Nuclear Science
2015

Handbook on Lead-bismuth Eutectic Alloy and Lead Properties, Materials Compatibility, Thermal-hydraulics and Technologies

2015 Edition

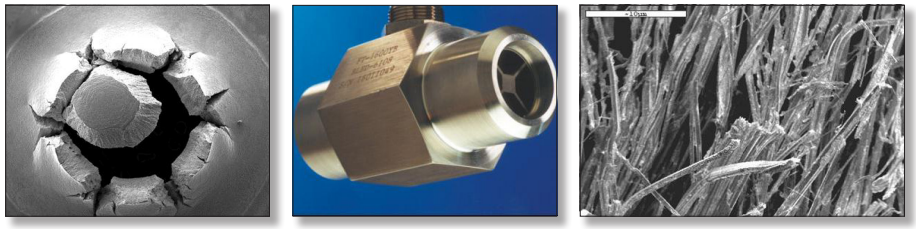

OECD
BETTER POLICIES FOR BETTER LIVES

NEA
NUCLEAR ENERGY AGENCY

Nuclear Science

Handbook on Lead-bismuth Eutectic Alloy and Lead Properties, Materials Compatibility, Thermal-hydraulics and Technologies

2015 Edition

© OECD 2015
NEA. No. 7268

NUCLEAR ENERGY AGENCY
ORGANISATION FOR ECONOMIC CO-OPERATION AND DEVELOPMENT

ORGANISATION FOR ECONOMIC CO-OPERATION AND DEVELOPMENT

The OECD is a unique forum where the governments of 34 democracies work together to address the economic, social and environmental challenges of globalisation. The OECD is also at the forefront of efforts to understand and to help governments respond to new developments and concerns, such as corporate governance, the information economy and the challenges of an ageing population. The Organisation provides a setting where governments can compare policy experiences, seek answers to common problems, identify good practice and work to co-ordinate domestic and international policies.

The OECD member countries are: Australia, Austria, Belgium, Canada, Chile, the Czech Republic, Denmark, Estonia, Finland, France, Germany, Greece, Hungary, Iceland, Ireland, Israel, Italy, Japan, Korea, Luxembourg, Mexico, the Netherlands, New Zealand, Norway, Poland, Portugal, the Slovak Republic, Slovenia, Spain, Sweden, Switzerland, Turkey, the United Kingdom and the United States. The European Commission takes part in the work of the OECD.

OECD Publishing disseminates widely the results of the Organisation's statistics gathering and research on economic, social and environmental issues, as well as the conventions, guidelines and standards agreed by its members.

This work is published on the responsibility of the Secretary-General of the OECD. The opinions expressed and arguments employed herein do not necessarily reflect the official views of the Organisation or of the governments of its member countries.

NUCLEAR ENERGY AGENCY

The OECD Nuclear Energy Agency (NEA) was established on 1 February 1958. Current NEA membership consists of 31 countries: Australia, Austria, Belgium, Canada, the Czech Republic, Denmark, Finland, France, Germany, Greece, Hungary, Iceland, Ireland, Italy, Japan, Korea, Luxembourg, Mexico, the Netherlands, Norway, Poland, Portugal, Russia, the Slovak Republic, Slovenia, Spain, Sweden, Switzerland, Turkey, the United Kingdom and the United States. The European Commission also takes part in the work of the Agency.

The mission of the NEA is:

- to assist its member countries in maintaining and further developing, through international co-operation, the scientific, technological and legal bases required for a safe, environmentally friendly and economical use of nuclear energy for peaceful purposes;
- to provide authoritative assessments and to forge common understandings on key issues, as input to government decisions on nuclear energy policy and to broader OECD policy analyses in areas such as energy and sustainable development.

Specific areas of competence of the NEA include the safety and regulation of nuclear activities, radioactive waste management, radiological protection, nuclear science, economic and technical analyses of the nuclear fuel cycle, nuclear law and liability, and public information.

The NEA Data Bank provides nuclear data and computer program services for participating countries. In these and related tasks, the NEA works in close collaboration with the International Atomic Energy Agency in Vienna, with which it has a Co-operation Agreement, as well as with other international organisations in the nuclear field.

This doument and any map included herein are without prejudice to the status of or sovereignty over any territory, to the delimitation of international frontiers and boundaries and to the name of any territory, city or area.

Corrigenda to OECD publications may be found online at: *www.oecd.org/publishing/corrigenda*.

© OECD 2015

You can copy, download or print OECD content for your own use, and you can include excerpts from OECD publications, databases and multimedia products in your own documents, presentations, blogs, websites and teaching materials, provided that suitable acknowledgment of the OECD as source and copyright owner is given. All requests for public or commercial use and translation rights should be submitted to *rights@oecd.org*. Requests for permission to photocopy portions of this material for public or commercial use shall be addressed directly to the Copyright Clearance Center (CCC) at *info@copyright.com* or the Centre français d'exploitation du droit de copie (CFC) *contact@cfcopies.com*.

Foreword

Prompted by several international projects dedicated to heavy liquid metal (HLM) nuclear systems designed for the transmutation of highly active nuclear waste, the Expert Group on Heavy Liquid Metal Technologies began its activities in 2003. The accelerator-driven system (ADS) was the reference system considered for this purpose, and several ADS concepts have been developed, for example, in Europe, Japan, Korea and the United States. The general layout of an ADS foresees three main components: i) the subcritical blanket loaded with minor actinide-bearing fuel and cooled with liquid lead-bismuth eutectic (LBE) or liquid lead (Pb); ii) an external neutron source made from a liquid LBE as a spallation target; and iii) a powerful proton accelerator. Several experimental campaigns on these key components were identified in a roadmap on the demonstration of ADS feasibility, with design, construction, operation and post-operation investigations of a neutron spallation target made of liquid LBE ensuing as an important task towards the demonstration of the ADS concept. The Megawatt pilot target experiment (MEGAPIE) was launched in this context to demonstrate the feasibility of a liquid, lead-bismuth (Pb-Bi) target for spallation facilities at a beam power level of 1 MW. MEGAPIE was supported by an international consortium composed of partners from Europe, Japan, Korea, the United States and the European Commission, demonstrating the transnational interest in this technology.

In addition to ADS development, other international projects continue to advance along other paths, including within the framework of the Generation IV International Forum (GIF), which has selected the lead-cooled fast reactor (LFR) as one of its six reference concepts; and through Russian projects to develop both the lead-cooled BREST and the LBE-cooled SVBR (Svintsovo-Vismutovyi Bystryi Reactor) concepts.

These activities and initiatives motivated the Expert Group on HLM Technologies to focus on the establishment of a common database in the form of a handbook so as to deliver a reference work for engineering design purposes. While the expert group was finalising the first version of the handbook, activities on HLM were expanding worldwide. For instance, in 2005, the European Commission supported project, EUROTRANS, was initiated. It gathered key European partners with significant ADS programmes and facilitated a collaboration framework with R&D programmes supported by the United States Department of Energy (US DOE) and at the time, the Japan Atomic Energy Agency Research Institute (now Japan Atomic Energy Agency). In parallel, international R&D projects on HLM technologies in support of the GIF LFR concept were also undertaken. The expert group thus perceived the necessity to edit, in a relatively short time span, a first version of the handbook in order to gather a set of relevant data for both ADS and LFR engineering design activities, but also to identify R&D gaps and needs as input towards future R&D programmes. At the time of the first edition's publication, it was evident that these newly initiated projects were producing highly relevant data worth including in a second edition of the handbook.

The second edition of the handbook was compiled and edited over a period of approximately seven years, and it includes new data that has helped in better understanding phenomena such as liquid metal embrittlement or turbulent heat transfer in a fuel bundle. In addition, new experimental data and updated and/or alternative explanations of phenomena such as post-irradiation examination of irradiated samples

The Expert Group on HLM Technologies hopes that this second edition of the *Handbook on Lead-bismuth Eutectic Alloy and Lead Properties, Materials Compatibility, Thermal-hydraulics and* Technologies will be considered as a reference in the field and act as a valuable tool for designers, researchers and all professional groups that have an interest in HLM technologies that are being actively pursued in several countries.

Acknowledgements

The 2015 edition of the *Handbook on Lead-bismuth Eutectic Alloy and Lead Properties, Materials Compatibility, Thermal-hydraulics and Technologies* was produced by members of the NEA Expert Group on Heavy Liquid Metal Technologies and by numerous contributors from related institutions (see Appendix 1), under the chairmanship of Dr Concetta Fazio from the Commission of the European Communities Joint Research Centre – Institute for Transuranium Elements.

The NEA would like to express its sincere gratitude to Dr Fazio for her devotion and excellent leadership, as well as to the chapter authors and contributors who dedicated their time and effort to the preparation of this second edition of the handbook.

Special thanks must also be conveyed to the peer reviewers (see Appendix 2).

Table of contents

1. Introduction 17

2. Thermophysical and electric properties of liquid lead, bismuth and lead-bismuth eutectic 27

2.1 Introduction 27
2.2 Pb-Bi system phase diagram 28
2.3 Normal melting point 31
2.3.1 Lead 32
2.3.2 Bismuth 32
2.3.3 LBE 35
2.4 Volume change at melting and solidification 36
2.5 Latent heat of melting at the normal melting point 40
2.5.1 Lead 40
2.5.2 Bismuth 41
2.5.3 LBE 42
2.6 Normal boiling point 43
2.6.1 Lead 43
2.6.2 Bismuth 44
2.6.3 LBE 46
2.7 Heat of vaporisation at the normal boiling point 46
2.7.1 Lead 47
2.7.2 Bismuth 48
2.7.3 LBE 49
2.8 Saturation vapour pressure 50
2.8.1 Lead 50
2.8.2 Bismuth 51
2.8.3 LBE 55
2.9 Critical point parameters 57
2.9.1 Lead 57
2.9.2 Bismuth 59
2.9.3 LBE 60
2.10 Surface tension 61
2.10.1 Lead 62
2.10.2 Bismuth 64
2.10.3 LBE 68
2.11 Density 70
2.11.1 Lead 70
2.11.2 Bismuth 73
2.11.3 LBE 75

2.12 Thermal expansion 78
2.13 Compressibility and sound velocity 79
2.13.1 *Lead* 80
2.13.2 *Bismuth* 83
2.13.3 *LBE* 86
2.13.4 *Bulk elastic modulus* 88
2.14 Heat capacity 89
2.14.1 *Lead* 89
2.14.2 *Bismuth* 93
2.14.3 *LBE* 96
2.14.4 *Enthalpy* 98
2.15 Equation of state 99
2.16 Viscosity 102
2.16.1 *Lead* 102
2.16.2 *Bismuth* 106
2.16.3 *LBE* 108
2.17 Electrical resistivity 111
2.17.1 *Lead* 111
2.17.2 *Bismuth* 114
2.17.3 *LBE* 116
2.18 Thermal conductivity and thermal diffusivity 118
2.18.1 *Lead* 119
2.18.2 *Bismuth* 122
2.18.3 *LBE* 125
2.18.4 *Thermal diffusivity* 128
2.19 Conclusions 128
References 131

3. Thermodynamic relationships and heavy liquid metal interaction with other coolants 143

3.1 Introduction 143
3.2 Enthalpies, entropies (solid and liquid state) – free energy and entropy of mixing 143
3.3 Chemical activities of Pb and Bi in Pb-Bi alloys 145
3.4 Purity requirements 147
3.5 Solubility data of metallic and non-metallic impurities in Pb, Bi and LBE 149
3.5.1 *Solubility data of some metallic elements in pure Pb, pure Bi and liquid eutectic Pb-Bi* 149
3.5.2 *Solubility data of oxygen in pure Pb, pure Bi and LBE* 155
3.5.3 *Oxygen/lead, bismuth, LBE interaction* 159
3.5.3.1 Reference states for oxygen activity in liquid metal 159
3.5.3.2 Relation between oxygen partial pressure and oxygen concentration 161
3.5.3.3 Phase diagrams Pb-O-Bi 163
3.6 Diffusivity 164
3.6.1 *Diffusivity data of some metallic elements* 164

3.6.2 *Oxygen diffusion coefficient* 167
3.7 Chemical interactions and ternary phase diagrams 169
3.8 Lead and LBE/water interaction 171
3.8.1 *Literature survey* 171
3.8.2 *Related risks* 173
3.8.3 *Numerical codes* 173
3.9 Lead or LBE and sodium interaction 174
3.10 LBE and Pb and organic compounds interaction 177
References 178
4. Chemistry control and monitoring systems 185
4.1 Introduction 185
4.2 Oxygen control in lead and LBE systems 186
4.2.1 *Upper oxygen limit for operational control* 186
4.2.2 *Lower limit of oxygen for operational control* 187
4.2.3 *Specifications for active oxygen control* 192
4.2.4 *Policy for a nuclear system* 195
4.2.5 *Oxygen control systems* 197
4.2.6 *The oxygen homogeneity issue* 200
4.3 Characterisation of impurities and requirements for control 201
4.3.1 *Impurity sources* 201
4.3.2 *Behaviour of impurities and requirements for purification* 204
4.3.3 *Active impurities* 207
4.3.4 *Production rate assessment* 208
4.3.5 *Consequences on operations* 209
4.4 Instrumentations for chemical monitoring 211
4.4.1 *Online electrochemical oxygen sensor* 211
4.4.1.1 Principle 212
4.4.1.2 Theory 215
4.4.1.3 Calibration 220
4.4.1.4 Characteristics of the oxygen sensors 222
4.4.1.5 Conclusions 225
4.4.2 *Development of sampling systems and analytical methods* 225
4.4.2.1 Dip sampler validation 226
4.4.2.2 Chemical analysis of lead-bismuth eutectic 227
4.4.2.3 Radioactive nuclides chemical analysis 229
4.4.2.4 Conclusions 230
4.5 Conclusions 230
References 232
5. Properties of irradiated lead-bismuth eutectic and lead 239
5.1 Introduction 239
5.1.1 *Chemical processes in a liquid metal facility* 240
5.1.2 *The chemical state of nuclear reaction products in a liquid metal target* 242
5.1.3 *Scope of this chapter* 242
5.2 Fundamental properties of binary and ternary systems with Pb, Bi and LBE 243

5.2.1 *Volatilisation of hazardous nuclides from liquid metals* 243
5.2.1.1 Equilibrium evaporation 245
5.2.1.2 Non-equilibrium evaporation 302
5.2.2 *Gas phase purification* 317
5.2.2.1 Mercury removal 318
5.2.2.2 Polonium removal 324
5.2.3 *Extraction of polonium from LBE* 324
5.2.4 *Extraction of other nuclear products from Pb, Bi and LBE* 327
5.2.5 *Removal of polonium from contaminated surfaces* 329
5.2.6 *Solubility of impurities in liquid lead, bismuth and LBE* 329
5.2.6.1 Results of solubility calculations for the elements of Group 1 to 16 in liquid lead, bismuth and LBE 330
5.2.6.2 Conclusions from the results of solubility calculations for nuclear systems 333
5.2.7 *Polonium migration and surface enrichment in solidified LBE* 333
5.2.7.1 Kinetic studies on the surface enrichment of polonium in solidified LBE 334
5.2.7.2 Solid state characterisation of LBE samples 337
5.2.8 *Evaluation of thermochemical data for binary systems by means of the semi-empirical Miedema model* 339
5.2.9 *Summary and conclusions on the review of simple model systems* 342
5.3 Experience from medium- and large-scale experiments 343
5.3.1 *Measurement of gas and volatile element production yields in a proton-irradiated molten lead-bismuth target in the ISOLDE facility* 343
5.3.1.1 The ISOLDE facility and target 344
5.3.1.2 Description of the experiment 345
5.3.1.3 The release process 346
5.3.1.4 Calculation methods 347
5.3.1.5 Results 347
5.3.1.6 Summary 353
5.3.2 *Distribution of radionuclides in the proton-irradiated LBE target from ISOLDE* 353
5.3.3 *Operational experiences from the MEGAPIE project* 358
5.3.3.1 Gas production in the MEGAPIE spallation target 358
5.3.3.2 Gas and volatile measurements 359
5.3.3.3 Gas and volatile production calculations 362
5.3.3.4 Gas and volatile release parameters estimation 364
5.3.3.5 Hydrogen and helium production 369
5.3.3.6 Conclusions of the gas production in the MEGAPIE target 371
5.3.4 *Estimation of the release of volatiles in accident scenarios for MEGAPIE licensing* 371
5.3.4.1 The reference accident case 371
5.3.4.2 Description of the source terms 371
5.3.4.3 Activity in the gas phase of the expansion volume 372
5.3.4.4 Activity released from spilled LBE 374

5.3.4.5 Activity released from the thin film of LBE adhering to the walls of the target 377
5.3.5 *LiSoR irradiation* 380
5.3.6 *Experience from accidents on Soviet nuclear-powered submarines* 381
5.3.7 *Summary and conclusions on the experience from medium- and large-scale experiments* 382
References 384
5.4 Appendix 398
5.4.1 *Thermodynamic properties of pure polonium (extrapolation results)* 398
5.4.2 *Thermodynamic data of polonium compounds (extrapolation results)* 400
5.4.3 *Results of solubility calculations* 407
5.4.4 *The Miedema model* 411

6. Compatibility of structural materials with lead-bismuth eutectic and lead: Standardisation of data, corrosion mechanism and rate 431

6.1 Introduction 431
6.2 Fundamentals 432
6.2.1 *Dissolution* 433
6.2.2 *Oxidation* 435
6.2.3 *Erosion corrosion* 440
6.2.4 *Fretting corrosion* 440
6.3 Corrosion tests 442
6.3.1 *Martensitic/ferritic steels* 442
6.3.2 *Austenitic steels* 445
6.3.3 *Results of experiments carried out under special conditions* 450
6.3.3.1 Influence of surface finishing and welds on the corrosion behaviour 450
6.3.3.2 Results of experiments with changing temperature and oxygen concentration 451
6.4 Oxidation-corrosion interaction model 451
6.4.1 *Modelling of long-term oxidation behaviour* 451
6.4.2 *Mass balance code for non-isothermal systems* 452
6.4.3 *Mechanistic modelling of dissolution rate and oxide growth* 453
6.5 Tables and figures of selected experimental results 455
6.6 Conclusions 469
6.7 Recommendations on corrosion test procedures (standardisation) 470
6.7.1 *Pre-test preparation* 470
6.7.1.1 Liquid metal: LBE and Pb 470
6.7.1.2 Materials 470
6.7.2 *Test conditions* 471
6.7.2.1 Static (no flow) tests 471
6.7.2.2 Dynamic tests 471
6.7.3 *Post-test analysis* 472
6.8 Tables 475
References 478

7. Effect of lead-bismuth eutectic and lead on mechanical properties of martensitic and austenitic steels 487

7.1 Introduction 487

7.2 The different manifestations of liquid metals on mechanical properties 490

7.2.1 Wetting: From ideal to real metallic systems 490

7.2.2 Definition and criteria of occurrence of LME 494

7.2.3 Liquid-metal-assisted damage (LMAD) 496

7.2.4 Environment-assisted cracking 496

7.3 Experimental results that point out LME effects: Case of T91 in contact with LBE or lead 497

7.4 Tensile behaviour of austenitic and ferritic/martensitic steels in contact with lead and LBE 499

7.4.1 Description of the test 499

7.4.2 Tensile behaviour of T91 in LBE 499

7.4.2.1 Tensile behaviour of T91 steel in its standard heat treatment in lead and LBE 499

7.4.2.2 Effect of heat treatment and effect of presence of flaws on the tensile behaviour of T91 steel in LBE 501

7.4.3 Effect of pre-exposure in LBE on tensile behaviour of T91 503

7.4.4 Role of oxide layer 505

7.4.5 Role of traces of impurities 508

7.4.6 Mechanical behaviour of welds in LBE 508

7.4.6.1 Description of the weld procedure 508

7.4.6.2 Mechanical response of the weld in LBE 510

7.4.7 Mechanical behaviour of silicon-enriched steels in LBE 512

7.4.8 Main requirements to prevent LME effects 517

7.5 Small punch test 517

7.5.1 Description of the test 517

7.5.2 T91 response in saturated oxygen LBE 519

7.5.2.1 Behaviour of T91 steel: Role of heat treatment 519

7.5.2.2 Behaviour of T91 steel: Role of oxide layer 521

7.5.3 316L stainless steel response in saturated oxygen LBE 523

7.5.4 Effect of temperature and of variable strain rate tests in low oxygen LBE 523

7.5.5 316L/T91 EB weld joint response in saturated oxygen LBE 525

7.6 Fracture toughness 528

7.6.1 Definition 528

7.6.2 Available data 529

7.6.3 Fracture toughness of T91 martensitic steel in LBE at 200 °C and 300 °C 530

7.6.3.1 Toughness assessment by DCT specimen 530

7.6.3.2 Toughness assessment by CCT specimen 531

7.6.4 Effect of pre-exposure 533

7.6.5 Effect of heat treatment on T91 534

7.6.6 Fracture toughness of 316L austenitic steel in LBE at 200°C and 300°C 535

7.7 Creep 535

7.7.1 Definition 535

7.7.2 *Liquid-metal-accelerated creep (LMAC)* 536
7.7.3 *Creep properties of martensitic and austenitic stainless steels in air or liquid metals other than lead or LBE* 536
7.7.4 *Creep of austenitic and ferritic/martensitic steels in lead or LBE* 537
7.7.4.1 Qualitative investigation of creep behaviour of T91 steel in contact with lead 538
7.7.4.2 Quantitative assessment of creep behaviour of T91 steel in contact with LBE 539
7.7.4.3 Role of GESA treatment on creep behaviour of T91 steel in contact with LBE 540
7.7.4.4 Quantitative assessment of creep behaviour of T91 steel in contact with lead 540
7.7.5 *Creep–to-rupture of P92 steel in lead* 541
7.8 Fatigue 543
7.8.1 *Definition* 543
7.8.2 *Low cycle fatigue behaviour of ferritic/martensitic steels in contact with oxygen-saturated LBE* 544
7.8.2.1 Role of LBE on cyclic accommodation 545
7.8.2.2 Role of LBE on fatigue resistance 545
7.8.2.3 Role of LBE on fatigue crack density 546
7.8.3 *Influence of hold time on fatigue behaviour of T91 in LBE* 546
7.8.4 *Influence of preliminary exposure to LBE on fatigue behaviour of T91* 548
7.8.5 *Low cycle fatigue behaviour of T91 steel in contact with low oxygen LBE* 549
7.8.6 *Low cycle fatigue resistance of 316L austenitic stainless steel in saturated oxygen LBE* 550
7.8.7 *Role of coating on fatigue crack initiation resistance of T91 steel* 550
7.8.8 *Influence of LBE on (long) fatigue crack growth of T91 and MANET II* 552
7.8.8.1 Qualitative analysis of the effect of LBE on fatigue crack propagation 552
7.8.8.2 Quantitative analysis of the effect of LBE on fatigue crack propagation 552
7.8.8.3 Influence of pre-exposure on fatigue crack propagation 554
7.9 Recommendations for testing procedures 555
7.9.1 *ASTM standards useful for mechanical tests in LBE* 555
7.9.2 *Adaptation of experimental installations for HLMs* 558
7.9.3 *Recommendations for testing procedures* 558
7.10 Conclusions 560
References 562

8. Irradiation effects on compatibility of structural materials with lead-bismuth eutectic 571
8.1 Introduction 571
8.2 LiSoR: Irradiation of T91 steel with 72 MeV protons in flowing LBE 571
8.2.1 *Irradiation experiments* 572
8.2.2 *Surface analyses* 574
8.2.3 *Tensile tests* 578
8.2.4 *Bend tests on LiSoR-6 samples* 579

8.2.4.1 The FeCrAlY coating....579
8.3 Irradiation with fission neutrons....583
8.3.1 Material and irradiation conditions....583
8.3.2 Testing conditions....585
8.3.3 Effect of irradiation and LBE on austenitic steels 316L and 15-15Ti....586
8.3.4 Effect of irradiation and LBE on FM steels T91, EM10 and HT9....588
8.3.4.1 T91 steel....588
8.3.4.2 EM10 steel....590
8.3.4.3 HT9 steel....591
8.3.5 Corrosion specimens irradiated in BOR60....592
8.4 Irradiation with proton and neutron spectrum in SINQ targets at PSI....592
8.4.1 Stressed capsules of EC316LN and 9Cr2WVTa irradiated in LBE....593
8.4.1.1 Materials and specimens....593
8.4.1.2 The EC316LN capsule....593
8.4.1.3 The 9Cr2WVTa capsule....594
8.4.2 SSRT tests on irradiated FM steels in LBE....596
8.4.2.1 Materials and specimens....596
8.4.2.2 SSRT tests....597
8.4.3 LBE effect on fracture toughness of irradiated T91 steel....600
8.5 MEGAPIE experiment....602
8.5.1 Target structure and irradiation....603
8.5.2 Visual inspection....605
8.5.3 Ultrasonic measurement....606
8.5.4 Analysis of LBE corrosion and erosion effects....607
8.5.4.1 Analysis of the T91 calotte....607
8.5.4.2 Analysis of the flow guide tube (FGT)....609
8.5.5 Mechanical testing....610
8.6 Conclusions....611
References....613

9. Corrosion protection in lead and lead-bismuth eutectic at elevated temperatures....617

9.1 Introduction....617
9.2 Methods of surface protection....618
9.2.1 Alloying with stable oxide formers....618
9.2.1.1 Surface alloying by the GESA process....619
9.2.1.2 Surface alloying by diffusion processes....621
9.2.2 Corrosion-resistant coatings....623
9.2.2.1 Al- or Si-containing coatings....623
9.2.2.2 Coatings with refractory metals....624
9.2.2.3 Oxide-, carbide- and nitride-based coatings....624
9.2.3 Corrosion inhibitors in LBE....625
9.3 Corrosion resistance of alloyed surfaces and coatings....626
9.3.1 Alloyed surfaces....626
9.3.2 Coatings....631

9.3.3 *Bulk alloys* 633
9.4 Mechanical properties 638
9.5 Concluding remarks 641
References 643
10. Low Prandtl number thermal-hydraulics 647
10.1 Background 648
10.1.1 The governing equations 648
10.1.1.1 Mass balance (continuity equation) 649
10.1.1.2 Momentum balance (Navier-Stokes equations) 649
10.1.1.3 Energy balance 650
10.1.1.4 Boundary conditions 650
10.1.2 Flow scenarios commonly found in HLM systems 651
10.1.2.1 Geometry: Wall-confined, free-surface or two-phase flows ..651
10.1.2.2 Steady-state duct flows: Fully developed or developing 651
10.1.2.3 Laminar or turbulent 652
10.1.2.4 Forced, mixed or natural convection 652
10.1.3 Specific features of liquid metals 653
10.1.3.1 Physical properties 653
10.1.3.2 Experimental conditions and extrapolation of results 655
10.2 Laminar flow and heat transfer in ducts 657
10.2.1 Fully developed flow in circular ducts 657
10.2.2 Developing flows in circular ducts 658
10.2.2.1 Thermally developing flow 659
10.2.2.2 Hydrodynamically developing flow 662
10.2.2.3 Simultaneously developing flow 663
10.2.3 Additional effects: Other geometries and axial thermal conduction 664
10.2.3.1 Non-circular geometries 664
10.2.3.2 Axial thermal conduction 665
10.3 Turbulent flow modelling 665
10.3.1 Reynolds equations for turbulent flows 667
10.3.2 Laws of the wall: Universal profiles in the boundary layers 668
10.3.3 Analytical Nusselt number correlations for turbulent parallel flow 669
10.3.4 Closure methods for the turbulent transport of momentum 671
10.3.4.1 Algebraic models (zero or one-half equations) 671
10.3.4.2 One-equation models 671
10.3.4.3 Two-equation models 672
10.3.4.4 Reynolds stress models (RSM) 673
10.3.5 Closure methods for the turbulent heat flux 673
10.3.5.1 Experimental observations 674
10.3.5.2 Semi-empirical methods of zero and first order 675
10.3.5.3 Turbulent Prandtl number from analytical solutions 677
10.3.5.4 Modelling by transport equations at different levels 679
10.3.6 Pool thermal-hydraulics 681
10.3.7 Direct numerical simulation (DNS) 682

10.4 Engineering correlations, models and experiences for liquid-metal flows 683
10.4.1 *Circular ducts* 683
10.4.1.1 Survey of experimental data in the open literature 684
10.4.1.2 Evaluation of analytical, empirical and semi-empirical correlations 687
10.4.2 *Flat channels (flow between parallel plates)* 693
10.4.3 *Concentric annulus* 695
10.4.4 *Rod bundles* 697
10.4.4.1 Bare rod bundles 698
10.4.4.2 Temperature profiles and the effects of spacers 701
10.4.5 *Some comments about the turbulent developing region* 703
10.4.5.1 Round tube 703
10.4.5.2 Flat channels 703
10.4.5.3 Concentric annulus 704
10.4.5.4 Rod bundles 705
10.4.6 *Buoyancy effects* 705
10.4.7 *Investigations on additional flow scenarios found in HLM systems* 707
10.4.7.1 Beam-entrance windows in spallation targets, e.g. for ADS 707
10.4.7.2 Free-surface and two-phase flows 709
10.5 Summary and conclusions 710
References 712
11. Instrumentation 731
11.1 Background of the measurement technique development 731
11.2 Flow meters 732
11.2.1 *Electromagnetic flow meters* 732
11.2.1.1 DC electromagnetic flow meters 732
11.2.1.2 Lorentz force velocimetry 736
11.2.1.3 AC electromagnetic flow meters 737
11.2.2 *Momentum-based flow meters* 747
11.2.2.1 Turbine flow meter 747
11.2.2.2 Coriolis flow meters 749
11.2.3 *Pressure- and counter-based flow meters* 750
11.2.3.1 Von Kármán vortex street flow meter 750
11.2.3.2 Obstacle flow meters, nozzle and orifice flow meters 751
11.2.4 *Ultrasound transit time method (UTT)* 754
11.3 Pressure sensors 757
11.3.1 *Types of pressure gauges and operation experience* 757
11.3.2 *Pressure correction in fully developed turbulent pipe flow* 758
11.4 Local velocity measurements 760
11.4.1 *Ultrasound Doppler velocimetry* 760
11.4.2 *Permanent magnet probes (PMP)* 764
11.4.3 *Electric-potential difference probes (EPDP)* 767
11.4.4 *Mechanical-based techniques* 767
11.4.4.1 Reaction probes (RP) 767

11.4.4.2 Fibre mechanics systems (FMS) 769
11.4.5 *Hot wire anemometry (HWA)* 771
11.4.6 *Transition time methods* 773
11.4.6.1 Temperature pulse method 773
11.4.6.2 Tracer studies 774
11.4.6.3 Dissolution and melting studies 775
11.4.7 *Neutron radiography* 776
11.4.8 *Pitot and Prandtl tubes* 776
11.4.8.1 General features and application 776
11.4.8.2 Viscous corrections for Pitot tubes 778
11.4.8.3 Turbulence correction for Pitot tubes 778
11.4.8.4 Velocity gradient correction for Pitot tubes 779
11.4.8.5 Displacement correction for Pitot tubes 780
11.4.8.6 Wall correction of Pitot tubes 780
11.4.8.7 Comments on displacement and corrections 781
11.4.9 *Flow field mapping* 781
11.4.9.1 Contactless inductive flow tomography (CIFT) 781
11.4.9.2 Radioscopic visualisation 784
11.5 Two-phase flow measurement 786
11.5.1 *Electromagnetic sensors* 787
11.5.1.1 DC permanent magnet void fraction sensors (PMVS) 787
11.5.1.2 AC electromagnetic void fraction sensors (EMVS) 788
11.5.2 *Local void determination* 790
11.5.2.1 Resistive or conductance probes 790
11.5.3 *Ultrasound Doppler velocimetry (UDV) for two-phase flows* 795
11.5.3.1 Further probe principles 797
11.5.4 *Tomographic flow mapping for multiphase flows* 798
11.5.4.1 Electromagnetic inductance tomography 798
11.5.4.2 X-ray, γ-ray and neutron radiography (NR) 798
11.6 Temperature measurement 809
11.6.1 *Thermocouples* 809
11.6.2 *Heat-emitting temperature sensing surfaces (HETSS)* 815
11.7 Level meters 817
11.7.1 *Direct contact sensors* 817
11.7.2 *Non-intrusive level sensors* 819
11.7.2.1 Electromagnetic level sensors 819
11.7.2.2 Light detection and ranging (LIDAR) 820
11.8 Free surface measurements 820
11.8.1 *Optical methods* 821
11.8.2 *Ultrasonic methods* 823
11.9 Summary and final comments 824
References 825
12. Existing heavy liquid metal facilities for experimental applications 841
12.1 Introduction 841

12.2 Technological facilities and their applications 842
12.3 Materials testing facilities and their applications 852
12.4 Thermal-hydraulics facilities and their applications 881

13. Safety guidelines 905

13.1 Effects of lead on human health and environment 906
13.2 Rules and regulations 909
13.3 Common safety controls and practices 913
13.4 Safe operations in HLM R&D 914
References 919

14. Perspectives and R&D priorities of heavy liquid metal coolant technologies 921

14.1 Introduction 921
14.2 Technology gaps, R&D needs and priorities for HLM systems operating at temperatures below 550°C 922
14.2.1 HLM thermal-physical properties 923
14.2.2 HLM chemical properties 923
14.2.3 Materials 923
14.2.4 Technologies 924
14.2.5 Thermal-hydraulics 925
14.2.6 Safety-related R&D 926

15. Guidelines for thermo-hydraulics modelling of pressure drop of the heavy liquid metal-cooled loops 927

15.1 Introduction 927
15.2 Description of the LACANES benchmarking procedure 927
15.2.1 Methods of LACANES benchmarking 927
15.2.2 Description of LBE thermo-hydraulic test loop HELIOS 928
15.3 Pressure loss correlations used in design and analysis models 930
15.3.1 Design and analysis codes used in benchmarking 930
15.3.2 Pipe wall friction loss correlations 931
15.3.3 Orifice 932
15.3.4 Spacers 933
15.3.5 Sudden area change 935
15.3.6 CFD modelling and comparison with correlations for complex components 936
15.4 Best practice guidelines 938
15.5 Summary and recommendations for future work 939
References 940

Appendix 1. List of contributors 943

Appendix 2. Peer reviewers 947

1. Introduction*

The main changes in this chapter since the 2007 edition of the handbook concern the sections related to the evolution of national and international programmes and, where available, new references have been added. An important step forward for heavy liquid metal (HLM) nuclear systems has been observed for example in Europe, the Russian Federation and in the framework of the Generation IV International Forum (GIF). Europe has defined its Strategic Research and Innovation Agenda (SRIA), where both lead-cooled fast reactors and lead-bismuth-cooled experimental reactors are being considered. Moreover, the irradiation of the MEGAPIE HLM neutron spallation target was successfully completed and postirradiation examination (PIE) activities have begun. In Russia, the small modular lead-bismuth-cooled SVBR is presently in the licensing stage.

Liquid metals have been studied since the early development of fission energy as reactor core coolants for fast reactors, fusion energy blanket applications and, more recently, for both accelerator-driven systems (ADS) proposed for high-level radioactive waste transmutation and for generation IV fast reactors. Moreover, heavy liquid metals are being proposed as target materials for high-power neutron spallation sources.

Accelerator-driven systems are nuclear fission reactors with a subcritical core (i.e. $k_{eff} < 1$). Therefore, to operate an ADS, an external neutron source is needed for a stable neutron economy in the core. One possible external neutron source is produced by a proton accelerator impinging on a spallation target (a heavy liquid metal is often considered). The protons hitting the heavy liquid metal generate neutrons which sustain the chain reaction in the subcritical core. A schematic view of an ADS is provided in Figure 1.1.

Figure 1.1: Schematic diagram of an ADS

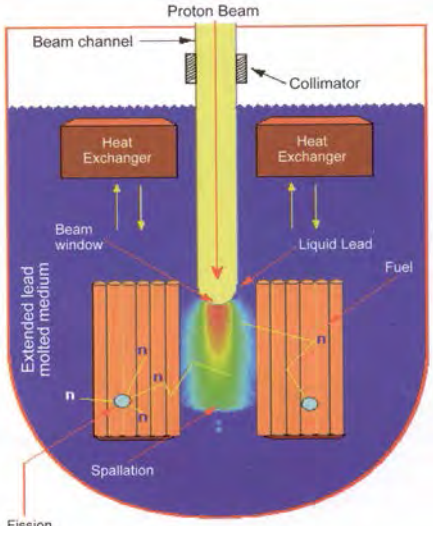

Source: ETWG (2001).

* Chapter lead: C. Fazio.

Neutron spallation targets are also being developed to provide a neutron source for other applications. For example, the MEGAPIE spallation neutron target (a schematic view of the MEGAPIE target is shown in Figure 1.2), which has been successfully tested at the SINQ facility of the Paul Scherrer Institute in Switzerland, has been designed and constructed in the framework of ADS development. The objective was to demonstrate the operability of such a liquid metal target while providing a neutron source for the typical applications at SINQ. Material investigation with neutrons has been achieved with a high degree of success (Fazio, 2008; Zanini, 2011; Wohlmuther, 2012).

Figure 1.2: Schematic diagram of the MEGAPIE target

1 – T91 window, 2 – lower target enclosure ($AlMg_3$), 3 – main flow guide tube, 4 – moderator, 5 – heater, 6 – bypass flow guide tube, 7 – LBE, 8 – central rod, 9 – bypass pump, 10 – main pump, 11 – heat exchanger, 12 – expansion volume, 13 – shielding, 14 – insulation gas (Ar), 15 – LBE leak detector

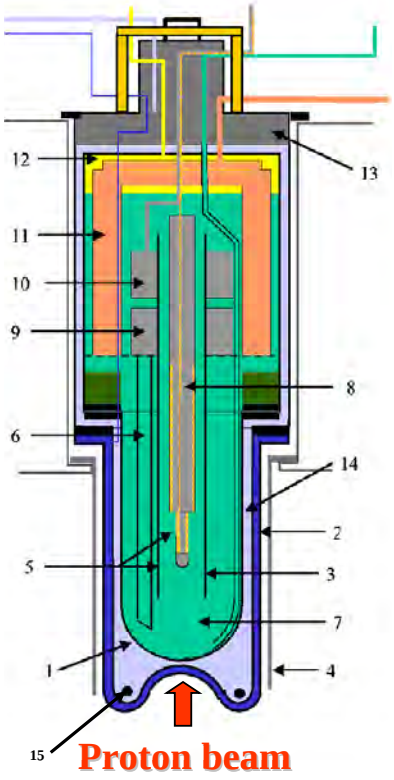

Source: FZK (2003).

Fast reactors are fission reactors where the neutron spectrum in the core is close to the fission neutron spectrum, since the neutrons are not thermalised as in a conventional light-water-cooled reactor. The fast reactor coolant is appropriately chosen in order to provide an effective heat transfer, without a significant thermalisation of the neutron spectrum. In order to achieve this goal, liquid metals (Na or Pb, Pb-Bi) or gas can be (or have been) used. A schematic view of a Pb-cooled fast reactor is provided in Figure 1.3.

HLM such as lead (Pb) or lead-bismuth eutectic (LBE) were proposed and investigated as coolants for fast reactors as early as the 1950s (e.g. in the United States). Sodium became the preferred choice in the 1960s, due to a higher power density achievable with this coolant, which resulted in lower doubling times, an important objective at that time (IAEA, 2002). However, LBE was chosen as the coolant for a number of alpha-class

submarine reactors in the former Soviet Union, which led to very extensive research and development (R&D) on coolant technology and materials, with particular emphasis on the chemistry control of the liquid metal to avoid plugging due to slag formation and to enhance corrosion resistance of the steels specifically developed for such services.

Figure 1.3: Schematic of Pb-cooled fast reactor

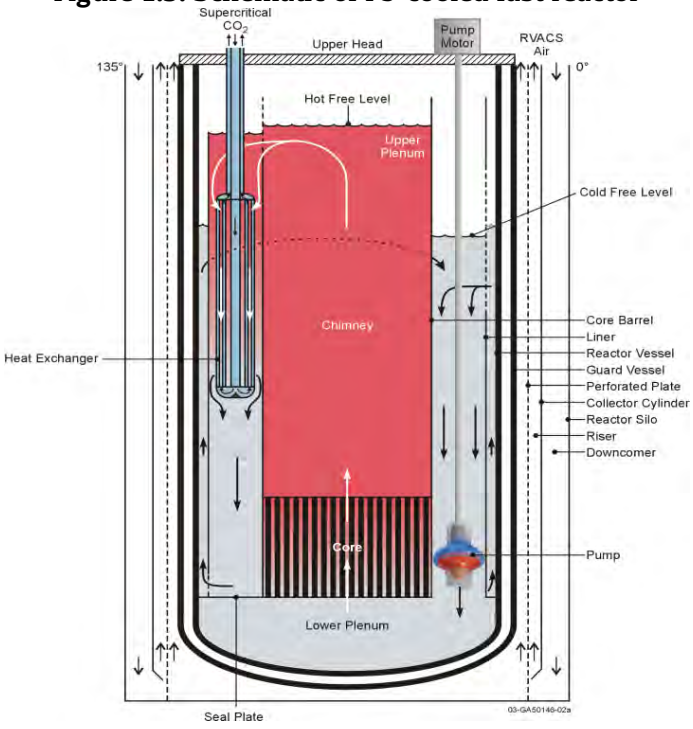

Source: Hejzlar (2004).

More recently, there has been renewed interest in Russia in lead and LBE coolants for civilian fast reactors (Kirillov, 1998, 2000, 2003; IAEA, 2012; Handbook, 2005). The lead-cooled BREST (Russian acronym for Pb-cooled fast reactor) (Filin, 2003) concept developed since the early 1990s is the most widely known, with the LBE-cooled SVBR (Russian acronym for lead-bismuth fast reactor) concept (Stepanov, 1998; IAEA, 2012) competing for attention. Their features and the associated technologies inspired several projects in the emerging field of ADS, and in particular lead cooling was associated, in the mid-1990s, with the proposal for an energy amplifier project together with LBE as a spallation target coolant and material. Subsequent development of ADS in Europe, Japan, Korea, and the United States, has adopted a heavy liquid metal (most often LBE) as the coolant for the subcritical core and as coolant and material for the spallation target which provides the external neutron source.

At the Korea Atomic Energy Research Institute (KAERI) and Seoul National University (SNU) in Korea, both ADS and LBE-cooled fast reactors (LFR) systems have been considered to explore proliferation-resistant and safe transmutation technology. KAERI's ADS, the Hybrid Power Extraction Reactor (HYPER) was designed to transmute TRU and some fission products such as ^{129}I and ^{99}Tc. HYPER uses Pb-Bi as both the coolant and target material. At SNU, a Pb-Bi-cooled transmutation reactor, the Proliferation-Resistant, Environment-Friendly, Accident-Tolerant, Continual and Economical Reactor (PEACER) was studied.

Research in the field of LBE technology at SCK•CEN (Belgium) since 1997 has been related to the Multi-Purpose Hybrid Research Reactor for High-Tech Applications

(MYRRHA) project and is aimed at the development of a research reactor driven by an accelerator, where LBE is used as a spallation target and coolant. Moreover, the European Programme that is defined within the Sustainable Nuclear Energy Technology Platform (SNETP) has launched the industrial initiative ESNII (2010), where, along with the MYRRHA system, a lead-cooled fast reactor system is also considered. The developments of both systems are supported through European Commission funded projects in the fields of design, safety, technology and materials.

In Japan, both ADS and LFR systems using LBE were studied. At the Japan Atomic Energy Agency (JAEA), an ADS with the thermal power of 800 MW was designed, where 250 kg of minor actinides and some long-lived fission products (LLFP) can be transmuted annually. R&D has been conducted on ADS using LBE as a spallation target and a coolant, and research using J-PARC was planned as well. At present, Japan is revising its overall R&D programme. The LFR systems using LBE as a coolant have been studied both at Tokyo Institute of Technology (TIT) and the Japan Nuclear Cycle Development Institute (JNC) separately. One of the LFR systems studied at TIT is designated as the Pb-Bi-cooled direct contact water fast reactor (PBWFR).

Finally, in the framework of the Generation IV International Forum (GIF), a class of Pb-LBE-cooled fast reactors (LFR) has been chosen as one of six system concepts for further development. Originally, a host of new missions were proposed for LFR, made possible by the properties of Pb-LBE, including hydrogen production, nuclear waste transmutation, and small modular reactors with long-life cores for supplying electricity and heat in remote areas and/or developing economies. In this context, a multi-year project at the Idaho National Laboratory and the Massachusetts Institute of Technology investigated medium power lead-alloy-cooled systems with the aim of producing low-cost energy and, at the same time, of burning actinides (Todreas, 2004). More recently a work presented in the context of GIF (Alemberti, 2013) has highlighted following current development directions:

- the European lead-cooled fast reactor (ELFR) for the large, central station plant (600 MWe);
- the BREST-OD-300 (300 MWe) for the medium-sized plant;
- the Small Secure Transportable Autonomous Reactor (SSTAR – 20 MWe) for the small system.

In the area of fusion technology programmes, the eutectic alloy Pb-17Li has been extensively studied as a breeder and as a coolant. A wide range of activities have been conducted in order to characterise materials and develop appropriate technologies (Kleykamp, 2002).

The selection criteria for the use of liquid metals as heat-transfer media in a nuclear environment include the following:

- Neutronics, related to the fast spectrum necessary for breeding, fuel conversion and actinide transmutation in the next generation of fast reactors and ADS concepts. In this case the coolant should have:
  - small (fast) capture cross-section (for small parasitic loss of neutrons);
  - high scattering cross-section (for small leakage of neutrons from the core);
  - small energy loss per collision (for small spectrum softening [moderating] effect);
  - high boiling temperature (for prevention of reactivity effects from boiling-related coolant voiding).
- Materials:

  - acceptable corrosion and mechanical degradation of structural and containment materials, and lifetime of equipment;
  - high stability of the liquid metal (e.g. limited chemical reactions with secondary coolants and air or formation of spallation products).
- Thermal-hydraulics:
  - moderate power requirement for circulating the liquid metal;
  - high heat transfer coefficient and small size of heat exchanger.
- Safety:
  - controllable chemical and radioactive hazards;
  - simple and reliable safety measures and systems.
- Economics.

Based on these factors and on the results presented in Table 1.1, it can be concluded that heavy liquid metals are well suited for fast reactor cores (see for example Todreas [2004]). Indeed, the use of heavy liquid metals (e.g. Pb-LBE) allows the achievement of a harder neutron spectrum, which results in better neutron economy (essential for burning actinides). Other favourable features of LBE use in nuclear systems are related to LBE's high boiling temperature and low melting temperature. The high boiling temperature is an important safety feature, essentially eliminating pressurisation and boiling concerns while enhancing the inherent safety of reactor cores. Higher allowable operating temperatures also improve the efficiency and feasibility of other energy products. The relatively low melting point facilitates use at low temperatures with reduced risk of uncontrolled freezing. High density and a wider range of possible operating temperatures offer increased design space for passive safety. A comprehensive comparative assessment of thermo-physical and thermo-hydraulic characteristics of lead, lead-bismuth eutectic alloy and sodium is also given in IAEA-TECDOC-1289 (2002).

Table 1.1: Basic characteristics of reactor coolants

Coolant	Atomic mass (g/mol)	Relative moderating power	Neutron absorption cross-section (1 MeV) (mbarn)	Neutron scattering cross-sections (barn)	Melting point (°C)	Boiling point (°C)	Chemical reactivity (with air and water)
Pb	207	1	6.001	6.4	327	1 737	Inert
LBE	208	0.82	1.492	6.9	125	1 670	Inert
Na	23	1.80	0.230	3.2	98	883	Highly reactive
H_2O	18	421	0.1056	3.5	0	100	Inert
D_2O	20	49	0.0002115	2.6	0	100	Inert
He	2	0.27	0.007953	3.7	–	-269	Inert

Source: Todreas (2004).

Other potentially favourable features of HLM are: lower reactivity associated with hypothetical voiding of the coolant; better shielding against gamma rays and energetic neutrons; high solubility of the actinides in the coolant, which could help to minimise the potential for re-criticality events upon core melting, and no energetic reaction with air and water, thereby eliminating the possibility of fire. One drawback associated with the use of liquid metal coolants is the potential complexity of in-service inspection and repair. Methods have been developed for under-sodium viewing (Young-Sang, 2013).

With respect to spallation neutron sources, there is a general consensus that above 1 MW of beam power, solid targets are hardly feasible from a heat removal point of view. Therefore, liquid metal targets are the best choice (see e.g. Bauer, 2001); among the liquid

metals, lead-alloy-based liquid metal targets are preferred if high operating temperatures are required. Properties that make heavy liquid metals ideal as spallation materials for neutron sources are listed in Table 1.2.

Table 1.2: Some relevant properties of possible liquid metal target candidate materials

Coolant	Composition (at %)	Density at 20°C (g/cm^3)	Density liquid (g/cm^3)	Linear coefficient of thermal expansion 10^{-5}/K (solid)	Linear coefficient of thermal expansion 10^{-5}/K (400°C)	Volume change upon solidification (%)	Specific heat (J/gK)	Thermal neutron absorption (barn)
Pb	Elem.	11.35	10.7	2.91	4	3.32	0.14	0.17
Bi	Elem.	9.75	10.07	1.75	–	-3.35	0.15	0.004
Pb-Mg eutectic	Pb 97.5% Mg 2.5%		10.6	–	–	0	0.15	0.17
Pb-Bi eutectic	Pb 45% Bi 55%	10.5	10.5			0	0.15	0.11
Hg	Elem.		13.55		6.1		0.12	389

Source: Bauer (2001).

The emerging worldwide interest in the application of HLM coolants has led to many R&D activities in the fields of materials, thermal-hydraulics, physical chemistry, among others. When the first edition of this handbook was published, it was clear and perceived as urgent that a HLM handbook would be needed for designers of HLM systems and for researchers in this field. Such a handbook should be a comprehensive compilation of all relevant properties, material test results, primary monitoring and control techniques, and instrumentation. Just as important, the handbook should highlight state of the art in research methodology and R&D resources (test facilities), and suggest a commonly accepted reporting and analysis protocol for systematic advancement of the scientific understanding and technological applications of HLM.

Several liquid metal handbooks have been issued since the 1950s, with the data available at the time. However, this data was limited due to restrictions associated with strategic national programmes. Although it has been reported that Russia has a manual or database for designers, it is not publicly available. The United States Advanced Accelerator Application (AAA) programme included in its materials handbook a brief chapter on this topic. However, none of these can fulfil the demanding needs of today's vibrant and diverse international research community.

In this context, the Nuclear Energy Agency (NEA), in the framework of the former Working Party on Partitioning and Transmutation (WPPT), now the Working Party on Scientific Issues of the Fuel Cycle (WPFC), launched the HLM coolant handbook project. The original plans to include in its scope the relatively more mature LBE coolant technology and materials has been expanded to include Pb for higher temperature and high-performance next generation of nuclear systems. The higher availability of basic property data for Pb can serve as a reference, and in some cases, serve as proxy for relatively scarce LBE property data. Conversely, the higher availability of LBE test data and facilities can benefit R&D for Pb. It is also envisaged that this handbook will be an evolving and working document of continued R&D efforts around the world in the next several years, with increasing utility for designers. Indeed, the expert group had decided to issue this new edition of the HLM handbook in order to include new and relevant results that have been published in recent years.

The structure of this handbook is as follows: four chapters are dedicated to HLM properties; the next four chapters cover materials and testing issues; and the subsequent two chapters summarise key aspects of thermal-hydraulics and system technologies. In the last three chapters, other issues such as existing test facilities, safety guidelines, open issues and perspectives are presented.

HLM properties are reported in Chapters 2-5. Chapter 2 compiles the thermo-physical and electrical properties of the LBE and Pb (e.g. density, molar volume, isobaric heat capacity, viscosity, thermal and electrical conductivity) reported in the open literature. In some cases, significant discrepancies exist among the different sources, and recommendations based on the "best fit" of data are offered.

Chapter 3 addresses thermodynamic relations, transport properties and the chemistry of HLM, such as the solubility and diffusivity of oxygen and metallic elements in the liquid metal. In Chapter 4, chemistry control and monitoring systems are discussed. The main chemistry issue is the monitoring and adjustment of the oxygen level in HLMs for the mitigation of corrosion and coolant contamination problems. For this purpose, the development, calibration and performance of electrochemical oxygen sensors and oxygen control systems are extensively described.

Chapter 5 deals with the properties of irradiated LBE and Pb. For this topic, very little data is available and most of them have been produced in the framework of the international MEGAPIE initiative and CERN experiments.

Materials issues are covered in Chapters 6-9. The compatibility of ferritic/martensitic and austenitic steels with the liquid metals is given in terms of corrosion (Chapter 6) and the effects on the mechanical properties in stagnant and flowing liquid metals (Chapter 7). While a substantial amount of corrosion test results are available from many sources, most results pertain to relatively short durations (up to a few thousand hours). Although several key qualitative conclusions can be drawn, the wide ranging test conditions and materials render it very difficult at present to derive a consistent set of correlations for design use, especially in long-term applications. It should also be noted that the data on the mechanical property changes is fairly scarce.

In Chapter 8, a collection of data is given representing the combined effects of proton irradiation and HLM on the properties of structural materials. These data have been produced principally at the Paul Scherrer Institute (Switzerland) and in the framework of the MEGAPIE initiative, with contributions from Los Alamos National Laboratory (United States). More data on the effects of irradiation on the compatibility of structural materials with Pb and LBE in the neutron field will be available at the end of the next five-year period, after the completion of the experiments described in this chapter.

Chapter 9 is dedicated to corrosion protection methods. In particular, two types of methods are under development and testing – the *in situ* growth and control of a "self-healing" protective oxide layer on the steel surface, and the deposition of a Fe-Al-based surface coating. Other types of coatings, such as *in situ* formation of carbides and nitrides via addition of inhibitors, have been tested but not as extensively.

Chapters 10 and 11 address the thermal-hydraulic behaviour and instrumentation needed for scientific, technological and operational purposes. For thermal-hydraulic quantities, the available set of data appears to be insufficient for a complete validation of computational fluid dynamics (CFD) codes and for the development of reliable and realistic physical models. Additional data is still needed for reliable models including data from long-term experiments at multiple temperatures and flow rates.

A compilation of existing NEA experimental facilities with their main parameters and key objectives is given in Chapter 12. Chapter 13 briefly reviews the effects of HLM containing Pb and Bi on human and environmental health and safety, and outlines safety guidelines for the use of HLMs. Finally, in Chapter 14, the open issues and the strategic outlook for R&D are summarised.

A new chapter has been added to this edition of the handbook, which includes the benchmark exercise performed on the experimental results obtained from the Heavy Eutectic Liquid Metal Loop for the Investigation of Operability and Safety (HELIOS) facility located at Seoul National University.

References

Abderrahim, H.A. et al. (2001), "MYRRHA: A Multipurpose Accelerator Driven System for Research & Development", *Nuclear Instruments & Methods in Physics Research*, A 463, pp. 487-494.

Abderrahim, H.A. (2005a), "MYRRHA: A Multipurpose ADS for R&D, Progress Report at End 2004", *ICONE 13*, Beijing.

Abderrahim, H.A. and D. de Bruin (eds.) (2005b), *MYRRHA, A Future for Nuclear Research. Pre-Design (DRAFT 2) Report*, SCK•CEN, Mol, Belgium.

Alemberti, A. et al. (2013), "The Lead-cooled Fast Reactor: Past Activities, Present Status and Future Directions", *GIF Symposium Proceedings, 2012 Annual Report*, San Diego, CA, 14-15 November 2012, NEA No. 7141, OECD/NEA, Paris.

Bauer, G.S. (2001), "Physics and Technology of Spallation Neutron Sources", *Nuclear Instruments and Methods in Physics Research*, Vol. 463, Issue 3, pp. 505-543.

ESNII (2010), *A Contribution to the EU Low Carbon Energy Policy: Demonstration Programme for Fast Neutron Reactors*, ESNII Executive Board, Sustainable Nuclear Energy Technology Platform (SNETP), October 2010, European Sustainable Nuclear Industrial Initiative.

ETWG (2001), *A European Roadmap for Developing Accelerator Driven Systems (ADS) for Nuclear Incineration*, Italian National Agency for New Technologies (ENEA), Rome, ISBN 88-8286-008-6.

Fazio, C. et al. (2008), "The MEGAPIE-TEST Project: Supporting Research and Lessons Learned in First-of-a-kind Spallation Target Technology", *Nuclear Engineering and Design*, Vol. 238, Issue 6, pp. 1471-1495.

Filin, A.I. et al. (2003), "Design Features of BREST Reactors and Experimental Work to Advance the Concept of BREST Reactors", *Power Reactors and Sub-critical Blanket Systems with Lead and Lead-Bismuth as Coolant and/or Target Material*, IAEA-TECDOC-1348, pp. 31-40, IAEA, Vienna.

FZK (2003), *Proceedings. of the 4th MEGAPIE Technical Review Meeting*, C. Fazio, J.U. Knebel and F. Gröschel (eds.), Paris, 18-19 March 2003, FZKA 6876, Forschungszentrum Karlsruhe, Karlsruhe.

Handbook on Thermo-physical Properties of Materials for Nuclear Engineering (2005), pp. 180 (in Russian).

Hejzlar, P. et al. (2004), "Design Strategy and Constraints for Medium Power Lead-alloy-cooled Actinide Burners", *Nuclear Technology*, Vol. 147, 3, pp. 321-343.

Hwang, I.S. et al. (2000), "The Concept of Proliferation Resistant, Environment-friendly, Accident-tolerant, Continual and Economical Reactor (PEACER)", *Progress in Nuclear Energy*, Vol. 37, 1-4, pp. 217-222.

IAEA (2002), *Comparative Assessment of Thermophysica and Thermohydraulic Characteristics of Lead, Lead-bismuth and Sodium Coolants for Fast Reactors*, IAEA-TECDOC-1289, International Atomic Energy Agency, Vienna.

IAEA (2012), "Liquid Metal Coolants for Fast Reactors Cooled by Sodium, Lead and Lead-bismuth Eutectic", *IAEA Nuclear Energy Series*, No. NP-T-1.6, International Atomic Energy Agency, Vienna.

EUROTRANS (2004), EC project No. FI6W-CT-2004-516520, http://cordis.europa.eu/project/rcn/85226_en.pdf.

Kirillov, P.L. (1998), *Thermophysical Properties of Lead, Bismuth and Their Eutectic Alloy*, FEI-0286, pp. 28 (in Russian).

Kirillov, P.L. and N. Deniskina (2000), *Thermophysical Properties of Liquid Metal Coolants*, Tables and Correlations, FEI-0291, pp. 41 (in Russian).

Kirillov, P.L. (ed.) (2003), *Knowledge Preservation Initiative – Generalization of Data on Hydrodynamics and Heat/Mass Transfer Processes in Liquid Metal Cooled Reactors*, prepared at the IPPE, pp. 660; 200 tables, 400 figures, more than 1 000 references (in Russian and English).

Kleykamp, H. et al. (2002), "Proceedings of the 10th International Conference on Fusion Reactor Materials (ICFRM-10)", *Journal of Nuclear Materials*, Vols. 307-311.

Knebel, J.U. et al. (2005), "Overview on Integrated Project EUROTRANS: EURopean Research Programme for the TRANSmutation of High Level Nuclear Waste in an Accelerator Driven System", *3rd Annual Idaho ADSS Experiments Workshop*, Pocatello, ID, 1-2 June.

Mukaiyama, T. (2003), "OMEGA Programme in Japan and ADS Development at JAERI", *Review of National Accelerator Driven System Programmes for Partitioning and Transmutation*, IAEA-TECDOC-1365, pp. 153-165, IAEA, Vienna.

Oigawa, H. et al. (2004), "R&D Activities on Accelerator-Driven Transmutation System in JAERI", *Proceedings of the 8th Information Exchange Meeting on Actinide and Fission Product Partitioning & Transmutation (IEMPT-8)*, Las Vegas, 9-11 November, OECD/NEA, Paris.

Park, W.S. et al. (1996), "Development of Nuclear Transmutation Technology", KAERI/ RR-1702/96, *Proceedings of International Conference on Heavy Liquid Metal Coolants in Nuclear Engineering*, Vol. 1 and 2, p. 824, 5-9 October, Obninsk, IPPE.

Sasa, T. et al. (2004), "Research and Development on Accelerator-driven Transmutation System at JAERI", *Nuclear Engineering and Design*, Vol. 230, 1-3, pp. 209-222.

Song, T.Y. et al. (2004), "HYPER Project", *Proceedings of the 4th International Workshop on Utilisation and Reliability of High Power Proton Accelerators*, Daejeon, 16-19 May 2004, OECD/NEA, Paris.

Stepanov, V.S. et al. (1998), "SVBR-75: A Reactor Module for Renewal of WWER 440 Decommissioning Reactors – Safety and Economic Aspects", *Nuclear Heat Applications: Design Aspects and Operating Experience*, IAEA-TECDOC-1056, pp. 165-176, IAEA, Vienna.

Takahashi, M. et al. (2004), "Design and Experimental Study for Development of Pb-Bi Cooled Direct Contact Boiling Water Small Fast Reactor (PBWFR)", *Proceedings of ICAPP'04*, Pittsburgh, 13-17 June 2004, paper No. 4058.

Todreas, N.E. et al. (2004), "Medium-power Lead Alloy Reactors: Missions for this Reactor Technology", *Nuclear Technology*, Vol. 147, 3, p. 305.

US DOE (2003), *Report to Congress on Advanced Fuel Cycle Initiative: The Future Path for Advanced Spent Fuel Treatment and Transmutation Research*, US Department of Energy, Office of Nuclear Energy, Science and Technology.

Wohlmuther, M and W. Wagner (2012), "PIE Preparation of the MEGAPIE Target", *Journal of Nuclear Materials*, Vol. 431, 1-3, pp. 10-15.

Young-Sang, J. et al. (2013), "Performance Test of a Plate-Type Ultrasonic Waveguide Sensor in Sodium", *AIP Conference Proceedings* 1511, Denver, 15-16 July, 1670, doi: 10.1063/1.4789242;

Zanini, L. et al. (2011), "Experience from the Post-test Analysis of MEGAPIE", *Journal of Nuclear Materials*, Vol. 415, 3, pp. 367-377.

2. Thermophysical and electric properties of liquid lead, bismuth and lead-bismuth eutectic*

2.1 Introduction

Among different heavy liquid metals (HLM), lead (Pb) and lead-bismuth eutectic (LBE: 44.5 wt.% Pb + 55.5 wt.% Bi) are considered at present as potential candidates for the coolant of new generation fast spectrum nuclear reactors and accelerated-driven systems (ADS) and for liquid spallation neutron sources (Sobolev, 2012). The main problem of these coolants is a rather high corrosion rate of steels at high temperatures (> 773 K ~ 500°C). Therefore LBE, due to its lower melting temperature (398 K ~ 125°C compared to 600 K ~ 327°C for lead) allowing lower operation temperature range resulting in lower corrosion rates and in easier maintenance, is considered as favourite in most projects. The production of the alpha-active polonium because of radiative capture of neutrons by bismuth is a disadvantage of LBE. Other alloys of lead that do not contain bismuth (Bi), such as lead-lithium eutectic (LLE: 99.32 wt.% Pb + 0.68 wt.% Li) with a melting temperature of about 508 K ~ 235°C and lead-magnesium eutectic (LME: 97.5 wt.% Pb + 2.5 wt.% Mg) with the melting temperature of about 522 K ~ 249°C, are studied as possible alternatives. LLE is also proposed as breeder-coolant in fusion reactors. However, using of LLE and LME requires very low oxygen content in coolant; moreover, their properties have not been well measured yet.

This chapter compiles data on the main thermophysical properties (e.g. characteristic temperatures, pressures and enthalpies, surface tension, density, compressibility, heat capacity, viscosity, thermal and electrical conductivity, etc.) of molten lead-bismuth eutectic, lead and bismuth (as the component of LBE) reported in the open literature. In some cases, significant discrepancies exist among the values given by different sources. Therefore, recommendations based on the "best fit" of the available data are usually proposed. Published data on the properties of the lead alloys of interest are still limited. The main sources are materials handbooks published in the 1950s and 1960s and later reviews. The first compilations of the main thermophysical properties of Pb and LBE were assembled by Lyon (1954), Kutateladze (1958) and Nikol'skii (1959). In the later handbooks most of data were either reproduced without changes (Mantell, 1958; Lyon, 1960; Bonilla, 1964; Crean, 1964) or with addition of new results (Friedland, 1966; Hultgren, 1963, 1973a, 1973b; Kubaschewski, 1979, 1993; Iida, 1988; Gurvich, 1991; Cheynet, 1989, 1996). During the last ten years several review-reports and chapters in handbooks have been published where previous data were reanalysed (Cevolani, 1998; Imbeni, 1998, 1999; Kirillov, 2000a, 2000b, 2008; Bogoslovskaya, 2002; Sobolev, 2002, 2005, 2007a, 2007b, 2008a, 2008b, 2009, 2011, 2012). The data, the recommendations and conclusions in this chapter are mainly based on the later review (Sobolev, 2011) and on the previous version of Chapter 2 (Sobolev, 2007b) included in the NEA handbook published in 2007.

In comparison with the previous version, the recommendations of this chapter for many properties were extended to higher temperatures. Some new experimental data appeared after publication of the first edition (e.g. Hayashi, 2007; Greenberg, 2008, 2009;

* Chapter leads: V.P. Sobolev and A. Gessi.

and Plevachuk, 2008) and other data which had not been included in the previous version was found. Consequently, missing information was added and some corrections were made in the recommended correlations. However, some publications and compilation reports issued in the former Soviet Union, in Russia and other countries have not yet been taken into account in this version of Chapter 2 because of difficulties in accessing the content.

The reliability of data depends on the method used for their production and the care with which the method is used. In general, data concerning metals in the liquid or vapour state show a significant dispersion, with the exception of the melting points. Only a few authors of compilations have paid adequate attention to dispersion and standard deviation of the reported values (e.g. Hultgren, 1973a, 1973b; and Gurvich, 1991).

The database in this chapter is presented in the form of a set of tables. Each table is devoted to one parameter and contains information about the references used, year of publication, measurement method, precision, temperature range and simplified composition of a sample. Sometimes values of the parameters from the reference and correlation obtained based on the available data are given. Often it was not possible to access the original sources of data. In this case, the data selected from handbooks and other compilations were used to fill in the database. In the case where information concerning precision or/and method was not available, a question mark "?" is used; if this information can be deduced or suggested using other sources then brackets "(…)" are used to indicate that the presented data should be used with caution. Values in the column "values" are given in the same unit system as provided in the original bibliographic sources. In all recommended correlations and values, the SI unit system is used, where temperature is given in the degrees of Kelvin ("kelvins"). In some cases the abbreviation "n/a" (non-applicable) is used.

A summary of the recommended correlations and the ranges of their validity is presented at the end of the chapter in Section 2.19.

2.2 Pb-Bi system phase diagram

One of the first more or less complete phase diagrams for the binary Pb-Bi system was published in the handbook of Hiers (1948); it was later reproduced in the well-known Smithells Metal Reference Book (SMRB) (1955).

Later, it was also reproduced almost without changes in the book of Ageron et al. (1959) and in the later editions of SMRB (Smithells, 1967, 1983, 2004).

This phase diagram presented in Figure 2.2.1 shows:

- an eutectic point at 55.5 wt.% Bi with a melting temperature of 124°C (397 K);
- a peritectic point at 32.2 wt.% Bi with a melting temperature of 184°C (457 K);
- solubility limits in solid state at 21.5 wt.% Bi in Pb (α-phase region) and 0.5 wt.% Pb in Bi (γ-phase region);
- an intermetallic compound phase (β-phase region);
- liquidus and solidus lines.

Hansen (1958) presented the Pb-Bi phase diagram with some new experimental results. This diagram with additional revisions was reported in Elliott (1965). Some parameters were changed in comparison with the diagram reproduced in Figure 2.2.1:

- the eutectic point at 56.7 wt.% Bi (56.3 at.% Bi) with a melting temperature of 124.7°C (398 K);
- the peritectic point at 36.2 wt.% Bi (36 at.% Bi);
- the solubility limit of Bi in Pb in the solid state is reported to be 23.4 wt.% (23.3 at.%).

Figure 2.2.1: Phase diagram of the Pb-Bi system

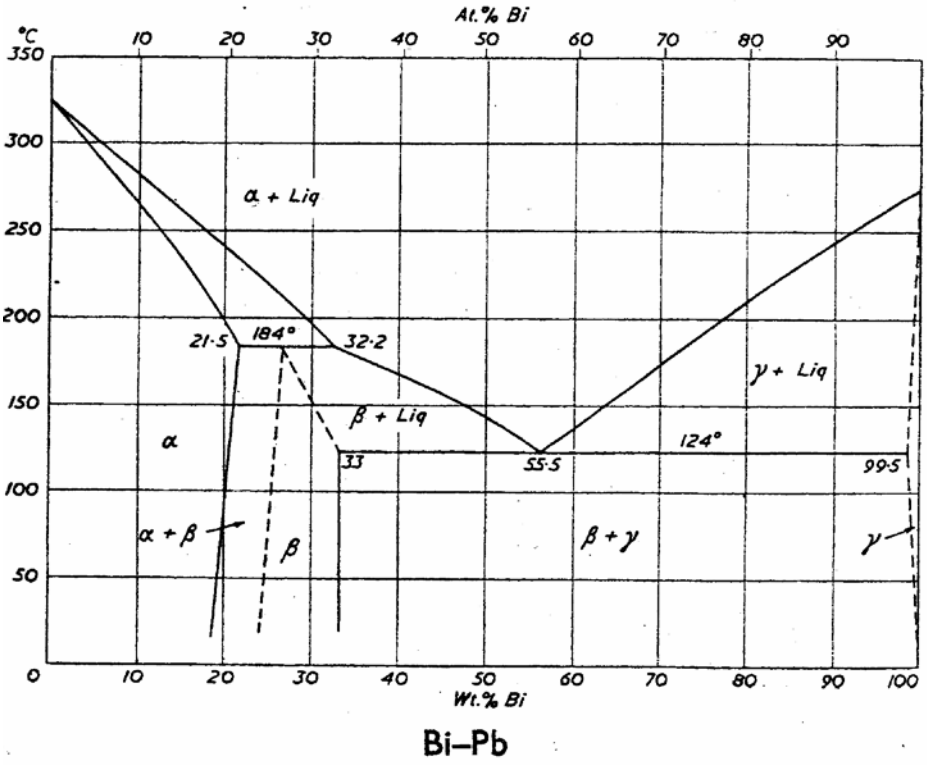

Source: Smithells (1955).

In 1973, the Pb-Bi phase diagram with refinements of the boundaries of the ε-phase, given by Predel (1967), and boundaries of γ-phase, given by Nosek (1967), was published by Hultgren (1973a). This diagram is reproduced in Figure 2.2.2.

This diagram provides the same eutectic and peritectic points as those proposed by Elliott (1965), but gives:

- the melting point of Bi at 271.22°C (544.52 K);
- the melting point of Pb at 327.3°C (600.6 K);
- the solubility limit of Pb in Bi in the solid state: 5 at.%;
- the solubility limit of Bi in Pb in the solid state: 24 at.%;
- an eutectoid point at 72.5 at.% Pb and -46.7°C (227 K);
- ε-phase region.

In 1992, Gokcen (1992) proposed a few modifications for some characteristic points (Figure 2.2.3):

- more precise melting points of elements at the normal atmospheric pressure: $T_{M,0(Bi)}$ = 271.442°C (544.592 K); $T_{M,0(Pb)}$ = 327.502°C (600.652 K);
- the eutectic point at 45.0 at.% Pb with $T_{M,0(LBE)}$ = 125.5°C (398.65 K);
- the peritectic point at 71 at.% Pb and 187°C (460.15 K);
- the lower limits of the elements solubility in the solid state: 0.5 at.% Pb in Bi and 22 at.% Bi in Pb.

Figure 2.2.2: Phase diagram of the Pb-Bi system

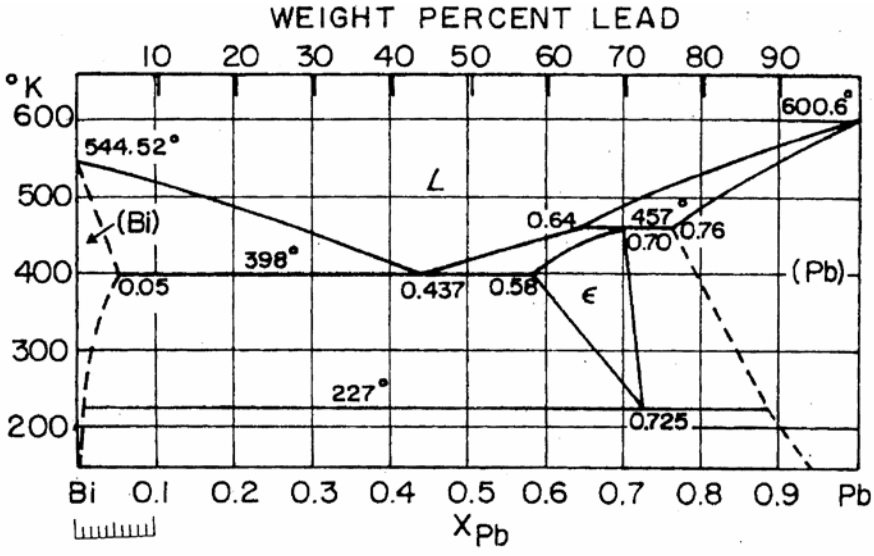

Source: Hultgren (1973a).

Figure 2.2.3: Phase diagram of the Pb-Bi system

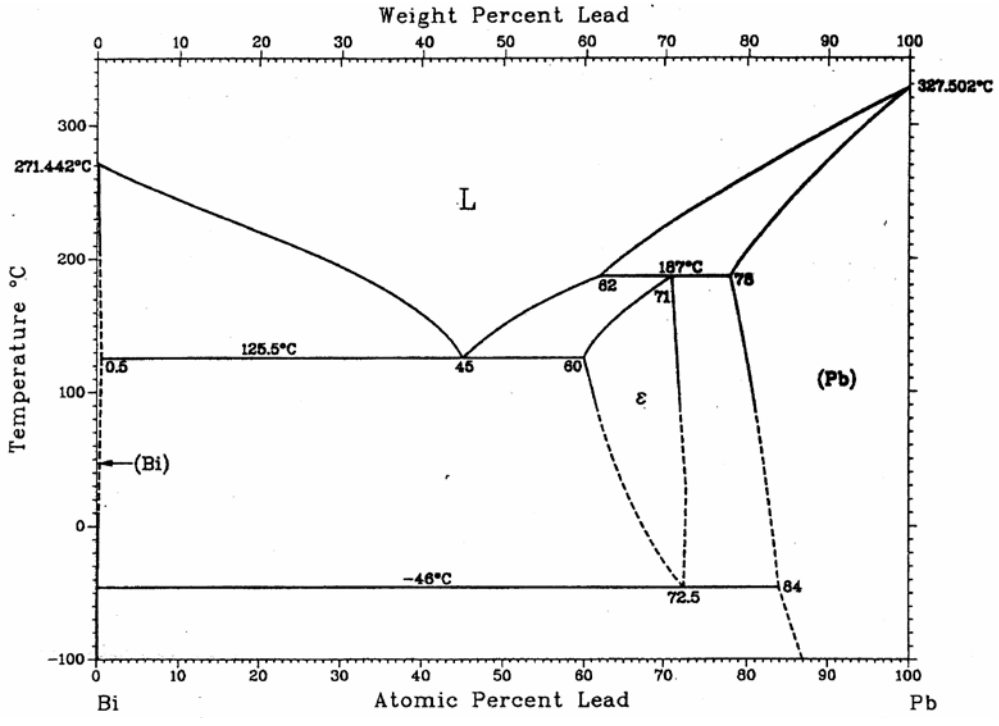

Source: Gokcen (1992).

The same year these modifications were reproduced in a Pb-Bi phase diagram published in the ASM Handbook (Baker, 1992).

In 1994, Okamoto cited the Pb-Bi phase diagram developed on the basis of the available experimental results by Taskinen (1992) (Figure 2.2.4) with the following parameters:

- $T_{M,0(Bi)}$ = 271.37°C (544.52 K); $T_{M,0(Pb)}$ = 327.502°C (600.652 K);
- the eutectic point at ~56 at.% Bi with $T_{M,0(LBE)}$ = 127.5°C (400.65 K);
- the peritectic point at 28.4 at.% Bi;
- the eutectoid point at 26.2 at.% Bi and -45.15°C (228.0 K);
- the limits of the elements solubility in the solid state of 0.1 at.% Pb in Bi and 24.8 at.% Bi in Pb.

However, it was pointed out that some of the used data are older than those used in Gokcen (1992).

Figure 2.2.4: Phase diagram of the Pb-Bi system

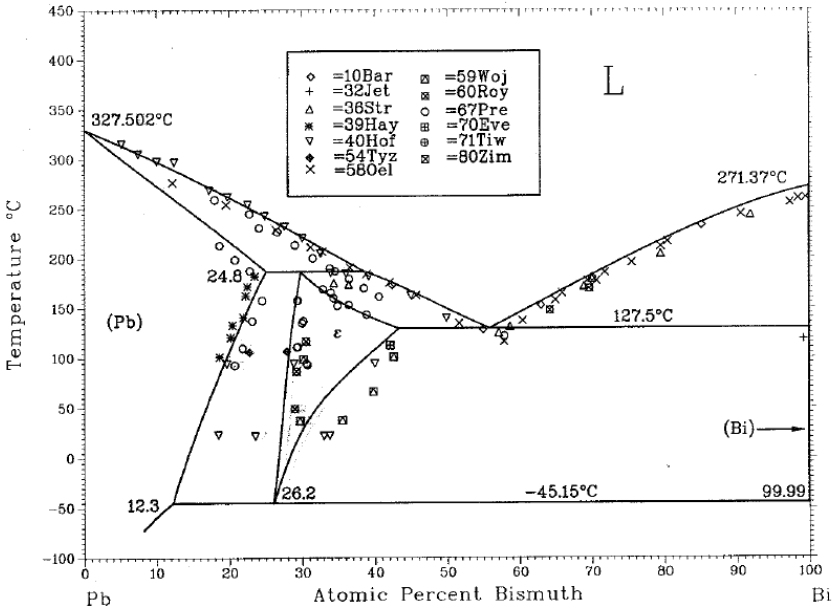

Source: Taskinen (1992).

In many Russian publications (Orlov, 1997, 2003), followed recently by other authors, a phase diagram is often presented which gives the LBE eutectic composition at 55.5 wt.% Bi and 44.5 wt.% Pb with the eutectic melting temperature of 123.5°C (396.65 K); the temperature is probably reproduced from Kutateladze (1958).

Recommendation

Gokcen's (1992) phase diagram reproduced in the ASM Handbook (Figure 2.2.3) is recommended for use in engineering and design calculations with the exception of the eutectic point. The Pb-Bi eutectic composition with 55.5 wt.% Bi and 44.5 wt.% Pb was selected with the eutectic melting temperature of 398 K (124.85°C) (see Section 2.3.3).

2.3 Normal melting point

Melting temperature at normal atmospheric pressure (normal melting point $T_{M,0}$) provides the lower boundary to the temperature range of operation of a liquid metal coolant. It is also an important characteristic of interatomic forces, which correlates with some thermodynamic properties.

2.3.1 Lead

The values of the lead melting temperatures were found in the following handbooks and reviews: Miller, 1951, 1954; Lyon, 1954, 1960; Kutateladze, 1958; Friedland, 1966; Hofmann, 1970; Hultgren, 1973b; Lucas, 1984a; Iida, 1988; Kubaschewski, 1979, 1993; Gokcen, 1992; Cheynet, 1996; Imbeni, 1998; Kirillov, 2000a; Smithells, 2004; and IAEA reports (Bogoslovskaya, 2002; Kirillov, 2008).

Friedland (1966) reproduced the values of the Pb melting temperature from Lyon (1954, 1960). The compilation of Imbeni (1998) presented data on the lead melting temperature from different sources with the conclusion that dispersion is not large. In the handbook (Kirillov, 2000a) and in the IAEA reports (Bogoslovskaya, 2002; Kirillov, 2008) the lead melting temperature presented in the earlier compilation (Kutateladze, 1958) was repeated. These sources have not been included in the database on the Pb melting point.

Hofmann (1970) refers to an evaluation of the literature data performed by Kohlraush (1956). Hultgren (1973b) collected data from many earlier sources, and recommended average values and uncertainties. Iida (1988) took data from the Iwanami Dictionary of Physics and Chemistry (Tamamushi, 1981). Kubaschewski (1979, 1993), cited the JANAF Thermochemical Tables (Chase, 1978, 1982; Knacke, 1991; Pankratz, 1982; Hultgren, 1973b). The compilation (Cheynet, 1996) references the JANAF Thermochemical Tables (Chase, 1985; Barin, 1989; Cheynet, 1989; Knacke, 1991). In Gokcen (1992) the value of 600.652 K is given for the high purity Pb that is used as the secondary reference point in the International Practical Temperature Scale. The last edition of SMRB (Smithells, 2004) presented the melting temperatures from the 82nd edition of the CRC Handbook of Chemistry and Physics (2002).

The data for the melting temperature of lead, extracted from the above selected sources, are presented in Table 2.3.1.

All selected data yield approximately the same value within their error limits. The most probable value for the melting temperature of technically pure lead obtained on the basis of the data presented in the table is:

$$T_{M,0(Pb)} = 600.6 \pm 0.1 \text{ K} \tag{2.1}$$

The melting point of lead increases by 0.0792 K per 1 MPa when pressure increases from about 15 up to 200 MPa. The increase continues at a lower rate, 0.0671 K per 1 MPa, in the range of 800-1 200 MPa; an increase of 5.4 K for a pressure increase from about 2 to 3 GPa was cited in Hofmann (1970).

2.3.2 Bismuth

The database for the normal melting point of bismuth is extracted from about the same sources as for lead (Section 2.3.1) and is presented in Table 2.3.2.

The melting temperature of bismuth is uncertain in the cited data in the first digit after the decimal point. The normal melting point of the high purity Bi: $T_{M,0(Bi)} = 544.592$ K is used as the secondary reference point in the International Practical Temperature Scale. Therefore, the recommended mean value for the technically pure Bi is as follows:

$$T_{M,0(Bi)} = 544.6 \pm 0.3 \text{ K} \tag{2.2}$$

The bismuth melting point increases with pressure and reaches about 569 K (296°C) at pressure 38 GPa (Klement, 1963).

Table 2.3.1: Selected database on the normal melting temperature of lead

Reg. No.	Parameter	Measurement method	Estimated accuracy	Temperature range, K	Pressure range, Pa	Values	Ref.
3.1.1	Melting temperature	Temperature vs. power	0.1°C	n/a	~10^5	327.4°C	Miller (1954)
	Interpolation function: $T_{M,0}$ = 600.65 K						
	Comments: Unknown purity						
3.1.2	Melting temperature	Temperature vs. power	0.1°C	n/a	~10^5	327.4°C	Kutateladze (1958)
	Interpolation function: $T_{M,0}$ = 600.65 K						
	Comments: Unknown purity						
3.1.3	Melting temperature	n/a	(0.1°C)	n/a	~10^5	327.3°C	Hofmann (1970)
	Interpolation function: $T_{M,0}$ = 600.55 K						
	Comments: Unknown purity						
3.1.4	Melting temperature	Temperature vs. power	0.1°C	n/a	~10^5	600.6 K	Hultgren (1973b)
	Interpolation function: $T_{M,0}$ = 600.6 K						
	Comments: Unknown purity						
3.1.5	Melting temperature	?	0.05 K	n/a	~10^5	600.55 K	Iida (1988)
	Interpolation function: $T_{M,0}$ = 600.55 K						
	Comments: Unknown purity						
3.1.6	Melting temperature	?	(0.005°C)	n/a	~10^5	327.502°C	Gokcen (1992)
	Interpolation function: $T_{M,0}$ = 600.652 K						
	Comments: High purity						
3.1.7	Melting temperature	?	?	n/a	~10^5	601 K	Kubaschewski (1993)
	Interpolation function: $T_{M,0}$ = 601 K						
	Comments: Unknown purity						
3.1.8	Melting temperature	?	(0.1°C)	n/a	~10^5	327.4°C	Cheynet (1996)
	Interpolation function: $T_{M,0}$ = 600.65 K						
	Comments: Unknown purity						
3.1.9	Melting temperature	?	(0.005°C)	n/a	~10^5	327.462°C	Smithells (2004)
	Interpolation function: $T_{M,0}$ = 600.612 K						
	Comments: Unknown purity						

Table 2.3.2: Selected database on the normal melting temperature of bismuth

Reg. No.	Parameter	Measurement method	Estimated accuracy	Temperature range, K	Pressure range, Pa	Values	Ref.
3.2.1	Melting temperature	Temperature vs. power	0.1°C (?)	n/a	~10^5	271.0°C	Miller (1954)
	Interpolation function: $T_{M,0}$ = 544.15 K						
	Comments: Unknown purity						
3.2.2	Melting temperature	Temperature vs. power	1°C (?)	n/a	~10^5	271°C	Kutateladze (1958)
	Interpolation function: $T_{M,0}$ = 544.15 K						
	Comments: Unknown purity						
3.2.3	Melting temperature	Temperature vs. power	0.05 K	n/a	~10^5	544.52 K	Hultgren (1973b)
	Interpolation function: $T_{M,0}$ = 544.52 K						
	Comments: Unknown purity						
3.2.4	Melting temperature	?	(1 K)	n/a	~10^5	545 K	Kubaschewski (1993)
	Interpolation function: $T_{M,0}$ = 545 K						
	Comments: Unknown purity						
3.2.5	Melting temperature	?	0.05 K	n/a	~10^5	544.10 K	Iida (1988)
	Interpolation function: $T_{M,0}$ = 544.10 K						
	Comments: Unknown purity						
3.2.6	Melting temperature	?	(0.005°C)	n/a	~10^5	271.442°C	Gokcen (1992)
	Interpolation function: $T_{M,0}$ = 544.592 K						
	Comments: High purity						
3.2.7	Melting temperature	?	(0.005°C)	n/a	~10^5	271.37°C	Tashien (1992)
	Interpolation function: $T_{M,0}$ = 544.52 K						
	Comments: High purity						
3.2.8	Melting temperature	?	(0.05°C)	n/a	~10^5	271.40°C	Smithells (2004)
	Interpolation function: $T_{M,0}$ = 544.55 K						
	Comments: High purity						

2.3.3 LBE

The data sources for the LBE normal melting temperature included in this handbook are Miller (1954), Kutateladze (1958), Hultgren (1973a), Smithells (1955), Eliot (1965), Gokcen (1992), Taskinen (1992), Kirillov (2008) and Plevachuk (2008). Most of these data were reproduced in later handbooks (Lyon, 1960; Kirillov, 2000a; Smithells, 1983), compilations and articles (Cevolani, 1998; Imbeni, 1999; Sobolev, 2005, 2007a, 2011; Bogoslovskaya, 2002). The selected sources included in the database (Table 2.3.3) give $T_{M,0(LBE)}$ = 123.5-127.5°C (396.7-400.7 K) for the LBE melting temperature at normal atmospheric pressure.

The value of:

$$T_{M,0(LBE)} = 398 \pm 1 \text{ K} \tag{2.3}$$

is recommended as the most reliable on the basis of the data presented in Table 2.3.3.

The eutectic point of Pb-Bi(e) is shifted to lower Pb contents and higher melting temperature with pressure increase. The eutectic temperature increases from 398 K at normal atmospheric pressure to ~422 K at pressure of 0.75 GPa and to ~481 K at 1.8 GPa (Ponyatovsky, 1970).

Table 2.3.3: Selected database on the LBE normal melting temperature

Reg. No.	Parameter	Measurement method	Estimated accuracy %	Temperature range, K	Pressure range, Pa	Values	Ref.
3.3.1	Melting temperature	?	?	n/a	~10^5	125°C	Miller (1954)
	Interpolation function: $T_{M,0}$ = 398.15 K						
	Comments: 44.5 wt.% Pb + 55.5 wt.% Bi, unknown purity						
3.3.2	Melting temperature	?	?	n/a	~10^5	123.5°C	Kutateladze (1958)
	Interpolation function: $T_{M,0}$ = 396.65 K						
	Comments: 44.5 wt.% Pb + 55.5 wt.% Bi, unknown purity						
3.3.3	Melting temperature	?	?	n/a	~10^5	398 K	Hultgren (1973a)
	Interpolation function: $T_{M,0}$ = 398 K						
	Comments: 43.7 at.% Pb + 56.3 at.% Bi, unknown purity						
3.3.4	Melting temperature	?	?	n/a	~10^5	124°C	Smithells (1955)
	Interpolation function: $T_{M,0}$ = 397.15 K						
	Comments: 44.8 wt.% Pb + 55.2 wt.% Bi, unknown purity						
3.3.5	Melting temperature	?	?	n/a	~10^5	125°C	Eliot (1965)
	Interpolation function: $T_{M,0}$ = 398.15 K						
	Comments: 43.7 at.% Pb + 56.3 at.% Bi, unknown purity						
3.3.6	Melting temperature	?	?	n/a	~10^5	125.5°C	Gokcen (1992)
	Interpolation function: $T_{M,0}$ = 398.65 K						
	Comments: 45.0 at.% Pb + 55.0 at.% Bi, unknown purity						

Table 2.3.3: Selected database on the LBE normal melting temperature (*cont.*)

Reg. No.	Parameter	Measurement method	Estimated accuracy %	Temperature range, K	Pressure range, Pa	Values	Ref.
3.3.7	Melting temperature	?	?	n/a	~10^5	127.5°C	Taskinen (1992)
	Interpolation function: $T_{M,0}$ = 400.65 K						
	Comments: 44 at.% Pb + 56 at.% Bi, high purity						
3.3.8	Melting temperature	?	?	n/a	~10^5	398.5 K	Plevachuk (2008)
	Interpolation function: $T_{M,0}$ = 398.5 K						
	Comments: 46 at.% Pb + 54 at.% Bi, high purity ±0.02 at.%						
3.3.9	Melting temperature	?	?	n/a	~10^5 (?)	398 K	Kirillov (2008)
	Interpolation function: $T_{M,0}$ = 398 K						
	Comments: 44.5 at.% Pb + 55.5 at.% Bi, unknown purity						

2.4 Volume change at melting and solidification

Knowledge of volume (density) changes in metals and alloys at their melting points is of critical importance for their application as liquid metal coolants and for the understanding of melting and solidification processes (Iida, 1988).

- *Solid lead*. Similar to the majority of metals with the FCC crystal structure, lead exhibits a volume increase upon melting. At normal conditions, a volume increase of 3.81% has been observed in pure lead (Iida, 1988). In several engineering handbooks, a value of ~3.6% is given for lead of technical purity (Miller, 1954; Bogoslovskaya, 2002; Kirillov, 2008).
- *Solid bismuth*. Solid bismuth shows a volume contraction during melting, similar to other semimetals. The anisotropic rigid bonds are apparently broken on melting, and the neighbouring atoms are packed closer one to another. According to Iida (1988), pure bismuth contracts approximately 3.87% upon melting. A contraction of 3.32% was reported by Miller (1954) in the handbook (Lyon, 1954) and a value of ~3.3% was recommended in the IAEA reports (Bogoslovskaya, 2002; Kirillov, 2008) for Bi coolant.
- *Solid LBE*. A negligible volume change on melting of solid LBE at normal atmospheric pressure was published in the handbook (Lyon, 1954). This recommendation was repeated in later handbooks and compilations. The LBE volume change of +0.5% was reported in the last IAEA compilation (Kirillov, 2008).

Recommendations for the mean values of the volume change upon melting are summarised for Pb, Bi and LBE in Table 2.4.1. It is recommended that for very slow melting (quasi-equilibrium conditions) the volume change upon melting be close to zero for LBE.

The situation is more complicated for LBE freezing and melting accompanied by a rapid temperature change. In the handbook of Lyon (1954) a 1.43 vol.% contraction of LBE on freezing with a subsequent expansion of the solid of 0.77 vol.% at an arbitrary temperature of 65°C has been reported. A contraction of 1.52 ± 0.1 vol.% of the solid phase after solidification of LBE has also been mentioned in Hofmann (1970).

Table 2.4.1: Relative change of volume of technically pure lead, bismuth and LBE at melting (p ~ 0.1 MPa)

	Pb	Bi	LBE
$\Delta V_{M,0}/V_{M,0}$	+0.037	-0.037	~0.00

The problems of freezing and melting of LBE in the reactor circuits were analysed by Pylchenkov (1999). He pointed out that the results of the freezing/de-freezing experiments are very sensitive to the experimental conditions and that very long times (> 100 d) are usually required to reach equilibrium. Some of his results are shown in Figure 2.4.1. The volume effect upon freezing/de-freezing depends very strongly on the phase structure of local transformations in the solid state related to the mutual solubility of LBE components (see the LBE phase diagram in Figure 2.2.3). A negligible volume change has been observed in some experiments. According to Pylchenkov (1999), post-solidification expansion may occur in a metastable alloy as a result of local changes in the composition. An excess in γ-phase precipitation during freezing can result in a volume increase. He pointed out the general tendency: the volume effect of LBE melting-solidification is minimal for pure eutectic materials.

Figure 2.4.1: Solid LBE volume evolution as a function of time after heat-up from 25 to 125°C

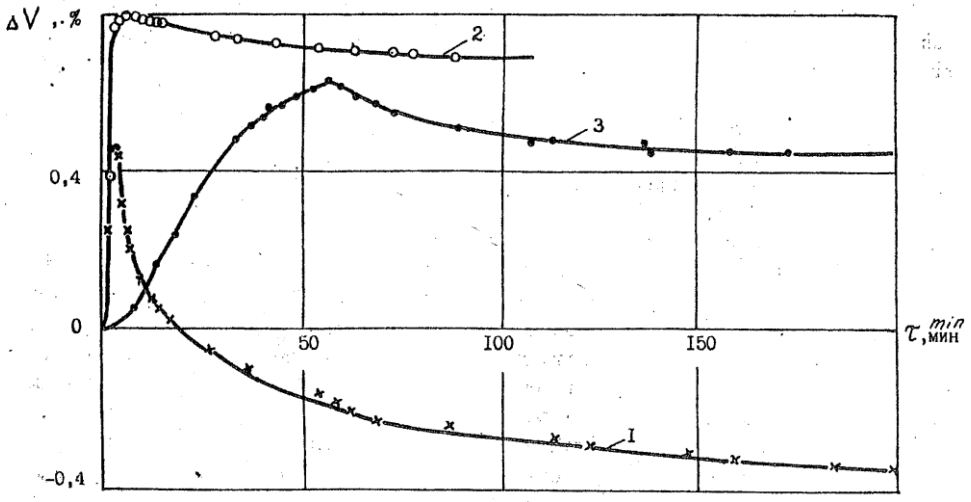

1. Fast heat-up (prehistory: few years at 20-25°C).
2. Fast heat-up (prehistory: cooling down to 25°C after solidification and exposure during 65 hours)
3. Heat-up time is one hour (prehistory: 3 hours of exposure at 124°C followed by 15 hours of exposure at 25°C)

Source: Pylchenkov (1999).

The results of measurements of LBE expansion over time at room temperature after solidification and rapid cooling has been reported by Glasbrenner (2005). In these results, shown in Figure 2.4.2, one can see that after solidification and cooling the studied material contracted about 0.35%. After about 100 minutes of exposure at room temperature, its volume returns to the initial value, but after one year, its linear size increases by about 1.2%.

Figure 2.4.2: Linear expansion of LBE as a function of time after solidification and cooling down to room temperature

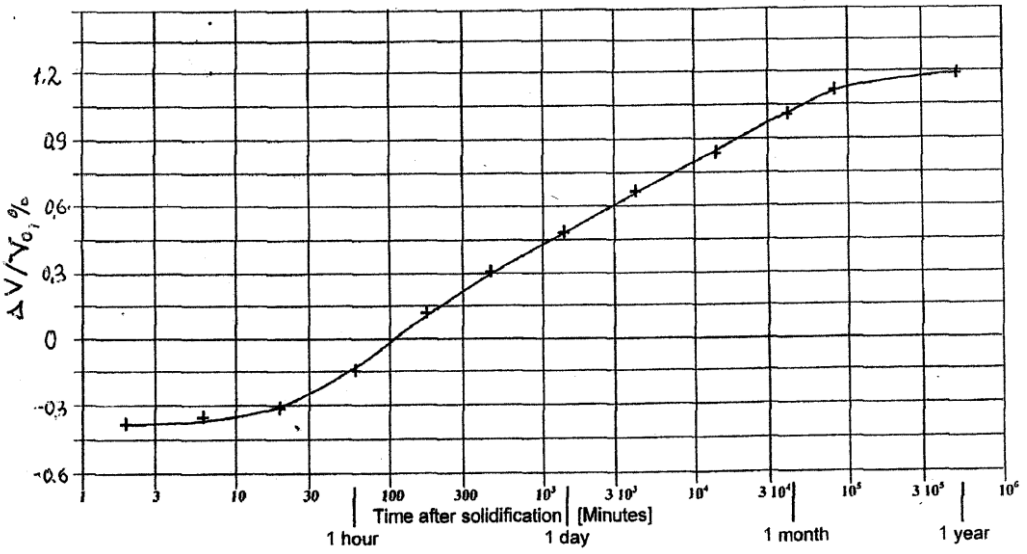

Source: Glasbrenner (2005).

Glasbrenner (2005) showed that solid phase transformations at the level of a crystal grain are responsible for the expansion of LBE after freezing. In their experiments, two phases were identified immediately after rapid solidification of LBE:

- β-phase: an intermetallic compound with 42 at.% Bi (at the freezing point) and a hexagonal closed packed structure;
- γ-phase: a solid solution of Pb in Bi (~0.4 at.% Pb) with a rhombohedra structure.

The β-phase formed at freezing is not stable at room temperature. With time it is partly transformed into a β-phase with a lower Bi content (about 35 at.%) and γ-phase (Takeda, 1997; Agostini, 2004). As the γ-phase needs much more space, the transformation produces an expansion of the material.

Measurements of this kind of LBE expansion performed at room temperature (Gröschel, 2005) showed that it is reduced by a factor of six when slow cooling is used to 60-90°C (333-363 K) in the place of quenching. Moreover, Takeda's experiments (1997) showed that the first period of a faster expansion (which ranges from two hours at 110°C [383 K] to three months at 20°C [293 K]) is followed by a second one with a lower expansion rate. The final increase in volume rarely exceeds 1.3% in one year.

On the other hand, Agostini (2004) and Zucchini (2005) showed that the consequences of LBE volume expansion caused by solid phase transformations (re-crystallisation) at freezing could lead to severe damages to pipeworks. The numerical and experimental studies described show that over-stressing due to LBE solid phase transformations and expansion in containment vessels, such as in the MEGAPIE target, must be taken into account during the design phase of the containment structures and can be managed by means of engineering rules. To avoid over-stressing of structures it is proposed to reduce:

- the height of each solid LBE layer;
- the presence of internal structures;
- the LBE yield strength.

Reduction of the LBE yield strength can be attained by raising the temperature at which re-crystallisation takes place and by adding, if possible, internal metallic balloons for expansion. The height of expanding LBE can be reduced by an appropriate freezing procedure, where the vessel is solidified in consecutive steps from bottom to top. Another important factor significantly affecting the yield stress is the strain rate. It has been shown that a realistic combination of the former effects can lead to a significant reduction of the LBE yield strength down to values of 3 MPa. As for the effect of γ-phase segregation, we could not evidence a significant difference between "aged" (3 months) and relatively "fresh" (5 h) samples (see Figures 2.4.3[a] and 2.4.3[b]). Further steps have to be made to compare the numerical approach with a validating experience and to formulate specific indications for the design.

Figure 2.4.3(a): Stress-strain graphs for the 5 h aged ("fresh") at 110°C LBE sample

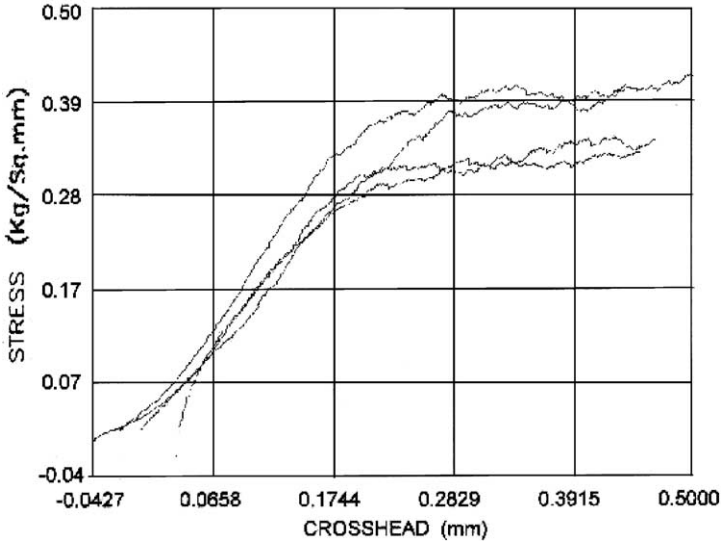

Source: Zucchini (2005).

Figure 2.4.3(b): Stress-strain graphs for the 3 months aged at 110°C LBE sample

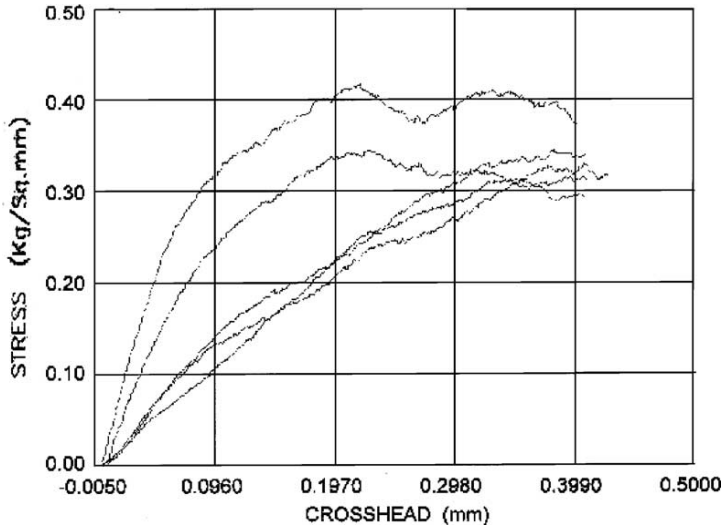

Source: Zucchini (2005).

2.5 Latent heat of melting at the normal melting point

Latent heat (enthalpy) of melting at normal pressure and melting temperature is an important calorimetric parameter, which correlates with some other thermodynamic properties and is used in analysis of melting and solidification of coolant material. It depends very weakly on the presence of impurities.

2.5.1 *Lead*

Values of the heat of melting of lead at the normal melting point (the enthalpy change on melting) was taken from about the same sources as for the melting temperature: Miller (1954), Hultgren (1973b), Lucas (1984a), Iida (1988), Kubaschewski (1993), Cheynet (1996), Stølen (1999) and Kirillov (2008). Cevolani (1998) took the Pb melting heat from Friedland (1966), who reproduced it from the chapter written by R.R. Miller (1954) in the well-known Lyon handbook (1954). This value was selected from an earlier handbook (Quill, 1950), and it was also given in many later handbooks and reviews. Stølen (1999) performed the critical assessment of the enthalpy of melting of many pure metals (including Pb) used as enthalpy standards at the normal atmospheric pressure. In the recent IAEA report (Kirillov, 2008) the same value is given as in the previous report (Bogoslovskaya, 2002) with a reference to the Russian reference book (Babichev, 1991). The selected database is presented in Table 2.5.1.

The selected values for lead lie in the range of 4.76-5.11 kJ mol^{-1}. The value deduced in the critical review (Stølen, 1999) is recommended for the latent heat of melting of the pure lead at the normal melting point:

$$Q_{M,0(Pb)} = 4.78 \pm 0.03\,\text{kJ mol}^{-1} = 23.07 \pm 0.14\,\text{kJ kg}^{-1} \tag{2.4}$$

Table 2.5.1: Selected database on the latent heat of melting of lead at the normal melting point

Reg. No.	Parameter	Measurement method	Estimated accuracy	Temperature range, K	Pressure range, Pa	Values	Ref.
5.1.1	Heat of melting	?	?	n/a	~10^5	5.89 cal/g	Miller (1954)
	Interpolation function: $Q_{M,0}$ = 24.7 kJ/kg = 5.11 kJ/mol						
	Comments: Unknown purity						
5.1.2	Heat of melting		42 J/mol	n/a	~10^5	4 799 J/mol	Hultgren (1973b)
	Interpolation function: $Q_{M,0}$ = 23.2 kJ/kg = 4.80 kJ/mol						
	Comments: Unknown purity						
5.1.3	Heat of melting	?	?	n/a	~10^5	5 109 J/mol	Lucas (1984a)
	Interpolation function: $Q_{M,0}$ = 24.7 kJ/kg = 5.11 kJ/mol						
	Comments: Unknown purity						
5.1.4	Heat of melting	?	?	n/a	~10^5	4.81 kJ/mol	Iida (1988)
	Interpolation function: $Q_{M,0}$ = 23.2 kJ/kg = 4.81 kJ/mol						
	Comments: Unknown purity						

Table 2.5.1: Selected database on the latent heat of melting of lead at the normal melting point *(cont.)*

Reg. No.	Parameter	Measurement method	Estimated accuracy	Temperature range, K	Pressure range, Pa	Values	Ref.
5.1.5	Heat of melting	?	(0.5 kJ/mol)	n/a	~10^5	4.8 kJ/mol	Kubaschewskin (1993)
	Interpolation function: $Q_{M,0}$ = 23 kJ/kg = 4.8 kJ/mol						
	Comments: Unknown purity						
5.1.6	Heat of melting	?	?	n/a	~10^5	4 761 J/mol	Cheynet (1996)
	Interpolation function: $Q_{M,0}$ = 23.0 kJ/kg = 4.76 kJ/mol						
	Comments: Unknown purity						
5.1.7	Heat of melting	n/a	22 J/mol	n/a	~10^5	4 782 J/mol	Stølen (1999)
	Interpolation function: $Q_{M,0}$ = 23.07 kJ/kg = 4.78 kJ/mol						
	Comments: Pure Pb.						
5.1.8	Heat of melting	?	?	n/a	~10^5	24.7 kJ/kg	Kirillov (2008)
	Interpolation function: $Q_{M,0}$ = 24.7 kJ/kg = 5.11 kJ/mol						
	Comments: Unknown purity						

2.5.2 Bismuth

The selected database for the latent heat of melting of bismuth is presented in Table 2.5.2. In Iida (1988) the value was reproduced from Kubaschewski (1979); in Cheynet (1996) it was extracted from the same source as that of Hultgren (1973b). As in the case of Pb, Cevolani (1998) took the Bi melting heat from Friedland (1966), who reproduced it from the chapter written by Miller (1954) in Lyon (1954). This value was taken from an earlier handbook (Quill, 1950). Therefore the values from Friedland (1966), Cheynet (1996) and Cevolani (1998) have not been included in the database.

In the case of Bi, the difference between the maximum and minimum values of the heat of melting is about 0.9 kJ mol^{-1}. The value deduced in the critical review of Stølen (1999) is recommended for the latent heat of melting of the pure bismuth at the normal melting point:

$$Q_{M,0(Bi)} = 11.15 \pm 0.06\,\text{kJ mol}^{-1} = 53.3 \pm 0.3\,\text{kJ kg}^{-1} \tag{2.5}$$

Table 2.5.2: Selected database on the latent heat of melting of bismuth at the normal melting point

Reg. No.	Parameter	Measurement method	Estimated accuracy	Temperature range, K	Pressure range, Pa	Values	Ref.
5.2.1	Heat of melting	?	?	n/a	~10^5	12.0 cal/g	Miller (1954)
	Interpolation function: $Q_{M,0}$ = 50.2 kJ/kg = 10.5 kJ/mol						
	Comments: Unknown purity						

Table 2.5.2: Selected database on the latent heat of melting of bismuth at the normal melting point (*cont.*)

Reg. No.	Parameter	Measurement method	Estimated accuracy	Temperature range, K	Pressure range, Pa	Values	Ref.
5.2.2	Heat of melting	?	209 J/mol	n/a	~10^5	11 297 J/mol	Hultgren (1973b)
	Interpolation function: $Q_{M,0}$ = 54.1 kJ/kg = 11.3 kJ/mol						
	Comments: Unknown purity						
5.2.3	Heat of melting	?	?	n/a	~10^5	10.5 kJ/mol	Lucas (1984a)
	Interpolation function: $Q_{M,0}$ = 50.2 kJ/kg = 10.5 kJ/mol						
	Comments: Unknown purity						
5.2.4	Heat of melting	?	0.2 kJ/mol	n/a	~10^5	10.89 kJ/mol	Kubaschewski (1979)
	Interpolation function: $Q_{M,0}$ = 52.1 kJ/kg = 10.9 kJ/mol						
	Comments: Unknown purity						
5.2.5	Heat of melting	?	(0.5 kJ/mol)	n/a	~10^5	11.3 kJ/mol	Kubaschewski (1993)
	Interpolation function: $Q_{M,0}$ = 54.1 kJ/kg = 11.3 kJ/mol						
	Comments: Unknown purity						
5.2.6	Heat of melting	n/a	54 J/mol	n/a	~10^5	11 145 J/mol	Stølen (1999)
	Interpolation function: $Q_{M,0}$ = 55.3 kJ/kg = 11.15 kJ/mol						
	Comments: Pure Bi						
5.2.7	Heat of melting	?	?	n/a	~10^5	54.7 kJ/kg	Bogoslovskaya (2002)
	Interpolation function: $Q_{M,0}$ = 54.7 kJ/kg = 11.4 kJ/mol						
	Comments: Unknown purity						
5.2.8	Heat of melting	?	(0.1 kJ/kg)	n/a	~10^5	50.15 kJ/kg	Kirillov (2008)
	Interpolation function: $Q_{M,0}$ = 50.15 kJ/kg = 10.48 kJ/mol						
	Comments: Unknown purity						

2.5.3 *LBE*

Values of the heat of melting of LBE at the normal atmospheric pressure were found in only three sources: Cevolani (1998), Bogoslovskaya (2002) and Kirillov (2008). In the review of Cevolani (1998), the calculated value is presented based on the heats of melting of lead and bismuth given in Friedland (1966). The recent IAEA compilations (Bogoslovskaya, 2002; Kirillov, 2008) provide slightly higher values. In the last compilation (Kirillov, 2008), a reference is given the earlier Russian reference book of Babichev (1991). The data from these sources are included in Table 2.5.3. Kopp's law yields $Q_{M,0(LBE)}$ = 36.4 kJ kg^{-1}, if the recommended above melting enthalpies of Pb and Bi are used for the calculation.

The mean value for the LBE melting heat of:

$$Q_{M,0(LBE)} = 8.04 \pm 0.06\,\text{kJ mol}^{-1} = 38.6 \pm 0.3\,\text{kJ kg}^{-1} \quad (2.6)$$

is the recommended value at the normal atmospheric pressure.

Table 2.5.3: Selected database on the latent heat of melting of LBE at the normal melting point

Reg. No.	Parameter	Measurement method	Estimated accuracy %	Temperature range, K	Pressure range, Pa	Values	Ref.
5.3.1	Heat of melting	?	?	n/a	~10^5	38 124 J kg^{-1}	Cevolani (1998)
	Interpolation function: $Q_{M,0}$ = 38.1 kJ/kg = 7.94 kJ/mol						
	Comments: Unknown purity						
5.3.2	Heat of melting	?	?	n/a	~10^5	38.8 kJ kg^{-1}	Bogoslovskaya (2002)
	Interpolation function: $Q_{M,0}$ = 38.8 kJ/kg = 8.08 kJ/mol						
	Comments: 44.5 wt.% Pb + 55.5 wt.% Bi, unknown purity						
5.3.3	Heat of melting	?	?	n/a	~10^5	38.9 kJ kg^{-1}	Kirillov (2008)
	Interpolation function: $Q_{M,0}$ = 38.9 kJ/kg = 8.09 kJ/mole						
	Comments: 44.5 wt.% Pb + 55.5 wt.% Bi, unknown purity						

2.6 Normal boiling point

Boiling temperature at normal atmospheric pressure (normal boiling point $T_{B,0}$) provides the upper boundary for the temperature range of operation of a liquid metal coolant. It is also an important parameter of interatomic forces, which correlates with some other thermodynamic properties.

2.6.1 Lead

For the boiling temperature of lead at the normal atmospheric pressure, the following sources were analysed: Lyon (1954, 1960), Kutateladze (1958), Hultgren (1973b), Iida (1988), Kubaschewski (1979, 1993), Bogoslovskaya (2002), Smithells (2004), Hammond (2004), Rashed (2008) and Kirillov (2008).

Miller (1954) in Lyon (1954) took the Pb boiling temperature from Ditchburn (1941). In Lyon (1960) the value is repeated from Lyon (1954). Kutateladze (1958) and Hultgren (1973b) did not give the explicit references. In Iida (1988) the value from Kubaschewski (1979) was reproduced, with the Pb boiling temperature probably taken from Hultgren (1973b). In the IAEA reports (Bogoslovskaya, 2002; Kirillov, 2008), the same value for the Pb boiling point is given, which was reproduced from Babichev (1991). In SMRB (Smithells, 2004) and in Kubaschewski (1993), the value was taken from Kubaschewski (1979).

The data for the boiling temperature of lead extracted from the above-mentioned sources are presented in Table 2.6.1.

Table 2.6.1: Selected database on the normal boiling temperature of lead

Reg. No.	Parameter	Measurement method	Estimated accuracy	Temperature range, K	Pressure range, Pa	Values	Ref.
6.1.1	Boiling temp.	Temperature vs. power	(10°C)	n/a	~10^5	1 737°C	Miller (1954)
	Interpolation function: $T_{B,0}$ = 2 010 K						
	Comments: Unknown purity						
6.1.2	Boiling temp.	Temperature vs. power	(10°C)	n/a	~10^5	1 740°C	Kutateladze (1958)
	Interpolation function: $T_{B,0}$ = 2 013 K						
	Comments: Unknown purity						
6.1.3	Boiling temp.	?	(5 K)	n/a	~10^5	2 023 K	Hultgren (1973b)
	Interpolation function: $T_{B,0}$ = 2 023 K						
	Comments: Unknown purity						
6.1.4	Boiling temp.	?	(5 K)	n/a	~10^5	1 750°C	Kubaschewski (1979)
	Interpolation function: $T_{B,0}$ = 2 023 K						
	Comments: Unknown purity						
6.1.5	Boiling temp.	Temperature vs. power	(5°C)	n/a	~10^5	1 749°C	Hammond (2004)
	Interpolation function: $T_{B,0}$ = 2 022 K						
	Comments: Unknown purity						
6.1.6	Boiling temp.	?	(5 K)	n/a	~10^5	2 024 K	Rashed (2008)
	Interpolation function: $T_{B,0}$ = 2 024 K						
	Comments: Unknown purity						
6.1.7	Boiling temp.	?	(5°C)	n/a	~10^5	1 745°C	Kirillov (2008)
	Interpolation function: $T_{B,0}$ = 2 018 K						
	Comments: Unknown purity						

The variation in the lead boiling temperature between the selected sources is more than for the melting temperature and is a large as 14 K. If the oldest sources (Miller, 1954; Kutateladze, 1958) are disregarded, then the most probable value of:

$$T_{B,0(Pb)} = 2021 \pm 3 \text{ K} \tag{2.7}$$

can be recommended for the boiling temperature of technically pure lead at the normal atmospheric pressure.

2.6.2 Bismuth

For the Bi boiling point the following sources were analysed: Lyon (1954, 1960), Kutateladze (1958), Howe (1961), Hultgren (1973b), Iida (1988), Kubaschewski (1979, 1993), Smithells (2004), Hammond (2004), Draggan (2007) and the IAEA reports (Bogoslovskaya, 2002; Kirillov, 2008).

Miller (1954) and Lyon (1954) took the Bi boiling temperature from Ditchburn (1941). In Lyon (1960) the value is repeated from Lyon (1954). Kutateladze (1958) and Hultgren (1973b) do not provide the explicit references. In Kubaschewski (1979) the same value was given as in Hultgren (1973b). Iida (1988) references to Tamamushi (1981). In SMRB (Smithells, 2004) the value was taken from Kubaschewski (1979). Kirillov (2008) give the same value as in Bogoslovskaya (2002) referencing to an earlier Russian reference book (Babichev, 1991). The CRC Handbook (Hammond, 2004) and the Encyclopedia of Earth (Draggan, 2007) recommend the same value as Kubaschewski (1979) without giving references. The sources on the normal boiling point of bismuth included in the selected database are presented in Table 2.6.2.

Table 2.6.2: Selected database on the normal boiling temperature of bismuth

Reg. No.	Parameter	Measurement method	Estimated accuracy	Temperature range, K	Pressure range, Pa	Values	Ref.
6.2.1	Boiling temp.	Temperature vs. power	(10°C)	n/a	~10^5	1 477°C	Miller (1954)
	Interpolation function: $T_{B,0}$ = 1 750 K						
	Comments: Unknown purity						
6.2.2	Boiling temp.	Temperature vs. power	(10°C)	n/a	~10^5	1 490°C	Kutateladze (1958)
	Interpolation function: $T_{B,0}$ = 1 763 K						
	Comments: Unknown purity						
6.2.3	Boiling temp.	?	?	n/a	~10^5	1 627°C	Howe (1961)
	Interpolation function: $T_{B,0}$ = 1 900 K						
	Comments: Unknown purity						
6.2.4	Boiling temp.	?	(5 K)	n/a	~10^5	1 837 K	Hultgren (1973b)
	Interpolation function: $T_{B,0}$ = 1 837 K						
	Comments: Pure Bi						
6.2.5	Boiling temp.	Temperature vs. power	10°C	n/a	~10^5	1 564°C	Kubaschewski (1979)
	Interpolation function: $T_{B,0}$ = 1 837 K						
	Comments: Unknown purity						
6.2.6	Boiling temp.	?	5 K	n/a	~10^5	1 833.15 K	Iida (1988)
	Interpolation function: $T_{B,0}$ = 1 833 K						
	Comments: Unknown purity						
6.2.7	Boiling temp.	?	(5 K)	n/a	~10^5	1 837 K	Hammond (2004)
	Interpolation function: $T_{B,0}$ = 1 837 K						
	Comments: Pure Bi						
6.2.8	Boiling temp.	?	(5 K)	n/a	~10^5	1 837 K	Draggan (2007)
	Interpolation function: $T_{B,0}$ = 1 837 K						
	Comments: Pure Bi						
6.2.9	Boiling temp.	?	(5 K)	n/a	~10^5	1 825 K	Kirillov (2008)
	Interpolation function: $T_{B,0}$ = 1 825 K						
	Comments: Technically pure Bi						

A significant level of dispersion exists in the data for the boiling point of bismuth with a range of about 150 K between the maximum and the minimum in the earlier handbooks: Lyon (1954, 1960), Kutateladze (1958), Howe (1961). The most reliable values are given by more recent sources. The following value and the uncertainty is recommended for the boiling temperature of the technically pure bismuth at the normal atmospheric pressure:

$$T_{B,0(Bi)} = 1831 \pm 6\,K \tag{2.8}$$

2.6.3 LBE

The boiling point of LBE at the normal atmospheric pressure is given in the handbook of Lyon (1954), and by Kutateladze (1958). The first references to the reports of the American Smelting and Refining Company, the second points out researchers of the Academy of Science of the USSR. However, both sources give the same value of $T_{B,0(LBE)}$ = 1 670°C (1 943 K). This value was reproduced later in other publications (Friedland, 1966; Hultgren, 1973a; Cevolani, 1998; Imbeni, 1999; Bogoslovskaya, 2002). In the recent collection of data by the IAEA (Kirillov, 2008) $T_{B,0(LBE)}$ = 1 638°C (1 911 K) is given. The recommendations included in the database are presented in Table 2.6.3.

Table 2.6.3: Selected database on the LBE normal boiling temperature

Reg. No.	Parameter	Measurement method	Estimated accuracy	Temperature range, K	Pressure range, Pa	Values	Ref.
6.3.1	Boiling temp.	?	?	n/a	~10^5	1 670°C	Miller (1954)
	Interpolation function: $T_{B,0}$ = 1 943 K						
	Comments: 44.5 wt.% Pb + 55.5 wt.% Bi, unknown purity						
6.3.2	Boiling temp.	?	?	n/a	~10^5	1 670°C	Kutateladze (1959)
	Interpolation function: $T_{B,0}$ = 1 943 K						
	Comments: 44.5 wt.% Pb + 55.5 wt.% Bi, unknown purity						
6.6.3	Boiling temp.	?	?	n/a	~10^5	1 638°C	Kirillov (2008)
	Interpolation function: $T_{B,0}$ = 1 911 K						
	Comments: 44.5 wt.% Pb + 55.5 wt.% Bi, unknown purity						

Based on the results of Table 2.6.3 the following value and uncertainty is recommended for the normal boiling temperature of the technically pure LBE:

$$T_{B,0(LBE)} = 1927 \pm 16\,K \tag{2.9}$$

2.7 Heat of vaporisation at the normal boiling point

The latent heat (enthalpy) of vaporisation is a measure of the cohesive or binding energy of atoms in a liquid metal (i.e. the energy required to break all the bonds associated with one of its atoms). Therefore, it correlates with surface tension and thermal expansion. Latent heat correlates with some other thermodynamic properties and used in analysis of boiling and condensation of liquid metal coolant. It depends very weakly on the presence of impurities.

2.7.1 Lead

The information on the latent heat of vaporisation of lead at the normal boiling point (the enthalpy change of boiling) was found in the following sources: Miller (1954), Friedland (1966), Lucas (1984a), Iida (1988), Kubaschewski (1979, 1993), Cevolani (1998), Bogoslovskaya (2002), Smithells (2004), Kirillov (2008) and Rashed (2008). Miller (1954) selected the Pb vaporisation heat from an earlier handbook (Quill, 1950). Friedland (1966) reproduced it from Miller (1954). Cevolani (1998) took the value from Friedland (1966). In two IAEA reports (Bogoslovskaya, 2002; Kirillov, 2008) the same value was reported, therefore only the second source was taken, which gives reference to Babichev (1991). The selected database is presented in Table 2.7.1.

Table 2.7.1: Selected database on the latent heat of vaporisation of lead at the normal boiling point

Reg. No.	Parameter	Measurement method	Estimated accuracy	Temperature range, K	Pressure range, Pa	Values	Ref.
7.1.1	Heat of boiling	?	(2 cal/g)	n/a	~10^5	204.6 cal/g	Miller (1954)
	Interpolation function: $Q_{B,0}$ = 856.7 kJ/kg = 177.5 kJ/mol						
	Comments: Unknown purity						
7.1.2	Heat of boiling	?	0.5 kcal/mol	n/a	~10^5	42.5 kcal/mol	Kubaschewski (1979)
	Interpolation function: $Q_{B,0}$ = 858.8 kJ/kg = 177.9 kJ/mol						
	Comments: Unknown purity						
7.1.3	Heat of boiling	?	(0.5 kJ/mol)	n/a	~10^5	177.5 kJ/mol	Lucas (1984a)
	Interpolation function: $Q_{B,0}$ = 856.8 kJ/kg = 177.5 kJ/mol						
	Comments: Unknown purity						
7.1.4	Heat of boiling	?	(1 kJ/mol)	n/a	~10^5	178 kJ/mol	Iida (1988)
	Interpolation function: $Q_{B,0}$ = 859 kJ/kg = 178 kJ/mol						
	Comments: Unknown purity						
7.1.5	Heat of boiling	?	?	n/a	~10^5	178.8 kJ/mol	Smithells (2004)
	Interpolation function: $Q_{B,0}$ = 862.9 kJ/kg = 178.8 kJ/mol						
	Comments: Unknown purity						
7.1.6	Heat of boiling	?	?	n/a	~10^5	856.8 kJ/kg	Kirillov (2008)
	Interpolation function: $Q_{B,0}$ = 856.8 kJ/kg = 177.5 kJ/mol						
	Comments: Unknown purity						
7.1.7	Heat of boiling	?	?	n/a	~10^5	178 kJ/mol	Rashed (2008)
	Interpolation function: $Q_{B,0}$ = 859 kJ/kg = 178 kJ/mol						
	Comments: Unknown purity						

The literature values are very close, with the difference between maximum and minimum values less than 1%. The mean value and the mean deviation are:

$$Q_{B,0(Pb)} = 177.9 \pm 0.04\,\text{kJ mol}^{-1} = 858.6 \pm 1.9\,\text{kJ kg}^{-1} \quad (2.10)$$

These values are recommended for the latent heat of vaporisation for pure lead at the normal boiling point.

2.7.2 Bismuth

The data on the latent heat of boiling of molten bismuth at the normal boiling point were found in the following sources: Miller (1954), Howe (1961), Friedland (1966), Lucas (1984a), Iida (1988), Kubaschewski (1979), Smithells (2004), Cevolani (1998), Bogoslovskaya (2002), Draggan (2007) and Kirillov (2008). The value presented in Howe (1961) was taken from Miller (1954). As in the case of Pb, Cevolani (1998) took the Bi vaporisation heat from Friedland (1966), who reproduced it from the chapter written by Miller (1954) in Lyon (1954). Therefore, the values from Howe (1961), Friedland (1966) and Cevolani (1998) were not included in the database. In the last edition of SMRB (Smithells, 2004), the Bi vaporisation latent heat was corrected in comparison with the value given in previous editions. The selected sources are presented in Table 2.7.2.

The recommended value for the latent heat of vaporisation of the technically pure bismuth at the normal boiling point and its deviation are:

$$Q_{B,0(Bi)} = 178.9 \pm 0.04\ \text{kJ mol}^{-1} = 856.2 \pm 1.9\ \text{kJ kg}^{-1} \tag{2.11}$$

Table 2.7.2: Selected database on the heat of boiling of bismuth at the normal boiling point

Reg. No.	Parameter	Measurement method	Estimated accuracy	Temperature range, K	Pressure range, Pa	Values	Ref.
7.2.1	Heat of boiling	?	?	n/a	~10^5	204.3 cal/g	Miller (1954)
	Interpolation function: $Q_{B,0}$ = 855.4 kJ/kg = 178.8 kJ/mol						
	Comments: Unknown purity						
7.2.2	Heat of boiling	?	2 kcal/mol	n/a	~10^5	42.8 kcal/mol	Kubaschewski (1979)
	Interpolation function: $Q_{B,0}$ = 856.7 kJ/kg = 179.1 kJ/mol						
	Comments: Unknown purity						
7.2.3	Heat of boiling	?	(1 kJ/mol)	n/a	~10^5	178.8 J/mol	Lucas (1984a)
	Interpolation function: $Q_{B,0}$ = 855.6 kJ/kg = 178.8 kJ/mol						
	Comments: Unknown purity						
7.2.4	Heat of boiling	?	(1 kJ/mol)	n/a	~10^5	179 kJ/mol	Iida (1988)
	Interpolation function: $Q_{B,0}$ = 856.5 kJ/kg = 179 kJ/mol						
	Comments: Unknown purity						
7.2.5	Heat of boiling	?	(8 kJ/kg)	n/a	~10^5 (?)	852 kJ/kg	Bogoslovskaya (2002)
	Interpolation function: $Q_{B,0}$ = 852 kJ/kg = 178.1 kJ/mol						
	Comments: Unknown purity						
7.2.6	Heat of boiling	?	?	n/a	~10^5	179.2 kJ/mol	Smithells (2004)
	Interpolation function: $Q_{B,0}$ = 857.5 kJ/kg = 179.2 kJ/mol						
	Comments: Unknown purity						

Table 2.7.2: Selected database on the heat of boiling of bismuth at the normal boiling point (*cont.*)

Reg. No.	Parameter	Measurement method	Estimated accuracy	Temperature range, K	Pressure range, Pa	Values	Ref.
7.2.7	Heat of boiling	?	(1 kJ/mol)	n/a	~10^5	179 kJ/mol	Draggan (2007)
	Interpolation function: $Q_{B,0}$ = 856.5 kJ/kg = 179 kJ/mol						
	Comments: Unknown purity						
7.2.8	Heat of boiling	?	(8 kJ/kg)	n/a	~10^5	857 kJ/kg	Kirillov (2008)
	Interpolation function: $Q_{B,0}$ = 857 kJ/kg = 179.1 kJ/mol						
	Comments: Unknown purity						

2.7.3 LBE

Information about the latent heat of vaporisation of LBE at the normal boiling point was found in only three sources: Cevolani (1998), Bogoslovskaya (2002) and Kirillov (2008). A value of 856.7 kJ kg^{-1} was published in the review of Cevolani (1998), who calculated it based on the heats of boiling of lead and bismuth presented in the handbook of Friedland (1966). In the IAEA compilations of Bogoslovskaya (2002) and Kirillov (2008) slightly different values were provided: Bogoslovskaya (2002) recommends 852 kJ kg^{-1}, while 862 kJ kg^{-1} is given by Kirillov (2008). Kopp's law yields $Q_{B,0(LBE)}$ = 857.3 kJ kg^{-1}, if the recommended above vaporisation enthalpies of Pb and Bi at their normal boiling points are used for the calculation. The sources included in the database are listed in Table 2.7.3.

Table 2.7.3: Selected database on the heat of vaporisation of LBE at the normal boiling point

Reg. No.	Parameter	Measurement method	Estimated accuracy %	Temperature range, K	Pressure range, Pa	Values	Ref.
7.3.1	Heat of boiling	?	?	n/a	~10^5	856 722 J/kg	Cevolani (1998)
	Interpolation function: $Q_{B,0}$ = 856.7 J/kg = 178.4 J/mol						
	Comments:						
7.3.2	Heat of boiling	?	?	n/a	~10^5	852 kJ/kg	Bogoslovskaya (2002)
	Interpolation function: $Q_{B,0}$ = 852 J/kg ≈ 178 J/mol						
	Comments: 44.5 wt.% Pb + 55.5 wt.% Bi, unknown purity						
7.3.3	Heat of boiling	?	?	n/a	~10^5	862 kJ/kg	Kirillov (2008)
	Interpolation function: $Q_{B,0}$ = 862 J/kg = 179.2 J/mol						
	Comments: 44.5 wt.% Pb + 55.5 wt.% Bi, unknown purity						

The following value is recommended for the latent heat of vaporisation of the pure LBE at the normal boiling point:

$$Q_{B,0(LBE)} = 178 \pm 1\,\text{kJ mol}^{-1} = 856 \pm 5\,\text{kJ kg}^{-1} \quad (2.12)$$

2.8 Saturation vapour pressure

The vapour pressure of a liquid metal as a function of temperature is an important property of coolants, which determines the dependence of the boiling temperature on pressure and heat-mass transfer in the cover gas space. It is directly related to the latent heat (enthalpy) of vaporisation. At the equilibrium between liquid and vapour phases on the liquid-vapour phase transition line, the Clausius-Clapeyron equation states (Iida, 1988):

$$\left(\frac{dp}{dT}\right)_{l\to v} = \frac{H_v - H_l}{T_B\left(V_v - V_l\right)} \tag{2.13}$$

where H_l and H_v are molar enthalpies, and V_l and V_v are molar volumes of the liquid and gas phases respectively. Assuming that the vapour behaves as a perfect gas and neglecting the volume of liquid in comparison with that of the gas, it can be obtained from Eq. (2.13) that the saturation vapour pressure (p_s) is:

$$p_s\left(T_B\right) = A \cdot \exp\left(-\frac{\Delta H_B}{R \cdot T_B}\right) \tag{2.14}$$

where A is a constant of integration and $\Delta H_B = H_v - H_l$ is the heat (enthalpy) of evaporation.

The above equation can provide approximate values for equilibrium vapour pressures over a wide range of temperature due to the relatively small variation of ΔH_B with temperature at low pressures. Closer fits of the experimental results can sometimes be obtained by adding supplementary temperature dependent terms, for instance, the following equation is frequently used:

$$\ln\left(p_s\left(T_B\right)\right) = A_1 + \frac{B}{T_B} + C \cdot \ln\left(T_B\right) \tag{2.15}$$

2.8.1 Lead

The data for the saturation vapour pressure of lead at different temperatures were found in the following publications: Lyon (1954, 1960), Friedland (1966), Hultgren (1973b), Iida (1988), Kubaschewski (1979, 1993), Cheynet (1996), Imbeni (1998) and in SMRB (Smithells, 1983, 2004).

Miller (1954) in Lyon (1954) used data on the Pb vapour pressure from Ditchburn (1941). Friedland (1966) presented plots based on the data from Lyon (1954). Hultgren (1973b) analysed different sources and presented a table with the recommended data in the range from the melting to the boiling temperature. Kubaschewski (1979) collected the data from Gross (1948), Eucken (1936) and Kelley (1935) and presented their own correlation. Iida (1988) reproduced the correlation of Kubaschewski (1979). Cheynet (1996) recompiled results communicated by himself earlier (1989) and by Chase (1985), Barin (1989) and Knacke (1991). Imbeni (1998) and SMRB (Smithells, 1983, 2004) recommended using the correlation of Kubaschewski (1979). The selected data sources are described in Table 2.8.1.

Figure 2.8.1(a) shows the saturated vapour pressure of molten lead taken from the above-cited literature and plotted as a function of temperature. At first glance, it can be seen that the agreement among the different sources is satisfactory. The correlation proposed by Kubaschewski and Alcock renormalised to obtain $p_s = 0.1013$ MPa at $T_{B,0(Pb)} = 2\,021$ K is thus recommended in Sobolev (2011) for the saturated vapour pressure of liquid lead. It can be presented as follows (where temperature is in kelvins):

$$p_{s(Pb)}\left[\text{Pa}\right] = 1.88 \times 10^{13} \cdot T^{-0.985} \cdot \exp(-23325/T) \tag{2.16}$$

The deviation of the selected literature data on the saturated vapour pressure of liquid lead from the recommended correlation (2.16) is plotted in Figure 2.8.1(b) (reproduced from Sobolev [2011]). One can see that, except for old data from Miller (1954), agreement is rather good: the deviation at temperatures higher than 1 100 K is less than 5% and increases to about 15% close to the melting temperature.

Using the selected data and Eq. (2.14) the following simplified correlation was also obtained (Sobolev, 2011):

$$p_{s(\mathrm{Pb})}[\mathrm{Pa}] = 5.76 \times 10^{9} \cdot \exp(-22131/T) \tag{2.16a}$$

The deviation of the selected database from the correlation (2.16a) is up to 18%.

2.8.2 *Bismuth*

The data on the saturation vapour pressure of liquid bismuth as a function of temperature were found in the following handbooks and compilations: Lyon (1954, 1960), Hove (1961), Hultgren (1973b), Kubaschewski (1979, 1993), Cheynet (1996), Imbeni (1998a) and SMRB (Smithells, 1983, 2004).

Miller (1954) in Lyon (1954) used data on the Bi vapour pressure from Ditchburn (1941). Hove (1961) based his compilation on the data presented in Lyon (1954), Smithells (1955), Hansen (1958) and other older sources. Hultgren (1973b) reported values selected on the basis of a critical assessment of many previously published data. Kubaschewski (1979) presented correlations for vapour pressure of Bi and Bi_2 with reference to a report of Brackett (1957). Iida (1988) reproduced the correlations of Kubaschewski (1979). Cheynet (1996) recompiled results communicated by himself earlier (1989) and by Chase (1985), Barin (1989) and Knacke (1991). Imbeni (1998) and SMRB (Smithells, 1983, 2004) recommended using the correlations of Kubaschewski (1979). The selected data are described in Table 2.8.2.

Table 2.8.1: Selected recommendations on the saturated vapour pressure of liquid lead

Reg. No.	Parameter	Measurement method	Estimated accuracy	Temperature range, K	Pressure range, Pa	Values	Ref.
8.1.1	Saturated pressure	?	?	1 260-1 884	10^{2}-10^{5}	–	Miller (1954)
	Interpolation function: $p_s = 5\,863 \times 10^{9} \cdot \exp(-22\,240/T)$						
	Comments: Unknown purity						
8.1.2	Saturated pressure	n/a	?	601-2 100	10^{-7}-10^{5}	–	Hultgren (1973b)
	Interpolation function: $p_s = 7.994 \times 10^{9} \cdot \exp(-22\,338/T)$						
	Comments: Unknown purity						
8.1.3	Saturated pressure	n/a	?	601-2 023	10^{-7}-10^{5}	–	Kubaschewski (1979)
	Interpolation function: $\log(p_s) = 2.1249 - 10\,130/T - 0.985 \cdot \log(T) + 11.16$						
	Comments: Unknown purity						
8.1.4	Saturated pressure	n/a	?	750-3 000	10^{-3}-10^{6}	–	Cheynet (1996)
	Interpolation function: $p_s = 5.343 \times 10^{9} \cdot \exp(-21\,955/T)$						
	Comments: Unknown purity						

Figure 2.8.1(a): Saturated vapour pressure of liquid lead versus temperature

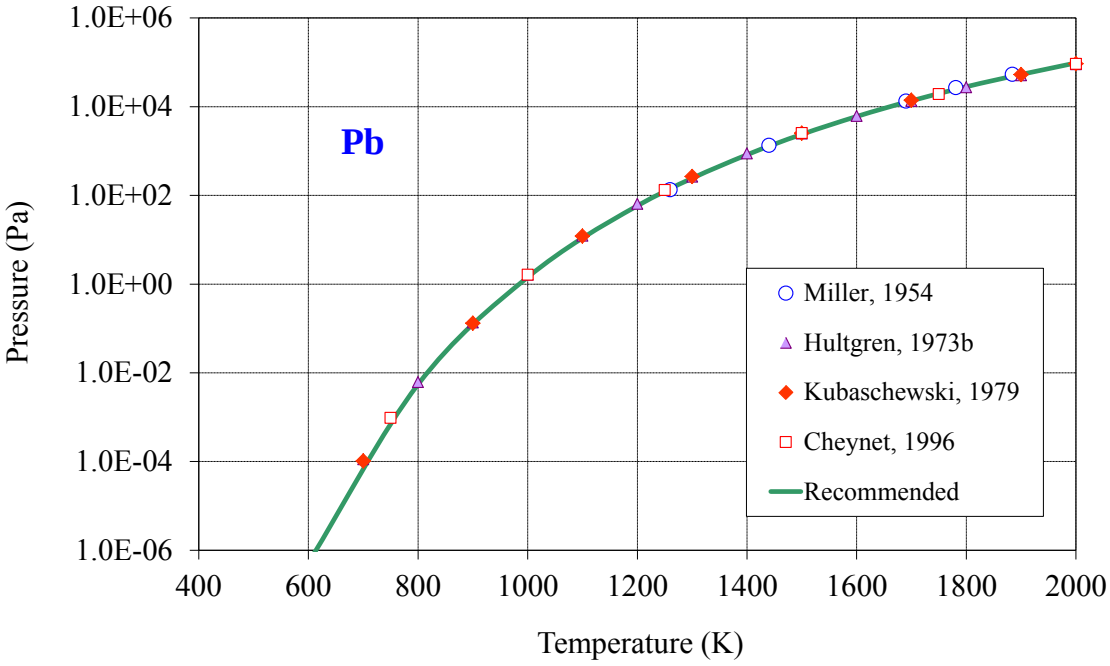

Source: Sobolev (2011).

Figure 2.8.1(b): Deviation of the selected literature data on the saturated vapour pressure of liquid lead from the recommended correlation (2.16)

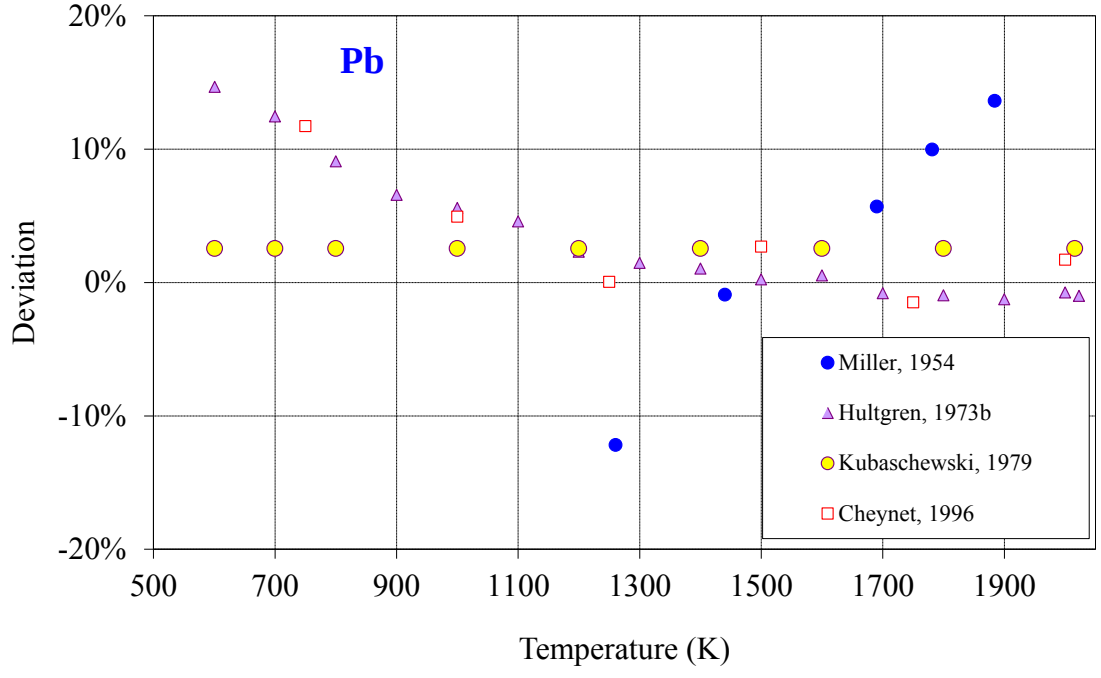

Source: Sobolev (2011).

Table 2.8.2: Selected recommendations on the saturated vapour pressure of liquid bismuth

Reg. No.	Parameter	Measurement method	Estimated accuracy	Temperature range, K	Pressure range, Pa	Values	Ref.
8.2.1	Saturated pressure	?	?	1 190-1 673	10^2-10^4	–	Miller (1954)
	Interpolation function: $p_s = 1.388 \times 10^{11} \cdot \exp(-24\,722/T)$						
	Comments: Unknown purity						
8.2.2	Saturated pressure	?	?	1 193-1 773	10^2-10^4	–	Hove (1961)
	Interpolation function: $p_s = 1.137 \times 10^{10} \cdot \exp(-21\,925/T)$						
	Comments: Unknown purity						
8.2.3	Saturated pressure	n/a	?	545-2 000	10^{-8}-10^5	–	Hultgren (1973b)
	Interpolation function: $p_s = 2.435 \times 10^{10} \cdot \exp(-22\,621/T)$						
	Comments: Unknown purity						
8.2.4	Saturated pressure	n/a	?	545-1 833	10^{-8}-10^5	–	Kubaschewski (1979)
	Interpolation function: $\log(p_{s(Bi1)}) = 2.1249 - 10\,400/T - 1.26*\log(T) + 12.35$ $\log(p_{s(Bi2)}) = 2.1249 - 10\,730/T - 3.2*\log(T) + 18.1$						
	Comments: Unknown purity						
8.2.5	Saturated pressure	n/a	?	750-2 000	10^{-3}-10^5	–	Cheynet (1996)
	Interpolation function: $p_s = 2.016 \times 10^{10} \cdot \exp(-22\,363/T)$						
	Comments: Unknown purity						

Figure 2.8.2(a) shows the values for the saturated vapour pressure of liquid bismuth from the above-cited sources plotted as a function temperature.

It can be seen that the agreement in temperature dependence given by the different sources is satisfactory. However, a significant scatter exists in values. Therefore, Eq. (2.14) was chosen to construct an empirical correlation allowing calculation of the saturated vapour pressure of liquid bismuth as a function of temperature. Using the selected data, the following correlation was obtained in Sobolev (2011), where temperature is in kelvins:

$$p_{s(\mathrm{Bi})}[\mathrm{Pa}] = 2.67 \times 10^{10} \cdot \exp(-22858/T) \qquad (2.17)$$

This correlation is recommended for temperatures up to the normal boiling point.

The deviation of the selected literature data for the saturated vapour pressure of liquid bismuth from the recommended correlation (2.17) is illustrated in Figure 2.8.2(b) (reproduced from Sobolev [2011]). One can see that a very large difference exists between the selected sources. The recommended correlation (2.17) gives the "best estimate" values with a maximum uncertainty of about 40%, if the earliest data presented in Miller (1954) are disregarded. Under these circumstances, it is not possible to develop a more precise correlation.

Figure 2.8.2(a): Saturated vapour pressure of liquid bismuth versus temperature

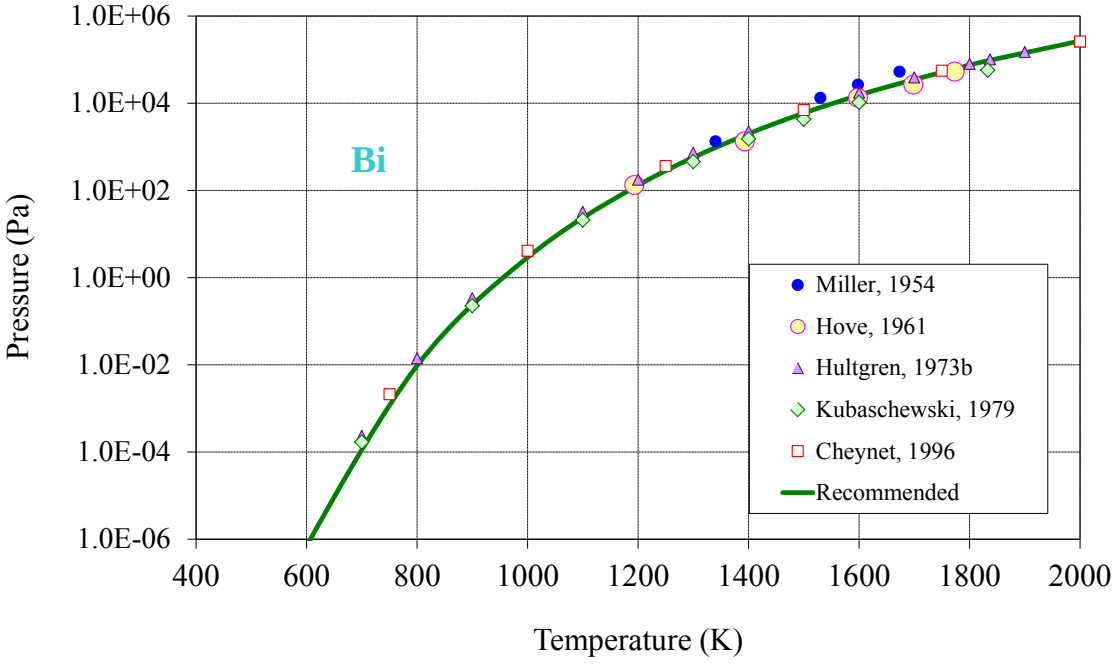

Source: Sobolev (2011).

Figure 2.8.2(b): Deviation of the selected literature data on the saturated vapour pressure of liquid bismuth from the recommended correlation (2.17)

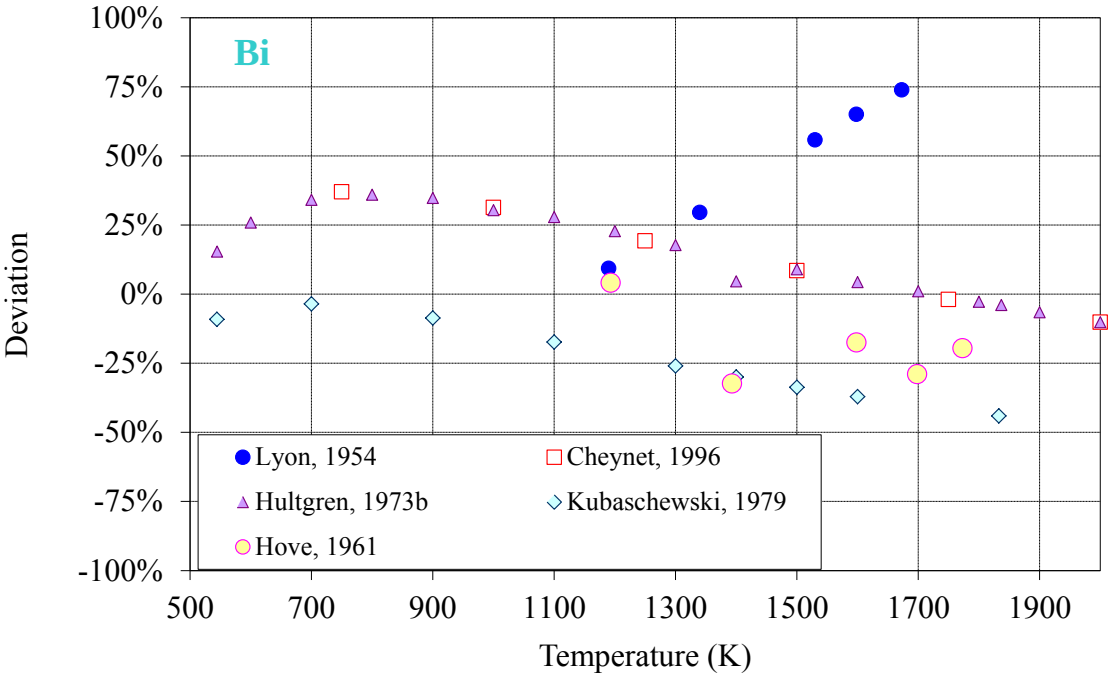

Source: Sobolev (2011).

2.8.3 LBE

Tupper (1991) studied polonium evaporation from LBE and published some experimental results on the LBE saturated vapour pressure at temperatures 235-268 and 520-550°C (508-541, 793-823 K). Later, Orlov (1997) published experimental values for the saturation pressure of the LBE vapour at equilibrium with the liquid phase at five different temperatures. However, both publications mentioned that a very large uncertainty in the pressure measurement exists at low temperatures (< 500°C ~ 773 K). The results of Orlov (1997) were reproduced later in Gromov (1999) and Cevolani (1998). New results have been communicated by Michelato (2003), Schuurmans (2005), and published by Ohno (2005). Cevolani (1998) fit a four-term logarithmic formula to the experimental data of Orlov (1997). Imbeni (1999) also used data of Orlov (1997), but recommended more simple correlations of type (2.14) and (2.15). Morita (2006) proposed a four-term correlation, which takes into account the formation of Bi_2 molecules in the LBE vapour phase. The sources included in the database are presented in Table 2.8.3 and their results are plotted in Figure 2.8.3(a).

Table 2.8.3: Selected database on the saturated vapour pressure of liquid LBE

Reg. No.	Parameter	Measurement method	Estimated accuracy	Temperature range, K	Pressure range, Pa	Values, Pa	Ref.
8.3.1	Saturated pressure	Evaporation/ condensation	?	523-823	10^{-6}-10^{-2}	–	Tupper (1991)
	Interpolation function: $p_s = 4.816 \times 10^7 \cdot \exp(-16\,429/T)$						
	Comments: 55.5 wt.% Bi + 44.5 wt.% Pb						
8.3.2	Saturated pressure	?	?	508-793	10^{-6}-10^{-3}	–	Orlov (1997)
	Interpolation function: $p_s = 1.207 \times 10^8 \cdot \exp(-16\,956/T)$						
	Comments: 55.5 wt.% Bi + 44.5 wt.% Pb						
8.3.3	Saturated pressure	(Direct)	?	723-923	10^{-7}-10^{-3}	–	Michelato (2003)
	Interpolation function: $p_s = 7.97 \times 10^{11} \cdot \exp(-30\,597/T)$						
	Comments:						
8.3.4	Saturated pressure	Direct	(10%)	673.15	n/a	3×10^{-5}	Schuurmans (2005)
	Interpolation function: $p_s = 1.138 \times 10^{10} \cdot \exp(-22\,597/T)$						
	Comments:						
8.3.5	Saturated pressure	Transpiration	5-25%	723-1 023	10^{-4}-10^{0}	–	Ohno (2005)
	Interpolation function: $p_s = 3.015 \times 10^9 \cdot \exp(-21\,447/T)$						
	Comments:						
8.3.6	Saturated pressure	n/a	(30-60%)	700-1 943	10^{-4}-10^{5}	–	Morita (2006)
	Interpolation function: $\ln(p_s) = 35.773 + 2.8006 \times 10^{-4} \cdot T - 24\,053/T - 1.6402 \cdot \ln(T)$						
	Comments: 55.5 wt.% Bi + 44.5 wt.% Pb						

Figure 2.8.3(a): Saturated vapour pressures of liquid LBE versus temperature

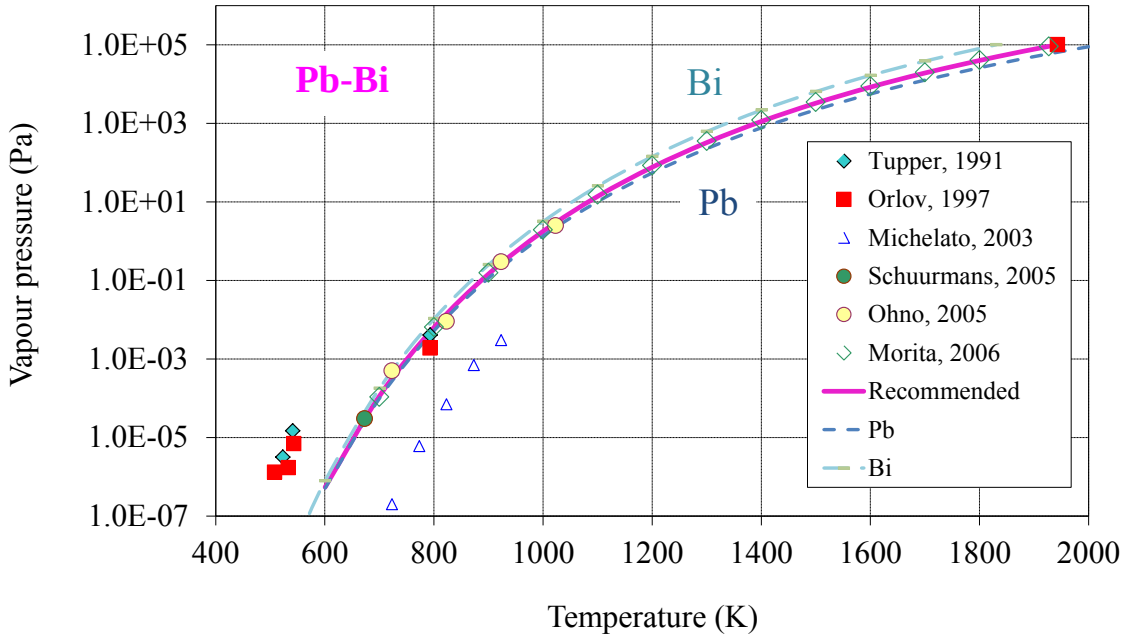

Source: Sobolev (2011).

Figure 2.8.3(a) illustrates that in the temperature range 650-1 940 K, the experimental values for LBE vapour pressure available from Tupper (1991), Orlov (1997), Schuurmans (2005) and Ohno (2005) are very close. The results of Michelato (2003) are systematically lower than the body of data. At temperatures of 500-550 K (227-277°C), Tupper (1991) and Orlov (1997), give a LBE vapour pressure that is an order of magnitude higher than the liquid-vapour equilibrium lines of lead and bismuth extrapolated to the lower temperatures. It should be noticed that at the expected level of saturated pressure (~10^{-8} Pa) it is very difficult to measure the pressure correctly, and overestimation by several orders of magnitude can often be obtained due to contamination of the liquid metal or of the experimental rig. Therefore it is proposed to not consider these points at present.

The selected data set was used to determine the coefficients for a simplified equilibrium Eq. (2.14), taking into account $p_s \approx 0.1$ MPa at the normal boiling temperature. The values of ΔH_B and A thus obtained were: $\Delta H_B = 187.5$ kJ mol^{-1} and $A = 12.2 \times 10^9$ Pa (Sobolev, 2011). The obtained value of ΔH_B is in a good agreement with the value of the latent heat of LBE vaporisation at the normal boiling point recommended in Section 2.7.3 (178 kJ mol^{-1}), taking into account the large uncertainty in the experimental results used for its calculation. The following simplified correlation for the saturation vapour pressure of molten LBE is recommended, where temperature is in kelvins:

$$p_{s(\mathrm{LBE})}[\mathrm{Pa}] = 1.22 \times 10^{10} \cdot \exp(-22552/T)\mathrm{K} \qquad (2.18)$$

This correlation is similar to those proposed above for lead and bismuth. The deviation of the selected experimental values from this correlation is illustrated in Figure 2.8.3(b). The maximum deviation in the temperature range of 673-1 927 K (400-1 654°C) is about ±60%. (There is no agreement at all at the lower temperatures.) In spite of this significant deviation, it was decided not to search for a more sophisticated formula, given the very large dispersion of data obtained from different sources.

Figure 2.8.3(b): Deviation of the selected data on the saturated vapour pressures of liquid LBE from the recommended correlation (2.18)

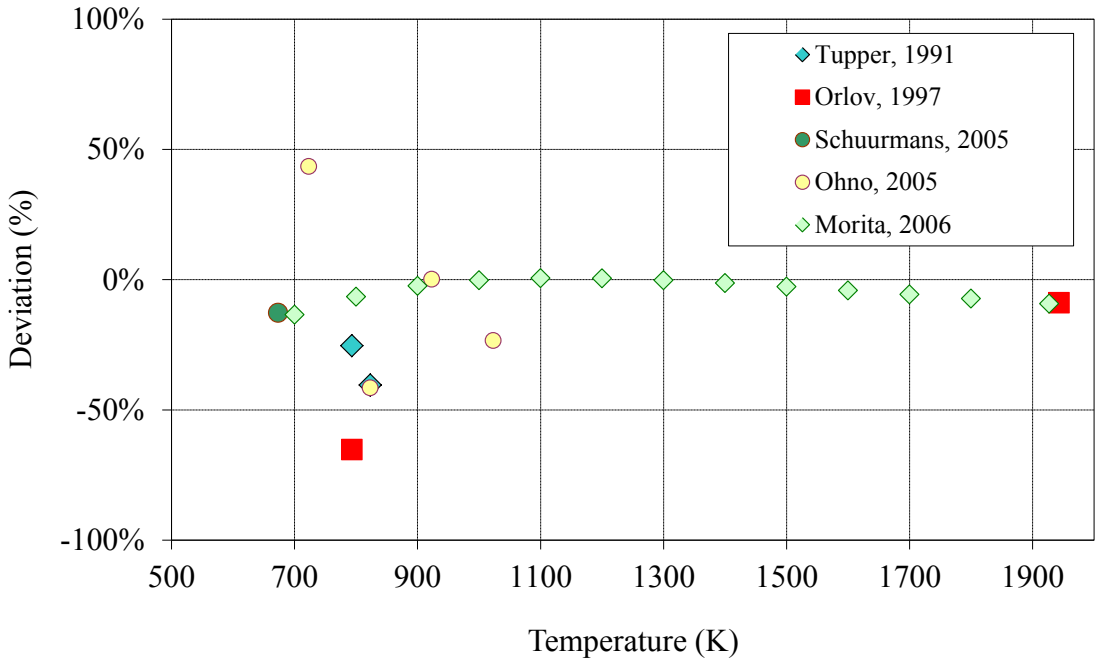

Source: Sobolev (2011).

2.9 Critical point parameters

The critical temperature (T_c), the critical pressure (p_c) and the critical density (ρ_c) (or the critical specific or molar volume V_c) are very important parameters for the development of an equation of state (EOS) and the extension of information on the available thermophysical data to higher temperatures and pressures. A very large uncertainty still exists in the critical temperatures, pressures and densities of heavy metals of interest. The critical compressibility Z_c is often used to compare different substances. It is determined as follows:

$$Z_c \equiv \frac{p_c \cdot V_c}{R \cdot T_c} = \frac{p_c \cdot M}{R \cdot T_c \cdot \rho_c} \tag{2.19}$$

where M is the molecular mass.

The following sources were analysed to prepare recommendations for the critical parameters of Pb, Bi and LBE in this handbook: Grosse (1961), Cahill (1968), Fortov (1975), Pottlacher (1990, 1998), Martynyuk (1983, 1998), Azad (2005), Morita (2006, 2007), Kirillov (2008) and Sobolev (2008a, 2008b, 2009, 2011).

2.9.1 *Lead*

Many experimental results were obtained for the Pb critical parameters, but with a large dispersion.

Grosse (1961) estimated the Pb critical temperature $T_{c(Pb)} \approx 5\,400$ K (2 127°C) with the principle of corresponding states using mercury (Hg) as the reference fluid and the enthalpy of the Pb vaporisation $\Delta H_{B,0}$ at the normal boiling point from an earlier source (Stull, 1956).

Martynyuk (1983) measured the Pb critical temperature and pressure using the pulse-heating method. Based on the experimental results and the Pb enthalpy and heat capacity values given in Hultgren (1973b), he obtained $T_{c(Pb)}$ = 4 460 K (4 187°C). Another value $T_{c(Pb)}$ = 4 140 K (3 867°C) was obtained using the correlation between T_c and the normal boiling enthalpy $\Delta H_{B,0}$ with the coefficients deduced from data for alkali metals and mercury. Then $p_{c(Pb)}$ = 160 MPa was found and $\rho_{c(Pb)}$ = 2 950 kg m^{-3} were calculated using few approximate semi-empirical correlations between T_c, p_c, $\Delta H_{B,0}$ and the density at the normal boiling point.

Pottlacher (1990) published a summary of experimentally determined and theoretically estimated parameters for the critical point of lead available in the literature at the time. Sixteen (16) sets of data as well as their own estimations were considered based on the experimental results obtained using the pulse-heating technique. Their summary shows that the experimental and theoretical data on the critical temperature of lead lie within the range of 3 584-6 000 K (3 311-5 727°C), while their own estimation yields $T_{c(Pb)}$ = 5 400 ± 400 K (5 127 ± 400°C). Their recommendations for the lead critical pressure and density are $p_{c(Pb)}$ = 250 ± 30 MPa and $\rho_{c(Pb)}$ = 3 200 ± 300 kg m^{-3}.

Martynyuk (1998) also estimated the Pb critical point parameters by determining parameters of the generalised Van der Waals (VdW) equation (see Section 2.15) using experimental data on the liquid phase density in the temperature range from the triple point to the normal boiling point and the heat of Pb vaporisation. The calculated results for lead were compared with the experimental data and estimations obtained by Martynyuk earlier (1983). Poor agreement between the theoretical and experimental values on the critical pressure and density was explained by very low accuracy of the experimental data. Values of $T_{c(Pb)}$ = 4 766 K (4 493°C), $p_{c(Pb)}$ = 90 MPa, $\rho_{c(Pb)}$ = 2 259 kg m^{-3} were recommended for the critical point of lead.

Azad (2005) estimated the critical temperatures of lead using a simple equation of state for the Pb liquid phase, based on the concept of internal pressure of liquids (see Section 2.15) and extrapolated to higher temperatures the data on the Pb density from Lyon (1954), on the Pb heat capacity from Kubaschewski (1979), Barin (1973) and on the sound velocity from Kleppa (1950), Gordon (1959) and Mustafin (1983). The obtained values of $T_{c(Pb)}$ = 3 369-3 391 K (3 096-3 118°C) are significantly lower than reported in other sources.

Morita (2007) calculated $T_{c(Pb)}$ = 4 756 K (4 483°C) with Kopp's correlation (1967) (bounding T_c with $\Delta H_{B,0}$) and $T_{c(Pb)}$ = 4 967 K (4 694°C) with Watson's method (1933) and Chawla's correlation (1981), which used an empirical relationship between T_c, $T_{B,0}$ and a liquid density at the normal boiling point. The enthalpy of Pb vaporisation at the normal boiling temperature was taken from Sobolev (2007) and the Pb density at the boiling point from Kirshenbaum (1961). Using the last value of T_c = 4 967 K (4 694°C), they also calculated the Pb critical density of $\rho_{c(Pb)}$ = 2 463 kg m^{-3} based on the law of "rectilinear diameter" (Cailletet, 1986). Then $p_{c(Pb)}$ = 103 MPa was obtained using the Pb critical compressibility of Z_c = 0.21 recommended in Martynyuk (1998).

In the recent IAEA publication (Kirillov, 2008) the following parameters were given for the critical point of lead: $T_{c(Pb)}$ = 5 000 ± 200 K (4 723 ± 200°C), $p_{c(Pb)}$ = 180 ± 30 MPa and $\rho_{c(Pb)}$ = 3 250 ± 100 kg m^{-3} with the reference to an older handbook published in the former USSR (Babichev, 1991).

A summary of data on the critical point parameters of lead extracted from the above-cited literature is presented in Table 2.9.1 (the data reviewed in Pottlacher [1990] are not included – only the final recommendation from this source is reproduced in the table).

Table 2.9.1: Summary of the critical point data for lead

Reference	T_c [K]	ρ_c [kg m^{-3}]	p_c [MPa]	Z_c
Grosse (1961) (calcul.)	5 400	–	–	–
Martynyuk (1983) (exper.)	4 460	2 950	160	0.30
Pottlacher (1990) (exper.)	5 400 ± 400	3 200 ± 300	250 ± 30	0.36
Martynyuk (1998) (calcul.)	4 776	2 259	90	0.2084
Pottlacher (1998) (calcul.)	4 961	2 720	(114)	(0.21)*
Azad (2005) (calcul.)	3 369-3 391	–	–	–
Morita (2007) (calcul. 1)	4 967	2 463	(103)	(0.21)*
Morita (2007) (calcul. 2)	4 756	–	–	–
Kirillov (2008) (handbook)	5 000 ± 200	3 250 ± 100	180 ± 30	0.276

* A rounded value taken from Martynyuk (1998).

From Table 2.9.1 one can see that the later results of Martynyuk (1998), Pottlacher (1998), Morita (2007) and Kirillov (2008) are in a rather good agreement. Concerning p_c, in Pottlacher (1998) and Morita (2007) its values were calculated with the same postulated Z_c taken from Martynyuk (1998), i.e. they are interdependent.

Taking into account a very large uncertainty in the estimations, the following values of the critical temperature, pressure and density of lead taken from the recent compilation of IAEA (Kirillov, 2008) are temporarily recommended in Sobolev (2011):

$$T_{c(Pb)} = 5000 \pm 200 \text{ K}, \rho_{c(Pb)} = 3250 \pm 100 \text{ kg m}^{-3}, p_{c(Pb)} = 180 \pm 30 \text{ MPa K} \quad (2.20)$$

2.9.2 Bismuth

Very limited results were found for the critical parameters of bismuth. Grosse (1961) estimated the critical temperature of bismuth ($T_{c(Bi)}$ = 4 620 K = 4 347°C) by applying the principle of corresponding states to the enthalpy of vaporisation and using Hg as the reference fluid.

Cahill (1968) compared the $T_{c(Bi)}$ value obtained in Grosse (1961) with one estimated ($T_{c(Bi)}$ ~ 5 000 K ≈ 4 727°C) by the method of rectilinear diameter (Cailletet, 1986) (which assumes that the average density of the liquid and the saturated vapour changes linearly with temperature).

Fortov (1975) calculated theoretical values for bismuth of the critical temperature ($T_{c(Bi)}$ = 4 200 K ≈ 3 927°C), pressure ($p_{c(Bi)}$ = 126 MPa) and density ($\rho_{c(Bi)}$ = 2 660 kg m^{-3}), based on traditional approaches such as the Grosse method described above and on the law of rectilinear diameter.

The experimental results were communicated by Martynyuk (1983), who estimated $T_{c(Bi)}$ = 3 780 K (3 507°C), $p_{c(Bi)}$ = 132 MPa and $\rho_{c(Bi)}$ = 3 010 kg m^{-3} from the pulse-heating experiments.

The critical temperature of bismuth estimated by Azad (2005), lower than recommended by other authors, is $T_{c(Bi)}$ = 2 042-2 106 K ≈ 1 769-1 883°C. His estimations were based on the concept of the internal pressure of liquids (see Section 2.15) and on the extrapolated to higher temperatures data on the Bi density, heat capacity and sound velocity from Lyon (1954), Strauss (1960), Kubaschewski (1979) and Jarzynski (1963).

Morita (2007) performed the estimation of the Bi critical parameters using the Watson method (1931) and the rectilinear diameter law with the liquid Bi density from Sobolev (2007) and obtained: $T_{c(Bi)}$ = 4 354 K and $\rho_{c(Bi)}$ = 2 705 kg m^{-3}. A similar estimation yields $T_{c(Bi)}$ = 4 420 K and $\rho_{c(Bi)}$ = 2 720 kg m^{-3}, and is performed with the density taken from Alchagirov (2003); with $Z_{c(Bi)}$ = 0.29 from Martynyuk (1983) $p_{c(Bi)}$ = 139 MPa was then obtained. Kopp's correlation (1967) yields $T_{c(Bi)}$ = 4 842 K, if the molar enthalpy of the Bi vaporisation at the normal boiling temperature is taken from Sobolev (2007).

In the recent IAEA compilation (Kirillov, 2008) the following parameters were presented for the critical point of bismuth with the reference to Babichev (1991): $T_{c(Bi)}$ = 5 100 ± 200 K, $p_{c(Bi)}$ = 150 MPa and $\rho_{c(Bi)}$ = 2 660 ± 200 kg m^{-3}.

A summary of the critical point parameters for bismuth, available in the analysed literature, is presented in Table 2.9.2.

Table 2.9.2: Summary of the critical point data of bismuth

Reference	T_c [K]	ρ_c [kg m^{-3}]	p_c [MPa]	Z_c
Grosse (1961) (calcul.)	4 620			
Cahill (1968) (calcul.)	5 000			
Fortov (1975) (calcul.)	4 200	2 660	126	0.28
Martynyuk (1983) (exper.)	3 780	3 010	132	0.29
Azad (2005) (calcul.)	2 042-2 106			
Morita (2007) (calcul. 1)	4 354	2 705		
Morita (2007) (calcul. 2)	4 420	2 720	(139)	(0.29)*
Morita (2007) (calcul. 3)	4 842			
Kirillov (2008) (handbook)	5 100 ± 200	2 660 ± 200	150	0.278

* A value taken from Martynyuk (1983).

Based on the results summarised above and disregarding a very low $T_{c(Bi)}$ given by Azad (2005), the following set of critical parameters can be recommended for Bi (Sobolev, 2011):

$$T_{c(Bi)} = 4500 \pm 500 \text{ K}, \rho_{c(Bi)} = 2800 \pm 200 \text{ kg m}^{-3}, p_{c(Bi)} = 135 \pm 15 \text{ MPa K} \quad (2.21)$$

2.9.3 *LBE*

No publications are currently available in the open literature with the results of measurement of the LBE critical parameters. Only three theoretical estimations were found: one in Azad (2005) and two others in Morita (2006, 2007).

Azad (2005) estimated the LBE critical temperatures using a simple equation of state (EOS) for the liquid phase based on the concept of internal pressure of liquids (see Section 2.15) and assuming that data on the LBE density, heat capacity and sound velocity are known. The gas phase was described with the perfect gas equation. The LBE melt density was taken from Alchagirov (2003). The LBE heat capacity and the sound velocity were calculated with Kopp's law using literature data on heat capacities and sound velocities of lead and bismuth from Hultgren (1973b), Kubaschewski (1979), Mustafin (1983) and Jarzynski (1963). The recommended calculated values for the LBE critical temperature and pressure are $T_{c(LBE)}$ = 2 411 K (2 138°C) and $p_{c(LBE)}$ = 244 MPa.

Morita (2006) used a method proposed by Martynyuk (1998), which is based on the generalised equation of Van der Waals (see Section 2.15). In Martynyuk (1998) its

constants are expressed through the melting and boiling temperatures, the latent heats of melting and boiling, and the liquid molar volume in the melting and boiling points. The LBE liquid density was taken from Alchagirov (2003) and the heat of the LBE vaporisation was calculated using the Clapeyron equation and the estimated vapour pressure curve. The following critical parameters of LBE were obtained: $T_{c(LBE)}$ = 4 890 K (4 617°C), $\rho_{c(LBE)}$ = 2 170 kg m^{-3} and $p_{c(LBE)}$ = 87.8 MPa.

In Morita (2007), $T_{c(LBE)}$ = 4 880 K was obtained with Kopp's correlation (1967), using the LBE evaporation enthalpy at the normal boiling temperature from Morita (2006). Using the Watson method $T_{c(LBE)}$ = 4 750 K was obtained with the liquid LBE density at the normal boiling temperature from Alchagirov (2003) and $T_{c(LBE)}$ = 4 720 K with the LBE density taken from Sobolev (2007).

A summary of the critical parameters of LBE is given in Table 2.9.3.

Table 2.9.3: Summary of the critical point data for LBE

Reference	T_c [K]	ρ_c [kg m^{-3}]	p_c [MPa]	Z_c
Morita (2006) (calcul.)	4 890	2 170	87.8	0.207
Azad (2005) (calcul.)	2 411	–	244	–
Morita (2007) (calcul. 1)	4 880	–	–	–
Morita (2007) (calcul. 2)	4 720, 4 750	–	–	–

It should be noted that the critical temperature of LBE obtained by Azad (2005) is more than by factor 2 lower and the critical pressure is 3 times higher than those calculated by Morita (2006, 2007). One of the reasons for a lower critical temperature (obtained in the calculations of Azad) may be the use of an incorrect temperature dependence of the sound velocity (he calculated the sound velocity in molten LBE based on Vegard's law [Azad, 2005], using the extrapolation of Mustafin [1983] for the sound velocity in lead and the extrapolation of the data of Jarzynski [1963] for the sound velocity in bismuth).

A very large uncertainty still exists in the estimation of the LBE critical parameters. More detailed analysis and comparison with other heavy metals is needed in order to provide recommendations. In the absence of better data, the following rounded values are recommended for approximate estimations with maximum uncertainties of the critical parameters of Pb and Bi (Sobolev, 2011):

$$T_{c(LBE)} = 4800 \pm 500 \text{ K}, \rho_{c(LBE)} = 2200 \pm 200 \text{ kg m}^{-3}, p_{c(LBE)} = 160 \pm 70 \text{ MPa K} \qquad (2.22)$$

2.10 Surface tension

A tension of liquid surfaces is related to tendency to minimise their surface energy. Quantitatively, the surface tension is characterised by the surface free energy per unit surface area. It is of primary importance in determination of wetting of solid surfaces by liquid metal coolants. The surface tension depends strongly on the presence of impurities. As most soluble elements are highly surface active in liquid metals, the accurate determination of the surface tension for pure liquid metals or alloys is very difficult, especially at high temperatures.

The surface tension (σ) decreases with temperature and reduces to zero at the critical temperature (T_c) where difference disappears between liquid and gas phases. According to Eötvös' law (see Iida [1988], Agrawal [1989]) for normal liquids, this relationship can be described by formula:

$$\sigma = K_\sigma \cdot V_a^{2/3} \cdot (T_c - T) \qquad (2.23)$$

where V_a is the molar volume. The coefficient K_σ is about the same for normal liquid metals.

Keene (1993) reviewed many data on the surface tension of pure metals and concluded that the temperature dependence of the surface tension is linear for most liquid metals:

$$\sigma = a + b \cdot T \tag{2.24}$$

2.10.1 Lead

Using the analysis of Imbeni (1998) as a starting point, the following sources were considered to include in the database for the surface tension of molten lead as a function of temperature at the normal atmospheric pressure: Miller (1954), Friedland (1966), Allen (1972), Kasama (1976), Smithells (1983, 2004), Lucas (1984a), Jauch (1986), Iida (1988) and Keene (1993). Moreover, later data from Eustathopoulos (1996), Novakovic (2002), Bogoslovskaya (2002), Alchagirov (2003), Kirillov (2000a, 2008) and Plevachuk (2008) were analysed.

Miller (1954) in Lyon (1954) presented the smoothed curve data from Hogness (1921). Friedland (1966) references to Lyon (1954) and Hogness (1921). Kasama (1976) made a review of the previous measurements and measured the Pb surface tension with the sessile drop method. The Smithells Metals Reference Book (1983, 2004) reproduced a relationship from the book of Allen (1972), who took it from Harvey (1961). Lucas (1984a) used the correlation proposed by Joud (1972). Iida (1988) reproduced a correlation from Kasama (1976). Keene (1993) reviewed many previous works to obtain values of the coefficients in his linear empirical correlation. The coefficients obtained by him based on all considered sources are very close to those recommended by Jauch (1996). Eustathopoulos (1996) revised the previous article of Lucas (1984a), but recommended the same correlation. Novakovic (2002) and Alchagirov (2003) measured the surface tension of very high purity Pb with the sessile drop method in the range of 623-773 K. Kirillov (2000a) gives a table of the recommended data without reference to sources. The data recommended in the IAEA reports (Bogoslovskaya, 2002; Kirillov, 2008) are very similar to those presented in Kirillov (2000a), but have slightly higher values. Kirillov (2008) references to Pokrovsky (1969), however, extrapolate their correlation from 773 K, given in the original source, up to 1 273 K. Plevachuk (2008) measured the Pb surface tension with the "large" drop method as a reference for measurement of the LBE surface tension. The selected sources are described in Table 2.10.1.

Table 2.10.1: Selected database on liquid lead surface tension at normal pressure

Reg. No.	Parameter	Measurement method	Estimated accuracy %	Temperature range, K	Pressure range, Pa	Values	Ref.
10.1.1	Surface tension	Maximum drop pressure	(5-10)	623-773	~10^5	–	Miller (1954)
	Interpolation function: $\sigma = (490.2 - 0.077 \cdot T) \times 10^{-3}$ N m^{-1}						
	Comments: Unknown purity						
10.1.2	Surface tension	Maximum bubble pressure	(5)	601-(873)	~10^5	–	Harvey (1961)
	Interpolation function: $\sigma = (548.3 - 0.133 \cdot T) \times 10^{-3}$ N m^{-1}						
	Comments: (> 99.9% Pb)						

Table 2.10.1: Selected database on liquid lead surface tension at normal pressure (*cont.*)

Reg. No.	Parameter	Measurement method	Estimated accuracy %	Temperature range, K	Pressure range, Pa	Values	Ref.
10.1.3	Surface tension	Drop weight	(5)	623-773	~10^5	–	Pokrovsky (1969)
	Interpolation function: $\sigma = (484.0 - 0.064 \cdot T) \times 10^{-3}$ N m^{-1}						
	Comments: (> 99.9% Pb)						
10.1.4	Surface tension	Sessile drop	2	620-1 280	~10^5	–	Joud (1972)
	Interpolation function: $\sigma = (528.1 - 0.11 \cdot T) \times 10^{-3}$ N m^{-1}						
	Comments: 99.9999% Pb						
10.1.5	Surface tension	Sessile drop	2	601-1 373	~10^5	–	Kasama (1976)
	Interpolation function: $\sigma = (548.3 - 0.128 \cdot T) \times 10^{-3}$ N m^{-1}						
	Comments: 99.99% Pb						
10.1.6	Surface tension	(Sessile drop)	2	601-1 250	~10^5	–	Jauch (1986)
	Interpolation function: $\sigma = (525.9 - 0.113 \cdot T) \times 10^{-3}$ N m^{-1}						
	Comments: (99.999% Pb)						
10.1.7	Surface tension	n/a	(3)	601-1 373	~10^5	–	Keene (1993)
	Interpolation function: $\sigma = (564.7 - 0.156 \cdot T) \times 10^{-3}$ N m^{-1}						
	Comments: Pure Pb						
10.1.8	Surface tension	Sessile drop	(0.1)	623-773	~10^5	–	Novakovic (2002)
	Interpolation function: $\sigma = (501.8 - 0.0861 \cdot T) \times 10^{-3}$ N m^{-1}						
	Comments: 99.9999 wt.% Pb						
10.1.9	Surface tension	Sessile drop	1	623-773	~10^5	–	Alchagirov (2003)
	Interpolation function: $\sigma = (492.8 - 0.080 \cdot T) \times 10^{-3}$ N m^{-1}						
	Comments: 99.9985 wt.% Pb						
10.1.10	Surface tension	n/a	(5-10)	603-1 273	~10^5	–	Kirillov (2008)
	Interpolation function: $\sigma = (484.4 - 0.064 \cdot T) \times 10^{-3}$ N m^{-1}						
	Comments: (> 99.9 wt.% Pb)						
10.1.11	Surface tension	"Large" drop	0.5	403-1 000	~10^5	–	Plevachuk (2008)
	Interpolation function: $\sigma = (448.05 - 0.0799 \cdot T) \times 10^{-3}$ N m^{-1}						
	Comments: (99.98 wt.% Pb)						

Figure 2.10.1(a) (reproduced from Sobolev [2011]) shows the values of surface tension of lead taken from the selected sources. The maximum difference of ±(4-5)% exists between the surface tension values given by different sources at $T < 1\,300$ K (1 027°C). In the region of the melting temperature the lowest values are given by Miller (1954) and the highest by Keene (1993). The values calculated using the correlation given in Joud (1972), Jauch (1986) and Plevachuk (2008) are very close in this temperature range. At higher temperatures, the scatter increases. The temperature slopes of the different correlations can differ for up to ±50%.

Figure 2.10.1(a): Liquid lead surface tension as a function of temperature

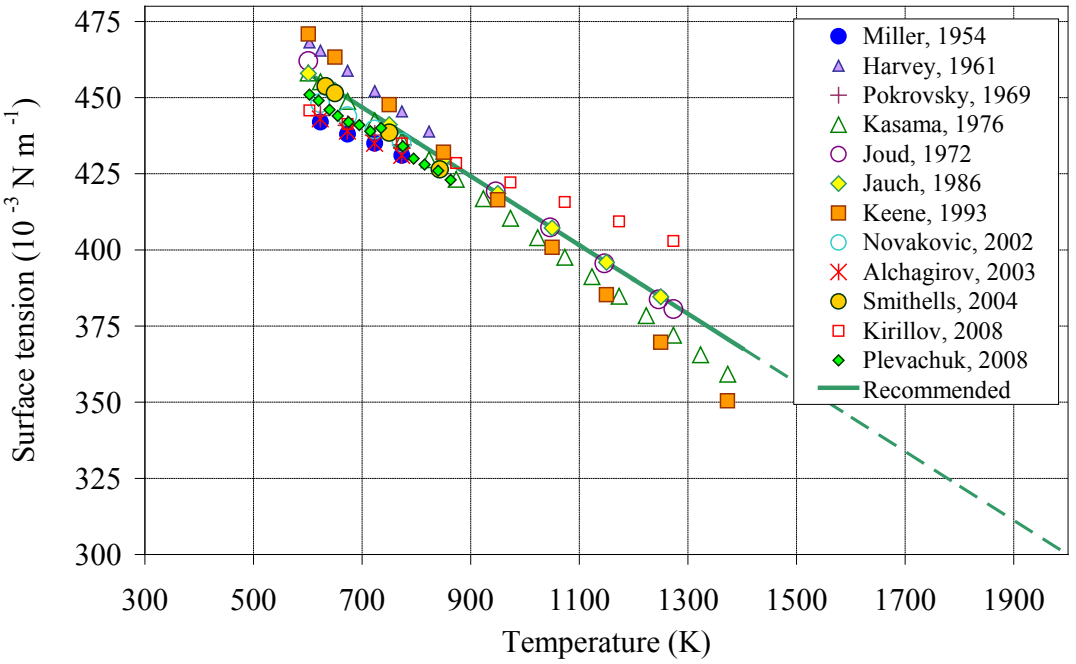

Source: Sobolev (2011).

The correlation proposed by Jauch (1986) allows a compromise represented by the following formula where temperature is in kelvins:

$$\sigma_{Pb}\left[\mathrm{Nm^{-1}}\right] = (525.9 - 0.113 \cdot T) \times 10^{-3} \tag{2.25}$$

Unfortunately, the temperature range of validity is not reported in most of the literature sources. In light of this, a conservative validity range of from the melting temperature of 600.6 K to 1 300 K (327.6-1 027°C) is considered acceptable. The maximum deviation of the selected literature data on the molten lead surface tension from the recommended correlation (2.25) is less than 5% (see Figure 2.10.1[b] reproduced from Sobolev [2011]) in this temperature range.

2.10.2 Bismuth

As in the case of lead, the results of analysis of Imbeni (1998) were used as a starting point. The data on the bismuth surface tension as a function of temperature were analysed from Lyon (1954), Howe (1961), Pokrovsky (1969), Allen (1972), the Smithells Metals Reference Book (1955, 2004), Kasama (1976), Lang (1977), Lucas (1984a), Iida (1988), Keene (1993), Eustathopoulos (1996), Novacovic (2002), Alchagirov (2003) and Plevachuk (2008).

Figure 2.10.1(b): Deviation of the selected database on the molten lead surface tension from the recommended correlation (2.25)

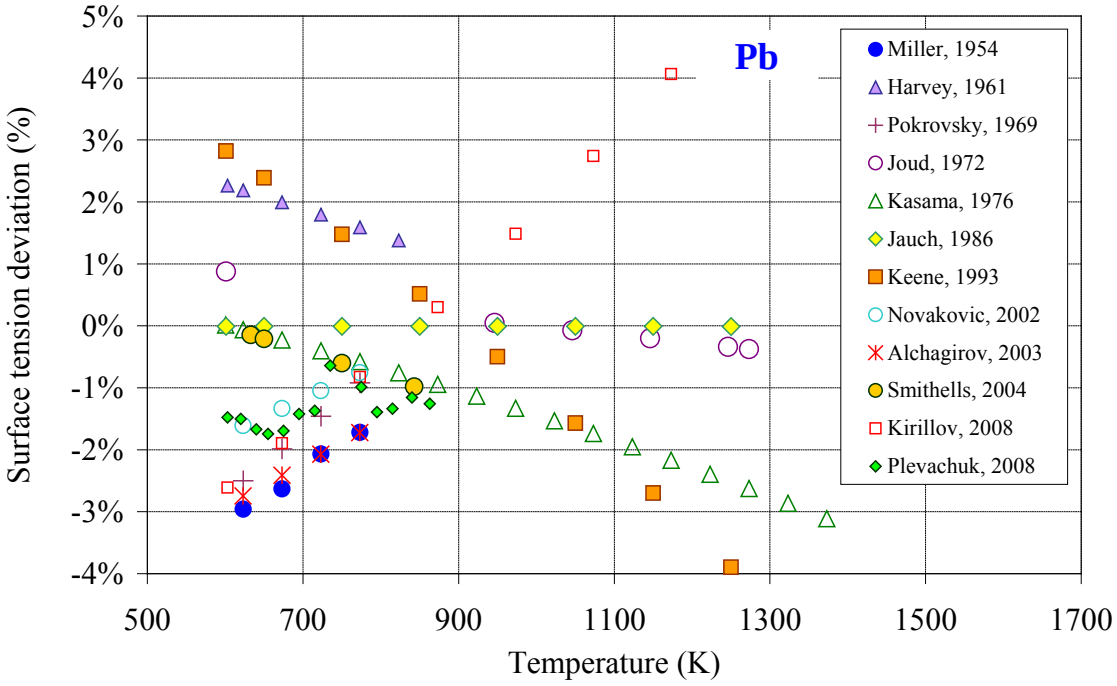

Source: Sobolev (2011).

Miller (1954) reproduced the Bi surface tension values from Krynitsky (1933) replotted from the data of Hogness (1921). Howe (1961) took two points from the data cited by Miller (1954) in Lyon (1954) and one supplementary point from Smithells (1955). Pokrovsky (1969) measured the surface tension of Bi with the drop weight method in the range of 573-773 K (300-500°C). Lucas (1984a) used two sets of the experimental data taken from Lang (1977) to obtain the coefficients of his linear correlation. Iida (1988) reproduced the constants of the linear correlation from Kasama (1976), who took the Bi surface tension at the melting temperature from Hogness (1921) and its temperature coefficient from other earlier sources. In the last edition of the Smithells Metals Reference Book (2004) a linear correlation was reproduced from the review of Allen (1972), who cited Addison (1963) as the source. Keene (1993) recommended a linear correlation with the coefficients obtained from an analysis of many previous sources, however (as in the case of lead), in his final recommendation, he based his recommendation on only six sources giving the highest values of the Bi surface tension. Eustathopoulos (1996) revised the previous article of Lucas (1984a), but recommended the same correlation. Novakovic (2002) and Alchagirov (2003) measured the surface tension of very high purity Bi with the sessile drop method in the range of 623-773 K. Plevachuk (2008) measured the Bi surface tension with the "large" drop method up to about 1 000 K. The sources included in the selected database are described in Table 2.10.2.

Figure 2.10.2(a) (reproduced from Sobolev [2011]) shows the analysed data on the surface tension of the molten bismuth in the range of temperature.

Table 2.10.2: Selected database on liquid bismuth surface tension at normal pressure

Reg. No.	Parameter	Measurement method	Estimated accuracy %	Temperature range, K	Pressure range, Pa	Values	Ref.
10.2.1	Surface tension	n/a	(5-10)	573-1 053	~10^5	–	Howe (1961)
	Interpolation function: $\sigma = (414.3 - 0.0667 \cdot T) \times 10^{-3}$ N m^{-1}						
	Comments: (> 99.9% Bi)						
10.2.2	Surface tension	Drop weight	(5)	573-773	~10^5	–	Pokrovsky (1969)
	Interpolation function: $\sigma = (417.2 - 0.0766 \cdot T) \times 10^{-3}$ N m^{-1}						
	Comments: (> 99.9% Bi)						
10.2.3	Surface tension	?	(5-10)	573-(773)	~10^5	–	Allen (1972)
	Interpolation function: $\sigma = (416.1 - 0.07 \cdot T) \times 10^{-3}$ N m^{-1}						
	Comments: (> 99.9% Bi)						
10.2.4	Surface tension	Sessile drop	2	573-(773)	~10^5	–	Kasama (1976)
	Interpolation function: $\sigma = (448.7 - 0.13 \cdot T) \times 10^{-3}$ N m^{-1}						
	Comments: (> 99.9% Bi)						
10.2.5	Surface tension	Sessile drop	2	558-992	~10^5	–	Lang (1977)
	Interpolation function: $\sigma = (420.4 - 0.089 \cdot T) \times 10^{-3}$ N m^{-1}						
	Comments: 99.999% Bi						
10.2.6	Surface tension	Maximum bubble pressure	4	619-838	~10^5	–	Lang (1977)
	Interpolation function: $\sigma = (414.1 - 0.070 \cdot T) \times 10^{-3}$ N m^{-1}						
	Comments: 99.999% Bi						
10.2.7	Surface tension	n/a	(3)	423-573	~10^5	–	Keene (1993)
	Interpolation function: $\sigma = (441.7 - 0.097 \cdot T) \times 10^{-3}$ N m^{-1}						
	Comments: Pure Bi						
10.2.8	Surface tension	Sessile drop	(0.1)	623-773	~10^5	–	Novakovic (2002)
	Interpolation function: $\sigma = (394.3 - 0.0502 \cdot T) \times 10^{-3}$ N m^{-1}						
	Comments: 99.9999 wt.% Bi						
10.2.9	Surface tension	Sessile drop	1	623-773	~10^5	–	Alchagirov (2003)
	Interpolation function: $\sigma = (421.7 - 0.0821 \cdot T) \times 10^{-3}$ N m^{-1}						
	Comments: 99.98 wt.% Bi						
10.2.10	Surface tension	"Large" drop	0.5	560-960	~10^5	–	Plevachuk (2008)
	Interpolation function: $\sigma = (410.9 - 0.0694 \cdot T) \times 10^{-3}$ N m^{-1}						
	Comments: 99.98 wt.% Bi						

Figure 2.10.2(a): Bismuth surface tension as a function of temperature

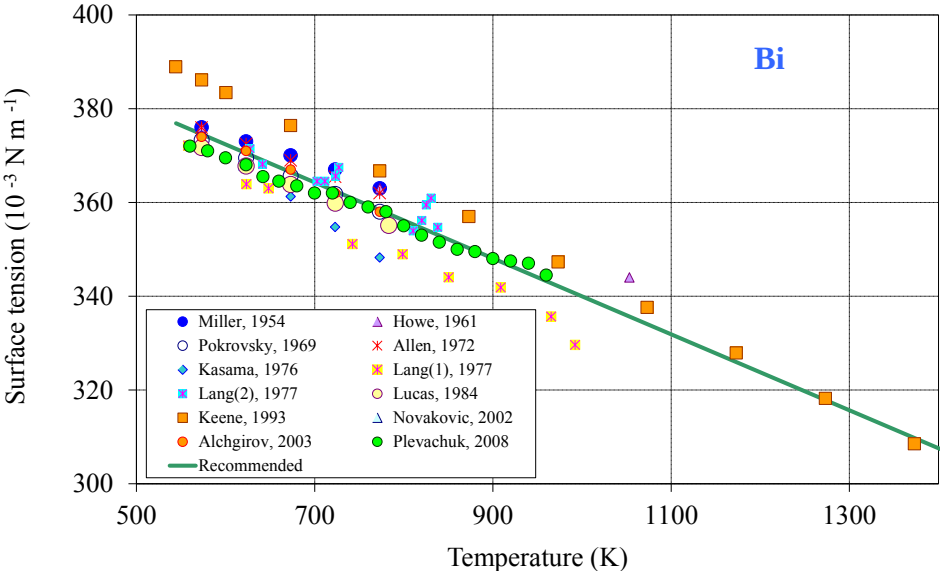

Source: Sobolev (2011).

A good compromise can be obtained with the linear correlation (Sobolev, 2011):

$$\sigma_{Bi}\left[\mathrm{Nm^{-1}}\right] = \left(420.8 - 0.081 \cdot T\right) \times 10^{-3} \tag{2.26}$$

where temperature is in kelvins. The expected validity range is $T_{M,0(Bi)}$ = 1 400 K (1 127°C). The maximum deviation of the selected literature data on the molten bismuth surface tension from the recommended correlation (2.26) is about ±3% (see Figure 2.10.2[b] from Sobolev [2011]).

Figure 2.10.2(b): Deviation of the database values on the molten bismuth surface tension from the recommended correlation (2.26)

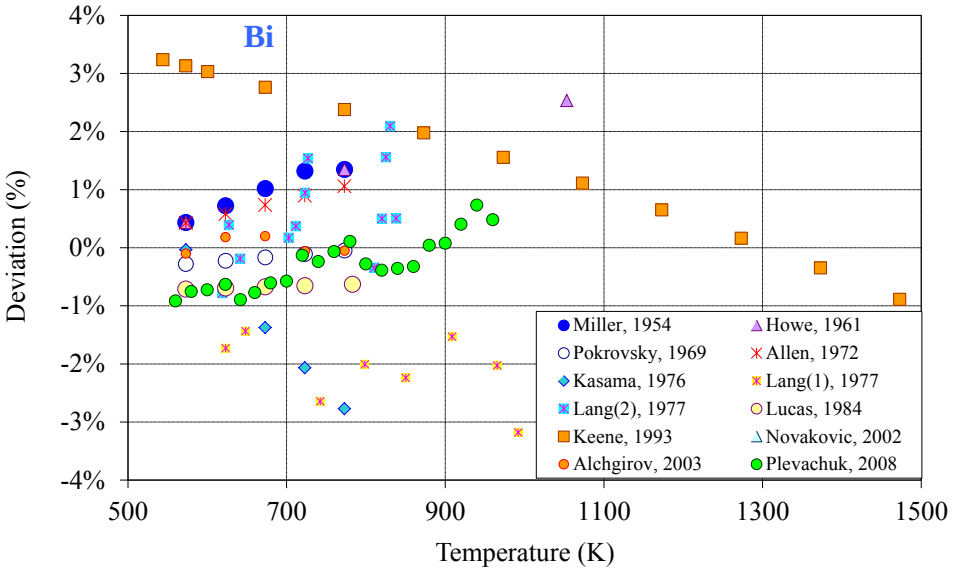

Source: Sobolev (2011).

2.10.3 LBE

The sources of data on the surface tension of the molten LBE, found in the open literature and analysed to include in the selected database (Table 2.10.3), are from Miller (1951), Lyon (1954), Semenchenko (1961), Pokrovsky (1969), Kazakova (1984), Novacovic (2002), Giuranno (2002), Bogoslovskaya (2002), Pastor Torres (2003), Kirillov (2000a, 2008) and Plevachuk (2008).

Table 2.10.3: Selected database on liquid LBE surface tension at normal pressure

Reg. No.	Parameter	Measurement method	Estimated accuracy %	Temperature range, K	Pressure range, Pa	Values, N m^{-1}	Ref.
10.3.1	Surface tension	n/a	(5-10)	(473-1 073)	~10^5	–	Miller (1951, 1954)
	Interpolation function: $\sigma = (421.26 - 0.0665 \cdot T) \times 10^{-3}$ N m^{-1}						
	Comments: Unknown composition and purity						
10.3.2	Surface tension	?	(5)	1 073-1 373	~10^5	–	Semenchenko (1961)
	Interpolation function: $\sigma = (421.26 - 0.0665 \cdot T) \times 10^{-3}$ N m^{-1}						
	Comments: Unknown composition and purity						
10.3.3	Surface tension	Drop weight	(5)	573-773	~10^5	–	Pokrovsky (1969)
	Interpolation function: $\sigma = (451.5 - 0.081 \cdot T) \times 10^{-3}$ N m^{-1}						
	Comments: 48.2 wt.% Pb + 51.8 wt.% Bi, unknown purity						
10.3.4	Surface tension	Sessile drop	2	(573)-1 073	~10^5	–	Kazakova (1984)
	Interpolation function: $\sigma = (415.7 - 0.047 \cdot T) \times 10^{-3}$ N m^{-1}						
	Comments: 43.3 wt.% Pb + 56.7 wt.% Bi, elements purity 99.999%						
10.3.5	Surface tension	Sessile drop	(0.1)	623-773	~10^5	–	Novacovic (2002)
	Interpolation function: $\sigma = (445.419 - 0.0801 \cdot T) \times 10^{-3}$ N m^{-1}						
	Comments: 44.7 wt.% Pb + 55.3 wt.% Bi, elements purity 99.9999%						
10.3.6	Surface tension	Pendent drop	2	423-573	~10^5	–	Pastor Torres (2003)
	Interpolation function: $\sigma = (450.86 - 0.0873 \cdot T) \times 10^{-3}$ N m^{-1}						
	Comments: 44.5 wt.% Pb + 55.5 wt.% Bi, elements purity > 99.99%						
10.3.7	Surface tension	?	?	403-1 073	~10^5	–	Kirillov (2008)
	Interpolation function: $\sigma = (444.0 - 0.0703 \cdot T) \times 10^{-3}$ N m^{-1}						
	Comments: 44.5 wt.% Pb + 55.5 wt.% Bi						
10.3.8	Surface tension	"Large" drop	0.5	403-1 000	~10^5	–	Plevachuk (2008)
	Interpolation function: $\sigma = (448.05 - 0.0799 \cdot T) \times 10^{-3}$ N m^{-1}						
	Comments: 44 at.% Pb + 56 at.% Bi, uncertainty of 0.02%						

Miller presented LBE surface tension values at 200, 300 and 400°C (1951), and later at 800 and 1 000°C (1954), obtained with data from Semenchenko (1937). Semenchenko (1961) reproduced his own data from the earlier publications. Pokrovsky (1969) measured the surface tension of Pb-Bi alloys with the drop weight method from their melting points up to 773 K (500°C). Kazakova (1984) measured surface tension of Pb-Bi melts using the sessile drop method at temperatures up to 800°C (1 073 K). Novacovic (2002) and Giuranno (2002) also used the sessile-drop method to study a molten Pb-Bi alloy with almost eutectic composition (43.9 wt.% Pb) over the temperature range of 623-773 K (350-500°C). Pastor Torres (2003) measured LBE surface tension with the pendent drop method in an inert atmosphere at temperatures from 423 to 573 K (150-300°C). However, the results obtained at T < 473 K (200°C) were discarded because of difficulties related to oxidation. Plevachuk (2008) used the "large" drop method in the temperature range from the melting temperature to about 1 000 K. The data presented in the handbook of Kyrillov (2000a) on the surface tension of molten LBE were corrected later in the IAEA reports (Bogoslovskaya, 2002; Kirillov, 2008). The data from the above-cited sources are included in the selected database presented in Table 2.10.3 and Figure 2.10.3(a) (Sobolev, 2011).

The selected LBE data can be described with an uncertainty of less than 3% by the following liner correlation of Plevachuk (2008):

$$\sigma_{LBE}\left[\mathrm{Nm^{-1}}\right] = (448.5 - 0.0799 \cdot T) \times 10^{-3} \qquad (2.27)$$

where temperature is in kelvins. The above correlation is recommended for estimation of the surface tension of molten LBE at normal pressure up to 1 400 K (1 127°C). The deviation of the selected data from the recommended correlation (2.26) in the temperature range is shown in Figure 2.10.3(b) (reproduced from Sobolev [2011]).

Figure 2.10.3(a): Surface tension of molten LBE versus temperature

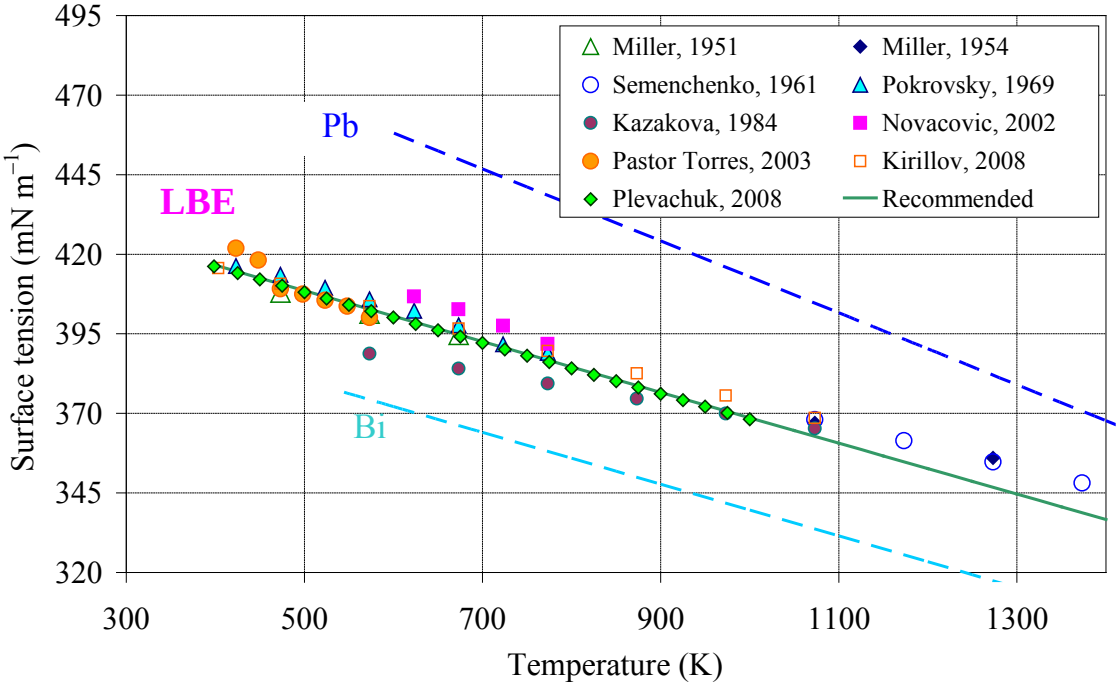

Source: Sobolev (2011).

Figure 2.10.3(b): Deviation of the selected database on surface tension of molten LBE from the recommended correlation (2.27)

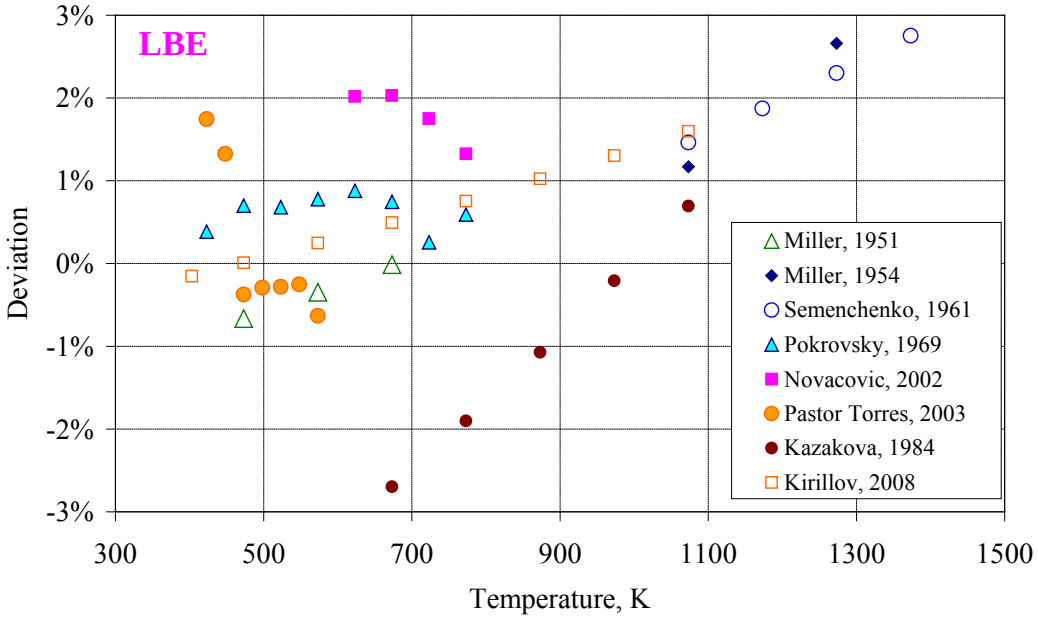

Source: Sobolev (2011).

2.11 Density

The density of liquid metal coolants is a property of primary importance. The temperature and pressure dependence of density provides essential information for the development of an equation of state. In engineering practice, it is used to determine the concentration of atoms in unit volume and hydraulic regime parameters of coolants in installations. In addition, the measurement or calculation of basic physical properties (e.g. viscosity, surface tension, thermal diffusivity) often requires knowledge of density.

2.11.1 Lead

The data for the density of the molten lead found in Miller (1954), Kutateladze (1958), Lyon (1960), Kirshenbaum (1961), Crean (1964), Friedland (1966), Weeks (1971), Ruppersberg (1976), Smithells (1983, 2004), Lucas (1984a), Iida (1988) and later compilations and articles of Imbeni (1998), Onistchenko (1999), Kirillov (2000a, 2008) and Bogoslovskaya (2002) were analysed to include in the present handbook database.

Miller (1954) selected data on liquid Pb density from Been (1950). Kutateladze (1958) references to data obtained in the laboratory of the Academician Mikheev of the Academy of Sciences of the former USSR. Lyon (1960) repeated values published by Miller (1954) in Lyon (1954). Kirshenbaum (1961) presented experimental results on molten lead density from the normal melting point up to temperature close to the normal boiling point. Ruppersberg (1976) measured liquid Pb density in the temperature range 636-829 K (363-556°C). Crean (1964) presented a graph with Pb density versus temperature prepared with data from older handbooks. SMRB (Smithells, 1983) provides recommendations on the Pb density based on the data taken from Kirshenbaum (1961) and from Strauss (1960). Lucas (1984a) reported values obtain by himself earlier (1969). Iida (1988) used a correlation recommended by Steinberg (1974). Imbeni (1998) analysed different sources and recommended a parabolic correlation based on the data of Lucas (1984a). Onistchenko

(1999) used the method of pseudopotentials and perturbation theory to calculate the pure liquid Pb density at p = 0.1 MPa as a function of temperature.

The recent IAEA report (Kirillov, 2008) repeats without reference the data from the earlier IAEA report (Bogoslovskaya, 2002), therefore only one of these sources was included in the Pb density database.

The recommendations of Friedland (1966) and Weeks (1971) have not been taken into account because they repeat the data from Lyon (1954), Smithells (1955) and Strauss (1960) already included in the database sources.

The selected database for density of molten lead at the normal atmospheric pressure is presented in Table 2.11.1.

Figure 2.11.1(a) shows the molten lead density values from the selected sources versus temperature.

A set of the selected data can be described by the linear temperature dependence proposed in Sobolev (2008a), where temperature is in kelvins:

$$\rho_{Pb}\left[\mathrm{kg\ m^{-3}}\right] = 11441 - 1.2795 \cdot T \tag{2.28}$$

The deviation of the selected source values from Eq. (2.28) is illustrated in Figure 2.11.1(b) (from Sobolev [2011]). One can see that maximum difference does not exceed 1% for most of the sources (except Lucas [1984a] and Onistchenko [1999]) in the temperature range from the normal melting point to 1 500 K; it increases up to about 2% when temperature increases up to the normal boiling point.

Table 2.11.1: Selected database on the density of molten lead at normal pressure

Reg. No.	Parameter	Measurement method	Estimated accuracy	Temperature range, K	Pressure range, Pa	Values	Ref.
11.1.1	Density	?	?	673-1 273	~10^5	–	Miller (1954)
	Interpolation function: ρ = 11 291 – 1.165·T kg m^{-3}						
	Comments: Unknown purity						
11.1.2	Density	?	?	673-1 073	~10^5	–	Kutateladze (1958)
	Interpolation function: ρ = 11 380 – 1.169·T kg m^{-3}						
	Comments: Unknown purity						
11.1.3	Density	Immersed sinker	(0.03%)	633-1 973	~10^5	–	Kirshenbaum (1961)
	Interpolation function: ρ = 11 470 – 1.318·T kg m^{-3}						
	Comments: 99.9% Pb						
11.1.4	Density	?	?	601-1 340	~10^5	–	Crean (1964)
	Interpolation function: ρ = 11 307 – 1.177·T kg m^{-3}						
	Comments: Unknown purity						
11.1.5	Density	Max. bubble pressure	< 1%	636-829	~10^5	–	Ruppersberg (1976)
	Interpolation function: ρ = 11 417 – 1.350·T kg m^{-3}						
	Comments: 99.99% Pb						

Table 2.11.1: Selected database on the density of molten lead at normal pressure (*cont.*)

Reg. No.	Parameter	Measurement method	Estimated accuracy	Temperature range, K	Pressure range, Pa	Values	Ref.
11.1.6	Density	?	?	?	~10^5	–	Smithells (1983)
	Interpolation function: $\rho = 11\,470 - 1.3174 \cdot T$ kg m^{-3}						
	Comments: Unknown purity						
11.1.7	Density	?	?	601-1 823	~10^5	–	Lucas (1984a)
	Interpolation function: $\rho = 11\,418 - 1.301 \cdot T + 6.278 \times 10^{-5} \cdot T^2$ kg m^{-3}						
	Comments: Unknown purity						
11.1.8	Density	?	?	601-2 000	~10^5	–	Iida (1988)
	Interpolation function: $\rho = 11\,463 - 1.32 \cdot T$ kg m^{-3}						
	Comments: Unknown purity						
11.1.9	Density	n/a	(~2%)	601-1 700	1×10^5	–	Onistchenko (1999)
	Interpolation function: $\rho = 11\,772 - 2.067 \cdot T + 4.353 \times 10^{-4} \cdot T^2$ kg m^{-3}						
	Comments: Pure Pb (model)						
11.1.10	Density	?	?	603-1 273	~10^5	–	Bogoslovskaya (2002)
	Interpolation function: $\rho = 11\,420 - 1.242 \cdot T$ kg m^{-3}						
	Comments: Unknown purity						

Figure 2.11.1(a): Density of molten lead as function of temperature at normal pressure

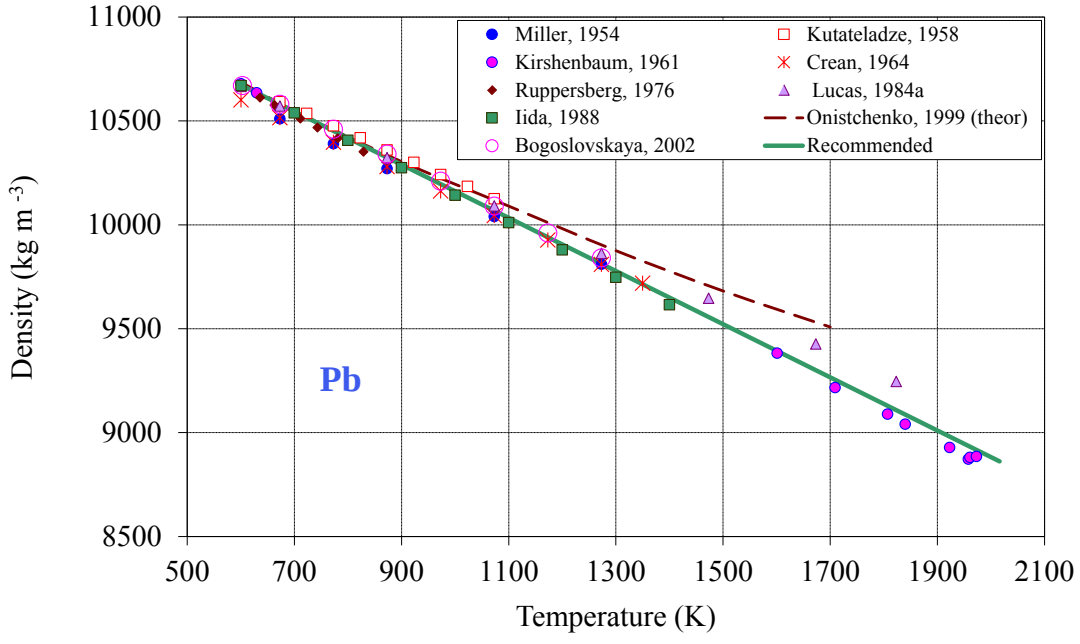

Source: Sobolev (2011).

Figure 2.11.1(b): Deviation of the database values on melted lead density from Eq. (2.28)

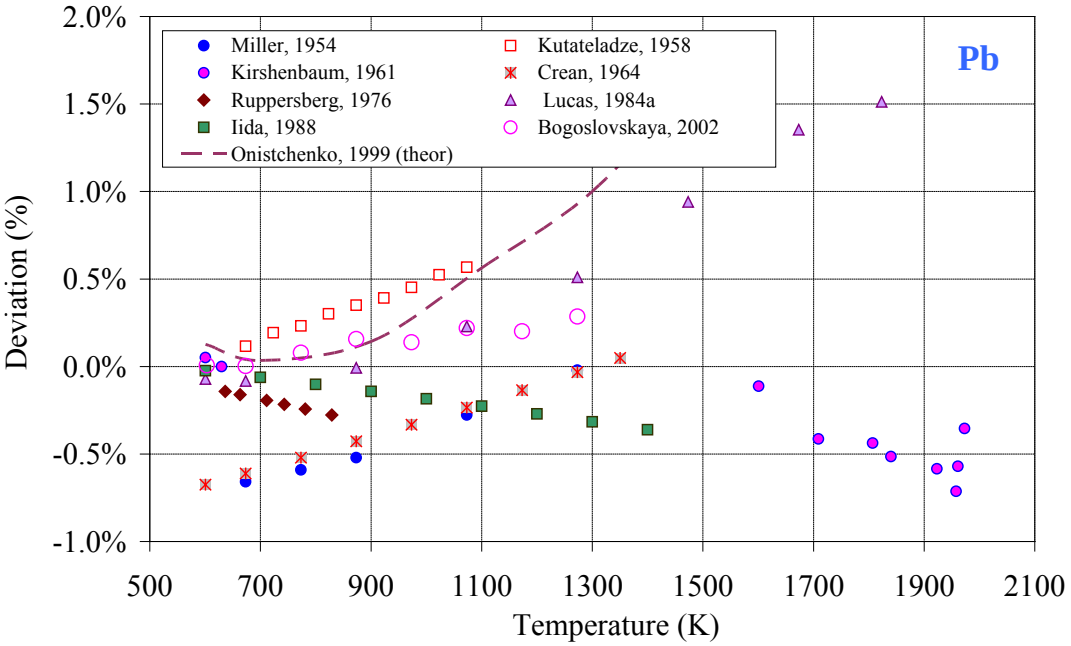

Source: Sobolev (2011).

2.11.2 *Bismuth*

The data for liquid bismuth density that have been included in the database were taken from Miller (1954), Kutateladze (1958), Cahill (1963), Crean (1964), Bonilla (1964), Lucas (1984a), Iida (1988), Makeev (1989) and Imbeni (1998).

Miller (1954) took data on liquid Bi density from Bircumshaw (1927). Kutateladze (1958) reference to data obtained in the laboratory of the Academician Mikheev of the Academy of Sciences of the former USSR. Cahill (1963) measured the molten bismuth density in the temperature range from the normal melting point up to the boiling temperature. Bonilla (1964) reported values that were obtained by interpolation of data collected from a number of sources. Crean (1964) presented a graph with the temperature dependence of Bi density prepared with data from older handbooks. Lucas (1984a) took recommendations from Lucas (1962). Iida (1988) references to Steinberg (1974). Makeyev (1989) measured the Bi density with the γ-attenuation method in the temperature range of 300-1 600 K and obtained slightly higher values than those given by the previous sources. Imbeni (1998) analysed different sources and proposed a linear correlation based on the data of Lucas (1984a). Onistchenko (1999) used the method of pseudopotentials and the perturbation theory to calculate the pure liquid bismuth density at p = 0.1 MPa as a function of temperature. Alchagirov (2004) performed accurate measurement of the liquid Bi density at temperatures between 746 and 702 K (473°C and 429°C) and recommended a linear correlation valid up to 750 K (477°C). Greenberg (2009) measured the Bi density using the γ-attenuation method and registered an anomaly at ~1 013 K (740°C).

Data from Smithells Metal Reference Book (1983), Friedland (1966) and Weeks (1971) have not been included in the database because they reproduce the results already presented in the above-cited sources.

The selected database on the density for molten bismuth is presented in Table 2.11.2.

Table 2.11.2: Selected database on density of molten bismuth at normal pressure

Reg. No.	Parameter	Measurement method	Estimated accuracy	Temperature range, K	Pressure range, Pa	Values	Ref.
11.2.1	Density	?	?	573-1 235	~10^5	–	Miller (1954)
	Interpolation function: $\rho = 10\,755 - 1.258 \cdot T$ kg m^{-3}						
	Comments: Unknown purity						
11.2.2	Density	?	?	553-973	~10^5	–	Kutateladze (1958)
	Interpolation function: $\rho = 10\,744 - 1.243 \cdot T$ kg m^{-3}						
	Comments: Unknown purity						
11.2.3	Density	Immersed sinker	13 kg cm^{-3}	630-1 730	~10^5	–	Cahill (1963)
	Interpolation function: $\rho = 10\,665 - 1.182 \cdot T$ kg m^{-3}						
	Comments: 99.972% Bi						
11.2.4	Density	?	?	589-1 033	~10^5	–	Bonilla (1964)
	Interpolation function: $\rho = 10\,722 - 1.211 \cdot T$ kg m^{-3}						
	Comments: Unknown purity						
11.2.5	Density	?	?	566-1 266	~10^5	–	Crean (1964)
	Interpolation function: $\rho = 10\,700 - 1.3174 \cdot T$ kg m^{-3}						
	Comments: Unknown purity						
11.2.6	Density	Buble max. pressure	(0.3%)	545-1 273	~10^5	–	Lucas (1984a)
	Interpolation function: $\rho = 10\,725 - 1.22 \cdot T$ kg m^{-3}						
	Comments: Unknown purity						
11.2.7	Density	?	?	545-(1 000)	~10^5	–	Iida (1988)
	Interpolation function: $\rho = 10\,692 - 1.18 \cdot T$ kg m^{-3}						
	Comments: Unknown purity						
11.2.8	Density	n/a	(~ 2%)	545-1 700	1×10^5	–	Onistchenko (1999)
	Interpolation function: $\rho = 10\,680 - 1.1928 \cdot T$ kg m^{-3}						
	Comments: Pure Bi (model)						
11.2.9	Density	γ-attenuation	~ 2%	300-1 600	~10^5	–	Makeyev (1989)
	Interpolation function: $\rho = 10\,156 - 1.20 \cdot T$ kg m^{-3}						
	Comments: 99.99% Bi						
11.2.10	Density	Picnometer	0.1%	546-702	~10^5	–	Alchagirov (2004)
	Interpolation function: $\rho = 10\,688 - 1.159 \cdot T$ kg m^{-3}						
	Comments: 99.98% Bi						
11.2.11	Density	γ-attenuation	(1%)	488-1 130	~10^5	–	Greenberg (2009)
	Interpolation function: $\rho = 10\,830 - 1.397 \cdot T$ kg m^{-3}						
	Comments: Unknown purity						

Figure 2.11.2(a) (from Sobolev [2011]) shows the molten bismuth density values from the selected sources versus temperature.

All sets of the selected data can be described with linear temperature dependence recommended by Imbeni (1998) based on the data of Lucas (1984a):

$$\rho_{Bi}\left[\mathrm{kg\ m^{-3}}\right] = 10725 - 1.22 \cdot T \qquad (2.29)$$

where temperature is in kelvins.

The deviation of the selected source values from Eq. (2.29) is illustrated in Figure 2.11.2(b) (reproduced from Sobolev [2011]). One can see that maximum difference does not exceed 0.5% in the temperature range from the normal melting point to the normal boiling point (except the data of Makeyev [1989], which are about 1-1.3% higher and the data of Greenberg [2009] at $T > 750$ K, which are slightly lower).

2.11.3 LBE

The data included in the database for molten LBE density are from Miller (1954), Kutateladze (1958), Bogoslovskaya (2002), Alchagirov (2003) and Khairulin (2005); they are described in Table 2.11.3.

Miller (1954) selected data on liquid LBE density from Been (1950). Kutateladze (1958) reference to studies of the Academy of Sciences of the former USSR. Imbeni (1999) proposed to use the same linear correlations as Cevolani (1998) based on data presented in the handbook Mantell (1958). The IAEA report (Bogoslovskaya, 2002) does not provide explicit reference. Alchagirov (2003) measured density of liquid LBE in the range of 410-726 K. Khairulin (2005) determined the LBE density with γ-ray attenuation technique over the temperature range from 293 to 750 K. In the recent IAEA report (Kirillov, 2008) LBE density was evaluated on the basis of the additivity law using densities and weight fractions of Pb and Bi; the obtained results are practically the same as given in the previous IAEA report (Bogoslovskaya, 2002).

Figure 2.11.2(a). Density of molten bismuth as a function of temperature at normal pressure

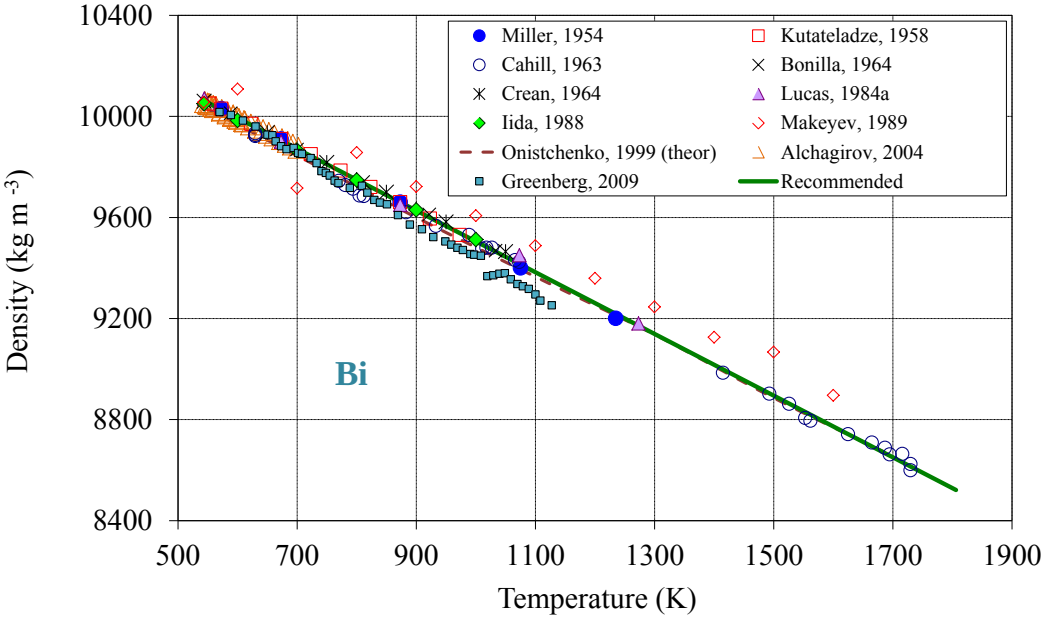

Source: Sobolev (2011).

Figure 2.11.2(b): Deviation of the database values on the bismuth density from Eq. (2.29)

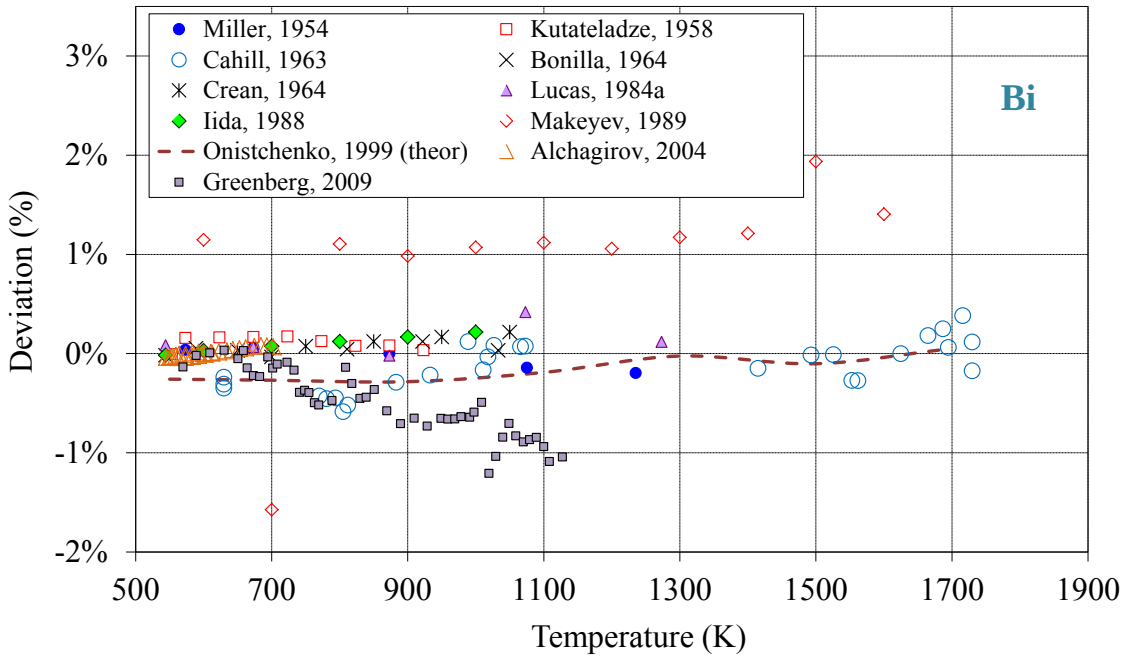

Source: Sobolev (2011).

Table 2.11.3: Selected database on density of molten LBE at normal pressure

Reg. No.	Parameter	Measurement method	Estimated accuracy	Temperature range, K	Pressure range, Pa	Values	Ref.
11.3.1	Density	?	?	473-1 273	~10^5	–	Miller (1954)
	Interpolation function: $\rho = 11\,113 - 1.375 \cdot T$ kg m^{-3}						
	Comments: Unknown data on eutectic composition and purity						
11.3.2	Density	Picnometer	2%	403-973	~10^5	–	Kutateladze (1958)
	Interpolation function: $\rho = 11\,062 - 1.2175 \cdot T$ kg m^{-3}						
	Comments: 44.5 wt.% Pb + 55.5 wt.% Bi, unknown purity						
11.3.3	Density	(Picnometer)	?	403-1 073	~10^5	–	Bogoslovskaya (2002)
	Interpolation function: $\rho = 11\,047 - 1.2564 \cdot T$ kg m^{-3}						
	Comments: 44.5 wt.% Pb + 55.5 wt.% Bi, unknown purity						
11.3.4	Density	Picnometer	0.1%	410-726	~10^5	–	Alchagirov (2003)
	Interpolation function: $\rho = 10\,981.7 - 1.1369 \cdot T$ kg m^{-3}						
	Comments: 44.6 wt.% Pb + 55.4 wt.% Bi; purity Pb – 99.9985 wt.%, purity Bi – 99.98 wt.%						
11.3.5	Density	γ-attenuation	(0.5%)	293-750	~10^5	–	Khairulin (2004)
	Interpolation function: $\rho = 10\,526 - 1.4378 \cdot (T - 397.9) + 0.00047 \cdot (T - 397.9)^2$ kg m^{-3}						
	Comments: 44.5 wt.% Pb + 55.5 wt.% Bi, unknown purity						

The data presented by Bonilla (1964), Crean (1964) and Hofmann (1970) were obtained by the interpolation of the results of Miller (1954) and Lyon (1960). The above-mentioned sources were therefore not included in the database.

The extracted density values as a function of temperature at normal atmospheric pressure are presented in Figure 2.11.3(a). The temperature dependence of the densities of pure molten lead and pure molten bismuth, calculated with the empirical correlations recommended in preceding sections are also reproduced for comparison.

The linear regression of values presented in Figure 2.11.3(a) yields for the LBE density:

$$\rho_{LBE}\left[\mathrm{kg\ m^{-3}}\right] = 11065 - 1.293 \cdot T \tag{2.30}$$

where the temperature is in kelvins.

Figure 2.11.3(b) shows that the deviation of the selected literature data for molten LBE density from Eq. (2.30) does not exceed 0.8% in the temperature range of 400-1 273 K.

Figure 2.11.3(a) also presents the calculation results of the LBE density using Vegard's law. Vegard's law allows to expresses the molar volume of LBE through the molar fractions ($x_{\mu(Pb)}$ and $x_{\mu(Bi)}$) and the molar volumes ($v_{\mu(Pb)}$ and $v_{\mu(Bi)}$) of lead and bismuth as follows:

$$v_{\mu(LBE)} = \left(x_{\mu(Pb)} \cdot \sqrt[3]{v_{\mu(Pb)}} + x_{\mu(Bi)} \cdot \sqrt[3]{v_{\mu(Bi)}}\right)^3 \tag{2.31}$$

Then Eq. (2.31) yields for LBE density the following equation:

$$\rho_{LBE} = \frac{\mu_{LBE}}{\left(x_{\mu(Pb)} \cdot \sqrt[3]{\frac{\mu_{Pb}}{\rho_{Pb}}} + \left(1 - x_{\mu(Pb)}\right) \cdot \sqrt[3]{\frac{\mu_{Bi}}{\rho_{Bi}}}\right)^3} \tag{2.32}$$

where μ(Pb), μ(Bi) and μ(LBE) are the molar masses of Pb, Bi and LBE respectively. Eq. (2.32) allows calculating the LBE density using as input the densities of pure molten lead and pure molten bismuth, which can be predicted with better precision than that of LBE.

From Figures 2.11.3(a) and 2.11.3(b) one can see that Vegard's law gives very good results up to at least 1 300 K (1 027°C).

Figure 2.11.3(a): Density of the melted LBE versus temperature

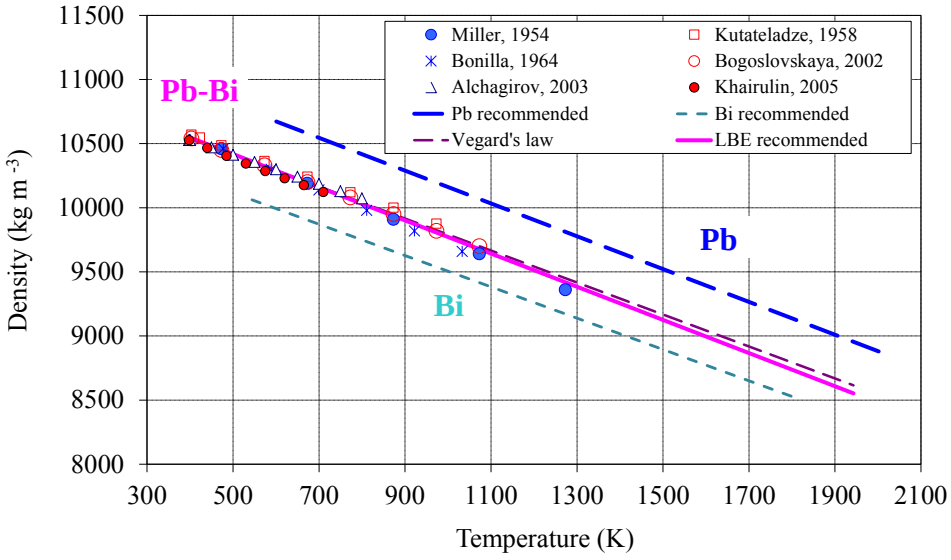

Source: Sobolev (2011).

Figure 2.11.3(b): Deviation of the selected data sources for melted LBE density from the Eq. (2.30)

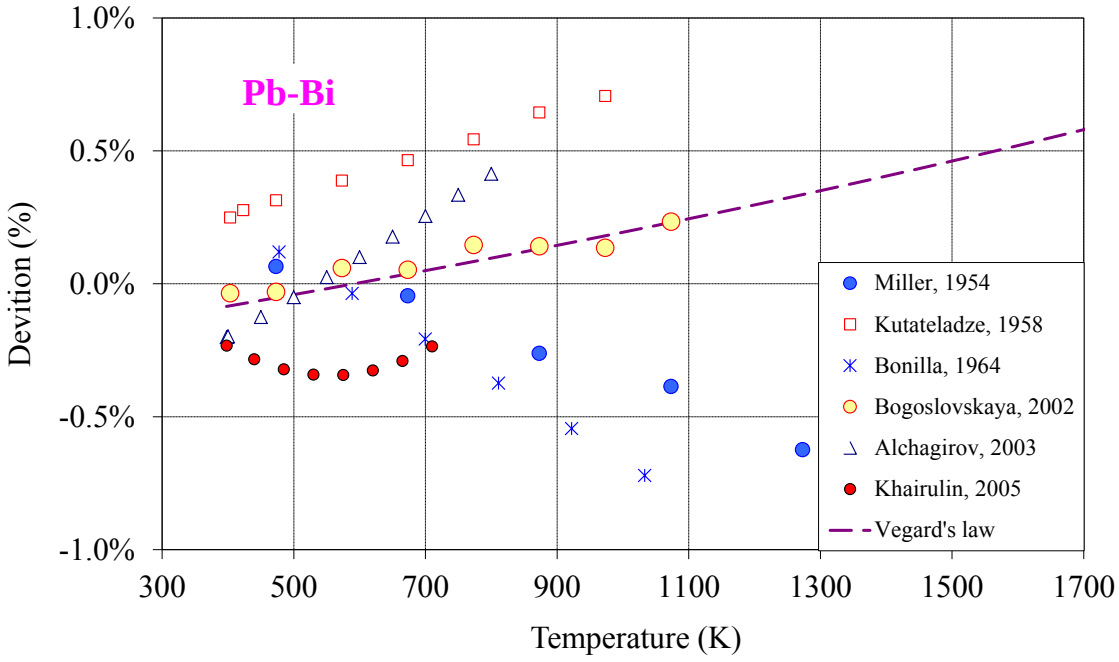

Source: Sobolev (2011).

2.12 Thermal expansion

The density of liquid metals changes with temperature due to thermal expansion related to anharmonicity of interatomic forces. In a general case, a link between the density and the coefficient of volumetric thermal expansion (CVTE) at constant pressure p is defined by the following formula:

$$\alpha_p(T) \equiv \frac{1}{V}\cdot\left(\frac{\partial V}{\partial T}\right)_p = -\frac{1}{\rho}\cdot\left(\frac{\partial \rho}{\partial T}\right)_p \tag{2.33}$$

Literature sources describing a direct measurement of CVTE of molten Pb, Bi and LBE were not found. Therefore, available information on the temperature dependence of their density (see Section 2.11) was used for deduction of the isobaric CVTE. Substituting the correlations for density recommended in Section 2.11 into (2.33) yields the following formulae for the isobaric CVTE of molten lead, bismuth and LBE respectively:

- Lead:

$$\alpha_{p(Pb)}\left[K^{-1}\right] = \frac{1}{8942 - T} \tag{2.34}$$

- Bismuth:

$$\alpha_{p(Bi)}\left[K^{-1}\right] = \frac{1}{8791 - T} \tag{2.35}$$

- LBE:

$$\alpha_{p(LBE)}\left[K^{-1}\right] = \frac{1}{8558 - T} \tag{2.36}$$

The results obtained with these formulae are presented in Figure 2.12.1.

Comparison of the isobaric volumetric CVTE of molten lead, bismuth and LBE, obtained with the formulae above, shows that LBE has the highest CVTE. In principle, this can be explained by the lower attractive forces between Pb and Bi atoms in LBE than in pure lead and in pure bismuth. However, it could also be due to a large uncertainty of the determination of the thermal expansion coefficient by using the procedure of differentiation of the density correlations.

Eqs. (2.34), (2.35) and (2.36) are recommended for practical applications as "the best choice" (because of their consistency with the correlations recommended above in Section 2.11) for calculation of the CVTE of the liquid lead, bismuth and LBE, respectively, at the normal atmospheric pressure.

Figure 2.12.1: Isobaric volumetric thermal expansion coefficients of molten lead, bismuth and LBE versus temperature

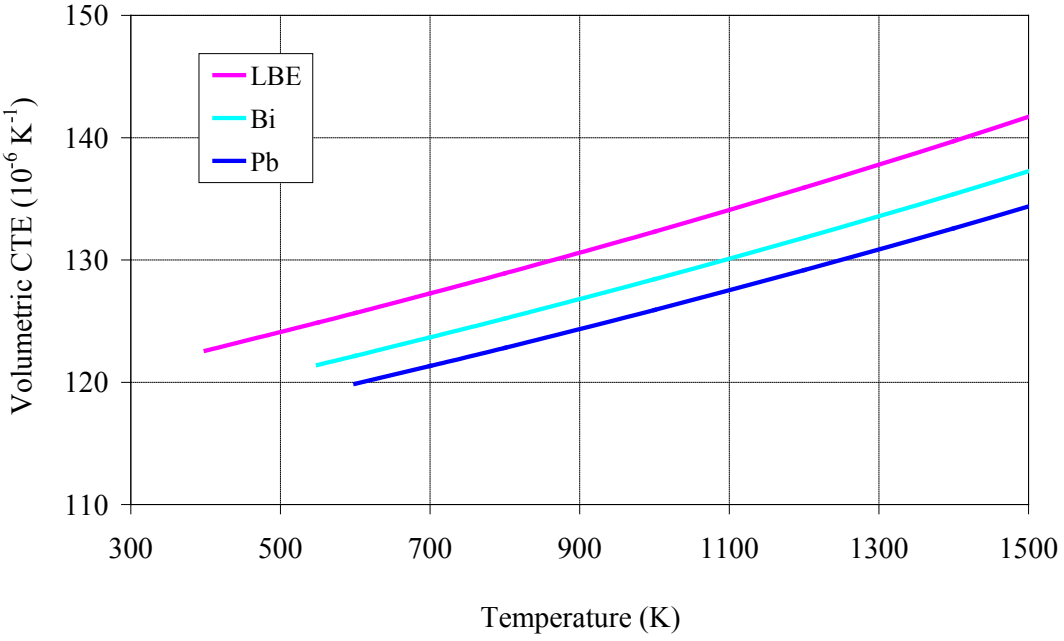

Source: Sobolev (2011).

2.13 Compressibility and sound velocity

Compressibility and sound velocity are basic thermodynamic properties of substances. There are no results for direct measurement of the compressibility for molten lead, bismuth and LBE in literature. Usually, the adiabatic (isentropic) compressibility β_S (or the adiabatic elastic modulus $B_S \equiv \beta_S^{-1}$) is found from the results of measurement of the sound velocity u_s and of the density ρ by using the following thermodynamic relationship (Dreyfus, 1971):

$$B_S \equiv \frac{1}{\beta_S} \equiv -V \cdot \left.\frac{\partial p}{\partial V}\right|_S = \rho \cdot \left(\left.\frac{\partial \rho}{\partial p}\right|_S\right)^{-1} = \rho \cdot u_s^2 \tag{2.37}$$

The sound velocity is an important thermophysical parameter, which correlates with many other properties. In the most of liquid metals, including Pb, Bi and LBE, it decreases monotonically with temperature. The correct measurement of the sound velocity in the considered heavy LM at high temperatures is very difficult, because of problems related to control of their purity, to dissolution attack on materials of sound transducers and measuring cells and to stability of temperature field in the cell. Therefore rather large dispersion exists between the experimental data obtained by different authors far away from the melting point.

The following bibliographic sources, containing information on the velocity of sound propagation in the heavy liquid metals of interest, were analysed: Kleppa (1950), Kutateladze (1958), Gordon (1959), Jarzynski (1963), Hill (1965), Gitis (1966), Filippov (1966), Konyuchenko (1969), Beyer (1972), Stremousov (1975), Tsu (1979), Mustafin (1983), Hixson (1986), Iida (1988), Kažys (2002), Hirabayashi (2005), Hayashi (2007) and Greenberg (2008).

2.13.1 Lead

The velocity of propagation of the longitudinal sound waves in molten lead at normal pressure was measured by Kleppa (1950) and by Gordon (1959) close to the melting point, by Filippov (1966) over a temperature interval from the melting temperature up to about 1 000 K, by Gitis (1966) up to about 1 440 K (~1 170°C), by Konyuchenk (1969) over the temperature range of 673-973 K (400-700°C), by Stremousov (1975) from 623 K up to 1 073 K (350-800°C), by Tsu (1979) in the range of 640-1 050 K (367-777°C), by Hayashi (2007) in the interval of 610-1 078 K (337-805°C) and by Greenberg (2008) in the interval of $T_{M,0}$-1 408 K ($T_{M,0}$-1 135°C). Hixon (1986) measured the lead sound velocity in the region close to the Pb critical point at pressures 0.1-0.3 GPa and temperatures up to 5 300 K. In Kutateladze (1958) the recommendation of Kleppa (1950) was reproduced. Beyer (1972) recommended a correlation for the temperature dependence of the Pb sound velocity based on five different sources (including Kleppa [1950] and Gitis [1966]). Mustafin (1983) analysed experimental data of different authors on sound velocity and enthalpy of few liquid metals and provided a table with recommended values of the sound velocity in the temperature range of 100-2 000 K. Iida (1988) reproduced correlations from Beyer (1972), Filippov (1966) and Tsu (1979) without giving the temperature limits and their own recommendations.

The data included in the database are presented in Table 2.13.1 and plotted in Figure 2.13.1(a).

Table 2.13.1: Selected database on velocity of sound in liquid lead

Reg. No.	Parameter	Measurement method	Estimated accuracy %	Temperature range, K	Pressure range, Pa	Values m s^{-1}	Reference
13.1.1	Sound velocity	Pulse propagation	2	601-653	~10^5	–	Kleppa (1950)
	Interpolation function: $u_s = 1\,790 - 0.5\cdot(T - T_{M,0}) = 2\,090 - 0.5\cdot T$ m s^{-1}						
	Comments: 99.93% Pb						
13.1.2	Sound velocity	Pulse propagation	0.1	601-643	~10^5	–	Gordon (1959)
	Interpolation function: $u_s = 1\,776 - 0.277\cdot(T - T_{M,0}) = 1\,942 - 0.277\cdot T$ m s^{-1}						
	Comments: 99.5% Pb						

Table 2.13.1: Selected database on velocity of sound in liquid lead (*cont.*)

Reg. No.	Parameter	Measurement method	Estimated accuracy %	Temperature range, K	Pressure range, Pa	Values m s^{-1}	Reference
13.1.3	Sound velocity	Pulsed interferometer	0.5	601-1423	~10^5	–	Gitis (1966)
	Interpolation function: $u_s = 2\,000 - 0.3 \cdot T$ m s^{-1} at T = 601-1 173 K $u_s = 2\,035 - 0.33 \cdot T$ m s^{-1} at T = 1 173-1 420 K						
	Comments: 99.998% Pb						
13.1.4	Sound velocity	Pulse propagation	(~1)	601-1 073(?)	~10^5	–	Filippov (1966)
	Interpolation function: $u_s = 1\,810 - 0.38 \cdot (T - T_{M,0}) = 2\,038 - 0.38 \cdot T$ m s^{-1}						
	Comments: Unknown purity						
13.1.5	Sound velocity	(Pulse propagation)	(~1)	673-973	~10^5	–	Konyuchenko (1969)
	Interpolation function: $u_s = 2\,014 - 0.318 \cdot T$ m s^{-1}						
	Comments: Unknown purity						
13.1.6	Sound velocity	n/a	(1)	601-1 423	~10^5	–	Beyer (1972)
	Interpolation function: $u_s = 1\,820 - 0.28 \cdot (T - T_{M,0}) = 1\,988 - 0.28 \cdot T$ m s^{-1}						
	Comments: Pure lead						
13.1.7	Sound velocity	Pulsed interferometer	(0.2)	623-1 073	~10^5	–	Stremousov (1975)
	Interpolation function: $u_s = 1\,995 - 0.289 \cdot T$ m s^{-1}						
	Comments: 99.99% Pb						
13.1.8	Sound velocity	Pulse propagation	(3)	601-1 000	~10^5	–	Tsu (1979)
	Interpolation function: $u_s = 1826 - 0.278 \cdot (T - T_{M,0}) = 1\,993 - 0.278 \cdot T$ m s^{-1}						
	Comments: Pb of high purity (4N = 99.99% Pb)						
13.1.9	Sound velocity	n/a	2	601-2 000	~10^5	–	Mustafin (1983)
	Interpolation function: $u_s = 1\,962 - 0.3535 \cdot T + 7.847 \times 10^{-5} \cdot T^2$ m s^{-1}						
	Comments: Pure lead						
13.1.10	Sound velocity	Pulse propagation	< 1	626-1 078	~10^5	–	Hayashi (2007)
	Interpolation function: $u_s = 1\,990\text{-}0.286 \cdot T$ m s^{-1}						
	Comments: 99.99% Pb						
13.1.11	Sound velocity	Pulse propagation	< 0.4	601-1 408	~10^5	–	Greenberg (2008)
	Interpolation function: $u_s = 1\,985\text{-}0.254 \cdot T$ m s^{-1}						
	Comments: Pb of extra high purity (5N = 99.999 Pb %)						

Figure 2.13.1(a): Velocity of ultrasound in liquid lead in function of temperature

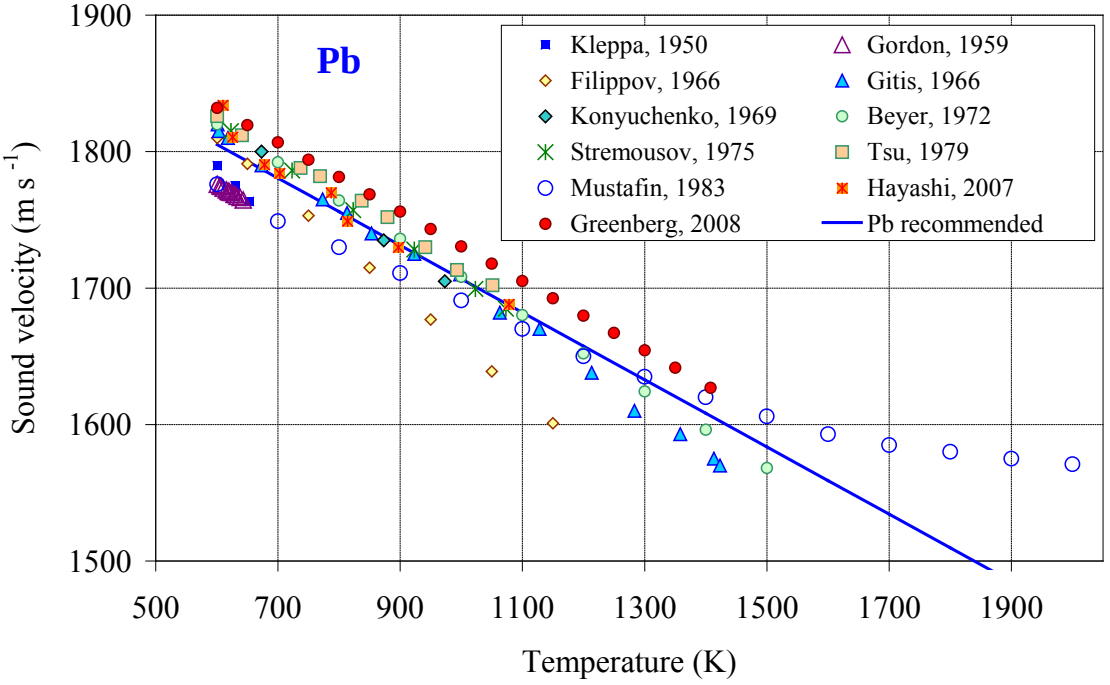

Source: Sobolev (2011).

Figure 2.13.1(b): Deviation of the selected literature data on the sound velocity in liquid lead from the Eq. (2.38)

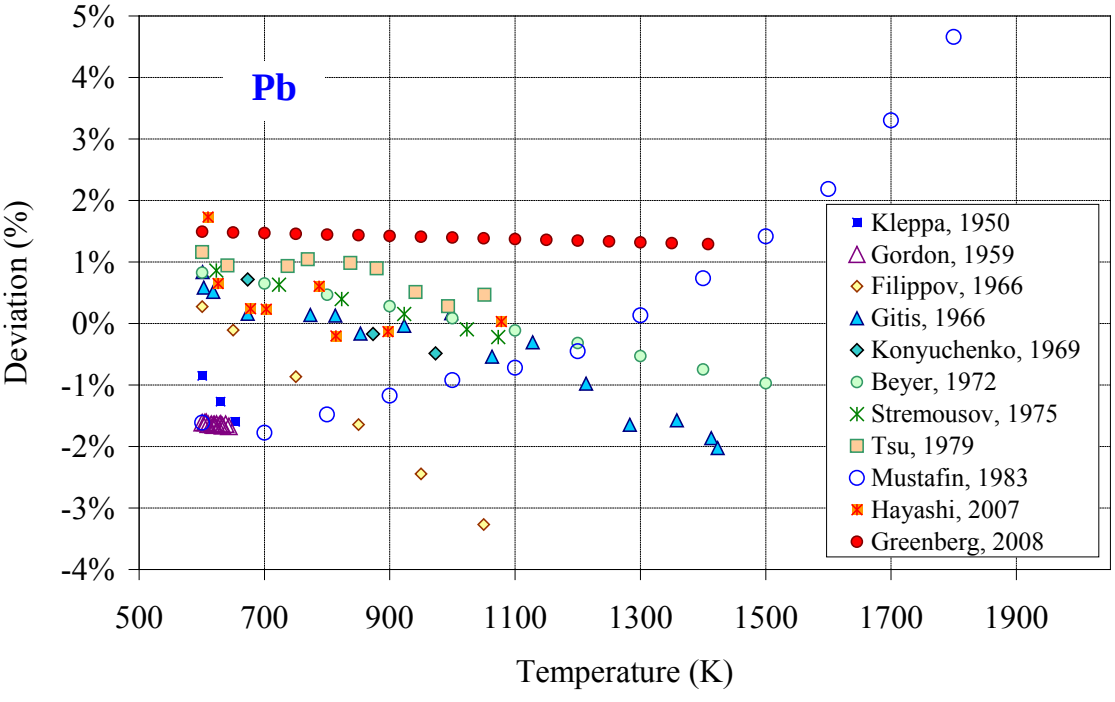

Source: Sobolev (2011).

At temperatures below 900 K, rather reasonable dispersion (±2%) is observed (Figure 2.13.1[a]) around the mean value, the temperature dependence of which can be described by the following linear correlation (Sobolev, 2011):

$$u_{s(Pb)}\left[\mathrm{m\,s^{-1}}\right] = 1953 - 0.246 \cdot T \tag{2.38}$$

With the same error this correlation can be extended to the temperature interval of 900-1 400 K, if the data of Gitis (1966) are discarded. At higher temperatures only the prognosis of Mustafin (1983) exists, which strongly deviates from the liner temperature dependence and provides higher values of the Pb sound velocity. Finally, it was decided not to take into account this estimation at $T > 1\,400$ K and recommend Eq. (2-38) for the estimation of the sound velocity in liquid lead for the temperature range of $T_{M,0}$-2 000 K at normal pressure. The deviation of the available data from the recommended correlation is illustrated in Figure 2.13.1(b).

2.13.2 Bismuth

The velocity of sound propagation in molten bismuth at normal pressure was measured by Kleppa (1950) in the temperature range close to the melting point, by Jarzynski (1963) from 578 K up to 715 K (305-442°C), by Hill (1965) in the interval of 553-685 K (280-412°C), by Gitis (1966) up to about 1 043 K (770°C), by Stremousov (1975) from 583 K up to 1 073 K (310-800°C), by Tsu (1982) in the temperature interval of 577-805 K (304-532°C), by Kanai (1993) from 553 K up to 1 173 K (280-900°C) and by Greenberg (2008) in the range $T_{M,0}$-1 273 K ($T_{M,0}$-1 000°C). In Kutateladze (1958) the recommendation of Kleppa (1950) was reproduced. Beyer (1972) cited different sources (including Kleppa [1950] and Gitis [1966]) and recommended the linear correlation, though indicating that uncertainty in the line slope is large. Iida (1988) reproduced correlations from Beyer (1972), Filippov (1966) and Tsu (1982) without giving the temperature limits and their own recommendations. The works included in the database are shown in Table 2.13.2.

Table 2.13.2: Selected database on velocity of sound in liquid bismuth

Reg. No.	Parameter	Measurement method	Estimated accuracy %	Temperature range, K	Pressure range, Pa	Values	Reference
13.2.1	Sound velocity	Pulse propagation	2	545-638	~10^5	–	Kleppa (1950)
	Interpolation function: $u_s = 1\,635 - 0.5\cdot(T - T_{M,0}) = 1\,907 - 0.5\cdot T$ m s^{-1}						
	Comments: 99.99% Bi						
13.2.2	Sound velocity	Pulse propagation	0.5	578-715	~10^5	–	Jarzynski (1963)
	Interpolation function: $u_s = 2\,111 - 0.78\cdot T$ m s^{-1}						
	Comments: 99.98% Bi						
13.2.3	Sound velocity	Pulse propagation	0.1	553-685	~10^5	–	Hill (1965)
	Interpolation function: $u_s = 1\,590 + 0.261\cdot T - 2.921 \times 10^{-4}\cdot T^2$ m s^{-1} at T = 593-853 K						
	Comments: 99.999% Bi						

Table 2.13.2: Selected database on velocity of sound in liquid bismuth (*cont.*)

Reg. No.	Parameter	Measurement method	Estimated accuracy %	Temperature range, K	Pressure range, Pa	Values	Reference
13.2.4	Sound velocity	Pulsed interferometer	0.5	545-1 000	~10^5	–	Gitis (1966)
	Interpolation function: u_s = 1 670 m s^{-1} at T = 545-593 K u_s = 1 777 – 0.18·T m s^{-1} at T = 593-853 K u_s = 1 811 – 0.22·T m s^{-1} at T = 853-1 043 K						
	Comments: 99.998% Bi						
13.2.5	Sound velocity	n/a	(1-2)	545-(700?)	~10^5	–	Beyer (1972)
	Interpolation u_s = 1 647 – 0.1·(T – $T_{M,0}$) = 1 701 – 0.1·T m s^{-1}						
	Comments: Technically pure Bi (?)						
13.2.6	Sound velocity	Pulsed interferometer	(0.2)	583-1 073	~10^5	-	Stremousov (1975)
	Interpolation function: u_s = 1 655 m s^{-1} at T = 545-583 K u_s = 1 742 – 0.15·T m s^{-1} at T = 583-783 K u_s = 1 787 – 0.207·T m s^{-1} at T = 783-1 073 K						
	Comments: 99.99% Bi						
13.2.7	Sound velocity	Pulse propagation	1	578-805	~10^5	–	Tsu (1982)
	Interpolation function: u_s = 1 571 + 0.376·T – 3.654 × 10^{-4}·T^2 m s^{-1}						
	Comments: Pb of extra high purity (6N = 99.9999% Bi)						
13.2.8	Sound velocity	Pulse propagation	(0.5)	553-1 173	~10^5	-	Kanai (1993)
	Interpolation function: u_s = 1 733 – 0.141·T m s^{-1} at T = 553-733 K u_s = 1 772 – 0.202·T m s^{-1} at T = 733-1 173 K						
	Comments: Bi of extra high purity (5N = 99.999% Bi)						
13.2.9	Sound velocity	Pulse propagation	< 1	545-1 273	~10^5	–	Greenberg (2008)
	Interpolation function: u_s = 1 650 m s^{-1} at T = 545-603 K u_s = 1 759 – 0.18·T m s^{-1} at T = 603-853 K u_s = 1 818 – 0.25·T m s^{-1} at T = 853-1 273 K						
	Comments: Bi of extra high purity (5N = 99.999% Bi)						

Based on the selected data presented in Table 2.13.2, the following correlation is recommended for the estimation of the sound velocity in molten bismuth in the temperature range $T_{M,0}$-1 800 K (Sobolev, 2011), where temperature is in kelvins:

$$u_{s(Bi)}\left[\mathrm{m\,s^{-1}}\right] = 1616 + 0.187 \cdot T - 2.2 \times 10^{-4} \cdot T^2 \qquad (2.39)$$

The data included in the database and the recommended Eq. (2.39) are presented in Figure 2.13.2(a). The temperature dependence of the sound velocity in liquid bismuth is non-linear. The velocity is almost constant from the melting temperature up to about 600 K and then decreases with increasing rate. (Some authors subdivide the temperature

range into intervals where this dependence is almost linear.) This behaviour is explained by the increase in bismuth density at melting followed by structural changes.

The deviation of the most of the data from Eq. (2.39) in the considered temperature interval is ±(1-2)% (see Figure 2.13.2[b]). Only results of two works (Kleppa, 1950; Jarzynski, 1963) strongly deviate from the recommended correlation with temperature.

Figure 2.13.2(a): Velocity of ultrasound in the molten bismuth as a function of temperature

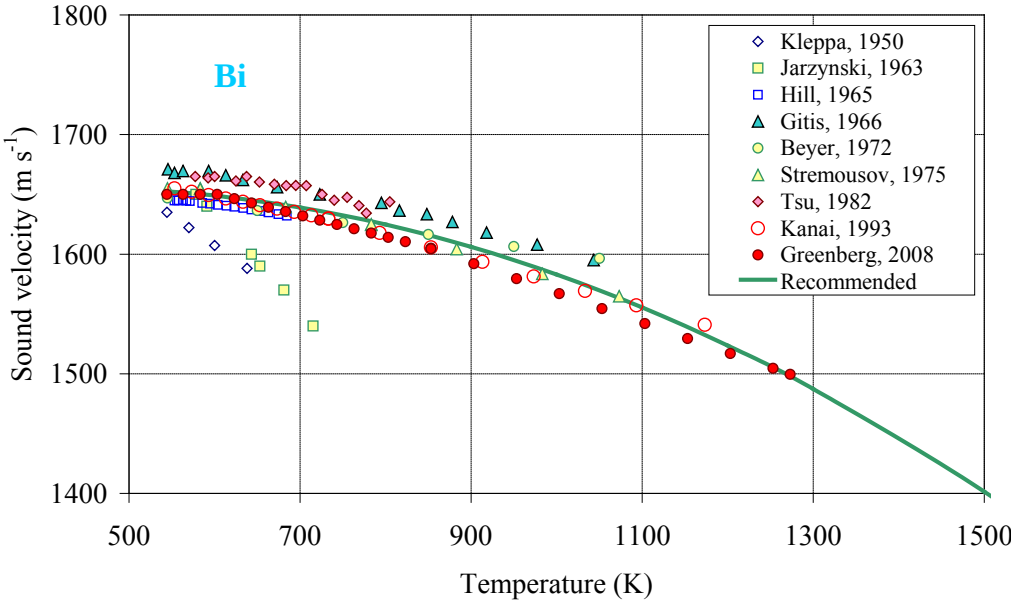

Source: Sobolev (2011).

Figure 2.13.2(b): Deviation of the selected literature data on the sound velocity in liquid bismuth from the Eq. (2.39)

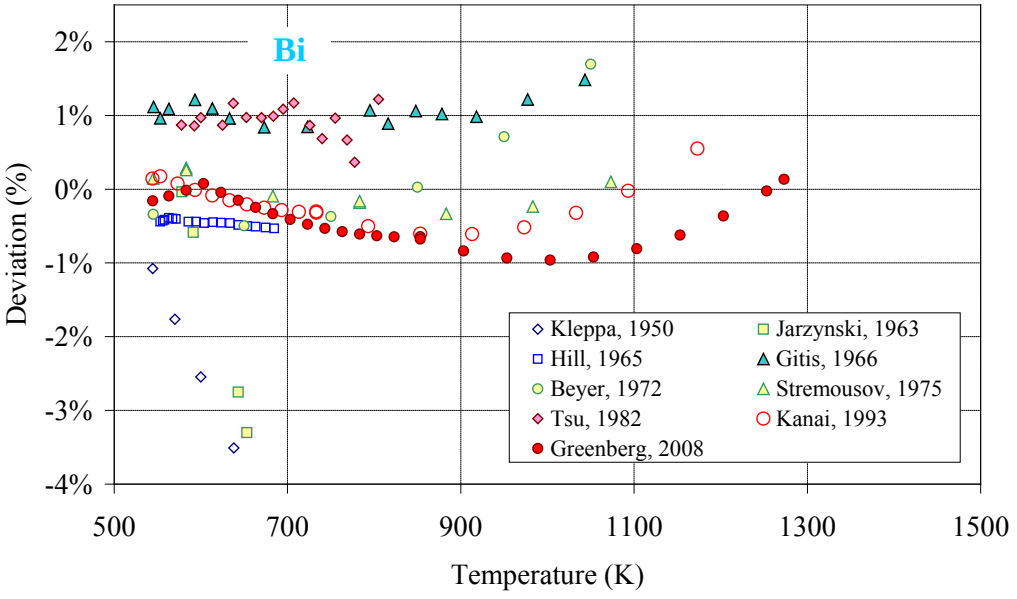

Source: Sobolev (2011).

2.13.3 LBE

Only three sources were found with data on sound velocity in molten LBE. Stremousov (1975) measured from 448 K up to 1 073 K (175-800°C), Kažys (2002) over the temperature range 433-603 K (160-330°C) and Hirabayashi (2005) in the interval of 460-680 K (187-407°C). The results of these publications have been included in the database presented in Table 2.13.3.

The values for the sound velocity in LBE are plotted in Figure 2.12.3(a) together with plots of the recommended correlations for lead (2.38) and bismuth (2.39). Values calculated with Vegard's law are also presented:

$$u_{s(LBE)} = x_{\mu(Pb)} \cdot u_{s(Pb)} + x_{\mu(Bi)} \cdot u_{s(Bi)} \tag{2.40}$$

where $x_{\mu(Pb)}$ and $x_{\mu(Bi)}$ are the atomic fractions of Pb and Bi in LBE.

One can see that all experimental data on the LBE sound velocity are in good agreement and lay between the recommended lines for Pb and Bi. Vegard's law gives a reasonable prediction of the LBE sound velocity at T = 600-1 100 K (where experimental results exist).

Taking into account that only three experimental data sets (Stremousov, 1975; Kažys, 2002; Hirabayashi, 2005) were found, the linear correlation for the LBE sound velocity is recommended (Sobolev, 2011):

$$u_{s(LBE)}\left[\mathrm{m\,s^{-1}}\right] = 1855 - 0.212 \cdot T \tag{2.41}$$

where temperature is in kelvins. The difference between the available experimental data on the LBE sound velocity and those obtained with Eq. (2.41) is less than 1% in the considered temperature range (Figure 2.13.3[b]).

Table 2.13.3: Selected database on sound velocity of the melted LBE at normal pressure

Reg. No.	Parameter	Measurement method	Estimated accuracy %	Temperature range, K	Pressure range, Pa	Values	Ref.
13.3.1	Sound velocity	Pulsed interferometer	(0.2)	583-1 073	~10^5	–	Stremousov (1975)
	Interpolation function: u_s = 1 851 – 0.193·T m s^{-1} at T = 348-723 K u_s = 1 895 – 0.254·T m s^{-1} at T = 723-1 073 K						
	Comments: 43 wt.% Pb + 57 wt.% Bi, purity: 99.99% Bi and 99.99% Pb						
13.3.2	Sound velocity	Pulse propagation	< 0.5	433-733	~10^5	–	Kažys (2002)
	Interpolation function: u_s = 1 806.5 – 0.02592·T – 1.605 × 10^{-4}·T^2 m s^{-1}						
	Comments: 44.5 wt.% Pb + 55.5 wt.% Bi, technical purity: 99% Pb and 99% Bi						
13.3.3	Sound velocity	Pulse propagation	0.5	460-780	~10^5	–	Hirabayashi (2005)
	Interpolation function: u_s = 1 871.5 – 0.258·T m s^{-1}						
	Comments: 44.5 wt.% Pb + 55.5 wt.% Bi, unknown purity						

Figure 2.13.3(a): Sound velocity in molten LBE, Pb and Bi versus temperature

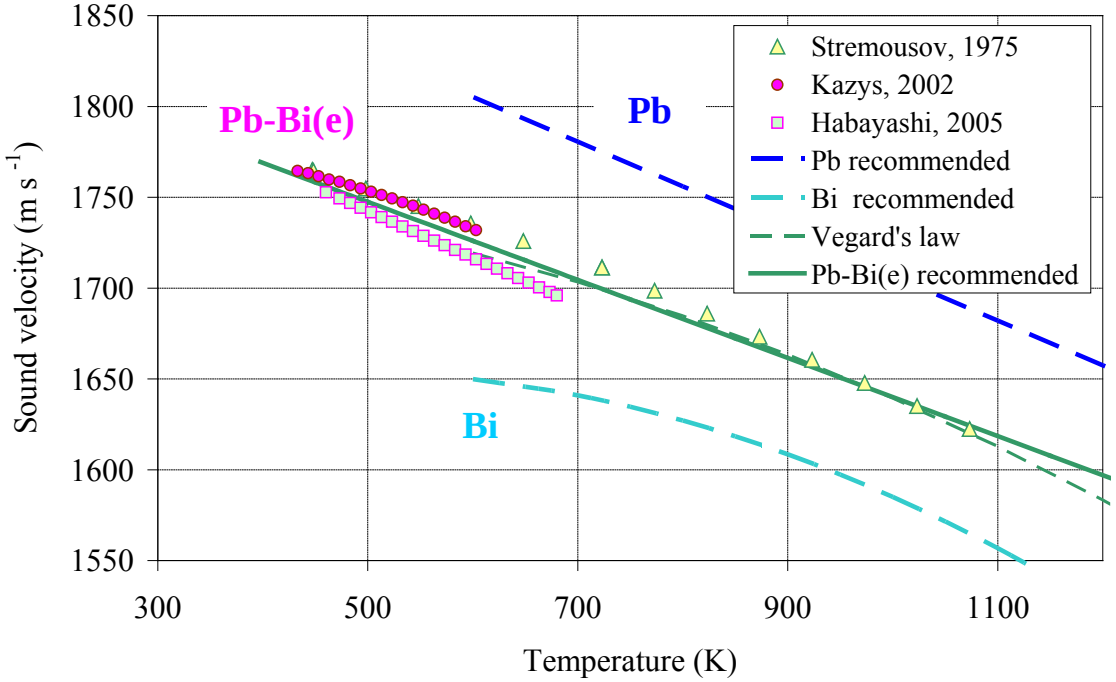

Source: Sobolev (2011).

Figure 2.13.3(b): Deviation of the literature data on the sound velocity in the molten lead-bismuth eutectic from the Eq. (2.40)

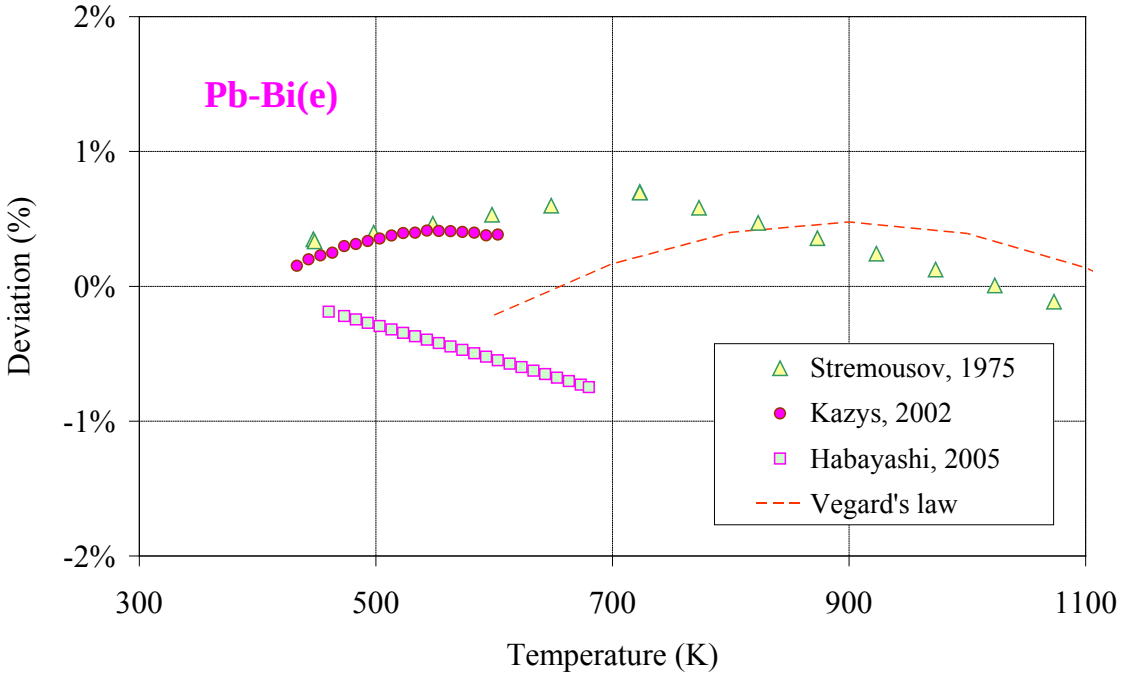

Source: Sobolev (2011).

2.13.4 *Bulk elastic modulus*

The results of the calculations of the isentropic (adiabatic) bulk elastic modulus B_S (and the isentropic compressibility β_S) of the molten lead, bismuth and LBE at normal pressure obtained with Eq. (2.37):

$$B_S(T) \equiv \frac{1}{\beta_S} = \rho(T) \cdot u_s^2(T)$$

using the recommended above correlations for density and sound velocity are presented below in Figure 2.13.4.

From Figure 2.13.4 it can be seen that the isentropic bulk modulus of LBE is higher than that of Bi but lower than that of Pb at the same temperature (the isentropic compressibility of LBE is lower than that of Bi and higher than of Pb).

In the respective temperature range and at the normal atmospheric pressure, the temperature dependence of the elastic moduli of Pb, Bi and LBE can be described with the help of parabolic functions:

- Lead:

$$B_{s(Pb)}[\text{Pa}] = \left(43.50 - 1.552 \times 10^{-2} \cdot T + 1.622 \times 10^{-6} \cdot T^2\right) \times 10^9 \quad (2.42)$$

- Bismuth:

$$B_{s(Bi)}[\text{Pa}] = \left(30.09 - 2.441 \times 10^{-3} \cdot T - 3.913 \times 10^{-6} \cdot T^2\right) \times 10^9 \quad (2.43)$$

- LBE:

$$B_{s(LBE)}[\text{Pa}] = \left(38.02 - 1.296 \times 10^{-2} \cdot T + 1.320 \times 10^{-6} \cdot T^2\right) \times 10^9 \quad (2.44)$$

where temperatures is in kelvins.

Figure 2.13.4: Isentropic bulk elastic modulus and compressibility of the molten Pb, Bi and LBE versus temperature

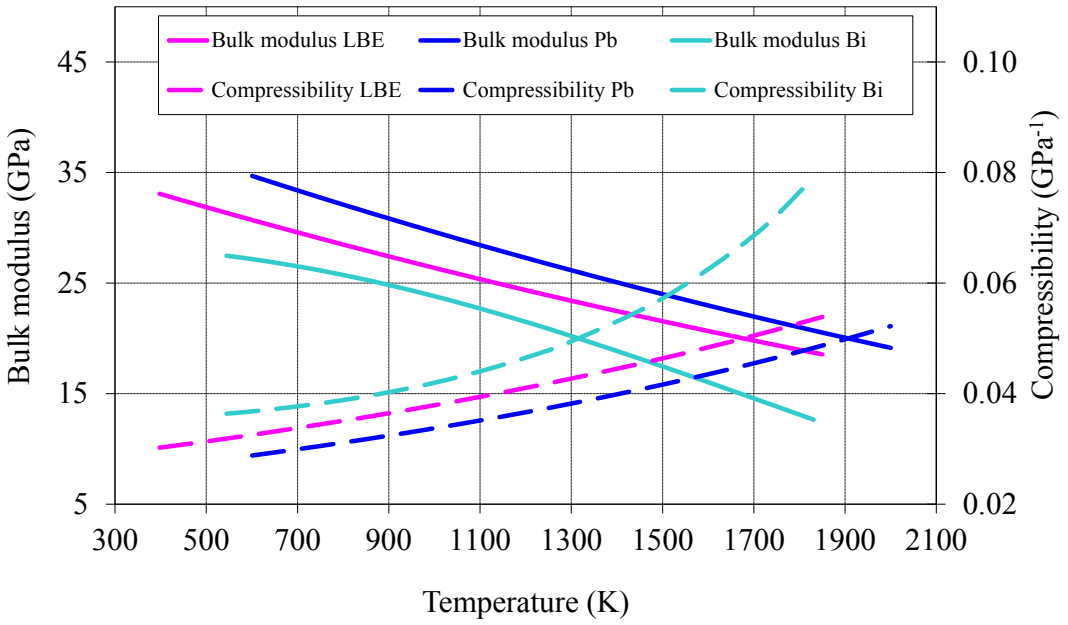

Source: Sobolev (2011).

The isothermal bulk modulus B_T (or the isothermal compressibility β_T) can be expressed through the isentropic bulk modulus B_S (or the isentropic compressibility β_S), the isobaric thermal expansion coefficient α_p, density ρ and the isobaric specific heat c_p (c_p is presented in Section 2.14):

$$B_T = \left(\frac{1}{B_S} + \frac{T \cdot \alpha_p^2}{\rho \cdot c_p} \right)^{-1} \quad \beta_T = \beta_S + \frac{T \cdot \alpha_p^2}{\rho \cdot c_p} \tag{2.45}$$

2.14 Heat capacity

Heat capacity is one of the most important properties of a coolant. Calculation of the coolant enthalpy change in function of temperature requires knowledge of the isobaric heat capacity. Available experimental data on the heat capacity of heavy liquid metals are not numerous. The theoretical calculation of heat capacity of liquid metals is restricted by the extreme complexity of the motion of atoms in liquids. Usually the isobaric heat capacity is measured, and then empirical correlations are used to fit the experimental results. The heat capacity of mixtures and alloys follows well the additivity low. Therefore, the effect of impurities on the heat capacity of technically pure liquid metals is weak. An extensive review of the existing experimental data on the heat capacity of liquid lead, bismuth and LBE was performed by Imbeni (1998, 1999).

When the isobaric specific heat capacity (c_p) is known, then the isochoric specific heat capacity (c_v) can be expressed through c_p, α_p, ρ and B_T (or B_S) as follows:

$$c_V = c_p - \frac{\alpha_p^2 \cdot B_T \cdot T}{\rho} = c_p \cdot \left(1 + \frac{\alpha_p^2 \cdot B_S \cdot T}{\rho \cdot c_p} \right)^{-1} \tag{2.46}$$

2.14.1 Lead

The heat capacity data and recommendations for liquid lead taken from Miller (1954), Lyon (1960), Kutateladze (1958), Friedland (1966), Touloukian (1970), Hultgren (1973b), Kubaschewski (1979, 1993), Iida (1988), Gurvich (1991), Cheynet (1996), Imbeni (1998), Smithells (1983, 2004) and Kirillov (2000a, 2008) have been analysed to include in the current database.

Miller (1954) reproduces in the Lyon handbook (1954) the lead heat capacity values at three temperatures from Klinkhardt (1927). Friedland (1966) used data of Douglas (1953) and the linear interpolation formula of Stull (1956). In the handbook of Touloukian (1970a) five sets of data on the heat capacity of liquid lead were reproduced from different sources. Two of them were discarded (one provides very high values; the second was reproduced in Lyon [1954]). Three others, Umino (1926), Dixon (1927) and Douglas (1954), were included in the database as Touloukian 1970(1), 1970(2) and 1970(3), respectively. Hultgren (1973b) analysed values selected from many previous publications, but in the temperature range of 601-1 200 K they seem to use data from Douglas (1953, 1954) and the correlation from Stull (1956). At higher temperatures, they recommend using the constant heat capacity value. Iida (1988) reproduced an analytical equation from Kubaschewski (1979), who in turn references many previous sources (Kelley, 1960; Stull, 1956, 1971; Chase, 1978), but also recommends a very similar correlation for the liquid lead heat capacity. In the later edition of Kubaschewski (1993), a few more recent sources were cited (Glushko, 1981; Pankratz, 1982; Chase, 1982; Knacke, 1991), however, almost the same correlation was recommended. Practically the same correlation was presented in the 82nd edition of the CRC Handbook (2002). Gurvich (1991) gave tables with data obtained by models benchmarked on the existing experimental data and proposed a polynomial for the heat capacity of the liquid lead in a whole temperature range from

melting to boiling. Cheynet (1996) provides the correlations for a large temperature range based on the previous studies (1989) and on other sources (though these are not referenced). The last edition of SMRB (Smithells, 2004) reports the linear correlation obtained with values taken from Hultgren (1973b) in the temperature range of $T_{M,0}$-1 300 K, but also gives some values taken from an earlier source.

Data on the heat capacity of the molten lead presented by Kirillov (2000a, 2008) repeat those of Kutateladze (1958), therefore they were not included in the selected database.

The selected sources are described in Table 2.14.1 and their data are presented in Figure 2.14.1(a).

Table 2.14.1: Selected database on the isobaric heat capacity of molten lead at normal pressure

Reg. No.	Parameter	Measurement method	Estimated accuracy, %	Temperature range, K	Pressure, Pa	Value, J kg^{-1} K^{-1}	Ref.
14.1.1	Specific heat	?	(5)	600 673 773	~10^5	163 155 155	Miller (1954)
	Interpolation function: *n/a*						
	Comments: Unknown purity						
14.1.2	Specific heat	Direct heating	(5)	673-1 073	~10^5	–	Kutateladze (1958)
	Interpolation function: c_p = 147 J kg^{-1} K^{-1}						
	Comments: Unknown purity						
14.1.3	Specific heat	?	(5)	601-1 170	~10^5	–	Friedland (1966)
	Interpolation function: $c_p = 154.3 - 0.0145 \cdot T$ J kg^{-1} K^{-1}						
	Comments: Unknown purity						
14.1.4	Specific heat	?	(5)	648-1 023	~10^5	–	Touloukian [1970 (1)]
	Interpolation function: c_p = 136.5 J kg^{-1} K^{-1}						
	Comments: 99.977% Pb						
14.1.5	Specific heat	?	1	601-1 200	~10^5	–	Touloukian [1970(2)]
	Interpolation function: $c_p = 148.6- - 0.0118 \cdot T$ J kg^{-1} K^{-1}						
	Comments: C.P. grade Pb purity						
14.1.6	Specific heat	?	(5)	601-1 200	~10^5	–	Touloukian [1970(3)]
	Interpolation function: $c_p = 156.8 - 0.0148 \cdot T$ J kg^{-1} K^{-1}						
	Comments: > 99.9% Pb						
14.1.7	Specific heat	Heat evolution	5	601-1 100	~10^5	–	Hultgren (1973b)
	Interpolation function: $c_p = 156 - 0.0144 \cdot T$ J kg^{-1} K^{-1} at $T \leq$ 1 300 K = 138 J kg^{-1} K^{-1} at $T >$ 1 300 K						
	Comments: Unknown purity						

Table 2.14.1: Selected database on the isobaric heat capacity of molten lead at normal pressure (*cont.*)

Reg. No.	Parameter	Measurement method	Estimated accuracy, %	Temperature range, K	Pressure, Pa	Value, J kg^{-1} K^{-1}	Ref.
14.1.8	Specific heat	n/a	6-15	601-2 016	~10^5	–	Gurvich (1991)
	Interpolation function: $c_p = 175.1 - 4.961 \times 10^{-2} \cdot T + 1.985 \times 10^{-5} \cdot T^2 - 2.099 \times 10^{-9} \cdot T^3 - 1.524 \times 10^6 \cdot T^{-2}$ J kg^{-1} K^{-1}						
	Comments: Pure Pb						
14.1.9	Specific heat	n/a	(5-15)	601-2 016	~10^5	–	Cheynet (1996)
	Interpolation function: $c_p = 156.8 - 0.0149 \cdot T$ J kg^{-1} K^{-1} at $T \leq 1\,200$ K $c_p = 87.9 + 3.06 \times 10^{-2} \cdot T - 3.426 \times 10^{-6} \cdot T^2 + 2.761 \times 10^7 \cdot T^{-2}$ J kg^{-1} K^{-1} at $T > 1\,200$ K						
	Comments: Pure lead						
14.1.10	Specific heat	n/a	(5)	601 673 773 873	~10^5	152 144 137 135	Smithells (2004)
	Interpolation function: $c_p = 316 - 0.418 \cdot T + 2.4 \times 10^{-4} \cdot T^2$						
	Comments: Unknown purity						

From Figure 2.14.1(a) it can be seen that Miller (1954) gives higher values for the heat capacity of lead than those reported by other sources. The values recommended by Kutateladze (1958) are independent of temperature. At temperatures higher than 1 300 K (1 027°C) two extrapolation tendencies are observed. According to that of Friedland (1966), the specific heat of lead decreases linearly with temperature, while according to Hultgren (1973b) it remains constant. In the recommendations of Gurvich (1991) and Cheynet (1996) it slightly increases with temperature at $T > 1\,500$ K.

A theoretical calculation of the Pb isobaric heat capacity performed by Onistchenko (1999) indicates that it should decrease with temperature after melting, then passes through a large plateau and begins increasing.

A reasonable choice for the isobaric (p = 0.1 MPa) heat capacity of the pure liquid lead in the temperature range of $T_{M,0}$ to 2 000 K (1 027°C) is the recommendation of Gurvich (1991) (renormalised to other units):

$$c_{p(Pb)}\left[\mathrm{J\,kg^{-1}\,K^{-1}}\right] = 175.1 - 4.961 \times 10^{-2} \cdot T + 1.985 \times 10^{-5} \cdot T^2 - 2.099 \times 10^{-9} \cdot T^3 - 1.524 \times 10^{6} \cdot T^{-2} \quad (2.47)$$

where temperature is in kelvins. The estimated uncertainty is 5-7% at $T = T_{M,0}$-1 500 K and 7-15% at higher temperatures where no experimental data were found in literature.

Taking into account a rather large uncertainty, a more compact correlation is proposed for use in design calculations (Sobolev, 2011):

$$c_{p(Pb)}\left[\mathrm{J\,kg^{-1}\,K^{-1}}\right] = 176.2 - 4.923 \times 10^{-2} \cdot T + 1.544 \times 10^{-5} \cdot T^2 - 1.524 \times 10^{6} \cdot T^{-2} \quad (2.48)$$

Figure 2.14.1(b) shows that the recommended Eq. (2.47) is in a very good agreement (< 3%) with the data presented in Freeland (1966), Touloukian (1970), Hultgren (1973b) and Cheynet (1996) and also with the theoretical model of Onistchenko (1999). Some earlier recommendations presented in Lyons (1954), Kutateladze (1958) (reproduced in Kirillov

[2000a, 2008]) and in Umino (1926) (reproduced in Touloukian [1970a]) deviate from the recommended Eq. (2.48) for about 7-10% (Figure 2.14.1[b]).

Figure 2.14.1(a): Heat capacity of molten lead as a function of temperature at normal pressure

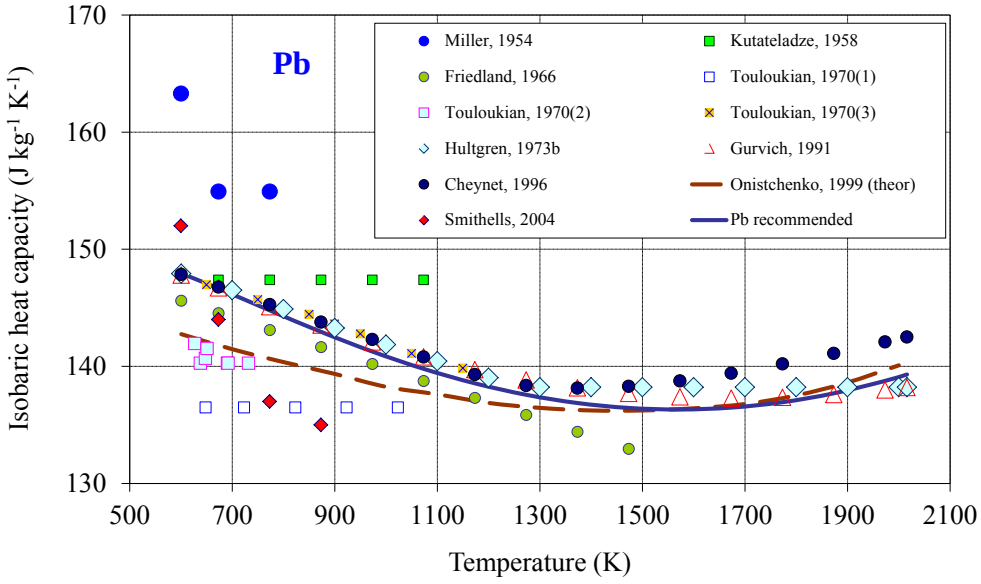

Source: Sobolev (2011).

Figure 2.14.1(b): Deviation of the selected data on the isobaric heat capacity of liquid lead from the Eq. (2.48)

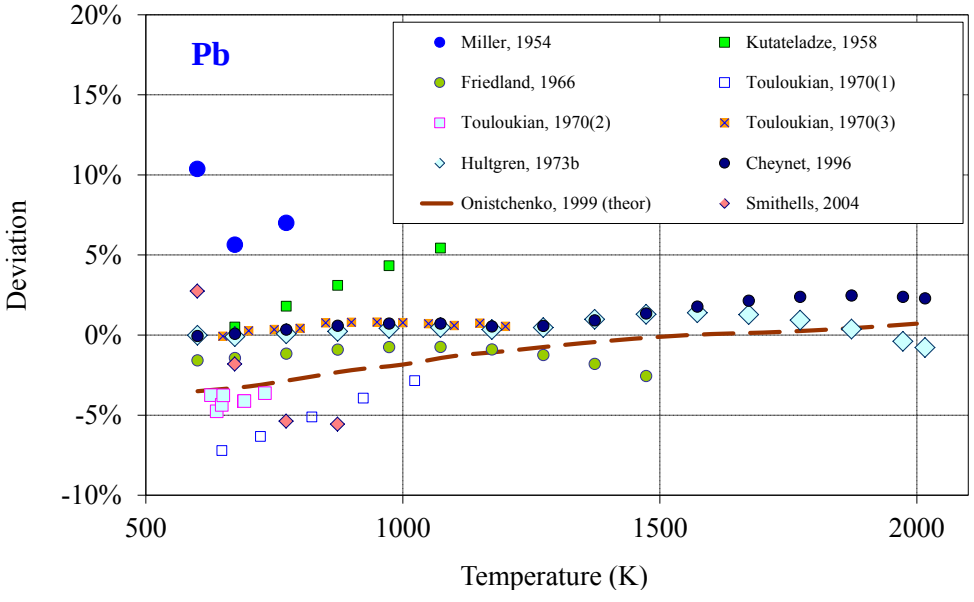

Source: Sobolev (2011).

2.14.2 Bismuth

The data for the heat capacity of bismuth as a function of temperature analysed in this handbook have been taken from Miller (1954), Kutateladze (1958), Howe (1961), Touloukian (1970a), Hultgren (1973b), Iida (1988), Kubaschewski (1979, 1993), Cheynet (1996) and Smithells (1983, 2004).

Howe (1961) and Crean (1964) reported values given earlier in Miller (1954) and Lyon (1960) and was not included in the database.

Miller (1954) reproduced the bismuth heat capacity values presented in the old Gmelins Handbook (1924). The same source was used in Reis (1959). In the handbook of Touloukian (1970a) three sets of the results on the heat capacity of liquid bismuth were reproduced from the earlier publications. The oldest one (Umino, 1926) gives a rather high constant value (0.0373 cal g^{-1} K^{-1} or 156 J kg^{-1} K^{-1}) for the temperature range of 545-873 K (272-600°C). Two others (Carpenter, 1932; Bell, 1960) were included in the selected database as Touloukian 1970(1) and 1970(2), respectively. Hultgren (1973b) presented values selected based on the critical assessment of the previously published data and extended the recommendations up to the bismuth boiling temperature. Iida (1988) reported an analytical equation taken from the compilation of Kubaschewski (1979) (where the results of Hultgren [1963] were cited). Kubaschewski (1993) reproduced Knacke's (1991) recommendations. In the old CRC Handbook of 1984 only one value (7.6 cal mol^{-1} $°C^{-1}$ or 156 J kg^{-1} K^{-1}) was given. Cheynet (1996) recommended two different correlations for two temperature intervals. SMRB (Smithells, 2004) presented a set of values with references to Grosse (1966), Stull (1956) and Hultgren (1963) (a point of this set at 673 K with anomalous high value was removed from the database). Moreover, Hultgren (1973b) was cited in this handbook and the correlation from Kubaschewski (1979) was recommended. In the previous edition of the handbook (Smithells, 1983), the references to Samsonov (1969), Viswanath (1972) and Bush (1963) were also given. The selected database on the isobaric heat capacity of liquid bismuth is presented in Table 2.14.2.

Figure 2.14.2(a) shows the values of heat capacity for molten bismuth obtained from the selected literature sources in the temperature range of interest. As it can be seen, the values reported in Miller (1954) increase with temperature and those of Kutateladze (1958) and of one set of Touloukian (1970[0]) remain constant, in contrast with the results published later by other authors. These data were not used in the development of the recommended correlation.

A theoretical calculation of the liquid Bi isobaric heat capacity performed by Onistchenko (1999) indicates that it shows the similar temperature dependence as that of the liquid lead (Figure 2.14.2[a]).

Based on analogy with other liquid metals the data were chosen with the heat capacity values decreasing with temperature after melting, and the correlation proposed by Imbeni (1998) (transformed to other units) is recommended for use in the isobaric specific heat of molten bismuth:

$$c_{p(\mathrm{Bi})}\left[\mathrm{J\,kg^{-1}\,K^{-1}}\right] = 118.2 + 5.934\times10^{-3}\cdot T + 7.183\times10^{6}\cdot T^{-2} \qquad (2.49)$$

In Imbeni (1998) this correlation was recommended for the temperature interval from $T_{M,0}$ to 1 300 K. However, as can be seen from Figure 2.14.2(a), the temperature range of applicability of Eq. (2.49) can be extended to a whole temperature range of liquid bismuth at normal pressure: from $T_{M,0}$ to $T_{B,0}$. The deviation of the analysed literature data from Eq. (2.49) is presented in Figure 2.13.2(b). Taking into account that the oldest data from Miller (1954), Kutateladze (1958) and one set from Touloukian (1970a) were discarded, the deviation of the selected database from Eq. (2.49) does not exceed about 2%.

Table 2.14.2: Selected database on the isobaric heat capacity of molten bismuth at normal pressure

Reg. No.	Parameter	Measurement method	Estimated accuracy, %	Temperature range, K	Pressure, Pa	Value	Ref.
14.2.1	Specific heat	Direct heating	(5)	553-973	~10^5	–	Kutateladze (1958)
	Interpolation function: c_p = 151 J kg^{-1} K^{-1}						
	Comments: Unknown purity						
14.2.2	Specific heat	?	(5)	546-644	~10^5	–	Touloukian [1970(1)]
	Interpolation function: $c_p = 170 - 0.046 \cdot T$ J kg^{-1} K^{-1}						
	Comments: 99.9% Bi						
14.2.3	Specific heat	?	(5)	545-802	~10^5	–	Touloukian [1970 (2)]
	Interpolation function: $c_p = 241 - 0.261 \cdot T + 1.6 \times 10^{-4} \cdot T^2$ J kg^{-1} K^{-1}						
	Comments: 99.9999 Bi						
14.2.4	Specific heat	Power evolution	5-15	545-1 800	~10^5		Hultgren (1973b)
	Interpolation function: $c_p = 199 - 0.134 \cdot T + 6.75 \times 10^{-5} \cdot T^2$ J kg^{-1} K^{-1} at $T \leq 1\,200$ K c_p = 130.2 J kg^{-1} K^{-1} at $T > 1\,200$ K						
	Comments: Pure Bi						
14.2.5	Specific heat	n/a	(5)	545-802	~10^5	–	Kubaschewski (1993)
	Interpolation function: $c_p = 91.1 + 4.967 \times 10^{-2} \cdot T - 1.9 \times 10^{-5} \cdot T^2 + 1.01 \times 10^{7} \cdot T^{-2}$ J kg^{-1} K^{-1} at $T \leq 1\,200$ K c_p = 130.2 J kg^{-1} K^{-1} at $T > 1\,200$ K						
	Comments: Pure Bi						
14.2.6	Specific heat	n/a	(5-15)	545-1 800	~10^5	–	Cheynet (1996)
	Interpolation function: $c_p = -248.1 + 0.7207 \cdot T - 3.875 \times 10^{-4} \cdot T^2 + 3.461 \times 10^{7} \cdot T^{-2}$ J kg^{-1} K^{-1} at $T \leq 800$ K $c_p = 101.2 + 0.02451 \cdot T - 5.8 \times 10^{-6} \cdot T^2 + 1.098 \times 10^{7} \cdot T^{-2}$ J kg^{-1} K^{-1} at $T > 800$ K						
	Comments: Pure Bi						
14.2.7	Specific heat	?	?	544-873	~10^5	–	Smithells (2004)
	Interpolation function: $c_p = 167 - 4.38 \times 10^{-2} \cdot T + 6.57 \times 10^{-6} \cdot T^2$ J kg^{-1} K^{-1}						
	Comments: Unknown purity						

Figure 2.14.2(a): Heat capacity of molten bismuth versus temperature at the normal pressure

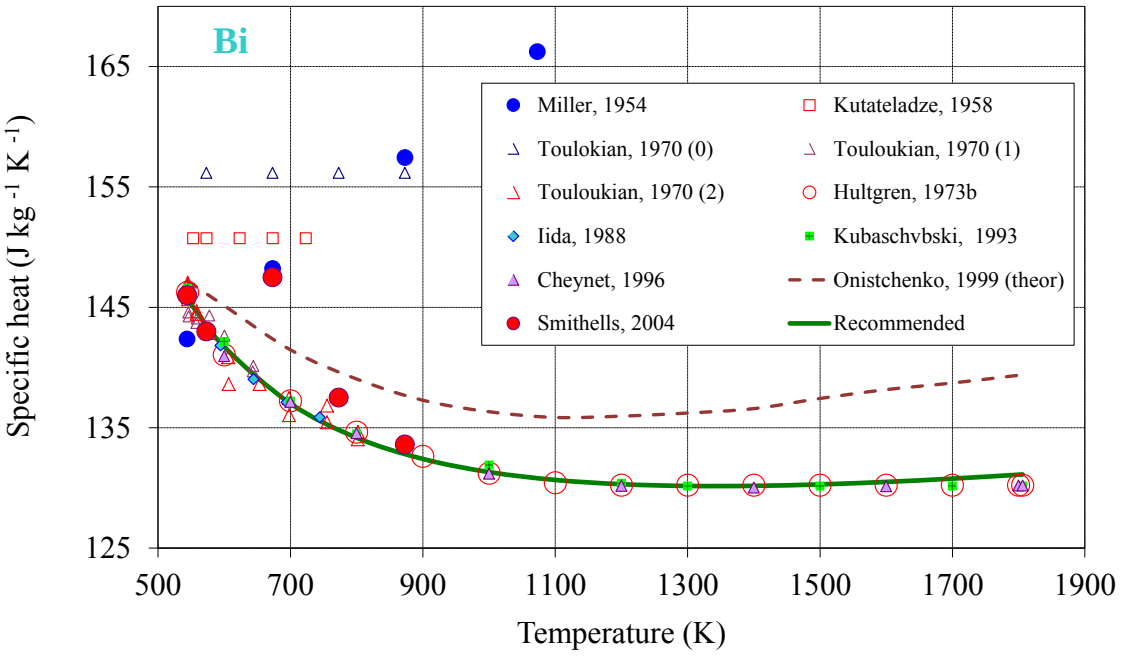

Source: Sobolev (2011).

Figure 2.14.2(b): Deviation of the literature data on the isobaric heat capacity of molten bismuth from the Eq. (2.49)

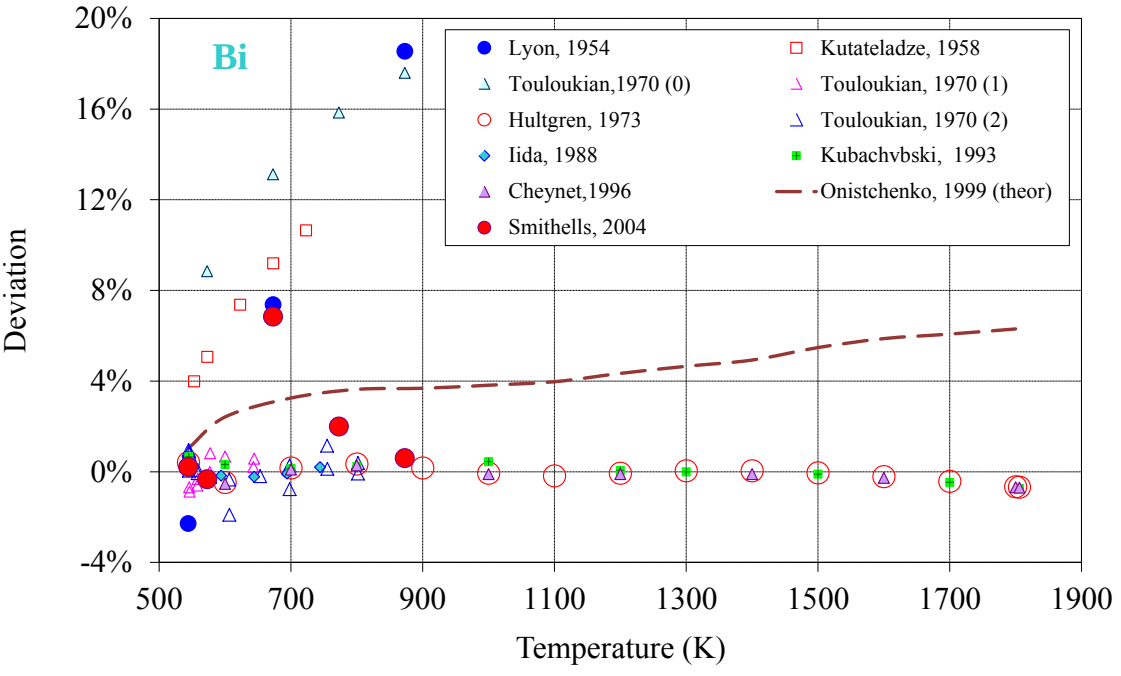

Source: Sobolev (2011).

2.14.3 LBE

Available data on the heat capacity of LBE are very limited. Only three independent sources were found: Miller (1954), Kutateladze (1958) and Hultgren (1973). The two older publications recommend the same value of the LBE specific heat (0.035 cal g^{-1} °C^{-1} or 146.5 J g^{-1} K^{-1}) for a range of temperatures. Kutateladze (1958) recommended this value for temperatures from 130°C to 700°C (403-973 K). This recommendation was reproduced in later handbooks (Mantell, 1958; Lyon, 1960; Bonilla, 1964; Crean, 1964; Friedland, 1966), and some of them even extended it to higher temperatures without any explanation. The value (146 J kg^{-1} K^{-1}) was repeated by Cevolani (1998) and by Kirillov (2000a, 2008). The only source which reports the LBE heat capacity depending on temperature is that of Hultgren (1973a), which refers to a report of Douglas (1953) as the original source. The data from Hultgren (1973a) were reprinted in later compilations, and a linear interpolation based on these data in the temperature range of $T_{M,0}$ to 1 100 K was proposed to use in Imbeni (1999) and in Morita (2006). Based on an analysis of the available data, the information from three sources (Miller, 1954; Kutateladze, 1958; Hultgren, 1973a) is included in the selected database shown in Table 2.14.3.

Figure 2.14.3(a) shows plots of the specific heat capacity of molten LBE as a function of temperature. A line obtained in the temperature range 601-1 800 K with the additive Kopp's law (often used for calculation of the heat capacity and enthalpy of the binary systems) was determined as follows:

$$c_{p(LBE)} = x_{Pb} \cdot c_{p(Pb)} + x_{Bi} \cdot c_{p(Bi)} \tag{2.50}$$

where $c_{p(Pb)}$ and $c_{p(Bi)}$ are the specific heat capacities of lead and bismuth, x_{Pb} and x_{Bi} are the weight fractions of Pb and Bi in LBE.

A rather good agreement exists between the values obtained with Kopp's law and those recommended in Hultgren (1973a).

Table 2.14.3: Selected database on the isobaric heat capacity of molten LBE at normal pressure

Reg. No.	Parameter	Measurement method	Estimated accuracy, %	Temperature range, K	Pressure, Pa	Value, J kg^{-1} K^{-1}	Ref.
14.3.1	Specific heat	?	(5)	417-631	~10^5	146.5 average	Miller (1954)
	Interpolation function: *n/a*						
	Comments: 44.5 wt.% Pb + 55.5 wt.% Bi, unknown purity						
14.3.2	Specific heat	Direct heating	(5)	403-973	~10^5	–	Kutateladze (1958)
	Interpolation function: $c_{p(LBE)}(T)$ = 146.5 J kg^{-1} K^{-1}						
	Comments: 44.5 wt.% Pb + 55.5 wt.% Bi, unknown purity						
14.3.3	Specific heat	Heat evolution	5	400-1 100	~10^5	–	Hultgren (1973a)
	Interpolation function: $c_{p(LBE)}(T) = 160 - 0.024 \cdot T$ J kg^{-1} K^{-1}						
	Comments: 45.3 wt.% Pb + 54.7 wt.% Bi, unknown purity						

Figure 2.14.3(a): Specific heat of molten LBE versus temperature

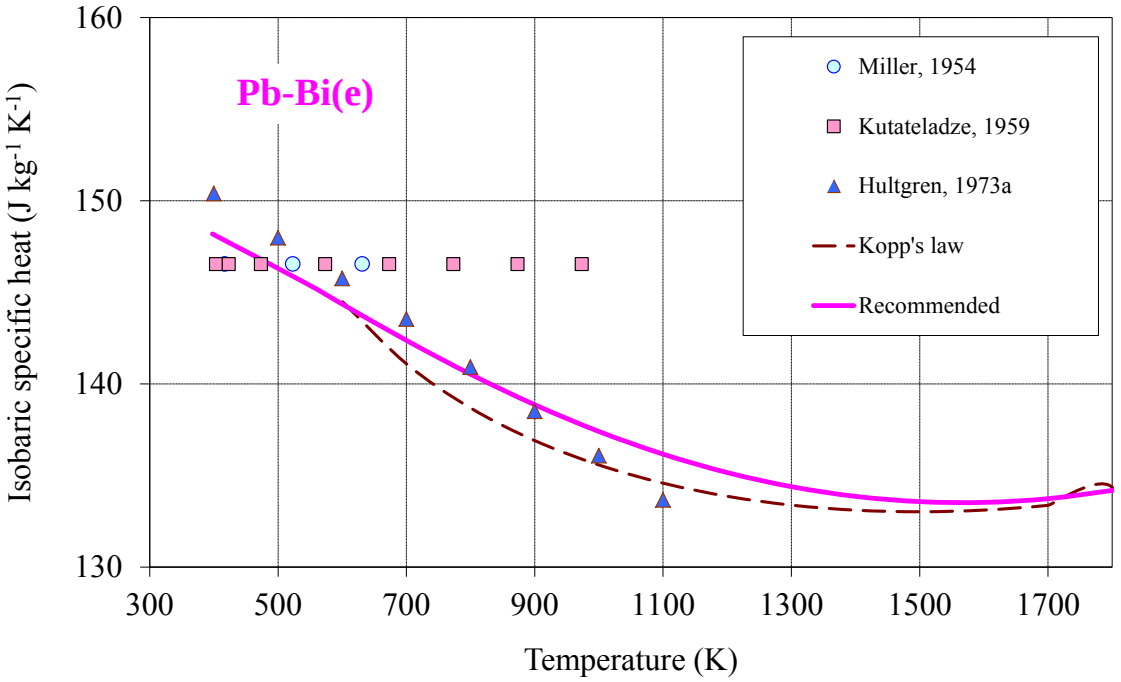

Source: Sobolev (2011).

Figure 2.14.3(b): Deviation of the available data on heat capacity of molten LBE from Eq. (2.51)

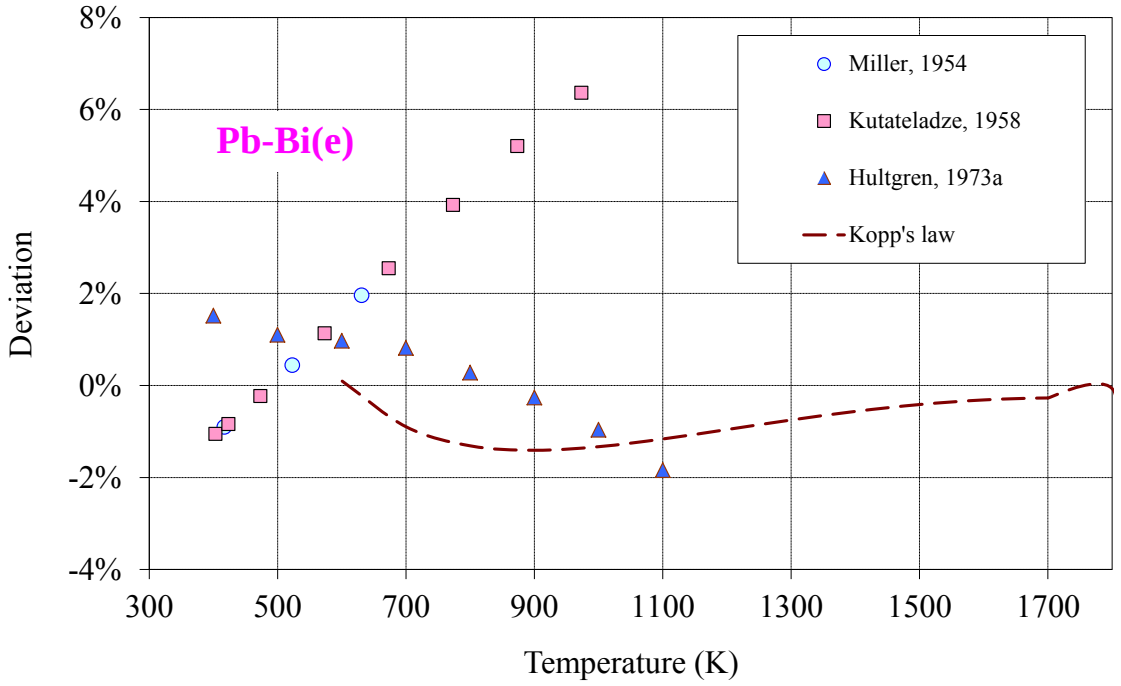

Source: Sobolev (2011).

Attempting, on the one hand, to take into account the similarity between LBE and its components (Pb and Bi) and, on other hand, to use the available experimental data on LBE specific heat, a fitting of the data set was developed using values given above with a polynomial (also taking into account the values obtained with Kopp's law) in the temperature range of 400-1 100 K (127-827°C) with the results as follows (Sobolev, 2011):

$$c_{p(\mathrm{LBE})}\left[\mathrm{J\,kg^{-1}\,K^{-1}}\right] = 164.8 - 3.94\times10^{-2}\cdot T + 1.25\times10^{-5}\cdot T^{2} - 4.56\times10^{5}\cdot T^{-2} \qquad (2.51)$$

where temperature is in kelvins.

The deviation of the data included in the data set from the recommended Eq. (2.51) is illustrated by Figure 2.14.3(b). One can see that the deviation of the selected values of the LBE specific heat from the recommended Eq. (2.51) does not exceed 5% in the temperature range of 400-1 100 K (127-827°C). The deviation of the values obtained using Kopp's law is about 1-2%. Expecting that the validity of Kopp's law for LBE is even better at high temperatures, it is recommended to extend the temperature region of applicability of Eq. (2.51) to the normal boiling temperature of LBE.

2.14.4 *Enthalpy*

The specific enthalpy (h) as a function of temperature at the given pressure is found by integration of the isobaric specific heat capacity over temperature:

$$h(T,p) = h(T_{\mathrm{M}},p) + \int_{T_{\mathrm{M}}}^{T} c_{\mathrm{p}}(T,p)\,dT \qquad (2.52)$$

where $h(T_{\mathrm{M}},p)$ is the value of enthalpy (after the melting) at the melting temperature T_{M} and pressure p; $c_{\mathrm{p}}(T,p)$ is the isobaric heat capacity; T_{M} is the melting temperature at pressure p.

Based on Eq. (2.52) and on the recommended above correlations for the specific heats of Pb, Bi and LBE, the increment of enthalpy of molten Pb, Bi and LBE from their melting points up to the given temperature at normal pressure can be presented as follows (Sobolev, 2011):

- Lead:

$$\begin{aligned}\Delta h_{\mathrm{Pb}}\left(T_{\mathrm{M},0},T,p_0\right)\left[\mathrm{J\,kg^{-1}}\right] &= 176.2\cdot\left(T - T_{\mathrm{M},0}\right) - 2.4615\times10^{-2}\cdot\left(T^{2} - T_{\mathrm{M},0}^{2}\right)\\ &+5.147\times10^{-6}\cdot\left(T^{3} - T_{\mathrm{M},0}^{3}\right) + 1.524\times10^{6}\cdot\left(T^{-1} - T_{\mathrm{M},0}^{-1}\right)\end{aligned} \qquad (2.53)$$

- Bismuth:

$$\begin{aligned}\Delta h_{\mathrm{Bi}}\left(T_{\mathrm{M},0},T,p_0\right)\left[\mathrm{J\,kg^{-1}}\right] &= 118.2\cdot\left(T - T_{\mathrm{M},0}\right) + 2.967\times10^{-3}\cdot\left(T^{2} - T_{\mathrm{M},0}^{2}\right)\\ &-7.183\times10^{6}\cdot\left(T^{-1} - T_{\mathrm{M},0}^{-1}\right)\end{aligned} \qquad (2.54)$$

- LBE:

$$\begin{aligned}\Delta h_{\mathrm{LBE}}\left(T_{\mathrm{M},0},T,p_0\right)\left[\mathrm{J\,kg^{-1}}\right] &= 164.8\cdot\left(T - T_{\mathrm{M},0}\right) - 1.97\times10^{-2}\cdot\left(T^{2} - T_{\mathrm{M},0}^{2}\right)\\ &+4.167\times10^{-6}\cdot\left(T^{3} - T_{\mathrm{M},0}^{3}\right) + 4.56\times10^{5}\cdot\left(T^{-1} - T_{\mathrm{M},0}^{-1}\right)\end{aligned} \qquad (2.55)$$

The temperature dependence of the enthalpy increments of Pb, Bi and LBE calculated with the correlations (2.53), (2.54) and (2.55) is presented in Figure 2.14.4.

Figure 2.14.4: Increment of the specific enthalpy of molten Pb, Bi and LBE versus temperature at normal pressure

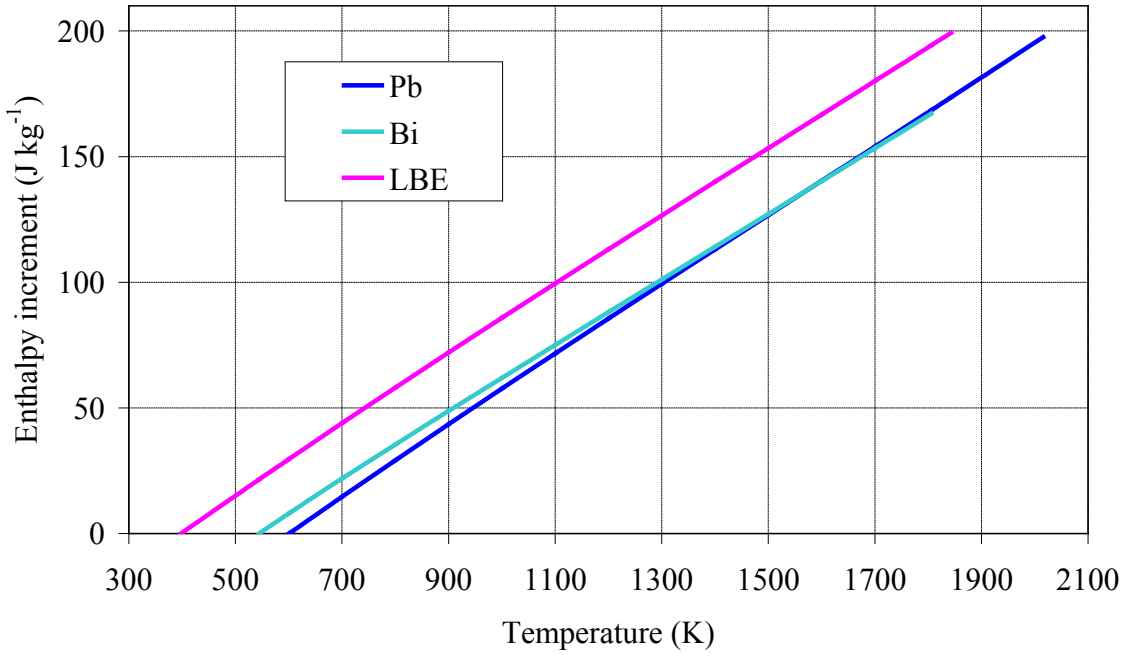

Source: Sobolev (2011).

2.15 Equation of state

The thermophysical data for Pb, Bi and LBE at high temperatures is rather scarce, and an equation of state (EOS) based on available experimental data and thermodynamic theory could be used for their prognosis (Azad, 2005; Morita, 2006, 2007; Sobolev, 2008a, 2008b, 2009, 2011, 2012).

Martynyuk (1998) has proposed to use the following generalised three-parameter equation of Van der Waals for liquid metals:

$$p\left(V_\mu, T\right) = \frac{R \cdot T}{V_\mu - b} - \frac{a}{V_\mu^n} \tag{2.56}$$

where V_μ is the molar volume, and a, b and n are the constants to be determined form experimental data. He also proposed to express the thermodynamic constants a, b and n through the heat of fusion ($\Delta H_{M,0}$), the heat of vaporisation ($\Delta H_{B,0}$) and the liquid phase molar volumes ($V'_{M,0}$) and ($V'_{B,0}$) at the normal melting and boiling points, respectively, as follows:

$$a = \frac{R \cdot (n-1)}{2} \cdot \left(V_{M,0}'^{(n-1)} \cdot \left(\Delta H_{M,0} - R \cdot T_{M,0} \right) + V_{B,0}'^{(n-1)} \cdot \left(\Delta H_{B,0} - R \cdot T_{B,0} \right) \right) \tag{2.57}$$

$$b = \frac{V'_{M,0} \cdot V'_{B,0} \left(\frac{\Delta H_{M,0}}{R \cdot T_{M,0}} - \frac{\Delta H_{B,0}}{R \cdot T_{B,0}} \right)}{V'_{M,0} \cdot \left(\frac{\Delta H_{M,0}}{R \cdot T_{M,0}} - 1 \right) - V'_{B,0} \cdot \left(\frac{\Delta H_{B,0}}{R \cdot T_{B,0}} - 1 \right)} \tag{2.58}$$

$$n = \frac{1}{2}\cdot\left(\frac{V'_{M,0}}{\left(V'_{M,0}-b\right)}\cdot\frac{R\cdot T_{M,0}}{\left(\Delta H_{M,0}-R\cdot T_{M,0}\right)}+\frac{V'_{B,0}}{\left(V'_{B,0}-b\right)}\cdot\frac{R\cdot T_{B,0}}{\left(\Delta H_{B,0}-R\cdot T_{B,0}\right)}\right) \tag{2.59}$$

This EOS was also used in Martynyuk (1998) for calculation of the critical parameters of lead and other liquid metals, which are related with the thermo dynamical constants a, b and n:

$$T_c = \frac{4a}{R\cdot b^{n-1}}\cdot\frac{n(n-1)^{n-1}}{(n+1)^{n+1}} \tag{2.60}$$

$$V_c = \frac{b(n+1)}{n-1} \tag{2.61}$$

$$p_c = \frac{a}{b^n}\cdot\left(\frac{n-1}{n+1}\right)^{n+1} \tag{2.62}$$

Eslami (2005) applied a perturbed hard-sphere-chain EOS developed by Song (1994) to liquid lead. For the considered HLM this EOS can be presented as follows:

$$p(T,V) = \frac{R\cdot T}{V}\cdot\left(1+\frac{b(T)\cdot V\left(V-0.125\cdot b(T)\right)}{\left(V-0.25\cdot b(T)\right)^3}-\frac{a(T)}{R\cdot T\cdot V}\right) \tag{2.63}$$

The coefficients $a(T)$ and $b(T)$ are expressed through the parameters of the intermolecular potential function of the given metal (a depth φ_{min} and a position r_{min} of the minimum) and trough an universal function of the reduced temperature τ:

$$a(T) = \frac{2\pi\cdot N_A^2\cdot r_{min}^3\cdot\varphi_{min}}{3}\cdot\left(a_1\cdot e^{-a_2\cdot\tau}+a_3\cdot e^{-a_4\cdot\tau^{1.5}}\right) \tag{2.64}$$

$$\tau = \left(\frac{k_B T}{\varphi_{min}}\right) \tag{2.65}$$

The constants a_i and b_i are determined only once by fitting to the reference substance of the given fluid type.

A simple EOS for liquid phase, developed by Srinivasan (1983) based on the concept of the internal pressure of liquids, was used by Azad (2005) for calculation of the LBE critical parameters. This EOS expresses the liquid metal pressure through its density, isobaric volumetric thermal expansion coefficient, isobaric and isochoric heat capacities and sound velocity:

$$\frac{p+p_i}{T} = u_s\cdot\alpha_p\cdot\rho\cdot\frac{C_p}{C_v} \tag{2.66}$$

where p_i is the liquid internal pressure. The left hand side of Eq. (2.66) is described with the linear empirical function:

$$\frac{p+p_i}{T} = A - B\cdot T \tag{2.67}$$

The coefficients A and B are fit to the right hand side of Eq. (2.66). Then the following system of two equations allows calculating T_c and p_c:

$$p_c = T_c\cdot(A - B\cdot T_c) \tag{2.68}$$

$$T_c = \frac{B \cdot T_i + \sqrt{(B \cdot T)^2 - 4B \cdot p_c}}{2B} \tag{2.69}$$

Morita (2006), proposed an EOS for the LBE vapour phase. They used the modified Redlich-Kwong (MRK) equation extended to a reacting system, where vapour consists of monomer and dimmer components. The functional form of the MRK equation extended to a reacting system is as follows:

$$p = \frac{R \cdot T}{M \cdot (1 + y_2) \cdot (v - a_1)} - \frac{a(T)}{v(v + a_3)} \tag{2.70}$$

with:

$$a(T) = a_2 \cdot \left(\frac{T}{T_c}\right)^{a_4} \qquad T \le T_c \tag{2.71}$$

$$a(T) = a_2 + \left.\frac{da}{dT}\right|_{T_c} \cdot (T - T_c) \qquad T > T_c \tag{2.72}$$

where v is the specific volume (per unit mass), y_2 is the dimer fraction, and a_1, a_2, a_3 and a_4 are the model parameters. From the definition, y_2 is related to the equilibrium constant k_2 given by:

$$k_2 = \frac{p_2}{(p_1)^2} = \frac{y_2}{(1 - y_2)^2 \cdot p} \tag{2.73}$$

where the total pressure p is the sum of the monomer pressure p_1 and the dimer pressure p_2:

$$p = p_1 + p_2 \tag{2.74}$$

Eq. (2.70) was applied to LBE, assuming that the LBE vapour consists of monatomic and diatomic components and representing the diatomic component as the diatomic bismuth molecule. Therefore, Eq. (2.74) was given by:

$$p = p_{Pb} + p_{Bi} \tag{2.75}$$

$$p_2 = p_{Bi2} \tag{2.76}$$

where p_{Pb}, p_{Bi} and p_{Bi2} are the partial pressure of monatomic lead, monatomic bismuth and diatomic bismuth, respectively.

The equilibrium constant k_2 of LBE in Eq. (2.73) was evaluated based on the vapour pressure data taken from the "best values" tabulated by Hultgren (1973a) for lead and bismuth as used for the estimation of the LBE vapour pressure. The results in the temperature range of 700-2 000 K (427-1 727°C) were fit to the following equation:

$$k_2 = \exp\left(-24.611 + \frac{23511}{T}\right) \tag{2.77}$$

where k_2 is in Pa^{-1} and T is in K.

The EOS parameters a_1, a_2 and a_3 in Eq. (2.70) were determined from the estimated values of the critical constants (Morita, 2006), and the fact that the critical isotherm on a pressure-volume p-v diagram has an inflection point at the critical point. The parameter a_4 was fit to the slope of the vapour pressure curve (Morita, 2006) at the critical temperature of 4 617°C (4 890 K).

A similar approach was used by Morita (2007) for construction of the EOS for lead and bismuth.

For pressures and temperatures significantly lower than the critical pressure and temperature, Sobolev (2008a, 2008b, 2009) proposed to construct a simplified thermal EOS for liquid phase of HLM based on available information on temperature and pressure dependence of density:

$$\rho(p,T) = \rho(p_0,T) + \left(\frac{1}{u^2_{\text{sound}}(T)} + \frac{T \cdot \alpha^2_p(T)}{c_p(T)} \right)_{p=p_0} \cdot (p - p_0) \tag{2.78}$$

where p_0 is the normal atmospheric pressure.

Applicability of the different EOS described above to HLM of interest was analysed in Sobolev (2009, 2011), and it was concluded that better results in a large temperature and pressure range can be obtained with the MRK EOS improved by Morita (2006, 2007) and with the perturbed hard-sphere-chain EOS developed by Song (1994). However, it was stressed that new experimental data on key thermodynamic parameters of the HLM at high temperatures and pressures are required for their validation.

2.16 Viscosity

Viscosity is a measure of friction among atoms of liquids. The presence of impurities can modify its value, however, data on this effect in liquid metals are very rare. As a thermophysical parameter of liquid metal coolants, viscosity is indispensable in all thermohydraulic calculations.

Accurate and reliable data on viscosity of liquid metals are not abundant. Some discrepancies between experimental data can be attributed to the high reactivity of metallic liquids, to the difficulty of taking precise measurements at elevated temperatures, and to a lack of a rigorous formula for calculations. All considered heavy liquid metals are believed to be Newtonian liquids. The temperature dependence of their dynamic viscosity η is usually described by an Arrhenius-type equation:

$$\eta = \eta_0 \cdot \exp\left(E_\eta / RT\right) \tag{2.79}$$

where E_η is activation energy of motion for viscous flow.

In engineering hydrodynamics, the kinematic viscosity (ν) is often used, which is a ratio of the dynamic viscosity to the liquid density:

$$\nu = \eta / \rho \tag{2.80}$$

2.16.1 Lead

The viscosity data for liquid lead analysed to include in the present handbook were taken from Miller (1954), Kutateladze (1958), Hofmann (1970), Beyer (1972), Iida (1975), Lucas (1984b), Iida (1988), Kyrillov (2000a), two IAEA reports (Bogoslovskaya, 2002; Kirillov, 2008) and SMRB (Smithells, 2004).

Miller (1954) references to the International Critical Tables (ICT, 1933). Kutateladze (1958) mentioned the results of Nikol'skii (1959), which were published one year later. Hofmann (1970) presented data of older measurements published in Gering (1935). Beyer (1972) referenced to an older publication of Ofte (1963). Lucas (1984b) considered a number of sources and probably used the lead viscosity values from Ofte (1967). Iida (1988) presented data from Iida (1975). In the review of Imbeni (1998) the correlation based on the recommendations of Schultz (1991) and empirical equations of Gmelins (1972) was

recommended. Data from Kirillov (2000a, 2008) and Bogoslovskaya (2002) are very close to those of Kutateladze (1958) at temperatures up to 1 073 K (800°C). In the recent IAEA report (Kirillov, 2008) an empirical formula of type (2.79) is given for the kinematic viscosity of liquid Pb on the basis of experimental data obtained by Nikol'skii (1959). However, the values presented in the table give the Pb kinematic viscosity up to 1 273 K (1 000°C) and show the viscosity increasing after about 1 083 K (810°C). Only one (Bogoslovskaya, 2002) of these three sources was included in the selected database. SMRB (Smithells, 2004) used the parameters of Eq. (2.79) from Beyer (1972) and Wittenberg (1970). The selected database sources are presented in Table 2.16.1. Figure 2.16.1(a) shows the values of molten lead viscosity taken from the cited literature.

Good agreement exists among the different sets of experimental data and the values calculated by means of the empirical equations, except the high temperature recommendations of Kirillov (2008). A reliable choice of an empirical equation to describe the temperature dependence of the dynamic viscosity of molten pure lead at normal pressure can be obtained by fitting the selected values into the Arrhenius-type Eq. (2.79):

$$\eta_{Pb}\left[\text{Pa s}\right] = 4.55 \times 10^{-4} \cdot \exp\left(\frac{1069}{T}\right) \tag{2.81}$$

where temperature is in kelvins. This correlation is valid in the temperature range from $T_{M,0}$ to 1 473 K (1 200°C); the estimated uncertainty is ±5%. The deviation of the literature data from the recommended Eq. (2.81) is presented in Figure 2.16.1(b).

Table 2.16.1: Selected database on dynamic viscosity of liquid lead

Reg. No.	Parameter	Measurement method	Estimated accuracy %	Temperature range, K	Pressure range, Pa	Values	Reference
16.1.1	Dynamic viscosity	?	(5)	714-1 117	~10^5	–	Miller (1954)
	Interpolation function: $\ln \eta = \frac{1186.1}{T} - 7.7929$ (η in Pa s)						
	Comments: Unknown purity						
16.1.2	Dynamic viscosity*	Torsional oscillations	(5)	673-1 073	~10^5	–	Kutateladze (1958)
	Interpolation function: $\ln \eta = \frac{1004.3}{T} - 7.5988$ (η in Pa s)						
	Comments: Unknown purity						
16.1.3	Dynamic viscosity	?	(5)	623-873	~10^5	–	Hofmann (1970)
	Interpolation function: $\ln \eta = \frac{1178.1}{T} - 7.820$ (η in Pa s)						
	Comments: Unknown purity						

Table 2.16.1: Selected database on dynamic viscosity of liquid lead (*cont.*)

Reg. No.	Parameter	Measurement method	Estimated accuracy %	Temperature range, K	Pressure range, Pa	Values	Reference
16.1.4	Dynamic viscosity*	Capillary method	0.5	603-1 273	~10^5	–	Iida (1975)
	Interpolation function: $\ln \eta = \frac{1032.2}{T} - 7.6354$ (η in Pa s)						
	Comments: 99.9999% Pb						
16.1.5	Dynamic viscosity	n/a	(5)	610-1 473	~10^5	–	Lucas (1984b)
	Interpolation function: $\eta = 4.486 \times 10^{-4} \cdot e^{\frac{8657}{RT}}$ Pa s						
	Comments: Unknown purity						
16.1.6	Dynamic viscosity	n/a	?	601-1 400	~10^5	–	Imbeni (1998)
	Interpolation function: $\eta = 4.12 \times 10^{-4} \cdot e^{\frac{9710}{RT}}$ Pa s						
	Comments: Unknown purity						
16.1.7	Dynamic viscosity**	n/a	(3)	603-1 073	~10^5 (?)	–	Bogoslovskaya (2002)
	Interpolation function: $\eta = 5.43 \times 10^{-4} \cdot e^{\frac{938.5}{T}}$ (η in Pa s)						
	Comments:						
16.1.8	Dynamic viscosity	n/a	(3)	(601-1 000) ?	~10^5	–	Smithells (2004)
	Interpolation function: $\eta = 4.636 \times 10^{-4} \cdot e^{\frac{8610}{RT}}$ Pa s						
	Comments: Unknown purity						

* The data on the Pb dynamic viscosity have been calculated with Eq. (2.80) using the data on the kinematic viscosity from Iida (1975) and the density calculated with Eq. (2.28).

** The data on the Pb dynamic viscosity have been calculated with Eq. (2.80) using the data on the kinematic viscosity from Kutateladze (1958) and the density presented in the same source.

Figure 2.16.1(a): Dynamic viscosity of liquid lead versus temperature at normal pressure

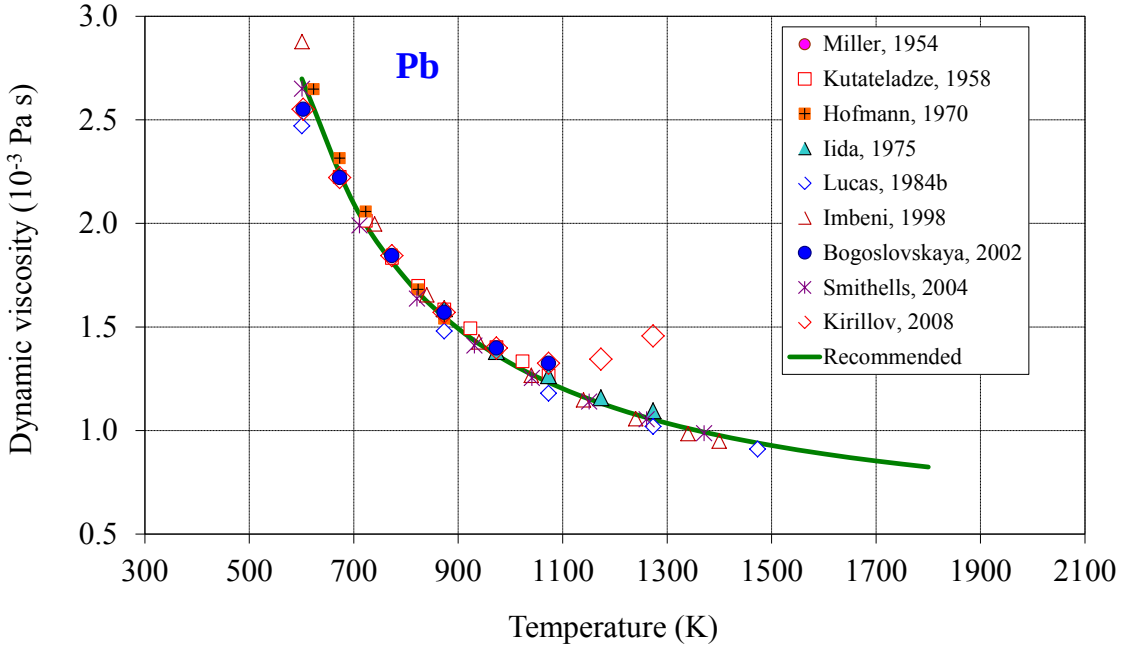

Source: Sobolev (2011).

Figure 2.16.1(b): Deviation of the literature data on dynamic viscosity of liquid lead from the recommended Eq. (2.81)

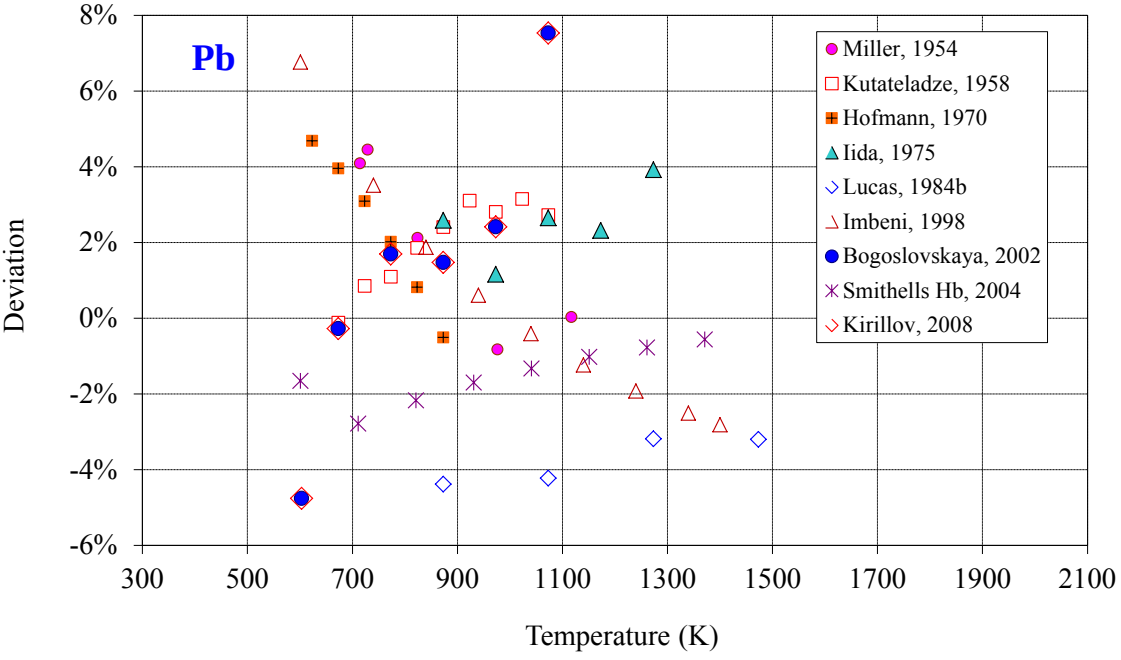

Source: Sobolev (2011).

2.16.2 Bismuth

Most of analysed viscosity data for bismuth as a function of temperature are from about the same sources as for lead: Lyon (1954), Kutateladze (1958), Bonilla (1964), Beyer (1972), Lucas (1984b), Iida (1988) and SMRB (Smithells, 2004).

Miller (1954) in Lyon (1954) presented the bismuth viscosity values from Sauerwald (1926). Kutateladze (1958) mentioned the results of Nikol'skii (1959) published one year later. The values reported by Bonilla (1964) were obtained by interpolation of data from a number of previous sources, however, they are very high as compared with those given by other analysed sources, and therefore they were disregarded. Beyer (1972) references to an older publication of Ofte (1963). Lucas (1984b) considered data from different sources and provided recommended values and constants of the Arrhenius-type Eq. (2.79). Iida (1988) reproduced the Bi viscosity data from Iida (1975). Imbeni (1998) recommended the correlation proposed by Lucas (1984b). SMRB (Smithells, 2004) gives the parameters of Eq. (2.79) deduced with the experimental results from Wittenberg (1970) and Beyer (1972). The selected sources are described in Table 2.16.2 below.

Figure 2.16.2(a) shows the values of viscosity taken from the cited literature for bismuth. A reasonable choice for an empirical correlation to calculate the bismuth viscosity as a function of temperature is that proposed by Lucas (1984b):

$$\eta_{Bi}\left[\text{Pa s}\right] = 4.456 \times 10^{-4} \cdot \exp\left(\frac{780}{T}\right) \tag{2.82}$$

where temperature is in kelvins. This correlation is valid in the temperature range from $T_{M,0}$ to 1 300 K (1 027°C). Rather satisfactory agreement is observed for most of them (except the discarded source Bonilla [1964]). The values given in Iida (1975) are lower than those given by other sources at temperatures below ~900 K (627°C). The deviation of the analysed data from Eq. (2.82) is illustrated in Figure 2.16.2(b).

Table 2.16.2: Selected database on dynamic viscosity of liquid bismuth

Reg. No.	Parameter	Measurement method	Estimated accuracy %	Temperature range, K	Pressure range, Pa	Values	Reference
16.2.1	Dynamic viscosity	?	?	553-873	~10^5	–	Miller (1954)
	Interpolation function: $\ln \eta = \frac{839}{T} - 7.8473$ (η in Pa s)						
	Comments: Unknown purity						
16.2.2	Dynamic viscosity*	Torsional oscillations	(5)	553-973	~10^5	–	Kutateladze (1958)
	Interpolation function: $\ln \eta = \frac{838.2}{T} - 7.8228$ (η in Pa s)						
	Comments: Unknown purity						
16.2.3	Dynamic viscosity**	Capillary method	0.5	553-1 273	~10^5	–	Iida (1975)
	Interpolation function: $\ln \eta = \frac{614.6}{T} - 7.581$ (η in Pa s)						
	Comments: 99.9999% Bi						

See notes on page 107.

Table 2.16.2: Selected database on dynamic viscosity of liquid bismuth (*cont.*)

Reg. No.	Parameter	Measurement method	Estimated accuracy %	Temperature range, K	Pressure range, Pa	Values	Reference
16.2.4	Dynamic viscosity	n/a	?	548-1 273	~10^5	–	Lucas (1984b)
	Interpolation function: $\eta = 4.456 \times 10^{-4} \cdot e^{\left(\frac{6485}{RT}\right)}$ Pa s						
	Comments: Unknown purity						
16.2.5	Dynamic viscosity	n/a	?	(545-1 000) ?	~10^5	–	Smithells (2004)
	Interpolation function: $\eta = 4.458 \times 10^{-4} \cdot e^{\left(\frac{6450}{RT}\right)}$ Pa s						
	Comments: Unknown purity						

* The data on the Bi dynamic viscosity have been calculated with Eq. (2.80) using the data on the kinematic viscosity from Kutateladze (1958) and the density presented in the same source.

** The data on the Bi dynamic viscosity have been calculated with Eq. (2.80) using the data on the kinematic viscosity from Iida (1975) and the density calculated with Eq. (2.29).

Figure 2.16.2(a): Dynamic viscosity of liquid bismuth versus temperature at normal pressure

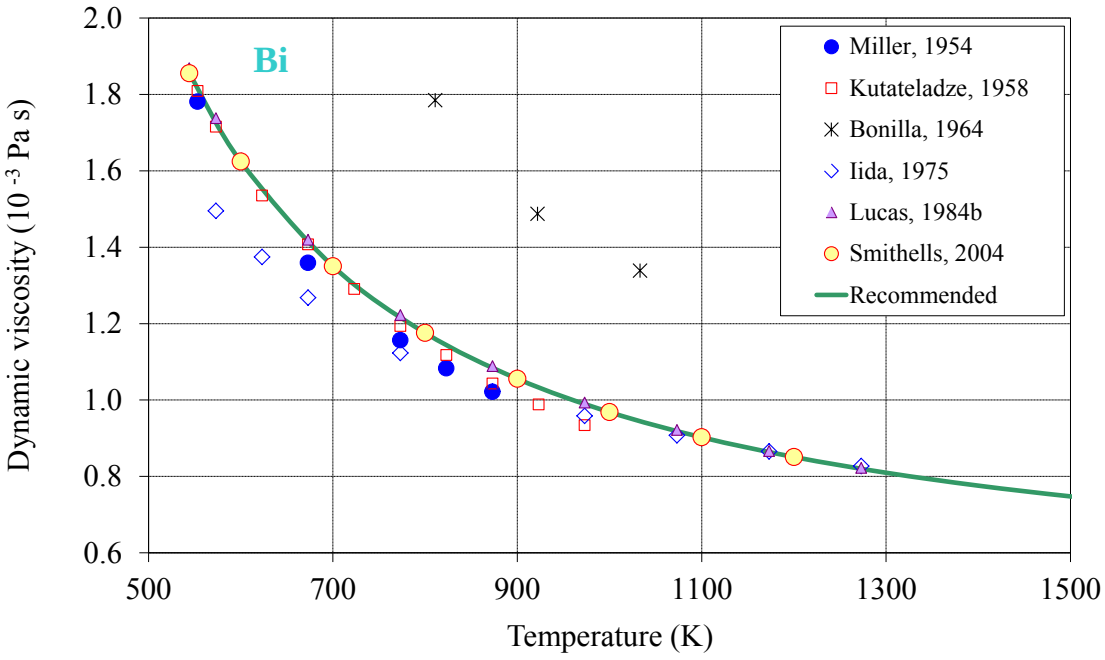

Source: Sobolev (2011).

Figure 2.16.2(b): Deviation of the literature on liquid bismuth viscosity from the recommended correlation (2.82) as a function of temperature

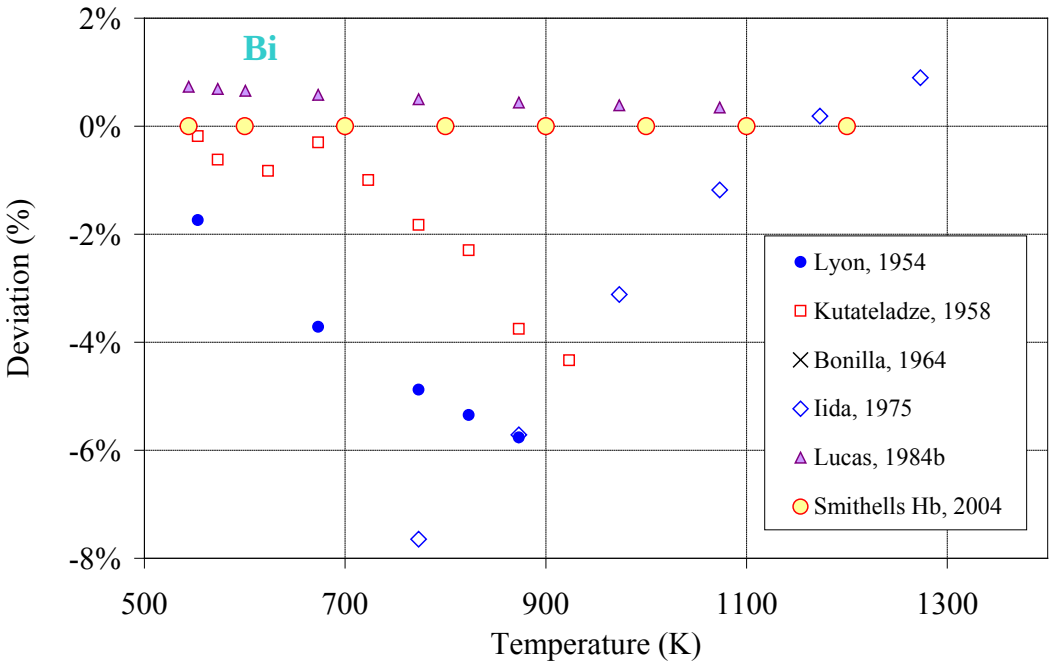

Source: Sobolev (2011).

2.16.3 *LBE*

The data on LBE viscosity were found in Lyon (1954, 1960), Mantell (1958), Kutateladze (1958), Bonilla (1964), Holman (1968), Kaplun (1979), Bogoslovskaya (2002), Kyrillov (2000a, 2008) and Plevachuk (2008).

Miller (1954) in Lyon (1954) references to a publication of Bienias (1927). In the handbook of Mantell (1958) the data from Lyon (1954) were used. Kutateladze (1958) mentioned the results of Nikol'skii (1959) published later. The values reported by Bonilla (1964) were obtained by interpolation of data from a number of previous sources. Later, some data were reported by Holman (1968). Kaplun (1979) performed more detailed measurements in the temperature range from the LBE melting point up to about 1 180 K (907°C). Cevolani (1998) proposed to use a parabolic correlation fitted to data presented in Mantell (1958). Imbeni (1999) provided an Arrhenius equation to describe the Bi viscosity graph presented in Crean (1964). The data from Kirillov (2000b) were repeated in Bogoslovskaya (2002) and then in Kirillov (2008). They are probably based on the experimental data of Nikol'skii (1959), but slightly differ from those of Kutateladze (1958). At temperatures higher than 900 K (627°C) they deviate to higher values (probably due to the presence of oxides or other impurities). Plevachuk (2008) measured the liquid LBE dynamic viscosity using the oscillating cup device. The sources included in the selected database are described in Table 2.16.3.

The data extracted from the selected sources are presented in Figure 2.16.3(a). Fitting the parameters of Eq. (2.79) to the LBE viscosity database presented above yields the following correlation:

$$\eta_{LBE}\left[\text{Pa s}\right] = 4.94 \times 10^{-4} \cdot \exp\left(\frac{754.1}{T}\right) \tag{2.83}$$

where temperature is in kelvins.

Table 2.16.3: Selected database on dynamic viscosity of liquid LBE

Reg. No.	Parameter	Measurement method	Estimated accuracy %	Temperature range, K	Pressure range, Pa	Values	Reference
16.3.1	Dynamic viscosity	n/a	(5)	605-873	~10^5 (?)	–	Miller (1954)
	Interpolation function: $\ln \eta = \frac{738}{T} - 7.6$ (η in Pa s)						
	Comments: 51.3 wt.% Pb + 48.7 wt.% Bi, unknown purity						
16.3.2	Dynamic viscosity*	Torsional oscillations	(5)	403-973	~10^5	–	Kutateladze (1958)
	Interpolation function: $\ln \eta = \frac{739}{T} - 7.54$ (η in Pa s)						
	Comments: 44.5 wt.% Pb + 55.5 wt.% B, unknown purity						
16.3.3	Dynamic viscosity	?	(5)	403-1 073	~10^5	–	(Holman (1968)
	Interpolation function: $\ln \eta = \frac{615.6}{T} - 7.44$ (η in Pa s)						
	Comments: Unknown composition and purity						
16.3.4	Dynamic viscosity	?	5	396-1 180	~10^5	–	Kaplun (1979)
	Interpolation function: $\eta = 4.656 \times 10^{-4} \cdot e^{\left(\frac{773.2}{T}\right)}$ Pa s						
	Comments: 44.5 wt.% Pb + 55.5 wt.% Bi, purity of components: 99.99%						
16.3.5	Dynamic viscosity	n/a	(5)	403-1 073	~10^5	–	Kirillov (2008)
	Interpolation function: $\eta = (7.37 - 1.337 \times 10^{-2} \cdot T + 7.278 \times 10^{-6} \cdot T^2) \times 10^{-3}$						
	Comments: 44.5 wt.% Pb + 55.5 wt.% Bi, unknown purity						
16.3.6	Dynamic viscosity	Oscillating cup	3	400-1 000	~10^5	–	Plevachuk (2008)
	Interpolation function: $\eta = 5.886 \times 10^{-4} \cdot e^{\left(\frac{5845}{RT}\right)}$ Pa s						
	Comments: 44 at.% Pb + 56 wt.% Bi, uncertainty 0.02%						

* The data on the LBE dynamic viscosity have been calculated with Eq. (2.80) using the data on the kinematic viscosity from Kutateladze (1958) and the density presented in the same source.

Figure 2.16.3(a) shows the viscosity of liquid LBE calculated with the recommended Eq. (2.83) in comparison with the data included in the database (Table 2.16.3), along with the recommended correlations for the dynamic viscosity of molten lead and of molten bismuth. It can be seen that viscosity of LBE is significantly lower than that of lead (especially at lower temperatures) and very close to the viscosity of bismuth. This is not surprising because it is known that in most cases viscosity does not respect the additive law for binary mixtures or alloys. These data indicate that the excess viscosity of LBE regarding the viscosity given by the additivity law is negative. It could indirectly be anticipated taking into account that the viscosity of normal pure liquid metals decreases with its melting temperature (Iida, 1988).

The maximum difference between the LBE viscosity given by (2.83) and the database set is about 6-8% in the temperature range of 400-1 173 K (127-900°C) as shown in Figure 2.16.3(b). Most of the discrepancies in the experimental data on the LBE viscosity can be attributed to impurities appeared due to its high reactivity.

Figure 2.16.3(a): Dynamic viscosity of the molten LBE versus temperature at normal pressure

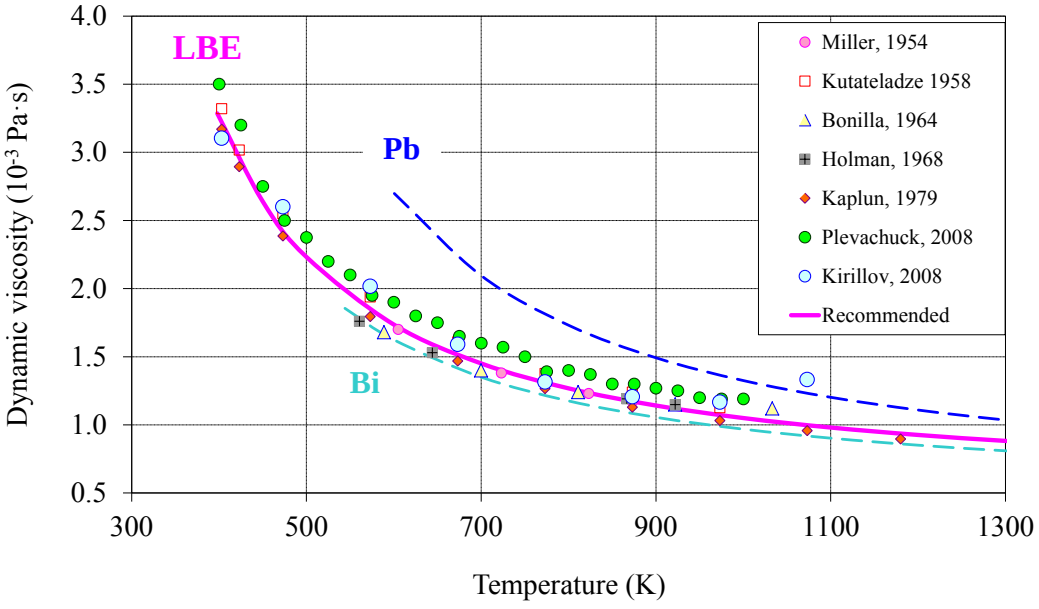

Source: Sobolev (2011).

Figure 2.16.3(b): Deviation of the literature data on dynamic viscosity of liquid LBE from the Eq. (2.83)

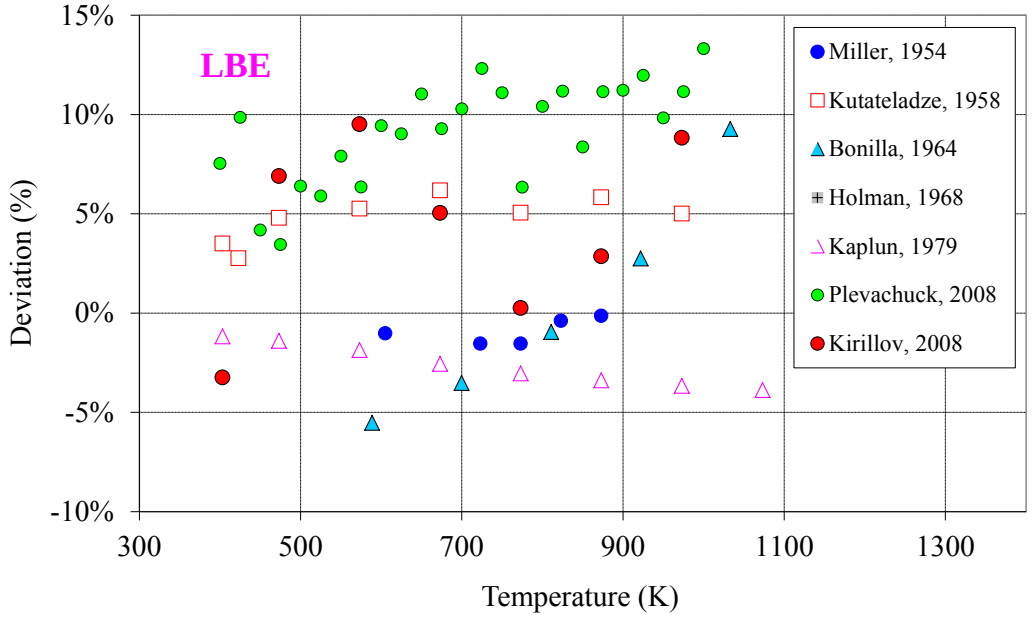

Source: Sobolev (2011).

The kinematic viscosity can be determined from Eq. (2.80) using the recommended correlations for the dynamic viscosity and the density. Its dependence on temperature is illustrated by Figure 2.16.4. The kinematic viscosity of LBE is 1.2-1.5 times smaller than that of lead in the temperature range of 600-1 100 K (327-827°C); it is very close to the kinematic viscosity of bismuth. This behaviour is close to that of the dynamic viscosities (see Figure 2.16.3[a]) and can be explained by the fact that the difference between the densities of Pb, Bi and LBE, which are present as the denominator in Eq. (2.80), is only 5-10% in the considered temperature range (see Figure 2.11.3[a]).

Figure 2.16.4: Kinematic viscosity of the melted lead, bismuth and LBE versus temperature

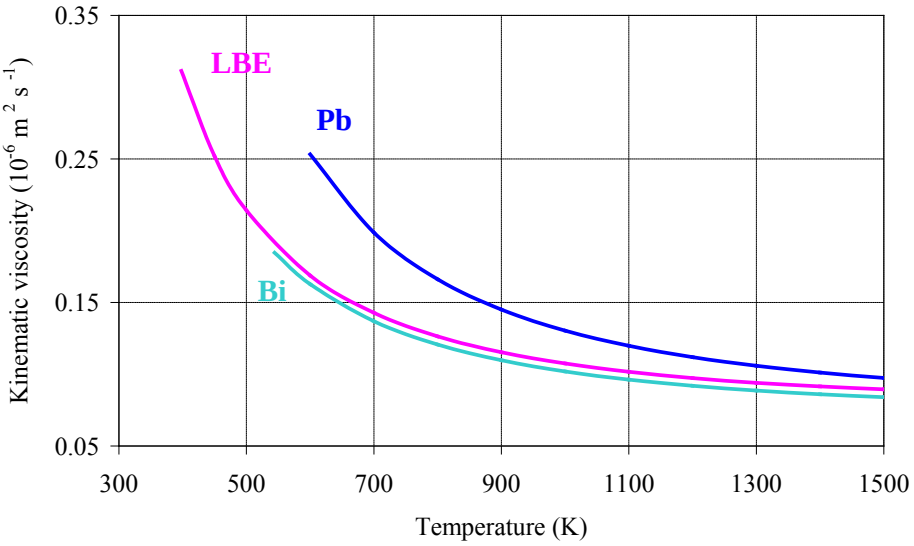

2.17 Electrical resistivity

Electrical resistivity is an important physical parameter of liquid metal coolants, which is used in magnitodynamics calculations and in design of electromagnetic pumps. It correlates with the electronic component of thermal conductivity and can also be used for its estimation. Metals in general are characterised by a very low electrical resistance, which increases with temperature and about doubles at melting. The electrical resistivity of liquid metals, with rare exceptions, increases linearly with temperature (in the temperature region of interest) and therefore can approximately be represented as follows:

$$r = r_0 + b_e \cdot T \tag{2.84}$$

In general, the electrical resistivity of liquid metals also increases, when impurities enter the melt and follow the additivity law. However, in the case of liquid alloys composed of polyvalent components, the resistivity sometimes shows a negative deviation from the additivity law (Iida, 1988).

2.17.1 Lead

The data on the electrical resistivity of liquid lead analysed to be included in this handbook were taken from Lyon (1954, 1960), Friedland (1966), Hofmann (1970), Banchila (1973), Smithells (1983, 2004), Iida (1988), Bretonnet (1988), Bogoslovskaya (2002), Smithells (1983, 2004) and Kirillov (2000a, 2008).

In the Liquid Metal Handbook of Lyon (1954) the data on Pb electrical resistivity were reproduced from the NBS report by Miller (1954). Hofmann (1970) cited a number of works

and provided a table with the recommended values of the Pb specific resistance in the range from 20.4 K (-252.9°C) up to 1 129 K (856°C). Banchila (1973) measured the electric resistivity of lead in capsules in the range of 1 190 K to 2 425 K (917-2 152°C). The upper limit of this range is beyond the normal boiling temperature of lead; that indicates that pressure within the capsule was higher than the normal atmospheric pressure.[1] Iida (1988) reproduced the coefficient of the linear correlation taken from Cusack (1960). Bretonnet (1988) treated different sources to obtain his correlation for the lead electric resistivity: Tschirner (1969), Davies (1970) and Mera (1972). SMRB (Smithells 1983, 2004) gave the recommended values of the lead electric resistivity based on the data taken from Ho (1968) and Davies (1970). Kirillov (2008) proposed to use a linear correlation from a review of Pashaev (1982) at temperatures up to 1 200 K and a cubic correlation proposed by Banchila (1973) at higher temperatures. However, in the table with the recommended values and in the earlier reviews of Kirillov (2000a) and Bogoslovskaya (2002) only the values based on the linear correlation from Pashaev (1982) were given in the temperature range from 403 K (130°C) up to 1 273 and 1 073 K respectively (1 000°C and 800°C).

Friedland (1966) reproduced data from Lyon (1960) and therefore was not included in the database. The sources included in the selected database are described in Table 2.17.1.

Figure 2.17.1(a) shows the values of the electrical resistivity for molten lead taken from the literature cited above.

The agreement between different sources is very good in the temperature range of 601-1 273 K (328-1 000°C). A linear interpolation equation is proposed for prognosis of the electrical resistivity of liquid lead at these temperatures and normal pressure:

$$r_{\mathrm{Pb}}\left[\Omega\,\mathrm{m}\right] = \left(67.0 + 0.0471 \cdot T\right) \times 10^{-8} \tag{2.85}$$

The deviation of the selected data from this correlation is less than 2%, except the high temperature data of Banchila (1973) and two points of Hofmann (1970) (see Figure 2.17.1[b]).

Table 2.17.1: Selected database on electrical resistivity of liquid lead at normal pressure

Reg. No.	Parameter	Measurement method	Estimated accuracy %	Temperature range, K	Pressure range, Pa	Values	Ref.
17.1.1	Electrical resistivity	?	(1)	601-1 273	~10^5	–	Miller (1954)
	Interpolation function: $r = (66.9 + 0.0462 \cdot T) \times 10^{-8}$ Ω m						
	Comments: (> 99.9% Pb)						
17.1.2	Electrical resistivity	Potentiometer	0.3	601-1 273	~10^5	–	Cusack (1960)
	Interpolation function: $r = (66.6 + 0.0479 \cdot T) \times 10^{-8}$ Ω m						
	Comments: (> 99.9% Pb)						
17.1.3	Electrical resistivity	n/a	(3)	601-1 129	~10^5	–	Hofmann (1970)
	Interpolation function: $r = (72.5 + 0.042 \cdot T) \times 10^{-8}$ Ω m						
	Comments: Unknown purity						

1. Estimation with Eq. (2.16) yields the saturation pressure of about p_s = 0.65 MPa at T = 2 425 K.

Table 2.17.1: Selected database on electrical resistivity of liquid lead at normal pressure (*cont.*)

Reg. No.	Parameter	Measurement method	Estimated accuracy %	Temperature range, K	Pressure range, Pa	Values	Ref.
17.1.4	Electrical resistivity	Potentiometer	< 3	1 190-(2 425)	$(1\text{-}7) \times 10^5$	–	Banchila (1973)
	Interpolation function: $r = (-84.51 + 0.3655 \cdot T - 2.135 \times 10^{-4} \cdot T^2 + 4.77 \times 10^{-8} \cdot T^3) \times 10^{-8}$ Ω m						
	Comments: 99.995% Pb						
17.1.5	Electrical resistivity	n/a	(1)	601-1 273	~10^5	–	Bretonnet (1988)
	Interpolation function: $r = (64.653 + 0.05068 \cdot T) \times 10^{-8}$ Ω m						
	Comments: (> 99.99% Pb)						
17.1.6	Electrical resistivity	n/a	(1)	–	~10^5	–	Smithells (2004)
	Interpolation function: $r = (67.4 + 0.0463 \cdot T) \times 10^{-8}$ Ω m						
	Comments: Unknown purity						
17.1.7	Electrical resistivity	n/a	(0.5-1)	603-1 273	~10^5	–	Kirillov (2008)
	Interpolation function: $r_{Pb}(T) = (65.73 + 0.0465 \cdot T) \times 10^{-8}$ Ω m						
	Comments: (> 99.99% Pb)						

Figure 2.17.1(a): Electrical resistivity of molten lead versus temperature

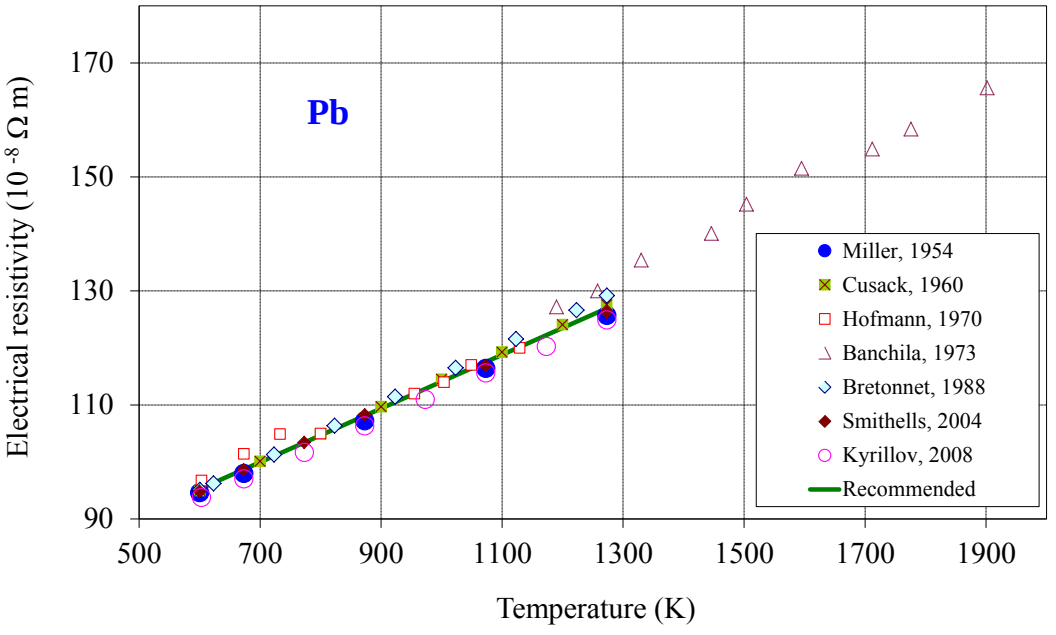

Source: Sobolev (2011).

Figure 2.17.1(b): Deviation of the database on lead electrical resistivity from the recommended correlation (2.85) as a function of temperature

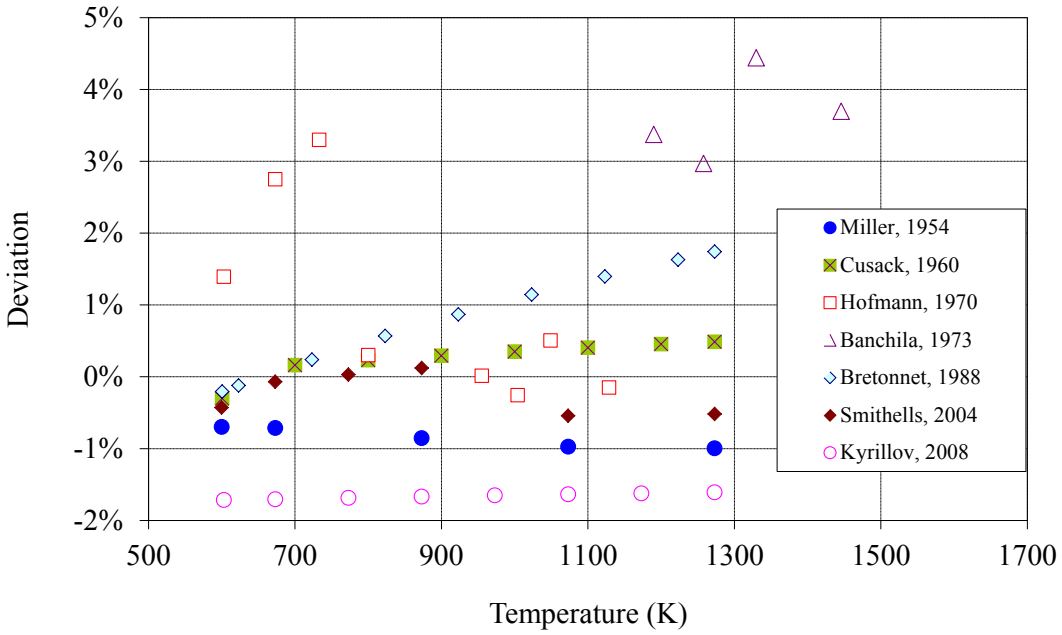

Source: Sobolev (2011).

2.17.2 Bismuth

The data for the electrical resistivity of molten bismuth analysed to include in this handbook were taken from Lyon (1954, 1960), Beer (1972), Iida (1988), Bretonnet (1988) and Smithells (2004).

Miller in Lyon (1954) provides the chosen values from one very old publication (Northrup, 1913). Lee (1972) in Beer (1972) reproduce only few points taken from Roll (1957) and Tomlinson (1969). Iida (1988) recommended a correlation from Cusack (1960). Bretonnet (1988) obtained his formula using the data of Roll (1957), Gasser (1984) and Ohno (1975). SMRB (Smithells, 2004) only reported the Bi resistivity value at the melting point with the reference to Grosse (1966), however, in the older version (Smithells, 1967) the values are given in the temperature interval from the melting point to 1 073 K (271-800°C). The selected sources are described in Table 2.17.2.

Figure 2.17.2(a) shows the values of electrical resistivity for liquid bismuth taken from literature, in the range of temperature of interest.

Table 2.17.2: Selected database on electrical resistivity of liquid bismuth

Reg. No.	Parameter	Measurement method	Estimated accuracy %	Temperature range, K	Pressure range, Pa	Values	Ref.
17.2.1	Electrical resistivity	?	(5)	573-1 023	~10^5 (?)	–	Miller (1954)
	Interpolation function: $r = (97.4 + 0.0548 \cdot T) \times 10^{-8}$ Ω m						
	Comments: Unknown purity						

Table 2.17.2: Selected database on electrical resistivity of liquid bismuth (*cont.*)

Reg. No.	Parameter	Measurement method	Estimated accuracy %	Temperature range, K	Pressure range, Pa	Values	Ref.
17.2.2	Electrical resistivity	Potentiometer	0.3	545-1 423	~10^5	–	Cusack (1960)
	Interpolation function: $r_{Bi} = (99.2 + 0.057 \cdot T) \times 10^{-8}$ Ω m						
	Comments: Unknown purity						
17.2.3	Electrical resistivity	?	?	545-1 073	~10^5	–	Smithells (1967)
	Interpolation function: $r = (98.0 + 0.0583 \cdot T) \times 10^{-8}$ Ω m						
	Comments: Unknown purity						
17.2.4	Electrical resistivity	Inductive and rotating field	(3)	573-815	~10^5	–	Lee (1972)
	Interpolation function: $r = (94.6 + 0.06 \cdot T) \times 10^{-8}$ Ω m						
	Comments: Unknown purity						
17.2.5	Electrical resistivity	n/a	(0.5-1)	545-1 423	~10^5	–	Bretonnet (1988)
	Interpolation function: $r = (99.119 + 0.05534 \cdot T) \times 10^{-8}$ Ω m						
	Comments: Unknown purity						

Figure 2.17.2(a): Electrical resistivity of liquid bismuth versus temperature

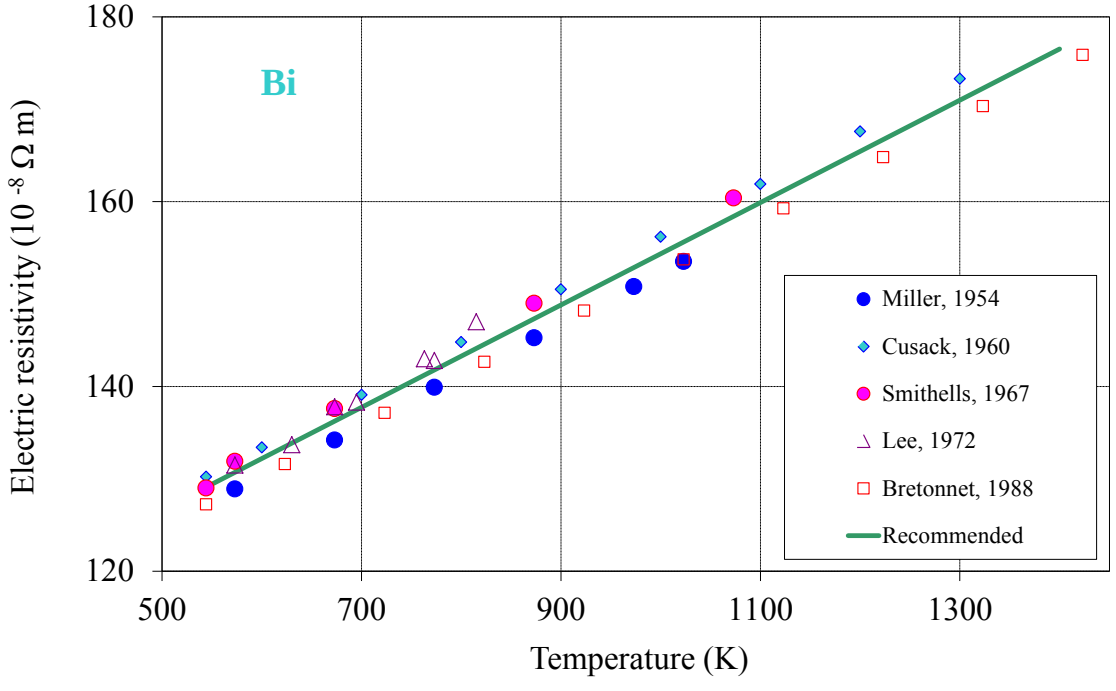

Source: Sobolev (2011).

The agreement between the selected sources is rather good. Applying the linear interpolation to the selected data set yields the following correlation:

$$r_{Bi}\left[\Omega\,\mathrm{m}\right] = \left(98.96 + 0.0554 \cdot T\right) \times 10^{-8} \tag{2.86}$$

where temperature is in kelvins. The deviation of the data set from this correlation is presented in Figure 2.17.2(b) as a function of temperature in the temperature range of 545-1 423 K (272-1 150°C). The maximum deviation is less than 2%.

Figure 2.17.2(b): Deviation of the selected database on bismuth electrical resistivity from the recommended correlation (2.86) as a function of temperature

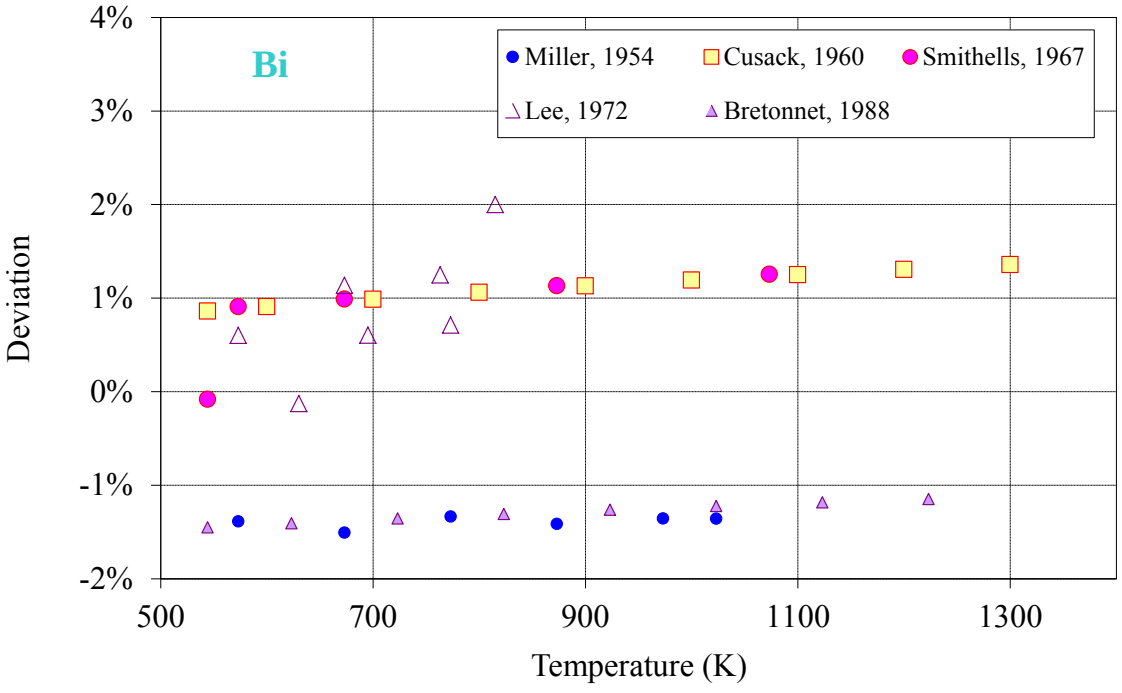

Source: Sobolev (2011).

2.17.3 LBE

Only a few reliable data sources on the electric resistivity of liquid lead-bismuth eutectic were found in open literature: Lyon (1954, 1960), Friedland (1966), Bogoslovskaya (2002), Kirillov (2000a, 2008) and Plevachuk (2008).

Miller (1954) in Lyon (1954) presented data obtained by interpolation of the results published in the reports of the American Smelting and Refining Company. Friedland (1966) reported only one value at 1 000°F (811 K) obtained by extrapolation of data from Lyon (1954). In the IAEA reports (Bogoslovskaya, 2002; Kirillov, 2008), data and interpolation formula were communicated with reference to Krzhizhanovski (1975). Plevachuk (2008) presented the results of measurements of the electric conductivity of liquid LBE from the melting point up to about 1 000 K (124-727°C) and gave the interpolation formula.

The data from Miller (1954), Kirillov (2008) and Plevachuk (2008) were included in the database shown in Table 2.17.3.

The selected data on the LBE electrical resistivity are presented in Figure 2.17.3(a) together with those recommended for the electric resistivity of liquid lead and of liquid bismuth.

Table 2.17.3: Selected database on electrical resistivity of liquid LBE

Reg. No.	Parameter	Measurement method	Estimated accuracy %	Temperature range, K	Pressure range, Pa	Values	Ref.
17.3.1	Electrical resistivity	?	?	473-773	~10^5	–	Miller (1954)
	Interpolation function: $r = (89.343 + 0.05 \cdot T) \times 10^{-8}$ Ω m						
	Comments: 44.5 wt.% Pb + 55.5 wt.% Bi, unknown purity						
17.3.2	Electrical resistivity	?	(1)	403-1 073	~10^5	–	Kirillov (2008)
	Interpolation function: $r = (83.35 + 0.0523 \cdot T) \times 10^{-8}$ Ω m						
	Comments: 44.5 wt.% Pb + 55.5 wt.% Bi, unknown purity						
17.3.3	Electrical resistivity	Potentiometer	2	398-1 000	~10^5	–	Plevachuk (2008)
	Interpolation function: $r = \dfrac{0.01}{8308.41 - 3.5228 \cdot (T - T_{M,0}) + 9.8112 \times 10^{-4} \cdot (T - T_{M,0})^2}$ Ω m						
	Comments: 44 at.% Pb + 56 wt.% Bi; 99.98%						

Figure 2.17.3(a): Electric resistivity of molten LBE versus temperature at normal pressure

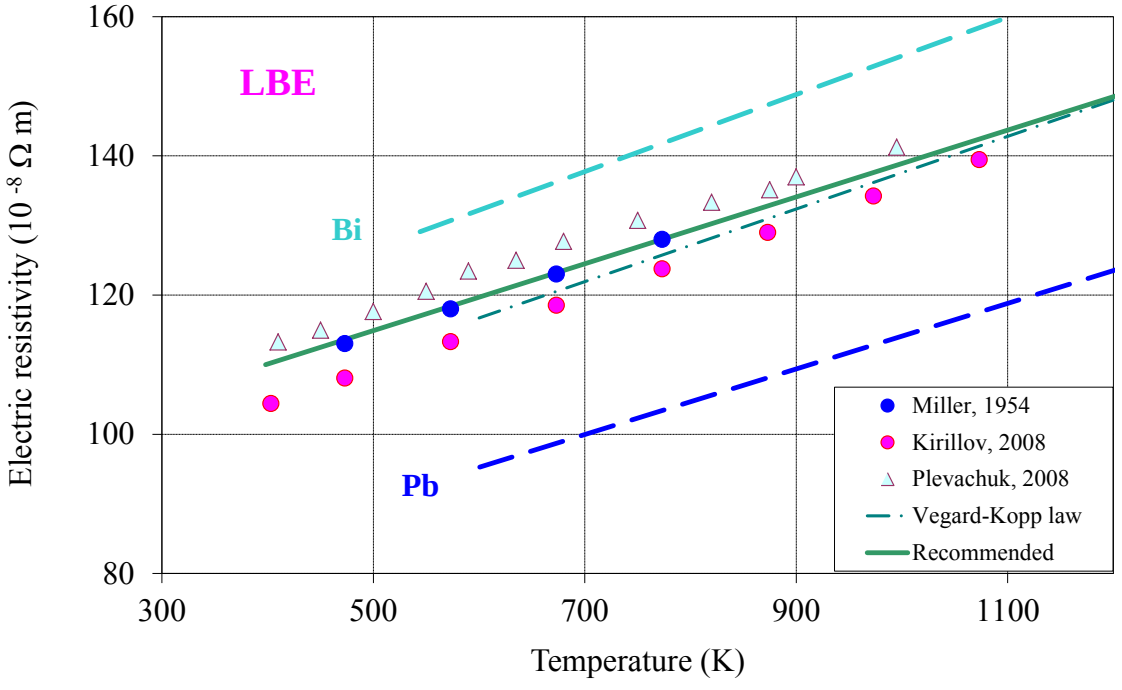

Source: Sobolev (2011).

In Figure 2.17.3(a) one can see that the LBE resistivity data recommended in Kirillov (2008) fit very well the line calculated with the "Vegard-Kopp" law using the resistivities of the liquid lead and the liquid bismuth. The data of Miller (1954) and Plevachuk (2008) have higher values. Taking into account that the Vegard-Kopp law is not applicable in the general case to transport properties of binary systems, and that only three independent sources are available, all data points were used for the development of the recommended linear interpolation correlation presented below:

$$r_{LBE}\left[\Omega\,\mathrm{m}\right] = \left(90.9 + 0.048 \cdot T\right) \times 10^{-8} \tag{2.87}$$

where temperature is in kelvins.

The deviation of the data found for the electric resistivity of liquid LBE from the recommended correlation (2.87) in the temperature range of 400-1 100 K (127-823°C) is illustrated in Figure 2.17.3(b). A maximum difference of almost ±6% is observed at lower temperatures; at higher temperatures it decreases to ±2%.

Figure 2.17.3(b): Deviation of the literature data on electric resistivity of LBE from the recommended Eq. (2.87)

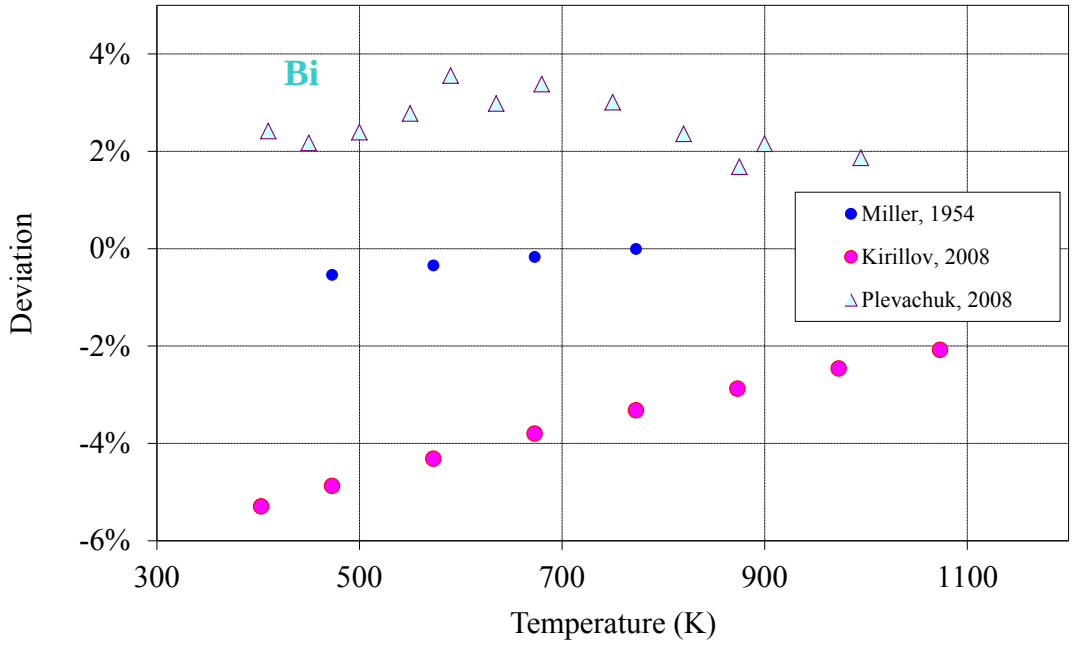

Source: Sobolev (2011).

2.18 Thermal conductivity and thermal diffusivity

Thermal conductivity is the fundamental thermophysical parameter of liquid metal coolants, which is used in all heat transfer calculations. The accuracy of its determination for liquid metals is poor and usually large discrepancies exist among different sets of data (Iida, 1988). It reduced when impurities appear in liquid metal, but this effect decreases with temperature due to domination of phonon mechanism of scattering of the energy carriers.

At present, few experimental data are available on thermal conductivity of Pb, Bi and LBE. The experimental determination of thermal conductivity of liquid metals is difficult

because of problems related to convection and to wetting, therefore large discrepancies exist between different sets of experimental results. The high thermal conductivity of liquid metals is mainly due to free electrons. A simple theoretical relation exists for pure metals between electrical and thermal conductivities known as Wiedemann-Franz-Lorenz (WFL) law (Kittel, 1956):

$$\lambda_e = L_0 \cdot T / r \tag{2.88}$$

where λ_e is the electronic thermal conductivity, r is the electrical resistivity and $L_0 = 2.45 \times 10^{-8}$ W Ω K^{-2} is the Lorenz Number.

This law has been confirmed for many normal liquid metals (Beer, 1972; Iida, 1988; Giordanengo, 1999). The contribution of phonons to the thermal conductivity of metals of interest is small in the temperature range of 400-1 200 K (127-927°C). Therefore, the approximate prediction of thermal conductivity of normal liquid metals and several alloys is possible by combining WFL law and the existing, reliable values of the electrical resistivity.

2.18.1 Lead

The following data on the liquid lead thermal conductivity were analysed for the handbook: Lyon (1954, 1960), Kutateladze (1958), Crean (1964), Friedland (1966), Dutchak (1967), Hofmann (1970), Touloukian (1970b), Viswanath (1972), Filippov (1966), Filippow (1973), Jauch (1986), Iida (1988), Hemminger (1989), Zinoviev (1989), Nakamura (1990), Mills (1996), Bogoslovskaya (2002), Yamasue (2003), Smithells (1983, 2004) and Kirillov (2008).

Miller (1954) in Lyon (1954) reproduced the Pb thermal conductivity values from Konno (1919, 1920) and Gmelins (1924). Kutateladze (1958) mentioned the works of Nikol'skii (1959) that were published later and recommended the data set obtained by interpolation and extrapolated it to a larger temperature range. Friedland (1966) used values given in Lyon (1954) and in Kutateladze (1958). Hofmann (1970) cited Konno (1920) and Bidwell (1940), but gave preference to the last. Touloukian (1970b) collected results on the liquid Pb thermal conductivity from many previous sources (Konno, 1919; Bidwell, 1940; Rosenthal, 1953; Powell, 1958; Filippov, 1966; Dutchak, 1967) and provided their own recommendation extrapolated to temperature 1 000 K (727°C). Viswanath (1972) used data from the handbook of Brooks (1955), which gives the same values as in Miller (1954). Jauch (1986) took their data from Touloukian (1970b). Iida (1988) presented graphs of values taken from the handbook of Powell (1972), where probably were reproduced the results presented in Powell (1958). Hemminger (1989) used steady-state method to measure the Pb thermal conductivity up to 773 K (500°C). Zinoviev (1989) presented values of the Pb thermal conductivity obtained from the data on thermal diffusivity, heat capacity and density. Nakamura (1990) measured the thermal conductivity of molten lead to confirm the reliability of their experimental installation based on the transient hot wire method. Mills (1996) considered few sources appearing after the publication of the review of Touloukian (1970b) and recommended the linear correlation for the temperature dependence of the Pb thermal conductivity. Yamasue (2003) measured the lead thermal conductivity with a non-stationary wire method up to 1 373 K (1 100°C). SMRB (Smithells, 1983) cited Ho (1968) and Davies (1970) as sources. In Bogoslovskaya (2002) and Kirillov (2000b, 2008) the works of Nikol'skii (1959) were cited, however, they probably also used some other sources and presented the interpolated corrected results.

The thermal conductivity of liquid lead, based on the analysed sources, is presented as a function of temperature in Figure 2.18.1(a) (Sobolev, 2011). All data on the Pb heat conductivity are in good agreement close to the melting temperature (except those of Bidwell [1940] selected in Hofmann [1970], which should be discarded because of unrealistically high values). However, data from different sources differ in the temperature dependence. Most of the sources give the Pb thermal conductivity monotonically increasing with temperature. On the other hand, the results reported in Konno (1919),

Miller (1954), Filippov (1966) and Yamasue (2003) show that the Pb thermal conductivity decreases with temperature after melting. The data presented in Kutateladze (1958) show anomalous behaviour where the Pb thermal conductivity increases with increasing rate with temperature. This behaviour is in contradiction with WFL law. The mentioned discrepancies could be explained by effects of impurities, oxidation and by irrelevant experimental conditions and techniques. Therefore, these five sources were not included in the database. The selected sources are described in Table 2.18.1 below.

Table 2.18.1: Selected database on thermal conductivity of liquid lead

Reg. No.	Parameter	Measurement method	Estimated accuracy %	Temperature range, K	Pressure range, Pa	Values	Ref.
18.1.1	Thermal conductivity	Comparative	(10)	617-755	~10^5	–	Rosenthal (1953)
	Comments: 99.8% Pb						
	Interpolation function: $\lambda = -5.53 + 0.0555 \cdot T - 2.94 \times 10^{-5} \cdot T^2$ W m^{-1} K						
18.1.2	Thermal conductivity	Comparative	(10)	623-873	~10^5	–	Powell (1958)
	Interpolation function: $\lambda = 9.2 + 0.0113 \cdot T$ W m^{-1} K^{-1}						
	Comments: 99.995% Pb						
18.1.3	Thermal conductivity	Comparative	(10)	627-870	~10^5	–	Dutchak (1967)
	Interpolation function: $\lambda = 9.65 + 0.0115 \cdot T$ W m^{-1} K^{-1}						
	Comments: Unknown purity (> 99.9% Pb)						
18.1.4	Thermal conductivity	n/a	(10)	601-1 000	~10^5	–	Touloukian (1970b)
	Interpolation function: $\lambda = -0.833 + 0.0346 \cdot T - 1.23 \times 10^{-5} \cdot T^2$ W m^{-1} K^{-1}						
	Comments: (> 99.9% Pb)						
18.1.5.	Thermal conductivity	Steady state	3	617-773	~10^5	–	Hemminger (1989)
	Interpolation function: $\lambda = 7.84 + 0.0129 \cdot T$ W m^{-1} K^{-1}						
	Comments: 99.99% Pb						
18.1.6	Thermal conductivity	Non-stationary	(10)	600.7 800 1 000	~10^5	15.5 19.0 21.4	Zinoviev (1989)
	Interpolation function: $\lambda = -1.73 + 0.037 \cdot T - 1.39 \times 10^{-5} \cdot T^2$ W m^{-1} K^{-1}						
	Comments: 99.99% Pb						
18.1.7	Thermal conductivity	Transient hot wire	(10)	623-975	~10^5	–	Nakamura (1990)
	Interpolation function: $\lambda = 10.9 + 0.0061 \cdot T$ W m^{-1} K^{-1}						
	Comments: (>99.9% Pb)						
18.1.8	Thermal conductivity	n/a	> 5	603-(1 273)	~10^5	–	Mills (1996)
	Interpolation function: $\lambda = 10.5 + 0.0075 \cdot T$ W m^{-1} K^{-1}						
	Comments: (> 99.9% Pb)						

Table 2.18.1: Selected database on thermal conductivity of liquid lead (*cont.*)

Reg. No.	Parameter	Measurement method	Estimated accuracy %	Temperature range, K	Pressure range, Pa	Values	Ref.
18.1.9	Thermal conductivity	?	?	601-873	~10^5	–	Smithells (2004)
	Interpolation function: $\lambda = -3.26 + 0.0426 \cdot T - 1.93 \times 10^{-5} \cdot T^2$ W m^{-1} K						
	Comments: (> 99.9% Pb)						
18.1.10	Thermal conductivity	Absolute axial	(5-10)	603-1 273	~10^5	–	Kyrillov (2008)
	Interpolation function: $\lambda = 9.32 + 0.0108 \cdot T$ W m^{-1} K^{-1}						
	Comments: unknown purity (> 99.9% Pb)						

Figure 2.18.1(a): Thermal conductivity of molten lead versus temperature at normal pressure

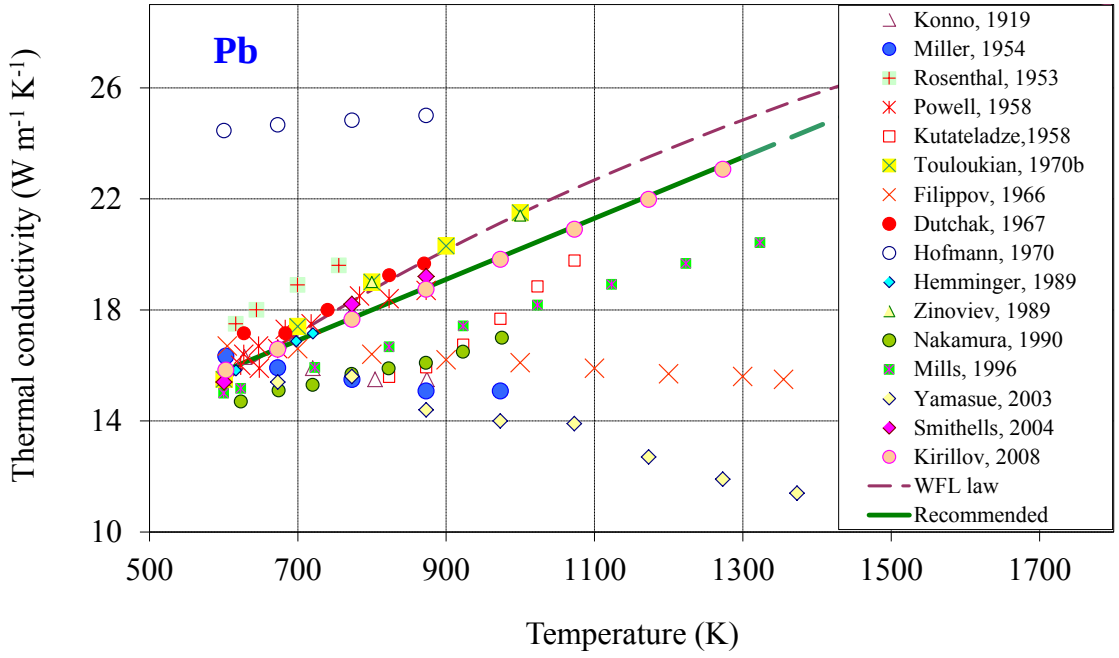

Source: Sobolev (2011).

In an effort to find a physically reasonable compromise between the available data and the WFL law (2.88), the following linear correlation was chosen as recommendation for the thermal conductivity of the technically pure liquid lead at normal pressure:

$$\lambda_{Pb}\left[\mathrm{W\ m^{-1}\ K^{-1}}\right] = 9.2 + 0.011 \cdot T \qquad (2.89)$$

where temperature is in kelvins. This correlation is applicable in the temperature range of $T_{M,0}$-1 300 K (1 027°C). The estimated uncertainty is ±15% (Figure 2.18.1[b] from Sobolev [2011]).

Figure 2.18.1(b): Deviation of the selected data set on thermal conductivity of liquid lead from the Eq. (2.89)

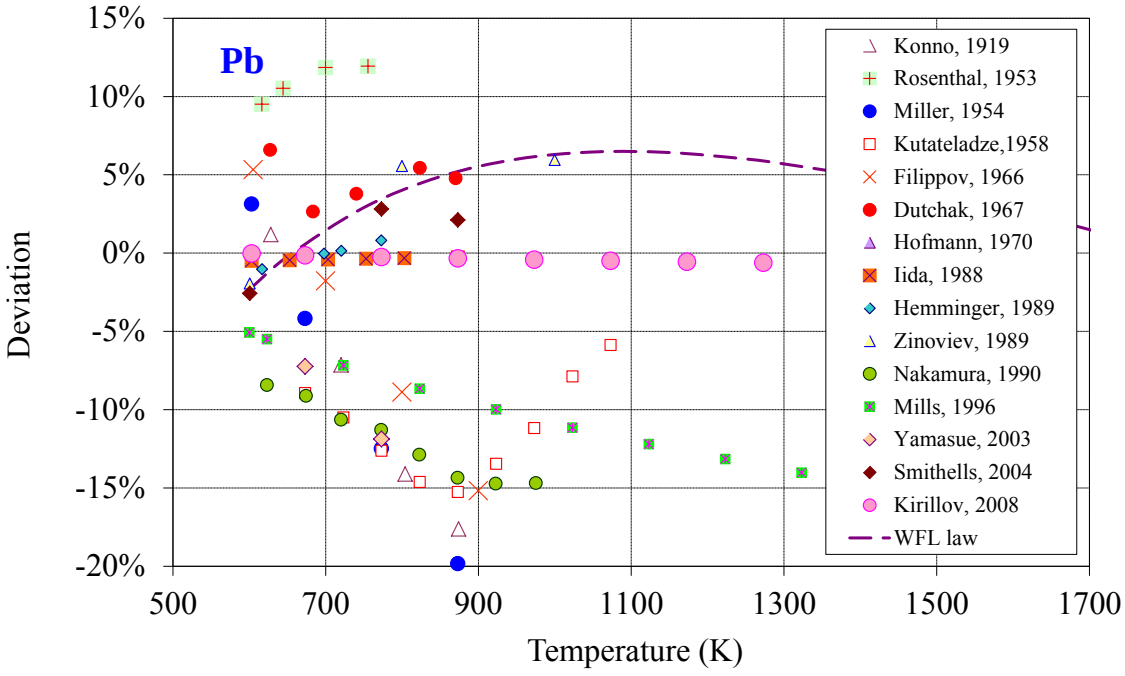

Source: Sobolev (2011).

2.18.2 *Bismuth*

The data for the liquid bismuth thermal conductivity analysed in this handbook were taken from Lyon (1954), Kutateladze (1958), Pashaev (1961), Crean (1964), Dutchak (1967), Touloukian (1970), Viswanath (1972), Iida (1988), Mills (1996) and Smithells (1983, 2004).

Miller (1954) in Lyon (1954) reproduced the Bi thermal conductivity values from Konno (1920), and mentioned that about the same values were given in the Smithells Metal Reference Book issued in 1949. Kutateladze (1958) provided interpolated values with the reference to the works of Nikol'skii (1959) published later. Crean (1964) probably used the same sources as Miller (1954). Touloukian (1970b) reproduced the thermal conductivity values for liquid Bi from Konno (1919), Powell (1958), Nikol'skii (1959), Pashaev (1961) and Dutchak (1967), and also gave recommended values extrapolated to higher temperatures. Viswanath (1972) used data from the handbook of Brooks (1955), which gives the same values as Miller (1954). Iida (1988) presented plots of the Bi thermal conductivity in function of temperature taken from the handbook of Powell (1972), who reproduced data from Powell (1958). Mills (1996) compared the recommendation on the liquid bismuth thermal conductivity from the compilation of Touloukian (1970b) with the experimental data published in Filippow (1973) and provided a recommendation, which is close to that of Touloukian (1970b). In the Smithells Metal Reference Book (2004) the same data were given as in Lyon (1954). The selected data set on the liquid Bi thermal conductivity is described in Table 2.18.2.

Figure 2.18.2(a) shows the values of thermal conductivity of liquid bismuth, taken from the analysed literature, plotted in the range of temperatures of interest.

Table 2.18.2: Selected database on thermal conductivity of liquid bismuth

Reg. No.	Parameter	Measurement method	Estimated accuracy %	Temperature range, K	Pressure range, Pa	Values, W m^{-1} K^{-1}	Ref.
18.2.1	Thermal conductivity	Stationary axial	(> 10)	559-857	~10^5	–	Konno (1919)
	Interpolation function: $\lambda = 67.8 - 0.194 \cdot T + 2.4 \times 10^{-4} \cdot T^2 - 9.94 \times 10^{-8} \cdot T^3$ W m^{-1} K^{-1}						
	Comments: Unknown purity						
18.2.2	Thermal conductivity	(Stationary axial) ?	(> 10)	573-973	~10^5	–	Miller (1954)
	Interpolation function: $\lambda = 91.1 + 0.222 \cdot T + 1.6 \times 10^{-4} \cdot T^2$ W m^{-1} K^{-1} at T = 573-673 K λ = 15.5 W m^{-1} K^{-1} at T > 673 K						
	Comments: Unknown purity						
18.2.3	Thermal conductivity	Comparative	(10)	573-823	~10^5	–	Powell (1958)
	Interpolation function: $\lambda = 5.34 + 0.0104 \cdot T$ W m^{-1} K^{-1}						
	Comments: 99.99% Bi						
18.2.4	Thermal conductivity	n/a	(~10?)	573-973	~10^5	–	Kutateladze (1958)
	Interpolation function: $\lambda = 9.5 + 0.009 \cdot T$ W m^{-1} K^{-1}						
	Comments: (99.9% Bi)						
18.2.5	Thermal conductivity	Stationary axial	(~10)	464-902	~10^5	–	Nikol'skii (1959)
	Interpolation function: $\lambda = 9.6 + 0.0088 \cdot T$ W m^{-1} K^{-1}						
	Comments: (> 99.9% Bi)						
18.2.6	Thermal conductivity	Axial	5	556.8 573.2 598.6 629.7	~10^5	14.2 13.8 14.2 14.2	Pashaev (1961)
	Interpolation function: n/a						
	Comments: (> 99.9% Bi) ?						
18.2.7	Thermal conductivity	Comparative	(7-10)	555.2 619.2 712.2 770.2	~10^5	12.97 13.81 14.65 14.65	Dutchak (1968)
	Interpolation function: $\lambda = 8.7 + 0.008 \cdot T$ W m^{-1} K^{-1}						
	Comments: (> 99.9% Bi)						
18.2.8	Thermal conductivity	n/a	(~10)	545-1 000	~10^5	–	Touloukian (1970)
	Interpolation function: $\lambda = 7.34 + 0.0095 \cdot T$ W m^{-1} K^{-1}						
	Comments: (> 99.9% Bi) ?						
18.2.9	Thermal conductivity	n/a	(~10)	545-(850)	~10^5	–	Mills (1996)
	Interpolation function: $\lambda = 6.55 + 0.01 \cdot T$ W m^{-1} K^{-1}						
	Comments: (> 99.9% Bi) ?						

Figure 2.18.2(a): Thermal conductivity of molten bismuth versus temperature

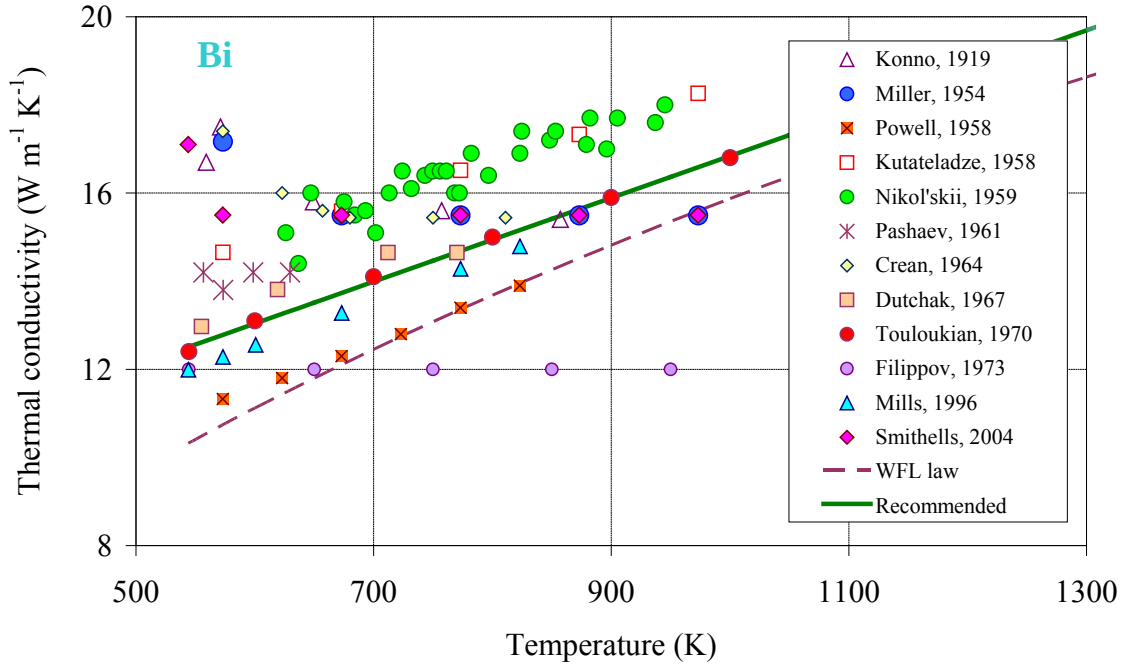

Source: Sobolev (2011).

Figure 2.18.2(b): Deviation of the analysed data on thermal conductivity of liquid bismuth from Eq. (2.90) versus temperature

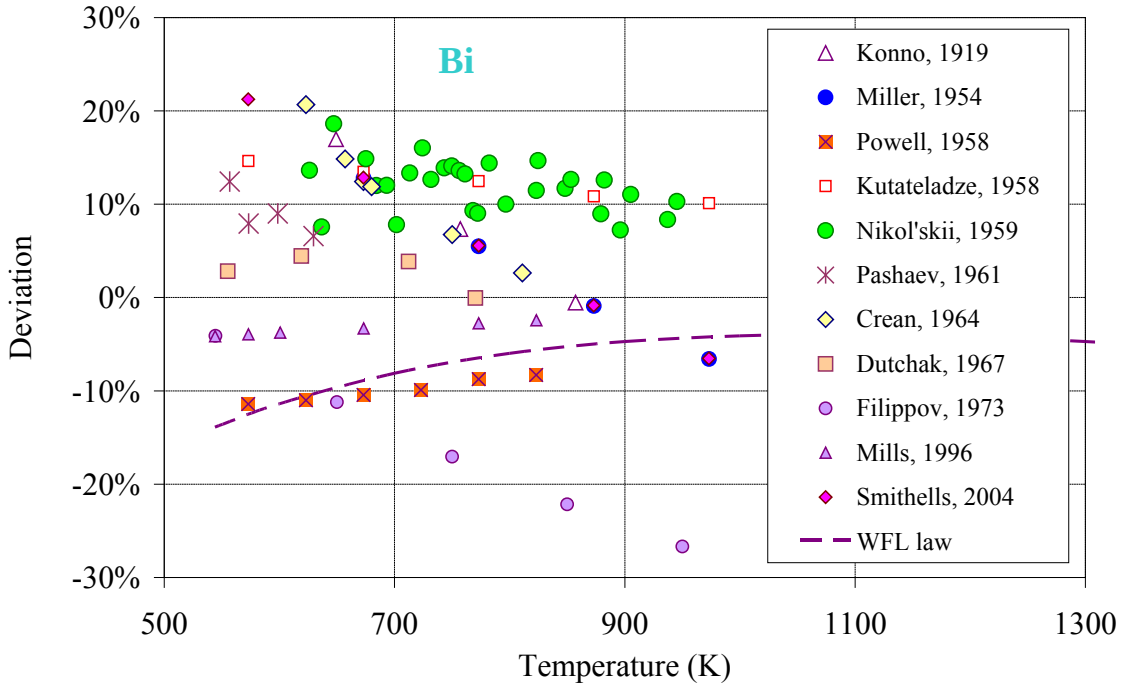

Source: Sobolev (2011).

A large discrepancy (±15-20%) exists between different sources in the considered temperature range. All recommendations can be subdivided into two groups. The first set of data shows a decrease of the Bi thermal conductivity with temperature up to about 600-650 K (327-377°C) and a constant value at higher temperatures; in the second set the thermal conductivity monotonically increases with temperature. The WFL law yields the Bi thermal conductivity increasing with temperature.

In this handbook, the following empirical correlation, recommended in Touloukian (1970b), was chosen:

$$\lambda_{Bi}\left[\mathrm{W\ m^{-1}\ K^{-1}}\right] = 7.34 + 9.5\times10^{-3}\cdot T \tag{2.90}$$

where temperature is in kelvins. It is expected that this correlation will be applicable in the temperature range from $T_{M,0}$ to about 1 000 K (727°C). The deviation of the analysed data set from the recommended Eq. (2.90) is illustrated by Figure 2.18.2(b) (reproduced from Sobolev [2011]), indicating that uncertainty of about ±15% can be fixed for the recommended correlation in the considered temperature range.

2.18.3 LBE

Information on thermal conductivity for molten LBE first comes from older handbooks. The most cited are Lyon (1954) and Kutateladze (1958). In the first source Miller (1954) referenced to Brown (1923). In the second, the works of Nikol'skii are mentioned (though published later in 1959) and some interpolated values were given. Most of later handbooks or reviewers reference these data. Touloukian (1970b) reproduced values of the liquid LBE thermal conductivity from Brown (1923), Mikryukov (1956), Powell (1958) and Nikol'skii (1959) without giving their own recommendations. Viswanath (1972) used data from Brown (1923). In the handbook of Powell (1972) the values from Powell (1958) were reproduced. Iida (1988) presented a graph with the temperature dependence of the LBE thermal conductivity from Powell (1972). In the recent Russian literature, new data were summarised in the handbook of Kirillov (2000a) without direct references to the sources. These recommendations were practically reproduced later in an IAEA technical document (Bogoslovskaya, 2002) and then in a more recent IAEA publication (Kirillov, 2008). In the latter source, it was indicated that the data for the LBE thermal conductivity were obtained using the additivity law and the thermal conductivities of Pb and Bi recommended in the same publication. These values are in agreement with the experimental result presented in Nikol'skii (1959). Recently the LBE thermal conductivity was measured and compared with a few previous recommendations by Plevachuk (2008). The data set for the LBE thermal conductivity included in the database is described in Table 2.18.3.

The values of the LBE thermal conductivity extracted from the analysed sources are presented in Figure 2.17.3(a) (reproduced from Sobolev [2011]) together with the values obtained with the WFL law and with the recommended values for thermal conductivities of lead and bismuth.

A non-negligible difference exists between the different recommendations at lower temperatures. The WFL law gives values close to the recommendations of Powell (1972) and the results of Plevachuk (2008) at lower temperatures: 400-800 K (127-527°C), and close to the recommendations of Kirillov (2008) at higher temperatures: 800-1 100 K (527-827°C).

Similar to viscosity and electric resistivity, the results on thermal conductivity are strongly affected by the purity and composition of LBE. Thermal conductivity is not an additive parameter and therefore the Vegard-Kopp law cannot be used to estimate it. Contrarily, the WFL law, which is valid for most metals, can be used.

Fitting the selected data set with a parabolic function yields the following recommended correlation for the liquid LBE thermal conductivity (Sobolev, 2011):

$$\lambda_{\mathrm{LBE}}\left[\mathrm{W\ m^{-1}\ K^{-1}}\right] = 3.284 + 1.617\times10^{-2}\cdot T - 2.305\times10^{-6}\cdot T^{2} \qquad (2.91)$$

where temperature is in kelvins.

The difference between the analysed data and the recommended Eq. (2.91) is plotted in Figure 2.18.3(b).

The maximum deviation is 10-15% for most of selected data. The WFL law can be used for an estimate of the LBE thermal conductivity if its electrical resistivity is known.

Table 2.18.3: Selected database on thermal conductivity of liquid LBE

Reg. No.	Parameter	Measurement method	Estimated accuracy %	Temperature range, K	Pressure range, Pa	Values, W m^{-1} K^{-1}	Ref.
18.3.1	Thermal conductivity	(Absolute)	(10)	439-558	~10^5	–	Brown (1923)
	Interpolation function: $\lambda = 4.25 + 0.0117\cdot T$ W m^{-1} K^{-1}						
	Comments: 46 wt.% Pb + 54 wt.% Bi, $T_{M,0}$ = 403 K						
18.3.2	Thermal conductivity	Absolute	(10)	433-593	~10^5	–	Lyon (1954)
	Interpolation function: $\lambda = 3.55 + 0.013\cdot T$ W m^{-1} K^{-1}						
	Comments: 44.5 wt.% Pb + 55.5 wt.% Bi, unknown purity						
18.3.3	Thermal conductivity	Direct electric heating	3	403.2 418.2 441.2	~10^5	7.20 7.15 8.37	Mikryukov (1956)
	Interpolation function: n/a						
	Comments: 45.44 wt.% Pb + 54.56 wt.% Bi, unknown purity						
18.3.4	Thermal conductivity	Comparative	(< 10)	423-773	~10^5	–	Powell (1958)
	Interpolation function: $\lambda = 3.44 + 0.0142\cdot T$ W m^{-1} K^{-1}						
	Comments: 44.5 wt.% Pb + 55.5 wt.% Bi; 99.995% Bi and 99.99% Pb						
18.3.5	Thermal conductivity	n/a	(~10)	403-973	~10^5	–	Kutateladze (1958)
	Interpolation function: $\lambda = 6.86 + 0.01\cdot T$ W m^{-1} K^{-1}						
	Comments: 44.5 wt.% Pb + 55.5 wt.% Bi, unknown purity						
18.3.6	Thermal conductivity	Stationary axial	(~10)	464-902	~10^5	–	Nikol'skii (1959)
	Interpolation function: $\lambda = 7.06 + 9.6\times10^{-3}\cdot T$ W m^{-1} K^{-1}						
	Comments: 44.5 wt.% Pb + 55.5 wt.% Bi (> 99.9% Bi and Pb)						
18.3.7	Thermal conductivity	n/a	(10)	403-1 073	~10^5	–	Kyrillov (2008)
	Interpolation function: $\lambda = 7.03 + 9.93\times10^{-3}\cdot T$ W m^{-1} K^{-1}						
	Comments: 44.5 wt.% Pb + 55.5 wt.% Bi, unknown purity						
18.3.8	Thermal conductivity	Absolute steady state	7	398-1 000	~10^5	–	Plevachuk (2008)
	Interpolation function: $\lambda = 0.72158 + 0.0233\cdot T - 8.1098\times10^{-6}\cdot T^2$ W m^{-1} K^{-1}						
	Comments: 44 at.% Pb + 56 wt.% Bi, 99.98% purity components						

Figure 2.18.3(a): Thermal conductivity of molten lead, bismuth and LBE versus temperature

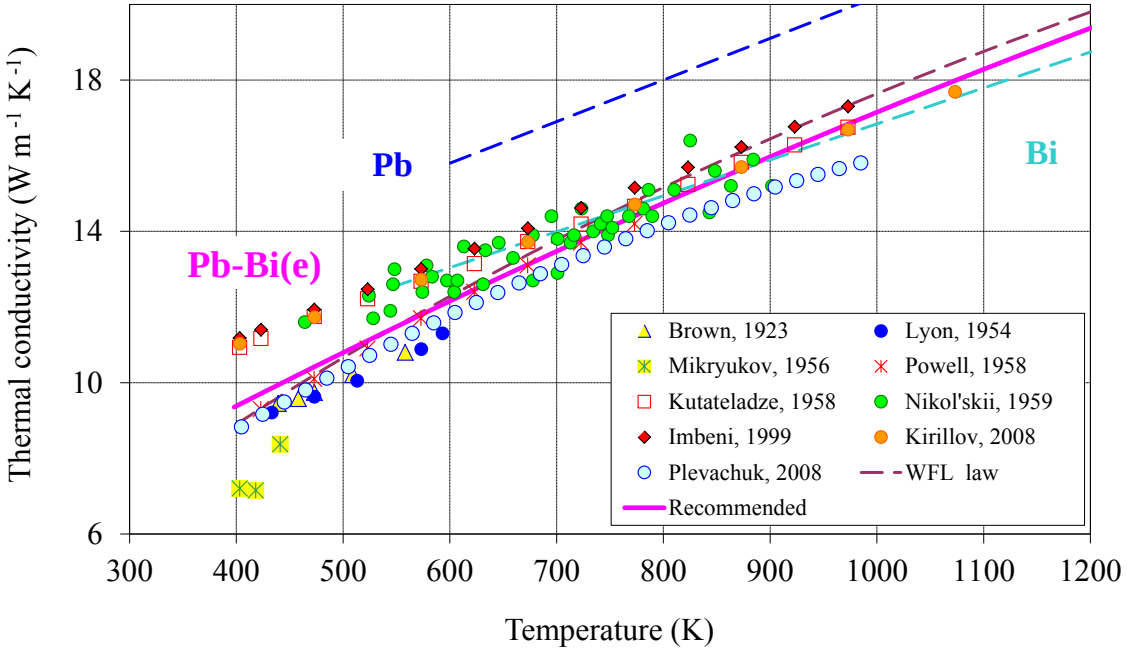

Source: Sobolev (2011).

Figure 2.18.3(b): Deviation of the available data set on thermal conductivity of liquid LBE from Eq. (2.91)

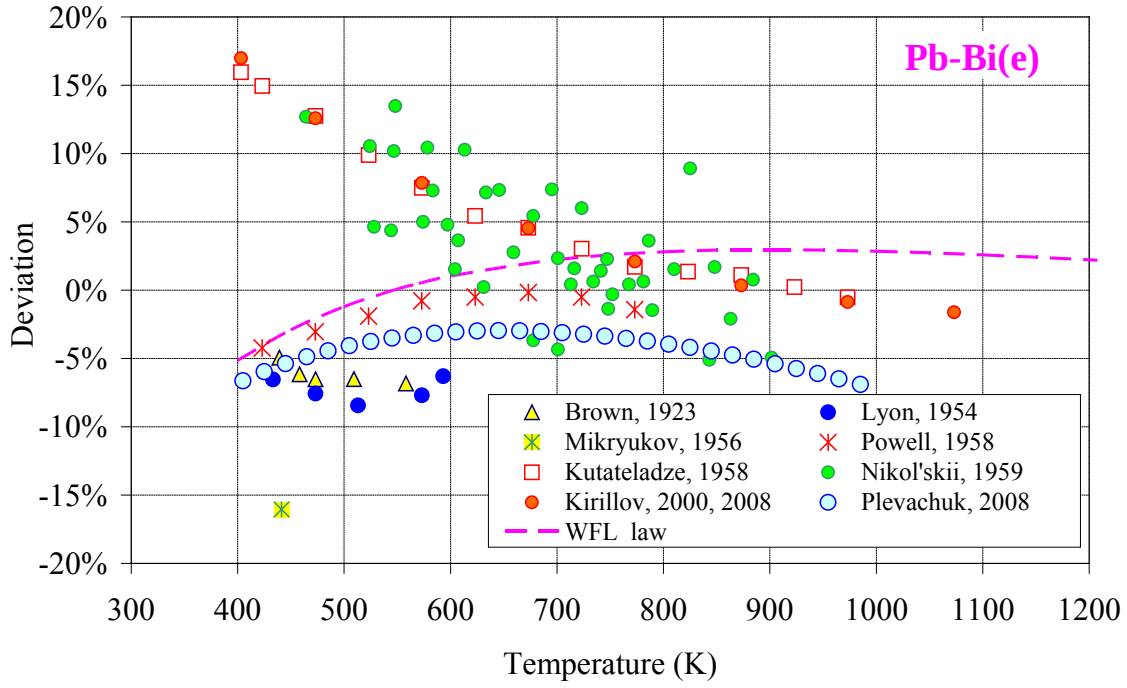

Source: Sobolev (2011).

2.18.4 *Thermal diffusivity*

Thermal diffusivity is often used in modelling of non-stationary heat conduction processes. It can be measure directly with non-stationary experimental methods. It is defined as follows:

$$a_p = \frac{\lambda}{\rho \cdot c_p} \tag{2.92}$$

So, it can be calculated using the recommended correlations for thermal conductivity, density and specific heat. The calculated thermal diffusivities of lead, bismuth and LBE are plotted as a function of temperature in Figure 2.18.4. The maximum uncertainty of thermal diffusivity calculated with Eq. (2.92) can reach 20-23%; the main contribution gives the uncertainty in thermal conductivity (±15%).

Figure 2.18.4: Thermal diffusivity of liquid lead, bismuth and LBE

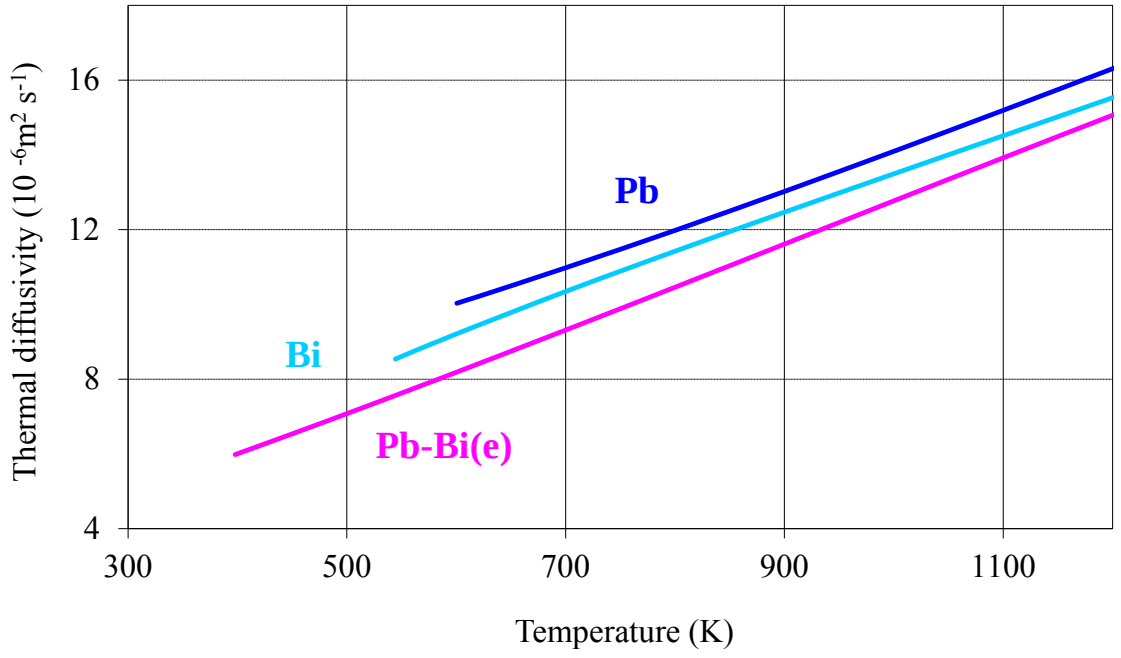

2.19 Conclusions

The data on thermophysical properties of liquid lead, bismuth and LBE are generally characterised by significant uncertainty (the exceptions are the melting point, the density and the electrical resistivity). In general, the reliability of data is satisfactory and good agreement among the different sources of experimental data is often observed. However, a large uncertainty still exists on saturated vapour pressure, heat capacity and thermal conductivity – different sources give even different temperature dependence of these parameters. A significant uncertainty also exists in the boiling temperature. The critical temperatures, the critical densities and the critical pressures of Pb, Bi and LBE are not well defined, and this hinders the development of equations of state for these coolants that can be applied for prognosis of their properties at high temperatures and pressures. Effects of impurities and dissolved additives on sensitive properties of liquid Pb, Bi and LBE coolants, such as surface tension, sound velocity, viscosity, electrical resistivity and thermal conductivity have not yet been studied. Extensive R&D is required to obtain the missing data.

Based on the review of the data and recommendations available in the literature and on the recent compilations performed for thermophysical properties of technically pure liquid lead, bismuth and lead-bismuth eutectic, correlations are proposed that can serve as temporary recommendations for engineering estimations and design calculations.

The recommended correlations for the main thermophysical properties of liquid Pb, Bi and LBE are summarised in Tables 2.19.1 to 2.19.3.

Table 2.19.1: Summary of the recommended correlations for main thermophysical properties of liquid lead (Pb)

$p \sim 0.1$ MPa, except the critical parameters and the saturated vapour pressure

Property, parameter	SI unit	Correlation	Temp. range (K)	Estimated error ±
Melting temperature	K	$T_{M,0} = 600.6$	n/a	0.1
Latent heat of melting	kJ kg^{-1}	$Q_{M,0} = 23.07$	n/a	0.14
Boiling temperature	K	$T_{B,O} = 2\,021$	n/a	3
Latent heat of boiling	kJ kg^{-1}	$Q_{B,0} = 858.6$	n/a	1.9
Critical temperature	K	$T_c = 5\,000$	n/a	200
Critical density	kg m^{-3}	$\rho_c = 3\,250$	n/a	100
Critical pressure	MPa	$p_c = 180$	n/a	30
Saturated vapour pressure	Pa	$p_s = 1.88 \times 10^{13} \cdot T^{-0.985} \cdot \exp(-23\,325/T)$ or $p_s = 5.76 \times 10^{9} \cdot \exp(-22\,131/T)$	601-2 021	15% 18%
Surface tension	N m^{-1}	$\sigma = (525.9 - 0.113 \cdot T) \times 10^{-3}$	601-1 300	4%
Density	kg m^{-3}	$\rho = 11\,441 - 1.2795 \cdot T$	601-1 900	1%
Sound velocity	m s^{-1}	$u_s = 1\,953 - 0.246 \cdot T$	601-2 000	2%
Bulk modulus	Pa	$B_s = (43.50 - 1.552 \times 10^{-2} \cdot T + 1.622 \times 10^{-6} \cdot T^2) \times 10^{9}$	601-1 900	5%
Isobaric specific heat	J kg^{-1} K^{-1}	$c_p = 176.2 - 4.923 \times 10^{-2} \cdot T + 1.544 \times 10^{-5} \cdot T^2$ $- 1.524 \times 10^{6} \cdot T^{-2}$	601-1 300	5%
Dynamic viscosity	Pa s	$\eta = 4.55 \times 10^{-4} \cdot \exp(1\,069/T)$	601-1 500	5%
Electric resistivity	Ω m	$r = (67.0 + 0.0471 \cdot T) \times 10^{-8}$	601-1 300	2%
Thermal conductivity	W m^{-1} K^{-1}	$\lambda = 9.2 + 0.011 \cdot T$	601-1 400	(15%)

Table 2.19.2: Summary of the recommended correlations for main thermophysical properties of molten bismuth (Bi)

p ~ 0.1 MPa, except the critical parameters and the saturated vapour pressure

Property, parameter	SI unit	Correlation	Temp. range (K)	Estimated error ±
Melting temperature	K	$T_{M,0} = 544.6$	n/a	0.3
Latent heat of melting	kJ kg^{-1}	$Q_{M,0} = 53.3$	n/a	0.3
Boiling temperature	K	$T_{B,O} = 1\,831$	n/a	6
Latent heat of boiling	kJ kg^{-1}	$Q_{B,0} = 856.2$	n/a	1.9
Critical temperature	K	$T_c = 4\,500$	n/a	500
Critical density	kg m^{-3}	$\rho_c = 2\,800$	n/a	200
Critical pressure	MPa	$p_c = 135$	n/a	15
Saturated vapour pressure	Pa	$p_s = 2.67 \times 10^{10} \cdot \exp(-22\,858/T)$	545-1 831	40%
Surface tension	N m^{-1}	$\sigma = (420.8 - 0.081 \cdot T) \times 10^{-3}$	545-1 400	3%
Density	kg m^{-3}	$\rho = 10\,725 - 1.22 \cdot T$	545-1 300	0.5%
Sound velocity	m s^{-1}	$u_s = 1\,616 + 0.187 \cdot T - 2.2 \times 10^{-4} \cdot T^2$	545-1 800	2%
Bulk modulus	Pa	$B_s = (30.09 - 2.441 \times 10^{-3} \cdot T - 3.913 \times 10^{-6} \cdot T^2) \times 10^9$	545-1 300	5%
Isobaric specific heat	J kg^{-1} K^{-1}	$c_p = 118.2 - 5.934 \times 10^{-3} \cdot T + 7.183 \times 10^6 \cdot T^{-2}$	545-1 300	4%
Dynamic viscosity	Pa s	$\eta = 4.456 \times 10^{-4} \cdot \exp(780/T)$	545-1 300	5%
Electric resistivity	Ω m	$r = (98.96 + 0.0554 \cdot T) \times 10^{-8}$	545-1 420	1.5%
Thermal conductivity	W m^{-1} K^{-1}	$\lambda = 7.34 + 9.5 \times 10^{-3} \cdot T$	545-1 000	(15%)

Table 2.19.3: Summary of the recommended correlations for main thermophysical properties of molten LBE

p ~ 0.1 MPa, except the critical parameters and the saturated vapour pressure

Property, parameter	SI unit	Correlation	Temp. range (K)	Estimated error ±
Melting temperature	K	$T_{M,0} = 398$	n/a	1
Latent heat of melting	kJ kg^{-1}	$Q_{M,0} = 38.6$	n/a	0.3
Boiling temperature	K	$T_{B,O} = 1\,927$	n/a	16
Latent heat of boiling	kJ kg^{-1}	$Q_{B,0} = 856$	n/a	5
Critical temperature	K	$T_c = 4\,800$	n/a	500
Critical density	kg m^{-3}	$\rho_c = 2\,200$	n/a	200
Critical pressure	MPa	$p_c = 160$	n/a	70
Saturated vapour pressure	Pa	$p_s = 1.22 \times 10^{10} \cdot \exp(-22\,552/T)$	670-1 927	60%
Surface tension	N m^{-1}	$\sigma = (448.5 - 0.08 \cdot T) \times 10^{-3}$	420-1 400	3%
Density	kg m^{-3}	$\rho = 11\,065 - 1.293 \cdot T$	400-1 300	0.8%
Sound velocity	m s^{-1}	$u_s = 1\,855 - 0.212 \cdot T$	400-1 100	1%
Bulk modulus	Pa	$B_s = (38.02 - 1.296 \times 10^{-2} \cdot T + 1.32 \times 10^{-6} \cdot T^2) \times 10^9$	400-1 100	3%
Isobaric specific heat	J kg^{-1} K^{-1}	$c_p = 164.8 - 3.94 \times 10^{-2} \cdot T + 1.25 \times 10^{-5} \cdot T^2 - 4.56 \times 10^5 \cdot T^{-2}$	400-1 100	7%
Dynamic viscosity	Pa s	$\eta = 4.94 \times 10^{-4} \cdot \exp(754.1/T)$	400-1 200	8%
Electric resistivity	Ω m	$r = (90.9 + 0.048 \cdot T) \times 10^{-8}$	403-1 100	6%
Thermal conductivity	W m^{-1} K^{-1}	$\lambda = 3.284 + 1.617 \times 10^{-2} \cdot T - 2.305 \times 10^{-6} \cdot T^2$	403-1 100	(15%)

References

Addison, C.C. and J.B. Raynor (1966), "Liquid Metals. Part XII. The Surface Tension of Liquid Bismuth in Pure And Impure Hydrogen, in Other Gases, And *in Vacuo*", *Journal of the Chemical Society A: Inorganic, Physical, Theoretical*, Issue 0, pp. 965-967.

Ageron, P. et al. (1959), "Matériaux", *Technologie des réacteurs nucléaires*, Vol. 1, Edition Eyrolles, Paris.

Agostini, P. et al. (2004), "The Re-crystallization Issue in Lead-bismuth Technology", *Journal of Nuclear Materials*, Vol. 335 (2), pp. 275-279.

Agrawal, D.C. and V.J. Menon (1989), "Surface Tension, Evaporation and eotvos Law for Liquid Metals", *Journal of Physics: Condensed Matter*, Vol. 1, p. 4161.

Alchagirov, B.B., T.M. Shamparov and G.A. Mozgovoi (2003), *High Temperature*, Vol. 41 (2), p. 210 (translated from *Teplofizika Vysokikh Temperatur*, Vol. 41 [2], p. 247).

Alchagirov, B.B., G.A. Mozgovoi and T.M. Shamparov (2004), *High Temperature*, Vol. 42 (3), p. 493 (translated from *Teplofizika Vysokikh Temperatur*, Vol. 42 [3], p. 487).

Allen, B.C. (1972), "The Surface Tension of Liquid Metals", *Liquid Metals*, S.Z. Beer (ed.), Marcel Dekker, New York, pp. 161-212.

Azad, A-M. (2005), "Critical Temperature of the Lead-bismuth Eutectic (LBE) alloy", *Journal of Nuclear Materials*, Vol. 341, Issue 1, pp. 45-52.

Babichev, A.P. et al. (1991), "Physical Quantities", *Handbook of Physical Quantities*, I.S. Grigoriev, E.Z. Meilikhov (eds.), Énergoatomizdat (in Russian), Moscow.

Banchila, S.N. and L.P. Filippov (1973), *High Temp*. (USSR), Vol. 11, p. 602 (translated from *Teplofizika Vysokikh Temperatur*, Vol. 11 [6], p. 1301).

Baker, H. (ed.) (1992), "Alloy Phase Diagrams", *ASM Handbook*, Vol. 3, ASM International, Metals Park.

Barin, I. and O. Knacke (1973), *Thermochemical Properties of Inorganic Substances*, Springer-Verlag, Berlin.

Barin, I. et al. (1989), *Thermochemical Data of Pure Substances*, Vol. 2, VCH Verlagsgesellschaft mbH, Weinheim.

Been, S.A. et al. (1950), "The Density of Liquids at Elevated Temperatures. I. The Density of Lead, Bismuth, Lead-Bismuth Eutectic, and Lithium in the Range Melting Point to 1000°C (1 832 F)", *Report NEPA 1585*, Fairchild Engine and Airplane Corp., Oak Ridge

Beer, S.Z. (ed.) (1972), *Liquid Metals Chemistry and Physics*, Marcel Dekker, New York.

Bell, H. and Hultgren, R. (1960), *Technical Report No. 1,* Univ. California.

Beyer, R.T. and E.M. Ring (1972), "Sound Propagation in Liquid Metals", *Liquid Metals Chemistry and Physics*, S.Z. Beer (ed.), Marcel Dekker, New York, p. 411-430.

Bidwell, C.C. (1940), "Thermal Conductivity of Metals", *Physical Review*, Vol. 58, p. 561.

Bienias, A. and F. Sauerwald (1927), *Journal for Inorganic and General Chemistry*, Vol. 93, p. 51.

Bircumshaw, L.L. (1927), *Philosophical Magazine*, Vol. 3 (7), p. 1286.

Bogoslovskaya, G.P. et al. (2002), *Comparative Assessment of Thermophysical and Thermohydraulic Characteristics of Lead, Lead-Bismuth and Sodium Coolants for Fast Reactors*, TECDOC-1289, IAEA, Vienna.

Bonilla, C.F. (1964), "Heat Transfer", Chapter 2 in *Reactor Handbook*, 2nd Ed. (rev., enl.), Vol. IV, Engineering, S. McLain and J.H. Martens (eds.), Interscience Publishers, New York, pp. 46-51.

Brackett, E. and L. Brewer (1957), "University of California Radiation Laboratory Report" UCRL-3712, March 1957.

Bretonnet, J.L. (1988), Conductivité électrique des métaux liquides, *Techniques de l'Ingénieur, Materiaux métal-liques*, n° M153, Form M69, 1.

Brooks, H. et al. (1955), *Reactor Handbook Engineering*, US Atomic Energy Commission, McGraw-Hill.

Brown, W.B. (1923), "Thermal Conductivities of Some Metals in The Solid and Liquid States", *Physical Review*, Vol. 22, p. 171.

Bystrov, P.M. et al. (1988), *Liquid Metal Coolants of Heat Pipes and Power Plants,* V.A. Kirilin (ed.), Nauka, Moscow (in Russian).

Bush, G. and J. Tieche (1963), *Journal of Physics: Condensed Matter*, Vol. 1, p. 78.

Cahill, J.A. and A.D. Kirshenboum (1963), "The Density of Liquid Bismuth From Its Melting Point to Its Normal Boiling Point and an Estimate of Its Critical Constants", *Journal of Inorganic and Nuclear Chemistry*, Vol. 25, p. 501.

Cahill, J.A., G.M. Krieg and A.V. Grosse (1968), "Electrical Conductivity of Tin, Lead, and Bismuth near Their Boiling Points with Estimates to Their Critical Temperatures", *Journal of Chemical and Engineering Data*, Vol. 13, p. 504.

Cailletet, L. and E. Matthias (1986), *Comptes Rendus de l'Académie des Sciences,* Paris, Vol. 102, p. 1202.

Carpenter, L.G. and T.F. Harle (1932), "The Atomic Heat of Bismuth at Higher Temperatures", *Proceedings of the Royal Society of London*, London, Vol. 136A, Issue 829.

Cevolani, S. (1998), *Review of the Liquid Lead-Bismuth Alloy Physical Properties*, ENEA Report DT.SBD.00004, ENEA, Rome.

Chase, M.W. et al. (eds.) (1978), "Thermochemical Tables", JANAF, *Journal of Physical and Chemical Reference Data*, Vol. 7, p. 793.

Chase, M.W. et al. (eds.) (1982), Thermochemical Tables, JANAF, *Journal of Physical and Chemical Reference Data*, Vol. 11, p. 695.

Chase, M.W. et al. (eds.) (1985), Thermochemical Tables, JANAF, *Journal of Physical and Chemical Reference Data*, Vol. 14, Suppl. No. 1.

Chawla, T.C. et al. (1981), "Thermophysical Properties of Mixed Oxide Fuel and Stainless Steel Type 316 for Use in Transition Phase Analysis", *Nuclear Engineering and Design*, Vol. 67, p. 57.

Cheynet, B. (1989), *Thermodynamic Properties of Inorganic Materials*, Vol. 2, Elsevier.

Cheynet, B., J.D. Dubois and M. Milesi (1996), *Données thermodynamiques des éléments chimiques*, Techniques de L'Ingénieur, Materiaux metalliques, No. M153, Form M64.

CRC Handbook of Chemistry and Physics (2002), 82nd edition, CRC Press, Boca Raton, Florida.

Crean, L.E. and W.E. Parkins (1964), "Liquid Metal Cooled Reactors", Chapter 17 in *Reactor Handbook*, 2nd Ed. (rev., enl.), Vol. IV, Engineering, S. McLain and J.H. Martens (eds.), Interscience Publishers, New York, pp.612-681.

Cusack, N. and J.E. Enderby, (1960), "A Note on the Resistivity of Liquid Alkali and Noble Metals", *Proceedings of the Physical Society*, Vol. 75, Issue 3, p. 395.

Davies, H.A. and J.S.L. Leach (1970), "The Electrical Resistivity of Liquid Indium, Tin and Lead", *Physics and Chemistry of Liquids*, Vol. 2, Issue 1.

Ditchburn, R.W. and J.C. Gilmour (1941), "The Vapor Pressures of Monatomic Vapors", *Reviews of Modern Physics*, Vol. 13, p. 310.

Dixon, A.L. and W.A. Rodebush (1927), "The Heat Capacities of Liquid Metals", *Journal of the American Ceramic Society*, Vol. 49, p. 11162.

Douglas, T.B. and J.L. Dever (1953), "Report NBS-2544", National Bureau of Standards.

Douglas, T.B. and J.L. Dever (1954), "Heat Content of Lead from 0 to 900°, and the Heat of Fusion", *Journal of the American Chemical Society*, Vol. 76, p. 4824.

Draggan, S. (2007), "Bismuth", *Encyclopaedia of Earth*, Cutler J. Cleveland (ed.), Washington, D.C., Environmental Information Coalition, National Council for Science and the Environment.

Dreyfus, B. and A. Lacaze (1971), *Cours de thermodynamique*, Dunod, Paris.

Dutchak, Ya.I. and P.V. Panasyuk (1967), *Soviet physics, Solid state*, Vol. 8 (9), p. 2244.

Elliott, R.P. (1965), *Constitution of Binary Alloys*, I-Supplement, McGraw-Hill Book Co., Inc., New York.

Eslami, H. (2005), "A Perturbed Hard-Sphere-Chain Equation of State for Liquid Metals", *Journal of Nuclear Materials*, Vol. 336, p. 135.

Eucken, A. (1936), *Metallwirtsch*, Vol. 15, 63.

Eustathopoulos, N., E. Ricci and B. Drevet (1996), *Tension superficielle*, Techniques de l'Ingénieur, traité Materiaux métalliques, N° M153, Form M67.

Filippov, S.I., N.B. Kazakov and L.A. Pronon (1966), *Izvest. VUZ Chern. Met.*, Vol. 9 (3), p. 8.

Filippow, L.P. (1973), "Research of Thermophysical Properties at the Moscow State University", *International Journal of Heat and Mass Transfer*, Vol. 16, Issue 5, pp. 865-885.

Fortov, V.E., A.N. Dremin and Leont'ev, A.A. (1975), *High Temperture*, vol 13, p. 984.

Friedland, A.J. (1966), "Coolant Properties, Heat Transfer and Fluid Flow of Liquid Metals", Chapter 2 in *Fast Reactor Technology: Plant Design*, J.G. Yevick (ed.), M.I.T. Press, Cambridge (MA).

Gasser, J.G. et al. (1984), "Electrical Resistivity of Bismuth and Bismuth-germanium Alloys in the Liquid State", *Journal of Non-Crystalline Solids*, Vol. 61-62, p. 1237.

Gering, K. and F. Sauerwald (1935), *Journal of Inorganic and General Chemistry*, Vol. 223, p. 204.

Giordanengo, B. et al. (1999), "Thermal Conductivity of Liquid Metals and Metallic Alloys", *Journal of Non-Crystalline Solids*, Vol. 250-252, p. 377.

Gitis, M.B. and I.G. Mikhailov (1966), *Soviet physics – Acoustics,* 11, 372 (translated from *Akust. Zh.,* 11 [1965], 434).

Giuranno, D. et al. (2002), "Surface Tension and Wetting Behaviour of Molten Bi-Pb alloys", *Intermetallics*, Vol. 11, p. 1313.

Glasbrenner, H. et al. (2005), "Expansion of Solidified Lead Bismuth Eutectic", *Journal of Nuclear Materials,* Vol. 343, p. 341.

Glushko, W.P. and V.A. Medvedev (eds.) (1981), *Termicheskie Konstanty Veschestv*, Part III, N, P, As, Sb, Bi (1968); Part IV, C, Si, Ge, Sn, Pb (1970); Part X, Alkaline Metals, *Akad. Nauk*, Moscow.

Gmelin, L. (1924), *Handbuch der Anorganischen Chemie*, Verlag Chemie, Berlin.

Gmelin, L. (1972), *Gmelins Handbuch der Anorganischen Chemie*, 8th edition, Yeil B1, Syst.-Nr. 47, Verlag Chemie GmbH, Weinheim.

Gokcen, N.A. (1992), "The Bi-Pb (Bismuth-lead) System", *Journal of Phase Equilibria*, 13, 21.

Gordon, R.B. (1959), "Propagation of Sound in Liquid Metals: The Velocity in Lead and Tin", *Acta Materialia*, 7, 1.

Greenberg, Y. et al. (2008), "High Precision Measurements of the Temperature Dependence of the Sound Velocity in Selected Liquid Metals", *Journal of Non-Crystalline Solids,* 354, 4094.

Greenberg, Y. et al. (2009), "Evidence For a Temperature-Driven Structural Transformation in Liquid Bismuth", *EPL,* 86, 3, 36004.

Gromov, B.F. et al. (1999), "The Problems of Technology of the Heavy Liquid Metal Coolants (Lead-bismuth, Lead)", *ProcEedings of the Conference. on Heavy Liquid Metal Coolants in Nuclear Technology (HLMC'98)*, 5-9 October 1998, Obninsk, Russia, SSC RF-IPPE, Vol. 1, pp. 87-100.

Gross, P. et al. (1948), "On Some Equilibria Involving Aluminium Monohalides", *Discussions of the Faraday Society*, 4, 206.

Grosse, A.V. (1961), "The Viscosity of Liquid Metals and an Empirical Relationship between their Activation Energy of Viscosity and Their Melting Points", *Journal of Inorganic Nuclear Chemistry*, 23, 333.

Grosse, A.V. (1966), *Revue haute température et réfractaires*., 3, 115.

Gröschel, G.F. and J. Patorski (2005), *PSI Scientific Report 2004*, Vol. III, p. 200, ISSN 1423-7326, March 2005.

Gurvich, L.V. and I.V. Veyts (1991), *Thermodynamic Properties of Individual Substances*, 4th edition, Vol. 2, Parts 1 and 2, Hemisphere Pub. Corp., New York.

Hammond, C.R. (2004), "The Elements", in *Handbook of Chemistry and Physics*, 81st edition, CRC Press.

Hansen, M. and K. Anderko (1958), *Constitution of Binary Alloys*, 2nd ed., McGraw-Hill Book Co., Inc., New York, USA.

Harvey, D. (1961), *Trans. AIME*, 221, 266.

Hayashi, M. et al. (2007), "Temperature dependence of the velocity of sound in liquid metals of group XIV", *International Journal of Thermophysics*, 28, 83.

Hemminger, W. (1989), "Thermal Conductivity of Lead in the Range – 180 to 500°C", *Int. J. Thermophys*., 10 (4), 765.

Hiers, G.O. (1948), *Metals Handbook*, Cleveland, Ohio, USA.

Hill, J.E. and A.L. Ruoff (1965), "Temperature Dependence of the Velocity of Sound in Some Liquid Metals and Eutectic Alloys", *J. Chem. Phys*., 43 (2), 2150-2151.

Hirabayashi, M. et al. (2005), "Development of Ultrasonic Flow Meter for Liquid Lead-bismuth Flow", *Proc. 13th International Conference on Nuclear Engineering*, Beijing, China, 16-20 May 2005, ICONE13-50346.

Hixson, S. et al. (1986), "Sound Speed in Liquid Lead at High Temperatures", *International Journal of Thermophysics*, 7 (1), 161.

Ho, C.Y., R.W. Powell and P.E. Liley (1968), *Thermal Conductivity of Selected Materials, Part 2*, NSRDS-NBS 16, National Standard Reference Data Series, National Bureau of Standards, Feb. 1968.

Hofmann, W. (1970), *Lead and Lead Alloys*, Springer-Verlag, Berlin, New York.

Hogness, T.R. (1921), "The Surface Tensions and Densities of Liquid Mercury, Cadmium, Zinc, Lead, Tin and Bismuth", *J. Am. Chem. Soc.,* 43, 1621.

Holman, J.P. (1968), *Heat Transfer*, MacGraw-Hill, USA.

Howe, H.E. (1961), "Bismuth", in *Rare Metals Handbook*, 2nd ed., C.A. Hampel, Reinhold Publishing Corp.

Hultgren, R. et al. (1963), *Selected Values of the Thermodynamic Properties*, J. Wiley, USA.

Hultgren, R. et al. (1973a), *Selected Values of the Thermodynamic Properties of Binary Alloys*, ASM, Metals Park, Ohio, USA.

Hultgren, R. et al. (1973b), *Selected Values of the Thermodynamic Properties of the Elements*, J. Wiley, New York, USA.

IAEA (International Atomic Energy Agency) (2009), *Thermophysical Properties of Materials for Nuclear Engineering: A Tutorial and Collection of Data*, IAEA-THPH, IAEA, Vienna.

Iida, T., Z. Morita and S. Takeuchi (1975), *Journal of the Japan Institute of. Metals*, 39, 1169.

Iida, T. and R.I.L. Guthrie (1988), *The Physical Properties of Liquid Metals*, Clarendon Press, Oxford.

Imbeni, V. et al. (1998), "Stato dell'arte sulle proprietà chimico-fisiche del Pb e Pb-Bi. Parte I. Proprietà di Pb, Bi, Li, Na", in *Studio di un acceleratore superconduttivo di protoni di grande potenza e studio di un sistema sottocritico da esso sostenuto per il bruciamento dei residui radioattivi, Sottotema 2: Prove di corrosione,* BoMet, Accordo di programma ENEA/INFN-MURST, Settore Ambiente, December 1998 (in Italian).

Imbeni, V. et al. (1999), "Stato dell'arte sulle proprietà chimico-fisiche del Pb e Pb-Bi. Parte II. Proprietà di Pb e Pb-Bi, Na", in *Studio di un acceleratore superconduttivo di protoni di grande potenza e studio di un sistema sottocritico da esso sostenuto per il bruciamento dei residui radioattivi, Sottotema 2: Prove di corrosione, BoMet*, Accordo di programma ENEA/INFN-MURST, Settore Ambiente, December 1999 (in Italian).

Jarzynski, J. (1963), "Ultrasonic Propagation in Liquid Bismuth and Mercury", *Proceedings of the Physical Soc*ierty., 81, 745.

Jauch, U. and B. Schulz (1986), *Estimation of the Thermophysical Properties in the System Li-Pb*, Report KfK 4144, Kernforschungszentrum, Karlsruhe.

Joud, J.C., N. Eustathopoulos and P. Desre (1972), "Mesure des tensions et entropies superficielles de cuivre, de l'argent at du plomb liquid par la méthode de la goutte posée sur support de graphite", *C.R. Acad. Sc. Paris*, Série C, t. 274, 549, Gauthier-Villars, Paris.

Kanai, S. and T. Yoshimi (1993), "Sound Velocity in the Liquid Bismuth-zinc System", *J. Phys. Soc. Jap.*, 62, 2388.

Kaplun, B. et al. (1979), *Teplofizicheskie svoystva veshestv i materialov*, Novosibirsk.

Kasama, A., T. Iida and Z. Morita (1976), *Journal of the Japan Institute of Metals*, 40, 1030.

Kazakova, I.V., S.A. Lyamkin and B.M. Lepinskikh (1984), *Russian Journal of Physical Chemistry* 58, 932.

Kažys, R.A. et al. (2002), "Investigation of Ultrasonic Properties of a Liquid Metal Used as a Coolant in Accelerator Driven Reactors", *2002 IEEE International Ultrasonics Symposium Proceedings*, ISSN 1051-0117, Munich, pp. 794-797.

Kelley, K.K. (1935), *Critical Evaluations of Vapour Pressures and Heats of Evaporation of Inorganic Substances*, US Bureau of Mines Bulletin No. 393.

Kelley, K.K. (1960), *Evaluation of High-Temperature Heat Capacities of Inorganic Compounds*, US Bureau of Mines Bulletin.

Keene, B.J. (1993), "Review of Data for the Surface Tension of Pure Metals", *International Metal Reviews*, 38, 157.

Khairulin, R.A. et al. (2005), "Crystallization and Relaxation Phenomena in the Bismuth-lead Eutectic", *Journal of Alloys and Compounds*, 387 (1-2), 183.

Kirillov, P.L. and G.P. Bogoslovskaya (2000a), "Heat Transfer in Nuclear Installations", *Energoatomisdat*, Moscow (in Russian).

Kirillov, P.L. and N.B. Deniskina (2000b), *Thermophysical Properties of Liquid Metal Coolants*, Tables and Correlations, Review FEI-0291, Obninsk, IPPE (in Russian).

Kirillov, P.L. et al. (eds.) (2008), *Thermophysical Properties of Materials for Nuclear Engineering: A Tutorial and Collection of Data*, IAEA, Vienna.

Kirshenbaum, A.D., J.A. Cahill and A.V. Grosse (1961), "The Density of Liquid Lead from the Melting", *Journal of Inorganic Nuclear Chemistry*, 22, 33.

Kittel, C. (1956), *Introduction to Solid State Physics*, Wiley, NY.

Klement, W., A. Jayaraman and G.C. Kennedy (1963), "Phase diagrams of arsenic, antimony, and bismuth at pressures up to 70 kbars", *Phys. Rev.*, 131, 632.

Kleppa, O.J. (1950), "Ultrasonic Velocities of Sound in Some Metallic Liquids. Adiabatic and Isothermal Compressibilities of Liquid Metals at their Melting Points", *Journal of Chemical Physics*, 18, 1331.

Klinkhardt, H. (1927), "Messung von wahren spezifischen Wärmen bei hohen Temperaturen durch Heizung mit Glühelektronen", *Annalen der Physik*, 389, 167.

Knacke, O., O. Kubaschewski and K. Hesselmann (1991), *Thermodynamic Properties of Inorganic Substances*, Vol. 2, 2nd ed., Springer-Verlag.

Kohlraush, F. (1956), *Praktische Physik*, II, Bände Teubner, Stuttgart.

Konno, S. (1919), *Science Reports of the Tohoku Imperial University*, 8, 169.

Konno, S. (1920), "LXV. On the Variation of Thermal Conductivity during the Fusion of Metals", *Phil. Mag.*, 40, 542.

Konyuchenko, G.V. (1969), *Teplofizika Vysokikh Temperatur*, 10, 309.

Kopp, I.Z. (1967), *Russian Journal of Physical Chemistry*, 41, 782.

Krynitsky, A.I. (1933), *Metals & Alloys*, 4, 79.

Krzhizhanovski, R.E. et al. (1975), *Inzhenerno-Phyzicheskiy Zhournal,* Vol. 29 (2), 322.

Kubaschewski, O. and C.B. Alcock (1979), *Metallurgical Thermochemistry*, 5th edition, Pergamon Press, Oxford.

Kubaschewski, O., C.B. Alcock and P.J. Spencer (1993), *Materials Thermochemistry*, 6th edItion, Pergamon Press, NY.

Kutateladze, S.S. et al. (1958), *Liquid-Metal Heat Transfer Media*, Cons. Bur. Inc., New York (transl. from Russian, *Atomnaia Energiia*, *Suppl. 2*).

Lang, G. et al. (1977), *Z. Metallk.*, 68, 113.

Lee, D.N. and B.D. Lichter (1972), "Relation between Thermodynamic and Electrical Properties of Liquid Alloys", *Liquid Metals*, S.Z. Beer (ed.), Marcel Dekker, New York, pp. 81-160.

Lucas, L.D. and G. Urbain (1962), "Densité du silicium, du germanium, de l'antimoine et du bismuth à l'état liquide", *C.R. Acad. Sci.*, T 255, 2414, Gauthier-Villars, Paris.

Lucas, L.D. (1969), "Densité du plomb à l'état liquide entre 330 35 1550°", *C.R. Acad. Sci.*, Série C 268, 1081, Gauthier-Villars, Paris.

Lucas, L.D. (1984a), "Données physico-chimiques des principaux métaux et métalloïdes", *Techniques de l'Ingénieur, Materiaux métalliques*, N° M153, Form M65a.

Lucas, L.D. (1984b), "Viscosité", *Techniques de l'Ingénieur, Materiaux métalliques*, N° M153, Form M66.

Lyon, R.N. (ed.) (1954), *Liquid Metals Handbook*, 2nd Ed., Report NAVEXOS P-733, Atomic Energy Commission and Dept. of the Navy, Washington, DC, USA, June 1952 (Rev. 1954).

Lyon, R.N. (1960), "Liquid Metals", Chapter 49 in *Reactor Handbook*, 2nd Ed. (rev., enl.), Vol. I: Materials, Sect. F: Coolant Materials, C.R. Tipton, Jr. (ed.), Interscience Publishers, New York, USA.

Makeyev, V.V., Y.L. Dyomina and P.S. Poppel (1989), *Teplofiz. Vys. Temp.*, 27, 889.

Mantell, C.L. (ed.) (1958), *Engineering Material Handbook*, McGraw-Hill, USA.

Martynyuk, M.M. (1983), *Russian Journal of Physical Chemistry*, 57, 494.

Martynyuk, M.M. (1998), *Russian Journal of Physical Chemistry*72, 13.

Mera, Y., Y. Kita and A. Adachi (1972), *Technical Report*, Osaka University, 22, 445.

Michelato, P. et al. (2003), "The TRESCO-ADS Project Windowless Interface: Theoretical and Experimental Evaluations", *Proc. Int. Workshop on P&T and ADS Development*, Mol, Belgium, 6-8 October 2003.

Mikryukov, V.E. and N.A. Tyapunina (1956), *Fiz. Met. i Metaloved.*, Akad. Nauk. SSSR, Ural. Filial, 3, 31.

Miller, R.R. (1951), "Physical Properties of Liquid Metals", *Liquid Metals Handbook*, Report NAVEXOS, R.N. Lyon (ed.), US Gov. Pt. Office, Washington DC, 2nd edition (rev.), ORNL, Tennessee.

Miller, R.R. (1954), "Physical Properties of Liquid Metals", *Liquid Metals Handbook*, R.N. Lyon (ed.), 2nd edition, Report NAVEXOS P-733, Atomic Energy Commission and Dept. of the Navy, Washington, USA, June 1952 (rev. 1954).

Mills, K.C., B.J. Monaghan and B.J. Keene (1996), "Thermal Conductivities of Molten Metals: Part 1 Pure Metals", *Int. Mat. Reviews*, 41, 209.

Morita, K. et al. (2006), "thermophysical Properties of Lead-bismuth Eutectic Alloy in Reactor Safety Analyses", *J. Nucl. Sci. Technology*, 43 (5), 526.

Morita, K., V. Sobolev and M. Flad (2007), "Critical Parameters and Equation of State for Heavy Liquid Metals", *J. Nucl. Mater.*, 362, 227.

Mustafin, G.M. and G.F. Shaikhiev (1983), *Russian Journal of Physical Chemistry,* 57 (3), 421.

Nakamura, S., T. Hibiya and F. Yamamoto (1990), "Thermal Conductivity of GaSb and InSb in Solid and Liquid States", *J. Appl. Phys.*, 68 (10), 5125.

Nikol'skii, N.A. et al. (1959), "Thermal and Physical Properties of Molten Metals and Alloys", *Voprosy Teploobmena*, Akad. Nauk SSSR, Energet. Inst. G.M. Krzhizhanovskogo, pp. 11-45 (in Russian).

Northrup, E.F. and V.A. Suydam (1913), "Resistivity of a Few Metals through a Wide Range of Temperature", *J. Franklin Inst.*, 175, 153.

Nosek, M.V., G.V. Sang-Sho-Hsyan and N.V. Semibratova (1967), *Tr. Inst. Khim*, Nauk Akad. Nauk Kaz. SSR, 15, 150.

Novacovic, R. et al. (2002), "Surface Properties of Bi-Pb Liquid Alloys", *Surface Science*, 515, 377.

NEA (2007), *Handbook on Lead–bismuth Eutectic Alloy and Lead Properties, Materials Compatibility, Thermal hydraulics and Technologies*, NEA No. 6195, OECD/NEA, Paris.

Okamoto, H. (1994), "Survey of Current Literature", *J. Phase Equilibria*, 15 (3), 361.

Ofte, D. and L.J. Wittenberg (1963), "Viscosity of Bismuth, Lead, and Zinc to 1000°C", *Trans. Met. Soc. AIME*, 227, 706.

Ofte, D. (1967), "The Viscosities of Liquid Uranium, Gold and Lead", *Journal of Nuclear Materials*, 22, 28.

Ohno, S. and S. Tamaki (1975), "Electronic Properties of Liquid in-Bi Alloys", *J. Phys. Soc. Japan*, 38, 538.

Ohno, S., S. Miyahara and Y. Kurata (2005), "Experimental Investigation of Lead-bismuth Evaporation Behaviour", *J. Nucl. Sci. and Techn.* 42, 593.

Onistchenko, V.P., O.F. Kutirkin and A.Yu. Boykov (1999), *High Temp. – High Pres.*, 31, 113.

Orlov, Y.I. (1997), "Technology of PbBi and Pb Coolants", *Seminar on the Concept of Lead-Cooled Fast Reactor*, Cadarache, France, 22-23 September, 1997.

Orlov, Yu., B.F. Gromov and V.A. Gylevskiy (2003), "Bases of Technology of Pb-Bi Coolant", *ATW Workshop*, Washington, DC, 16-18 February 2003.

Pankratz, L.B. (1982), *Thermodynamic Properties of Elements and Oxides*, US Department of the Interior, Bureau of Mines, 672, USA.

Pashaev, B.P. et al. (1982), *Reviews on Thermophysical Properties of Materials,* M.: IVTAN, N°3 (35) (*in Russian)*.

Pastor Torres, F.C. (2003), *Surface Tension Measurement of Heavy Liquid Metals Related to Accelerator Driven Systems (ADS)*, Diploma Thesis, FZK (IKET), KALLA.

Plevachuk, Yu. et al. (2008), "Some Physical Data of the Near Eutectic Liquid Lead-bismuth", *Journal of Nuclear Materials*, 373, 335.

Pokrovsky, N.L., P.P. Pugachevich and N.A. Golubev (1969), *Zhurnal Fizicheskoy Khimii,* 43 (8), 2158.

Ponyatovsky E.G. and A.G. Rabinkin (1970), *Fizika Metallov i Metallovedenie*, 3, 606.

Pottlacher, G. and H. Jäger (1990), "Measurement of Thermophysical properties of lead by a submicrosecond pulse-heating method in the range 2000-5000 K", *Int. J. Thermophysics*, 11, 719.

Pottlacher, G. (1998), personal communication.

Powell, R.W. and R.P. Tye (1958), "Experimental Determinations of the Thermal Conductivities of Molten Metals", *Proc. Conf. Thermodynamic and Transport Properties of Fluids. Inst. Mech. Eng.*, London, pp. 182-187.

Powell, R.L. and G.E. Childs (1972), *American Institute of Physics Handbook*, McGraw-Hill Book Company, Inc., New York.

Predel, B. and W. Schwerman (1967), *Z. Metallk.*, 58, 553.

Pylchenkov, E.H. (1999), "The Issues of Freezing-Defreezing Lead-bismuth Liquid Metal Coolant in Reactor Facilities Circuits", *Proc. Conf. on Heavy Liquid Metal Coolants in Nuclear Technology (HLMC'98)*, 5-9 October 1998, Obninsk, Russian Federation, SSC RF-IPPE, Vol. 1, pp. 110-119.

Quill, L.L. (1950), *Chemistry and Metallurgy of Miscellaneous Materials*, McGraw-Hill Book Company, Inc., New York.

Rashed, M. (2008), "Lead", *Encyclopaedia of Earth*, Cutler J. Cleveland (ed.), Washington, DC, Environmental Information Coalition, National Council for Science and the Environment, First published in the *Encyclopaedia of Earth*, December 2006 (revised January 2008).

Reis, T. et al. (1959), *Technologie des réacteurs nucléaires*, *Tome 1 – Matériaux*, Eyrolles, Paris.

Roll, A. and H. Motz (1957), *Zeitung Metallk.,* 48, 272.

Rosenthal (1953), Ph. D. Thesis, MIT, United States.

Ruppersberg, H. and W. Speicher (1976), *Zeitung Naturforschung*, 319, 47.

Samsonov, G.V., A.D. Panasyuk and E.M. Dudnik (1969), *Izv. Vuz. Tsvet. Met.*, 12, 110.

Sauerwald, F. and K. Topler (1926), *Z. Anorg. Chem.*, 157, 117.

Schulz, B. (1991), "Thermophysical Properties of the Li(17)Pb(83) Alloy", *Fusion Eng. Des.*, Vol. 14, p. 199.

Schuurmans, P. et al. (2006), R&D Support for a Windowless Liquid Metal Spallation Target in MYRRHA ADS (private communication).

Semenchenko, V.K. and N.L. Pokrovsky (1937), *Uspekhi Khim.*, 6, 777.

Semenchenko, V.K. (1961), *Surface Phenomena in Metals and Alloys*, Pergamon Press, London.

Smithells, C.J. (1955), *Metals Reference Book,* 2nd Edition, Vol. I. Interscience Punl. Inc. New York, Butterworths Scientific Publ., London.

Smithells, C.J. (1967), *Metals Reference Book,* 4th Edition, Vol. III. Interscience Punl. Inc. New York, Butterworths Scientific Publ., London.

SMRB (Smithells Metals Reference Book) (1983), "The Physical Properties of Liquid Metals", Chapter 8, *Thermochemical Data*, E.A. Brandes (ed.), 6th edition, Butterworths, London.

SMRB (2004), W.F. Gale, T.C. Totemeier (eds.), 8th edition, Elsevier, Amsterdam.

Sobolev, V. (2005), *MYRRHA ADS Database: Part I. Thermophysical Properties of the Molten Lead-Bismuth Eutectic*, SCK•CEN report BLG-1014, Mol, Belgium, August 2005 (rev. December 2005).

Sobolev, V. (2007a), "Thermophysical Properties of Lead and Lead-bismuth Eutectic". *Journal of Nuclear Materials*, 362, 235-247.

Sobolev, V. and G. Benamati (2007b), "Thermophysical and Electric Properties", Chapter 2, *Handbook on Lead-Bismuth Eutectic Alloy and Lead Properties, Materials Compatibility, Thermal hydraulics and Technologies*, NEA No. 6195, OECD/NEA, Paris, pp. 25-99.

Sobolev, V., P. Schuurmans and G. Benamati (2008a), "Thermodynamic Properties and Equation of State of Liquid Lead and Lead-bismuth Eutectic", *J. Nucl. Mater.*, 376, 358.

Sobolev, V. (2008b), "Thermodynamic Properties and Equation of State of Heavy Liquid Metals (Brief Review)", *Proceedings of the Workshop on Utilisation and Reliability of High Power Proton Accelerators*, Mol, Belgium, 6-9 May 2007, OECD/NEA, Paris.

Sobolev, V. (2009), "Thermodynamic Equations of State for Heavy Liquid MetalCoolants", Fifth Edition of the International Workshop on Materials for HLM-Cooled Reactors and Related Technologies (HeLiMERT-2009), Mol, Belgium, 20-22 April 2009, SCK•CEN, Mol, Belgium, pp. 149-156.

Sobolev, V. (2011), *Database of Thermophysical Properties of Liquid Metal Coolants for GEN-IV*, SCK•CEN report BLG-1069, Mol, Belgium, December 2010 (rev. December 2011).

Sobolev, V. (2012), "Properties of Liquid Metal Coolants", *Comprehensive Nuclear Materials*, Vol. 2, R.J.M. Konings (ed.), Elsevier, Amsterdam, pp. 373-392.

Song, Y., S.M. Lambert and J.M. Prausnitz (1994), "A Perturbed Hard-sphere-chain Equation of State for Normal Fluids and Polymers", *IEC Res.*, 33, 1047.

Srinivasan, G.M. and S. Ganesan (1983), "A New Approach for the Estimation of the Critical Temperature: Application to Sodium", *Journal of Nuclear Materials,* 114, 108.

Steinberg, D.J. (1974), "A Simple Relationship between the Temperature Dependence of the Density of Liquid Metals and Their Boiling Temperatures", *Met. Trans.*, 5, 1341.

Stølen, S. and F. Grønvold (1999), "Critical Assessment of the Enthalpy of Fusion Metals Used as Enthalpy Standards at Moderate to High Temperatures", *Thermochimica Acta*, 327, 1.

Strauss, S.W., L.E. Richards and B.F. Brown (1960), "The Density of Liquid Lead and of Dilute Solutions of Nickel in Lead", *Nucl. Sci. Eng.*, 7, 442.

Stremousov, V.I. and B.A. Solomin (1975), *Zhurnal Fiz. Chim.* XLIX (8).

Stull, D.R. and G.C. Sinke (1956), *Thermodynamic Properties of the Elements*, Am. Chem. Soc., Washington

Stull, D.R. et al. (eds.) (1971), *Thermochemical Tables*, JANAF, US Department of Commerce, National Bureau of Standards, US Government Printing Office.

Takeda, Y. (1997), *Volume Change of LBE After Solidification*, PSI TM-97-02-01.

Tamamushi, B. et al. (eds.) (1981), *Iwanami Dictionary of Physics and Chemistry (Iwanami rikagaku jiten)*, 3rd edition, Iwanami Shoten Publishers, Tokyo.

Taskinen, P. and O. Teppo (1992), *Scand. J. Metall.,* 21 (4), 181.

Tomlinson, J.L. and B.D. Lichter (1969), The Electrical Resistivity of the Liquid Alloys of Cd-Bi, Cd-Sn, Cd-Pb, In-Bi, and Sn-Bi", *Trans. AIME*, 245, 2261.

Touloukian, Y.S. and E.H. Buyco (1970a), "Specific Heat: Metallic Elements and Alloys", *Thermphysical Properties of Matter*, Vol. 4, IFI/Plenum, New York – Washington.

Touloukian, Y.S. et al. (1970b), "Thermal Conductivity: Metallic Elements and Alloys", *Thermophysical Properties of Matter*, Vol. 1, IFI/Plenum, New York – Washington.

Tschirner, H.U. (1969), *Z. Metallk.*, 60, 46.

Tsu, Y. et al. (1979), *Journal of the Japan Institute of Metals,* 43, 439.

Tsu, Y. et al. (1982), *Transactions of the Japan Institute of Metals,* 23, 1.

Tupper, R.B. et al. (1991), "Polonium Hazards Associated with Lead-Bismuth Used as a Reactor Coolant", *Proc. Int. Conf on Fast Reactors and Related Fuel Cycles*, Kyoto, 28 October-1 November 1991, Vol. 4, pp. 5.6-1 – 5.6-9.

Umino, S. (1926), *Sci. Repts.,* Tohoku Impl. Univ., 15 (Ser. 1), 597.

Viswanath, D.S. and B.C. Mathur (1972), "Thermal Conductivity of Liquid Metals and Alloys", *Met. Trans*., 3, 1769.

Von Wartenberg, H. and R. Schütte (1933), *Z. Anorg. Chem*., 211, 222.

Washburn, E.W. (1933), *International Critical Tables of Numerical Data, Physics, Chemistry and Technology*, published for the National Research Council by McGraw-Hill Book Co. Inc., New York.

Watson, K.M. (1931), "Prediction of Critical Temperatures and Heats of Vaporization", *Ind. Eng. Chem*., 23, 360.

Weeks, J.R. (1971), "Lead, Bismuth, Tin And Their Alloys As Nuclear Coolants", *Nucl. Eng. Des*., 15, 363.

Wittenberg, L.J. and D. Ofte (1970), "Viscosity of Liquid Metals", *Techniques of Metals Research*, Vol. 4, Part 2, Interscience, New York.

Yamasue, Y.E. et al. (2003), "Deviation from Wideman-Franz Law for the Thermal Conductivity of Liquid Tin and Lead at Elevated Temperature", *Int. J. Thermophys*. 24, 713.

Zinoviev, V.E. (1989), "Properties of Metals", *Atomnaya Energia*, Moscow (in Russian).

Zucchini, A., P. Agostini and F. Baicchi (2005), "Lead-bismuth Eutectic Recrystallization Studies for the MEGAPIE Target", *Journal of Nuclear Materials*, 336 (2-3), 291.

3. Thermodynamic relationships and heavy liquid metal interaction with other coolants*

3.1 Introduction

This chapter collates:

- enthalpies, entropies, free energy and entropy of mixing for LBE;
- purity requirements for use of LBE in a nuclear system;
- solubility and diffusivity values of various elements, especially metallic elements and oxygen, in pure Pb, pure Bi and LBE; interaction between oxygen and liquid Pb, Bi and LBE is considered, links between oxygen partial pressure and dissolved oxygen concentration in the liquid metal is given;
- ternary and pseudo-binary phase diagrams;
- finally, the interaction of liquid Pb and LBE with other coolants such as water, sodium or oil is also considered.

Revisions have been made to the previous handbook edition according to the revisions performed in Chapter 2 (Sobolev, 2011), but also taking into account the latest literature results.

3.2 Enthalpies, entropies (solid and liquid state) – free energy and entropy of mixing

The heats of formation of six solid Pb-Bi alloys were measured at 400 K in a liquid lead solution calorimeter by Roy (1959). It was found that these alloys obey Kopp's law of additivity and the heats of formation are therefore temperature independent. The lead and bismuth used in these experiments were reported to be 99.999% pure. Using these results, integral free energies and entropies of formation for solid Pb-Bi alloys were calculated at 400 K as a function of the Pb content.

The main thermodynamic functions of interest are enthalpy H, free energy F, Gibbs potential Φ and entropy S. The enthalpy and other thermodynamic potentials of pure substances in the condensed liquid state at the standard pressure can be presented as follows:

$$H(T,P_0) = H(0,P_0) + \int_0^{T_m} C_p(T,P_0)dT + \Delta H_m(T_m,P_0) + \int_{T_m}^{T} C_p(T,P_0)dT$$

* Chapter lead: L. Martinelli. For additional contributors please see Appendix 1.

Figure 3.2.1: Nomenclature

$C_p(T)$	Heat capacity at constant pressure (J mol^{-1} K^{-1})
$H_X(T)$	Enthalpy of the element X at temperature T (J mol^{-1})
$\Delta H_m(T)$	Latent enthalpy of melting (J mol^{-1})
$\Delta H_X^{(298)}(T)$	Increment of enthalpy of the element X at temperature T, considering 298 K as the reference standard temperature (J mol^{-1})
T	Temperature (K)
T_m	Melting temperature (K)
P	Pressure (Pa)
P_0	Standard (normal) pressure (Pa)
$S(T)$	Entropy (J mol^{-1} K^{-1})
$\Phi(T)$	Gibbs energy function (J mol^{-1})

And thus for T higher than T_m at constant pressure P_0:

$$H(T,P_0) - H(T_m,P_0) = \int_{T_m}^{T} C_p(T,P_0)\,dT \tag{3.1}$$

$$S(T) = \int_0^{T_m} \frac{C_p(T)}{T}\,dT + \frac{\Delta H_m(T_m)}{T_m} + \int_{T_m}^{T} \frac{C_p(T)}{T}\,dT \tag{3.2}$$

For the considered systems it was supposed that $S^{o}(0) = 0$ in agreement with the third law of thermodynamics:

$$\Phi(T) = H(T) - T \cdot S(T) \tag{3.3}$$

Usually the values of the thermodynamics functions are tabulated using the temperature of 298.15 K and the pressure of $1.01325 \cdot 10^5$ Pa as the reference standard state (STP).

In order to be consistent with Chapter 2 of this handbook (Sobolev, 2011), the enthalpies were calculated with Eq. (3.1) above and the recommended correlations for heat capacities of the molten Pb, Bi and LBE presented in Chapter 2. This transformation yields the following relationships at P_0 = 1 atm:

$$H_{Pb}(T,P_0) - H_{Pb}(T_m,P_0) = 36.5(T - T_m) - 0.51 \times 10^{-2}\left(T^2 - T_m^2\right) + 1.067 \times 10^{-6}\left(T^3 - T_m^3\right) - 3.158 \times 10^5 \frac{(T - T_m)}{T T_m} \tag{3.4}$$

$$H_{Bi}(T,P_0) - H_{Bi}(T_m,P_0) = 24.70(T - T_m) + 0.62 \times 10^{-3}\left(T^2 - T_m^2\right) + 1.501 \times 10^6 \frac{(T - T_m)}{T T_m} \tag{3.5}$$

$$H_{LBE}(T,P_0) - H_{LBE}(T_m,P_0) = 34.3(T - T_m) - 0.41\times10^{-2}(T^2 - T_m^2) + 8.667\times10^{-7}(T^3 - T_m^3) - 9.5\times10^4\frac{(T - T_m)}{TT_m} \quad (3.6)$$

The recommended curves based on Eqs. (3.4), (3.5) and (3.6) are presented in Figure 3.2.2.

Figure 3.2.2: Variations of the lead, the bismuth and the LBE enthalpy with temperature

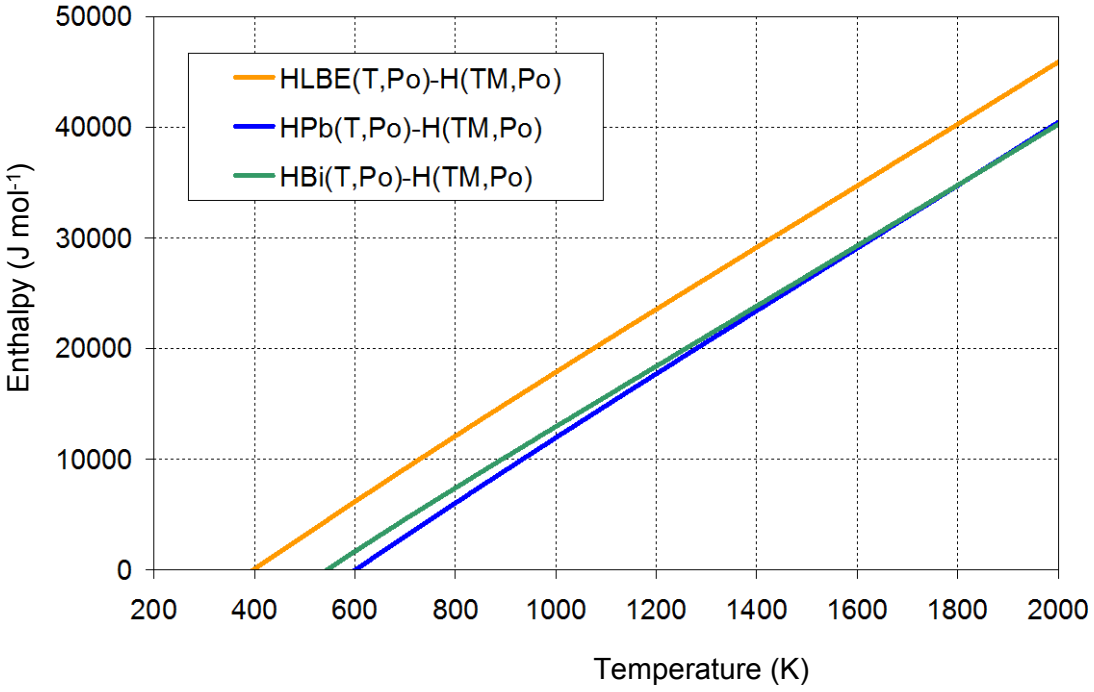

3.3 Chemical activities of Pb and Bi in Pb-Bi alloys

Activities of Pb and Bi in the Pb-Bi alloys can be given by the following relation:

$$a_M = \gamma_M x_M$$

with a_M the activity of M (Pb or Bi), γ_M the acitivity coefficient of the element M (Pb or Bi) and x_M the molar fraction of M (Pb or Bi) in the Pb-Bi alloy. According to Moser (1973) the activity coefficient for Pb and Bi can be written as:

$$\ln\gamma_M = \omega(T)(1 - x_M)^2$$

with M the element Pb or Bi, $\omega(T)$ a function depending on temperature and T the temperature in K. The same function $\omega(T)$ is given for Pb and Bi. Values of $\omega(T)$ are given in Table 3.3.1.

Table 3.3.1: ω(T) for Pb and Bi in Pb-Bi alloys

$$\omega(T) = -A - B/T$$

Reference	A	B	Temperature range (K)
Mose (1973)	0.2025	447	670-760
Prasa (1977)	0.2693	391.5	1 150-1 320
Orlov (1998)	0.2026	446.97	All range

Source: Zhang (2008).

In his paper, Gossé (2014) proposes a fit of the Bi and Pb activities at LBE composition as a function of temperature. These calculations were performed using the assessment of Yoon (1998); the activities referred to are the pure liquids. Bi and Pb activities show the non-ideal attractive interactions in the liquid responsible for the eutectic reaction (see Figure 3.3.2). From this study, the Bi and Pb activities at LBE composition can be written as:

$$a_{Bi} = 0.53381 - \frac{56.2}{T} \text{ from 399 to 1 173 K}$$

$$a_{Pb} = 0.42206 - \frac{63.2}{T} \text{ from 399 to 1 173 K}$$

Figure 3.3.1 and Figure 3.3.2 represent respectively activities data for Pb and Bi in LBE proportions from various authors, and activities of Pb and Bi calculated by Gossé (2014) as a function of Pb molar fraction in the Pb-Bi alloy for various temperatures.

Figure 3.3.1: Bi and Pb chemical activities at LBE composition as a function of temperature referred to pure Bi (black) and Pb (red) liquids

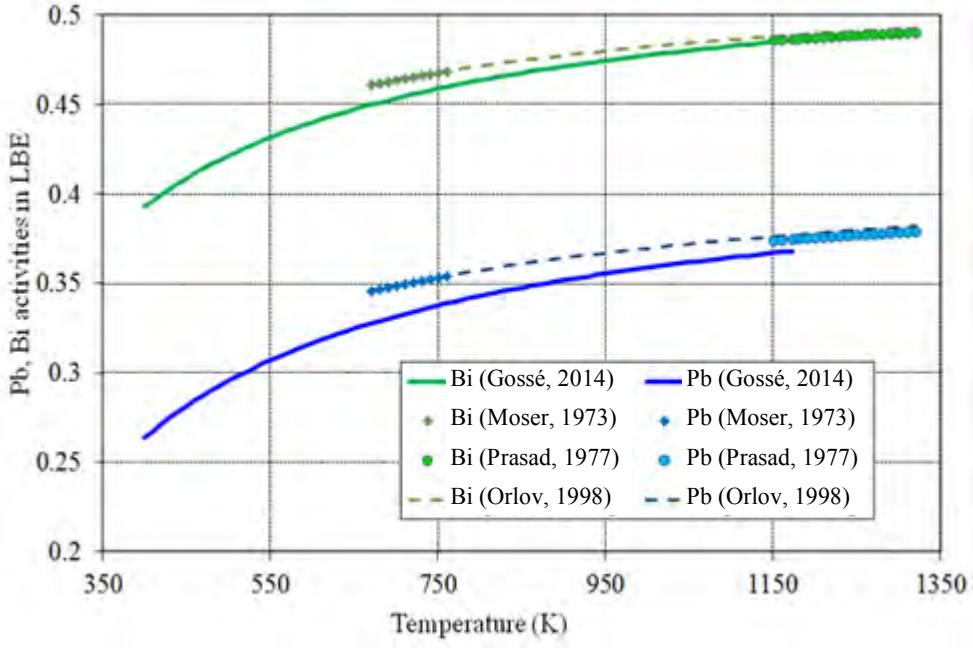

Figure 3.3.2: Bi and Pb chemical activities calculated at 473 K (solid lines), 573 K (dash-dot lines), 673 K (dot lines) and 773 K (dash lines) as a function of Pb molar fraction; reference state is pure liquids

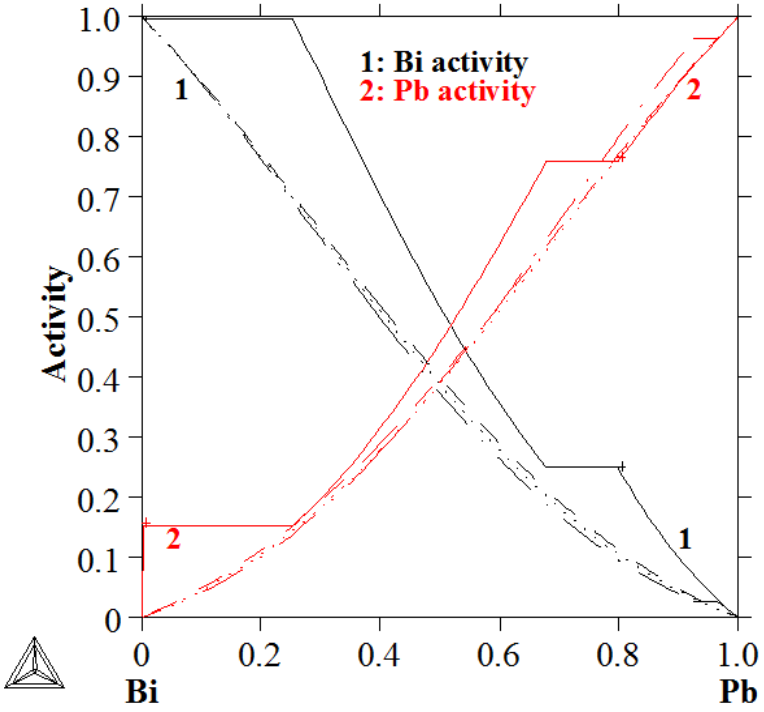

Source: Yoon (1998).

3.4 Purity requirements

The chemical composition of lead or LBE is of importance for the operating conditions of a nuclear system in the following ways:

- First, the formation of radioactive elements due to irradiation induces a contamination of the circuits and components. It may also have an influence on physical parameters of the reactor.
- Second, a high content of some impurity elements in the coolant partly drives the coolant chemistry control and affects the corrosion resistance of structural steels.
- Third, if some impurities react with other elements produced under irradiation. For instance, the surface enrichment of polonium in solidified LBE presents different behaviour due to the impurities in LBE. Moreover, impurities can induce solid precipitation at the surface of the primary circuit components and may strongly affect thermal and hydraulic characteristics of the reactor. Otherwise, mass transfer from a thermal gradient for example can induce precipitation of solids in the coldest parts of the circuit which may result in flow blockages or instabilities.

The main sources of impurities in the heavy metal coolant in nuclear systems are:

- metallic impurities due to the limits of the refining process and their ingress during casting;
- corrosion and erosion products resulting from the interaction of structural materials with the heavy liquid metal coolant;

- coolant interaction with gas in the circuit;
- spallation or fission products due to proton or neutron beam/material interactions;
- release of fission products to the coolant in case of clad rupture. Some important fission products are radioisotopes of iodine (^{131}I, ^{133}I, ^{135}I) and caesium (^{134}Cs, ^{136}Cs, ^{137}Cs);
- processes related to purposeful adding of impurities (oxygen for example) to the coolant.

In this chapter, we only look at the impurities in the lead or LBE before use. The impurities and fission products generated during operation are considered in Chapter 4 together with the methods for their control and removal.

At the moment, no nuclear specifications exist for lead or LBE. However, different commercial materials seem to have an appropriate purity for nuclear applications. Commercial grades of lead content up to 99.98 wt.% of the basic metal are available. Typical lead and LBE impurity contents are given as examples in Table 3.4.1. Ivanov (2003) recommends C00 or C0 purity for lead and the chemical composition of LBE used for MEGAPIE experiment is given in Table 3.4.2 (Safety, 2002).

Silver is the only noticeable impurity which may be relevant for activation. It is activated under the neutron flux through the following reaction: ^{109}Ag (n,γ) ^{110m}Ag, 250 d.

In addition to metallic impurities, there are some amounts of oxygen, nitrogen and hydrogen in the initial lead or LBE resulting from the conditions of cooling down of commercial material, overall dimensions of ingots and conditions of its further storage. Of concern is not only oxygen distributed in the volume of ingots but also oxygen in the near-surface layer of ingots as lead oxide (PbO). As a result of long storage of unprotected ingots in humid atmosphere, adsorbed moisture is transformed on their surface to the lead hydroxide according to the reaction:

$$PbO + H_2O = Pb(OH)_2$$

Table 3.4.1: Chemical composition of commercial lead, wt.%

Elements	Lead brand			Elements	Lead brand		
	C00	C0	C1		C00	C0	C1
Ag	0.00001	0.0004	0.001	Tl	0.0001	–	–
Cu	0.00001	0.0005	0.001	Ca	0.0001	–	–
Zn	0.0001	0.001	0.001	Na	0.0001	–	–
Bi	0.0005	0.004	0.006	Cd	0.00005	–	–
As	0.0001	0.0005	0.001	Al	0.00005	–	–
Sn	0.0001	0.0005	0.001	Hg	0.00005	–	–
Sb	0.0001	0.0005	0.001	In	0.00001	–	–
Mg	0.0001	–	–	Mg+Ca+Na		0.002	0.003
Fe	0.0001	0.001	0.001	Pb	99.99852	99.992	99.985

Table 3.4.2: Metallic impurities in the LBE for MEGAPIE experiment

Element	Content (μg/g)
Ag	25.6
Cd	2.2
Cr	0.19
Cu	26.5
Fe	1.4
In	14.4
Ni	2
Sn	5.9

Source: Safety (2002).

3.5 Solubility data of metallic and non-metallic impurities in Pb, Bi and LBE

3.5.1 *Solubility data of some metallic elements in pure Pb, pure Bi and liquid eutectic Pb-Bi*

The procedures used for the determination of the solubility in the liquid metals cause some problems because subsequent chemical reaction or exchange of impurities (oxygen, nitrogen, carbon…) between the liquid metal and the solid metal or compound may occur.

Generally, when the experimental technique is described, the solubility of a metallic element X in the considered liquid metals is obtained by putting the metal X (as a specimen or the crucible containing the melt) in contact with the liquid for several hours. Then a filtered few grams of this latter are sampled at the temperature of the test. The samples are then analysed by various techniques.

For a metallic element with a large solubility, a specimen is immersed in a liquid bath and the weight loss of the metallic specimen is regularly measured. When it is constant, then it is considered that the solubility limit of X element is reached. It is equal to the weight loss of the metallic specimen divided by the liquid bath volume.

A large amount of solubility data have been reported in IAEA (2002) (which is a compilation of data available in Kozlov [1983] and Arnoldov [1998]). In this review, the Fe solubility in liquid Pb comes from Weeks (1969), who determined two temperature laws from 673 to 873 K and from 873 to 1 023 K. Unfortunately, only the low temperature range was used in IAEA (2002). So, these extrapolated values must be discarded above 873 K. The values of metallic solubility in LBE mentioned by Li (2002) coming from Gromov (1997), Orlov (1997) and Adamov (1998) are in agreement with all those data.

Recently, Gossé (2014) developed a thermodynamic database using the Calphad method (Lukas, 2007), to evaluate the solubility limits and the chemical activities of Cr, Ni and Fe in Bi, Pb and LBE. In this work, the thermodynamic data on the Cr-Fe-Ni + Bi-Pb quinary system was reviewed and the Bi-Cr and Cr-Pb binary phase diagrams were assessed. Fe, Cr and Ni solubilities (in at. fraction, T in K) at LBE composition were calculated as a function of temperature. Table 3.5.1 gives the values of A, B of the following equation used to characterise the solubility values as a function of temperature and the temperature range when it is specified:

$$\log S\ (\text{wt.\%}) = A - B/T \tag{3.7}$$

with T, the temperature in (K) and S the solubility limit in wt.%.

The elements for which the solubility limit is presented in Table 3.5.1 are mainly metallic elements but some non-metallic elements are also concerned, as carbon. N_2 is not soluble in lead or LBE.

Weeks (1969) measured iron solubility limits in Pb-Bi alloys as a function of composition and temperature. Weeks proposed solubility laws from his experimental work, under the form $\log_{10}$ S (wt ppm) = A – B/*T*. Linear regression on experimental data given by Weeks (1969) were done; the values of A and B calculated in Weeks' laws are presented in Figure 3.5.1.

Among this series of fit, Weeks' law for Bi concentration equal to 52.6 wt.% is not in agreement with its own experimental data as shown in Figure 3.5.1. Then the values of A and B in $\log_{10}$ S (wt ppm) relation are directly assessed from his experimental data for this composition; all the results from Weeks are gathered together with the erroneous law given in Weeks (1969) (see Table 3.5.1).

However, the iron solubility limit at the exact LBE proportion (Bi concentration equal to 55 wt.%) is not given by Weeks (1969). Consequently, and as shown in Figure 3.5.1, the values of A and B were extrapolated from his experimental data for the general solubility law ($\log_{10}$ S (wt ppm) = A – B/*T*). As it can be seen in Figure 3.5.1(a) that the value of A ($\log_{10}$ S (wt ppm) = A – B/*T*) seems constant for Bi concentration ranging from 0 to 83.8 wt.%, then a mean of these values is taken equal to 5.85 for iron solubility in wt. ppm, leading to an iron solubility equal to 1.85 in wt.%. Figure 3.5.1(b) shows that the value of B is a linear function of the Bi concentration. Then, the extrapolation at LBE proportions is easily done leading to B equal to -4 164.

To conclude, for iron solubility limit in wt.%, the A and B values for LBE proportions extrapolated from Weeks' experimental data (1969) are slightly corrected. The retained A and B coefficients are considered to be 1.85 and -4 164, respectively. This new law coming from Weeks' experimental data (1969) is included in Table 3.5.1.

Figure 3.5.1: Solubility data of iron in liquid Pb-Bi alloys; $\log_{10}$ S (wt ppm) = A – B/T

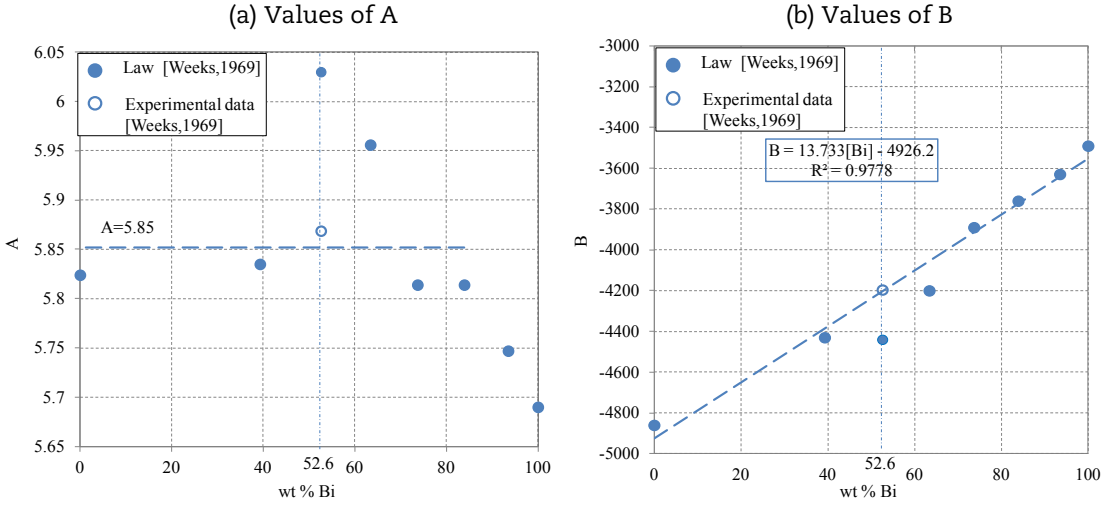

In Figures 3.5.2, 3.5.3 and 3.5.4, the different solubility data for iron, chromium and nickel in Pb, Bi and LBE are presented. The two iron solubility laws given in Bi and in LBE are so close that they can be considered as equal and moreover they are validated one by one. However the iron solubility in pure Pb is given by three different laws. Considering the limited available information about the experimental method of determining these three laws, no recommended law is given.

Table 3.5.1: Solubility of some elements in liquid Pb, Bi and Pb-Bi. $\log_{10}$ S (wt%) = A - B/T

The recommended laws are written in bold type

Pb					*LBE*				*Bi*			
Element	Ref.	T (K)	A	B	Ref.	T (K)	A	B	Ref.	T (K)	A	B
Ni	(Tecdoc, 2002)	603-1 573	2.78	1 000	(Tecdoc, 2002) (Rosenblatt, 1969)	723-823	1.7	1 000	(Weeks, 1998)	723-903	2.61	1 538
Ni	(Alden 1958)	645-1 350 1 351-1 517	1.7 3.7	1 670 4 257	(Martynov, 1998)	673-1 173	1.53	843				
Ni					(Martinelli, 2010)	603-712 712-1 173	5.2 1.7	3 500 1 009				
Ni	(Gossé, 2014)	598-917	1.36	1 395	(Gossé, 2014)	528-742	4.32	2 933	(Gossé, 2014)	543-738	3.81	2 429
						742-1 173	1.74	1 006		738-918	2.05	1 131
										918-1 173	1.35	484
Mn	(Tecdoc, 2002)	600-1 473	2.02	1 825								
Mn	(Pelzel, 1956)	747-1 273	3.0445	3 272								
Mn	(Elliot, 1965)	623-1 073	6.32	2 690								
Co	(Tecdoc, 2002)	623-1 923	2.60	4 400	(Rosenblatt, 1969)	673-823	1.3	2 834				
Cu	(Tecdoc, 2002)	600-1 273	2.72	2 360	(Rosenblatt, 1969)	673-823	2.41	1 920				
Fe	(Tecdoc, 2002)	330-910	0.34	3 450	(Martynov, 1998)	823-1 053	2.01	4 380	(Massalski, 1990)	973-1 173	2.18	3 980
Fe	(Weeks, 1969) (Amoldov, 1999)	673-873 873-1 023	0.34 1.824	3 450 4 860	(Weeks, 1998) [Bi]=52.6wt%	773	Log (S) = -3.55		(Weeks, 1998)	713-998	1.832	3 589
Fe	(Stevenson, 1961)	1 023-1 573	2.53	5 314	(Weeks, 1969) [Bi]=52.6wt%*	823-1 053	2.03	4 440				
α Fe	(Ali-Khan, 1982)	1 273-1 923	3.67	2 450	(Weeks, 1969) [Bi]=52.6wt%**	823-1 053	1.87	4 196				
α Fe	(Stevenson, 1961)		2.96	6 100	(Weeks, 1969) ***	823-1 053	1.85	4 164				

* Law given by Weeks (Weeks, 1969) for 52.6 wt% Bi, but this law is not reliable as it is not in agreement with his own experimental data.

** Recommended law for the 52.6 wt% composition obtained by linear regression on Weeks' experimental values (Weeks, 1969).

*** Recommended law extrapolated from Weeks' experimental work (Weeks, 1969) for Bi concentration equal to 55 wt% (LBE proportions).

Table 3.5.1: Solubility of some elements in liquid Pb, Bi and Pb-Bi. log10 S (wt%) = A - B/T *(cont.)*

The recommended laws are written in bold type

Pb					*LBE*				*Bi*			
Element	Ref.	T (K)	A	B	Ref.	T (K)	A	B	Ref.	T (K)	A	B
γ Fe	(Ali-Khan, 1982)	1 273-1 923	7.66	7 100								
γ Fe	(Stevenson, 1961)		1.83	4 800								
Fe	(Gossé, 2014)	600-1 173	2.11	5 225	(Gossé, 2014)	399-1 173	2.00	4 399	(Gossé, 2014)	545-1 173	2.20	3 930
Cr	(Tecdoc, 2002) (Alden, 1958)	1 181-1 483	3.74	6 750	(Courouau, 2004)	643-813	1.07	3 022	(Venkatraman, 1988)	658-901	2.34	3 610
Cr	(Venkatraman, 1988)	1 173-1 473	3.7	6 720	(Tecdoc, 2002) (Martynov, 1998)	673-773	-0.02	2 280	(Weeks, 1998)	663-998	2.5	3 717
Cr	(Gossé, 2014)	601-1 773	*3.62*	6 648	(Gossé, 2014)	399-1 173	1.12	3 056	(Gossé, 2014)	545-1 773	2.34	3 610
Mo	(Tecdoc, 2002)	1 273	$<10^{-3}$ wt%									
Mo	(May, 1982)	873-973	$<10^{-6}$ wt%									
Mo	(Shunk, 1969)	1 073-1 473	1.6	6 000								
Mo	(Brewer, 1980)		2.92	10 553.5								
W	(Shunk, 1969)	1 473-2 013	6.55	7 150								
Si	(Tecdoc, 2002)	1 323-1 523	3.886	7 180								
Zr	(Tecdoc, 2002)	773	~1.2 10^{-9} wt%		(Tecdoc, 2002) (Weeks, 1969)	500-998	0.15	3 172				
Nb	(Tecdoc, 2002)	1 273	$< 10^{-5}$ wt%									
Ti	(Tecdoc, 2002)	773	~5.6 10^{-4} wt%									
U	(Tecdoc, 2002)	673-1 073	3.921	5121								
C	(Tecdoc, 2002)	1 443-1 828	1.026	3 850	(Tecdoc, 2002)		-1.36	1 870				

* Law given by Weeks (Weeks, 1969) for 52.6 wt% Bi, but this law is not reliable as it is not in agreement with his own experimental data.

** Recommended law for the 52.6 wt% composition obtained by linear regression on Weeks' experimental values (Weeks, 1969).

*** Recommended law extrapolated from Weeks' experimental work (Weeks, 1969) for Bi concentration equal to 55 wt% (LBE proportions).

Figure 3.5.2: Solubility data of iron in liquid Pb, Bi and LBE

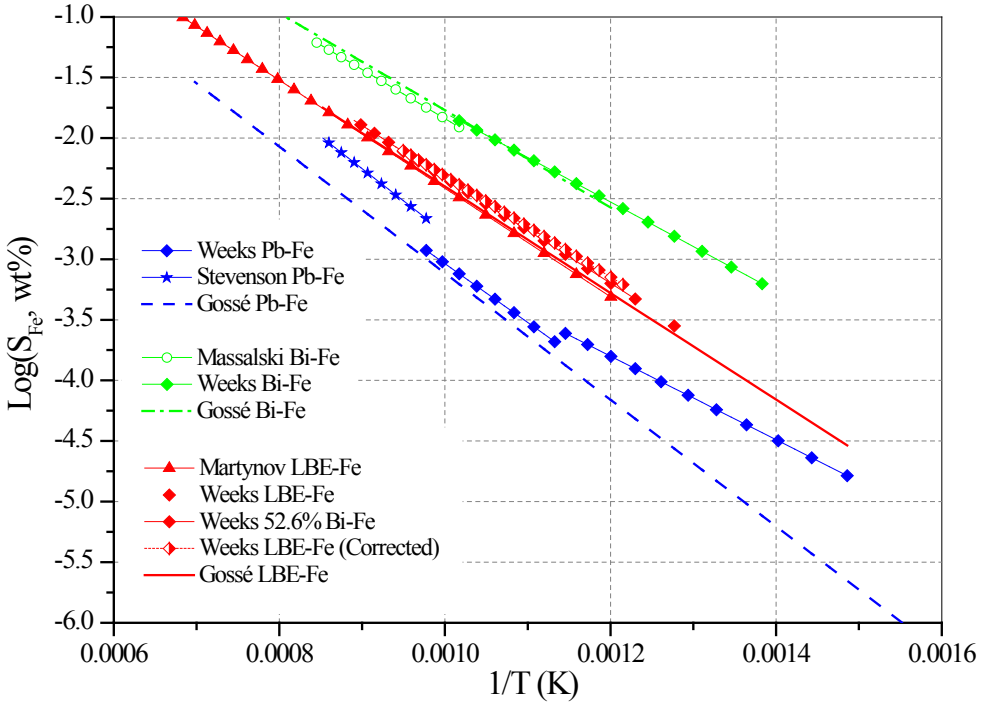

Figure 3.5.3: Solubility data of chromium in liquid Pb, Bi and LBE

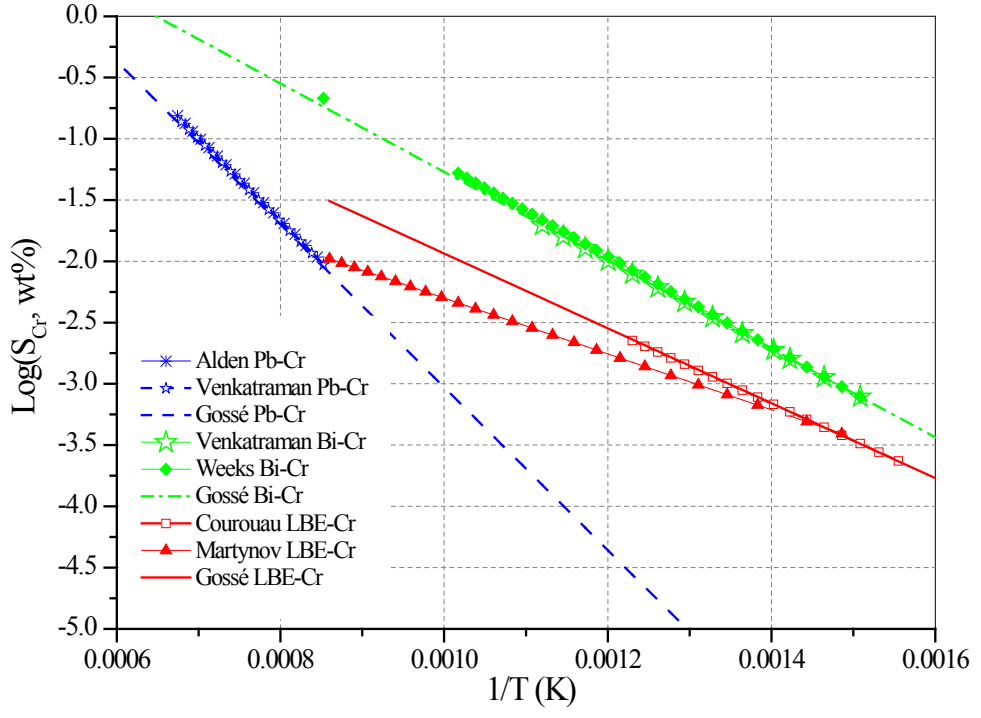

Figure 3.5.4: Solubility data of nickel in liquid Pb, Bi and LBE

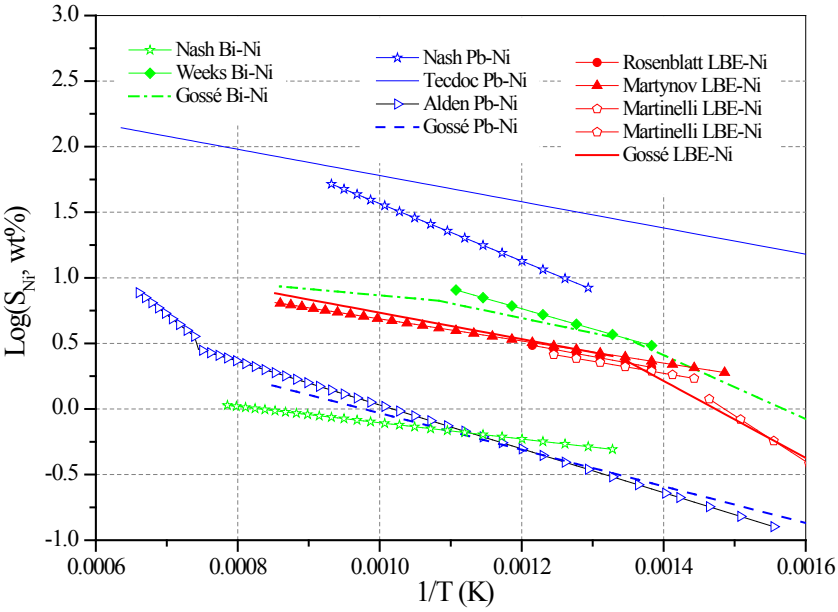

For chromium, the two solubility laws given in Pb and Bi are so close that they can be considered as equal; moreover they have been validated independently. Concerning Cr solubility in LBE, three sets of data (Martynov, 1998a; Courouau, 2004; Gossé, 2014) are consistent up to approximately 723 K. Above this temperature Martynov (1998a) exhibits a light drift towards lower values.

The solubility of metallic species is often higher in liquid Bi than in LBE and higher in LBE than in liquid Pb. However in case of nickel, the solubility limit in Pb, given in the IAEA (2002) reference, is higher than that in Bi. This fit, which exhibits high Ni solubility, is shown in the review by Arnoldov (1998).

On the contrary, Ni solubility by Alden (1958) is very low and shows a change of slope above 1 350 K towards the miscibility gap in the liquid phase. According to the recent thermodynamic assessment of the Ni-Pb system by Vaajamo (2013), it can be shown that the data of Alden (1958) are fully consistent with numerous sets of data. Therefore, the Ni solubility law in liquid Pb calculated by Gossé (2014) using the Calphad modelling of Vaajamo (2013) should be recommended.

In addition, these solubility limits are not consistent with the phase diagrams of Pb-Ni and Bi-Ni (Hansen, 1958). These data should thus be validated. Consequently, a recommended law is only given for Ni solubility limit in LBE. Otherwise, experimental solubility limits are not always in good agreement with theoretical predictions (see Chapter 5). Many explanations can be proposed (see discussion in Chapter 5): thermodynamic model are too simplified, enthalpies used in predictions are not sufficiently accurate and experimental data are overestimated due to analysis of precipitate and dissolved particles in LBE. Accurate solubility measurements should be made for the irrelevant data.

A comparison of the solubility of some metallic elements of interest from a corrosion point of view shows that, as reported by Borgstedt (1992), these data follow the general trends in the solubility of transition metals reported by Guminski (1990): Ni and Mn dissolve to a large extent in low melting point metals while molybdenum has a very low solubility. Moreover, in order to model the corrosion phenomena, the solubility limit of Fe in pure Pb and Ni in pure Bi and pure Pb should be determined and the Fe and Cr solubility limits should be validated in LBE.

3.5.2 *Solubility data of oxygen in pure Pb, pure Bi and LBE*

Different determinations of the oxygen solubility limit in Pb and Pb-Bi have been performed. At the lowest temperatures (~773 K), sampling methods are generally used. At higher temperature, experimental techniques rest on rare earth stabilised zirconia probes (see Chapter 4). These probes allow not only the measurement but also the control (for small quantities of Pb-Bi) of dissolved oxygen in Pb-Bi.

Different techniques have been used to determine the solubility limit of oxygen in Pb-Bi such as:

- After oxygen has been inserted in the liquid Pb bath, the bath is sampled. The Pb sample is melted again in a graphite crucible. The CO_2 production is then measured and converted to an oxygen concentration in the bath (Steen, 1982).
- The oxygen content is obtained from calorimetric measurements (Rodigina, 1961).
- Solid PbO is dissolved in the liquid and the oxygen content dissolved in the liquid is continuously measured by means of a rare earth stabilised zirconia probe (Taskinen, 1979).
- Oxygen is introduced into the liquid by electrochemical techniques using a rare earth stabilised zirconia probe. The dissolved oxygen content is followed in parallel with a rare earth stabilised zirconia probe (Ghetta, 2002).
- The oxygen solubility limit in LBE is deduced from the oxygen solubility limits in pure liquids Pb and Bi by thermodynamical calculations using Gibbs energy of PbO and Bi_2O_3 oxides (Müller, 2003).

In a bibliographic review on the compatibility of structural steels with liquid lead, Flament (1988) reported on a study from Steen (1982) which compared the data obtained at temperatures lower than 823 K from various authors. These data are shown in Figure 3.5.5. Steen (1982) observed large discrepancies between them and concluded that the discrepancies are probably due to the presence of stray oxide particles in the liquid lead and that in the 673- 773 K temperature range, the oxygen solubility is low. From his work, he suggested a value of about 1 ppm.

Figure 3.5.5: Data of oxygen solubility in lead reported in Steen (1982)

1 – Reinert, 2 – Worner, 3 – Baker, 4 – Hansen, 5 – Bartfeld, 6 – Zausznica, 7 – Carlsson

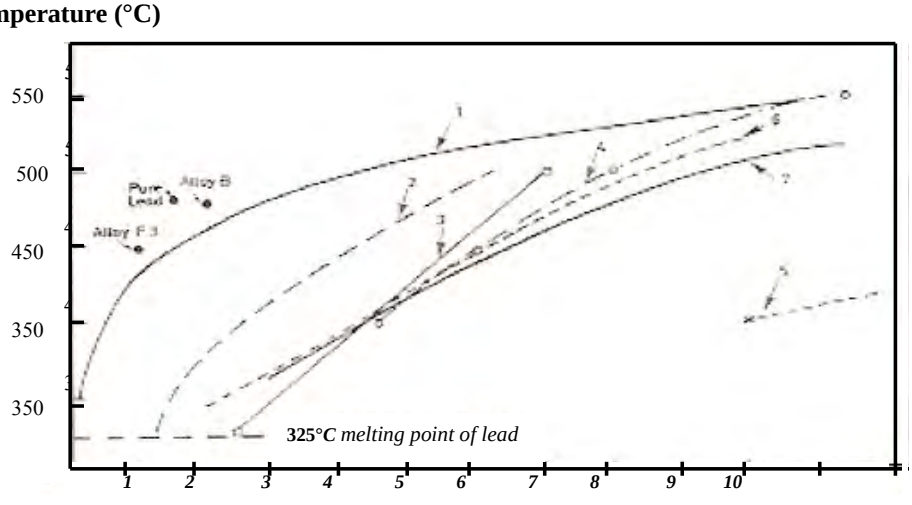

Recently, Ganesan (2006b) reviewed some literature data on oxygen solubility in liquid Pb and LBE and reported the new results. Based on the uncertainties on the data obtained from sampling methods (Risold, 1998), Ganesan (2006b) considers only the data obtained mostly at high temperature by electrochemical methods. Moreover, Ganesan gathers together several literature data on oxygen solubility limits in pure bismuth in his PhD thesis (2006a). These data are presented along with other literature data in Table 3.5.2.

Selected oxygen solubility data in lead, LBE and bismuth are reported in Table 3.5.2. The A and B parameters refer to Eq. (3.7), log (S, wt.%) = A – B/*T*, with S, the oxygen solubility limit, expressed in wt.%, in lead alloys and *T* the temperature in K.

The oxygen measurement performed in liquid metal using a stabilised zirconia probe is very accurate. Consequently, the solubility values obtained by this method are considered more reliable than the measurements obtained by the other methods.

Figure 3.5.6 represents the high temperature experimental data on oxygen solubility in liquid lead obtained by electrochemical techniques. From this figure, it appears that the data of Szwarc (1972) and Charlé (1976) deviate from the others. Ganesan (2006b) explains that the use of chromel wire as electrical lead would have contributed to this deviation due to the interaction of dissolved Cr and Ni with oxygen in molten Pb. The other data are in good agreement, except those of Conochie (1981) at low temperatures. Consequently, a linear regression of the values given by Alcock (1964), Rodigina (1961), Taskinen (1979), Isecke (1977), Gromov (1999) and Ganesan (2006b), is taken as recommended law for oxygen solubility limit in pure lead. This value is then:

$$\log (S, \text{wt.\%}) = 3.23 - 5043/T \text{ in pure lead with } T \text{ in (K)} \quad \text{and } 573\ \text{K} < T < 1\,373\ \text{K} \tag{3.8}$$

Figure 3.5.6: Data of oxygen solubility in molten lead from Table 3.5.2

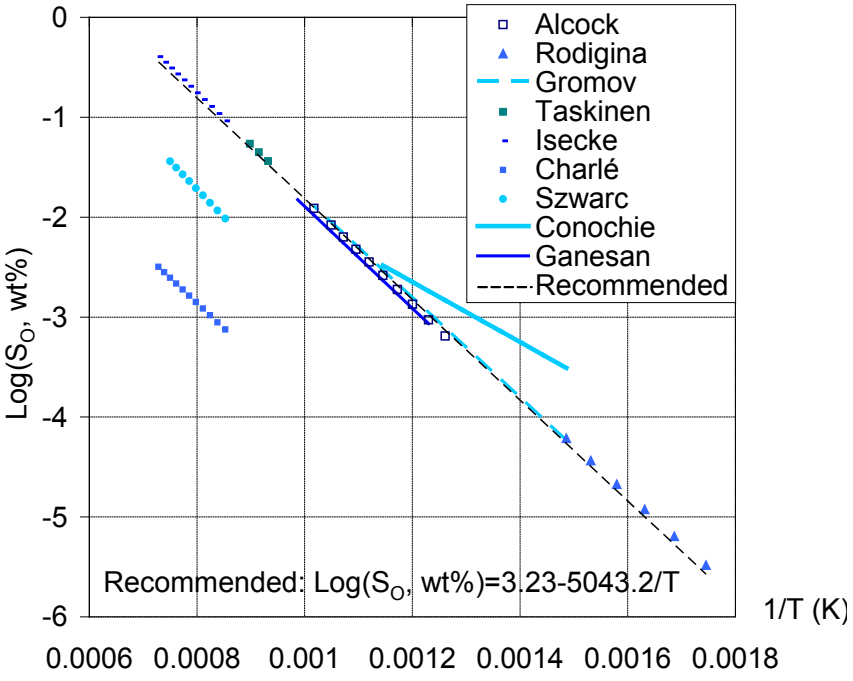

Figures 3.5.7 and 3.5.8 compare the values of oxygen solubility in molten LBE and in pure bismuth reported in Table 3.5.2.

Table 3.5.2: Oxygen solubility data in liquids Pb, Bi and LBE

Recommended laws are written in bold

Pb				LBE				Bi			
Ref.	T (K)	A	B	Ref.	T (K)	A	B	Ref.	T (K)	A	B
Richardson (1954)	1 213-1 513 573-673	1.9 3.2	3 521 5 050	Gromov (1998) Martynov (1998)	673-973	1.2	3 400	Martynov (1998)	673-1 033	1.48	3 400
Rodigina (1961)	573-673	3.07	4 900	Ghetta (2004)	673-773	3.27	4 852	Heinzel (2003)	562-1 000	2.76	4 451
Heinzel (2003)	573-1 053	1.64	3 503	Müller (2003)	473-923	2.52	4 803	Griffith (1953)	673-1 023	1.40	3 317
Alcock (1964)	783-973	3.42±0.14	5 240±120	Courouau (2004)	623-773	3.34	4 962	Isecke (1979)	1 002-1 623	3.27	5 138
Szwarc (1972)	1 170-1 353	2.76	5 600	Ganesan (2006)	813-1 013	2.42	4 287	Hahn (1979)	1 073-1 223	-0.086	3 064
Charlé (1976)	1 173-1 373	1.19	5 061	Anik (1987)	1 173	0.23 wt.%		Fitzner (1980)	988-997 997-1 181	3.84 3.07	5 543 4 778
Isecke (1977)	1 173-1 373	3.38	5 182	Abella (2011)	733	9.2×10^{-6}					
Taskinen (1979)	1 073-1 118	3.38	5 170		773	1.2×10^{-6}		Heshmatpour (1981)	1 023-1 273	0.41	2 780
Conochie (1981)	728-879	0.96	3 007		813	1.6×10^{-5}		Recommended	673-1 003 1 003-1 573	2.29 3.04	4 066.5 4 810
Gromov (1999)	673-873	3.2	5 000	Recommended	673-1 013	2.25	4 125				
Ganesan (2006)	813-1 013	3.21	5 100								
Recommended	673-1 373	3.23	5 043								

In LBE, Figure 3.5.7 shows that there is a higher discrepancy in the experimental results than in pure lead. Indeed, different techniques are used to obtain the oxygen solubility limit: Martynov (1998a) dissolved PbO pellets, Müller (2003) performed thermodynamic calculations, Courouau (2004) used calibration line of the zirconia oxygen probe while Abella (2011), Ghetta (2004) and Ganesan (2006b) used the most reliable electrochemical technique with the zirconia oxygen probe. However, the results given by Abella (2011) are two orders of magnitude lower than that of Ghetta and Ganesan which are both consistent. This difference could be explained by the use of only one zirconia probe for oxygen measurement and oxygen control by Abella while Ghetta used one probe for oxygen measurements and another one for oxygen control. Indeed, the oxygen control step involves application of a current across the zirconia which could disturb the measurement made without current. Consequently, a linear regression of the solubility limits given by Ganesan (2006b) at high temperatures and Ghetta (2004) at low temperatures should be a reliable alternative for the oxygen solubility limit in LBE. This recommended value is thus:

$$\log (S, \text{wt.\%}) = 2.25 - 4125/T \text{ in LBE with } T \text{ in (K)} \quad \text{and } 673\ \text{K} < T < 1\,013\ \text{K} \tag{3.9}$$

Figure 3.5.7: Data of oxygen solubility in molten LBE from Table 3.5.2

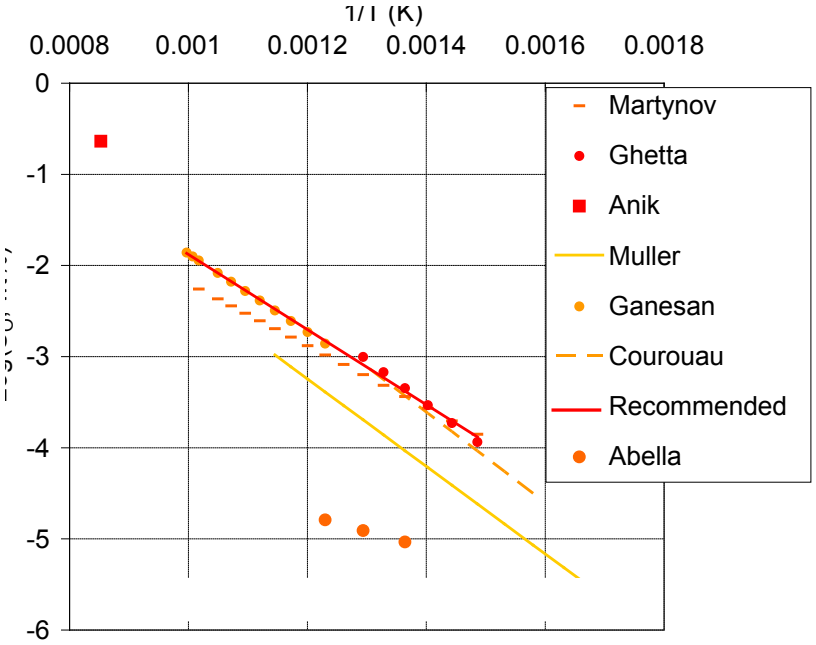

In pure bismuth, there are good agreement between the different data, except those of Heshmatpour (1981) and Hahn (1979). However, a change of slope, corresponding to the straight line of oxygen solubility limit, is observed in Figure 3.5.8 for temperatures close to 983-1 003 K (710-730°C). This must be due to a change of the oxide structure in equilibrium with liquid bismuth at saturation level. Indeed, Figure 3.5.10 shows that, from 573 to 1 002 K (300°C to 729°C), the oxide in equilibrium with liquid bismuth at saturation level is α-Bi_2O_3 or bismite which has monoclinic crystal structure while from 1 002 K to 1 573 K (729 to 1 300°C) the oxide in equilibrium with oxygen saturated Bi is δ-Bi_2O_3 or sphaerobismoite which has tetragonal structure. Consequently, the recommended solubility value is represented by two laws, corresponding to the linear regression of the data given by Martynov (1998b), Griffith (1953), Isecke (1979) and Fitzner (1980):

$$\log (S, \text{wt.\%}) = 2.30 - 4066/T \text{ in pure bismuth with } T \text{ in (K)} \quad \text{and } 573\ \text{K} < T < 1\,002\ \text{K} \tag{3.10}$$

$$\log (S, \text{wt.\%}) = 3.04 - 4810/T \text{ in pure bismuth with } T \text{ in (K)} \quad \text{and } 1\,002\ \text{K} < T < 1\,573\ \text{K} \tag{3.11}$$

Figure 3.5.8: Data of oxygen solubility in molten bismuth from Table 3.5.2

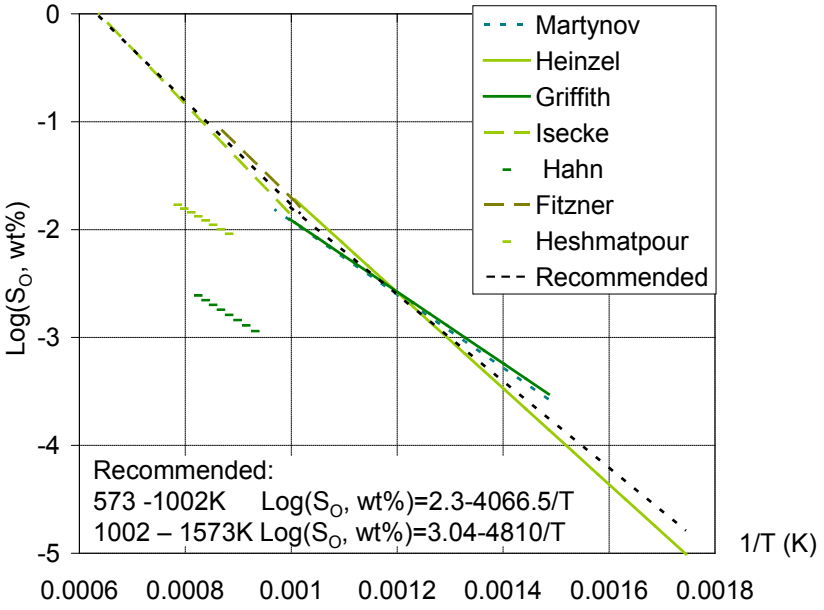

3.5.3 *Oxygen/lead, bismuth, LBE interaction*

In the framework of corrosion studies, it is often necessary to determine the oxygen partial pressure in equilibrium with the oxygen concentration dissolved in the liquid metal. The free energy of the following reaction must then be evaluated:

$$\frac{1}{2}O_2(g) = O^{LM}$$

In order to determine this free energy, literature proposed different reference states (in relation to the standard state for gaseous species: $P^0_{O_2} = 1$ atm) for oxygen activity in the liquid metal. These reference states are detailed in the following paragraph. Then the relations between the oxygen partial pressure in the above gaseous atmosphere and the oxygen concentration in equilibrium in the liquid metal are given. Finally, phase diagrams involving lead, bismuth and oxygen are presented.

3.5.3.1 *Reference states for oxygen activity in liquid metal*

Oxygen activity is characterised by the following relations:

- $a_O = \gamma x_O$ with γ the oxygen activity coefficient and x_O the oxygen molar fraction dissolved in the liquid metal;
- or $a_O = \gamma(C_O/C_{ref})$ with γ the oxygen activity coefficient, C_O the oxygen concentration dissolved in the liquid metal and C_{ref} the reference concentration for oxygen in liquid metal.

The different reference states for oxygen in liquid metal are the following:

- The first reference state, called in this chapter Reference 1, has often been chosen to characterise the reaction $\frac{1}{2}O_2(g) = O^{LM}$. The oxygen activity in the liquid metal

is considered equal to 1 ($a_O^0 = 1$) for the extrapolated and fictive state of an equilibrium between the dissolved oxygen concentration and the gaseous oxygen of which partial pressure is equal to 1 atm ($P_{O_2} = 1\,\text{atm}$). This reference state is fictive as the liquid metal cannot be at equilibrium with an oxygen partial pressure equal to 1 atm. Indeed, the oxygen solubility limit is reached for oxygen partial pressure much lower.

However the interest of this reference state does not consist of its chemical meaningful aspect but of its simplicity: it implies that the reaction equilibrium constant $Kd^{(1)}$ is equal to 1. The oxygen activity is written $a_O^{(1)} = \gamma^{(1)} x_O$ and the oxygen molar fraction and the oxygen activity coefficient are linked to the oxygen partial pressure in equilibrium with the oxygen concentration in the liquid metal by: $\gamma^{(1)} x_O = Kd^{(1)} P_{O_2}^{1/2}$ with $Kd^{(1)} = 1$.

- The second reference state, called Reference 2, is the one chosen by Chang (1989) to compare the free energy of the reaction $\frac{1}{2}O_2(g) = O^{LM}$ for different liquid metals. Consequently he needed a reference state in which the oxygen molar fraction is identical whatever the considered liquid metal.

  In this reference state, oxygen activity is equal to 1 ($a_O^0 = 1$) for an oxygen concentration equal to 1 at.%, leading to an oxygen molar fraction equal to 0.01 ($x_O = 0.01$). The oxygen activity is either written $a_O^{(2)} = \gamma^{(2)} x_O$, implying an activity coefficient $\gamma^{(2)}$ equal to 100, or $a_O = \gamma^{(2')}\left(C_O / C_{ref}^{(2')}\right)$ implying an activity coefficient $\gamma^{(2)}$ equal to 1 (Henry's law) and a reference concentration equal to 1 at.% with C_O expressed in at.%.

  The equilibrium constant of the reaction $\frac{1}{2}O_2(g) = O^{LM}$ is written: $\gamma^{(2)} x_O = Kd^{(2)} P_{O_2}^{1/2}$ with a standard free energy ($\Delta G^{0(2)} = -RT \ln Kd^{(2)}$) which has been determined in literature for pure Pb and Bi and for LBE.

- The third reference state for reaction $\frac{1}{2}O_2(g) = O^{LM}$, called Reference 3, has been chosen by Russian researchers and then by the researchers involved in European programmes such as TECLA, MEGAPIE and then DEMETRA. The main interest of this reference state is its chemically meaningful aspect.

  Indeed, the oxygen activity a_O^0 is equal to 1 for an oxygen concentration equal to its solubility limit C_O^{sat} at the considered temperature ($a_O^0 = 1$ for $C_O = C_O^{sat}$).

  When the oxygen concentration in the liquid metal reaches its solubility limit, the most stable oxide precipitates and then the dissolved oxygen activity and the oxide activity are both equal to 1. The oxygen activity is either written $a_O^{(3)} = \gamma^{(3)} x_O$, implying $\gamma^{(3)} = 1/x_O^{sat}$ (with x_O^{sat} the oxygen molar fraction when oxygen solubility limit is reached), or $a_O = \gamma^{(3')}\left(C_O / C_{sat}^{(3')}\right)$ implying an activity coefficient $\gamma^{(3')}$ equal to 1 (Henry's law) and a reference concentration equal to the oxygen solubility limit C_{sat}. C_{sat} and C_O must be expressed in the same units.

  This reference state necessitates to determine the oxygen solubility limit in the liquid metal in order to determine the reaction constant $Kd^{(3)}$.

For a given oxygen partial pressure P_{O_2}, in equilibrium with the liquid metal, the molar fraction of the dissolved oxygen does not depend on the reference state.

Consequently, $\frac{\gamma^{(i)}}{\gamma^{(j)}} = \frac{Kd^{(i)}}{Kd^{(j)}}$ with $\gamma^{(i)} x_O = Kd^{(i)} P_{O_2}^{1/2}$.

Reference state 1 is thus linked to reference state 2 according to:

$$\ln \gamma^{(1)} = -\ln Kd^{(2)} + \ln \gamma^{(2)} = \frac{\Delta G^{0(2)}}{RT} + \ln 100$$

As the free energies $\Delta G^{0(2)}$ are given for pure Pb and pure Bi (Chang, 1989) (with activity coefficients $\gamma^{(2)}$ equal to 100), the link between the two systems is immediate.

Furthermore, reference states 3 and 2 are linked by the following relation:

$$\ln Kd^{(3)} = \ln Kd^{(2)} + \ln \frac{\gamma^{(3)}}{\gamma^{(2)}} = -\frac{\Delta G^{0(2)}}{RT} - \ln 100 x_O^{sat}$$

3.5.3.2 *Relation between oxygen partial pressure and oxygen concentration*

The free energies ΔG^0 values for the reaction $\frac{1}{2} O_2(g) = O^{LM}$ permit to calculate the oxygen partial pressure in equilibrium with the liquid metal as a function of the oxygen concentration in the liquid metal and the temperature according to:

$$\log P_{O_2} = 2 \log x_O + 2 \log \gamma + 2 \frac{\Delta G^0}{RT \ln 10}$$

Different free energies ($\Delta G^0 = H^0 - TS$), expressed in Reference 2 ($\gamma = 100$ for oxygen concentration expressed in molar fraction), are given in Table 3.5.3. Considering the free energies of Table 3.5.3, the oxygen partial pressure can be expressed as a function of the oxygen concentration in wt.% according to:

$$\log P_{O_2} = 2 \log(C_O, \text{wt.\%}) + 2 \log\left(\frac{M_{LM}}{M_O}\right) + \frac{2}{2.3R}\left(\frac{H^0}{T} - S\right) \tag{3.12}$$

with M_{LM} and M_O the molecular mass of the liquid metal and of the oxygen (equal to 16 g.mol^{-1}) respectively.

Using this relation the oxygen partial pressure is presented versus oxygen concentration in Pb, Bi and LBE at 823 K (550°C) in Figure 3.5.9.

The oxygen partial pressure in equilibrium with the dissolved oxygen in liquid LBE can thus be written as a function of oxygen concentration and temperature according to:

$$\log P_{O_2} = 2 \log(C_O, \text{at.\%}) + \frac{2}{2.3R}\left(\frac{-127398}{T} + 27.938\right) \tag{3.13}$$

with T in (K), C_O in at.% and 812 K < T < 1 012 K.

$$\log P_{O_2} = 2 \log(C_O, \text{wt.\%}) + 2 \log\left(\frac{208}{16}\right) + \frac{2}{2.3R}\left(\frac{-127398}{T} + 27.938\right) \tag{3.14}$$

with T in (K), C_O in wt.% and 812 K < T < 1 012 K.

$$\log P_{O_2} = 2 \log(x_O) + 4 + \frac{2}{2.3R}\left(\frac{-127398}{T} + 27.938\right) \tag{3.15}$$

with T in (K), x_O in molar fraction and 812 K < T < 1 012 K.

Table 3.5.3: Data for free energy of equilibrium ($\Delta G° = H° - TS$ in J.mol^{-1}) $\frac{1}{2}O_2(g) = O^{LM}$ in Pb, Bi and LBE according to reference 2

Standard state for O_2 is: $P^0_{O_2} = 1$ atm and oxygen activity equal to 1 for an oxygen concentration equal to 1 at.%

Pb				LBE				Bi			
Ref.	T (K)	H (J.mol^{-1})	-S (J.mol^{-1})	Ref.	T (K)	H (J.mol^{-1})	-S (J.mol^{-1})	Ref.	T (K)	H (J.mol^{-1})	-S (J.mol^{-1})
Otsuka (1979) Otsuka (1981)	1 073-1 673 1 023-1 273	-118 600 -117 170	14.1 12.9	Ganesan (2006)	812-1 008	-127 398	27.938	Chang (1989)		-99 730	13.2
Ganesan (2006)	815-1 090	-121 349	16.906	Ghetta (2005)		-127 140	27.2	Fitzner (1980)	988-1 181	-95 502	9.69
Chang (1989)		-119 100	14.6	Recommended	812-1 008	-127 398	27.938	Isecke (1979)	973-1 473	-101 098	15.66
Alcock (1964)	783-973	-119 411	12.222					Hahn (1979)	1 073-1 223	-68 156	14.14
Szwarc (1972)	1 012-1 353	-105 855	18.661					Heshmatpour (1981)	1 023-1 273	-95 437	3.78
Charlé (1976)	1 173-1 373	-119 840	15.794								
Isecke (1977)	1 173-1 373	-120 376	16.255								
Taskinen (1979)	1 073-1 203	-116 717	12.699								
Fischer (1966)	903-1 253	-106 395	10.254								

Figure 3.5.9: Oxygen partial pressure (atm) towards oxygen concentration (wt.%) at 823 K (550°C)

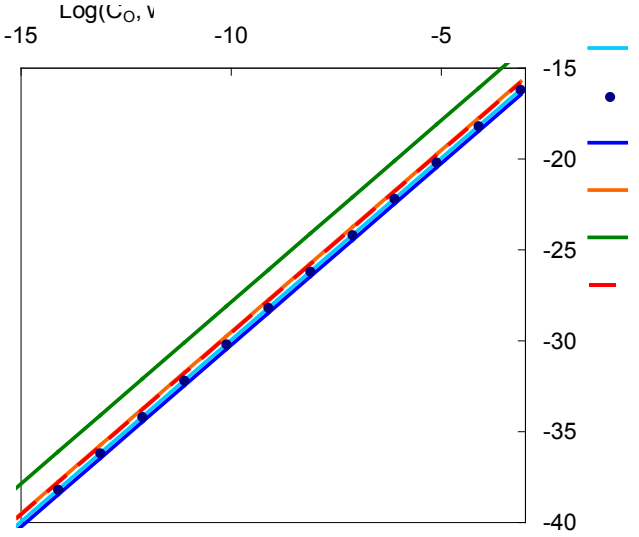

3.5.3.3 *Phase diagrams Pb-O-Bi*

Figure 3.5.10 presents the phase diagram of Pb-O and Bi-O for temperatures higher than the melting point of Pb-Bi and lower than the melting point of the lowest melting oxide, at the oxygen saturation level, lead and bismuth are in equilibrium with the different polymorphs of PbO and Bi_2O_3. The binary phase diagram Bi_2O_3-PbO according to the Calphad modelling by Diop is presented in Figure 3.5.11. It shows that several mixed oxides $PbO{\cdot}Bi_2O_3$ may exist as a function of temperature and composition. Only a few ternary Pb-O-Bi phase diagrams are available in the literature but some isotherms can be represented merging the databases by Risold (1995, 1998), Yoon (1998) and Diop (2009). Figure 3.5.12 exhibits two phase diagrams determined at 823K (550°C) by Ganesan (2008) and calculated at 1 173K (900°C) by Anik (1987).

Figure 3.5.10: Phase diagram Pb-O (left) and Bi-O (right)

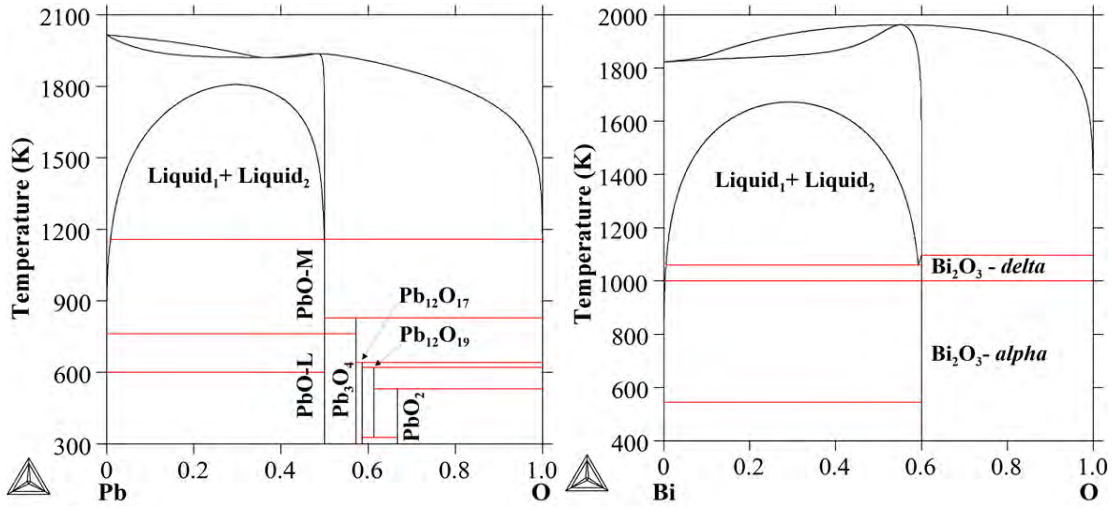

Source: Left image from Risold (1998), right image from Risold (1995).

Figure 3.5.11: PbO-Bi_2O_3 section of the ternary phase diagram Pb-Bi-O

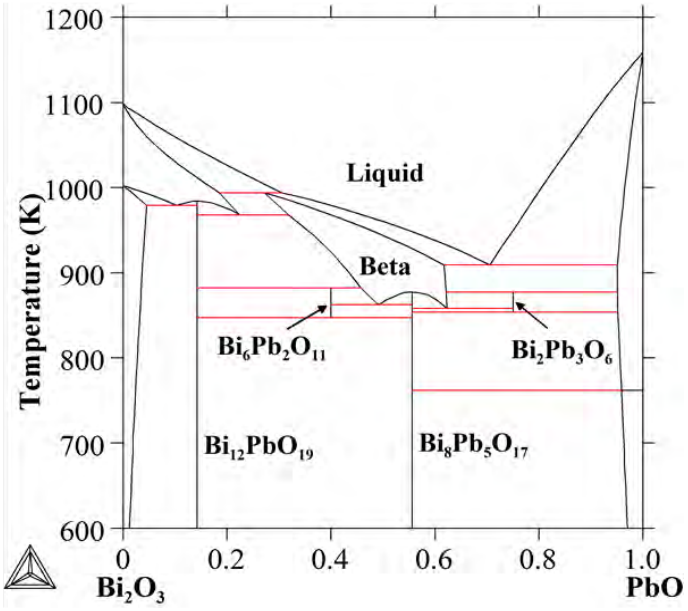

Source: Diop (2009).

Figure 3.5.12: Ternary phase diagram Pb-O-B

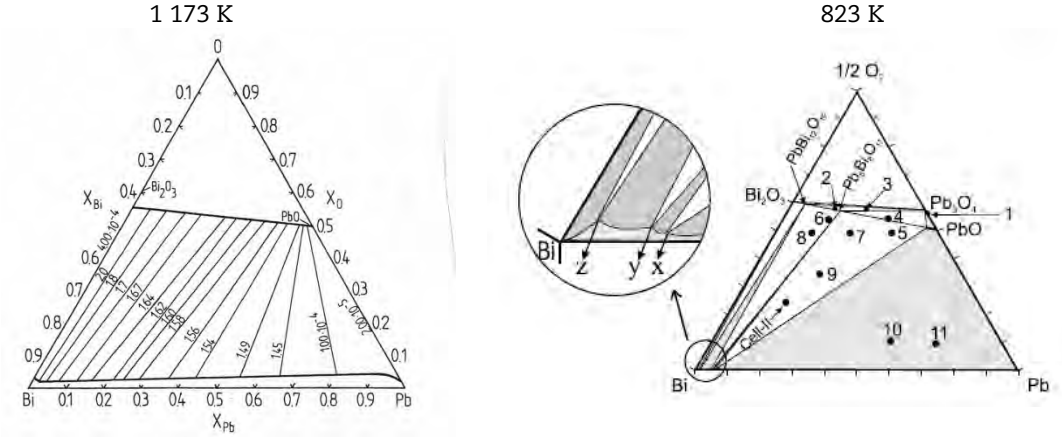

Source: Left diagram from Anik (1987); right diagram from Ganesan (2008).

3.6 Diffusivity

3.6.1 Diffusivity data of some metallic elements

The diffusion coefficient of a solute in a melt is a fundamental quantity required to characterise mass-transport rates. However, accurately measuring diffusion coefficients in liquid metals is very difficult, the main issue being the problem of mass transport by bulk motion of the fluid due to natural convection. This is driven by buoyancy forces produced by any temperature or concentration gradients which lead to decrease of liquid density with depth. For instance, in case of temperature gradient, the highest temperature is at the highest depth in order to decrease the liquid density at the highest depth. Several

different techniques exist to determine the diffusion coefficient in molten metals and generally the error on the measurement is many per cent. A survey of these techniques is available in Kubicek (1983) and Shimoji (1986).

Experimental techniques

- *Capillary techniques*. Many diffusion coefficients in molten metals have been determined by means of capillary techniques. These techniques include:
  - *Capillary reservoir methods (with finite or semi-infinite capillary tubes)*. In this technique a long capillary tube containing the pure molten metal is immersed in a large reservoir of the same molten metal containing a known concentration of the metal whose diffusion rate is desired to be measured. Concentration of the diffusing species is successfully determined by using radionuclides or X-ray spectral analysis.

  Some specific arrangements have been developed to improve these methods. For example, a shearing cell consisting of six discs that can rotate around an axial pin has been developed. The capillaries in three of the discs are filled with pure melt and a fourth is filled with melt containing a radioactive diffusing species. The outmost disc serves to close off the capillaries. As soon as the capillaries are aligned, diffusion starts. After a certain period, the discs are revolved to shear the column into four segments. Sometimes, the capillary reservoir method has been combined with use of a high temperature galvanic cell in particular to determine the oxygen diffusion coefficients in various liquid metals. The main advantage of this method is that the diffusion coefficient is measured *in situ*, not by subsequent analysis.

  - *Stationary diffusion source methods*. With this method the species for which diffusion is to be investigated is allowed to come into contact with the liquid through a gaseous phase. This method avoids some of the shortcomings of the capillary reservoir technique and is efficient with radionuclides.
  - *Reactive diffusion methods*. With this method the solid phase is allowed to come into contact with the melt.

  These methods suffer from several deficiencies, including convection (during immersion of the tube or due to difference of density, mechanical effects, thermal gradient), inaccurate initial or boundary conditions, surface diffusion, inaccuracy in determining the concentration profiles of the diffusing species or phenomena arising during solidification.

- *Controlled forced convection techniques*. The errors due to convection can be suppressed by imposing controlled force convection. When the dissolution of a solid in a liquid is diffusion controlled in the liquid boundary layer, the method of rotating disc dissolution can be used. This method uses a rotating disc which dissolves in a static melt. The rate of rotation is chosen so that laminar flow is achieved. The weight loss of the disc combined with the time of dissolution and angular velocity allow determination of the diffusion coefficient. The control of convection can also be ensured by applying electromagnetic stirring.

- *Electrochemical methods*. Electrochemical techniques are especially suitable for the determination of diffusion coefficients in the melt because convection is suppressed or eliminated. The experiments last only a few seconds in contrast to the capillary methods and the wall effects are not encountered. Of these methods, the most important in the study of diffusion in melts are chronopotentiometry and Rotating Disc Electrode (RDE). Linear voltammetry and polarography have limited application.

In the chronopotentiometry method, a pulse of current density is used to disturb the system from its equilibrium and the potential variation with time of the investigated electrode is measured. In the rotating disc method, an increasing voltage is applied to the RDE and the current is measured. In the linear voltammetry method, an increasing potential is applied to the working electrode. The current intensity variations with time and its maximum are measured.

Available data

Only a few data for diffusion coefficients of metallic elements in liquid lead and lead-bismuth are available in the literature. Special attention is paid to the iron coefficient because iron diffusion in liquid lead alloys is the limiting step of the corrosion of iron and iron chromium alloys such as T91 (Fe-9Cr).

The iron diffusion coefficient in lead has been determined by analysing the grooving of grain boundaries by the liquid metal (Robertson, 1968). With this method the liquid metal in contact with the solid dissolves the grain boundaries to form grooves. The groove width is linked to the diffusion coefficient of solid elements in the liquid, which is determined equal to:

$$\log\left(D, \mathrm{cm^2 s^{-1}}\right) = -2.31 - \frac{2295}{T} \quad 973\ \mathrm{K} < T < 1\,273\ \mathrm{K}\ (700\text{-}1\,000°\mathrm{C})$$

The iron diffusion coefficient in LBE is known at only four temperatures:

- 673 K: 3.5×10^{-7} cm^2.s^{-1} (oxygen concentration = 10^{-11} wt.% during experiments) (Balbaud, 2004);
- 740 K: 4×10^{-6} cm^2.s^{-1} and 4.5×10^{-6} cm^2.s^{-1} (oxygen concentration = 3×10^{-14} wt.% during experiments) (Abella, 2011);
- 743 K: 7.6×10^{-6} cm^2.s^{-1} (oxygen concentration = 3×10^{-12} wt.% during experiments) (Balbaud, 2004);
- 1 023 K: 2.27×10^{-5} cm^2.s^{-1} (Barnerjee, 1974).

These data have been obtained by means of experiments with an iron rotating disk specimen (Barnerjee, 1974) or a T91 steel (Fe-9Cr) cylinder (Balbaud, 2004; Abella, 2011). The specimen dissolution rate is limited by iron diffusion in the boundary layer and is determined by a weight loss measurement. The weight loss depends on the temperature, time, rotating speed, liquid viscosity, the solubility and diffusivity of the solute.

Figure 3.6.1 shows that the diffusion coefficients for iron in liquid Pb and LBE are not very different. The data determined at low temperature are not far from the extrapolated values for iron from high temperatures (973-1 273 K) (Robertson, 1968). In case of iron diffusion in LBE, Barnerjee (1974) and Balbaud (2004) consider that the corrosion rate of the rotating disk/cylinder is limited by the iron diffusion in the boundary layer. This assumption should be verified even if their results are close to those of Robertson in pure lead.

As there is no other available data for iron diffusion in LBE and as that given by Robertson (1968) in pure lead is close to those given by Barnerjee (1974), Balbaud (2004) and Abella (2011) in LBE, the Robertson's values are often used in LBE.

Selected diffusion coefficient data for different metallic elements in lead are also reported in the literature and given in Table 3.6.1.

Figure 3.6.1: Iron diffusion coefficient in pure Pb and eutectic Pb-Bi

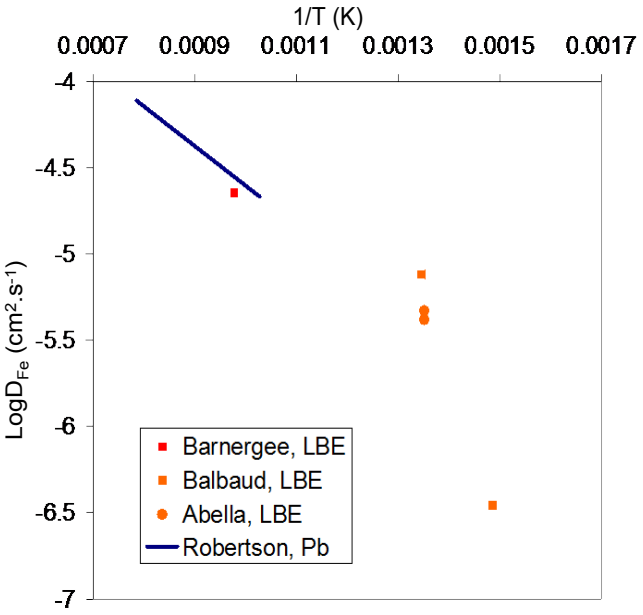

Table 3.6.1: Diffusion coefficients of some metallic elements in liquid lead

Element	Temperature range (K)	Diffusion coefficient ($cm^2\ s^{-1}$); R (J mol-1 K^{-1})	Reference
Co	1 023-1 273	$4.6 \cdot 10^{-4}$ exp(-22 154/RT)	Robertson (1968)
Se	823-1 173	$3.4 \cdot 10^{-4}$ exp(-12 958/RT)	Lozovoy (1981)
In	723-1 173	$3.1 \cdot 10^{-4}$ exp(-13 794/RT)	Lozovoy (1981)
Tl	723-1 173	$3.1 \cdot 10^{-4}$ exp(-15 884/RT)	Lozovoy (1981)

3.6.2 Oxygen diffusion coefficient

Different techniques have been used to determine the oxygen diffusion coefficient:

- Electrochemical measurement with a rare earth stabilised zirconia electrode (Szarc, 1972; Bandyopadhyay, 1971; Honma, 1971). The principle is to perform amperometries at the oxygen reduction potential. The variations of the current intensity are related to the diffusion coefficient of oxygen in the liquid metal.
- Electrochemical measurements with a rare earth stabilised zirconia electrode on each side of a horizontal column of liquid metal. One probe is used to introduce oxygen into the liquid. The other, on the opposite side of the liquid metal column is used to measure oxygen concentration as a function of time via its potential. This data is then to determine the oxygen diffusion coefficient.
- Measurement of the weight loss of a PbO rotating disc (Gromov, 1996). The dissolution kinetics of PbO in liquid lead or LBE depends on the oxygen solubility, the rotation speed of the disc, the viscosity of the liquid and the diffusion coefficient of oxygen at the temperature.

Selected oxygen diffusion coefficient data in pure lead, LBE and pure bismuth are given in Table 3.6.2 and presented in Figure 3.6.2.

Table 3.6.2: Data on oxygen diffusion coefficient in liquid lead and LBE

Liquid	Temperature range (K)	Diffusion coefficient of oxygen ($cm^2 s^{-1}$), R ($J\ mol^{-1}\ K^{-1}$)	Reference
Pb	973-1 173	$6.32 \cdot 10^{-5}$ exp(-14 979/RT)	Arcella (1968)
Pb	1 073-1 373	$(9.65 \pm 0.71) 10^{-5}$ exp(-20 083±6 067/RT)	Homna (1971)
Pb	1 023	$1.29 \cdot 10^{-5}$	Bandyopadhyay (1971)
Pb	1 013-1 353	$(1.44 \pm 0.45) 10^{-3}$ exp(-25 942±2 803/RT)	Swzarc (1972)
Pb	1 173-1 373	$(1.48 \pm 0.6) 10^{-3}$ exp(-19 497±10 711/RT)	Otsuka (1975)
Pb	1 173-1 373	$1.90 \cdot 10^{-3}$ exp(-20 927/RT)	Charlé (1976)
Pb	673-1 273	$6.6 \cdot 10^{-5}$ exp(-16 158/RT)	Gromov (1996)
Pb	823-1 053	$2.79 \cdot 10^{-3}$ exp(-45 587/RT)	Ganesan (2006b)
Pb	1 063	$1.30 \cdot 10^{-5}$	Kawakami (1973)
LBE	473-1 273	$2.39 \cdot 10^{-2}$ exp(-43 073/RT)	Gromov (1996)
LBE	813-973	0.154 exp(-69 069/RT)	Ganesan (2006b)
LBE	733	$2.50 \cdot 10^{-6}$	Abella (2011)
LBE	773	$2.65 \cdot 10^{-6}$	
LBE	813	$2.80 \cdot 10^{-6}$	
Bi	951-1 100	$1.07 \cdot 10^{-2}$ exp(-49 229/RT)	Fitzner (1980)
Bi	1 023-1 273	$1.98 \cdot 10^{-4}$ exp(-26 610/RT)	Heshmatpour (1981)

Figure 3.6.2: Oxygen diffusion coefficient in liquid lead, LBE and bismuth

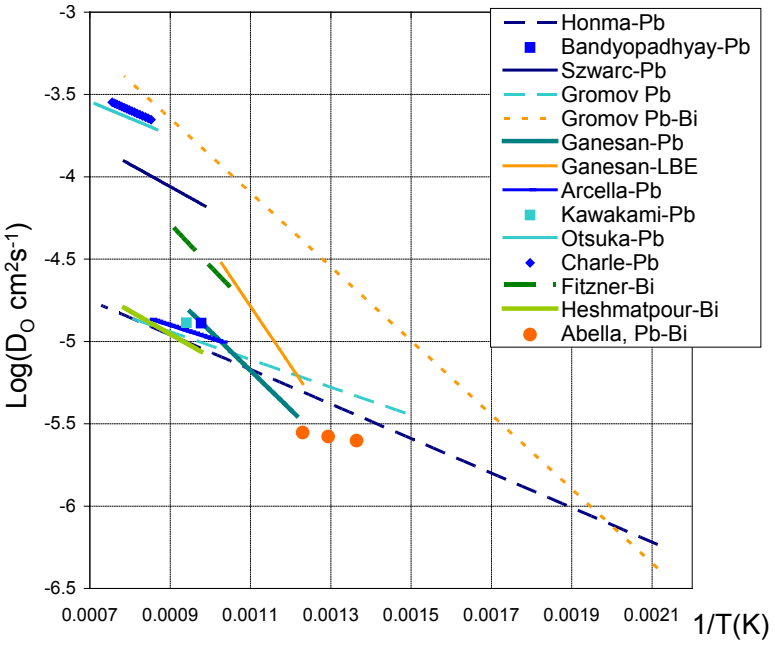

The following observations are made:

- The differences between the data in lead may result from the differences between materials used for the rare earth stabilised zirconia probe.
- The results obtained with the rare earth stabilised zirconia probe are not very different from those obtained with a rotation disc.
- There is a significant scatter of the different values except in the 873-973 K (600-700°C) temperature range.
- The oxygen diffusion coefficients in LBE are higher than those in lead, except for those of Abella (2011).
- Discrepancy in the results of oxygen diffusion coefficient in pure bismuth and in LBE is lower than one order of magnitude.

3.7 Chemical interactions and ternary phase diagrams

During operation, a lot of spallation products will be generated in the LBE target. In particular mercury is expected to be the most generated species. Therefore, the ternary Pb-Bi-Hg system has been investigated (Maître, 2002). Phase limits and invariant equilibria were determined using differential scanning calorimetry (DSC). The phase diagram computation was performed using the Calphad method (Kaufman, 1970) with Thermocalc software. Only one ternary intermetallic compound has been identified with composition close to $Bi_{0.35}$ $Hg_{0.20}$ $Pb_{0.45}$.

The Thermocalc nomenclature is given in Figure 3.7.1. Two isothermal sections at 310 K and 355 K of the ternary phase diagram are given in Figures 3.7.2 and 3.7.3.

The 310 K section, Figure 3.7.2., emphasises a peritectic equilibrium:

$$C = Liq + Fcc(Pb) + Rhombo_A7(Bi)$$

where C is $Bi_{0.35}$ $Hg_{0.20}$ $Pb_{0.45}$.

The 355 K section shows another invariant:

$$Liq + hcp_\varepsilon(Bi,Pb) = Fcc(Pb) + Rhombo_A7(Bi)$$

The isopleth section (X_{Pb}/X_{Bi} = 0.45/0.55 (Figure 3.7.4) shows the decrease in liquidus and solidus temperature as the Hg content increases.

Figure 3.7.1: Thermocalc nomenclature

Fcc (Pb)	Pb solid solution (face centred cubic)
Rhombo_A7(Bi)	Bi solid solution (rhombic)
hcp_ε(Bi,Pb)	Non-stoichiometric intermetallic compound Pb-Bi (hexagonal compact) admitting a low Hg extension in the ternary system Pb-Bi-Hg
C	$Bi_7Hg_4Pb_9$ ternary intermetallic compound
Liq	Liquid

Figure 3.7.2: Isothermal section at 310 K for the ternary Pb-Bi-Hg system

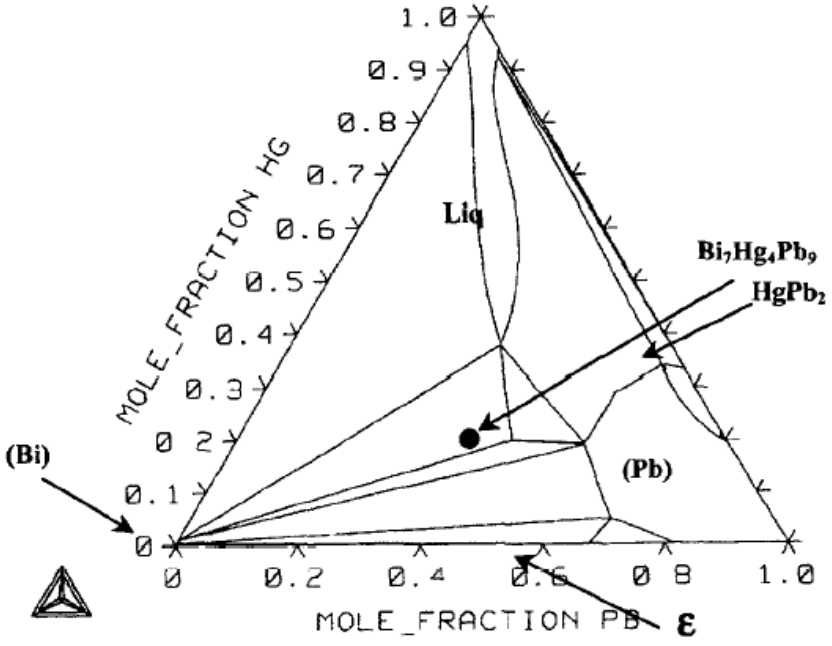

Source: Maître (2002).

Figure 3.7.3: Isothermal section at 355 K for the ternary Pb-Bi-Hg system

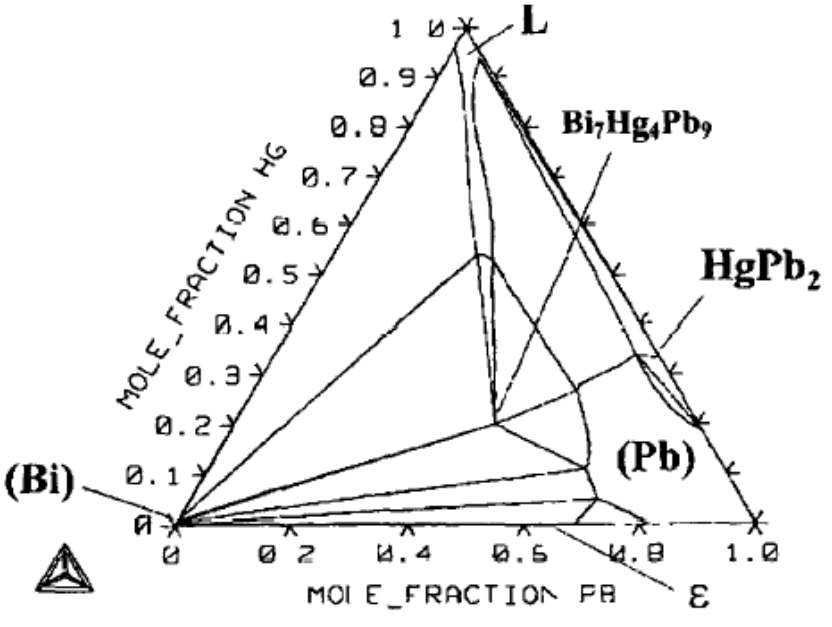

Source: Maître (2002).

Figure 3.7.4: Isopleth section (X_{Pb}/X_{Bi} = 0.45/0.55) in Pb-Bi-Hg

Temperature is given in K

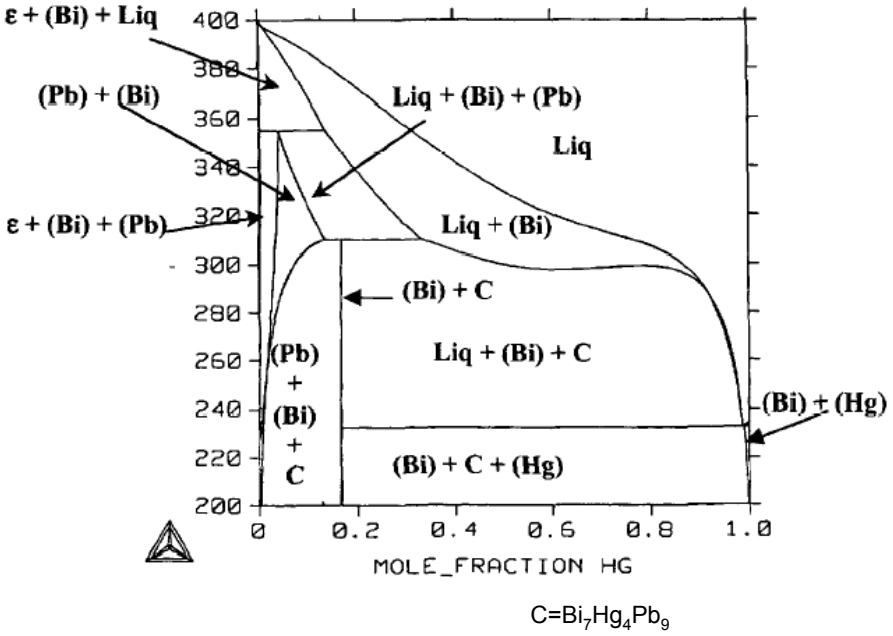

Source: Maître (2002).

3.8 Lead and LBE/water interaction

The increasing interest in heavy liquid metal reactors, based on either lead or lead-bismuth eutectic coolants, raises the question of the effects of their possible interaction with water. The preliminary designs of the lead fast reactor (LFR) and of subcritical transmutation systems prototypes presently foresee the use of steam generation modules in direct contact with the liquid metal of the main vessel. This configuration is not recommended for safety reasons, unless the formation mechanism of highly volatile polonium species in the presence of water is thoroughly understood. Moreover, with this configuration an accidental leakage of water into the core vessel cannot be excluded. Moreover, an incidental scenario which could cause a physical interaction between LBE and heavy water has been considered and studied for the MEGAPIE experiment (MSR, Jacobs). The consequences of such an event must be thoroughly examined due to its impact on the design, maintenance and economics of these future reactors.

It should be pointed out that, unlike the cases of sodium or lithium and its alloys, for Pb and Pb-Bi there is no chemical interaction with water and the resulting effects are significantly different.

3.8.1 Literature survey

From a literature review, three main categories of experiments were found:

- Pb-17Li large scale experiments (Kottowski, 1991; Ciampichetti, 2003a, 2003b);
- Small scale experiments involving Pb, Pb-17Li, 2Pb-7Li, and Li (Kranert, 1991);
- Small scale Pb-Bi experiments (Sibamoto, 2001; Corradini, 1988; Nakamura, 1999; Hibiki, 2000; Suzuki, 2003).

Large scale experiments

Large scale experiments were mainly performed in Ispra and Brasimone with Pb-17Li for fusion applications. Their characteristics are given in Table 3.8.1.

Table 3.8.1: Large scale experiments

Water pressure	Water temperature	Injected mass of water	Liquid metal temperature	Volume of the reaction vessel
40-155 bar	498-598 K	2.7-4.6 kg	623-773 K	50-100 litres

Due to the chemical and physical interactions, strong and rapid pressure and temperature rises were observed. In some tests, spikes were detected above the water injection pressure.

LIFUS 5 and BLAST experiments (Kottowski, 1991; Ciampichetti, 2003a, 2003b) dealt with the interaction between Pb-17Li alloy and hot pressurised water coming from large leaks, simulating a cooling tube rupture inside the water-cooled liquid lead-lithium (WCLL) blanket. Due to the production of hydrogen in these experiments, it is not possible to extend the results to the accident scenarios foreseen in lead reactors.

Small scale experiments

Small scale experiments done by JRC Ispra (Kranert, 1991), consisted of the injection of water from the top of an expansion tube (d = 9 mm, L = 2 m) into a reaction capsule containing the alloy (d = 24 mm, L = 170 mm) without cover gas buffer. The test conditions are given in Table 3.8.2.

Table 3.8.2: Conditions of small scale experiments

Water pressure	Water subcooling temperature	Injected mass of water	Liquid metal temperature
1-25 bar	283 – 316 – 348 K	1.2-200 g	773-1 073 K

Source: Kranert (1991).

The results of the tests carried out with lead and a water injection pressure of 1 bar showed a pressure rise of up to 18 bar due to the coolant column impact on the alloy surface. The 18 bar pressure rise is the highest observed value, excluding the tests with lithium. In fact, an important conclusion of this work was that the chemical reaction between the alloys containing lithium and water inhibits a violent thermo-hydraulic reaction due to the attenuating effect of the hydrogen produced.

A small scale LBE experiment was performed at JAERI in the framework of reactor safety. The liquid metal was dropped into a water pool having the features shown in Table 3.8.3 (Sibamoto, 2001; Nakamura, 1999).

Table 3.8.3: Conditions of the JAERI small scale experiment

Water pressure	Water temperature	Liquid metal temperature	Mass of water	Mass of LBE
1 bar	373 K	523 K	80 g	1.8 Kg

These experiments demonstrated that the melt accumulation in the water pool is accompanied by vigorous steam generation at the initial point of contact of the Pb-Bi with water. A violent vapour expansion occurred and was well predicted by a simplified one-dimensional model. The evolution of steam production and expansion was measured by a neutron radiography technique.

For the development and validation of the SIMMER code, Hibiki (2000) and Suzuki (2003) reported some experimental studies on flow characteristics in gas-molten metal pool. Corradini (1988) presents some criteria to predict the conditions for a vapour explosion.

3.8.2 Related risks

The main risk for the structures is associated with the occurrence of a vapour explosion. A vapour explosion is a physical event in which a hot liquid rapidly fragments and transfers its internal energy to a colder, more volatile liquid which in turn vaporises at high pressure and expands, doing work on its surroundings. The vapour explosion criterion advanced by Fauske (1973) is based on the comparison between interface temperature and the spontaneous nucleation temperature. For fluids hardly wetting, like water and LBE, the spontaneous nucleation temperature is very close to the homogeneous nucleation temperature which is approximately 583 K for water. This criterion, even if not universally accepted, was confirmed by recent observations collected by Kurata (2004) which show that, at 1 atmosphere pressure, a steam explosion is possible over an interface temperature range from about 573 K to the water critical temperature. Other observations by Kurata (2004) are that:

- Vapour explosion can occur at initial melt temperatures and between about 673 K (400°C) and 773 K (500°C) at pressures under 0.1 MPa.
- Vapour explosions seem to occur when the water is sufficiently subcooled, and when the contact temperature is higher than the spontaneous bubble-nucleation temperature.
- Vapour explosions do not occur at pressures above 0.2 MPa.
- Decreasing droplet subcooling diminishes the explosion intensity.

In case where vapour explosions do not occur, the expansion of released water in LBE happens at a slower rate and simpler thermodynamic models can describe the behaviour.

In any case it is advisable that liquid metal/water interaction be studied by means of both experimental and numerical approaches.

3.8.3 Numerical codes

In view of the safety issues related to the severe core melting accident, several numerical codes have been developed in recent years to assess the effects of the interaction between liquid metals and water. Among these are:

- Mattina.
- SIMMER.

Mattina (Jacobs, 2002) was recently used to simulate a case of LBE/water interaction for the MEGAPIE project. Its limitations are that the code is not suitable for the treatment of film boiling conditions and that the equations of state for lead and lead-bismuth were not originally implemented.

SIMMER is a complex fluid-dynamic code coupled with a neutron kinetics model that has been used to model liquid metal/water interactions (Corradini, 1998; Hibiki, 2000; Suzuki, 2003). The fluid dynamic part is suitable for the modelling of liquid metal/coolant interactions having several different patterns and its database includes the physical properties of lead and LBE as well.

3.9 Lead or LBE and sodium interaction

There are a number of applications where lead or LBE are used in the same system as sodium. In these cases it is possible for lead or LBE to contact sodium. Such applications include: *i*) accelerator-driven technology for waste transmutation systems where LBE is used for the spallation target and sodium is used for the transmuter blanket; *ii*) in advanced intermediate heat exchangers (AIHX) for fast breeder reactors in which the secondary liquid sodium is replaced by LBE; *iii*) when a sodium-bonded metallic fuel is deployed inside a LBE-cooled blanket. In all the cases, the consequences of contact between the different liquids under accident conditions have to be considered and evaluated. The information given hereafter is taken from Crawford (2001).

Figures 3.9.1 and 3.9.2 show the binary phase diagrams for the Na-Pb and Na-Bi systems respectively (Borgstedt, 1996). While a ternary Na-Pb-Bi diagram would be more appropriate, the binaries allow an estimate of the potential stable phases for LBE/Na interaction.

These phase diagrams show that Bi is less soluble in Na than Pb but Bi is not insoluble, as can be seen from the following equation (Borgstedt, 1987) giving the variations of Pb and Bi solubilities in Na:

- $\log(S_{Pb}, \text{wt.\%}) = 6.1097 - \frac{2636}{T}$ in the 393-523 K (120-250°C) temperature range.
- $\log(S_{Bi}, \text{wt.\%}) = 2.15 - \frac{2103}{T}$ in the 398-563 K (125-290°C) temperature range.
- $\log(S_{Bi}, \text{wt.\%}) = 5.67 - \frac{4038}{T}$ in the 563-923 K (290-650°C) temperature range.

The Na-Pb compound melting temperatures are around 673 K or less while Na_3Bi melts at 1 113 K (840°C).

Moreover, the products formed in the reactions between Na and Pb or Na and Bi are listed in Table 3.9.1 along with their enthalpies of formation. The negative values of the enthalpies of formation indicate that these compounds are formed in exothermic reactions.

Figure 3.9.1: Na-Pb phase diagram

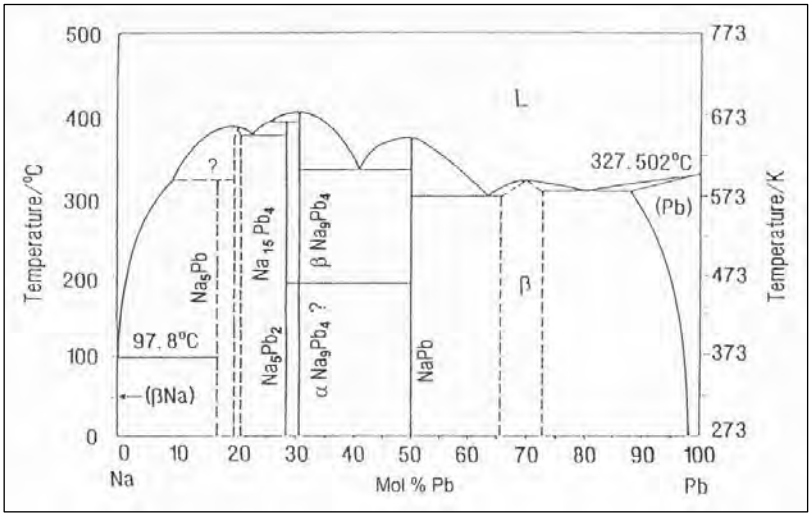

Source: Borgstedt (1996).

Figure 3.9.2: Na-Bi phase diagram

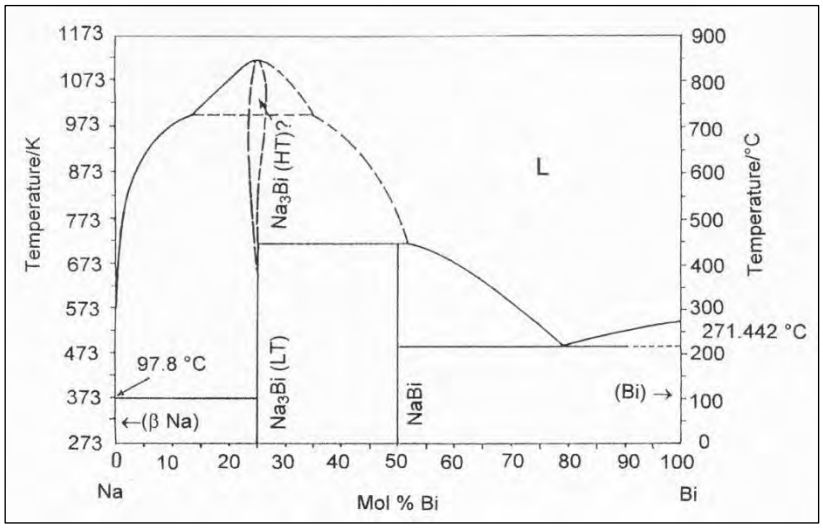

Source: Borgstedt (1996).

Table 3.9.1: Known reaction products from Na and Pb or Na and Bi reactions

Compounds	$\Delta H_f°$ (298), kJ/mole
Lead	
$Na_{15}Pb_4$	–
Na_5Pb_2	-146.3
Na_9Pb_4	–
NaPb	-48.49
$NaPb_3$	-63.54
Na_4Pb	-83.6
Bismuth	
Na_3Bi	-201.48
NaBi	-65.21

Experimental tests for phase identification consisted of placing measured quantities of Pb or Bi metal onto a measured quantity of solid Na in the bottom of a Petri dish. The metals were then heated in an argon atmosphere from 298 K to a temperature above the melting temperature of Na. Each experiment was terminated after the observed reaction was complete or after the metals had melted and mixed. It has been mentioned "no visible exothermic reaction was noticeable at the melting points of sodium or lead. Once the lead melted, it mixed well with the molten sodium." (Crawford, 2001) For the Na-Bi reaction, "A very vigorous exothermic reaction took place at the melting point of sodium. A grey-to-black friable material resulted from the exothermic reaction." (Crawford, 2001) The following accomplishments and/or general observations were made as a result of the experimental programme:

- Investigations and calculations are performed to evaluate the temperature excursion when Na and Bi are put in contact.

- The Na-Bi reaction is rapid and releases a relatively high amount of heat. The Na-Pb reaction seems less severe but the reason for that is not obvious based on the values of compound formation enthalpies.
- In the case of an Na-cooled transmuter blanket and an LBE target, phenomena to be considered in analysing the consequences of a blanket-target interface leak include:
  - The Na-Bi and Na-Pb reaction products might plug the leak, stopping the reaction and leading to a benign event.
  - The Na-Bi and Na-Pb reaction products might form in the leak area and stress the target wall, exacerbating the failure and leading to more but this seems not very likely because the material inboard of the target wall would be liquid LBE and there would be nothing solid to maintain the reaction products in a position to stress the original leak area.
  - The Na-Bi and Na-Pb reaction products could be swept away by the flowing Na coolant, where they might dissolve or might simply disperse as solids in the coolant. Looking at the Na-Bi and Na-Pb phase diagrams indicates that the Na-Pb intermetallic is unstable in dilute solutions of Pb in Na, but that the Na_3Bi intermetallic would be present in dilute solutions of Bi in Na up to temperatures near 873 K. Furthermore, the Na_3Bi reaction product would likely remain solid at coolant temperatures, whereas the $Na_{15}Pb_4$ reaction product, if at sufficiently high Pb content to remain stable, could precipitate out of Na solution at coolant inlet temperatures. Therefore, it is possible that some reaction products will remain solid in the Na coolant. These products could potentially block flow channels depending on their amount and on their degree of dispersion.
  - If the supply of reacting Na and Bi is not mitigated, significant heat energy from the reaction might be deposited to the blanket or target components but the ability of Na and LBE to dissipate heat and the available volume of Na to absorb the heat would likely prevent such a development.
- In conclusion, a reaction between sodium and bismuth appears to be sufficiently exothermic that local temperatures could increase substantially, either adversely affecting further reaction, or perhaps introducing reaction products that might block flow channels. Experiments and calculations to assess reaction kinetics and the phenomenology of the reaction in representative conditions of the considered system are needed to properly estimate the consequences on the contact between Na and Bi and Pb.

Some experiments have also been conducted by Saito (2005) to investigate the reaction between LBE and sodium. They consist in introducing some small amounts of LBE as droplets into a sodium bath. The tests were performed at different temperatures of Na and LBE (between 573 and 673 K) and with various LBE amounts (40 to 140 g as 1-2 mm diameter droplet for 1 100 g of Na). The following results were obtained:

- The sodium temperature immediately rises by dropping LBE into liquid sodium due to an exothermic reaction between Na and LBE.
- The reaction between Na and LBE occurs more quickly when the temperature of the melts is high.
- Fine reaction products are formed and they mainly consist of $BiNa_3$ intermetallic compound. The amount of LBE affects the amount of reaction products and reaction heat.
- The reaction heat deduced from the temperature increase is comparable to the calculated $BiNa_3$ standard formation enthalpy value.

3.10 LBE and Pb and organic compounds interaction

The MEGAPIE spallation neutron target uses Diphyl THT (DTHT, produced by Bayer) oil as coolant to cool the LBE target. In case of a heat exchanger leak, high pressure DTHT will enter the low pressure LBE. Therefore, the consequences of such an event, particularly from a safety point of view, must be evaluated by investigating the chemical and thermal interactions between DTHT and LBE. Therefore, a set of experiments were carried out and are reported in Leung (2003). These experiments consisted of putting DTHT with and without LBE in an autoclave at 623 K under an argon atmosphere.

The results show that:

- No chemical reaction occurs between oil and LBE which induces an increase of temperature and pressure detrimental to MEGAPIE experiment.
- There is a significant difference between apparent gas production rates of the DTHT and DTHT-LBE mixture at elevated temperature, but the net gas production at room temperature was virtually the same in the two cases. This suggests the production of a condensable gas in the experiment with only DTHT.
- There is a lower pressure rise than that which would be expected from the supplier information.

References

Abella, J. et al., (2011), "Fundamental Data: Solubility of Nickel and Oxygen and Diffusivity of Iron and Oxygen in Molten LBE", *Journal of Nuclear Materials*, 415, p. 329.

Adamov, E.O. and Y.I. Orlov (1998), "Nuclear Development on the Basis of New Concepts of Nuclear Reactors and Fuel Cycle", *Proceedings of Heavy Liquid Metal Coolant in Nuclear Technology (HLMC 1998)*, SSRF-IPPE-Obninsk 1999, p. 24.

Alcock, C.B. and T.N. Belford (1964), "Thermodynamics and Solubility of Oxygen in Liquid Metals from E.M.F. Measurements Involving Solid Electrolytes", *Transactions of the Faraday Society*, 60, pp. 822-835.

Ali-Khan, I. (1982), Material Behaviour and Physical Chemistry in Liquid Metal Systems, H.U. Borgstedt (ed.), New York, Plenum, pp. 237-242.

Alden, T., D.A. Stevenson and J. Wulff (1958), "Solubility of Nickel and Chromium in Molten Lead", J., *Trans. Metall. Soc AIME*, pp. 15-17.

Anik, S. and M.G. Frohberg (1987), "Thermodynamics and Solubility of Oxygen in Liquid Bismuth-Lead and Bismuth-Antimony Alloys", *Ber. Bunsenges. Phys. Chem*, 91, p. 790.

Arcella, F.G. and G.R. Fitterer (1968), *J. Metals*, 47A.

Arnoldov, M.N. et al. (1998), *Solubility and Corrosion of Materials in Lead and Lead-Bismuth*, Review FEI-0228 (in Russian).

Balbaud, F. et al. (2004), "Influence of Pb-Bi Hydrodynamics on the Corrosion Behaviour of Martensitic Steel T91", *J. Nucl. Mater.,* 335, pp. 204-209.

Banerjee, S. (1974), *Proceedings of the 5th International Congress on Metallic Corrosion*, Tokyo, NACE, Houston, Texas.

Bandyopadhyay, G.K. and H.S. Ray (1971), "Kinetics of Oxygen Dissolution in Molten Lead", *Metallurgical Transactions*, 2, p. 3055.

Bardfeld, K. (1955), Thesis, T.H. Braunschweig.

Baker, W.A. (1939), "The Estimation of Oxygen in Metals", *J. Inst. Met.*, 65, p. 345.

Biefeld, R.M. and S.S. White (1981), "Temperature/Composition Phase Diagram of the System Bi_2O_3-PbO", *J. Am. Cer. Soc.*, 64, p. 182.

Brewer, L. and R.H. Lamoreaux (1980), "Molybdenum Physico-Chemical Properties of Its Compounds and Alloys", L. Brewer (ed.), *Atomic Energy Review*, Special Issue No. 7, IAEA, Vienna p. 295.

Borgstedt, H.U. and C.K. Mathews (1987), *Applied Chemistry of the Alkali Metals*, Plenum Press, New York.

Borgstedt, H.U. and H. Feuerstein (1992), "The Solubility of Metals in Pb-17Li", *Journal of Nuclear Materials*, 191-194, pp. 988-991.

Borgstedt, H.U. and C. Guminski (1996), "Metals in Liquid Alkali Metals, Part II: Co to Bi", *Solubility Data Series*, Vol. 64, Oxford University Press, p. 270 and p. 314.

Carlsson, G. (1978), *Syrets löslighet bly* [Oxygen Solubility of Lead], Swedish Institute for Metals Research, IM 1327.

Chang, Y.A., K. Fitzner and X. Zhang (1989), "The Solubility of Gases in Liquid Metals and Alloys", *Progress in Materials Science*, Vol. 32, pp. 97-259.

Charlé, H. and J. Osterwald (1976), "Elektrochemische Gleichgewichts-und Diffusion-suntersuchungen am System Blei-Sauerstoff", *Z. Phys. Chem.*, 99, pp. 199-208.

Cheynet, B., J.D. Dubois and M. Milesi (1996), "Données thermodynamiques des éléments chimiques", *Techniques de L'Ingénieur*, Matériaux métalliques, No. M153, Forum M64.

Ciampichetti, A. et al. (2003a), "Water Large Leaks into Liquid Pb-17Li: First Experimental Results on LIFUS 5 Facility", *Fus. Eng. Des.,* 69, pp. 563-567.

Ciampichetti, A. et al. (2003b), *Water Large Leaks into Liquid Pb-17Li: Tests n. 6-7-8 on LIFUS* 5, ENEA Report LB-A-R-019, ENEA, Rome.

Conochie, D.S., C. Ebiogwu and D.G.C. Robertson (1984), "Oxygen Solubility in Molten Lead", *Trans. Inst. Miner. Metall.*, 93, C45-C48.

Corradini M.L. et al. (1988), "Vapor Explosions in Light Water Reactors: A Review of Theory and Modelling", *Progress in Nuclear Energy*, Vol. 22, No. 1.

Courouau, J.L. (2004), "Electrochemical Oxygen sensors for On-line Monitoring in Lead-Bismuth Alloys: Status of Development", *Journal of Nuclear Materials,* 335, pp. 254-259.

Crawford, D.C et al. (2001), *Discussion on the Sodium-bismuth Reaction*, ANL technical report, Argonne National Laboratory, Argonne, IL.

Diop, I. et al. (2009), "Experimental Investigations and Thermodynamic Description of the PbO-Bi_2O_3 System", *J. Chem. Thermodynamics*, 41, pp. 420-432.

Elliot, R.P. (1965), *Constitution of Binary Alloys*, McGraw-Hill, New York.

Fauske, H.K. (1973), "On the mechanisms of Uranium-Dioxide-Sodium Interactions", *Nucl. Sci. Engr*, Vol 51, pp 95-100.

Flament, T., P. Fauvet and J. Sannier (1988), *Compatibility of Structural Steels with Liquid Lead, A Bibliographic Study*, Commissariat à l'énergie atomique (CEA) report RT SCECF 108.

Fischer, W.A. and W. Ackerman (1966), *Arch. Eisenhüttenwes.*, 37, p. 43.

Fitzner, K., (1980), "Diffusivity, Activity and Solubility of Oxygen in Liquid Bismuth", *Thermochimica Acta*, 35, p. 277.

Ganesan, R. (2006a), Thesis, Indian Institute of Technology, Mumbai.

Ganesan R., T. Gnanasekaran and R.S. Srinivasa (2006b), "Diffusivity, Activity and Solubility of Oxygen in Liquid Lead and Lead-Bismuth Eutectic Alloy by Electrochemical Methods", *Journal of Nuclear Materials*, 349, pp. 133-149.

Ganesan R., T. Gnanasekaran and R.S. Srinivasa (2008), "Standard Molar Gibbs Energy of Formation of $Pb_5Bi_8O_{17}$ and $PbBi_{12}O_{19}$ and Phase Diagram of the Pb-Bi-O System", *Journal of Nuclear Materials*, 375, pp. 229-242.

Ghetta, V., A. Maître and J.C. Gachon (2004), Oral communication, MEGAPIE meeting, Nantes.

Ghetta, V et al. (2001), "Experimental Setup for Steel Corrosion Characterization in Lead Bath", *Journal of Nuclear Materials,* 296, p. 295.

Gossé, S. (2014), "Thermodynamic Assessment of Solubility and Activity of Iron, Chromium, and Nickel in Lead Bismuth Eutectic", *Journal of Nuclear Materials,* 449, pp. 122-131.

Griffith, C.B. and M.W. Mallett (1953), "The Solubility of Carbon and Oxygen in Liquid Bismuth", *J. Am. Chem. Soc.*, 75, p. 1832.

Gromov, B.F. and B.A. Shmatko (1996), *Journal of Obninsk*, No. 4, IPPE No. ISSN 0204-3327.

Gromov, B.F. et al. (1997), "Use of Lead-bismuth Coolant in Nuclear Reactors and Accelerator-Driven Systems", *Nucl. Eng. Des.,* 173, p. 207.

Gromov, B.F. et al. (1998) "The Problems of Technology of the Heavy Liquid Metal Coolants (Lead-bismuth, Lead)", *Proceedings of the Conference of the Heavy Liquid Metal Coolants in Nuclear Technology*, Obninsk, Russian Federation, 5-9 October, pp. 87-100.

Guminski, C. (1990), "Solubility of Metals in Liquid Low Melting Metals", *Z. Metallk.*, 81, pp. 105-110.

Gurvich, L.V. et al. (1991), *Thermodynamic Properties of Individual Substances*, Fourth Edition, Vol. 2, Parts 1 and 2, Hemisphere Pub. Corp., New York.

Hahn, S.K. and D.A. Stevenson (1979), "Thermodynamic Investigation of Antimony + Oxygen and Bismuth + Oxygen Using Solid State Electrochemical Techniques", *J. Chem. Thermodynamics*, 11, p. 627.

Hansen, M. (1958), in *Constitution of Binary Alloys*, McGraw-Hill, New York.

Heinzel, A. (2003), *Korrosionsverhalten von Stählen in sauerstoffbeladenem, flüssigem Pb55,5%Bi unter Berücksichtigung von Oberflächenmodifikationen*, Thesis, Universität Karlsruhe 2002, FZK report FZKA 6823, Forschungszentrum Karlsruhe (FZK), Karlsruhe.

Heshmatpour, B. and D.A. Stevenson (1981), "An Electrochemical Study of the Solubility and Diffusivity of Oxygen in the Respective Liquid Metals Indium, Gallium, Antimony and Bismuth", *J. Electroanal. Chem.*, 130, p. 47.

Hibiki, T. et al. (2000), "Study on Flow Characteristics in Gas-Molten Metal Mixture Pool", *Nuclear Engineering and Design*, Vol. 196, p. 233.

Honma, S., N. Sano and Y. Matsushita (1971), "Electrochemical Measurement of the Diffusivity of Oxygen in Liquid Lead", *Metallurgical Transactions*, 2, p. 1494.

Hultgren, R. et al. (1973), *Selected Values of the Thermodynamic Properties of Binary Alloys*, American Society for Metals (ASM), Metals Park, Ohio.

Hultgren, R. et al. (1974), *Selected Values of the Thermodynamic Properties of the Elements*, J. Wiley, New York.

IAEA (International Atomic Energy Agency) (2002), *Comparative Assessment of Thermophysical and Thermohydraulic Characteristics of Lead, Lead-bismuth, and Sodium Coolants for Fast Reactors*, TECDOC-1289, IAEA, Vienna.

Isecke, B. (1977), *Equilibria Studying the Bismuth-, Antimony-, and Lead-Oxygen Systems*, Thesis, TU Berlin, Berlin.

Isecke, B. and J. Osterwald (1979), *Z. Phys. Chem. Neue Folge Bd.*, 115, p. 17.

Ivanov, K.D. et al. (2003), "Impurities in Lead and Lead-bismuth Coolants", *Proceedings of the Fast Neutrons Reactors Conference*, Obninsk, Russian Federation, 8-12 December (in Russian).

Jacob, K.T. and J.H.E. Jeffes (1971), "Thermodynamics of Oxygen in Liquid Copper, Lead and Copper-Lead Alloys", *Trans. Inst. Miner. Metall.*, 80, p. C32.

Jacobs, H. (2002) *Untersuchung zum Sicherheitskonzept des MEGAPIE Targets in der Spallations-Neutronenquelle SINQ: Druckentwicklung im Strahlrohr der Anlage in dem angenommenen Störfall, Bruch der Strahlfenster an Targetbehälter und Sicherheitshülle*, FZK Report FZKA 6637, Forschungszentrum Karlsruhe (FZK), Karlsruhe.

Kaufman, L. and H. Bernstein (1970), *Computer Calculations of Phase Diagrams*, Academic Press, New York.

Kozlov, F.A. et al. (1983), "Liquid Metal Coolants for Nuclear Power", *Energoatomizdat,* Moscow (in Russian).

Kottowski, H.M. et al. (1991), "Lithium-Lead/Water Interaction. Large Break Experiments", *Fus. Eng. Des.*, 17, pp. 343-349.

Kranert, O. and H. Kottowski (1991), "Small Scale Lithium-Lead/Water Interaction Studies", *Fus. Eng. Des.*, 15, pp. 137-154.

Krysco, W.W. (1974), *Proceedings of the 5th International Conference on Lead*, Paris, pp. 215-221.

Kubicek, P. and T. Peprica (1983), "Diffusion in Molten Metals and Melts: Application to Diffusion in Molten Iron", *International Metals Reviews*, 28, pp. 131-147.

Kurata, Y. (2004) "Summary of PbBi-Water Interaction Experiments at CRIEPI in Japan", Presentation at MEGAPIE meeting.

Kawakami, M. and M. Goto (1973), *J. Iron Steel Inst. Japan*, 59, p. 196.

Lukas, H., S.G. Fries and B Sundman (2007), *Computational Thermodynamics: The Calphad Method*, Cambridge University Press, Cambridge.

Leung, W., H. Wagner and K. Woloshun (2003), "Experimental Results from DTHT-LBE Interaction Experiments and DTHT Irradiation Experiments", *Proceedings of the 4th MEGAPIE Technical Review Meeting*, Paris, 18-19 March.

Li, N. (2002), "Active Control of Oxygen in Molten Lead-bismuth Eutectic Systems to Prevent Steel Corrosion and Coolant Contamination, *Journal of Nuclear Materials*, 300, pp. 73-81.

Lozovoy, V.I. and V.I. Ogloblya (1981), *Akad. Nauk. SSR. Metallofiz,* 3 (1), pp. 92-96.

Maître, A. et al. (2002), "Preliminary Study of Some Parts of the Quinary System Bi-Fe-Hg-O-Pb, *J. Phys. IV France*, 12, pp. 163-174.

Martinelli, L. et al. (2010), "Nickel Solubility Limit in Liquid Lead-bismuth Eutectic", *Journal of Nuclear Materials*, 400, pp. 232-239.

Martynov, P.N. and K.D. Ivanov (1998a), "Nuclear Heat Application: Design Aspect and Opening Experiments", Proceedings of four technical meetings held between December 1995 and April 1998, pp. 177-184.

Martynov, P.N. (1998b), Performance of Works Under Contract N°501068B049630 Between RF IPPE and Research Centre Cadarache, Obninsk.

Massalski T.B. (ed.), *Binary Alloys Phase Diagrams*, The Materials Information Society, Materials Park, Ohio (1990).

Müller, G. et al. (2003), "Control of Oxygen Concentration in Liquid Lead and Lead-bismuth", *Journal of Nuclear Materials,* 321, pp. 256-262.

May, S. and D. Picot (1982), CEA Report, 82/464.

Moser, Z. (1973), *Z. Metallkd.*, 64, p. 40, cited by Zhang (2008).

Nakamura, H. et al. (1999), "Visualization of Simulated Molten Fuel Behaviour in a Pressure Vessel Lower Head Using High-frame-Rate Neutron Radiography", *Nuclear Technology,* Vol. 125.

Nash, P. (1985), "The Bi-Ni (Bismuth-Nickel) System", *Bull. Alloy Phase Diagrams*, 6, p. 345.

Orlov, Y.I. (1997), "Stages of Development of Lead-bismuth as a Coolant for Nuclear Reactors in Russia", *Int. Workshop on Physics of Accelerator Driven System for Nuclear Transmutation in Energy Production*, Trento, Italy, 28 September-03 October.

Orlov, Y.I. (1998), "The Main Impurities and Their Condition in the Pb-Bi Coolant", contract SSC RF IPPE/CEA-DRN-DER 5010 6 8 B049630, Substage 2.1, Obninsk, cited by Zhang (2008).

Otsuka, S. and Z. Kosuka (1975), "The Diffusivity of Oxygen in Liquid Lead by Electrochemical Measurements", *Metallurgical Transaction B*, 6B, p. 389.

Otsuka, S. and Z. Kosuka (1979), "Activities of Oxygen in Liquid Lead and Antimony from Electrochemical Measurements", *Metallurgical Transaction B*, Vol. 10, p. 565.

Otsuka, S. and Z. Kosuka (1981), "Further Study on the Activities of Oxygen in Liquid Pb and Sb by a Modified Coulometric Titration Method", *Metallurgical Transaction B*, Vol. 12, p. 616.

Prasad, R., V. Venugopal and D.D. Sood (1977), "A Thermodynamic Study of Lead + Bismuth Using a Transpiration Technique", *J. Chem. Thermodyn.*, 9, p. 765, cited by Zhang (2008).

Pelzel, E. (1956), *Metall.*, 10, p. 717.

Reiner, M. (1974), "Discussion of [Krysco]", *Proceedings of the 5th International Conference on Lead*, Paris, pp. 227-229.

Richardson, Webb (1954-5), *Trans. Inst. Min. Met*, 64, p. 529.

Risold, D. et al. (1995), "The Bismuth-oxygen System", *J. Phase Equilibria*, 16, No. 3, p. 223.

Risold, D., J-I. Nagata and R.O. Suzuki (1998), "Thermodynamic Description of the Pb-O System", *J. Phase Equilibria*, 19, No. 3, p. 213.

Robertson, W.M. (1968), *Trans. Met. Soc. AIME*, 242, pp. 2139-2142.

Rodigina, E.N., K.Z. Gomel'skii and V.F. Luginina (1961), *Zhur. Fiz. Khim.*, 35, p. 1799.

Rosenblatt, G. and J.R. Wilson (1969), Proceedings of Session IV on "Corrosion by Liquid Metals" of the 1969 Fall Meeting of the Metallurgical Society of AIME, Philadelphia, Pennsylvania.

Roy, P., R.L. Orr and R. Hultgren (1959), *The Thermodynamics of Bismuth-Lead Alloys*, 2nd Techn. Report Ser. No. 126, Issue No. 2, MRL, University of California, Berkeley.

PSI (Paul Scherrer Institute) (2002), *Safety Report About the MEGAPIE Experiment with a Lead Bismuth Eutectic Target in the SINQ Neutron Source of PSI West*, PSI, Villigen.

Saito, J. (2005), "Reaction Behavior of Lead-bismuth Eutectic with Liquid Sodium", *13th International Conference on Nuclear Engineering (ICONE 13)*, Beijing, China, 16-20 May 2005.

Shimoji, M. and T. Itami (1986), "Diffusion and Defect Data", *Solid State Data*, Vol. 43.

Shunk, F.A. (1969), *Constitution of Binary Alloys*, McGraw-Hill, New York.

Sibamoto, Y. et al. (2001), "Neutron Radiography Flow Visualization of Liquid Metal Injected into an Empty Vessel and a Vessel Containing Saturated Water", *Nucl. Tech.*, 133, pp. 119-132.

Sobolev, V. and A. Gessi, Chapter 2, this document.

Steen, H. and O. Grinder (1982), "Short Communication on Solubility of Oxygen in Lead and Two Lead Alloys", *Scand. J. Metall.*, 11, pp. 152-157.

Stevenson, D.A. and J. Wulff (1961), "Liquid-Solid Phase Distribution Studies in the Systems Iron-Lead, Cobalt-Lead, Chromium Tin and Nickel-Silver", *Trans. Met. Soc. AIME*, 221, pp. 271-275.

Suzuki, T. et al. (2003), "Analysis of Gas-Liquid Metal Two Phase Flows Using a Reactor Safety Code SIMMER III", *Nuclear Engineering and Design*, Vol. 220.

Szwarc, R., K.E. Oberg and R.A. Rapp (1972), "The Diffusivity and Solubility of Oxygen in Liquid Lead from Electrochemical Measurements", *High Temperature Science*, 4, pp. 347-356.

Taskinen, A. (1979), "Thermodynamics and Solubility of Oxygen in Liquid Lead", *Scandinavian Journal of Metallurgy*, 8, pp. 185-190.

Vaajamo, I., P. Taskinen and J.A. Gisby (2013), "A Solubility Study and Thermodynamic Description of the System Fe-Ni-Pb", *Calphad*, Vol. 42, pp. 66-75.

Venkatraman, M. and J.P. Neumann (1988), "The Bi-Cr (Bismuth-chromium) System", *Bull. Alloy Phase Diagrams*, 9, p. 271.

Walker, R.A. and J.N. Pratt (1970), "The Solubilities of Bismuth and Tellurium in Liquid Sodium", *Journal of Nuclear Materials*, 34, pp. 165-173.

Weeks, J.R. and A.J. Romano (1969), "Liquidus Curves and Corrosion of Fe, Ti, Zr and Cu in Liquid Bi-Pb Alloys", *Corrosion*, Vol. 25, No. 3, pp. 131-136.

Weeks, J.R. (1998), "Liquid Metal Compatibility of Structural Materials with Liquid Lead-bismuth and Mercury", *1997 TMS Annual Meeting*, Orlando, FL, 9-13 February, M.S. Wechsler et al. (eds.), The Minerals, Metals & Materials Society (TMS).

Worner, H.W. (1940), "The Determination of Oxygen in Lead and Some Lead Alloys", *J. Inst. Met.*, p. 131.

Yoon, S.W. and H.M. Lee (1998), "A Thermodynamic Study of Phase Equilibria in the Sn-Bi-Pb Solder System", *Calphad*, Vol. 22, No. 2, pp. 167-178.

Zhang, J. and N. Li (2008), "Review of the Studies on Fundamental Issues in LBE Corrosion", *Journal of Nuclear Materials*, 373, p. 351.

4. Chemistry control and monitoring systems*

4.1 Introduction

The development of heavy liquid metal chemistry control and monitoring is one of the issues that is critical for nuclear systems using lead alloys either as a spallation target or as a coolant from the contamination control point of view as well as from the corrosion point of view.

Corrosion rates at temperatures below 450°C are rather low and satisfactory operation in this temperature range can be achieved using many materials, including stainless steels and alloy steels. However, low temperature operation comes at a sacrifice of thermal efficiency, which will have a direct effect on the economics of plant operation for any power producing system. Thus, for applications where economic power generation is the goal, reduced temperature operation is not an acceptable solution. This is especially true for fast reactor systems where capital cost is generally considered higher than that for current light water reactor systems. In the case of ADS and other non-critical systems, however, operation at a temperature for which corrosion becomes acceptable is an option. Low temperature operation does not, however, eliminate the production of spallation and activation products or other contaminants, such as the oxygen or the corrosion products.

Thus, for operation of an HLM nuclear system, chemistry control and monitoring is a critical issue for at least three distinct requirements:

1) Contamination, the assurance of stable hydrodynamics and heat transfer during service lifetime requires that PbO production be avoided. Lead oxide production may result in plugging due to mass transfer in a non-isothermal system. Also, deposits of other contaminants may eventually reduce the overall heat transfer capacity, etc.

2) Corrosion and/or dissolution must be kept to a minimum to ensure sufficient resistance of the structural materials during the expected service lifetime. This might require the use of active oxygen control to promote and maintain a protective film, although other methods could be applied (see Chapter 6).

3) Activation due to corrosion, spallation and fission products might require liquid metal specific control to ensure safe management of the operation and maintenance phases.

The satisfaction of the above requirements makes chemistry control an essential element of nuclear system operation: control of oxygen and other relevant impurities including corrosion products, spallation and activation products. To this end, control processes, in conjunction with monitoring systems, must be developed and/or qualified for application to an ADS system for both the coolant loop and the spallation target loop. These issues will be discussed in detail in the following sections, which were updated from the previous version of the handbook in order to consider the data recommended in Chapter 3 as well as the latest understandings in the chemistry of liquid lead alloys.

* Chapter lead: J-L. Courouau.

4.2 Oxygen control in lead and LBE systems

Oxygen is clearly the most important chemical compound for any lead alloy system, because of its potential contamination rate, as well as because of its consequences on the contamination by solid oxides, and its main influence on the corrosion rate of iron-based structures (Shmatko, 2000; Zrodnikov, 2003; Martynov, 2003) (see also Chapter 6).

Oxygen results from start-up operations, from the maintenance phase and possibly from incidental contamination as well. During these operating steps oxygen saturation is more than likely (Courouau, 2003a, 2005a). On the contrary, its contamination source should be negligible during normal operating mode. If the oxygen concentration must be adjusted to a specified value for corrosion control, the issue of implementing an oxygen contamination source arises. Contrarily, systems for oxygen purification would be necessary for the start-up, restart or maintenance phases. Therefore, the following points that describe the requirements for operating a nuclear lead alloy system will be detailed hereafter:

1) the upper limit for oxygen to avoid contamination by coolant oxides;
2) the lower limit for oxygen to enhance corrosion protection through the self-healing oxide layer, which depends on the structural material – the iron-based alloy will be treated for illustration;
3) the oxygen control policy for nuclear operations, including the method to select the oxygen activity.

Finally, the issue of the homogeneity of the oxygen, which is present in very low concentrations in the lead alloys and submitted to various processes either consuming or releasing it, will be shortly discussed.

4.2.1 *Upper oxygen limit for operational control*

The contamination of coolant by its oxides is defined by the solubility of oxygen in lead alloys, giving a maximum allowable oxygen chemical activity in the liquid metal. The following relations define these limits for pure lead and LBE (Chapter 3), for which C_o^* stands for the dissolved oxygen concentration expressed in weight percentage:

- Lead (for 300°C < T < 1 100°C):

$$\log C^*_{o(\text{wt.\%})} = 3.23 - \frac{5043}{T_{(K)}} \tag{4.1}$$

- LBE (for 400°C < T < 740°C):

$$\log C^*_{o(\text{wt.\%})} = 2.25 - \frac{4125}{T_{(K)}} \tag{4.2}$$

These relations are recommended based on the assessment of the latest data available, for which a correct agreement is observed, and which is more accurate when compared to the previously used relation for the LBE (Chapter 3).

The main oxide formed in liquid LBE is lead monoxide (PbO), as it is the most stable oxide when compared to other lead oxides and bismuth oxides (Gromov, 1998). The upper oxygen chemical activity needed to avoid contamination is then defined by the lead monoxide solubility, although in case of a large oxygen contamination, both lead and bismuth oxides will be formed.

In order to calculate dissolved oxygen concentration, the hypothesis of an ideal solution is often made, and Henry's law is applied to the dissolved oxygen. Assuming solid lead monoxide as the standard state for the oxygen in lead alloy, oxygen activity, a_o, shall be equal to unity when saturation is reached (Borgstedt, 1987):

$$a_O = \frac{C_o}{C_o^*} \tag{4.3}$$

where C_o is the dissolved oxygen concentration and C_o^* is the saturated oxygen concentration.

The operating specification to avoid any oxide precipitation in the coolant is then:

$$a_O \leq 1 \quad \text{or} \quad C_o \leq C_o^* \tag{4.4}$$

This specification must be ensured for all operating temperatures at any point of the loop, both in the liquid bulk as well as at the wall interface.

Table 4.2.1 presents some values for the oxygen solubilities in lead and lead-bismuth eutectic at relevant temperature for a nuclear system operation with LBE using Eqs. (4.1) and (4.2). The sodium oxygen solubility values are given for comparison as being always between 2 and 5 orders of magnitude higher than the lead or LBE values. A main operating consequence is that the safety margin to avoid oxide precipitation is very limited, especially in the low temperature range, and its potential risk of circuits clogging is then a real issue. Indeed, any small change in the coolant chemical conditions may very quickly induce oxide precipitation that is not acceptable for a nuclear system.

Table 4.2.1: Oxygen solubilities in lead alloys and pure sodium expressed in weight percentage*

	130°C	200°C	330°C	400°C	500°C	600°C	700°C
Lead			7.4E-06	5.5E-05	5.1E-04	2.8E-03	1.1E-02
LBE	1.0E-08	3.4E-07	2.6E-05	1.3E-04	8.2E-04	3.4E-03	1.0E-02
Na**	4.8E-04	2.2E-03	1.5E-02	3.0E-02	6.6E-02	1.2E-01	2.0E-01

* Concentration expressed in weight percentage converts to μg/g (or ppm) by the multiplication by 104 or by addition of 4 in the log-type relation.

** Thorley (1989) sodium solubility relation log C^* = 1.153 – 1 803/T (114-526°C).

The upper limit for the oxygen that will be allowed in any non-isothermal system is generally defined by the point where oxide is formed first: the surface of the coldest point because of the thermal gradient between the wall and the liquid bulk, and because oxide can be formed there and thrown elsewhere in the circuits (Shmatko, 2000) (see Figure 4.2.2). For illustration, if the minimum temperature of the surface of a LBE system is 200°C, the upper oxygen limit for operation will be 3.4 10^{-7} wt.% (0.0034 ppm in weight).

Attention must be paid to the cold shutdown temperature which must comply with this specification.

4.2.2 *Lower limit of oxygen for operational control*

Almost all of the elements of significance for structural material development have a lower equilibrium oxygen partial pressure than lead and bismuth for their oxides. It is then possible, from a theoretical point of view, to promote a protective oxide film by assuring that the oxygen potential in the liquid metal is above the potential for film formation on the structural material for use in the high temperature range (> 450°C) (see also Chapter 6). This active oxygen control scheme for corrosion protection has been

widely studied for steel structures by the formation of an iron-chromium-oxide film (magnetite and spinel oxide) (Gorynin, 1998). Russian test data on steels in liquid lead alloy have shown that there exist three different yet distinctive corrosion regimes as a function of oxygen concentration. When the oxygen concentration is too low for a stable oxide film, dissolution of metal occurs. At high oxygen concentrations, rapid oxidation occurs which results in degradation of the structure and/or the formation of Pb oxides. Between these two extremes, a transition region exists where the kinetics transitions between dissolution and oxidation and the overall reaction rate is kept very small (Ballinger, 2004).

The reliance of an oxide film based on an alloying element of the structure requires that the oxygen potential be controlled within a narrow band, the upper oxygen potential being defined by Pb oxide contamination, and the lower oxygen potential by the formation conditions of the protective oxide. The following structural elements are foreseen for corrosion protection by the formation of oxide film, except iron: Cr, Zr, Si, Al (Ballinger, 2004). ZrO_2, Al_2O_3, SiO_2 or SiC can be considered as low-solubility materials or used as barriers layers to limit the corrosion. From the viewpoint of active oxygen control, the lower oxygen limit is initially determined by the relative thermodynamic stability of the oxide when compared to Pb oxide, the more stable the lower the oxygen potential, and the largest operational temperature range.

First, the stability of various oxides is compared using their free energies of formation (Ellingham diagram). Reactions are written for the consumption of one mole of di-oxygen:

$$\frac{2x}{y} Me_{(dissolved)} + O_{2(dissolved)} \longrightarrow \frac{2}{y} Me_X O_Y \tag{4.5}$$

The unit is then expressed in J/mol of oxygen O_2. Calculation is made with HSC database software (HSC, V4.1), and the coefficients of the linear regression in the temperature range 400-1 000 K (127-727°C) are computed to give the standard free enthalpies of formation in the useful operating range, and reported in Table 4.2.2. Indeed, the construction of the $\Delta G - T$ diagram is useful to determine the relative areas of stability for oxides, using the activities product of the previous reaction:

$$\Delta G = RT \cdot \ln P_{O_2} \text{ and } \Delta G^o = RT \cdot \ln P^o_{O_2} \tag{4.6}$$

All points of such a $\Delta G - T$ diagram are then meaningful:

- For $\Delta G > \Delta G^o$, the system is outside its equilibrium conditions, and only oxide is present.
- For $\Delta G = \Delta G^o$, the system follows its redox equilibrium, where both oxide and the metal are present.
- For $\Delta G < \Delta G^o$, the system is outside its equilibrium conditions, and no oxide is stable.

The corresponding $\Delta G - T$ diagram is plotted in Figure 4.2.1, presenting clearly the more stable and the least stable oxides from a thermodynamic point of view in liquid lead alloy. The isoconcentration lines of dissolved oxygen for respectively 10^{-6} wt.% and 10^{-14} wt.% (0.01 and 10^{-10} ppm in weight) in LBE melt are also plotted for comparison. In particular, it can be seen that the window for an active oxygen control for corrosion protection by iron oxide film corresponds to the narrow area delimited by the PbO line (below) and the Fe_3O_4 line (above). Alternatively, all other potential oxides for other structure candidate materials, SiO_2, Cr_2O_3, Al_2O_3, and ZrO_2 present oxides that will be stable over the whole range of oxygen potential in the liquid metal alloys, including in the higher temperature range. One has to keep in mind that thermodynamically possible reactions might be kinetically controlled; actual reaction rates must be studied by experimentation.

Table 4.2.2: Main oxides free enthalpy coefficients for the 400-1 000 K temperature range, and for one mole of oxygen computed from HSC v4.1

$\Delta G^o = \Delta H^o - T \cdot \Delta S^o$	ΔH^o (400-1 000 K) kJ/mol	ΔS^o (400-1 000 K) J/mol/K
4/3 Al + O_2 = 2/3 Al_2O_3	-1 117.15	-209.8
4/3 Bi + O_2 = 2/3 Bi_2O_3	-389.14	-192.6
4/3 Cr + O_2 = 2/3 Cr_2O_3	-755.41	-171.8
4/3 Fe + O_2 = 2/3 Fe_2O_3	-544.13	-171.2
3/2 Fe + O_2 = 1/2 Fe_3O_4	-551.99	-156.9
2 Fe + O_2 = 2 FeO	-529.19	-131.4
2 H_2 + O_2 = 2 H_2O(g)	-490.31	-104.5
2 Ni + O_2 = 2 NiO	-473.69	-175.7
3/2 Pb + O_2 = 1/2 Pb_3O_4	-357.93	-192.1
2 Pb + O_2 = 2 PbO (litharge < 762 K)	-439.87	-198.8
2 Pb + O_2 = 2 PbO (massicot)	-437.61	-199.1
Pb + O_2 = PbO_2	-273.60	-195.5
Si + O_2 = SiO_2	-909.32	-179.6
Zr + O_2 = ZrO_2	-194.54	-187.21

Figure 4.2.1: Ellingham diagram for lead-bismuth eutectic melt with indication of some oxygen concentration expressed in weight percentage

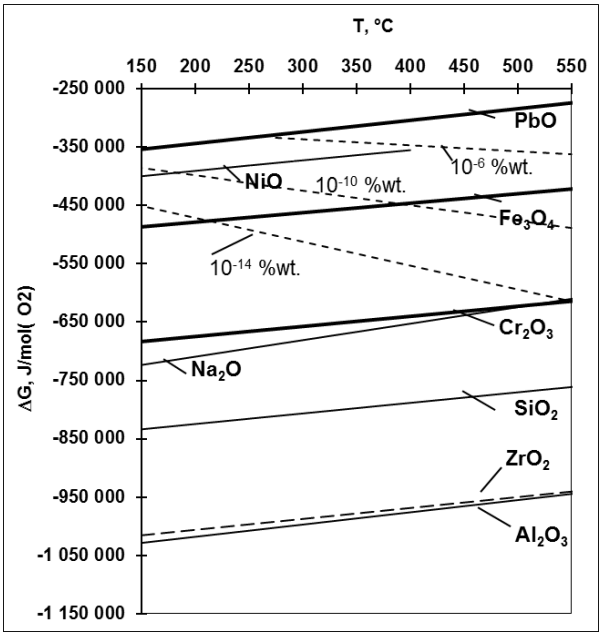

Figure 4.2.1 is plotted with activity of all impurities equal to unity, meaning that all elements are dissolved in the LBE up to their solubility limit. This is unlikely to happen in a nuclear system where impurities from the alloying elements of the structure as well as dissolved oxygen are subject to mass transfer within the circuits, including release to the liquid metal by corrosion/dissolution of the structure as well as precipitation/oxidation, so the actual activity results from a dynamic equilibrium, which may be very far from unity. Detailed analysis of the iron-based structure is given hereafter to illustrate the methodology used for specifying the lower limit of the oxygen for operational control.

Assuming iron-based alloys and corrosion protection through a self-healing oxide layer, the oxygen potential must ensure the conditions for the formation of iron oxide in any part of the system, in the liquid bulk as well as at the wall interface, for all operating conditions. Indeed, the magnetite being the least stable oxide of the layer, it defines the minimum allowable oxygen concentration. The same kind of development could similarly be made for another kind of protective oxide. The reaction of the iron oxidation in liquid lead alloys is assumed to be as follows:

$$\frac{3}{4}\mathrm{Fe} + \mathrm{PbO}_{(\mathrm{dissolved})} \longrightarrow \frac{1}{4}\mathrm{Fe_3O_4} + \mathrm{Pb}_{(\mathrm{liquid})} \tag{4.7}$$

where oxygen is supposed in solution in the form of dissolved PbO below its saturation limit. This is equivalent to consider that a cloud of Pb atoms surrounds the O atom. Dissolved oxygen chemical activity is then referring to dissolved PbO activity. Computed from Table 4.2.1, the standard free enthalpy of reaction is then:

$$\Delta_r G^o{}_{(\mathrm{J/mol})} = -57190 - 21.1 \cdot T_{(\mathrm{K})} \tag{4.8}$$

Lead activity is equal to unity in pure lead solution, and is given by the following Russian relation in LBE solution as quoted in Courouau (2002b), which is slightly lower than 0.45:

$$\ln a_{\mathrm{Pb}} = -\frac{135.21}{T_{(\mathrm{K})}} - 0.8598 \tag{4.9}$$

The iron solubility in lead and LBE is expressed as follows (Gromov, 1998; IAEA, 2002), and as illustrated in Table 4.2.3 (relations proposed in Chapter 3):

- Lead (for 330°C < T < 910°C):

$$\log C^{\mathrm{s}}_{\mathrm{Fe(wt.\%)}} = 0.34 - \frac{3450}{T_{(\mathrm{K})}} \tag{4.10}$$

- LBE (for 550°C < T < 780°C):

$$\log C^{\mathrm{s}}_{\mathrm{Fe(wt.\%)}} = 2.01 - \frac{4380}{T_{(\mathrm{K})}} \tag{4.11}$$

Table 4.2.3: Iron solubilities in pure lead, LBE and pure sodium expressed in weight percentage*

	130°C	200°C	330°C	400°C	500°C	600°C	700°C
Lead	6.1E-09	1.1E-07	4.2E-06	1.6E-05	7.5E-05	2.4E-04	6.2E-04
LBE	1.4E-09	5.7E-08	5.6E-06	3.2E-05	2.2E-04	9.9E-04	3.2E-03
Na**	3.2E-10	1.0E-08	7.9E-07	4.0E-06	2.5E-05	1.0E-04	3.1E-04

* Concentration expressed in weight percentage converts to μg/g (or ppm) when multiplied by 10^4.

** Sodium solubility relation recommended by Borgstedt (1987).

Unlike the liquid sodium, the iron presents solubility in liquid lead alloys of the same order of magnitude when compared to oxygen. This fact is one of the keys of lead alloy chemistry understanding: no dominant chemical species is found in the lead alloys for all operating conditions.

The activity product of the reaction of formation of magnetite in lead alloys is then as follows for equilibrium conditions:

$$\ln\left(a_O \cdot a^{3/4}{}_{Fe}\right) = \ln a_{Pb} + \frac{\Delta_r G^o}{RT} \tag{4.12}$$

When the iron reaches saturation at the liquid metal interface, the iron activity equals one, and the minimum allowable oxygen activity at the structure interface for assuring magnetite stability can then be calculated from Eq. (4.12). However, for a non-isothermal system where mass transfer occurs, the actual activity results from a dynamic equilibrium, which is most probably far from unity, so that the real oxygen concentration required for maintaining the magnetite thermodynamically stable could be orders of magnitudes higher. This is discussed in more detail hereafter, as the recent understanding of the oxide scale formation allows discussing either the conditions for the formation of the oxide, or the conditions of its dissolution, in other words: the conditions of its thermodynamic stability.

According to the oxidation mechanism recently evidenced (Martinelli, 2008), the oxide growth occurs both at the liquid/oxide interface and at the steel/oxide interface leading to duplex oxide scales. FeCr spinel oxide is formed at the inner interface by reaction of the steel with molecular oxygen that transfers through connected nanoporosities in the oxide scales according to the "available space model", while magnetite is formed at the liquid/oxide interface by reaction of iron, which diffused from the steel matrix throughout the oxide scales with oxygen dissolved in the liquid metal diffusing through the boundary layer from the liquid metal bulk. The conditions for the formation of the magnetite will then be derived from Eq. (4.12) taking into account the iron activity in the magnetite and the dissolved oxygen activity at the liquid metal/oxide interface. As the kinetics of diffusion in the oxide and the conditions of convection and mass transfer in the liquid metal boundary layer will control the actual activities at the interface, both iron and oxygen activities are unknown, so that thermodynamic calculations are made hereafter by taking into account the liquid metal bulk activity for dissolved oxygen and steel matrix iron activities as first approximations, although both activities are most probably lower due to oxygen transfer from the liquid metal bulk and iron diffusion though the oxide scale from the steel matrix. Although complex, ongoing research is in progress to determine the actual oxygen activities at the various interfaces (Martinelli, 2008-2011).

Defining the iron activity similarly to the oxygen activity, $a_{Fe} = C_{Fe}/C'_{Fe}$, it is equal to one when the iron is saturated in the solution, and defining the minimum oxygen concentration required for effective corrosion protection for iron-based alloys, $C_{o\,min}$ (wt.%), the following relations are derived:

- Lead:

$$\log C_{O\,min(\%wt.)} = -\frac{3}{4}\log C_{Fe(\%wt.)} + 2.38 - \frac{10618}{T_{(K)}} \tag{4.13}$$

- LBE:

$$\log C_{O\,min(\%wt.)} = -\frac{3}{4}\log C_{Fe(\%wt.)} + 2.28 - \frac{10456}{T_{(K)}} \tag{4.14}$$

If the system enters the dissolution area, and if *in situ* oxide layers protect the structure, there will be a certain time lag corresponding to the time required to dissolve the magnetite and spinel oxide layers. This somehow introduces a safety margin. Conversely, when going back to the right oxygen level, there will be some delay. During these periods, simple measurement of oxygen is not enough, as oxygen concentration will be kept stable as defined by the iron oxide chemical reaction equilibrium. This is analogous to a buffer effect. The only way to detect if the oxide layer is dissolving or growing would be to measure directly its thickness using an electrical resistance probe measurement (Provorov, 2003).

The lower limit for the oxygen that will be allowed in any non-isothermal system is generally defined by the point where the iron oxide will be dissolved first: the surface of the hottest point because of the thermal gradient between the wall and the liquid bulk. For a primary reactor circuit, the maximum temperature at cladding surface generally defines the hot spot. For illustration, if the maximum temperature of the surface of an LBE system operating with a structure made of iron-based alloy is 650°C, the lower oxygen limit for ensuring the iron oxide formation would be about 10^{-7} wt.% with LBE saturated in iron.

4.2.3 *Specifications for active oxygen control*

The oxygen concentration areas of operation to ensure both no contamination, required for any system, and possibly corrosion protection for higher operating temperature are similar for the liquid lead or the lead-bismuth eutectic:

$$C_{O\,min} \leq C_O \leq C_O^* \tag{4.15}$$

The operating specifications for oxygen are evaluated from Figure 4.2.2 drawn with the previous relations illustrated for active control of iron-based structure, keeping in mind that for other non-ferrous structure materials, the specification for active oxygen control for corrosion protection would be less restrictive.

Figure 4.2.2: Oxygen specifications in LBE

Bulk temperature of 400-480°C, 520°C at hot spots and 350°C at cold spots, showing in shaded area the allowable oxygen operating range, as well as the contamination ($C_O = C_O^*$), the oxidation ($C_{O\,min} < C_O < C_O^*$) and the dissolution ($C_O < C_{O\,min}$) areas, with $C_{O\,min}$ defined for iron activity equal to one, either considering coolant bulk temperatures or the hot and cold spots ($4.3 \cdot 10^{-5}$ wt.% at 350°C, $1.3 \cdot 10^{-5}$ wt.% at 400°C) ($1.8 \cdot 10^{-9}$ wt.% at 480°C, $5.4 \cdot 10^{-9}$ wt.% at 520°C)

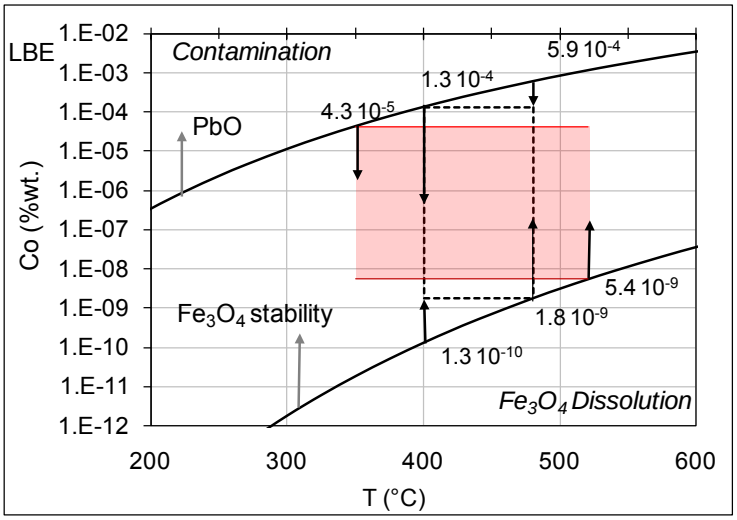

For non-isothermal systems, the temperature at the interface is different from the bulk temperature because of the heat transfer process. However, if the oxide layer protection is required, the minimum oxygen content must be ensured at the wall temperature, where the chemical reaction is actually taking place, which will define another oxygen concentration range when compared to the range defined by the liquid metal bulk temperature. As illustrated in Figure 4.2.2 where operating conditions present a bulk coolant temperature range of 400-480°C, a maximum fuel clad temperature of 520°C and a minimum steam generator wall temperature of 350°C, the resulting operating range is narrowed to $4.3{\cdot}10^{-5}$ wt.% for the upper limit to prevent coolant oxidation at 350°C and to $5.4{\cdot}10^{-9}$ wt.% to keep oxide protection at 520°C for saturated iron activity in the liquid metal ($a_{Fe} = 1$).

If the same kind of conditions is required for lead coolant, the oxygen to ensure no contamination and stability of the iron oxide would range from $1.4{\cdot}10^{-5}$ wt.% at 350°C down to $1.0{\cdot}10^{-8}$ wt.% at 520°C, which presents a similar operating window when compared to LBE.

One can note as well the larger the temperature gradient in the system, the narrower the oxygen operating window. The operating window might be reduced to a single line at 10^{-7} wt.% for liquid LBE, if the cold spot temperature is reduced to 173°C and the hot peak temperature increased to 650°C, leaving no operating margins. For higher temperature gradients, the operating window disappears, meaning the system will operate with continuous contamination and/or oxide layer dissolution. In practice, such high gradient can be decreased by reducing the efficiency of the system, meaning decreasing the temperature difference in the heat exchanger (larger exchange area, higher capital cost), or decreasing the temperature difference in between the reactor inlet and outlet (lower Carnot efficiency for energy conversion).

However, the condition that dissolved iron be present in saturated condition at the oxide/liquid interface is foreseeable in static condition, but unlikely in dynamic loop condition where mass transfer plays a role. Indeed, in a non-isothermal system, the iron is released from the hot structural wall and transferred to locations with lower temperature, where it can precipitate. If the dissolved activity is defined by the cold leg temperature, where thermodynamic equilibrium occurs, then the lowest iron concentration that can be foreseen in such a system may reasonably be assumed. Figure 4.2.3 illustrates this: decreasing the iron concentration reduces the oxidation area, the higher the temperature the higher the reduction, and the lower the iron concentration and the higher the reduction. In the example presented in Figure 4.2.3 the oxygen operating window is somewhat narrowed from $5.4{\cdot}10^{-9}$ to $7.3{\cdot}10^{-8}$-$4.3{\cdot}10^{-5}$ wt.%. This assumption supposes, in fact, first, that the iron content is constant over the circuit, second, that it is saturated at the cold point temperature, and lastly, that the bulk concentration equalise the interface concentration. In other words, it supposes a total deposition of iron at each passage of the coolant in the cold leg and a negligible iron release at each passage for a significant modification of the iron concentration, which is assumed as conservative as regards the operating window for dissolved oxygen.

This operating window clearly presents some operational margins for the oxygen control, as well as some margins for the real concentrations at the interface although unknown. For operation in nuclear system, one should prefer this thermodynamic set of specifications as much as possible, even though the oxide dissolution kinetics could be assumed as slow. Indeed, nuclear operation means long service life time, for which kinetics, usually negligible, may eventually affect the system over the long term.

In any case, it seems reasonable to verify the constant oxygen concentration hypothesis over a pilot scale experiment representative of the required system, in order to confirm the choice and to check that there is no limitation from the kinetics, either for the oxide formation or for the oxide dissolution. Based on these comments, it appears as

well that the initial oxide formation for corrosion protection would most probably require specific operations, as the conditions for the effective oxide growth would most probably be different from normal operating conditions.

Figure 4.2.3: Oxygen specifications in LBE with the iron saturated at the cold spot and with the oxygen dominant species hypothesis for preferred operational range

Bulk temperature of 400-480°C, 520°C at hot spots and 350°C at cold spots, showing in shaded area the allowable oxygen operating range considering the contamination ($C_O = C_O^*$) at the cold spot and the lower threshold defined by the oxygen dominant species at the hot spot ($4.3 \cdot 10^{-5}$ wt.% at 350°C and $3.04 \cdot 10^{-6}$ wt.% at 520°C) as well as the lower limit that is defined for dissolved iron supposed constant and saturated at the cold spot (10^{-5} wt.% at 350°C for iron)

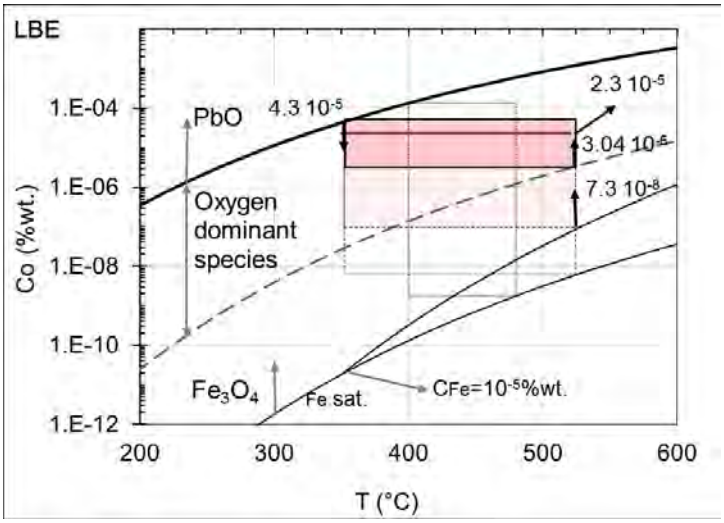

In addition to this analysis, which allowed determining a conservative operating window for the dissolved oxygen where both conditions for contamination control and oxide stability could be thermodynamically ensured, one should consider the effect of the mixed O-Fe domain. The chemical interactions among species presenting equivalent concentrations are believed to introduce an unnecessary complexity in the chemical monitoring of the liquid alloy.

Indeed, the iron concentration is difficult to measure and impossible to monitor online up to now. To date, the lower detection limit is $5 \cdot 10^{-4}$ wt.% using chemical analysis and could possibly be lowered to $5 \cdot 10^{-5}$ wt.%, which is still higher than the expected iron concentration. There is no straightforward solution to control the iron content, but oxygen should be controlled and monitored online to keep control on one parameter.

The oxygen dominant species domain can then be preferred from an operational point of view, so as to set the system in oxygen controlled chemistry rather than in a mixed domain. As illustrated in Figure 4.2.3 (blue dotted line) where the oxygen dominant species line is plotted, the new oxygen window would then be ranging from $3.04 \cdot 10^{-6}$ wt.% to $4.3 \cdot 10^{-5}$ wt.%. A choice for an oxygen specification could be set to the mean value, $2.3 \cdot 10^{-5}$ wt.% for liquid LBE.

There are many other impurities that would be present in a real liquid metal system apart from iron and would interact with dissolved oxygen as well, which further supports the recommended choice for the oxygen dominant species area. In this domain, any variation of oxygen due to other impurities should be negligible, so that the oxygen control would be steadier.

As a consequence, the oxygen specification is determined using the following equation, as this complies with the contamination requirement, the magnetite stability area as well as the oxygen dominant species area:

$$\begin{cases} C_O\left(\text{Contamination} \middle/ \text{and corrosion control}\right) = \dfrac{C_o^*(\text{cold spot}) + C_O^{dom}(\text{hot spot})}{2} \\ \log C_O^{dom}(\%) = 2.08 - \dfrac{5974.85}{T(K)} \; for\ LBE \;\&\; \log C_O^{dom}(\%) = 2.15 - \dfrac{6067,29}{T(K)} \; for\ lead \end{cases} \quad (4.16)$$

where the oxygen dominant chemical species threshold, C_O^{dom}, is determined by equating the number of moles of oxygen and iron in the same volume of liquid alloys.

This thermodynamic analysis was made thanks to some assumptions and could be more or less well applied to perlite steel (Fe 100%). Therefore, real operating limits should be measured on test facilities in representative operating conditions and for relevant materials. These limits will definitely be influenced by alloying elements like Cr or Al. Ferritic martensitic steels containing around 10% Cr form duplex oxide layers with a dense spinel layer below the magnetite which acts as a diffusion barrier for iron and has an oxygen activity some orders of magnitude lower than that of magnetite. Therefore, if the magnetite layer were dissolved in the loop by LBE, the stable, dense spinel layer would prevent the steel from dissolution attack. Alloying Al into the steel surface should also provide a stable protective oxide layer in LBE containing oxygen.

The cold shutdown temperature must, in principle, comply with this specification, so that the condition of the cold spot temperature and cold shutdown temperature would have to be analysed when available.

As the oxygen is supposed constant over the non-isothermal circuit, strictly speaking only one oxygen sensor should be required to monitor the oxygen concentration, but this will require validation on test facilities in representative operating conditions and for relevant materials.

4.2.4 *Policy for a nuclear system*

Oxygen control is thus a basic requirement for relevant nuclear systems for which long service lifetime is expected. This translates to interventions for components and fuel handling, repair and maintenance, requiring oxygen purification before any restart, along with a requirement for an operating temperature as high as possible, which might require corrosion control by self-healing oxide layer on the structural iron-based materials.

Contamination represents the main issue during the initial operations (first filling, start-up…) (Ivanov, 2003a; Courouau, 2004c, 2005a), as well as during the maintenance and repair phases: air ingress can occur and the oxygen is released from the structural materials as well as from the LBE itself. It is critical to ensure that the liquid metal is kept clean and that no solid oxides are formed, as these could possibly clog narrow sections of the facility, or deposit on the heat exchanger surface, such that the overall cooling capacity of the system can be affected. However, it is reported (Martynov, 2005), and usually well observed, that there are no difficulties during the start-up of facilities from the viewpoint of the coolant purity and cleanliness, meaning that a few per cent of solid lead oxide in the liquid metal melt appears to remain compatible with flowing conditions. However, oxide accumulation over long-term operation, if not treated regularly, will eventually hinder facility operation by affecting its cooling capacity (clogging, deposits on pipes). The amount of solid oxide and circuit deposits were recorded up to 5 wt.% of the coolant mass in the circuit (Martynov, 2005). These deposits are mainly composed of PbO and LBE, with traces of iron, and are not affected by high temperature or by low oxygen concentration. The occurrence of a two-phase flow is not acceptable for nuclear operation, so the contamination must first be reduced to the minimum, and systems for regular purification must be implemented (Martynov, 2005).

Known major oxide slag formation failures date back from the 1960s: the initial run of the KV/27 land nuclear reactor based at IPPE and the project 645 nuclear submarine failure on cruise (Ivanov, 2003b). For the latter, a sudden ingress of slag in the core during sea trials in 1968 caused a loss of power due to negative temperature reactivity effect. The crew tried to restore the power by levelling off the control rods that led to partial melting of the core. In fact, there were at least two sources of contamination for the coolant: oxygen accumulated during the maintenance phases and oil contamination from the rotating shaft of the primary pumps. As there were no quality monitoring devices or purification processes, the slow, ongoing contamination and accumulation could not be detected or treated, eventually leading to the nuclear failure of the system.

By contrast, during normal operating mode, oxygen contamination sources are negligible, such that, due to the various sources of oxygen consumption, low or very low oxygen content in the liquid metal loop can be expected (Shmatko, 2000). Corrosion control through active oxygen control could then be critical during that operating period, depending on the choice of materials, and the operating temperatures (Weisenburger, 2014). For iron-based alloys and for temperatures higher than 450°C, for which the corrosion rates by dissolution become significant, active oxygen control would be required. The use of other, low-solubility materials such as composite SiC, ceramic Al_2O_3 and ZrO_2, which present low solubility in lead alloys or might be applied on substrate materials as barriers layers (Ballinger, 2004), may present such a large area of use as regards the oxygen that the lower oxygen limit may not be achievable in practice, excluding any requirement for active oxygen control.

The requirements for oxygen control systems could then be divided into:

1) oxygen purification during start-up or restart to prevent the formation of lead monoxide;

2) active oxygen control for corrosion protection during normal operating mode, and possibly at the initial stage to promote the formation of a protective oxide layer.

The first requirement consists in ensuring the contamination control in any part of the circuit and for any operating condition, in order to avoid the oxide formation of primarily the coolant oxides. This requirement is common to all nuclear systems.

The second requirement consists in active oxygen control for promoting a protective oxide film formation on the structure by controlling the oxygen potential in the liquid metal. This requirement depends on the design specifications of the systems, firstly its operating temperatures, and then on the choice of the materials.

If no corrosion control is required, the contamination specifies the upper threshold for the oxygen control as follows:

$$C_o \text{ (contamination control only)} \leq C_o^* \text{(cold leg wall temperature)} \qquad (4.17)$$

This determination was made for the MEGAPIE target (Fazio, 2008), thanks to the choice of low operating temperature (< 400°C peaks) for the short service lifetime (6 months). Figure 4.2.4 represents the expected oxygen concentration during its service lifetime, from its start-up tests to the on-beam operations. Its service lifetime was assessed as compliant with the corrosion by dissolution of the steel at the chosen low operating temperature. However, Figure 4.2.4 clearly indicates that the conditions for dissolution would be achieved after a certain delay, necessary for the residual oxygen present in the liquid bulk as well as the residual oxide layer present on the steels to dissolve, which may take weeks or months depending on the initial oxide layer and the production of hydrogen and spallation products. This time lag will limit the overall corrosion later on.

Figure 4.2.4: Oxygen expected behaviour for the MEGAPIE target

During start-up operation (integral test stand – MITS), and during beam steady-state operation where the oxygen will be reduced first down to the iron oxide stability threshold, and then even further down when all iron oxide will be reduced after a certain delay (Courouau, 2005a)

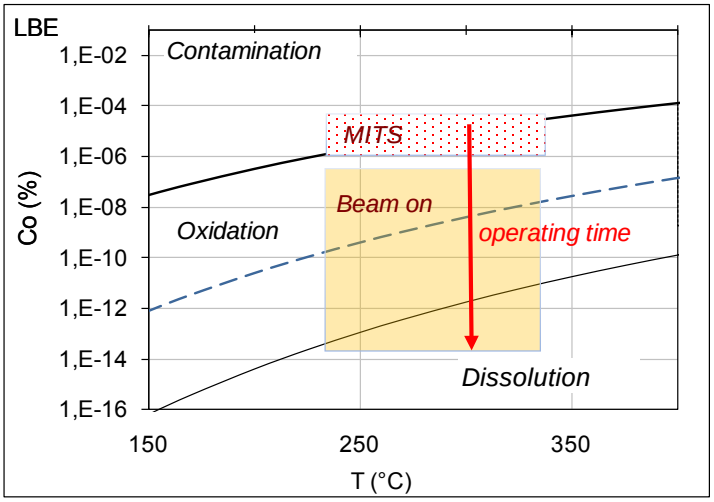

4.2.5 *Oxygen control systems*

The first requirement consists in ensuring the contamination control in any part of the circuit and for any operating condition, firstly in order to avoid oxide formation of the coolant oxides. This requirement is common to all nuclear systems.

For any nuclear lead alloys circuits, it is necessary to provide the following systems for the oxygen control:

- oxygen measurement systems for online monitoring for the cover gas and the liquid metal;
- oxygen control systems for purification, and possibly for active oxygen control.

Indeed, the oxygen will behave accordingly between the cover gas and the liquid phase in normal operating condition, where equilibrium will most certainly be reached. As the main contamination sources are not part of normal operation, it is important to be able to detect the transient due to contamination as soon as possible. As the transient could be very different from one phase to another, because of the large difference in volume, oxygen measurement in both media is required. This was the main lesson learnt from the 1990 air contamination at sodium-cooled fast reactor SUPERPHENIX, where only liquid metal quality sensors were implemented. Although the plugging-metres were actually indicating the contamination, the correct interpretation did not take place. Since then, and as was already performed on sodium-cooled fast reactor PHENIX since the beginning, gas chromatography of the cover gas allows detecting any variation of nitrogen content that will allow detecting any air ingress quickly, as the oxygen reacts quickly with sodium.

The oxygen monitoring system for the liquid metal bulk, also referred to as the oxygen sensor, is part of a complete development in itself and will be detailed hereafter in a specific section. Measuring devices for the oxygen in the gas phase are commercially available.

The oxygen control processes will be briefly detailed hereafter.

Processes for oxygen control in lead-bismuth systems are basically of two different kinds:

- gas phase control;
- solid phase control.

The principle of the gas phase control is based on gas/liquid equilibrium between the cover gas and the liquid bulk when the liquid is below saturation. Controlling the oxygen partial pressure in the gas phase would set the dissolved oxygen content.

In practice, pure oxygen or hydrogen are flowed in the cover gas, usually in dilution with argon, which is easy to achieve over flowing liquid in vessel, provided the interface is well mixed, or directly with the help of a bubbling line for a larger exchange area, in order to oxidise or reduce the liquid lead alloys according to the following reactions:

$$Pb_{(liquid)} + O_{2(gas)} \Leftrightarrow PbO_{(dissolved)} \tag{4.18}$$

$$PbO_{(dissolved)} + H_{2(Gas)} \Leftrightarrow H_2O + Pb_{(liquid)} \tag{4.19}$$

The use of hydrogen gas allows recovering from oxide accumulation after a large contamination, for start-up or maintenance, or after prolonged operation in order to restore the thermal-hydraulic performances of the system. The mechanical impact of bubbles is reported to increase the efficiency of the process by putting particles of deposit back into solutions, which should be used together with a filtration system (Papovyants, 1998). The use of getter addition, such as Zr, or Mg, will reduce the oxygen to low concentration but will simultaneously produce other solid oxides that would have to be purified by some means. Hydrogen presents the main advantages as it produces only a gaseous reaction product that is easily evacuated, in practice through the vent line.

However, it is not easy to achieve the very low oxygen potential that is required for active oxygen control in the cover gas, so the use of a ternary gaseous mixture is more practicable. Indeed, by fixing the ratio of steam over hydrogen for instance, the oxygen potential in the liquid metal is determined by the thermodynamic equilibrium (Gulevski, 1998; Müller, 2000; Shmatko, 2000). In principle, the use of other reaction systems could be used, such as the CO/CO_2 system, but are not favoured for practical and safety reasons. This can be used for the purification processes of a system where oxide film is protecting the structure, in order to protect the oxide film from dissolution (Martynov, 2005). Moreover, the use of a CO/CO_2 system should be evaluated with a special focus on the potential carburisation effects on the structural material.

The process parameters of the gaseous systems are related to the mass exchange at the gas-liquid interface that limits the equilibrium process in practice. Bubbling, which increases the exchange area greatly, favours the exchange, and then the time to reach the thermodynamic equilibrium. Temperature is the second main parameter for the hydrogen reduction of solid lead oxide (Ricapito, 2002), the higher the better, which might be related to the solubility. On the other hand, the oxidation is fast, which may lead to solid oxide formation rather than dissolved oxygen, which can be transferred and settled in another part of the facility, then requiring subsequent purification. This is why oxidation at a slower rate is better achieved when adjusting directly the gas phase composition with the help of a ternary gas mixture.

To avoid the excessive oxidation and solid oxide formation within the system, solid mass exchange was proposed (Gromov, 1996; Zrodnikov, 2003). It consists in dissolving solid lead oxide, the physical form of which is mechanically stable, e.g. pellet (Figure 4.2.5), in a device where the thermal-hydraulics are controlled. Indeed, the dissolution rate depends on temperature and flow rate (Askhadullin, 2003, 2005; Simakov, 2003), which gives rise to the automated control of the oxygen by adjusting the consumption due to the oxidation with the contamination rate delivered to the system. The solid mass exchange unit can be designed as a consumable item or for the whole service lifetime of a small

device such as spallation target, avoiding the handling requirement. Such a system would spare the need for complex gas circuits to be operated in a nuclear environment, except probably a regular venting out of the spallation residues, thus enhancing the confinement and the overall safety of the system. Expected oxygen consumption rates may present a maximum in the range of tenth of micrograms per square metre per hour (72 μg/m²/s [Schroer, 2011a]), although depending on numerous design and operating parameters. For a 10 000 m² system, the maximum oxygen required would then account to roughly 0.7 g/h. Accurate assessments of the oxygen consumption as well as the effective release rates are necessary for the effective design and operation of any system (Weisenburger, 2014; Marino, 2014).

Figure 4.2.5: Lead monoxide pellet device for oxygen supply to the coolant using the solid phase method

G – liquid flow rate

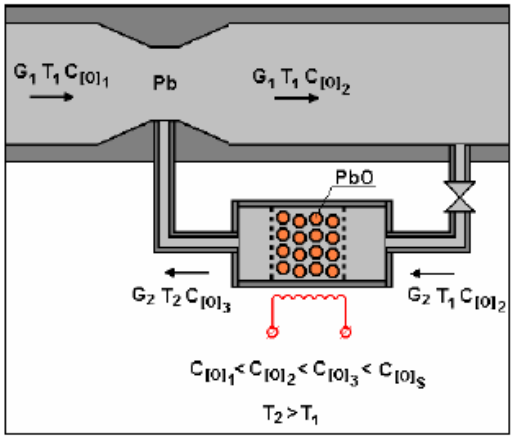

Source: Martynov (2003) and Askhadullin (2005).

The flow direction is to be noted, as it results from an important operational feedback relating to the behaviour of the dissolved iron impurity. If the active iron – dissolved iron in liquid alloy able to react with other species, to dissolve or to crystallise – enters into contact with solid lead oxide pellet, a thin iron oxide film covers the pellet and does not allow any further dissolution, as the magnetite cannot be dissolved in the conditions of the mass exchanger unit. The same mechanism occurs during normal operation; if the start-up purification was not performed at 100% the remaining lead oxide reacts with dissolved iron, and inactive impurities are formed in the liquid metal system. It is present but does not react with other species, nor does it dissolve. Alternatively, reversing the liquid metal flow as illustrated in Figure 4.2.5 oxidises the active iron impurities first, so that they becomes inactive and able to enter into the mass exchange unit (Martynov, 2003; Askhadullin, 2005).

The conditions for the effective fabrication of solid lead oxide pellet were recently experimentally determined as were the process design parameters and conditions of operation as illustrated in Figure 4.2.6 (Askhadullin, 2007).

However, the application of this process requires the prior control of the impurities in the loop in order to be effective (Brissonneau, 2011), so that it can only be viewed as a part of the solution for the chemistry control of the liquid lead alloys. Nonetheless, this process demonstrated its efficiency on a pilot scale loop and presented outstanding stability of the controlled oxygen, with no comparison with the usual gas phase control. It can only be recommended, after the necessary verification and commissioning on pilot scale experiment before its implementation in a nuclear system in representative operating conditions and for relevant materials.

Figure 4.2.6: Solid lead oxide control

Illustration of LBE oxygen control by means of MX-type mass exchangers on the IPPE-SM-2 test rig in the years 2000-2005

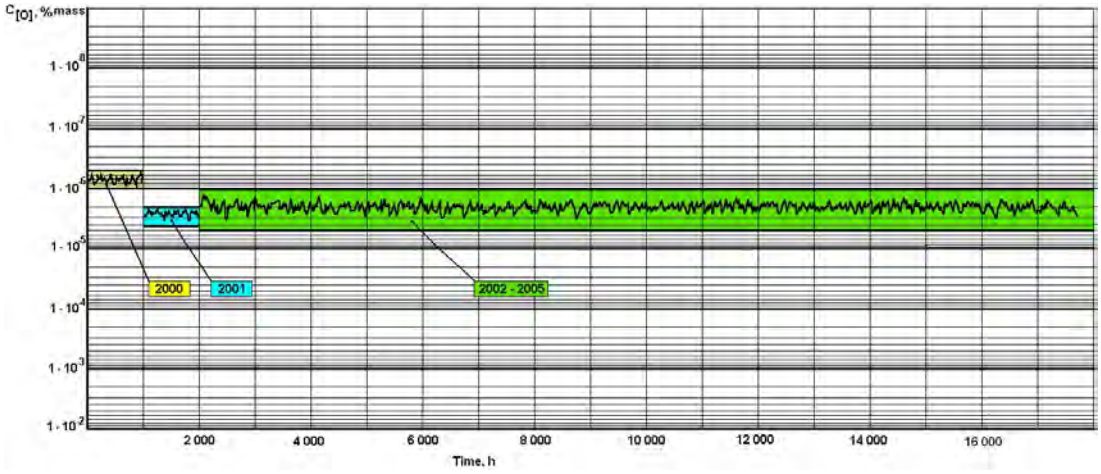

Source: Askhadullin (2007).

4.2.6 *The oxygen homogeneity issue*

Considering the oxygen as perfectly homogenised within the circuit (Shmatko, 2000; Orlov, 2005), i.e. that there is no limitation to the mass transfer because of the little convection/diffusion rate of the dissolved oxygen within the liquid metal, the oxygen concentration would be constant over the whole system. However, the condition for oxygen homogeneity is questionable. In the case of the corrosion protection, the oxygen range will be rather low, such that the process will only be qualified if the oxygen behaviour is controlled over all parts of the circuits for all operating conditions. This means no lower oxygen spots where corrosion could occur, nor higher oxygen spots where lead oxide can build up. This depends on the various convection and diffusion data for oxygen in lead alloy systems (see also Chapter 3), which are known as rather limited (Zrodnikov, 2003). However, the low oxygen diffusivity in lead alloys could be somehow compensated for by higher convection in the system, ensuring the vigorous stirring of the liquid metal, and then its homogeneity.

In small scale systems, such as SVBR-75 (Toshinsky, 2000) or the Angstrem concepts (IAEA, 1998), the liquid is renewed hundreds of times per hours, as illustrated in Table 4.2.4, so the liquid phase can be assumed to be perfectly stirred and homogeneous. In addition, as the volume of the coolant is small, there should be no stagnation zones. However, the highest flow velocity does not exceed 2 m/s on the fuel cladding walls. For larger systems the homogeneity might not be ensured, especially because of the lower convection. For instance, in pool-type liquid metal reactors such as BREST or sodium-cooled reactors, the system mass change rates are ten times lower than for the small scale reactors (Table 4.2.4), primarily because these reactors hold considerably larger coolant volume. Dealing with the system mass change rate, the circulation loop-type reactor, when compared to pool-type, would be more efficient from the homogeneity point of view, even though it would be necessary to compare in much more detail distribution of Reynolds number in various parts of the reactors. The main event that can modify the distribution of impurities throughout the reactor (loop or pool type) is the shutdown or isothermal stand-by, which may affect the impurity distribution between hot plenum and cold plenum.

Table 4.2.4: Typical design parameters for core coolant circulation for various reactors

	Core flow rate	Primary coolant	System mass change rate	Temperature
PHENIX – 350 MWe (Na)	10 260 t/h (3 * 0.95 t/s)	840 t	12 times/h	400-550°C (150°C)
SUPERPHENIX – 1 500 MWe (Na)	61 056 t/h (4 * 4.24 t/s)	3 250 t	19 times/h	395-545°C (150°C)
EFR – 1 470 MWe (Na)	61 170 t/h	2 100 t	29 times/h	395-545°C (150°C)
PWR – 1 300 MWe (light water)	68 000 t/h	380 m^3	179 times/h	286-323°C (37°C)
SVBR – 75 MWe (LBE)	3 492 m^3/h (11.18 t/s)	18 m^3	194 times/h	275-439°C (164°C)
NPHP Angstrem – 30 t (LBE)	382 m^3/h	3 m^3	127 times/h	280-465°C (185°C)
BREST – 300 MWe (Pb)	143 640 t/h (3.8 m^3/s)	600 m^3 (6 300 t)	23 times/h	420-540°C (120°C)
BREST – 1 200 MWe (Pb)	570 240 t/h (158.4 t/s)	2 500 m^3 (26 250 t)	22 times/h	420-540°C (120°C)

The recommendation from Shmatko (2000) is to provide at the circuit design stage provisions to avoid any perturbation of the flow (junction, abrupt turns, etc.), and to exclude any stagnation zones. This would in principle limit the contamination, accumulation and potential rapid release due to thermos-hydraulic instability such as during hot stand-by and shutdown of the reactor. Another recommendation would be to take into account maintenance and cleaning operation at the design stage.

However, the only possibility to validate a design for the safety authorities as regards corrosion protection by self-healing oxide would be to model the mass transfer within the system, using accurate data on convection and diffusion of impurities, and appropriate relations to represent the corrosion/precipitation phenomena in circuits (Zrodnikov, 2003; Balbaud, 2001; Li, 2002).

4.3 Characterisation of impurities and requirements for control

4.3.1 *Impurity sources*

One of the main, and most important, impurities is oxygen. However, there are other sources of contamination that could present some macroscopic effects on the operation even though occurring at a microscopic rate.

Apart from oxygen, other main contamination sources include: *i)* corrosion products (Fe mainly, Ni, Cr, etc.) expected to be generated continuously at a rate depending on the operating temperature, liquid metal flow rate, etc.; *ii)* activation products from spallation, corrosion product activation, or fission (Po, Hg, Tl, Cs, Mn,...); *iii)* light particle production such as hydrogen (including tritium) within the reactor core, the subcritical assembly or the spallation target.

In addition, if a self-healing iron oxide film corrosion protection method is applied for iron-based alloys, the oxygen must be controlled within a very narrow range, above the Fe_3O_4 formation potential but below the PbO formation potential (see Section 4.2.3). Advanced alloy systems that rely on either Si- or Al-based oxide formation for protection will expand the acceptable oxygen potential range. However, the effect of impurities, whether from the corrosion process itself, or due to contaminants introduced by other

means, can have a significant effect on the oxygen level required for protection, especially during transient phenomena such as reactor hot or cold shutdown, which may dramatically affect the impurity distribution and stability within the liquid metal system. For this reason it is important that a complete determination of the potential impurities/contaminants be identified and characterised.

The sources of impurities can be listed by analysing the reactor system conditions during various operating modes including: *i)* initial start-up before the first irradiation; *ii)* normal operating conditions, including start-up and shutdown; *iii)* transient and accidental conditions. Table 4.3.1 gives a synthesis of the various contamination sources expected for an accelerator-driven system (IAEA, 1993, 2002; Courouau, 2003a, 2004b).

Table 4.3.1: Typical impurity sources in nuclear HLM systems

A = coolant system of a critical or subcritical reactor system, B = spallation target of an ADS

	Pollution sources	A	B	Species	Impact
Normal operating conditions	Cover gas renewal	x	x	O, H_2O	Negligible
	Steam leak from SG	x		H_2O, (O, H)	Major if microleak or tube rupture
	Spallation residues, ternary fission and proton beam	x	x	H, tritium	Release to the environment
			x	Po, Hg, Tl, Au, Os and Ir	Release in case of loss of confinement
	Fuel/fuel cladding	x		^{54}Mn, ^{51}Cr, ^{59}Ni, ^{58}Co, ^{60}Co, ^{110m}Ag-110m	Coolant activation
	Corrosion products	x	x	Fe, Cr, Ni	Plugging/deposits
Initial start-up, restart after maintenance or repair	Dissolved oxygen	x	x	O	Plugging/deposits
	Intrinsic pollution	x	x	Ag, Cu, Sn,...	Grade definition
	Gas adsorption in structures during maintenance	x		O, H_2O	Plugging/deposits
	Air inlet	x		O, H_2O	Plugging/deposits
Off-normal pollution sources	Fuel cladding failure	x		^{239}Pu, ^{235}U, ^{85}Kr, minor actinides and Cs, I, Kr, Xe nuclides	Activation on the long term
	Air ingress	x	x	O, H_2O	Plugging/deposits
	Steam ingress	x		H_2O	Cover gas pressurisation, plugging/deposits
	Casual pollution (oil, Hg,…)	x		Oil, Hg, Pb-Sn,…	Plugging/deposits

During normal operation, the only sources of contamination for an ADS system (primary circuit) will thus be hydrogen and transition metal or metalloid impurities resulting either from corrosion in the whole circuit or from spallation reactions in the target. An additional and incidental source of radio-contamination of a critical system would be from any failed fuel cladding.

A potential source of hydrogen in the intermediate circuits comes from the permeation from the steam generator units, if the energy conversion is performed with a Rankine cycle with steam, because of the steel aqueous corrosion as well as the thermal decomposition of the hydrazine (N_2H_4) added (in excess to the dissolved oxygen) in the

water/steam circuits to reduce the aqueous corrosion. Actual diffusion rate will depend on the hydrogen partial pressure difference as well as on the oxide film thickness at the liquid lead alloy interface of the steam generator unit.

Another source of residual hydrogen would be from the proton beam in the spallation target and light element production by ternary fission that includes tritium. The degassing of hydrogen adsorbed during some fuel elaboration processes should also be mentioned, though almost negligible, can also be mentioned.

For an ADS system, protons from the beam itself represent an intrinsic hydrogen source, as not all the protons injected into the system will result in a spallation reaction: unused protons will be thermalised and dissolved into the liquid metal as ionic hydrogen. The residual amount of hydrogen is however not well known. Spallation reactions generate hydrogen as well, in quantities that have been roughly assessed for instance for the MEGAPIE experiment to several litres of hydrogen, including about 10% of tritium (69 l of LBE, 200 days of irradiation, 1.74 mA), the order of magnitude of which is not negligible, especially since the amount steadily increases with the irradiation time, which could give rise to an accumulation effect in the spallation target, even though part of it reacts with oxide films or adsorbed gases. In addition, tritium, like other hydrogen isotopes, diffuses throughout the hot metallic component and eventually to the environment, engendering a potential safety issue during operation or when dismantling.

The ternary fission must be accounted for, as it is usually not negligible. Production depends on the ternary fission yields for ^{239}Pu, ^{235}U and ^{238}U. This produces all of the hydrogen nuclides continuously but at low rates, which is usually not negligible for the tritium with regard to the contamination release issue. As this impurity is produced inside the fuel rod, diffusion towards liquid metal is a function of the fuel cladding material, its operating temperature, and of the surface state of the material in contact with the liquid metal: steel retains almost no hydrogen or tritium, whereas zirconium alloys retain all hydrogen. Real transfer rate would have to be assessed for HLM systems, especially if a specific coating (alumina) or surface modification treatment (GESA) is used (Müller, 2000), as it can significantly reduce the share of the contamination effectively transferred to the liquid media. In addition, if the use of neutron absorbers such as boron carbide is foreseen, its contribution to the tritium source would have to be accounted for, as its share might not be negligible when compared to the ternary fission contribution (Courouau, 2003a).

The steam generator units, if any, are normally designed to be leak-proof. However, some micro leaks can be expected, either because of the lower detection limit of the leak detection system, or because of some agreed-upon operational tolerance (a few litres/hour). From the liquid sodium reactor experience, a null leak rate between water-steam circuit and the secondary sodium circuit is, however, achievable, with extra constraints on the nuclear operation for the leak detection system and steam generator design. From the Russian experience (Toshinsky, 2000; Shmatko, 2000), operation with small leaks is reported for some time without significant deviation of the designed technological parameters, which allowed repairs to be made at a convenient time. Indeed, the actual rate of oxidation in case of a small steam leak appears to be limited (Shmatko, 2000) and does not induce the formation of solid lead oxide in excess, but rather to a dynamic equilibrium in the intermediate oxygen range (Martynov, 2003). This observation gives rise to the principle of direct contact steam generator (Martynov, 2003, 2005), as well as to the concept of a Pb-Bi-cooled direct contact boiling water small fast reactor (PBWR) (Takahashi, 2003). Accurate knowledge of the possible micro leak rate is critical, if any, as it will most probably exceed all other contamination rates in oxygen. The relation giving the oxidation of lead by water is provided in Martynov (2005): oxidation stops once the oxygen activity reaches 10^{-3} of its saturation limits. The potential impact of larger leaks relates to the pressurisation of the cover gas, which induces specific safety requirements.

The other initial contamination consists in the residual compounds in lead or LBE after manufacturing: it is not the most important one, but represents a source that can be easily dealt with, either by the choice of a "nuclear grade" lead or lead alloy (see Chapter 3), or by the application of specific procedures that would enable to start the nuclear operation with the lowest impurity level achievable.

During the initial start-up, or any restart after maintenance or repair, oxygen is clearly the largest contaminant at this stage of the operation of the nuclear facility (Ivanov, 2003b; Courouau, 2004c, 2005a). Chemical control and monitoring will enable to control the chemistry of the lead alloys prior to its first irradiation, as well as prior to any operating cycle. Moist air is adsorbed on the residual lead alloy layer as well as on the structural steels in a comparatively high amount that will have to be purified before any restart of the system. This contamination source was neglected for the first submarine named "project 645", and led to the gradual accumulation of oxide in the primary circuit, which eventually concluded, together with the chronic oil leakages of the pumps, with an at-sea accident in 1968 (Ivanov, 2003b). This accident occurred a few months after the second core had been loaded, and is at the origin of the intensive studies undertaken by the Russians related to liquid lead alloy technology control in the 1970s.

The evaluation of the release rates of corrosion products to the liquid metal is rather difficult as it depends firstly on the choice of materials (iron-based steels, ceramics, refractory metals…), on the corrosion mechanisms as well as on the corrosion protection policy chosen (none, self-oxide healing for steels, coating), on the oxygen activity, on the structural materials and on the operating conditions (see Chapter 6). However, the order of magnitude for iron, chromium and nickel for the coolant loop account to a few kilograms per year when iron-based steels would be used for a primary circuit of significant size. This impurity source is thus not negligible over years of operation, and should be accounted for, even though it is only roughly assessed for the moment; variations in the estimations could be very large.

4.3.2 *Behaviour of impurities and requirements for purification*

As previously listed, most of the contamination by impurities can be expected to remain limited in mass, except for oxygen and corrosion residues. Corrosion products potentially present long-term and cumulative effects, mainly because of the dynamic mass transfer equilibrium that will occur in a non-isothermal system. Pipes clogging due to corrosion products were experienced in several loops, which is a specific issue of the HLM: hot or cold stand-by may lead to a rapid redistribution of the deposited impurities within a few hours, eventually clogging the cold pipes as was observed on the CICLAD loop (see Chapter 12) and as illustrated in Figure 4.3.1. This effect was observed within a few hours, as impurities were first accumulated in some cold spot within the loop, then following a change in the loop temperature distribution, the pump duct became the lowest temperature spot in the loop and got plugged. Such observations are reported for almost all research facilities operating with lead alloys and would not be acceptable for any nuclear system.

The noble elements, the oxides of which are less stable than the lead monoxide, will be dissolved in the liquid metal melt up to their solubility limit, and then be present probably as particles (see Chapter 3). In addition, depending on the level of oxygen controlled in the facility, the impurities might be present either in the oxide or dissolved form according to the Ellingham diagram. In any case, mass transfer from the hot part to the cold part, as well as from the liquid metal bulk to the walls, will occur, thus generating an operating risk for long-term operation, such that it would be required to propose a continuous purification process to control these continuous contamination sources.

Figure 4.3.1: CICLAD, Ni pin precipitation in the EMP duct that eventually led to complete plugging

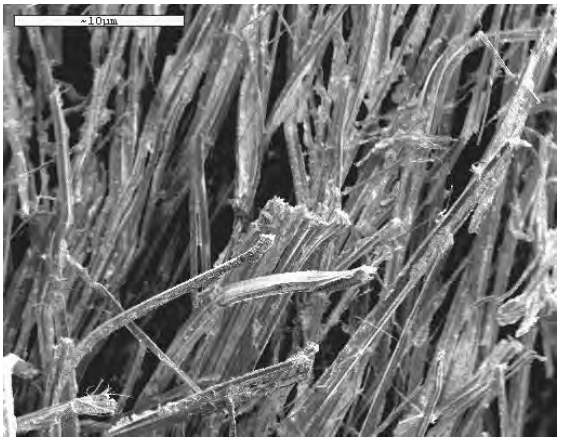

Source: F. Balbaud-Célérier, CEA Saclay.

Purification requirements

For a lead alloy coolant system which is foreseen to operate for 30 years or longer, as well as for target loop systems, which, due to operating conditions, are expected to be operated only a few years, it appears necessary to continuously trap the impurities in a specific unit. A specific purification campaign during isothermal stand-by and cold shutdown should be foreseen as well.

In principle, only the solid impurities, insoluble particles or oxides should be gathered in a bypass line equipped with the required chemical engineering process units such as filters, crystallisers or settling units. Lower operating temperature will allow minimising the amount of dissolved species. In addition, temperature gradients or packing may efficiently promote crystallisation of these metals and increase the efficiency of the purification unit.

As some homogeneous crystallisation might occur, the conditions to provide sufficient sedimentation and residence time for the existing particles in a cold quasi-stagnant auxiliary vessel should therefore be investigated as an alternative purification system for some specific needs, e.g. start-up purification prior to the filling operation. Particles could then be skimmed off from the gas/liquid interface, as most probably some will be settled up at the interface. This interface could be arranged in specific unit, rather than in the loop, as this will affect the gas/liquid equilibrium with non-metallic impurities (oxygen, hydrogen,…) because of the formation of an oxide film at the interface. It may be a specific issue to assess the localisation of the cold point in a particular system and to compare it to the interface temperature, so as to avoid as far as possible the formation of a thick impurity layer on the interface. This purification by sedimentation is the choice made for the MEGAPIE experiment, prior to its filling operation; oxides and impurities will be kept in storage vessels (Courouau, 2004c, 2005a), but validation will still be required for larger systems.

The filtration system, possibly at the coldest point of the facility, appears as one of the most suitable processes for the lead alloy coolant. This operation is typically a chemical engineering operation, difficult and complex to investigate in liquid metal. Its efficiency depends on numerous parameters, constants or variables during the operations. The main factors of importance are as follows:

- location in the systems, geometry, etc.;
- driving force that induces the flow through the media, regeneration ability;

- operating parameters: flow rate, temperature, etc.;
- solid: nature, form and size, concentration, and particle size distribution;
- filter medium: nature, surface, thickness, pore size, hydrodynamic resistance, mechanical resistance, mode of operation (continuous or batch), pressure and temperature for the filtration, etc.

The particle size distribution defines the choice of the filtration medium. The liquid presenting a large amount of particles of small size (1 μm or less, colloidal) will quickly clog the filtration medium by the formation of little, permeable and compact deposits on the filtration medium ("cake"). The filtration rate will slow down drastically. Particle size distribution might be modified by some process such as coagulation to increase the filtration efficiency. If particles are roughly spherical, the cake will have good liquid permeability, and thus a large filtration rate. Another illustration is available for the elastic or compressible particles that will act as valves, as any increase in the driving force will decrease the filtration rate, due the compaction of the cake, and a sharp decrease of the pore size (Perry, 1997).

There are typically two types of filtration mechanisms that could be applied to liquid metal technology for separating a solid from a liquid (Perry, 1997):

- deep bed filtration where solids are trapped within the pores or body of the filter medium;
- cake filtration where solids are stopped at the surface of a filter medium and pile upon one another to form a cake of increasing thickness.

From the lead alloys' operating feedback, the following filtering media for deep bed filtration is reported: alumina fibre in the form of textile; glass fibre; metallic mesh textile like or sintered metal filter (Zrodnikov, 2003; Orlov, 2005).

From the aluminium refinery technologies for advanced applications (aerospace), the use of filtering medium for deep bed filtration, such as alumina foam or zircon-mullite honeycomb medium is reported for the removal of tiny particles before the metal casting operation as a once-through operation. In addition, a magnetic field is reported to have promoted the nucleation and crystal growth as well as adsorption on specific metal. There is then a variety of solutions, but, as the basic data are missing, nature of particles, size, form, etc., as well as the filtration rate. Neither current design rules nor selection criteria are well defined, except for the pressed and sintered fibre metal medium developed for BREST-300 (Papovyants, 1998; Orlov, 2005), or the commercially available media (PALL Corporation™), which were recently successfully tested on the STELLA loop in conditions of heavy contamination of the liquid lead alloy (Figure 4.3.2) (Beauchamp, 2010). However, these studies were too preliminary although they clearly demonstrated the possibility of purification, but still require sustained efforts with a representative liquid metal loop to obtain the design parameter relations. These are necessary to design a purification process unit required for a larger scale system. One of the constraints of this kind of study is the monitoring of solid impurity concentration and accumulation in the liquid metal system, which could only be qualitatively assessed, although being one of the main process parameters.

As the unit will eventually be plugged, it sounds logical either to design the system for the whole service lifetime, or to provide systems with easy removal and replacement, or regeneration of the filtration medium.

Moreover, nuclear system purification must be designed to cope with incidental contamination such as the loss of cover gas tightness, water or other ingress (grease, oil, mercury, etc.), as their impact impinges on the loss of operating time because of the need for long and costly purification campaigns. In the latter case of contamination, oil ingress is by far the incident that happened the most often, as in the prototype fast reactor of

Dounray (150-200 l) (UK-PFR, 1991). Russian feedback reports the effect of such an event on a lead alloy system (KV-27 land reactor), which is very similar to the sodium-oil pyrolysis reaction giving solid materials (Ivanov, 2003a).

Figure 4.3.2: Purification of impurities by filtration

Pall-PMM-150™ cartridge test (standard sintered stainless steel mesh, removal rate of 9 μm), pressure drop in the filter test line versus time of operation at 400°C, 80 l/h, oxygen from 10^{-5} wt.% to 10^{-7} wt.% at the end (power outage at 167 h) achieved on the STELLA test rig. Cross-section of the filter media showing the accumulation of impurities on one side of the mesh (up to 200 μm) Pb_7Bi_3-Bi with PbO-Bi micron-size agglomerated particles forming filaments containing iron, chromium oxides in traces.

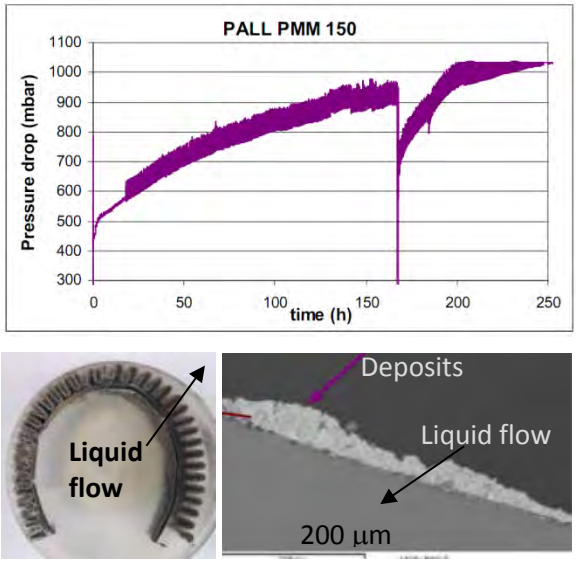

Source: Beauchamp (2010).

In addition to the purification of particles flowing in the liquid lead alloys, a process to recover from the possible fouling of the circuit must be developed and implemented at the design stage. Indeed, such an occurrence was observed in numerous pilot scale facilities, because of inefficient or absent purification systems, or because of incidental contamination. Both mechanical and chemical cleaning was applied (scratching and acid attack), which would not be applied in a nuclear system. Some remarkable developments were made by applying the techniques of microscopic bubble implosions at the fouling location to put the deposits back in solution, in association with hydrogen reduction for dissolution (Papovyants, 1998). This process requires a specific bubbling system for the formation and dispersion of the fine bubbles in the pilot scale loop, a modified centrifugal pump for injection of the gas in a specifically designed impeller ("dispergator"). Results obtained on pilot scale loop were successful. Its implementation on other loops is, however, required for verification and commissioning before any implementation in a nuclear system under representative operating conditions and materials. The issue of the high hydrogen content must also be analysed with regard to the issue of hydrogen embrittlement of the structural materials.

4.3.3 *Active impurities*

The control of the radioactive impurities topic will not be fully addressed, as it is allocated a complete section of specific study (see Chapter 5). Only some elements are given hereafter, and particularly supported by one fully documented case study (Petrovich, 2002), in order to sort out which of the active nuclides could be critical for

nuclear system operation, and to focus on some basic hard points for further studies, such as the behaviour of the volatile species (noble gas, Po, Hg, Cs, I), or the mobile species (tritium), or the long half-life nuclides that will affect the maintenance operations during shutdown, and later the waste management for decommissioning. Until now literature insisted mainly on polonium nuclide production.

4.3.4 *Production rate assessment*

The activation/spallation sources are continuous and important in term of activities as well as in terms of potential dose rate. However, this point should be more fully addressed in order to take provision for the fact that lead is often used as biological shielding to limit the dose rate.

To support the following analysis, figures that were assessed by Petrovich (2002) for a primary circuit of a subcritical system, which can be assumed as representative of a critical system, as well as for the spallation target circuit, will be taken into account. These calculations correspond to the TECLA project reference subcritical reactor: 300 MWth, 3.7 tonnes of LBE for the target, 2 000 tonnes for the LBE coolant loop, 3 mA for the nominal beam current, 0.6 to 1.5 GeV for the beam energy (Courouau, 2003a). The codes used for the following assessment are MCNPX and SP-FISPACT (Petrovich, 2002).

The most abundant nuclides produced by the spallation reactions are the nuclides close in mass to lead and bismuth, such as Po, Tl, Hg and Au, directly descending from the spallation and activation reactions, which basically peel off neutrons from the nucleus. In fact, including all direct reactions and daughter reactions, almost all the periodic table is produced with a clear peak close to the atomic number of lead or bismuth, and a second one at about half the value. There is about 3 to 4 orders of magnitude difference between the impurity concentrations observed in the target and in the coolant. As regards impurity production, the mass rates are low when compared to other potential sources of impurities in the system such as the corrosion source, except for Po in the primary loop where the amount of Bi under the neutron flux is very large, and Po, Hg, Tl, Au, Os and Ir for the target loop:

- Target loop: 180 g per operating year (163 g for Po, Hg, Tl, Au, Os and Ir).
- Primary loop: 2 970 g per operating year (2 940 g of Po and 29 g of Tl, Hg, Au and Pt).

As regards the chemistry of these systems, one can first only consider the influence of these few impurities:

- Target loop: Po, Hg, Tl, Au, Os and Ir.
- Primary loop: Po and to a lesser extent Tl, Hg and Au.

However, possible phenomena occurring in these systems and leading to a local accumulation (plugging), or local effect (corrosion inhibitors or promoters) are to be ascertained, as well as the gas/liquid interactions (Po, Hg, Cs, etc.) and the effect on the control of the dissolved oxygen content.

After one year of irradiation at 3 mA, the total activity of the LBE of the target loop is assessed as being 44 300 TBq for the 3.7 tonnes of LBE, which makes 12 TBq/kg or 320 Ci/kg. This level of activity appears exceptionally high when considering fluid activity in a typical nuclear power plant operation, although it is quite rational in the realm of the high neutron source. The total activity of the primary loop is assessed as being $1.1 \cdot 10^{18}$ Bq for the 2 000 tonnes of LBE, which makes 0.55 TBq/kg or 15 Ci/kg almost entirely due to ^{210}Bi (52%) and ^{210}Po (43%). The elements giving the highest activities after the coolant and polonium nuclides are the following: Tl, Hg, Au, Pt, Ir, Os and Re. While the activity of Tl is only about one order of magnitude lower when compared to the coolant, the Re activity is five orders of magnitude less. Except for the lead and bismuth isotopes, which represent the coolant activation itself and which are numerous as expected, most of the activity is due to the isotopes of Po, Tl, Hg, Au, Pt and Ir, listed in decreasing order of activity.

Then, after one year of radioactive decay, the total activity of the spallation target decreases by a factor of 35, but is still significant: 1 260 TBq that makes 0.340 TBq/kg. Main contributions are the following: ^{210}Po (75% of the total activity), ^{195}Au (9.5%), ^{207}Bi (4.5%), ^{204}Tl (3.5%), ^{195}Os (1.1%) and ^{208}Po (1.5%). The main nuclides responsible for the dose rate are then: ^{185}Os ($3.6 \cdot 10^6$ Bq/g), ^{88}Y ($2.55 \cdot 10^5$ Bq/g), ^{192}Ir ($2.24 \cdot 10^5$ Bq/g), ^{95}Zr ($6.9 \cdot 10^4$ Bq/g), with the assumption of a linear relation between the dose rate and the activity.

For the coolant loop, the residual nuclides responsible for 99% of the total dose rate are listed as follows in decreasing order of dose rate contribution: ^{207}Bi(γ β^+, 37.97 y – $2 \cdot 10^4$ Bq/g supposing a perfect homogeneity within coolant), ^{210}Po (α, 138.4 d – $4 \cdot 10^7$ Bq/g), ^{185}Os (γ β^+, 93.6 d – 73 Bq/g), ^{208}Bi (γ β^+, 3.67 y – 9 Bq/g), ^{144}Pm (γ β^+, 363.42 d – 16 Bq/g) and ^{195}Au (γ β^+, 186 d – 4 500 Bq/g).

The activation products should be added to the spallation residues for both the coolant and the target loops:

- activation of the coolant, lead and bismuth, which makes up, along with the spallation residues, the largest part of the total activity, as previously illustrated;
- activation of dissolved impurities by the neutron flux, intrinsic impurities from the supplied alloys such as Ag, corrosion products, etc.;
- release of activated products by the corrosion, dissolution of structures submitted to the neutrons.

Then, due to mass transfer and deposition, the activated corrosion products can plate out on different parts of the circuit, being for instance responsible for significant dose rates to which the personnel are exposed during maintenance and handling operations of some specific component such as pumps, heat exchangers, etc.

To the spallation and activation products, fissions products are released into the primary coolant loop: tritium and fissile products.

Tritium is produced by fission and spallation. This nuclide is rather particular for a reactor system, as it is very mobile throughout hot and metallic interfaces immersed in liquid metal. Although tritium has a low energy activity (beta), it is accounted for as it migrates, is present in sections of the reactor where no other radioactive product is expected and is finally released to the environment, where, as tritiated water ($^1H^3HO$), a significant dose impact may be observed. This is why tritium was studied for the prediction of release rates or inventories in various subsystems at the time of the design or during operation.

Fissile contamination sources in normal operation are due to surface contamination of the fuel cladding by traces of Pu or U. These traces migrate into the liquid metal, and account for fissile contamination of the coolant. In addition, when subjected to the neutron flux, fission products appear, such as caesium and iodine nuclides, but at very low levels. In case of fuel cladding failure, volatile fission products such as caesium, iodine, xenon and krypton nuclides are released into the system, mostly in the cover gas, in much larger quantities.

4.3.5 *Consequences on operations*

By contrast to the spallation target which presents a small service lifetime with no maintenance or repair, the primary circuit is planned for the entire reactor service lifetime (tens of years), which necessarily requires maintenance operations, component handling, refuelling, etc., and might require the use of a specific radioactivity control system.

The behaviour of these nuclides depends on their chemical form in the liquid lead alloys:

- dissolved, if the solubility is large when compared to the mass released (e.g. Au);
- dissolved, but submitted to precipitation if solubility is low enough in some part of the circuit when compared to the mass released;
- oxidised, if the oxide potential is lower than lead oxide, and depending on the oxygen potential of the liquid alloy.

As previously seen, some active nuclides may build up in specific parts of the system, such as the cold exchange surfaces of heat exchangers, or at the gas/liquid interface, or on other specific spots. This will not have any impact on operations, but during maintenance and component handling, it may lead to the necessity to perform cleaning and decontamination operations.

As the dose rate of the primary coolant is mainly due to ^{207m}Pb, with a level not comparable to any other nuclide, it is critical for designing the biological shielding. However, this nuclide disappears in less than one hour as its half-life is only of 0.8 s; other nuclides are thus to be considered for maintenance or handling operations, and even for dismantling.

The coolant activation itself influences the operations related to components of fuel handling for maintenance, or repair, as they may require specific operations to allow repair, increasing the overall reactor complexity, as:

- coolant cleaning process to remove the coolant itself;
- decontamination process by acid attack to remove the deposits and first micrometres of the structure, and decrease the activity and dose rate due to nuclides adsorbed into the steel.

In addition, the nuclides, which can transfer from the liquid coolant to another system such as a secondary or auxiliary system, cover gas control system, etc., are the main source of concern during normal operating mode, as they may require specific control and processes to keep them within the release authorisations specified by the safety authorities:

- tritium, as it makes up one of the main contributions to environmental release;
- volatile species such as Kr, Br, Xe, Ar, I, Cs, H, Po and Hg nuclides.

Depending on the cover gas system, various solutions can be implemented to control the activities, such as:

- Re-circulating cover gas loop, which can include some delay tanks to increase residence time and favour radioactive decay of short half-life products (Kr), or trapping on charcoal bed (Xe), or even cryogenic trap, all of which were used for the liquid sodium fast reactor systems. Other specific traps for Po compounds or mercury vapour could be designed to reduce coolant activity from those radioisotopes specific to lead alloy systems.
- Gas tight system, with venting from time to time to relieve the pressure, with the necessary gas decontamination before release to the stack, as foreseen for the MEGAPIE target operation.

It may be a solution for the polonium nuclides to use their volatility properties (PoPb compound) to eliminate it in the gas phase rather than in the liquid phase, as it could be easier. The effect of the oxygen control process that requires gas flowing to either oxidise or reduce the lead alloys is to be addressed from this activity control issue, as it will affect

the gas/liquid distribution of the active nuclides as well. This is especially true for the hydrogen/steam gaseous mixture bubbling or cover gas blowing, as:

- H_2Po, is volatile, so the process will enhance Po transfer to the gas phase.
- Tritium, as a hydrogen isotope, will react isotopically with H_2 from the gas phase as well as with the steam, so the reaction will favour tritium transfer to the gas phase.

During incidental events, such as a loss of coolant accident, the alpha emitter activity in the lead alloy is often the dimensioning event for the safety scenario. In that case, this allows setting up the specification of the maximum ^{210}Po nuclide that could be agreed in the coolant loop, so as to study and design the necessary control processes (Khorosanov, 2002; Buongiorno, 2004).

4.4 Instrumentations for chemical monitoring

4.4.1 *Online electrochemical oxygen sensor*

The accurate measurement of the oxygen concentration in the liquid lead-bismuth eutectic, as well as in the pure lead alloys for use as coolant in nuclear systems or as liquid spallation target for high neutron sources or accelerator-driven systems is a critical issue for defining the active oxygen control that will first of all prevent the contamination of the liquid system by lead and bismuth oxides, as well as, possibly, ensure efficient corrosion protection of the iron-based alloys structures if the self-healing oxide layer method is chosen.

The use of the ionic conduction properties of some solid electrolyte (Desportes, 1994), and in particular the zirconia-based ceramic, allow to make electrochemical cell assembly that permits the measurement of dissolved oxygen in liquid metal systems, the activity of which could be extremely low ($< 10^{-4}$). This is known as the electromotive force measurement in open circuit, or as the galvanic cell method.

This technique presents several well-known advantages such as:

- specific to the dissolved oxygen, but the bounded oxygen, such as in oxide, is not taken into account;
- rapid and continuous measurement that is able to be implemented directly online in the system, provided the seal in between the liquid metal and the ceramic is leak tight;
- wide concentration range covered by one single sensor, with a lower detection limit that is actually very low, as well as its potential operating temperature range;
- no relation with the size and contact area of the electrodes;
- no disturbance of the measured system.

However, its well-known limitation was its use at a rather high operating temperature, of the order of 750°C typically for a Pt-air reference system, because of the high cell resistance that increases with decreasing temperature, as well as the irreversibility of the cell. In addition, the poor thermal shock resistance requires special care to prevent high thermally induced stresses that can cause cracking of the solid electrolyte. A specific protection from rapid temperature fluctuation shall be provided. Another solution is to design sensor as a consumable item. The service life is often reported as being in the range of only tens to hundreds of hours.

Although the principle and the application have been well known since the 1950s, especially at the laboratory scale for the measurement of basics thermodynamic data, its real application as industrial oxygen sensors began in the late 1980s where its applications were multiple, from the automotive industries (lambda sensors) to glove box

gas control (Desportes, 1994). However, some particular and earlier applications such as the sensor for the steel making industry, which is used to measure C/CO ratio, as well as the sensor for the liquid sodium to be used as nuclear coolant (yttria-stabilised thoria), could be noted (Asher, 1988). In addition, the Russian institutes developed a specific application for the oxygen control in lead-bismuth eutectic to be used as coolant in nuclear submarines in the late 1970s-1980s (Gromov, 1997, 1998; Shmatko, 2000), whose teams paved the ways for this very specific instrumentation in heavy liquid metal coolant with the use of very specific multi-layer pellet-type sensors (Shmatko, 2000). This specific design of the solid electrolyte, although very complicated and costly to produce (pellet-type, multi-layer ceramics, metal-to-ceramic bonding, etc.), allowed a very accurate measurement of the oxygen together with an exceptionally long service lifetime of 10 years. Some of these sensors are still in use in Russia, as well as in Italy (Azzati, 2003), but are apparently no longer produced. Since the mid-1990s, development and testing of new sensor design based on yttria-stabilised zirconia or magnesia-stabilised zirconia were conducted worldwide, including in Russia (Askhadullin, 2003, 2005; Chernov, 2003; Colominas, 2004; Courouau, 2002b, 2004a; Fernandez, 2002; Ghetta, 2002; Konys, 2001, 2004; Li, 2003; Muscher, 2001; Zrodnikov, 2003; Takahashi, 2002; Nam, 2008; Lim, 2012, 2013; Schroer, 2011b).

The main requirements for an online oxygen sensor are as follows: accurate in such a low oxygen concentration range, reliable, predictable and safe for long-term nuclear operation. For instance, one of the main constraints as regards safety for such system is related to the ceramic breakdown; any leaks of radioactive liquid metal outside the system must be prevented, as well as any ceramic pieces running in the nuclear loop. However, some limitations appeared on sensors using the commercially available yttria-doped zirconia thimble (Courouau, 2005b), such as the ceramic relative fragility, as well as the time drift that is often observed that will delay for a while their direct implementation in nuclear systems. However, the new Russian sensor design (Zrodnikov, 2003) was already used in the nuclear loop of the BOR-60 lead channel (Korotkov, 2003), which operated for about 100 days. For this sensor, not only the shape (conical when compared to a one-end-closed tube) but also the composition and the microstructure of the solid electrolyte are adjusted to enhance the ceramic resistance to thermally induced stresses (Askhadullin, 2005).

4.4.1.1 Principle

Sensors are based on the potential measurement method at null current for a galvanic cell built with a solid electrolyte: zirconia doped with either magnesia, calcia or yttria, as this doping element stabilises the ceramic into the tetragonal form that conducts oxygen ions under certain temperature and oxygen conditions. Although the Russian feedback indicated the achievement of such sensors for the low operating conditions expected of the lead alloys (Gromov, 1997; Shmatko, 2000), their assembly was not straightforward at first, as it was considered that such electrodes and cells would not work for the temperature of interest for lead alloy applications (400 to 550°C), because of the irreversibility of the electrode, and because of the too-high cell resistance.

The electrodes define either the liquid metal phase where the dissolved oxygen is to be measured, the working electrode, as well as the reference electrode, which is the constant oxygen potential reference system, as illustrated in Figure 4.4.1.

Sensor assembly takes place within the laboratory and is now considered as a routine procedure, as illustrated in Figure 4.4.2, where the use of the one-end-closed tube allows separating easily the reference (inside) from the measurement medium (outside). One of the critical elements for the design of such a sensor is then the sealing between the ceramic tube and the structure of the liquid metal system, which must be leak tight as well as electrically insulated.

Figure 4.4.1: Galvanic cell principle

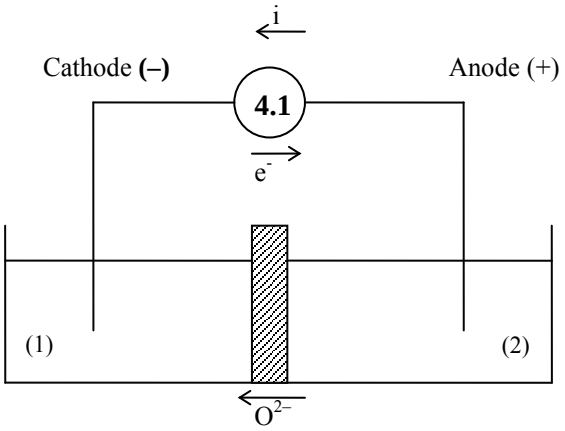

Figure 4.4.2: Generic implementation scheme

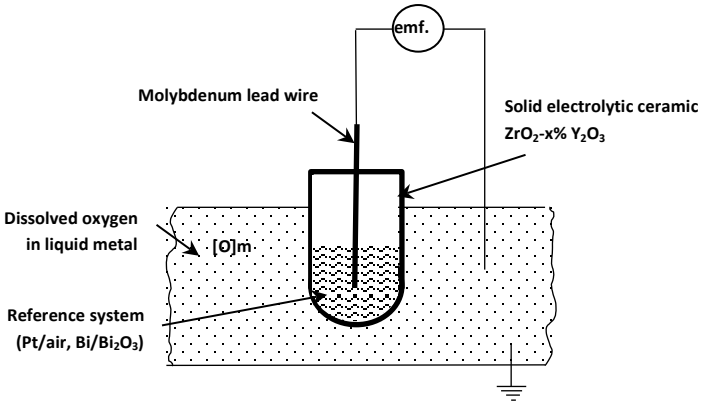

The solid electrolyte supplied by FRIATEC AG company (yttria-doped zirconia, FzY grade, 8.1% in yttria) was used by Courouau (2003b) and Konys (2001) for instance whereas the FERROTROM company supplied the ceramic used by IQS (both magnesia- and yttria-stabilised zirconia) (Colominas, 2004). Various other suppliers can be found throughout the world (Li, 2003), e.g. the Nikkato Corporation (Ganesan, 2006). On-purpose ceramic can be synthesised and fired with the required characteristics and shape (Shmatko, 2000; Askhadullin, 2005). This supplier list is not exhaustive.

Assembly is done in the open air. Ingots of pure metal and oxide powder are mixed to get a liquid metal internal reference at the operating temperature with only a slight excess of its oxide; 10% to 50% of oxides in excess are reported as satisfactory (Courouau, 2003a). The air in excess is consumed during the first use, corresponding to the activation of the sensor, to form the reference metal oxide. The activation of the sensor is done during the calibration procedure or during its first use, the first step of which is the immersion of the sensor in an LBE melt followed by a temperature increase. Once the sensor provides a stable potential output (electromotive force – emf), the reference is considered to be at the thermodynamic equilibrium, and is designated activated or ready for operation. This process occurs over a matter of minutes at 450-500°C.

The choice of the reference system is critical. It greatly depends on various parameters (Desportes, 1994), such as the oxygen partial pressure of the reference, which must be close to the partial pressure to be measured, the good knowledge of the equilibrium value of the reference system, a good buffering effect in case of slight disturbances to keep the

partial pressure stable, and good compatibility between the lead wire and the reference systems. The use of gas (air, or oxygen) presents some advantages, as the partial pressure is accurately known, whereas the thermodynamic data of the liquid metal reference couple metal/metal oxide could be less accurately known, requiring a calibration (Desportes, 1994).

Usually air is used with platinum coated on the ceramic surface for a better junction at the interface, and a Pt lead wire, making the Pt/air electrode, with a well-known limitation in its operating temperature, because of the resistance of the junction between the gas and the solid phase. The operating temperature must be higher than 450°C for such a cell (Desportes, 1994; Konys, 2004). In addition, some difficulty is reported for assuring constant oxygen partial pressure in the ceramic tube, which usually requires a small air flow inside the sensor. Alternatively, liquid metal reference systems provide a better contact with the solid electrolyte, and then a lower cell resistance at comparatively lower temperature. The use of low melting point metal allows favouring the use of the sensor in the required temperature range of a lead alloy system (400-500°C), without an additional heating system.

The effect of thermal cycling on the solid electrolyte when a liquid metal reference is used can be critical. Indeed, the melting/cooling of the internal reference can induce wear on the solid electrolyte, promoting the growth of microcracks, eventually leading to rupture (Courouau, 2005), whereas the air/Pt electrode used under the same liquid metal electrode conditions exhibited a much higher service lifetime (Konys, 2004; Schroer, 2011b).

The contact lead wire must be compatible with the liquid metal melt of the reference. For instance, molybdenum presents a low solubility in bismuth, which is favourable. Platinum or iridium metal, however, which are the typical lead wired for such an electrochemical cell, dissolve in liquid bismuth, excluding their use for the long term. However, molybdenum is sensitive to oxidation which is more stable than bismuth oxide. If the temperature is high enough, the kinetics become significant, so that it limits in practice the maximum operating temperature to about 450°C over the long term.

The reference electrode must not chemically react with the solid electrolyte, leading to the formation of reaction products on the interface, modifying the potential outputs. Similarly, it must not represent a source of contamination in case of ceramic failure. Bismuth is chemically close to lead, fully miscible, and its oxide is less stable than lead oxide. On the other hand, indium (extensively for the Harwell oxygen metre) forms more stable oxide than lead, so that it will reduce the oxygen potential of the liquid lead alloys, but is totally miscible in the liquid alloys.

The range of the readings for the latter indium reference electrode system includes null voltage output, which does not mean that the sensor is broken. This clearly represents an operating difficulty, as in that case there is no clear possibility to determine either the effectiveness or the failure of the sensor. An example of that behaviour was observed during STELLA operation (Figure 4.4.3) (Courouau, 2010), where the In sensor was believed broken for several days when its output was close to the null value. This point would have disqualified, a priori, this reference system for nuclear operation, but systematic and standard calibrations were developed for a periodic verification of the sensor (Schroer, 2011b).

These considerations explain why the choice for the reference systems focused mainly on either the gas system (air/Pt lead wire) or the bismuth (mp. 271°C)/bismuth oxide or indium (mp. 157°C)/indium oxide systems for the reference electrode with Mo as lead wire, although other reference could be used in principle. From the safety point of view, the gas reference system will not be favoured for use in a nuclear system, as it requires the constant flowing of gas inside in the reference electrode, making a route for the contamination of activated lead alloys outside the confinement in case of solid electrolyte failure. If chosen however, its implementation requires the design and validation of a specific system to offset the consequences of a leak.

Figure 4.4.3: STELLA absolute time drift observation for two sensors implemented at the same location at the same time (1 500 hours of service life)

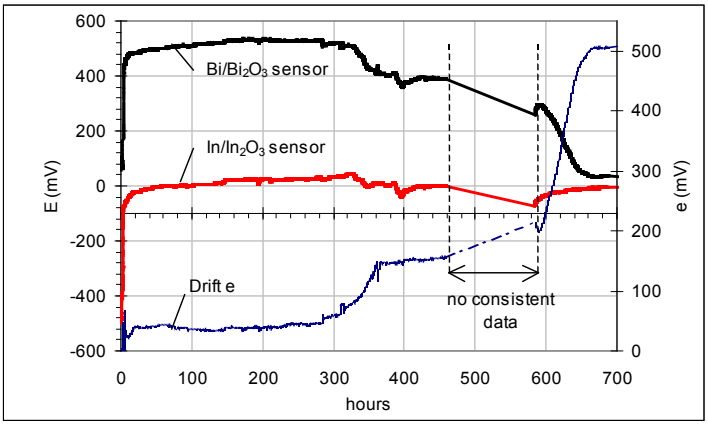

4.4.1.2 *Theory*

This analysis is done for pure lead as well as for the lead-bismuth (55% in weight) eutectic.

The method of potential measurement with null current can be applied to the measurement of dissolved oxygen in liquid lead-bismuth alloys. A typical electrochemical galvanic cell that will subsequently be referred to as "EC sensor" is as follows:

Mo, Metal + metal oxide (reference) // $ZrO_2 + Y_2O_3$ // Pb + PbO (lead alloy solution), steel

where the yttria-stabilised zirconia (YSZ) ceramic, which specifically conducts oxygen ions, separates two medias showing different oxygen activities: an electromotive force (emf) is then formed across the solid electrolyte. If one of the media is defined to act as a reference, so as to maintain the oxygen partial pressure constant to a defined value, then the emf is a function of the oxygen activity in the other medium.

Assuming pure ionic conduction in the solid electrolyte, and assuming that all transfers at the various interfaces developed in the electrochemical cell are reversible, the Nernst relation giving the theoretical emf, noted E_{th}, can be written:

$$E_{th} = \frac{RT}{4F} \cdot \ln \frac{P_{O2(reference)}}{P_{O2}} \tag{4.20}$$

with E_{th} in Volts, R the perfect gas constant (8.31441 J/mol/K), F the Faraday constant (96 484.6 C/mol), T the temperature (Kelvin), and P_{O2} the oxygen partial pressure in the lead alloy.

The oxygen partial pressure of the reference, $P_{O2\,(reference)}$, is defined by the following reaction, in case of a metal (M)/metal oxide (M_xO_y) reference, where x and y are respectively the stoichiometric coefficients for the metal and the oxygen.

$$\frac{2x}{y} M_{(liquid)} + O_2 \Leftrightarrow \frac{2}{y} M_x O_{y\,(solid)} \tag{4.21}$$

All reactions are written so that they corresponds to the consumption of one mole of oxygen. The units of the free enthalpies of formation are then expressed in J/mol of oxygen O_2.

As the reference is built so as to present a constant oxygen partial pressure, both the metal and its oxide are present in excess to ensure the thermodynamic equilibrium of

the reaction. In addition, the liquid solution corresponds to the pure metal, so that the activities of both the reference and its oxide are equal to one and then:

$$\ln P_{O2\ reference} = \frac{\Delta_r G^0_{reference}}{RT} \tag{4.22}$$

The oxygen partial pressure in the lead alloy melt is given by the thermodynamic equilibrium of lead monoxide, considering that it is the most stable oxide in lead-bismuth eutectic:

$$2Pb_{(liquid)} + O_{2(gas)} \Leftrightarrow 2PbO_{(dissolved)} \tag{4.23}$$

The activities product of the lead oxide reaction of formation in lead alloys is then as follows using the oxygen activity defined in Eq. (4.3):

$$\Delta_r G^0_{PbO} = -RT \cdot \ln \frac{a^2_{PbO}}{a^2_{Pb} \cdot P_{O2}} \text{ and then } \ln P_{O2} = \frac{\Delta_r G^o{}_{PbO}}{RT} + 2 \cdot \ln \frac{a_O}{a_{Pb}} \tag{4.24}$$

The saturated oxygen concentration for lead and LBE are derived from Eq. (4.1) and Eq. (4.2):

- Lead:

$$\ln C^*_{o(\text{wt.\%})} = A - \frac{B}{T_{(K)}} \text{ with } A = 7.44 \text{ and } B = 11\,612 \tag{4.25}$$

- LBE:

$$\ln C^*_{o(\text{wt.\%})} = A' - \frac{B'}{T_{(K)}} \text{ with } A' = 5{,}18 \text{ and } B' = 9\,498 \tag{4.26}$$

Lead activity is equal to unity in pure lead solution, and is given by the following Russian relation in LBE solution as quoted in Courouau (2002b):

- LBE:

$$\ln a_{Pb} = -\alpha - \frac{\beta}{T_{(K)}} \text{ with } \alpha = 0.8598 \text{ and } \beta = 135.21 \tag{4.27}$$

The free enthalpies of formation for the various oxides are expressed by the following relations, assuming that all relations are given for the consumption of one mole of O_2:

$$\Delta G^o_{(J/mol)} = \Delta H^o - \Delta S^o \cdot T_{(K)} \tag{4.28}$$

Calculations are made with the help of the HSC database software (HSC, v4.1), which represents a compilation of some of the latest thermodynamic data available. The free energies of formation are linearly regressed on a limited temperature range, 400-1 000 K, so as to determine the standard enthalpy and entropy by the least mean squares method. The latter data, standard enthalpy and entropy, are constant over the temperature range (cf. Table 4.4.1)

The general relationship for a metal-metal oxide reference could then be derived from the Nernst relation, assuming a pure ionic conduction in the solid electrolyte:

$$E_{th} = \frac{\Delta G^o_{reference} - \Delta G^o_{PbO}}{4F} - \frac{RT}{2F} \ln \frac{a_O}{a_{Pb}} \tag{4.29}$$

Table 4.4.1: Main oxides free enthalpy coefficients for the 400-1 000 Kelvin temperature range per mole of oxygen O_2 consumed

$\Delta G^{o}_{(J/mol)} = \Delta H^{o} - \Delta S^{o} \cdot T_{(K)}$	ΔH^{o} (400-1 000 K) J/mol	ΔS^{o} (400-1 000 K) J/mol/K
4/3 Bi + O_2 = 2/3 Bi_2O_3	-389 140	-192.6
2 Pb + O_2 = 2 PbO	-437 608	-199.1
4/3 In + O_2 = 2/3 In_2O_3	-618 674	-216.8

By using the following constants:

$$a = \frac{\Delta H^{o}_{reference} - \Delta H^{o}_{PbO}}{4F} \tag{4.30}$$

$$b = -\frac{\left(\Delta S^{o}_{reference} - \Delta S^{o}_{PbO}\right)}{4F} \tag{4.31}$$

$$c = -\frac{R}{2F} \tag{4.32}$$

These constants allow to writing down simplified relations:

- Lead:

$$E_{th(V)} = a + b \cdot T_{(K)} + c \cdot T_{(K)} \cdot \ln a_o \tag{4.33}$$

- LBE:

$$E_{th(V)} = (a + c\beta) + (b + c\alpha) \cdot T_{(K)} + c \cdot T_{(K)} \cdot \ln a_o \tag{4.34}$$

Hence for saturated oxygen solution, the previous relations depend only on the temperature:

- Lead:

$$E^{SAT}{}_{th(V)} = a + b \cdot T_{(K)} \tag{4.35}$$

- LBE:

$$E^{SAT}{}_{th(V)} = (a + c\beta) + (b + c\alpha) \cdot T_{(K)} \tag{4.36}$$

Finally, these general relations could be simplified by using the (a, b, c) constants and the concentration expressed in wt.%:

- Lead:

$$E_{th(V)} = (a + cB) + (b - cA) \cdot T_{(K)} + c \cdot T_{(K)} \cdot \ln C_{o(wt.\%)} \tag{4.37}$$

- LBE:

$$E_{th(V)} = (a + c\beta + cB') + (b + c\alpha - cA') \cdot T_{(K)} + c \cdot T_{(K)} \cdot \ln C_{o(wt.\%)} \tag{4.38}$$

The free energies are in good agreement with the respective energies computed with the use of other databases (JANAF) (NIST 2013; Barin, 1989). The slight inaccuracy of these data will affect the theoretical electromotive force calculation by a few millivolts that are

assumed as reasonable. Another source of scattering is due to the data resulting from the lead activity relation in LBE, which only slightly affect the emf by a maximum of 10 mV, as well as from the oxygen solubility relation, which on the contrary can affect the emf to a much greater extent. This is why it is essential to know with a relatively high accuracy the oxygen solubility data (cf. Chapter 3). All calculations presented here are made with Eq. (4.1) and Eq. (4.2) respectively for lead and LBE.

The constants of the Nernst relations can then be calculated, and are reported in the next table for Bi/Bi_2O_3 and In/In_2O_3 reference electrodes for a cell immersed in a lead alloy melt according to the following emf (E) vs. temperature (T) and oxygen concentration (C_O) relationships:

$$E_{(mV)} = K_1 + K_2 \cdot T_{(K)} + K_3 \cdot T_{(K)} \cdot \ln C_{O(\%)} \text{ for } E > E^{SAT} \tag{4.39}$$

$$E^{SAT}{}_{(mV)} = K + K' \cdot T_{(K)} \text{ for } E = E^{SAT} \tag{4.40}$$

Table 4.4.2 synthesises the most useful relations for In and Bi reference sensor in LBE melts.

Table 4.4.2: Theoretical relations for Bi/Bi_2O_3 and In/In_2O_3 references for LBE melts

E in mV, P in bar, T in Kelvin, C in weight percentage

LBE	Bi/Bi_2O_3 reference (melting point 271°C)	In/In_2O_3 reference (melting point 157°C)
$E^{SAT}(T)$	$E^{SAT}{}_{(mV)} = 119.8 - 0.0539 \cdot T$	$E^{SAT}{}_{(mV)} = -475 + 0.0088 \cdot T$
$E(T, a_o)$, $E > E^{SAT}$	$E_{(mV)} = 119.8 - 0.0539 \cdot T - 0.0431 \cdot T \cdot \ln a_o$	$E_{(mV)} = -475 + 0.0088 \cdot T - 0.0431 \cdot T \cdot \ln a_o$
$E(T, C_o)$, $E > E^{SAT}$	$E_{(mV)} = -289 + 0.169 \cdot T - 0.043 \cdot T \cdot \ln C_{O(wt.\%)}$	$E_{(mV)} = -884 + 0.232 \cdot T - 0.232 \cdot T - 0.043 \cdot T \cdot \ln C_{O(wt.\%)}$
$\ln a_o(T,E)$ $E > E^{SAT}$	$\ln a_o = -23.209 \cdot \frac{E_{(mV)}}{T} + \frac{2779.5}{T} - 1.251$	$\ln a_o = -23.209 \cdot \frac{E_{(mV)}}{T} - \frac{11024}{T} + 0.20$
$\ln C_o(T,E)$ $E > E^{SAT}$	$\ln C_{O(\%)} = -23.209 \cdot \frac{E_{(mV)}}{T} - \frac{6719}{T} + 3.93$	$\ln C_{O(\%)} = -23.209 \cdot \frac{E_{(mV)}}{T} - \frac{20522}{T} + 5.385$
$\ln P_{sat}(T)$, $E = E^{SAT}$	$\ln P^{SAT}{}_{O2} = -\frac{52362}{T} + 25.67$	
$\ln P(T,E)$ $E > E^{SAT}$	$\ln P_{O2} = -\frac{46803}{T} - 46.418\frac{E_{(mV)}}{T} + 23.16$	$\ln P_{O2} = -\frac{74410}{T} - 46.418\frac{E_{(mV)}}{T} + 26.075$

Using another kind of reference sensor, the air/platinum reference sensor, described as follows, similar relations could be derived:

$$Pt, O_2 \text{ (reference) // } ZrO_2 + Y_2O_3 \text{ // } Pb + PbO \text{ (lead alloys solution), steel} \tag{4.41}$$

- Lead:

$$E^{SAT}{}_{th(V)} = \left(\frac{-\Delta H^o_{PbO}}{4F}\right) + \left(\frac{\Delta S^o_{PbO}}{4F} - \frac{c}{2} \cdot \ln 0.21\right) \cdot T_{(K)} \tag{4.42}$$

- Lead:

$$E_{th(V)} = \left(\frac{-\Delta H^{o}_{PbO}}{4F} + cB \right) + \left(\frac{\Delta S^{o}_{PbO}}{4F} - \frac{c}{2} \cdot \ln 0.21 - cA \right) \cdot T_{(K)} + c \cdot T_{(K)} \cdot \ln C_{O\,(wt.\%)} \quad (4.43)$$

- LBE:

$$E^{SAT}{}_{th(V)} = \left(\frac{-\Delta H^{o}_{PbO}}{4F} + c\beta \right) + \left(\frac{\Delta S^{o}_{PbO}}{4F} - \frac{c}{2} \cdot \ln 0.21 + c\alpha \right) \cdot T_{(K)} \quad (4.44)$$

- LBE:

$$E_{th(V)} = \left(\frac{-\Delta H^{o}_{PbO}}{4F} + cB' + c\beta \right) + \left(\frac{\Delta S^{o}_{PbO}}{4F} - \frac{c}{2} \cdot \ln 0.21 - cA' + c\alpha \right) \cdot T_{(K)} + c \cdot T_{(K)} \cdot \ln C_{O(wt.\%)} \quad (4.45)$$

Finally, these relations are calculated for the saturation using the data previously given using the oxygen concentration expressed in weight percentage:

- Lead:

$$E^{SAT}{}_{(mV)} = 1133.9 - 0.550 \cdot T_{(K)} \quad (4.46)$$

- Lead:

$$E_{(mV)} = 633.6 - 0.229 \cdot T_{(K)} - 0.043 \cdot T_{(K)} \cdot \ln C_{O\,(\%)} \text{ for } E > E^{SAT} \quad (4.47)$$

- LBE:

$$E^{SAT}{}_{(mV)} = 1128.1 - 0.587 \cdot T_{(K)} \quad (4.48)$$

- LBE:

$$E_{(mV)} = 718.8 - 0.363 \cdot T_{(K)} - 0.043 \cdot T_{(K)} \cdot \ln C_{O\,(\%)} \text{ for } E > E^{SAT} \quad (4.49)$$

These relations enable to plot the E vs. T (C_O as parameter) diagram as illustrated in Figure 4.4.4, which is most useful for reading sensor output as well as for sensor calibration (Konys, 2001; Gromov, 1998). It allows easily plotting the reading and comparing the relative position of the oxygen in relation to the PbO saturation line, defining the lower potential value achievable, which must be avoided to keep clear of contamination by PbO precipitation. Similarly, other oxide stability thresholds can be plotted for pertinent information on the position of the oxygen potential when compared for instance to the stability of the magnetite.

Apart from the data used for the theoretical assessment, there may be other causes for the sensor not to behave according to the theoretical relations: electrolyte conduction properties (slight electronic conduction, impurities in the ceramic, etc.), the influence of the reaction at the electrode/electrolyte interface (liquid metal/zirconia reaction, or even traces of impurities depositing on the interface), cell irreversibility (equilibrium not reached due to an oxygen transfer rate limitation especially at very low oxygen partial pressure), as well as the instrumental uncertainties. This is why calibration methods are often required (Subbarao, 1980; Courouau, 2003b).

Figure 4.4.4: Diagram *E* vs. *T* for the oxygen sensor reading in LBE

Indicates the oxygen and iron isoconcentration lines in weight percentage regularly set every order of magnitude, as well as the PbO and Fe_3O_4 saturation line, the respective oxide being stable below the line, and the oxygen dominant species area, the oxygen being dominant below the line. As an illustration the oxygen operating window presented in Figure 4.2.3 is plotted in the shaded area

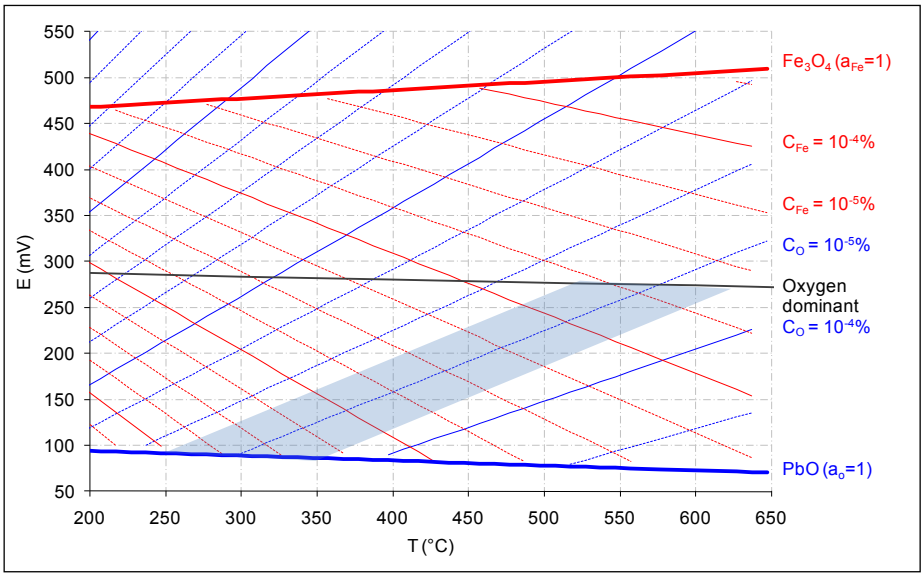

4.4.1.3 *Calibration*

Calibration is based on the comparison of the potential measurements (E) with the expected theoretical emf (E_{th}) for defined oxygen concentrations. The main difficulty for lead alloy melts consists in exactly defining the oxygen concentration of the melt. As oxygen is present in traces and subject to other impurities, its actual value is experimentally difficult to assess and to keep stable, particularly at dynamics facilities. Several methods were developed under static conditions based on specific operating procedures to maintain stable oxygen for a certain delay (temperature variation), or based on chemical equilibrium (dissolved impurity, or gaseous couple):

- the temperature variation close to the oxygen saturation (Konys, 2001; Courouau, 2002b), as illustrated in Figure 4.4.5, which allows accurately defining the oxygen content of a liquid melt, supposing its stable concentration during measurement;
- the comparison against the metal/metal oxide couple that buffers the oxygen concentration to the equilibrium level (Colominas, 2004);
- the comparison to the known gas phase oxygen content such as the steam/hydrogen gaseous mixture (Konys, 2004) that defines the oxygen concentration in the liquid bulk when the gas/liquid equilibrium is achieved.

Another method is based on the coulometric titration method, requiring a well-designed static facility to control all the sources of oxygen contamination. First, the residual oxygen is removed thanks to hydrogen. Then, a defined amount of oxygen is added thanks to an electrochemical oxygen pump up to the saturation at a given temperature (Ghetta, 2002).

All of these methods concluded in a rather good agreement between the sensor voltage output and the theoretical emf, and usually justified the use of the theoretical emf relation for the calculation of the oxygen concentration from the sensor readings.

Figure 4.4.5: Calibration with the inflexion point technique

Oxygen in LBE concentration; temperature diagram illustrating the principle of the calibration by the variation of temperature close to the saturation and example of actual calibration points obtained on the ARTOIS glove box following a specific operating procedure where oxygen remains constant for a while, allowing measuring the inflexion point that exactly defines the saturation temperature, here 420°C, allowing to calculate K1, K2, K and K′, assuming K3 constant

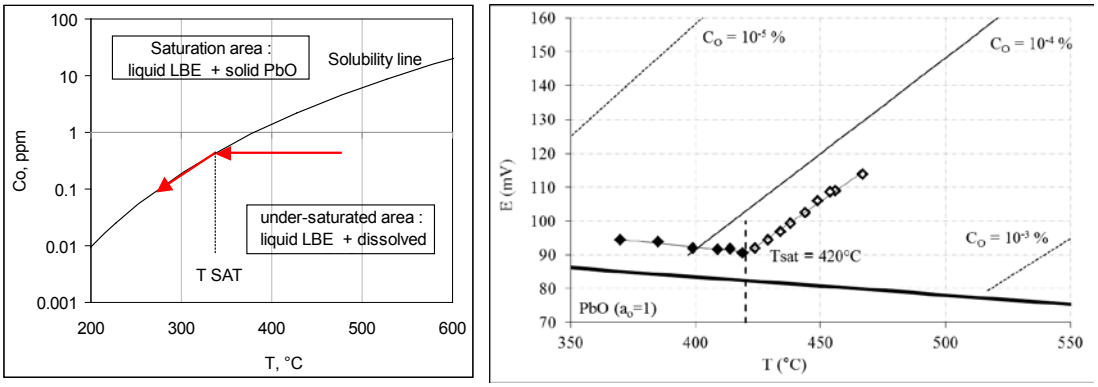

However, a slight scatter of a few millivolts, up to several tens of millivolts is always observed from this theoretical behaviour that is not yet fully understood. The effect of the other impurities might be the source of the errors, by reacting at the solid electrolyte interface and forming a metal/metal oxide couple interfering with the electrode potential. This must be understood more clearly as this side effect on the calibration process may limit the reliability of the sensors. The second source of errors is interpreted as coming from the zirconia intrinsic properties: slight impurity content variations in the fabrication process may be part of the explanation (Subbarao, 1980).

The temperature variation close to the oxygen saturation calibration method was repeated a great number of times so that mean statistical constants could be derived from it, and are thus recommended instead of the theoretical constants (Courouau, 2003b):

$$Bi/Bi_2O_3 \begin{cases} E^{SAT}_{(mV)} = 137 - 0.067 \cdot T_{(K)} \\ E_{(mV)} = -323 + 0.23 \cdot T - 0.0431 \cdot T \cdot \ln C_{O(wt.\%)} \end{cases} \quad (4.50)$$

$$In/In_2O_3 \begin{cases} E^{SAT}_{(mV)} = -412 - 0.051 \cdot T_{(K)} \\ E_{(mV)} = -937 + 0.71 \cdot T - 0.0431 \cdot T \cdot \ln C_{O(wt.\%)} \end{cases} \quad (4.51)$$

The accuracy is assessed within 5% of the voltage readings (25 mV maximum scattering for a 500 mV reading) that affect the concentration by 40% for the high concentration range to 80% for the low concentration range.

Calibration was, in any case, recommended to achieve a better accuracy. However, since the oxygen solubility relation is now considered as more accurate and since the source of deviation of the output is now understood and independent from the sensor (see Section 4.4.1.4), the thermodynamic relations as indicated in Table 4.2.2 are now recommended.

However, the availability of a method to achieve a reliable calibration in the field is necessary to significantly increase long-term accuracy, in order to regularly assess the proper operation of the sensor. Different methods were developed and are now available (Shroer, 2010).

4.4.1.4 *Characteristics of the oxygen sensors*

Sensors have been tested for thousands of hours in both static and dynamic conditions in stable and unstable chemical conditions that validate their effective and reliable use for dynamic loop operation (Schroer, 2011b; Askhadullin, 2005; Ghetta, 2002; Colominas, 2004; Courouau, 2003b; Gromov, 1997; Konys, 2004; Shmatko, 2000). These tests allowed gaining a large operating feedback representative of long-term operations over a wide variety of operating conditions. The characteristics observed up to now on these oxygen prototype sensors are thus satisfactory and confirm previous observations as regards the operating range (370-550°C for the Bi/Bi_2O_3 reference electrode), the oxygen concentration range, the response time, the accuracy and reproducibility, as well as the service life (several thousands of hours, longer expected in stable conditions). An operating temperature lower than 350°C is possible but with a reduced accuracy, as the sensor outputs deviate from ideal behaviour most probably because of an increasing irreversibility of the cell.

The time to react to a concentration change is fast for an oxygen contamination. The recovery time is linked to the chemical reaction kinetics that are limited by the mass transfer phenomenon (gas/liquid interface, oxygen diffusion in liquid bulk). From a general point of view, the transient phase of one system is not absolutely reliable as the oxygen content is globally inhomogeneous. However, this effect disappears under steady-state conditions. The sensor gives only the local oxygen content, such that loop implementation is important to obtain reliable information about a homogenous system (Orlov, 2005).

Time drift can affect sensor outputs over the long term as illustrated in Figure 4.4.3 because of the deposition of impurities at the electrolyte interface, which eventually creates a separate and different liquid metal environment measured by the oxygen sensor (Courouau, 2010). The oxygen in this environment presents behaviour different from the liquid bulk, firstly because the surface/volume ratio changed from a very low value in the liquid metal bulk to a very high value. The relative proportion of impurities is different, which can significantly affect the oxygen concentration. For instance, the oxygen may react with impurities such as aluminium, even if present in very low concentration, decreasing the dissolved oxygen locally. The use of a metallic sheath to protect the ceramic thimble is reported to favour the deposition of impurities. As a confirmation, the sheath protected by pack cementation presented fouling and gave oxygen outputs corresponding to dissolved aluminium/aluminium oxide in LBE. The mechanism of fouling is illustrated in Figure 4.4.6; the sensor keeps monitoring the concentration at the ceramic/liquid interface, $[O]_i$. If at first the oxygen interfacial concentration was representative of the liquid bulk concentration, the formation of deposits gradually modified the liquid metal system to a local one, the concentration of which evolved independently from the liquid metal bulk.

The time drift that was observed on several occasions on static device was repeated on the STELLA loop operation (Figure 4.4.3). The drift appeared only after a certain delay of several hundreds of hours, when the lead alloys was submitted to thermal and oxygen variations. Then, the drift gradually and almost constantly increases. In this specific example, the time drift of the Bi sensor is illustrated by plotting on the graph the absolute difference between the theoretical deviation of two different reference electrodes (here 546 mV), and the difference between the two sensors' readings, according to Eq. (4.52):

$$e = 546 - \left(E\left(Bi/Bi_2O_3\right) - E\left(In/In_2O_3\right)\right) \tag{4.52}$$

When a sensor is fouled by impurities, it can be recovered from by applying a cleaning procedure. Figure 4.4.6 presents one of the STELLA sensors that presented a drift right after its extraction from the loop: it was then cleaned with acidic solution, recalibrated and efficiently reused.

Figure 4.4.6: Mechanism of formation of an isolated liquid metal volume at the interface of the sensing part of the electrochemical sensor by the combined effect of sheath and impurities

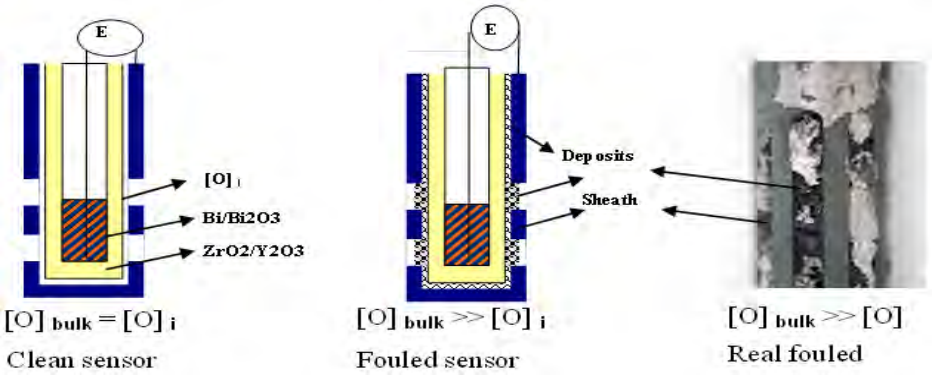

Source: Courouau (2010).

Although yttria-doped zirconia is known to present a better thermal shock resistance (temperature gradient, temperature cycling) as well as a better mechanical resistance when hot (vibrations, contact, etc.) when compared to other solid electrolytes such as yttria-stabilised thoria, a number of failures has been observed (Figure 4.4.7). The point of breakdown is often observed at the central point localised at the bottom of the ceramic thimble. The internal reference electrode when localised in a closed-end tube is itself a source of major mechanical wear during its solidification. Optic observations of the ruptured ceramic surface (Figure 4.4.7) indicate the gradual insertion of bismuth into microcracks, most probably due to the positive volumetric change of Bi during its solidification. Lowering the height of the internal reference electrode will reduce this effect. The use of conical shape for the solid electrolyte is most favourable from this particular point of view, as the solidification constraints will exert preferentially upwards towards the free level rather than radially towards the ceramic. This conclusion is further evidenced by the experimental observations from the CORRIDA loop (Konys, 2004): the air/Pt reference sensor exhibited a much higher service lifetime when compared to the Bi/Bi_2O_3 reference sensor used within the same operating conditions, and with the same electrolyte. The use of specific temperature ramps when heating, and especially when cooling, is recommended (1°C/min or lower for instance).

Figure 4.4.7. Bi/Bi_2O_3 sensor operated for 1 400 hours on the STELLA loop and details of the point of rupture

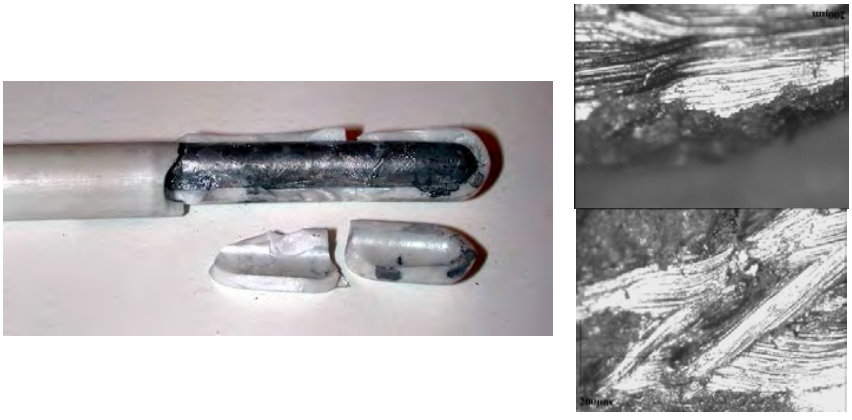

Source: Courouau (2005b).

Another method to reduce failures is to use a proper design for the ceramic housing, together with the use of special procedure for operation. This was typically used for the liquid sodium sensor (Westinghouse, Harwell) and is known to be efficient (Asher, 1988). Figure 4.4.8 presents one of the designs for such a housing that has been achieved (Courouau, 2005b), and that must be validated on the STELLA loop. A similar design is used at the Karslruhe Lead Laboratory (Konys, 2001). Its main characteristics consist in having the seal, ensuring the tightness of the facility between the ceramic and the metallic structure localised in the cold area, which is made possible thanks to the ceramic length and the cooling fins. The seal is then a simple O-ring. The ceramic is protected with a metallic sheath reducing shocks, both thermal and mechanical, and keeping ceramic pieces in case of rupture. Leak detection is ensured at the cap location with a specific temperature measurement. Any liquid metal coming up there should in principle stay confined thanks to this metallic cap. This kind of design proved efficient in liquid sodium technology, as the sensor service lifetime was not dependent on the sealing medium, which, if localised in the bottom area, would be in contact with high temperature liquid metal, eventually leading to a short circuit, or the loss of the leak-proof feature.

Figure 4.4.8: CEA sensor housing to be tested on the STELLA loop

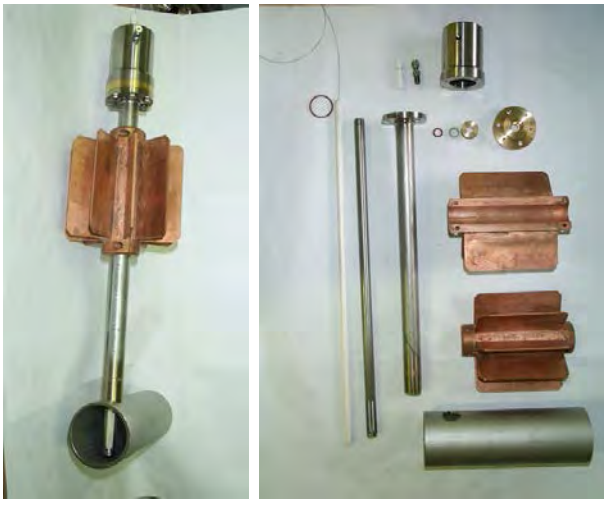

Source: Courouau (2005b).

Although the closed-end tube shape is commercially available and easily separates the two electrodes, the working and the reference electrodes, it might have to be replaced by other less fragile shapes, like a conical shape sealed with graphite or tantalum (Li, 2003) or fused with a metal-to-ceramic bound (Chernov, 2003) to a metallic tube that is reported as far more resistant. However, implementation becomes more complex because of the issue of the metal-to-ceramic sealing and fusing that must be compatible with the liquid metal over the long term. The Russian model, dating from the early 1990s, and which is now registered in the Russian state standard committee (Figure 4.4.9), was, for instance, implemented on the BOR-60 lead channel and operated most satisfactorily during irradiation (Korotkov, 2003). Recent developments include the inclusion of impurities, such as particles of alumina (nano size), as well as the specific firing procedure to exceptionally improve the mechanical resistance of the solid electrolyte (Askhadullin, 2005, 2007). The US model (Figure 4.4.10) is based on the solid electrolyte used in the car industry for the lambda sensor, the ceramic part of which is quite widely available at low cost. It is awaiting validation under representative conditions as pertains to the long-term behaviour of the seal. In addition, a reactive braze for the bound was recently developed within the framework of a specific MIT-Ceramtec agreement with promising results up to now (Ballinger, 2006).

Figure 4.4.9: A schematic cross-sectional view of the oxygen sensor developed by IPPE

Source: Zrodnikov (2003) and Askhadullin (2007).

Figure 4.4.10: LANL ceramic element with the graph-lock gasket and the metallic sheath with the seating ring and the reactive braze bound

Source: Li (2003) and Ballinger (2006).

4.4.1.5 *Conclusions*

The oxygen monitoring system is quite compulsory for any lead alloy system, at least to ensure the contamination control. It is now clear that sensors based on solid electrolyte electrochemical cell proved efficient for measuring the dissolved oxygen of the lead alloy systems, despite a number of limitations, which are quite typical of this kind of measurement. However, it is not commercially available, so that for a day-to-day use on experimental facilities, the theoretical background and know-how given in this section will allow the assembly of a sensor from available parts, as well as its basic use at the laboratory scale. The interpretation of its outputs is now more closely related to the liquid chemistry rather than on the operation of the sensor itself.

Several concepts were designed and are presently at different levels of achievement, but all are under rapid progress for a reliable use in a nuclear system. One can notice in particular the outstanding level of achievement of the Russian design (Askhadullin, 2007), which presents, apparently, none of the limitations identified and described in this section, and was successfully used in a nuclear environment. It avoids the use of a metallic sheath, which presents another advantage as regards the fouling issue.

4.4.2 *Development of sampling systems and analytical methods*

The impurities monitoring system for the liquid phase is typical of the liquid metal fast reactors: a system that allows getting a liquid metal sample, in order to perform a chemical or radiochemical analysis of the impurities. Periodic sampling enables in principle to monitor the behaviour of the dissolved impurities over the long term as well as to assess the gradual activation of the coolant.

4.4.2.1 *Dip sampler validation*

There are two main types of sampling system:

- dip sampling throughout an airlock system, which is the reference sampling system in liquid metal reactors such as the sodium-cooled;
- circulation in a tube-sampling device in a bypass line, which was partly given up because of representativeness difficulties as regards the corrosion products (potential accumulation due to deposits on the walls), although this is questionable depending on the impurities to be measured.

The objective is to be able to take a sample of liquid LBE in any facility to perform subsequent chemical analysis of the impurities. The following specifications are usually required for any sampling system:

- to obtain an homogeneous liquid metal sample;
- to provide a sampling system that does not pollute liquid metal samples;
- to design an easy-to-use system that complies with a nuclear environment;
- to provide a system that may be quickly cooled.

Such a device was already developed for the lead-lithium eutectic alloy that is studied for the tritium-breeding blanket of a fusion reactor (Desreumaux, 1993). The basic principle was to adapt the sampler to the LBE melt and achieve a first qualification on a static facility. The scheme and a view of this dip sampler developed for the lead-lithium alloy is provided hereafter in Figure 4.4.11 along with the LBE sample obtained (Courouau, 2002a).

Figure 4.4.11: Scheme, view of the dip sampling system, which is then hooked to a stem and immersed throughout an air lock, as well as the resulting LBE sample

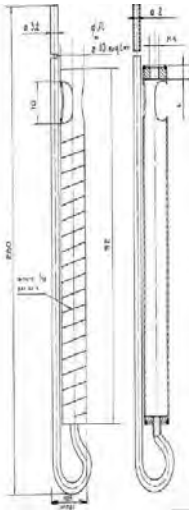

The tube on the bottom part, opposite to the hole for the inlet of the melt, was necessary to ensure a good filling of the sampler by enabling degassing. This tube should not really be needed for lead-bismuth alloy because of its higher density. The dip sampler fabrication could then be simplified. The stripy marks done during fabrication on the external surface of the dip sampler enable, in principle, an easy discarding of the steel, like the opening of a tin, delivering the LBE sample ready for its analysis.

The nature of the material used up to now is stainless steel. Its effect on the dissolved impurity content was not assessed. However, a pure material presenting very low solubilities in lead alloys is recommended. Elements such as Fe, Cr, Nb, Mo, Co, Ti, Si and Zr present very low solubilities in the liquid lead alloys eutectic, and could be efficiently used for the dip sampling material. However, as Fe and Cr are two of the impurities to be analysed, it is recommended they be avoided for the candidate material. Carbon in the form of graphite or a composite such as SiC can possibly be used.

The issue of the representativeness of the measurement has not been treated due to the lack of any sampling under loop operating conditions. This issue is to be further investigated, as the sampling system might not be homogeneous for all nuclides. Indeed, some impurities might be concentrated on the walls of the sampling system, so that the conditions of sampling (temperature, immersion time, temperature decrease gradient, etc.) are to be optimised on the basis of the future experimental feedback. In addition, the topic of the possible contamination of the sampling system during immersion by the free surface oxides is not addressed. The feedback from past development should be taken into account for the liquid metal sample optimisation, such as for instance multiple sampling systems for a larger amount of metal sampled such as the "harp sampler" (Figure 4.4.12) (Borgstedt, 1989), and especially for a technique and know-how developed for achieving representative sampling (Borgstedt, 1989). The use of alternative techniques, such as the online distillation technique that was once studied and applied for liquid sodium, should be reassessed.

Figure 4.4.12: Schematic drawing of an overflow multiple sampler for flowing alkali metals

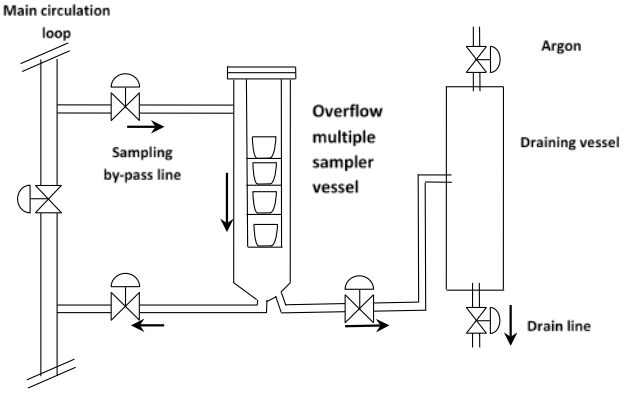

4.4.2.2 *Chemical analysis of lead-bismuth eutectic*

Various techniques are used for lead alloy characterisation, as follows (Desreumaux, 1998):

- composition analysis;
- characterisation of metallic impurities;
- oxygen present in the alloy measurement.

The composition analysis techniques are based on calorimetry, surface spectroscopy analysis or atomic absorption spectroscopy (AAS). The calorimetric method principle is to measure the thermal flux absorbed or produced by a sample subjected to a temperature increase. The results enable deducing the respective reaction temperatures, the eutectic and peritectic points, as well as the reaction specific heat. But this kind of analysis is not sufficient in and of itself, as several compositions are often possible when referring to a phase diagram.

The surface spectroscopy analysis consists of X-ray analysis, scanning electron microscopy (SEM) or wavelength dispersive X-ray fluorescence (WDXRF). When energy dispersive X-ray spectrometer (EDS) is coupled to a scanning electron microscope, the measure of the alloy composition is possible at any point of the surface of the sample. The mean value of several points (10 at least) could be used to determine the mean composition of the alloys. The scanning electron microscope enables determining the general state of the alloys, through the study of its enriched or depleted zone. The latter method, WDXRF, enables the measurement of virtually all the periodic table ($Z > 11$) for concentrations above 500 μg/g (Desreumaux, 1998). This method is thus well adapted to the alloy composition determination, but not for the measurement of impurities.

Metallic impurity analyses are achieved first by dissolution of the lead alloy, and then by the use of inductive coupled plasma/mass spectrometry (ICP/MS) or AAS. The ICP/MS method enables the measurement of a wide range of impurities such as Fe, Ni, Cr, Ag, Cd, Cu, Sn, Sb, etc.

The iron impurity has an isobaric interference with ArO gaseous mixture (Ar being the plasma gas) that increases the lower detection limit to 50 μg/g. For the iron impurity, the AAS technique coupled with the spiking method is then a better choice than the ICP-MS technique, resulting in a lower detection limit decreased to 5 μg/g.

For the nickel impurity, because of the contamination coming from the nickel cones of the transfer chamber of the ICP/MS apparatus, the lower detection limit is high when compared to the other impurities. There are two methods for decreasing the lower detection limit: changing the cones to platinum cones, or measuring nickel by AAS with a spiking method that decreases the lower detection limit to 5 μg/g as well.

The analytical measurement of oxygen in a sample can be made by two methods (Desreumaux, 1998). The first method is based on the reductive fusion of the sample in a graphite crucible. The resulting carbon dioxide is measured by infrared spectroscopy. This technique is used with careful calibration in the expected range, and with devoted preparation procedures for the sample in order to reduce any superficial oxide. It measures the total amount of oxygen present in the alloys: either the dissolved oxygen or the oxides. The other method is based on electrochemical measurement as described in the next subtask with laboratory scale electrochemical cells. It measures only the dissolved oxygen present in the liquid metal solution.

The methods were applied to LBE samples performed on the alloy supplied by METALEUROP to CEA Cadarache (Desreumaux, 1998) (Table 4.4.3).

Table 4.4.3: Composition of the METALEUROP LBE

	Calorimetry		WDXRF	
	Melting point	Enthalpy	%Pb	%Bi
Measurements	126.2°C	17.0 J/g	41.7±2	57.3±2

Table 4.4.4 gives the impurities measured, as well as the values of the pure lead and bismuth characterised by the supplier for comparison. During the cooling phase of the dip sampling, a segregation phenomenon occurs, resulting in a relative heterogeneity of the lead alloy depending on the method used for composition characterisation. Typically, a better composition measurement is obtained by dissolution of the whole sample, rather than on parts of the sample.

The table provides the metallic impurity concentrations measured in the alloys with the different analysis techniques. This compares well to one of the other characterisations available (Glasbrenner, 2004b) made on the LBE supplied by Impag AG (Switzerland) which contained a few μg/g of impurities: Ag 11.4, Fe 0.78, Ni 0.42, Sn 13.3,Cd 2.89, Al 0.3, Cu 9.8, Zn 0.2.

Table 4.4.4: Metallic impurities measured in the METALEUROP LBE

	Analytical technique	EPB measured (μg/g)	Bi (theoretical) (μg/g)	Pb (theoretical) (μg/g)
Sn	ICP/MS	< 2	< 1	< 2
Fe	AAS	< 5	< 1	
Ni	AAS	< 5	1.4	< 1
Ag	ICP/MS	3	1	6
Cu	ICP/MS	< 2	< 1	< 2
Zn	ICP/MS	< 2	< 1	
Cd	ICP/MS	< 1	< 1	< 2
Sb	ICP/MS	< 2	< 3	< 2
As	ICP/MS	< 2	< 1	< 2
Te	ICP/MS	< 1	< 1	< 3

The first tests for oxygen measurement were made with a LECO apparatus calibrated with a steel matrix, giving thus a different fusion temperature. The results showed dispersed values for the lead alloy sample, from 1 μg/g to 5 μg/g. A different approach based on calibration of the apparatus with a 1 μg/g lead sample did not allow lowering the detection limit. Actually, the apparatus used for these measurements proved insufficient for this kind of study: background level of the LECO apparatus is too high and its resulting sensitivity appeared too low when compared to the effective operating oxygen concentration range (0.01 μg/g).

4.4.2.3 Radioactive nuclides chemical analysis

The regular radio activation measurement of the coolant is typical for nuclear system operation, as it can affect the reactor operation (handling or repair during maintenance operation, fuel cladding failure, transfer or accumulation on a specific part of the system…). All nuclides being gamma emitters can be measured by gamma spectrometry. This is typically achieved after having dissolved the metal sample in an aqueous solution (nitric acid). However, other nuclides, which are specific to the spallation reaction, or due to the activation of the heavy liquid metal coolant, are only beta-emitters (most of the Bi, Tl, Hg, Au, Pt nuclides), or even alpha-emitters (^{208,209,210}Po). Their measurement therefore requires specific procedures in order to be able to measure traces, and in some case to be able to measure each of the isotopes produced for one particular nuclide (Po).

Preliminary investigations were achieved for Po isotope speciation by Lacressonniere (2003), which was applied to one of the first LiSoR irradiated samples (36 hours, 2002). Measurements gave: 3 752 Bq/g of ^{208}Po, 22 Bq/g of ^{209}Po, 19 Bq/g of ^{210}Po, which corresponds to the measurement achieved independently by the Paul Scherrer Institute (Glasbrenner, 2004b), as well as to the nuclear production assessment. The technique is based on concentration of the nuclides in a first step (ferric co-precipitation, and liquid/liquid extraction with tri-butyl-phosphate), then in a second step by the self-deposition on an argent disk for alpha-spectrometry measurement.

The technique that was under study for the trace measurement of the mercury concentration is the atomic absorption spectrometry coupled with a vapour generator. The detection limit achieved by this method is 0.06 μg/g (60 10^{-9} g/g) (Chabert, 2003).

4.4.2.4 *Conclusions*

The dip sampling system that was originally developed for Pb-Li alloys got a first validation in LBE. The issue of the representation is to be further assessed, in order to eventually propose an optimised design. Indeed, the sample must be representative of the liquid metal bulk, which is depending of the location of the sampling, and then of the design of the nuclear system.

The analytical techniques for metallic impurities measurement: Fe, Ni, Cu, Sn, Ag, Zn, Cd, Sb, As, Te, for which either ICP-MS or AAS with spiking method have been used, were as well demonstrated. However, the lower detection limit of 5 μg/g cannot be further lowered, unless another ICP-MS apparatus, more costly, is used to lower the detection limit by one order of magnitude: 0.5 μg/g. Industrial analytical laboratories are usually equipped with such equipment. A cross-comparison benchmark with such laboratories is necessary, however, to confirm the lower detection limit and accuracy of the measurement, including, in particular all the crucial preparation steps of the samples.

Concerning the radioactive impurities, measurement techniques were developed only for the speciation of the polonium and mercury, as the techniques for low alpha or beta activities measurement are not straightforward. Further developments for the speciation methods should concern the main spallation and activation products isotopes that are expected for normal operating conditions: Po, Bi, Pb, Hg, Au, Pt, Ir, Re, Ta, Hf. The techniques for solvatation, concentration, etc., are part of the development envisaged.

However, during normal operating conditions in an anisothermal system, the equilibrium concentration of the main impurities involved in the corrosion and mass transfer processes will be lower or even far lower than the lower detection limit available (5 μg/g or even 0.5 μg/g). This makes really difficult the iron monitoring, for instance. There is no straight solution foreseeable to solve that issue, except the use of an indirect measurement method. Indeed, the steel making industry uses the oxygen measurement to check the dissolved carbon, as the dissolved oxygen is defined by the C/CO chemical equilibrium in that particular condition. Detecting the iron oxide stability threshold, providing the availability of precise data and good sensor accuracy could be one of the solutions.

4.5 Conclusions

Chemistry control in a nuclear system appears as a quite complex issue, particularly the necessity to keep the corrosion under control in a wider operating temperature range, as well as to keep the coolant free of any contamination by oxides, which is basically the first requirement. The radiochemistry control appears to be difficult as well, as production rates are relatively inaccurate, and as the transport phenomena as well as associated purification processes are to be better understood and developed.

However, chemistry control is usually not critical for operation if taken into account at the early design stage as well as during start-up and shutdown procedures. This is why it should not be neglected in designing any kind of systems, especially in the view of the potential operating difficulties that could result. Well-designed and well-operated facilities could be run, in principle, with a rather high confidence under the no-oxygen conditions. Higher operating temperatures require the validation of oxygen control systems at a specified medium range concentration over the long term for larger systems, and especially for pure lead.

There are some similarities in the chemistry analysis of water, liquid sodium and lead alloy systems. They all present quite identical requirements for both monitoring and processes. However, the consequences for an LBE system are much more critical, such as the loss of cooling capacity due to plugging or the loss of confinement due to corrosion, which makes this issue as one of the most important one when operating such a system.

Some points remains open for further studies, such as process optimisation of oxygen control systems, the improvement of the reliability of the associated instrumentation (such as the oxygen sensor), as well as the basic phenomena for aerosols, particles and mass transfer, even of impurities present in traces such as the active contaminants, within a close and tight system over the long term, for which basic understanding must still be increased.

Real operating limits for the processes should be measured on test facilities in representative operating conditions and for relevant materials before any implementation in a nuclear system.

References

Asher, R.C. et al. (1988), "Recent Developments in the Design, Performance and Application of HARWELL Oxygen Sensors and Harwell Carbon Meters", 4th *Int. Conference on Liquid Metal Engineering and Technology (LIMET)*, Avignon, France, 17-21 October.

Askhadullin, R.S. (2007), *Development of Oxygen Sensors, Systems of Control of Oxygen Content in Lead Coolants for Test Loops and Facilities – Final Project Technical Report on the Work Performed from 1 May 2005 to 30 April 2007*, ISTC project n°3020.

Askhadullin, R.S. et al. (2003), "Regulation of the Thermodynamic Activity of Oxygen in Lead and Lead-Bismuth by the Dissolution of the Oxides in Heat Transfer Systems", *Proceedings of the Fast Neutrons Reactors Conference*, Obninsk, Russian Federation, 8-12 December (in Russian).

Askhadullin, R.S. et al. (2005), *Development of Oxygen Sensors, Systems of Control of Oxygen Content in Lead Coolants for Test Loops and Facilities*, International Science and Technology Centre, Contract No. 3020.

Azzati, M., A. Gessi and G. Benamati (2003), *Experimental Results on Oxygen Control Systems*, TECLA D28, ENEA FIS ENG Technical Note.

Balbaud-Célérier, F. and F. Barbier (2001), "Investigation of Models to Predict the Corrosion of Steels in Flowing Liquid Lead Alloys", *Journal of Nuclear Materials*, Vol. 289, pp. 227-242.

Ballinger, R.G. (2006), private communication.

Ballinger, R.G. and J. Lim (2004), "An Overview of Corrosion Issues for the Design and Operation of High Temperature Lead and Lead-bismuth Cooled Reactor Systems", *Nuclear Technology*, Vol. 147, pp. 418-435.

Barin, I. (1989), *Thermochemical Data of Pure Substances*, VCH Editions, Weinheim Germany.

Beauchamp, F. et al. (2010), "A Review of Lead-Bismuth Alloys Purification Systems in Regard with the Latest Results Achieved on STELLA Loop", *Conference on Technology and Components for Accelerator Driven Systems (TCADS-1)*, Karlsruhe, Germany, 15-17 March 2010, OECD/NEA, Paris.

Blochin, V.A. et al. (1998), "Experience of Development and Operation of Oxides Electrolytic Sensors in Lead-bismuth Coolant", *Proceedings of the Conference of the Heavy Liquid Metal Coolants in Nuclear Technology*, Obninsk, Russian Federation, 5-9 October, pp. 87-100 (in Russian).

Borgstedt, H.U. and C.K. Mathews (1987), *Applied Chemistry of the Liquid Alkali Metals,* Plenum Press, New York, London.

Borgstedt, H.U. and Z. Peric (1989), "Sampling of Alkali Metals in Nuclear Applications", *Erzmetall*, Vol. 42, No. 11, pp. 504-507.

Brissonneau, L. et al. (2011), "Oxygen Control Systems and Impurity Purification in LBE: Learning from DEMETRA Project", *Journal of Nuclear Materials*, Vol. 415, No. 3, pp. 348-360.

Buongiorno, J. et al. (2004), "Studies of the Polonium Removal from Molten Lead-bismuth for Lead Alloys Cooled Reactor Applications", *Nuclear Technology*, Vol. 147, pp. 406-417.

Buongiorno, J., N.E. Todreas and M.S. Kasimi (2002), "Heavy Metal Transport in Lead-bismuth Cooled Fast Reactor with In-Vessel Direct Contact Steam Generation", *Nuclear Technology*, Vol. 138, pp. 30-43.

Chabert, C. (2003), personal notes.

Chernov, M.E., P.N. Martynov and V.A. Gulevskiy (2003), "Development of Electrochemical Capsule Oxygen Sensor for Control and Monitoring of Heavy Metal Coolant Condition", *Proceedings of the Fast Neutrons Reactors Conference*, Obninsk, Russian Federation, 8-12 December (in Russian).

Colominas, S., J. Abella and L. Victori (2004), "Characterisation of an Oxygen Sensor Based on In/In_2O_3 Reference Electrode", *Journal of Nuclear Materials*, Vol. 335, pp. 260-263.

Courouau, J-L. (2000), "Oxygen Control Systems, Comparison between Oxygen Probes", *Proceedings of the 1st MEGAPIE Technical Review Meeting*, Cadarache, France, 14-15 June.

Courouau, J-L. et al. (2002a), "Impurities and Oxygen Control in Lead Alloys", *Journal of Nuclear Materials*, Vol. 301, pp. 53-59.

Courouau, J-L., P. Deloffre and R. Adriano (2002b), "Oxygen Control in Lead-bismuth Eutectic: First Validation of Electrochemical Oxygen Sensor in Static Conditions", *Journal de Physique IV*, France 12, Pr. 8, pp. 141-153.

Courouau, J-L. (2003a), "Impurities and Purification Processes in Lead-bismuth Systems", Deliverable No. 25, TECLA, 5th EURATOM Framework Programme No. FIKW-CT-2000-00092.

Courouau, J-L. et al. (2003b), *Report on the Long Term Validation of Electrochemical Sensor*, Deliverable No. 32, TECLA, 5th EURATOM Framework Programme No. FIKW-CT-2000-00092.

Courouau, J-L. (2004a), "Electrochemical Oxygen Sensors for On-line Monitoring in Lead-bismuth Alloys: Status of Development", *Journal of Nuclear Materials*, Vol. 335, pp. 254-259.

Courouau, J-L. and J-C. Robin (2004b), "Chemistry Control Analysis of Lead Alloys Systems to be Used as Nuclear Coolant or Spallation Target", *Journal of Nuclear Materials*, Vol. 335, pp. 264-269.

Courouau, J-L. et al. (2004c), "Initial Start-Up Operations Chemistry Analysis for MEGAPIE", *Proceedings of the 5th MEGAPIE Technical Review Meeting*, Nantes, France, 24-26 May.

Courouau, J-L. et al. (2005a), "Review of the Oxygen Control for the Initial Operations and Integral Tests of the MEGAPIE Spallation Target", *Proceedings of the 6th MEGAPIE Technical Review Meeting*, Mol, Belgium, 27-29 June.

Courouau, J-L. et al. (2005b), "Electrochemical Oxygen Sensor for On-line Measurement in Liquid Lead Alloys Systems at Relatively Low Temperature", *AFINIDAD (AFINAE) Revista de Quimica teorica y aplicada (Journal of Theoretical and Applied Chemistry)*, Vol. 62, No. 519, pp. 464-468.

Courouau J-L. et al. (2010), "Demonstration of the Effect of Impurities on the Long-term Behaviour of Electrochemical Oxygen Sensor During the STELLA 2006 Tests", *Conference on Technology and Components for Accelerator Driven Systems (TCADS-1)*, Karlsruhe, Germany, 15-17 March 2010, OECD/NEA, Paris.

Desportes, C. et al. (1994), *Électrochimie des solides*, EDP Sciences – Presses universitaires de Grenoble, ISBN 2.7061.0585.1 (in French).

Desreumaux, J. (1998), *Caractérisation de lingots d'alliage plomb-bismuth de deux provenances différentes*, Technical Note CEA DER/STML/LEPE 98/061 (in French).

Desreumaux, J. et al. (1993), "Development of a New Plugging Indicator and Experimental Tests in a Lithium-lead Facility", *Conference on Liquid Metal Systems*, Karlsruhe, Germany, 16-18 March.

Fazio, C., M. Azzati and G. Benamati (2000), *Oxygen Control Strategies in Large Loop, Critical Analysis of the Different Process*, ENEA FIS ENG Technical Note HS-A-R—007.

Fazio, C. et al. (2008), "The MEGAPIE-TEST Project: Supporting Research and Lessons Learned in First-of-a-kind Spallation Target Technology", *Nuclear Engineering and Design*, Vol. 238, No. 6, pp. 1471-1495.

Fernandez, J.A. et al. (2002), "Development of an Oxygen Sensor for Molten 44.5% Lead_55.5% Bismuth Alloy", *Journal of Nuclear Materials*, Vol. 301, pp. 47-52.

Ganesan, R., T. Gnanasekaran and R.S. Srinivasa (2006), "Diffusivity, Activity and Solubility of Oxygen in Liquid Lead and Lead-bismuth Eutectic Alloy by Electrochemical Methods", *Journal of Nuclear Materials*, Vol. 349, pp. 133-149.

Ghetta, V. et al. (2001), "Experimental Setup for Steel Corrosion Characterization in Lead Bath", *Journal of Nuclear Materials*, Vol. 296, pp. 295-300.

Ghetta, V. et al. (2002), "Control and Monitoring of Oxygen Content in Molten Metals, Application to Lead and Lead-bismuth Melts", *Journal de Physique IV*, France 12, Pr. 8, pp. 123-140.

Ghetta, V., A. Maître and J-C. Gachon (2004), "Thermodynamic and Corrosion Studies Related to Liquid PbBi", *Proceedings of the 5th MEGAPIE Technical Review Meeting*, Nantes, France, 24-26 May.

Glasbrenner, H. and F. Gröschel (2004a), "Bending Test on T91 Steel in Pb-Bi Eutectic, Bi and Pb-Li Eutectic", *Journal of Nuclear Materials*, Vol. 335, pp. 239-243.

Glasbrenner, H. et al. (2004b), "Polonium Formation in Pb-55.5Bi Under Proton Irradiation", *Journal of Nuclear Materials*, Vol. 335, pp. 270-274.

Gorynin, V. et al. (1998), "Structural Materials for Power Plants with Heavy Liquid Metal Systems as Coolant", *Proceedings of the Conference of the Heavy Liquid Metal Coolants in Nuclear Technology*, Obninsk, Russian Federation, 5-9 October, pp. 120.

Gromov, B.F. and B.A. Shmatko (1996), "Physico-chemical Properties of Lead-bismuth Alloys", *Izvestiya Vischikh Uchebnikh Zavedenii – iyadernii energiya (Transaction of Higher Educational Institutions – Nuclear Energy)*, No. 4, pp. 35-41 (in Russian).

Gromov, B.F. and B.A. Shmatko (1997), *Izvestiya Vischikh Uchebnikh Zavedenii – iyadernii energiya (Transaction of Higher Educational Institutions – Nuclear Energy)*, No. 6, pp. 14-18 (in Russian).

Gromov, B.F. et al. (1998), "The Problems of Technology of the Heavy Liquid Metal Coolants (Lead-bismuth, Lead)", *Proceedings of the Conference of the Heavy Liquid Metal Coolants in Nuclear Technology*, Obninsk, Russian Federation, 5-9 October, pp. 87-100.

Gulevskiy, V.A., P.N. Martynov and Yu.I. Orlov (1998), "Application of Hydrogen/Water Vapor Mixtures in Heavy Coolant Technology", *Proceedings of the Conference of the Heavy Liquid Metal Coolants in Nuclear Technology*, Obninsk, Russian Federation, 5-9 October, pp. 668-674.

Gulevskiy, V.A. et al. (2003), "Water and Hydrogen in Heavy Metal Coolant Technology", *Proceedings of the Fast Neutrons Reactors Conference*, Obninsk, Russian Federation, 8-12 December (in Russian).

Hugon, M. et al. (2005), "Euratom R&D Programmes on the Back-End of the Fuel Cycle", *Revue générale du nucléaire (RGN)*, No. 2, March-April.

HSC Chemistry for Windows Version 4.1, Chemical Reaction and Equilibrium Software, Outokumpu.

NIST (National Institute of Standards and Technology) (2013), JANAF Thermochemical Tables, accessed 13 December 2014, http://kinetics.nist.gov/janaf/.

IP-EUROTRANS (Integrated Project-EUROTRANS) (2004), 6th EURATOM Framework Programme, No. FI6W-CT-2004-516520.

International Atomic Energy Agency (IAEA) (1993), *Fission and Corrosion Product Behaviour in Liquid Metal Fast Breeder Reactors (LMFBRs)*, TECDOC-687, IAEA, Vienna.

IAEA (1998), *Nuclear Heat Applications: Design Aspects and Operating Experience*, IAEA-TECDOC-1056, IAEA, Vienna.

IAEA (2002), *Comparative Assessment of Thermophysical and Thermohydraulic Characteristics of Lead, Lead-bismuth, and Sodium Coolants for Fast Reactors*, TECDOC-1289, IAEA, Vienna.

IAEA (2003), *Power Reactors and Sub-critical Blanket Systems with Lead and Lead-bismuth as Coolant and/or Target Material*, IAEA-TECDOC-1348, IAEA, Vienna.

Ivanov, K.D. et al. (2003a), "Impurities in Lead and Lead-bismuth Coolants", *Proc. of the Fast Neutrons Reactors Conference*, Obninsk, Russian Federation, 8-12 December (in Russian).

Ivanov, K.D., P.N. Martynov and Yu.I. Orlov (2003b), "Pb-Bi Coolant Technology on NPP of Generation I and II", *Proceedings of the Fast Neutrons Reactors Conference*, Obninsk, Russian Federation, 8-12 December (in Russian).

Jacob, K.T. and W.W. Shim (1981), "Gibbs Energy of Formation of Lead Zirconate", *Journal of the American Ceramic Society*, Vol. 64, No. 10.

Kawahara, H. et al. (2004), "Replacement of Secondary Heat Transport System Components in the Experimental Fast Reactor JOYO", *Proceedings of ICONE 12*, Arlington, Virginia.

Khorosanov, G.L., A.P. Ivanov and A.I. Blokhin (2002), "Polonium Issue in Fast Reactor Lead Coolants and One of the Ways of its Solution", *Proceedings of ICONE 10*, No. 22330, Arlington, Virginia.

Konys, J. et al. (2001), "Development of Oxygen Meters for the Use in Lead-bismuth", *Journal of Nuclear Materials*, Vol. 296, pp. 289-294.

Konys, J. et al. (2004), "Oxygen Measurements in Stagnant Lead-bismuth Eutectic Using Electrochemical Sensors", *Journal of Nuclear Materials*, Vol. 335, pp. 249-253.

Korotkov, V.V., K.D. Ivanov and S.V. Salayev (2003), "The Results of the Experimental Investigations Using IPPE Test Facilities in Support of the Technological Regimes of Maintaining the Lead Coolant Quality and the Purity of Self Contained BOR-60 Reactor Channel", *Proceedings of the Fast Neutrons Reactors Conference*, Obninsk, Russian Federation, 8-12 December (in Russian).

Lacressonniere, C. (2003), "Méthode de séparation des isotopes du polonium 208, 209 et 210", CEA Technical Note DEN/DTN/STR/LCEP 03/032.

Lefhalm, C.H., J.U. Knebel and K.J. Mack (2001), "Kinetics of Gas Phase Oxygen Control System (OCS) for Stagnant and Flowing Pb-Bi Systems", *Journal of Nuclear Materials*, Vol. 296, pp. 301-304.

Loewen, E.P and A.T. Tokuhiro (2003), "Status of Research and Development of the Lead Alloys Cooled Fast Reactor", *Journal of Nuclear Science and Technology*, Vol. 40, No. 8, pp. 614-627.

Li, N. (2002), "Active Control of Oxygen in Molten Lead Bismuth Eutectic Systems to Prevent Steel Corrosion and Coolant Contamination", *Journal of Nuclear Materials*, Vol. 300, pp. 73-81.

Li, N. (2003), in *Advanced Fuel Cycle Initiative*, Quarterly Report, Vol. 1, Sand2003-2060P, January-March.

Li, N. (2004), personal notes.

Lim, J. et al. (2013), "Performance of Potentiometric Oxygen Sensors with LSM-GDC Composite Electrode in Liquid LBE at Low Temperatures", *Sensors and Actuators B: Chemical*, Vol. 188, pp. 1048-1054.

Lim, J. et al. (2012), "Accuracy of Potentiometric Oxygen Sensors with Bi/Bi_2O_3 Reference Electrode for Use in Liquid LBE", *Journal of Nuclear Materials*, Vol. 429, No. 1-3, pp. 270-275.

Mariën, A. et al. (2012), "Solid Electrolytes for Use in Lead-bismuth Eutectic Cooled Nuclear Reactors", *Journal of Nuclear Materials*, Vol. 427, No. 1-3, pp. 39-45.

Marino, A. et al. (2014), "Temperature Dependence of Dissolution Rate of a Lead Oxide Mass Exchanger in Lead-bismuth Eutectic", *Journal of Nuclear Materials*, Vol. 450, No. 1-3, pp. 270-277.

Martinelli, L. et al. (2005), "High Temperature Oxidation of Fe-9Cr Steel in Stagnant Liquid Lead-bismuth", *Proceedings of the EUROCOOR Conference*, Lisbon, Portugal, 4-8 September.

Martinelli, L. et al. (2008), "Oxidation Mechanism of a Fe-9Cr-lMo Steel by Liquid Pb-Bi Eutectic Alloy (Part III)", *Corrosion Science*, Vol. 50, No. 9, 2549-2559.

Martinelli, L., M. Auroy and J. Fouletier (2011), "Mesure de l'activité en oxygène en surface de couches d'oxydes formées par oxidations des Fe-9Cr", Ateliers Gédépéon, Bilan des actions soutenues en 2010, 12-13 January (www.gedeon.prd.fr).

Martinelli, L., J-L. Courouau and F. Balbaud-Celerier (2011), "Oxidation of Steels in Liquid Lead Bismuth: Oxygen Control to Achieve Efficient Corrosion Protection", *Nuclear Engineering and Design*, Vol. 241, No. 5, pp. 1288-1294.

Martynov, P.N. and Y.I. Orlov (1998), "Slagging Processes in Lead-bismuth Loop. Prevention and Elimination of Critical Situations", *Proceedings of the Conference of the Heavy Liquid Metal Coolants in Nuclear Technology*, Obninsk, Russian Federation, 5-9 October, pp. 565-576.

Martynov, P.N. et al. (2005), "Water and Hydrogen in Heavy Liquid Metal Coolant Technology", *Progress in Nuclear Energy*, Vol. 47, No. 1-4, pp. 604-615.

Martynov, P.N. and K.D. Ivanov (1998), "Properties of Lead-bismuth Coolant and Perspectives of Non-Electric Applications of Lead-bismuth Reactor", *Nuclear Heat Applications: Design Applications and Operating Experience*, IAEA-TECDOC-1056, IAEA, Vienna, pp. 177-184.

Martynov, P.N. et al. (2003), "Lead-bismuth and Lead Coolants in New Technologies of Reprocessing of Liquids and Gases", *Proceedings of the Fast Neutrons Reactors Conference*, Obninsk, Russian Federation, 8-12 December (in Russian).

Müller, G., G. Schumacher and F. Zimmermann (2000), "Investigation on Oxygen Controlled Liquid Lead Corrosion of Surface Treated Steels", *Journal of Nuclear Materials*, Vol. 278, pp. 85-95.

Müller, G. et al. (2003), "Control of Oxygen Concentration in Liquid Lead and Lead-bismuth", *Journal of Nuclear Materials*, Vol. 321, pp. 256-262.

Muscher, H. et al. (2001), *Measurement of Oxygen Activity in Lead Bismuth Eutectic by Means of the EMF Method*, FZKA Report 6690, Forschungszentrum Karlsruhe (FZK), Karlsruhe, Germany.

Nam, H. et al. (2008), "Dissolved Oxygen Control and Monitoring Implementation in the Liquid Lead–bismuth Eutectic Loop: HELIOS", *Journal of Nuclear Materials*, Vol. 376, No. 3, pp. 381-385.

Obara, T. et al. (2003), "Preliminary Study of the Removal of Polonium Contamination by Neutron-Irradiated Lead-bismuth Eutectic", *Annals of Nuclear Energy*, Vol. 30, pp. 497-502.

Nuclear Energy Agency (NEA) (2005), *Fuels and Materials for Transmutation – A Status Report*, NEA No. 5419, OECD/NEA, Paris.

Orlov, Y.I. et al. (2005), "Hydrodynamic Problems of Heavy Liquid Metal Coolant Technology in Loop-type and Monoblock-type Reactor Installations", *Proceedings of the 11th International Topical Meeting on Nuclear Reactor Thermal-hydraulics (NURETH-11)*, Avignon, France, 2-6 October, Paper No. 220.

Pankratov, D. et al. (2003), "Estimation of ^{210}Po Losses from the Solid ^{209}Bi Irradiated in a Thermal Neutron Flux", *Annals of Nuclear Energy*, Vol. 30, pp. 785-791.

Papovyants, A.K. et al. (1998), "Purifying Lead-bismuth Coolant from Solid Impurities by Filtration", *Proceedings of the Conference of the Heavy Liquid Metal Coolants in Nuclear Technology*, Obninsk, Russian Federation, 5-9 October, pp. 675-682 (in Russian).

Perry, R.H. (1997), *Perry's Chemical Engineers' Handbook*, 7th edition, McGraw-Hill, New York.

Petrovich, C. (2002), *Evaluation of Spallation Products in Lead Bismuth Cooling Systems of ADS-DF*, TECLA Deliverable No. 5, ENEA Technical Note FIS-P130-001, 12 December.

Provorov, A.A. et al. (2003), "Methods and Device for Indication of Passivation Films on the Surface of Structural Materials in Heavy Liquid Metal Coolants", *Proceedings of the Fast Neutrons Reactors Conference*, Obninsk, Russian Federation, 8-12 December (in Russian).

Ricapito, I., C. Fazio and G. Benamati (2002), "Preliminaries Studies on PbO Reduction in Liquid LBE by Flowing Hydrogen", *Journal of Nuclear Materials*, Vol. 301, pp. 60-63.

Salayev, S.V. et al. (2003), "Estimation of the Diffusion Output of Metallic Alloying Elements from the Structural Steels to the Exposure with Heavy Liquid Metal Coolants", *Proceedings of the Fast Neutrons Reactors Conference*, Obninsk, Russian Federation, 8-12 December (in Russian).

Shmatko, B.A. and A.E. Rusanov (2000), "Oxide Protection of Materials in Melts of Lead and Bismuth", *Materials Science*, Vol. 36, No. 5, pp. 689-700.

Schroer, C., O. Wedemeyer and J. Konys (2011a), "Gas/Liquid Oxygen-Transfer to Flowing Lead Alloys", *Nuclear Engineering and Design*, Vol. 241, No. 5, pp. 1310-1318.

Schroer, C. et al. (2011b), "Design and Testing of Electrochemical Oxygen Sensors for Service in Liquid Lead Alloys", *Journal of Nuclear Materials*, Vol. 415, No. 3, pp. 338-347.

Simakov, A.A. et al. (2003), "Development and Experimental Operations of Mass-Exchange Apparatuses for Guaranteeing the Assigned Oxygen Regime in the Heavy Liquid Metal Coolant", *Proceedings of the Fast Neutrons Reactors Conference*, Obninsk, Russian Federation, 8-12 December (in Russian).

Subbarao, E.C. (1980), *Solid Electrolyte and Their Applications*, Plenum Press, New York.

Takahashi, M. et al. (2002), "Experimental Studies on Flow Technology and Steel Corrosion of Lead-bismuth", *Proceedings of ICONE 10*, Arlington, VA, 14-18 April 2002, No. 22226.

Takahashi, M. et al. (2003), "Design of Pb-Bi Cooled Direct Contact Boiling Water Small Fast Reactor (PBWFR)", *Proceedings of the Fast Neutrons Reactors Conference*, Obninsk, Russian Federation, 8-12 December (in Russian).

TECLA (Technologies, Materials and Thermal-Hydraulics for Lead Alloys) (2000), 5th EURATOM Framework Programme, No. FIKW-CT-2000-00092.

Thorley, A.W. (1989), "Solubility of Oxygen in Sodium", Risley Northern Research Laboratories, UK AEA, NRL-R-1043 (R).

Toshinsky, G.I. et al. (2000), "Multipurpose Reactor Module SVBR-75/100", *Proceedings of ICONE 8*, No. 8072, Baltimore, MD, 2-6 April.

Ulyanov, V.V. et al. (2003), "Investigations for the Hydrogen Cleaning Technology of Lead and Lead-bismuth Coolants of Nuclear Tank Facilities", *Proc. of the Fast Neutrons Reactors Conference*, Obninsk, Russian Federation, 8-12 December (in Russian).

Warin, D. (2002), "Transmutation Studies in Europe", *Revue générale du nucléaire (RGN)*, No. 4, August-September.

Weisenburger, A. et al. (2014), "Oxygen for Protective Oxide Scale Formation on Pins and Structural Material Surfaces in Lead-Alloy Cooled Reactors", *Nuclear Engineering and Design*, Vol. 273, 584-594.

Zhang, J. and N. Li (2004), "Corrosion/Precipitation in Non-Isothermal and Multi-Modular LBE Loop Systems", *Journal of Nuclear Materials*, Vol. 326, pp. 201-210.

Zrodnikov, A.V. et al. (2003), "Heavy Liquid Metal Coolants Technology (Pb-Bi and Pb)", *3rd International Workshop on Materials for Hybrid Reactors and Related Technologies*, Rome, October 2003.

5. Properties of irradiated lead-bismuth eutectic and lead*

5.1 Introduction

Lead and LBE possess favourable properties for use as both a spallation neutron target material and as a coolant for ADS and reactor systems. For ADS applications, these properties include: *i)* a high neutron yield in spallation reactions with high-energy protons; *ii)* both melts have a small neutron absorption cross-section; *iii)* a small scattering cross-section. As coolants, lead and LBE exhibit: *i)* high boiling points; *ii)* good heat removal efficiency; *iii)* inert behaviour with respect to reaction with water. The properties of the pure target materials are discussed in detail in Chapter 2 of this handbook. In this chapter, we focus on the effects of impurities generated by nuclear reactions in liquid metals used in nuclear systems.

During the operation of large-scale nuclear systems such as reactors, spallation targets and ADS, impurities will be introduced into the liquid metal by nuclear reactions. The spectrum of impurities produced is very specific for the different individual systems. For instance, in the reactor core activation by low energy particles will dominate, while in a spallation unit employing a target material with atomic number Z, a much wider product spectrum, ranging from atomic number 1 to $Z + 1$ is produced by various different nuclear reaction pathways such as spallation, fission and activation. In recent years, large effort was put into the development and validation of nuclear Monte Carlo codes that can be used to predict the amount of impurities generated by nuclear reactions in such systems. For example, both within the preparation and evaluation phase of the MEGAPIE prototype liquid LBE spallation target different codes and nuclear reaction models were used to predict the nuclide inventory. The results of different calculations were compared to each other, and were further validated using experimental data on neutronic performance, emission of delayed neutrons and gas release during the MEGAPIE experiment (Zanini, 2008a). Generally, in many cases a reasonable agreement between prediction and experiment was observed, while other aspects still require further study. Concerning the topic of impurity generation within the liquid metal of a spallation system, it has to be stated that while the main predictions of different nuclear codes and models produced within the MEGAPIE project are consistent among each other, a detailed experimental validation of the nuclide production through radiochemical analyses of material from spallation target materials is still lacking. Material from the MEGAPIE target and from a smaller LBE target irradiated at the ISOLDE facility at CERN will be analysed in detail in the coming years. Results of the analyses of gas production within the MEGAPIE target and preliminary results of the analyses of the aforementioned ISOLDE target will be presented in this chapter. However, at present one largely has to rely on the predictions made using nuclear codes to estimate the amounts of nuclear reaction-generated impurities that are produced in operating liquid Pb/alloy-based nuclear facilities. In the pool of a liquid-metal-cooled reactor, the rupture of a fuel element may lead to additional impurities from partial dissolution of the fuel. Apart from nuclear reaction products, additional impurities may be present in the source material as obtained from the supplier. Furthermore, impurities may be introduced into the liquid

* Chapter lead: J. Neuhausen. For additional contributors please see Appendix 1.

metal by corrosion processes from the structural materials or ingressed through the cover gas. In this section, we will focus on those phenomena that originate from the nuclear reaction induced impurities. Hence, we will discuss processes involving corrosion products and other "conventional" impurities only briefly in the introductory section to provide an overview of the chemical situation. Further discussions on these "conventional" impurities will be limited to situations where they are relevant to the behaviour of nuclear reaction products. For the treatment of phenomena involving these non-nuclear reaction-generated impurities we refer to Chapters 3, 4 and 6 of this handbook.

5.1.1 *Chemical processes in a liquid metal facility*

From a physicochemical point of view, a liquid metal spallation target – and also to a lesser extent the core of a liquid-metal-cooled reactor – is an extremely complex heterogeneous multi-component system, comprising macroscopic phases such as construction materials, the liquid metal and the cover gas plenum, as well as a large variety of micro-components. The latter can be present in different concentrations and chemical states, depending on operating conditions such as temperature, pressure, liquid metal flow, redox potential and proton dose. These micro-components are of different origin. Gaseous impurities include oxygen, nitrogen and water that may be ingressed in small amounts from the environment. The construction materials contribute oxides, nitrides and carbides, apart from their main metallic components and alloying elements. Furthermore, nuclear reaction products will accumulate in the system during operation. The spectrum of nuclear reaction induced impurities that are generated during operation in an LBE-based spallation target ranges from atomic number 1 (hydrogen) to 84 (polonium). In detail, the inventory produced in the facility will depend on its design and operation conditions. Typical amounts and concentrations of impurities that have to be expected for different facilities according to predictions using nuclear codes are in the range of several grams (mole fractions in the order of 10^{-6}) for the MEGAPIE target (800 kW, 850 kg LBE, 123 days irradiation) (Zanini, 2008a) to kg (mole fractions in the order of 10^{-4}) for an LBE-based European Spallation Source (5 MW, 10 t LBE, 40 years irradiation) (ESS, 2010b). For these spallation facilities, elements with atomic numbers close to the target material will dominate the product spectrum. For the cores of recent ADS designs, the activation is dominated by ^{210}Po for the LBE-cooled XT-ADS (660 g, mole fraction $3{\cdot}10^{-7}$) but in the assessment of accident scenarios the dissolution of fission products from failed fuel elements also has to be considered. For the lead-cooled EFIT, masses of 200 g (mole fraction $5{\cdot}10^{-8}$) and 2.4 kg (mole fraction $6{\cdot}10^{-7}$) have been considered for iodine and caesium in accident scenarios (Jolkkonen, 2009). The reader is referred to the original works for more details.

These micro-components can undergo chemical reactions with the macro-components and among each other. By far the most important physicochemical process involving impurities generated by irradiation in a liquid metal target or reactor pool is the volatilisation of radioactive species. Such processes play the dominant role in the assessment of radioactivity release both under normal operation and in accident scenarios. Therefore, it is essential for the licensing of liquid-metal-based nuclear facilities and their safe operation to thoroughly understand the underlying fundamental processes and to have physicochemical data at hand that allow a reliable prediction of the release of radioactivity that can occur under various scenarios.

Furthermore, in the liquid metal system a continuous transport of material is caused by the flow of the liquid metal as well as gradients in temperature and chemical potential. As a result, mobilisation, transport and deposition processes can occur in the system. Here, mobilisation processes are mainly dissolution processes such as leaching and corrosion. Additionally, the fast flowing liquid metal can cause erosion of the construction materials. This effect can be strongly enhanced by the presence of hard solid particles suspended in the liquid that can be formed by precipitation of insoluble phases as well as by breaking-off crystallites from the construction materials in corrosion processes.

Furthermore, gas phase transport processes involving gaseous or volatile species can occur. Surface properties of the construction materials may be altered by diffusion processes, where materials can be transported from the construction materials to the liquid phase or in opposite direction, i.e. from the liquid to surface layers and/or the bulk solid phase. These diffusion processes are enhanced by the strong radiation field, especially in vicinity of the target window, but also to a lesser extent in the complete target system. Precipitation processes can include formation of local coatings as well as formation of mobile insoluble particles. As a consequence of the chemical complexity of the system, the nature of precipitations is expected to be extremely complex. In principle, formation of metallic or intermetallic platings on metal surfaces have to be considered as well as the precipitation of particles of intermetallic phases, oxides, salts, nitrides or hydrides. These materials, depending on their wetting properties, their density difference compared to the liquid metal and their particle size, can remain suspended in the liquid or accumulate, e.g. at the liquid/gas interface, at the walls of the target, the reactor vessel or the liquid metal loop or sediment at the bottom at positions with low flow rate or during maintenance periods when the liquid metal flow is stopped. Taken as a whole, transport processes cause a continuous chemical stress for the integrity of the complete liquid metal system. This also includes the degradation of passivating surface layers and embrittlement of construction materials caused by dissolution or incorporation of certain components. The presence of halogens and chalcogens produced by nuclear reactions can have catalysing effects on degradation and corrosion processes. The hydrogen-water vapour pressure ratio, which is determining the reductive potential, is one parameter that is decisive for the chemical state of different components. This ratio is not known *a priori*, nor is it constant within the operation period of the target unless special measures such as integration of an oxygen control system are taken. For a detailed discussion on this topic, we refer to Chapters 3 and 4 of this handbook that discuss the fundamental thermodynamics of redox processes in Pb and LBE and their practical consequences, respectively. In this chapter, we will discuss solely the possible influences of the oxygen potential on the chemical behaviour of radiogenic impurities (see for instance the formation of Cs oxide in Section 5.2.1.1.11.6).

As a consequence of these processes, an inhomogeneous distribution of nuclear reaction products is to be expected for a liquid metal target or reactor core system. The implications for its operation and maintenance are numerous: the formation of surface layers throughout the system and the distribution of radionuclides between surfaces and bulk liquid metal are largely dependent on the operating conditions. At start-up, nuclear reaction and corrosion product concentration is very small. Therefore, homogeneous surface layers cannot be formed. On the other hand, because of the high ratio of adsorption sites on surfaces compared to the number of impurity atoms present at an early stage of operation, it is likely that a substantial fraction of the radionuclides produced are adsorbed on the surfaces. With increasing irradiation time the concentrations of nuclear reaction and corrosion products will get larger and larger. This can lead to an overall increasing ratio of radionuclides carried with the liquid metal, compared to the adsorbed material. Additionally, coatings can be formed, preferably at special positions such as the heat exchanger, where elements or compounds with low solubility could precipitate at the relatively low temperatures present. This will lead to changes in heat conduction, resulting in a change of performance of the heat exchanger. In general, an inhomogeneous distribution of decay heat and radiation has to be taken into account. This has consequences e.g. for shielding calculations or maintenance operations at different components. Furthermore, the accumulation of nuclear reaction products in the form of insoluble chemical compounds with lower density compared to the liquid metal at the liquid/gas interface may lead to enhanced evaporation of volatiles, caused by decay heat.

5.1.2 *The chemical state of nuclear reaction products in a liquid metal target*

Apart from its function as target material and heat transfer medium, the liquid metal in a liquid metal spallation target acts as a solvent and reaction medium for nuclear reaction and corrosion products. Initially, nuclear reaction products will be present in the target in atomically dispersed form until reaching a certain saturation concentration, unless they react with another chemical species to form a compound. After such a reaction, the solubility of this compound in the liquid metal determines the state of the element under consideration within the system. The solvent lead or LBE, which is present in a large excess, has to be considered to be a principal reaction partner for nuclear reaction products that are present in the system in a highly excited state and hence are very reactive. However, there are compounds that are much more stable than the corresponding compounds of nuclear reaction products with lead or bismuth. Consequently, the solvent elements can be displaced from the primary chemical reaction products by other impurities. Therefore, it is expected that finally various other compounds are formed from all the elements present, leading to a minimisation of the Gibbs free energy of the system. With increasing irradiation time, reactions of nuclear reaction products among each other become more probable because of the increased concentrations.

From the situation described above, it is concluded that the solubility of elements and compounds plays an important role in the understanding of nuclear reaction product behaviour in the liquid metal. Though there are compilations of literature data on the solubility of metals in lead and LBE, these data concentrate on steel alloying elements, while data for most of the prominent nuclear reaction products formed in a lead or LBE spallation target are missing. Furthermore, the interaction of nuclear reaction products with the liquid metal and among themselves will have a decisive influence on their chemical state within the target system. In principle, the chemical state of the different components can be evaluated based on thermodynamic data, e.g. using the method of Gibbs free energy minimisation. However, this requires a complete and consistent set of thermodynamic data (enthalpies and entropies as well as their temperature dependence) for all possible species/phases/compounds that could be formed in the system. For a system comprised of more or less all elements of the periodic table such as a liquid lead or LBE target, i.e. a system comprising more than 80 different elements, this is unrealistic: approximately 3 500 binary combinations would have to be considered, whereas the ternary combinations already amount to approximately 95 000. In reality, the number of possible phases or species will be even much larger because there may well be more than one phase/species/compound per binary system, and the formation of ternary, quaternary and more complex phases can be expected. Even the formation of hitherto unknown phases is possible. On the other hand, even for binary combinations literature values for thermodynamic data are incomplete. Consequently, a complete and consistent data set comprising all possible phases and species, whether obtained from experimental investigations or from first principles calculations, is out of reach. Thermodynamic data are however extremely important to describe almost all of the chemical phenomena that are important for a safe and reliable operation of a liquid-metal-based nuclear system, including evaporation, dissolution and precipitation processes as well as purification methods that can be used for the removal of hazardous activation products from the cover gas or the liquid metal itself.

5.1.3 *Scope of this chapter*

In principle, two approaches can be used to tackle the problem of describing such a complex system. In a bottom-up approach, one can start from investigations of the most simple model systems, i.e. binary or ternary systems of one impurity element with Pb, Bi and LBE. In this way, one can acquire an understanding of the fundamental processes and obtain the fundamental physical and chemical parameters that are needed to derive predictions for the more complex system. In a top-down approach, one can study the properties and behaviour of complex systems and materials that are similar to a real

spallation target or reactor core environment. In practice, these two approaches are complementary: while the results from the studies of complex systems may be very difficult to interpret in detail, they allow a validation of the predictions made based on fundamental parameters derived from simple model systems.

As a consequence of the situation described above, the present chapter is divided into two parts. In part one we will present the information that can be derived from simple model systems such as binary and ternary systems of single elements with lead, bismuth and LBE. Much of this chapter will be devoted to a discussion of fundamental volatilisation processes, the compilation of the corresponding substance-specific data and the derivation of recommended relations for the estimation of the maximum possible release of volatile radioactive species. We will also point out where substantial information is lacking and discuss practical issues of handling volatile radioactivity in large-scale facilities. We will also present the current state of knowledge concerning the removal of hazardous radioactive species from the cover gas as well as from the liquid metal itself. Additional sections are devoted to the behaviour of irradiation-induced impurities in the condensed phase, including the solubility of elements in liquid lead, bismuth and LBE and the migration of the extremely hazardous element polonium in solidified LBE. In the final section, a method for the calculation of approximate thermodynamic data in a large number of binary systems comprised of metals and semi-metals will be discussed. From the collected data, we derive qualitative predictions for the nuclear reaction product behaviour in nuclear systems employing liquid lead or LBE as target or coolant material.

The second part of the chapter will be devoted to more complex systems that realistically represent a spallation target environment. The presented results include data on the volatilisation of radionuclides from a proton-irradiated LBE target from the ISOLDE facility at CERN and their distribution in the irradiated target. Furthermore, the experiences gained from the MEGAPIE prototype LBE target operated in 2006 at PSI will be presented. The results are discussed with respect to the predictions made from the data derived from fundamental studies. Finally, the licensing procedure for MEGAPIE is briefly described.

5.2 Fundamental properties of binary and ternary systems with Pb, Bi and LBE

5.2.1 *Volatilisation of hazardous nuclides from liquid metals*

The gaseous and volatile elements relevant for emission from a liquid-lead-based or lead-alloy-based reactor or target facility can be divided into different categories according to their physical and chemical properties.

Hydrogen is gaseous under the operation conditions of a liquid metal target or reactor. For this element, chemical reactions with the liquid metal, impurities contained therein and with nuclear reaction products have to be considered. In principle, hydrogen can form e.g. hydrides, water, hydroxides or more complex chemical compounds. Here, the stable phases present in the system will depend on the redox potential of the system, which will vary with irradiation/operation time. Because of the very complex nature of the system, quantitative predictions on the hydrogen-containing species and phases present in an operating spallation target or reactor system are extremely complicated. Even a qualitative assessment of the production of hydrogen-containing chemical species is difficult and hence not approached in this section. While it can be safely stated that all these compounds will have lower volatility compared to elemental hydrogen, for the purpose of conservative estimations of emissions in worst case scenarios, hydrogen can be assumed to be completely and instantaneously released to the cover gas. This approach was chosen in the licensing procedure of the MEGAPIE prototype experiment performed at PSI in 2006 (Groeschel, 2006). To obtain more precise information on the hydrogen behaviour in liquid-lead-alloy-based systems, extensive experimental studies would be necessary. Such studies may prove greatly helpful – if not mandatory – for the licensing of large-scale facilities.

The noble gases are chemically inert. Thus, there is no chemical retention of these gases in the liquid metal. In reality, the release of noble gases will be decelerated by kinetic phenomena such as diffusion in the liquid metal, bubble formation and the like. Indeed, a small amount of noble gases was found to remain in a proton-irradiated LBE target even under elevated temperature and vacuum conditions (Zanini, 2010). However, the rate of these processes is not known and is difficult to estimate, and the remainder was in the range of 1/1 000 of the totally produced activity. Additionally, as shown below (Section 5.3.3), the release rate was roughly measured during MEGAPIE operation, showing that the release time in a real target is of the order of days. Nevertheless, we recommend that under the current state of knowledge, all of the produced noble gases should be assumed to be immediately released from the liquid metal for safety assessments.

Oxygen and nitrogen can form a variety of chemical compounds such as oxides, nitrides, nitrites, nitrates and the like. The stable phases again will depend on the redox potential of the system. Since these elements only form relatively short-lived radionuclides with half-lives of minutes or even lower, and as they are not produced in large quantities in the systems discussed, they will not be considered here.

For certain elements that are gaseous or show a non-negligible volatility under the operation conditions of a liquid metal target or reactor, chemical state and volatility can be assessed using equilibrium data. The most important elements of this class that are produced in liquid metal targets and reactors based on lead alloys are mercury and polonium, and to a lesser extent cadmium, thallium, the halogens bromine and iodine and the alkaline metals rubidium and caesium. The latter are not only produced within a spallation target, but can also be dissolved in the liquid metal pool of a reactor in case of a fuel element failure. Finally, the target and coolant materials lead and bismuth also show a low but measurable volatility in the considered temperature range.

The equilibrium evaporation of lead, bismuth, polonium and the fission products iodine, caesium and strontium has been carefully reviewed in a recent study concerned with accident scenarios for liquid-lead-alloy-cooled reactors within the EC-FP6 programme EUROTRANS (Jolkkonen, 2009). We base our discussion of these elements and the evaluation concerning their possible volatilisation on that study. The behaviour of mercury, cadmium, bromine and rubidium in a liquid spallation target has been assessed within the licensing procedure of the MEGAPIE target (Neuhausen, 2005c-e). The recommendations presented here concerning the evaporation of these elements will be based on the results of the latter study. The systems of rubidium and bromine in lead alloys are only briefly discussed and still require more careful evaluation.

For the elements mentioned above, we will derive recommended relations to estimate the maximum gas phase concentrations of radionuclides in the cover gas of liquid metal targets and reactor systems based on equilibrium vapour pressures. For the purpose of such estimations, the target or reactor system is considered a closed system. The estimated maximum gas phase concentrations can be lowered by physical or chemical means (i.e. trapping of condensable gases or chemical absorption of reactive gases) in a dedicated purification device. Options for such purification will be discussed later on.

Phenomena like the evaporation from a free surface to an infinite volume or aerosol formation that are more related to accident conditions will be discussed in a later section of this chapter. Whereas aerosols are certainly also formed in the cover gas of the reactor or target under normal operation conditions, they can be removed very efficiently using particulate filters (Borisov, 1995a). However, combined mechanisms of gas phase transport that may be comprised of chemical reactions, evaporation, recoil mechanisms caused by α-decay and transport of particulate matter may play a larger role in materials containing α-emitters. These phenomena can be complicated and are not yet fully understood. The current state of knowledge is presented and critically discussed in a section dealing with "abnormal" polonium volatilisation.

5.2.1.1 *Equilibrium evaporation*

5.2.1.1.1 Methods for estimation of equilibrium vapour pressure

We shall attempt to identify the most stable chemical form (e.g. compound) for a given element, with regard to the elemental composition and temperature of the system. Especially in liquid and gaseous systems at high temperatures, at which chemical equilibrium is reached rapidly, this is the form the element will (predominantly) be found in. In liquid-metal-based nuclear facilities, the amounts of solvent (lead and/or bismuth) are very large relative to that of the studied radioactive impurities. Therefore, the solvent can be regarded as a constant factor regardless of the degree of contamination.

The dissolved fraction of a nuclear reaction product will be in equilibrium with, and thus determine the partial pressure of the gaseous fraction of the same. More specifically, when a species is at a particular degree of dilution in a particular solvent (here lead or LBE) the dilution and any chemical interaction with the solvent will change the *thermodynamical activity* of the species; one of the most easily observed manifestations of that property is the vapour pressure. (The pressure of a gas not involved in the studied reactions such as the cover gas does not influence the *equilibrium*, although evaporation *rates* are typically lower in a denser atmosphere.)

With this data and some properties of the target or reactor system, it is possible to calculate what fractions and amounts of the radioisotopes will be found in gas phase and in the liquid metal, respectively. In case of a breach to the exterior, that is, loss of cover gas pressure or a liquid metal spill, non-equilibrium conditions apply and net transport of vapour from the liquid metal to the atmosphere will take place until a new equilibrium is attained (which may be never, if the volume of gas is unlimited or replenished). These aspects will be dealt with in Section 5.2.1.1.2.

While there are combinations of nuclear reaction products that in principle would form compounds with each other (e.g. caesium and iodine), their relative concentrations in the liquid metal are so low that compounds with lead or bismuth will overwhelmingly dominate the overall composition unless both have negligible affinity for these metals; as we shall see, most of the radioactive products studied here do form compounds with lead or bismuth.

5.2.1.1.2 Units and conventions

Unless otherwise stated, standard units are used, as for example K, Pa and J for temperature, pressure and energy, respectively. For certain thermodynamical calculations, units of atmospheres have been used internally without necessarily pointing it out in each case (as the most common definition of "standard state" is the pure substance at 1 atm and 298.15 K). Temperatures in Celsius are frequently used in the text, in legends and in stating ranges of validity, nevertheless mathematical expressions are based on absolute temperatures. When temperature limits are not stated for a function, the formal range of validity is unclear from the literature but assumed to coincide reasonably well with the interval we are studying.

Indices and attributes, such as overstrike for molar quantities and indices denoting the standard state, are used sparingly; these specifics should be clear from the context and the associated units. The plimsoll ($^{\ominus}$) is written here as ($^{\circ}$) and used to indicate properties corresponding to one or several criteria of standard (e.g. the pure substance, atmospheric pressure, or relative to the component elements). The asterisk (*) indicates extrapolated or apparent properties, such as expressions for Henry constants.

5.2.1.1.3 Volatility of solutes

For an *ideal solution* of components *A* and *B*, in which the atoms are randomly distributed and have equal bonding energy *AA* and *AB*, the vapour pressure of component *A* equals

the vapour pressure of the pure component P_A^o adjusted for its molar fraction X_A in the solution, as formulated in Raoult's Law:

$$P_A = P_A^o \cdot X_A \pi \tag{5.1}$$

While this is hardly ever strictly valid for real solutions, it is often a sufficiently good approximation for the purpose of estimating the volatility of a component with a reasonable degree of accuracy. The attraction of this model is that the properties of the mixture can be calculated knowing only the properties of the pure substances.

The more realistic case of a *regular solution* allows for a certain degree of preferential association *AA* or *AB*, but still assumes a random distribution of atoms. The vapour pressure can then be expressed by correcting for the enthalpy of mixing (the entropy of mixing is assumed not to differ from the ideal case). Thus, we need only the additional information of the difference in bonding energy between *AA* and *AB*. A semi-empirical model to determine approximate values for bonding in a large number of binary systems *AB* will be discussed in Section 5.2.7.

In *any* non-ideal case, the vapour pressure of *A* will be related to the *thermodynamic activity* of *A* (denoted as a_A) in the *AB* solution. This term can be loosely regarded as the "effective concentration", and is unity in the pure condensed phase and, by convention, in a pure gas at atmospheric pressure.

In non-ideal solutions a_A is obtained by multiplying the corresponding parameter (here X_A) with the thermodynamic activity coefficient γ_A, which will be characteristic for the component pair, the concentrations, temperature, pressure, etc. Thus the partial pressure of *A* in the gas phase over the *AB* solution is:

$$P_A = P_A^o \cdot a_A \tag{5.2}$$

where the activity of the component *A* in the solution is $a_A = \gamma_A \cdot X_A$. If we instead would choose to combine $P_A^o \cdot \gamma_A = K_{H,A}$, we would arrive at Henry's Law:

$$P_A = K_{H,A} \cdot X_A \tag{5.3}$$

where K_H is the Henry constant, essentially a "virtual P°" reached by extrapolating the low concentration segment of the curve to $X = 1$. It is useful to realise that Eqs. (5.2) and (5.3) state exactly the same thing, namely, that:

$$P_A = P_A^o \cdot \gamma_A \cdot X_A \tag{5.4}$$

In very dilute solutions of any type, the solvent can be regarded as an essentially pure substance with $\gamma = 1$. The solute, on the other hand, can have a γ several orders of magnitude lower. A solution is said to be *ideal dilute* when the individual solute molecules experience an environment of pure solvent and virtually no solute-solute interaction takes place. Below this limit it stands to reason that additional dilution should not further influence the thermodynamic activity coefficient; the activity itself will of course still depend on the concentration, but γ remains constant, which is the reason that the Henry constant does not change with concentration in sufficiently dilute solutions. (The concept of an "ideal dilute solution" should not be confused with an ideal solution, as an ideal dilute solution may be strongly non-ideal in the thermodynamical sense.)

Thus, as it is the volatility of the highly diluted nuclear reaction products that we are assessing, we shall have to calculate each one with respect to its individual concentration and thermodynamic activity coefficient in the solvent and at the temperature in question.

At equilibrium conditions, the *chemical potential* μ of a volatile substance *A* is the same in the condensed and in the gas phase; the same holds true for other two-phase equilibria such as dissolved and undissolved *A* in a saturated solution, and μ is further

the key property for estimating chemical reaction equilibria. The chemical potential is, simply put, the molar Gibbs energy of A under the prevailing conditions, and varies with temperature and activity according to:

$$\mu_A = \mu_A^\circ + R \cdot T \cdot \ln a_A \tag{5.5}$$

where μ_A° is the molar Gibbs energy at the standard state (pure substance at 25°C, 1 atm pressure) and thus equal to $\overline{G_A^\circ}$, which can be obtained from standard tables (not to be confused with the Gibbs energy of formation $\Delta\overline{G_{f,A}^\circ}$). R is, of course, the gas constant, 8.314472 J $K^{-1}mol^{-1}$.

To return to the task immediately at hand, we will see in Section 5.2.1.1.11.3 that e.g. the Cs-Pb system is a strongly non-regular solution, and the value of γ will thus be hard to determine solely by calculations from known thermodynamic parameters. Extrapolations from known experimental data can also be problematic, as the relation between γ and concentration (or temperature) may well be complex in nature (for instance in the case of a limiting lower concentration for the formation of ionic clusters). As a theoretical approach to the behaviour of the extremely diluted and strongly interacting binary and ternary systems in question could get both difficult and – considering that they are incompletely investigated – unreliable, we shall instead apply the pragmatic approach of applying the available experimental data to evaluate the vapour pressures, and largely ignore the underlying causes for deviations from regular behaviour.

5.2.1.1.4 The liquid target and coolant material

Even in the case of severe contamination, the amounts of nuclear-reaction-induced impurities are too small to affect the physicochemical properties of the much larger quantity of liquid metal. We can thus regard it as chemically pure in our calculations, and shall therefore note here some properties of liquid lead, bismuth and LBE that will find application in the following sections.

5.2.1.1.4.1 Lead

Lead vapour is essentially monatomic (Kim, 1966). The vapour pressure of pure liquid lead, from the melting to the boiling point, follows the expression (Kubaschewski, 1979):

$$P_{Pb}^\circ = 10^{-\frac{10130}{T}+13.2848-0.985\log T} \tag{5.6}$$

A more detailed review of all the available literature data arriving at the same recommended function can be found in Chapter 2, Section 2.8.1 of this handbook. In the entire liquid range, the vapour pressure of pure lead is from one-half to one-third that of pure bismuth.

5.2.1.1.4.2 Bismuth

There are several determinations of the vapour pressure over liquid bismuth. It has been measured in the range of 1 196 to 1 268 K (Fischer, 1966):

$$P_{Bi}^\circ = 10^{-\frac{9150.3}{T}+9.7575} \tag{5.7}$$

This is in fairly good agreement with another determination between 850 and 950 K (Kim, 1966):

$$P_{Bi}^\circ = 10^{-\frac{9656.4}{T}+10.2464} \tag{5.8}$$

The data found in Kubaschewski (1979) (attributed to "private communication" with Brackett and Brewer) is split into two separate expressions for monomeric and dimeric bismuth vapour, valid from the melting to the boiling point; when graphed, the resulting sum of these pressures nearly overlaps with Eq. (5.8) within the region of 500 to 1 200 K. Chapter 2, Section 2.8.2 of the present handbook gives a thorough and critical review of all literature data available on the saturated vapour pressure of bismuth.

Due to the mixed molecular state of Bi in the gas phase, the content of Bi in the vapour is not linearly related to its partial pressure, which will have some consequences for certain calculations.

An expression for the average molecular mass of gaseous bismuth as function of temperature, in the range 849 to 954 K, was presented by Kim (1966):

$$M_{Bi(g)} = 10^{\frac{93.6117}{T} + 2.43354} \tag{5.9}$$

This was also experimentally confirmed to be valid at extrapolation to 1 173 K (Fischer, 1966). Clusters of more than two Bi atoms are present only in small amounts (Böwering, 1998). Thus the average mass of typically 350 to 325 between 849 and 1 173 K indicates roughly equal amounts of monatomic and diatomic Bi in the vapour, something that can also be inferred from the above-mentioned separate functions (Kubaschewski, 1979).

A recent critical comparison of dimerisation data (Morita, 2006) appears to confirm these estimates, and, despite a certain scattering of the different groups of results reviewed, indicates that the monomeric fraction, as can be expected from its larger contribution to the entropy of the system, continues to increase up to 2 000 K (Figure 5.2.1).

Figure 5.2.1: Mole fraction of dimeric bismuth in pure bismuth vapour

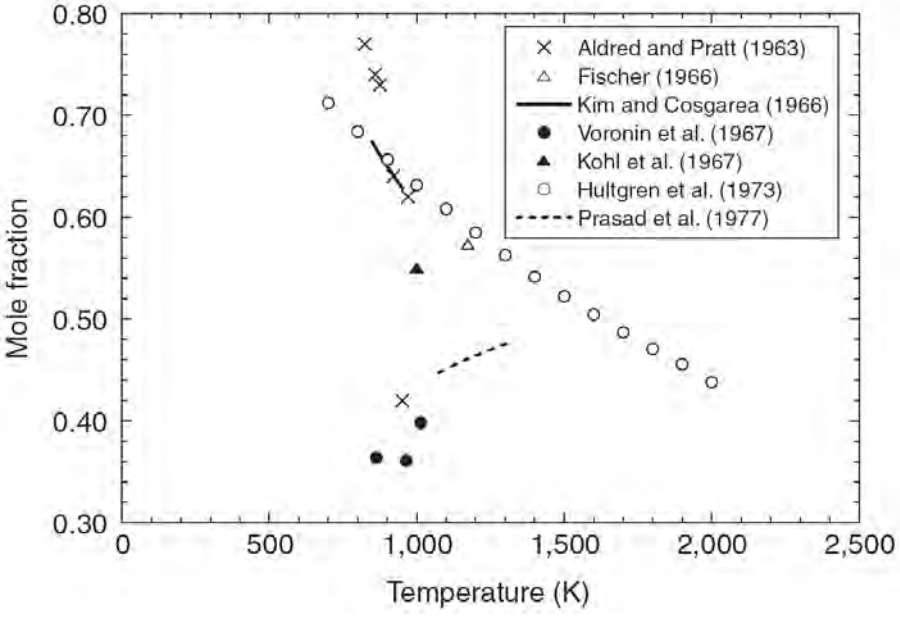

Source: Reproduced with permission of Taylor & Francis from Morita (2006).

5.2.1.1.4.3 LBE

Lead-bismuth mixtures exhibit a moderate, symmetrical, negative deviation from Raoult's Law. As can be seen from Figure 5.2.2, the thermodynamic activity (and consequently also the vapour pressure) is decreased by about 20% in the equimolar

mixture. For most calculations, LBE (55% Bi, 45% Pb; atom and weight per cent are nearly equivalent as the atomic weights differ only by 0.5%) can be approximated with an equimolar, ideal solution of Pb and Bi, as the uncertainties in the activity coefficients of the highly diluted contaminants are larger, and their concentrations are impossible to predict with exactitude. For somewhat more precise estimates of the thermodynamic activities of the components, they can, in the neighbourhood of 700 K, be assumed 0.48 (for Bi) and 0.34 (for Pb), or the following functions (Prasad, 1977), formally valid for 1 150 to 1 320 K, can be used for the respective thermodynamic activity coefficients at other compositions and temperatures:

$$\gamma_{Bi(Pb-Bi)} = e^{-\left(\frac{391.5}{T} + 0.2693\right)\left(1 - X_{Bi}\right)^{\to 2}} \tag{5.10}$$

$$\gamma_{Bi(Pb-Bi)} = e^{-\left(\frac{391.5}{T} + 0.2693\right)\left(1 - X_{Pb}\right)^{2}} \tag{5.11}$$

For simple conservative estimations, we can recommend to use the values for 700 K given in Prasad (1977), leading to the following equations for the Henry constant of lead and bismuth at the eutectic composition:

$$K_{H(Pb(LBE))} = 10^{-\frac{10130}{T} + 12.8163 - 0.985\log T} \tag{5.12}$$

and:

$$K_{H(Bi(LBE))} = 10^{-\frac{9656.4}{T} + 9.9272} \tag{5.13}$$

Figure 5.2.2: Thermodynamic activity as function of concentration in the Bi-Pb system at 700 K

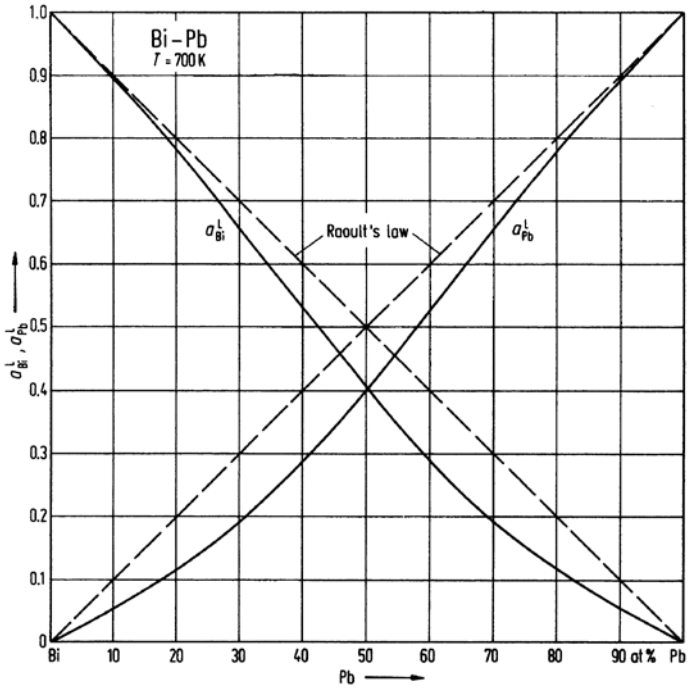

Source: Reproduced with permission of Springer Science+Business Media from Landolt-Börnstein (1992).

For a more detailed review on the topic of the specific composition and pressure of the vapours over non-contaminated LBE at different temperatures we would like to direct the reader's attention to the exhaustive review of Morita (2006) and the critical review on various LBE vapour pressure data compiled in Chapter 2, Section 2.8.3 of this handbook.

5.2.1.1.5 Polonium

While some of the fundamental physical and physicochemical properties of elemental polonium are reasonably well known, those properties for which determination is disturbed by the radioactive decay of the sample are known with lower accuracy, and the corresponding literature requires critical evaluation. In particular, the chemistry of polonium compounds is largely uncharted territory. This has several reasons. All isotopes are unstable, and the most easily produced isotope (^{210}Po) has a half-life of only 138 days; thus it generates considerable decay heat (140 W/g) and macroscopic amounts of any except the most stable compounds will rapidly decompose under the combined effects of heat and radiolysis. Even in micro-scale, the decay heat makes calorimetric measurement of heat capacities and reaction enthalpies virtually impossible. The hazardous nature and limited commercial availability of ^{210}Po present additional restrictions on the amounts that can be used in experimental work.

The more stable ^{209}Po (half-life 103 years) would be better suited for chemical investigations using weighable quantities of material, but it is only available in small quantities and at an extraordinarily high price, which prohibits its use in any larger quantity.

Thus, at the present state of affairs, most of our knowledge of polonium chemistry is based on theoretical calculations, analogy with other chalcogens such as Se and Te, and a handful of isolated observations over the span of ninety years.

5.2.1.1.5.1 Metallic polonium

An expression for the vapour pressure of pure Po referred to as "IPPE data" (Li, 1998), is identical to the radiometric determination of Abakumov (1974a, 1982) for 368-604°C:

$$P_{Po}^{o} = 10^{-\frac{5440 \pm 60}{T} + 9.46 \pm 0.05} \tag{5.14}$$

In this approximate temperature range, expression (5.14) gives about 10% lower Po vapour pressure than an older determination by direct pressure measurement at 438 to 745°C (Brooks, 1955):

$$P_{Po}^{o} = 10^{-\frac{5377.8 \pm 6.7}{T} + 9.3594 \pm 0.0068} \tag{5.15}$$

Thus, Eqs. (5.14) (Abakumov, 1974a) and (5.15) (Brooks, 1955) are in fairly good agreement. However, a detailed review of the experimental work together with estimations of the vapour pressure over metallic polonium obtained by extrapolation from the thermodynamic properties of its lighter homologues in the chalcogens group (Eichler, 2002) indicates that the experimental results of Abakumov and Brooks may be affected by effects of the radioactive decay of the ^{210}Po samples used in the measurements, possibly leading to an overestimation of vapour pressures derived from the experiments. The deviations between their experimental results (squares and triangles in Figure 5.2.3) and the extrapolational results obtained by Eichler (circles in Figure 5.2.3) are larger at low temperatures, where thermal effects of the polonium decay may play a significant role, while they diminish – for the extrapolation of the vapour pressure of Po_2 molecules – approaching the boiling point. Interestingly, exactly this effect has been predicted theoretically considering the effect of radioactive decay on the evaporation equilibrium (Kopytin, 1961). In addition to possible thermal effects of polonium

decay on the evaporation, non-thermal effects such as sputtering (see Section 5.2.1.1.5.5.1) can lead to increased polonium vapour phase concentrations and thus an overestimation of the equilibrium vapour pressure. These effects will dominate at low temperatures and thus could explain the large discrepancy between the single experimental data point for the vapour pressure over solid polonium (asterisk in Figure 5.2.3) (Ausländer, 1956) and Eichler's extrapolations. For more details on the experimental difficulties concerning the determination of equilibrium vapour pressure data for polonium and the reliability of various data sets the reader is referred to the original literature (Eichler, 2002).

The convergence of experimental and theoretical data when approaching the boiling point indicates that the results of the extrapolations of Eichler (2002) are reasonable. Still, the results of the theoretical evaluations are of limited accuracy and therefore we cannot recommend relying solely on them for safety-related estimations. In this respect, a redetermination of the polonium vapour pressure using the more long-lived isotope ^{209}Po would deliver tremendous insight. It seems likely that the vapour pressure of this isotope will agree much better with the theoretically estimated temperature function of Eichler (2002), which can be regarded as an estimation of the vapour pressure function of a fictive, non-radioactive polonium isotope. Nevertheless, the thermodynamic data of polonium extrapolated by Eichler forms a consistent set of data that is provided as Appendix 5.4.1 to this chapter to facilitate further investigations on this topic.

Figure 5.2.3: Comparison of various experimental vapour pressure data and theoretically estimated data

The solid-liquid transition temperature is indicated by an arrow

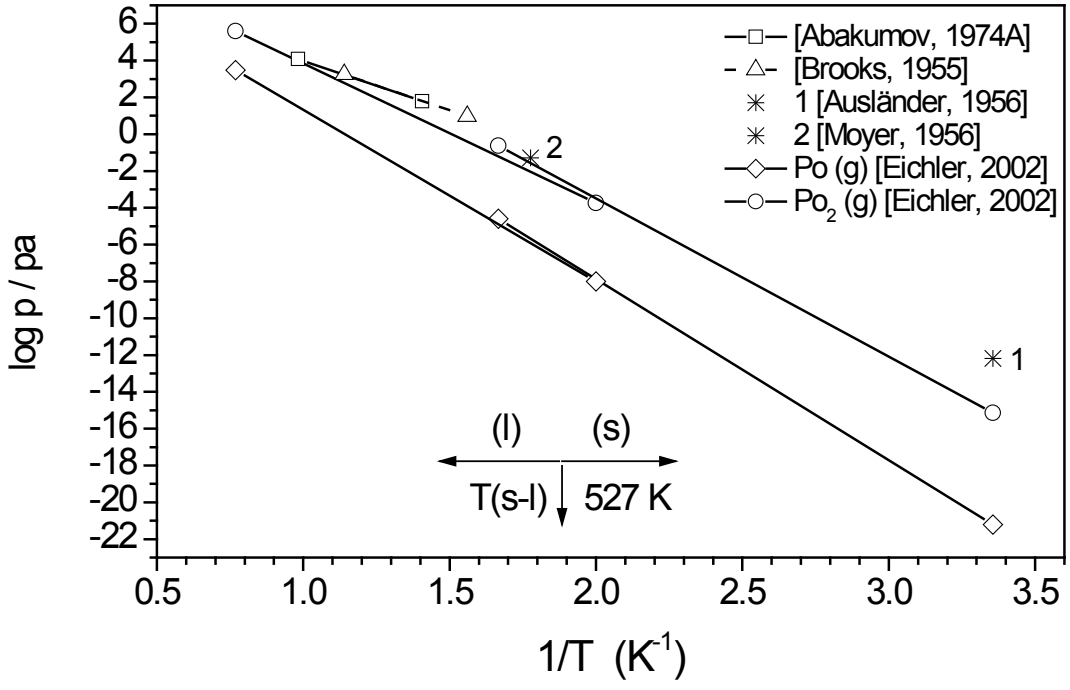

Source: Reproduced, with a correction of one reference, from Eichler (2002).

There is some uncertainty about the predominating species in the gas phase. Abakumov (1982) concludes, from a comparison of direct pressure measurement (~ number of gaseous atoms and molecules) with radiometric measurements of the gas (~ number of Po nuclei) that "there is a small portion of diatomic molecules in polonium vapour". Eichler (2002) from his extrapolation in the chalcogen group concludes that Po_2 molecules

are expected to be the dominating vapour phase species over pure polonium. It is a reasonable assumption that the degree of dimerisation will increase with Po concentration. Thus, a significant fraction of gas phase polonium may be present as diatomic molecules in the case of pure polonium, which is discussed in this section, but at very high dilution and consequently low partial pressure – as present in an LBE-based nuclear facility – the monatomic species will be favoured, unless gas phase species containing the constituents of the liquid metal such as PbPo or BiPo are formed.

The vapour pressures of pure polonium are as such of little use to us, since polonium in lead or lead alloys exhibits large deviation from ideal behaviour. We therefore need to estimate its volatility from the LBE medium by other methods. For most *practical* purposes, it is in fact of little importance to know exactly what chemical state the polonium has in the gas phase; we are mainly interested in the total amount or concentration of polonium over the liquid metal surface and can use experimentally determined, apparent vapour pressures. As it typically is not the physical partial pressure that has been measured, but the radioactivity in a given volume, and as this contribution to the overall gas pressure in any case is completely negligible, we can in many cases convert the radioactivity measurements to a fictional pressure of monatomic Po vapour and express it as such.

One practical case where this approach may be inadequate is that of low temperatures. Several authors have noted pronounced aberrations from normal evaporation behaviour and attributed them to a recoil mechanism caused by the high α-activity of ^{210}Po (see Section 5.2.1.1.5.5.1). Most notably, there is a measurable evaporation of ^{210}Po samples at temperatures way below the point where thermal evaporation would effectively be zero. In one experiment (Borisov, 1995a) clean metal plates were exposed, in vacuum, to highly active preparations of ^{210}Po (surface films electrodeposited on copper and cooled to -196°C). Clearly, at this temperature the vapour pressure predicted by classical mechanisms is negligible. Nevertheless, after an exposure time of "several seconds", ^{210}Po contamination could be autoradiographically detected on the plates. From the registered decay patterns, the authors estimated the "emission" of polonium to range from single or few atoms per event up to clusters of ≈3 500 atoms. Obviously, in pure ^{210}Po, this can lead to a significant spreading of radioactivity, but in very dilute alloys (LBE, < 1 ppm Po) very few of the ejected clusters will contain even a single additional ^{210}Po atom beyond the one decayed when producing the recoil event. However, in surfaces enriched in polonium such effects could contribute significantly to volatilisation.

Also when, as at some distance from a heated Po source, the vapour assumes ambient temperature, classical physical chemistry would predict condensation of the vapour, either onto surfaces or as an aerosol that should be retained in a microporous filter. Yet there are reports to the contrary, and these observations have been interpreted as evidence that under certain circumstances, ^{210}Po is partially or predominantly in the state of a gaseous compound at ambient temperature. Again, that assumption does not correspond with the simple expedience of treating the evaporated ^{210}Po as monatomic Po vapour.

In short, the mathematical expression for an "apparent" vapour pressure of monatomic ^{210}Po that also estimates low-temperature evaporation correctly would be of rather complex and unfamiliar form. But at high temperatures and dilutions, as in a liquid metal reactor pool or spallation target, the contribution by recoil mechanisms should be quite small relative to the thermal evaporation (Riehl, 1964), and we shall use the experimentally determined vapour pressures, as function of temperature, without trying to estimate how much, if any, is a contribution from decay events. Yet one should exercise great caution in extrapolating these functions to room temperature (e.g. airborne particles, solidified spills or contaminated cool surfaces) as they may very well underestimate the effective volatilisation of ^{210}Po in the low-temperature region. Such effects will be discussed in Section 5.2.1.1.5.5.

5.2.1.1.5.2 Polonium alloys and intermetallic polonium compounds

Both lead and bismuth spontaneously react with polonium vapour above 350°C (Abakumov, 1982). Thus the total polonium content in the vapours over lead and LBE is significantly lowered primarily through the formation of metal-polonium complexes or lead and/or bismuth polonides, e.g. PbPo or Bi_2Po_3. These complexes or compounds bind Po in the liquid phase. According to Li (1998), PbPo is also considered the predominating Po species in the gas phase over LBE. Although being in agreement with both general chemical reasoning and the observed Po vapour pressure data over solutions in LBE, this assumption still remains to be confirmed experimentally. A similar effect is observed in liquid bismuth (Bradley, 1968). The volatility of Po will therefore be governed not only by the properties of the pure element itself, but to a large extent by its interaction with the metallic solvent and the intermetallic species formed. Thus, it would be misleading to discuss these effects separately. It is worth noting that as both elemental polonium and the lead/bismuth polonides have higher vapour pressure than lead and bismuth, there is a possibility that ^{210}Po is "distilled" from the LBE and deposited at higher concentration on cooler surfaces; this seems to be confirmed in evaporation experiments in vacuum at 550°C, resulting in a thousand-fold enrichment of ^{210}Po (Tupper, 1991). In contrast, at 250°C the condensed vapours had ^{210}Po levels similar to those of the melt (ibid.). Similarly, in a report on ^{210}Po adsorption and desorption (Obara, 2005b, 2005c), the presented data indicates a twenty-fold enrichment in ^{210}Po content when the vapours over contaminated LBE at 900°C were condensed on plates of quartz glass at 600°C.

It is unlikely that the earlier mentioned recoil mechanism significantly enhances the primary volatilisation of ^{210}Po from contaminated lead alloys at elevated temperatures; however, it can be expected to be an important secondary volatilisation mechanism in polonium-enriched fractions (e.g. surface films) formed by condensation of primary vapour.

Estimates of parameters for calculating polonium partial pressures over dilute solutions in bismuth alloys date back to at least 1954. Unfortunately, the reports are often unclear on the units of temperature and pressure, and even the base of logarithms used is sometimes in question. Several recent reports seem to be quoting older estimates, expressed in non-SI units, without giving due consideration to or making mention of this matter.

There are three slightly different approaches to the problem of predicting the evaporation of Po from the heavy liquid metal target and coolant material, and they differ more in the assumptions than in the actual measurements.

The first approach, making the minimum number of assumptions, is to use an experimentally determined expression for the "apparent" vapour pressure of Po over the heavy liquid metal without taking the actual chemical state of Po into consideration; if the expression correctly describes the total amount of Po radioactivity in the vapours, and if that is the only parameter we are interested in, it is a simple and practical approach. By relating the obtained expression, an apparent Henry constant, to the vapour pressure of pure metallic polonium, a thermodynamical activity coefficient for Po in the solution can be obtained. While one may in this context, for convenience, often speak in terms of dissolved polonium metal and polonium vapour, we should however keep in mind that both the dissolved and the gaseous state is, most probably, in fact metal-polonium complexes and polonides and not elemental polonium.

The second approach is to apply the thermodynamical activity coefficient for polonium *metal* in the dilute solution (which deviates strongly from unity as the solution is highly non-ideal) in combination with the existing data on the vapour pressure of pure polonium. Obviously, if the thermodynamical activity coefficient is based on vapour pressure measurements, this is nothing more than the reversal of the process by which the thermodynamical activity coefficient was determined, and is for every practical, predictive purpose equivalent to the first method. Nevertheless, the activity coefficient is a good way of visualising and comparing the polonium-binding properties of different

liquid metal compositions – in this case, the tendency to form less volatile polonides. However, when derived from vapour pressure measurements, its correctness will be affected by the accuracy of the vapour pressure measurements for the pure element. For a detailed critical review of these measurements for Po see Eichler (2002).

The third approach is to estimate the actual chemical state of Po in the liquid and gaseous phases (which is easier done for the latter than for the former) and use the vapour pressure of that particular compound (typically *assumed* to be PbPo in lead-based solutions) with corrections for the dilution and assuming near-ideal behaviour. Of course, all three approaches should arrive at similar results.

Below we shall compare a number of estimates from various sources, obtained by different methods. Unless stated otherwise, temperatures are in Kelvin and pressures in Pa. In some cases, the original form of the expression has been converted to these units to simplify comparison. Unless the temperature range is given, it is unclear over what range the expression is considered valid.

5.2.1.1.5.2.1 Polonium in pure lead

Polonium forms a stable intermetallic compound with lead (Witteman, 1960). It is generally assumed that polonium dissolved in liquid lead will evaporate as molecular lead polonide (PbPo). In a joint report by investigators at LANL and IPPE, in which evaporation rates rather than equilibrium concentrations are discussed, it is estimated that in near vacuum at 400°C, 99.8% of the total Po evaporation from LBE is in the form of PbPo and 0.2% as "pure Po", with no mention of any bismuth polonides (Li, 1998).

The vapour pressure of pure PbPo was determined in the range of 640 to 850°C (Abakumov, 1974a, 1982):

$$P^{o}_{PbPo} = 10^{-\frac{7270 \pm 80}{T} + 9.06 \pm 0.07} \tag{5.16}$$

This function is the same as that referenced as "IPPE data" in Li (1998), and most likely also the source used for Eq. (7.2) of IAEA (2002), with the difference that the IAEA report – without stating it clearly – persists in the use of torr. It should be noted that these experimental determinations may suffer from radiation-induced effects similar to those observed for pure polonium.

Any systematic determination of the activity coefficient of dilute PbPo in liquid lead or LBE could not be found, but it is not unreasonable to approximate it with unity (see the preceding section), something that is done explicitly in Li (1998) and implicitly in IAEA (2002). In Section 5.2.1.1.5.2.3, we will review experimental data showing that dilute Po solutions in LBE have evaporation characteristics that are within experimental error indistinguishable from those of a near-ideal solution of PbPo. Eq. (5.16) can thus in principle be used as a Henry constant, in combination with the molar ratio, to estimate the vapour pressure of PbPo – assumed nearly equal to the total vapour pressure of Po – over liquid lead alloys.

Apart from being envisioned as reactor coolant and target materials in spallation sources, liquid lead alloys (with lithium rather than bismuth) are considered as blanket material in fusion reactors. A similar polonium production problem will thus be encountered and is being investigated in that field of research. The application of those experimental results to liquid lead and LBE may be complicated by the possible formation of Li_2Po, which could influence the evaporation characteristics. We have found no experimentally determined thermodynamical data for Li_2Po, but analogous alkali metal compounds are expected to have enthalpies of formation in the neighbourhood of ΔH_f = -340 kJ/mol (Abakumov, 1982; Krestov, 1962), while estimations based on a semi-empirical model yield a value of ΔH_f = -158 kJ/mol (Neuhausen, 2003) (see also Section 5.2.7 and Appendix 5.4.4). A theoretical estimation predicted ΔH_f = -35.4 kJ/mol for PbPo (Eichler, 2004a). Other theoretical estimates of ΔH_f of PbPo range from -7.4 to

-68 kJ/mol (Neuhausen, 2003). We further have no real knowledge of the vapour pressure of Li_2Po, or of its thermal stability.

If we apply the expression for the activity coefficient for Po (determined at $X_{Po} = 1.5 \cdot 10^{-13}$) in $Li_{0.17}Pb_{0.83}$ eutectic, determined in the range of 400 to 680°C (Feuerstein, 1992):

$$\gamma_{Po(PbLi)} = e^{-\frac{1329}{T} - 4.77} \tag{5.17}$$

on the vapour pressure over pure Po (Eq. 5.14), we arrive at a Henry constant of:

$$K_{H(Po(PbLi))} = 10^{-\frac{6017}{T} + 7.39} \tag{5.18}$$

The authors argue that polonium forms mainly PbPo also in lead-lithium melts, basing this conclusion on the agreement of their results (ibid.) with PbPo experimental data (Abakumov, 1982). It appears that Eq. (5.17) is based on only seven measurements that exhibit a distinct scattering ([Feuerstein, 1992], see Figure 5.2.4) and that the slope would change considerably if just one of the points were excluded. While the reported partial pressures and γ values agree reasonably well with the corresponding curves for lead and LBE solutions of Po in the studied temperature range, one should probably exercise caution in extrapolating Eqs. (5.17) and (5.18) too far. These equations are further evaluated in Section 5.2.1.1.5.3.

Another series of measurements (Schipakin, 1995) of α-activity in the gas phase, in units of Ci/dm^3, was performed over irradiated $Li_{0.17}Pb_{0.83}$ eutectic containing ^{210}Po in an amount corresponding to a molar ratio of roughly $2 \cdot 10^{-11}$. Assuming that the only detected radioisotope is ^{210}Po with a specific activity of 4 500 Ci/g (Figgins, 1961), the measured total Po concentrations over the clean liquid surface ([Schipakin, 1995], see Figure 5.2.4) can be converted to units of pressure, as monatomic Po vapour, and fitted to the function:

$$P_{Po(PbLi)} = 10^{-\frac{3428}{T} - 3.98} \tag{5.19}$$

where P is in Pa and T in K. It should be stressed that the function is based on only three points in the interval of 350 to 450°C, extracted from a graph, and that the precision is thus low. If we similarly extrapolate to $X_{PbPo} = 1$, we get a Henry constant of:

$$K_{H(Po(PbLi))} = 10^{-\frac{3428}{T} + 6.72} \tag{5.20}$$

This deviates from other estimates by three orders of magnitude.

The Schipakin (1995) report is rather confusing at several points, such as the statement on page 167: "With a ^{210}Po content in the eutectic of 10^{-7} Ci g^{-1} the value of M is $95 \cdot 10^{-11}$." (M here indicates "its molar fraction in the eutectic", which is more commonly written as X_{Po}). The "average atomic mass" of $Li_{0.17}Pb_{0.83}$ is 173 g/mol. The reported molar ratio of $95 \cdot 10^{-11}$ (we shall assume that this somewhat non-standard notation is not due to a missing decimal point, but intentional and equals $9.5 \cdot 10^{-10}$) corresponds to $1.15 \cdot 10^{-9}$ g ^{210}Po per gram eutectic. The statement thus amounts to saying that the specific radioactivity of ^{210}Po is 87 Ci/g, which is 52 times lower than the commonly accepted value. If the specific ^{210}Po radioactivity of the melt was 10^{-7} Ci g^{-1}, then the molar ratio was in fact about $2 \cdot 10^{-11}$, which is the value we have used in deriving Eq. (5.20) from Schipakin's data. Considering this and other unclarities in the report, and the poor agreement with other data (see Table 5.2.1), we do not recommend using Eq. (5.20).

5.2.1.1.5.2.2 Polonium in pure bismuth

While pure bismuth is not being considered as reactor coolant or target material for spallation sources, it is the material of choice for industrial production of ^{210}Po, and as the

product is typically purified by distillation, the vapour pressure of Po in Bi has been determined with high accuracy in large-scale experiments. As Bi is the main component in LBE, we have reason to review this data.

The polonium-bismuth system is poorly researched, but a compound Bi_2Po_3 has been reported (Yefimov, 1996). Also, the chemical analogue tellurium forms stable bismuth tellurides (Brebrick, 1968), and there is also evidence for Bi-Te complex formation in the liquid state (Mudry, 1998). We should therefore expect Po solutions in Bi to deviate strongly from ideality. This is confirmed by experimental data.

The activity coefficient for dilute ($10^{-10} \leq X_{Po} \leq 10^{-6}$) polonium in bismuth in the temperature interval 450-850°C, derived from careful measurements of the equilibrium vapour pressure of polonium over dilute solutions in liquid bismuth using both the Langmuir and Knudsen methods (Joy, 1963; Moyer, 1956), follows the expression:

$$\gamma_{Po(Bi)} = 10^{-\frac{2728.3}{T} + 1.1176} \tag{5.21}$$

This estimate is also quoted and used in Li (1998) and Pankratov (2003), but in the latter paper the log operator has been omitted before γ, possibly due to poor proofreading. Thus the expression found in Pankratov (2003) yields a negative activity coefficient at all temperatures below 2 441 K (e.g. γ_{Po} = -1.61 at 1 000 K).

A report on the Po to Bi ratio in the vapour phase during distillation of ^{210}Po-contaminated Bi (Bradley, 1968) offers another possibility to estimate γ for Po in liquid Bi. The experimentally determined (at 923 to 1 038 K) relative volatilities $\alpha_{eff,\ Po/Bi}$ were obtained at non-equilibrium conditions and underestimate the equilibrium value $\alpha_{Po/Bi}$ due to Po depletion at the surface. This deviation becomes more pronounced at higher temperatures (ibid.), resulting in a lower effective relative volatility of Po, and thus an apparently lower activity coefficient.

As the relative volatility was determined as total amounts of Po and Bi in the collected, condensed vapour, we have adjusted the Bi amount by $209/M_{Bi(g)}$, where $M_{Bi(g)}$ is the average molar mass of the partially dimeric Bi gas (Eq. [5.9]), in order to obtain a parameter directly proportional to the physical pressures of Po and Bi vapour, respectively. In absence of more accurate data, we did not correspondingly adjust the Po amount, but assume gaseous Po to be chiefly monatomic at low partial pressure.

We thus arrive at a thermodynamic activity coefficient of:

$$\gamma_{Po(Bi)} = 10^{-\frac{2272.7}{T} + 0.1316} \tag{5.22}$$

Eqs. (5.21) and (5.22) are further evaluated in Section 5.2.1.1.5.4.

5.2.1.1.5.2.3 *Polonium in LBE*

A recent experimental report (Ohno, 2006) describes a carefully performed determination of the total ^{210}Po activity in a known volume of argon over an LBE melt containing 0.21-0.22 ppb ^{210}Po, using the transpiration method. Though equilibrium was only verified by flow rate dependent measurements at the lowest temperature investigated, this study represented the most convincing experimental investigation of polonium vapour pressure over dilute solutions in LBE available at the time of writing of the present chapter. In the range of 450 to 750°C the "apparent" vapour pressure of Po based on measurements in the vicinity of molar ratio $X_{Po} = 2 \cdot 10^{-10}$ corresponds to the Henry constant:

$$K_{H(Po(LBE))} = 10^{-\frac{8348}{T} + 10.5357} \tag{5.23}$$

The authors also calculated (ibid.) the apparent thermodynamica activity coefficient for elemental Po in LBE from the collected data, without in any way suggesting that Po would in fact appear in elemental state in this system. This follows the expression:

$$\gamma_{Po(LBE)} = 10^{-\frac{2908}{T} + 1.079} \tag{5.24}$$

As this thermodynamical activity coefficient was derived from Eq. (5.14) combined with Eq. (5.23), we gain no advantage from using it for further calculations; that would only be an exercise in circularity. It is nevertheless included in Figure 5.2.4 for comparison.

A similar approach was employed in an earlier determination (Buongiorno, 2003), although the authors there explicitly assume the results to describe the partial pressure of PbPo in a gas phase of 1 MPa argon. The molar ratio of ^{210}Po (referred to as PbPo) in LBE was approximately $2.5 \cdot 10^{-8}$ and measurements were made in the range of 392 to 550°C. A linear extrapolation to $X_{PbPo} = 1$, that is, pure lead polonide, gives us the Henry constant for, as it was assumed, PbPo in LBE:

$$K_{H(PbPo(LBE))} = 10^{-\frac{6790 \pm 1840}{T} + 8.46 \pm 1.26} \tag{5.25}$$

While Eq. (5.25) gives vapour pressures very similar to other estimates (Table 5.2.1), one should note that the stated error margins of the coefficients are very large; coefficients at the upper and lower extremes of these intervals produce partial pressure values that differ by six to seven orders of magnitude. On the other hand, several other reports do not state any error margins at all.

Although this approach can appear more pleasing to the chemist, as it is based on a clearly stated model of the actual chemical state of the system, the *a priori* assumption of a PbPo species is rather unnecessary. The known parameter was the ^{210}Po concentration in the liquid phase; the measured parameter was the concentration of ^{210}Po atoms in the gas phase, and the chemical state of the polonium is in fact irrelevant for the experiment.

Yet it is interesting to note that Eq. (5.16) and Eq. (5.25) agree within the experimental error. Since Eq. (5.16) was obtained by measurements over a sample of PbPo at very high concentration in lead ($X_{PbPo} = 0.6$) (Abakumov, 1974a), where γ_{PbPo} should approach unity, the assumption that the liquid phase can, even at low Po concentrations, be regarded as a near-ideal solution of PbPo in LBE is consistent with the available data. Reversing the argument, this appears to justify the application of the "third approach" mentioned in Section 5.2.1.1.5.2.

Thus, we can take the view that the solution of PbPo in Pb and LBE is near-ideal and that Po evaporates mainly as PbPo, and may thus use Eq. (5.16) in combination with Eq. (5.14) (the vapour pressure of pure Po) to construct yet another expression for the activity coefficient of Po in dilute lead and LBE solution:

$$\gamma_{Po(LBE)} = 10^{-\frac{1830}{T} - 0.40} \tag{5.26}$$

This estimate agrees reasonably well with the majority of the determinations (Figure 5.2.4). The application of Eq. (5.26) is for every practical purpose equivalent to using Eq. (5.16) as a Henry constant, to be multiplied with the molar ratio of Po in Pb or LBE.

5.2.1.1.5.3 Evaluation of thermodynamic activity data in the Po-Pb-Bi system

An overview of data from five sets of experiments (Figure 5.2.4) illustrates the general consensus that the thermodynamic activity of Po is strongly depressed in liquid Pb and Bi alloys, the effect being about two orders of magnitude at 1 000 K and even more pronounced at lower temperatures.

Figure 5.2.4: Activity coefficients for very dilute solutions of Po in liquid Pb and Bi alloys

A (in Bi, Eq. [5.21]) from Moyer (1956); B (in LBE, Eq. [5.24]) from Ohno (2006); C (in Bi, Eq. [5.22]), calculated from evaporation data published in Bradley (1968); D (as PbPo, as ideal solution in Pb, Eq. [5.26]), from Abakumov (1974a, 1982); E (in $Li_{0.17}Pb_{0.83,}$ Eq. [5.17]), from Feuerstein (1992).

Note that extrapolations below the melting points of the pure metals (Bi: 545 K, Pb: 601 K) are relevant for the liquid state only (viz. LBE melting point 397 K)

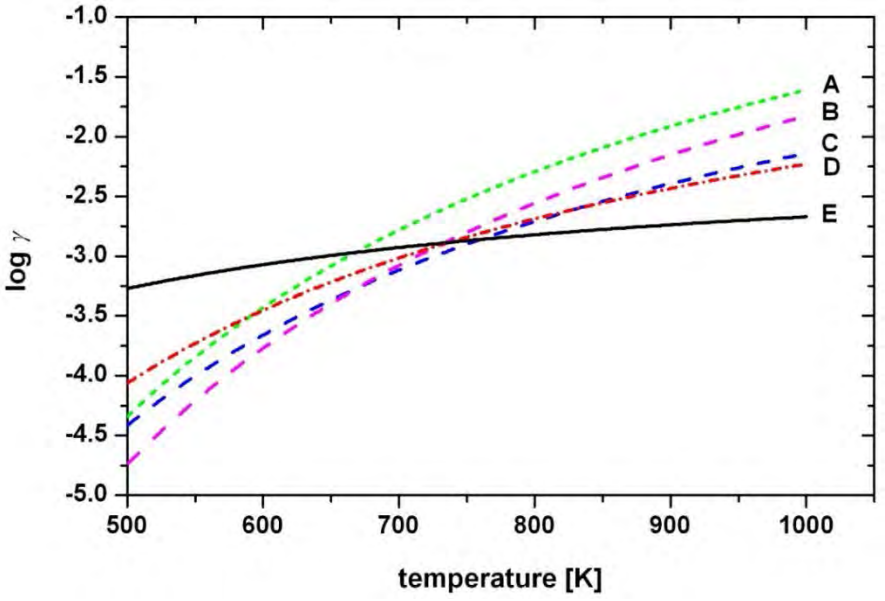

A comparison of Curves A and C (γ of Po in Bi, Eqs. [5.21] and [5.22]) shows that with increasing temperature Curve C, being based on non-equilibrium measurements, progressively falls below the equilibrium value given by Curve A. This may be attributed to the aforementioned effect of surface depletion. Furthermore, we noted in Section 5.2.1.1.5.2.1 that the slope of Curve E (γ of Po in $Li_{0.17}Pb_{0.83}$, Eq. [5.17]) may be questioned. If we therefore choose to compare the activity coefficients for Po in Bi as estimated in Curve A (Eq. [5.21]) and for Po in Pb as estimated in Curve D (Eq. [5.26]), we find that above the melting point of pure lead (601 K), Pb appears to interact more strongly with Po than Bi does, while the opposite is indicated at lower temperatures. However, Curve D is based on measurements performed above 913 K, and the extrapolation to temperatures around 600 K can certainly not be trusted. Curve B (γ for Po in LBE, Eq. [5.24]) should in any case follow fairly close to Curve D at higher temperatures. Because Pb, the component that is more strongly binding in this temperature range, has a lower thermodynamic activity due to its diluted state in LBE and thus a lower efficiency in forming compounds with Po, Curve B should be expected to lie somewhat above Curve D, as it is indeed seen to do above 750 K. We cannot with reasonable accuracy make a similar comparison at low temperatures, where Bi may or may not be the stronger binding component, as none of the data sets that the curves are based on extend below 723 K.

It stands to reason that at a temperature where Bi and Pb have the same affinity for Po, a mixture of Bi and Pb should also have similar Po affinity as the pure metals (in the absence of ternary compound formation). This holds approximately true for the triplet of Curves B (LBE), C (Bi) and D (Pb), which intersect each other in the region of 670 to 830 K, but not for Curve A (Bi). On the other hand, Curve A intersects Curve D at a temperature

far below the validity range of any of the curves, which is why this cannot be taken as proof either for or against the consistency of that combination of estimates of γ for Po in the respective solvents. Also, the combination of Curves B, C and D appears inconsistent in that the value of γ for Po in LBE, at high temperatures, would be higher than in either of the pure components.

We will therefore accept Eqs. (5.21) (Curve A) and (5.26) (Curve D) as the best available estimates of γ for Po in Bi and Pb, respectively. As the experimental work that Curve B is based on (Eq. [5.23] [Ohno, 2006]) appears highly convincing, and the corresponding estimate of the thermodynamic activity of Po in LBE assumes reasonable values with respect to the thermodynamic activity in the pure components, we recommend using Eq. 5.23 as Henry constant for calculations of Po volatilisation from LBE. Caution should nevertheless be taken in extrapolating Eq. (5.23) to lower temperatures.

Addendum

During the phase of peer review and revision of the present chapter, new results on polonium volatilisation became available. These results are immensely important, both for the practical use of the recommendations derived in the present and the following section as well as for the fundamental understanding of polonium volatilisation from liquid metals. Therefore, these new results will be briefly discussed in the following:

In a recent study, the evaporation of Po from its dilute solution in liquid lead-bismuth eutectic (LBE) was measured again at temperatures between 700 and 1 000°C in Ar/5%H_2 using the transpiration method (Gonzalez, 2014a). Concurrent measurements of the evaporation of LBE could be well reproduced by calculations using literature data. This allowed to model the Po evaporation data and extract accurate temperature correlations for the Henry constant for Po dissolved in LBE at two different Po concentrations. Extrapolations of the new correlations were in excellent agreement with existing data at lower temperature, in particular with those represented by Eqs. (5.23) and (5.25) extracted from Ohno (2006) and Buongiorno (2003). Thus, these new correlations confirm the validity of the assessment given above for high temperatures. In another, more detailed recent study, polonium evaporation from LBE into Ar and Ar/5%H_2 was measured as a function of time and carrier gas flow rate at temperatures between 600 and 1 000°C (Gonzalez, 2014b). The experimental results, together with a theoretical analysis of polonium diffusion in LBE, provided evidence that correlations such as Eqs. (5.23) and (5.25) closely describe true equilibrium between dissolved and vapour polonium in the investigated temperature range.

However, in another recent study, the evaporation behaviour of polonium from liquid bismuth and LBE has been measured at lower temperatures, similar to the expected operation temperatures of liquid-metal-cooled facilities, i.e. 164-500°C and 300-500°C for LBE and Bi, respectively (Rizzi, 2014). The Henry constant data determined in this study for polonium over the dilute liquid metal solutions in the cited temperature ranges deviate significantly from those measured in Ohno (2006), Buongiorno (2003) and Gonzalez (2014a, 2014b), indicating much higher volatility of polonium at temperatures < 500°C compared to what would be expected from extrapolating Eq. (5.23) to this temperature range. Possible mechanisms responsible for the increased polonium volatility, involving impurities in the carrier gas and an oxide layer on the liquid metal samples are speculatively discussed in Rizzi (2014). The cause of the increased polonium evaporation observed in Rizzi (2014) was further investigated in a follow-up study (Gonzalez, 2014c). In this study, the time-dependent release of polonium from LBE samples in Ar/5%H_2 and Ar was measured between room temperature and 500°C. These experiments also showed enhanced polonium volatilisation, similar to the observations of Rizzi (2014). In addition, the study revealed that the majority of polonium in the LBE samples evaporated according to established temperature correlations for the Henry constant of polonium in LBE represented by Eq. (5.23), while only a small fraction of

polonium in the LBE behaved differently, causing a relatively large but transient polonium release at the start of the evaporation experiments. The study also revealed that this volatile fraction of polonium was located near the sample surface and was formed after prolonged exposure of the samples to air at room temperature (Gonzalez, 2014c). Thus, it can be speculated that the peculiar evaporation behaviour of this surface polonium is caused by enrichment and association with an oxide layer.

Another recent study investigated the evaporation and deposition behaviour of the element polonium and its compounds without contact to a liquid metal matrix in a temperature gradient tube made of fused silica using carrier gases with varied redox potential (Maugeri, 2014). The results obtained in this study show that under inert and reducing conditions in the absence of moisture, elemental polonium (or possibly BiPo in samples where Po was produced by proton irradiation of Bi-metal) is evaporated and deposited around 250 to 325°C in the silica tube. Polonium compounds more volatile than elemental polonium can be formed if traces of moisture are present in both inert and reducing carrier gas. This indicates that the hypothesised very volatile polonium compound H_2Po (see Section 5.2.1.1.5.5.3) is not formed when polonium interacts with pure hydrogen gas. The fact that highly volatile polonium species are formed when moisture is present in the carrier gas rather indicates that highly volatile polonium hydroxides exist that are formed under the conditions prevailing in the experiments of Maugeri (2014). The use of dried oxygen as carrier gas in the experiments of Maugeri (2014) lead to the formation of polonium oxides which are less volatile than elemental polonium. It was also found that the volatility of polonium oxides increases with increasing oxidation state. In the presence of moisture in an oxidising carrier gas, species are formed that are more volatile than the oxides and less volatile than elemental polonium. Considering the redox potential of the carrier gas those species were concluded to likely be oxyhydroxides.

Summarising these new findings, it can be stated that the evaporation behaviour of polonium from diluted solutions in LBE at temperatures ≥ 500°C is reasonably well understood, documented by consistent results from different independent studies. At temperatures below 500°C however, the evaporation behaviour of polonium from dilute LBE solutions is more complex than expected. The increased polonium volatility observed in the more recent experiments seems to be associated with small fractions of the polonium located near the surface of LBE samples, having a different chemical state compared to the polonium in the bulk. The most recent results indicate that this surface layer is most likely of oxidic nature, and the chemical reactions leading to enhanced volatilisation likely involve moisture causing the formation of volatile polonium hydroxides. The causes of these phenomena are currently under intensive study. A more extensive review on these studies may be issued by the expert group when more results become available. *For the moment we conclude this discussion by emphasising that the recommended temperature function derived below for polonium volatilisation from the liquid metals Pb, Bi and LBE was confirmed to be valid between 600 and 1 000 °C, but should not be used below 500 °C.*

5.2.1.1.5.4 Evaluation of polonium thermal evaporation data

In light of the new results obtained after compilation and review of the present chapter that were briefly described at the end of the preceding section, we emphasise once again that the following points 1-3 are valid only for temperatures above 500 °C.

1) Whether Po, at low concentration, is dissolved in lead or in LBE has little importance for its effective vapour pressure. Both metals lower the thermodynamic activity of Po, and the observed vapour pressures are similar to such degree that one can draw no obvious conclusion regarding the effect of differences in solvent composition (Table 5.2.1). Also from Figure 5.2.4 it can be concluded that there is no obvious difference in the thermodynamic activity of Po in LBE and lead that cannot be attributed to experimental error and extrapolation beyond the range of experimental data.

Table 5.2.1: Effective pressures (in Pa) of polonium over a 1 ppm solution in liquid lead and LBE; comparison of different estimates

Note that the temperature range of the table may exceed that in which the different sets of evaporation data were collected

	Eq. (5.23)	Eq. (5.25)	Eq. (5.16)	Eq. (5.18)	Eq. (5.20)
Reference	Ohno (2006)	Buongiorno (2003)	Abakumov (1982)	Feuerstein (1992)	Schipakin (1995)
Solvent	LBE	LBE	Pb*	$Li_{0.17}Pb_{0.83}$	$Li_{0.17}Pb_{0.83}$
Determined at	$X_{Po} = 2{\cdot}10^{-10}$	$X_{Po} = 2.5{\cdot}10^{-8}$	X_{Po} = Unknown	$X_{Po} = 1.5{\cdot}10^{-13}$	$X_{Po} = 2{\cdot}10^{-11}$
Normalised to	$X_{Po} = 1{\cdot}10^{-6}$	$X_{Po} = 1{\cdot}10^{-6}$	$X_{Po} = 1{\cdot}10^{-6}$	$X_{Po} = 1{\cdot}10^{-6}$	$X_{Po} = 1{\cdot}10^{-6}$
T (K)	$P_{Po,tot}$(Pa)				
500	$6.91{\cdot}10^{-13}$	$7.59{\cdot}10^{-12}$	$3.31{\cdot}10^{-12}$	$2.27{\cdot}10^{-11}$	$7.31{\cdot}10^{-7}$
600	$4.19{\cdot}10^{-10}$	$1.39{\cdot}10^{-9}$	$8.78{\cdot}10^{-10}$	$2.30{\cdot}10^{-9}$	$1.02{\cdot}10^{-5}$
700	$4.07{\cdot}10^{-8}$	$5.75{\cdot}10^{-8}$	$4.72{\cdot}10^{-8}$	$6.23{\cdot}10^{-8}$	$6.65{\cdot}10^{-5}$
800	$1.26{\cdot}10^{-6}$	$9.39{\cdot}10^{-7}$	$9.39{\cdot}10^{-7}$	$7.39{\cdot}10^{-7}$	$2.72{\cdot}10^{-4}$
900	$1.82{\cdot}10^{-5}$	$8.23{\cdot}10^{-6}$	$9.60{\cdot}10^{-6}$	$5.06{\cdot}10^{-6}$	$8.15{\cdot}10^{-4}$
1 000	$1.54{\cdot}10^{-4}$	$4.68{\cdot}10^{-5}$	$6.17{\cdot}10^{-5}$	$2.36{\cdot}10^{-5}$	$1.96{\cdot}10^{-3}$
1 100	$8.84{\cdot}10^{-4}$	$1.94{\cdot}10^{-4}$	$2.82{\cdot}10^{-4}$	$8.32{\cdot}10^{-5}$	$4.01{\cdot}10^{-3}$
1 200	$3.79{\cdot}10^{-3}$	$6.33{\cdot}10^{-4}$	$1.00{\cdot}10^{-3}$	$2.38{\cdot}10^{-4}$	$7.30{\cdot}10^{-3}$

* Assumed PbPo in ideal solution in Pb.

2) With the exclusion of one outlier set of data (Eq. [5.20]), the remaining four experiments show surprisingly good agreement (considering the experimental difficulties and differing experimental conditions) on the effective vapour pressure (Table 5.2.1). We recommend using Eq. (5.23) for the evaluation of Po evaporation from activated LBE; while it gives somewhat higher estimates of the effective vapour pressure, this may very well be due to the commendable thoroughness in ensuring equilibrium conditions and saturation of the gas phase during the experiments. In accordance with item No. 1, Eq. (5.23) can be used for liquid lead alike.

3) We note that despite the fact that the concentrations of Po in the melt differ by five orders of magnitude between Feuerstein's determination of the activity coefficient and Buongiorno's measurements of vapour pressures, the respective functions are in fairly good agreement in the range of 600 to 1 100 K; in fact, all data except Schipakin's show satisfactory agreement above 700 K regardless of the differences in Po concentration. This indicates that the thermodynamic activity coefficient for Po in lead-alloy melts is constant within this concentration range, a characteristic of an ideal dilute solution (see Section 5.2.1.1.3). It is noted that this is also the case in pure bismuth; the activity coefficient was found to be constant over a concentration range of four orders of magnitude (Moyer, 1956). We therefore find it appropriate to apply Eq. (5.23) within a wide range of Po concentrations, despite the lack of experimental data for the highest concentrations that may be encountered in strongly activated liquid metals. As these concentrations are still below $X_{Po} = 10^{-5}$ it appears more reasonable to assume that there will be no significant solute-solute interaction than the opposite.

4) There is reason to believe that Po-enriched films may form by condensation on surfaces above the liquid metal level, if the temperature difference is sufficient. While Eq. (5.23) should describe volatilisation of Po from very dilute lead and LBE solution with good accuracy, it should not be applied to Po-rich alloys at low temperatures.

Thus, from Eqs. (5.3) and (5.23), the vapour pressure of polonium over liquid lead and LBE in the range of 500 to 750°C will be fairly well approximated by:

$$P^{*}_{Po(Pb,LBE)} = X_{Po} \cdot K_{H(Po(LBE))} = X_{Po} \cdot 10^{-\frac{8348}{T}+10.5357} \tag{5.27}$$

5.2.1.1.5.5 Abnormal polonium volatilisation

5.2.1.1.5.5.1 Aggregate recoil/sputtering

A well-known property of α-decaying substances is their ability to volatilise even at room temperature. This effect was first observed at the beginning of the last century, when walls of a closed vessel containing a surface source of RaA (^{218}Po) were detected to be contaminated by its daughter product, RaB (^{214}Pb) (Brooks, 1904). This observation led to the hypothesis that during α-decay, the daughter product is expelled in the opposite direction of the emitted α-particle. Due to momentum conservation, such a heavy particle acquires a kinetic energy of roughly 100 keV, which is enough to overcome the binding forces at the sample surface. Thus, a recoiled daughter atom is able to leave the sample containing its mother and to settle down on nearby surfaces.

Further observations showed that not only the daughter product itself, but the α-active parent as well may be transported by recoil. Working with radium decay products (Makower, 1910) or polonium (Lawson, 1919), a significant mobility of the parent was observed. This "pseudo-recoil" effect could not be explained by the simple theory behind daughter recoil, as the latter implies the transport of only one single atom expelled during α-decay. It was then assumed that groups of atoms may also be expelled during one decay, generating aggregates containing the undecayed substance. This phenomenon was termed *aggregate recoil*. It implies the formation of chunks of the radioactive substance at the surface of a sample, which are then expelled by radioactive decay. These clusters are then transported further by either diffusion or other decay events, thus forming a radioactive aerosol phase (Natanson, 1956) containing the original mother isotope.

The basic principle of this theory was developed in the first decades of the last century and is nowadays still an accepted explanation for the high mobility of ^{210}Po. Nevertheless, there are several contradictions, which may not be explained by this simple theory (Trenn, 1980). Observations with curie quantities of polonium suggest that the spread of contamination is largely dependent on the volatility of the polonium compound involved (Bagnall, 1957). Experiments on polonium volatility in different atmospheres also indicate the existence of a volatile polonium compound (see Section 5.2.1.1.5.5.3) rather than a process based on recoil. Nonetheless, there seems to exist the consensus that recoil may partly explain high mobility of α-active solid samples (Icenhour, 2005; Whitehead, 1994), but for the case of polonium, diffusion, electrostatic attraction and air current effects also play an important role for its transport (Borisov, 1980). Interestingly, there is a lack in scientific research investigating these phenomena, and the fundamentals of the involved processes remain obscure.

For the process behind aggregate recoil, many parallels may be found by consulting literature on the theory of sputtering in particle physics. Here, the ejection of atoms is usually caused by a beam of accelerated ions that hit a target material. The term *sputtering* is therefore predominantly used if the source of energy comes from outside of the target. In analogy, the process of aggregate recoil may be considered as a sputtering effect caused by intrinsic irradiation. Both effects in reality differ by the origin of the kinetic energy transmitted to a target, but are essentially describing the same process occurring

on an atomic level. The advantage of describing aggregate recoil as a sputtering effect lies in the huge knowledge gained from particle physics experiments.

Based on the sputtering theory developed by Sigmund (1969), sputtering was estimated for the MEGAPIE prototype LBE target considering the α-decay of the ^{210}Po isotope (Groeschel, 2006). At the end of MEGAPIE irradiation, with about four months of operation at an average of 1 mA, the calculated total activity of ^{210}Po in the target is in the order of $1.3 \cdot 10^{14}$ Bq, which corresponds to a mole fraction of $x_{210Po} = 9 \cdot 10^{-7}$. The number of emitted atoms from a full LBE leak covering a surface of 4 m^2 is $\Phi_{Sput} = 9 \cdot 10^{15}$ atoms/m^2 per day (Perret, 2002). Therefore $8 \cdot 10^9$ ^{210}Po atoms can be emitted in one day and the number of disintegrations in one day within the emitted material is less than 500. This corresponds to a very low activity due to sputtering of about $6 \cdot 10^{-3}$ Bq per s and m^2 of LBE surface. It should also be noted that sputtering will significantly contribute to the release of β- and γ-active species.

It should be stressed that in reality the fraction of sputtered material is expected to be higher than predicted by theory because of the following reasons:

1) The above calculations are based on the assumption that the distribution of Po inside LBE will be homogeneous, which is known not to be the case. Po was found to concentrate at grain boundaries and to segregate towards LBE surfaces (Tammann, 1932; Obara, 2004b), see also Section 5.2.6. Such enrichment of polonium may significantly contribute to higher sputtering rates than would be expected assuming a homogeneous distribution.

2) Another reason for an increase in sputtering may result from the oxidation of lead at its surface. Changes in density or the sputtering mechanism may contribute to significantly higher release rates. A significant increase in the release of activity was observed for ^{238}Pu pellets if exposed to an atmosphere containing moisture (Steward, 1963). The authors of this work, however, did not consider sputtering to be a possible cause of ^{238}Pu to become airborne, but referred their observation to breakaway of oxide by the air current. This indicates a possible change in total sputtering for oxidised metals compared to their pure state.

5.2.1.1.5.5.2 *Volatility at room temperature*

The mobility of radioactive substances at ambient temperature is a phenomenon not yet fully understood. Open α-active sources and sources undergoing fission are said to contaminate their surroundings in quite short time. Especially ^{210}Po is observed to creep against gas flows and penetrate regions impossible to reach by normal gas dynamics (Stang, 1966). To minimise the escape of polonium particles through orifices of a polonium laboratory, a minimum gas flow velocity of 1.5 m/s is suggested in Ershova (1974). ^{210}Po is moreover a well-known nuclide in terms of posing strong contamination issues in α-spectroscopy. Open sources are often observed to contaminate the detector system to a significantly larger extent than other nuclides do, a fact explained by its high volatility and relatively short half-life (Sill, 1970). Even cooling the samples to the temperature of liquid nitrogen does not prevent contamination (Kurakado, 1981). Similar findings were obtained by Riehl (1964), where the volatility of polonium was observed to be independent of temperature below -40°C. This behaviour is not only restricted to polonium. The ability of $^{238}PuO_2$ to become highly mobile was described in a report on the experience from a plutonium processing facility (Icenhour, 2005). Such effects are, in any case, only observed if very large activities exceeding the curie-level are processed. For laboratories working with small α-activities these effects are of minor importance.

It should also be stressed that in comparison to their stable or differently decaying isotopes, the apparent physical and chemical properties of α-decaying nuclides may significantly change (Kopytin, 1962). Even different half-lives of two α-decaying isotopes of one element may lead to different macroscopic behaviour. Such effects can significantly

alter properties such as apparent vapour pressure at low temperatures, the melting point and diffusion constants in different matrices. Depending on the half-life and activity of the isotope involved, the volatilisation behaviour of polonium at low temperatures will significantly deviate from predictions done by extrapolations from vapour pressure curves as the volatilisation will become independent from temperature. This is the direct consequence of the sputtering effect and should be kept in mind while dealing with large quantities of any polonium isotope. This circumstance is not only limited to polonium; every other element decaying by α or fission will exhibit such behaviour. For example, the solubility of ^{238}Pu in water is larger by a factor of 200 than for its longer-lived homologue ^{239}Pu (Fleischer, 1977), which approximately corresponds to the ratio of their half-lives. However, up to now little effort was put into measuring such discrepancies and experiments studying such effects are rather scarce.

One should be aware that α-active aerosols can penetrate regular particle filters by the physical mechanism of α-recoil significantly faster than expected from the claimed efficiency of the filters (Ryan, 1975; McDowell, 1977). Other researchers have attributed the penetration of polonium through particulate filters as proof for a chemical conversion of polonium to a gaseous compound. Usually referred to as a "gaseous fraction of polonium" or PoH_2, it has found its way into scientific textbooks although its existence has never been confirmed.

5.2.1.1.5.5.3 Polonium hydride

Several investigators have reported Po volatilisation in excess of what would be expected from thermal evaporation of elemental Po or its intermetallic compounds with Pb and Bi and attributed this deviation to the formation of a gaseous polonium compound. There is wide disagreement on what relevance, if any, polonium hydride may have for such volatilisation of ^{210}Po from contaminated, liquid or solid heavy metal alloys. Most of the reasonably well established properties of PoH_2 are listed and discussed in a supplement volume to the Gmelin Handbook (Bagnall, 1990); this is in fact a very limited amount of data which, additionally, is often based on experiments performed nearly one century ago.

Lead polonide may, in principle but not necessarily in practice, react with moisture according to:

$$PbPo + H_2O \leftrightarrow H_2Po + PbO \tag{5.28}$$

From very early on it has been argued that PoH_2, if it exists, would be a highly unstable compound (Mendeleev, 1889). It was nevertheless reported to appear in trace amounts when polonium metal reacts with hydrogen gas (Lawson, 1915), or with dilute hydrochloric acid in the presence of metallic magnesium (Paneth, 1918).

Pure polonium hydride has never been produced in sufficient quantity to determine its physical properties. By extrapolation from the hydrides of sulphur, selenium and tellurium, a boiling point of 37°C was estimated (Bagnall, 1966). Thus, if PoH_2 were formed by reaction with water or moist air, it would be gaseous above a spill of liquid LBE. It has therefore been given attention in several reports on safety issues related to activated LBE coolant (Li, 1998; Levanov, 1999; Pankratov, 2004).

The observations interpreted as evidence for the formation of a gaseous Po compound in the presence of e.g. water vapour are basically of two types: an increase in total ^{210}Po in the gas phase or the appearance of a non-filterable fraction of ^{210}Po in the cooled vapour. In some cases, both effects have been studied during the same experiment. A review paper (Borisov, 1999) summarises the Russian observations and interpretations of these phenomena.

From evaporation experiments with irradiated bismuth dissolved in LBE it was concluded that in the presence of water vapour, PoH_2 is the predominating form of ^{210}Po in the gas phase (Buongiorno, 2003). If this holds true, it would greatly increase the ^{210}Po release in certain accident scenarios, for instance if the activated target material came

into contact with water. Experimentally determined functions for formation energies and partial pressures of PoH_2 under various experimental conditions have been published (Buongiorno, 2003, 2004), but are typically based on differences between expected and observed total polonium content in the gas phase, assuming that this difference represents the contribution from PoH_2. Thus, to accept these functions, one must be convinced that the excess over what would be expected from thermal evaporation alone is almost exclusively due to the presence of molecular PoH_2. Several other mechanisms that might explain the observed discrepancies have been suggested (see above and end of this section), and as there is also poor agreement between experiments performed by different groups as well as completely negative results, it would be premature to recommend even a tentative expression for the partial pressure of PoH_2 over activated target material.

The idea of PoH_2 as the predominant gaseous component in these experiments has also been strongly questioned on a theoretical basis. It is widely acknowledged that this compound appears to be thermodynamically unstable and does not spontaneously form in any significant quantity (Buongiorno, 2004; Eichler, 2004a). Thus the equilibrium ought to be strongly shifted towards the elements or, in a heavy liquid lead-alloy target, possibly lead polonide and hydrogen. In fact, even dedicated attempts to produce PoH_2 by various methods, in order to prove its very existence and determine some of its properties, have either failed or resulted in very low yields (a review is given by Weigel [1959], Abakumov [1982], Bagnall [1990]). While there is some reason to believe that the compound does in fact exist, PoH_2 has never been successfully isolated in weighable quantity and, if we allow ourselves to doubt the pioneering work on this elusive compound, never been obtained at all by simple reaction of polonium metal with hydrogen.

Other experiments (Neuhausen, 2004) interestingly show no significant difference between polonium volatilisation in argon/hydrogen mixture and argon/steam mixture, respectively. If indeed there were production of PoH_2, this ought to be much larger in the presence of hydrogen gas, which is a more reactive donor of hydrogen atoms than the thermodynamically more stable water molecule. Theoretical estimates of thermodynamic data of PoH_2 and other polonium compounds were derived from data of homologous chalcogen compounds in Eichler (2004a) (provided as Appendix 5.4.2 at the end of this chapter). The equilibrium constant for formation of PoH_2 from PbPo calculated using these thermodynamic data is several orders of magnitude smaller for the reaction with water than for that with hydrogen (Figure 5.2.5).

It must be stressed that while the thermodynamic parameters for PbPo and PoH_2 used to derive the equilibrium constants (Eichler, 2004a) are theoretical estimates with large uncertainties, this error is cancelled out when we study the *difference* between these two reactions; thus we can say with confidence that the two reactions should exhibit a large difference in PoH_2 yield, a difference that was not observed.

Figure 5.2.5: Equilibrium constants for formation of polonium hydride from solid (left) and gaseous (right) lead polonide and different sources of hydrogen; positive values of log(K_T) indicate that the equilibrium is shifted towards the products, and vice versa

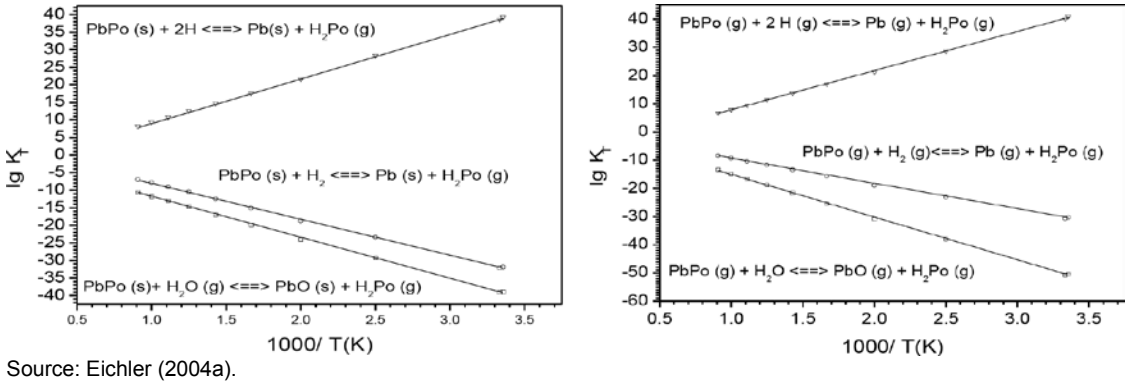

Source: Eichler (2004a).

As seen from Figure 5.2.5, thermodynamical calculations (Eichler, 2004a) further indicate that PoH_2 could not be produced in any appreciable amount by simple reaction with steam or hydrogen. The equilibrium constants for formation of PoH_2 from PoPb are very small except for reaction with monatomic hydrogen, and even if PoH_2 were formed through the action of short-lived, energetic hydrogen radicals that were present in the high radiation field of a spallation target, it would tend to spontaneously decompose ($PoH_2 + Pb \rightarrow PoPb + H_2$).

In another investigation on this topic (Borisov, 1995a), the apparently non-condensable (at near-ambient temperature) fraction of the ^{210}Po release was determined separately. Any metallic Po as well as the PbPo intermetallic compound, after being evaporated from the hot melt, would be expected to condense upon cooling and be present as an aerosol that is retained when the gas stream passes through a particulate filter. Significant and sometimes quite large amounts of activity, however, were found to penetrate the filter. The authors argue that this is due to the formation of PoH_2; this conclusion is repeated in a related paper (Petryanov, 1992). The same authors propose that a small fraction of thermodynamically unstable, short-lived PoH_2, formed from metallic Po in a humid atmosphere (Borisov, 1995b), is sufficient for producing this effect. This would be due to a state of equilibrium between metallic aerosol particles and gaseous PoH_2 that makes the aerosol essentially unfilterable, as trapped ^{210}Po would briefly form $^{210}PoH_2$, be carried across the filter by the gas stream, and then revert to metallic aerosol. The authors further mention a combination of particulate filters with active charcoal adsorbent as proven quite efficient in retaining airborne ^{210}Po activity (Borisov, 1995b, 1999).

There are several aspects of the reported observations (Borisov, 1995a) that would require further investigation and analysis, and in our opinion a deeper discussion of certain peculiarities would have constituted a highly appropriate addition to the report:

1) The total release of ^{210}Po was found to be lower in humid atmosphere (air or argon) than in dry atmosphere. This was, reasonably enough, ascribed to the visibly denser surface layer of oxides formed under humid conditions, which would hinder the evaporation kinetics (in other words, the experiments were performed under non-equilibrium conditions). However, in one experiment where an oxide film, described as being "loose", was mechanically removed, the total ^{210}Po release decreased 48-fold. The explanation for this observation (that the loose film provided an increased interaction surface) seems insufficient for an effect of this magnitude. In any case, other experiments indicate that the effect of an oxide layer on evaporation rates is fairly complex and depends strongly on experimental conditions such as temperature and pressure (Tupper, 1991), which may contribute to the somewhat confusing nature of the results.

2) The relative fraction of "gaseous" ^{210}Po differed greatly (5 to 83% of total) between experiments but showed no obvious trend with regard to evaporation temperature. However, if we would assume that a low-temperature, gas phase equilibrium between airborne solids and gaseous hydride establishes itself in the cooler parts of the apparatus (as the authors suggest – see above), then the evaporation temperature would only influence the total levels of airborne ^{210}Po and not the observed relative amounts of aerosol and gaseous compound. Also, in the same experiment quoted in item No. 1 above, the "gaseous" fraction of the total release decreased by 53% when the "loose" film was removed. Such a dependence on the evaporation source is not in accord with the concept of a gas-phase equilibrium determining the relative fraction of PoH_2.

3) At 350°C, the relative fraction of "gaseous" ^{210}Po was greater in dry argon (67%) than in moist argon (41%). The authors offer no explanation and do not even comment on the peculiar result that their "polonium hydride" is, at this temperature, most readily formed in the absence of hydrogen.

4) The data can at best be described as scattered, and there is no mention of the number of replicates (if any), nor any estimation of the magnitude and sources of experimental error.

The investigators do not describe the filter that was used in any greater detail, but unless it in fact was inadequate for retention of aerosols, which seems unlikely, then the experiment shows in a rather conclusive way that a great part of the airborne ^{210}Po behaves much like a gas at some distance from the source. Thus, this report, despite its shortcomings, merits attention.

In a related paper (Petryanov, 1992) the production of a "gaseous fraction of polonium" was studied at lower temperatures, using pure polonium deposited on copper or filter material. The rate of emission of "gaseous" Po into a stream of moist air[1] at 20°C increased two- to five-fold with increasing humidity, and the concentration of "gaseous" Po reached in moist helium and moist hydrogen, at 80°C, was more than ten times higher than in the corresponding dry gases.

Yet another experiment has been described, in which the volatilisation of Po from LBE increased in a regular and consistent manner with increasing admixture of hydrogen gas to the inert carrier (Larson, 2002a, 2002b). The highest ^{210}Po concentrations obtained in the gas phase were somewhat below $5{\cdot}10^{-14}$ mol/dm^3 at 40 000 ppm H_2, as compared to about $5{\cdot}10^{-16}$ mol/dm^3 at 1 000 ppm H_2. These results clearly represent a real phenomenon and cannot be dismissed as coincidence or over-interpretation.

All this considered, the results present a very puzzling picture, and it is difficult to draw any definite conclusions from these experiments. We can neither accept the formation of molecular PoH_2 on the basis of the reported observations alone, nor can we rule out the possibility that ^{210}Po may assume a gaseous or at least gas-like state under conditions where classic chemical reasoning would predict otherwise.

5.2.1.1.5.5.4 *Polonium aerosols*

Apart from airborne polonium species which are present in atomic or molecular form, polonium atoms may to a large extent be attached to dust particles dispersed in air. This fraction, usually referred to as polonium aerosols, has attracted significant attention by scientists in the former Soviet Union. Several Soviet scientists performed many pioneering investigations on aerosols formed by polonium and have developed several filtering systems capable of mitigating problems resulting thereof (Natanson, 1956; Borisov, 1980; Fillatov, 2007).

As with any aerosol, those with polonium are usually formed by either dispersion of solids or liquids containing Po or its compounds or by condensation of its vapours on airborne particles. Any mechanical treatment such as cutting, grinding or sawing thus producing fine powders of solid Po-containing materials may significantly contribute to the formation of dispersed radioactive aerosol. Condensation and agglomeration of oversaturated vapours usually occurs, involving inert nucleation cores as dust or fines present in the gaseous phase (Stewart, 1963).

Recoil sputtering presents a special case for polonium aerosol formation, as it is a process occurring without any outer force. Within this process, single atoms and aggregates can be expelled to the surroundings. These aggregates are usually positively charged due to stripping of electrons during the decay process. As such, they easily attract liquid and solid material thus forming clusters of atoms or particles in the nanometre region. In air containing water vapour these clusters are mostly hydrated and attach themselves to existing aerosol particles within minutes. Apart from the dynamics of

1. The English translation of the legend to Table 2 is in error; the Russian original (Doklady Akademii nauk SSSR, Vol. 322, No. 3, 1992) clearly states that the experiment was performed in air and not, as the English version would have it, in hydrogen.

particle size growth, the presence of polar molecules such as water vapour and trace gases (NO_x, NH_3, SO_2) also significantly contributes to the charge neutralisation of radioactive polonium clusters (Papastefanou, 2008). From experiments with ^{220}Rn emanations it was also shown that polarity of trace gases influences the agglomeration dynamics and the concentration of condensation nuclei for radioactive aerosols (Natanson, 1956).

Borisov (1995b) and Ito (1987) have measured the charge distribution of airborne polonium species. They found it to obey the standard distribution function with the majority of particles being neutral; aerosols with higher specific activity show increasing shifts towards positive charges. Due to α-radiation, the charge of aerosol particles is continuously changing and is in equilibrium with the surrounding air which is also permanently ionised. The charge of radioactive aerosols contributes to a large extent to the sticking of these particles to surfaces by electrostatic forces. Polarity and electrostatic attraction may indeed play a significant role in the spread of radioactivity of airborne polonium particles.

5.2.1.1.5.5.5 *Summary*

There is still no scientifically proven method to quantitatively assess the spread of polonium at ambient temperatures. This circumstance has not changed significantly during the last 50 years, as indicated in the 1966 report on the migration of radioactive material (Stang, 1966):

> *It has been postulated that … [during polonium decay] sufficient recoil energy is imparted to other atoms with which the decayed atom has been associated so as to move the small agglomerate a short distance…*
>
> *Another theory attributes the migration of polonium to its relatively high vapour pressure.*
>
> *Still another school of thought rejects both of these theories and holds that polonium is transported only by outside agents…*

As a last point, polonium hydride may be added as a possible explanation for the high mobility of polonium. The first two effects, volatility and recoil sputtering, certainly play a role for the observed abnormal spreading of substances containing polonium. However, it has not been clear up to now to what extent each of these effects contribute to the room temperature volatility observed for polonium. It should clearly be stated that none of them may be favoured up to now, and it seems mandatory to perform careful systematic experiments to clarify the nature of this peculiar volatilisation behaviour of polonium to ensure the safe operation of LBE-based nuclear facilities.

5.2.1.1.5.6 Polonium dioxide

PoO_2 is readily formed from metallic polonium, typically in solid state. In pure oxygen at 1 atm it sublimates upon heating to 885°C (Bagnall, 1966). Vapours of PoO_2 are in chemical equilibrium with the component elements, and will decompose in an oxygen-poor atmosphere. At 500°C, an oxygen partial pressure of 8.5 kPa is required to suppress dissociation; this value increases with temperature (Abakumov, 1982). Thus vapours of PoO_2 will be stable up to high temperatures in air but not in the cover gas of a heavy-metal-cooled reactor or a liquid metal spallation loop.

It follows that the PoO_2 partial pressure will depend on oxygen partial pressure as well as on temperature, and that unless the oxygen partial pressure is fairly high, we need to distinguish between the PoO_2 partial pressure and the combined Po pressure in the system. At high O_2 pressure, the partial pressure of PoO_2, in Pa, is (Abakumov, 1974b):

$$P^{o}_{PoO_2} = 10^{-\frac{10070 \pm 150}{T} + 11.129 \pm 0.11} \tag{5.29}$$

The above expression corresponds to Curve E in Figure 5.2.6; it can be seen that the pressure is lower than for metallic polonium (Curve A, corresponding to Eq. [5.14]).

Figure 5.2.6: Vapour pressures (in mm Hg)

A – metallic polonium
E – polonium dioxide under conditions preventing dissociation of the oxide

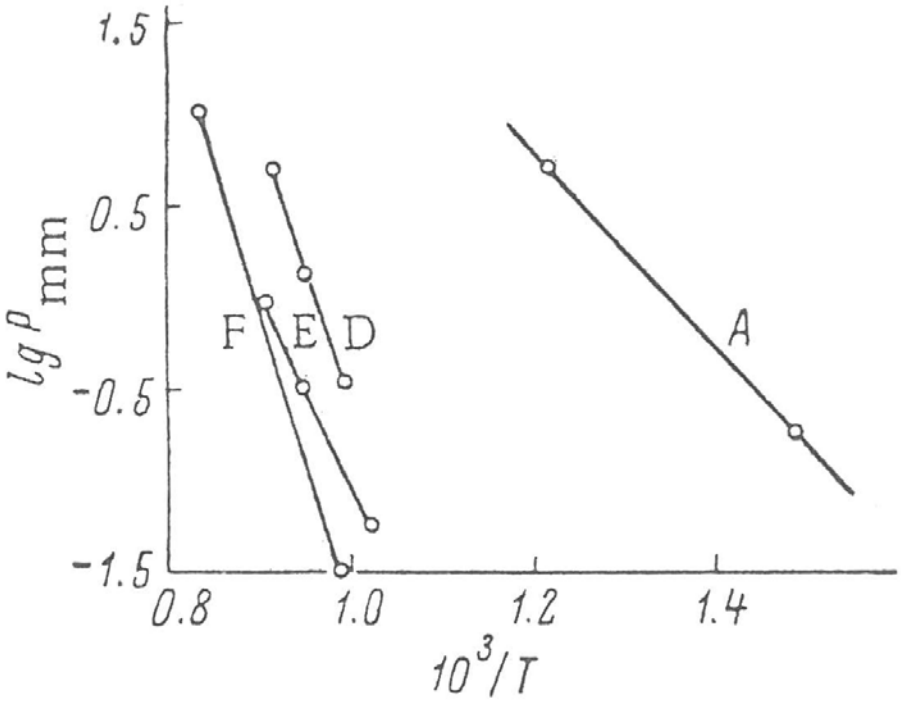

Source: Abakumov (1974b).

PoO_2 is a less volatile form of polonium than the metal itself, it does not offer an explanation for the observed anomalies in evaporation as it should be unstable in the presence of H_2 or metallic lead and bismuth, and it is unlikely to present any additional complications for the issue of polonium volatilisation from activated coolant or target material. As the interaction of water with the target material is likely to produce, by purely physical mechanism, aerosol particles of activated lead or lead alloy, these particles having large evaporation surface and potential for airborne transport, the design of the target loop and associated safety components should nevertheless aim to exclude that possibility.

5.2.1.1.6 Mercury

5.2.1.1.6.1 Metallic mercury

Mercury is known to be the only metal which is liquid at ambient conditions. Owing to the relatively weak cohesion in the condensed state, it also has a low boiling point of 356.73°C and consequently a very high vapour pressure at typical operating conditions of a lead-alloy-based spallation target or reactor. Pure mercury is known to evaporate as monatomic vapour (Wiberg, 1985). The vapour pressure of metallic mercury has been determined to a high degree of accuracy. For its temperature dependence, we will use here the function recommended in the compilation from Landolt-Börnstein (1960):

$$\log P^{o}_{Hg} = -3332.7/T + 12.6706 - 0.848 \cdot \log T \qquad (5.30)$$

5.2.1.1.6.2 Mercury in lead, bismuth and LBE

From the phase diagrams of the Pb-Hg and Bi-Hg systems (Figures 5.2.7 and 5.2.8 [Landolt-Börnstein, 1991]), one can see that mercury is completely soluble in the pure liquid metals. Intermetallic phases are only observed at low temperature in the case of Pb-Hg, whereas no such phases have been found in the Bi-Hg system. It can be concluded that the chemical interaction of mercury with the elements of an LBE target is not strong. Therefore, mercury can be considered to be dissolved in atomically disperse form within the liquid metals.

This is in agreement with the thermodynamic activities found for mercury in both metals (Figures 5.2.9 and 5.2.10), which are slightly larger than 1. Investigations on the thermodynamic properties of solutions of Hg in lead and bismuth using both vapour pressure and emf measurements are summarised in Landolt-Börnstein (1991) and Hultgren (1973). The values for thermodynamic activity coefficients of mercury in Pb and Bi at temperatures close to 600 K for concentrations of mercury ranging from $X_{Hg} = 0$ to $X_{Hg} \cong 0.1$ recommended in these reviews are compiled in Table 5.2.2.

Figure 5.2.7: Phase diagram of the Pb-Hg system

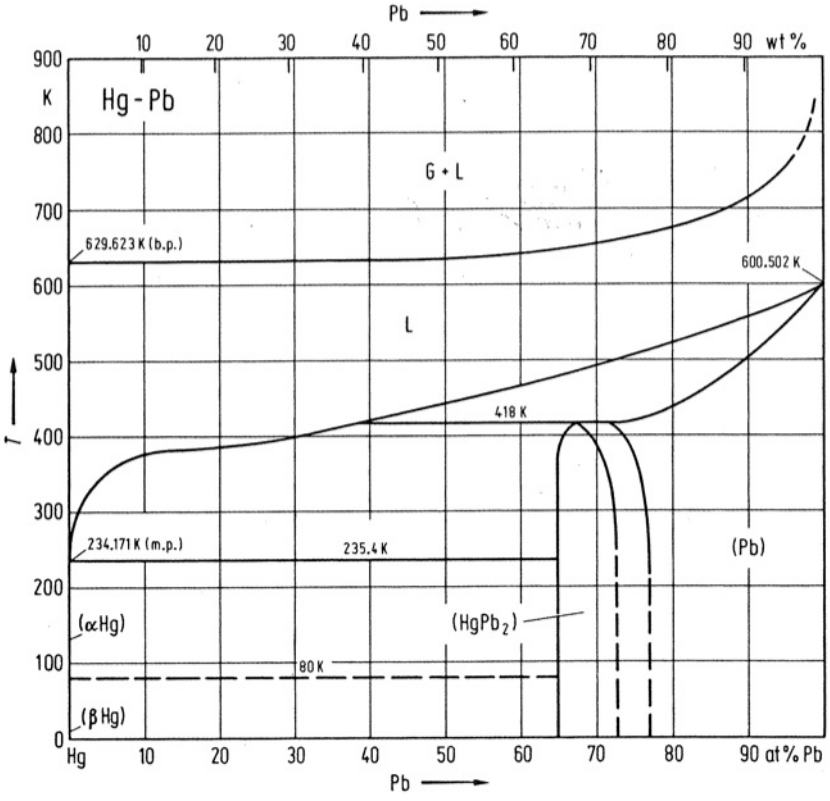

Source: Reproduced with permission of Springer Science+Business Media from Landolt-Börnstein (1991).

Figure 5.2.8: Phase diagram of the Bi-Hg system

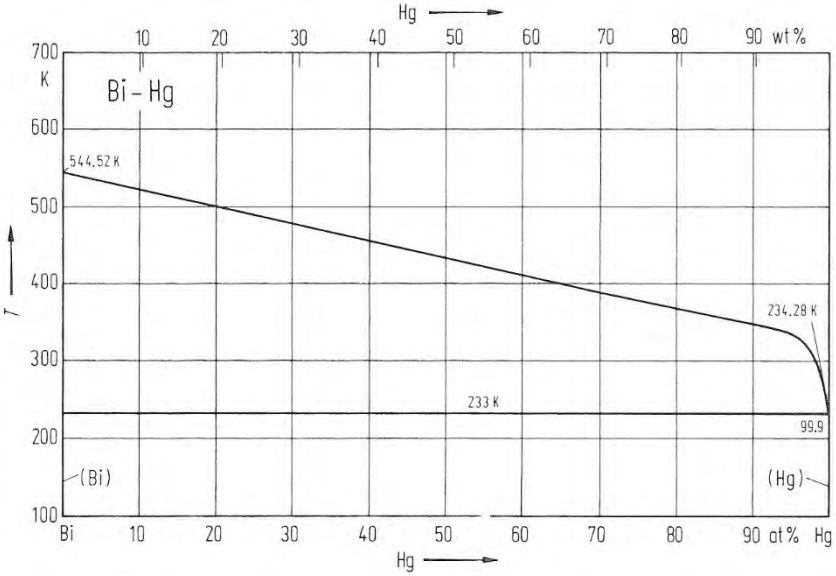

Source: Reproduced with permission of Springer Science+Business Media from Landolt-Börnstein (1991).

Figure 5.2.9: Thermodynamic activities in the Pb-Hg system

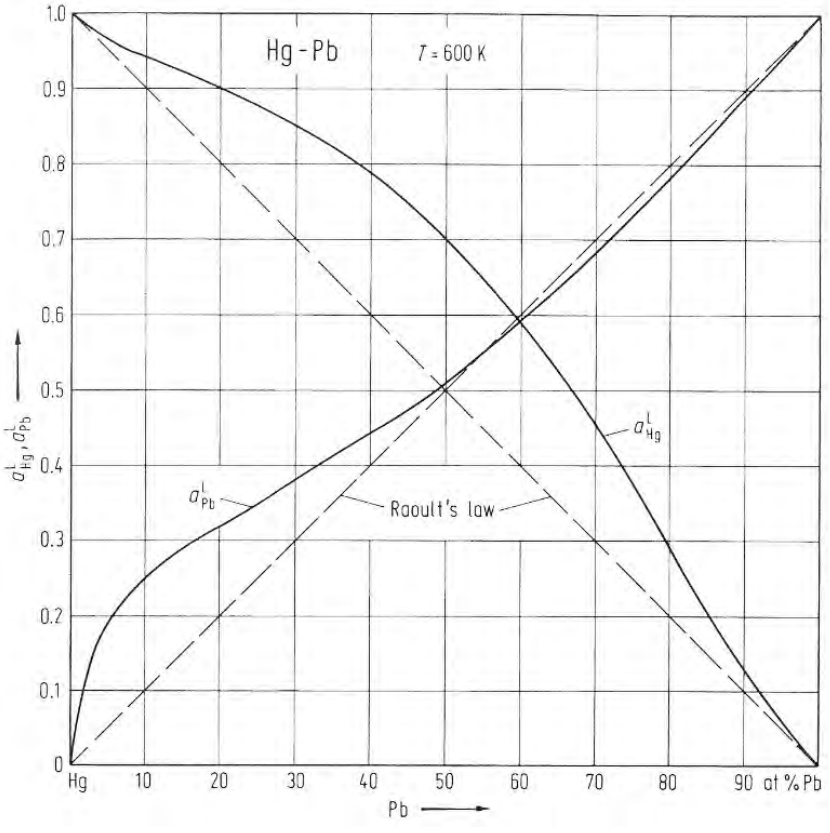

Source: Reproduced with permission of Springer Science+Business Media from Landolt-Börnstein (1991).

Figure 5.2.10: Thermodynamic activities in the Bi-Hg system

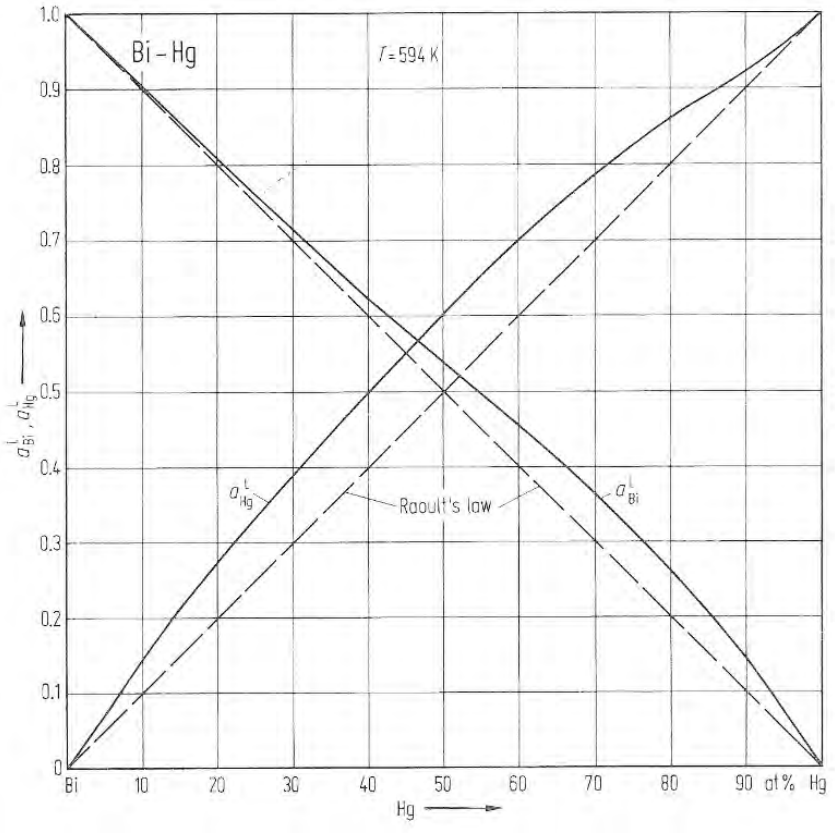

Source: Reproduced with permission of Springer Science+Business Media from Landolt-Börnstein (1991).

Table 5.2.2: Literature values for the thermodynamic activity coefficient of mercury in liquid lead and bismuth

Activity coefficient γ_{Hg}	Mole fraction X_{Hg}	Temperature (K)
$\gamma_{Hg(Pb)}$ = 1.358 (Landolt-Börnstein, 1991)	0.101	597.15
$\gamma_{Hg(Pb)}$ = 1.34 (Hultgren, 1973)	0.1	600
$\gamma_{Hg(Bi)}$ = 1.461 (Landolt-Börnstein, 1991)	0.063	594.05
$\gamma_{Hg(Bi)}$ = 1.41 (Hultgren, 1973)	0	594
$\gamma_{Hg(Bi)}$ = 1.386 (Hultgren, 1973)	0.1	594

These values are consistent and very similar for both solvents. The temperature for which the reported activity coefficients are valid coincides well with the maximum operation temperatures expected for a lead-alloy-based spallation target (where the production of mercury by spallation reactions is a major concern), while typical operating temperatures of heavy-liquid-metal-cooled reactors are significantly higher.

Because of the weak interaction of mercury with both solvent metals, no compound formation is expected in the gas phase. In principle, mercury can form compounds with various elements that are formed by nuclear reactions, both in the condensed and in the

gaseous phase. The most simple and at the same time most stable of these compounds are the halogenides and chalcogenides. However, since at the same time numerous other and more reactive metals are produced by nuclear reactions, these will form much more stable compounds with the halogens and chalcogens. As a consequence, it is expected that the formation of mercury compounds will neither lead to a strong retention in the condensed phase nor contribute significantly to the mercury partial pressure observed above the liquid metal.

Experiments were performed at PSI on the release of Hg from LBE (Neuhausen, 2005a, 2006a). In one series of experiments (Neuhausen, 2005b), LBE samples were irradiated with neutrons in SINQ, where ^{203}Hg is formed by (n,α) reactions from ^{206}Pb (a variety of thallium and shorter-lived mercury nuclides are also formed by (n,xn) reactions of the sample materials and subsequent electron capture or β^+ decay of Pb and Bi nuclides). Typical concentrations of non-carrier-added mercury in LBE achieved in these preparations amounted to $X_{Hg} \cong 10^{-13}$. A second series of experiments (Neuhausen, 2006a) was devoted to study the influence of the gas phase composition on the release of mercury from LBE. For these experiments, a Cd/Hg alloy was neutron-irradiated in SINQ. The activated mercury, also containing mainly the isotope ^{203}Hg, was removed from cadmium by distillation and subsequently mixed with LBE, yielding samples that contain inactive mercury as carrier with mole fractions in LBE of $X_{Hg} \cong 7 \cdot 10^{-5}$, a concentration that is expected for long-term irradiated high power spallation targets. Typically, the samples used for release experiments had a weight of a few grams.

The release of mercury from liquid LBE under flowing gas (reducing Ar/H_2, inert N_2 and oxidising N_2/O_2 mixtures) has been studied using these samples in the temperature range from 408 to 1 292 K using γ-ray spectroscopy. For this purpose, the amount of mercury present in the condensed phase was quantitatively determined before and after each experiment using the 279 keV γ emission of ^{203}Hg and applying corrections for γ-ray absorption by the LBE. The relative experimental errors of the individual γ-ray measurements, arising mainly from the approximate nature of the absorption correction and variations of the shapes of the strongly absorbing samples, are estimated to be in the range of ±20%.

Qualitatively, the results of these experiments show that significant amounts of mercury begin to evaporate from liquid LBE at temperatures starting from about 475 K (Figure 5.2.11). A high percentage of the mercury present (80%) was released from the samples within one hour at temperatures higher than 625 K, indicating that the possibility of mercury release has to be seriously considered in safety assessments for lead-alloy-based spallation targets. The release of mercury is strongly depressed in oxidising atmospheres, probably caused by oxide layers that were formed on the surface of the liquid metal in presence of oxygen.

From the amounts of Hg evaporated in these experiments as a function of temperature, the temperature dependence of the vapour pressure of Hg over the LBE solution was calculated, assuming that the gas phase was saturated with mercury (Neuhausen, 2011a). Here, it should be pointed out that the saturation condition was not experimentally validated. The evaluation of the two sets of experiments at different concentration levels yielded two distinct temperature functions for the effective vapour pressure of mercury. The corresponding relations, both normalised to a mole fraction of $X_{Hg} = 1$, are given in Eqs. (5.31) and (5.32) and depicted in Figure 5.2.12 together with the temperature function of the vapour pressure of pure Hg, i.e. Eq. (5.30):

$$\log P^*_{Hg} = -3115/T + 8.9 \text{ (measurement at } X_{Hg} \cong 10^{-13}\text{, normalised to } X_{Hg} = 1) \quad (5.31)$$

$$\log P^*_{Hg} = -3093/T + 9.7 \text{ (measurement at } X_{Hg} \cong 7 \cdot 10^{-5}\text{, normalised to } X_{Hg} = 1) \quad (5.32)$$

Figure 5.2.11: Comparison of the fractional release of Hg from liquid LBE under different gas atmospheres and different Hg concentrations

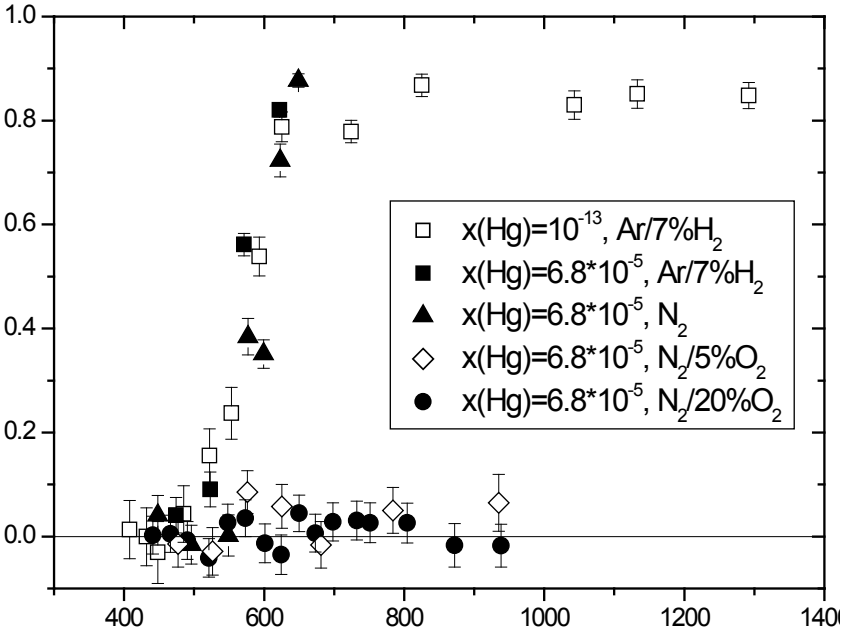

Source: Reproduced with permission of Elsevier Ltd. from Neuhausen (2006a).

Figure 5.2.12: Comparison of literature data of the vapour pressure of pure Hg (Eq. [5.30]) and Hg vapour pressure over dilute solutions of Hg in LBE, normalised to $X_{Hg} = 1$, deduced from experimental data

Eq. (5.32): with carrier, $X_{Hg} \cong 7 \cdot 10^{-5}$, Eq. (5.31): non-carrier-added, $X_{Hg} \cong 10^{-13}$

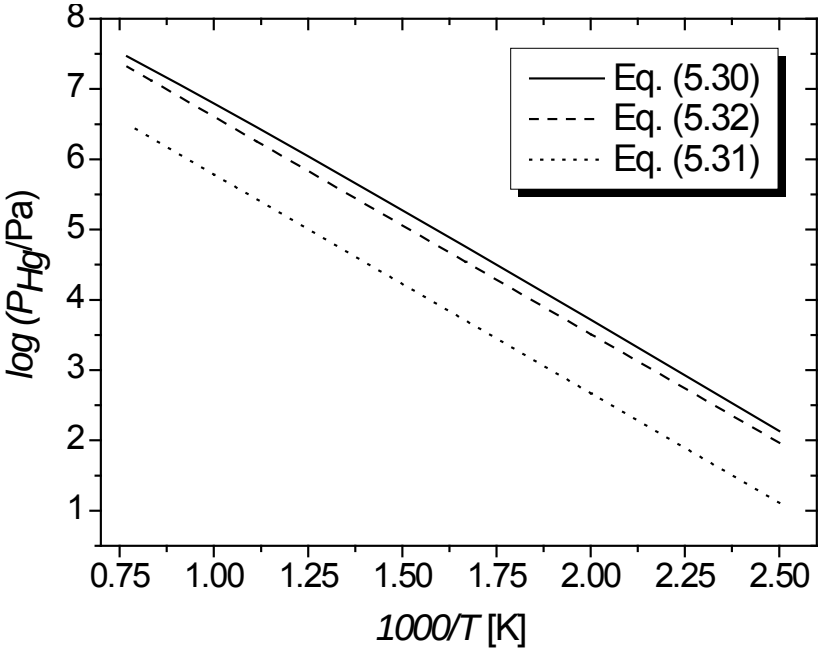

Source: Reproduced with permission of Elsevier Ltd. from Neuhausen (2011a).

The figure shows that the temperature dependence of the vapour pressure of mercury observed over LBE at both concentration levels is very similar to that of pure mercury, i.e. the slopes of the three graphs are very similar. However, the normalised functions obtained from the two sets of experiments at different concentration levels yield systematically differing values for the absolute values of the mercury vapour pressure. While the relation derived from experiments performed at higher concentrations of $X_{Hg} \cong 7 \rightarrow 10^{-5}$ show only slightly lower values of mercury vapour pressure compared to equation (5.30), the relation derived from experiments performed at $X_{Hg} \cong 10^{-13}$ show significantly lower values throughout the temperature range considered here. In other words, at $X_{Hg} \cong 7 \cdot 10^{-5}$ the behaviour of mercury in these experiments can be described by Eq. (5.4) with apparent thermodynamic activity coefficients γ_{Hg} only slightly smaller than unity, i.e. close to ideal behaviour, while for $X_{Hg} \cong 10^{-13}$ apparent activity coefficients of $\gamma_{Hg} \cong 0.14$ are obtained.

In contrast to the thermodynamic activity coefficients of mercury in both pure lead and pure bismuth given in the literature (see Table 5.2.2), the LBE experiments yield activity coefficients smaller than unity. While the agreement of the results at higher concentrations with the data for the pure solvent metals still seems acceptable given the error margins stated for the γ measurements, the activity coefficient of Hg calculated for LBE samples containing non-carrier-added mercury is clearly smaller than unity. It is not clear if this apparent negative deviation from ideal behaviour observed in the LBE experiments is caused by peculiarities of the chemical interaction in the ternary system or if it is caused by the extremely low concentrations. A diffusion limitation of the evaporation process may lead to unsaturated conditions in the experiments and thus the vapour pressure values derived from experiments under the assumption of mercury saturation in the gas phase would be systematically underestimated. However, deviations from saturated conditions are generally expected to be temperature dependent, a behaviour that is not observed in the results of Neuhausen (2011a). Finally, the behaviour of mercury in LBE remains to be clarified in additional experiments under systematic variation of temperatures, concentrations and gas flow, explicitly assuring mercury saturation in the gas phase.

Summarising, the values of mercury activity coefficients in pure lead and pure bismuth given in the literature are consistent and very similar. They are valid for a temperature that coincides well with the operation temperatures expected for a lead-alloy-based spallation target, where significant production of mercury will occur. Furthermore, they are in reasonable agreement with the (slightly smaller) values derived from those LBE experiments performed using mercury concentrations comparable to those expected for spallation loops. For conservative estimations we therefore recommend to use values close to the reported literature data. For simplicity and to add even more conservativism, we recommend using a still somewhat larger value of 2 for the thermodynamic activity coefficient of mercury in LBE for estimation of its vapour pressure in diluted lead or LBE solutions:

$$\gamma_{Hg(LBE)} = 2 \tag{5.33}$$

and thus from Eqs. (5.3), (5.4), (5.30) and (5.33):

$$K_{H(Hg,LBE)} = 10^{-\frac{3332.7}{T} + 12.9716 - 0.848 \log T} \tag{5.34}$$

Given the high volatility of mercury and its large production rate in lead-alloy-based spallation systems, additional experiments concerning the evaporation behaviour of mercury from LBE under various conditions are highly recommended to clarify the peculiar behaviour observed in the few experiments performed so far.

Addendum

After finalising the present chapter, new experimental results became available on mercury volatilisation from LBE (Aerts, 2014). In this study, the equilibrium evaporation of mercury from dilute solutions in liquid lead-bismuth eutectic (LBE) was studied in argon atmosphere. Mercury present as impurity in LBE was evaporated and detected by atomic fluorescence spectroscopy, and a method which accurately simulates the experimental data was developed. In this way, coefficients of the temperature function of the Henry constant for mercury dissolved in LBE were determined. Experiments with samples from several different batches of LBE revealed that mercury at mole fractions between 10^{-6} and 10^{-12} and temperatures between 150 and 350°C evaporated from liquid LBE close to ideal behaviour, confirming the assessment presented above. Evaporation of mercury from *solid* LBE on the other hand was found to be unexpectedly high.

5.2.1.1.7 Cadmium

5.2.1.1.7.1 Metallic cadmium

Like its higher homologue in the periodic table, Cd is a rather low melting and volatile metal. However, compared to mercury, its boiling point under ambient pressure is considerably higher (767°C). Consequently, its vapour pressure is much lower than that of mercury. According to Landolt-Börnstein (1960), the temperature dependence of the vapour pressure of pure Cd can be expressed as (with the correction of a sign error in the log*T*-term):

$$P^{\circ}_{Cd} = 10^{-\frac{5711}{T} + 13.78 - 1.0867 \log T} \tag{5.35}$$

5.2.1.1.7.2 Cadmium in lead, bismuth and LBE

The Pb-Cd and Bi-Cd systems both show eutectic behaviour (Figures 5.2.13 and 5.2.14 [Landolt-Börnstein, 1991]). Cadmium is completely miscible with the solvent metals Pb and Bi at temperatures higher than 600 K. No intermetallic compounds are known. In conclusion, no strong attractive interactions between Cd and the solvent metals and, hence, no retention effects are expected for Cd in liquid Pb, Bi and LBE.

Figure 5.2.13: Phase diagram of the Pb-Cd system

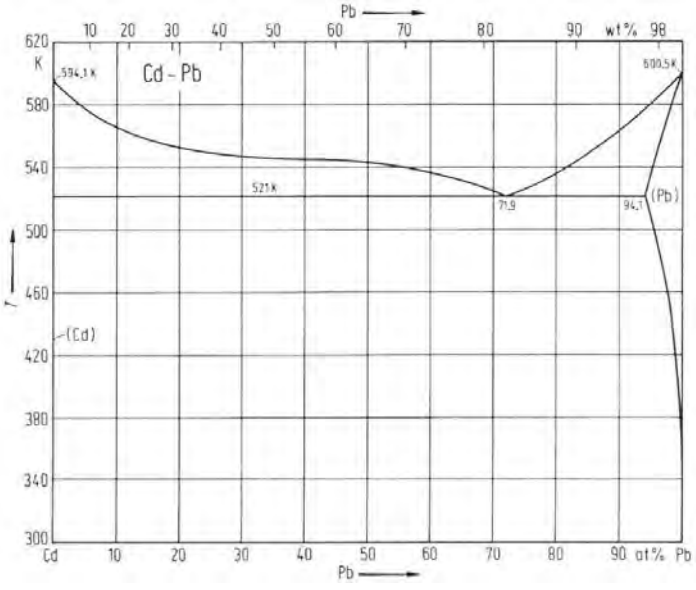

Source: Reproduced with permission of Springer Science+Business Media from Landolt-Börnstein (1991).

Figure 5.2.14: Phase diagram of the Bi-Cd system

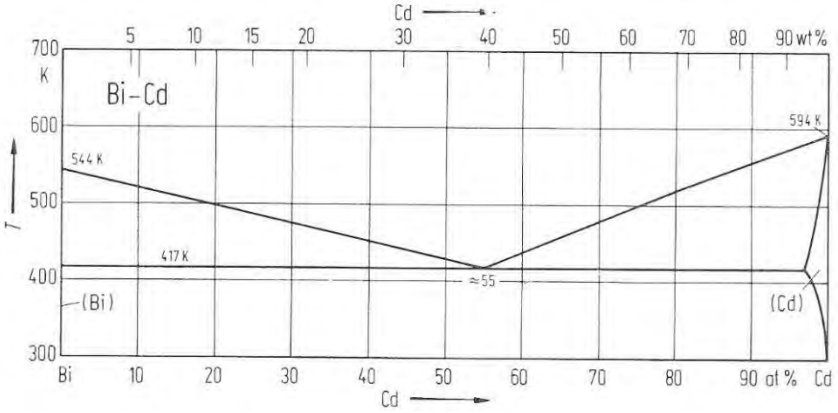

Source: Reproduced with permission of Springer Science+Business Media from Landolt-Börnstein (1991).

Thermodynamic properties of these systems determined by various methods are reviewed in Landolt-Börnstein (1991) and Hultgren (1973). The results show that the interaction between cadmium and lead indeed shows positive deviation from ideality, i.e. $\gamma_{Cd} > 1$ for the complete composition range, while for the cadmium bismuth system the deviation from ideality is much weaker, and γ changes its sign from positive on the Cd-rich side to negative on the Bi-rich side (Figures 5.2.15 and 5.2.16). From the results of the thermodynamic investigations, the following data on thermodynamic activity coefficients have been extrapolated to $X_{Cd} = 0$ and 773 K (Hultgren, 1973):

$$\gamma_{Cd(Pb)} = 3.376 \text{ and } \gamma_{Cd(Bi)} = 1 \tag{5.36}$$

Figure 5.2.15: Thermodynamic activities in the Pb-Cd system

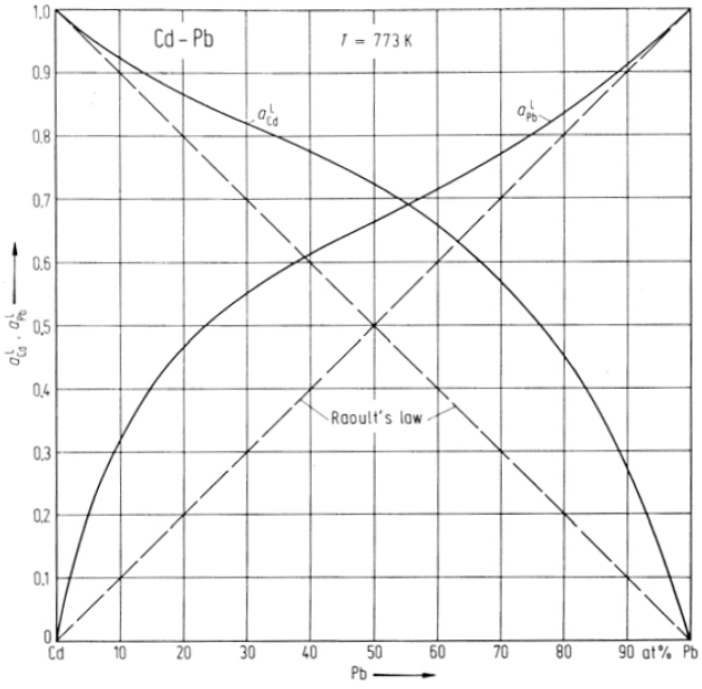

Source: Reproduced with permission of Springer Science+Business Media from Landolt-Börnstein (1991).

Figure 5.2.16: Thermodynamic activities in the Bi-Cd system

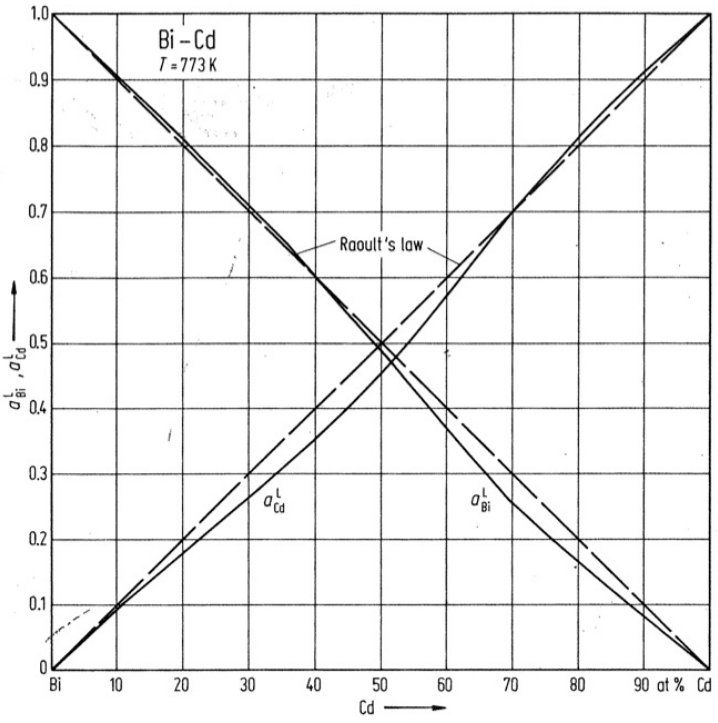

Source: Reproduced with permission of Springer Science+Business Media from Landolt-Börnstein (1991).

This indicates that the Cd-Pb interaction is significantly weaker than the Cd-Cd interaction, leading to an increase of vapour pressure compared to that expected for an ideal solution. The behaviour of Cd in Bi is almost ideal at high dilution. The ternary system Cd-Pb-Bi has not been investigated; however it is reasonable to assume that the activity coefficient of Cd in LBE will not exceed the maximum value observed for the two pure solvent metals. It is also not expected that the lower operation temperatures of a spallation loop will lead to a significantly increased activity coefficient. Nevertheless, because of the uncertainties concerning the behaviour in the ternary system and the temperature dependence, we recommend to use a slightly increased value for the activity coefficient of Cd in LBE for the calculations of maximum gas phase concentrations. Furthermore, it is desirable to verify the statements made above with experimental studies of the ternary Cd-Pb-Bi system:

$$\gamma_{Cd(LBE)} = 4 \tag{5.37}$$

resulting in:

$$K_{H(Cd,LBE)} = 10^{-\frac{5711}{T} + 14.38 - 1.0867 \log T} \tag{5.38}$$

5.2.1.1.8 Thallium

5.2.1.1.8.1 Metallic thallium

Tl is a low melting (304°C) and slightly volatile metal. However, compared to mercury and cadmium, its boiling point under ambient pressure is considerably higher (1 473°C). Accordingly, its vapour pressure is much lower than that of mercury and even Cd at the same temperature. Nevertheless, we will include it into our considerations since it is

formed in large amounts in a lead or lead-alloy-based spallation target by spallation reactions. For the temperature dependence of the vapour pressure of pure Tl the following relation is found in Landolt-Börnstein (1960):

$$P^{o}_{Tl} = 10^{-\frac{9463}{T} + 13.364 - 0.892 \log T} \tag{5.39}$$

5.2.1.1.8.2 Thallium in lead, bismuth and LBE

For both systems, Pb-Tl and Bi-Tl, it can be concluded from the phase diagrams that Tl will show a solubility in the liquid solvent metals that is considerably higher than the concentrations of Tl that will be produced by nuclear reactions (Figures 5.2.17 and 5.2.18) (Landolt-Börnstein, 1991). In the Pb-Tl system, on the Pb-rich side the liquid phase is in equilibrium with a more Tl-rich solid solution of Tl in Pb. Some Tl-rich intermetallic phases have been reported. However, the situation on the Tl-rich side is unclear and not important for the topic studied here. We conclude that no strong chemical interaction between Pb and Tl is to be expected that could cause a chemical retention. The Bi-Tl system shows quite complicated behaviour, with multiple eutectic points and indications for intermetallic phase formation at intermediate to high Tl content and low temperatures. The Bi-rich side of the system has the characteristics of a eutectic with Bi and the δ-phase forming the constituents of the solidified eutectic. The presence of this eutectic with the occurrence of the δ-phase indicates a certain affinity between Bi and Tl. Therefore, $\gamma_{Tl(Bi)}$ can be expected to be < 1 and a certain degree of retention of Tl release from bismuth is expected.

Figure 5.2.17: Phase diagram of the Pb-Tl system

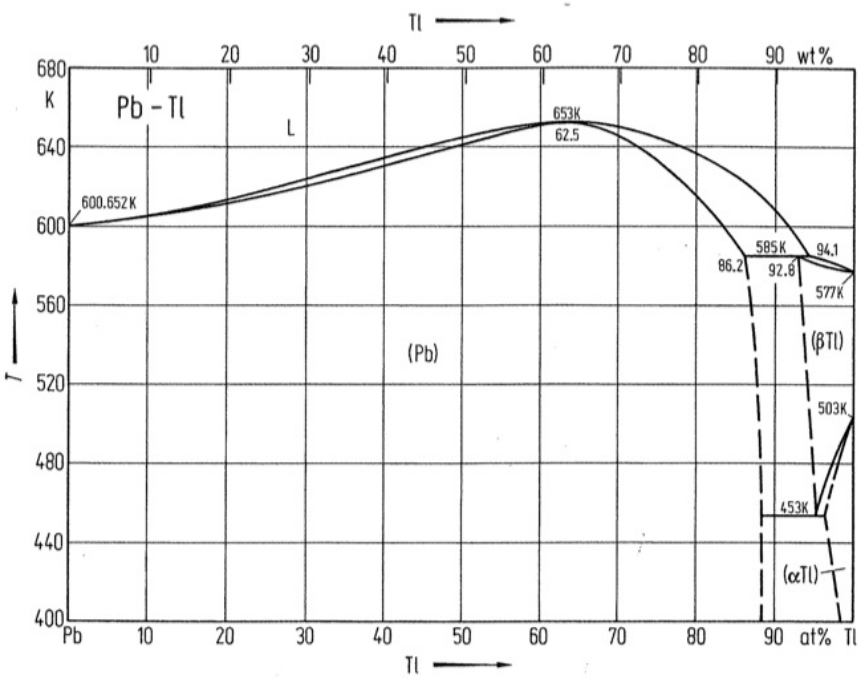

Source: Reproduced with permission of Springer Science+Business Media from Landolt-Börnstein (1991).

Figure 5.2.18: Phase diagram of the Bi-Tl system

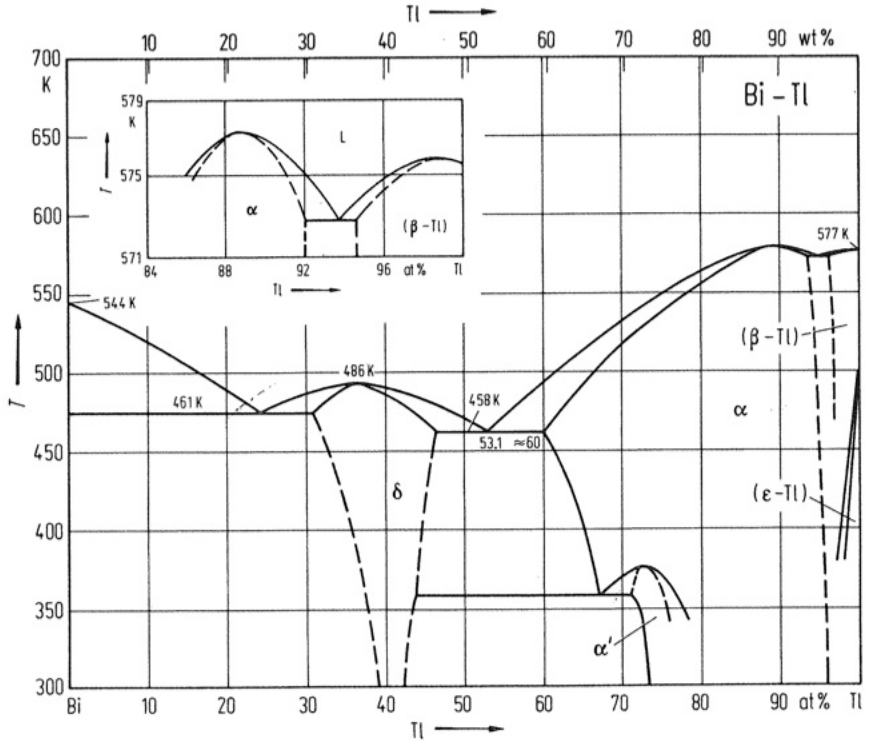

Source: Reproduced with permission of Springer Science+Business Media from Landolt-Börnstein (1991).

Thermodynamic properties of these systems determined by various methods are reviewed in Landolt-Börnstein (1991) and Hultgren (1973). Indeed, the results show that as expected from the above considerations, the interaction between thallium and lead is relatively small compared to that with bismuth. For both solvent metals activity coefficients < 1 are obtained for the Tl-poor side of the system (Figures 5.2.19 and 5.2.20). Thermodynamic investigations have led to the extrapolation of the following data on thermodynamic activity coefficients for $X_{Cd} = 0$ and temperatures of 773 and 750 K, respectively (Hultgren, 1973):

$$\gamma_{Tl(Pb)} = 0.796 \tag{5.40}$$

and:

$$\gamma_{Tl(Bi)} = 0.238 \tag{5.41}$$

Thermodynamic data for the ternary system Tl-Pb-Bi are not available. We expect retention of the release of Tl from LBE, primarily due to its interaction with bismuth. However, since it is not possible to accurately predict its behaviour in LBE and because of uncertainties with respect to the temperature dependence of its activity coefficient, we recommend using the larger of the two values for the Tl activity coefficient determined for the binary mixtures, i.e. the one for Tl in Pb for conservative estimations of its vapour pressure over LBE, hence:

$$\gamma_{Tl(Pb)} = 0.8 \tag{5.42}$$

and thus:

$$K_{H(Tl,LBE)} = 10^{-\frac{9463}{T} + 13.264 - 0.892 \log T} \tag{5.43}$$

Figure 5.2.19: Thermodynamic activities in the Pb-Tl system

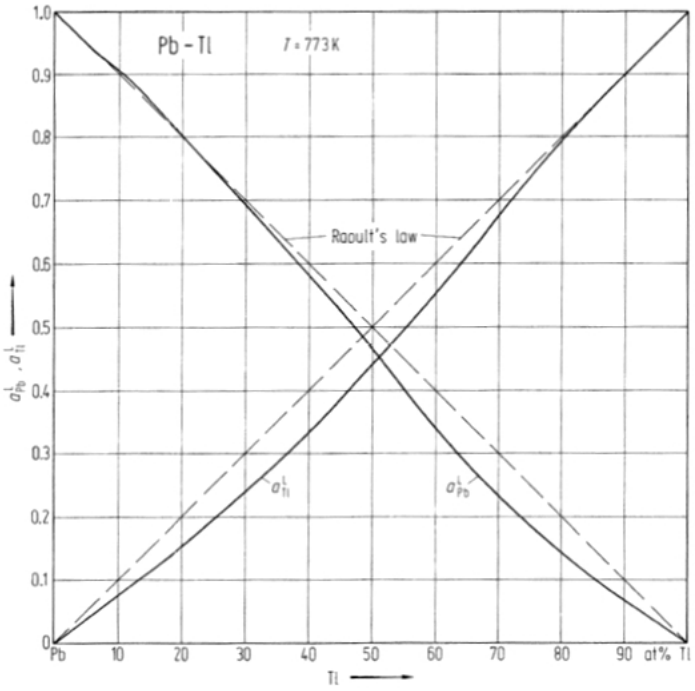

Source: Reproduced with permission of Springer Science+Business Media from Landolt-Börnstein (1991).

Figure 5.2.20: Thermodynamic activities in the Bi-Tl system

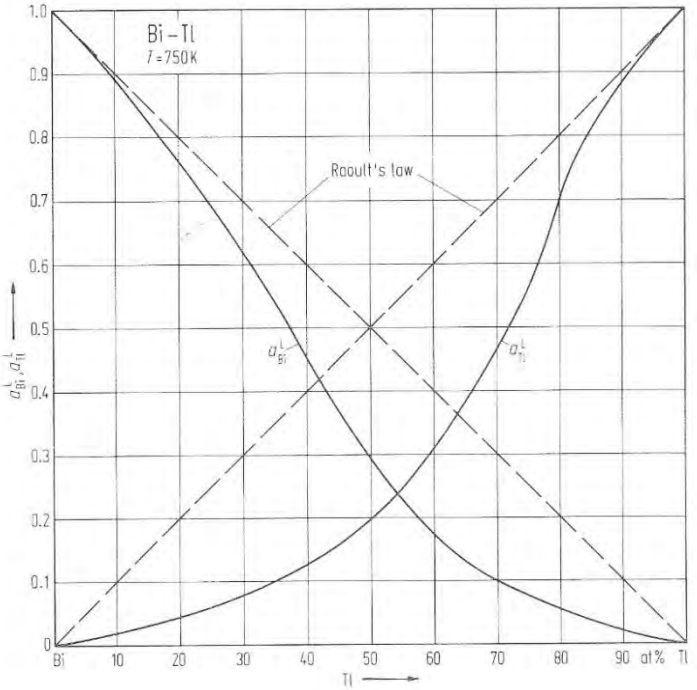

Source: Reproduced with permission of Springer Science+Business Media from Landolt-Börnstein (1991).

In laboratory scale experiments performed on the release of Hg and Tl from LBE (Neuhausen, 2005) discussed previously in Section 5.2.1.1.6.2, no measurable Tl release was observed for temperatures up to 1 000°C (see Figure 5.2.21), indicating that Tl is not released in substantial amounts from LBE samples even at very high temperatures in a flowing gas atmosphere. This is a combined effect of high dilution, low volatility of Tl itself and possibly also retention in the liquid metal by chemical interactions. It should be mentioned that the experimental error of the experiments (Neuhausen, 2005) are in the order of 10-20%. Thus, a fraction of Tl in this order of magnitude still could have been released to the gas phase. However, given the fact that even at 1 000°C the majority of the thallium dissolved remains in LBE, the experiments definitely confirm that the release of Tl from LBE under reducing conditions will be marginal in a closed spallation loop at typical operating temperatures of at maximum 500°C, and that even in an open system the release will not be high unless volatile thallium compounds are formed. Thallium oxides and hydroxides are fairly volatile, but their formation in a reducing atmosphere of a closed loop is unlikely. For an accident case however, a contribution of these compounds to Tl evaporation may play a role. Therefore, further experimental studies on the formation of volatile Tl compounds are recommended.

Figure 5.2.21: Comparison of the fractional release of Hg and Tl from liquid LBE under Ar/7%-H_2 atmosphere

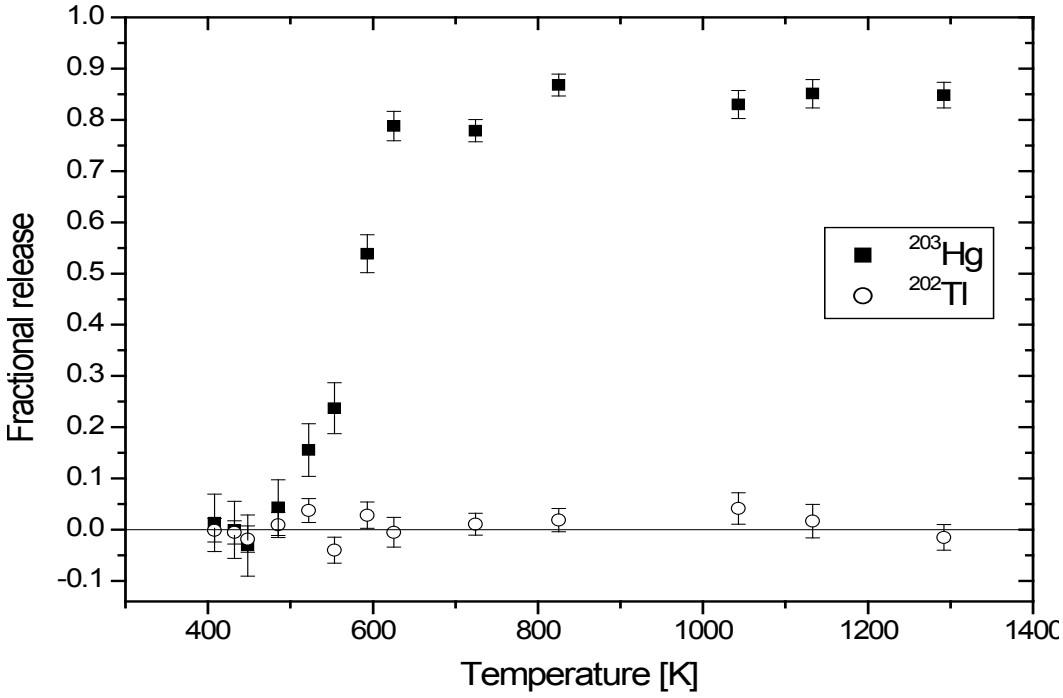

Source: Reproduced with permission of De Gruyter from Neuhausen (2005a).

5.2.1.1.9 Iodine

As shown in Figure 5.2.23 and Section 5.2.1.1.9.5, iodine is almost exclusively present as a compound with lead and bismuth in the liquid metal and in the gas phase. The properties of these compounds are well investigated, and there is no need to derive them from the corresponding properties of elemental iodine. It is therefore unnecessary to review the properties of pure iodine here.

5.2.1.1.9.1 Iodine in pure lead

PbI, PbI_2, PbI_3, PbI_4 (McBride, 2002) and Pb_2I_4 (Barin, 1993) have been observed in the gas phase. In solid form, lead iodide crystallises only as PbI_2, having $T_m = 408 \pm 2°C$ (Stull, 1975; Konings, 1995; Knacke, 1991) and a calculated $T_b = 1\,393°C$ (Knacke, 1991).

One thermodynamical analysis of the Pb-I system Rybak (2002) attempts to predict the degree of dissociation of gaseous PbI_2. We note that the authors base some of their calculations on unrealistic assumptions, in one case postulating a PbI_2 partial pressure of 10^5 Pa at a temperature of 400 K, thus ignoring both the fact that the PbI_2 is a solid at that temperature and that the vapour pressure over a condensed phase and the temperature cannot simultaneously be fixed at arbitrary values. Yet some of the conclusions regarding the composition in the temperature range where the materials are indeed wholly or partially gaseous can be of interest. Essentially, the calculations indicate that above 800 K, the vapour will consist primarily of monatomic iodine and lead, while molecular PbI_2 dominates at lower temperatures (Figure 5.2.22). Mass spectrometric analysis of the vapour over pure PbI_2 was said to have detected mainly molecular PbI_2 up to 600°C (Rybak, 2002), although none of the actual experimental data was included in the report.

In the presence of excess lead, free iodine levels will of course also be considerably depressed at high temperatures; see Section 5.2.1.1.9.5 for a detailed discussion on this topic.

Figure 5.2.22: Thermodynamical prediction of the composition of the gas phase over PbI_2 at a postulated, fixed total pressure of 100 Pa

* = PbI_2, × = PbI, ▲ = Pb, ■ = I_2, ♦ = I

The low-temperature region of the graph is unrealistic as it ignores the condensation of gaseous PbI_2

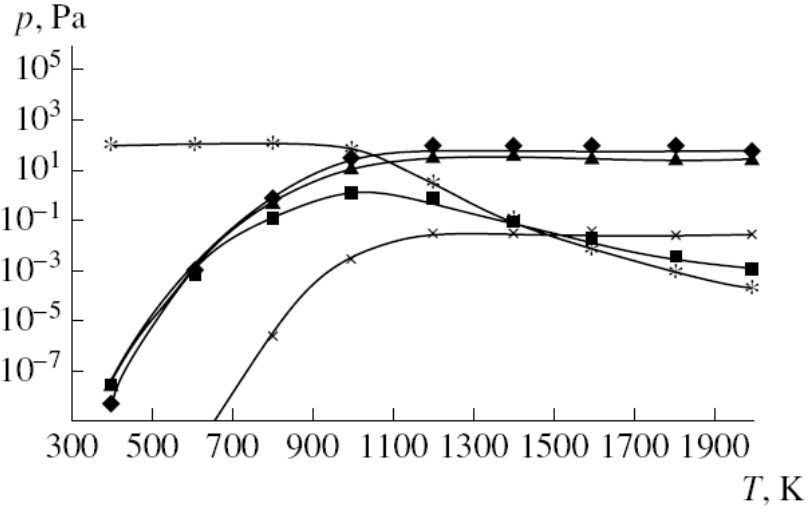

Source: Reproduced with permission of Springer Science+Business Media from Rybak (2002).

The Pb-I phase diagram (Figure 5.2.23) shows a narrow region of solubility of PbI_2 in liquid lead up to 660 K, where solubility rapidly increases. While slight, this is quite sufficient to dissolve the small fraction (relative to liquid metal) of PbI_2 formed from nuclear reaction products. As was argued in the case of polonium (Section 5.2.1.1.5.2), the strong retention of I_2 ($\gamma << 1$) can also be attributed to the formation of stable complexes with lead. The solution, regarded as PbI_2 in lead, should thus exhibit a thermodynamical activity coefficient closer to unity, although it is obvious from the phase diagram

(Figure 5.2.23, right) that more concentrated solutions are non-ideal below 400°C, with a positive deviation from Raoult's Law (as seen from the fact that PbI_2 segregates). Nevertheless, experimental data (Figure 5.2.27) indicate that below the ideal-dilute limit, $\gamma_{PbI2(LBE)}$ is in fact near unity.

Figure 5.2.23: Phase diagrams of the Pb-I system (left) and the Bi-I system (right)

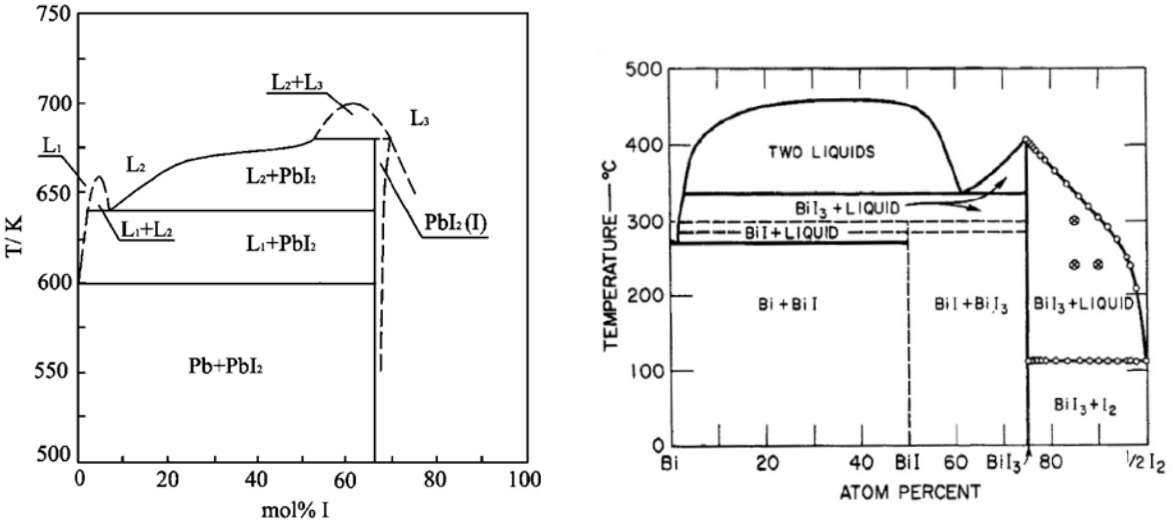

Source: Revised version (Zhu, 2006) of the phase diagram on the left published in Konings (1995), reproduced with permission of Wiley-VCH. Phase diagram on the right reprinted with permission from Rosztoczy (1965), © 1965 American Chemical Society.

According to experimental investigation (Konings, 1996), the vapour pressure of pure solid PbI_2 (Figure 5.2.24) between 580 K and 621 K follows the equation:

$$P^{o}_{PbI_2(s)} = 10^{-\frac{8691 \pm 84}{T} + 13.814 \pm 0.140} \tag{5.44}$$

When extrapolated to higher temperatures, this expression agrees fairly well with an older estimate (Knacke, 1991), which in turn is based on yet older data. We thus regard it as valid up to the melting point. A comparison with yet other determinations is found in Figure 5.2.24.

The vapour pressure of pure liquid PbI_2 is (Knacke, 1991):

$$P^{o}_{PbI_2(l)} = 10^{-\frac{9087}{T} - 6.16 \log T + 31.897} \tag{5.45}$$

An older expression (Kelley, 1935) gives virtually the same values as Eq. (5.45) in the range of 400 to 1 200 K.

In accordance with the above, we can use Eq. (5.44) below 697 K (424°C) and Eq. (5.45) above 697 K as Henry constants for calculating the total iodine levels, expressed as gaseous PbI_2, over contaminated liquid lead. (The two equations used come from different sources, and while the difference in pressure is minute near the experimentally determined melting point of ≈ 681 K, they intersect each other somewhat above that temperature; hence the breakpoint at 697 K).

Figure 5.2.24: Vapour pressure of pure PbI_2 below its melting point

Data sets include Niwa (Δ), Duncan and Thomas (▽), Hilpert (□) and original data from Konings (1996) (O); for detailed references, see Konings (1996)

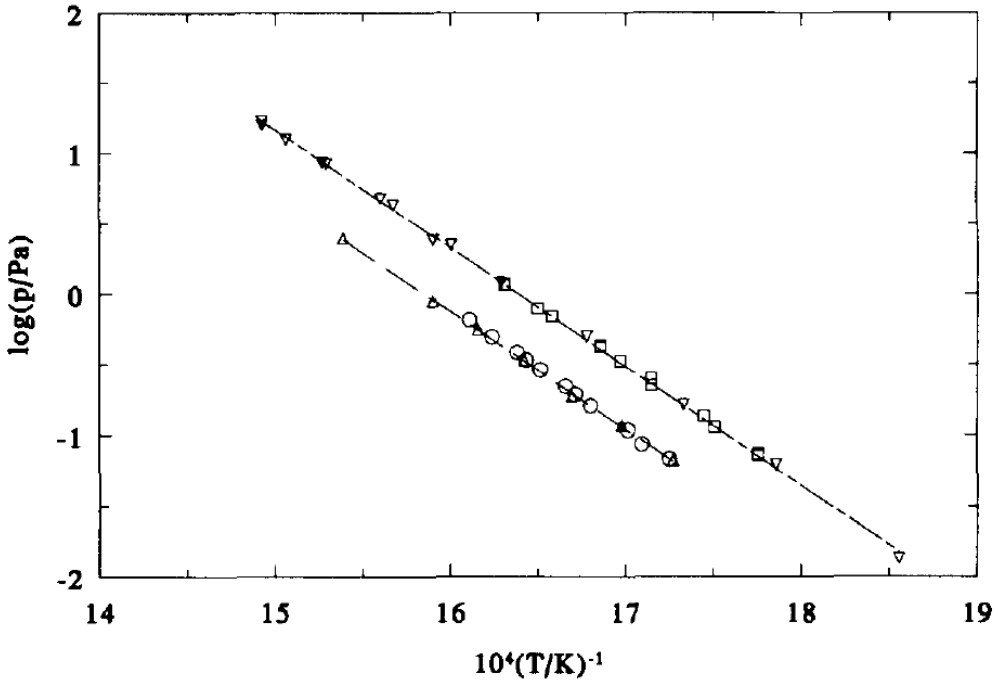

Source: Reproduced from Konings (1996) with permission of Elsevier.

5.2.1.1.9.2 Iodine in pure bismuth

There are at least two easily recognised forms of bismuth iodide. BiI has been reported to undergo peritectic melting (that is, decomposition into a liquid and a solid, here liquid bismuth and solid BiI_3) at 330°C (Dikarev, 1987). Other investigations indicate that BiI typically decomposes to BiI_3 and metallic bismuth or lower sub-iodides already at 312°C (Kurzhupova, 1978; von Schnering, 1978) and that while very pure samples of BiI can be heated up to approximately 327°C (600 K) without visible decomposition, the mono-iodide is to be regarded as metastable at that temperature (von Schnering, 1978).

BiI_3 melts at 408±2°C (Cubicciotti, 1959; Yosim, 1962; Rosztoczy, 1965; Predel, 1971; Knacke, 1991) and has a calculated T_b = 539°C (ibid.). Dissociation into BiI and I_2 becomes significant at temperatures above 630°C (ibid.).

Two sub-iodides corresponding to the empirical formula $Bi_{3.3}I$ and $Bi_{4.4}I$ were reported to have melting points in the neighbourhood of 300°C (Kurzhupova, 1978; Dikarev, 1987); these were later found to have the exact compositions $Bi_{14}I_4$ and $Bi_{18}I_4$. An updated, albeit brief, review of the bismuth-iodine system, with additional references, can be found in Lindsjö (2005).

As can be seen from the phase diagram (Figure 5.2.23), not only the solid but also the liquid phase of BiI_3 exhibits a fairly limited tendency to dissolve in or mix with metallic bismuth. For this reason, we suspect that there is little lowering of the thermodynamic activity of the triiodide in this system.

Above 458°C there is full miscibility over the whole concentration range (Yosim, 1962); only very low concentrations of iodine remain dissolved down to the solidification temperature of bismuth. While the iodine in bismuth solution does not seem to be

present as actual triiodide molecules, but rather as lower iodides or ionic clusters (Yosim, 1962; Ichikawa, 1985), we shall nevertheless for simplicity regard the bismuth-iodine melt as a solution of BiI_3 in bismuth, as BiI_3 is the well-defined solid phase most closely in equilibrium with the solution (emerging upon cooling or saturation).

While the solution is nearly ideal at iodine-rich composition, it shows positive deviation from Raoult's Law as the bismuth/iodine ratio exceeds 0.5 (Cubicciotti, 1959). This is illustrated by Figure 5.2.25, which indicates a rapidly increasing thermodynamic activity coefficient for BiI_3 in bismuth with decreasing concentrations of the iodide; the graph also confirms the observation (ibid.) that this effect is especially pronounced at lower temperatures. That is a predictable consequence of the low solubility of BiI_3 in liquid bismuth at low temperatures; the BiI_3 solution is then closer to the saturation limit, at which limit the activity of dissolved BiI_3 will equal that of the pure substance.

Yet the phase diagram shows (Figure 5.2.23) that at concentrations below a few per cent, BiI_3 will be completely dissolved in liquid bismuth, which allows us to at least draw the conclusion that the iodine content in the vapours over an ideal-dilute iodine solution in liquid bismuth will be much lower than that over pure BiI_3 at the same temperature.

Figure 5.2.25: Thermodynamic activity of BiI_3 (downward sloping curves) in liquid Bi

The activity coefficient $\gamma_{BiI3} = a_{BiI3}/X_{BiI3}$; as can be seen, γ_{BiI3} is dependent on both concentration and temperature, and extrapolation in order to obtain a reliable value for the extremely high dilution in contaminated LBE is difficult

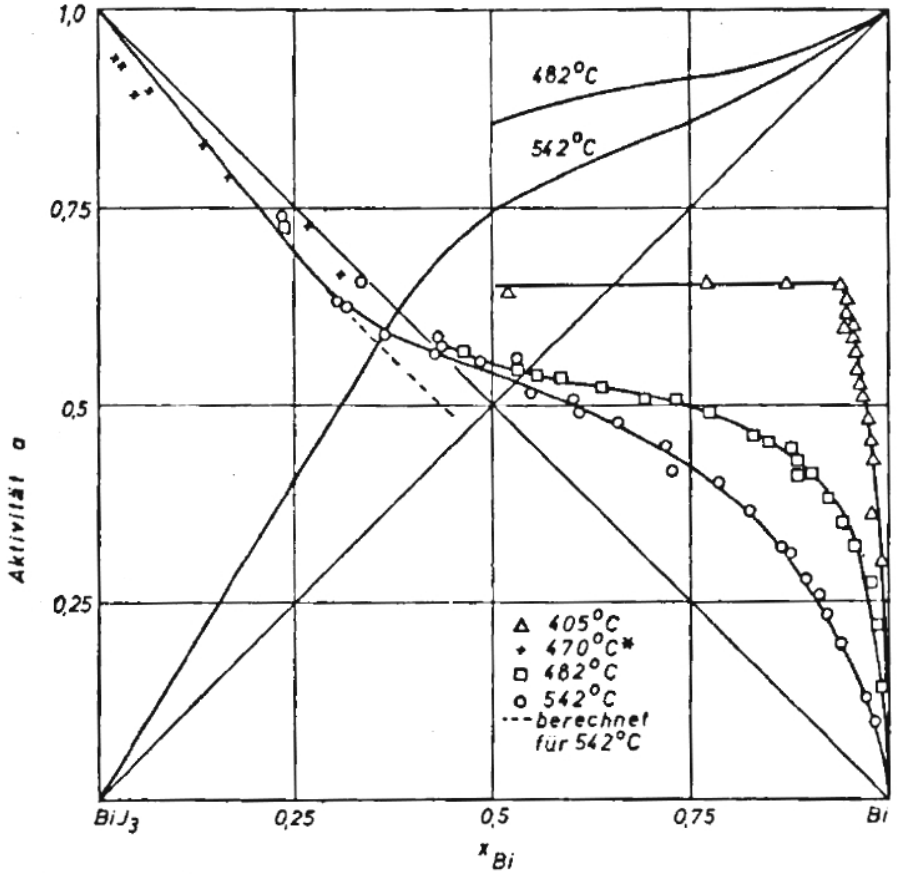

Source: Reproduced with permission of Elsevier Ltd. from Predel (1971).

The vapour over pure BiI_3 consists of gaseous BiI_3 with a small contribution of I_2 (ibid.). Even a very modest (10%) addition of metallic Bi lowers the I_2 levels below the detection limit (ibid.). We can therefore assume that the only iodine-containing species in the vapours over a dilute iodine solution in liquid bismuth will be BiI_3.

The vapour pressure of pure liquid BiI_3 is (ibid.):

$$P^{o}_{BiI_3(l)} = 10^{-\frac{4310}{T} + 10.29} \tag{5.46}$$

This gives essentially the same pressures in the liquid region of 682 to 812 K as the expression recommended in Knacke (1991).

Below the melting point of BiI_3, Eq. (5.46) will further overestimate the vapour pressure of dissolved BiI_3, which will, with increasing concentration, rather approach the limiting, and lower, value of the vapour pressure over pure *solid* BiI_3 (reached in the saturated solution). Consequently, we may use Eq. (5.46) as a conservative estimate of the iodine content in the vapours over iodine-contaminated liquid bismuth. This is in all likelihood a gross overestimation of the actual vapour pressure over a dilute solution, and in fact already gives quite high pressures at modest temperatures. However, as shall be seen in the next section, the relevant iodine compound in contaminated LBE is not BiI_3, but PbI_2.

5.2.1.1.9.3 Iodine in LBE

While some trends can be observed from experiments with macroscopic amounts of the iodides of lead and bismuth, these cannot be extrapolated to very high dilution with impunity. Also, most of the experiments have been performed at moderately high temperatures, and especially in the case of BiI_3, below the boiling point of the iodide. Fortunately, some experimental results are available from investigations at higher temperatures and extreme dilution (Eichler, 2003).

It is of considerable interest to note that while iodine is completely retained in LBE – within the limits of experimental error – up to 700 K (Figure 5.2.26), its release accelerates dramatically above 800 K and is nearly quantitative at 1 000 K (Neuhausen, 2006b). However, it should be noted that the experiment was done with a small sample (~1 g) in a gas stream and thus driven by continuous removal of the vapour. Therefore the most interesting result is that even at these conditions, iodine is very efficiently retained in the melt below 700 K.

For an estimate of the vapours released from massive amounts of LBE in a relatively stagnant atmosphere, an equilibrium calculation is more appropriate. Data from the same dynamical evaporation experiments were used (Neuhausen, 2005c, 2005d) to estimate an equilibrium vapour pressure (as monatomic iodine) expressed as a Henry constant (to be multiplied by the molar ratio of iodine, as a monatomic species, in the melt to obtain values of vapour pressure [Eq. 5.3]):

$$K_{H(I,LBE)} = 10^{-\frac{10407}{T} + 14.56} \tag{5.47}$$

At high temperatures (> 700°C), Eq. (5.47) gives nearly the same results as a Raoult's Law calculation for the corresponding amount of liquid PbI_2 in ideal solution. At lower temperatures, Eq. (5.47) gives progressively lower pressure compared to the PbI_2 curve (Figure 5.2.27). A direct comparison of Eq. (5.47) with Eq. (5.45) shows the same trend. This can be interpreted either as an indication that, quite unlike the Bi-BiI_3 system, PbI_2 shows a negative deviation from ideality in lead at lower temperatures ($\gamma_{PbI2(Pb)} < 1$) or that the use of dynamic measurements for equilibrium calculations has introduced a systematical error, a possibility which the authors acknowledge.

Figure 5.2.26: Evaporation of iodine from very dilute solution in LBE

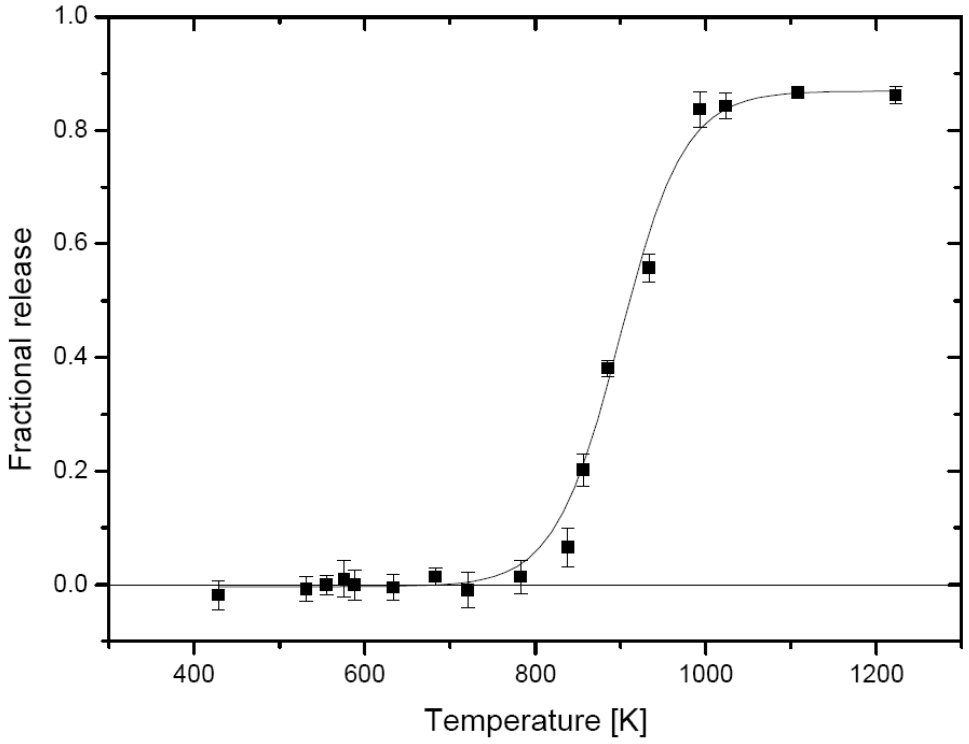

Source: Reproduced with permission of De Gruyter from Neuhausen (2006b).

5.2.1.1.9.4 Evaluation of iodine evaporation data

The retention of iodine in LBE is caused mainly by its chemical interaction with lead. The partial pressure of iodine could be estimated either with Eq. (5.47), or more conservatively, by the function for the vapour pressure of pure PbI_2 (Eqs. [5.44], [5.45]) combined with its molar fraction in the melt, thus using Eqs. (5.44) and (5.45) as Henry constants. Using the molar fraction of monoatomic iodine, being twice that of the postulated PbI_2, with the latter functions results in a value twice the partial pressure of actual PbI_2. We recommend using this quantity, Eqs. (5.44) and (5.45) multiplied by two times the molar fraction of PbI_2, as a hypothetical but practical "$Pb_{0.5}I$" partial pressure. Thus the concentration in the liquid metal and the calculated content in the gas phase will conveniently be expressed on monoatomic iodine basis.

5.2.1.1.9.5 Iodides in the gas phase

In addition to the question of the chemical properties of iodine in lead and bismuth melts, there has been some discussion regarding what the major iodine-bearing species in the gas phase is. As gaseous Pb and Bi are in thermodynamic equilibrium with the melt (meaning that the chemical potential of the gaseous and liquid fractions is equal), and also in chemical equilibrium with the gaseous metal iodides, we can choose the following reaction for our study:

$$3\ Pb(l) + 2\ BiI_3(g) \rightarrow 2\ Bi(l) + 3\ PbI_2(g) \qquad (5.48)$$

A simple thermodynamic calculation shows that the Gibbs energy of reaction (5.48) is negative for all temperatures above the melting point of LBE. Furthermore, it decreases with increasing temperature (Figure 5.2.28), which is typical for a reaction that increases the number of gaseous molecules and thus the entropy of the system.

Figure 5.2.27: Comparison of experimentally estimated pressures of iodine-containing vapours with calculations assuming different evaporating species

Crosses correspond to Eq. (5.47); note that while PbI_2 was in absence of better data on the activity coefficient assumed to be in ideal solution, a value of $\gamma_{BiI3(Bi)} = 50$ was estimated from Predel (1971)

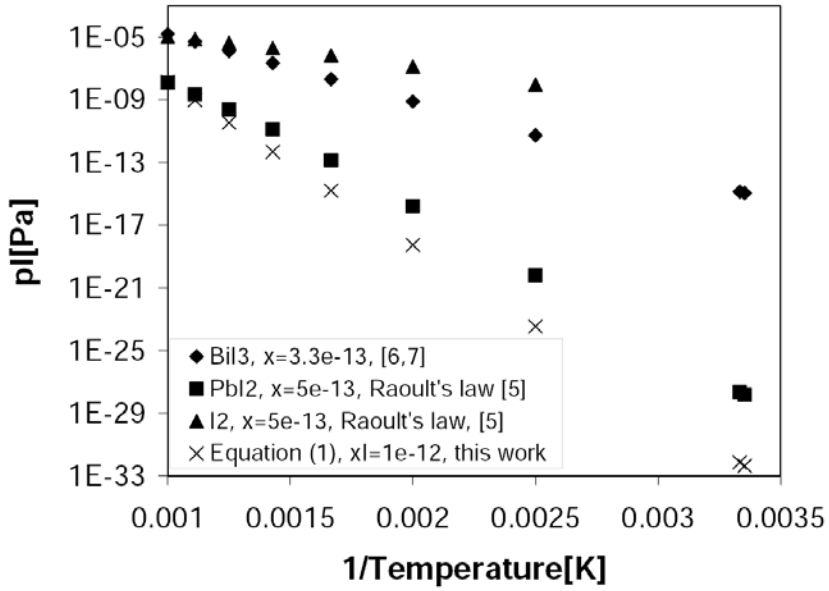

Source: Neuhausen (2005c).

Figure 5.2.28: Standard Gibbs energy for the reaction 3 Pb(l) + 2 BiI_3(g) ↔ 2 Bi(l) + 3 PbI_2(g)

As the thermodynamical activities of Bi and Pb are about equal in the nearly equimolar mixture (LBE), no particular correction has been made for their respective concentrations in the melt

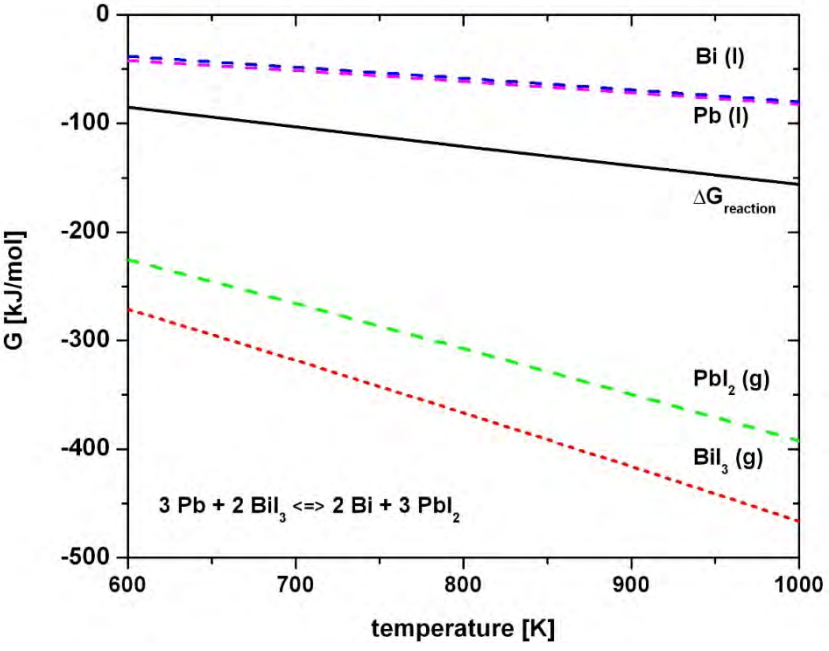

It thus appears established that the dominating iodine-bearing species over liquid lead and LBE will be lead diiodide rather than bismuth triiodide. However, the equilibrium concentration (partial pressure) of lead vapour will be defined by evaporation/condensation of the large reservoir of liquid lead (or LBE), not by the dissociation of PbI_2. Starting from the standard Gibbs energy of reaction for the formation of lead iodide in the gas phase according to:

$$Pb(g) + I_2(g) \leftrightarrow PbI_2(g) \tag{5.49}$$

and knowing that:

$$\Delta G^{\circ}_{reaction} = -RT \ln \frac{P_{PbI_2}}{P_{Pb} \cdot P_{I_2}} \tag{5.50}$$

(where the activities are approximated with partial pressures in units of atmospheres), and obtaining P_{Pb} from Eq. (5.6), we can see (Figure 5.2.29) that the ratio of lead diiodide to free iodine is very large over the relevant temperature range. In other words, the levels of free iodine will be negligible.

Figure 5.2.29: Ratio between partial pressures of PbI_2 and I_2 over liquid lead

For convenience, the ordinate is drawn in base 10 logarithmic scale

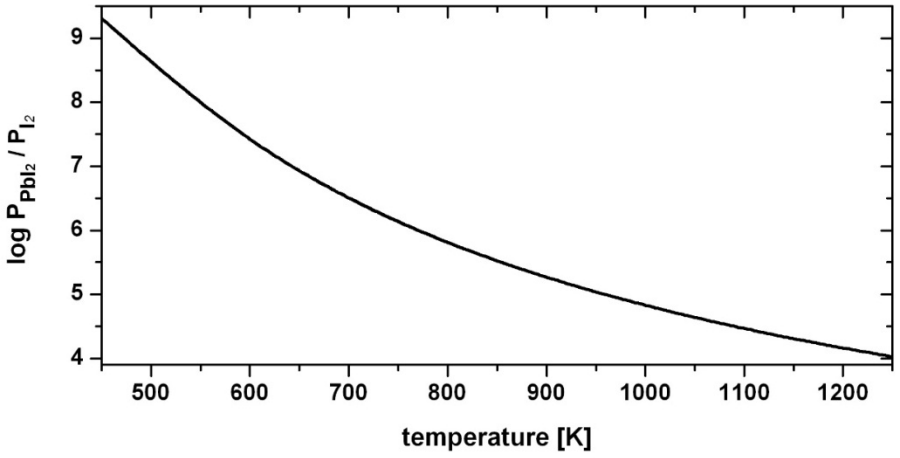

5.2.1.1.10 Bromine

5.2.1.1.10.1 Elemental bromine

With a boiling point of 59°C, elemental bromine is even more volatile than elemental iodine. However, similar as shown for iodine, bromine will almost exclusively be present as compounds with lead and bismuth in the liquid metal and in the gas phase. Therefore, properties of pure bromine will not be reviewed here.

5.2.1.1.10.2 Bromine in lead, bismuth and LBE

According to its standard Gibbs enthalpy of formation at 298 K of -261 kJ/mol, $PbBr_2$ is even more stable than PbI_2 (-174 kJ/mol) (Barin, 1993). The phase diagram of the Bi-Br system and the thermodynamic activities in the Bi-$BiBr_3$ system are depicted in Figure 5.2.30. The situation is qualitatively similar to that of the Bi-I system, however the bromine-rich phases are liquid throughout the typical operation temperatures of a spallation target or reactor system. We presume that bromine present in concentrations relevant for a spallation loop will be dissolved in the liquid metal. The strong interaction of bromine with lead indicates that in the diluted solutions the formation of aggregates of Br with the solvent atoms can be assumed that will lead to a very efficient retention of bromine.

Figure 5.2.30: Phase diagram of the Bi-Br system (left); thermodynamic activities in the Bi-$BiBr_3$ system (right)

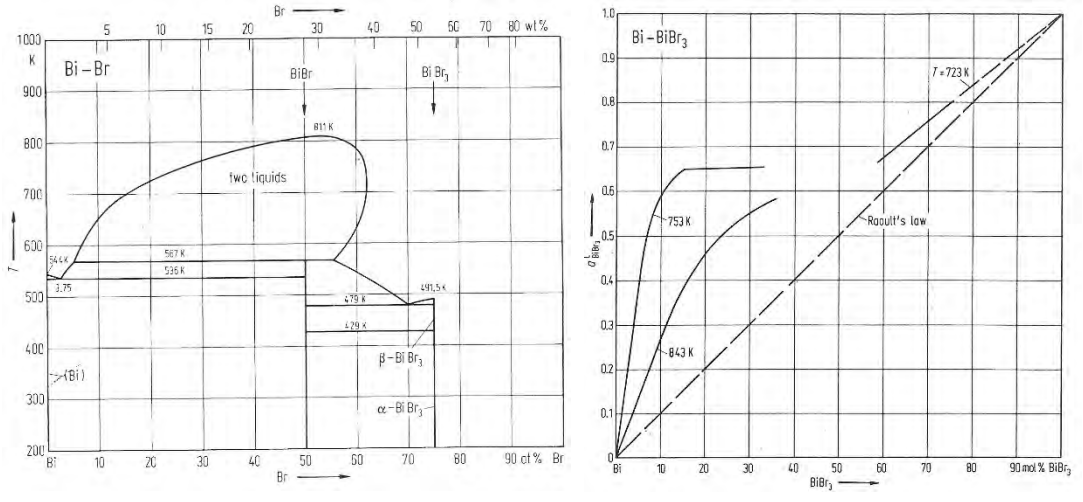

Source: Both reproduced with permission of Springer Science+Business Media from Landolt-Börnstein (1991).

Therefore, the volatility of dissolved bromine in a liquid-lead-alloy-cooled reactor system or a spallation loop is expected to be strongly decreased by chemical interaction with the LBE components. We propose that this volatility may be estimated from the vapour pressure of metal bromides assuming ideal behaviour in the same way that was used for the iodine-LBE system. However, a final judgement of these systems that will allow a reasonably reliable quantitative assessment of gas phase concentrations will require a thorough review of the corresponding literature data on the thermodynamic properties of Pb- and Bi-bromides as well as an experimental verification. Therefore, we will not give quantitative results for the bromine content of the cover gas in this report.

However, qualitative investigations of the behaviour of gaseous halogens over liquid LBE in laboratory scale experiments confirm the above assumptions on the halogen behaviour in LBE (Neuhausen, 2005c). In these studies, approximately 200 mg of iodine or bromine were applied on the surface of 250 g of liquid LBE kept at 250°C in a glass flask. After about 30 min in the case of iodine and approximately 15 min in the case of bromine, the gas phase was completely colourless, indicating that the halogens in the gas phase readily react with the LBE. The relative rates of decolourisation for bromine and iodine correspond to the relative stabilities of their lead and bismuth compounds, i.e. bromine reacted faster with the liquid metal than iodine.

5.2.1.1.11 Caesium

5.2.1.1.11.1 Metallic caesium

Metallic caesium, which melts at as low a temperature as 29°C and boils at 671°C, will obviously be quite volatile unless highly diluted in the liquid metal or retained by a chemical affinity to the same. As we shall show, both of these criteria are fulfilled.

The vapour pressure of liquid metallic caesium in the range of 370 to 660°C has been determined with great accuracy (Hill, 1996):

$$P_{Cs}^{o} = 10^{-\frac{4979.5799}{T} - 9.3234247\log T + 0.0044733132T - 8.684092\cdot10^{-7}T^{2} + 34.573234} \quad (5.51)$$

While we do not need quite such high precision in the study at hand, we shall use this expression rather than the older and simpler, but somewhat conflicting expressions found in the common handbooks.

5.2.1.1.11.2 Intermetallic compounds and Zintl phases

In the solid state, lead forms well-defined intermetallic compounds with caesium, as can be seen from the suggested phase diagram of the Cs-Pb system reproduced in Figure 5.2.31. A list of some binary intermetallic compounds is also provided in Table 5.2.3.

Figure 5.2.31: Phase diagram of the Cs-Pb system

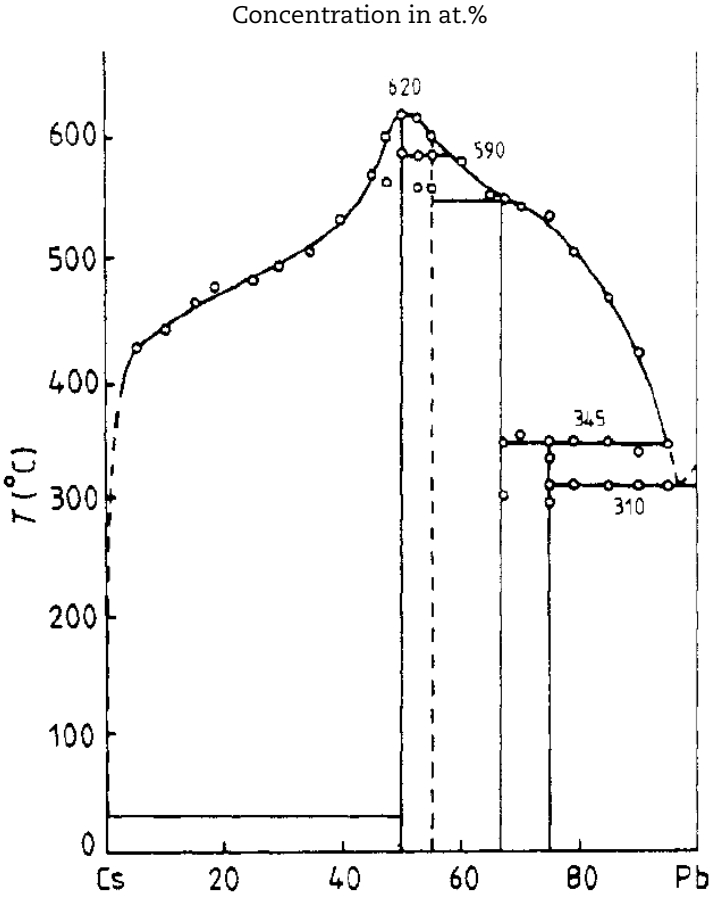

Source: Reproduced with permission of IOP Publishing from Meijer (1986).

Table 5.2.3: Some binary intermetallic compounds in the Cs-Pb and Cs-Bi systems

Empirical formula	T_m (°C)	Comment	Reference
CsPb	596	First, "plastic" phase transition	Saboungi (1988)
$CsPb_2$	345		Meijer (1986)
Cs_3Bi	660	Deviates from Gnutzmann's results	Zhuravlev (1958)
Cs_3Bi_2	501	Incongruent melting	Gnutzmann (1961)
Cs_5Bi_4	418	Incongruent melting	Gnutzmann (1961)
$CsBi_2$	595	Deviates from Zhuravlev's results	Gnutzmann (1961)

While most of these compounds have melting points in excess of 500°C, the minute quantity formed (compared to the body of lead or LBE) can safely be assumed to be in the liquid state due to dissolution in the liquid metal, as is also indicated by the liquidus line of the phase diagram. The existence of these compounds *as a chemical species* in the dilute liquid solution is a matter of definition, as the constituent atoms will associate and dissociate in a stochastic manner to form loosely ordered clusters.

The Cs-Pb compounds can be regarded as constituted of tetrahedrical Pb_4^{4-} polyanions, formed through a redox reaction where the highly electropositive caesium atoms donate the electrons and the Cs^+ cations thus formed balance the negative charge. The Pb_4^{4-} polyanions belong to the class of Zintl ions (van der Lugt, 1996), and such Cs-Pb compounds are correspondingly classified as Zintl compounds or Zintl phases (Sevov, 2002).

It should be pointed out that the above description of Zintl compounds has been condensed and very much simplified; more accurate and systematic definitions are proposed and discussed in several of the references to this section.

Interestingly, the Zintl ions themselves largely retain their integrity in the molten state (Reijers, 1990; Winter, 1996), and in the equi-atomic Cs-Pb melt, Pb_4^{4-} tetrahedra are present up to 1 900 K (Hochgesand, 1998; Kurzhöfer, 2000) (see Figure 5.2.32). They thus also associate with and exert a co-ordinating influence on the cations in the melt, causing its properties to deviate towards non-metallic. In the case of the Pb_4Cs_4 clusters, the ionic radius of the surrounding, associated Cs^+ ions is sufficient to entirely segregate the central Pb_4 clusters from each other in the equimolar mixture. The $Cs_{0.5}Pb_{0.5}$ melt thus has peculiar, semi-crystalline properties, exhibits a semi-liquid to liquid phase transition around 920 K, and behaves as a semiconductor (Price, 1991; Saboungi, 1992). While such macroscopic effects naturally would not be discernible in the very dilute Cs solution we are discussing here, the strong association between Cs and Pb also remains in very dilute solutions.

Figure 5.2.32: Visualisation of structural ordering in liquid Cs-Pb solution

Snapshot of molecular dynamics simulation

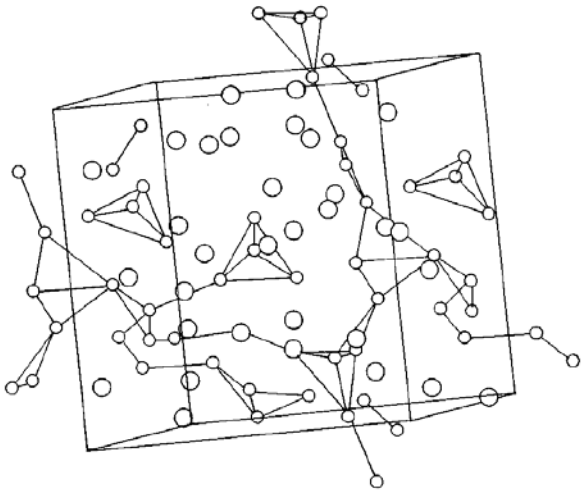

Source: Reproduced with permission of AIP Publishing from de Wijs (1995).

While the corresponding binary systems with Bi are less thoroughly investigated, a similar formation of a series of intermetallic compounds has been established (Figure 5.2.33, Table 5.2.3). Compound formation in the liquid state can also be observed in Cs-Bi (Meijer, 1986).

Figure 5.2.33: Phase diagram of the Cs-Bi system

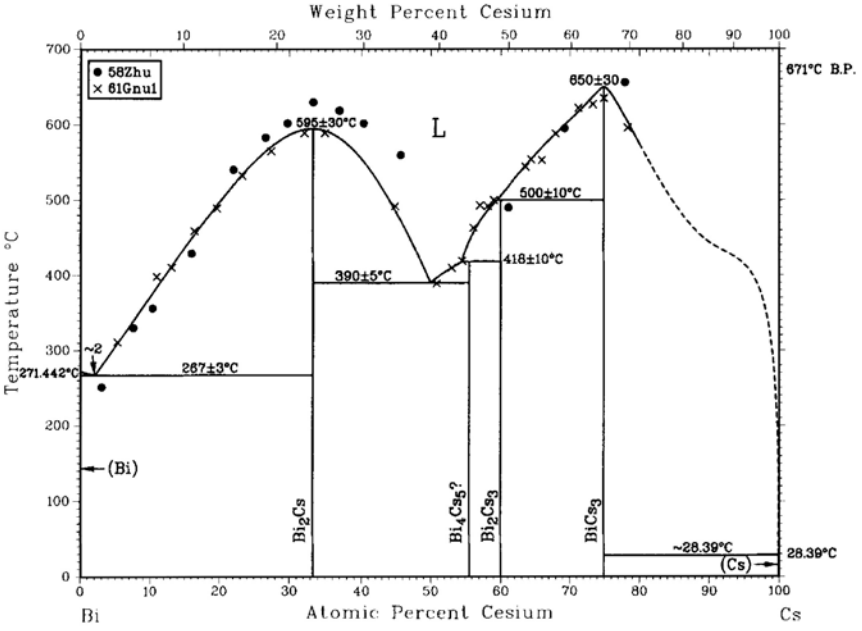

Source: Reproduced with permission of Springer Science+Business Media from Sangster, (1991).

There are more stringent as well as looser definitions of Zintl compounds, and to what extent the various binary intermetallic compounds mentioned in this text should be classified as Zintl compounds is somewhat beside the point in the current context; discussions on this topic can be found elsewhere (Schäfer, 1973; Hurng, 1989). These melts are characterised by strong hetero-atomic interaction, ionic clustering and non-random mixing, which is why the application of simple textbook methods for the calculation of physicochemical properties is ruled out. We shall therefore rely on the few experimental studies that have been done on the thermodynamical properties of these systems.

5.2.1.1.11.3 Caesium in pure lead

Some of the known, solid Cs-Pb intermetallic compounds are listed in Table 5.2.3. The activity coefficient for Cs in liquid lead has been measured by electrochemical methods (Yamshchikov, 2001) and is indicative of strong hetero-atomic interaction. As the investigators simultaneously varied the concentration (X_{Cs} = 0.0056 to 0.0982, almost certainly reaching above the ideal-dilute limit) and the temperature (953 to 1 104 K), it is difficult to separate these two effects on the value of the activity coefficient; nevertheless, the authors propose an expression for the temperature dependence:

$$\gamma_{Cs(Pb)} = 10^{-\frac{2540 \pm 960}{T} + 0.69 \pm 0.94} \tag{5.52}$$

valid for concentrations up to 10 mol% Cs, and ignore the possible (in our opinion, rather likely) effects of differences in concentration. The corresponding graph is reproduced below as Figure 5.2.34.

From the tabulated data (Yamshchikov, 2001) we find that for the lowest concentrations (below 2 mol% Cs), values of γ are 0.0095 to 0.012 at temperatures in the vicinity of 690°C, and reach 0.028 at 830°C; this indicates that partial pressures of Cs will be 105 to 36 times lower than in an ideal solution at the respective temperatures.

Figure 5.2.34. Thermodynamic activity coefficient of Cs in lead as function of temperature, disregarding any effects of differences in concentration

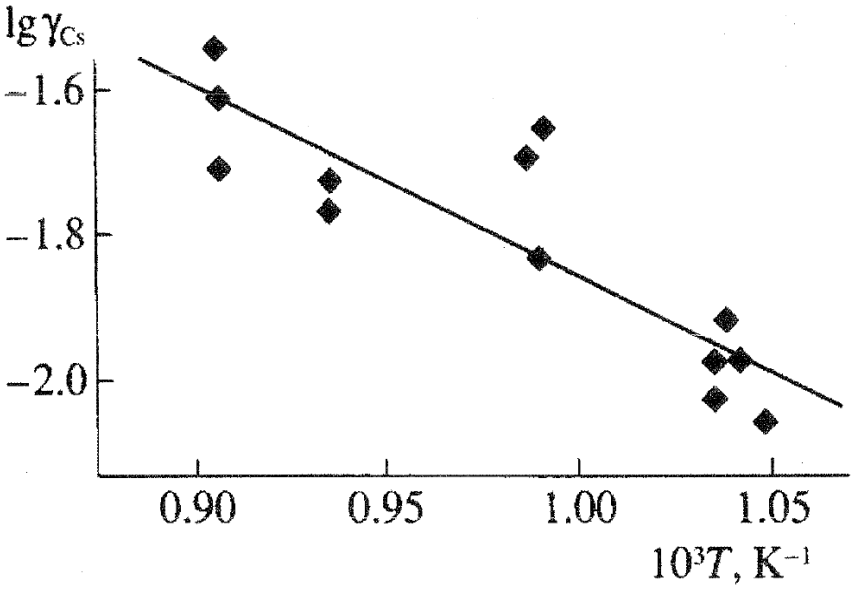

Source: Reproduced with permission of Nauka Publishers from Yamshchikov (2001).

Considering that the activity coefficient for caesium in liquid lead is not known with very high accuracy, we recommend using the fixed value:

$$\log \gamma_{Cs(Pb)} = -1.5 \tag{5.53}$$

in calculations as a conservative estimate for dilute solutions of caesium in liquid lead at temperatures up to 1 100 K. Thus (Eqs. [5.3], [5.4], [5.51] and [5.53]) the Henry constant of caesium over liquid lead in the range of 370 to 660°C *will be less than:*

$$K_{H(Cs,Pb)} = 10^{-\frac{4980}{T} - 9.323\log T + 0.004473T - 8.684\cdot 10^{-7}T^2 + 33.07} \tag{5.54}$$

5.2.1.1.11.4 Caesium in pure bismuth

Bismuth also forms a series of intermetallic compounds with caesium (Table 5.2.3), indicating an appreciable degree of affinity between the two elements. We have calculated the thermodynamic activity coefficients γ for bismuth-rich liquid caesium alloys (Figure 5.2.35) from published vapour pressure data (Gverdtsiteli, 1984), using Eq. (5.51) as reference (pure caesium). As the experiments were performed with rather high Cs content ($X_{Cs} \geq 0.19$) and in a limited temperature range (for the highest dilution, 952-1 250 K), it would be imprudent to extrapolate the results to a general expression to be applied to higher dilutions at lower temperatures. However, a comparison of the two highest dilutions ($X_{Cs} = 0.191$ and 0.257, respectively) shows no obvious dependence on concentration; at 1 000 K they respectively give $\log \gamma = -2.73$ and $\log \gamma = -2.69$, and at 800 K the corresponding values are -3.23 and -3.45. Thus we can use the fixed value:

$$\log \gamma_{Cs(Bi)} = -2.5 \tag{5.55}$$

as a conservative estimate of the actual activity coefficient of caesium in liquid bismuth at a concentration of less than 10 at.% Cs and at temperatures up to 1 000 K.

Figure 5.2.35: Activity coefficients for Cs in liquid Bi solution, calculated from vapour pressure data

It should be noted that the individual curves are extrapolated to cover the entire temperature range; the experimental vapour pressure data for each composition only spans an interval of 200-300 K between 952–1 250 K

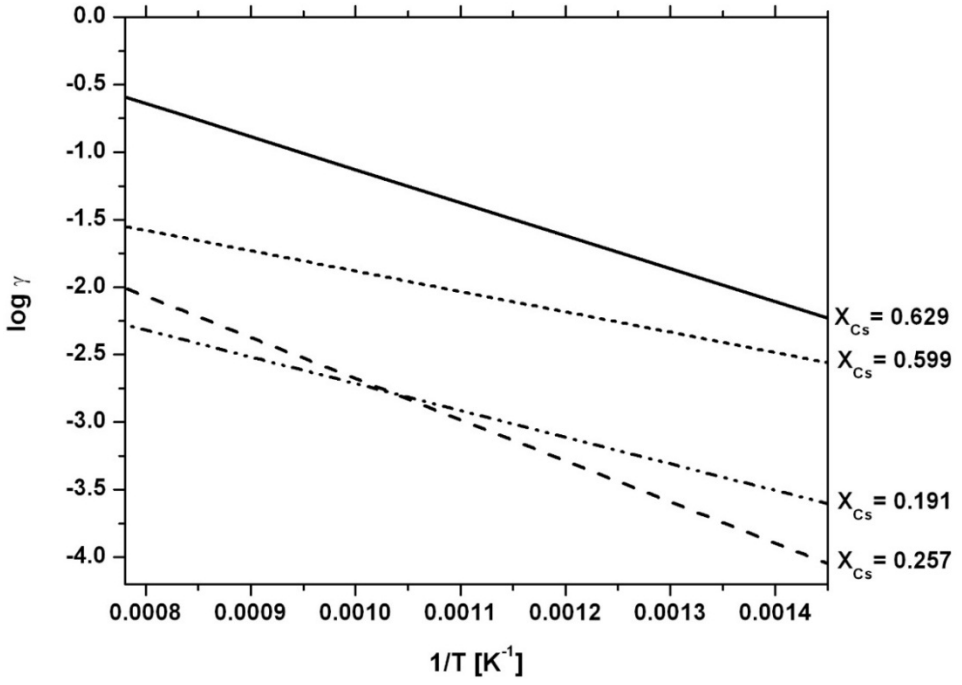

Source: Gverdtsiteli (1984).

5.2.1.1.11.5 Caesium in LBE

Considering the data for the Cs-Pb and Cs-Bi systems discussed above, it is expected that the activity, and thus the vapour pressure, of caesium should be lower in LBE than in pure lead, due to the stronger interaction with bismuth; yet it will be higher than in pure bismuth, as the thermodynamic activity of bismuth is only about 0.5 in LBE (see Section 5.2.1.1.4.3). One would expect that compounds or aggregates between Cs and Bi would dominate the intermetallic interactions. However, since we do not know the stoichiometry of these intermetallic compounds or clusters, which may be of a variable and perhaps ternary ($Cs_xBi_yPb_z$) nature, we cannot apply our knowledge of the bismuth activity to predict the magnitude of the effect on the Cs activity in LBE.

In a recent investigation (Ohno, 2007), the evaporation of caesium from LBE was studied. Seven experiments were performed at four different temperatures in the range from 450 to 750°C using samples with a caesium mole fraction of $6.4 \cdot 10^{-3}$. The results of the individual experiments show a considerable scatter. We have extracted the results given in form of a graph of gas-liquid partition coefficients vs. temperature in Ohno (2007) and converted them to thermodynamic activity coefficients for caesium in LBE using an approximate relation given in Ohno (2006). When fit against the inverse absolute temperature, Eq. (5.56) is obtained. The resulting activity coefficients range from 0.001 at 450°C to 0.013 at 750°C, indicating that – as expected – caesium is retained in LBE:

$$\gamma_{Cs(LBE)} = 10^{-\frac{2677 \pm 863}{T} + 0.75 \pm 0.98} \tag{5.56}$$

A comparison of the different data on activity coefficients for Cs in lead (Yamshchikov, 2001), bismuth (Gverdtsiteli, 1984) and LBE (Ohno, 2007) is shown in Figure 5.2.36. The temperature function derived from Ohno's data for caesium in LBE (Eq. [5.56]) agrees well with the equation suggested by Yamshchikov (2001) for caesium in lead (Eq. [5.52]) and gives considerably higher values compared to those observed by Gverdtsiteli (1984) for Cs in liquid bismuth. Given the large scatter of the data for caesium in LBE, we still recommend using the conservative constant value of the thermodynamic activity coefficient for caesium in liquid lead stated in Eq. (5.53) and also use Eq. (5.54) for estimations of the vapour pressure of caesium over diluted solutions in LBE until more reliable data become available.

Figure 5.2.36: Comparison of data on activity coefficients for Cs in liquid Pb, Bi and LBE solution

Squares: Cs in LBE, calculated from experimentally determined vapour-liquid partition coefficient data from Ohno (2007)
Solid line: Cs in LBE, least squares fit obtained from the Ohno (2007) data (Eq. [5.56])
Dashed line: Cs in Pb, Eq. (5.52) given by Yamshchikov (2001)
Open circles: Cs in Bi, derived from vapour pressure data for the lowest Cs concentrations used in Gverdtsiteli (1984)

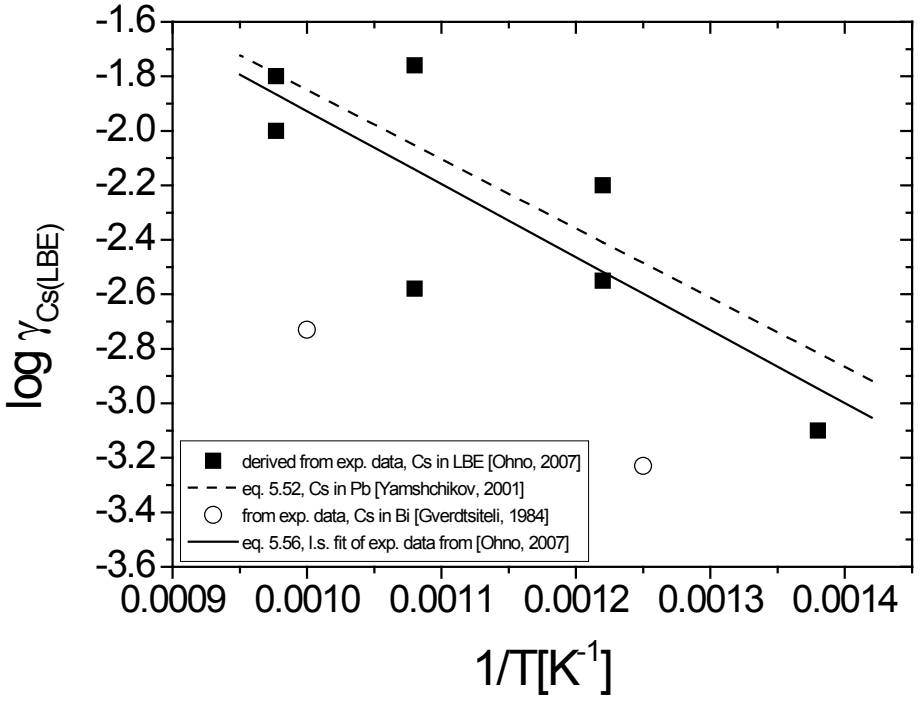

5.2.1.1.11.6 Gas phase reactions

In the preceding sections, we have discussed the partial pressure of Cs in the gas phase above the liquid metal as elemental vapours. This is not a completely accurate model of the system, since the compounds formed in the melt may evaporate in molecular form and further reactions can take place between the gaseous components, and thus this approach could underestimate the overall concentration of a given element (which will be the equilibrium concentration of elemental vapour plus the sum over the gaseous compounds of the element). The resulting equilibrium cannot easily be calculated in detail due to the very large number of possible compounds (see Figure 5.2.37) and the lack of thermodynamic data, especially for the heavier Cs_nPb_m clusters. On the other hand, some

of the experimental data has been produced with the explicit (Gverdtsiteli, 1984) or implicit assumption that all the gaseous caesium is monoatomic; thus we can expect it to be valid even if compound formation occurs in the gaseous state. Furthermore, the intermetallic compounds typically have fairly high melting points in the pure state (Table 5.2.3), suggesting that their vapour pressure, and thus their fraction in the gas phase, will be low.

Figure 5.2.37: Mass spectrogram of Cs-Pb clusters produced by reaction between the metallic vapours in helium gas

The highest peaks correspond to $Cs_3Pb_2^+$ and $Cs_3Pb_5^+$ ions

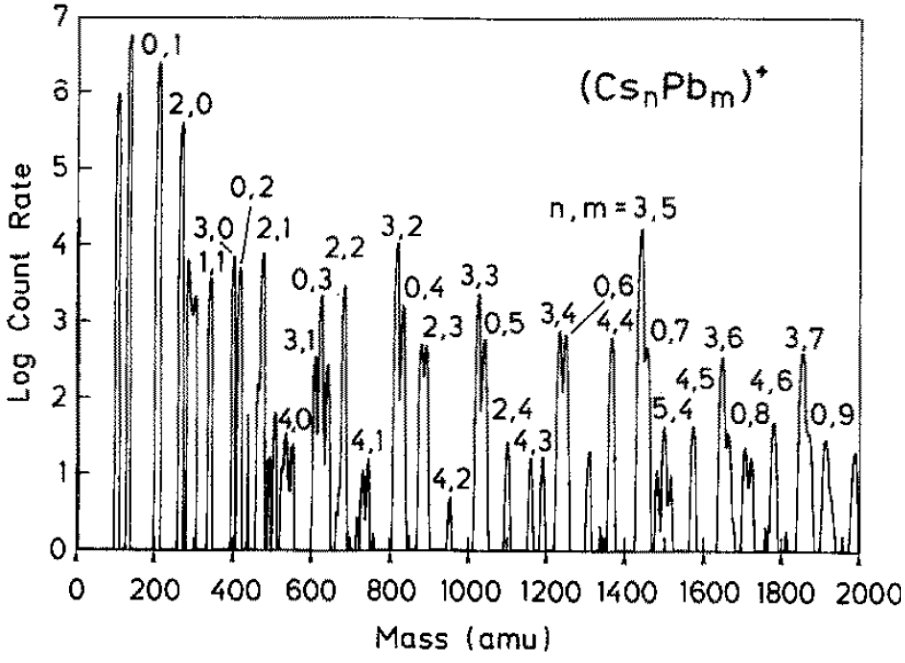

Source: Reproduced with permission of Springer Science+Business Media from Martin (1986).

It is sometimes assumed that the nuclear reaction products could combine with each other, for instance, that CsI could be formed from the elements. CsI is indeed more stable than PbI_2, which might lead to the impression that it should preferentially form in the liquid metal. However, compounds between the different trace elements will be virtually absent in the liquid metal and the vapours over it due to the skewed mass balance; compounds with the major components, lead and bismuth, are thermodynamically favoured, as the major components have higher thermodynamic activity by dint of their immensely higher concentration.

For completeness, we will nevertheless discuss the formation of Cs_2O, which may have significant volatility at high temperatures and thus might contribute to Cs levels in the gas phase. There is significant disagreement on the thermodynamical properties of Cs_2O. It is generally agreed that it melts in the vicinity of 765 K, but while some (Knacke, 1991) estimate its boiling point to 1 815 K, others (Glushko, 1979) place it as low as 1 420 K. Also the Gibbs energy of formation for gaseous Cs_2O is disputed, and thus there is no certain value for its dissociation coefficient at high temperatures. Using the values recommended in Glushko (1979), which relate the partial pressure of Cs_2O to that of caesium and oxygen at a given temperature, we have tried to estimate the contribution from Cs_2O to total Cs in the gas phase.

The oxygen potential in a spallation target system will be a function of irradiation time, mainly caused by the formation of reducing agents such as hydrogen and electropositive metallic nuclear reaction products. Thus, the oxygen potential will tend to decrease with increasing irradiation time unless it is kept constant by active means using an oxygen control system. A general requirement for the safe operation of a lead-based spallation system is to keep the oxygen concentration low enough to prevent the formation of solid lead oxide slags at the minimum liquid metal temperature. On the other hand, the oxygen concentration should be kept above the threshold value for the dissolution of oxide layers of the construction materials to prevent corrosion problems (see Chapter 4 of this handbook for more details). Therefore, in large-scale nuclear facilities based on lead alloys, an active oxygen control is mandatory to ensure reliable operation. In any case, even in the absence of active oxygen control and at the very beginning of the irradiation, P_{O2} cannot, in the closed loop or reactor vessel, exceed a value determined by the equilibrium pressure over pure PbO at the corresponding temperature; any excess oxygen would then be consumed by reaction with the large reservoir of lead. (The maximum oxygen potential in the melt itself is, of course, the same as that described above, and corresponds to the saturation concentration of oxygen in the liquid metal. This holds true even when there is a non-equilibrium pressure of oxygen in the gas phase, as in the case of a spill or oxygen ingress into the loop.)

Thus the theoretical maximum value of P_{O2} can be obtained from the dissociation coefficient (and hence, from the Gibbs energy of formation [Barin, 1993]) for pure PbO at the studied temperature. For 1 000 K, it is about $3.5 \cdot 10^{-13}$ atm, or twice that if expressed as P_O. The partial pressure of caesium in the system can be obtained through Eq. (5.54) and will of course depend on the Cs concentration in the coolant.

At 1 000 K, the dissociation coefficient of Cs_2O is (Glushko, 1979):

$$\frac{\left(P_{Cs}\right)^2 \cdot P_O}{P_{Cs_2O}} = 10^{-18.4769} \tag{5.57}$$

At higher temperatures, the equilibrium is shifted towards the elements, and vice versa (ibid.). The lowest monatomic Cs pressure at which Cs_2O vapour represents 50% of the total gaseous caesium, over oxygen-saturated lead and at 1 000 K, is $2.4 \cdot 10^{-7}$ atm or 0.024 Pa. For comparison, this caesium pressure is about an order of magnitude greater than that obtained by modelling (Jolkkonen, 2009) of Cs evaporation at 1 000 K in LBE- and lead-cooled reactors with limited core damage.

We thus conclude that Cs_2O will not be a major contributor to caesium volatilisation at high temperatures except under conditions of near oxygen saturation of the coolant and extensive caesium contamination of the same. The fraction of Cs_2O can however be significant at lower temperatures, but the total Cs levels are then correspondingly lower.

5.2.1.1.12 Rubidium

Rubidium is very similar in its chemical behaviour to its higher homologue caesium. Therefore, it can certainly be expected to be retained in lead alloys in an analogous way. According to Landolt-Börnstein (1960) the vapour pressure of metallic rubidium can be described using the following equation:

$$P_{Rb}^{o} = 10^{-\frac{4588}{T} - 1.45 \log T + 14.110} \tag{5.58}$$

The available literature data on the Pb-Rb and Bi-Rb systems have not been reviewed as thoroughly as the corresponding Cs systems thus far. The Pb-Rb phase diagram (Landolt-Börnstein, 1991) depicted in Figure 5.2.38 very much resembles the Pb-Cs system both concerning phase relations and transition temperatures. Interestingly, a very simple conservative estimation performed within the MEGAPIE licensing procedure (Neuhausen,

2005c) came to very similar results for the activity coefficients of alkaline metals in LBE, i.e. $\gamma_{Rb,Cs(LBE)} \cong 0.01$ compared to the results obtained for caesium in the preceding section. In a paper studying the thermodynamic properties of liquid Rb-Pb alloys, values of $\gamma_{Rb(Pb)} = 0.014$ were found at 878 K for Rb mole fractions of $X_{Rb} = 0.02$ (Tumidajski, 1990). We conclude that a thermodynamic activity coefficient of $\gamma_{Rb(LBE)} \cong 0.02$ used along with the vapour pressure function of metallic Rb and appropriate estimations of the Rb inventory should allow reasonably conservative estimates for the vapour phase concentration of this element over a lead-alloy pool. However, a more thorough review of literature data and supporting experiments are necessary to confirm this statement.

Figure 5.2.38: Phase diagram of the Pb-Rb system; concentration in at.%

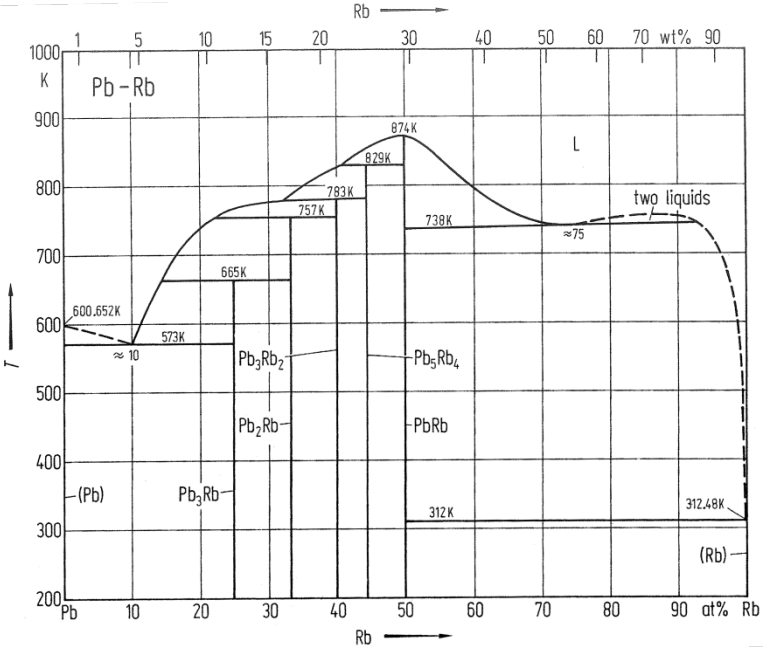

Source: Reproduced with permission of Springer Science+Business Media from Landolt-Börnstein (1991).

5.2.1.1.13 Summary and conclusions

5.2.1.1.13.1 Recapitulation

Based on the recommended functions for the partial pressures of Pb, Bi, Po, Hg, Cd, Tl, I and Cs in lead and LBE solution, as derived in the previous sections of this chapter and summarised below, and the theoretical maximum concentration in the liquid metal determined on the basis of the entire nuclear reaction product inventory, one can calculate the equilibrium partial pressure of each solute at an – within limits – arbitrary temperature. These partial pressures constitute a concentration in the gas phase, which we identify here with the cover gas volume of the respective reactor or target design, representing the amount of volatiles that are to be handled within the cover gas system to prevent hazardous releases from the system. This concentration also corresponds to the maximum concentration/activity that can be *instantly* released from the loop when opened for maintenance operations or in an accident case. With the insertion of other values for the amount of liquid metal, gas phase volume, inventory and temperature, the data allow similar calculations for other scenarios and different facility designs.

As the amounts of evaporated activity will scale linearly with the volume of gas that is in contact with contaminated liquid metal, the data might also be useful to estimate volatilisation in the case of a liquid metal leak into a closed containment. This presupposes

sufficient time for a solute-gas equilibrium to be established, which is contingent on liquid metal quantity, temperature and cooling rate. While it appears unlikely that a large volume of air would be saturated by evaporation from a moderate spill before the liquid cools and solidifies, the values thus obtained may be useful as theoretical upper limits for risk assessment purposes. Furthermore, the equilibrium vapour pressure of volatiles over diluted liquid metal solutions is one of the fundamental parameters necessary for a prediction of their evaporation kinetics in open systems, which is crucial for the evaluation of releases in accident scenarios. This will be addressed in more detail in the following section.

Applying ideal gas laws, the amounts of volatiles in a given gas volume are easily obtained from the partial pressures. The error arising from assuming ideal gas behaviour is insignificant compared to the uncertainties in activity coefficients. Thus, the total radioactivity resulting from Pb, Bi, Po, Hg, Cd, Tl, I, and Cs decay in the gas phase can be calculated from the respective amount $N_{(g)}$ in the appropriate gas volume, the specific radioactivity A_m of the isotopes and their relative abundance. The slight difference between the atomic mass of one specific isotope and the average atomic mass over the actual isotopic vector can be ignored, as the approximation is insignificant in this context.

5.2.1.1.13.2 Volatilisation from LBE in reactor or spallation facilities: Recommended data

Table 5.2.4 compiles data and functions that we can recommend for use for the estimation of maximum equilibrium vapour phase concentrations of volatiles over liquid LBE. These correspond to the current state of knowledge on the volatility of the discussed elements over diluted solutions in liquid lead, bismuth and LBE and will allow conservative estimations of releases that have to be expected in nuclear facilities using these liquid metals as spallation target material or reactor core coolant. Examples for such assessments and discussions on the consequences of their results on nuclear systems can be found in Jolkkonen (2009) and ESS (2010) for ADS reactor cores and spallation facilities, respectively.

Table 5.2.4: Recommended values and functions for volatiles in LBE

Element	Estimated log (γ)	Recommended function for Henry constant K_H (Pa)	
		Function	Nominal range
Pb	Eq. (5.11)	Eq. (5.12) (for X_{Pb} = 0.45)	Around 423°C
Bi	Eq. (5.10)	Eq. (5.13) (for X_{Bi} = 0.55)	Around 423°C
Po*	Eq. (5.24)	Eq. (5.23)	500-750°C
Hg	< 0.3	Eq. (5.34)	Around 330°C
Cd	< 0.6	Eq. (5.38)	Around 500°C
Tl	< -0.1	Eq. (5.43)	Around 500°C
I	0 (PbI_2 in LBE)	Eq. (5.44) Eq. (5.45)	307-424°C 424-847°C
Br	Not quantitatively evaluated	Behaviour similar to iodine expected	Not assessed
Cs	< -1.5 (Cs metal in Pb) < -2.5 (Cs metal in Bi)	Eq. (5.54)	370-660°C
Rb	Estimated ≈ -1.7 (in Pb)	Eq. (5.58) times γ_{Rb}	Around 600°C

* Note added in proof: In view of the results of the most recent experiments that were briefly discussed in the addendum to Section 5.2.1.1.5.3, we emphasise again that Eqs. (5.23) and (5.24) should not be used to assess the evaporation behaviour of polonium at temperatures below 500°C. The low-temperature evaporation behaviour of polonium in liquid Pb, Bi and LBE needs to be studied in more detail.

However, we strongly recommend that additional systematic experimental studies should be performed to verify the recommended functions for those systems of volatiles in LBE where no or insufficient data are available and the recommended functions are solely based on conclusions from the related binary systems. An even more important requirement for the licensing of future lead-alloy-based nuclear facilities will be to gain an understanding of release processes different from evaporation in elemental form. The most prominent example for systems where such phenomena play a crucial role is the Po-LBE system, where under certain conditions, discussed in Section 5.2.1.1.5, much higher gas phase concentrations than expected from equilibrium evaporation data have been observed. In this context, not only processes involving molecular evaporation but also recoil mechanisms and aerosol formation, transport and deposition have to be understood in detail. A clarification of these phenomena will require substantial experimental and theoretical efforts.

5.2.1.2 *Non-equilibrium evaporation*

5.2.1.2.1 Introduction

As an extension of the assessment of volatiles' behaviour for closed systems, based on equilibrium vapour pressure data presented in Section 5.2.1, we discuss here the treatment of volatilisation under non-equilibrium conditions, i.e. for an open system. The methods discussed are primarily important for the estimation of evaporation rates for accident scenarios, but can also be applied for an estimation of the possible mass transfer from the liquid metal to a purification unit located in the cover gas system of a spallation loop or reactor core that continuously removes and traps the evaporated material, thus preventing the establishment of equilibrium. Since a fast release of the gaseous elements from the liquid metal to the gas phase is likely to occur, we will assume complete release of these elements from the liquid metal to the cover gas during operation. Therefore, we will focus on those elements and their compounds that are not gaseous in their standard state but have a considerable volatility under the operating conditions of a spallation source or reactor. As shown in Section 5.2.1.1, these elements will for the most part remain within the liquid metal system during normal operation and thus form an additional source term that plays a critical role for accident scenarios. In this section, we will present the available literature data on the evaporation kinetics of these elements from liquid lead, bismuth and LBE and discuss methods for estimation of maximum evaporation rates using the equilibrium evaporation data compiled in Section 5.2.1.1. With the assessment of release kinetics presented in this section we lay the foundation for accident studies on lead and lead-alloy-cooled nuclear facilities. We will point to open issues that deserve further study.

Results obtained using the methods discussed below can be used as a source term for estimations of the radiological hazard of accident scenarios. As an example for such estimations, in Section 5.3.4 of this chapter we will show how such data were used within the assessment of accident scenarios within the licensing procedure for the MEGAPIE liquid LBE target irradiated in 2006 at Paul Scherrer Institute (PSI).

5.2.1.2.2 Theoretical methods for the estimation of evaporation rates

5.2.1.2.2.1 Evaporation rate calculation using Langmuir's method

The maximum rate of evaporation of a pure substance into a vacuum was shown by Langmuir (1913) to be:

$$R_m = \sqrt{\frac{M}{2\pi RT}} p^{\circ} \tag{5.59}$$

with R_m mass evaporation rate;

M molecular or atomic mass;

T absolute temperature in K;

R universal gas constant;

$P°$ vapour pressure of the pure substance.

In the theoretical derivation of this relation, it was postulated that the *rate of vaporisation* of atoms or molecules from a liquid surface in a high vacuum is the same as the rate of vaporisation in the presence of a saturated vapour of these atoms or molecules. The *rate of condensation* is determined by the pressure of the vapour. Thus, it is zero in vacuum, while in equilibrium the rates of vaporisation and condensation are equal, yielding a net *evaporation rate* of zero. Thus, the rate of vaporisation can be calculated from the rate of condensation, which in turn can be derived from the kinetic theory of gases (for a detailed derivation see e.g. Langmuir [1913] and McNeese [1967]).

The assumptions implicit in the use of Eq. (5.59) for calculating the rate of evaporation from a liquid surface include the following (McNeese, 1967):

1) The liquid surface is plane.
2) The liquid surface is of infinite extension, i.e. collisions of molecules with the vessel walls in the vapour space must exert a negligible influence on the rate of vaporisation.
3) The vapour phase behaves as an ideal gas.
4) Every part of the liquid surface is within a fraction of the mean free path from every other part or from a condensing surface, i.e. the effect of collisions between evaporating molecules among themselves or with molecules of a cover gas on the rate of evaporation is negligible.
5) The number of molecules leaving the liquid surface is not affected by the number striking the surface.
6) Vapour molecules striking the liquid surface are absorbed and re-vaporised in a direction given by a cosine relation, which is independent of the direction of approach at the moment of absorption.

With respect to an assessment of the evaporation rate of a volatile element A dissolved in a liquid metal in an accident scenario relevant for a spallation source or liquid-metal-cooled reactor, or within a cover gas system equipped with a purification unit for continuous removal of the evaporated material, estimations can be made by substituting the vapour pressure of the pure substance in Eq. (5.59) by the effective vapour pressure or Henry constant K_H, as defined in Eq. (5.3), of the diluted volatile dissolved in LBE multiplied by its mole fraction in the diluted solution as derived in Section 5.2.1.1, thus yielding:

$$R_{m\,(\mathrm{A})} = \sqrt{\frac{M}{2\pi RT}} K_{H,\mathrm{A\,(Pb,LBE)}} X_{\mathrm{A\,(Pb,LBE)}} \tag{5.60}$$

with $K_{H,\mathrm{A\,(Pb,LBE)}}$ Henry constant of the element A in a Pb or LBE solution;

$X_{\mathrm{A\,(Pb,LBE)}}$ mole fraction of the dissolved element A.

The molar evaporation rate can then be simply calculated by dividing R_m by the molar mass of the evaporated species:

$$R_{n\,(\mathrm{A})} = R_{m\,(\mathrm{A})}/M \tag{5.61}$$

For the effective vapour pressure of the most important volatile species formed by nuclear reactions within a lead-alloy-based spallation target, i.e. Po, Hg, Cd, Tl, I and Cs, the relations derived in Section 5.2.1.1 and compiled in Table 5.2.4 can be used and values for the mole fractions can be obtained e.g. from inventory calculations performed using nuclear Monte Carlo codes. Evaporation rates can then be calculated using Eq. (5.60). Nevertheless, assumptions No. 2 and No. 4 used in the derivation of Eq. (5.59) are not met for accident scenarios in nuclear facilities. Especially, assumption No. (4) is not fulfilled because in the scenarios the presence of a vapour phase will cause a significant amount of re-condensation of the vaporised atoms or molecules. Therefore, evaporation rates observed in practice will be considerably lower than those predicted using Eq. (5.60). Nevertheless, Eq. (5.60) together with the relations for effective vapour pressure can be used for simple and extremely conservative estimations of the maximum possible rates of evaporation of volatiles from a liquid metal surface for cases where no experimental data are available, which is the case for most of the volatile elements discussed here.

5.2.1.2.2.2 Mass transport calculations

The phenomenon of evaporation can be treated more sophistically using the theories developed to describe mass transfer in multi-component systems. In single phase systems comprising more than one component, where the concentrations of components vary from point to point, a natural tendency exists to minimise these concentration differences. This minimisation is achieved by the transfer of material from the higher concentration regions to those with lower concentration. Similarly, in two-phase systems a transfer of material from one phase to the other takes place when there is a difference in the chemical potential of the component of interest across the phase boundary. In the case studied here, radionuclides dissolved in dilute solution in a liquid metal will be transferred to the gas phase, the driving force being the difference in chemical potential of the considered radionuclide in the liquid and in the gas phase. The chemical potential of the radionuclide in the liquid phase can be expressed in the form of its thermodynamic activity in the liquid metal which is related to its vapour pressure as demonstrated in Section 5.2.1.1.3, Eqs. (5.2) to (5.5). The chemical potential of the radionuclide in the gas phase is given by its thermodynamic activity in the gas phase, which can be expressed by its partial pressure in case of ideal behaviour. For instance, in an accident case a pool of spilled liquid metal containing radionuclides may be exposed to ambient air. In this case, the chemical potential of the radionuclides is given by their thermodynamic activities, which can be estimated based on the thermodynamic activity coefficients as derived in Section 5.2.1.1, compiled in Table 5.2.4. The chemical potential in the gas phase will be zero at the time the accident occurs and will increase afterwards.

Generally, in the theory of mass transfer, the molar mass flux can be expressed in the form of the simple equation:

$$R_{n\,(A)} = k\,\Delta a_A \tag{5.62}$$

with R_n molar mass flux (in our case corresponding to molar evaporation rate in $mol \cdot cm^{-2} \cdot s^{-1}$);

k mass transfer coefficient (in case of use of a dimensionless thermodynamic activity in $mol\ cm^{-2} s^{-1}$);

Δa_A difference in the thermodynamic activity of element *A* between liquid and gaseous phase (dimensionless when based on mole *fraction*).

Determination of the mass transfer coefficient is extremely complex and dependent on the experimental boundary conditions of the phenomenon to be studied. For the case of evaporation of volatile species from diluted solutions of radionuclides in a liquid metal it may – depending on the scenario studied – contain diffusivity parameters of the species involved in both the liquid metal and gas phases, parameters describing convective effects in both phases, heat transfer parameters and, when applicable, parameters

describing chemical reactions, all of them as a function of temperature. We will not go into detail concerning this type of calculation. The fundamentals of such calculations are described in numerous textbooks, e.g. Rohsenow (1961) and Welty (2008). Many models for describing mass transfer under various boundary conditions are described in these references. However, analytical forms of the mass transfer coefficient are only available for a few simple geometries and boundary conditions such as gas flow over a circular pool or through circular or rectangular channels. These models may already prove very valuable for the assessment of accident scenarios of future liquid-metal-based nuclear facilities, but possibly numerical methods for solving the differential equations for mass transfer have to be applied in safety studies. From a physicochemical point of view, the fundamental parameters required for such calculations are vapour pressure and diffusivity data for the involved species. Concerning vapour pressure data, the current knowledge has been discussed in detail in Section 5.2.1.1 and condensed into Table 5.2.4. Regarding the diffusivity, no comprehensive and systematic review of all the available data on diffusivities of impurities in the liquid metals under consideration here has thus far been undertaken. Most studies focused on the diffusion of oxygen and steel alloying elements. These studies are discussed in Chapter 3 of this handbook. For elements, when no or only unreliable experimental data on diffusivities are available, approximations such as the Stokes-Einstein relation (see e.g. Welty [2008]) may be used to estimate reasonable parameters for the diffusion in the liquid. For the estimation of diffusivities of molecular species in the gas phase, a variety of approximate methods have been developed from kinetic gas theory (ibid.). However, for the elements that are important with respect to the release of radioactivity from liquid metal nuclear facilities, we recommend that a comprehensive review and analysis of the literature data should be undertaken to clarify the necessity of additional experimental investigations.

5.2.1.2.3 Experimental studies on the evaporation of volatile elements from liquid lead and LBE

Experimental studies concerning their evaporation rate from liquid lead or LBE have been performed for only for a few of the volatile elements considered here. However, these include the most hazardous elements polonium and mercury. In the following, we will summarise these experimental studies and their results.

5.2.1.2.3.1 Polonium evaporation from liquid lead-bismuth eutectic

Early works on the separation of polonium from bismuth by evaporation were conducted primarily at Mound Laboratory (Joy, 1963; Endebrock, 1953; Moyer, 1956) and at Savannah River Laboratory (Bradley, 1970) during the 1950s and 1960s. However, quantitative information on the evaporation rate of polonium is difficult to extract from these reports.

Tupper (1991) measured the evaporation of polonium from activated LBE in a glass apparatus depicted in Figure 5.2.39. In this series of experiments, polonium containing LBE was prepared by neutron irradiation and the evaporation of polonium was measured at two different temperatures, approximately 250°C (523 K) and 550°C (823 K), both at ambient pressure in an argon atmosphere and under vacuum (approximately 2 Pa). One measurement at ambient pressure under air was also performed to determine the influence of an oxide layer present on the liquid metal surface on the evaporation rate of polonium. In these experiments, the glass walls of the evaporation apparatus served as condensation surfaces. The amount of evaporated polonium was deduced from radiochemical analyses of the material deposited on these surfaces.

The results of atmospheric pressure experiments in an Ar-atmosphere and air at 250°C indicate that the evaporation of polonium is not influenced by the presence of an oxide layer. The observed polonium flux was approximately two orders of magnitude lower than that predicted by calculation. At 550°C, the observed polonium flux was “three or four” orders of magnitudes lower than the calculated values. Unfortunately, the calculations performed are not described in the paper. The use of the term “Raoult’s law”

seems to indicate that the calculations of the polonium evaporation rate stated in the paper were performed using an equation similar to Eq. (5.60), but using the vapour pressure of pure polonium instead of the effective vapour pressure. This approach would neglect the chemical interaction of polonium with LBE, i.e. the system would be regarded as an ideal solution. The differences observed in the calculated and measured evaporation rates observed in Tupper (1991) could thus arise from both shortcomings in the assumptions used for the derivation of the relations for calculating evaporation rates (i.e. the neglect of condensation effects) and from neglecting the chemical interaction between solute and solvent. We will use the numerical data for the evaporation rate of polonium from LBE given in Tupper (1991) for the two temperatures 250 and 550°C later in this review, when we compare the results of different experiments and calculations performed using Eq. (5.60).

Figure 5.2.39: Glass apparatus used by Tupper for the measurement of polonium evaporation rate from LBE

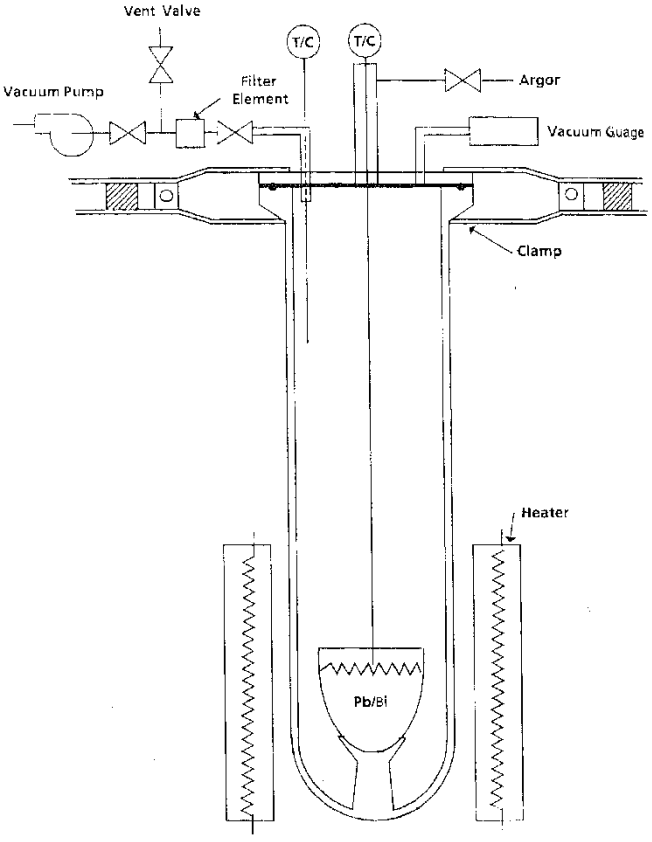

Source: Tupper (1991).

In another series of experiments, γ-active ^{206}Po was implanted into LBE samples at CERN-ISOLDE. The evaporation behaviour of polonium dissolved in liquid LBE was studied at various temperatures in the range from 482 K up to 1 330 K under a continuous flow of Ar/H_2 or Ar/H_2O using γ-ray spectroscopy. Two types of experiments were performed at various temperatures: short-term isochronous (1 h) release experiments at various temperatures and long-term isothermal release studies for several days up to weeks at different temperatures with intermittent determination of the remaining radioactivity. The experimental set-up of the polonium release studies from LBE are described in detail in Neuhausen (2004).

Within short-term (1 h) experiments, measurable amounts of polonium were evaporated only at temperatures above 968 K (Figure 5.2.40). Long-term experiments revealed that a slow evaporation of polonium already occurs at temperatures around 867 K, resulting in a fractional polonium loss of the melt around 1% per day (Figure 5.2.41).

A quantitative evaluation of the results of the experiments described above was undertaken in order to determine values for the polonium flux from liquid LBE and its temperature dependence (Neuhausen, 2005b). The amount of polonium in the samples was deduced from its activity including corrections for absorption of γ-rays by LBE. The surface area of the samples was conservatively estimated from the sample dimensions. The fractional release of polonium was determined as the difference of the count rate for several suitable γ-lines before and after the heating experiment, normalised to the count rate before heating. The amount of polonium released, in terms of moles or mass, can then be calculated by multiplying fractional release and the moles or mass of polonium present in the sample before the experiment, respectively. The molar or mass flux in mol $cm^{-2}\ s^{-1}$ or $g\ cm^{-2}\ s^{-1}$ can then be calculated from the surface area of the sample and experiment duration.

To facilitate a comparison with the results obtained by Tupper (1991), the determined evaporation rates were normalised by the mole fraction of polonium in the measured samples. Indeed, a linear dependence of vapour pressure of polonium to its concentration was found for diluted solutions of polonium in bismuth over a large concentration range (mole fractions from 10^{-6} to 10^{-10}) indicating that Henry's law is valid for the bismuth polonium system under these conditions (Joy, 1963). Based on the results of the detailed literature review on the Po-Bi (Pb, LBE) systems in Section 5.2.1.1 of this chapter, we assume that the behaviour of polonium in liquid LBE is analogous to that in bismuth, i.e. Henry's law is applicable.

An evaluation of the long-term release experiments described in Neuhausen (2004, 2005b) shows that the kinetics of polonium release follows a first order law, i.e. the differential loss of polonium is proportional to the amount of polonium present in the sample:

$$-dn_{\mathrm{Po,LBE}}/dt = kn_{\mathrm{Po,LBE}} \tag{5.63}$$

with $n_{\mathrm{Po,LBE}}$ amount of polonium dissolved in the LBE sample (mol);

t time;

k rate constant.

Thus, after integration one obtains:

$$\ln\left(n_{\mathrm{Po,LBE}}/n_{0,\mathrm{Po,LBE}}\right) = -kt \text{ or } n = n_0 e^{-kt} \tag{5.64}$$

with $n_{0,\mathrm{Po,LBE}}$ being the initial amount (mol) of polonium in the sample at t = 0.

The rate constants for three temperatures, 867, 916 and 968 K were determined as the slope of linear fits of $\ln(n/n_0)$ versus time (see Figure 5.2.42). The instantaneous evaporation rate at the beginning of the experiment was than calculated as:

$$dn/dt_{(t=0)} = -kn_0 \tag{5.65}$$

Figure 5.2.40: Comparison of the release of polonium from LBE (1 h experiments) in Ar/7%-H_2 and water saturated Ar atmospheres as a function of temperature

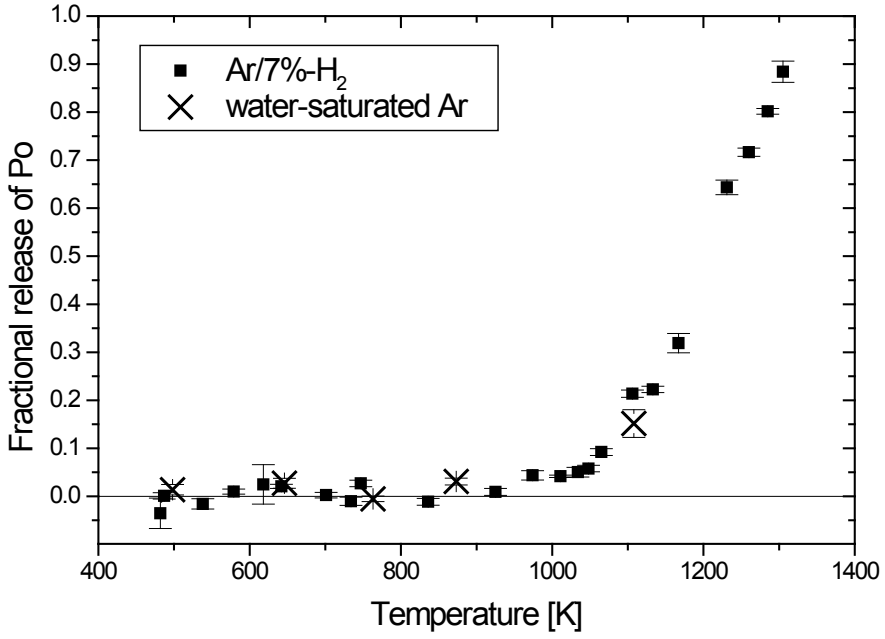

Source: Reproduced with permission of De Gruyter from Neuhausen (2004).

Figure 5.2.41: Comparison of the long-term polonium release from LBE in an Ar/7%-H_2 atmosphere at different temperatures as a function of heating time

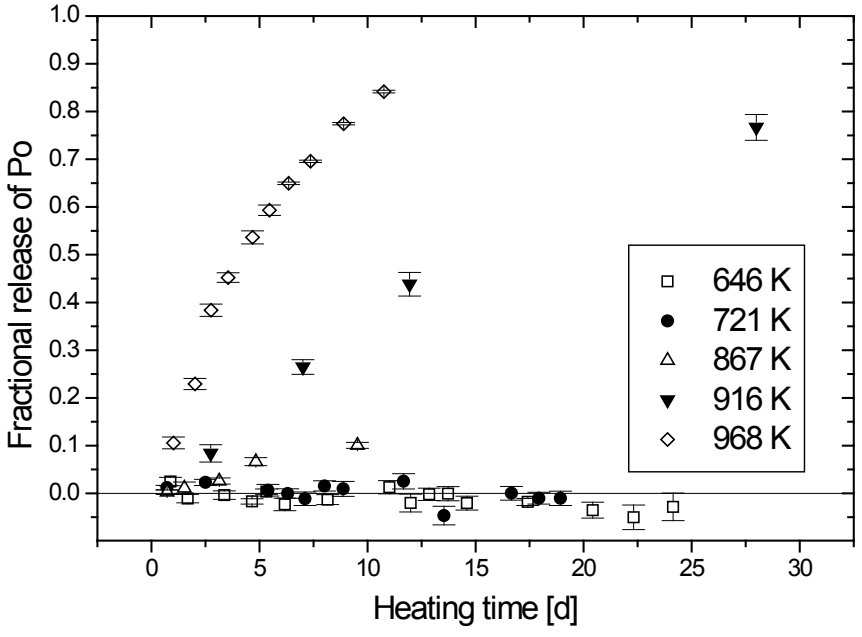

Source: Reproduced with permission of De Gruyter from Neuhausen (2004).

Figure 5.2.42: Linear fit of $\ln(n/n_0)$ vs. time for polonium release from liquid LBE at 968 K

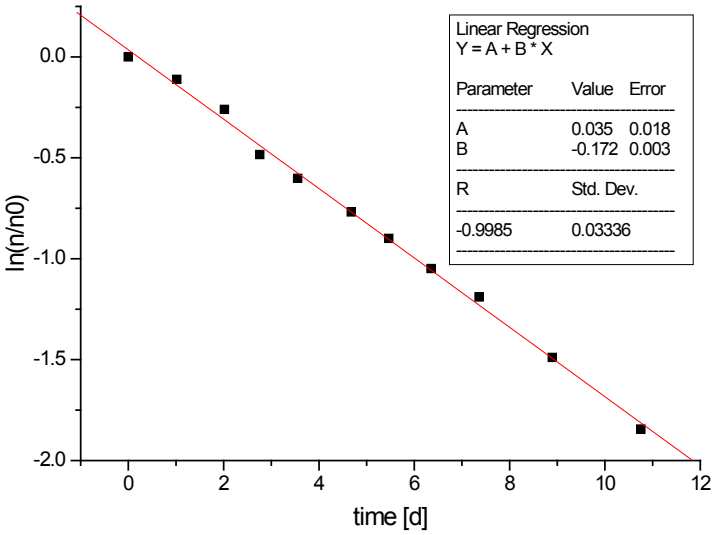

The flux is then obtained by dividing by the surface area of the sample. To obtain a broader set of data, some of the 1 hour release experiments from Neuhausen (2004) were also evaluated quantitatively. Those selected for evaluation included only experiments for which on the one hand a significant release was observed, though on the other hand the released fraction of polonium was relatively small compared to the total amount present. The latter condition was applied to limit the error introduced by the continuous decrease of polonium concentration during the 1 hour experiment that practically leads to a decrease of evaporation rate within the duration of the experiment. Finally, data were taken from experiments performed within the temperature range from 974 K to 1 167 K, yielding between 4 and 32% fractional release of polonium. For these data, the evaporation rate was calculated by multiplying the initial amount of polonium with the fractional release and dividing by the duration of the experiment.

Table 5.2.5 shows a summary and comparison of the results obtained in Tupper (1991) and Neuhausen (2005b). A graphical representation of these data is shown in Figure 5.2.43. The figure indicates that both series of experiments yield consistent values for the molar flux of polonium from liquid LBE. The temperature dependence of the molar flux of polonium in both experimental studies, covering a different temperature range, is consistent as well. These facts are notable in connection with the discussion about polonium release in the form of polonium hydride, H_2Po. Since the experiments described in Neuhausen (2004) were performed in a hydrogen-containing atmosphere, the formation of this compound would be one of the release paths to be considered. However, the results presented in Neuhausen (2005b) do not show any indication of an increased polonium flux under a hydrogen-containing atmosphere as compared to the data taken by Tupper (1991) in an argon atmosphere. A linear fit of the logarithm of the normalised molar flux of polonium from LBE versus inverse temperature using both sets of data (Figure 5.2.44) yields the following parameters:

$$\log\left(R_n / X_{Po}\right) = \left(-1.38 \pm 0.23\right) - \left(6027 \pm 213\right)/T \tag{5.66}$$

with a correlation coefficient of -0.99319 and a standard deviation of 0.19576, where:

R_n molar flux of polonium in mol cm^{-2} s^{-1};

X_{Po} mole fraction of polonium in liquid LBE;

T temperature in K.

Table 5.2.5: Comparison of polonium evaporation rate in different experiments

Temperature (K)	Pressure	Atmosphere	Mole fraction X_{Po} at start of experiment	Po flux R_n/X_{Po} mol cm^{-2} s^{-1}
Tupper (1991)				
531.15	Ambient	Ar	$7.5 \cdot 10^{-11}$	$2.910 \cdot 10^{-13}$
838.15	Ambient	Ar	$7.5 \cdot 10^{-11}$	$1.324 \cdot 10^{-9}$
Neuhausen (2004, 2005b) long-term experiments				
867.15	Ambient	Ar/7%H_2	$4.76 \cdot 10^{-14}$	$2.029 \cdot 10^{-9}$
916.15	Ambient	Ar/7%H_2	$2.91 \cdot 10^{-14}$	$9.029 \cdot 10^{-9}$
968.15	Ambient	Ar/7%H_2	$8.7 \cdot 10^{-13}$	$2.010 \cdot 10^{-8}$
Neuhausen (2004, 2005b) short-term experiments				
974.15	Ambient	Ar/7%H_2	$2.48 \cdot 10^{-12}$	$5.095 \cdot 10^{-8}$
1 011.15	Ambient	Ar/7%H_2	$1.62 \cdot 10^{-12}$	$4.577 \cdot 10^{-8}$
1 034.15	Ambient	Ar/7%H_2	$1.60 \cdot 10^{-12}$	$5.984 \cdot 10^{-8}$
1 048.15	Ambient	Ar/7%H_2	$2.30 \cdot 10^{-12}$	$6.744 \cdot 10^{-8}$
1 065.15	Ambient	Ar/7%H_2	$1.57 \cdot 10^{-12}$	$1.097 \cdot 10^{-7}$
1 106.15	Ambient	Ar/7%H_2	$2.89 \cdot 10^{-12}$	$2.332 \cdot 10^{-7}$
1 133.15	Ambient	Ar/7%H_2	$1.55 \cdot 10^{-12}$	$2.443 \cdot 10^{-7}$
1 167.15	Ambient	Ar/7%H_2	$1.45 \cdot 10^{-12}$	$3.801 \cdot 10^{-7}$

Source: Tupper (1991); Neuhausen (2004, 2005b).

Figure 5.2.43: Graphical representation of molar flux data for polonium from liquid LBE as a function of temperature

Triangles – data from Tupper (1991)
Open circles – data derived from long-term experiments described in Neuhausen (2004)
Squares – data derived from 1 h experiments described in Neuhausen (2004)

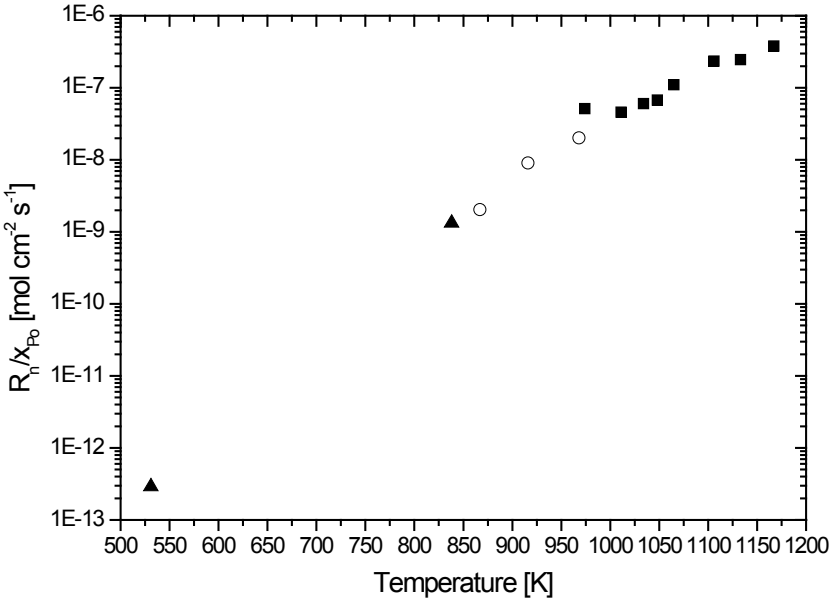

Figure 5.2.44: Linear fit of the logarithm of the molar flux of polonium in mol cm^{-2} s^{-1}, normalised to the polonium mole fraction, versus inverse temperature

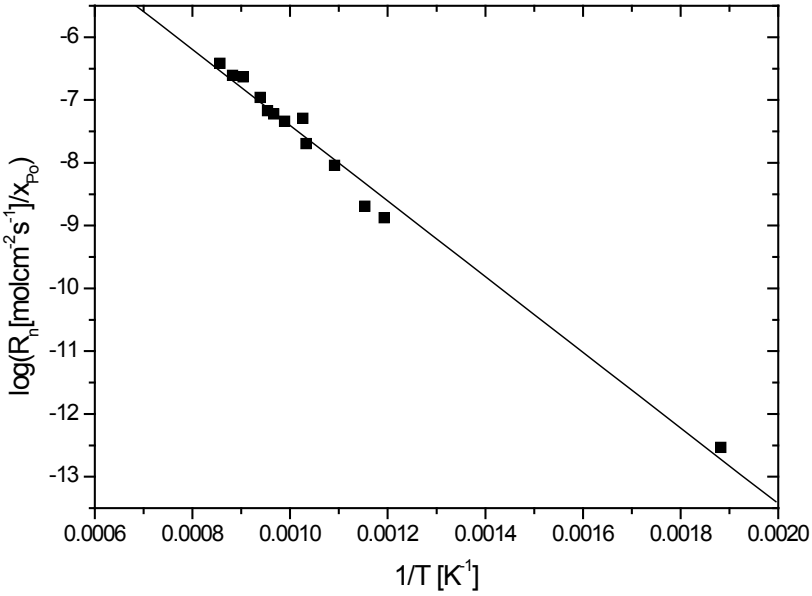

Additionally, from the experimental data of Neuhausen (2004) the apparent vapour pressure of polonium within the transported gas was calculated assuming ideal behaviour of the gaseous phase (Neuhausen, 2005c/e). The results, normalised to a mole fraction of $X_{Po} = 3.3 \cdot 10^{-6}$ (the concentration expected for the MEGAPIE target at the end of irradiation), are compared to determinations of the *equilibrium* vapour pressure of polonium over liquid bismuth (Joy, 1963) and LBE (Buongiorno, 2003; Eichler, 2004a) in Figure 5.2.45. The good agreement shows that obviously the dynamic experiments in Neuhausen (2004) were performed close to saturated conditions concerning the polonium concentrations in the gas phase. This lets us conclude that under non-saturated conditions, e.g. at higher gas fluxes across the liquid metal surface, higher evaporation rates than expressed by Eq. (5.66) are possible, until at very high gas fluxes a diffusion limitation will occur. Nevertheless, Eq. (5.66) was employed in the licensing procedure of the MEGAPIE experiment to estimate polonium evaporation rates, and its use was accepted by the authorities. We point out that for the licensing of larger facilities a more detailed study of polonium evaporation kinetics including the influences of the variation of carrier gas composition and fluxes as well as the experimental geometries is desirable. Such a study would also allow the determination of other fundamental parameters for polonium evaporation kinetics such as diffusivities in the liquid metal.

5.2.1.2.3.2 Measurements of mercury vaporisation from molten lead

Experiments were conducted to measure the rate of vaporisation of elemental mercury from molten lead to provide a basis for estimating radiological source terms for the Accelerator Production of Tritium (APT) project lead blanket (Greene, 1998). In this study, molten pools of lead with 0.01% to 0.10% mercury were prepared under inert conditions. Experiments were conducted which varied in duration from several hours to as long as a month to measure the mercury vaporisation from the lead pools. The melt pools and gas atmospheres were controlled at 340°C during the tests, above the melting temperature of lead. Parameters which were varied in the tests included the mercury concentrations, gas flow rates over the melt, circulation in the melts, gas atmosphere compositions and the addition of aluminium (as a source for the formation of surface oxide layers that could hinder the release of Hg) to the melts. The apparatus used is depicted in Figure 5.2.46. The relevant experimental parameters are compiled in Tables 5.2.6 and 5.2.7.

Figure 5.2.45: Comparison of various data of polonium vapour pressure over diluted liquid metal solutions, normalised to a mole fraction of $X_{Po} = 3.3 \cdot 10^{-6}$

The regions depicted with full symbols correspond to the temperature range where actual experimental data were obtained, while the open symbols correspond to extrapolations to lower or higher temperatures

- ♦ Equilibrium vapour pressure of polonium over bismuth (Knudsen cell experiment in vacuum [Joy, 1963])
- ▲ Equilibrium vapour pressure of polonium over LBE in Ar-atmosphere (Buongiorno, 2003)
- ● Vapour pressure of polonium over LBE in Ar/7%H_2-atmosphere (Neuhausen, 2004)
- \+ Calculated from thermodynamic data of polonium extrapolated in Eichler (2002), assuming dimeric polonium in the gas phase and a thermodynamic activity coefficient of polonium derived from semi-empiric modelling of the interaction of polonium with liquid lead and bismuth using parameters determined in Neuhausen (2003, 2005c)

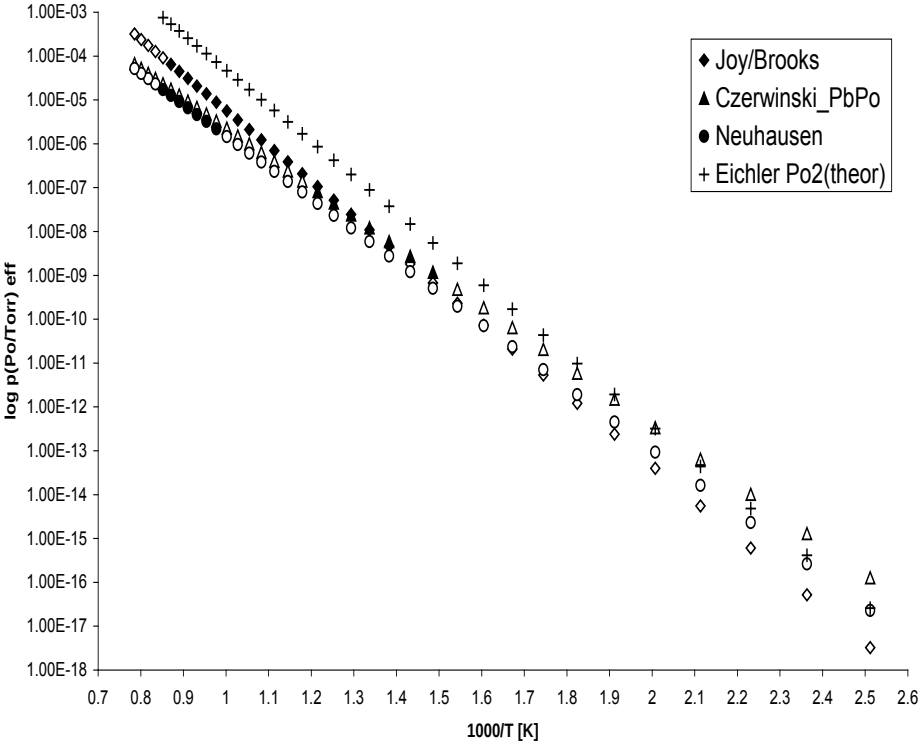

The vaporisation of mercury was found to scale roughly linearly with the concentration of mercury in the pool. Variations in the gas flow rates were not found to have any effect on the mass transfer. However, circulation of the melt by a submerged stirrer did enhance the mercury vaporisation rate, indicating that the evaporation rate under these conditions is limited by diffusion in the liquid and the vapour phase in the un-stirred experiments was not saturated with mercury vapour.

The rate of mercury vaporisation under a high-purity argon atmosphere was found to exceed that for an air atmosphere by as much as a factor of 10 to 20. The reason for this variation was presumably the formation of an oxide layer over the melt pool with the air atmosphere which retarded mass transfer across the melt-atmosphere interface. Aluminium was introduced into the melt to investigate its effect upon the mercury vaporisation rate. No effect was observed for an experiment under a high-purity argon atmosphere, which suggests that there are no chemical effects of aluminium dissolved in the liquid metal on the vaporisation kinetics. With an air atmosphere, the presence of

aluminium in the melt reduced the mercury vaporisation by an additional factor of six in comparison to the identical test but without aluminium, suggesting that aluminium retards the vaporisation of mercury by creating a surface oxide layer in addition to the lead-oxide layer or by changing the character of the lead-oxide layer, thereby increasing its mass transfer resistance. Figure 5.2.47 summarises these results.

Figure 5.2.46: Apparatus used for experiments to determine mercury vaporisation from liquid lead

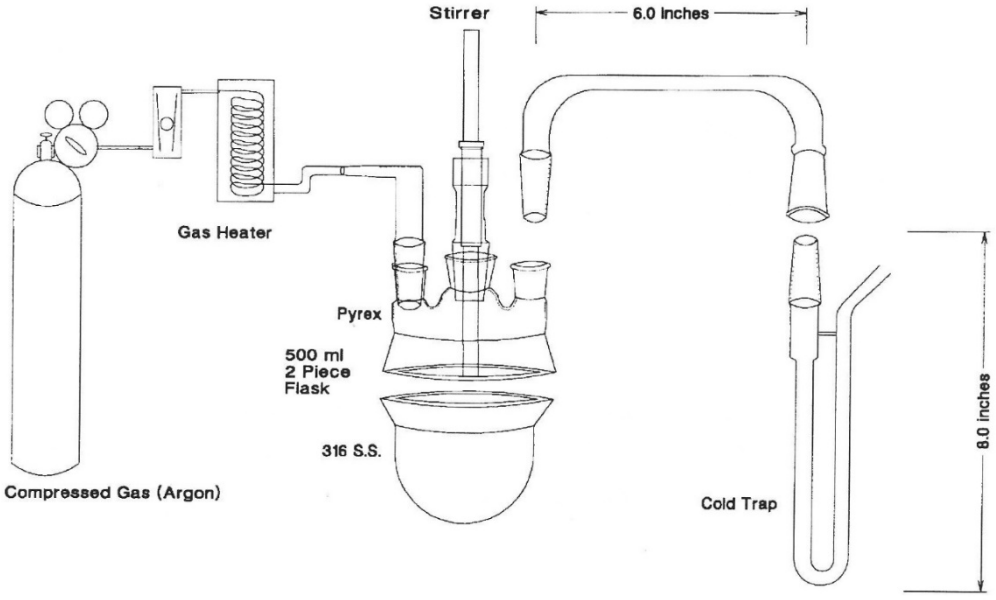

Source: Greene (1998).

Table 5.2.6: Ranges of parameters for experiments studying mercury evaporation from a lead pool

Parameter	Nominal value and uncertainty
Nominal lead mass	2.5 kg
Lead surface area	93.3 cm^2
Nominal mercury concentration (weight)	0.01%, 0.10%, 1.0%
Lead temperature	340°C±2.5°C
Atmosphere temperature	340°C±2.5°C
Gas flow rate	200 ml/min±6%, 750 ml/min±2%
Atmosphere composition	Argon (pre-purified, 99.998%), air
Melt stirring rate	None, 1 rpm
Aluminium in melt	Yes, no

Source: Greene (1998).

Table 5.2.7: Specifications for individual mercury evaporation experiments

Test (-)	Hg (wt.%)	Cover gas	Gas flow	Pool agitation	Aluminium in melt	Purpose/comments
00	0.0	Argon	Low	No	No	Shakedown test, measure of the lead carryover
01	1.0	Argon	Low	No	No	Effect of very high mercury concentration
02	0.1	Argon	Low	No	No	Bounding (5-year APT) mercury concentration
03	0.01	Argon	Low	No	No	Nominal (1-year APT) mercury concentration
04	0.1	Argon	High	No	No	Effects of changes in the gas flow rate
05	0.1	Argon	Low	Yes	No	Effects of agitation of the melt pool
06	0.1	Air	Low	No	No	Effects of an oxidising air atmosphere
08	0.01	Air	Low	No	No	Effects of air at nominal mercury concentration
09	0.1	Air	Low	No	Yes	Effects of aluminium in the melt with air
10	0.1	Argon	Low	No	Yes	Effects of aluminium in the melt with argon
11	0.1	Argon	Low	No	No	Repeat of Hg-Pb/O_2 with improved procedures

Source: Greene (1998).

Figure 5.2.47: Comparison of the effects of atmosphere composition and aluminium addition to the melt on the rate of evaporation of elemental mercury from a lead pool

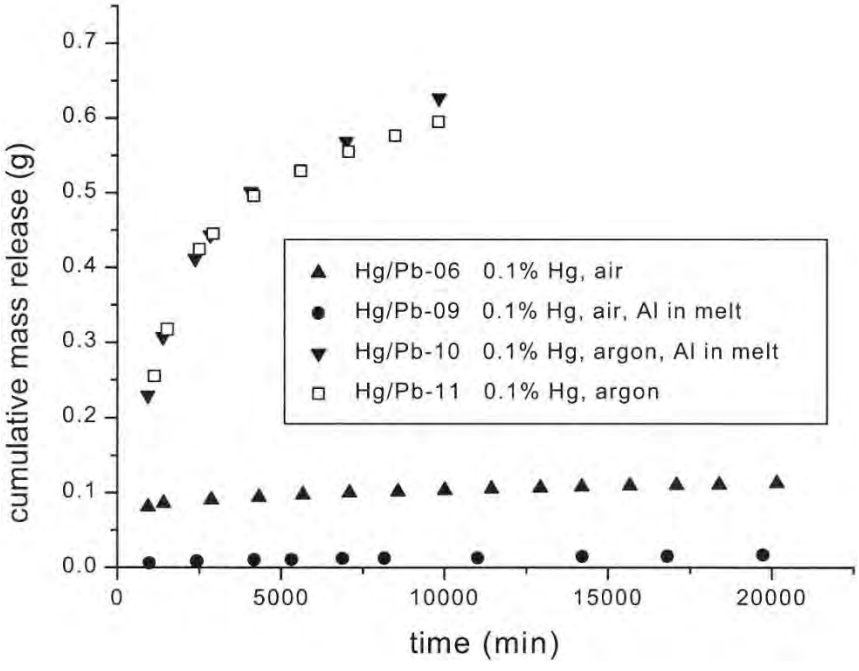

Source: Greene (1998).

In a spallation source, similar effects can be expected, resulting from the formation of layers that consist of oxides of electropositive spallation products such as for instance the lanthanides. Such layers could significantly reduce the amount of mercury released in accident scenarios in case a stable oxide layer is formed. A study of these effects is still not available.

Studies were also performed using LBE as the solvent for mercury (Neuhausen, 2005a, 2006a). Qualitatively, the results of these studies agree with the results of Greene (1998) with respect to the retardation of mercury release under oxidising atmospheres. However, quantitative evaluations of the latter studies indicate larger release rates than observed in Greene (1998). This result may be explained by the much smaller sample size used in Neuhausen (2005a, 2006a) compared to Greene (1998). The results of Greene (1998) indicate that in their set-up mass transport in the liquid plays a significant role, limiting the mercury release in the un-stirred experiments. On the other hand, a quantitative evaluation of the experiments of Neuhausen (2005a, 2006a) in terms of vapour pressure (discussed in more detail in Section 5.2.1.1.6) indicates that the results of such dynamic experiments are indeed strongly influenced by sample size and concentration of the solute (Neuhausen, 2011a). Thus, diffusion effects will be dramatically reduced in smaller samples. It can be concluded that some basic knowledge of the evaporation behaviour of mercury from lead and LBE is available, but fundamental experimental data are still missing, for example the temperature dependency of mercury vaporisation from liquid metals, diffusion data of mercury and modelling of its transport in the liquid metal.

5.2.1.2.3.3 Measurements of the evaporation of lead and bismuth from liquid LBE

A few experiments have been performed to measure the evaporation of the elements constituting the target material, i.e. Pb and Bi, from the liquid melt. In the same series of experiments dealing with polonium evaporation, Tupper (1991) also studied the evaporation of lead and bismuth from LBE at 250 and 550°C under vacuum as well as an inert and an oxidising atmosphere at ambient pressure. The results of this study are not easily comprehensible using chemical reasoning. Under vacuum at 250°C, much larger evaporation of lead and bismuth than predicted by calculation was observed, the quantity of lead in the condensate being much larger than that of bismuth. Furthermore, no enrichment of polonium in the condensate was observed. At 550°C on the other hand the measured quantities of lead and bismuth in the condensate agree reasonably well with those predicted by calculation, the composition of the condensate was much closer to the eutectic composition and an enrichment of polonium in the condensate was observed. The results obtained at 550°C agree reasonably well with the thermodynamic properties of the systems that were discussed in detail in Section 5.2.1, though a consistent interpretation of the results obtained at 250°C is unavailable. For the experiments performed under an inert atmosphere at ambient pressure, contradictory results are given in the paper. While the text states for the experiments performed at both 250 and 550°C no detectable quantities of lead and bismuth were observed, the table summarising the experiments gives numerical values for the LBE flux observed under these conditions. The results concerning the effects of an oxide scum on the surface of the liquid metal on the evaporation rate are equally puzzling. The fact that incomprehensible and contradictory results are given for those experiments performed at low temperature and/or at ambient pressure, i.e. those conditions that give rise to a low rate of evaporation, raises the suspicion that the quantities of LBE evaporated in these experiments were actually near to or below the limit where reliable quantification is possible. Unfortunately, the paper (Tupper, 1991) does not give details on the analysis procedure and the methods used for the calculations. Overall, the information concerning the evaporation of lead and bismuth from LBE that can be extracted from Tupper (1991) is not satisfactory. Results of studies on lead and bismuth evaporation from LBE are also reported in Michelato (2004, 2007) and Ohno (2005). The results of these measurements qualitatively support the statements made in Section 5.2.1 concerning the thermodynamic activity and relative volatility of Pb and Bi in LBE, i.e. thermodynamic activity coefficients of both constituents in the eutectic are < 1 and Bi is the more volatile component compared to Pb. However, no numerical relations describing the evaporation rate as a function of experimental parameters are derived from the experimental data. To improve this situation, a study of the evaporation behaviour of the LBE constituents was initiated at SCK•CEN in Belgium to provide a reliable foundation for the design of windowless spallation targets (Rosseel, 2009).

Generally, from the assessment of physicochemical data on the volatility of lead and bismuth presented in Section 5.2.1.1.4 it seems reasonable to assume that their contribution to the released radioactivity will be low and less hazardous in comparison to that of mercury and polonium.

5.2.1.2.4 Theoretical estimations of volatile release from LBE using Langmuir's equation

For the remaining volatile elements, i.e. the alkaline metals, halogens, thallium and cadmium, no experimental data are available concerning their evaporation rate from a surface of liquid lead, bismuth or LBE. For these elements, estimations of their evaporation rates may be made using Eq. (5.60) using the recommended values of effective vapour pressure compiled in Section 5.2.1.1.13 together with concentrations of the respective elements derived from the results of nuclear calculations. The results of such calculations will however clearly overestimate the evaporation rate because the assumptions used in the derivation of the equations, in particular the absence of a cover gas phase that back-reflects the evaporated particles to the liquid metal surface, are not fulfilled for evaporation to a cover gas at ambient pressure. In Figure 5.2.48, we compare normalised molar evaporation rates calculated using Eq. (5.60) and (5.61) and Eq. (5.27) recommended in Section 5.2.1.1.13 for the effective equilibrium vapour pressure of polonium over LBE with those obtained using Eq. (5.66), which is based on experimental results. It is clearly seen that for the temperature range of interest for the operation of spallation targets the theoretical approach gives 1 to 3 orders of magnitude higher evaporation rates than those found in the experiment. The disagreement of the two approaches increases with increasing temperature, in agreement with the comparisons made in Tupper (1991) between their experimental results and predictions. A similar degree of overestimation can be expected when one uses the Langmuir approach for the estimation of evaporation rates of volatiles from LBE in those cases for which no

Figure 5.2.48: Comparison of normalised molar polonium evaporation rate from liquid LBE calculated using a theoretical approach (Eqs. [5.60] and [5.61]) and a mathematical relation derived from experimental data (Eq. [5.66])

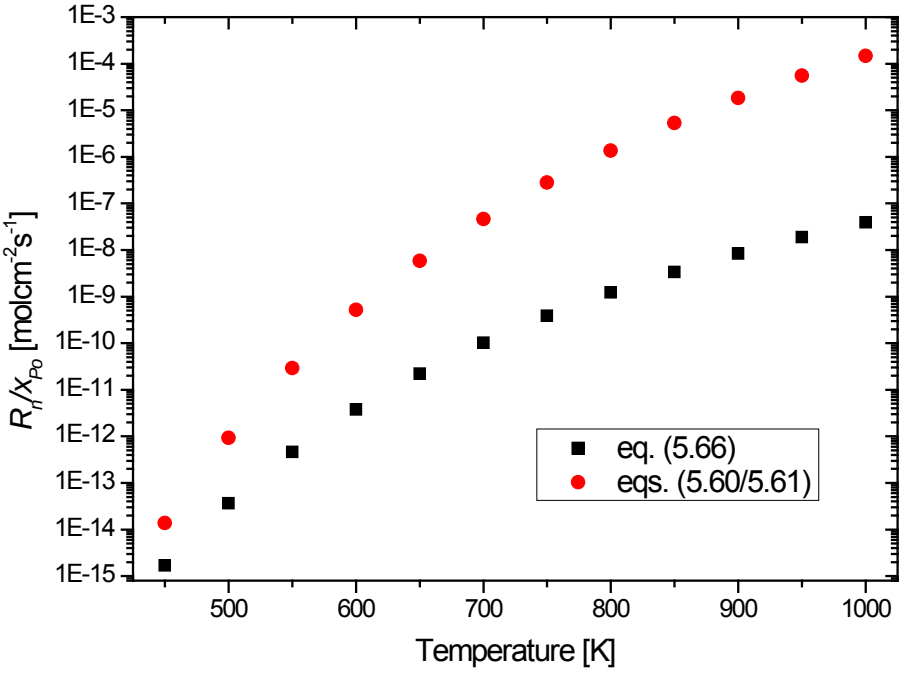

experimental data are available. In many cases, the relations recommended for the effective vapour pressures of volatiles over LBE used for the theoretical calculations are based on conservative estimates of the respective thermodynamic activity coefficients (see Section 5.2.1), leading to another source of conservativeness in the calculations. Thus, such calculations can be used to estimate the maximum possible release of volatiles from an open surface of liquid LBE. In case it turns out that the results obtained by these extremely conservative estimations lead to results that do not comply with the safety limits, more sophisticated calculations based on the mass transfer approach discussed in Section 5.2.1.2.2.2 must be performed. In any case, experimental studies on the evaporation behaviour of these volatiles under conditions relevant for accident scenarios may play a crucial role in validating such calculations.

5.2.2 Gas phase purification

On the basis of current knowledge described in the previous sections, trace amounts of hazardous radionuclides will volatilise into the cover gas above the LBE coolant under normal operating conditions of ADS systems. However, even these trace amounts (order of ppm and lower in the gas phase) may present a substantial radiation hazard because of their high radiotoxicity. The radioactivity transported with the cover gas has to be handled in a safe manner, e.g. it has to be removed before exhaust gases are released to the public. For this purpose, it is useful to study the performance of getter materials that can bind the volatile radioactivity and hence remove it from the gas phase.

In an ADS system, the highest concentrations of contaminants will occur in the cover gas. Direct treatment of the cover gas is, therefore, advantageous from both the safety and economical points of view; in case of gaseous discharges from the reactor, external contamination is minimised and the gas treatment system will be more cost effective because lower flow rates are involved.

The two volatile elements considered most critical are Po and Hg. Methods for the removal of Hg are well studied for application in natural gas processing and in the treatment of effluent gases of coal-fired power plants. Mercury removal technologies based on adsorption on high-surface area materials have been found to be efficient (Pavlish, 2003). Typically activated carbons are employed, loaded as granules in an adsorption bed through which the effluent gas flows. The sorption efficiency of such carbons can be improved by impregnation with iodine or sulphur (Krishnan, 1994; Lee, 2004). In the presence of impregnants, it has been proposed that Hg forms strong chemical bonds with the surface of the adsorbent (chemisorption) instead of interacting through relatively weak intermolecular forces (physisorption). Immobilisation through chemisorption is the preferred method for control of Hg and Po. Carbon-based adsorbents present certain disadvantages such as flammability and reduced performance under conditions of high humidity. These operational limitations may be circumvented by using inorganic adsorbents such as zeolites, porous alumina or silica, loaded with noble metals. Currently, gold-loaded alumina is used to remove mercury from a He off-gas stream at the Spallation Neutron Source (SNS) (McManamy, 2008).

The available data on polonium capturing are very limited. In solution, Po is known to adsorb strongly on silver surfaces (Bagnall, 1983, 1990). Carbon-based sorbents were reported to be capable of highly effective removal of gaseous Po (Borisov, 1999). Experiments by Obara (2008) showed that polonium evaporated from neutron-irradiated LBE can be collected by stainless steel wire meshes. However, the interaction between steel and Po is probably not optimal for the purpose of polonium capturing.

The affinity of noble metals (Ag, Au, Pd, Pt) for Hg vapours over LBE was suggested by thermodynamic calculations using semi-empirical models and was demonstrated by experiment (Eichler, 2004b, 2005; Neuhausen, 2010). Similar calculations indicate that these metals could also be efficient absorbers for polonium. The corresponding results are discussed in more detail in the sections below.

Adsorbents under consideration for Po and Hg removal are currently used for iodine control in PWR and BWR. Impregnated activated carbons as well as silver-loaded inorganic porous materials can be applied as adsorbents for removal of anorganic and organic iodide forms (Jubin, 1996; Kovach, 1998; Mineo, 2000). As mentioned above, iodine enhances mercury adsorption on carbons. Thus, the presence of iodine contaminants in the off-gas, even in small quantities, may have a synergistic effect on mercury adsorption. Conversely, other contaminants can reduce the efficiency of an adsorbent. In the presence of hydrogen, noble metals may catalyse the formation of volatile Po compounds. Obviously, these effects can have important repercussions on the design of a gas treatment system, but were not investigated to date.

Meanwhile, an experimental programme has been started at SCK•CEN in Mol (Belgium) to investigate in detail the efficiency of such gas phase absorber systems for the removal of mercury and polonium, paying special attention to the conditions prevalent in the off-gas system of an ADS.

5.2.2.1 Mercury removal

The binding of mercury on selected metals, their distribution between these metals and LBE in the presence of an excess of LBE, similar to the environment present in a spallation system, and the retention of Hg on a high-surface metal-coated absorber material has been studied at PSI (Neuhausen, 2010).

Those metals that form the most stable compounds with mercury (and also with the halogens and polonium) are the alkaline and alkaline earth metals and the lanthanides. However, these metals readily react with oxygen and moisture. Therefore, they are not suitable for use as absorber materials in a spallation system, where oxygen and moisture may be present as impurity in the cover gas system, and an air environment will be present in case of accidents. Therefore, in the choice of suitable metallic getter materials, one is limited to more noble metals that do not suffer from surface oxidation.

To limit the choice of materials and to provide the theoretical background for the interpretation of the experimental results, semi-empiric calculations were performed to evaluate the strength of interaction of mercury with various noble metals. For this purpose, the enthalpies of solution, adsorption and segregation of mercury with the amalgam-forming noble metals palladium, platinum, silver and gold and with the target materials lead and bismuth were calculated using the Miedema model (de Boer, 1988) and the Eichler-Miedema model for adsorption properties (Eichler, 1979). A detailed discussion of the method of calculation can be found in Neuhausen (2003). Thermodynamically, the process of release of an element dissolved in the liquid metal to the gas phase can be equivalently represented by its segregation to the surface and subsequent desorption or by reversal of the dissolution process and subsequent evaporation of the pure element. On the other hand, the gettering process can be described by the adsorption from the gas phase to the metal surface that may be followed by an incorporation of the adsorbed species from the surface to the bulk metal (formally a reversal of segregation). Figure 5.2.49 illustrates these processes and the involved thermochemical quantities.

In our case we have to consider the evaporation of mercury from LBE and its adsorption on noble metals with the corresponding enthalpies. Table 5.2.8 compiles the results of thermochemical calculations for the interaction of the components of the target material and the noble metals Pd, Ag, Pt and Au.

From the results compiled in Table 5.2.8, it can be concluded that the enthalpies of solution of mercury in the liquid target components are small and positive. Hence, the chemical interaction between mercury and the components of the liquid metal is weak and repulsive. This is consistent with thermodynamic activity coefficients slightly larger than unity that are actually observed in the Hg-Pb and Hg-Bi systems (Hultgren, 1973). In conclusion, a decrease of the vapour pressure of mercury in solution in the liquid metal, apart from that arising from the high dilution, will not occur. On the other hand, mercury

shows a significant affinity to the solid noble metals in the order Ag < Au < Pt < Pd, indicated by the negative heats of solution. Thus, mercury will show a tendency to be enriched in these noble metals in a system that separately contains liquid LBE and one of the noble metals in an equilibrium that is established over the gas phase transport of mercury (Eichler, 2004b). This is even more pronounced for the adsorption of mercury on the surface of the noble metals, where strongly negative net enthalpies of adsorption are calculated. Hence, from the enthalpic point of view, the adsorption to the surface is favoured compared to the incorporation into the bulk.

Figure 5.2.49: Thermochemistry of adsorption of an element *A* on a metal surface *B*

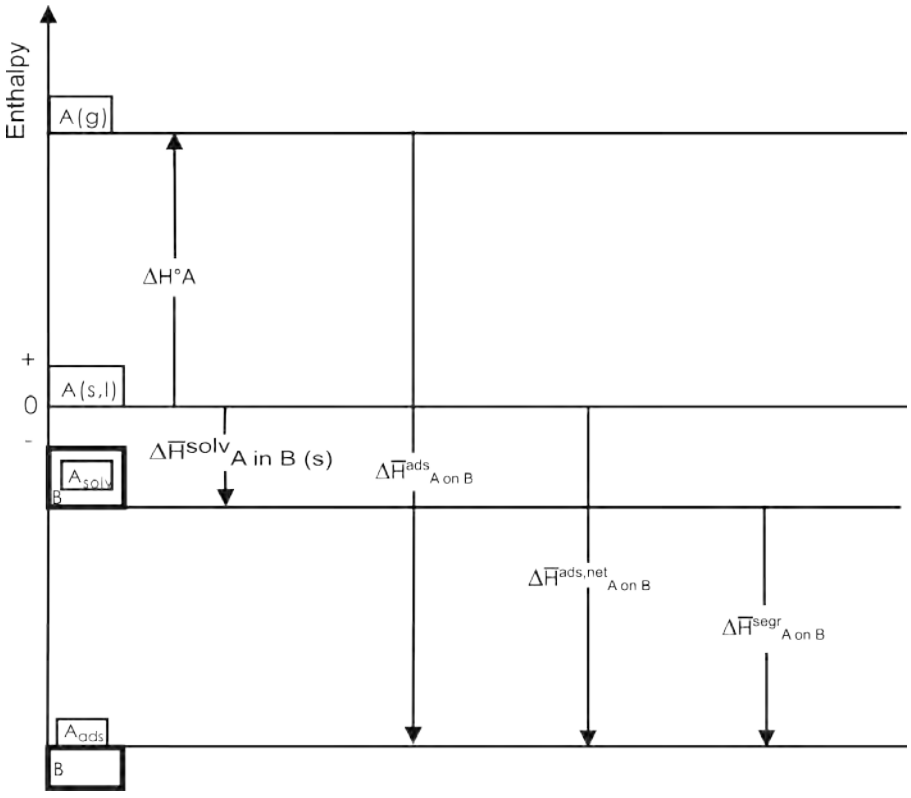

Table 5.2.8: Calculated enthalpies for processes involved in the evaporation of Hg from LBE and its adsorption to noble metals

The evaporation enthalpy of mercury is 61.8 kJ/mol (Barin, 1995)

Element	Enthalpy of solution (kJ/mol)	Enthalpy of adsorption (kJ/mol)	Net enthalpy of adsorption (kJ/mol)	Enthalpy of segregation (kJ/mol)
Pb(l)	5.0	-64.3	-2.6	-7.6
Bi(l)	4.4	-64.5	-2.8	-7.2
Pd(s)	-109.8	-196.3	-134.5	-24.7
Ag(s)	-8.9	-94.7	-33.0	-24.1
Pt(s)	-68.5	-161.0	-99.2	-30.7
Au(s)	-27.0	-110.0	-48.3	-21.3

For practical purposes, with respect to the use of noble metal absorbers for the removal of mercury from the cover gas in a liquid LBE spallation target the following predictions can be made from the result of these calculations.

Because the affinity of mercury to the noble metals is higher compared to its affinity to the components of LBE, an enrichment of mercury in the noble metals can be expected when they are placed in the cover gas system. However, in a spallation target, the LBE phase will be orders of magnitude larger compared to the size and capacity of the absorbers.

Therefore, a substantial part of the mercury will still remain dissolved in the liquid LBE, and the chemical equilibrium – and in consequence the maximum gas phase concentration of mercury that can be reached – will in principle be determined by the equality of the chemical potential of mercury in the three phases, i.e. the liquid metal, the absorber and the gas phase. On the other hand, kinetic effects may hinder the establishment of equilibrium. Such retardation effects should especially occur for the evaporation of mercury from the liquid metal and for its incorporation into the bulk noble metal, both because of the involvement of diffusion processes. However, the adsorption to the surface of the noble metal should be a fast process, unless the surface of the noble metal is heavily contaminated. Based on these considerations, it should be feasible to reduce the gas phase concentration of Hg in the cover gas over LBE by continuously purging the gas over a noble metal absorber that offers a high surface area. Thus, one relies on surface adsorption, which is the most favourable process both from the thermodynamic and from the kinetic points of view. However, the absorber will have to be exchanged frequently, when its surface is saturated. Large noble metal surface areas can be provided by soaking materials with high specific surface area, e.g. molecular sieves, with aqueous solution of noble metal salts and subsequent reductive heat treatment. Due to the approximate nature of our calculations and the lack of knowledge on kinetic data, we abstain from quantitative predictions.

Various series of experiments were performed to validate the predictions based on the results of thermochemical calculations (Neuhausen, 2010). In the first series, radioactive mercury was placed inside sealed quartz tubes together with one of the noble metals Pd, Ag, Pt and Au, keeping the metals separated from the mercury by a plug and heating the tubes to temperatures indicated in Figure 5.2.50. After the heating, the activity of mercury in the noble metal and different parts of the quartz tubes was determined by γ-spectroscopy. For all four metals Pd, Ag, Pt and Au, more than 99.5% of the mercury was found to be absorbed on or in the metals. (No attempt has been made to assess the distribution of mercury between surface and bulk metal using activity measurements.) On the remainders of the quartz tubes, almost no radioactivity was detected. Visually, the platinum sample showed a black colour and a brittle nature after the treatment. The other metals were still ductile after the experiments, all showing a silver lustre. Thus, the amalgamation is also visually detectable for the gold sample. The results show that in agreement with the predictions mercury shows a tendency to absorb in or on the metals examined here. In subsequent experiments, the metals loaded with mercury were heated in a quartz tube under a flow of Ar/7%H_2 at temperatures close to the boiling point of mercury. For all metals, a significant mercury release was observed in these experiments.

Figure 5.2.50: Experiments for absorption of activated Hg in noble metals in evacuated quartz tubes

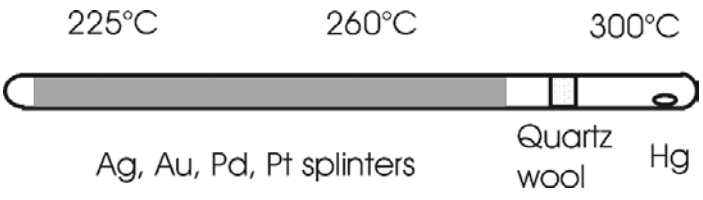

Source: Neuhausen (2010).

Especially for the platinum sample the release was relatively fast. In consequence, because of the embrittlement observed in platinum after amalgamation and the relatively fast release of mercury in the heat treatment, platinum was discarded from further examination.

In a second series of experiments, the distribution of mercury between an excess of LBE and noble metals Pd, Ag and Au placed in the cover gas at elevated temperatures was examined in evacuated quartz tubes (Neuhausen, 2010). The arrangement of the experiments is shown in Figure 5.2.51. After heating in the indicated temperature profile, distribution of the radioactive mercury inside the tube was determined by γ-spectroscopy with roughly 1 cm spatial resolution. Depicted in Figure 5.2.51, the experimental results show that for all of the noble metals a substantial part of the radioactivity is transferred to the LBE phase, as was expected for the reasons explained above. Surprisingly however, on the solid silver absorber a large accumulation of mercury was detected, while on palladium and gold no enrichment of mercury was observed. This surprising result is not explainable with the results of the thermochemical calculations and merits further study. While the absence of mercury in palladium and gold may be explained by the temperature gradient, which was chosen to study the suitability of the absorber materials under the worst conditions, the observed mercury deposition on silver seems to indicate a much stronger affinity of mercury to silver compared to the two other noble metals, which is not predicted by the calculations. In a real spallation target or ADS system, temperature gradients resulting in lower temperatures in the gas phase, compared to those of the liquid metal, will usually occur. Under such conditions, gold and palladium may also show enrichment effects.

Based on these results, silver and palladium foils were built into the cover gas of the MEGAPIE target prior to its irradiation in 2006. The choice of metals was driven by the favourable behaviour of silver in the experiments described above and by the results of theoretical predictions that indicate palladium as the most suitable absorber metal. The efficiency of these absorbers within a real high power target can thus be studied in the post-irradiation examination of MEGAPIE. However, systematic laboratory studies with temperature and composition variations should be performed so as to achieve a better understanding of the underlying processes. From the first experimental results presented here, silver promises to be an efficient, yet affordable, absorber material for mercury. Based on its known chemical properties, it should also be suitable to bind halogens from the gas phase.

In another series of experiments concerning the suitability of noble metal absorbers for the removal of radioactive mercury from the cover gas of a spallation target, the retention of mercury on palladium-coated alumina in a gas flow was studied (Neuhausen, 2010). For this purpose, a quartz tube was filled with approximately 10 g of Al_2O_3 impregnated with palladium, which was dried before in a stream of 60 ml/min Ar/7%H_2 at 600°C for 16 hours. The absorber material was fixed within the tube by a plug made of quartz wool placed on each side. At the exhaust side, the column was filled with charcoal to catch the mercury that will be released from the palladium absorber in the experiments. The tube containing the absorber was placed inside a tube furnace in such a way that the complete palladium absorber material and a part carrying the inflowing gas are located within the furnace, while the part containing the charcoal catcher was located outside the furnace. Thus, it was assured that the charcoal catcher had a temperature low enough to effectively retain the mercury. The absorber material was very slowly charged with radioactive mercury by placing a droplet of mercury approximately 1 cm upstream of the absorber and heating the furnace to 230°C in a gas stream of 60 ml/min Ar/7%H_2 for a period of 6 days. After the charging, the distribution of mercury within the tube was measured using γ-spectroscopy. Then, the charged absorber tube was successively heated at different temperatures for 23 hours under the same flow conditions, and the Hg distribution was determined after each heating experiment. More experimental details can be found in Neuhausen (2010). The results of the experiments are shown in Figure 5.2.52.

At temperatures up to 327°C no transport of the adsorbed mercury can be detected. At 378 and 430°C, i.e. above the boiling point of mercury, a transport of mercury with the gas flow is detectable, leading to a shoulder in the mercury distribution. After heating to 484°C for 23.5 hours, the mercury activity is smeared over the palladium column, and a small amount of activity can be detected on the charcoal absorber located outside of the furnace. At still higher temperatures, the transport becomes faster, leading to an almost complete release of mercury during a day at 633°C. The results indicate that high surface materials coated with palladium can be used for purification of the cover gas of a spallation target unit. The mercury is efficiently retained on the palladium surface at temperatures below the boiling point of mercury, while above the boiling point a significant transport of the volatile metal is observed. A transfer to technical scale however will require additional systematic studies with respect to both fundamental and technical aspects.

Some information on how cover gas purification can be realised on a technical scale may be obtained from the existing high power liquid spallation target facilities SNS at ORNL, USA (ORNL-Web) and JSNS at J-PARC, Japan (JAEA/KEK, 2011). These facilities both use mercury as liquid spallation target material. Therefore, much larger quantities of mercury in the cover gas have to be handled, but the radioactivity associated with the mercury will not necessarily be higher compared to those in an LBE-based ESS because of lower operating temperatures and less intense irradiation in the two spallation target facilities. One major difference compared to LBE-based systems is that no polonium will form in mercury, so in this respect no information can be obtained from mercury facilities.

Figure 5.2.51: Experimental set-up and results of experiments for the determination of Hg distribution in a system containing a noble metal absorber in the gas phase of an evacuated quartz tube and an excess of LBE

The radioactivity distribution over the length of the quartz tube after the heating experiment is depicted in the lower part

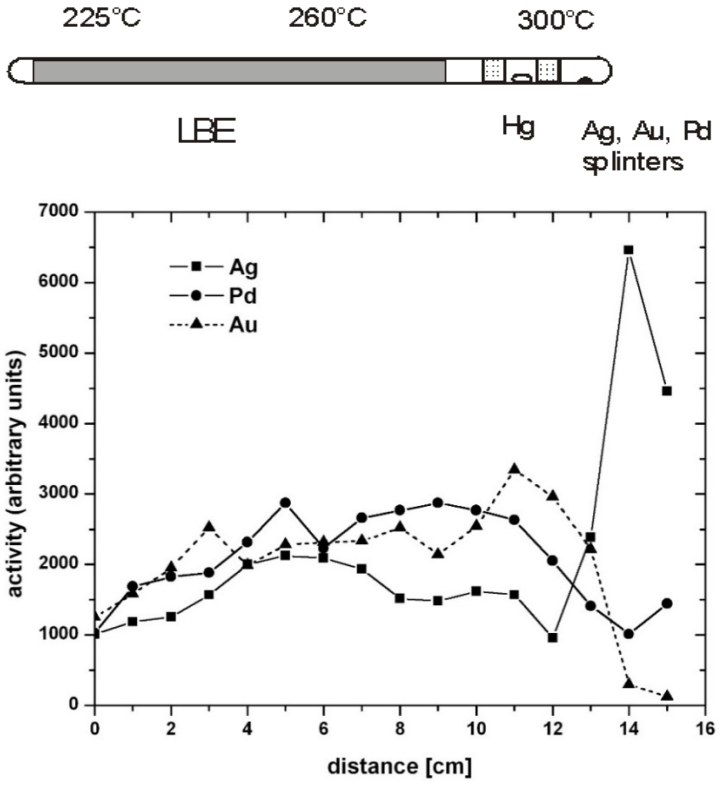

Source: Neuhausen (2010).

Figure 5.2.52: Results of experiments studying the Hg retention on palladium-coated alumina

The radioactivity distribution over the length of the quartz tube filled with the absorber material after various heating experiments is depicted in the upper part. The lower part shows a sketch of the experimental set-up indicating the positioning of the absorber material.

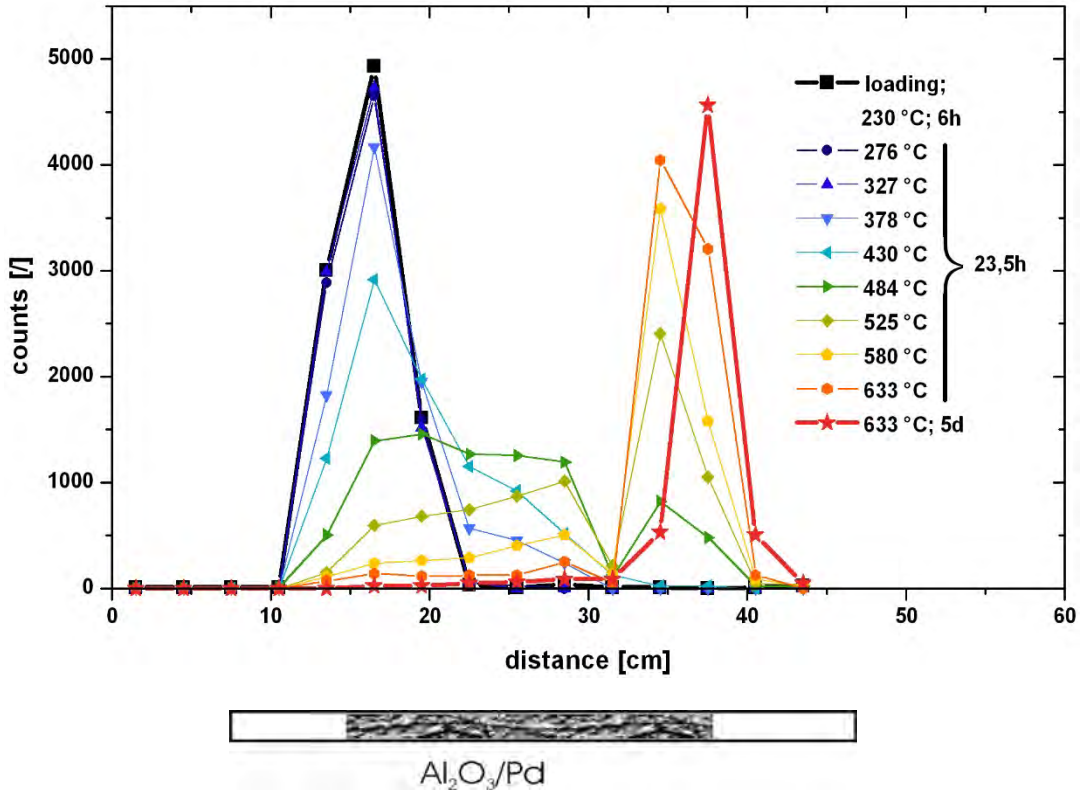

The off-gas system of SNS consists of a series of different absorbers, consisting of two absorbers for binding mercury on a special gold-on-alumina substrate, a CuO-reactor for converting the gaseous hydrogen isotopes to water and two molecular sieves for the absorption of the produced water. Finally, the gas flows over a liquid-nitrogen-cooled charcoal adsorber to remove the heavier noble gases and residual activity (DeVore, 2007). After some operational problems that occurred in the first year of operation, the system and its handling was optimised, and meanwhile the off-gas of the SNS can be efficiently and safely treated using these purification devices.

The off-gas processing system of JSNS is used to handle the contaminated helium cover gas before the target chamber is replaced. In particular, it is designed to remove radioactive mercury vapours as well as tritium and ^{127}Xe. For this purpose, the cover gas is pumped over a mercury absorber made of sulphur-impregnated charcoal into a decay tank, where it is stored for up to one year to ensure ^{127}Xe decay before it is released through the exhaust (Kai, 2014). The decay tank is connected to a loop containing another mercury absorber and a molecular sieve that serve to remove remaining mercury and tritiated water before the gas is released. In a bypass line of this loop, an oxidation catalyst is installed that can be used to transform gaseous tritiated hydrogen to tritiated water.

A transfer of these gas purification concepts from high power liquid metal spallation targets to ADS seems feasible. However, the efficiency of these systems for polonium trapping remains to be demonstrated.

5.2.2.2 *Polonium removal*

Regarding the possibility of adsorption of the extremely hazardous polonium from the gas phase, we have performed additional thermochemical calculations. The results are presented in Table 5.2.9. From these results, palladium in particular is predicted to be suitable as an absorber material. However, the predictive power of these calculations for the purpose intended here remains to be proven; this can be accomplished with dedicated future experiments as well as by an analysis of the absorber foils incorporated in the MEGAPIE target.

Table 5.2.9: Calculated enthalpies for processes involved in the evaporation of polonium from LBE and its adsorption to noble metals

For the evaporation enthalpy of polonium, the value of 188.9 kJ/mol from Eichler (2002) was used

Metal	Enthalpy of solution (kJ/mol)	Enthalpy of adsorption (kJ/mol)	Net enthalpy of adsorption (kJ/mol)	Enthalpy of segregation (kJ/mol)
Pb(l)	-10.2	-207.8	-18.9	-8.7
Bi(l)	-7.3	-204.8	-15.9	-8.6
Ag(s)	4.2	-219.4	-30.5	-34.8
Au(s)	47.0	-179.7	9.2	-37.8
Pt(s)	-21.2	-260.0	-71.1	-49.9
Pd(s)	-105.5	-333.3	-144.4	-38.8

In a study that has been performed to develop a filter for polonium in gas phase (Obara, 2006; 2008), stainless steel mesh samples which were made of thin wires were tested for their polonium filtering capability. The experimental results suggest that such meshes efficiently collect polonium which was evaporated from neutron-irradiated LBE. The authors expect that almost the same effect can be obtained by using other metallic wire meshes, indicating that they do not consider a specific interaction of polonium with the filter material used. Possibly, in these experiments aerosols rather than gaseous polonium species were present. Generally, the topic of polonium filtering from the gas phase needs further detailed study to gain the level of understanding that is required for licensing and operation of large-scale facilities. In particular, efficient polonium filters will inevitably cause the accumulation of materials containing high polonium activity concentrations, which are prone to the abnormal volatilisation effects discussed in Section 5.2.1.1.5.5. Furthermore, the accumulation of polonium will cause a temperature increase in the filters caused by decay heat. All these effects will limit the efficiency of the filtering system in large-scale facilities.

5.2.3 *Extraction of polonium from LBE*

Handling the radioactive liquid LBE in spallation targets as well as in reactors requires severe safety precautions, especially concerning the hazardous polonium isotopes $^{208\text{-}210}$Po, which are formed in considerable amounts by various nuclear reactions (Zanini, 2008a; Cetnar, 2010). One way to avoid polonium release by evaporation or sputtering effects from LBE and minimise contamination in case of reactor leakage could be a continuous removal of polonium from the liquid metal. For this purpose, a liquid-liquid extraction technique using molten alkaline hydroxides was proposed (Yefimov, 1998). Recently, experiments were performed to determine polonium removal efficiency as a function of the main process variables (Heinitz, 2011).

In these experiments, neutron-irradiated LBE samples containing ^{210}Po were brought into contact with eutectic mixtures of NaOH and KOH under variation of the relative amounts of the metallic and ionic phases, temperatures and cover gas atmospheres.

The results of these systematic experiments show that reducing conditions, e.g. provided by hydrogen as cover gas, facilitates efficient extraction of polonium from the liquid metal to the liquid alkaline salt melt as compared to inert conditions (Figure 5.2.53). Conversely, under oxidising conditions polonium removal is less efficient.

Figure 5.2.53: Extraction ratio of polonium using different gas blankets

Experiments were performed at 250°C, 30 min of extraction time and $\mu = 2$

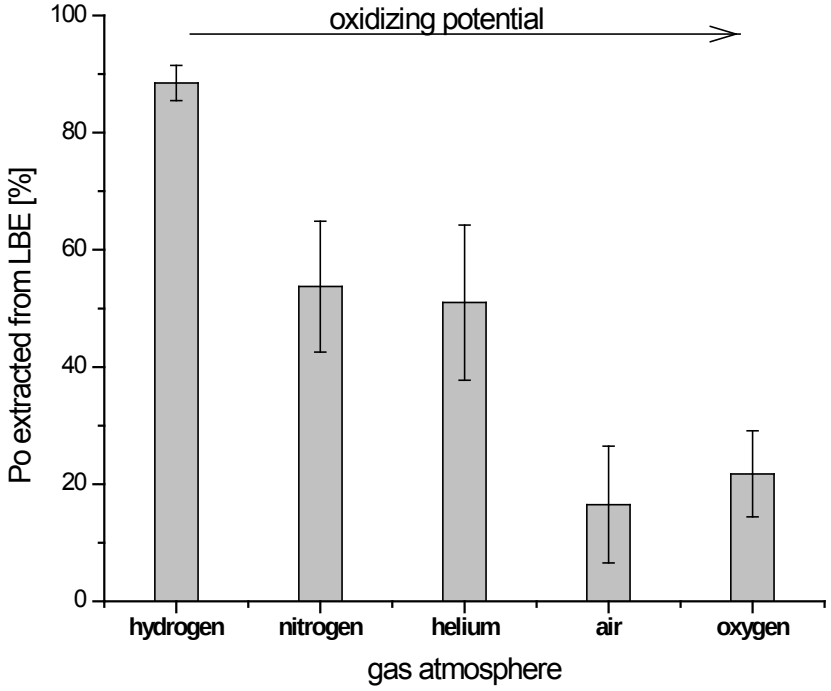

Source: Reproduced with permission of Elsevier Ltd. from Heinitz (2011).

The extraction process was also studied under varying temperature and with dried and moist cover gas (Figure 5.2.54[a]), showing that the extraction efficiency increases with increasing temperature and increasing dryness of the cover gas.

A third series of experiments was performed in an effort to reveal the amounts of alkaline salt melt necessary for an efficient polonium extraction. For this purpose, the hydroxide to LBE mass ratio μ was varied in the range of 10^{-1} to 10^{1} under a constant temperature of 250°C for both H_2 and N_2 atmospheres. The results given in Figure 5.2.54(b) clearly show that under an H_2 atmosphere the amount of hydroxide needed to extract the same amount of Po is dramatically lower compared to that needed under N_2. As expected, polonium removal efficiency is reduced when the ratio of extracting agent to liquid metal is lowered. In practice, this can be overcome by raising the temperature. It was shown in Schulz (1969) that more than 99% of polonium can be extracted at a ratio of $\mu \leq 0.5$ at 500°C in N_2 (for NaOH and pure Bi). For a hydrogen gas blanket or with other reducing agents, even much smaller μ ratios could be used.

Figure 5.2.54(a): Influence of water content on the extraction coefficient as function of temperature

The upper graph shows the water release from hydroxide as a function of temperature; the lower part shows the ratio of polonium content of the alkali and the liquid metal phase as a function of temperature

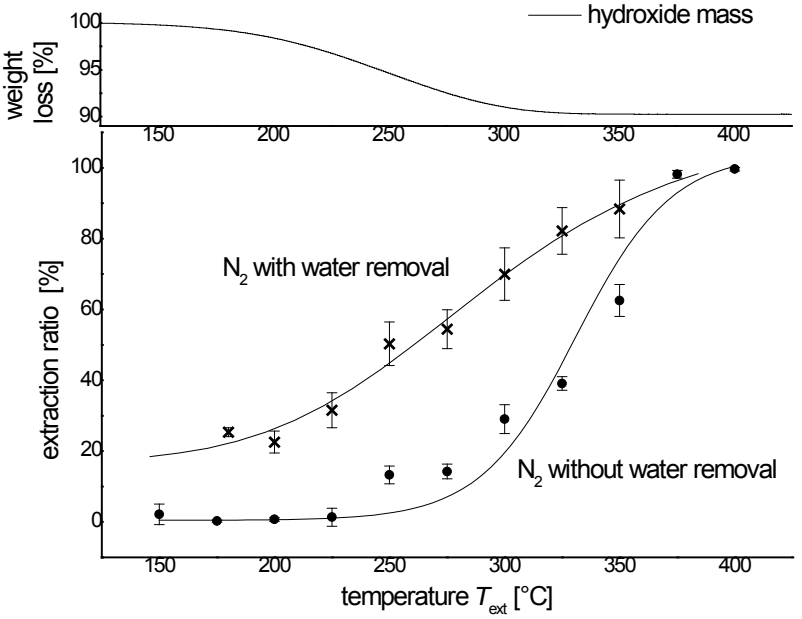

Source: Reproduced with permission of Elsevier Ltd. from Heinitz (2011).

Figure 5.2.54(b): Dependence of polonium extraction on hydroxide to LBE mass ratio for hydrogen and nitrogen gas blankets

Temperature of extraction 250°C; extraction time 30 min

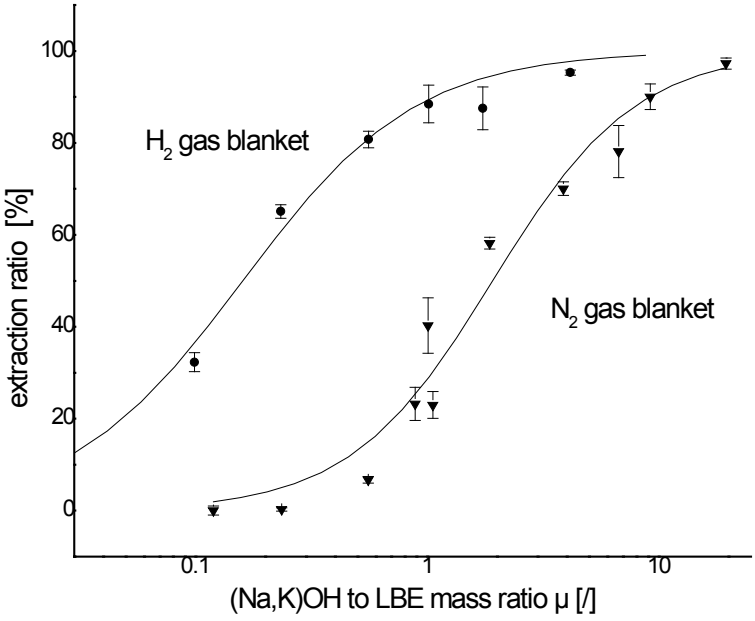

Source: Reproduced with permission of Elsevier Ltd. from Heinitz (2011).

In order to investigate the Po extraction process in more detail, kinetic experiments were performed by Heinitz (2013). Results of these investigations have shown that the behaviour of polonium in the system LBE-NaOH/KOH is very sensitive to traces of oxygen and moisture at temperatures below 300°C. The extraction efficiency varies significantly depending on whether the system is under agitation or not. At 200°C, almost complete Po transfer was observed for extractions under stagnant conditions after very short experiment times, down to one minute. Upon agitation or after longer contact times, polonium is transferred from the alkaline phase back to the metallic phase. This peculiar behaviour was explained by a two-step reaction process, where a very fast reductive transfer of Po to Po^{2-} ions dissolved in the alkaline melt is followed by a slow oxidative back-extraction to the metallic phase. The second oxidative step is believed to be caused by the gradual uptake of trace oxygen impurities from the inert gas environment. Stirring facilitates the ingress of oxygen, promoting the reverse extraction.

Despite these effects, it can be concluded that alkaline extraction of polonium from liquid LBE under reducing conditions is a promising technique for reducing the polonium content of LBE in nuclear systems. However, the process remains to be optimised and brought to a technical scale that can be implemented in a nuclear system, solving e.g. materials issues.

5.2.4 *Extraction of other nuclear products from Pb, Bi and LBE*

Apart from polonium isotopes that are formed via neutron activation of Bi or produced via (p,*x*n) reactions in the target material, many different additional nuclear reaction products can be present in the liquid metal, including spallation products from the spallation target of an ADS and fission products released from defective fuel elements (see Section 5.1). In order to be able to reduce the potential hazards caused by these nuclear reaction products during the operation of nuclear heavy liquid metal facilities, it may be useful to have methods for their removal from the liquid metal at hand. Therefore, the behaviour of a wide spectrum of different elements in the alkaline liquid-liquid extraction process was studied using qualitative experiments with irradiated Pb, Bi and LBE samples from various sources, containing radionuclide mixtures that may be considered typical of real spallation systems and also contain some important fission products.

A Pb sample weighing 42.7 mg originating from Target 4 of the PSI SINQ spallation neutron source was fused with 355.5 mg of NaOH/KOH at 350°C for 0.5 h under stirring in a nitrogen atmosphere. Additionally, a sample of 3.04 g Bi irradiated with ^{40}Ar ions at the PSI Philips cyclotron was fused with 1.03 g of the eutectic alkaline mixture for 2 h under similar conditions. Finally, 462.3 mg of proton irradiated LBE from the experiment at the CERN-ISOLDE facility (see Section 5.3.1.2) was fused with 0.9 g of eutectic NaOH/KOH and stirred for 1 h at 300°C at a nitrogen atmosphere. The measurement of the distribution of the radionuclides between both phases was performed via γ-spectroscopy. See Heinitz (2013) for experimental details and the applied methods.

The results of this investigation are graphically shown in Figure 5.2.55. A periodic chart of elements is given for each investigated sample. Nuclides detected in the samples are highlighted in different colours representing their individual extraction behaviour: elements marked in green were successfully extracted from the metal (> 90% extraction efficiency), red indicates no or poor transfer to the alkaline phase (< 10% efficiency).

Most elements were found to behave identically in Pb, Bi or their eutectic mixture. Easily extractable are alkali and alkaline earth elements, the 3-D metals, the chalcogens and the lanthanides. Noble metals of the 5^{th} and 6^{th} period of the periodic table such as Ag, Ru, Rh, Ir, Pt, Au, Hg as well as Tl may not be separated by the alkaline extraction technique. In general, the behaviour of each element within the liquid metal/liquid hydroxide extraction system depends upon its oxidation potential relative to that of Pb or Bi. With traces of oxygen present in the system, elements with high affinity to oxygen are oxidised first and are transferred into the alkaline phase. With excess oxygen present,

first all elements with higher oxygen affinity than Pb or Bi are oxidised and transferred to the alkaline phase. After this, oxidiation of the metallic matrix material will start.

For the chalcogens including Po, extraction most efficiently occurs via reduction, not via oxidation. For a more detailed analysis of the processes involved, refer to Heinitz (2013).

Figure 5.2.55: Chart of detected elements qualitatively indicating their extraction behaviour with eutectic NaOH/KOH from irradiated (a) Pb; (b) Bi; (c) LBE

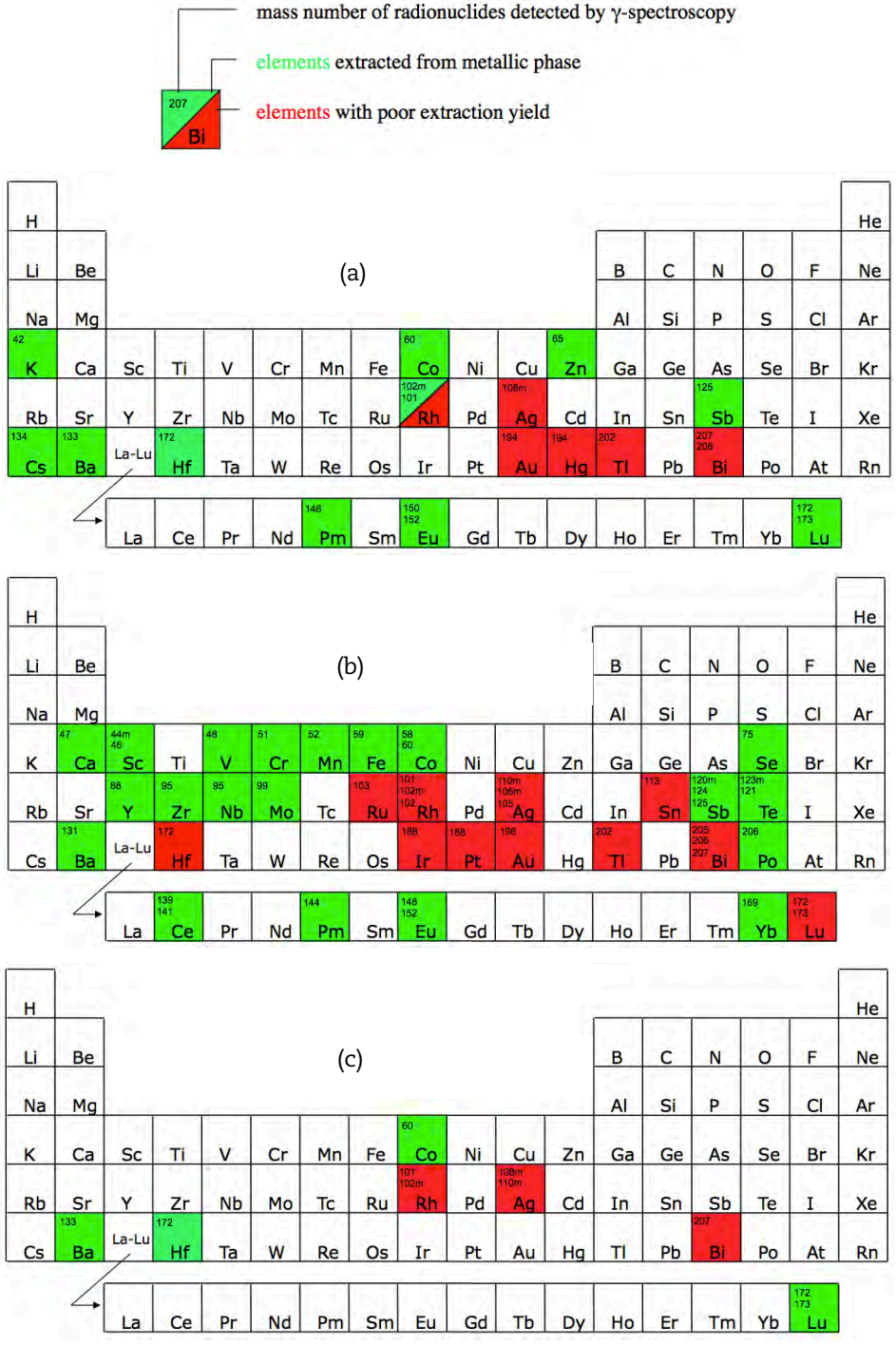

5.2.5 *Removal of polonium from contaminated surfaces*

A method to remove polonium contamination without using solvent or liquid was studied in Obara (2001, 2002, 2003, 2004a, 2005d) and Miura (2003, 2004a, 2005b, 2006). In the described experiments, polonium that is adhered on a material surface, e.g. quartz or stainless steel, is released by heating the contaminated material under vacuum. The released polonium was collected in a cold trap. The experimental results showed that the polonium could be removed by heating at 500°C, but other non-radioactive material could not be removed by the heating. It is stated that the polonium collected in the cold trap has to be cooled to avoid its release from the trap, probably caused by the "abnormal" polonium volatilisation effects discussed in Section 5.2.1.1.5.5.

5.2.6 *Solubility of impurities in liquid lead, bismuth and LBE*

As explained in the introduction, apart from its function as target material and heat transfer medium, LBE in a liquid metal spallation target acts as a solvent and reaction medium for nuclear reaction and corrosion products. In consequence, the solubility of elements and compounds in the liquid metal plays an important role in the understanding of impurity behaviour within a liquid metal target or reactor system. To obtain a consistent set of solubility data and close the gaps concerning experimental data, solubility data for elements in Pb and Bi were recently calculated in the framework of the European ADS project EUROTRANS, based on thermodynamic relations and data obtained using a semi-empirical method (Neuhausen, 2007). The results were compared with literature data and the consequences for a liquid LBE target were discussed.

Data for the solubility of many elements in Pb, Bi and LBE that have been extracted from different sources are compiled in Courouau (2003). Generally, much more data are present for the solubilities in the pure metals lead and bismuth, while only few data for the solubility of metals in LBE are reported. The latter are restricted to ten metals comprising iron and other typical alloying materials of steels. These values are used in Neuhausen (2007) for comparison with results of calculations.

Figure 5.2.56 shows a comparison of solubility data available in the literature and typical overall concentrations that were expected in the liquid LBE spallation target MEGAPIE, based on the nominally foreseen irradiation, i.e. approximately 900 kg of LBE irradiated for 200 days with 1.4 mA of 575 MeV protons (Zanini, 2005). It is obvious that there is a substantial lack of experimental data, especially for those elements that are primarily produced by spallation and fission reactions.

From chemical equilibrium considerations, the following equations were derived for the solubilities of elements *A* in a liquid metal *B*, distinguishing two cases, where the solute is in equilibrium either with the pure solid metal:

$$\ln x_A = \frac{(\Delta S_{melt}A_S + \Delta S_{melt}B_S + \Sigma\Delta S_{trans}A_S + \Delta\overline{S}_{ex})}{R} - \frac{(\Delta H_{melt}A_S + \Delta H_{melt}B_S + \Sigma\Delta H_{trans}A_S + \Delta\overline{H}_{mix}AB_l)}{RT} \quad (5.67)$$

or a solid intermetallic compound with the solvent element:

$$\ln x_A = \frac{1}{yRT}\left[-\Delta H_{form}\,A_yB_{1-y} + y\,\Delta H_{melt}A_s + (1-y)\Delta H_{melt}B_s + y\,\Delta H_{mix}AB_l + y\,\Sigma\Delta H_{trans}A_s\right] + \frac{1}{yR}\left[-\Delta S_{form}A_yB_{1-y} + y\,\Delta S_{melt}A_s + (1-y)\Delta S_{melt}B_s + y\,\Delta\overline{S}_{ex} + y\,\Sigma\Delta S_{trans}A_s\right] \quad (5.68)$$

with x_A mole fraction of the solute *A* in the solution;

y stoichiometric coefficient of *A* in a solid compound with the solvent *B*, A_yB_{1-y};

R universal gas constant;

T absolute temperature;

$\Delta H_{melt}\ A_s$, $\Delta H_{melt}\ B_s$ molar enthalpy of melting for pure solid elements *A* and *B*;

$\Delta \overline{H}_{mix} AB_l$ partial molar enthalpy of mixing of liquid element *A* with liquid element B saturated with element *A*;

$\Delta S_{melt}\ A_s$, $\Delta S_{melt}\ B_s$ molar entropy of melting of pure solid elements *A* and *B*;

$\Delta \overline{S}_{ex}$ partial molar excess entropy of the solution;

$\Delta H_{form} A_y B_{1-y}$ enthalpy of formation of the solid compound with composition A_yB_{1-y};

$\Delta S_{form} A_y B_{1-y}$ entropy of formation of the solid compound with composition A_yB_{1-y};

$\Sigma \Delta H_{trans}$ enthalpies for the solid state phase transformations of the elements;

$\Sigma \Delta S_{trans}$ entropies for the solid state phase transformations of the elements.

Details of the derivation of these equations, including assumptions, simplifications and limitations of their use are discussed in Neuhausen (2007).

5.2.6.1 *Results of solubility calculations for the elements of Group 1 to 16 in liquid lead, bismuth and LBE*

Using the equations given above, the solubilities of the elements of Group 1 to 16 of the periodic table in liquid lead and bismuth were calculated. For these calculations, the enthalpy and entropy values for phase transitions and melting were taken from literature (Barin, 1995). The excess entropies and formation entropies had to be neglected (set to 0) since generally no literature data were available. The enthalpies of mixing and formation were calculated using the semi-empirical Miedema model. For a detailed description of the Miedema model, its applications and limits we refer to the extensive monograph of de Boer (1988). This monograph also contains the parameters for elements from Group 1-15 of the periodic table of the elements used in Neuhausen (2007). An extension to the elements of Group 16, i.e. the chalcogens, is described in Neuhausen (2003). The elements of Groups 17 and 18 (halogens and noble gases) are not covered by the model and are therefore not treated. For the estimation of solubilities in LBE, interpolations were performed on the log(x) values obtained for the two metals Pb and Bi, giving the two metals a weight according to their mole fraction in the eutectic alloy, i.e. 0.45 and 0.55.

Figure 5.2.57 gives graphical representations of the results of solubility calculations for elements in LBE obtained by interpolation of the results obtained for pure lead and bismuth at 500 and 800 K. These temperatures correspond to a range expected for operating conditions of future ADS, spallation target systems or liquid-metal-cooled reactors. The figure compares the few data listed as experimental data in Courouau (2003) (solid squares) with the results of calculations, both for elements that are expected not to form compounds with the target material (open circles) and those that are known as compound formers at least with one of the elements Pb or Bi (open triangles). The concentrations of nuclear reaction products expected for the nominal MEGAPIE irradiation of 200 days with 1.4 mA of 575 MeV protons as calculated using FLUKA/ORIHET are indicated by crosses (Zanini, 2005). Here, it must be pointed out that for long-term irradiations considered for ADS targets, much higher concentrations of impurities can be reached. The reliability of both experimental and calculated data are discussed in detail in Neuhausen (2007). The results of solubility calculations from Neuhausen (2007) are compiled in Appendix 5.4.3 of this chapter.

Figure 5.2.56: Comparison of literature data on the solubility of elements in Pb, Bi and LBE at 600 K and the concentrations expected for the originally foreseen MEGAPIE irradiation

Concentrations are given as the logarithm of the mole fraction x calculated from the results of FLUKA/ORIHET simulations (Zanini, 2005)

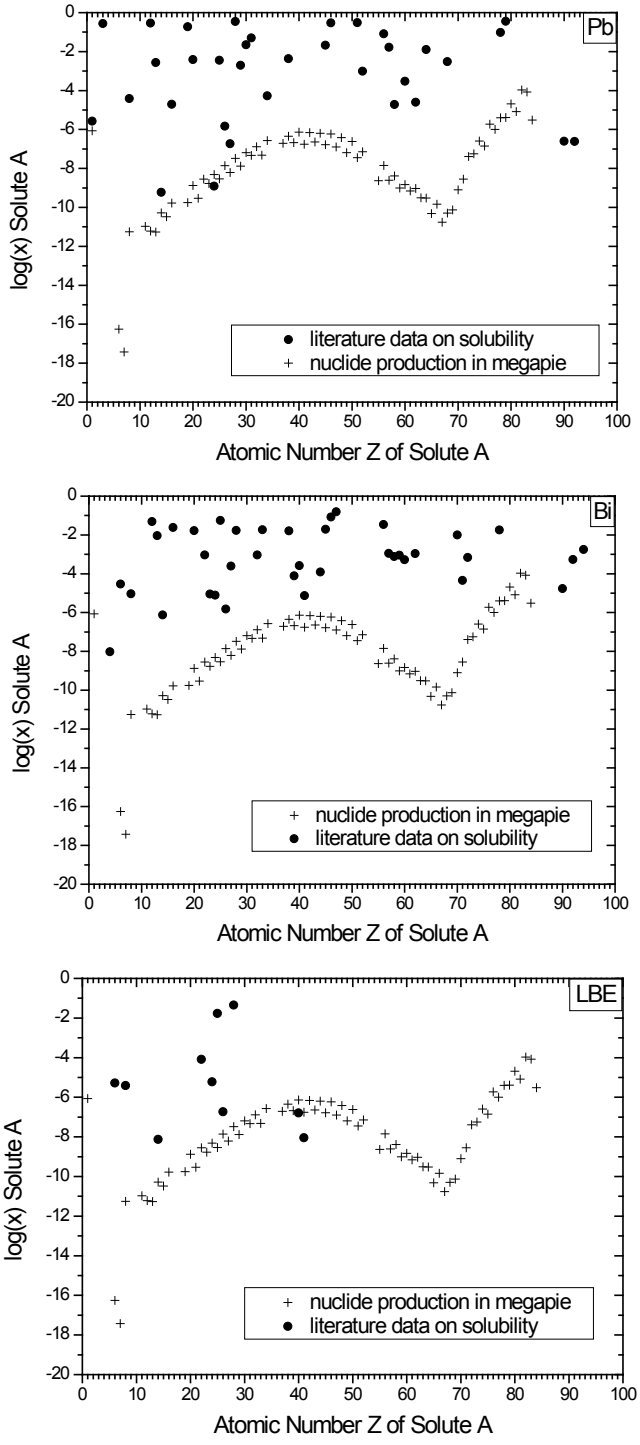

Source: Literature data on solubility from Courouau (2003).

Figure 5.2.57: Comparison of literature data (solid squares) on solubility of elements in LBE (Courouau, 2003) with calculated values for non-compound-forming (open circles) and compound-forming (open triangles) elements at 500 and 800 K

Calculated solubilities for LBE were obtained by interpolation; concentrations expected for the originally foreseen MEGAPIE irradiation (crosses) were calculated from the results of FLUKA/ORIHET simulations (Zanini, 2005)

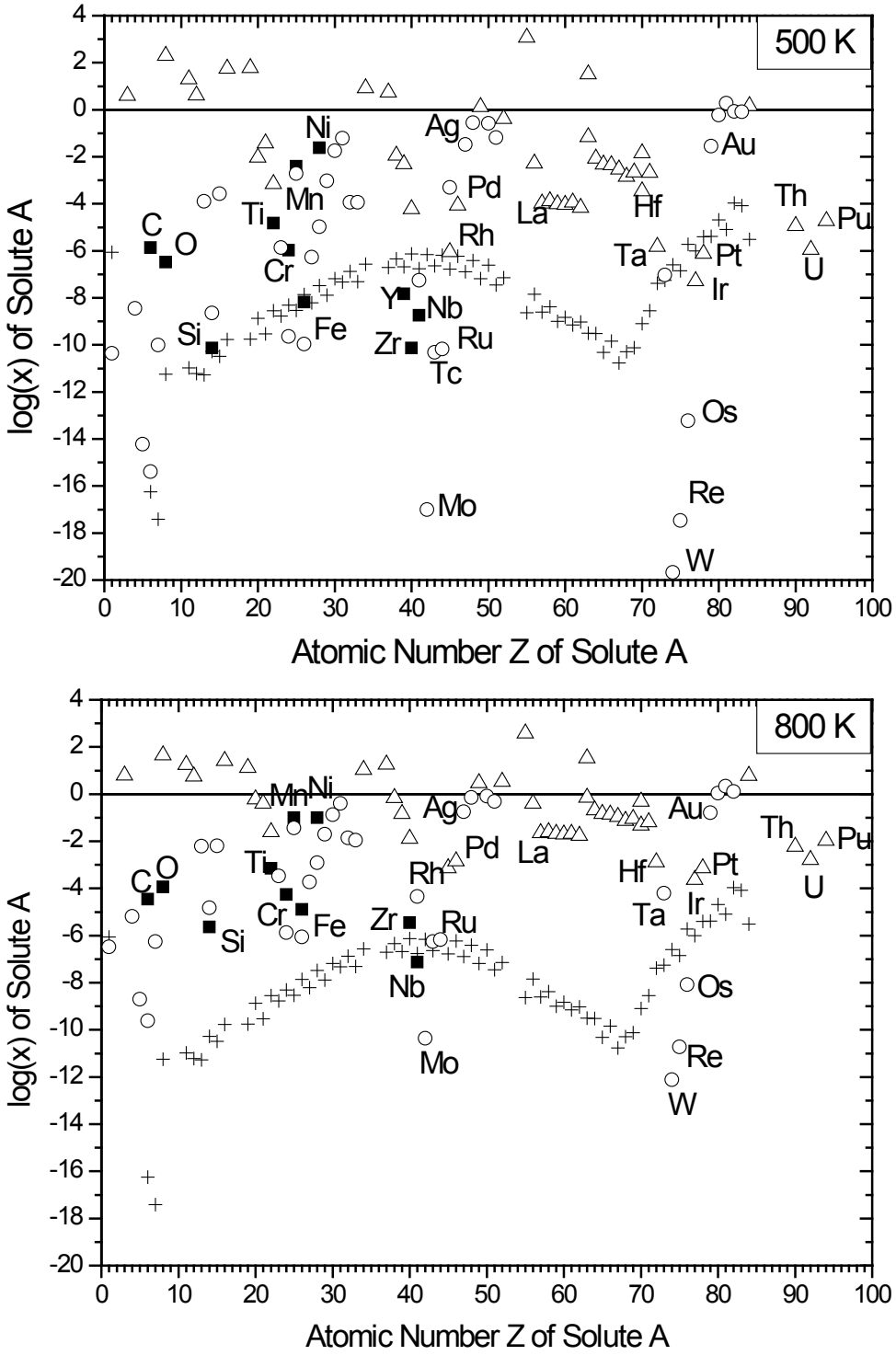

5.2.6.2 *Conclusions from the results of solubility calculations for nuclear systems*

Consequences that arise from the consideration of both literature and calculated data affect both the construction materials choice for target and reactor systems as well as the assessment of nuclear reaction product behaviour. For the construction materials, their solubility in LBE determines their resistance against dissolution in the liquid metal. Here it becomes clear that iron-based alloys are clearly preferable in comparison to nickel alloys. Alloying components can be expected to enhance or decrease corrosion resistance according to their solubility in the liquid metal. One example for this kind of behaviour is the known leaching of nickel from steels in LBE (Shrier, 1994) (see also Chapter 6). In comparison, Figure 5.2.57 indicates that alloying of refractory metals such as molybdenum or tungsten should increase corrosion resistance. Of course, in addition to the fundamental property of solubility in the liquid metal, the kinetics of corrosion processes will be greatly influenced by the presence of surface layers and their stability under the given operating conditions. The influence of alloying components on dissolution processes will also depend on their incorporation in intermetallic phases and its influence on the alloy microstructure. Therefore, the present data can only serve as a fundamental base for construction materials choice.

Concerning the behaviour of nuclear reaction products, it has to be noted that the operating conditions such as temperature, temperature gradients as well as changes in concentration under continuous irradiation will have a strong influence. Figure 5.2.57 indicates that the solubilities of some refractory metals such as Nb, Mo, Tc, Ru, W, Re, Os in LBE are predicted to be very small. Therefore, for these metals the solubility limit can already be reached with relatively short irradiations such as MEGAPIE. For these metals, precipitation could be possible, especially at relatively cold spots in the system. For the remaining d-metals the situation is less clear and will depend strongly on factors such as temperature, concentration, oxygen potential, etc. For most of the main group metals, Figure 5.2.57 indicates that the solubility limit will probably not be reached even in a long-term irradiated ADS target.

5.2.7 *Polonium migration and surface enrichment in solidified LBE*

The behaviour of polonium in solidified LBE may be of interest in the context of target or reactor coolant handling after operation and for final disposal. Literature indicates that the distribution of polonium in irradiated LBE samples becomes inhomogeneous after some time (Obara, 2004b; Muira, 2004b). In a related study, a method has been developed to estimate the detailed polonium depth distribution in irradiated solid LBE (Obara, 2004b; Mira, 2004b). The method employs a simple physical model and a mathematical unfolding technique to derive the depth distribution of polonium in the near surface region of irradiated LBE samples from their α-ray spectra. The results obtained for the specimen investigated shows two maxima of polonium concentration, one sharp maximum more or less directly on the surface of the sample and one broader maximum a few μm below the surface.

In the following section we will describe the recent work performed with respect to the distribution and surface enrichment of ^{210}Po in LBE samples irradiated in SINQ at PSI within the EU projects EUROTRANS, GETMAT and ANDES. Details of these experimental studies can be found in von Rohr (2008) and Müller (2009). The phenomenon of polonium surface enrichment and migration is, however, still far from being understood. Since polonium surface enrichment may lead to strongly enhanced transfer to the vapour phase by recoil mechanisms, the phenomenon is currently under investigation at PSI.

Polonium-containing LBE samples were produced by neutron irradiation of pieces of LBE in SINQ. The samples were stored at room temperature for two years. Afterwards, the distribution of ^{210}Po in the samples was determined by successively etching off a certain amount of the sample surface and analysing its ^{210}Po content by liquid scintillation counting (LSC) (von Rohr, 2008). Figure 5.2.58 shows the variation of the ^{210}Po concentration

in a typical sample as a function of mass remaining in the successive dissolution process. The diagram clearly shows that ^{210}Po is enriched in the surface region, while in the inner part of the sample its concentration remains more or less constant. The thickness of the enriched layer is estimated to be in the order of 20 μm, based on the sample shape and weight loss. The impetus for the segregation and its kinetics are topics for further study.

Figure 5.2.58: ^{210}Po activity concentration in LBE fractions successively dissolved from a ^{210}Po-containing LBE sample as a function of the amount of material that was etched off

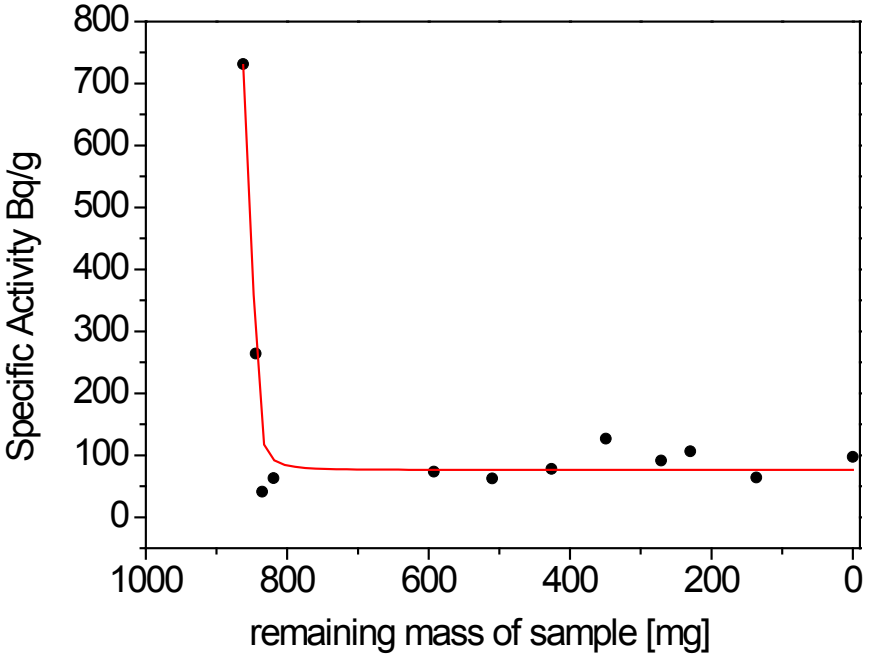

Source: von Rohr (2008).

For the preparation of homogenous polonium-containing LBE samples used in further studies, a method for homogenisation of the Po distribution was devised. Homogeneity can be achieved by heating the samples at 500°C in an H_2-atmosphere under mild agitation. Samples treated in this manner no longer show a surface enrichment of ^{210}Po immediately after solidification.

5.2.7.1 *Kinetic studies on the surface enrichment of polonium in solidified LBE*

The kinetics of polonium migration to the surface in natural lead samples has been discussed in several reports by Zastawny (1989, 1992) and Patrizii (2008). These reports however do not give a completely consistent picture. The kinetics of migration of polonium to the surface of solidified LBE samples was recently studied at PSI by means of α-spectroscopy using neutron-irradiated LBE samples. Samples that initially showed a homogeneous polonium distribution were obtained by melting in an H_2 stream at 600°C for 30-60 minutes. To study the variation of the surface α-activity with time at room temperature, these samples were placed into an α-measuring chamber directly after homogenisation, where spectra were recorded successively for periods up to 12 days using a batch routine (von Rohr, 2008). The change of the recorded α-spectra with time is illustrated in Figure 5.2.59. The spectra show a strong increase of the α-counts measured in the range between 4.9 and 5.3 MeV, indicating an enrichment of ^{210}Po in a near-surface layer of the LBE samples, ranging approximately 2 μm below the surface. Figure 5.2.60

shows the increase of the α-counts in this energy range, compared to the counts measured at starting time, as a function of time. A fit of this function, using a simplified model for diffusion out of a spherical sample (Crank, 1992), gives a diffusion coefficient in the order of 10^{-11} cm^2 s^{-1}. The nature of the diffusion process is still unclear. The enrichment of polonium in the grain boundaries of various p-group metals such as lead and bismuth has been observed (Tammann, 1932), suggesting a grain boundary diffusion mechanism.

Figure 5.2.59: Variation of α-spectra recorded from a solidified and homogenised ^{210}Po-containing LBE sample with time off

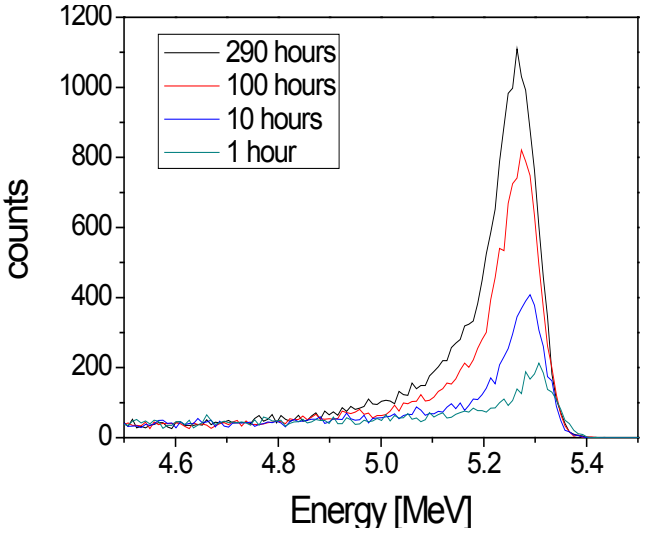

Source: von Rohr (2008).

Figure 5.2.60: Increase of surface activity in ^{210}Po-containing LBE sample as a function of time off

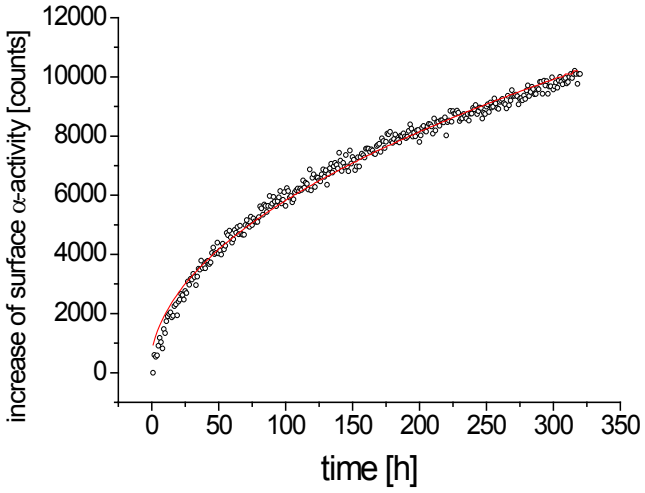

Source: von Rohr (2008).

However, fast impurity diffusion processes that do not involve grain boundaries were also observed in lead (Kärger, 1998). In the eutectic alloy, the situation is still more complex due to the presence of crystallites of two distinct phases. Dedicated experiments to study the diffusion mechanism of polonium in LBE are currently being performed at PSI.

Addendum

The work on diffusion of polonium in LBE mentioned above was completed while this chapter was undergoing the peer review process. The results can be found in Heinitz (2013).

In a subsequent series of experiments, the increase of surface radioactivity of Po-containing LBE samples with time was studied at different temperatures and under various gas blankets (Müller, 2009). The change of the recorded surface radioactivity of such samples with time at different temperatures is illustrated in Figure 5.2.61. It can be seen that the activity increases rapidly within the first days and almost doubles within four weeks for each measured temperature. Saturation was reached only for samples stored at 100°C, whereas at room temperature and 60°C the activity was still rising after 25 days. This effect is explained by an enhanced segregation rate at higher storage temperature, since the migration is expected to be a thermally activated process. In comparison to the first migration experiments described above, a significantly slower migration at room temperature was observed. Generally, it turned out to be very difficult to prepare samples having reproducible surface properties. scanning electron microscope (SEM) pictures of inactive LBE spheres show different surface patterns, even when the samples were cooled in the same manner (see Figure 5.2.62). Therefore, the initial Po concentration at the surface of the samples could also vary due to subtle changes within the solidification process. This can explain the different initial surface activities of the three samples in Figure 5.2.61 that were prepared under similar conditions and hence show similar bulk activities. These discrepancies originating from the crystallisation process could also cause changes in the migration rate. Experimental procedures to produce samples with reproducible surface activities and a defined micro-structural state must be developed for reliable experimental examination of the polonium migration process in LBE.

Figure 5.2.61: The increase of surface activity of LBE samples stored in air at different temperatures as a function of time

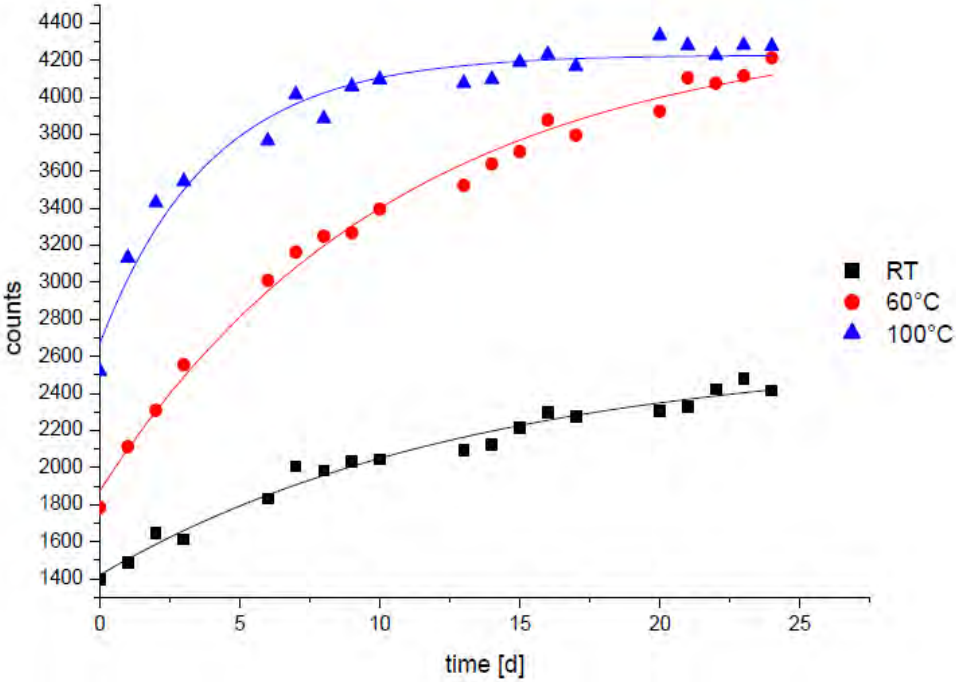

Source: Müller (2009).

Figure 5.2.62: Different surface structures of various LBE samples solidified under virtually equivalent conditions

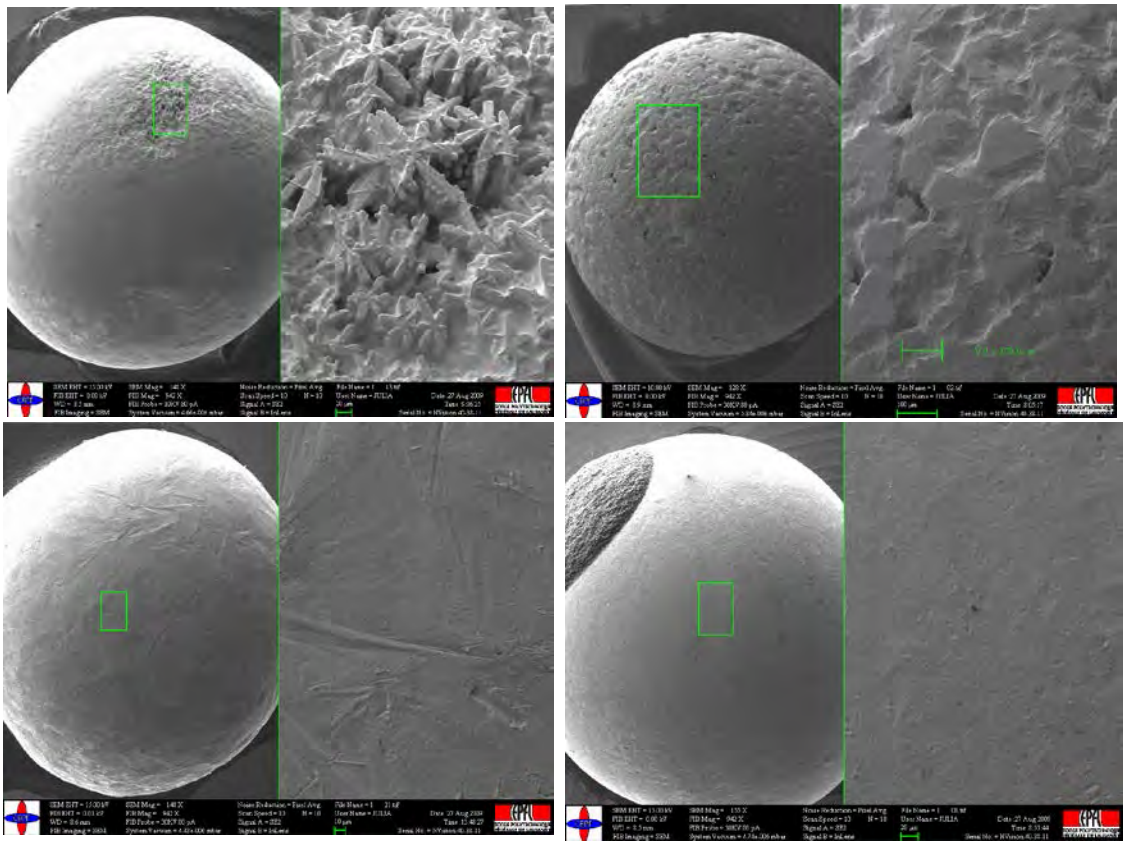

Source: Müller (2009).

5.2.7.2 *Solid state characterisation of LBE samples*

To gain a more thorough understanding of the driving force and mechanism of the polonium migration process observed in solidified (LBE) leading to an inhomogeneous polonium distribution, some basic bulk and surface solid state analyses were performed (von Rohr, 2008). For this purpose, polonium-containing samples of LBE were prepared in the method described above. The samples show a bright metallic lustre directly after homogenisation in a hydrogen flow. However, after some hours of storage under ambient air the appearance of the surface changes to a dull grey look. After months or years of storage, a surface layer is clearly visible (Figure 5.2.63). For a phase analysis, such a sample was mounted on a Seifert 3000P powder diffractometer equipped with Cu-anode and multi-layer optics. A diffractogram was recorded in the θ-2θ mode using Cu-Kα radiation. For chemical and micro-structural analysis, a similar sample was studied using a scanning electron microscope (SEM) equipped with an energy dispersive X-ray spectrometer (EDX). For this purpose, a part of the surface layer was mechanically removed, and EDX analysis was performed on both cleaned and not cleaned areas of the samples. An EDS-mapping of Pb and Bi was performed on the cleaned part of the surface to obtain information about the microstructure of the bulk material.

Figure 5.2.64 shows an X-ray diffractogram of an aged neutron-irradiated LBE sample. Additionally to the lines of a lead-rich Pb_7Bi_3-phase and a Bi-phase, lines of PbO are clearly visible. In agreement with this fact, an EDS analysis of the unmodified surface shows the presence of a significant amount of oxygen, while a scratched surface only

shows the constituents of the eutectic. An EDS mapping of a surface cleaned in this way (Figure 5.2.65) shows both grains of a lead-rich and a Bi-rich phase in agreement with the results of X-ray diffraction and the phase diagram known from literature (Hultgren, 1973). Already in a very early report on Po-distribution in solidified metals (Tammann, 1932) an enrichment of Po in grain boundaries of metals was observed after crystallisation.

These results indicate that a grain boundary diffusion process may explain the fast diffusion of Po in LBE, and the binding of Po in a surface oxide layer that is formed on LBE samples is a possible driving force for diffusion. However, a more careful analysis of the process is mandatory to elucidate the diffusion behaviour of Po in LBE.

Figure 5.2.63: Aged sample of neutron-irradiated LBE, showing surface oxide layer

Source: von Rohr (2008).

Figure 5.2.64: X-ray diffractogram of a neutron-irradiated LBE sample after several years of storage under air

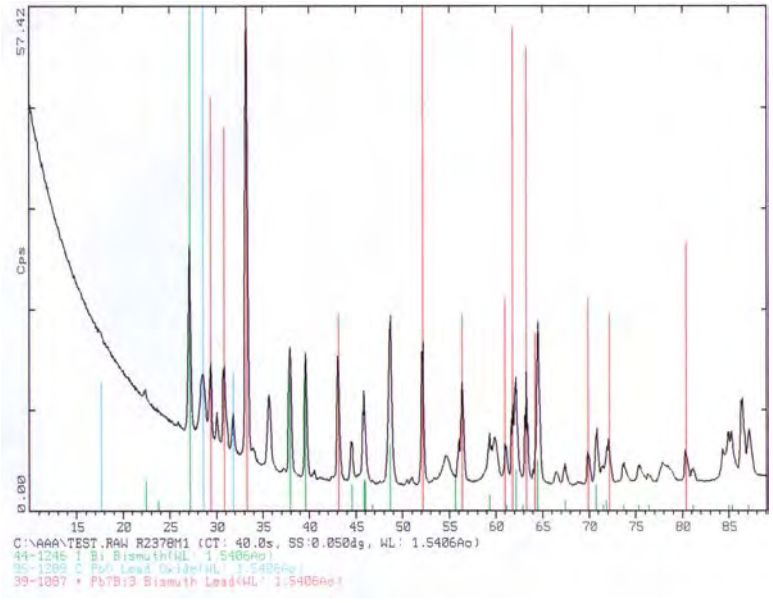

Source: von Rohr (2008).

Figure 5.2.65: EDS map of a scratched surface of a neutron-irradiated LBE sample

Image size approximately 80 × 100 μm; colours indicate the concentrations of the respective elements increasing from blue over green and yellow to red

Lead distribution (Lα) Bismuth distribution (Lα)

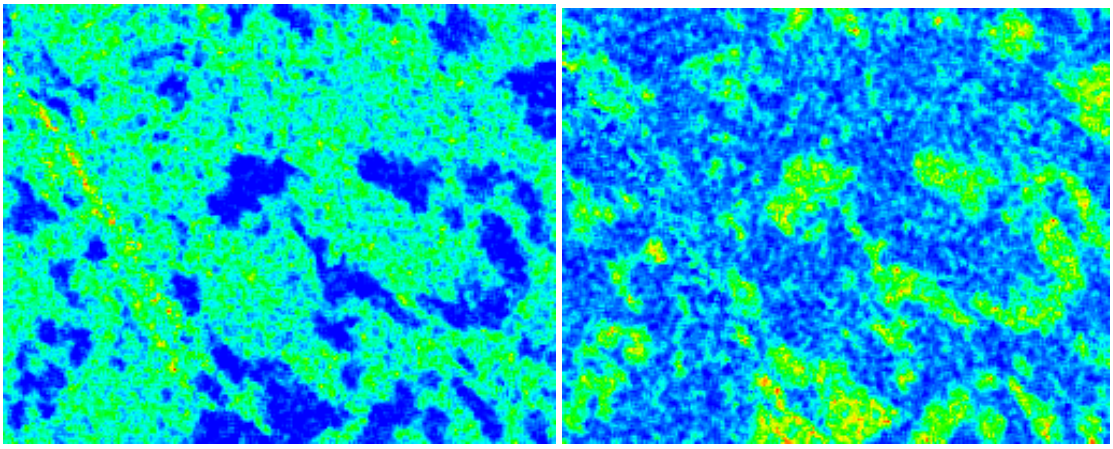

Source: von Rohr (2008).

5.2.8 *Evaluation of thermochemical data for binary systems by means of the semi-empirical Miedema model*

As explained in the introduction of this chapter, a complete set of thermodynamical data of a system comprising more than 80 components such as a lead-alloy-based liquid spallation target will be impossible to retrieve. On the other hand, a consideration of only binary interactions may already provide a means to allow the prediction of the behaviour of certain groups of elements in a liquid metal, neglecting multinary interactions. The Miedema model allows a convenient and – compared to more sophisticated quantum mechanical methods – extremely fast estimation of enthalpy values in binary systems of metals and semi-metals, such as the enthalpies of formation of binary compounds and enthalpies of mixing and solution. The method was used in the preparatory phase of the MEGAPIE project to facilitate an estimation of the strength of interaction of polonium with other metallic and semi-metallic elements. Since thermochemical data for polonium compounds are generally lacking, the Miedema method (de Boer, 1988) provides a valuable tool for their estimation. For the purpose of obtaining thermochemical data for binary metal-polonium systems, first a parameter set for the elements of the chalcogen group had to be elaborated (Neuhausen, 2003). Using this parameter set, thermochemical properties such as enthalpies of formation of solid metal chalcogenides, partial molar enthalpies of solution of chalcogens in liquid and solid metals, partial molar enthalpies of evaporation of the chalcogens from liquid metal solution into the monoatomic gaseous state, partial molar enthalpies of adsorption of chalcogenides on metal surfaces at zero coverage and partial molar enthalpies of segregation of the chalcogens in trace amounts within solid metal matrices have been calculated in Neuhausen (2003). These properties are compared with available experimental data and discussed with an emphasis on the periodic behaviour of the elements.

The model calculations show that a semi-quantitative description of the chalcogens' thermochemical properties is possible using the semi-empirical Miedema approach. General trends in the formation enthalpies of metal chalcogenides throughout the periodic table are represented reasonably well by the results of calculations. It should be pointed out that the computed enthalpy values should not be considered as highly

precise data. However, periodic trends and relative stabilities of series of compounds are reproduced well by the calculations. Therefore, the calculated properties can serve as a basis for the prediction of the chemical interactions for metal-chalcogen combinations that have not yet been studied experimentally, e.g. especially for metal polonium combinations. Figure 5.2.66 shows a summary of calculated formation enthalpies of metal polonides of composition $M_{0.5}Po_{0.5}$ and the experimentally known qualitative facts about those metal polonium systems. In general, the agreement is satisfactory. Negative enthalpies of formation are calculated for metal-polonium combinations for which compound formation is observed, whereas positive values are calculated for systems where no reaction is observed. Values for enthalpies of formation of binary compounds, enthalpies of solution, adsorption and segregation obtained for polonium-containing systems using the Miedema model are compiled in Appendix 5.4.3.

Figure 5.2.66: Experimental information and Miedema predictions of the stability of binary polonides throughout the periodic table of the elements

Each box corresponds to the binary system of the specified element with polonium. The atomic number of the element is given in brackets. The boxes are shaded as follows: white boxes = binary system not investigated; horizontally hatched boxes = no reaction is observed between the respective element and polonium; vertically hatched boxes = reaction is observed, but the product is not well characterised; cross-hatched boxes = contradictory evidence from different literature; diagonally hatched boxes = reaction is observed, reaction product characterised by X-ray diffraction or at least melting or decomposition temperature has been determined. Values for the enthalpies of formation of solid compounds of composition $M_{0.5}Po_{0.5}$ calculated using the Miedema model are given for each combination. The box for La(57) can be considered representative for the complete lanthanide series.

The evaluations of thermodynamical data of binary or ternary systems of volatile nuclear reaction products performed in Section 5.2.1 were based on interactions of the elements with the target material only, except for a few cases where oxides of polonium and caesium and the interaction of caesium and iodine were treated. Thus, interactions such as compound formation of the impurity elements among each other have been largely neglected thus far. These interactions can lead to behaviour of the system that is not comprehensible from the consideration of interactions of the impurities with the target/coolant material alone. For example, electropositive elements that – in their pure form – are highly soluble in lead and bismuth may form oxides with the oxygen dissolved in the liquid metal or by reducing the oxide layers on construction materials. These oxides are most probably almost insoluble in the liquid metal. This effect could lead to

precipitation of insoluble compounds and a simultaneous increased attack on the construction material. Such effects naturally become more important for increased operation times, i.e. with increasing overall concentrations of the impurities. Similarly, the behaviour of impurities can be influenced by formation of intermetallic phases.

A consistent and complete set of thermodynamic data for all phases/compounds and gas phase species that could possibly form in a target system is not – and probably will never be – available. It has been proposed however that one could try to obtain reasonable predictions on the typical character of compounds formed by different elements, or at least certain groups of elements, within the target system, based on the knowledge of its total composition (construction materials and their protective layers and impurities, target material and impurities, corrosion behaviour, nuclide production, ingress of gaseous impurities) using a mass balance. In this mass balance, the chemical products will be limited to binary compounds. Formally, of these compounds, the most stable one will be formed until one of its components is completely consumed. In subsequent steps, the next most stable compound is formed and so on, according to the hierarchy of stability of all possible binary compounds. To facilitate such an approach, a consistent set of binary interaction data is required. One possibility to quickly develop such a data set is to calculate formation enthalpies of all binary combinations of elements that can be treated by the Miedema model. Such calculations have been performed in Neuhausen (2007) for equimolar binary compounds of all elements of Groups 1 to 16. In the following section, we will briefly discuss the results.

A map of heats of formation for compounds of composition $A_{0.5}B_{0.5}$ obtained based on the Miedema model in Neuhausen (2007) is shown in Figure 5.2.67. The periodicity of the stability of the compounds is clearly visible. For example, the chalcogenides are particularly stable. Consequently, valleys of stability are found for the atomic numbers Z = 8 (O), 16 (S), 34 (Se), 52 (Te) and 84 (Po), indicated by large negative enthalpies of formation (blue zones) in Figure 5.2.67. The calculated values for these enthalpies of formation of the chalconides become less negative with increasing atomic number of the chalcogen. This result coincides well with the known periodic behaviour of these elements. When one looks at the enthalpies of formation of the chalcogenides with a second element as function of the atomic number of this second element, i.e. all compounds $A_{0.5}B_{0.5}$, where A is a chalcogen and B any other element ranging from Z = 1 to 110, one observes periodic behaviour again. Chalcogenides of electropositive elements, e.g. Group 1 to 4, show exceptional high stability. When one moves to the higher group numbers 5 to 16, the enthalpies of formation become less negative (for O, S, Se and Te) or even positive (for Po). In agreement with the calculations, in most of the binary polonium systems where positive formation enthalpies are calculated, no binary compounds could be prepared as of yet (Landolt-Börnstein, 1991). In contrast to the "valleys of stability" found for metal chalcogenides, there are areas of very large positive values for the calculated values of formation enthalpies, indicating no stable binary compounds, e.g. for combinations of the electropositive metals of Groups 1 and 2 with the refractory metals of Groups 5 to 8. This behaviour is consistent with experimental results on those systems. No information on compounds in these binary systems is found in Hultgren (1973) and only 3 compounds out of 59 binary systems of those metals (all with ruthenium) are mentioned in Landolt-Börnstein (1991).

Thus, though the results of Miedema calculations are only approximate values, they reflect the periodicity of the chemical behaviour of elements well. In a next step, the results can be used to make reasonable predictions about chemical processes within a liquid metal target. While the limitation to binary phases is clearly an over-simplification, it may, together with the data on solubility, give an indication on the specific behaviour of different elements or groups of elements. For example, it seems highly probable that those elements that form very stable oxides that are not reducible by hydrogen will tend to form oxides with impurity oxygen that can be accumulated on surfaces. Such assessments of the probable chemical state of various elements within a spallation

system will at least give a hint on their characteristic behaviour in the liquid metal system. As we shall see in Section 5.3.2, accumulation of electropositive metals, probably in the form of insoluble oxides, does actually occur in liquid metal targets. More detailed predictions using the mass balance calculations discussed above still remain to be done, also including the halogen compounds that are not accessible using the Miedema model. The validity of such predictions could be verified by detailed (radio)chemical analysis of material that represents the complex composition of a spallation system, i.e. the material from the ISOLDE target or finally on LBE samples taken within the post-irradiation examination programme for the MEGAPIE experiment.

Figure 5.2.67: Stability map for all binary combinations of elements from the periodic table accessible by the Miedema model

Stability is judged by the enthalpies of formation for binary compounds of composition $A_{0.5}B_{0.5}$ calculated using the Miedema model. Values for binary combinations containing halogens and noble gases (Group 17 and 18) which are not covered by the Miedema model are depicted with a formation enthalpy of 0

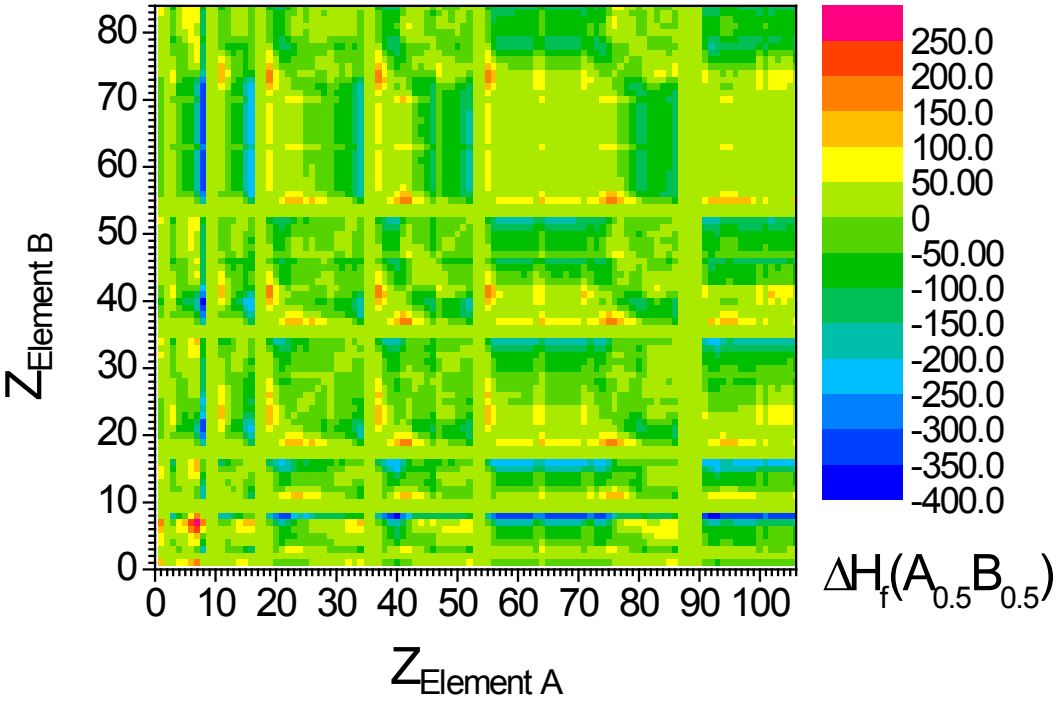

5.2.9 *Summary and conclusions on the review of simple model systems*

The liquid metal used as spallation target material or reactor core coolant in a nuclear system forms a highly complex chemical system with numerous impurity components produced by nuclear reactions as well as left over from the production of the material and incorporated from the construction materials during operation. The system is operated under strongly varying conditions concerning temperatures, liquid metal flow and a high irradiation field, which makes reliable predictions on the chemical behaviour of the micro-components very difficult. A rigorous thermodynamic treatment seems unrealistic, both because of the system's complexity and the lack of complete and consistent thermodynamic data. The first section of the present chapter compiles the information that can be derived from simple model systems that typically contain one element of interest dissolved in lead, bismuth or LBE and in some cases other chemical reagents.

To facilitate predictions on the physical and chemical behaviour, in the first section of this chapter we extensively reviewed the fundamental physicochemical data available for simple binary and ternary model systems, i.e. systems that contain lead, bismuth or LBE and one single impurity element, focused on those impurities that are expected to be particularly hazardous. From these data, it was possible to derive conservative relations for the thermodynamic activity coefficients of the impurities in diluted liquid lead, bismuth and LBE which in turn allow the estimation of their volatility from liquid metal solutions. These data should be crucial for the licensing of nuclear facilities based on liquid lead alloys. Nevertheless, more complete, accurate and reliable data on the volatility of elements in diluted lead-alloy solution should be acquired to facilitate such licensing procedures, especially clarifying the nature of those processes that can result in enhanced polonium volatilisation.

We have also discussed the release of volatiles by evaporation in open systems. Furthermore, the ongoing work concerning the removal of hazardous radioactive elements from the gas phase, from the liquid metal and from contaminated structure materials was presented. Additionally, we discussed the use of thermodynamic data for binary systems obtained using the semi-empirical Miedema model to estimate the solubility of elements in liquid lead, bismuth and LBE and more generally to assess the stability of binary compounds, in particular those of polonium, where no experimental data are available.

Conclusions for ADS systems were drawn concerning the choice of construction materials and processes that may lead to the accumulation and enrichment of elements in specific locations and components of a spallation system.

5.3 Experience from medium- and large-scale experiments

5.3.1 *Measurement of gas and volatile element production yields in a proton-irradiated molten lead-bismuth target in the ISOLDE facility*

The aim of the MEGAPIE project was to demonstrate the feasibility of a liquid lead-bismuth eutectic (LBE) target for spallation facilities at a beam power level of about 1 MW. During the design phase of such an innovative system, many safety aspects must be considered. One of the most important safety issues is related to the production and release of volatile elements during operation.

During the MEGAPIE experiment, volatile elements were produced, which diffused through the LBE and collected in an expansion volume of about 2 litres placed at the top of the target, above the LBE free surface.

In order to be able to license an experiment such as MEGAPIE, it was required to estimate in the design phase the amount of production and release of such gases and volatile elements. This work is particularly complex as we are dealing with a full-scale experiment, in which one has to take into account production, diffusion in the medium and evaporation. As a first approximation, the production yield of volatile elements was determined by Monte Carlo calculations. One can assume that all the produced amounts of volatiles are immediately released. However, this might be a simplification for such a complex target as MEGAPIE.

Following the launch of the ADS concept for nuclear waste transmutation, there has been renewed interest in the study of isotope production following spallation reactions in heavy materials (Michel, 1997; Titarenko, 2002). Experiments performed in inverse kinematics have allowed the investigation over large mass regions of production cross-sections in thin targets (Enqvist, 2001). These experiments, in combination with the further development of Monte Carlo transport codes, have led to a deeper understanding of the spallation process and to the development of new theoretical models (Boudard, 2002; Junghans, 1998; Benlliure, 1998). Production of noble gas isotopes by proton-induced

reactions on lead and lead-bismuth were measured by Leya (2005, 2006). Measurements were performed using the stacked foil technique (Leya, 2005; Gloris, 2001). In-flight measurements in inverse kinematics also allowed to measure short-lived radioisotopes (Enqvist, 2001). In parallel to new available data, development of spallation models has taken place.

In the case of an ADS target where production of isotopes originates in a large volume of LBE, it is important to consider not only the production of volatile elements, but also the kinetics of their release from the LBE volume. Both aspects are important: it is important to know the total amount of radioactive species produced inside the LBE volume, even if they are not released at a given temperature, to estimate the dose rates in case of accidental increase of the target temperature (following an accident) involving a higher release. It is also important to know the fraction of the volatile radioactive species produced in the target that is released to the cover gas in normal operating conditions because the amount and type of radionuclide inventory must be handled by a specially designed target ancillary system during operation.

Apart from gaseous elements, it is also important to measure the release of nuclides of less volatile elements, such as Br, I, Cd, At and Po. Astatine has polonium daughters which are highly radiotoxic. Polonium isotopes $^{208\text{-}210}$Po are α-emitters with long half-lives. Polonium isotopes will also be produced as spallation products inside the target but are not expected to be released in substantial amounts at the MEGAPIE operating temperatures based on the thermodynamic data compiled in Section 5.2.1. A more detailed discussion of releases in the case of accident scenarios for the MEGAPIE target will be presented in Section 5.3.4.

The degree of volatility is different for each element; moreover, the dimensions of the MEGAPIE target make it difficult to predict how much will be released, even for the noble gases, since the release may be delayed by diffusion in the large and geometrically complex target system. The behaviour of the other volatile elements is even less clear, since some of them might be trapped in the LBE or form chemical compounds. To study the production and release of volatile elements from an irradiated LBE target, a preparatory experiment with a molten Pb-Bi target was performed at the ISOLDE facility at CERN with proton beam energies of 1 and 1.4 GeV.

5.3.1.1 *The ISOLDE facility and target*

The proton injector for ISOLDE is the PS Booster (PSB). The PSB is an assembly of four small synchrotrons. The protons are delivered to the PSB from a linac and accelerated to 1 GeV or 1.4 GeV before being injected into the proton synchrotron (PS) or sent to the ISOLDE facility. The protons in the PSB are accelerated in pulses with one pulse being delivered every 1.2 seconds. One super-cycle to the PS is a multiple of this interval and for the present experiment it was of 14.4 or 16.8 seconds; up to half of the pulses could be used by ISOLDE. The number of protons in each pulse was between 10^{12} and 10^{13} during the experiment.

Drawings showing the dimensions and the internal structure of the actual ISOLDE target are shown in Figure 5.3.1. The target consisted of a Ta container filled with LBE. The container was a cylinder about 20 cm long, with an outer diameter of 2 cm and walls of 0.5 mm thickness. The beam entrance window was also made from Ta metal and had a spherical shape. The thickness of the beam entrance window is up to 6 mm to mitigate the effects of the pressure wave generated by the proton beam. About 550 g of LBE was put inside the Ta container. The target was heated allowing the LBE to reach temperatures up to 600°C. As shown in the figure, above the cylinder a chimney is mounted to allow released isotopes from the target to diffuse out of the target and to be successively ionised and accelerated to 30 or 60 kV by an ion source. A helix was placed inside the chimney to avoid splashing of target material into the ion source, which would lead to serious damage.

Figure 5.3.1: Drawings of the ISOLDE target

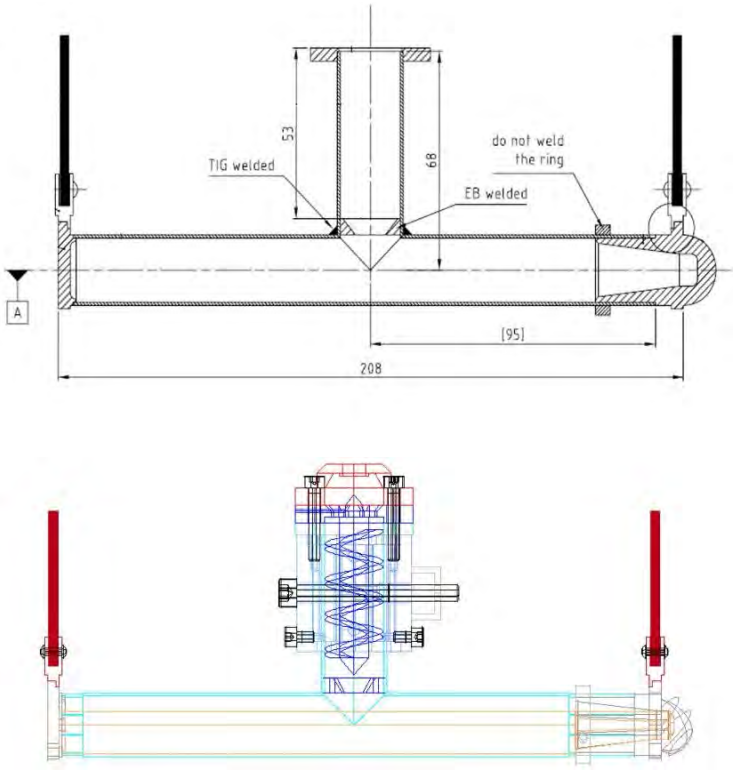

Nuclides formed in the LBE target during irradiation first diffuse out of the target material, evaporate and then effuse into the transfer line and further on to the ion source. The ion source ionises the produced nuclides so that they can be controlled and accelerated in an electric field. The efficiency of the ion source varies with both element number (Z) and the mass of the respective isotope. The goal is to produce a beam as pure as possible. Because of the different physical and chemical properties of the produced elements, such as volatilities, adsorption enthalpies and ionisation energies, the ion source and properties of the transfer line (e.g. material and temperature) are chosen so that the separation of the wanted radioactive element is optimised.

After ionisation, the produced radioactive nuclides are directed to a mass separator. The mass separator, together with the ion source, aims to produce a clean beam consisting of one selected mass. The General Purpose Separator (GPS) is one of two mass separators at ISOLDE. It can deliver three beams, of varying mass within 15%, to the General Low Mass (GLM) station, General High Mass (GHM) station and into a third beam line leading to other experiments at ISOLDE, at the same time.

The ion beams can be monitored along the target, separator and beam transport lines, by means of Faraday cups that can be inserted in the beam. Such Faraday cups have been used during the experiment to measure the intensity of some ion beams, and to measure the transmission and ion source efficiencies.

5.3.1.2 *Description of the experiment*

Various measurement techniques are available at ISOLDE, which can be subdivided in two categories according to the half-life of the nuclides measured. Off-line measurements using γ-spectroscopy are used for isotopes with half-lives from about 5 minutes to a few weeks. For on-line measurements two procedures were used to collect data: the Faraday cup and the tape station measurement. Measurements by Faraday cups are most useful

for measuring stable isotopes or long-lived radioisotopes. The tape station measures the release yield of radioisotopes with a very short half-life. After collection of the radioactive ion beams on the tape, it is transported to a germanium detector which carries out the on-line measurements.

Measurements were performed in two different runs each lasting about one week. In the first run, the typical irradiation conditions were 10^{13} protons per pulse (ppp), 1 pulse per super-cycle (pps), super-cycle length 16.8 seconds. For the second measurement run, the irradiation conditions were changing during the measurements. The beam intensity was about $0.9 \cdot 10^{13}$ ppp, the pulses per super-cycle were varying between 1 and 6 pps, and the super-cycle length was 14.4 seconds. Overall, the target took $1.3 \cdot 10^{17}$ protons in the first run with E = 1.4 GeV, and $1.3 \cdot 10^{18}$ protons in the second run, with E = 1.0 and 1.4 GeV.

5.3.1.3 *The release process*

The release of the volatile elements from a molten metal target is a complex process (Köster, 2000). Volatile species produced by spallation in the target are not emitted instantaneously but through diffusion to the molten metal surface, evaporation from this surface and then through effusion out of the container. The diffusion in the bulk material depends on the temperature and on the chemical properties of the produced elements. Following the diffusion through the bulk material, the elements evaporate from the liquid metal surface and effuse through the target container, the transfer line and the ion source. In a simple approximation, the evaporation rate can be assumed proportional to the vapour pressure of the given element over its dilute solution in the liquid metal, as outlined in Section 5.2.1.2 of the present chapter. The effusion time is given by the number of wall collisions times the average time between two wall collisions. For a real target and ion source unit the total release time is given by the sum of the diffusion, evaporation and the effusion times.

Solid targets are typically optimised to minimise diffusion times, e.g. by use of stacked thin metal foils or powders as targets and by operating at very high temperatures (< 2 000°C). At these high temperatures, evaporation will be almost instantaneous. For such targets typical release time constants of 1 second or less are reached (CERN, n.d.; Butler, 2011; Bergmann, 2003). For liquid metal targets, typically lower temperatures are used (e.g. in case of LBE avoiding significant evaporation of the target material limits the temperatures to about 700°C maximum), and the diffusion path cannot be optimised by using thin or fine-grained material. Because of the lower operating temperature, the evaporation rate may become the limiting factor for release. As a consequence, the average release time of volatile products from liquid targets is typically of the order of minutes, and decreases with increasing temperature.

The individual behaviour of different elements in the release process can be very different due to the specific diffusion behaviour of individual elements in the liquid material, different volatility of the elements in dilute liquid metal solution and other effects such as surface effects at the liquid metal surface which may inhibit or slow down the diffusion or evaporation process. Furthermore, the effusion behaviour depends on the adsorption interaction of the released atoms with the walls of the target container and transfer line. Thus it is element-specific as well.

All these processes combined lead to a delay in the release of volatile nuclides. Since it is difficult to disentangle the respective importance of diffusion, evaporation and effusion from the experimental data, we will take into account the combined effect by discussing a retention time that is characteristic for each chemical element in the target. This characteristic retention time can vary over a wide range of time scales for different chemical elements.

In the following, we will compare the amounts of radionuclides released from the liquid LBE target in the experiment described above, expressed as release yield (in units of

atoms per proton charge delivered to the target), to the amounts predicted to be produced under the given irradiation conditions using nuclear Monte Carlo codes, expressed as production yield (also in units of atoms per proton charge delivered to the target).

As a consequence of the complexity of both the nuclear processes involved in the production and decay of these radionuclides and the release process itself, interpretation of the results is complicated. For example, in cases where the experimentally determined release yield of a radionuclide is smaller than the predicted production yield, this may be caused by incomplete release of the nuclide during the experiment or an inadequate modelling of the production process, or both. In case of incomplete release, the extent of retention in the target will depend on the ratio of the life time of the radionuclide to its retention time in the target. For a nuclide, with a half-life shorter than its characteristic retention time in the target, a large fraction of the nuclide will have decayed before it is released from the target, while for longer-lived isotopes (having the same characteristic element-specific retention time) a larger fraction will be released. For isotopes with a half-life much longer than the characteristic retention time the release yield equals the production yield. In such cases, one should observe a systematic variation of the deviation between the release yield and the production yield with the half-life of different isotopes of the same element, with larger deviations observed for the shorter-lived isotopes. In principle, this deviation can be corrected for (David, 2013), if the characteristic retention time of the element is known. For some noble gases and mercury, the release yield has been measured as a function of time after one incident proton pulse (Tall, 2008b). From such measurements, the retention time can be deduced. For other elements, such data are not available, but reasonable estimates for retention times may still be deduced, e.g. based on the relative diffusivities or volatilities of the elements in LBE, or the relative strength of their chemical interaction with the target material that was discussed in Section 5.2.

Furthermore, for a reliable interpretation of such comparisons between predicted production yield and measured release yield it is immensely valuable to obtain information on the amount of nuclides remaining in the target after the experiment to assess the completeness of their release. For long-lived and stable nuclides, such information can be obtained from chemical or radiochemical analysis of the irradiated target. For some of the elements detected in the ISOLDE experiments such information is available from the post-irradiation analysis studies described in more detail in Section 5.3.2. For elements where direct information from post-irradiation analysis is not available, we will draw conclusions from the thermodynamic and kinetic assessment of release properties given in Section 5.2 and from release studies performed independently of the ISOLDE experiment.

5.3.1.4 *Calculation methods*

In the following sections, the experimental data for the release yields of radioisotopes of individual elements or groups of chemically related elements released from the target during the experiment and measured by off-line and on-line γ-spectroscopy are compared to the predicted production yields obtained from calculations using the Monte Carlo code MCNPX (Pelowitz, 2011).

Recent developments in the INCL4 Intranuclear Cascade Model (Boudard, 2013) were used, coupled with the evaporation model Abla07 (Kelic, 2008), inserted into a private version of MCNPX2.7.b at CEA Saclay (David, 2013). Calculations were also performed using the CEM03 model (Mashnik, 2006).

5.3.1.5 *Results*

5.3.1.5.1 Temperature dependence of release

Results from measurements performed at different target temperatures are shown in Figure 5.3.2. Note that in contrast to the subsequent Figures 5.3.3 to 5.3.6, the yields given

in this figure are not corrected for the ion source efficiency. Thus, they correspond to the number of atoms that has left the ion source and not to the amount of atoms that escaped the target and entered the ion source. As a consequence, the numbers in Figure 5.3.2 are systematically lower than those in the following figures and should not be directly compared to calculation results. Generally, the yields of Cd, Hg, Xe and At increase with increasing temperature. This was expected, since evaporation is endothermic, and also the diffusion of the dissolved radionuclides in the liquid metal is a thermally activated process. For Cd and At, the slope of the temperature function is much steeper than for Hg and Xe. The thermodynamic assessment presented in Section 5.2 revealed that the slope of the temperature function of the vapour pressure of Cd in dilute LBE solution is much steeper than that of Hg. Thus, the different behaviour of Cd and Hg in the ISOLDE experiment is in agreement with available thermodynamic data. For Xe and At, such thermodynamic data are not available. However, the thermodynamic data presented in Section 5.2 for the interaction of the lighter chemical homologues of At, iodine and bromine with LBE indicate that there is generally a strong retention of the elements of the halogen group in LBE. Consequently, their enthalpy of volatilisation from the liquid metal is large, leading to steep temperature functions of their vapour pressure above dilute solutions in LBE. On the other hand, for noble gases such as Xe there is no strong chemical interaction with LBE, and their enthalpies of vaporisation are low. Thus, one should expect comparatively low temperature dependence of their release from the liquid metal. In summary, we can state that the temperature dependence of the yields measured for radioisotopes of the elements Cd, Hg, Xe and At correlate well with their chemical retention in the liquid metal.

Figure 5.3.2: Temperature dependence of the release yield for the indicated isotopes, measured by collection at the GLM

Note that in contrast to the subsequent Figures 5.3.3 to 5.3.6, the yields given in this figure are not corrected for the ion source efficiency. Thus, they correspond to the number of atoms that has left the ion source and not to the amount of atoms that escaped the target and entered the ion source. As a consequence, the numbers in Figure 5.3.2 are systematically lower than those in the following figures and should not be directly compared to calculation results

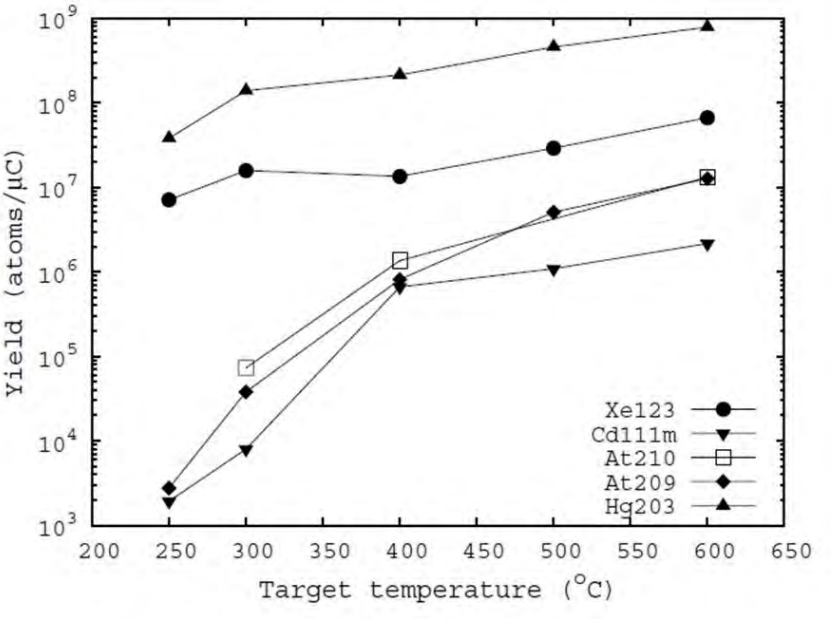

Source: Reproduced with permission of EDP Sciences from Tall (2007).

5.3.1.5.2 Noble gases

From the results of post-irradiation analysis it was found that the residual amount of stable isotopes of Xe and of the other noble gases in the LBE was small, at the level of about one per mil of the expected amount directly produced during the irradiation. For some noble gas nuclides larger amounts were detected, but their origin was clearly attributed to the decay of less volatile long-lived precursors after operation (Leya, 2014; Noah, 2012). Thus, one can quite safely assume almost complete release of noble gases during the experiment. Figure 5.3.3 shows a comparison between the predicted production of xenon isotopes and the amount of these isotopes released from the target and measured with online and off-line methods. We obtain good agreement between measured data and the results of simulations performed with the MCNPX code. Predictions by the MCNPX code are in good agreement with data for the krypton isotope release yields as well (see Figure 5.3.4). Krypton isotopes, like Xe isotopes, are produced in the later stage of the spallation process either by fission of highly excited spallation fragments, or in a two-step fission process induced by high-energy spallation neutrons, indicating that these nuclear reaction channels are well described by the nuclear physics models incorporated into the code.

5.3.1.5.3 Mercury

No indication of the presence of Hg isotopes was found in the post-irradiation analysis of the target described in Section 5.3.2. Considering its half-life of 444 y, the isotope ^{194}Hg should be detectable via its γ-emitting daughter ^{194}Au if it were still present in the target after irradiation. The fact that no ^{194}Hg/Au was detected in samples from the target indicates that the release of long-lived Hg isotopes during the ISOLDE experiment was nearly complete. This is supported by the results of experiments studying mercury release from LBE samples in a flow of gas (Neuhausen, 2005a; 2006a), where complete release of mercury within one hour was observed at temperatures > 300°C.

Figure 5.3.3: Measured release yields of Xe isotopes (in atoms for a proton charge of 1 μC on target) for 1 and 1.4 GeV protons (red and black dots, respectively)

Calculated production yields obtained using MCNPX with the INCL4.6-Abla07 model combination, for 1 and 1.4 GeV proton energy, and the CEM03 model, for 1GeV proton energy, are shown as lines

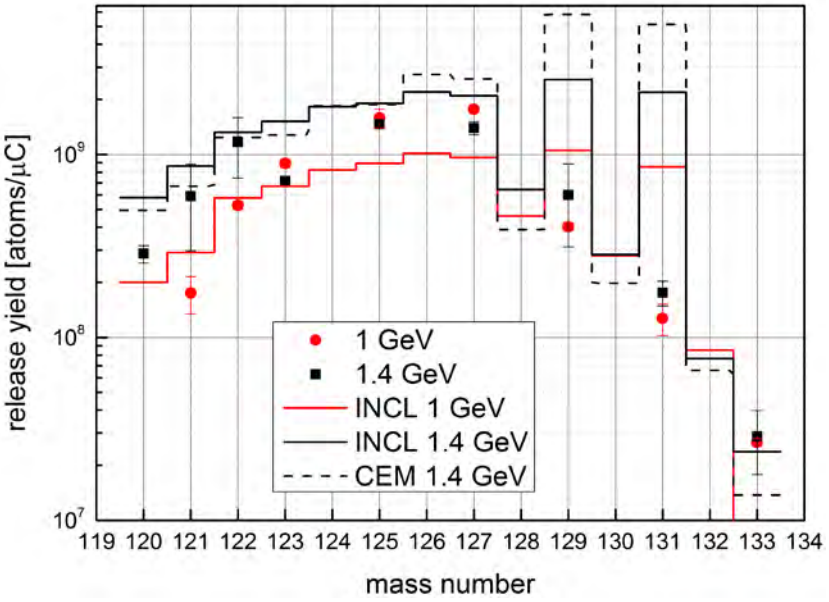

Source: Reproduced with permission from Zanini (2014).

Figure 5.3.4: Same as Figure 5.3.3 but for Kr isotopes

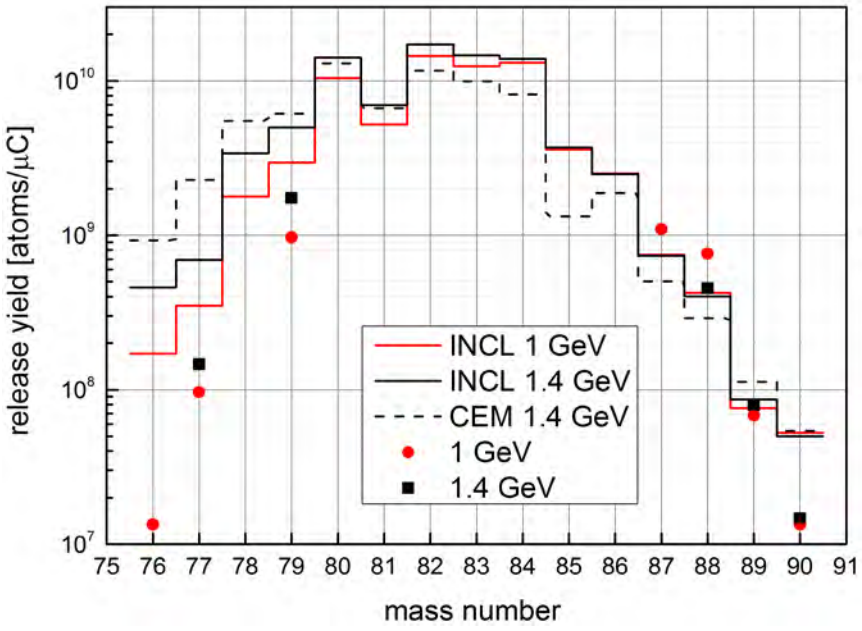

Source: Reproduced with permission from Zanini (2014).

An early evaluation and comparison of measured mercury release yields with predicted production yields (Tall, 2007) indicated systematically lower release yields for short-lived mercury isotopes. Measurements of the release of mercury isotopes vs. time indicates a characteristic retention time of 10-20 min at 600°C (Tall, 2008). This information was obtained from measurements done with a few proton pulses on target, followed by a measurement of the current of the released (ionised) mercury isotopes with Faraday cups up to about 30 minutes. After applying a correction taking into account this retention time (David, 2013) a much better agreement between experiment and prediction is achieved. In Figure 5.3.5 the measured cumulative release yields at 1 and 1.4 GeV for radioactive Hg isotopes are compared with the production yields, corrected for retention, predicted by calculations. The results of the simulations agree well with the results of the measurements.

5.3.1.5.4 Astatine and polonium

The astatine isotopes have short half-lives, ranging from 9.2 min for ^{204}At up to 8.3 h for ^{210}At, and are produced in low quantities in the target. However, astatine decays via ε and/or β+ decay to polonium, which is highly radiotoxic due to its long-lived α-emitting isotopes ^{208}Po (2.9 y), ^{209}Po (102 y) and ^{210}Po (138 d). It is therefore important to measure the release yields of astatine isotopes. For an assessment of a possible retention of astatine in the target, no measurements from post-irradiation analysis can be used because of the short half-lives of all At isotopes. However, from results on the release behaviour of astatine's lighter chemical homologue iodine from LBE (Neuhausen, 2006b) it seems likely that astatine release from the target will not be complete. Indeed, in an early evaluation of the experimental results (Tall, 2007) significant deviations between calculated production yields and measured release yields were observed, stimulating a more detailed evaluation that makes use of recent improvements in nuclear physics as well as the above-mentioned retention correction.

Figure 5.3.5: Same as Figure 5.3.3 but for Hg isotopes

Calculated production yields are corrected taking into account decay inside the target, considering a release time of 10 minutes

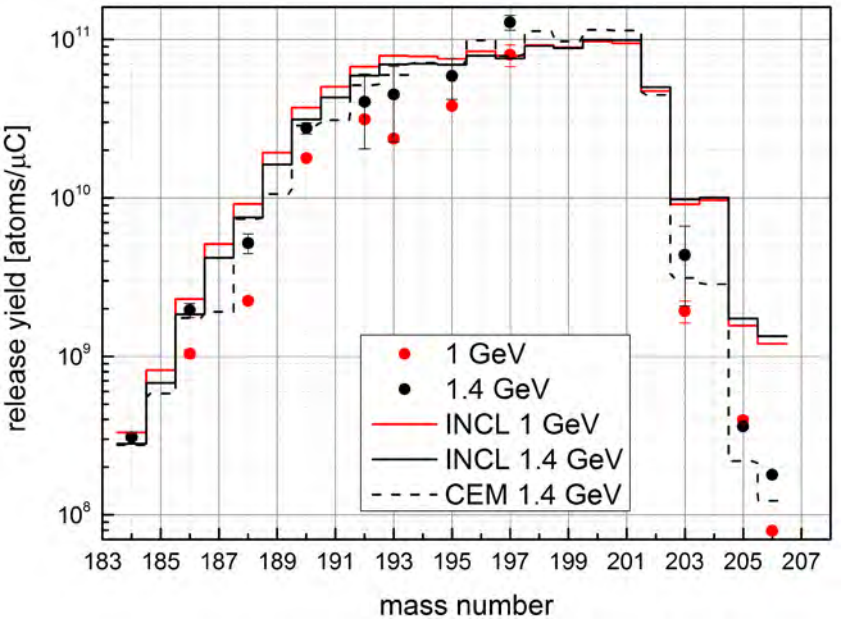

Source: Reproduced with permission from Zanini (2014).

Light particles (α, ^{3}He and pions) play a major role in the production of astatine isotopes (Clark, 1982). The dominating direct reactions are:

$$^{209}\text{Bi}\ (p\pi, xn)\ ^{210-x}\text{At}$$

However, for an extended target as used in this experiment, secondary reactions must be taken into account:

$$^{209}\text{Bi}\ (^{3}\text{He}, xn)\ ^{212-x}\text{At}$$

induced by spallation-produced ^{3}He and:

$$^{209}\text{Bi}\ (^{4}\text{He}, xn)\ ^{213-x}\text{At}$$

induced by spallation-produced ^{4}He.

Recent developments in the INCL4 Intranuclear Cascade Model (Boudard, 2013) have shown that astatine production can be successfully modelled if the pion exchange reactions and secondary reactions induced by ^{3,4}He are taken into account. Additionally, the retention time inside the bulk material must be considered for a precise comparison of nuclides of elements other than the noble gases, for which an almost instantaneous release can be safely assumed for the small ISOLDE target. Information on the diffusion time was only available for mercury (see also above; a retention time of about 10 minutes was measured for Hg at 600°C). For astatine, a retention time of about 10 hours had to be assumed for obtaining good agreement between predicted and experimentally measured yields (David, 2013). To judge whether the assumption of such a retention time is reasonable we have to resort to the notion that At in dilute LBE solution will behave similar to its lighter homologue iodine, since data on the release of At from LBE, or the diffusivity and vapour pressure of At in dilute solution in LBE are not available. The evaluation of thermodynamic data presented in Section 5.2 indicates a rather strong retention of iodine in LBE. Furthermore, observations from release experiments of iodine

from LBE (Neuhausen, 2006b) indicate that at 600°C about 20% of the iodine are released from an LBE sample much smaller than the ISOLDE target at ambient pressure within 1 hour. Assuming a similar degree of retention of astatine in LBE, a retention time of 10 hours seems reasonable.

A comparison of the release yields of astatine isotopes measured in the ISOLDE experiment with the predicted production yields is shown in Figure 5.3.6. With the proper contribution of secondary particles and the correction for the retention time, the INCL4/Abla model gives results in very good agreement with the experimental data.

Figure 5.3.6: Same as Figure 5.3.3 but for At isotopes

Calculated values are corrected taking into account
decay within the target, for a retention time of 10 hours

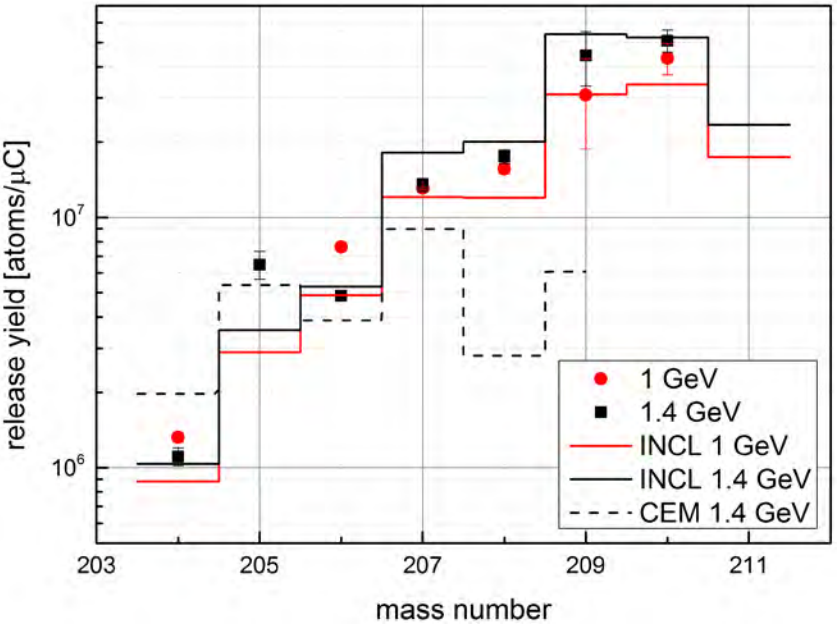

Source: Reproduced with permission from Zanini (2014).

5.3.1.5.5 Other isotopes

Other less volatile elements were also detected. The amount of Cd isotopes detected by γ-measurements was small and significantly lower than the amount that should have been produced according to the predictions. Since there are no γ-emitting long-lived isotopes of Cd, the retention of this element could not be confirmed by γ-spectrometry measurements on the irradiated target material performed several years after irradiation. From the chemical and thermodynamic properties of cadmium discussed in Section 5.2.1.1.7, there should be no strong attractive interaction with the liquid metal, but the volatility of the element Cd itself is fairly low. Thus, incomplete release of cadmium in the ISOLDE experiment is in accordance with its physicochemical properties.

The amount of iodine isotopes detected by γ-measurements was also systematically lower compared to the predictions. For iodine, strong retention in LBE was found in studies on the release of iodine from liquid lead-bismuth (Neuhausen, 2006b) which clearly show that the release of iodine from LBE is slow at 600°C and below. Similarly, the thermodynamic data on the interaction of iodine with Pb, Bi and LBE assessed in Section 5.2.1.1.9 point to strong retention of iodine in these metals. Furthermore, first

results on the analysis of ^{129}I in the irradiated target material by accelerator mass spectrometry (Hammer, 2010a) also indicate substantial retention of iodine in the target. Thus, chemical retention can be identified as the major cause of the discrepancies between the release yields of iodine isotopes observed in the ISOLDE experiment and the calculated production yields.

5.3.1.6 *Summary*

The complex process of production, diffusion and release of volatile elements in a molten metal target has been investigated at CERN/ISOLDE, giving very important results directly applicable to experiments such as MEGAPIE. For the comparison of the quantities of radionuclides measured in the experiment with the production predicted using nuclear codes it is important to take into account the chemical release behaviour of the different elements. Making use of results of the post-irradiation analysis of the target material as well as the assessment of thermodynamic properties of volatile elements in contact with LBE, it was possible to explain observed discrepancies between release data measured in the ISOLDE experiment and the predictions of nuclide production in the target obtained from Monte Carlo simulations. In all cases where the experimentally observed quantities of radionuclides released from the target were significantly and systematically smaller than their predicted production, incomplete release of the chemical element in question (I, At, Cd) was identified as the reason, either confirmed by actual analysis of the irradiated target material or from the assessment of thermodynamic data. On the contrary, in cases where complete release was achieved (i.e. noble gases), the agreement of experimentally determined and predicted amounts of radionuclides is good. Thus, despite the complexity of the processes involved, a consistent interpretation of the data was possible, confirming both a reasonable understanding of the chemical effects influencing the release of volatiles from liquid LBE and the capability of Monte Carlo codes used in the MEGAPIE neutronic design phase for predicting isotope production. The release of longer-lived Hg and noble gases isotopes is complete or nearly complete at 600°C. For short-lived Hg isotopes a retention time of about 10 minutes must be assumed to obtain a better agreement between data and calculations. A very interesting case is At, the release of which was observed for the first time from a molten ISOL target. The measured astatine release yields can be understood if secondary reactions and long retention times are included in the model calculations. When taking into account these effects, a good agreement of experimental and calculated data is achieved.

5.3.2 *Distribution of radionuclides in the proton-irradiated LBE target from ISOLDE*

In the following section, we will report the first results of radiochemical examinations on the target material of the ISOLDE target discussed above. The target, containing 547 g of LBE, was irradiated at the ISOLDE facility with 1.4 GeV protons in May 2004 and with 1.0 GeV and 1.4 GeV protons in August 2005. The proton doses applied in 2004 and 2005 were 1.3×10^{17} and 1×10^{18}, respectively. Since quantifying the release of gaseous and volatile elements during the irradiation at different temperatures was the major goal of this experiment, the target temperature was set to 400 and 600°C for the 2004 irradiation. For the second irradiation in 2005, the target temperature was varied between 250°C and 600°C. For more information on the irradiation see Tall (2008).

In 2008, the target was transported to PSI and dismantled in PSI's hot cell facility. Figures 5.3.7 and 5.3.8 show photographs of the irradiated target before and after dismantling, respectively. On the surface of the opened target, a surface layer is clearly visible. Four disk-shaped sections were cut at positions 2, 3, 5 and 7, as depicted in the schematic drawing shown in Figure 5.3.9. From each of these disks, a bar of approximately 15 mm length and 2×2 mm base area was cut in such a way that the former LBE-vacuum and LBE-tantalum interfaces can be assessed as illustrated in Figure 5.3.10. For more details on the cutting procedure see Boutellier (2008). To obtain an overview on the

radionuclide distribution, samples of a few mg of the material with a thickness of about 100 μm were hand-cut from one of the bars using a scalpel. Various samples were taken at the LBE-vacuum interface (designated as *a)* in Figure 5.3.10), approx. 100 μm below this interface, from the LBE-tantalum interface (designated as *b)* in Figure 5.3.10) and from the bulk, see Neuhausen (2011b, 2011c).

Figure 5.3.7: ISOLDE LBE target before dismantling

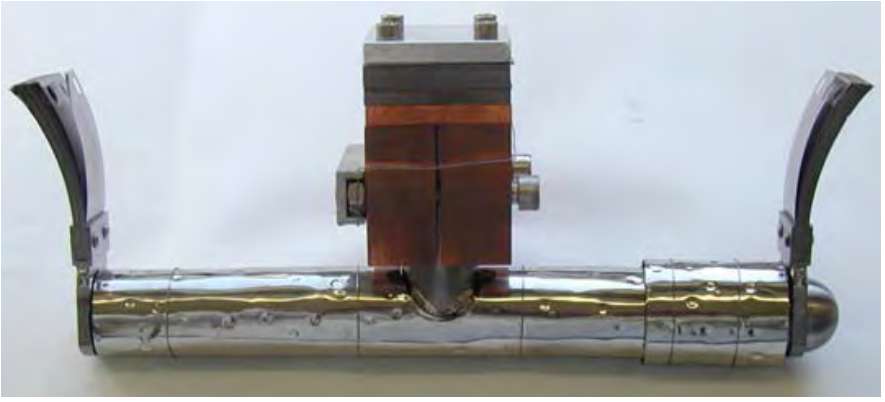

Source: Boutellier (2008).

Figure 5.3.8: Section of the target showing the tantalum hull and the free surface of LBE that was exposed to vacuum during irradiation

Note the brown surface layer

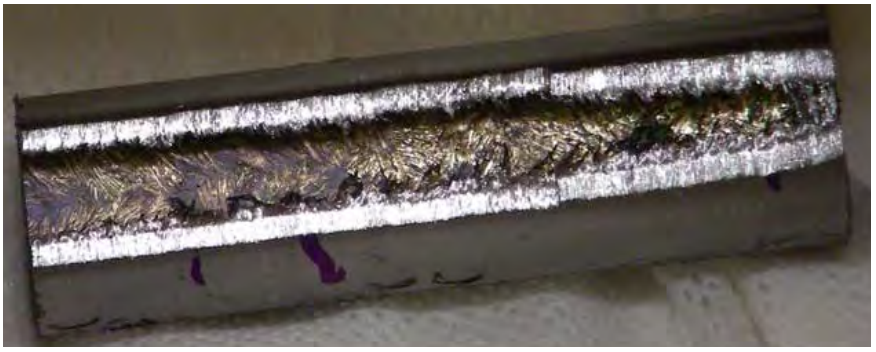

Source: Boutellier (2008).

Figure 5.3.9: Cutting scheme for the ISOLDE LBE target

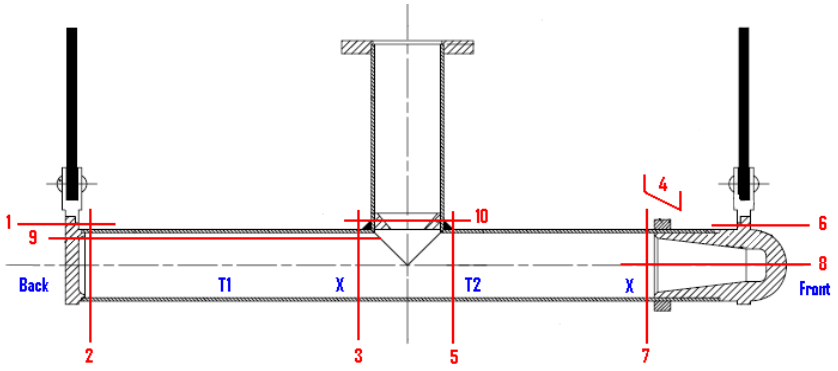

Source: Neuhausen (2011b).

Figure 5.3.10: Bar cut from one disk of the ISOLDE LBE target

The ends where the LBE-vacuum and LBE-tantalum interfaces were located are designated as a) and b)

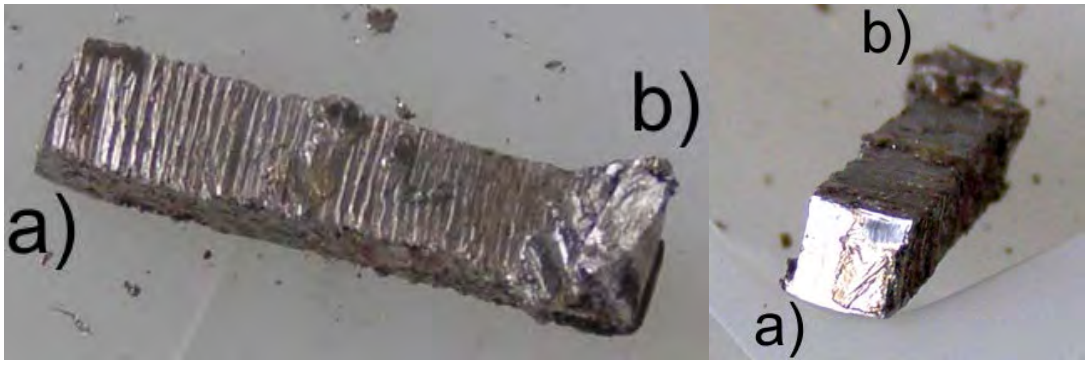

Source: Neuhausen (2011b).

The results obtained by α-spectrometry for the samples taken from four different locations are compared to the results of nuclear calculations in Table 5.3.1. The measured activity concentrations were decay-corrected to reflect the situation present at end of beam (EOB, 23 August 2005).

Table 5.3.1: Comparison of calculated bulk activity concentrations and measured activity concentrations of polonium isotopes in samples from different positions of the target

Reference time 23 August 2005 (EOB)

	^{208}Po	^{209}Po	^{210}Po
Sample position	A_{conc} (Bq/g)	A_{conc} (Bq/g)	A_{conc} (Bq/g)
LBE-vacuum interface	16 329	144	20 775
100 µm below LBE-vacuum interface	15 876	139	18 902
Bulk LBE	13 563	111	16 518
LBE-tantalum interface	15 367	134	19 243
Calculated (FLUKA)*	26 700	165	20 100

* Activity concentrations were calculated from the produced amounts reported in Zanini (2008b) assuming homogeneous distribution in the bulk LBE.

The calculation results are in reasonable agreement with the measured activity concentrations. While the calculated activity for ^{208}Po is about 70% higher than the measured ones, the calculated activities of ^{209}Po and ^{210}Po are in very good agreement with the experimental results. The activity concentrations measured in the samples seem to show a systematic trend, indicating enrichment towards the interfaces. However, the error of 10% quoted for the α-spectrometry results precludes a definite statement about surface enrichment from the α-spectrometry data. The results are however not contradictory to the observation of an approximately five-fold polonium enrichment

observed in a surface layer of a few μm thickness in Po-containing LBE samples (see Section 5.2.6 and von Rohr [2008]). Indeed, the presence of such a surface layer in a sample of ≈100 μm thickness would perfectly account for the differences in the α-spectrometry results for bulk and surface samples. More detailed studies of polonium surface enrichment in the ISOLDE target are underway (as of January 2011).

The results of γ-spectrometry studies are given in Tables 5.3.2 and 5.3.3. It is important to note that no indication of the presence of Hg isotopes was found in these γ-spectrometry measurements. Considering its half-life, the isotope ^{194}Hg (half-life 444 y) should be detectable via its γ-emitting daughter ^{194}Au if it were still present in the samples. Thus, the fact that no ^{194}Hg/Au was detected in the samples indicates that the release of Hg during the ISOLDE experiment was nearly complete.

Table 5.3.2: Comparison of calculated bulk activity concentration and measured activity concentrations of ^{172}Hf/Lu and ^{207}Bi in samples from different positions of the target

Reference time 23 August 2005 (EOB)

Sample position	Sample No.	Sample mass (mg)	^{172}Hf/Lu A_{conc} (kBq/g)	^{207}Bi A_{conc} (kBq/g)
LBE-vacuum interface	1 2	6.1 4.1	567 652	29 30
100 μm below LBE-vacuum interface	1 2	7.8 10.6	31 26	29 3
Bulk LBE	1 2 3 4	16.9 17.2 0.8 1.2	77 79 80 294	33 34 32 31
LBE-tantalum interface	1 2	2.64 1.88	221 187	37 34
Calculated (FLUKA)*			113	36

* Activity concentrations were calculated from the produced amounts reported in Zanini (2008b) assuming homogeneous distribution in the bulk LBE.

The results presented in Table 5.3.2 show that the distribution of radionuclides in the target is non-trivial. While ^{207}Bi is homogeneously distributed throughout the bulk, a depletion of this nuclide was observed in one of the samples taken approximately 100 μm below the former liquid metal-vacuum interface. Overall, the activity concentration of ^{207}Bi in the bulk agrees well with predictions from nuclear calculations. For ^{172}Hf/Lu an enrichment compared to the bulk is observed at the LBE-vacuum and LBE-tantalum interfaces (see example in Figure 5.3.11). Within the bulk, the majority of the samples have – in good agreement with theoretical predictions – ^{172}Hf/Lu-activity concentrations around 80 kBq/g, however one sample shows a significant enrichment of ^{172}Hf/Lu to 294 kBq/g. ^{60}Co, ^{102m}Rh, ^{133}Ba and ^{173}Lu show behaviour similar to ^{172}Hf/Lu, while ^{110m}Ag is not enriched at the surfaces. A possible explanation is that the more electropositive metals form insoluble oxides with the oxygen present in the liquid metal that separate from the liquid, while noble metals with a high solubility in LBE such as Ag remain dissolved.

Figure 5.3.11: Comparison of a section of the γ-spectra of a bulk LBE sample and a sample from the former LBE-vacuum interface of the ISOLDE LBE target

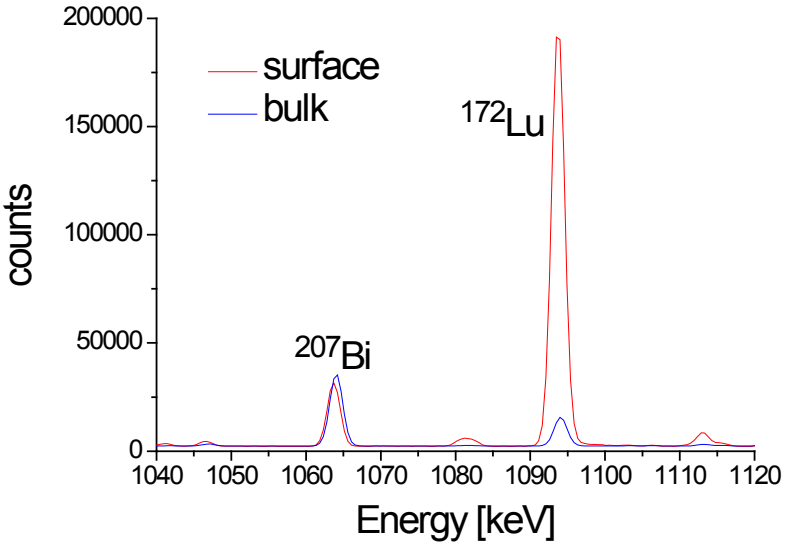

Source: Neuhausen (2011c).

Table 5.3.3: Comparison of measured and calculated activity concentrations of several nuclides in bulk LBE samples from the ISOLDE LBE target

Reference time 23 August 2005 (EOB)

Nuclide	A_{conc} (Bq/g) measured Bulk Sample 3	A_{conc} (Bq/g) measured Bulk Sample 4	A_{conc} (Bq/g) calculated (FLUKA)*
^{60}Co	820	2 210	2 157
^{102m}Rh	4 550	7 720	–
^{110m}Ag	23 100	19 000	–
^{133}Ba	900	3 350	1 540
^{172}Hf/Lu	79 700	294 000	113 000
^{173}Lu	107 000	512 000	122 000
^{207}Bi	31 600	31 400	36 200

* Activity concentrations were calculated from the produced amounts reported in Zanini (2008b) assuming homogeneous distribution in the bulk LBE.

Table 5.3.3 gives a comparison of activity concentrations of various nuclides in Samples 3 and 4 from the bulk LBE listed in Table 5.3.2. These samples were cut from one single LBE piece of 2 mg taken from the centre of a bar cut from the target. The results show that most of the detected radionuclides are strongly enriched in Sample 4, as compared to Sample 3. Possible explanations for this observation could be either the preferred deposition of radionuclides on dispersed particles that are suspended in the liquid metal or the precipitation of insoluble compounds that partly remain suspended in the liquid. A deeper exploration of these effects and a more detailed study of the spatial distribution of various radionuclides within the ISOLDE LBE target are ongoing. First results of these studies can be found in Hammer (2010b).

The preliminary results presented here indicate that a carefully planned sampling, including a sufficient number of samples from selected locations, is essential to extract reliable and meaningful results from the radiochemical analysis of liquid metal targets. The sampling plan for the post-irradiation examination (PIE) of the MEGAPIE target has been devised bearing in mind the expected inhomogeneity of the target material (Dai, 2009). Furthermore, the results on nuclide distribution in the ISOLDE target show that separation and deposition phenomena will occur in a liquid metal target that will influence its operation. Probably, one will have to deal with solid precipitations that can form platings on the surfaces of construction materials, depositions on the liquid metal and cover gas interfaces as well as remain within the liquid metal in the form of solid particulate matter. However, at the present state, it is difficult to predict the amount and the physical and chemical properties of the deposited material. Measures to mitigate the negative influences on operation of the facility such as plugging, reduction of heat removal capacity of heat exchangers, accumulation of radioactivity at the walls of construction materials and consequently increased doses during maintenance operations should be taken into account. The accumulation of radioactive material at the liquid metal-cover gas interface may also lead to enhanced transfer of radioactivity to the gas phase either by recoil mechanisms or by the additional heat caused by the radioactive decay in the near surface region.

Addendum

After the work on this chapter was concluded, new results from the PIE of the MEGAPIE target were obtained. Briefly, they show that polonium in the MEGAPIE target is homogeneously distributed in the bulk LBE, and the amounts of polonium found in the LBE agree reasonably well with the predicted amounts obtained using nuclear codes (Hammer, 2014b). Similar results were obtained for ^{207}Bi and ^{194}Hg/Au (Hammer, 2014a). For the electropositive metal lutetium, the distribution of the isotope ^{173}Lu was studied in detail. Similar to what was observed for ^{172}Hf/Lu in the ISOLDE target, an accumulation of lutetium on the walls of the target vessel and on the free surface of the LBE was observed. Compared to the ISOLDE target, the accumulation effect was much stronger in MEGAPIE. In the latter, the lanthanide nuclides and radionuclides of other electropositive elements such as ^{133}Ba and ^{54}Mn were not detected in bulk LBE samples but only at the interfaces (wall/free surface), indicating an almost complete separation of these elements from the liquid metal during operation of the target (Hammer, 2014a). Radionuclides of more noble elements such as mercury, gold and silver remain in the LBE.

5.3.3 *Operational experiences from the MEGAPIE project*

5.3.3.1 *Gas production in the MEGAPIE spallation target*

During the 575 MeV proton irradiation, produced volatile isotopes diffuse within the LBE and a fraction of them can be released at the level of the liquid metal free surface (see Figure 5.3.12). These processes are very complex (Neuhausen, 2005c). As the LBE circulates in a closed loop, diffusion, circulation and convection contribute to isotopic displacement inside the target. Some chemical recombinations are possible, such as oxide formation with the oxygen generated by spallation reactions, chemical reactions with structural materials or deposition at cold surfaces.

It is possible to classify volatile isotopes into specific groups according to the specific reaction by which they are produced from the interaction between the proton beam and the LBE:

- H and He are produced by intra-nuclear cascade and evaporation.
- Kr, Xe and I are produced by fission.
- Ne is created by both evaporation and fission.

- Hg is produced by the intra-nuclear cascade process.
- Po, generated by (p,xn) reactions on Bi, (α,xn) reactions on Pb, (n,γ) on ^{209}Bi and subsequent β-decay to ^{210}Po, or α or π exchange reactions on Bi leading to At and subsequent decay to Po.

During the MEGAPIE experiment gas measurements were performed in order to assess as many as possible of these produced radioelements. The high amount of radioactive volatile isotopes that ends in the gas handling system known as the cover gas system (CGS) requires specific safety measures during handling operations or in case of accident.

Figure 5.3.12: MEGAPIE target schematic view

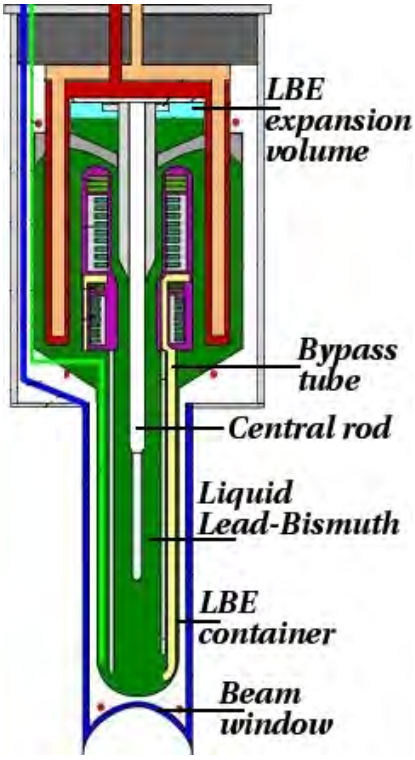

Source: Zanini (2008a).

5.3.3.2 *Gas and volatile measurements*

The CGS was connected to an expansion volume located at the top of the target where the released isotopes were collected. Figure 5.3.13 shows a schematic view of the CGS including the target expansion volume, the decay tank for the storage of radioactive gas, the sampling unit dedicated to activity measurement and some pressure transducers. Two fresh gas samplings were performed two days after the beginning of operation, which corresponds to 1 mA·h of accumulated charge on target. The first gas sampling procedure consisted in venting the expansion volume into the sampling unit.

This was followed by a dilution in the decay tank and the sampling unit was then removed to be analysed. The second fresh gas sampling was performed by venting a low fraction of the gas contained in the decay tank into a second sampling unit. The two sampling units were analysed by γ-spectroscopy (see Figure 5.3.14 for a typical γ-spectrum from the first gas sample).

Figure 5.3.13: Schematic view of the cover gas system

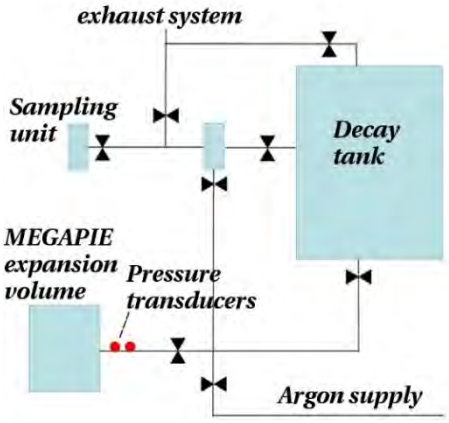

Source: Zanini (2008a).

Figure 5.3.14: First fresh gas sampling γ-spectrum with relevant γ-lines

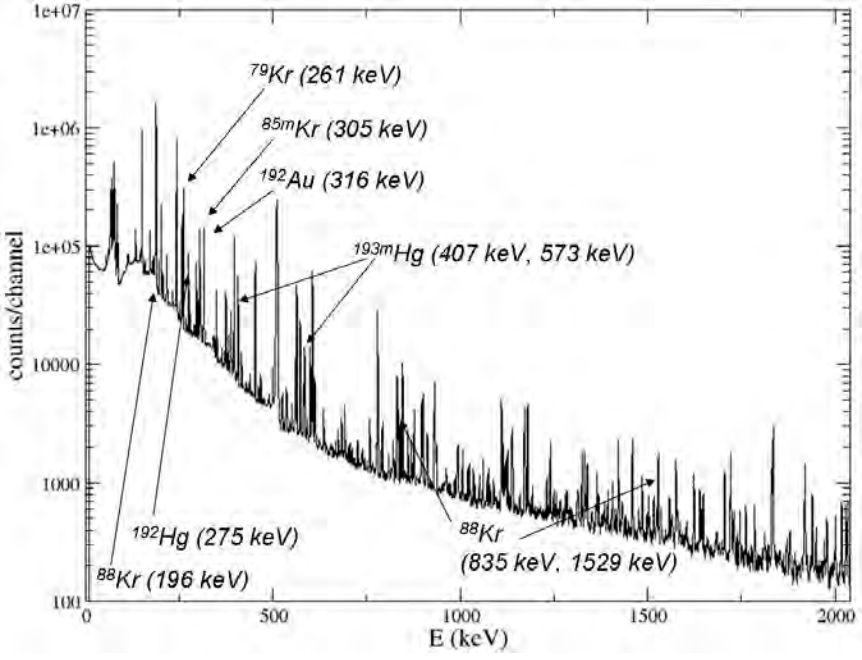

Source: Reproduced with permission of IEEE from Thiollière (2011).

The activities with their uncertainties obtained from the analysis of the two samples are presented in Table 5.3.4.

Radioisotopes of noble gases such as argon, krypton and xenon were detected. Heavier radionuclides were also measured, among these isotopes of gold and mercury. Note that detected gold isotopes are resulting from mercury decay. We notice the two following important points:

- Neither mercury nor gold were detected in the second sample.
- Noble gas activities were approximately 40% lower in comparison with the first sample and this deviation does not depend on isotope mass.

The latter result gives an order of magnitude on the systematic uncertainty in the noble gases measurements, as according to the sampling procedure, the amount of radioactive gases in both samples should have been the same. The behaviour of the mercury isotopes is more difficult to interpret but it seems to indicate that a fraction of the heavier isotopes have stuck to the pipe walls or the decay tank during the second sampling operations.

Table 5.3.4: Isotopes respective half-life and measured activity in the first gas sample

Nuclide	$T_{1/2}$	Activity (Bq) Sample 1	Activity (Bq) Sample 2
^{41}Ar	1.8 h	$3.2 \cdot 10^2$ (20%)	$2.4 \cdot 10^2$ (20%)
^{79}Kr	34.9 h	$4.5 \cdot 10^4$ (5%)	$3.1 \cdot 10^4$ (5%)
^{85m}Kr	4.5 h	$1.5\ 10^5$ (5%)	$1.1 \cdot 10^5$ (5%)
^{88}Kr	2.8 h	$2.7 \cdot 10^4$ (5%)	$1.9 \cdot 10^4$ (5%)
^{122}Xe	20.1 h	$1.4 \cdot 10^4$ (10%)	$9.3 \cdot 10^3$ (5%)
^{125}Xe	16.9 h	$9.5 \cdot 10^4$ (5%)	$6.5 \cdot 10^4$ (5%)
^{127}Xe	36.4 d	$5.0 \cdot 10^3$ (5%)	$3.6 \cdot 10^3$ (5%)
^{129m}Xe	8.9 d	$7.6 \cdot 10^3$ (5%)	$3.9 \cdot 10^3$ (50%)
^{135}Xe	9.1 h	$5.7 \cdot 10^2$ (10%)	$3.6 \cdot 10^2$ (5%)
^{192}Au	5.0 h	$3.4 \cdot 10^4$ (5%)	–
^{193}Au	17.7 h	$1.2 \cdot 10^4$ (10%)	–
^{195}Au	186 d	$1.2 \cdot 10^2$ (15%)	–
^{192}Hg	4.9 h	$1.8 \cdot 10^4$ (5%)	–
^{193m}Hg	11.8 h	$1.2 \cdot 10^4$ (5%)	–
^{195m}Hg	41.6 h	$2.9 \cdot 10^3$ (5%)	–
^{197}Hg	64.1 h	$2.1 \cdot 10^4$ (5%)	–
^{197m}Hg	23.8 h	$3.6 \cdot 10^3$ (5%)	–
^{203}Hg	46.6 d	$5.0 \cdot 10^1$ (5%)	–

In order to correlate the experimental activities presented in Table 5.3.4 with the activity in the expansion volume, which contains information on the actual volatile elements released, we define two groups, the noble gases and mercury, showing a similar behaviour from the production to the detection of their isotopes. Indeed, Ar, Kr and Xe are chemically inert noble gases with high volatility. It is thus reasonable to consider that noble gases behaviour will be ruled by similar mechanisms (Neuhausen, 2005c). The noble gases are considered as fully volatile during the sampling procedure. The gold isotopes are assumed to come from decay of mercury effused from the expansion volume to the sampling unit. The absence of Hg and Au in the second sample could be due to three possible scenarios that cover all possibilities that could occur in the CGS:

- s1: Mercury and gold are fully volatile during all the steps of the procedure. This is the standard scenario considered for the measured noble gases. It is, however, only theoretical because Hg and Au were only observed in the first sample.
- s2: All the mercury and gold diffuse into the first sampling unit and an unknown proportion sticks on the sampling unit, the decay tank walls and the linking pipes.
- s3: Mercury and gold stick on the pipes and walls somewhere between the expansion volume and the sampling unit even before the first sampling.

Each scenario has a specific normalisation factor, called sampling factor S, to be applied to the measured activity $A_{e\text{-}S}$ in order to obtain the activity in the MEGAPIE expansion volume $A_{e\text{-}EV}$. This factor is defined as:

$$A_{e-EV} = S \times A_{e-S} \tag{5.69}$$

The sampling factor represents the ratio between the number of atoms in the expansion volume and the sampling unit (see Figure 5.3.13). This ratio can be calculated by equating the pressure in the expansion volume to that in the rest of the system. Perfect gas behaviour is also assumed and volumes and temperatures are known with sufficient accuracy. Note that the temperature in the expansion volume is different from the temperature in the rest of the CGS.

For Scenario s1, we have calculated a sampling factor $S_{s1} = 3.33 \cdot 10^3$. This value is also used for the estimation of noble gas activity in the expansion volume.

For Scenario s2, the sampling factor value depends on the gas proportion that has stuck on the sampling unit walls. Therefore, it is contained within two limits. The lower limit represents the case where all the mercury has stuck before the dilution into the decay tank while the upper limit is the case described by Scenario s1. The calculation gives a Scenario s2 with a sampling factor $25 \leq S_{s2} \leq 3.33 \cdot 10^3$.

The lower limit of the third scenario corresponds to the mercury normal diffusion up to the sampling unit (represented then by Scenario s2). A calculation where the whole mercury sticking on the pipes between the expansion volume and the sampling unit gives the upper limit of Scenario s3 which leads to an infinite value of the sampling factor. The third scenario is then illustrated by the relation $25 \leq S_{s3} \leq \infty$. Since there is no argument for choosing between Scenarios s2 and s3, the sampling factor can only be defined by its lower limit:

$$S \geq 25 \tag{5.70}$$

5.3.3.3 *Gas and volatile production calculations*

In this section we compare the experimental activities with a set of calculations. We have employed several combinations of validated multi-particle transport codes coupled with evolution codes, in particular FLUKA (Ferrari, 2005) and MCNPX2.5.0/CINDER'90 (Pelowitz, 2005; Wilson, 2006). In addition, we have made calculations using the SNT code (Korovin, 1992). Concerning the MCNPX code, the most realistic set of spallation models describing the intra-nuclear cascade and the evaporation process have been defined after a detailed benchmark (David, 2007). As a consequence, we carried out calculations with Bertini (1969)/Dresner (1962), INCL4 (Boudard, 2002)/Abla (Junghans, 1998), ISABEL (Junghans, 1998)/Abla (Yariv, 1979) and CEM2k (Mashnik, 2001). A neutronic study has shown an agreement between simulated and experimental neutron flux (Panebianco, 2009) outside the target, thus validating the simulated geometry used. The evolution calculation takes into account the experimental irradiation time profile which includes 15 hours of cooling before the sample activity measurement (see Figure 5.3.15).

For each isotope excluding gold, the evolution takes into account spallation reactions, and decay and nuclear reactions with low energy neutrons (i.e. E < 20 MeV). Gold is not volatile and it is assumed to be generated only from the decay of released mercury. Its spallation production rate is then initialised to zero in the evolution calculation.

Table 5.3.5 shows that we could measure some metastable nuclide activities. The metastable production with MCNPX is taken into account via a data library used in the gamma emission module (Prael, 1998). With FLUKA, the isomeric production ratio is 0.5 for all nuclides with isomers. The yields of nuclei in metastable states induced by neutrons are simulated in SNT from the evaluations available in the European Activation File (Forrest, 2007) at energies below 20 MeV. For higher energies the isomeric ratio is

taken to be 0.5 for all cases. For proton-induced reactions the code SNT uses the Proton Activation Data File (Konobeyev, 2007) below 150 MeV including accurate evaluations for isomer yields. Above 150 MeV, the ratio is 0.5 once more. Results from the calculations are given in Table 5.3.5. Statistical uncertainties on provided activities are not directly computable since after the evolution calculation, they are a combination of the nuclide production uncertainties, the nuclide's parents' production uncertainties and the neutron flux. We mention in the table the uncertainty on independent spallation rate production provided by simulation codes when available. This represents an under estimation of the statistical error but it remains an acceptable order of magnitude.

Figure 5.3.15: Irradiation at the start-up of MEGAPIE

The dashed lines represent the irradiation model used in evolution calculations

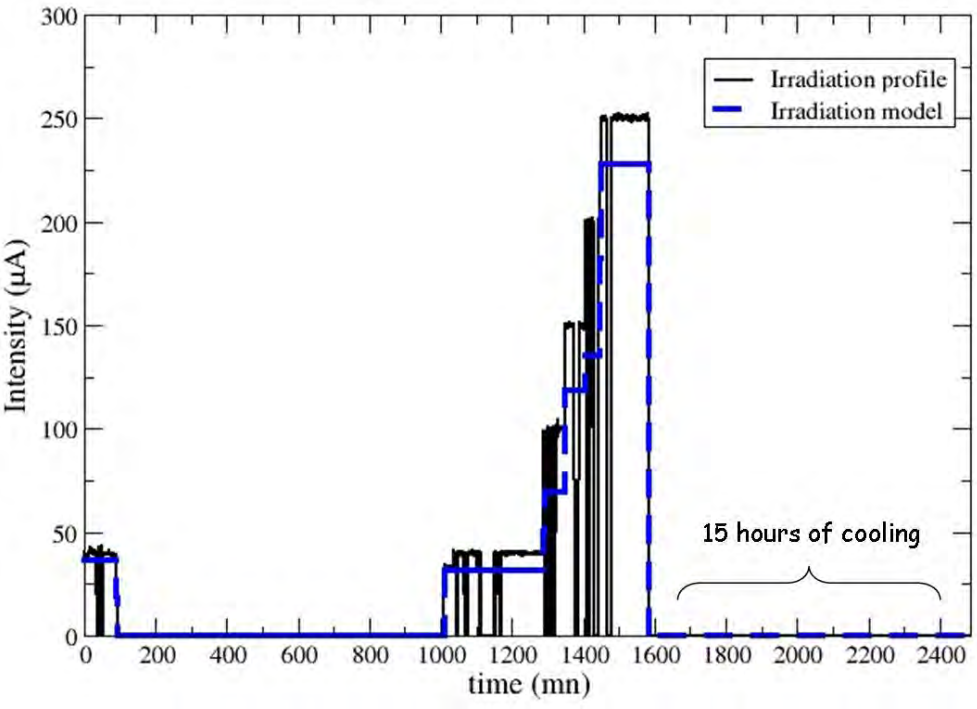

Source: Reproduced with permission of IEEE from Thiollière (2011).

Table 5.3.5: Activities measured (Probe 1) and calculated with MCNPX (with different model combinations), FLUKA and SNT

Activity values are expressed in Bq. Indicated uncertainty in brackets (%) is the error on the isotope spallation production rate provided by the codes. Calculated values are obtained from the total activities in LBE divided by the sampling factor $S_{s1} = 3.33 \cdot 10^3$.

Nuclide	Probe 1	MCNPX				FLUKA 2008	SNT
		Bertini/ Dresner	INCL4/ Abla	ISABEL/ Abla	CEM		
^{41}Ar	$3.2 \cdot 10^2$ (20)	$3.6 \cdot 10^4$ (10)	$1.4 \cdot 10^4$ (10)	$2.1 \cdot 10^4$ (10)	$1.5 \cdot 10^3$ (25)	$1.1 \cdot 10^4$	$2.7 \cdot 10^2$
^{79}Kr	$4.5 \cdot 10^4$ (5)	$5.2 \cdot 10^6$ (3)	$2.4 \cdot 10^6$ (4)	$3.1 \cdot 10^6$ (3)	$7.3 \cdot 10^6$ (2)	$2.8 \cdot 10^6$	$5.2 \cdot 10^6$
^{85m}Kr	$1.5 \cdot 10^5$ (5)	$1.1 \cdot 10^7$ (2)	$1.5 \cdot 10^7$ (1)	$1.2 \cdot 10^7$ (1)	$1.0 \cdot 10^7$ (1)	$2.0 \cdot 10^7$	$5.3 \cdot 10^6$
^{88}Kr	$2.7 \cdot 10^4$ (5)	$2.7 \cdot 10^6$ (2)	$2.0 \cdot 10^6$ (2)	$1.4 \cdot 10^6$ (3)	$8.5 \cdot 10^5$ (2)	$2.2 \cdot 10^6$	$1.3 \cdot 10^6$

Table 5.3.5: Activities measured (Probe 1) and calculated with MCNPX (with different model combinations), FLUKA and SNT (*cont.*)

Activity values are expressed in Bq. Indicated uncertainty in brackets (%) is the error on the isotope spallation production rate provided by the codes. Calculated values are obtained from the total activities in LBE divided by the sampling factor $S_{s1} = 3.33 \cdot 10^3$.

Nuclide	Probe 1	MCNPX				FLUKA 2008	SNT
		Bertini/ Dresner	INCL4/ Abla	ISABEL/ ABLA	CEM		
^{122}Xe	$1.4 \cdot 10^4$ (10)	$2.7 \cdot 10^6$ (4)	$1.2 \cdot 10^6$ (7)	$1.6 \cdot 10^6$ (6)	$1.1 \cdot 10^6$ (5)	$6.6 \cdot 10^5$	$2.6 \cdot 10^6$
^{125}Xe	$9.5 \cdot 10^4$ (5)	$6.2 \cdot 10^6$ (4)	$5.1 \cdot 10^6$ (4)	$5.6 \cdot 10^6$ (4)	$3.9 \cdot 10^6$ (3)	$3.8 \cdot 10^6$	$8.2 \cdot 10^6$
^{127}Xe	$5.0 \cdot 10^3$ (5)	$3.4 \cdot 10^5$ (3)	$2.7 \cdot 10^5$ (4)	$3.1 \cdot 10^5$ (4)	$2.2 \cdot 10^5$ (3)	$2.8 \cdot 10^5$	$4.0 \cdot 10^5$
^{129m}Xe	$7.6 \cdot 10^3$ (5)	$1.2 \cdot 10^5$ (3)	$9.2 \cdot 10^4$ (4)	$1.4 \cdot 10^5$ (4)	$6.0 \cdot 10^4$ (3)	$2.7 \cdot 10^5$	$1.2 \cdot 10^{-2}$
^{135}Xe	$5.7 \cdot 10^2$ (10)	$2.3 \cdot 10^6$ (6)	$1.4 \cdot 10^5$ (19)	$9.9 \cdot 10^4$ (29)	$6.5 \cdot 10^4$ (22)	$1.3 \cdot 10^5$	$7.2 \cdot 10^4$
^{192}Au	$3.4 \cdot 10^4$ (5)	$8.4 \cdot 10^8$ (0)	$9.6 \cdot 10^8$ (0)	$1.0 \cdot 10^9$ (0)	$1.3 \cdot 10^9$ (0)	$1.0 \cdot 10^9$	$1.4 \cdot 10^9$
^{193}Au	$1.2 \cdot 10^4$ (10)	$8.0 \cdot 10^8$ (0)	$8.7 \cdot 10^8$ (0)	$9.1 \cdot 10^8$ (0)	$1.0 \cdot 10^9$ (0)	$9.5 \cdot 10^8$	$1.2 \cdot 10^9$
^{195}Au	$1.2 \cdot 10^2$ (15)	$5.2 \cdot 10^6$ (0)	$5.7 \cdot 10^6$ (0)	$6.4 \cdot 10^6$ (0)	$5.9 \cdot 10^6$ (0)	$6.7 \cdot 10^6$	$7.1 \cdot 10^6$
^{192}Hg	$1.8 \cdot 10^4$ (5)	$3.4 \cdot 10^8$ (0.3)	$4.0 \cdot 10^8$ (0.5)	$4.1 \cdot 10^8$ (0.5)	$5.2 \cdot 10^8$ (0.3)	$4.0 \cdot 10^8$	$5.3 \cdot 10^8$
^{193m}Hg	$1.2 \cdot 10^4$ (5)	$1.7 \cdot 10^8$ (0.3)	$1.3 \cdot 10^8$ (0.5)	$1.3 \cdot 10^8$ (0.5)	$1.1 \cdot 10^8$ (0.3)	$8.7 \cdot 10^7$	$5.0 \cdot 10^7$
^{195m}Hg	$2.9 \cdot 10^3$ (5)	$5.8 \cdot 10^7$ (0.4)	$4.9 \cdot 10^7$ (0.5)	$4.5 \cdot 10^7$ (0.5)	$3.4 \cdot 10^7$ (0.4)	$4.1 \cdot 10^7$	$2.7 \cdot 10^7$
^{197}Hg	$2.1 \cdot 10^4$ (5)	$6.3 \cdot 10^8$ (0.5)	$6.5 \cdot 10^8$ (0.5)	$7.1 \cdot 10^8$ (0.6)	$6.2 \cdot 10^8$ (0.4)	$9.5 \cdot 10^8$	$7.2 \cdot 10^8$
^{197m}Hg	$3.6 \cdot 10^3$ (5)	$6.6 \cdot 10^7$ (0.5)	$6.7 \cdot 10^7$ (0.5)	$5.3 \cdot 10^7$ (0.6)	$4.4 \cdot 10^7$ (0.4)	$4.2 \cdot 10^7$	$5.7 \cdot 10^7$
^{203}Hg	$5.0 \cdot 10^1$ (5)	$2.2 \cdot 10^6$ (0.8)	$2.5 \cdot 10^6$ (0.8)	$1.8 \cdot 10^6$ (1)	$9.9 \cdot 10^5$ (0.9)	$7.8 \cdot 10^5$	$1.4 \cdot 10^6$

Simulation codes provide the evaluation of isotopes production inside the LBE while measurements give the amount released from the target. Moreover, a release fraction is defined as the amount of released atoms per produced atom in the LBE at the time of the measurement. The ratio between released and simulated in-target isotope values could be interpreted as the evaluation of the release fraction for the spallation model used at the time the measurement is made.

5.3.3.4 *Gas and volatile release parameters estimation*

For each code and model combination and for each measured isotope, the ratio $R(t_{irr})$ between experimental activity in the expansion volume and simulated in-target production has been extracted as:

$$R(t_{irr}) = \frac{A_{e-EV}}{A_{s-IT}} = S \times \frac{A_{e-S}}{A_{s-IT}} \tag{5.71}$$

This number depends on the irradiation profile and on the time the measurement is made, which we summarise by the variable t_{irr}. S is the sampling factor defined above. $A_{e\text{-}EV}$, $A_{e\text{-}S}$ and $A_{s\text{-}IT}$ are the experimental activity in the expansion volume, in the sampling unit and the simulated activity in the LBE target, respectively. Figure 5.3.16 shows the ratio $R(t_{irr})$ extracted for noble gases from the sampling factor S_{s1} as a function of mass number. The lower limit of the ratio $R(t_{irr})$ is also represented and estimated for gold and mercury from the sampling factor given by S = 25.

Figure 5.3.16: $R(t_{irr})$ as a function of isotope mass number

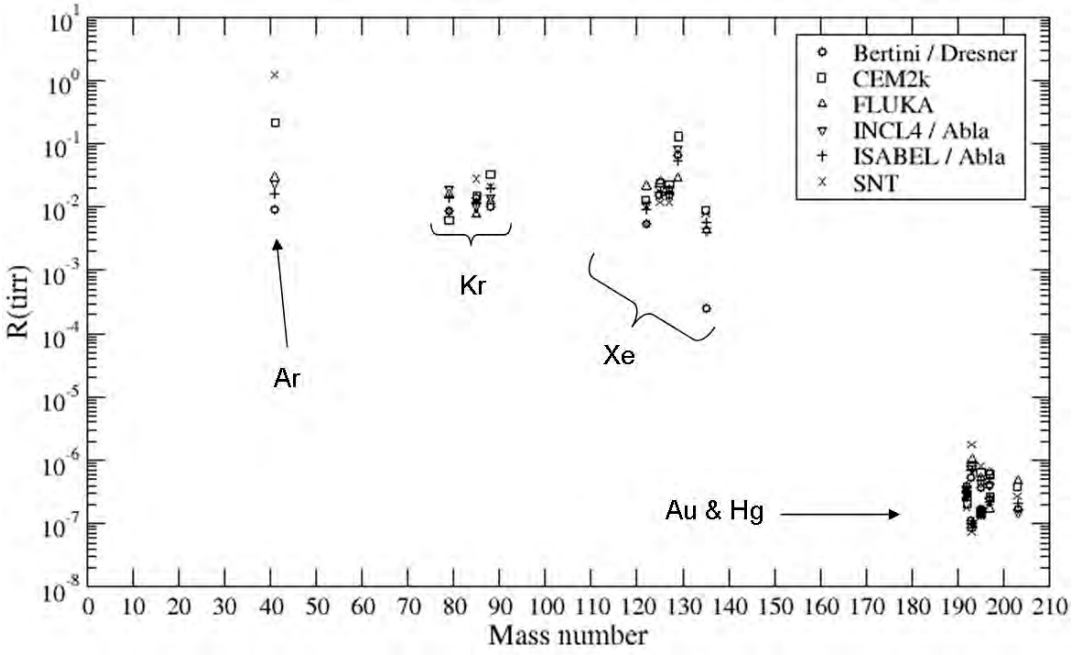

Source: Reproduced with permission of IEEE from Thiollière (2011).

We can distinguish two trends which discriminate noble gas and heavy nuclide behaviour. Concerning the noble gases, the extracted ratio $R(t_{irr})$ is reasonably constant except for the case of ^{41}Ar calculated with the code SNT and ^{135}Xe calculated by Bertini/Dresner. For the first isotope, the model predicts a sharp decrease of the fission yields for lead and bismuth isotopes with a decrease of the fragment mass for $A < 43$, which explains the strong deviation. The ^{135}Xe discrepancy is induced by the overestimated production rate using Bertini/Dresner. ^{41}Ar calculated with SNT and ^{135}Xe obtained with Bertini/Dresner are excluded for the calculation of the average value and the error is extracted as the standard deviation coupled with the 40% of systematic error. The mean ratio $R(t_{irr})$ obtained for 1 mA·h of accumulated charge and two days of irradiation is given by:

$$\left\langle R_{nb}\left(t_{irr}\right)\right\rangle = (2.3 \pm 1.5) \times 10^{-2} \tag{5.72}$$

Concerning heavy nuclides, we assume that the average ratio could be extracted as the mean value of the distribution while uncertainty is related to the distribution standard deviation and the 40% of systematic error. After 1 mA h of accumulated charge and two days of operation, the lower limit of the ratio $R(t_{irr})$ is given by:

$$\left\langle R_{Hg-s3}\left(t_{irr}\right)\right\rangle = (3.4 \pm 2.9) \times 10^{-7} \tag{5.73}$$

The ratio $R(t_{irr})$ for mercury shows the difficulty in understanding the mercury behaviour in a complex system such as MEGAPIE.

In order to evaluate if there is an effect of the nuclide half-life on the measurement results, we represented in Figure 5.3.17 the ratio $R(t_{irr})$ as a function of isotope half-life. The figure shows that there is no evident half-life effect in the calculated data for noble gases as well as for gold and mercury, as expected.

Figure 5.3.17: $R(t_{irr})$ as a function of isotope half-life

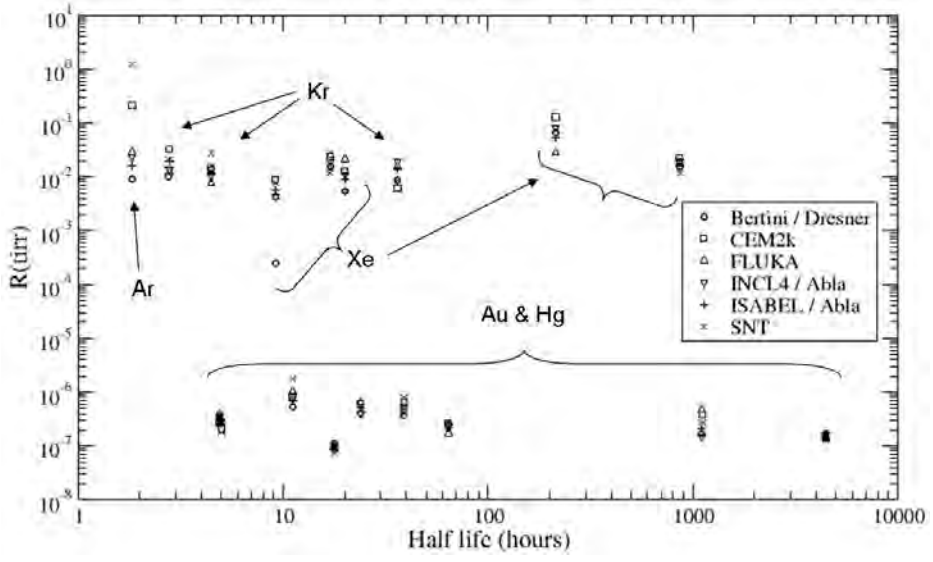

Source: Reproduced with permission of IEEE from Thiollière (2011).

We also calculated the mass in the expansion volume obtained from the activity in the sampling unit multiplied by the sampling factor of Scenario s1 in the case of noble gases. The lower limit of Scenario s3 is used in the case of heavy nuclides, which means that the calculated lower limit on the mass of produced isotopes in the expansion volume is given. Masses calculated by simulation are then multiplied by the noble gases ratio $R_{nb}(t_{irr})$ as determined above (with the respective heavy nuclide ratio being $R_{Hg-s3}[t_{irr}]$). Figure 5.3.18 and Figure 5.3.19 show the mass distributions for xenon, gold and mercury isotope production in the expansion volume of the MEGAPIE target, respectively.

Figure 5.3.18: Measured and calculated xenon mass in the expansion volume after two days of irradiation and 15 h cooling calculated with the sampling factor deduced from Scenario s1

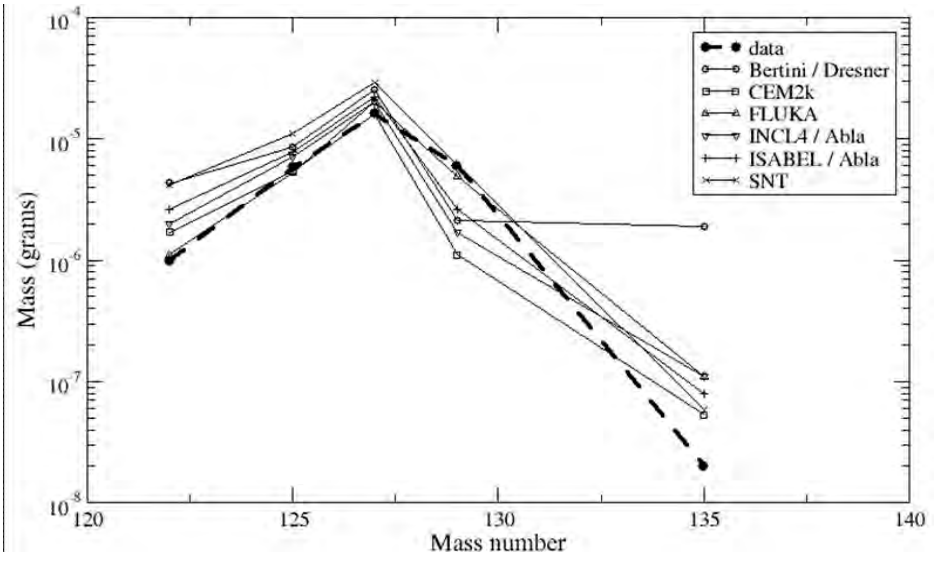

Source: Reproduced with permission of IEEE from Thiollière (2011).

Figure 5.3.19: Lower limit of measured and calculated gold and mercury masses in the expansion volume after two days of irradiation and 15 h cooling

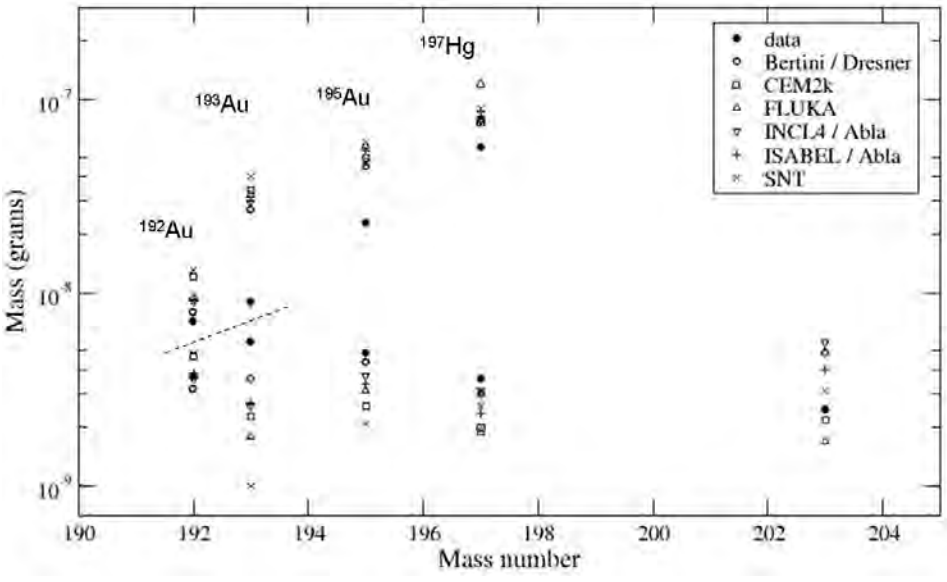

Source: Reproduced with permission of IEEE from Thiollière (2011).

In order to give a global view of the results, all points are represented as the ratio between experimental and simulated data on Figure 5.3.20. The grey lines highlight a factor 3 deviation from experimental data, which shows the most important deviations and improvement necessities.

Figure 5.3.20: Ratio between experimental and simulated data

The grey dash-dot lines show a factor of 3 deviation from experimental data

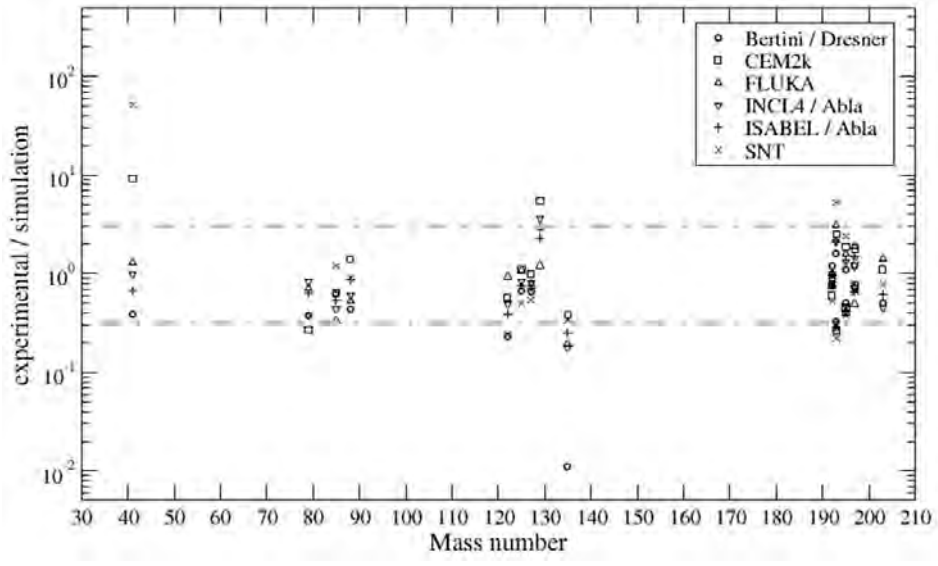

Source: Reproduced with permission of IEEE from Thiollière (2011).

The following is devoted to the characterisation of the release velocity from the LBE based on the most reliable calculations performed with the INCL4/Abla and CINDER'90 evolution codes. We define the probability $P_r(\Delta t)$ for a stable nuclide to be released within Δt after having been created (Ravn, 1979):

$$P_r(\Delta t) = 1 - \exp\left(-\frac{\Delta t}{\tau}\right) \tag{5.74}$$

The parameter τ is a characteristic release time representing the release velocity and depends on the LBE temperature. In our case, the release is slow so that Δt can be considered very small compared to τ, thus:

$$P_r(\Delta t) \approx \frac{\Delta t}{\tau} \tag{5.75}$$

On the other hand, the probability $P_d(\Delta t)$ that a radioactive nuclide, with a radioactive constant λ, has not decayed within Δt after its creation is given by:

$$P_d(\Delta t) = \exp(-\lambda \cdot \Delta t) \tag{5.76}$$

Let us consider the irradiation begins at $t = 0$. If t_r is the time after which the release is stopped and t_m the time at which the activity measurement is performed ($t_r \leq t_m$), the amount of the isotope released $N_r(t_r, t_m)$ at time t_r is given by:

$$N_r(t_r, t_m) \approx \int_0^{t_r} g(t) \cdot \left(\frac{t_r - t}{\tau}\right) \cdot dt \tag{5.77}$$

if $g(t)$ obeys the following relation: $g(t) = N_c(t) \cdot \exp(-\lambda \cdot (t_m - t))$.

$N_c(t)$ represents the nuclide production rate given by the temporal derivative of the absolute created amount $N_a(t)$, excluding the decay contribution. $N_a(t)$ is not directly accessible by the evolution calculation. As a consequence, the concerned nuclides are set as stable in the file that contains radioactive nuclides parameters used by the evolution code CINDER'90. The result of the calculation provides directly $N_a(t)$ which yields $N_c(t)$ after derivation in time.

The total amount $N_t(t_m)$ of nuclides generated within the time t_r and present at t_m inside and outside the LBE, taking decay into account, is given by:

$$N_t(t_r, t_m) = \int_0^{t_r} g(t) \cdot dt \tag{5.78}$$

At a specified temperature, the release fraction $R(t_r, t_m)$ defined as the amount of released atoms per produced atom in the LBE at the measurement time t_m is then given by the following ratio:

$$R(t_r, t_m) = \frac{N_r(t_r, t_m)}{N_t(t_r, t_m)} \tag{5.79}$$

This leads to the following expression for the factor τ:

$$\tau \approx \frac{1}{R(t_r, t_m)} \left(t_r - \frac{\int_0^{t_r} t \cdot g(t) \cdot dt}{\int_0^{t_r} g(t) \cdot dt} \right) \tag{5.80}$$

The LBE temperature in the MEGAPIE target has been measured to lie in the range between 290°C during irradiation and 220°C during standby near the LBE free surface (Dementjevs, 2010). As the release rate of volatiles in this temperature range is not exactly known, the volatile behaviour can be described by the following hypotheses:

- H1: volatile release is not affected by temperature fluctuations, which implies that the release is constant during the irradiation and the 15 hours of cooling according to the irradiation profile shown on Figure 5.3.15. That implies $t_r = t_m$.
- H2: the volatile nuclides release at 220°C is negligible compared to the release at 290°C and t_r is then the time the irradiation stopped, 15 hours before the activities measurement at t_m.

We consider for the calculation of τ that $R(t_r, t_m)$ is given by the estimated value of the ratio $R(t_{irr})$ with the associated uncertainty. Estimation of τ has been done from the average value obtained with INCL4/Abla and the error comes from the uncertainty on $R(t_{irr})$ which is dominant. The calculation for noble gases provides respectively for the hypotheses H1 and H2:

$$\tau_{NG-H1} = (31 \pm 20) \text{ days} \tag{5.81}$$

$$\tau_{NG-H2} = (4.7 \pm 3.1) \text{ days} \tag{5.82}$$

It is worth noting that there is a high deviation of the parameter τ according to the considered hypothesis. A dedicated experiment aiming at defining the temperature dependency of the release rate of noble gases could be a possible way to deduce a more precise value for this parameter from the present data.

5.3.3.5 *Hydrogen and helium production*

During the six months irradiation, the pressure in the expansion volume was measured by means of two pressure transducers (see Figure 5.3.13). A pressure evolution model based on calculations has been realised following these assumptions:

- Perfect gas behaviour is assumed.
- Pressure build-up comes from hydrogen and helium isotopes, with only a negligible fraction coming from other noble gases and from mercury.
- Hydrogen combines instantaneously into H_2.
- Initial pressure is a free parameter.
- The hydrogen and helium release time is lower than the characteristic time of the irradiation.

The pressure evolution is then given by:

$$P(t) = \frac{1}{V(t)}\left(V(0)P_0 + \frac{RT(t)n(t)}{N_a}\right) \tag{5.83}$$

where $V(t)$ is the expansion volume. The pressure depends on LBE volume evolution, which is a function of its temperature $T(t)$ that increases when the beam is on target. N_a is the Avogadro constant and $n(t)$ is the amount of gas atoms expressed as the sum of hydrogen, deuterium, tritium and helium:

$$n(t) = \frac{n_H(t) + n_D(t) + n_T(t)}{2} + n_{He}(t) \tag{5.84}$$

The temperature evolution $T(t)$ is measured by an in-line thermocouple. By fitting the initial pressure P_0, the pressure evolution was calculated. Results are shown in Figure 5.3.21 and are compared to the measured pressures. Measured and calculated pressures are in fair agreement. The shape of the experimental pressure is not reproducible without a non-linear gas leakage term which is not conceivable. The integrated amounts of released hydrogen and helium agree with experiment better than 25%. We present as a consequence simulated production of hydrogen and helium normalised for a proton source in Table 5.3.6. The results obtained with the INCL4/Abla version used in the MCNPX version used are known to be irrelevant for D, T and ^{3}He (Leray, 2008), so they were not included. Future versions of INCL4/Abla will include those light particle emissions (David, 2010).

Figure 5.3.21: Experimental and calculated pressure evolution superposed with experimental and average proton beam intensity

Experimental pressure evolution – grey line, calculated pressure evolution – black dots, experimental proton beam intensity – green line, average proton beam intensity – blue line

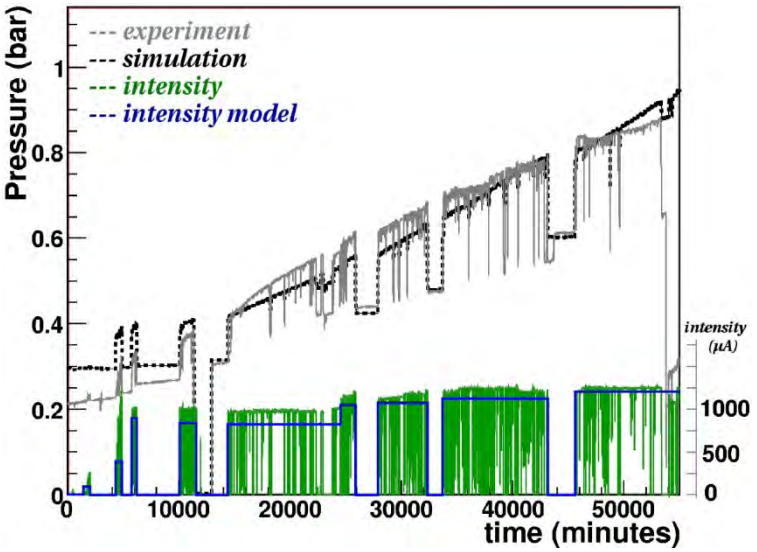

Source: Reproduced from Zanini (2008a).

Table 5.3.6: Calculated production rate per source proton of hydrogen and helium isotopes in the target

	Bertini/ Dresner	INCL4/ Abla	ISABEL/Abla
^{1}H	1.8	1.6	1.43
^{2}H	$8.9\cdot10^{-2}$	–	–
^{3}H	$4.8\cdot10^{-2}$	–	–
^{3}He	$1.3\cdot10^{-3}$	–	–
^{4}He	0.20	0.17	0.30
	CEM2k	FLUKA 2008	SNT
^{1}H	1.3	1.16	1.27
^{2}H	0.4	0.14	0.21
^{3}H	0.1	0.13	$5.7\cdot10^{-2}$
^{3}He	$3.1\cdot10^{-2}$	$5.3\cdot10^{-3}$	0.13
^{4}He	0.19	0.40	

5.3.3.6 *Conclusions of the gas production in the MEGAPIE target*

The MEGAPIE experiment has provided relevant information on spallation target neutronic and nuclear issues. The gas and volatile production is a major point concerning ADS safety. We have presented in this section a method to estimate the released quantity of noble gases and mercury. According to experimental results only a fraction (in the order of 10^{-2}) of the noble gases produced according to predictions are released from LBE after two days of operation. The fact that our calculations give comparable results for Ar, Kr and Xe underlines a similar release mechanism for noble gases. We mention that an additional measurement performed two months after the beginning of the experiment showed that the release was almost total. This is in agreement with the estimated parameter representing the release velocity. Mercury and gold have been measured and the lower limit of the expected release fraction has been extracted by considering three scenarios related to mercury diffusion in the cover gas system. In addition, the necessity to improve metastable state nuclide production in the Monte Carlo calculation is emphasised in this work. Finally, hydrogen and helium release have been observed via the pressure build-up in the expansion volume. The pressure evolution has been well reproduced by simulation codes.

5.3.4 *Estimation of the release of volatiles in accident scenarios for MEGAPIE licensing*

In the framework of licensing the MEGAPIE target, a reference accident case was defined. For this accident case, it had to be shown – using conservative assumptions – that the safety of the population living near the facility would not be endangered as a result of radioactivity emission. Additional safety measures were to be defined where required, based on the outcome of these assessments. In this section, we will summarise the licensing procedure, focusing on the methodology used for dealing with the hazard caused by the evaporation of volatiles from the liquid metal melt and draw conclusions from the experience of MEGAPIE that may prove valuable for the licensing of larger-scale facilities. A detailed treatise of the MEGAPIE reference accident case can be found in Groeschel (2006).

5.3.4.1 *The reference accident case*

Two scenarios were considered that differ in their consequences with respect to the containment of the radioactivity released from the target itself:

- *Internal failure*. In this case, the target window breaks, resulting in a destruction of the target and a complete spill of the liquid metal, leaving behind a thin layer of LBE sticking to the still-hot walls of the target. However, the outer enclosure as well as the off-gas systems of SINQ and PSI remain intact and work according to their specifications. Therefore, the emission of radioactivity will proceed through the filter systems of these off-gas systems.
- *Failure caused by external effects*. In this case, e.g. caused by a heavy earthquake, in addition to the destruction of the target itself, the ancillary systems such as the off-gas systems are at least temporarily unavailable and a leak in the outer enclosure leads to an unfiltered emission of radioactivity.

5.3.4.2 *Description of the source terms*

The inventory used within the MEGAPIE licensing procedure was calculated for an irradiation of 200 days with a proton current of 1.4 mA (575 MeV) (Pitcher, 2002). The inventory of volatile elements in the LBE is compiled in Table 5.3.7. This inventory is distributed over three source terms:

- the gas phase of the expansion volume;
- spilled LBE below the target;
- LBE surface film adhering to the inner surfaces of the target.

Table 5.3.7: Inventory of volatile elements produced by nuclear reactions in the LBE of the MEGAPIE target after 200 days of irradiation with 1.4 mA/575 MeV protons

Element	Total (g)	Radioactive nuclides (g)	Activity EoI (Bq)
Bi	508E+03	21.7	3.25E+15
Pb	414E+03	18.0	3.96E+15
Hg	14.8	1.63	1.47E+15
Tl	6.76	0.828	3.62E+15
Po	1.61	1.61	7.32E+14
At	2.58E-09	2.58E-09	3.53E+12
Ar	7.43E-10	4.86E-11	3.66E+05
Kr	0.115	0.0145	3.11E+13
Xe	0.0682	2.22E-03	7.50E+12
Br	0.028	1.64E-04	3.69E+13
I	0.0275	0.0121	1.69E+13
Cs	0.0126	7.07E-03	1.16E+13
Cd	0.163	0.0105	1.71E+13
Rb	0.0497	0.0265	4.00E+13
H	0.535	0.0359	1.28E+13
He	0.202	0	0

Source: Pitcher (2002).

The amount of volatile nuclear reaction products in LBE at the end of irradiation was calculated to be 64.1 g (approximately 70 mppm). Of that, 43.6 g are radioactive nuclides. The activity of the single elements predicted for MEGAPIE is about one order of magnitude lower than that expected for a larger-scale facility such as an LBE-based ESS at the end of its irradiation (ESS, 2010b), which is in turn expected to be smaller than that of the spallation unit of an ADS.

5.3.4.3 *Activity in the gas phase of the expansion volume*

The elements formed in the spallation zone are transported in the LBE stream. The transport to the inlet of the heat exchanger requires about 10 s. From here, they can be transferred to the expansion volume, which is connected to the liquid metal loop via a few thin pipes. The volume contraction of the liquid metal caused by interruptions in the proton beam leads to a mass exchange between expansion volume and the lower target system, which in turn results in a fast equalisation of the concentrations. For the estimation of the activities in the cover gas phase of MEGAPIE the following conservative assumptions and relations were used:

- Noble gases and hydrogen are completely and instantaneously released to the cover gas phase.
- For the remaining elements, an equilibrium concentration is quickly reached in the gas phase. This concentration is calculated from the vapour pressure relations of the pure evaporating substances (this was assumed to be Pb-Po in case of polonium. The remaining elements were considered to evaporate in the elemental state) and their concentrations in the liquid metal, assuming ideal behaviour,

i.e. using Raoult's law. This approach neglects chemical interactions between the dissolved volatiles and the liquid metal. For those elements that show a retention in LBE such as the halogens and the alkaline metals, this approach is more conservative (but also less realistic) than that discussed in Section 5.2.1, whereas for Cd and Hg the gas phase concentrations in the melt will be underestimated by a factor of 4 and 2, respectively. The analysis of literature data presented in Section 5.2.1 was, however, not available at the time MEGAPIE was licensed.

The expansion volume is vented to a decay tank every 50 days. Therefore, the activity of the noble gases and hydrogen is limited to the 50 day build-up. For the volatiles, the effect of venting is negligible because their fraction in the gas phase is very low. The maximum concentration reached at the end of the 200 d irradiation period was thus assumed. The activity in the decay tank was neglected in the accident assessment. The masses, activities and vapour pressures of gases and volatiles predicted for a temperature of 250°C in the MEGAPIE expansion tank are compiled in Table 5.3.8.

Table 5.3.8: Gaseous inventory in the expansion volume after 200 d irradiation with periodic venting of the cover gas every 50 days, calculated using the assumptions explained in the text

Element	Total mass (g)	Activity at end of irradiation (Bq)	Partial pressure (mbar)	Mass in gas phase (g)	Mass of radioactive isotopes (g)	Activity of gas phase (Bq)
Bi	508E+03	3.25E+15	6.0E-12	6.4E-14	21.7	0.41E-03
Pb	414E+03	3.96E+15	4.9E-12	5.2E-14	18.0	0.5E-03
Hg	14.8	1.47E+15	1.6E-03	1.63E-5	1.63	1.62E09
Tl	6.76	3.62E+15	1.41E-11	1.47E-13	0.828	78.5
Po**	1.61	7.32E+14	2.52E-13	5.36E-15	1.61	2.5
Ar* [a]	7.43E-10	3.66E+05	7.43E-10	ca. 1.0	4.86E-11	3.38E+04
Kr*	0.115	3.11E+13	0.115	0.029*	0.0145	3.10E+13
Xe*	0.0682	7.50E+12	0.0682	0.017*	2.22E-03	6.39E+12
Cs	0.0126	1.16E+13	7.5E-12	5.1E-14	7.07E-03	47
Cd	0.163	1.71E+13	1.13E-09	6.5E-12	0.0105	678
Rb	0.0497	4.00E+13	1.75E-08	8.9E-13	0.0265	716
H*	0.535	1.28E+13	0.134*	0.134*	0.0359	3.21E12
He*	0.202	0	0.051*	0.051*	0	0

* 50 day build-up; [a]Cover gas: 0.5 bar Ar at 250°C: ≅ 1 g; ** Po calculated as PbPo.

Source: Groeschel (2006).

As shown in Table 5.3.8, the noble gases, hydrogen and mercury are the prominent elements in the cover gas phase. The amount of polonium activity transferred to the gas phase by sputtering was estimated to be $1.2 \cdot 10^3$ Bq (Groeschel, 2006). This significantly increases the polonium concentration in the gas phase. The additional gas phase activity resulting from sputtering of β and γ emitters was predicted as $2.8 \cdot 10^4$ Bq (mainly Pb and Bi isotopes), which is negligible compared to the activity arising from evaporation.

Among the volatile elements, only the most hazardous mercury and polonium were considered in the assessment of the MEGAPIE reference accident case. Generally, for larger-scale facilities such as ADS much higher total gas phase radioactivities have to be expected arising from both the longer and more intense irradiation and from the larger cover gas volume. For instance, for an LBE-based ESS (5 MW LBE spallation target irradiated for 40 years), a factor of about 1 000 higher activities were estimated in the cover gas for some volatile nuclides (ESS, 2010a, 2010b).

5.3.4.4 *Activity released from spilled LBE*

In the analysis of the MEGAPIE reference accident case, it was assumed that the approximately 88 litres of LBE with a mean temperature of 300°C flow out of the target. To estimate the release from this spilled liquid metal, two factors had to be considered:

- Distribution of the LBE (finely dispersed liquid metal results in a large surface area, but also leads to fast cooling and solidification; a pool-like spill has a smaller surface, but cools slower).
- Interaction with water (coolant and/or moderators).

As a starting point to estimate the release from a pool of LBE, the model of a pool of 4 m^2 surface and a thickness of 2.2 cm introduced in the MEGAPIE safety report (Perret, 2002) was used. Based on the cooling curve for this pool given in Perret (2002), the evaporation behaviour of the volatile nuclides can be calculated using the methods described in Section 5.2.

In case of interaction with water, the cooling can be very fast, but the formation of vapour and aerosols that both can carry radioactivity has to be considered. However, the amount of radioactivity that can be released from LBE in these processes is difficult to estimate using the current knowledge of LBE-water interaction and the behaviour of the numerous nuclear reaction products under these conditions. Therefore, an estimation of the release path via vapour and aerosols was not possible in the MEGAPIE accident study. For large-scale facilities such as ADS or lead-alloy-cooled reactors with a larger radioactive inventory and much longer operation time compared to MEGAPIE, studies will have to be performed to clarify these issues. An extensive assessment for the estimation of the amount of water vapour that can be produced by interaction with LBE, the pressure wave induced by this evaporation and the amount of tritium and radioactive O, C and N isotopes carried with the vapour has been performed within the MEGAPIE accident study. However, in this section, we will confine ourselves to list the estimated amount of T, O, C and N released from water originating from the window cooling and the moderator tank.

An estimation of the amount of radioactivity released due to the pressure increase caused by LBE-water interaction comprises the inventory of:

- the expansion volume (^{3}H, Kr, Xe, Hg und Po);
- the tritiated water vapour (^3H_2O);
- gases dissolved in the heavy water of window cooling and moderator (O, N, C).

It was shown in extensive studies (Groeschel, 2006) that about 13.5% of this material could reasonably be assumed to be released from the target facility within the boundary conditions of the reference accident case, leading to the activities listed in Table 5.3.9.

Table 5.3.9: Activity from expansion volume, moderator and window cooling, released in the pressure wave caused by LBE-water interaction

Element	Activity from expansion volume, (Bq)	13.5%
Hg	1.62E+09	2.2E+08
Po	1.2E+03 (sputtering)	31.6E+02
Kr*	3.10E+13	4.2E+12
Xe*	6.39E+12	8.6E+11
Tritium	3.21E+12	4.2E+11
Activity from moderator and cooling		
Tritium	1.05E+11	1.4E+10
CNO	2.8E+12	3.8E+11

* 50 day build-up.

Source: Groeschel (2006).

For the calculation of the activity release from the spilled pool of LBE, the "dry" case with slow cooling was considered. It was calculated that in this case the LBE pool cools down to the melting point in about 11 minutes and afterwards takes about 34 minutes to solidify. It was assumed that the activity released in this scenario would encompass the release in the – difficult to assess – case of interaction with water leading to fast cooling and water evaporation with entrainment of radioactivity. The estimations performed were limited to the evaporation of Hg and Po, because these nuclides pose the by far most hazardous constituents.

For the evaporation rate of polonium, data from Perret (2002) derived by interpolation from data given in Tupper (1991) were used:

- Po evaporation rate at 340°C: $2 \cdot 10^{-8}$ Bq $m^{-2}s^{-1}$ per Bq/kg LBE.
- The temperature dependence of the evaporation rate was incorporated based on the temperature dependence of the vapour pressure of pure Pb-Po given in Abakumov (1974).

For the calculation of the evaporation of mercury from LBE, values for the evaporation rate determined by Greene (1998) were used, corresponding to the evaporation of mercury from a lead pool under air:

- Hg evaporation rate at 340°C: $1.97 \cdot 10^{-7}$ g $cm^{-2}s^{-1}$ at a concentration of 108 mass ppm mercury.
- The temperature dependence of the evaporation rate was incorporated based on the temperature dependence of the vapour pressure of pure mercury given in CRC (1989).

Figure 5.3.22 shows the cooling behaviour of the LBE pool (Perret, 2002), while the cumulative mercury and polonium evaporation from the pool is depicted in Figures 5.3.23 and 5.3.24. The graphs show that the major part of the activity is released in the first 5 minutes. The calculated cooling curve mainly results from heat transfer to the concrete floor. It has to be pointed out that the amount of polonium released calculated for this scenario becomes almost a factor 3 lower when one uses Eq. (5.66) given in this report, which was derived in the final stages of MEGAPIE licensing (Neuhausen, 2005b) and can be considered more reliable than the original approach used for the MEGAPIE intermediate safety report. The amount of activity released by sputtering within 24 hours after the spill was also estimated and found to be low compared to that released by evaporation during solidification (see Section 5.2.1.1.5.5).

Figure 5.3.22: Calculated cooling curve of an LBE spill of 4 m²

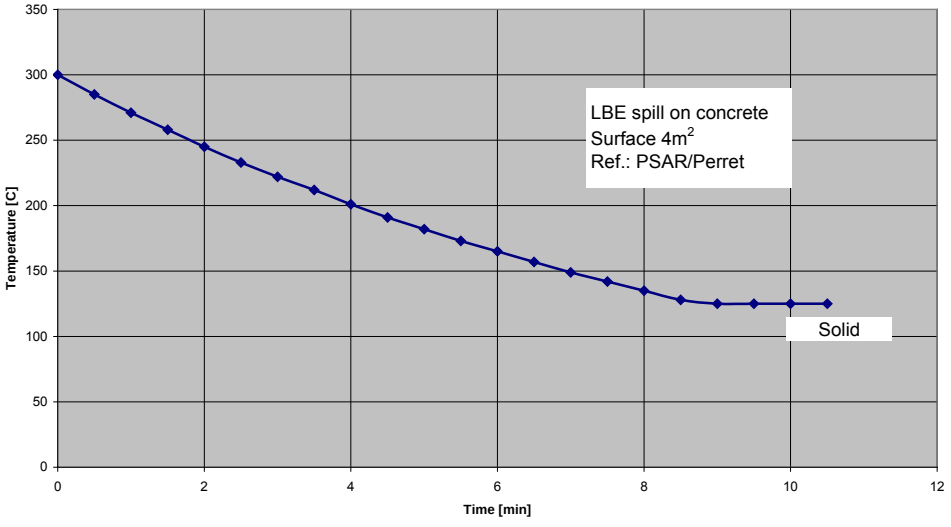

Source: Curve calculated by Perret (2002), reproduced from Groeschel (2006).

Figure 5.3.23: Cumulative Hg evaporation from LBE spill

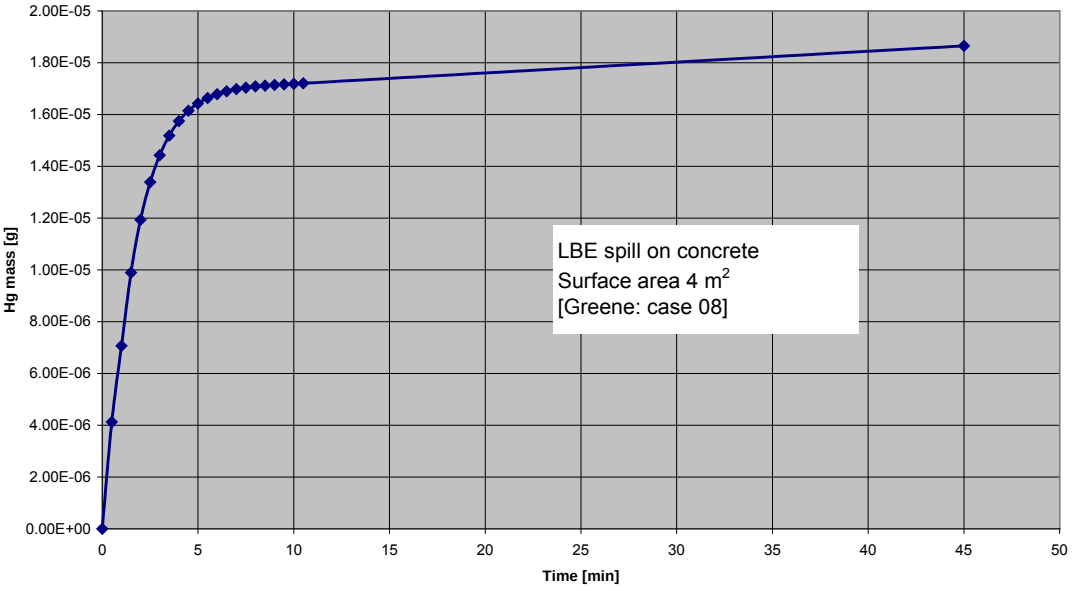

Source: Groeschel (2006).

Figure 5.3.24: Cumulative evaporation of Po from LBE spill

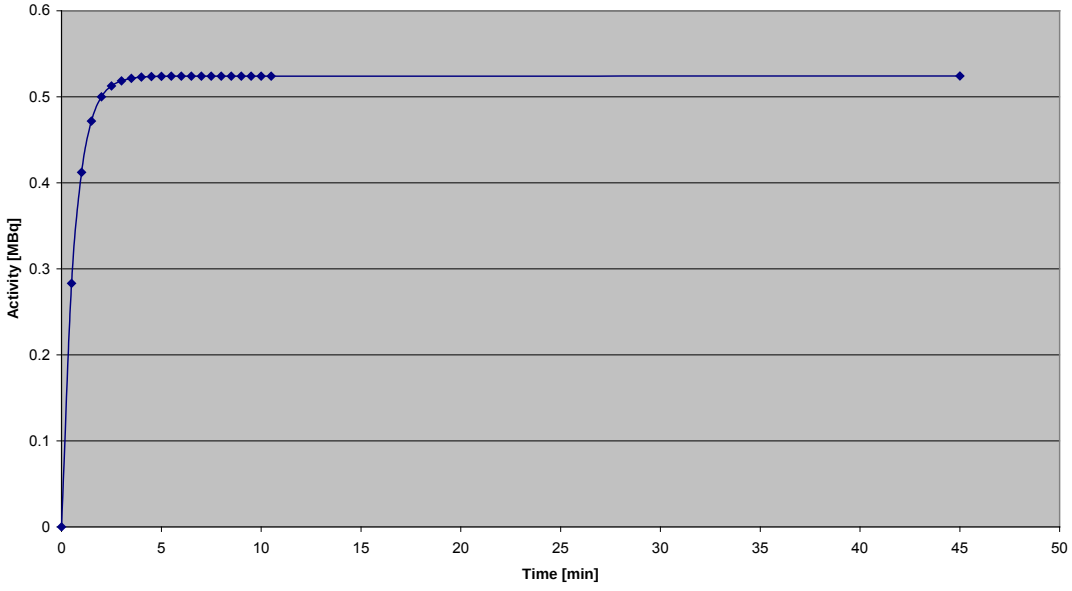

Source: Groeschel (2006).

Table 5.3.10 summarises the amounts of radioactivity released from the pool within the first 24 h after the spill.

The evaporated and sputtered material will mix with the gas volume in the proton beam line cellar, where the spill will occur and can then be transported through the facility to be released to the environment.

Table 5.3.10: Activity released from an LBE spill (4 m^2) within the first 24 h

Element	Inventory in LBE EoI (g)	Inventory in LBE EoI (Bq)	Evaporated mass (g)	Evaporated activity (Bq)	Sputtered activity (Bq)
Hg	14.8	1.47E+15	1.8655E-5g	1.86E+09	
Pb+Bi					1.48E+06
Po	1.61	7.32E+14	–	5.25E+05	6.4E+05

Source: Groeschel (2006).

5.3.4.5 *Activity released from the thin film of LBE adhering to the walls of the target*

After the liquid metal flowed out of the target, a thin film of LBE will remain on the wetted surfaces of the walls of the target. According to experiences with other LBE loops, the thickness of this film was estimated to be about 20 μm. This corresponds to a mass of 3.5 kg (0.4% of the total LBE in the target) deposited on 16.7 m^2. After the LBE has flown out, these structures slowly cool down via heat conduction, radiation and convection. The cooling curves of different target components were calculated to estimate the release of mercury and polonium from these surfaces in a subsequent step. More details of these calculations can be found in the original work (Groeschel, 2006) and a more thorough analysis using computer modelling (Mikityuk, 2008). We limit our discussion in this report to a description of the main results. Three main scenarios were studied:

1) Target head remains closed; slow cooling; slow diffusion of radioactive gas.
2) Target head contains disrupted gas and coolant pipes. This case was divided in two sub-scenarios 2a) and 2b) with different gas flow conditions within the target (see Groeschel [2006] for details), both with faster cooling, but also faster transport of radioactivity as compared to Case 1.

As an example, Figure 5.3.25 shows the cooling behaviour calculated for various components of the target for one of these scenarios.

For the three scenarios, the cumulative evaporation of mercury and polonium was estimated using the same methods employed for calculating the release from spilled LBE. Examples of the results for both mercury and polonium are shown in Figures 5.3.26 and 5.3.27. The results for all three cases are compiled in Table 5.3.11.

After solidification, further activity is released by sputtering. However, this activity was estimated to be three orders of magnitude lower compared to that resulting from evaporation, based on the knowledge available at that time. Considering the experiences concerning sputtering made at PSI during the last years indicating that sputtering from polonium-containing LBE samples are orders of magnitude higher than calculated using the methods used in Perret (2002) and Groeschel (2006), we strongly recommend that these phenomena be studied in more detail for the licensing of large-scale facilities.

Using these values for evaporated and sputtered activities, various accident scenarios have been analysed. In these analyses it was proven that the goals in radioprotection for the environment can be achieved for MEGAPIE. However, additional safety measures had to be taken compared to the routine operation of a solid target in SINQ:

1) The atmosphere of the proton beam line cellar had to be rendered inert by lowering its oxygen concentration to exclude a fire caused by ignition of the organic liquid used as secondary coolant.
2) The SINQ exhaust gas system had to be equipped with additional charcoal – and aerosol filters, earthquake-resistant shut-off flaps and an autonomously operating

high capacity suction and filtering system that ensures a directed flow of gas even in the case of significant leaks.

3) Furthermore, a mobile suction and filtering unit had to be provided that serves as a back-up of the off-gas filtering systems mentioned above.

Using these additional measures it was proven to the licensing authorities that even under severe accident scenarios the population living in the environment of the facility would not be exposed to doses higher than 1 mSv. For more details on the accident analysis, see the original reports (Perret, 2002; Groeschel, 2006).

Figure 5.3.25: Cooling of target components in the upper part of the target in case of a closed target head

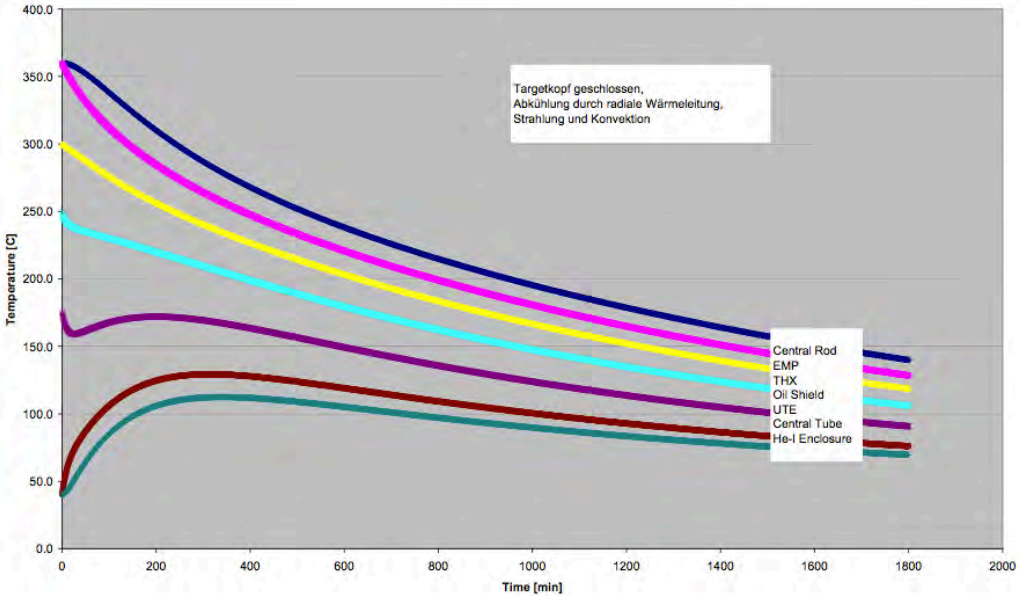

Source: Groeschel (2006).

Figure 5.3.26: Evaporation of Hg from the thin LBE film on the surface of the inner target structures, accident scenario with closed target head

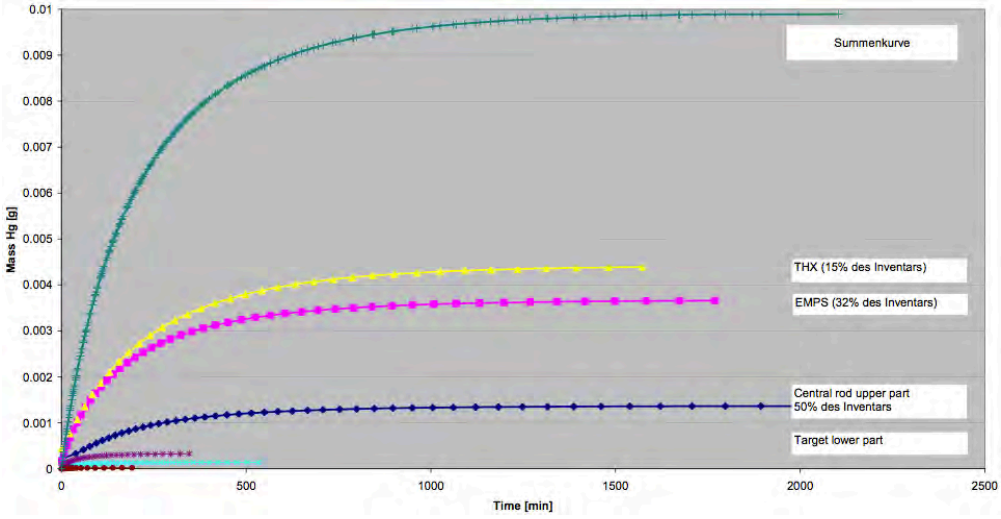

Source: Groeschel (2006).

Figure 5.3.27: Evaporation of Po from the thin LBE film on the surface of the inner target structures, accident scenario with closed target head

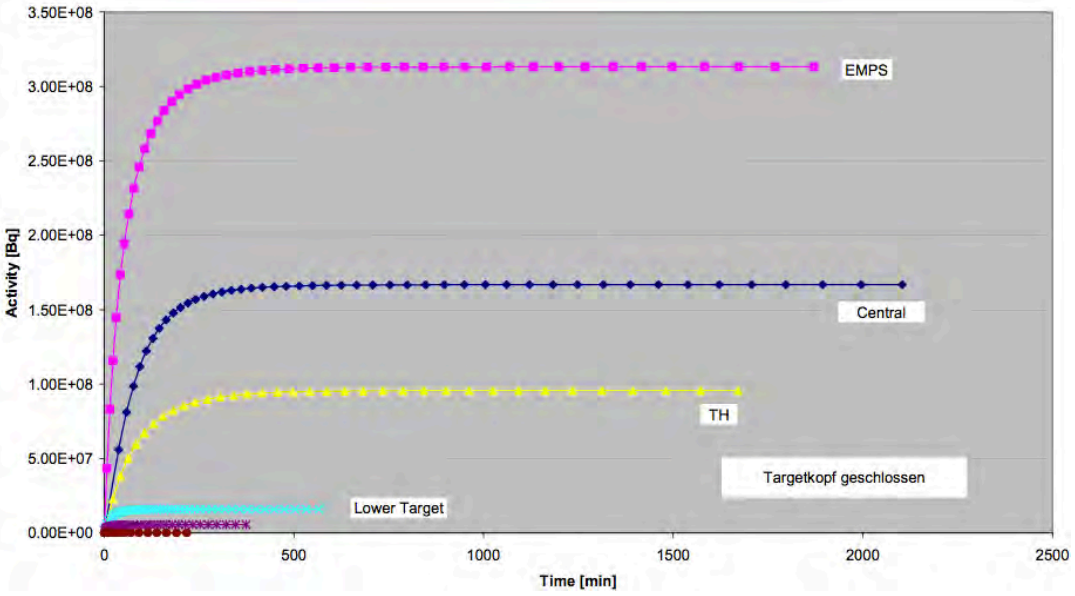

Source: Groeschel (2006).

Table 5.3.11: Mass and activity of mercury and polonium released by evaporation (until solidification) and sputtering (within the first 24 h) from the LBE film adhering to the inner target structures for different scenarios

Element	Inventory in film (g)	Inventory in film (Bq)	Evaporated mass (g)	Evaporated activity (Bq)	Sputtered activity (Bq)
Scenario 1	Target head closed				
Hg	0.0569	5.65E12	0.0099	9.83E+11	
Pb/Bi					5.291E+06
Po	0.0062	2.82E12		5.97E+08	2.34E+05
Scenario 2a	Target head open				
Hg	0.0569	5.65E12	0.0065	6.45E+11	
Pb/Bi					3.848E+06
Po	0.0062	2.82E12		4.90E08	1.7E+05
Scenario 2b	Target head open				
Hg	0.0569	5.65E12	0.0041	4.06E+11	
Pb/Bi					3.848E+06
Po	0.0062	2.82E12		1.7528E08	1.7E+05

5.3.5 *LiSoR irradiation*

The Liquid Metal – Solid Metal Reaction (LiSoR) loop is a unique facility which was designed to simultaneously investigate the influence of flowing lead-bismuth eutectic (LBE), static stress and irradiation by protons onto materials specimens.

The loop with the test section was designed and constructed by Subatech, France; the liquid metal pump and flow meter was delivered from IPUL, Latvia; assembling, cabling, isolating and commissioning was performed at PSI, Switzerland. The LiSoR test facility installed in the IP1 bunker is connected to a beam line from the Philips PSI accelerator. The beam energy on the target was about 72 MeV maximum for the five irradiation experiments, while different beam currents between 15 and 50 μA were chosen for each irradiation period.

The loop was fabricated of austenitic stainless steel 316L whereas in the test section ferritic steel T91 was used. The flow rate of the pump is up to 0.3 l/s, which corresponds to a flow velocity of about 1 m/s in the test section. The total amount of LBE in the melting vessel was about 18 l, of which approximately 15 l were filled into the loop for operation.

Up to 2005, five LiSoR test sections have been irradiated. After each irradiation cycle the loop was drained and the irradiated LBE was collected in the storage tank together with the non-irradiated remaining 5 l. After a reasonable decay time the test section was disconnected from the loop and transported into a hot cell for disassembly and examination. LBE was never changed or refilled, i.e. most of LBE was irradiated during all the experiments, except the part remaining in the storage tank. The isotopes generated during irradiation are mostly short-lived nuclides with half-life times in the range days at most. Only the isotopes ^{207}Bi ($T_{1/2}$ = 31.55 y) and ^{208}Po ($T_{1/2}$ = 2.898 y) have relatively long half-lives. The other isotopes except ^{207}Bi and ^{208}Po formed during irradiation experiments 1 to 4 decayed. The time between irradiation experiment No. 4 (ended after only 144 h of irradiation on 25 June 2003) and No. 5 (irradiation started on 21 April 2004) was nearly 10 months, enough time for decay of the short-lived nuclides.

The eutectic LBE (44.8 wt.% Pb and 55.2 wt.% Bi) alloy which was used for filling LiSoR was supplied by Impag AG, Switzerland and contained a very low concentration of impurities: Ag 11.4, Fe 0.78, Ni 0.42, Sn 13.3, Cd 2.89, Al 0.3, Cu 9.8 and Zn 0.2 ppm respectively. During the commissioning phase (approximately 2 000 h of operation with LBE temperatures between 473 and 573 K without irradiation) and during the five irradiation periods the impurity levels should have increased due to corrosion products (dissolving of steel elements) and formation of stable decay products.

The irradiated LBE was analysed after the LiSoR 2 experiment with high-resolution α-spectroscopy on chemically separated solutions (Glasbrenner, 2005). Nuclear calculations were also made in order to compare the experimentally determined activities with predictions by calculations. In Table 5.3.12, the calculated values are compared with the experimental ones. The analysis was carried out about half a year after the irradiation was completed. Thus, only Po isotopes with relatively long half-life time could be analysed. Calculations taking the correct beam parameters into account also indicated the generation of the Po isotopes 202, 203, 204, 205 and 207. It is believed that these isotopes were present during and directly after irradiation but due to their short half-lives they had already decayed when the analysis was started. A comparison of the calculated and the experimental activities achieved for the Po isotopes 206 and 208 shows a reasonable agreement between the calculated and experimentally determined values, whereas the theoretical prediction of the ^{210}Po activity is too low. The generation of the ^{210}Po isotope requires thermal neutrons and the FLUKA code used for predictions at that time had only included reactions with fast neutrons. It is definitely possible that during the irradiation a small fraction of thermal neutrons is generated, and these will then inevitably be a source of ^{210}Po production from the bismuth.

Table 5.3.12: Values of Po isotopes revealed by neutronic calculation in comparison with experimental data

Isotope	Bq/calc.	Bq/g calc	Bq/g exp
^{202}Po	$3.1 \cdot 10^{9}$	$1.6 \cdot 10^{4}$	
^{203}Po	$2.3 \cdot 10^{11}$	$1.2 \cdot 10^{6}$	
^{204}Po	$9.9 \cdot 10^{11}$	$5.3 \cdot 10^{6}$	
^{205}Po	$1.1 \cdot 10^{12}$	$5.9 \cdot 10^{6}$	
^{206}Po	$9.1 \cdot 10^{10}$	$4.8 \cdot 10^{5}$	$9.95 \cdot 10^{5}$
^{207}Po	$7.9 \cdot 10^{11}$	$4.2 \cdot 10^{6}$	
^{208}Po	$5.9 \cdot 10^{8}$	$3.1 \cdot 10^{3}$	$4.8 \cdot 10^{3}$
^{210}Po	$2.0 \cdot 10^{6}$	11	150

5.3.6 *Experience from accidents on Soviet nuclear-powered submarines*

Within the military naval programme of the Soviet Union, considerable effort was put into the development of a compact lead-bismuth-cooled nuclear reactor for driving ships or submarines. The major work on the reactor design was performed at the Institute of Physics and Power Engineering (IPPE) in Obninsk, Russia, where a prototype reactor (27/VT, 70 MW_{th}) was built and operated since 1959 (Suvorov, 1999). In total, eight nuclear submarines (one prototype "Project 645", seven of "Project 705") were built and put into service as of 1971. During their period of service, three submarines suffered serious accidents involving partial core melting as well as spills of the coolant material into the reactor compartment, causing significant contamination by ^{210}Po and its α-active aerosols.

Only a few reports on the research performed during development of these reactors and the experience gained with Soviet LBE-cooled nuclear systems, including practical experience dealing with leaks of activated coolant material, are accessible to western scientists, since a major part of this research still remains classified. In Pankratov (1999) some general procedures are described in handling spilled LBE containing high levels of ^{210}Po in the order of 1 Ci/kg.

By monitoring the activity of airborne ^{210}Po and the degree of contamination on surfaces after spills and during decontamination work, the following measures were found to minimise the spread of radioactivity from spilled LBE:

1) *Removal of ingots of the solidified metal.* Solidified LBE ingots have to be removed prior to decontamination procedures as they largely contribute to recontamination of previously cleaned surfaces and the release of ^{210}Po into the surroundings. Presumably sputtering largely drives the spread of radioactivity from solidified spills of LBE containing polonium. This effect may be similar to the spontaneous formation of dust observed on lava-like fuel containing materials in the debris of the Chernobyl reactor core (Baryakhtar, 2002).

2) *Cutting or welding in high-contaminated areas should be avoided.* Mechanical cutting of the coolant material resulted in a significant increase of the airborne ^{210}Po activity, most likely due to the formation of aerosol particles. Such procedures have to be avoided, if possible.

3) *Decontamination/covering of surfaces with strippable films.* Highly contaminated surfaces were coated by polymer films for "protection and deactivation" purposes. These films are claimed to vastly improve the radiation situation by decreasing the surface activity to permissible levels and also decreasing the release of airborne polonium. High moisture content is reported to decrease the protection efficiency. A more detailed description of the films is not yet available.

5.3.7 *Summary and conclusions on the experience from medium- and large-scale experiments*

In the preceding sections we collected valuable results from experiments involving LBE irradiation beyond the laboratory scale, focusing on the behaviour of radioactive impurities generated in the LBE during irradiation. These results were discussed in context with the fundamental physicochemical properties reviewed in Section 5.2.

In an experiment at the ISOLDE facility at CERN, an LBE target was irradiated with protons to study the production of gaseous and volatile nuclear reaction products and their release from the target. The production of these nuclear reaction products was predicted by state-of-the-art nuclear physics models. In the experiment, it was found that isotopes of the noble gases were released from the rather small target without noticeable delay, while for isotopes of other volatile elements such as mercury, cadmium, iodine and astatine a significant retention in the target was observed. This retention can be caused both by interaction of the element with the liquid metal matrix and by adsorption to walls in the experimental facility. In qualitative agreement with the physicochemical data and results of laboratory scale evaporation experiments discussed in Section 5.2, this retention is rather weak for mercury isotopes but much stronger for cadmium, iodine and astatine. The retention leads to a partial decay of short-lived nuclides before they can be detected. When this retention is taken into account and the latest nuclear physics models are used for calculations, a good agreement between the predicted amounts of radionuclides and experimental data is achieved. It is however difficult to extract precise information on the complex mechanism of release from the available data.

More information on the release of volatiles from LBE in a complex installation was obtained from the analysis of the cover gas of the liquid LBE spallation target MEGAPIE. The experimental results indicate that only a fraction (in the order of 10^{-2}) of the noble gases produced according to predictions are released from LBE after two days of operation of this much larger and more complex target system. Additional measurements performed two months after the beginning of the irradiation experiment showed that noble gas release was almost complete at that time. Hydrogen and helium release were measured via the pressure build-up in the expansion volume. The pressure evolution has been well reproduced by nuclear simulation codes. Finally, a lower limit of the release fraction of mercury isotopes was extracted by considering different scenarios for mercury diffusion in the cover gas system. The results are in qualitative agreement with the volatilisation behaviour found in the ISOLDE target and the physicochemical data presented in Section 5.2. However, because of the larger size and higher complexity of the MEGAPIE target as compared to the ISOLDE target, release from MEGAPIE was generally slower.

A summary is given explaining how the amount of radioactivity possibly released from the MEGAPIE target under normal operation and specific accident scenarios was estimated for its licensing. Based on this assessment, the MEGAPIE experiment was successfully licensed, and finally the target was safely operated for four months. The data collected during its operation concerning the evaporation of volatiles were found to be consistent with the understanding of release processes. This experience should prove valuable for the licensing of future facilities, but it should be kept in mind that MEGAPIE was a prototype with limited power and lifetime. For industrial-scale facilities more detailed analysis may be required because of their still higher complexity and the longer operation times, higher power and thus larger amounts of radioactivity produced.

Radionuclide distribution in the LBE of the ISOLDE target after end of irradiation was analysed using radiochemical methods. These studies revealed inhomogeneities in the distribution of radionuclides of electropositive elements, which tend to accumulate on the free surface of the liquid metal and the walls of the target container. Indications were also found that small particles remain suspended in the liquid metal containing these elements. It is speculated that these electropositive elements are oxidised and the formed oxides separate from the liquid metal. On the other hand, noble metals such as silver,

gold and also polonium remain more or less homogeneously distributed in the bulk liquid metal. Similar effects were meanwhile also found – to a much larger extent – in samples from the irradiated MEGAPIE target.

Finally, short accounts are given summarising results of the LiSoR experiment and the scarce information available in the open literature on the experience with Russian submarines driven by LBE-cooled reactors.

Overall, the experiences from these medium- and large-scale facilities and experiments indicate that the production of the most relevant gaseous and volatile radionuclides can be predicted with reasonable reliability using the most recent nuclear physics models. The release behaviour of volatile radionuclides observed in the experiments and facilities discussed in this section seems fairly well understood. Noble gases are released relatively quickly from liquid LBE because they are extremely volatile and show no retentive chemical interaction with the liquid metal. Nevertheless, their release from large and complex facilities may be retarded by diffusion as shown in the MEGAPIE gas analysis. The release of volatiles such as mercury, iodine and polonium is much less pronounced, caused by their lower volatility as compared to the noble gases and also, in the cases of iodine and polonium, because of a distinct attractive chemical interaction with the liquid metal. As a consequence, for mercury isotopes relatively short retention times were observed in the ISOLDE experiment, and in MEGAPIE mercury isotopes were detected in the cover gas analysis. On the other hand, iodine release from the ISOLDE target was extremely retarded and in MEGAPIE no iodine was detected in the cover gas. In both experiments, no polonium activity was detected except for trace amounts that can be explained by decay of more volatile astatine released to the gas phase. These observations, i.e. increasing volatility in the order noble gases $\rightarrow$ mercury $\rightarrow$ iodine $\rightarrow$ polonium, are in good agreement with the volatility assessment given in Section 5.2. Despite this apparently good understanding the latest polonium evaporation experimental results (see addendum to Section 5.2.1.1.5.3) show that under certain circumstances increased volatilisation may occur. The experiences from MEGAPIE and ISOLDE indicate that these processes did not cause significant polonium evaporation under the operational conditions of these systems. However, it cannot be ruled out that such phenomena may play a significant role in scenarios where the polonium-containing liquid metal enters into contact with moisture, e.g. steam generator tube ruptures. Thus, these processes have to be studied in more detail to understand the parameters governing the occurrence of enhanced polonium volatilisation and to develop countermeasures to cope with possible consequences. Further research should also be devoted to the transfer of fission products from defective fuel elements to the liquid metal and their transport and deposition within and their release from the system under various conditions.

Thus, results from larger-scale experiments indicate that heavy-liquid-metal-cooled nuclear systems can be operated safely when the liquid metal remains cold and well contained, and the radioactivity in the cover gas is properly controlled. However, there remain both safety-related and operational problems that have to be addressed to ensure this operational safety, many of them related to the transport and deposition of radioactive impurities within the system. In the present chapter, we have compiled both fundamental data and practical experiences that should provide a basis to solve these problems.

References

Abakumov, A.S. and Z.V. Ershova (1974a), "Vapor Tension of Polonium and Lead Polonide, Radiokhimiya", Vol. 16, pp. 397-401, *Soviet Radiochemistry*, Vol. 16, pp. 396-399.

Abakumov, A.S. and Z.V. Ershova (1974b), "Vapor Tension and Thermal Dissociation of Polonium Dioxide", *Soviet Radiochemistry*, Vol. 16, pp. 400-403.

Abakumov, A.S. (1982), "Thermal Reactions of Polonium", *Russ. Chem. Rev.*, Vol. 51, pp. 622-629.

Ausländer, J.S. and J.I. Georgescu (1956), "On the Vapour Pressure of Polonium at Room Temperature", *1st International Conference on the Peaceful Use of Atomic Energy*, Geneva, 1955, pp. 389-391.

Bagnall, K.W. (1957), *Chemistry of Rare Radioelements, Polonium – Actinium*, Butterworths, London.

Bagnall, K.W. (1966), *The Chemistry of Selenium, Tellurium and Polonium*, Elsevier, New York.

Bagnall, K.W. (1983), "The Chemistry of Polonium", *Radiochim. Acta*, 32, pp. 153-161.

Bagnall, K.W. (1990), "Compounds of Polonium: Polonium and Hydrogen", *Gmelin Handbook of Inorganic and Organometallic Chemistry, Polonium*, Supplement Vol. 1, pp. 286-288, Springer-Verlag, Berlin.

Barin, I. (1993), *Thermochemical Data of Pure Substances*, 2nd Ed., VCH, Weinheim.

Barin, I. (1995), *Thermochemical Data of Pure Substances*, 3th Ed., VCH, Weinheim.

Baryakhtar, V., et al. (2002), "Radiation Damages and Self-Sputtering of High-Radioactive Dielectrics: Spontaneous Emission of Submicronic Dust Particles", *Condensed Matter Physics*, Vol. 5, 3 (31), pp. 449-471.

Benlliure, J. et al. (1998), "Calculated Nuclide Production Yields in Relativistic Collisions of Fissile Nuclei", *Nuclear Physics A*, 628 (3) pp. 458-478.

Bergmann, U.C. et al. (2003), "Production Yields of Noble-Gas Isotopes from ISOLDE UC_x/Graphite Targets", *Nucl. Instr. and Meth. in Phys. Res.*, B204, pp. 220-224.

Bertini, H.W. (1969), "Intranuclear-Cascade Calculation of the Secondary Nucleon Spectra from Nucleon-Nucleus Interactions in the Energy Range 340 to 2900 MeV and Comparisons with Experiment", *Phys. Rev.*, Vol. 188, pp. 1711-1730.

Böwering, N. et al. (1998), "Spin-Resolved Photoelectron Spectroscopy in the Auto-Ionization Region of Atomic Bismuth", *J. Phys. B: At. Mol. Opt. Phys.*, 31, pp. 5221-5232.

Borisov, N.B. et al. (1980), "Radiatsionnaya bezopasnost pri rabote s polonijem-210", *Atomizdat*, Moscow.

Borisov N.B. et al. (1995a), "Specific Properties of Polonium Aerosols", *Colloid J. Russ. Acad. Sci.*, 57, pp. 7-10.

Borisov, N.B. et al. (1995b), "Investigation of the ^{210}Po Yield from Lead-Lithium Eutectic in Application to the Conditions of the Blanket of a Thermonuclear Reactor", *Atomic Energy*, 79, pp. 702-705.

Borisov, N.B. (1999), "On the 275th Anniversary of the Russian Academy of Sciences: Research on Polonium Aerosols and Appropriate Safety Measures under the Leadership of I.V. Petryanov-Sokolov", *Atomic Energy*, 86, pp. 385-387.

Boudard, A. et al. (2002), "Intranuclear Cascade Model for a Comprehensive Description of Spallation Reaction Data", *Phys. Rev. C*, Vol. 66, No. 044615.

Boudard, A. et al. (2013), "New Potentialities of the Liège Intranuclear Cascade Model for Reactions Induced by Nucleons and Light Charged Particles", *Phys. Rev. C*, Vol. 87, No. 014606.

Boutellier, V. (2008), *ISOLDE-Target*, Technical Note TM 43-08-14, Paul Scherrer Institut, Villigen.

Bradley, R.F. (1968), *Surface Depletion in the Vacuum Distillation of Metals from Bismuth,* Report DPMS6852, Savannah River Site, DOE.

Bradley, R.F., L.F. Landon and G.W. Gibson (1970), *Separation of ^{210}Po from Bismuth by Liquid Metal Distillation*, Report TID-4500, US Atomic Energy Commission, Savannah River Laboratory, Aiken, South Carolina.

Brewer, L. (1953), "Thermodynamic Properties of the Oxides and their Vaporization Processes", *Chem. Rev.*, Vol. 52 (1), pp. 1-75.

Brooks, H. (1904), "A Volatile Product from Radium", *Nature*, 70, p. 270.

Brooks, L.S. (1955), "The Vapour Pressure of Polonium", *J. Am. Chem. Soc.*, Vol. 77, p. 3211.

Brebrick, R.F. (1968), "Characterization of Phases in the 50-60 at.% Te Region of the Bi-Te System by X-ray Powder Diffraction Patterns", *J. Applied Crystallography*, 1, pp. 241-246.

Buongiorno, J., C. Larson and K.R. Czerwinski (2003), "Speciation of Polonium Released from Molten Lead Bismuth", *Radiochim. Acta*, Vol. 91, pp. 153-158.

Buongiorno, J. et al. (2004), "Studies of Polonium Removal from Molten Lead-bismuth for Lead-alloy-cooled Reactor Applications", *Nuclear Technology*, 147, pp. 406-417.

Butler, P.A. (2011), "ISOL Techniques to Reach Radioactive Nuclei: From Birth to EURISOL", *Proceedings of the International School of Physics "Enrico Fermi"*, Vol. 178, From the Big Bang to the Nucleosynthesis, A. Bracco, E. Nappi (eds.), IOS, Amsterdam, DOI 10.3254/978-1-60750-974-5-173.

CERN (European Organisation for Nuclear Research) (n.d.), *ISOLDE: The Radioactive Ion Beam Facility: Targets and Separators* (web page), accessed 15 July 2014, CERN, Switzerland, http://isolde.web.cern.ch/targets-and-separators.

Cetnar, J. and G. Domanska (2010), "Evaluation of Circuit Activation and Radiotoxicity in the LBE Cooled XADS Experimental Accelerator Driven System Using Monte Carlo Method MCB", *Nukleonika*, 55 (1), pp. 119-125.

Clark, J.L. et al. (1982), "Inclusive π-Production with 200 MeV Protons – Radiochemical Study of the ^{209}Bi (π,xn) At^{210-x} Reactions", *Physical Review C*, 26 (5), pp. 2073-2083.

Courouau, J.L. (2003), Technical Note NT STR LCEP 2003/001, CEA.

Crank, J. (1992), *The Mathematics of Diffusion*, Clarendon Press, Oxford.

CRC (1989), *CRC Handbook of Chemistry and Physics*; 69th edition.

Cubicciotti, D. and F.J. Keneshea (1959), "The Vapor Pressures of BiI Over Liquid Bi-BiI$_3$ Solutions", *J. Phys. Chem.*, 63, pp. 295-296.

Dai, Y. et al. (2009), *Specimen Extraction Plan for MEGAPIE PIE,* MEGAPIE-Report MPR-11-DY34-001-2, Paul Scherrer Institut, Villigen, Switzerland.

David, J.C. et al. (2007), *Benchmark Calculations on Residue Production Within the EURISOL DS Project,* Saclay internal report DAPNIA-07-59/04, CEA, France.

David, J-C. (2010), "INCL4.5 and Abla0 – Improved Versions of the Intranuclear Cascade (INCL4) and Deexcitation (Abla) Models", *Proceedings to the Shielding Aspects of Accelerators, Targets and Irradiation Facilities*, CERN, Meyrin, Switzerland.

David, J.C. et al. (2013), "Modeling Astatine Production in Liquid Lead-bismuth Spallation Targets", *Eur. Phys. J.* A, 49: 29, DOI 10.1140/epja/i2013-13029-4.

de Boer, F.R. et al. (1988), *Cohesion in Metals, Transition Metal Alloys*, North-Holland, Amsterdam.

Dementjevs, S. (2010), private communication.

DeVore, J.R. and D.W. Freeman (2007), "Treatment of Mercury Target Off-Gas at SNS", *Proc. 8th Int. Topical Meeting on Nuclear Applications and Utilization of Accelerators (AccApp07)*, Pocatello, Idaho, 29 July-2 August, ANS, LaGrange Park, Illinois..

de Wijs, G.A. et al. (1995), First-Principles Molecular-Dynamics Simulation of Liquid Cs-Pb, *J. Chem. Phys.*, 103, pp. 5031-5040.

Dikarev, E.V., V.A. Trifonov and B.A. Popovkin (1987), "New Data on the T-x Equilibrium Diagram of the Bi-BiI_3-System in the Range of Existence of Lower Crystalline Bismuth Iodides", *Russ. J. Inorg. Chem.*, Vol. 32, p. 238.

Dresner, L. (1962), *EVAP – A Fortran Program for Calculating the Evaporation of Various Particles from Excited Compound Nuclei*, ORNL-TM-196, Oak Ridge National Laboratory, Oak Ridge, TN.

Eichler, B. (1979), *Bestimmung der Adsorptionswärme gasförmiger Metalle auf festen Metalloberflächen bei Nullbedeckung (Empirisches Modell)*, Report ZfK-396, Rossendorf, Germany.

Eichler, B. (2002), *Die Flüchtigkeitseigenschaften des Poloniums*, PSI-Report No. 02-12, Paul Scherrer Institut, Villigen, Switzerland.

Eichler, B. and J. Neuhausen (2003), *Analyse der Thermochemischen Beziehungen des Iods in einem Blei-Wismut-Spallationstarget*, TM 18-03-01, Paul Scherrer Institut, Villigen, Switzerland.

Eichler, B. and J. Neuhausen (2004a), *Verflüchtigungspfade des Poloniums aus einem Pb-Bi-Spallationstarget (Thermochemische Kalkulation)*, PSI-Report Nr. 04-06, ISSN 1019-0643.

Eichler, B. and J. Neuhausen (2004b), *Radiochemische Untersuchung der Sorption und Desorption von Quecksilber an Silber*, Technical Note TM-18-04-01, Paul Scherrer Institut, Villigen, Switzerland.

Eichler, B. and J. Neuhausen (2005), "Radiochemical Investigations of the Sorption and Desorption Behaviour of Mercury on Noble Metals", *Ann. Rep. Lab. For Radio- and Environ. Chemistry*, University of Bern and PSI, Switzerland, p. 47.

Endebrock, R.W. and P.M Engle (1953), *The Separation of Polonium from Liquid Bismuth by Distillation*, Report US Atomic Energy Commission AECD-4146, Mound Laboratory, Miamisburg, Ohio.

Enqvist, T. et al. (2001), "Isotopic Yields and Kinetic Energies of Primary Residues in 1 A GeV ^{208}Pb + p Reactions", *Nucl. Phys.* A, 686, pp. 481-521.

Ershova, Z.V. and A.G. Volgin (1974), "Polonii i ego primeneniye", *Atomizdat*, Moscow.

ESS (2010a), *Environmental Compliance Report Concerning the Target Material,* EC-FP7 Project ESS-PP Deliverable D 8.1, Paul Scherrer Institut, Villigen, Switzerland.

ESS (2010b), *Environmental Compliance Report Concerning the Radioactive Inventory,* EC-FP7 Project ESS-PP Deliverable D 8.2, Paul Scherrer Institut, Villigen, Switzerland.

Feuerstein, H., J. Oschinski and S. Horn (1992), "Behaviour of Po-210 in Molten Pb17-Li", *J. Nucl. Mat.*, 191-194, pp. 288-291.

Figgins, P.E. (1961), *The Radiochemistry of Polonium,* National Academy of Sciences, National Research Council, Nuclear Science Series, Radiochemistry of the Elements, NAS3037, US Atomic Energy Commission, Washington, DC.

Fillatov, Y., A. Budyka and V. Kirichenko (2007), *Electrospinning of Micro- and Nanofibers: Fundamentals and Applications in Separation and Filtration Processes*, Begell House Inc, New York.

Fischer, A.K. (1966), "Vapor Pressure of Bismuth", *J. Chem. Phys.*, 45, pp. 375-377.

Fleischer, R.L. and O.G. Raabe (1977), "Fragmentation of Respirable PuO_2 Particles in Water by Alpha Decay – A Mode of 'Dissolution'", *Health Phys.*, 32, pp. 253-257.

Ferrari, A. et al. (2005), *FLUKA: A Multi-Particle Transport Code*, CERN-2005-10, INFN/TC_05/11, SLAC-R-773.

Forrest, R.A., J. Kopecky and J-Ch. Sublet (2007), *The European Activation File: EAF-2007 Neutron-Induced Cross Section Library*, EASY Documentation Series, UKAEA FUS 535.

Glasbrenner, H., Y. Dai and F. Gröschel (2005), "LiSoR Irradiation Experiment and Preliminary Post Irradiation Examinations", *Journal of Nuclear Materials*, Vol. 343, pp. 267-274.

Gloris, M., R. Michel and F. Sudbrok (2001), "Proton-Induced Production of Residual Radionuclides in Lead at Intermediate Energies", *Nucl. Instr. and Methods*, A 463, p. 593.

Glushko, V.P. (ed.) (1979), *Termodinamicheskie Svoistva Individualnykh Veshchestv*, Vol. IV, Nauka, Moscow.

Gnutzmann, G. and W. Klemm (1961), "Das Verhalten der Alkalimetalle zu Halbmetallen. IV. Die Systeme des Kaliums, Rubidiums und Caesiums mit Wismut", *Z. anorg. allg. Chem.*, 309, pp. 181-188.

Gonzalez Prieto, B. et al. (2014a), "Equilibrium Evaporation of Trace Polonium from Liquid Lead-bismuth Eutectic at High Temperature", *Journal of Nuclear Materials,* 450, pp. 299-303.

Gonzalez Prieto, B. et al. (2014b), "Use of the Transpiration Method to Study Polonium Evaporation from Liquid Lead-bismuth Eutectic at High Temperature", *Radiochim. Acta*, DOI 10.1515/ract-2014-2263.

Gonzalez Prieto, B. et al. (2014c), "Non-Uniform Polonium Distribution in Lead-bismuth Eutectic Revealed by Evaporation Experiments", *J. Radioanal. Nucl. Chem.*, DOI 10.1007/s10967-014-3264-1.

Greene, G.A. and C.C. Finfrock (1998), *Vaporization of Elemental Mercury from Molten Lead at Low Concentrations*, Report BNL-52622, Brookhaven National Laboratory, Upton, New York, US-DOE Contract DE-AC02-98CH10996.

Groeschel, F. et al. (2006), *Intermediate Safety Report, Treatment of the Reference Accident Case*, Deliverable D14 of WP1 of the MEGAPIE-TEST programme, 5th EURATOM Framework Programme, Paul Scherrer Institut, Villigen, Switzerland.

Gverdtsiteli, I.G., A.G. Kalanparishvili and V.G. Kashiya (1984), "Interaction Kinetics and Sorption Isosteres of Caesium in the Caesium-Bismuth System", *Russ. J. Phys. Chem.*, 58, pp. 1189-1191.

Hammer, B. et al. (2010a), *Determination of Long-Lived Radionuclides in a LBE-Target from ISOLDE: Part II: First Results*, Annual Report 2010, Laboratory for Radiochemistry and Environmental Chemistry, Paul Scherrer Institut, Villigen, Switzerland, p. 37.

Hammer, B. (2010b), *Production and Distribution of Long-Lived Radionuclides in a Lead-bismuth Target from ISOLDE*, Master Thesis, University of Bern, Switzerland.

Hammer, B. et al. (2014a), "Analysis of the ^{207}Bi, ^{194}Hg/Au and ^{173}Lu Distribution in the Irradiated MEGAPIE Target", *Journal of Nuclear Materials*, 450, pp. 278-286.

Hammer, B. et al. (2014b), "Radiochemical Determination of Polonium in Liquid Metal Spallation Targets", *Nuclear Data Sheets*, Vol. 119, p. 280ff.

Heinitz, S., J. Neuhausen and D. Schumann (2011), "Alkaline Extraction of Polonium from Liquid Lead Bismuth Eutectic", *J. Nucl. Mater.*, 414, pp. 221-225.

Heinitz, S. (2013), *Investigations on Physico-Chemical Aspects of Lead-Based Alloys for Nuclear Applications*, PhD Thesis, University of Bern, Switzerland.

Hill, K.D. and M. Gotoh (1996), "The Vapour Pressure of Caesium between 370°C and 660°C", *Metrologia*, 33, pp. 307-317.

Hochgesand, K. et al. (1998), "Polyanionic Clustering and Electronic Properties of the Expanded Equiatomic Liquid Alloy Caesium-Lead", *Ber. Bunsen Ges. Phys. Chem.*, 102, pp. 1259-1265.

Hultgren, R. et al. (1973), *Selected Values of the Thermodynamic Properties of Binary Alloys*, American Society for Metals, Metals Park, Ohio.

Hurng, W.M. and J.D. Corbett (1989), "Alkaline-Earth-Metal Antimonides and Bismuthides with the A_5Pn_3-Stoichiometry, Interstitial and Other Zintl Phases Formed on Their Reactions with Halogen or Sulphur", *Chem. Mater.*, 1, pp. 311-319.

IAEA (International Atomic Energy Agency) (2002), *Comparative Assessment of Thermophysical and Thermohydraulic Characteristics of Lead, Lead-bismuth and Sodium Coolants for Fast Reactors,* IAEA-TECDOC-1289, IAEA, Vienna.

Icenhour, A.S. (2005), *Transport of Radioactive Material by Alpha Recoil*, ORNL/TM2005/22, Oak Ridge National Laboratory, Oak Ridge, Tennessee.

Ichikawa, K. (1985), "Heat Capacity and Internal Motion of Molten Bi + BiI_3 Mixtures", *J. Phys. C: Solid State Phys.*, 18, pp. 4631-4638.

Ito, S. and N. Maeda (1987), "Charge Distributions of Alpha-Recoil Atoms from Electrodeposited ^{210}Po Source", *Nucl. Instrum. Methods Phys. Res., Sect. B*, Vol. 28 (3), pp. 331-335.

JAEA/KEK (Japan Atomic Energy Agency/High-Energy Accelerator Research Organization) (2011), *Japan Proton Accelerator Research Complex (J-PARC)*, website, JAEA/KEK, Japan, accessed 28 July 2014, http://j-parc.jp/researcher/MatLife/en/index.html.

Jolkkonen, M. (2009), *Report on Source Term Assessment for XT-ADS and the Lead Cooled EFIT*, EUROTRANS DM1 DESIGN Deliverable D1.63/64, KTH, Stockholm.

Joy, E.F. (1963), *The Vapour-Liquid Equilibrium of Dilute Solutions of Polonium in Liquid Bismuth,* Mound Laboratory Report MLM-987, US Atomic Energy Commission, Miamisburg, Ohio.

Jubin, R. and R. Counce (1996), "Diffusional Analysis of the Adsorption of Methyl Iodide on Silver Exchanged Mordenite", *Proc. of the 24th DOE/NRC Nuclear Air Cleaning and Treatment Conference*, Portland, Oregon, 15-18 July 1996, NUREG/CP-0153, US Nuclear Regulatory Commission, Washington, DC.

Junghans, A.R. et al. (1998), "Projectile-Fragment Yields as a Probe for the Collective Enhancement in the Nuclear Level Density", *Nuclear Physics A*, 629, p. 635.

Kärger, J., P. Heitjans and R. Haberlandt (1998), *Diffusion in Condensed Matter*, Vieweg, Braunschweig-Wiesbaden.

Kai, T. et al. (2014), "Experiences on Radioactivity Handling for Mercury Target System in MLF/J-PARC", *Progress in Nuclear Science and Technology*, 4, pp. 380-383.

Kelic, A., M.V. Ricciardi and K-H. Schmidt (2008), "ABLA07 – Towards a Complete Description of the Decay Channels of a Nuclear System from Fission to Multifragmentation", *Proceedings of the Joint ICTP-IAEA Advanced Workshop on Model Codes for Spallation Reactions*, Trieste, Italy, 4-8 February 2008, IAEA INDC(NDS)-0530, D. Filges et al. (eds.), IAEA, Vienna, pp. 181-222.

Kelley, K.K. (1935), "Critical Evaluations of Vapour Pressures and Heats of Evaporation of Inorganic Substances", *US Bureau of Mines Bulletin* No. 383.

Kim, J.H. and A. Cosgarea (1966), "Study of the Vapors of Liquid Lead and Bismuth", *J. Chem. Phys.*, 44, pp. 806-809.

Knacke, O., O. Kubaschewski and K. Hesselmann (1991), *Thermochemical Properties of Inorganic Substances*, 2nd ed., Springer-Verlag, Verlag Stahleisen, Berlin, New York, Düsseldorf.

Köster, U. (2000), *Ausbeuten und Spektroskopie radioaktiver Isotope bei LOHENGRIN und ISOLDE*, PhD Thesis, Technical University of Munich, Munich.

Köster, U. (2001), "ISOLDE Target and Ion Source Chemistry", *Radiochim. Acta*, Vol. 89, pp. 749-756.

Konings, R.J.M., A. Kok-Scheele and E.H.P. Cordfunke (1995), "On the Phase Diagrams of the Systems Pb-PbI_2, PbI_2-NaI and PbI_2-ZnI_2", *Thermochimica Acta*, 261, pp. 221-225.

Konings, R.J.M. et al. (1996), "The Infrared Spectrum and Vapour Pressure of Lead Di-Iodide", *Thermochimica Acta*, 273, pp. 231-238.

Konobeyev, A.Yu. et al. (2007), "The Proton Activation Data File PADF-2007 in ENDF-6 Format", *International Conference on Nuclear Data for Science and Technology*, pp. 709-713.

Kopytin, L.M. and Yu.V. Gagarinskii (1961), "The Effect of Radioactivity of Substances on Their Physicochemical Properties", *Atomnaya Energiya*, Vol. 10, No. 3, pp. 238-243.

Korovin, Yu.A., A.Yu. Konobeyev and P.E. Pereslavtsev (1992), "The Code for the Calculation of Nuclide Composition and Activity of Irradiated Materials", *J. Nuclear Constants*, Issue 3-4, pp. 117-121.

Kovach, L.S. (1998), "History of Radioiodine Control", *Proceedings of the 25th DOE/NRC Nuclear Air Cleaning and Treatment Conference*, Minneapolis, MN, 3-6 August 1998, NUREG/CP-0167, US Nuclear Regulatory Commission, Washington, DC.

Krestov, G.A. (1962), "Thermodynamic Properties of Some Astatine and Polonium Compounds", *Radiokhimiya*, Vol. 4 (6), pp. 690-696.

Krishnan, S.V., B.K. Gullett and W. Jozewicz (1994), "Sorption of Elemental Mercury by Activated Carbons", *Environmental Science & Technology*, 28, pp. 1506-1512.

Kubaschewski, O. and C.B. Alcock (1979), *Metallurgical Thermochemistry*, 5th ed. Pergamon Press, Oxford.

Kurakado, M., S. Ito and Y. Isozumi (1981), "Prevention of Contamination by ^{210}Po Alpha-Ray Sources", *J. Appl. Rad. Isot.*, 32 (4), pp. 229-232.

Kurzhöfer, R. (2000), *Untersuchungen der elektrischen Leitfähigkeit der flüssigen Legierungen Cs-Pb, K-Sb, und K-Bi in Abhängigkeit von Druck und Temperatur*, FB 03, Universität Dortmund (dissertation).

Kurzhupova et al. (1978), "On the Existence of a Lowest Crystalline Bismuth Iodide", *Zhurnal Neorganicheskoi Khimii*, 23, pp. 1741-1743.

Landolt-Börnstein (1960), *Landolt-Börnstein: Zahlenwerte und Funktionen aus Physik, Chemie, Astronomie, Geophysik und Technik*, Band II, Teil 2a, Springer, Berlin.

Landolt-Börnstein (1991), *Numerical Data and Functional Relationships in Science and Technology, New Series*, O. Madelung (ed.), Group IV: Macroscopic and Technical Properties of Matter, Vol. 5, Phase Equilibria, Crystallographic and Thermodynamic Data of Binary Alloys, Springer, Berlin.

Landolt-Börnstein (1992), *Numerical Data and Functional Relationships in Science and Technology, New Series*, O. Madelung (ed.): Group IV: Macroscopic and Technical Properties of Matter, Vol. 5b, Phase Equilibria, Crystallographic and Thermodynamic Data of Binary Alloys, Springer, Berlin.

Langmuir, I. (1913), "The Vapour Pressure of Metallic Tungsten", *Phys. Rev. Second Series*, 2, pp. 329-342.

Larson, C.L. (2002a), *Polonium Extraction Techniques for a Lead-bismuth Cooled Fast Reactor*, Master's Thesis, MIT Nuclear Engineering Department.

Larson, C.L. (2002b), "Polonium Hydride Stripping and Formation of Rare-Earth Polonides", *Design of an Actinide Burning, Lead or Lead-bismuth Cooled Reactor that Produces Low Cost Electricity, FY02 Annual Report*, October 2002, INEEL/EXT0201249/ MITANPPR092, Idaho National Engineering and Environmental Laboratory/Bechtel BWXT Idaho, LLC.

Latimer, W.M. (1952), *The Oxidation States of the Elements and Their Potentials in Aqueous Solution*, 2nd ed., Prentice-Hall, Englewood Cliffs, p. 88.

Lawson, R.W. (1915), "Über die Existenz einer Polonium-Wasserstoffverbindung", *Mitteilungen aus dem Institut für Radiumforschung*, 80, pp. 845-852.

Lawson, R.W. (1919), "The Aggregate Recoil of Radioactive Substances Emitting α-Rays", *Nature*, 102, p. 464.

Lee, S.F. et al. (2004), "Removal of Gas-Phase Elemental Mercury by Iodine- and Chlorine-Impregnated Activated Carbons", *Atmospheric Environment*, 38, pp. 4887-4893.

Leray, S. et al. (2008), *Recent Improvements of Spallation Models for Better Predictions of Helium and Tritium Production*, CEA Report DAPNIA-07-286.

Lettry, J. et al. (1997), "Release from ISOLDE Molten Metal Targets Under Pulsed Proton Beam Conditions", *Nucl. Instrum. Meth. B*, Vol. 126, pp. 170-175.

Levanov, V.I., D.V. Pankratov and E.F. Yefimov (1999), "The Estimation of Radiation Danger of Gaseous and Volatile Radionuclides in Accelerator Driven System with Pb-Bi Coolant", *Proceedings of the 3rd International Conference on Accelerator-Driven Transmutation Technologies and Applications*, Prague, Czech Republic, 7-11 June 1999.

Leya, I. et al. (2005), "Production of Noble Gas Isotopes by Proton-Induced Reactions on Lead", *Nucl. Instr. Meth. B*, Vol. 229, pp. 1-23.

Leya, I. et al. (2006), "Production of Noble Gas Isotopes by Proton-Induced Reactions on Lead and Bismuth", *Nucl. Instr. Meth. A*, Vol. 562 (2), pp. 760-763.

Leya, I. et al. (2014), forthcoming.

Li, N., E. Yefimov and D. Pankratov (1998), *Polonium Release from an ATW Burner System with Liquid Metal Lead-bismuth Coolant,* LA-UR-98-19-95, Los Alamos National Laboratory, Los Alamos, NM.

Lindsjö, M. (2005), *On the Nature of Main-Group Polycations – An Odyssey*, doctoral thesis, Royal Institute of Technology, Stockholm, Sweden.

Makower, W. and S. Russ (1910), "The Recoil of Radium C from Radium B", *Philosophical Magazine*, 19 (6), p. 100.

Martin, T.P. (1986), "Compound Clusters", *Z. Phys. D Atoms, Molecules and Clusters*, 3, pp. 211-217.

Mashnik, S.G. and A.J. Sierk (2001), "CEM2k – Recent Developments in CEM", *Proc. AccApp2000*, Washington, DC, La Grange Park, IL, pp. 328-341.

Mashnik, S.G. et al. (2006), "CEM03 and LAQGSM03 – New Modeling Tools for Nuclear Applications", *J. Phys.: Conf. Ser.*, 41, 340 (2006), doi:10.1088/1742-6596/41/1/037.

Maugeri, E.A. et al. (2014), "Thermochromatography Study of Volatile Polonium Species in Various Gas Atmospheres", *Journal of Nuclear Materials*, 450, pp. 292-298.

McBride, B.J., M.J. Zehe and S. Gordon (2002), *NASA Glenn Coefficients for Calculating Thermodynamic Properties of Individual Species*, NASA/TP2002211556, Glenn Research Center, Cleveland, Ohio.

McDowell, W.J., F.G. Seeley and M.T. Ryan (1977), "Penetration of HEPA-Filters by Alpha Recoil Aerosols", *Health Physics*, 32, pp. 445-447.

McManamy, T. et al. (2008), "Overview of the SNS Target System Testing and Initial Beam Operation Experience", *Journal of Nuclear Materials*, 377, pp. 1-11.

McNeese, L.E. (1967), *Considerations of Low Pressure Distillation and Its Application to Processing of Molten-Salt Breeder Reactor Fuels*, ORNL-TM-1730, Oak Ridge National Laboratory, Oak Ridge, Tennessee.

Meijer, J.A., G.J.B. Vinke and W. van der Lugt (1986), "Resistivity of Liquid Rb-Pb and Cs-Pb Alloys", *J. Phys. F: Met. Phys.*, 16, pp. 845-851.

Mendeleev, D. (1889), "The Periodic Law of the Chemical Elements", *J. Chem. Soc.*, 55, pp. 634-656.

Michel, R. et al. (1997), "Cross Sections for the Production of Residual Nuclides by Low- and Medium-Energy Protons from the Target Elements C, N, O, Mg, Al, Si, Ca, Ti, V, Mn, Fe, Co, Ni, Cu, Sr, Y, Zr, Nb, Ba and Au", *Nucl. Instrum. Methods B*, Vol. 129, pp. 153-193.

Michelato, P. et al. (2004), "Theoretical and Experimental Evaluation of the Windowless Interface for the TRASCO-ADS Project", *J. Vacuum Science & Technol. A*, 22 (4), pp. 1810-1815.

Michelato, P. et al. (2007), "Vacuum Interface Analysis of a Windowless Spallation Target for Accelerator-Driven Systems", *Nuclear Science and Engineering*, 157, pp. 95-109.

Miedema, A.R., R. Boom and F.R. de Boer (1975), "On the Heat of Formation of Solid Alloys", *Journal of the Less Common Metals*, 41 (2), pp. 283-298.

Mikityuk, K., P. Coddington and F. Gröschel (2008), "Analysis of Radioactivity Releases in the MEGAPIE Reference Accident", *Nucl. Eng. Des.*, 238, pp. 1838-1844.

Mineo, H. et al. (2000), "Development of Treatment Technology for Dissolver Off-Gas of Spent Fuel, *Proceedings of the 26th DOE/NRC Nuclear Air Cleaning and Treatment Conference*, Richland, Washington, 11-12 September 2000, US Dept. of Energy, Office of Health, Safety and Security, Washington, DC.

Miura, T., T. Obara and H. Sekimoto (2003), "Removal of Polonium Contamination by Lead-bismuth Eutectic in Nuclear Systems", *11th International Conference on Nuclear Engineering (ICONE11)*, Tokyo, 20-23 April 2003, ICONE11-36045.

Miura, T., T. Obara and H. Sekimoto (2004a), "Characteristics of Polonium Contamination from Neutron Irradiated Lead-bismuth Eutectic", *12th International Conference on Nuclear Engineering (ICONE12)*, Arlington, VA, USA, 25-29 April 2004, ICONE12-49153.

Miura T., T. Obara and H. Sekimoto (2004b), "Unfolding of Polonium Distribution in Depth of Irradiated Lead-bismuth Eutectic from α-Particle Pulse-Height Distribution", *Applied Radiation and Isotopes*, 61, pp. 1307-1311.

Miura, T., T. Obara and H. Sekimoto (2005b), "Polonium Contamination Removal Experiment For Lead-bismuth Cooled Fast Reactor", *Proc. of the 2005 Int. Congress on Advances in Nuclear Power Plants (ICAPP'05)*, Seoul, Korea, 15-19 May 2005, Paper 5088.

Miura, T., T. Obara and H. Sekimoto (2006), "Investigation of Polonium Decontamination from Stainless Steel Surfaces Using the Baking Method", *Nuclear Technology*, 155, pp. 78-89.

Morita, K. et al. (2006), "Thermophysical Properties of Lead-bismuth Eutectic Alloy in Reactor Safety Analyses", *Journal of Nuclear Science and Technology*, 43, pp. 526-536.

Moyer, H.V. (ed.) (1956), *Polonium*, US Atomic Energy Commission Report TID-5221.

Mudry, S.I. (1998), "The Structure of Liquid Bi_2Te_3 Alloys Near the Stoichiometric Region", *Journal of Alloys and Compounds*, 267, pp. 100-104.

Müller, S. (2009), *Behaviour of Po-210 in LBE*, Internship Report, Paul Scherrer Institut, Villigen, Switzerland.

Natanson, G.L. (1956), "Radioaktivnye Aerozoli", *Uspekhi Khimii*, 25 (12), p. 1429.

Neuhausen, J. and B. Eichler (2003), *Extension of Miedema's Macroscopic Atom Model to the Elements of Group 16 (O, S, Se, Te, Po)*, PSI Report 03-13, Paul Scherrer Institut, Villigen, Switzerland.

Neuhausen, J., U. Köster and B. Eichler (2004), "Investigation of Evaporation Characteristics of Polonium and Its Lighter Homologues Selenium and Tellurium from Liquid Pb-Bi-Eutecticum", *Radiochim. Acta*, Vol. 92, pp. 917-923.

Neuhausen, J. and B. Eichler (2005a), "Study of the Thermal Release Behaviour of Mercury and Thallium from Liquid Eutectic Lead-bismuth Alloy", *Radiochimica Acta,* Vol. 93, pp. 155-158.

Neuhausen, J. (2005b), *Reassessment of the Rate of Evaporation of Polonium from Liquid Eutectic Lead Bismuth Alloy*, PSI Report TM-18-05-01, Paul Scherrer Institut, Villigen, Switzerland.

Neuhausen, J. (2005c), *Gas Phase Concentrations of Volatile Nuclear Reaction Products in the MEGAPIE Expansion Tank*, PSI Report TM-18-05-02, Paul Scherrer Institut, Villigen, Switzerland.

Neuhausen, J. (2005d), "Gas Phase Concentrations of Volatile Nuclear Reaction Products in the MEGAPIE Expansion Tank, Part 3: Hg and I Evaporation", *Annual Report 2005*, Laboratory for Radiochemistry and Environmental Chemistry, Paul Scherrer Institut, Villigen, Switzerland, p. 46.

Neuhausen, J. (2005e), "Gas Phase Concentrations of Volatile Nuclear Reaction Products in the MEGAPIE Expansion Tank, Part 2: Polonium Evaporation", *Annual Report 2005*, Laboratory for Radiochemistry and Environmental Chemistry, Paul Scherrer Institut, Switzerland, p. 45.

Neuhausen, J. (2006a), "Investigations on the Release of Mercury from Liquid Eutectic Lead Bismuth Alloy Under Different Gas Atmospheres", *Nucl. Instrum. Methods Phys. Res., Sect. A*, 562, pp. 702-705.

Neuhausen, J. and B. Eichler (2006b), "Investigations on the Thermal Release of Iodine from Liquid Eutectic Lead-bismuth Alloy", *Radiochim. Acta*, 94, pp. 239-242.

Neuhausen, J. et al. (2007), *Report on Semi-Empirical Modeling of Thermodynamical Data for the Assessment of the Solubility and Chemical Behavior of Nuclear Reaction and Corrosion Products in a liquid Lead-bismuth Spallation Target,* EUROTRANS Domain 4 DEMETRA Report D4.32., Paul Scherrer Institut, Villigen, Switzerland.

Neuhausen, J. (2010), *Final Report on Po, I, Hg Production and Deposition*, EC-FP6-IP EUROTRANS Deliverable D4.66, Paul Scherrer Institut, Villigen, Switzerland.

Neuhausen, J. and D. Schumann (2011a), "Vapour Phase Concentrations of Volatile Nuclear Reaction Products in the MEGAPIE Cover Gas", *J. Nucl. Mater.*, 415, pp. 361-366.

Neuhausen, J. et al. (2011b), "Distribution of Radionuclides in a Proton Irradiated LBE Target from ISOLDE. Part 1: Sample Cutting and α-Spectrometry", *Annual Report 2010*, Laboratory for Radiochemistry and Environmental Chemistry, Paul Scherrer Institut, Villigen, Switzerland, p. 34.

Neuhausen, J. et al. (2011c), "Distribution of Radionuclides in a Proton Irradiated LBE Target from ISOLDE. Part 2: γ-Spectroscopy", *Annual Report 2010*, Laboratory for Radiochemistry and Environmental Chemistry, Paul Scherrer Institut, Villigen, Switzerland, p. 35.

Noah, E. et al. (2012), "Post-Irradiation Analysis of the Tantalum Container of an ISOLDE LBE Target", *Journal of Nuclear Materials*, 431, pp. 60-65.

Obara, T. et al. (2001), "Removal of Polonium Contamination on Quartz Glass by Baking", *Trans. American Nuclear Society*, 85, p. 49.

Obara, T. et al. (2002), "Removing Effect of Polonium Contamination by LBE in Various Baking Conditions", *Trans. American Nuclear Society*, 87, p. 539.

Obara, T. et al. (2003), "Preliminary Study of the Removal of Polonium Contamination by Neutron-Irradiated Lead-bismuth Eutectic", *Annals of Nucl. Energy*, Vol. 30, pp. 497-502.

Obara, T., T. Miura and H. Sekimoto (2004a), "Polonium Contamination Removal from Stainless Steel by Baking Method", *Trans. American Nuclear Society*, 91, pp. 483-484.

Obara, T., T. Miura and H. Sekimoto (2004b), "Polonium Distribution Analysis by Alpha-Ray Spectrum Unfolding Method", *Trans. American Nuclear Society*, 90, pp. 354-355.

Obara, T., T. Miura and H. Sekimoto (2005a), "Fundamental Study of Polonium Contamination by Neutron Irradiated Lead-bismuth Eutectic", *J. Nucl. Mat.*, 343, pp. 297-301.

Obara, T. et al. (2005b), "Development of Measure for Polonium Contamination in Pb-Bi Cooled Direct Contact Water FBR (PBWFR)", *Proc. of 2005 Int. Congress on Advances in Nuclear Power Plants (ICAPP'05)*, Seoul, Korea, 15-19 May 2005, Paper 5089.

Obara, T., T. Miura and H. Sekimoto (2005c), "Development of Polonium Surface Contamination Measure in Lead-bismuth Eutectic Coolant", *Progr. Nucl. Energy*, 47, pp. 577-585.

Obara, T. et al. (2006), "Preliminary Study on Polonium Filter for Lead Alloy Cooled Reactors", *Trans. American Nuclear Society*, 94, p. 762.

Obara, T. et al. (2008), "Polonium Evaporation and Adhesion Experiments for the Development of Polonium Filter in Lead-bismuth Cooled Reactors", *Progress in Nuclear Energy*, 50, pp. 556-559.

Ohno, S., S. Miyahara and Y. Kurata (2005), "Experimental Investigation of Lead-bismuth Evaporation Behaviour", *J. Nucl. Sci. Technol.*, 42, pp. 593-599.

Ohno, S. et al. (2006), "Equilibrium Evaporation Behaviour of Polonium and its Homologue Tellurium in Liquid Lead-bismuth Eutectic", *J. Nucl. Sci. Technol.*, 43, pp. 1359-1369.

Ohno, S., S. Miyahara and Y. Kurata (2007), "Test Results of Volatile Radionuclide Evaporation from Liquid Lead-bismuth and Their Comparison with Test from Sodium Pool", *Proc. 15th Int. Conf. Nucl. Eng. (ICONE15)*, Nagoya, Japan, 22-26 April 2007, ICONE15-10608.

ORNL (Oak Ridge National Laboratory) (n.d.), *Spallation Neutron Source*, webpage, accessed 28 July 2014, ORNL, Oak Ridge, TN, http://neutrons.ornl.gov/facilities/SNS/.

Panebianco, S. et al. (2009), "Neutronic Characterization of the MEGAPIE Target", *Annals of Nuclear Energy*, Vol. 36, pp. 350-354.

Paneth, F. (1918), "Über Wismutwasserstoff und Poloniumwasserstoff", *Berichte der Deutschen Chemischen Gesellschaft*, 51, pp. 1704-1728.

Pankratov, D.V. et al. (1999), "Polonium Problem in Nuclear Power Plants with Lead-bismuth as a Coolant", *Proc. HLMC98*, Obninsk, Russia, Vol. 1, pp. 101-109.

Pankratov, D. et al. (2003), "Estimation of ^{210}Po Losses from the Solid ^{209}Bi Target Irradiated in a Thermal Neutron Flux", *Annals of Nuclear Energy*, 30, pp. 785-791.

Pankratov, D.V. et al. (2004), "Analysis of the Polonium Hazard in Nuclear Power Systems with Lead-bismuth Coolant", *Atomic Energy*, 97, pp. 559-563.

Papastefanou, C. (2008), "Radioactive Aerosols", *Radioactivity in the Environment*, Vol. 12, Elsevier, Amsterdam, the Netherlands.

Patrizii, L. (2008), "Study of the Effects Induced by Lead on the Emulsion Films of the OPERA Experiment", *Journal of Instrumentation*, 3.

Pavlish, J.H. et al. (2003), "Status Review of Mercury Control Options for Coal-Fired Power Plants", *Fuel Processing Technology*, 82, pp. 89-165.

Pelowitz, D.B. (ed.) (2011), *MCNPX User's Manual, Version 2.7.0*, LANL Report LA-CP-11-00438, Los Alamos National Laboratory, Los Alamos, NM.

Perret, Ch. (2002), *Sicherheitsbericht zum MEGAPIE-Experiment an einem Target mit flüssigem Blei-Bismut-Eutektikum in der Neutronenquelle SINQ des PSI-West*, Paul Scherrer Institut, Villigen, Switzerland.

Petryanov, I.V. et al. (1992), "Formation and Emission of a Gaseous Fraction of Polonium from Its Solid Preparations", *Doklady Biophysics*, 322, pp. 49-51.

Pitcher E. (2002), "Summary Report on Neutronics Work in Support of MEGAPIE", *AAA Quarterly Report*, September.

Prael, R.E. and W.B. Wilson (1998), "Nuclear Structure Libraries for LAHET and MCNPX", *Proceedings of the 4th Workshop on Simulating Accelerator Radiation Environments*, Knoxville, Tennessee, 13-16 September 1998, Oak Ridge National Laboratory, Oak Ridge, Tennessee, p. 183.

Prasad, R., V. Venugopal and D.D. Sood (1977), "A Thermodynamic Study of Lead + Bismuth Using a Transpiration Technique", *J. Chem. Thermodyn.*, 9, pp. 765-772.

Predel, B. and D. Rothacker (1971), "Thermodynamische Untersuchung des Systems Wismut-Wismuttrijodid", *Thermochim. Acta*, 2, pp. 25-39.

Price, D.L. et al. (1991), "Two-Stage Melting in Caesium Lead Alloys", *Phys. Rev. Lett.*, 66, pp. 1894-1897.

Ravn, H.L. (1979), "Experiments with Intense Secondary Beams of Radioactive Ions", *Phys. Rep.*, Vol. 54, pp. 201-259.

Reijers, H.T.J. et al. (1990), "Formation of Zintl-Ions in Alkali-Lead Alloys", *J. Non-Crystalline Solids*, 117/118, pp. 56-59

Riehl, N. and R. Sizmann (1964), "Die abnorme Flüchtigkeit α-strahlender Substanzen", *Radiochim. Acta*, Vol. 3, p. 44.

Rizzi, M. et al. , "Polonium Evaporation from Dilute Liquid Metal Solutions", *J. Nucl. Mater.*, 450, 304-313.

Rohsenow, W.M and H.Y. Choi (1961), *Heat, Mass and Momentum Transfer*, Prentice-Hall, Englewood Cliffs, New Jersey.

Rosseel, K. et al. (2009), Presentation at IP EUROTRANS, DEMETRA Meeting, Bologna, Italy.

Rosztoczy, F.E. and D. Cubicciotti (1965), "The Bismuth Iodide-iodine Phase Diagram", *J. Phys. Chem.*, Vol. 69, pp. 124-127.

Ryan, M.T., K.W. Skrable and G. Chabot (1975), "Retention and Penetration Characteristics of a Glass Fiber Filter for ^{212}Pb Aggregate Recoil Particles", *Health Physics*, 29, pp. 796-798.

Rybak, O.V. and I.V Kurilo (2002), "Equilibrium Vapor Composition in the PbI_2-system", *Inorganic Materials*, 38, pp. 735-737.

Saboungi, M.L. et al. (1988), "Heat Capacity of Some Liquid Zintl Compounds: Equi-Atomic Alkali-Lead Alloys", *J. Chem. Phys.*, 89, pp. 5869-5875.

Saboungi, M.L. and D.L. Price (1992), "A Novel Phase Transition in Alloys", *J. Non-Crystal. Sol.*, 150, pp. 260-265.

Sangster, J. and A.D. Pelton (1991), "The Bi-Cs (Bismuth-Caesium) System", *J. Phase Equilibria*, 12, pp. 443-446.

Schäfer, H., B. Eisenmann and W. Müller (1973), "Zintl Phases: Transitions Between Metallic and Ionic Bonding", *Angew. Chem.* (in English), Vol. 12, pp. 694-712.

Schipakin, O., N. Borisov and S. Churkin (1995), "Experimental Study of ^{210}Po Release from 17Li-83Pb Eutectic", *Fus. Eng. Des.*, 29, pp. 164-169.

Schulz, W.W. and G.F. Schiefelbein (1969), "Pyrochemical Extraction of Polonium from Irradiated Bismuth Metal", *Ind. Eng. Chem. Process Design Develop.*, 8 (4), pp. 508-515.

Sevov, S.C. (2002) "Zintl Phases", *Intermetallic Compounds – Principle and Practice: Progress*, Vol. 3, J.H. Westbrook and R.L. Fleischer (eds.), John Wiley & Sons Ltd., Chichester, United Kingdom.

Shrier, L.L., R.A. Jarmin and G.T. Burstein (eds.) (1994), *Corrosion*, Vol. 1, Metal/Environment Reactions, Chapter 2.9, Butterworth-Heinemann Ltd., Oxford.

Sigmund, P. (1969), "Theory of Sputtering. I. Sputtering Yield of Amorphous and Polycrystalline Targets", *Phys. Rev.*, 184, pp. 383-416.

Sill, C.W. and D.G Olson (1970), "Sources and Prevention of Recoil Contamination of Solid-State Alpha Detectors", *Analytical Chemistry*, 42 (13), pp. 1596-1607.

Stang, L., Jr. (1966), "Radioactive Material, Migration of", *Encyclopaedic Dictionary of Physics*, Vol. 10, p. 258, Atomic Energy Research Establishment, Harwell, Oxford.

Stewart, K. (1963), "The Particulate Material Formed by the Oxidation of Plutonium", *Prog. Nucl. Energy*, Series IV, Vol. 5, pp. 535-579.

Stull, D.R. and H. Prophet (1975), JANAF Thermochemical Tables US Department of Commerce/National Bureau of Standards (1971), Supplements 1974, 1975.

Suvorov, G.P., O.V. Kuzko and M.I. Bugreev (1999), "Experience of 27/VT Facility Construction and Operation", *Proc. HLMC98*, Obninsk, Russian Federation, Vol. 1, pp. 67-75.

Tall, Y. et al. (2007), "Volatile Elements Production Rates in a Proton-Irradiated Molten Lead-bismuth Target", *International Conference on Nuclear Data for Science and Technology*, pp. 1069-1072.

Tall, Y. (2008), *Mesures de taux de production d'éléments gazeux et volatiles lors de réactions induites par des protons de 1 et 1,4 GeV sur des cibles épaisses de plomb et plomb-bismuth liquides*, PhD thesis, École Nationale Supérieure des Techniques Industrielles et des Mines de Nantes, France.

Tammann, G. and A. v. Löwis of Menar (1932), "Über das Verhalten des Poloniums bei der Kristallisation von Metallen", *Z. Anorg. Allg. Chem.*, 205, p. 145.

Thiollière, N. et al. (2011), "Gas Production in the MEGAPIE Spallation Target", *Nuclear Science and Engineering*, 169, pp. 178-187.

Titarenko, Yu.E. et al. (2002), "Cross Sections for Nuclide Production in 1 GeV Proton-Irradiated ^{208}Pb", *Phys. Rev. C*, Vol. 65, No. 064610.

Trenn, T.J. (1980), "Phenomenon of Aggregate Recoil – Premature Acceptance of an Essentially Incorrect Theory", *Annals of Science*, 37 (1), p. 81.

Tumidajski, P.J. et al. (1990), "Thermodynamic Properties of Liquid Rb-Pb Alloys", *J. Phys.: Condens. Matter*, 2, pp. 209-220.

Tupper, R.B. et al. (1991), "Polonium Hazards Associated with Lead Bismuth Used as a Reactor Coolant", *Int. Conf. on Fast Reactors and Related Fuel Cycles*, Kyoto, Japan, 28 October-1 November 1991, pp. 5.6-1 to 5.6-9.

van der Lugt, W. (1996), "Poly-Anions in Liquid Ionic Alloys: A Decade of Research", *J. Phys.: Condens. Matter*, 8, pp. 6115-6138.

von Rohr, F. et al. (2008), *Über das Verhalten von ^{210}Po in Blei-Wismut*, Technical Note TM-18-08-01, Pal Scherrer Institut, Villigen, Switzerland.

von Schnering, H.G., H. von Benda and C. Kalveram (1978), "Wismutmonojodid BiJ, eine Verbindung mit Bi(0) und Bi(II)", *Z. Anorg. Allg. Chem.*, 438, pp. 37-52.

Weigel, H. (1959), "Chemie des Poloniums", *Angew. Chemie*, 71, pp. 289-299.

Welty, J.R. et al. (2008), *Fundamentals of Momentum, Heat and Mass Transfer*, Wiley, New York.

Wiberg, N. (1985), *Holleman-Wiberg, Lehrbuch der anorganischen Chemie*, Walter de Gruyter, Berlin, New York.

Whitehead, N.E. (1994), "Recoil Sputtering from Sources of Alpha Emitters", *Proceedings of the 3rd SPERA Workshop*, Canberra, Australia, 15-17 February 1994, pp. 62-78.

Wilson, W.B. et al. (2006), *A Manual for CINDER'90 – Version 06.1 Codes and Data*, Advanced Fuel Cycle Program.

Winter, R. et al. (1996), "Survival of Polyanions in Expanded Liquid Zintl Alloys", *J. Non-Crystalline Solids*, 205-207, pp. 66-70.

Witteman, W.G., A.L. Giorgi and D.T. Vier (1960), "The Preparation and Identification of Some Intermetallic Compounds of Polonium", *J. Phys. Chem.*, 64, pp. 434-440.

Yamshchikov, L.F., S.P. Raspopin and V.N. Gusev (2001), "Thermodynamic Characteristics of Cs in Pb Melts", *Rasplavy*, 2, pp. 34-36.

Yariv, Y. and Z. Fraenkel (1979), "Intranuclear Cascade Calculation of High-Energy Heavy-Ion Interactions", *Phys. Rev. C*, Vol. 20, pp. 2227-2243.

Yefimov, E. (1996), *Removal and Containment of Polonium from Liquid Lead-bismuth Eutectic*, State Scientific Centre of Russian Federation Institute of Physics and Power Engineering, Obninsk, Russia.

Yefimov, E.I., D.V. Pankratov and S.V. Ignatiev (1998), "Removal and Containment of High-Level Radioactive Polonium from Liquid Lead-bismuth Coolant", *Mat. Res. Soc. Symp. Proc.*, 506, 679-686.

Yosim, S.J. et al. (1962), "The Bismuth-Bismuth Tribromide and Bismuth-Bismuth Triiodide System", *J. Phys. Chem.*, 66, pp. 28-31.

Zanini, L. (2005), *Summary Report for MEGAPIE R&D Task Group X9: Neutronic and Nuclear Assessment*, PSI Report 05-12, Paul Scherrer Institut, Villigen, Switzerland.

Zanini, L. et al. (2008a), *Neutronic and Nuclear Post-Test Analysis of MEGAPIE*, PSI Report 08-04, Paul Scherrer Institut, Villigen, Switzerland, ISSN 1019-0643.

Zanini, L. (2008b), personal communication.

Zanini, L. et al. (2010), "Post-Test Analysis of a Pb/Bi-Filled Ta Target at ISOLDE", *International Workshop on Technology and Components of Accelerator Driven Systems*, Karlsruhe, Germany, 15-17 March 2010, OECD/NEA, Paris.

Zanini, L. et al. (2014), "Measurement of Volatile Radionuclides Production and Release Rates Followed by a Post-Irradiation Analysis of a Pb/Bi Filled Ta Target at ISOLDE", *Nuclear Data Sheets*, 119, DOI: 10.1016/j.nds.2014.04.146.

Zastawny, A., J. Bialon and T. Sosinski (1989), "Changes in the Surface Radioactivity of Lead – The Effect of the Diffusion of Bismuth and Polonium Radioisotopes", *Appl. Rad. Isot.*, Vol. 40 (1), pp. 19-25.

Zastawny, A., J. Bialon and T. Sosinski (1992), "Migration of Po-210 in Lead to the Surface", *Appl. Rad. Isot.*, Vol. 43 (9), pp. 1147-1150.

Zhdanov, S.I. (1985), in *Standard Potentials in Aqueous Solution*, A.J. Bard, R. Parsons and J. Jordan (eds.), Dekker, New York, pp. 93-125.

Zhu, X.H. et al. (2006), "Synthesis and Characterization of PbI_2 Polycrystals", *Crystal Research and Technology*, Vol. 41 (3), pp. 239-242.

Zhuravlev, N.N. (1958), "Structure of Superconductors. XIII. Investigation of Bi-Cs Alloys", *Sov. Phys. JETP*, 34, pp. 571-573.

5.4 Appendix

5.4.1 *Thermodynamic properties of pure polonium (extrapolation results)*

Thermodynamic constants that describe the evaporation processes of polonium are summarised and critically discussed by Eichler (2002). Additionally, the systematic variations of the properties of the elements of the chalcogen group are analysed, empirical correlations are proposed and cyclic processes are balanced. Accordingly, the existing values of entropies for polonium are acceptable. Questionable, however, are those values of enthalpies, which have been deduced from results of the experimental investigations of the temperature dependency of the vapour pressure, melting point and boiling temperatures. Technical difficulties and possible error sources of the measurements resulting from the radioactive decay properties of ^{210}Po are discussed. Using extrapolative standard enthalpies and entropies as well as their temperature dependency, shown in Tables 5.4.1-5.4.3 (Eichler, 2002), the following empirical correlations for the equilibrium partial pressure of monomeric and dimeric polonium above the pure condensed phase and the equilibrium constant of the dimerisation reaction in the gas phase are derived:

$$\log p(Po(g))/Pa = (11.797 \pm 0.024) - (9883.4 \pm 9.5)/T;\ T = 298\text{-}600\ K \quad (5.85)$$

$$\log p(Po(g))/Pa = (10.661 \pm 0.057) - (9328.4 \pm 4.9)/T;\ T = 500\text{-}1300\ K \quad (5.86)$$

$$\log p(Po_2(g))/Pa = (13.698 \pm 0.049) - (8592.3 \pm 19.6)/T;\ T = 298\text{-}600\ K \quad (5.87)$$

$$\log p(Po_2(g))/Pa = (11.424 \pm 0.124) - (7584.1 \pm 98.1)/T;\ T = 500\text{-}1300\ K \quad (5.88)$$

$$\log K_d = (-4.895 \pm 0.012) + (11071 \pm 6)/T \quad (5.89)$$

with p as pressure in Pa, T the temperature in K and K_d the equilibrium constant of the dimerisation reaction $K_d = p(Po_2(g))/p(Po(g))^2$.

Table 5.4.1: Temperature dependent standard entropies (J mol^{-1}K^{-1}) and standard enthalpies (kJ mol^{-1}) of polonium (selected extrapolation results)

T (K)	S_TPo (g)	H_TPo (g)	S_TPo (l)	H_TPo (l)	S_TPo (s)	H_TPo (s)	S_TPo$_2$ (g)	H_TPo$_2$ (g)
298	187.13	188.9	–	–	55.20	0.00	282.24	166.2
300	187.28	188.9	–	–	55.36	0.05	282.49	166.3
400	193.20	190.9	–	–	66.16	2.74	294.22	170.4
500	197.89	192.9	96.13	16.88	69.68	5.75	303.40	174.5
600	201.75	194.9	99.97	20.38	75.39	8.94	310.98	178.7
700	205.06	197.0	104.08	24.51	80.54	12.36	317.47	182.9
800	207.36	199.1	107.94	28.36	–	–	323.15	187.1
900	210.52	201.3	111.94	32.06	–	–	328.22	191.4
1 000	212.89	203.4	115.20	35.83	–	–	332.80	195.8
1 100	215.02	205.6	118.20	39.60	–	–	337.00	200.2
1 200	217.00	207.9	120.85	43.37	–	–	340.88	204.7
1 300	218.83	210.1	123.22	46.37	–	–	344.49	209.2

Source: Eichler (2002).

Table 5.4.2: Temperature dependence of standard entropy of polonium (extrapolation)

Standard entropy: S^0_T ($Jmol^{-1}K^{-1}$) = A + BT + CT^2 + DT^3

	A	B	C	D
$S_TPo(g) \pm \Delta$	164.30495	0.0947	$-6.51757 \cdot 10^{-5}$	$1.89789 \cdot 10^{-8}$
298-1 300 K	0.708	0.0033	$4.60499 \cdot 10^{-6}$	$1.94088 \cdot 10^{-9}$
$S_TPo(l) \pm \Delta$	78.25652	0.02762	$2.25857 \cdot 10^{-5}$	$-1.32887 \cdot 10^{-8}$
500-1 300 K	2.40963	0.00876	$1.01247 \cdot 10^{-5}$	$3.73800 \cdot 10^{-9}$
$S_TPo(s) \pm \Delta$	21.06849	0.14888	$-1.33057 \cdot 10^{-4}$	$5.96463 \cdot 10^{-8}$
298-700 K	0.51653	0.00343	$7.21707 \cdot 10^{-6}$	$4.83576 \cdot 10^{-9}$
$S_TPo_2(g) \pm \Delta$	237.11031	0.18734	$-1.29537 \cdot 10^{-4}$	$3.77809 \cdot 10^{-8}$
298-1 300 K	1.31574	0.00618	$8.55737 \cdot 10^{-6}$	$3.6061 \cdot 10^{-9}$

Source: Eichler (2002).

Table 5.4.3: Temperature dependence of standard enthalpy of polonium (extrapolation)

Standard enthalpy: ΔH^0_T ($kJmol^{-1}$) = A + BT + CT^2 + DT^3

	A	B	C	D
$H_TPo(g) \pm \Delta$	183.22359	0.01829	$2.15156 \cdot 10^{-6}$	$-2.33463 \cdot 10^{-10}$
298-1 300 K	0.01493	$7.01599^{*}10^{-5}$	$9.70807 \cdot 10^{-8}$	$4.09105 \cdot 10^{-11}$
$H_TPo(l) \pm \Delta$	2.0991	0.02024	$2.33896 \cdot 10^{-5}$	$-9.77999 \cdot 10^{-9}$
500-1 300 K	1.37678	0.0055	$6.82892 \cdot 10^{-6}$	$2.66605 \cdot 10^{-9}$
$H_TPo(s) \pm \Delta$	-5.97236	0.014	$2.23597 \cdot 10^{-5}$	$-7.07494 \cdot 10^{-9}$
298-700 K	0.38876	0.00258	$5.43228 \cdot 10^{-6}$	$3.63987 \cdot 10^{-9}$
$H_TPo_2(g) \pm \Delta$	154.42684	0.03892	$2.44905 \cdot 10^{-6}$	$1.74859 \cdot 10^{-12}$
298-1 300 K	0.07976	$3.7491 \cdot 10^{-4}$	$5.18766 \cdot 10^{-7}$	$2.18611 \cdot 10^{-10}$

Source: Eichler (2002).

The results of the extrapolation for the standard enthalpy of the gaseous monomeric polonium and the dimerisation enthalpy are:

$$\Delta H^0_{298}Po\ (g) = 188.9\ kJ/mol \text{ and } \Delta H^0_{298}(form)\ Po_2\ (g) = 211.5\ kJ/mol \quad (5.90)$$

The preferred evaporation of pure polonium in the dimeric state requires new interpretations of the thermodynamic relations of polonium in mixed phases (activity coefficients) if the experimental conditions exclude a formation of the dimers due to low concentrations.

The thermodynamic data derived by extrapolation (Eichler, 2002), while not highly accurate, at least represent a consistent set of data. To acquire more reliable data that are essential for the prediction of polonium behaviour in a technical system, experimental thermodynamic studies using polonium isotopes which are less prone to radiation effects, such as ^{209}Po, are necessary.

5.4.2 *Thermodynamic data of polonium compounds (extrapolation results)*

For polonium compounds, almost no experimental thermodynamic data are available. Therefore, as a first step, a coherent set of thermodynamic data for polonium hydride, lead polonide and polonium dioxide was derived by Eichler et al. (2004a) using extrapolative procedures. The equilibrium constants of formation, dissociation and evaporation reactions were calculated using these data. Furthermore, equilibrium constants for the reactions of lead polonide and polonium dioxide with hydrogen, water vapour as well as with lead and bismuth were evaluated. It must be pointed out that such extrapolations do not produce results of high accuracy. However, precise measurements of thermodynamic data of polonium compounds that would be required for engineering purposes remain scarce, and generally the corresponding experiments are difficult to perform. The extrapolated data can thus be considered as best available estimates until better data become available. Detailed experimental studies of the discussed systems, preferably using isotopes that suffer less from decay effects compared to the frequently utilised ^{210}Po, are strongly recommended to produce reliable fundamental data. Furthermore, the influence of decay effects on the behaviour of polonium and the apparatus employed for measurements deserves attention.

Based on these thermodynamic data obtained by Eichler (2004a), possible volatilisation processes are evaluated. From this assessment, volatilisation of polonium from LBE most likely occurs in the form of intermetallic molecules Pb-Po or Bi-Po. Rates for the release of radioactivity and their temperature dependency have been calculated. The main results of this study are summarised in the following section.

The following temperature function is recommended for the entropy of polonium hydride:

$$\begin{aligned} S_T H_2Po(g) = {} & (206.07678 \pm 1.41) + (0.12098 \pm 0.00437) * T \\ & - \left(3.73042 * 10^{-5} \pm 2.97 * 10^{-6}\right) * T^2 \end{aligned} \tag{5.91}$$

Entropy values for polonium hydride together with those of polonium and hydrogen are compiled in Table 5.4.4.

Calculated entropy of formation values for polonium hydride are compiled in Table 5.4.5 for the six different formation reactions given below (Eqs. [5.92-5.97]). The corresponding enthalpy and Gibbs free energy values are given in Tables 5.4.6 and 5.4.7.

$$Po(cond) + H_2(g) \Leftrightarrow H_2Po(g) \tag{5.92}$$

$$Po(g) + H_2(g) \Leftrightarrow H_2Po(g) \tag{5.93}$$

$$0.5\, Po_2(g) + H_2(g) \Leftrightarrow H_2Po(g) \tag{5.94}$$

$$Po(cond) + 2\, H(g) \Leftrightarrow H_2Po(g) \tag{5.95}$$

$$Po(g) + 2\, H(g) \Leftrightarrow H_2Po(g) \tag{5.96}$$

$$0.5\, Po_2(g) + 2\, H(g) \Leftrightarrow H_2Po(g) \tag{5.97}$$

Entropy and enthalpy values for Pb-Po are compiled in Tables 5.4.8 and 5.4.9 together with the entropy of sublimation and the entropies of formation of gaseous and solid Pb-Po from the elements in their standard state at the given temperature. Gibbs free energy values for these formation reactions as well as the sublimation reaction are listed in Table 5.4.10 together with the corresponding equilibrium constants or vapour pressures, respectively.

The following temperature functions have been derived from Tables 5.4.8 and 5.4.9 for the entropy of gaseous and solid lead polonide (Eichler, 2004a):

$$S_T \text{ PbPo (g)} = 233.2798 + 0.19892\ T - 1.5756*10^{-4}\ T^2 + 5.19651*10^{-8}\ T^3 \quad (5.98)$$

$$S_T \text{ PbPo (s)} = 53.19976 + 0.27136\ T - 2.1165*10^{-4}\ T^2 + 7.16652*10^{-8}\ T^3 \quad (5.99)$$

This results in the following relation for the entropy of sublimation:

$$\Delta S_T(\text{subl}) \text{ PbPo} = 180.08004 - 0.07244T + 5.40902*10^{-5}T^2 - 1.97001*10^{-8}\ T^3 \quad (5.100)$$

Extrapolated entropy values for polonium dioxide are given in Table 5.4.11 together with its entropy of sublimation and formation.

Enthalpy data have been extrapolated for the formation of gaseous and solid polonium dioxide from the gaseous monoatomic elements, i.e. oxygen and polonium. These values are compiled in Table 5.4.12 together with the resulting values for enthalpy of sublimation and vapour pressure. The derived enthalpy values should be regarded cautiously because they are based on rather few literature data for chalcogen dioxides (SeO_2 and TeO_2) and the chemical bonding in these compounds (polar covalent) differs substantially from the bonding in PoO_2 (partially ionic).

Equilibrium constants for the following reactions were calculated from these entropy and enthalpy values:

Formation reaction: $$\mathrm{Po\,(cond) + O_2\,(g) \Leftrightarrow PoO_2\,(s)} \quad (5.101)$$

Dissociation: $$\mathrm{PoO_2\,(cond) \Leftrightarrow Po\,(g) + O_2\,(g)} \quad (5.102)$$

$$\mathrm{2\ PoO_2\,(cond) \Leftrightarrow Po_2\,(g) + 2\ O_2} \quad (5.103)$$

Reduction with H: $$\mathrm{PoO_2\,(s) + 2\ H_2\,(g) \Leftrightarrow Po\,(cond) + 2H_2O\,(g)} \quad (5.104)$$

Reduction with Pb: $$\mathrm{PoO_2\,(s) + 2\ Pb\,(cond) \Leftrightarrow Po\,(cond) + 2PbO\,(s)} \quad (5.105)$$

Reduction with Bi: $$\mathrm{3PoO_2\,(s) + 4\ Bi\,(cond) \Leftrightarrow 3Po\,(cond) + 2\ Bi_2O_3\,(s)} \quad (5.106)$$

The calculated equilibrium constants are shown in Table 5.4.13. The calculated values generally reflect the actually observed chemical behaviour of polonium dioxide (Bagnall, 1990). Nevertheless, it is possible that the enthalpy of formation of solid PoO_2 is overestimated. The dissociative volatilisation of PoO_2 observed in vacuum as observed opposed to the congruent sublimation of PoO_2 in the presence of oxygen cannot be explained by these data. However, it remains to be clarified to what extent radiolysis effects may play an additional role in the volatilisation process.

Table 5.4.4: Standard entropies of gaseous polonium hydride, dimeric and monoatomic gaseous polonium and hydrogen

T (K)	$S^0_T H_2Po$ (g) ($Jmol^{-1}K^{-1}$)	S^0_T Po (s;l) ($Jmol^{-1}K^{-1}$) Eichler (2002)	S_T Po (g) ($Jmol^{-1}K^{-1}$) Eichler (2002)	S_T Po_2 (g) ($Jmol^{-1}K^{-1}$) Eichler (2002)	$S^0_T H_2$ (g) ($Jmol^{-1}K^{-1}$) Barin (1995)	S_T H (g) ($Jmol^{-1}K^{-1}$) Barin (1995)
298	238.13	55.20	187.13	282.24	130.68	114.716
300	238.35	55.36	187.28	282.49	130.86	114.845
400	249.49	63.16	193.20	294.22	139.22	120.824
500	258.09	69.68	197.89	303.40	145.74	125.463
600	265.76	99.97	201.75	310.98	151.08	29.252
700	272.51	104.08	205.06	317.47	155.61	132.457
800	278.56	107.94	208.00	323.15	159.55	135.232
900	284.07	111.94	210.52	328.22	163.05	137.680
1 000	289.15	115.20	212.88	332.8	166.22	139.870
1 100	293.88	118.2	215.02	337.00	169.11	141.851
1 200	298.31	120.85	216.99	340.88	171.79	143.660

Table 5.4.5: Entropy of polonium hydride formation for different reactions (Eqs. [5.92] to [5.97])

T (K)	$\Delta S^0_{T,form} H_2Po$ (g) ($Jmol^{-1}K^{-1}$) Eq. (5.92)	$\Delta S_{T,form} H_2Po$ (g) ($Jmol^{-1}K^{-1}$) Eq. (5.93)	$\Delta S_{T,form} H_2Po$ (g) ($Jmol^{-1}K^{-1}$) Eq. (5.94)	$\Delta S_{T,form} H_2Po$ (g) ($Jmol^{-1}K^{-1}$) Eq. (5.95)	$\Delta S_{T,form} H_2Po$ (g) ($Jmol^{-1}K^{-1}$) Eq. (5.96)	$\Delta S_{T,form} H_2Po$ (g) ($Jmol^{-1}K^{-1}$) Eq. (5.97)
298	52.25	-79.68	-33.67	-46.50	-178.43	-132.42
300	52.13	-79.79	-33.76	-46.70	-178.62	-132.59
400	47.11	-82.93	-36.84	-55.32	-185.36	-139.27
500	42.67	-85.54	-39.35	-62.52	-190.73	-144.54
600	14.71	-87.07	-40.81	-92.71	-194.49	-148.23
700	12.82	-88.16	-41.84	-96.48	-197.46	-151.14
800	11.07	-88.99	-42.09	-99.84	-199.01	-153.48
900	9.08	-89.5	-42.57	-103.23	-201.81	-155.40
1 000	7.73	-89.95	-43.47	-105.79	-203.47	-156.99
1 100	6.57	-90.25	-43.73	-108.02	-204.84	-158.32
1 200	5.67	-90.47	-43.92	-109.86	-206.00	-159.45

Table 5.4.6: Standard formation enthalpy for polonium hydride and enthalpies for its formation from the elements in different reactions (Eqs. [5.92] to [5.97])

T (K)	$\Delta H^{o}_{T,form}H_2Po$ (g) (kJmol^{-1}) Eq. (5.92)	$\Delta H_{T,form}H_2Po$ (g) (kJmol^{-1}) Eq. (5.93)	$\Delta H_{T,form}H_2Po$ (g) (kJmol^{-1}) Eq. (5.94)	$\Delta H_{T,form}H_2Po$ (g) (kJmol^{-1}) Eq. (5.95)	$\Delta H_{T,form}H_2Po$ (g) (kJmol^{-1}) Eq. (5.96)	$\Delta H_{T,form}H_2Po$ (g) (kJmol^{-1}) Eq. (5.97)
298	163.0	-25.9	79.9	-273.0	-461.9	-356.1
300	165.9	-22.9	82.8	-270.1	-459.0	-353.2
400	164.9	-23.2	82.5	-272.3	-460.5	-354.8
500	166.2	-20.9	84.7	-272.2	-459.4	-353.7
600	152.0	-22.6	83.0	-187.8	-462.3	-356.8
700	149.1	-23.4	82.2	-291.8	-464.3	-358.8
800	146.7	-24.0	81.5	-295.4	-466.2	-360.6
900	144.6	-24.6	81.0	-298.7	-468.0	-362.4
1 000	141.9	-25.7	79.8	-302.6	-470.2	-364.7
1 100	140.4	-25.6	79.9	-305.2	-471.2	-365.7
1 200	137.6	-27.0	78.6	-309.1	-473.7	-368.1

Table 5.4.7: Gibbs free energy values for polonium hydride formation reactions (Eqs. [5.92] to [5.97])

T (K)	$\Delta G^{o}_{T,form}H_2Po$ (g) (kJmol^{-1}) Eq. (5.8)	$\Delta G_{T,form}H_2Po$ (g) (kJmol^{-1}) Eq. (5.9)	$\Delta G_{T,form}H_2Po$ (g) (kJmol^{-1}) Eq. (5.10)	$\Delta G_{T,form}H_2Po$ (g) (kJmol^{-1}) Eq. (5.11)	$\Delta G_{T,form}H_2Po$ (g) (kJmol^{-1}) Eq. (5.12)	$\Delta G_{T,form}H_2Po$ (g) (kJmol^{-1}) Eq. (5.13)
298	147.4	-2.2	89.9	-259.2	-408.8	-316.7
300	150.0	1.0	92.9	-256.2	-405.5	-313.5
400	146.1	10.0	97.2	-254.5	-390.6	-303.3
500	144.9	21.9	104.4	-249.4	-372.4	-289.8
600	143.1	29.7	107.5	-244.7	-358.2	-280.4
700	140.1	38.3	111.5	-241.0	-342.8	-269.7
800	137.9	47.2	115.6	-236.4	-327.1	-258.7
900	136.4	55.9	119.7	-230.9	-311.4	-247.5
1 000	134.1	64.2	123.3	-226.0	-295.9	-236.9
1 100	133.2	73.7	128.0	-219.7	-279.2	-224.9
1 200	130.8	81.6	131.3	-214.8	-263.9	-214.3

Table 5.4.8: Extrapolated entropy values of gaseous and solid lead polonide, sublimation entropy of PbPo and entropies for the formation of gaseous and solid PbPo from the elements in their standard state

T (K)	S_T (g) ($Jmol^{-1}K^{-1}$)	S_T (s) ($Jmol^{-1}K^{-1}$)	ΔS (subl) ($Jmol^{-1}K^{-1}$)	ΔS (form) PbPo (g) ($Jmol^{-1}K^{-1}$)	ΔS (form) PbPo (s) ($Jmol^{-1}K^{-1}$)
298	285.46	122.61	162.854	159.919	-2.941
300	285.57	122.92	162.651	159.722	-2.918
400	295.25	137.87	157.383	152.441	-6.139
500	304.85	149.72	155.130	150.807	-3.720
600	311.69	159.62	152.067	122.927	-29.143
700	317.46	168.19	149.273	112.128	-37.115
800	322.45	175.77	146.683	108.771	-37.911
900	326.84	182.60	144.245	106.330	-37.910
1 000	330.77	188.84	141.930	103.989	-37.940
1 100	334.31	194.60	139.715	101.814	-37.900

Source: Eichler (2004a).

Table 5.4.9: Extrapolated enthalpy values of gaseous and solid lead polonide, sublimation enthalpy of PbPo and enthalpies for the formation of gaseous and solid PbPo from the elements in their standard state

T (K)	H_T PbPo (g) ($kJmol^{-1}$)	H_T PbPo (s) ($kJmol^{-1}$)	ΔH_T (subl) PbPo ($kJmol^{-1}$)	ΔH_T (form) PbPo (g) ($kJmol^{-1}$)	ΔH_T (form) PbPo (s) ($kJmol^{-1}$)
298	184.2	-35.43	219.6	184.20	-35.43
300	183.7	-35.25	218.9	183.55	-35.36
400	186.6	-30.14	216.7	181.07	-35.66
500	190.4	-25.26	215.7	179.05	-36.60
600	195.1	-18.97	214.1	166.20	-47.84
700	199.7	-12.61	212.3	158.90	-53.43
800	204.0	-6.47	210.5	156.31	-54.16
900	208.3	-0.14	208.5	153.96	-54.51
1 000	212.4	5.93	206.5	151.34	-55.17
1 100	217.1	12.13	204.9	149.26	-55.66

Source: Eichler (2004a).

Table 5.4.10: Gibbs free energy for the formation and sublimation reactions of lead polonide and the corresponding equilibrium constants

T (K)	ΔG (form) PbPo (s) (kJmol^{-1})	lg K_{form}	ΔG (form) PbPo (g) (kJmol^{-1})	lg K_{form}	ΔG (subl) PbPo (s) (kJmol^{-1})	lg p_{PbPo} p/(bar)
298	-34.55	6.055	136.54	-23.931	171.09	-29.986
300	-34.48	6.003	135.63	-23.613	170.12	-29.616
400	-33.21	4.336	120.094	-15.680	153.30	-20.017
500	-33.744	3.629	103.65	-10.826	138.39	-14.455
600	-30.35	2.642	92.44	-8.047	122.80	-10.689
700	-27.45	2.048	80.41	-5.999	107.86	-8.047
800	-22.83	1.490	69.29	-4.524	92.12	-6.014
900	-20.39	1.183	58.26	-3.381	78.654	-4.564
1 000	-17.23	0.899	47.35	-2.473	64.58	-3.373
1 100	-13.97	0.663	37.26	-1.769	51.23	-2.433

Source: Eichler (2004a).

Table 5.4.11: Temperature dependence of the entropy of polonium dioxide, sublimation entropy of PoO_2 and entropy formation for gaseous and solid PoO_2

T (K)	S_T PoO_2 (g) (Jmol^{-1}K^{-1})	S_T PoO_2 (s) (Jmol^{-1}K^{-1})	ΔS_T (subl) PoO_2 (Jmol^{-1}K^{-1})	ΔS_T (form) PoO_2 (g) (Jmol^{-1}K^{-1})	ΔS_T (form) PoO_2 (s) (Jmol^{-1}K^{-1})
298	286.29	82.41	203.89	25.945	-177.94
300	286.57	82.84	203.73	25.878	-177.85
400	300.47	103.07	197.40	23.439	-173.96
500	312.20	118.45	193.76	21.83	-171.93
600	322.09	130.60	191.50	-4.327	-195.82
700	330.56	141.62	188.94	-4.984	-193.93
800	338.02	152.19	185.84	-5.839	-191.68
900	344.63	162.96	181.67	-7.238	-188.91
1 000	350.59	174.38	176.21	-8.189	-184.40
1 100	356.01	185.11	170.90	-9.108	-180.01

Source: Eichler (2004a).

Table 5.4.12: Temperature dependence of the enthalpy of polonium dioxide formation from gaseous monoatomic elements, sublimation enthalpy of PoO_2 and its vapour pressure

T (K)	ΔH^*_T (form) PoO_2 (g) ($kJmol^{-1}$)	ΔH^*_T (form) PoO_2 (s) ($kJmol^{-1}$)	ΔH_T (subl) PoO_2 ($kJmol^{-1}$)	log p_{PoO2} (bar)
298	-690.6	-1 054.2	363.7	-53.0847
300	-690.5	-1 054.1	363.6	-52.6527
400	-684.2	-1 053.8	369.6	-37.9440
500	-685.2	-1 053.2	368.0	-28.3177
600	-688.5	-1 052.4	364.0	-21.6786
700	-692.6	-1 051.1	358.5	-16.8783
800	-697.3	-1 050.6	353.3	-13.3618
900	-699.0	-1 049.9	350.9	-10.8769
1 000	-702.0	-1 049.0	347.0	-8.9211

Table 5.4.13: Equilibrium constants of formation, dissociation and some redox reactions of polonium dioxide

T (K)	lgK Eq. (5.101)	lgK Eq. (5.102)	lgK Eq. (5.103)	lgK Eq. (5.104)	lgK Eq. (5.105)	lgK Eq. (5.106)
298	55.0186	-91.9491	-151.6368	25.0874	11.0814	7.8522
300	54.5810	-91.2891	-150.5667	25.0030	11.0490	7.9350
400	38.6900	-67.4778	-113.3430	19.8000	7.9740	5.7201
500	29.1570	-53.2184	-89.1903	16.6250	6.1590	4.5029
600	22.4892	-43.7087	-73.8741	14.7848	5.2828	4.2965
700	17.8969	-36.9287	-62.9461	13.2791	4.3851	3.4093
800	14.5364	-31.9854	-54.9718	12.0496	3.6396	2.5329
900	11.9543	-28.1527	-48.8971	11.0517	3.0397	1.7910
1 000	10.0102	-25.1956	-44.2274	10.1218	2.4498	0.8614
1 100	8.4682	-22.8200	-40.4811	9.3079	1.9299	0.2755

5.4.3 *Results of solubility calculations*

Table 5.4.14: Literature data (Courouau, 2003) and values calculated using Eq. (5.67) for the solubility of pure elements in Pb at different temperatures

See also Section 5.2.5

Z	Element	log(x) (literature values)			log(x) (calculated)		
		600 K	700 K	800 K	600 K	700 K	800 K
1	H	-5.5731	-5.0058	-4.5867	-8.5894	-7.36235	-6.44205
4	Be	–	–	–	-7.00625	-5.96759	-5.18859
5	B	–	–	–	-11.75079	-10.00343	-8.69291
6	C	–	–	–	-12.66289	-10.8539	-9.49717
7	N	–	–	–	-8.01403	-6.86917	-6.01052
13	Al	-2.5692	-1.9832	-1.5485	-3.25525	-2.70458	-2.29158
14	Si	-9.229	-7.53	-6.2236	-6.95814	-5.74177	-4.82948
15	P	–	–	–	-2.80598	-2.38963	-2.07736
24	Cr	-8.9082	-7.3996	-6.0986	-8.59143	-7.30477	-6.33978
25	Mn	-2.4464	-2.0138	-1.6912	-2.75087	-2.26006	-1.89195
26	Fe	-7.711	-6.553	-5.686	-8.79311	-7.47434	-6.48526
27	Co	-6.733	-5.454	-4.8519	-5.62539	-4.74862	-4.09105
28	Ni		-2.3*	-1.9*	-4.50747	-3.78804	-3.24846
29	Cu	-2.7005	-2.1404	-1.7225	-2.64323	-2.19267	-1.85476
30	Zn	-1.6513	-1.1679	-0.9534	-1.4525	-1.16611	-0.95132
31	Ga	-1.3048	-0.9307	-0.6665	-0.95265	-0.67884	-0.47348
32	Ge	–	-4.4653	-3.0899	-3.00414	-2.34721	-1.8545
33	As	-0.95*	-0.52*	-0.28*	-3.00535	-2.38654	-1.92243
41	Nb	–	–	–	-6.90992	-5.85102	-5.05685
42	Mo	–	–	–	-14.8194	-12.60163	-10.93831
43	Tc	–	–	–	-9.05599	-7.69031	-6.66605
44	Ru	–	–	–	-8.89887	-7.55579	-6.54848
45	Rh	-1.68	-1.2579	-0.9486	-3.14057	-2.62011	-2.22976
47	Ag	-1.3*	-0.92*	-0.57*	-1.29081	-1.03811	-0.84858
48	Cd	–	–	–	-0.44655	-0.30497	-0.19878
50	Sn	–	–	–	-0.41453	-0.25148	-0.1292
51	Sb	-0.5149*	-0.291*	-0.1407*	-0.76003	-0.48745	-0.28301
73	Ta	–	–	–	-6.711	-5.68047	-4.90758
74	W	–	–	–	-17.07111	-14.5606	-12.67771
75	Re	–	–	–	-15.08506	-12.85824	-11.18813
76	Os	–	–	–	-11.46989	-9.75952	-8.47675
79	Au	-0.4454	-0.2639	-0.2007	-1.29163	-1.03703	-0.84608
80	Hg	–	–	–	-0.14442	-0.0529	0.01575
81	Tl	–	–	–	0.24078	0.26551	0.28405
83	Bi	–	–	–	0.11196	0.25073	0.3548

* From Landolt-Börnstein (1991/92).

Table 5.4.15: Literature data (Courouau, 2003) and values calculated using Eq. (5.67) for the solubility of pure elements in Bi at different temperatures

Z	Element	log(x) (Literature values)			log(x) (calculated)		
		600 K	700 K	800 K	600 K	700 K	800 K
1	H	–	–	–	-8.67449	-7.43528	-6.50587
4	Be	-8.02194	-6.63472	-5.45863	-6.99246	-5.95577	-5.17825
5	B	–	–	–	-11.78824	-10.03553	-8.72099
6	C	-4.52904	-4.45846	-4.45846	-12.95216	-11.10185	-9.71412
7	N	–	–	–	-8.60362	-7.37453	-6.45271
13	Al	-2.03456	-1.56709	-1.22416	-3.05695	-2.53462	-2.14286
14	Si	-6.12838	-5.12838	-4.52633	-6.93169	-5.71909	-4.80964
15	P	–	–	–	-3.08636	-2.62995	-2.28764
23	V	-5.04455	-4.43274	-3.98906	-4.20073	-3.52882	-3.02489
24	Cr	-5.10253	-4.25017	-3.61094	-7.46743	-6.34135	-5.49678
25	Mn	-1.2508	-0.77337	-0.58554	-1.65262	-1.3187	-1.06826
26	Fe	-5.82483	-4.82484	-4.14816	-7.78088	-6.60671	-5.72608
27	Co	-3.60523	-3.24631	-2.97491	-4.75441	-4.00207	-3.43782
29	Cu	-2.5*	-2*	-1.6*	-2.27465	-1.87675	-1.57832
30	Zn	-0.75*	-0.4*	-0.24*	-1.2833	-1.02109	-0.82443
31	Ga	–	–	–	-0.76597	-0.51883	-0.33347
32	Ge	-3.03724	-2.42755	-1.90866	-3.01934	-2.36023	-1.8659
33	As	-1.73303	-1.05815	-0.59021	-3.10006	-2.46772	-1.99346
41	Nb	-5.12943	-4.60655	-4.23298	-5.18455	-4.37213	-3.76282
42	Mo	–	–	–	-13.42889	-11.40976	-9.89542
43	Tc	–	–	–	-8.06615	-6.84187	-5.92367
44	Ru	-3.91121	-3.71885	-3.57458	-7.97741	-6.76597	-5.85739
45	Rh	-1.70503	-1.30343	-1.00827	-2.29053	-1.8915	-1.59223
47	Ag	-0.80593	-0.3279	-0.13889	-1.04733	-0.82941	-0.66597
48	Cd	–	–	–	-0.30224	-0.18127	-0.09055
49	In	–	–	–	0.52621	0.5077	0.49381
50	Sn	–	–	–	-0.3187	-0.16935	-0.05734
51	Sb	-0.89*	-0.43*	-0.18*	-0.8189	-0.53791	-0.32716
73	Ta	–	–	–	-5.0013	-4.21502	-3.62531
74	W	–	–	–	-15.7043	-13.38905	-11.65261
75	Re	–	–	–	-13.97183	-11.90405	-10.35321
76	Os	–	–	–	-10.50501	-8.93248	-7.75309
79	Au	-0.62*	-0.41*	-0.3*	-1.15344	-0.91858	-0.74244
80	Hg	–	–	–	-0.08853	-0.00499	0.05766
81	Tl	–	–	–	0.3521	0.36092	0.36754
82	Pb	–	–	–	0.0113	0.069	0.11227

* From Landolt-Börnstein (1991/92).

Table 5.4.16: Coefficients of the temperature functions log(x) = A – B/T for the solubility of pure elements in Pb obtained using Eq. (5.67)

Z	Element	A	B (K)
1	H	0	5 154
4	Be	0.2644	4 362
5	B	0.4807	7 339
6	C	0	7 598
7	N	0	4 808
13	Al	0.5994	2 313
14	Si	1.5565	5 109
15	P	0.1085	1 749
23	V	0.5026	3 629
24	Cr	0.4152	5 404
25	Mn	0.6848	2 061
26	Fe	0.4383	5 539
27	Co	0.5120	3 682
28	Ni	0.5286	3 022
29	Cu	0.5107	1 892
30	Zn	0.5522	1 203
31	Ga	0.9640	1 150
32	Ge	1.5944	2 759
33	As	1.3263	2 599
41	Nb	0.5024	4 447
42	Mo	0.7050	9 315
43	Tc	0.5038	5 736
44	Ru	0.5027	5 641
47	Ag	0.4781	1 061
48	Cd	0.5445	5 95
49	In	0.3966	24
50	Sn	0.7268	685
51	Sb	1.1481	1 145
73	Ta	0.5027	4 328
74	W	0.5025	10 544
75	Re	0.5027	9 353
76	Os	0.5027	7 184
78	Pt	0.5023	173
79	Au	0.4906	1 069
80	Hg	0.4962	384
81	Tl	0.4139	104
82	Pb	0.4152	249
83	Bi	1.0833	583

Table 5.4.17: Coefficients of the temperature functions log(x) = A – B/T for the solubility of pure elements in Bi obtained using Eq. (5.67)

Z	Element	A	B (K)
1	H	0	5 205
4	Be	0.2644	4 354
5	B	0.4807	7 361
6	C	0	7 771
7	N	0	5 162
13	Al	0.5994	2 194
14	Si	1.5565	5 093
15	P	0.1085	1 917
23	V	0.5026	2 822
24	Cr	0.4152	4 730
25	Mn	0.6848	1 402
26	Fe	0.4383	4 932
27	Co	0.5120	3 160
28	Ni	0.5286	2 532
29	Cu	0.5107	1 671
30	Zn	0.5522	1 101
31	Ga	0.9640	1 038
32	Ge	1.5944	2 768
33	As	1.3263	2 656
41	Nb	0.5024	3 412
42	Mo	0.7050	8 480
43	Tc	0.5038	5 142
44	Ru	0.5027	5 088
45	Rh	0.5027	1 676
47	Ag	0.4781	915
48	Cd	0.5445	508
50	Sn	0.7268	627
51	Sb	1.1481	1 180
73	Ta	0.5027	3 302
74	W	0.5025	9 724
75	Re	0.5027	8 685
76	Os	0.5027	6 605
79	Au	0.4906	986
80	Hg	0.4962	351
81	Tl	0.4139	37
82	Pb	0.4152	242

5.4.4 *The Miedema model*

The Miedema model is a semi-empirical model for the calculation of enthalpies of formation and enthalpies of mixing in solid and liquid binary metal systems. The element-specific constants involved in the calculations are derived from properties of the elements and subsequently adjusted to give the best possible fit to known experimental enthalpy data. In spite of this empirical character, the physical significance of the parameters is obvious. Therefore, the classification of the model as semi-empirical is justified. Through the process of adjustment of parameters to experimental data, the model incorporates the complete knowledge of enthalpy effects in binary alloy systems.

The Miedema model is a cellular model. The principles and applications of the model are discussed in detail in de Boer (1988). Within the framework of the model, an alloy is thought to be built up from atomic cells of the constituent elements, each with a defined atomic volume. When cells of two different elements A and B are brought into contact to form an alloy (Figure 5.4.1), there will be discontinuities of the electron density n_{ws} at the boundaries of their (Wigner-Seitz) atomic cells. To eliminate these discontinuities, a rearrangement of the electron distribution within the atomic cell is required. This involves a transfer of electrons into higher energy levels and thus leads to a positive contribution to the enthalpy of formation or mixing. This positive contribution is found to be proportional to the squared differences in cube root of the electron densities, $n_{ws}^{1/3}$, of the constituent elements in the state of a bulk metal.

Values for n_{ws} for transition metals have been derived from experimental data of the bulk modulus and molar volume. For non-transition metals, a superposition of the charge densities of free atoms placed at individual lattice points was found to be an acceptable approximation for n_{ws} (de Boer, 1988).

Figure 5.4.1: Schematic cellular model of the formation of an alloy AB from two pure metals A and B

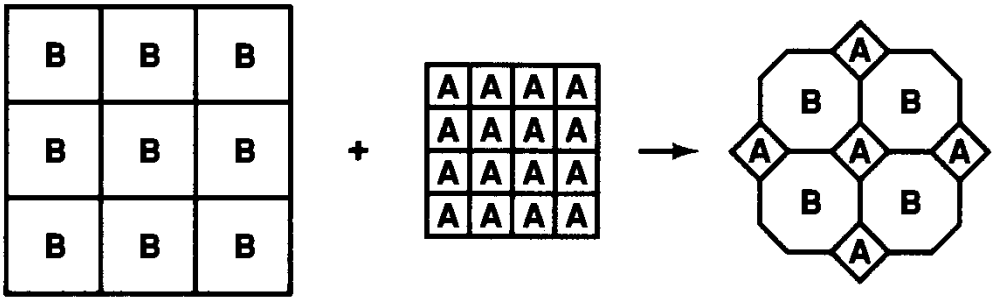

Source: Reproduced with permission of Elsevier Ltd. from Miedema (1975).

A negative contribution to the enthalpies of formation or mixing, which is stabilising with respect to the constituent elements, arises from the equalisation of the chemical potential of the electronic charge, Φ^*, between dissimilar atomic cells. Φ^*, also called Miedema electronegativity, was originally derived from the work functions of the pure metals and afterwards adjusted using available experimental data of enthalpies of formation. This contribution is proportional to the square of the differences of Miedema electronegativities of the constituent elements. Thus, for the interfacial enthalpy effect between neighbouring atomic cells we arrive at the following proportionality:

$$\Delta H^{interface} \propto -P\left(\Delta\Phi^*\right)^2 + Q\left(\Delta {n_{ws}}^{1/3}\right)^2 \qquad (5.107)$$

where $\Delta H^{interface}$ is the enthalpy effect at the interface between dissimilar atomic cells, P and Q are the empirical constants for specific combinations of metals, tabulated in

de Boer (1988), $\Delta\Phi^*$ is the difference of Miedema electronegativities of the constituents and Δn_{ws} is the difference of electron densities at the Wigner-Seitz cell boundary of the constituents.

A quantification of this relation, as discussed extensively in de Boer (1988), involves the introduction of several other group and element-specific constants and leads to the following equations for the enthalpies of formation of ordered solid alloys $A_{xA}B_{xB}$:

$$\Delta H^f A_{x_A}B_{x_B}(s) = x_A\, V_{A,alloy}\, 2/3 f_B^A \left[-P\left(\Delta\Phi^*\right)2 + Q\left(\Delta n_{ws}\, 1/3\right)2 - R_m \right] / \left[\left(n_{ws}A\right) - 1/3 + \left(n_{ws}B\right) - 1/3 \right] + x_A\, \Delta H^{trans}A + x_B\, \Delta H^{trans}B \quad (5.108)$$

and for the partial molar enthalpies of solution at infinite dilution in solid (liquid) mixtures of A and B:

$$\Delta \bar{H}^{solv}{}_{A\text{ in }B}(l) = 2\, V_{A,alloy}\, 2/3 \left[-P\left(\Delta\Phi^*\right)2 + Q\left(\Delta n_{ws}\, 1/3\right)2 - R_{m,liquid} \right] / \left[\left(n_{ws}A\right) - 1/3 + \left(n_{ws}B\right) - 1/3 \right] \quad (5.109)$$

with $\Delta H^f A_{x_A}B_{x_B}(s)$ enthalpy of formation of an alloy of composition $A_{xA}B_{xB}$;

$\Delta \bar{H}^{solv}{}_{A\text{ in }B}(l)$ partial molar enthalpy of solution of component A in B at infinite dilution;

x_A and x_B mole fraction of component A and B, respectively ($x_A + x_B = 1$);

$V_{A,alloy}$ atomic volume of component A within the alloy;

f_B^A degree to which an atomic cell of metal A is in contact with dissimilar atomic cells of metal B on average, has been determined empirical for statistically ordered and ordered alloys (de Boer, 1988);

P, Q empirical constants for specific combinations of metals, tabulated in de Boer (1988);

$\Delta\Phi^*$ difference of Miedema electronegativities of the constituents;

Δn_{ws} difference of electron densities at the Wigner-Seitz cell boundary of the constituents;

R_m hybridisation term that was introduced to account for an additional enthalpy contribution due to interaction of d- and p-orbitals in solid compounds of transition metals with non-transition metals, treated as a group-specific constant within the Miedema model;

$R_{m,liquid}$ for liquid mixtures a reduced hybridisation term has to be used: $R_{m,liquid} = 0.73R_m$;

$\Delta H^{trans}A,B$ enthalpies for the transformation of elements A and B into a hypothetical metallic state (for semi- or non-metallic elements).

For a detailed discussion of the model see de Boer (1988).

A consistent set of Miedema parameters was developed for the elements of the chalcogen group (Group 16 of the periodic table of the elements: O, S, Se, Te, Po) from the results of quantum chemical calculations as well as empirical correlations with physical properties related to electronegativity and electron density (Neuhausen, 2003). The values of these parameters are listed in Table 5.4.18. For details of the derivation of parameters we refer to the original literature (Neuhausen, 2003).

Table 5.4.18: Miedema parameters for the elements of the chalcogen group

Element	$n_{ws}^{1/3}$ [d.u.$^{1/3}$]	Φ^* [V]	$V^{2/3}$ [cm^{2}mol$^{-2/3}$]
O	1.70	6.97	2.656
S	1.46	5.60	4.376
Se	1.40	5.17	5.172
Te	1.31	4.72	6.439
Po	1.15	4.44	7.043
Hybridisation term R for the chalcogen group: 2.45 V^2		Valence factor *a* for the chalcogen group: 0.04	

Using this parameter set, thermochemical properties such as enthalpies of formation of solid metal chalcogenides, partial molar enthalpies of solution of chalcogens in liquid and solid metals, partial molar enthalpies of evaporation of the chalcogens from liquid metal solution into the monoatomic gaseous state, partial molar enthalpies of adsorption of chalcogenides on metal surfaces at zero coverage and partial molar enthalpies of segregation of the chalcogens in trace amounts within solid metal matrices have been calculated in Neuhausen (2003). These properties are compared with available experimental data and discussed with an emphasis on the periodic behaviour of the elements. Systematic errors of the model for specific element combinations are discussed as well in Neuhausen (2003).

The model calculations demonstrate that a semi-quantitative description of the thermochemical properties of the chalcogens using the semi-empirical Miedema approach is possible. General trends in the formation enthalpies of metal chalcogenides throughout the periodic table are represented reasonably well by the results of calculations. It should be pointed out that the computed enthalpy values should not be considered as highly precise data. However, periodic trends and relative stabilities of series of compounds are reproduced well by the calculations Therefore, the calculated properties can serve as a basis for the prediction of the chemical interactions for metal-chalcogen combinations that have not been studied experimentally so far, i.e. especially for metal polonium combinations. Enthalpy values for polonium-containing systems are compiled in Tables 5.4.19-5.4.21.

Table 5.4.19: Calculated enthalpies of formation ($\Delta H^f_{\mathrm{calc}}$) of solid binary polonides obtained using Miedema parameters derived in Neuhausen (2003) (Table 5.4.18)

All other Miedema parameters have been taken from de Boer (1988).
For comparison, the few available literature data and values calculated by other methods within Neuhausen (2003) have been included ($\Delta H^f_{\mathrm{Lit}}$).

Partner element	Composition $M_{1-x}Po_x$	$\Delta H^f_{\mathrm{calc}}$ [kJmol^{-1}]	$\Delta H^f_{\mathrm{Lit}}$ [kJmol^{-1}]
Ac	0.3333	-114.3	
	0.5000	-135.8	
	0.6000	-125.0	
	0.6667	-109.6	
Ag	0.3333	1.2	
	0.5000	1.2	
	0.6000	1.1	
	0.6667	0.9	

Table 5.4.19: Calculated enthalpies of formation (ΔH^{f}_{calc}) of solid binary polonides obtained using Miedema parameters derived in Neuhausen (2003) (Table 5.4.18) (*cont.*)

All other Miedema parameters have been taken from de Boer (1988).
For comparison, the few available literature data and values calculated by other methods within Neuhausen (2003) have been included (ΔH^{f}_{Lit}).

Partner element	Composition $M_{1-x}Po_x$	ΔH^{f}_{calc} [kJmol^{-1}]	ΔH^{f}_{Lit} [kJmol^{-1}]
Al	0.3333	12.9	
	0.5000	13.2	
	0.6000	11.3	
	0.6667	9.6	
Am	0.3333	-99.8	
	0.5000	-113.1	
	0.6000	-101.6	
	0.6667	-88.0	
As	0.3333	18.5	
	0.5000	20.2	
	0.6000	17.8	
	0.6667	15.2	
Au	0.3333	13.5	
	0.5000	14.5	
	0.6000	12.7	
	0.6667	10.8	
B	0.3333	82.2	
	0.5000	70.2	
	0.6000	57.0	
	0.6667	47.4	
Ba	0.3333	-115.0	
	0.5000	-149.3	-153[a] -161.5[b] -167.8[g] -137.7[h] -137.6[k]
	0.6000	-143.9	
	0.6667	-129.1	
Be	0.3333	51.0	
	0.5000	45.7	-28.6[b]
	0.6000	37.3	
	0.6667	31.1	
Bi	0.3333	-2.3	
	0.5000	-2.8	
	0.6000	-2.6	
	0.6667	-2.3	

See notes on page 424.

Table 5.4.19: Calculated enthalpies of formation (ΔH^{f}_{calc}) of solid binary polonides obtained using Miedema parameters derived in Neuhausen (2003) (Table 5.4.18) (*cont.*)

All other Miedema parameters have been taken from de Boer (1988).
For comparison, the few available literature data and values calculated by other methods within Neuhausen (2003) have been included (ΔH^{f}_{Lit}).

Partner element	Composition $M_{1-x}Po_x$	ΔH^{f}_{calc} [kJmol^{-1}]	ΔH^{f}_{Lit} [kJmol^{-1}]
Bk	0.3333	-100.1	
	0.5000	-112.1	
	0.6000	-100.0	
	0.6667	-86.3	
C	0.3333	127.5	
	0.5000	96.3	
	0.6000	77.1	
	0.6667	64.2	
Ca	0.3333	-103.3	
	0.5000	-123.3	-128[a] -140.4[b] -132.1[c] -135.9[g] -117.3[h] -121.3[k]
	0.6000	-112.9	
	0.6667	-98.7	
Cd	0.3333	-2.0	
	0.5000	-2.2	-1.8[b] -29.2[c]
	0.6000	-1.9	
	0.6667	-1.7	
Ce	0.3333	-108.7	
	0.5000	-129.6	
	0.6000	-119.6	
	0.6667	-105.0	
Cf	0.3333	-96.9 (Cf(II)) -99.9(Cf(III))	
	0.5000	-119.4 (Cf(II)) -111.2 (Cf(III))	
	0.6000	-111.6 (Cf(II)) -98.9 (Cf(III))	
	0.6667	-98.6 (Cf(II)) -85.3 (Cf(III))	
Cm	0.3333	-99.0	
	0.5000	-113.0	
	0.6000	-101.8	
	0.6667	-88.3	

See notes on page 424.

Table 5.4.19: Calculated enthalpies of formation (ΔH^{f}_{calc}) of solid binary polonides obtained using Miedema parameters derived in Neuhausen (2003) (Table 5.4.18) (*cont.*)

All other Miedema parameters have been taken from de Boer (1988).
For comparison, the few available literature data and values calculated by other methods within Neuhausen (2003) have been included (ΔH^{f}_{Lit}).

Partner element	Composition $M_{1-x}Po_x$	ΔH^{f}_{calc} [kJmol^{-1}]	ΔH^{f}_{Lit} [kJmol^{-1}]
Co	0.3333	15.1	
	0.5000	14.3	
	0.6000	11.9	
	0.6667	10.0	
Cr	0.3333	20.6	
	0.5000	19.8	
	0.6000	16.5	
	0.6667	13.8	
Cs	0.3333	-55.8	-114[a]
	0.5000	-79.1	
	0.6000	-80.9	
	0.6667	-74.5	
Cu	0.3333	6.5	
	0.5000	6.2	
	0.6000	5.1	
	0.6667	4.3	
Dy	0.3333	-104.9	
	0.5000	-121.1	-115.2[b] -154.0[g]
	0.6000	-109.8	
	0.6667	-95.5	
Er	0.3333	-103.6	
	0.5000	-118.7	
	0.6000	-107.2	
	0.6667	-93.1	
Es	0.3333	-116.0	
	0.5000	-143.9	
	0.6000	-134.9	
	0.6667	-119.3	
Eu	0.3333	-103.5 (Eu(II)) -42.3 (Eu(III))	
	0.5000	-126.6 (Eu(II)) -76.3 (Eu(III))	-147.8[b] -152.7[g] -111[h]
	0.6000	-117.5 (Eu(II)) -75.1 (Eu(III))	
	0.6667	-103.4 (Eu(II)) -67.1 (Eu(III))	

See notes on page 424.

Table 5.4.19: Calculated enthalpies of formation (ΔH^{f}_{calc}) of solid binary polonides obtained using Miedema parameters derived in Neuhausen (2003) (Table 5.4.18) (*cont.*)

All other Miedema parameters have been taken from de Boer (1988).
For comparison, the few available literature data and values calculated by other methods within Neuhausen (2003) have been included (ΔH^{f}_{Lit}).

Partner element	Composition $M_{1-x}Po_x$	ΔH^{f}_{calc} [kJmol^{-1}]	ΔH^{f}_{Lit} [kJmol^{-1}]
Fe	0.3333	28.6	
	0.5000	27.4	
	0.6000	22.9	
	0.6667	19.2	
Fm	0.3333	-111.1	
	0.5000	-132.4	
	0.6000	-121.3	
	0.6667	-106.1	
Ga	0.3333	3.4	
	0.5000	3.6	
	0.6000	3.1	
	0.6667	2.7	
Gd	0.3333	-106.3	
	0.5000	-124.1	
	0.6000	-113.2	
	0.6667	-98.8	
Ge	0.3333	28.4	
	0.5000	24.6	
	0.6000	20.4	
	0.6667	17.1	
H	0.3333	74.5	
	0.5000	56.0	
	0.6000	44.8	
	0.6667	37.3	
Hf	0.3333	-77.9	
	0.5000	-84.4	-2.8[b] -3.4[c]
	0.6000	-74.3	
	0.6667	-63.7	
Hg	0.3333	0.5	
	0.5000	0.6	-10.5[b] 3.7[c]
	0.6000	0.5	
	0.6667	0.4	

See notes on page 424.

Table 5.4.19: Calculated enthalpies of formation (ΔH^{f}_{calc}) of solid binary polonides obtained using Miedema parameters derived in Neuhausen (2003) (Table 5.4.18) (*cont.*)

All other Miedema parameters have been taken from de Boer (1988).
For comparison, the few available literature data and values calculated by other methods within Neuhausen (2003) have been included (ΔH^{f}_{Lit}).

Partner element	Composition $M_{1-x}Po_x$	ΔH^{f}_{calc} [kJmol^{-1}]	ΔH^{f}_{Lit} [kJmol^{-1}]
Ho	0.3333	-103.9	
	0.5000	-119.6	-116.8[b] -141.4[g] -132[h]
	0.6000	-108.2	
	0.6667	-94.1	
In	0.3333	-7.8	
	0.5000	-8.8	
	0.6000	-7.9	
	0.6667	-6.9	
Ir	0.3333	21.8	
	0.5000	22.3	
	0.6000	19.1	
	0.6667	16.2	
K	0.3333	-53.4	-123[a]
	0.5000	-70.4	
	0.6000	-67.5	
	0.6667	-60.1	
La	0.3333	-109.8	
	0.5000	-132.2	
	0.6000	-122.7	
	0.6667	-108.1	
Li	0.3333	-52.8	
	0.5000	-50.9	
	0.6000	-42.5	
	0.6667	-35.8	
Lu	0.3333	-103.0	
	0.5000	-116.8	-72.6[b] -8.8[c] -13.6[g]
	0.6000	-105.0	
	0.6667	-90.9	
Mg	0.3333	-25.9	
	0.5000	-27.5	-27[a] -56.9[c]
	0.6000	-23.9	
	0.6667	-20.4	

See notes on page 424.

Table 5.4.19: Calculated enthalpies of formation (ΔH^{f}_{calc}) of solid binary polonides obtained using Miedema parameters derived in Neuhausen (2003) (Table 5.4.18) (*cont.*)

All other Miedema parameters have been taken from de Boer (1988).
For comparison, the few available literature data and values calculated by other methods within Neuhausen (2003) have been included (ΔH^{f}_{Lit}).

Partner element	Composition $M_{1-x}Po_x$	ΔH^{f}_{calc} [kJmol^{-1}]	ΔH^{f}_{Lit} [kJmol^{-1}]
Mn	0.3333	-13.9	
	0.5000	-13.3	
	0.6000	-11.1	
	0.6667	-9.3	
Mo	0.3333	37.5	
	0.5000	38.3	
	0.6000	32.8	
	0.6667	27.7	
N	0.3333	130.4	
	0.5000	87.2	
	0.6000	68.9	
	0.6667	57.5	
Na	0.3333	-47.7	-116[a]
	0.5000	-54.2	
	0.6000	-48.0	
	0.6667	-41.3	
Nb	0.3333	-11.7	
	0.5000	-12.1	40.9[c]
	0.6000	-10.5	
	0.6667	-8.9	
Nd	0.3333	-107.5	
	0.5000	-126.5	
	0.6000	-116.0	
	0.6667	-101.5	
Ni	0.3333	10.7	
	0.5000	10.2	-23.6[b] 6.3[c] -23.4[h] -19.2[i]
	0.6000	8.5	
	0.6667	7.1	
Np	0.3333	-59.3	
	0.5000	-62.2	
	0.6000	-53.9	
	0.6667	-45.9	

See notes on page 424.

Table 5.4.19: Calculated enthalpies of formation (ΔH^{f}_{calc}) of solid binary polonides obtained using Miedema parameters derived in Neuhausen (2003) (Table 5.4.18) (*cont.*)

All other Miedema parameters have been taken from de Boer (1988).
For comparison, the few available literature data and values calculated by other methods within Neuhausen (2003) have been included (ΔH^{f}_{Lit}).

Partner element	Composition $M_{1-x}Po_x$	ΔH^{f}_{calc} [kJmol^{-1}]	ΔH^{f}_{Lit} [kJmol^{-1}]
O	0.3333	-79.9	-84.2 (8.4)[d] -84.4[e] -83.7[f]
	0.5000	-72.2	
	0.6000	-58.9	
	0.6667	-49.0	
Os	0.3333	40.6	
	0.5000	41.4	
	0.6000	35.3	
	0.6667	29.8	
P	0.3333	41.8	
	0.5000	39.7	
	0.6000	33.5	
	0.6667	28.2	
Pa	0.3333	-118.9	
	0.5000	-131.3	
	0.6000	-116.6	
	0.6667	-100.4	
Pb	0.3333	-3.1	
	0.5000	-3.7	-29.4[b] -18.2[c] -33.9[h] -28.3[k]
	0.6000	-3.5	
	0.6667	-3.0	
Pd	0.3333	-29.6	
	0.5000	-30.7	-29.4[c]
	0.6000	-26.3	
	0.6667	-22.3	
Pm	0.3333	-107.4	
	0.5000	-125.9	
	0.6000	-115.1	
	0.6667	-100.6	
Pr	0.3333	-107.6	
	0.5000	-127.0	
	0.6000	-116.6	
	0.6667	-102.1	

See notes on page 424.

Table 5.4.19: Calculated enthalpies of formation (ΔH^{f}_{calc}) of solid binary polonides obtained using Miedema parameters derived in Neuhausen (2003) (Table 5.4.18) (*cont.*)

All other Miedema parameters have been taken from de Boer (1988).
For comparison, the few available literature data and values calculated by other methods within Neuhausen (2003) have been included (ΔH^{f}_{Lit}).

Partner element	Composition $M_{1-x}Po_x$	ΔH^{f}_{calc} [kJmol^{-1}]	ΔH^{f}_{Lit} [kJmol^{-1}]
Pt	0.3333	-6.0	
	0.5000	-6.3	
	0.6000	-5.4	
	0.6667	-4.6	-23.3[b] -27.4[c] -13.8[h] -10.5[i]
Pu	0.3333	-84.9	
	0.5000	-89.2	
	0.6000	-77.4	
	0.6667	-65.9	
Rb	0.3333	-55.0	-112[a]
	0.5000	-75.4	
	0.6000	-74.6	
	0.6667	-67.4	
Re	0.3333	52.6	
	0.5000	53.9	
	0.6000	46.2	
	0.6667	39.1	
Rh	0.3333	4.1	
	0.5000	4.1	
	0.6000	3.5	
	0.6667	3.0	
Ru	0.3333	31.7	
	0.5000	32.0	
	0.6000	27.2	
	0.6667	23.0	
S	0.3333	-11.6	
	0.5000	-12.2	
	0.6000	-10.5	
	0.6667	-8.9	
Sb	0.3333	3.1	
	0.5000	3.7	
	0.6000	3.4	
	0.6667	3.0	

See notes on page 424.

Table 5.4.19: Calculated enthalpies of formation (ΔH^{f}_{calc}) of solid binary polonides obtained using Miedema parameters derived in Neuhausen (2003) (Table 5.4.18) (*cont.*)

All other Miedema parameters have been taken from de Boer (1988).
For comparison, the few available literature data and values calculated by other methods within Neuhausen (2003) have been included (ΔH^{f}_{Lit}).

Partner element	Composition $M_{1-x}Po_x$	ΔH^{f}_{calc} [kJmol^{-1}]	ΔH^{f}_{Lit} [kJmol^{-1}]
Sc	0.3333	-97.1	
	0.5000	-105.5	-81.1[b] -92.5[c] -76.7[g] -124[h]
	0.6000	-92.8	
	0.6667	-79.6	
Se	0.3333	1.5	
	0.5000	1.6	
	0.6000	1.5	
	0.6667	1.3	
Si	0.3333	51.5	
	0.5000	45.8	
	0.6000	38.1	
	0.6667	32.0	
Sm	0.3333	-106.4	
	0.5000	-124.4	
	0.6000	-113.6	
	0.6667	-99.2	
Sn	0.3333	-0.2	
	0.5000	-0.3	
	0.6000	-0.2	
	0.6667	-0.2	
Sr	0.3333	-106.6	
	0.5000	-135.1	-134[a] -155.6[b] -141.6[c] -156.2[g]
	0.6000	-128.2	
	0.6667	-114.0	
Ta	0.3333	-14.7	
	0.5000	-15.3	76.4[c]
	0.6000	-13.2	
	0.6667	-11.2	
	0.3333	-105.1	
	0.5000	-121.9	-112.7[b] -108.0[g]
	0.6000	-110.7	
	0.6667	-96.5	

See notes on page 424.

Table 5.4.19: Calculated enthalpies of formation (ΔH^{f}_{calc}) of solid binary polonides obtained using Miedema parameters derived in Neuhausen (2003) (Table 5.4.18) (*cont.*)

All other Miedema parameters have been taken from de Boer (1988).
For comparison, the few available literature data and values calculated by other methods within Neuhausen (2003) have been included (ΔH^{f}_{Lit}).

Partner element	Composition $M_{1-x}Po_x$	ΔH^{f}_{calc} [kJmol^{-1}]	ΔH^{f}_{Lit} [kJmol^{-1}]
Tc	0.3333	29.7	
	0.5000	30.3	
	0.6000	25.9	
	0.6667	21.9	
Te	0.3333	4.6	
	0.5000	5.4	
	0.6000	5.0	
	0.6667	4.3	
Th	0.3333	-108.7	
	0.5000	-128.3	
	0.6000	-118.2	
	0.6667	-103.7	
Ti	0.3333	-51.4	
	0.5000	-52.7	-29.6[b] -29.2[c] -47.5[g] -45.5[h] -24.8[i]
	0.6000	-45.2	
	0.6667	-38.3	
Tl	0.3333	-7.6	
	0.5000	-8.8	
	0.6000	-8.0	
	0.6667	-7.0	
Tm	0.3333	-103.4	
	0.5000	-117.9	-120.4[b] -144.8[g]
	0.6000	-106.2	
	0.6667	-92.1	
U	0.3333	-68.1	
	0.5000	-72.6	
	0.6000	-63.4	
	0.6667	-54.2	
V	0.3333	-7.2	
	0.5000	-7.1	43.1[c]
	0.6000	-6.0	
	0.6667	-5.0	

See notes on page 424.

Table 5.4.19: Calculated enthalpies of formation (ΔH^{f}_{calc}) of solid binary polonides obtained using Miedema parameters derived in Neuhausen (2003) (Table 5.4.18) (*cont.*)

All other Miedema parameters have been taken from de Boer (1988).
For comparison, the few available literature data and values calculated by other methods within Neuhausen (2003) have been included (ΔH^{f}_{Lit}).

Partner element	Composition $M_{1-x}Po_x$	ΔH^{f}_{calc} [kJmol^{-1}]	ΔH^{f}_{Lit} [kJmol^{-1}]
W	0.3333	51.2	
	0.5000	52.9	
	0.6000	45.4	
	0.6667	38.5	
Y	0.3333	-106.3	
	0.5000	-124.1	-100.4[b] -102.3[c] -38.8[g]
	0.6000	-113.2	
	0.6667	-98.8	
Yb	0.3333	-101.6 (Yb(II)) -75.9 (Yb(III))	
	0.5000	-119.8 (Yb(II)) -97.0 (Yb(III))	-114.0[b] -122.2[g] -125[h]
	0.6000	-108.9 (Yb(II)) -89.3 (Yb(III))	
Yb	0.6667	-94.9 (Yb(II)) -78.0 (Yb(III))	
Zn	0.3333	4.0	
	0.5000	3.9	-24.1[c]
	0.6000	3.3	
	0.6667	2.8	
Zr	0.3333	-94.1	
	0.5000	-102.5	-27.6[b] -38.1[c]
	0.6000	-90.5	
	0.6667	-77.7	

a Krestov (1962).

b LMTO calculations (Neuhausen, 2003).

c PP-PW calculations (Neuhausen, 2003).

d Brewer (1953).

e Latimer (1952).

f Zhdanov (1985).

g Calculated from Kapustinskii lattice energies, ionisation energies and sublimation enthalpies (Neuhausen, 2003).

h Estimated from linear correlations with lnA in homologous series MQ (Q = S, Se, Te) (Neuhausen, 2003).

i Estimated from linear correlations with covalent radius of the chalcogen in homologous series MQ (Q = S, Se, Te) (Neuhausen, 2003).

k Estimated from linear correlations with ionic radius of the chalcogen in homologous series MQ (Q = S, Se, Te) (Neuhausen, 2003).

Table 5.4.20: Calculated values for the partial molar enthalpy of solution of liquid Po in liquid elements B at infinite dilution and calculated partial molar enthalpies of evaporation of Po into the monoatomic state from liquid metal solutions

Symbol of element B	Atomic number Z	$\Delta\bar{H}^{solv}_{Po\ in\ B\ (l)}$ (calc.) [kJmol^{-1}]	$\Delta\bar{H}^{v}_{Po\ in\ B\ (l)}$ (calc.) [kJmol^{-1}]
Ac	89	-322.4	511.3
Ag	47	15.0	173.9
Al	13	46.5	142.4
Am	95	-279.3	468.2
As	33	63.0	125.9
Au	79	69.3	119.6
B	5	268.1	-79.2
Ba	56	-335.5	524.4
Be	4	218.1	-29.2
Bi	83	-7.3	196.2
Bk	97	-282.8	471.7
C	6	36.5	152.4
Ca	20	-309.6	498.5
Cd	48	-7.0	195.9
Ce	58	-301.8	490.7
Cf^{II}	98	-285.8	474.7
Cf^{III}	98	-283.3	472.2
Cm	96	-275.6	464.5
Co	27	136.3	52.6
Cr	24	158.4	30.5
Cs	55	-174.3	363.2
Cu	29	47.8	141.1
Dy	66	-293.8	482.7
Er	68	-290.6	479.5
Es	99	-342.5	531.4
Eu^{II}	63	-308.3	497.2
Eu^{III}	63	-296.7	485.6
Fe	26	188.4	0.5
Fm	100	-331.1	520.0
Ga	31	11.7	177.2
Gd	64	-296.7	485.6
Ge	32	41.7	147.2
Hf	72	-190.1	379.0
Hg	80	1.7	187.2

Table 5.4.20: Calculated values for the partial molar enthalpy of solution of liquid Po in liquid elements B at infinite dilution and calculated partial molar enthalpies of evaporation of Po into the monoatomic state from liquid metal solutions (*cont.*)

Symbol of element B	Atomic number Z	$\Delta\bar{H}^{solv}_{Po\ in\ B\ (l)}$ (calc.) [kJmol^{-1}]	$\Delta\bar{H}^{v}_{Po\ in\ B\ (l)}$ (calc.) [kJmol^{-1}]
Ho	67	-291.0	479.9
In	49	-25.8	214.7
Ir	77	155.7	33.2
K	19	-167.1	356.0
La	57	-304.1	493.0
Li	3	-192.1	381.0
Lu	71	-290.0	478.9
Mg	12	-89.0	277.9
Mn	25	23.4	165.5
Mo	42	214.1	-25.2
Na	11	-155.2	344.1
Nb	41	37.8	151.1
Nd	60	-299.4	488.3
Ni	28	119.1	69.8
Np	93	-131.4	320.3
Os	76	224.9	-36.0
P	15	109.5	79.4
Pa	91	-327.7	516.6
Pb	82	-10.2	199.1
Pd	46	-30.3	219.2
Pm	61	-299.5	488.4
Po	84	0	188.9
Pr	59	-299.4	488.3
Pt	78	55.3	133.6
Pu	94	-221.3	410.2
Rb	37	-171.7	360.6
Re	75	267.9	-79.0
Rh	45	91.6	97.3
Ru	44	193.3	-4.4
S	16	-41.0	229.9
Sb	51	10.2	178.7
Sc	21	-278.6	467.5
Se	34	5.1	183.8
Si	14	105.6	83.3

Table 5.4.20: Calculated values for the partial molar enthalpy of solution of liquid Po in liquid elements B at infinite dilution and calculated partial molar enthalpies of evaporation of Po into the monoatomic state from liquid metal solutions (*cont.*)

Symbol of element B	Atomic number Z	$\Delta\bar{H}^{solv}_{Po\ in\ B\ (l)}$ (calc.) [kJmol^{-1}]	$\Delta\bar{H}^{v}_{Po\ in\ B\ (l)}$ (calc.) [kJmol^{-1}]
Sm	62	-296.7	485.6
Sn	50	-0.7	189.6
Sr	38	-315.6	504.5
Ta	73	26.8	162.1
Tb	65	-293.8	482.7
Tc	43	185.0	3.9
Te	52	14.9	174.0
Th	90	-302.7	491.6
Ti	22	-106.4	295.3
Tl	81	-24.8	213.7
Tm	69	-290.6	479.5
U	92	-159.1	348.0
V	23	51.2	137.7
W	74	262.4	-73.5
Y	39	-296.7	485.6
Yb^{II}	70	-305.5	494.4
Yb^{III}	70	-290.6	479.5
Zn	30	14.7	174.2
Zr	40	-244.4	433.3

Source: Neuhausen (2003).

Table 5.4.21: Calculated values for the partial molar enthalpy of solution of polonium in solid elements B at infinite dilution, mechanism of polonium adsorption on/in solid surfaces of element B, see Neuhausen (2003), partial molar enthalpies of adsorption of polonium in/on solid surfaces of B at zero coverage, partial molar net enthalpies of adsorption of polonium in/on solid surfaces of B at zero coverage and partial molar enthalpies of segregation of polonium in a solid matrix of B

Element B	Atomic number Z	$\Delta\bar{H}^{solv}_{Po\ in\ B(s)}$ (calc.) [kJmol^{-1}]	Adsorption mechanism	$\Delta\bar{H}^{ads}_{Po\ in/on\ B}$ (calc.) [kJmol^{-1}]	$\Delta\bar{H}^{ads,net}_{Po\ in/on\ B}$ (calc.) [kJmol^{-1}]	$\Delta\bar{H}^{seg}$ Po (calc.) [kJmol^{-1}]
Ac	89	-369.8	In	-540.7	-351.8	18.1
Ag	47	4.2	In	-212.8	-23.9	-28.1
Al	13	46.5	In (on)	-167.8 (-227.8)	21.1 (-38.9)	-25.4 (-85.4)
Am	95	-330.1	In	-509.6	-320.7	9.3
As	33	63.0	On	-221.3	-32.4	-95.4
Au	79	47.0	In (on)	-175.8 (-254.6)	13.1 (-65.7)	-33.9 (-112.7)
B	5	268.1	On	-303.2	-114.3	-382.3
Ba	56	-361.3	In	-524.2	-335.3	26
Be	4	218.1	On	-243.9	-55	-273
Bi	83	-7.3	In	-203.6	-14.7	-7.3
Bk	97	-333.6	In	-511.4	-322.5	11.1
C	6	36.5	In	-375.2	-186.3	-222.8
Ca	20	-331.5	In	-501.6	-312.7	18.8
Cd	48	-7.0	In	-206.7	-17.8	-10.8
Ce	58	-351.3	In	-520.4	-331.5	19.8
Cf^{II}	98	-308.4	In	-503.6	-314.7	19.2
Cf^{III}	98	-333.9	In	-486.5	-297.6	10.8
Cm	96	-326.5	In	-508.8	-319.9	6.6
Co	27	58.6	On (in)	-318.5 (-187.4)	-129.6 (1.5)	-188.2 (-57.0)
Cr	24	79.6	On	-337.5	-148.6	-228.2
Cs	55	-174.3	In	-347.8	-158.9	15.4
Cu	29	25.5	In	-204.7	-15.8	-41.3
Dy	66	-343.8	In	-524.5	-335.6	8.2
Er	68	-340.8	In	-524.2	-335.3	5.5
Es	99	-368.2	In	-533.6	-344.7	23.4
Eu^{II}	63	-329.8	In	-514.0	-325.1	21.4
Eu^{III}	63	-346.5	In	-502.2	-313.3	16.5
Fe	26	109.8	On	-286.5	-97.6	-207.4
Fm	100	-357.3	In	-534.2	-345.3	12
Ga	31	11.7	In	-184.6	4.3	-7.4

Table 5.4.21: Calculated values for the partial molar enthalpy of solution of polonium in solid elements B at infinite dilution, mechanism of polonium adsorption on/in solid surfaces of element B, see Neuhausen (2003), partial molar enthalpies of adsorption of polonium in/on solid surfaces of B at zero coverage, partial molar net enthalpies of adsorption of polonium in/on solid surfaces of B at zero coverage and partial molar enthalpies of segregation of polonium in a solid matrix of B (*cont.*)

Element B	Atomic number Z	$\Delta\overline{H}^{solv}_{Po\ in\ B(s)}$ (calc.) [kJmol^{-1}]	Adsorption mechanism	$\Delta\overline{H}^{ads}_{Po\ in/on\ B}$ (calc.) [kJmol^{-1}]	$\Delta\overline{H}^{ads,net}_{Po\ in/on\ B}$ (calc.) [kJmol^{-1}]	$\Delta\overline{H}^{seg}$ Po (calc.) [kJmol^{-1}]
Gd	64	-346.5	In	-524.7	-335.8	10.7
Ge	32	41.7	In (on)	-179.0 (-252.9)	9.9 (-64.0)	-31.8 (-105.7)
Hf	72	-266.3	In	-477.0	-288.1	-21.8
Hg	80	1.7	In	-191.7	-2.8	-4.4
Ho	67	-341.0	In	-523.2	-334.3	6.7
In	49	-25.8	In	-219.5	-30.6	-4.8
Ir	77	78.0	On	-353.8	-164.9	-242.9
K	19	-167.1	In	-342.3	-153.4	13.7
La	57	-353.4	In	-523.5	-334.6	18.8
Li	3	-192.1	In	-371.0	-182.1	10
Lu	71	-340.4	In	-526.8	-337.9	2.6
Mg	12	-89.0	In	-286.5	-97.6	-8.5
Mn	25	-53.8	In	-279.7	-90.8	-37
Mo	42	134.6	On	-327.4	-138.5	-273.1
Na	11	-155.2	In	-333.7	-144.8	10.5
Nb	41	-41.2	In (on)	-286.4 (-407.7)	-97.4 (-218.8)	-56.2 (-177.6)
Nd	60	-349.0	In	-522.1	-333.2	15.8
Ni	28	41.7	In (on)	-201.6 (-325.6)	-12.7 (-136.7)	-54.4 (-178.4)
Np	93	-207.8	In	-395.3	-206.4	1.4
Os	76	146.4	On	-361.3	-172.4	-318.8
P	15	109.5	On	-191.3	-2.4	-111.9
Pa	91	-401.2	In	-583.4	-394.5	6.6
Pb	82	-10.2	In	-207.3	-18.4	-8.2
Pd	46	-105.5	In	-327.1	-138.2	-32.6
Pm	61	-349.3	In	-522.9	-334	15.3
Po	84	0	In	-196.8	-7.9	-7.9
Pr	59	-349.0	In	-520.7	-331.8	17.2
Pt	78	-21.2	In	-255.0	-66.1	-44.9
Pu	94	-296.7	In	-474.7	-285.8	10.9
Rb	37	-171.7	In	-345.9	-157	14.7

Table 5.4.21: Calculated values for the partial molar enthalpy of solution of polonium in solid elements B at infinite dilution, mechanism of polonium adsorption on/in solid surfaces of element B, see Neuhausen (2003), partial molar enthalpies of adsorption of polonium in/on solid surfaces of B at zero coverage, partial molar net enthalpies of adsorption of polonium in/on solid surfaces of B at zero coverage and partial molar enthalpies of segregation of polonium in a solid matrix of B (*cont.*)

Element B	Atomic number Z	$\Delta\bar{H}^{solv}_{Po\ in\ B(s)}$ (calc.) [kJmol^{-1}]	Adsorption mechanism	$\Delta\bar{H}^{ads}_{Po\ in/on\ B}$ (calc.) [kJmol^{-1}]	$\Delta\bar{H}^{ads,net}_{Po\ in/on\ B}$ (calc.) [kJmol^{-1}]	$\Delta\bar{H}^{seg}$ Po (calc.) [kJmol^{-1}]
Re	75	188.8	On	-341.9	-153	-341.8
Rh	45	14.7	In	-231.1	-42.2	-56.9
Ru	44	115.2	On	-329.6	-140.7	-255.9
S	16	-41.0	In	-234.9	-46	-4.9
Sb	51	10.2	In	-194.2	-5.3	-15.5
Sc	21	-329.5	In	-518.4	-329.5	0
Se	34	5.1	In	-194.1	-5.2	-10.3
Si	14	105.6	On	-260.7	-71.8	-177.4
Sm	62	-346.5	In	-521.0	-332.1	14.4
Sn	50	-0.7	In	-197.9	-9	-8.3
Sr	38	-336.6	In	-503.3	-314.4	22.2
Ta	73	-52.0	In	-307.8	-118.9	-66.9
Tb	65	-343.8	In	-523.4	-334.5	9.3
Tc	43	106.9	on	-314.1	-125.2	-232.1
Te	52	14.9	In	-187.2	1.7	-13.2
Th	90	-353.5	In	-537.5	-348.6	4.9
Ti	22	-183.7	In	-397.8	-208.9	-25.2
Tl	81	-24.8	In	-220.6	-31.7	-6.8
Tm	69	-340.8	In	-524.8	-335.9	4.9
U	92	-235.3	In	-428.0	-239.1	-3.7
V	23	-27.2	In	-269.7	-80.8	-53.6
W	74	182.7	On	-354.3	-165.4	-348
Y	39	-346.5	In	-527.9	-339	7.6
Yb^{II}	70	-327.5	In	-501.3	-312.4	15.1
Yb^{III}	70	-340.8	In	-510.2	-321.3	19.5
Zn	30	14.7	In	-192.6	-3.7	-18.4
Zr	40	-320.1	In	-517.2	-328.3	-8.2

6. Compatibility of structural materials with lead-bismuth eutectic and lead: Standardisation of data, corrosion mechanism and rate*

6.1 Introduction

Liquid metal corrosion might have various impacts on the operation of reactor systems. The loss of material due to corrosion can jeopardise the integrity of the structural and functional components. This issue is especially important for thin wall components like fuel cladding and heat exchanger tubes. Therefore, the LBE contains oxygen that causes an *in situ* formation of a protective oxide scale. The oxide layer grown on the metal surface may reduce the heat transfer through the metal walls. This is important for components for which heat transfer is part of the function, again the fuel cladding through which heat produced by nuclear reaction in fuel is transferred to the coolant and for heat exchanger tubes through which the heat exchange between primary and secondary circuit occurs. Therefore, besides corrosion, the thickness of the oxide layer may be one of the criteria to define the lifetime of these components. The corrosion products due to corrosion processes on metal surface and its release to the coolant may lead to deposition at the colder part of liquid metal circuits and block the flow paths; this effect is also known as plugging. Distribution and concentrations of various impurities in the coolant, which can be both consumed or produced by corrosion processes, are very important data, which should be provided for the development of appropriate coolant management strategies.

Dedicated experimental studies are performed to assess these corrosion degradation effects. Different approaches to analyse the experimental data so as to assess component performance should also be applied. For instance, the integrity assessment of components should be based on the maximum corrosion penetration, whereas the assessment of heat exchanger performance is usually based on the average coverage of the surface by the oxide films and their thermal conductivity. Prediction of corrosion effects for the components with the desired lifetime requires development of extrapolation methods based on good understanding of underlying processes, their mechanistic description and the set of reliable experimental data for extrapolation. These different approaches should be properly reflected in the recommendations for corrosion testing and for experimental data analysis.

The existing corrosion data obtained by examination of corrosion layers after exposure of steels to lead and LBE environment at similar conditions show significant scatter of the results. The possible reasons for the scatter are:

- different experimental procedures implemented in different labs;
- insufficient control of the key testing parameters;
- differences in measurements of corrosion damages and in interpretation and reporting of the experimental results.

* Chapter lead: F.J. Martín-Muñoz. For additional contributors, please see Appendix 1.

All these reasons should be evaluated by a critical assessment comparison of the existing experimental data and results of these exercises should be reflected upon. Therefore, from the numerous experimental data obtained thus far, those selected should be based on relevant experimental procedures with sufficiently controlled test parameters and reliable examination methods.

Various approaches to mitigate liquid metal corrosion (LMC) developed to date are the following:

- selecting corrosion-resistant materials and defining an appropriate range of coolant operating parameters including temperature and dissolved oxygen concentration;
- doping of steels with elements, which promotes the formation of protective oxide layers, e.g. Si and Al;
- applying protective coatings or surface alloying;
- adding inhibitors to the coolant, e.g. Zr.

The chemistry control of Pb and LBE is discussed in Chapter 2 of this handbook. Other corrosion mitigation approaches are discussed in more detail in Chapter 9.

Chapter 6 focuses on the compatibility of structural materials, mainly stainless steels, with lead-bismuth eutectic and lead, dealing with the corrosion mechanism and rates. First, the fundamentals of corrosion, protection methodologies by in situ oxide layer formation and oxidation-corrosion interaction models are discussed. Second, a critical review of the existing data on corrosion of structural steels in LBE and Pb is presented, with the main conclusions obtained from these data. Finally, recommendations on corrosion test procedures are proposed.

6.2 Fundamentals

According to ISO terminology corrosion is a physicochemical interaction leading to a significant deterioration of the functional properties of either a material or the environment with which it has interacted, or both. The most known types of corrosion are aqueous corrosion of metals exposed to liquid electrolytes and high temperature corrosion or oxidation, which usually takes place in gaseous environment. Another type is the liquid metal corrosion of which the corrosion in lead and in LBE is a particular case. An overview of LMC phenomena is provided by Tortorelli (2003). A comprehensive outline of the thermodynamic database available for lead and lead-bismuth is given in Chapter 3 of this handbook. Here, only the issues relevant to corrosion in lead-based alloys are discussed. LMC can manifest itself in various ways. The following categories may be used to classify relevant corrosion phenomena of steels in Pb and LBE:

- dissolution;
- oxidation;
- erosion corrosion;
- fretting corrosion.

Definitions and descriptions of these types of reactions are provided subsequently. However, it is important to know that these classifications are not commonly accepted and the terminology may vary. Moreover, the individual categories are not independent and two types of corrosion phenomena can take place simultaneously and in synergy on the same metal surface, as will be demonstrated.

The main driving forces of liquid metal corrosion are the differences in solubility limits of the alloying elements of the exposed steel in liquid metal (dissolution mode), by chemical reactions with non-metallic impurities present in liquid metal (oxidation mode,

carburisation) and high flow velocity of liquid metal (erosion corrosion). General discussions of the different types of corrosion in liquid metals and of the influence of several variables (temperature, temperature gradient, ratio metal solid area to liquid metal volume, velocity and others) can be found in Staudhammer (1992), Bagnall (1995) and Zhang (2008).

6.2.1 Dissolution

The simplest corrosion reaction that can occur in a liquid metal environment is direct dissolution. The net rate at which an elemental species enters solution is proportional to the difference between the solubility of that element and its actual concentration in the liquid metal. Under isothermal conditions, the rate of the dissolution reaction would decrease with time as the concentration of species in solution increases, and once the concentration reaches the solubility limit the dissolution reaction should stop. Therefore, corrosion by direct dissolution process can be minimised by selecting steels whose elements have low solubility limits in liquid metal and/or by saturating the melt with the alloying elements before exposure of steel. The latter will, however, cause problems in loops with temperature gradients as will be addressed further on.

Structural materials exposed to liquid metals can undergo corrosion by: *i)* direct dissolution of solid metal in the liquid metal by a surface reaction involving atoms from the solid and liquid metals or impurities present in the liquid metal; *ii)* by intergranular attack. In the dissolution process or leaching, one alloy component can be preferentially dissolved, as in the case of nickel that is leached from stainless steels by lead and lead-bismuth eutectic (Sheir, 1994). The first stage of the dissolution process involves "cleavage" of the bonds between atoms in the solid metal and the formation of new bonds with atoms of liquid metal or its impurities, in the boundary layer. Once this occurs, the dissolved atoms diffuse through the boundary layer into the liquid metal.

Corrosion processes resulting from dissolution in a non-isothermal liquid metal system consist of both dissolution at the hot part of the flow circuit and solute deposition at the colder parts. In a flowing recirculating system, the precipitation process in the cold leg or heat removal part of the circuit often controls the steady-state concentration of the solute. The material dissolved at the highest temperature will precipitate at the lowest temperature until a steady-state concentration of solute in liquid metal is reached. The corrosion rate is a function of both the maximum and minimum temperature in the circuit and the corrosion rate at the highest temperature can be reduced by increasing the minimum temperature or by reducing the maximum temperature (Weeks, 1997). This type of corrosion is termed thermal gradient mass transfer. It may be illustrated by circulating a corrosive metal such as bismuth around a thermal convection loop of the type shown in Figure 6.2.1 (Weeks, 1958). Mass is transferred from the hot zone to the cold zone and, after a period of time, plugging of the loop may occur. This type of corrosion does not decrease with time, contrary to that observed in isothermal conditions.

Mass transfer can also occur under isothermal conditions where concentration gradients exist. The dissolved elements from one alloy get transported by the liquid metal and precipitate or dissolve in another alloy, forming metal solid solutions or intermetallic compounds. In some cases selective dissolution can be of advantage for "masking" one region of the system by material dissolved from another region of the system. Masking may be described as the lowering of element loss from a downstream region because a region rich in these elements is located upstream. For example, the removal of nickel from nickel-containing alloys is an important factor determining the corrosion rate of these materials. If a high nickel source is placed upstream in an isothermal zone, the nickel removal rate from a region downstream could be reduced due to the higher Ni content in the coolant adjacent to this region, which reduces the activity difference between the surface and the bulk.

Figure 6.2.1: Thermal gradient mass transfer

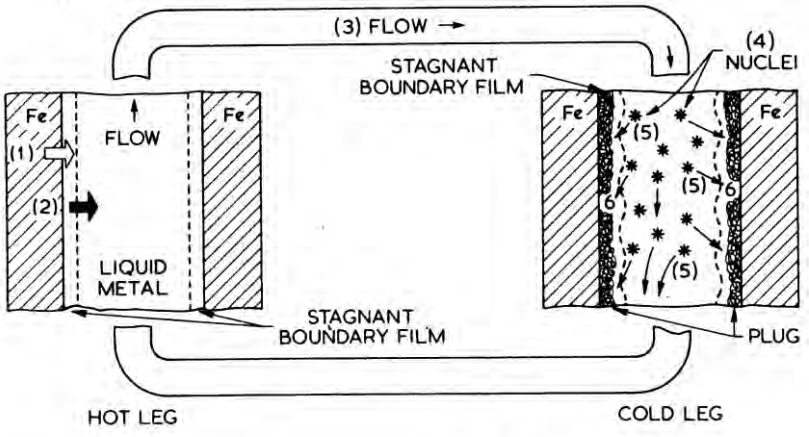

1. Solution
2. Diffusion
3. Transport of dissolved metal
4. Nucleation
5. Transport of crystallites
6. Crystal growth and sintering (plug formation)

Source: Weeks (1958).

Under certain conditions, dissolution of steels by liquid metals can lead to intergranular attack because the atoms at the grain boundary have a higher potential energy than the atoms inside the grains. Therefore, the activation energy of the grain boundary atoms for dissolution is lower and the probability of their transition to the melt higher and, hence, the dissolution rate, higher. If the concentration of higher solubility elements increases in the grain boundaries, the dissolution rate may increase due to the preferential dissolution of these elements (Gerasimov, 1983). Additionally, accelerated mass transport of alloying elements towards the surface of the metal might also enhance intergranular attack.

Preferential elemental dissolution from an alloy into liquid metal might result in a phase transformation in the corrosion layer. One of the examples is the preferential dissolution of nickel from the corrosion layer of austenitic stainless steels exposed to certain conditions in liquid metal which may cause phase transformation to a ferritic structure in the surface region.

In Pb and LBE systems the dissolution may be accomplished by penetration of liquid material through the corrosion layer.

As an example the long-term test conducted in the CORRIDA loop on austenitic 316L steel in oxygen-containing flowing lead-bismuth eutectic at 550°C is shown in Figure 6.2.2 (Schroer, 2010b). The velocity of the liquid metal flow was 2 m/s and the concentration of dissolved oxygen averaged 1.6×10^{-6} wt.%. A local dissolution attack was observed that increased with exposure time. It reached a depth of 270 μm after 7 518 h. The white spots in the figure are regions with penetrated LBE. Ni is practically completely leached out of the steel at the affected sites, accompanied by penetration of Pb and Bi into the steel. Additionally, Cr is significantly depleted (Figure 6.2.2 [right]). This local attack, in general, occurs at one to two sites on each specimen, with lateral dimensions significantly larger than the depth. However, the major part of the sample surface is covered and protected by a thin Cr-oxide scale with some enrichment of Si at the scale/steel interface. Thicker FeCr spinel layers (< 40 μm) were additionally observed at some sites. The selected temperature is obviously too high for application of 316L in LBE.

Figure 6.2.2: Local degradation of 316L by selective leaching of Ni and Cr in the course of the exposure to oxygen-containing flowing LBE at 550°C for 7 518 hours

Results of qualitative EDX analyses (line scan) are shown on the right

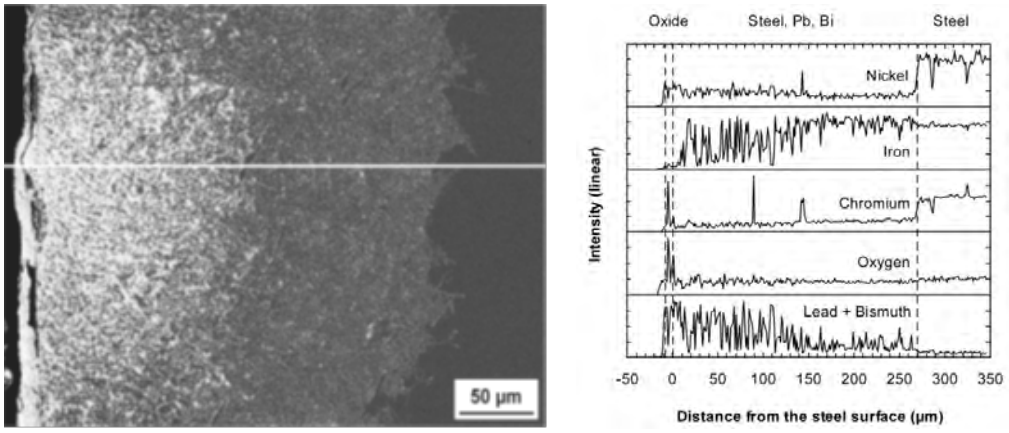

Source: Schroer (2010b).

6.2.2 Oxidation

Oxygen concentration in liquid lead alloys is a key parameter for the corrosion of structural materials. Several authors have correlated decreased dissolution resistance in Pb and LBE with low oxygen concentration. Gorynin (1999) determined the influence of oxygen concentration on the dissolution/oxidation process of two austenitic stainless steels (16Cr-11Ni-3Mo commercial steel, and 15Cr-11Ni-3Si-MoNb experimental steel alloyed with 3% Si) in experiments performed in flowing lead at 550°C for 3 000 hours. For oxygen concentrations between 10^{-8} and 10^{-10} wt.%, corrosion by dissolution occurs whereas for concentrations higher than 10^{-7}-10^{-6} wt.% oxidation of steels takes place (Figure 6.2.3). The dissolution observed for low oxygen concentrations (10^{-8}-10^{-10} wt.%) begins with the formation of pits on the material surface. During exposure, the pits grow and merge into a porous corrosion layer, whose thickness grows linearly with time. Figure 6.2.3 shows the effect of oxygen concentration on corrosion resistance for stainless steels. There is a minimum in material loss associated with the formation of a protective oxide film.

With an adequate control of the oxygen concentration in the liquid metal, formation of oxide films on the surface of the structural materials occurs, limiting further dissolution. For optimum effectiveness, the oxygen concentration in the liquid metal must be adequate to passivate the material but not sufficiently high to promote the precipitation of lead oxide. For Fe-containing alloys such as structural steels, minimum oxygen concentration is defined by the magnetite (Fe_3O_4) decomposition potential, considering this oxide is less stable than the others that can be formed on structural steels. The maximum value is fixed by precipitation of lead oxide. After formation of oxide films, dissolution of the structural materials, becomes negligible if the oxygen concentration is sufficient, as the oxidation reaction is quicker than that of dissolution. The ideal protective oxide layer should be pore-free, crack-free, stress-free at operating temperatures, and resistant to spalling or damage during cooling or heating (Stott, 1987). In addition, the oxygen and metal ions must have low diffusion coefficients through the scale and the recession rate of the original surface must be low enough during the desired service life (Kofstad, 1987). However, it is possible to optimise the self-healing layer by controlling the oxygen concentration in the liquid lead/lead-bismuth and the operating conditions or to use protective measures as described in Chapter 9. Finally, this optimisation has the scope to minimise the corrosion-dissolution process and the corrosion-oxidation process.

Figure 6.2.3: Dissolution/oxidation depth of stainless steels in lead at 550°C for different oxygen concentrations in the liquid metal

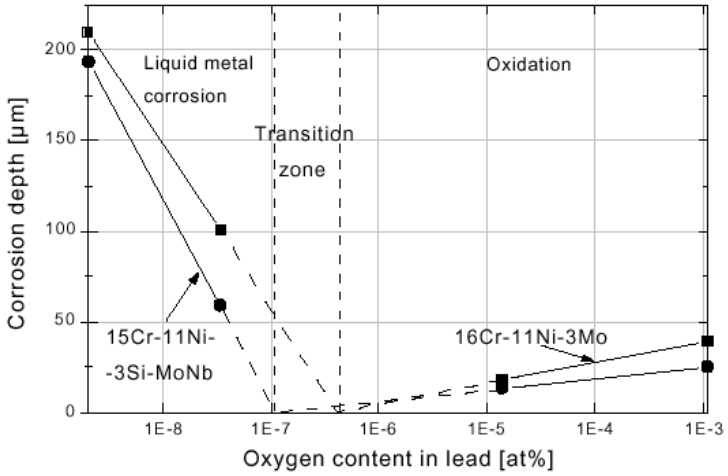

Source: Gorynin (1999).

The protective oxide layer on ferritic/austenitic steel in LBE or Pb containing the necessary oxygen content is a duplex oxide scale, while austenitic steels tend to develop partly duplex and thin, single oxide scales. Various theories have been suggested to explain the formation of duplex layers on these steels, the most widely accepted stipulating that the formation of oxides relies on the simultaneous diffusion of anions and cations (Müller, 2000). According to this theory, the first oxide that forms and grows inwards from the steel surface is Fe-Cr spinel ($Fe^{2+}O[Fe^{3+},Cr^{3+}]_2O_3$). Once a thin spinel layer is formed, iron cations from the steel bulk diffuse to the surface, where they get oxidised, forming a magnetite (Fe_3O_4) scale that grows outwards from the original steel surface. A schematic representation of this mechanism is shown in Figure 6.2.4. The continuous, concurrent counter-diffusion of O and Fe ions results in the growth of a duplex oxide scale (Müller, 2000).

Figure 6.2.4: Schematic representation of the oxidation mechanism of steels in liquid Pb

This mechanism was originally proposed for martensitic OPTIFER IVc and austenitic 1.4970 steels (Müller, 2000), but its basic principles are also applicable to the oxidation behaviour of other ferritic and austenitic steels in liquid LBE

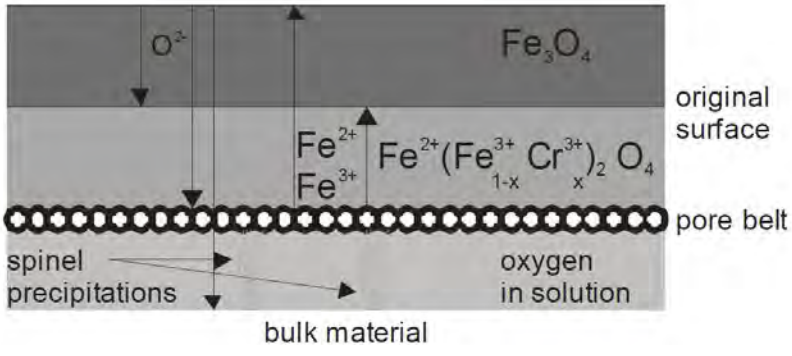

Figure 6.2.5 shows an example of an oxide duplex layer on T91 steel. The duplex oxide scale with an internal oxidation zone (IOZ) developed on the steel surface in LBE after 2 000 h at 480°C. The outer layer consists of Fe and O, the second layer also contains Cr and the IOZ consists of Cr-rich oxides at the steel grain boundaries. The outer layer is magnetite (Fe_3O_4) that is porous and penetrated by LBE. The second layer consists of Fe-Cr spinel and is more compact, thus being the stable protection layer on the steel surface (Figure 6.2.5, right). LBE penetrated the magnetite layer but was stopped at the interface between the magnetite and the spinel layer.

Figure 6.2.5: SEM cross-section of T91 steel after exposure to flowing LBE at 480°C for 2 000 hours

Results of qualitative EDX analyses (line scan) are shown on the right (DEMETRA, 2009a)

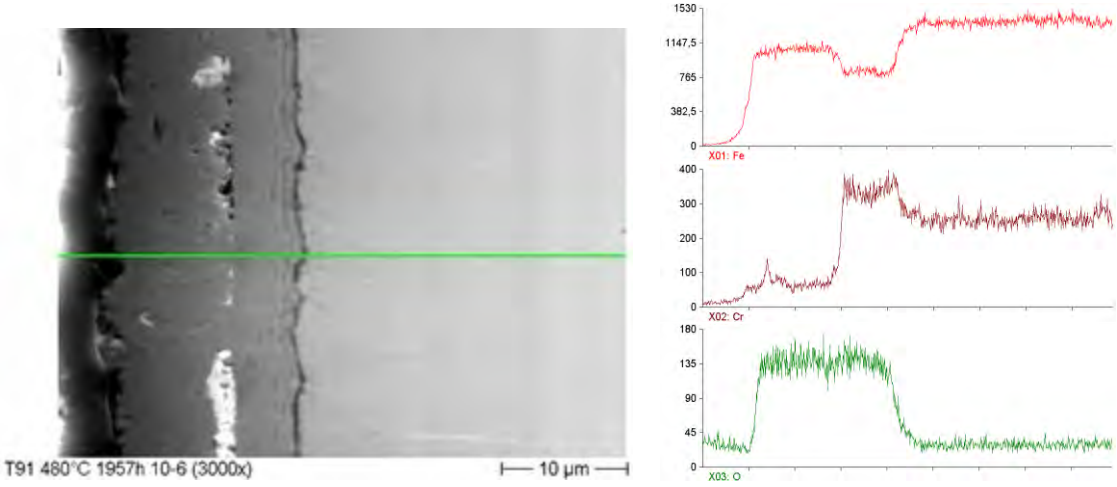

Austenitic steels have a different oxidation behaviour because they generally contain more Cr and Ni than martensitic steels. The oxide layer formed on austenitic steels has the following possible structures (Müller, 2000; Zhang, 2005):

- For temperatures below 450°C, the oxide layer is very thin and composed of the single-layer Fe-Cr spinel or Cr oxide, which can prevent direct dissolution.
- For temperatures above 450°C, the oxide layer may consist of two scale types, either duplex- or single-layer structure, depending on the surface and operating conditions. The duplex-layer oxide can also prevent steel component dissolution, though for long-term exposure there is an increasing risk of dissolution attack.
- For temperatures above 550°C, heavy dissolution attack occurs.

The different oxidation phenomenon on austenitic 316L steel are shown in Figure 6.2.6. One aspect of non-uniform oxidation is the localised formation of oxide-filled pits (middle image). The prolongation of steel LBE exposure usually leads to the lateral growth of the pits that eventually connect, forming a continuous scale (right image). EDS elemental analysis of these oxide pits indicated the presence of mixed Fe-Cr oxides, such as Cr-deficient spinels (Schroer, 2010). The formation of rather thick oxide scales (right image; oxide scale thickness ≈ 20 µm) has mostly been associated with the presence of mixed Fe-Cr oxides. Such oxides are believed to be less protective than the very thin (<1 µm) Cr- and Si-rich oxides that cover the steel surface in some cases (e.g. left image). The latter are more protective and were reported to maintain their sub-micrometre thickness for more than 15 000 h (Schroer, 2010). Quite interestingly, the steel matrix beneath such thin oxide scales is usually enriched in Ni, a fact underlining their efficiency

as diffusion barriers, and hence their protectiveness against LMC attack (Schroer, 2010). However, Ni segregation under the oxide scale bears the following risk: if the continuity of the oxide scale is locally disrupted and LBE reaches the stratum of Ni-enriched steel, steel dissolution may proceed very fast due to the high solubility of Ni in the LBE, which, however, may occur only after exceeding a temperature of 450°C.

Figure 6.2.6: Oxidation behaviour of 316L steel exposed to liquid LBE in the CORRIDA loop for 503 h (left), 4 015 h (middle) and 15 028 h (right) at 550°C

The LBE flow velocity was 2 m/s and the LBE oxygen concentration was $C_O \approx 1.6 \times 10^{-6}$ wt.% (Schroer, 2010)

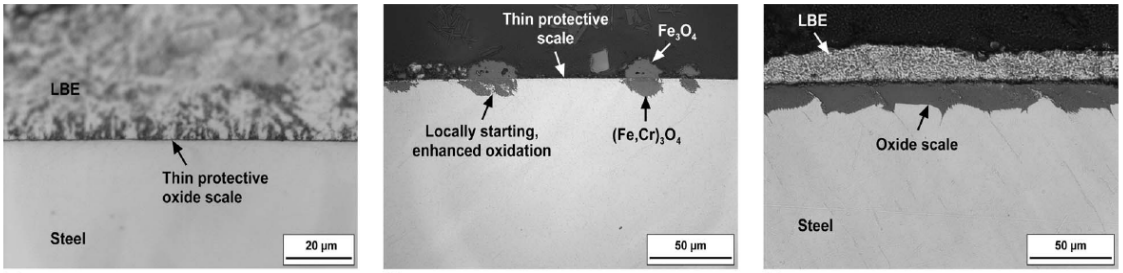

The high sensitivity of protective oxide scale formation to the oxygen concentration in LBE requires an active oxygen control technique that is based on the fact that lead and bismuth possess a lower affinity to oxygen than the major alloying elements of structural steels (Ni, Fe, Cr). The molar free energy of formation of the oxides of Ni, Fe and Cr is lower than that of lead and bismuth oxides, as can be seen in the Ellingham diagram in Figure 6.2.7.

Figure 6.2.7: Ellingham-Richardson diagram containing oxides of steel components and of Bi and Pb

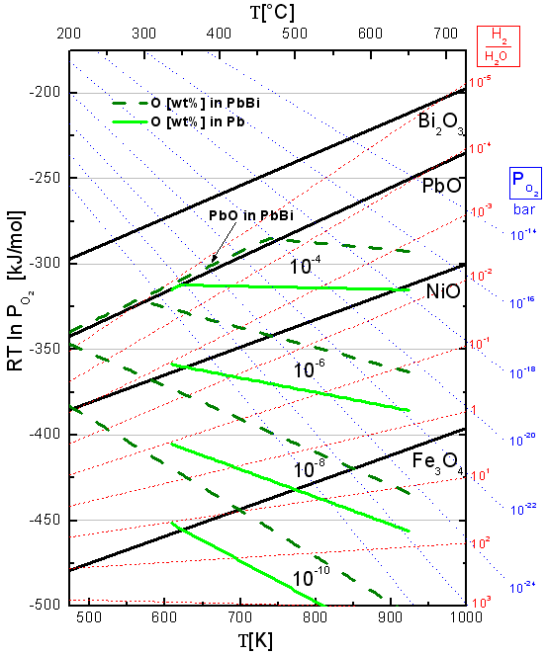

Source: Müller (2003).

To prevent PbO precipitation and to support Fe_3O_4 formation, the following conditions must be established:

$$2\,\Delta G^{\circ}_{PbO} > RT \ln p_{O2} > 0.5\,\Delta G^{\circ}_{Fe3O4} \tag{6.1}$$

where ΔG° is the Gibbs energy for formation of oxides, p_{O2} is the oxygen partial pressure, R is the gas constant and T is the absolute temperature. A detailed description of these processes is given in Chapter 4, Section 4.2, *Oxygen control in lead and LBE systems*.

The reaction resulting in the formation/dissolution of magnetite in liquid lead or lead-bismuth can be expressed as:

$$2\,O_2 + 3\,Fe \Leftrightarrow Fe_3O_4 \tag{6.2}$$

Neglecting the free energy for dissolution of the three substances, the free energy of reaction (6.2) assuming that the reaction occurs at steel surfaces at equilibrium can be approximated by that of the following relation:

$$\Delta G_{Fe_3O_4} = -RT \ln \frac{a_{Fe_3O_4}}{a_O^4 \cdot a_{Fe}^3} \tag{6.3}$$

where Fe, O and Fe_3O_4 are dissolved in the liquid metal, and a is the chemical activity of the substances present in solution. For the relation between the activities it follows:

$$\text{if } a_{Fe_3O_4} = 1 \Rightarrow a_O^4\, a_{Fe}^3 = \text{constant at constant } T \tag{6.4}$$

For example, at 400°C and for $a_{Fe} = 1$, the dissolved oxygen activity at equilibrium is 1×10^{-6} corresponding to an oxygen concentration of 1×10^{-10} wt.%. If $a_{Fe} < 1$, the oxygen activity will be higher (see Chapter 4, Section 4.2.2 for more details).

The oxygen activities in equilibrium with magnetite precipitation ($a[Fe_3O_4] = 1$) and the dissolved iron activity for different concentrations of iron are presented as a function of the temperature in Figure 6.2.8 (Li, 2002). The authors also draw the lines for the dissolved iron activities in equilibrium with magnetite precipitation and isoconcentration of oxygen. Steel corrosion via dissolution occurs below a minimum value of activity, a_{min}, for which Fe_3O_4 is unstable, whereas coolant contamination by lead oxide formation takes places for $a_O = 1$ by definition of the reference state used in the calculation (oxygen activity is equal to 1 when the oxygen saturation is reached, see Chapter 3, Section 3.4.3). Setting the maximum and minimum temperature values of the liquid metal in a loop and assuming the oxygen concentration at minimum temperature equal to the saturation value, the permissible range of oxygen activity values can be determined.

During system operation, different processes can change the oxygen activity to values out of the permissible range. Impurities present in the coolant, the oxides of which are more stable than iron oxide, can decrease the oxygen concentration down to values lower than that needed for the formation of magnetite. Transmutation elements generated by the proton beam in the coolant can disturb the chemical equilibrium in the loop. Reduction-oxidation reactions can occur with formation of non-soluble oxides, and with reduction of the oxide protective layers (Gromov, 1998). On the contrary, air in-leaks can increase the oxygen activity.

To control the oxygen activity in flowing liquid metal systems, several procedures have been developed in the past by Russian researchers (Efanov, 2001) and at present they are being revised in different laboratories in Europe and the United States (Knebel, 1999). A detailed description of these procedures is given in Chapter 4 of this handbook, Section 4.3, entitled *Oxygen control in lead and LBE systems*. For on-line oxygen control monitoring, electrochemical sensors for oxygen activity measurements were developed by Russian researchers and, recently, reference electrodes of In/In_2O_3, Bi/Bi_2O_3 and others are being developed and tested in several laboratories under various conditions. A detailed description of these sensors is given in Chapter 4, Section 4.4, *On-line electrochemical oxygen sensors*.

Figure 6.2.8: Oxygen concentration as a function of activity and temperatures

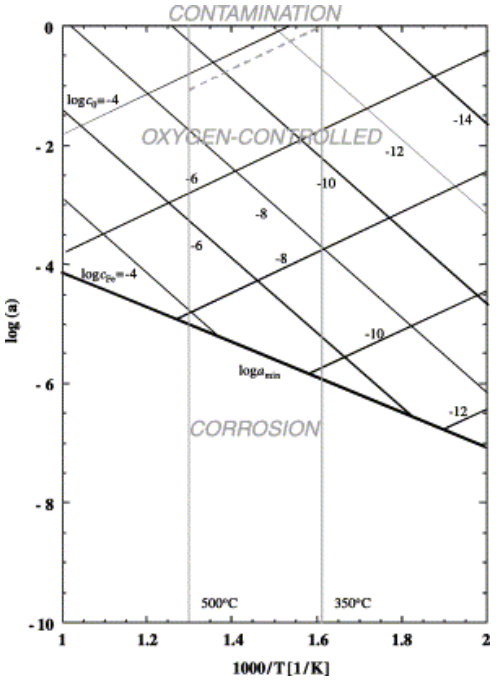

Source: Li (2002).

6.2.3 *Erosion corrosion*

If the liquid metal is flowing at high velocity, the structural materials could also be subject to erosion-corrosion. The erosion can be classified to the widely damaged surface along the flow as if fluid carries out the surface material by a strong dynamic pressure and the pitting-type erosion where material is deeply lost from narrow surface areas (Kondo, 2005).

The oxide scale may be removed due to mass transfer corrosion. In practice, erosion can occur at locations where the flow suddenly changes its direction, such as a bend, an expansion, at places where flow vortex is close to the surface of the materials, recirculation zones, etc. The liquid metal flow can erode the protective layer and the high shear stress may strip the layer away. Such attacks can enhance the oxidation mechanism and lead to a higher degradation rate of the surface. Chang (1990) classified erosion-oxidation phenomena into four categories: *i)* erosion of oxide only; *ii)* erosion enhanced oxidation; *iii)* oxidation affected erosion; *iv)* erosion of metal only. Rishel (1991) proposed that there are three types of erosion-enhanced oxidation ranges (Figure 6.2.9). However, the influence of liquid metal velocity on the type of erosion has not yet been examined. Combined erosion/corrosion processes can lead to severe damage of the protective layers and should be investigated thoroughly.

6.2.4 *Fretting corrosion*

Fretting is a specific type of wear that is expected to occur in molten lead-alloy-cooled nuclear reactors due to flow-induced vibrations and that mainly affects fuel claddings and heat exchanger tubes. A new facility (FRETHME) (Del Giaccio, 2012), designed to investigate this specific type of wear, studied fretting tests in liquid lead alloys under reactor-relevant conditions. Numerous fretting tests (Del Giaccio, 2012b) were performed under severe conditions (accelerated tests) on candidate steels such as the f/m T91 steel, austenitic 15-15 Ti steel and Al surface-alloyed T91 (GESA-T91).

Fretting damage increases with an increasing number of cycles/time and temperature. Fretting interacts with the corrosion mechanisms occurring in liquid Pb alloys (fretting corrosion) and destabilises the corrosion barriers, favouring e.g. dissolution attacks. Due to the high Ni content, the 15-15Ti steel is affected by dissolution-enhanced fretting, while oxidation-enhanced fretting characterises T91 steel at temperatures higher than 500°C.

Figure 6.2.9: Erosion-oxidation interaction regimes

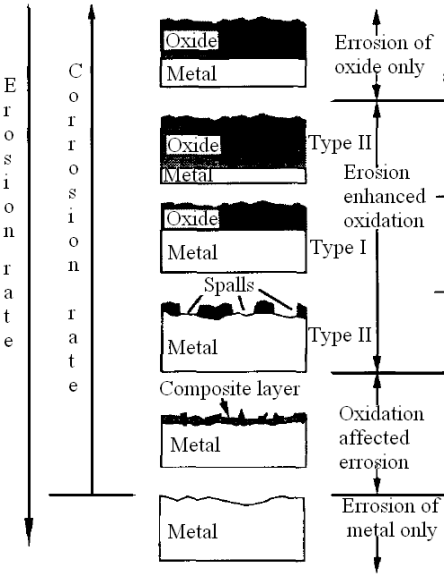

Source: Rishel (1991).

In most of the tests under accelerating conditions, 10% of fuel clad thickness was already eroded after quite short periods of time. To extrapolate the obtained results to conditions (load and amplitude) that allow long-term use of the respective component in Pb-cooled reactors, the concept of fretting maps was applied. Fretting maps were constructed using the obtained experimental data, particularly the fretting wear coefficient, which is a characteristic of a specific fretting regime.

The influence of amplitude/load combinations on the fretting process is represented in 3-D fretting maps like the one shown in Figure 6.2.10. The x- and y-axes are load and amplitude respectively, while for the z-axis different parameters like fretting depth, penetration rate or specific wear coefficient can be used to express the fretting wear severity. These 3-D maps were constituted starting from the experimental results and adding expected values of specific wear coefficients that are qualitatively predicted according to the expected fretting regimes for friction pairs of T91 and 15-15Ti. In this way, a wider overview of the wear process can be provided. In the 3-D fretting map, full circles correspond to values experimentally measured; empty circles represent the expected values according to the interpretation of the fretting regimes plot.

Figure 6.2.10 represents the fretting map for the friction pair of T91 relative to maximum fretting depth. It can be clearly seen that for short amplitudes (e.g. < 35 μm) and high loads (e.g. > 50 N) the fretting damage is minimised. However, in the case of unavoidable large amplitudes (> 75 μm), low loads (< 25 N) can also reduce the fretting damage.

In reactor constructions it is important to consider possible damages that could occur due to fretting. Amplitudes of 35 μm should not be exceeded to avoid intolerable damages during operation.

Figure 6.2.10: 3-D fretting map for friction pairs of T91

The maximum fretting depth (z axis) is plotted versus load (axis x)/amplitude (axis y) combinations; test parameters – 450°C, 10^{-6} wt.% [O], 10 Hz, $5.6 \cdot 10^6$ cycles, 150 h

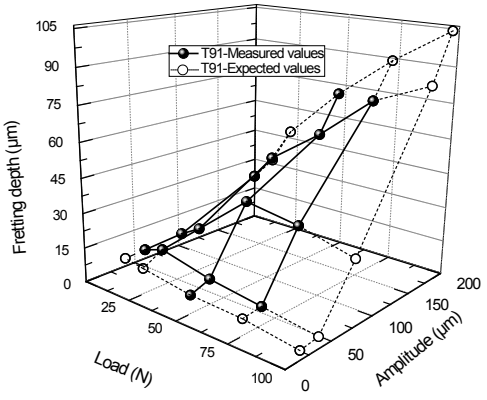

Source: Del Giaccio (2012).

6.3 Corrosion tests

A great number of tests have been conducted to explore the behaviour of relevant steels in liquid, stagnant and flowing LBE and Pb. The test temperatures extend from 300 to 600°C and the exposure times reach up to 15 000 h. Oxygen concentrations in LBE/Pb range from 10^{-10} wt.% up to the saturation limit. Many of the tests are just scoping tests and not relevant for judgement of the material suitability for liquid metal reactor application. Exposure times must be long enough to allow an extrapolation to reasonable operation life times in a reactor and oxygen concentrations must be in a range in which no plugging may occur in a loop due to reaching the saturation limit at the lower temperatures and no dissolution attack should take place because of too-low oxygen potential in any part of the loop. Therefore, the list of all the experiments attached to Chapter 6 is divided into two parts to facilitate examination of the results that may allow a reliable statement pertaining to material behaviour in a liquid-metal-cooled reactor.

In Section 6.3 we will first discuss typical material reactions like oxidation and dissolution of steel components for martensitic/ferritic, and then for austenitic steels. This separate treatment is due to the different oxidation behaviour and temperature stability of the steels. The former develop duplex oxide scales at all temperatures, while the latter form thin oxide scales below 450°C and additional duplex structures above this temperature.

6.3.1 Martensitic/ferritic steels

A great number of initial experiments in stagnant and flowing LBE were performed under saturated oxygen. This condition is not relevant for reactor conditions because of the temperature gradients in the coolant loop, but the development of the oxide scale is similar to that observed at oxygen concentrations around 10^{-6} wt.%. Figure 6.3.1 shows corrosion tests of T91 steels in stagnant Pb-Bi eutectic saturated by oxygen carried out at 500, 520, 540 and 560°C for 1 000 and 2 832 h (Yeliseyeva, 2008). The oxide layers grown under these conditions have the typical duplex structure scale that consists of an outer magnetite sub-layer, the upper part of which contained plumboferrites and an inner Cr-rich spinel layer.

It is obvious that the upper part of the duplex layer, which consists of martensite, divides into two parts A and B (as marked in Figure 6.3.1, 560°C) with different properties. Extensive examinations (Hosemann, 2008e) of the duplex layer on HT-9 steel after 3 000 h

at 550°C in LBE containing 10^{-6} wt.% oxygen revealed that both parts of the duplex layer consist, again, of two distinct areas. The upper part of the magnetite layer has a kind of columnar grain structure, the grains of which are directed perpendicular to the surface, while the inner part consists of undirected grains. The columnar structured grains in the upper part ease penetration of LBE into the layer along the grain boundaries and pores. The structures obtained after 2 832 hours in Figure 6.3.1 support the results of the examination. The entered LBE forms columns and reaches down to about the middle of the magnetite layer. The finding for the spinel part of the duplex layer (C and D in Figure 6.3.1, 560°C) is that the part at the interface to the steel bulk is enriched in Cr (Hosemann, 2008e), which is indeed found in several published line scans of this region, as also in Figure 6.2.5. The zone marked "E" is the internal oxidation zone that typically appears below the duplex oxide scale in ferritic/martensitic steels.

Figure 6.3.1: Morphology of scales formed on the surface of T91 steel after exposure to the oxygen-saturated Pb-Bi melt versus interaction temperature and time

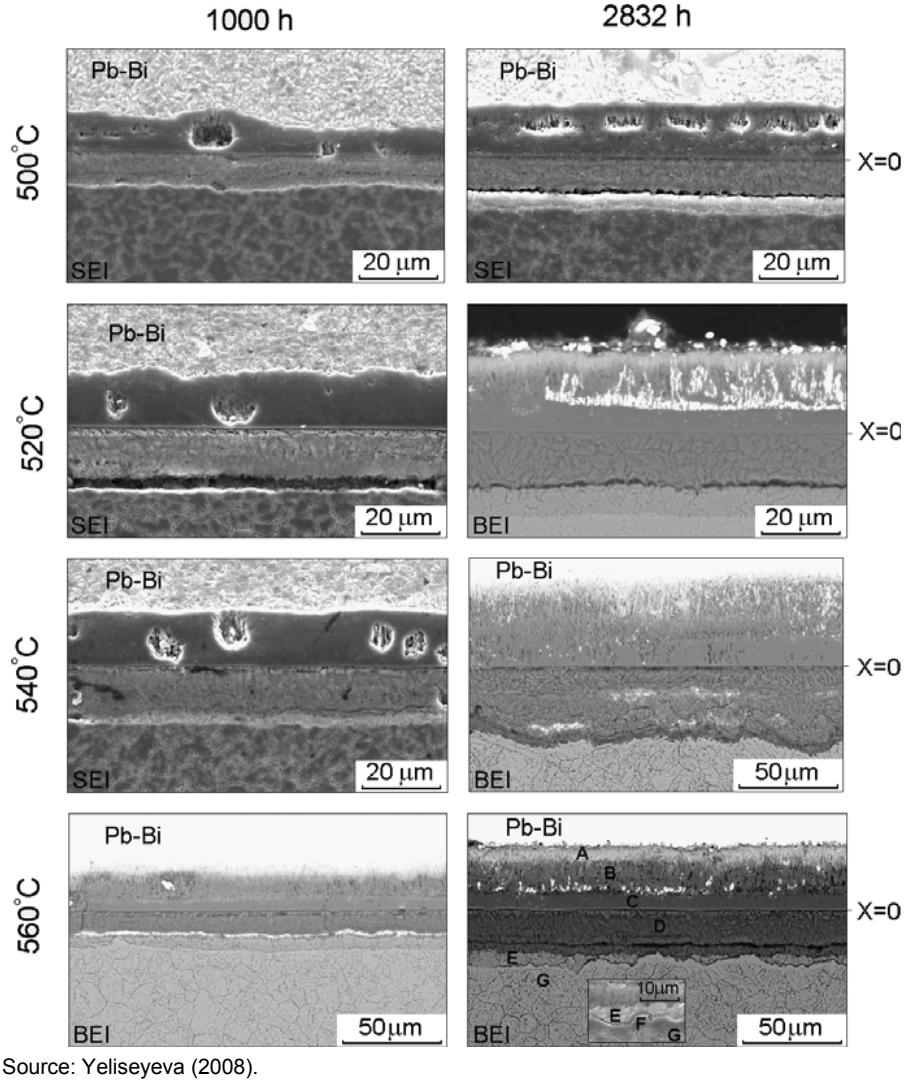

Source: Yeliseyeva (2008).

After long exposure to LBE, the oxide scale becomes very thick and it contains numerous LBE inclusions, as exhibits Figure 6.3.2 of a T91 specimen after 15 000 h of exposure to LBE at 550°C containing 10^{-6} wt.% oxygen. Contact of LBE is still prevented by an intact spinel layer. Remarkable is the fact that the internal oxidation zone did not grow proportional to the oxide scale. This corresponds to Weisenburger's (2011) observation that growth of the IOZ ends after 2 000 h, indicating that oxygen diffusion diminishes after that time. However, the thermal barrier for the heat flow through a pin with such a scale on the surface will be not tolerable. Thus, temperatures in this range require improved protection layers, e.g. those that are discussed in Chapter 9.

Figure 6.3.2: Oxide scale on T91 after 15 000 h at 550°C in LBE + $1.6{\cdot}10^{-6}$ wt.% oxygen

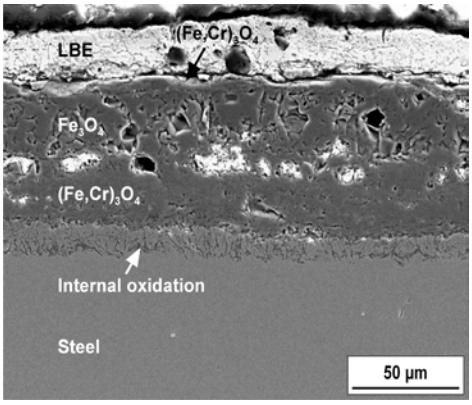

Source: Schroer (2010).

Another effect that requires attention is erosion of parts of the oxide layer in fast-flowing liquid metal. Figure 6.3.3 shows T91 surfaces that were exposed for 2 000 h to LBE containing 10^{-6} wt.% oxygen flowing with 1, 2, 3 m/s velocity at 550°C in the IPPE loop (Weisenburger, 2008). The magnetite layer is still present at 1 m/s flow velocity but at 2 m/s only small amounts are left, and it disappears entirely at 3 m/s. However the spinel layer continues to protect the steel still perfectly at 3 m/s.

Figure 6.3.3: T91 surfaces after 2 000 h exposure to flowing LBE containing 10^{-6} wt.% oxygen at 550°C with 1 (up), 2 (middle), 3 m/s (down) in the IPPA loop

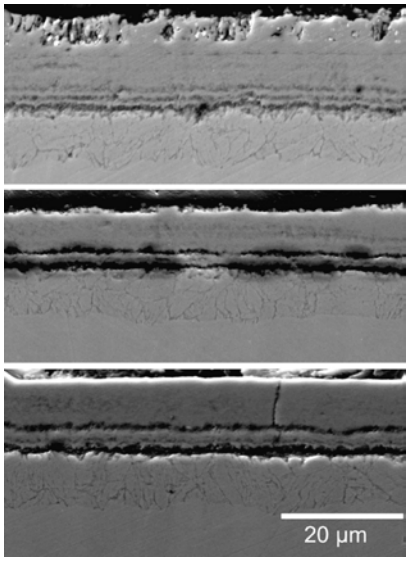

Source: Weisenburger (2008).

Dissolution attack on ferritic/austenitic steels T91 (Heinzel, 2008) and 410SS (Kurata, 2008) is represented in Figure 6.3.4 after exposure to LBE under unusual conditions. The oxygen concentration of $3 \cdot 10^{-9}$ wt.% is too low and the temperature of 600°C too high to allow protective oxide scale formation.

Figure 6.3.4: Dissolution attack on ferritic/austenitic steels, left T91 at 600°C after 2 000 h and right 410SS at 550°C ($3 \cdot 10^{-9}$ wt.% oxygen) after 3 000 h

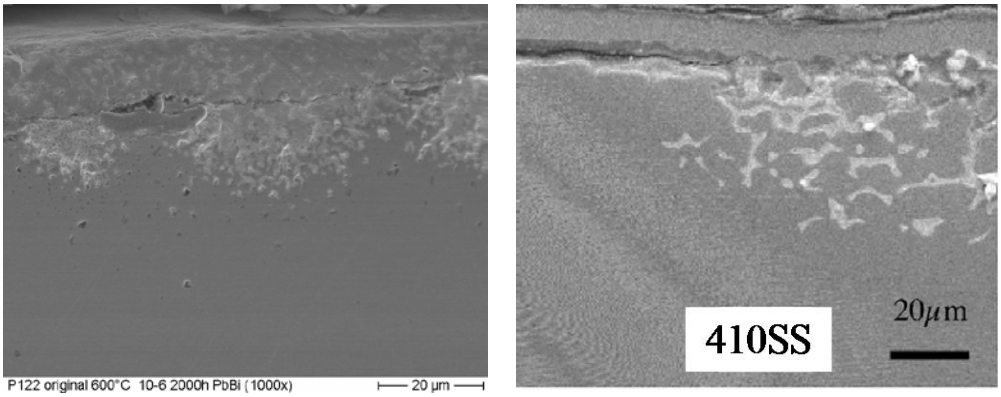

Source: Left image Heinzel (2008), right image Kurata (2008).

The oxide scales formed on ferritic/martensitic provide good protection against dissolution attack of liquid LBE and Pb, but attention has to be given to the thickness of the scales due to their low thermal conductivity. This concerns mainly the surfaces of the tube walls of fuel pins and heat exchangers that are exposed to high heat fluxes. Therefore, several examinations deal with the growth of oxide scales on these steels and with parameters that control the oxide thickness in the liquid metal environment (Weisenburger, 2013; Schroer, 2010b). A fit of the results of numerous reliable experiments on T91 steel in LBE containing 10^{-6} wt.% of oxygen in the temperature range of 420-550°C, results in the following empirical relation for oxide scale growth as function of time and temperature (Weisenburger, 2013):

$$\delta_S(t,T) = (-0.98 + 2.54 \cdot 10^{-3} T)\sqrt{t} \qquad [420°C < T < 550°C]$$

where $\delta_S(t,T)$ = oxide scale thickness (µm);

t = time (h);

T = temperature (°C).

As an example, after 15 000 h one obtains an oxide scale thickness of 9.77 µm at 420°C and 50.2 µm at 550°C. After a possible life time of three years, the scale would be 66.5 µm at 550°C. High heat fluxes will cause an increase of the temperature gradient across the oxide scale with time because of the growing scale thickness. The consequence is a higher temperature on the metal surface of the tubes which leads to higher oxidation rates.

6.3.2 *Austenitic steels*

As previously mentioned in Section 6.2.2, 316L steel is somewhat different in its oxidation behaviour. At low temperature (<450°C) the oxide scale is very thin on the austenitic steel surface even after 5 000 h of exposure to LBE; it is thus not visible on the magnification of 2 000 × in Figure 6.3.5. The white layer on top of the material on the left side consists of LBE. Increasing the temperature to 450°C partly causes development of duplex oxide structures after 5 000 h like that observed on ferritic martensitic steels (Heinzel, 2013). The layer growth starts at singular points with little nodes that connect later on to a continuous oxide scale covering the whole surface.

Figure 6.3.5: Oxide scale development on 316L and 1.4970 steel after 5 000 h

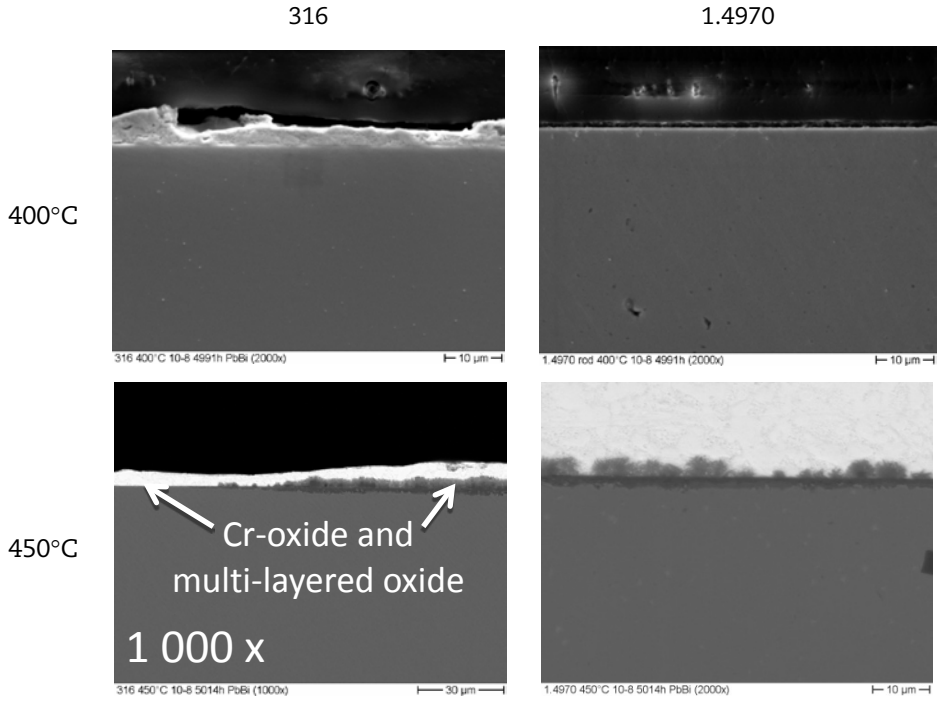

Source: Heinzel (2013).

Numerous studies have referred to the various aspects of the non-uniform oxidation behaviour of 316/316L steels; for example, the inwards-growing Fe-Cr spinel often develops preferentially along the grain boundaries of the base steel, as may be seen in Figure 6.3.6. It has been suggested that grain boundary oxidation penetrates deeper below the steel surface in coarse-grained steels than in fine-grained ones (Yeliseyeva, 2008). This process appears distinctly at high temperatures (Figure 6.3.6). At 560°C dissolution attack starts prior to reaching an exposure time of 1 000 h, indicating that application at temperatures above 500°C may only be possible after surface protection measures such as those discussed in Chapter 9.

The austenitic AISI 316L steel showed better resistance to oxidation than ferritic/martensitic T91, which was attributed to the higher content of chromium. However, with the increase in temperature and time, the defectiveness of the duplex scale increases and it becomes permeable for liquid metal. The penetration of the components of PbBi eutectic into the scale occurred selectively. Lead enters into the composition of plumboferrites while free bismuth was situated mainly in the pores of the scale (Figure 6.3.6).

The high solubility of certain steel elements (especially Ni and Cr) in the liquid LBE will unavoidably lead to steel dissolution, if the steel exposure conditions (especially the liquid metal oxygen concentration and the temperature) are such that either no protective oxide can be formed on the steel surface or the existing oxide scale is rendered insufficiently protective. Steel dissolution is aggravated as the temperature of steel exposure increases, due to the fact that the solubility and mobility of Ni, Cr and Fe in liquid LBE increase with temperature (Li, 2002). The current understanding of steel dissolution is as follows: first, Ni and Cr dissolve in the liquid metal and are thus removed from the area close to the steel surface. The removal of Ni and Cr, and to a less extent of Fe, creates vacancy clusters or pores in the steel matrix, which are then filled by Pb and Bi, as the liquid metal penetrates into the steel that has just undergone selective leaching.

Figure 6.3.6: Morphology of the scales formed on the surface of AISI 316L steel after exposure to the oxygen-saturated PbBi melt versus interaction temperature and time

X = 0 – initial interface "solid metal/liquid PbBi"

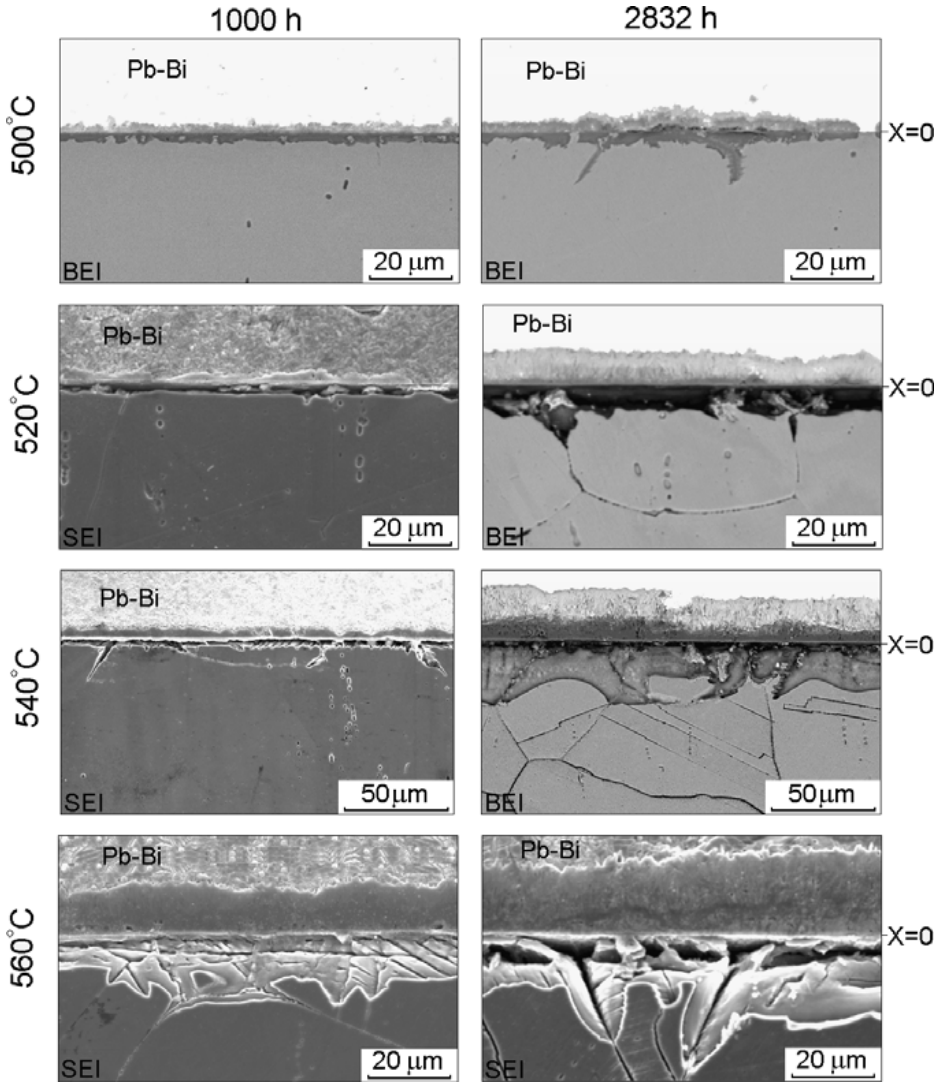

Source: Yeliseyeva (2008).

The steel depletion in Ni results in the destabilisation of the austenitic phase close to the steel surface and its transformation into ferrite (DEMETRA, 2009a; Schroer 2010; Benamati, 2005). Since steel *ferritisation* is one of the consequences of dissolution, it is not difficult to understand why it has been reported to be favoured either by low oxygen concentrations in the liquid metal (Figure 6.3.7) or high temperatures (Figure 6.3.8, right; Figure 6.3.9, bottom) or a combination of both. In fact, ferritisation has also been reported to occur at temperatures as low as 400°C, when the oxygen concentration in the liquid metal is low ($C_O < 10^{-8}$ wt.%, Figure 6.3.7).

Many similarities are reported as regards the dissolution behaviour of 316/316L and 15-15Ti steels, which is not so surprising if one considers their compositional similarities. The ferritisation rate of 15-15Ti type steels is usually reported to be lower than that of 316/316L steels under identical exposure conditions, possibly due to the smaller grain size that characterises cold-worked 15-15Ti steels. 15-15Ti steels exhibit both enhanced

dissolution and ferritisation rates when exposed to high temperatures and low oxygen concentrations in the liquid metal. For example, the thickness of the ferritic zone has been reported to increase from ~45 μm (Figure 6.3.10) for oxygen-saturated liquid (Kurata, 2004) LBE to ~220 μm for oxygen-depleted liquid LBE (Müller, 2005), after a few thousand hours of exposure at 550°C.

Figure 6.3.7: Superficial ferritisation of 316L steel to a maximum depth of 14 μm resulted from the steel exposure to liquid LBE in the LECOR loop for 1 500 h at 400°C

The LBE flow velocity was 1 m/s and the LBE oxygen concentration was $C_O \approx 10^{-10} \div 10^{-8}$

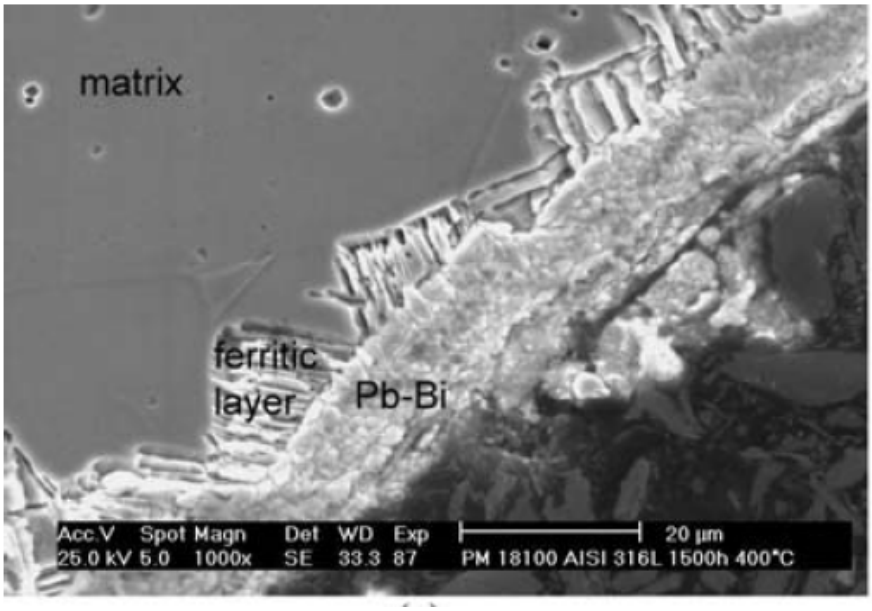

Source: Benamati (2005).

Figure 6.3.8: LMC behaviour of 316L steel exposed to stagnant liquid LBE for 500 h at 535°C (left), 550°C (middle), and 600°C (right)

The LBE oxygen concentration for the tests performed at 535°C and 550°C was $C_O \approx 3 \div 4 \times 10^{-6}$ wt.%, while that for the test performed at 600°C was $C_O \approx 8 \times 10^{-6}$ wt.%

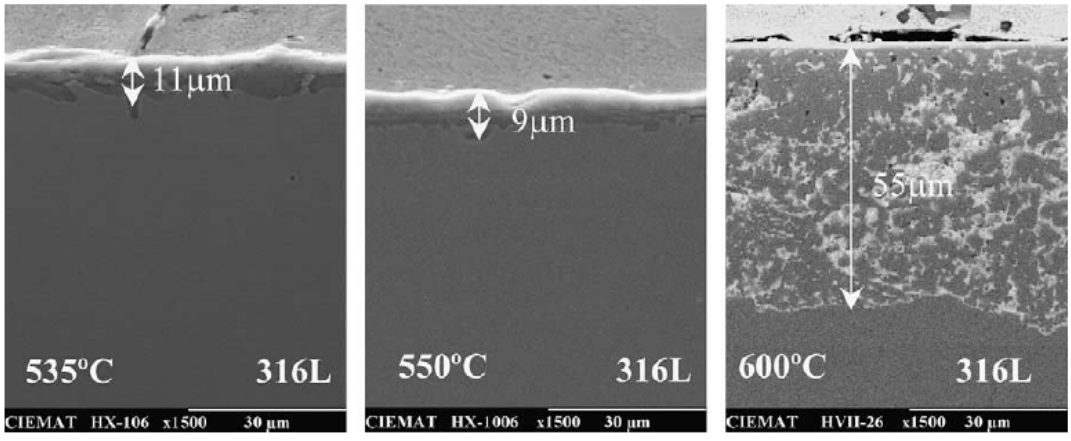

Source: Martin (2004).

Figure 6.3.9: LMC behaviour of 316L steel exposed to liquid LBE in two different forced convection loops (at IPPE and PROMETEY) for 2 000 h at 420°C (upper), 550°C (middle) and 600°C (bottom)

The LBE flow velocity was 2 m/s for the tests performed at 420°C and 600°C, and 0.5 m/s for the test performed at 550°C; the LBE oxygen concentration was $C_O \approx 1 \times 10^{-6}$ wt.% in all cases

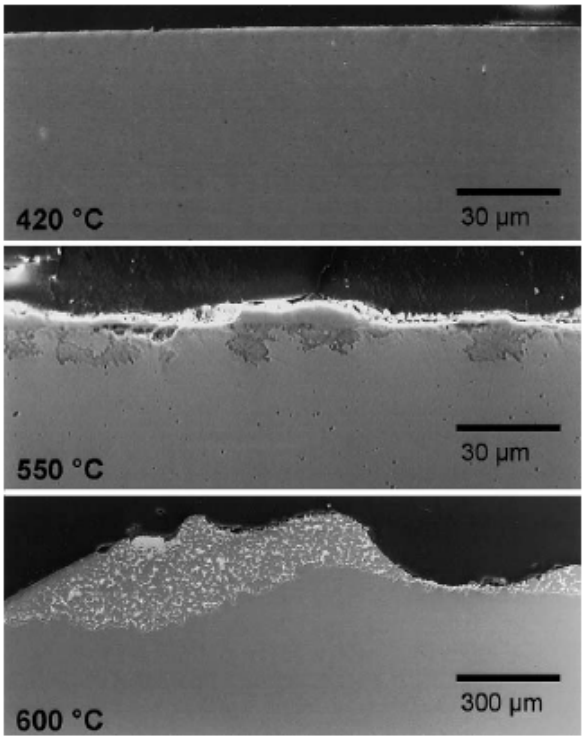

Source: Müller (2002).

Figure 6.3.10: Ferritisation of JPCA steel exposed to stagnant liquid LBE for 3 000 h at 550°C

The maximum thickness of the ferritic zone is 45 µm, and the liquid LBE was saturated in oxygen

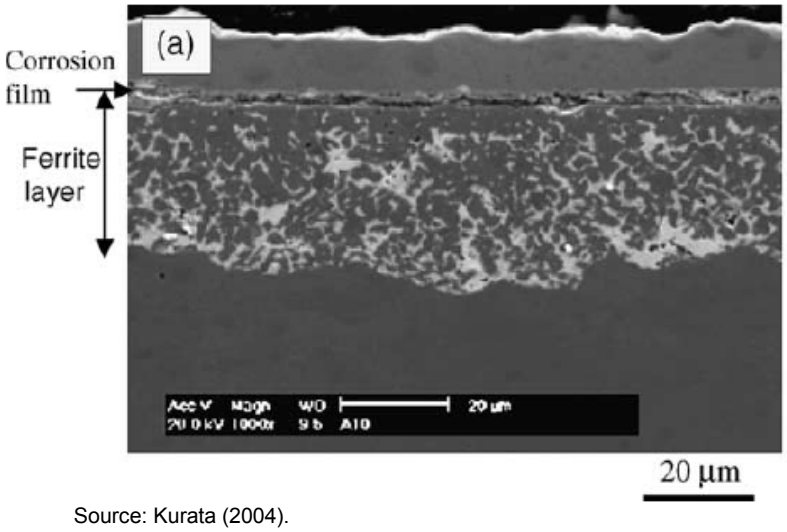

Source: Kurata (2004).

Due to their susceptibility to dissolution and ferritisation at high temperatures and low LBE oxygen concentrations, thin-walled components made of 316L (e.g. MYRRHA heat exchanger tubes) and 15-15Ti steels (e.g. MYRRHA cladding tubes) should not be exposed to such conditions, as component failure is expected to occur within a relatively short time span. One of the studies (Müller, 2005) illustrates the above reports with deep (~220 μm) dissolution attack and subsequent ferritisation of a 1.4970 steel tube after its exposure to (stagnant) oxygen-depleted LBE for 7 200 h at 550°C (Figure 6.3.11). Crack propagation in the ferritic zone could result in the premature failure (< 1 year) of such a tube during service under similar conditions.

Figure 6.3.11: Dissolution and ferritisation of 1.4970 steel tube exposed to liquid LBE in a forced convection loop at PROMETEY for 7 200 h at 550°C

Even though the outer tube surface was in contact with flowing LBE (flow velocity: 0.5 m/s), the tube interior was in contact with stagnant LBE that penetrated into the tube during the test. The oxygen concentration of the liquid LBE in contact with the outer tube surface was $C_O \approx 1 \times 10^{-6}$ wt.%, while the liquid LBE inside the tube was depleted in oxygen.

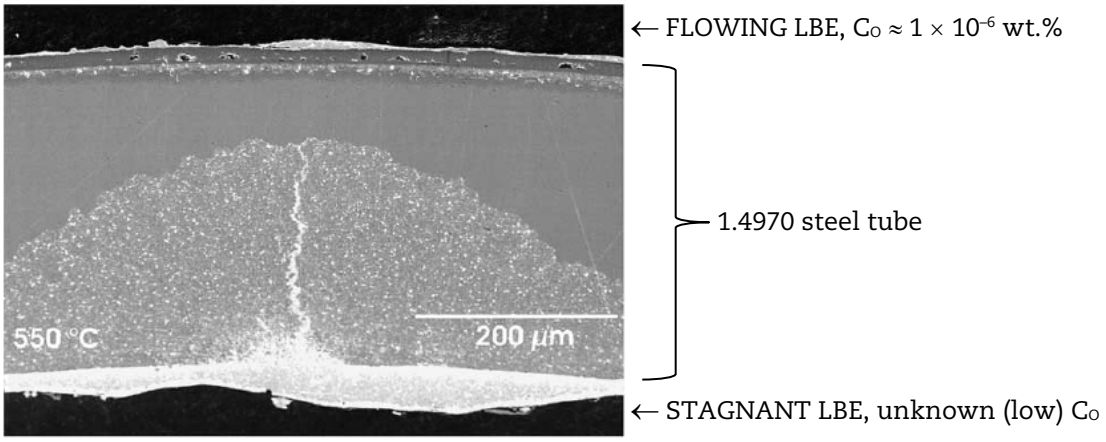

Source: Müller (2005).

6.3.3 Results of experiments carried out under special conditions

6.3.3.1 Influence of surface finishing and welds on the corrosion behaviour

Some authors have evaluated the corrosion behaviour of steels with "special conditions" in liquid metal. Some of these conditions are welded steels or those with different surface finishing.

Corrosion behaviour of a ferritic-martensitic F82H and an austenitic stainless steel JPCA (both parent and weld materials with electron beam welding) was studied in an LBE loop at temperatures of 450 and 550°C (Kikuchi, 2008). LBE velocity in the main channel was 0.5 m/s, oxygen concentration was controlled to 2-4 × 10^{-5} wt.% by adding hydrogen and/or moisture with argon carrier gas. The corrosion layer on F82H consisted of three structures: the outer oxide layer is magnetite Fe_3O_4, the inner layer a spinel-type $FeCr_2O_4$ followed by an oxygen diffusion layer. Corrosion depth increased with increasing time at 450°C, and with increasing test temperature. The corrosion layer at 500°C on F82H disintegrated during testing. The EB welded joint showed the same corrosion properties as the original materials. The corrosion behaviour in JPCA was characterised by the oxide layer Fe_3O_4 and pit formation. At 450°C, the oxide layer was 1-2 μm in depth after 3 000 h but pit depth was relatively large. The EB welded joint showed the same corrosion properties as the parent materials.

A study of the influence of surface finishing and welds on the corrosion behaviour of 316L and T91 steel specimens tested in stagnant LBE was performed (Martin, 2011). Tests were carried out at 500 and 550°C from 100 to 2 000 h in LBE containing 10^{-6} and 10^{-8} wt.% oxygen. The analysis of the T91 and 316L specimens with different surfaces finished (as-received, grinded, grinded and polished and electrolytically polished) tested in LBE showed a general behaviour in agreement with other results previously reported. T91 tested at 500 and 550°C under an oxidising atmosphere (10^{-6} wt.%O) showed compact and uniform oxide scales, with thicknesses of approximately 30 and 50 μm, respectively. The same steel tested under reductive atmosphere (10^{-8} wt.%O) presented a surface with general dissolution, especially after 2 000 h exposure in LBE. Also, as mechanised 316L stainless steel was tested under the same conditions as T91 steel results were in general according to expectations. Finally, the behaviour of specimens grinded, polished and electro-polished was not different from the result obtained with as-mechanised samples, for any of the conditions tested. Therefore, the general conclusion is that the effect of surface finishing on the corrosion/protection processes is not significant for the conditions tested. As concerns the weld materials (T91-T91 TIG and T91-316L) the general conclusions were that, whereas T91-T91 welded joints showed the same corrosion properties as the parent materials for the conditions tested, AISI 316L-T91 welded joints presented an important dissolution in the seam area which was associated with the fabrication process.

6.3.3.2 Results of experiments with changing temperature and oxygen concentration

The corrosion characteristics of several high chromium steels were investigated after immersion in Pb-Bi under transient temperature conditions (Rivai, 2010). Two cases were evaluated: in the first case, the specimen HCM12A was immersed in Pb-Bi at 550°C for 12 h and then the temperature was increased up to 800°C and kept there for 12 h; in the second case the specimens (SUS430, Recloy10) were immersed in Pb-Bi at 550°C for around 500 h, then the temperature was increased to 800°C and maintained for 15 h. The concentrations of oxygen were 10^{-6} (550°C) and 2×10^{-5} (800°C) for the transient temperature case-1, and 10^{-6} wt.% (550-800°C) for the transient temperature case-2. The results showed that, during the temperature transients all three steels suffered from dissolution attack by Pb-Bi that penetrated the oxide layer that was formed at 550°C.

The behaviour of protective oxide layers on P122 steel and its welds and of ODS steel in LBE were examined under conditions of changing temperatures and oxygen concentrations (Weisenburger, 2006). P122 (12Cr/HCM12A) and its welded joints were exposed to LBE at 550°C for 4 000 h with oxygen concentrations of 10^{-6} and 10^{-8} wt.% which changed every 800 h. It was found, as with the case of a constant oxygen concentration of 10^{-6} wt.%, a protective spinel layer ($Fe[Fe_{1-x}Cr_x]_2O_4$) was maintained on P122 and also on its welded joint. Two experiments with exposure times of 4 800 h were conducted on ODS steel, both with temperatures changing from 550 to 650°C and back every 800 h, one experiment with 10^{-6} and the other with 10^{-8} wt.% oxygen in LBE. Both experiments showed strong local dissolution attack after 4 800 h, which is in agreement with the behaviour of ODS in LBE at a constant temperature of 650°C.

6.4 Oxidation-corrosion interaction model

6.4.1 Modelling of long-term oxidation behaviour

Modelling long-term behaviour is of crucial interest for component lifetime prediction in liquid lead alloys. Forecasts based only on empirical data, without knowledge of the physical process and considering the experimental uncertainties, are always problematic. Two different approaches are presented for predicting the long-term performance of T91 in lead-bismuth eutectic: a mass transfer and a mechanistic model.

In the mass transfer model, the experimental data are incorporated in the mass transfer code (Steiner 2008; Zhang 2005, 2007, 2009), simulating oxide growth based on an experimentally determined rate law and dissolution/precipitation of oxide in/from flowing liquid metal based on the function of local equilibrium solubility of oxides at the scale surface and convective diffusion in the flowing liquid metal.

In the mechanistic model (Martinelli, 2008d), the oxide scale growth is calculated using physical and thermodynamic considerations.

6.4.2 Mass balance code for non-isothermal systems

For steel in liquid lead and lead-bismuth eutectic with oxygen control, there are two competitive processes proceeding simultaneously at the solid/liquid interface: oxidation and dissolution. Therefore, the growth of the oxide layer in liquid metal follows a very different time-dependent function compared with that in gas. The Tedmon model (1966), based on the experiments of Cr oxidation at high temperature with scale vaporisation, can be applied to the present oxidation process by replacing the vaporisation rate with the mass transfer corrosion rate. The model was rewritten in the following form:

$$\frac{d\delta}{dt} = K_{p,c} - Q_{c,o}$$

where δ is the thickness of the oxide layer and t is the time, $K_{p,c}$ and $Q_{c,o}$ are the oxide layer growth rate and oxide removal rate by the liquid metal, respectively. The oxide layer growth $K_{p,c}$ is derived from experimental data and $Q_{c,o}$ from assumptions based on general thermodynamic stability considerations. Both contain a high degree of uncertainty, due to the lack of reliable and consistent long-term oxidation data and due to unknown dissolution rates and stability of formed oxide scales in liquid lead alloys.

Zhang (2007) assumes parabolic oxidation and used oxidation rates mainly derived from short-term experiments, while the MATLIM code (Steiner, 2008) uses cubic rate laws for oxide growth on the steel surface with parameters fitted to experimental data for the specific steel at the temperature and oxygen concentration under consideration. With respect to the dissolution/formation of magnetite at the oxide-scale/liquid-metal interface, it is assumed that the local concentration of Fe and oxygen in the liquid metal at this interface is always given by the equilibrium concentration in the liquid metal oxide system. Additionally, one-dimensional convective transport of Fe and oxygen by the flowing liquid metal is considered. The code calculates the local oxide scale thickness, and the Fe and oxygen concentration in the liquid-metal bulk as a function of time, for discrete positions along the flow path of the liquid metal. Fixed parameters of the simulation are the liquid-metal mass flow (velocity profile) and the temperature profile along the flow path of the liquid metal. In addition, the influence of the flow velocity on the dissolution of magnetite is considered as well. The results of predicting the oxide scale thickness on T91 specimens in the test sections of the CORRIDA loop at different flow velocities are shown in Figure 6.4.1 (left). An increase in flow velocity from stagnant to 2 m/s reduces the oxide scale thickness from 80 to 45 μm after about 30 years. However, it must be underlined that the code does not consider erosive removal or spallation of oxide scales.

As an example of the MATLIM code application, in Figure 6.4.1 (right) the calculated oxide scale thicknesses of the steam generator of EFIT and the XT ADS heat exchanger as a function of lifetime and temperature are given. It is shown that, on the surface of the EFIT steam generator tubes, operated at 480°C, an oxide scale of about 65 μm would grow within 15 years. As consequence of such oxide scale growth rates an increase of the heat transfer surface of the steam generator must be considered already in the design phase (Mansani, 2009).

Figure 6.4.1: Simulation of oxide scale thickness of T91 using the MATLIM code

As a function of exposure time for different flow velocities (left)

Different ADS components as function of time (right)

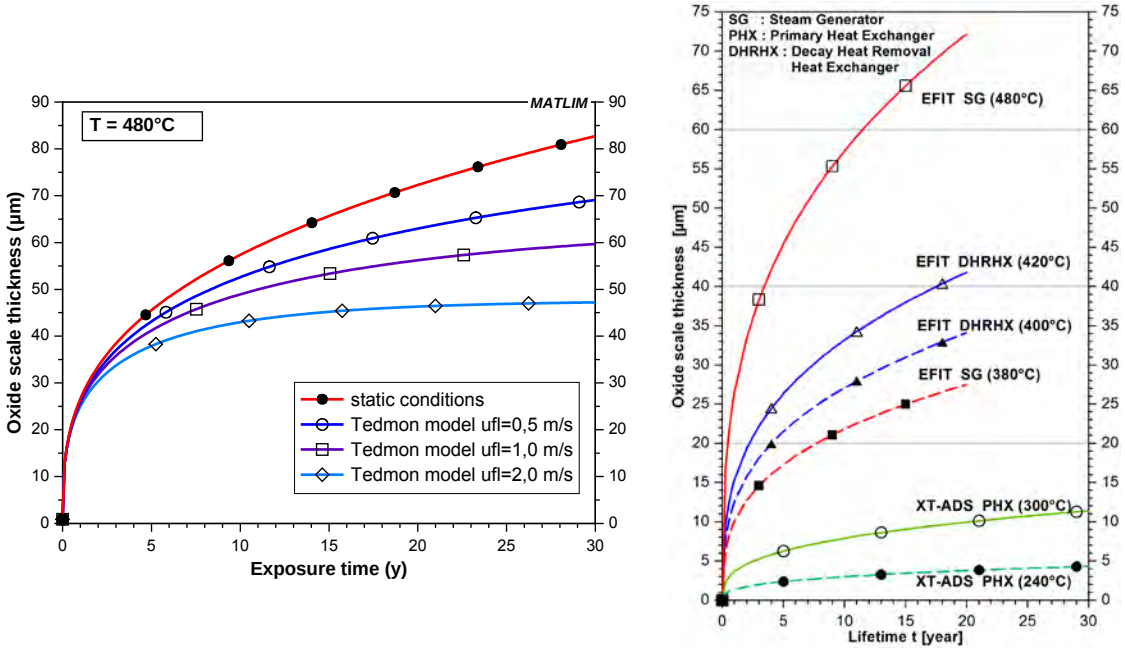

Source: Weisenburger (2009).

Zhang (2009) applied his model to experimental data of steels in flowing liquid lead and LBE obtained from various authors. He calculated the parameters K_p and Q_c for ferritic and austenitic stainless steels, with and without GESA treatment (see Chapter 9). The conclusion was that it is still impossible to develop any correlation with oxygen content and flow rate based on the current experimental data of steels in flowing liquid lead. For LBE, the results indicate that the oxidation constant and the corrosion rate are functions of the temperature, flow velocity, oxygen concentration, steel composition and the temperature difference. However, based on the results it is not possible to establish any correlations due to the scarcity of the experimental data.

6.4.3 *Mechanistic modelling of dissolution rate and oxide growth*

Dissolution of steel elements and oxidation are processes that determine corrosion in a Pb-PbBi liquid environment. The oxygen concentration in the liquid metal is an important parameter that determines which one of these processes prevails, as outlined in Section 6.2. Both corrosion processes are described by mechanistic models that are outlined here.

A model for the dissolution process (Balbaud-Celerier, 2011) differentiates between two dissolution conditions. At low liquid metal velocities the dissolution rates are controlled by mass transfer, while at high velocities they are activation-controlled. In the first case the mass transfer coefficient is much lower than the precipitation rate, in the second case it is much higher. Calculations assuming only mass-transfer-controlled dissolution attack result in much too high amounts of dissolved iron on the surface. Figure 6.4.2 shows a plot of the calculated corrosion effects as a function of the angular velocity of specimens rotating in liquid Pb-Bi at different temperatures compared to data obtained in experiments conducted at 400°C (Fe), 470°C (Fe, T91) and 500°C (Fe) in CICLAD (Balbaud-Celerier, 2004, 2010). The ordinate contains the ratio of the corrosion rate to the difference between the solubility, S_{Fe}, and concentration C_{Fe} of Fe in liquid Pb-Bi. When a

mixed mass transfer and activation-controlled process is assumed, the course of the curves fit the experimental values in an acceptable manner. However, the precipitation rates calculated do not follow the Arrhenius law, which may be due to inconsistent results or caused by the lack of reliable physico-chemical data in the Pb-Bi technology.

Figure 6.4.2: Corrosion of rotating steel T91 in LBE at 400-540°C/<10^{-8} wt.% oxygen as function of angular velocity

Ordinate: ratio of the corrosion rate to the difference between the solubility, S_{Fe}, and concentration C_{Fe} of Fe in liquid PbBi

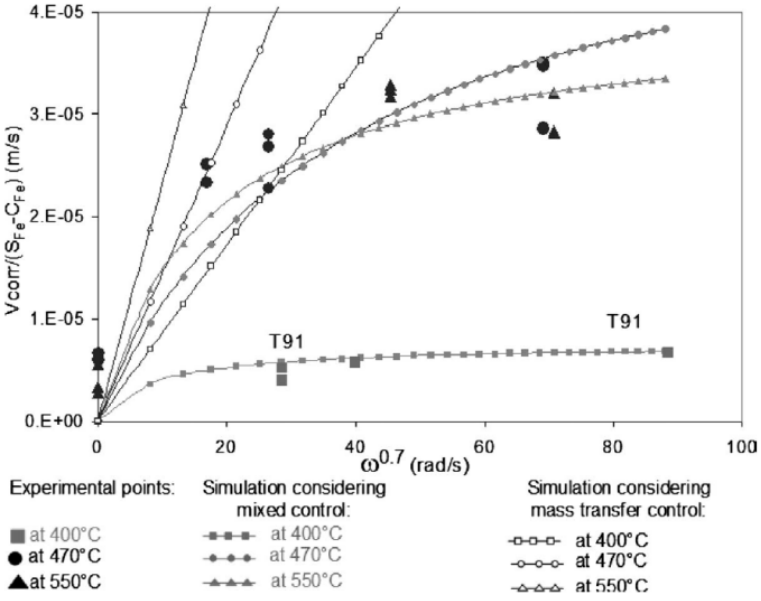

Source: Balbaud-Celerier (2004, 2010).

Oxidation experiments of T91 with ^{18}O tracer in ^{18}O-^{16}O saturated Pb-Bi at 470°C (Martinelli, 2008) showed that the Fe-Cr spinel layer grows by oxygen diffusion into the metal surface region, while magnetite grows due to iron diffusion to the surface and into the oxide scale at the magnetite/liquid metal (environment) interface.

The mechanistic model is based on the "available space model" process (Martinelli, 2008b; Brückman, 1965; Atkinson 1988). According to this model, the outwardly diffusing iron that forms the magnetite layer results in a vacancy accumulation in the Fe-Cr steel. These vacancies can segregate at the interface steel/oxide to form micro-cavities. These cavities will be filled with the spinel that forms by reaction of Fe and Cr with the diffusing oxygen. The limiting mechanism is the iron diffusion that allows the creation of available space for the Fe-Cr spinel growth (Martinelli, 2008b). According to these assumptions, the Fe-Cr spinel layer thickness depends on the capability of magnetite formation.

The magnetite scale thickness is calculated considering the mechanisms described above and Wagner's theory of oxidation (Martinelli, 2008c; Wagner, 1933). Most required parameters for the simulation, like diffusion coefficients, etc., are literature values (Backhaus-Ricoult, 1986; Töpfer, 1995). However, some constants mainly describing the differences of iron diffusion in magnetite and spinel are derived from fittings of experimental results (Martinelli, 2011).

Several exposure experiments performed at different temperatures and oxygen concentrations were compared with simulations (Figure 6.4.3).

Figure 6.4.3: Comparison modelling/experiment for oxygen saturation concentration at 470°C, 550°C, 600°C, 620°C (left) and for low oxygen concentration (right)

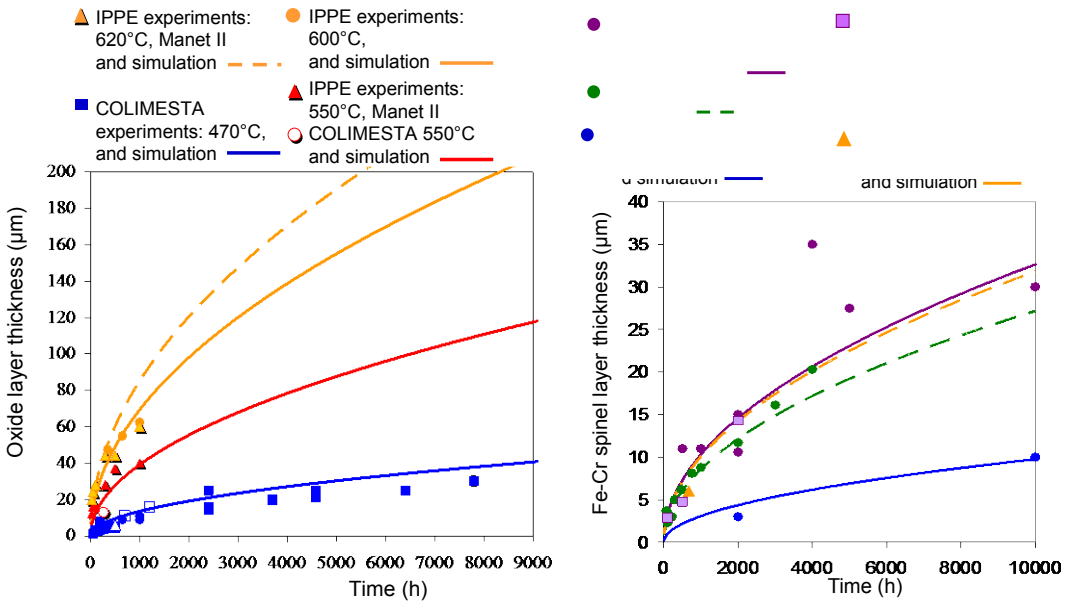

Source: Experimental points in left image from Martinelli (2008d), experimental points in right image in dynamic and static LBE from Weisenburger (2009).

Experimental values of oxide scale thickness of T91 after exposure to oxygen-saturated LBE are in good agreement with the simulated values for all temperatures (Figure 6.4.3 left). Unfortunately, long-term experimental data were only available at a temperature of 470°C. With lower oxygen content (Figure 6.4.3 right), which means under more reactor relevant conditions, some parameters required for the simulation were derived from the experiments to be simulated. Under these conditions, a general agreement between simulation and experiments can be anticipated. Indeed, the experiment in the LINCE loop at 450°C is very well simulated. Experiments performed by the CEA in the COLIMESTA facility at 530°C (Martinelli, 2011) slightly deviate from the simulated ones for longer exposure times. Finally, the deviation of the calculated trend from the experiments is noticeable in the data from the CORRIDA experiments, where an evident scatter of experimental values was observed.

Therefore, both simulation approaches presented here require further study of parameters for modelling the corrosion processes and experimental validation, especially at long exposure time for realistic and reliable long-term prediction.

6.5 Tables and figures of selected experimental results

Corrosion tests of a wide variety of materials under wide ranging conditions have been carried out in both stagnant and flowing LBE/Pb. The steels tested include Fe-Cr steels, with chromium contents from 1.2 to 17.84 wt.% and austenitic stainless steels. The composition of these steels is shown in Table 6.8.1 and 6.8.2., respectively. However, only part of all the data collected from corrosion tests are considered by the authors of this chapter to be relevant for judgement of material suitability for application in LBE loops. Tables 6.5.1 and 6.5.2 contain the data for ferritic/martensitic and austenitic steels, respectively, that were selected. They cover the temperature region of 300-650°C, exposure times from 100 to 15 000 hours and oxygen concentration in LBE/Pb from 10^{-12} wt.% to saturation. Tables are not shown for pure refractory materials (such as W, Nb, Mo...) or ceramic materials (SiC, Ti_3SiC_2...). They can be found in Chapter 9.

Table 6.5.1(a): Summary of experimental data of 9Cr and 12Cr f/m steels T91, Manet II, EM19, F82H, Optifer and P122 exposed to stagnant LBE or Pb

Exposure time ≥ 2 000 h, data used for Figures 6.5.1 and 6.5.2

Material	HLM	T (°C)	Time (h)	C_O (wt.%)	LMC layer (μm)	Ref.
Manet II	LBE	300	5 000	5.9×10^{-6}	<< 1	Fazio (2001)
T91	LBE	35	3 000	1×10^{-14} (with Zn)# 7×10^{-8} (no Zn)	-0.07	Deloffre (2004)
Manet II	LBE	400	5 000	9.81×10^{-5}	5	Fazio (2001)
T91	LBE	425	2 300	1×10^{-11}	-1.0	Sapundjiev (2006)
T91	LBE	425	3 000	1×10^{-11}	-5.6	Sapundjiev (2006)
T91	LBE	445	2 300	1×10^{-11}	-1.0	Sapundjiev (2006)
T91	LBE	445	3 000	1×10^{-11}	-1.4	Sapundjiev (2006)
T91	LBE	450	2 400	1.1×10^{-8}	< 1	Soler (2004)
F82H	LBE	450	2 400	1.1×10^{-8}	< 1	Soler (2004)
EM10	LBE	450	2 400	1.1×10^{-8}	< 1	Soler (2004)
T91	LBE	450	3 000	6×10^{-8}	30 12 (p)	Gómez (2004)
F82H	LBE	450	3 000	6×10^{-8}	11 14 (p)	Gómez (2004)
EM10	LBE	450	3 000	6×10^{-8}	11 9 (p)	Gómez (2004)
F82H	LBE	450	3 000	2.99×10^{-4}	8.4	Kurata (2005)
T91	LBE	450	3 000	5×10^{-8}	-0	Kurata (2008a, 2008b)
F82H	LBE	450	3 000	5×10^{-8}	-0	Kurata (2008a, 2008b)
T91	LBE	450	3 000	2.99×10^{-4}	8	Kurata (2005, 2008, 2009, 2011)
F82H	LBE	450	3 000	2.99×10^{-4}	8	Kurata (2005, 2008, 2009, 2011)
T91	LBE	470	3 700	4.47×10^{-4}	21	Martinelli (2008c, 2011)
T91	LBE	470	2 300	4.47×10^{-4}	16	Hwang (2010)
T91	LBE	470	2 409	4.47×10^{-4}	25	Martinelli (2008b)
T91	LBE	470	3 682	4.47×10^{-4}	20	Martinelli (2008b)
T91	LBE	470	3 800	4.47×10^{-4}	19	Hwang (2010)
T91	LBE	470	4 500	4.47×10^{-4}	24	Hwang (2010)
T91	LBE	470	4 545	4.47×10^{-4}	25	Martinelli (2008b)
T91	LBE	470	6 300	4.47×10^{-4}	24.5	Hwang (2010)
T91	LBE	470	6 364	4.47×10^{-4}	25	Martinelli (2008b)
T91	LBE	470	7 773	4.47×10^{-4}	30.4	Martinelli (2008b, 2005)

See notes on page 458.

Table 6.5.1(a): Summary of experimental data of 9Cr and 12Cr f/m steels T91, Manet II, EM19, F82H, Optifer and P122 exposed to stagnant LBE or Pb (*cont.*)

Exposure time ≥ 2 000 h, data used for Figures 6.5.1 and 6.5.2

Material	HLM	T (°C)	Time (h)	C_O (wt.%)	LMC layer (μm)	Ref.
T91	LBE	490	2 300	1×10^{-11}	-3.9	Sapundjiev (2006)
T91	LBE	490	3 000	1×10^{-11}	-6.1	Sapundjiev (2006)
F82H	LBE	500	2 000	7.88×10^{-4}	17.3	Kurata (2002)
P122	LBE	500	2 000	1^{E}-6	15	Müller (2002)
T91	LBE	500	2 832	7.88×10^{-4}	29÷30*	Yeliseyeva (2008)
T91	LBE	500	2 832	7.88×10^{-4}	15**	Yeliseyeva (2008)
Optifer IVc	LBE	500	3 000	1×10^{-6}	15	Heinzel (2002)
P122	LBE	500	5 000	1×10^{-6}	20	Müller (2002) (JNC)
P122	LBE	500	10 000	1×10^{-6}	60-70	Müller (2003) (JNC)
T91	LBE	502	2 000	4×10^{-8}	-20 ÷ -24	Martín-Muñoz (2011)
T91	LBE	520	2 832	1.12×10^{-3}	42*	Yeliseyeva (2008)
T91	LBE	520	2 832	1.12×10^{-3}	21**	Yeliseyeva (2008)
T91	LBE	535	2 300	1×10^{-11}	-43.5	Sapundjiev (2006)
T91	LBE	535	3 000	1×10^{-11}	-57.4	Sapundjiev (2006)
F82H	LBE	535	3 000	3×10^{-7}	-6	Martín (2004)
T91	LBE	535	3 000	3×10^{-7}	-26	Martín (2004)
EM10	LBE	535	3 000	3×10^{-7}	-45	Martín (2004)
T91	LBE	540	2 832	1.57×10^{-3}	67*	Yeliseyeva (2008)
T91	LBE	540	2 832	1.57×10^{-3}	34**	Yeliseyeva (2008)
P122	LBE	550	2 000	1×10^{-6}	13	Müller (2002) (JNC)
P122	LBE	550	2 000	1×10^{-4}	22	Müller (2003) (JNC)
P122	LBE	550	2 000	1×10^{-8}	-2	Müller (2003) (JNC)
T91	LBE	550	2 000	3.9×10^{-9}	-30	Gnecco (2004)
Optifer IVc	Pb	550	3 000	8×10^{-6}	30.4	Müller (2000)
Optifer IVc	Pb	550	3 000	1×10^{-6}	Spall off	Heinzel (2002)
T91	LBE	550	3 000	4×10^{-7}	Diss.	Martín (2004)
T91	LBE	550	3 000	4×10^{-6}	Diss.	Martín (2004)
F82H	LBE	550	3 000	4×10^{-7}	-14	Martín (2004)
F82H	LBE	550	3 000	4×10^{-6}	Diss.	Martín (2004)
F82H	LBE	550	3 000	1.2×10^{-3}	14	Kurata (2005)
EM10	LBE	550	3 000	4×10^{-7}	-65	Martín (2004)
EM10	LBE	550	3 000	4×10^{-6}	-15	Martín (2004)

See notes on page 458.

Table 6.5.1(a): Summary of experimental data of 9Cr and 12Cr f/m steels T91, Manet II, EM19, F82H, Optifer and P122 exposed to stagnant LBE or Pb (*cont.*)

Exposure time ≥ 2 000 h, data used for Figures 6.5.1 and 6.5.2

Material	HLM	T (°C)	Time (h)	C_O (wt.%)	LMC layer (μm)	Ref.
T91	LBE	550	3 000	1.85×10^{-3}	14	Kurata (2005)
F82H	LBE	550	3 000	1.85×10^{-3}	13.9	Kurata (2005)
T91	LBE	550	3 000	3×10^{-9}	-50	Kurata (2008)
F82H	LBE	550	3 000	3×10^{-9}	-35	Kurata (2008)
P122	LBE	550	5 000	1×10^{-6}	10-20	Müller (2002) (JNC)
P122	LBE	550	5 000	1×10^{-4}	7	Müller (2003) (JNC)
P122	LBE	550	5 000	1×10^{-8}	-1	Müller (2003) (JNC)
P122	LBE	550	10 000	1×10^{-6}	oxide	Müller (2003) (JNC)
T91	LBE	560	2 832	2.17×10^{-3}	29**	Yeliseyeva (2008)
T91	LBE	575	2 300	1×10^{-11}	-42.1	Sapundjiev (2006)
T91	LBE	575	3 000	1×10^{-11}	-8.4	Sapundjiev (2006)
F82H	LBE	600	2 000	3.93×10^{-3}	21.3 -26.6	Kurata (2009)
P122	LBE	600	2 000	1×10^{-6}	-20	Müller (2002) (JNC)
T91	LBE	600	3 000	8×10^{-10}	***-150 ÷ -200***	Deloffre (2004)
T91	LBE	600	3 000	8×10^{-5}	***-130***	Martín (2004)
F82H	LBE	600	3 000	8×10^{-5}	-80	Martín (2004)
EM10	LBE	600	3 000	8×10^{-5}	-16	Martín (2004)
P122	LBE	600	5 000	1×10^{-6}	-30	Müller (2002) (JNC)
P122	LBE	600	1 0000	1×10^{-6}	-200	Müller (2003) (JNC)
T91	LBE	605	3 000	1×10^{-11}	-4.7	Sapundjiev (2006)
P122	LBE	650	2 000	1×10^{-6}	-12	Müller (2002) (JNC)
P122	LBE	650	5 000	1×10^{-6}	-40	Müller (2002) (JNC)
P122	LBE	650	10 000	1×10^{-6}	diss	Müller (2003) (JNC)

Cases of localised dissolution are highlighted in ***red, bold, italic characters***.

[#] Zn was used as an oxygen getter.

* Magnetite + spinel + internal oxidation zone (IOZ); ** Spinel + IOZ; [&] Spinel.

Table 6.5.1(b): Summary of experimental data of 9Cr and 12Cr f/m steels T91, Manet II, T410, E911, HCM12A, Optifer and P122 exposed to *flowing* LBE or Pb

Exposure time ≥ 2 000 h, data used for Figures 6.5.1 and 6.5.2

Material	HLM	T (°C)	Time (h)	C_O (wt.%)	v (m/s)	LMC layer (μm)	Ref.
T91	LBE	300	3 116	1×10^{-6}	1.9	Oxidised	Barbier (2001)
Optifer IV	LBE	300	3 116	1×10^{-6}	1.9	Oxidised	Barbier (2001)
T91	LBE	300	10 000	1×10^{-8}	1	Oxidised	Martín-Muñoz (2008)
T91	LBE	302	2 000	1×10^{-8}	1	< 2	Martín-Muñoz (2011)
T91	LBE	302	5 000	1×10^{-8}	1	< 2	Martín-Muñoz (2011)
T91	LBE	302	10 000	1×10^{-8}	1	0	Martín-Muñoz (2011)
Optifer IV	Pb	400	2 000	3×10^{-5}	2	44	Glasbrenner (2001)
T91	LBE	400	3 000	3×10^{-6}	1	6	Aiello (2004)
Optifer IV	Pb	400	3 027	3×10^{-5}	2	49	Glasbrenner (2001)
T91	LBE	400	4 500	3×10^{-10}	1	-14	Aiello (2004) Long (2003)
ManetII	LBE	420	2 000	1×10^{-6}	1.3	8	Müller (2002) Heinzel (2002)
ManetII	LBE	420	4 300	1×10^{-6}	1.3	11	Müller (2004) Heinzel (2002)
ManetII	LBE	420	7 200	1×10^{-6}	1.3	20	Müller (2004) Heinzel (2002)
T91	LBE	450	2 000	1×10^{-8}	1	-10	Weisenburger (2011)
T91	LBE	450	2 014	1.1×10^{-6}	2	9.7	Schroer (2012a, 2012b)
T91	LBE	450	5 000	1.1×10^{-6}	1	30	DEMETRA (2009a) (LECOR)
T91	LBE	450	5 016	1.1×10^{-6}	2	13.7	Schroer (2012a, 2012b)
T91	LBE	450	8 039	1.1×10^{-6}	2	16.0	Schroer (2012a, 2012b)
E911	LBE	450	8 039	1.1×10^{-6}	2	*-125*	Schroer (2012)
T91	LBE	452	2 000	1×10^{-8}	1	3	Martín-Muñoz (2011)
T91	LBE	452	5 000	1×10^{-8}	1	3	Martín-Muñoz (2011)
T91	LBE	452	10 000	1×10^{-8}	1	10	Martín-Muñoz (2011)

See notes on page 461.

Table 6.5.1(b): Summary of experimental data of 9Cr and 12Cr f/m steels T91, Manet II, T410, E911, HCM12A, Optifer and P122 exposed to *flowing* LBE or Pb (*cont.*)

Exposure time ≥ 2 000 h, data used for Figures 6.5.1 and 6.5.2

Material	HLM	T (°C)	Time (h)	C_O (wt.%)	v (m/s)	LMC layer (μm)	Ref.
HT-9	LBE	460	2 000	1×10^{-6}	1.9	12-14	Zhang (2005)
T-410	LBE	460	2 000	1×10^{-6}	1.9	12-14	Zhang (2005)
HT-9	LBE	460	3 000	1×10^{-6}	1.9	14-16	Zhang (2005)
T-410	LBE	460	3 000	1×10^{-6}	1.9	4-20	Zhang (2005)
Optifer IVc	LBE	470	2 000	1×10^{-6}	2	18 (p)	Barbier (2001)
Optifer IVc	LBE	470	3 116	1×10^{-6}	2	22 (p)	Barbier (2001)
T91	LBE	470	3 116	1×10^{-6}	2	16 (p)	Barbier (2001)
T91 (tube)	LBE	480	2 000	1×10^{-6}	1.3	25	Weisenburger (2008)
T91 (tube)	LBE	480	4 630	1×10^{-6}	1.3	28	DEMETRA (2009a) (IPPE)
HCM12A	LBE	480	5 500	5×10^{-6}	18	0.08	Kikuchi (2012)
T91 (tube)	LBE	480	6 587	1×10^{-6}	1.3	30	DEMETRA (2009a) (IPPE)
T91	Pb	500	2 000	1×10^{-5}	1	20	Gessi (2008)
T91 (B)	LBE	550	1 991	1.6×10^{-6}	2	23**	Schroer (2012b)
Optifer, IV	Pb	550	2 000	3×10^{-5}	2	41	Glasbrenner (2001)
T91 tube	LBE	550	2 000	1×10^{-6}	1.3	31	DEMETRA (2009a) (IPPE)
T91 tube	LBE	550	2 000	1×10^{-6}	1	22	Weisenburger (2008)
HT-9	LBE	550	2 000	1×10^{-6}	1.9	32-36	Zhang (2005)
T-410	LBE	550	2 000	1×10^{-6}	1.9	1-50	Zhang (2005)
P122	LBE	550	2 018	1×10^{-6}	2	26	Schroer (2010, 2005)
T91	LBE	550	2 998	1×10^{-6}	2	16	Schroer (2006)
HT-9	LBE	550	3 000	1×10^{-6}	1.9	12-15	Hosemann (2008)
HT-9	LBE	550	3 000	1×10^{-6}	1.9	38-44	Zhang (2005)
T-410	LBE	550	3 000	1×10^{-6}	1.9	4-36	Zhang (2005)
EM10	Pb	550	3 027	3×10^{-5}	2	34	Glasbrenner (2001)
Optifer, IV	Pb	550	3 027	3×10^{-5}	2	46	Glasbrenner (2001)
T91 (B)	LBE	550	4 015	1.6×10^{-6}	2	44**	Schroer (2012b)

See notes on page 461.

Table 6.5.1(b): Summary of experimental data of 9Cr and 12Cr f/m steels T91, Manet II, T410, E911, HCM12A, Optifer and P122 exposed to *flowing* LBE or Pb (*cont.*)

Exposure time ≥ 2 000 h, data used for Figures 6.5.1 and 6.5.2

Material	HLM	T (°C)	Time (h)	C_O (wt.%)	v (m/s)	LMC layer (μm)	Ref.
T91 tube	LBE	550	4 630	1×10^{-6}	1.3	31	DEMETRA (2009a) (IPPE)
T91 (A)	LBE	550	5 012	1.6×10^{-6}	2	46**	Schroer (2012b)
T91	LBE	550	5 016	1×10^{-6}	2	26	Schroer (2006)
P122	LBE	550	5 016	1×10^{-6}		30	Schroer (2005, 2010)
T91 tube	LBE	550	6 587	1×10^{-6}	1.3	40	DEMETRA (2009a) (IPPE)
T91 (B)	LBE	550	7 518	1.6×10^{-6}	2	41**	Schroer (2012b)
T91	Pb	500	10 000	1×10^{-6}	1	32$	Gessi (2008)
T91 (A)	LBE	550	10 002	1.4×10^{-6}	2	48**	Schroer (2012b)
P122	LBE	550	10 006	1×10^{-6}		35	Schroer (2005, 2010)
T91 (B)	LBE	550	10 021	1.6×10^{-6}	2	43**	Schroer (2012b)
P122	LBE	550	15 017	1×10^{-6}	2	Oxide	Schroer (2010)
T91 (A)	LBE	550	15 028	1.6×10^{-6}	2	*-200*	Schroer (2012b)
T91 (B)	LBE	550	15 028	1.6×10^{-6}	2	*-150*	Schroer (2012b)
P122	LBE	550	20 039	1×10^{-6}	2	Oxide	Schroer (2010)
T91 (A)	LBE	550	20 040	1.6×10^{-6}	2	58**	Schroer (2012b)

* Magnetite + spinel + internal oxidation zone (IOZ); ** Spinel + IOZ; & Spinel; ***, $ Magnetite + spinel.

(A), (B): These studies tested two different T91 heats, i.e. T91-A (A) and T91-B (B).

(p) Pre-oxidised.

Cases of localised dissolution are highlighted in ***red, bold, italic characters***.

Table 6.5.2(a): Summary of experimental data of 316L, 316, and 304L and 15-15Ti steels exposed to *static* liquid LBE for duration ≥ 2 000 h

Data used for Figures 6.5.3 and 6.5.4

Material	T (°C)	Time (h)	C_O (wt.%)	LMC layer (μm)	Reference
316L	300	5 000	1.84×10^{-5}	≤ 1	Fazio (2001) Benamati (2002)
316L	400	5 000	1.41×10^{-4}	1	Fazio (2001) Benamati (2002)
316L	425	3 000	1×10^{-11}	-1.3	Sapundjiev (2006)
316L	445	2 300	1×10^{-11}	-2.3	Sapundjiev (2006)
316L	445	3 000	1×10^{-11}	-1	Sapundjiev (2006)

Table 6.5.2(a): Summary of experimental data of 316L, 316, and 304L and 15-15Ti steels exposed to *static* liquid LBE for duration ≥ 2 000 h (*cont.*)

Data used for Figures 6.5.3 and 6.5.4

Material	T (°C)	Time (h)	C_O (wt.%)	LMC layer (μm)	Reference
316	450	3 000	2.99×10^{-4}	2.5	Kurata (2008b, 2005, 2010)
316	450	3 000	5×10^{-8}	< 1 -80	Kurata (2008a, 2008b)
JPCA	450	3 000	5×10^{-8}	Ferrit.: 4.7	Kurata (2008)
JPCA	450	3 000	Saturated	4	Kurata (2005, 2008, 2009)
316L	500	2 540	$\leq 1 \times 10^{-8}$	≤ 2	Yamaki (2011)
JPCA	500	2 000	Saturated	2	Kurata (2009)
1.4970	500	3 000	5×10^{-7}	6	Heinzel (2002)
316L	500	3 045	$\leq 1 \times 10^{-8}$	≤ 2 -31	Yamaki (2011)
316L	500	5 000	1×10^{-6}	Nodes	Müller (2003) (JNC)
316L	500	10 000	1×10^{-6}	-40	Müller (2003) (JNC)
316L	520	2 832	1.12×10^{-3}	18 8.5 (IOZ)	Yliseyeva (2008)
316L	535	2 300	$<10^{-11}$	-57.2	Sapundjiev (2006)
316L	535	3 000	$<10^{-11}$	-59.2	Sapundjiev (2006)
316L	535	3 000	$3\text{-}4 \times 10^{-6}$	Oxidation	Martín (2004)
304L	535	3 000	$3\text{-}4 \times 10^{-6}$	0	Martín (2004)
316L	535	3 000	3×10^{-7}	Dissolution	Martín (2004)
304L	535	3 000	3×10^{-7}	0	Martín (2004)
316L	540	2 832	1.57×10^{-3}	50 25 (IOZ)	Yliseyeva (2008)
316L	550	2 000	3.9×10^{-9}	-60	Gnecco (2004)
316L	550	2 000	1.85×10^{-3}	7 ÷ 8	Gnecco (2004)
316L	550	2 000	1×10^{-4}	Dissolution attack	Müller (2003) (JNC)
316L	550	2 000	1×10^{-4}	Dissolution attack	Müller (2003) (JNC)
316L	550	2 000	1×10^{-8}	-100	Müller (2003) (JNC)
316L	550	2 000	1×10^{-6}	15 ÷ 35	Furukawa (2004) Müller (2002) (JNC)
304L	550	3 000	$3 \div 4 \times 10^{-6}$	0	Martín (2004)
316L	550	3 000	$3 \div 4 \times 10^{-6}$	Oxidation	Martín (2004)
304L	550	3 000	$3 \div 4 \times 10^{-7}$	0	Martín (2004)
316L	550	3 000	$3 \div 4 \times 10^{-7}$	Dissolution	Martín (2004)
316L	550	3 000	1.17×10^{-3}	< 1 -50	Benamati (2002)

See notes on page 463.

Table 6.5.2(a): Summary of experimental data of 316L, 316, and 304L and 15-15Ti steels exposed to *static* liquid LBE for duration ≥ 2 000 h (*cont.*)

Data used for Figures 6.5.3 and 6.5.4

Material	T (°C)	Time (h)	C_O (wt.%)	LMC layer (μm)	Reference
316	550	3 000	*1.85×10^{-3}*	≤ 2 -20	Kurata (2004)
316	550	3 000	*1.85×10^{-3}*	1.7 -22.4	Kurata (2008b, 2009, 2005)
316	550	3 000	*3×10^{-9}*	< 1 *-350*	Kurata (2008a, 2008b)
1.4970	550	3 000	5×10^{-7}	16-20	Heinzel (2002)
JPCA	550	3 000	3×10^{-9}	Ferrit.: 40	Kurata (2009)
JPCA	550	3 000	Saturated	47 Oxide: 3 Ferrit.: 44	Kurata (2005, 2008, 2009)
316L	550	5 000	1×10^{-6}	Nodes	Müller (2003) (JNC)
316L	550	10 000	1×10^{-6}	-200 μm	Müller (2003) (JNC)
316L	552	2 000	1.4×10^{-6}	11 ÷ 26	Martín-Muñoz (2011)
316L	552	2 000	1.4×10^{-7}	-25 ÷ -33	Martín-Muñoz (2011)
316L	560	2 832	*2.17×10^{-3}*	48 23.5 (IOZ) -30	Yeliseyeva (2008)
316L	565	2 300	*$<10^{-11}$*	-58.1	Sapundjiev (2006)
316L	565	3 000	*$<10^{-11}$*	-123	Sapundjiev (2006)
316L	570	2 300	*$<10^{-11}$*	-163	Sapundjiev (2006)
316L	570	3 000	*$<10^{-11}$*	-132.2	Sapundjiev (2006)
316L	600	2 000	*1×10^{-6}*	-20	Müller (2002, 2003) (JNC)
316L	600	2 000	*3.93×10^{-3}*	17 *-559*	Kurata (2008)
JPCA	600	2 000	Saturated	67 Oxide: 10 Ferrit.: 57	Kurata (2009)
316L	600	3 000	8×10^{-10}	-200 ÷ -220	Kikuchi (2003)
316L	600	5 000	*1×10^{-6}*	-20	Müller (2003) (JNC)
316L	600	10 000	*1×10^{-6}*	-180	Müller (2003) (JNC)

IOZ = Internal oxidation zone.

Cases of localised dissolution are highlighted in ***red, bold, italic characters***.

Table 6.5.2(b): Summary of experimental data of 316L, 316, 1.4571, 15-15Ti (1.4970, D9) and 16Cr11Ni3Mo steels exposed to *flowing* liquid LBE for duration ≥ 2 000 h

Data used for Figures 6.5.3 and 6.5.4

Material	HLM	T (°C)	Time (h)	C_O (wt.%)	v (m/s)	LMC layer (μm)	Ref.
316L	LBE	300	2 000	$1 \div 2 \times 10^{-6}$	1.9	< 1	Barbier (2001)
316L	LBE	300	3 000	$1 \div 2 \times 10^{-6}$	1.9	< 1	Barbier (2001)
316L	LBE	300	5 000	1×10^{-8}	1	0	Martín-Muñoz (2011)
316L	LBE	300	10 000	1×10^{-8}	1	0	Martín-Muñoz (2011)
1.4970**	LBE	300	2 000 3 116	$(1\text{-}2) \times 10^{-6}$	1.9±0.1	<1	Barbier (2001)
316L	LBE	400	4 500	$10^{-10} \div 10^{-8}$	1	-10	Long (2003); Aiello (2004); Benamati (2005)
316L	LBE	420	2 000	1×10^{-6}	2	< 1	Müller (2002)
316L	LBE	420	4 000	1×10^{-6}	1.3	< 1	Müller (2004)
1.4970**	LBE	420	2 000	1×10^{-6}	2	<1	Müller (2002)
1.4970**	LBE	420	4 000	1×10^{-6}	1.3	<1	Müller (2004)
316	LBE	450	3 000	*$10^{-9} \div 10^{-8}$*	1	*-100*	Kikuchi, 2003
316L	LBE	450	3 600	*$10^{-9} \div 10^{-8}$*	0.7	*-390*	Saito (2012)
316L	LBE	452	2 000	$10^{-10} \div 10^{-8}$	1	-2	Martín-Muñoz (2011)
316L	LBE	452	5 000	$10^{-10} \div 10^{-8}$	1	2 -10 *-300*	Martín-Muñoz (2011)
316L	LBE	452	10 000	$10^{-10} \div 10^{-8}$	1	-24 ÷ -50	Martín-Muñoz (2011)
316	LBE	460	2 000	$3 \div 5 \times 10^{-6}$	1.9	2 ÷ 4	Zhang (2005); Li (2001)
316L	LBE	460	2 000	$3 \div 5 \times 10^{-6}$	1.9	< 1	Zhang (2005); Li (2001)
D9**	LBE	460	2 000	$(3\text{-}5) \times 10^{-6}$	1.9	4-6	Zhang (2005)
316L	LBE	460	3 000	$3 \div 5 \times 10^{-6}$	1.9	1	Zhang (2005); Li (2001)
D9**	LBE	460	3 000	$(3\text{-}5) \times 10^{-6}$	1.9	2-6	Zhang (2005)
316L	LBE	470	2 000	$1 \div 2 \times 10^{-6}$	1.9	< 1	Barbier (2001)
316L	LBE	470	3 000	$1 \div 2 \times 10^{-6}$	1.9	< 1	Barbier (2001)
1.4970**	LBE	470	2 000 3 116	$(1\text{-}2) \times 10^{-6}$	1.9±0.1	<1	Barbier (2001)
316L	Pb	500	2 000	$10^{-6} \div 10^{-4}$	1	< 1	Gessi (2008)
316L	Pb	500	10 000	1×10^{-6}	1	≤ 10	Weisenburger (2011)
316L	LBE	550	1 991	1.6×10^{-6}	2	< 1 6 -90	Schroer (2010)
316L	LBE	550	2 000	1×10^{-6}	0.5	12	Müller (2002)

See notes on page 466.

Table 6.5.2(b): Summary of experimental data of 316L, 316, 1.4571, 15-15Ti (1.4970, D9) and 16Cr11Ni3Mo steels exposed to *flowing* liquid LBE for duration ≥ 2 000 h (*cont.*)

Data used for Figures 6.5.3 and 6.5.4

Material	HLM	T (°C)	Time (h)	C_O (wt.%)	v (m/s)	LMC layer (μm)	Ref.
316	LBE	550	2 000	$3 \div 5 \times 10^{-6}$	1.9	16 ÷ 20	Zhang (2005)
316L	LBE	550	2 000	$3 \div 5 \times 10^{-6}$	1.9	1 ÷ 12 *-160*	Zhang (2005)
1.4970**	LBE	550	2 000	1×10^{-6}	0.5	<30	Müller (2002)
D9**	LBE	550	2 000	$(3\text{-}5) \times 10^{-6}$	1.9	20-36	Zhang (2005)
316L	LBE	550	3 000	$3 \div 5 \times 10^{-6}$	1.9	1 ÷ 10 *-220*	Zhang (2005)
Cr16Ni11Mo3	Pb	550	3 000	$\sim 10^{-6}$	?	20-33	Gorynin (1999)
Cr16Ni11Mo3	Pb	550	3 000	$\sim 10^{-10}$		*-130*	Gorynin (1999)
316/316L	LBE	550	3 000	$3 \div 5 \times 10^{-6}$	1.9	< 1	Johnson (2004)
316L annealed	LBE	550	3 000	1×10^{-6}	2	25	Hosemann (2012)
316L Cold rolled	LBE	550	3 000	1×10^{-6}	2	2 spinel	Hosemann (2012)
D9**	LBE	550	3 000	$(3\text{-}5) \times 10^{-6}$	1.9	12-40	Zhang (2005)
1.4571 (s)	LBE	550	3 495	1×10^{-6}	2	< 1-*350 ÷ -450*	Schroer (2011)
316L	LBE	550	4 000	1×10^{-6}	0.5	≤ 12	Müller (2004)
316L	LBE	550	4 015	1.6×10^{-6}	2	< 1/15 ÷ 24	Schroer (2010)
1.4970**	LBE	550	4 000	1×10^{-6}	0.5	20	Müller (2004)
1.4571 (s)	LBE	550	5 016	$1 \times 10^{-9} \div 3 \times 10^{-5}$	2	*-600*	Schroer (2011)
1.4571 (t)	LBE	550	6 000	1×10^{-6}	1.7	10 ÷ 23/0 ÷ -2	Schroer (2011)
316L	LBE	550	7 200	1×10^{-6}	0.5	≤ 5	Müller (2004)
1.4970**	LBE	550	7 200	1×10^{-6}	0.5	-300	Müller (2004)
Cr16Ni11Mo3	LBE	550	9 000	$\sim 10^{-6}$	?	~75	Gorynin (1999)
316L	LBE	550	10 021	1.6×10^{-6}	2	< 1/16 ÷ 28/*-350*	Schroer (2010)
1.4571 (s)	LBE	550	12 564	1×10^{-6}	2	25/*-1 000*	Schroer (2011)
316L	LBE	550	15 028	1.6×10^{-6}	2	< 1 /8 ÷ 28/*-350*	Schroer (2010)
1.4571 (t)	LBE	550	23 000	*1×10^{-6}* (*)	1.7	2 ÷ 37/-1 ÷ -70 *-110 ÷ -240*	Schroer (2011)
1.4571 (t)	LBE	550	29 000	*1×10^{-6}* (*)	1.7	4 ÷ 11 /-60 ÷ -95/*-120 ÷ -350*	Schroer (2011)

See notes on page 466.

Table 6.5.2(b): Summary of experimental data of 316L, 316, 1.4571, 15-15Ti (1.4970, D9) and 16Cr11Ni3Mo steels exposed to *flowing* liquid LBE for duration ≥ 2 000 h (*cont.*)

Data used for Figures 6.5.3 and 6.5.4

Material	HLM	T (°C)	Time (h)	C_O (wt.%)	v (m/s)	LMC layer (μm)	Ref.
1.4571 (t)	LBE	550	40 000	1×10^{-6} (*)	1.7	10 ÷ 26 -1 ÷ -80	Schroer (2011)
316L	LBE	600	2 000	1×10^{-6}	2	*-270*	Müller (2002)
1.4970**	LBE	600	2 000	1×10^{-6}	2	30	Müller (2002)
1.4970**	LBE	600	4 000	1×10^{-6}	1.3	>100	Müller (2002)

(t) = tubes; (r) = rods; (s) = specimens; (g) ground; (p) passivated by means of pre-oxidation for 50 h at 400°C; passivation was performed in a gaseous mixture of steam with 5% H_2.

+ 08X16H11M3: X = Cr (16%), H = Ni (11%), M = Mo (3%).

The actual test duration was not 8 760 h; the reported thickness of the corrosion layers was an extrapolation based on shorter-term experimental data.

(*) These tubes were not exposed for the whole test to liquid LBE with $C_O \approx 10^{-6}$ wt.%. During the first 3 500 h of loop operation, the liquid LBE C_O fluctuated a lot: for ~1 000 h, it was $10^{-8} < C_O < 10^{-7}$ wt.%, and for another ~1 000 h, it was $10^{-9} < C_O < 10^{-8}$ wt.%.

Selected data are obtained from tests with exposure times of ≥ 2 000 h to allow reasonable extrapolation to the lifetime in a reactor and to avoid data from the initial process of scale formation (incubation time). Furthermore the materials should have relevant compositions (e.g. Cr content ≥ 9 wt.%). An important point is the manner in which the experiment is conducted. The conditions should be kept constant during the test, to obtain reliable data for an extrapolation to longer time periods. Therefore, the course of the experiments was thoroughly studied to be aware of the way the test was carried out. The selected data listed in Tables 6.5.1 and 6.5.2 are applied to conduct a first screening of the data using only the qualitative corrosion behaviour (oxidation or dissolution). With these data, an analysis was made, representing the general corrosion behaviour in graphics of temperature versus oxygen concentration. These graphics are shown in Figures 6.5.1-6.5.4.

The behaviour of ferritic/martensitic steels during exposure to LBE for ≥ 2 000 h is presented in Figure 6.5.1, which has two clearly defined regions; the upper part shows the formation of protective oxide scales and the lower displays an LBE attack on steel. The border between both regions is the line drawn from the first data point at 300°C/10^{-8} wt.% oxygen to 450°C/10^{-8} wt.% and then with increasing oxygen concentration up to 550°C/10^{-4} wt.%. The diagram shows that the conditions of compatibility between steel and LBE exist inside a large region of temperatures up to 550°C and oxygen concentrations down to 10^{-8} wt.%. Above 550°C there is a large risk of scale failure and dissolution attack onto the steel. Comparison of Figure 6.5.1 with 6.5.2, describing the situation for tests with a duration of more than 4 000 h, shows that probability of long time failure in the region with protective scale formation is small. This gives a hint that extrapolation of results obtained after 3 000-4 000 h is reliable. When failure occurs, it mostly happens before 4 000 h are reached. It should be noted that exposure times of only two protected steels reached 10 000 h and one 15 000 h in the temperature range 450-550°C.

Experimental results of corrosion tests on austenitic steels are represented in Figure 6.5.3. As for the Fe-Cr steels the diagram divides into two parts, separated by the line from 400°C/10^{-8} wt.% to 500°C/10^{-5} wt.% up to 540°C/10^{-3} wt.%. It should, however, be noted that above 500°C the risk of dissolution attack by leaching out of Ni is high. At 550°C all the specimens fail even in LBE saturated in oxygen. As expected, the border for

protective oxide scale formation is higher than for Fe-Cr steels. Unfortunately there were not many long-term experiments performed in the region where surface protection is expected (Figure 6.5.4). Therefore, more experiments are necessary to improve the reliability of extrapolations for the lifetimes of reactor structures. It is however obvious that the region for operation with protective oxide scales is much smaller than for the ferritic/austenitic steels. This concerns mainly the high temperature area of the diagram.

Figure 6.5.1: Fe-Cr steels after exposure to LBE/Pb for ≥ 2000 h at temperatures ranging from 400-650°C

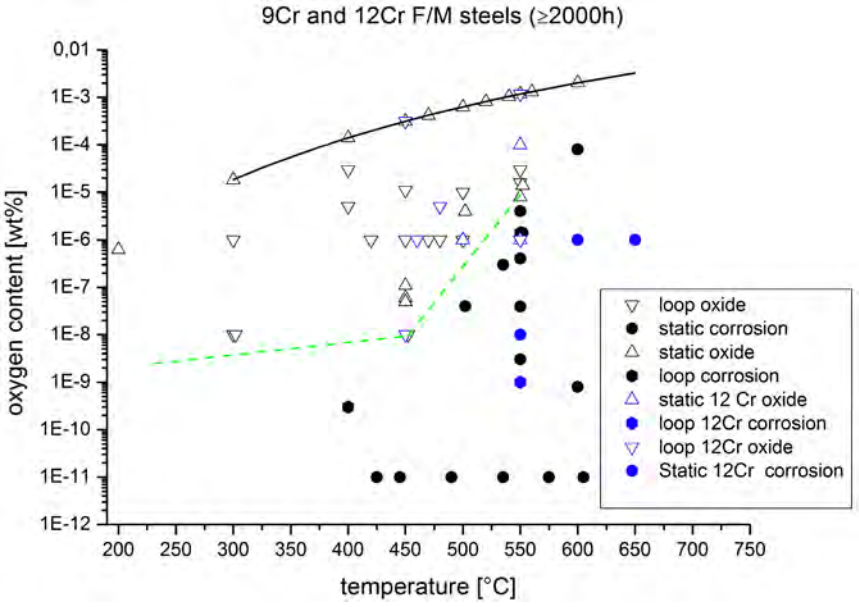

Figure 6.5.2: Fe-Cr steels after exposure to LBE/Pb for ≥ 4 000 h at temperatures ranging from 400-650°C

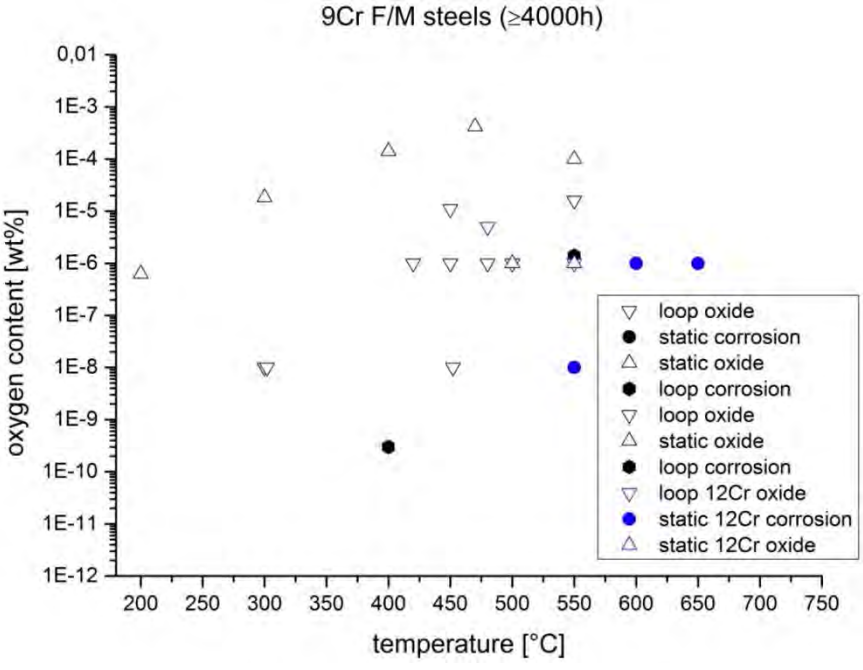

Figure 6.5.3: Fe-Cr-Ni steels after exposure to LBE/Pb for ≥ 2 000 h at temperatures ranging from 400-600°C

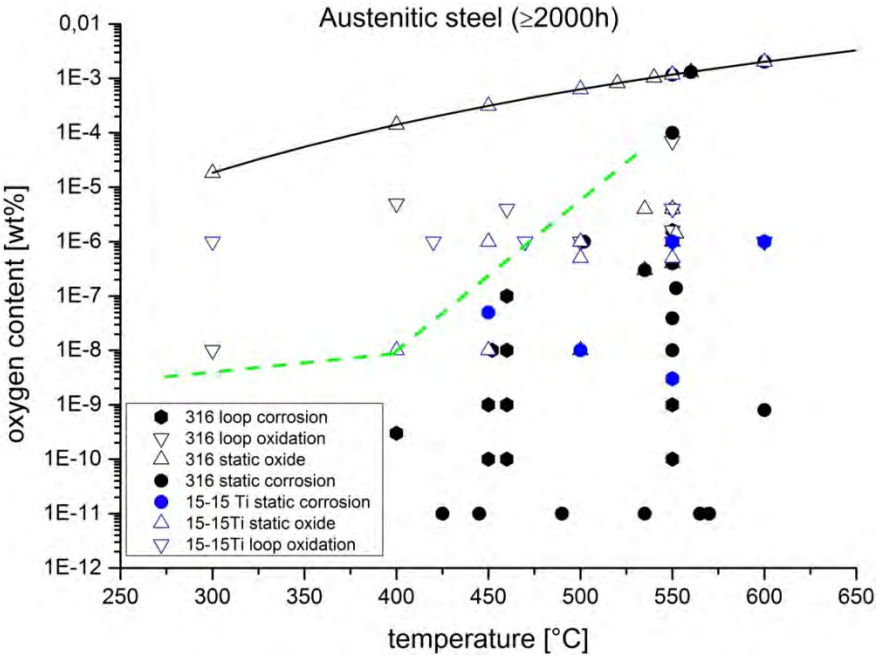

Figure 6.5.4: Fe-Cr-Ni steels after exposure to LBE/Pb for ≥ 4 000 h at temperatures ranging from 400-600°C

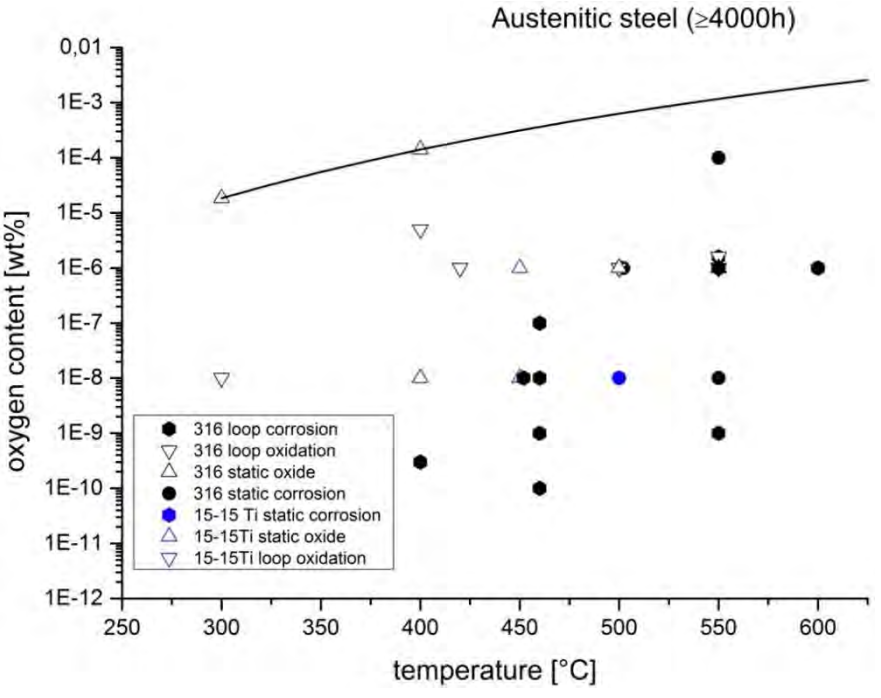

6.6 Conclusions

Ferritic/martensitic (Fe-Cr) and austenitic (Fe-Cr-Ni) steels exhibit different behaviour when exposed to liquid LBE or Pb. This is mainly caused by the Ni content and the higher Cr concentration in the austenitic steels. The following properties are characteristic for the steels:

- Fe-Cr steel:
  - Formation of duplex oxide scales that grow up to several 10 μm depending on temperature, exposure time and oxygen concentration.
  - Lower border of oxygen concentration region for stable oxide scale formation: 10^{-8} wt.% at temperatures < 450°C increasing up to 10^{-4} wt.% between 450 and 550°C.
  - At temperatures and oxygen concentrations outside the range of stable oxide scale formation dissolution attack is to be expected after local destruction of the oxide scale. However, it proceeds much slower than in austenitic steels.
  - Highest temperature for stability of a protected steel surface, 550°C.
  - Ablation of magnetite layer in loops with flow velocities ≥ 2 m/s. However, spinel layer stays intact and ensures surface protection.
  - After long exposure times at high temperatures oxide scales may be, especially at low flow velocities (< 2 m/s), too thick for the required heat transfer. Typical scale thickness in LBE with 10^{-6} wt.%O after an exposure time of 10 000 h is depending on temperature, e.g. 480°C → 23 μm; 500°C → 28 μm; 550°C → 41 μm (including magnetite scale). A scale thickness of 50 μm on heat exchanger tubes would require an increase of the exchanger area of 15% in the case of EFIT. Special surface protection (e.g. alloying of Al) would be an advantage for high temperature surfaces (see Chapter 9).
- Fe-Cr-Ni steel:
  - Formation of very thin high-Cr oxide scales < 450°C and duplex scales above this temperature which cover part of the whole surface after long exposure time.
  - Oxygen concentration range for stable oxide scale formation, 10^{-6}-10^{-4} wt.% depending on temperature.
  - Highest temperature for protected steel surface, 500°C.
  - Risk of Ni leaching at scale defects with high temperature (> 450°C) and/or low oxygen concentration in LBE and Pb followed by ferritisation of the steel.

Prediction of material behaviour by modelling all the processes that determine the corrosion of steels in liquid Pb and PbBi requires enhanced attention to the important parameters in the experiments and to the principal processes of oxidation, solution and diffusion involved in corrosion.

There are only few experiments conducted in liquid Pb. Although those experiments give a hint that there may be no great differences in behaviour it appears to be necessary to study material behaviour in pure Pb in more detail, because of the much higher solubility of Ni in Bi.

6.7 Recommendations on corrosion test procedures (standardisation)

Analysis of the available data indicates that a wide range of experimental conditions has been tested: temperatures from 300 to 650°C, times from 100 to 15 000 hours and oxygen concentration in LBE/Pb from 10^{-12} wt.% to saturation.

Thirty-four (34) Fe-Cr steels and eleven (11) Ni alloys have been tested. However, there are not enough data for each condition and, in some cases, not all the experimental conditions are reported. The result has been that much of the data cannot be properly interpreted. This indicates that more systematic work is necessary to be able to standardise the test procedures, but it is possible to give some general recommendations. Within the framework of the VELLA initiative two guidelines and procedures for the performance of tests of materials' compatibility with lead-bismuth eutectic (LBE) or lead (Pb) were developed (Gómez-Briceño, 2008, 2009).

The approach to testing in LBE or Pb involves design and placement of samples, design of test system, the control and monitoring of tests conditions and the measurement and evaluation of corrosion damage. The general recommendations that follow are based on Bagnall (1995).

In order to assure valid results, tests should be well documented, and the following systematic parameters should be reported.

6.7.1 Pre-test preparation

6.7.1.1 Liquid metal: LBE and Pb

- Impurity analysis of the LBE or Pb should be made before and after each test (see Chapter 4).
- Total mass of LBE/Pb. The ratio of the specimen surface area to the liquid LBE volume should be sufficient to ensure that LBE is not saturated with corrosion product at end of test.

6.7.1.2 Materials

Compositions, thermal treatments and mechanical properties as well as the type of product (plate, tube, thick wall tube, etc.) of the materials to be tested should be reported. Basic characterisation of the material microstructure should be carried out.

It is common practice to test only one specimen of each material or lot of materials for each test condition. However, as a minimum, duplicate and preferably triplicate specimens should be tested for any given test period to determine the variability in the oxidation/corrosion behaviour.

Size and shape of the specimens vary and selection is a matter of convenience: rectangular plates, disks, cylinders, tubes, etc. can be used. For flat specimens, the preparation of the surface is easier. Cut edges might corrode much faster than the rest of the surface. A large surface to mass ratio and a small ratio of edge area to total area are recommended.

The specimen surface should be finished in a reproducible way. Mechanical polishing of the surface with No. 600 abrasive paper or cloth of higher No. is a common practice. Other types of finishing, such as turning or electropolishing, are also adequate. In some cases, the material should be tested in as-received condition. Measurement of the roughness of the final surface is recommended in particular in the latest case. Finishing of the surface should be done with care to prevent work hardening of the surface. Specimens should be finally degreased, rinsed in water and in a suitable solvent (such as acetone, methanol, etc.) and dried.

Dried specimens should be weighted on an analytical balance to an accuracy of at least ± 0.01 mg and the total exposed surface area of the specimen should be calculated with an accuracy of at least 1%.

If Method A is used to quantify the degradation of material after testing, specimen thickness should be measured with sufficient accuracy to allow a reliable quantification of the loss of material. For example, if the expected loss of bulk material in a cylindrical specimen is around 10 μm (20 μm change in diameter) the accuracy should be at least of ±1 μm.

The method of specimen preparation should be described when reporting test results to facilitate interpretation of the data.

The samples should be correctly identified using a technique that will not be destroyed during the test.

6.7.2 Test conditions

The compatibility of materials with heavy liquid metals can be studied using static, thermal convection and forced convection conditions. A detailed description of the typical systems is included in Chapter 12.

6.7.2.1 Static (no flow) tests

In isothermal devices for tests in stagnant LBE/Pb, the container can serve as the test specimen, or the test specimen can be incorporated. In any case, the container and test specimen should be either of the same composition or, better, the container should be inert to corrosion in liquid metals. Relative surface areas of different metals and surface/liquid metal volume ratios are important points to consider when designing small scale tests to examine corrosion trends. The liquid metal volume to exposed area metal ratio should be high enough to avoid saturation of main steel elements in the liquid metal. In general, materials with large compositional differences should not be exposed together to determine relative corrosion behaviour.

The temperature should be uniform in the liquid metal contained in the device. If a temperature gradient exists, it must be measured and given. The oxygen content in LBE or Pb should be homogenised and known during the test period.

Stagnant tests are very useful for a first screening of experimental conditions and contribute to the establishment of a corrosion mechanism in LBE/Pb. However, under isothermal conditions, the rate of dissolution reaction would decrease with time as the concentration of the main steel elements dissolved in the liquid metal increases. After a period, the actual elemental concentration becomes equal to the solubility and the dissolution rate is zero.

6.7.2.2 Dynamic tests

The simplest non-isothermal flowing system where processes associated with dissolution and deposition occur is one in which the flow is induced by thermal convection. This is accomplished by heating one leg of a closed loop and cooling another leg. The flow rate is dependent on the height of the heated and cooled sections, on the temperature gradient and on the physical properties of the liquid. Thermal convection loops can be destructively examined after operation and specimens can be removed and replaced numerous times for cumulative periods without interruption of liquid metal flow. However, the utility of thermal convection loops is limited by the low flow velocities that can practically be achieved (maximum of about 60 mm/s), making extrapolations to the higher velocities in operating systems doubtful.

Higher flow velocities are obtained in forced convection loops where the liquid is pumped through the loop with an electromagnetic or mechanical pump. Test specimens of various materials are generally placed in the hot leg and the effect of the flowing liquid on the specimen is determined from changes in weight, dimensions, mechanical properties and microstructure. Such an approach yields data on maximum corrosion rates as a function of temperature and liquid metal flow rate. The chemical balance between dissolution and deposition is strongly influenced by all materials (i.e. containment and tests specimens) exposed to the circulating LBE or Pb. The containment material has its own effect on test results in systems in which dissimilar metals or alloys are involved.

The parameters that should be taken into account during tests under flowing LBE or Pb are:

- *Materials*. Steel composition of the loop and test specimens must be analysed and reported. The test specimen distribution in the loop should always be given in detail when reporting corrosion results. Relative corrosion sources and sinks are of vital importance in the analysis of corrosion specimens.
- *Temperature*. Maximum and minimum temperature of the loop must be measured and reported during the loop operation. However, corrosion rate/temperature relationships are strongly influenced by system geometry. For this reason, loop geometry and temperature distribution along the loop should also be measured and reported during a test.
- *Flow rate and hydraulic diameter with specimens in the pipe*. In general, flow rate influences corrosion rate by LBE or Pb. If the liquid metal is flowing at high velocity, the structural materials could also be subject to erosion. It is necessary to measure and report the flow rate at several points of the loop, especially at the test sections. Knowing that the introduction of specimens in the pipe reduces the hydraulic diameter of the pipe, the velocity increases in the test section due to the specimen introduction. Consequently it is necessary to give the flow velocity and the hydraulic diameter with and without specimens in the test section.
- *Time*. Accurate kinetic measurements must be made over an extended period for useful comparison and predictive analysis. The proposed exposure intervals are 2 000, 5 000, 10 000 and 15 000 hours. Accelerated corrosion takes place in the first hours of exposure, depending on the material and temperature, but 2 000 hours seems a reasonable time to detect this period. After this initial period, a steady-state corrosion rate is usually attained.
- *Oxygen concentration in LBE or Pb*. Corrosion inhibition is dependent on formation of protective surface films and control of oxygen in the liquid metal is essential for this process. The oxygen control system used to adjust and assure the required oxygen in the LBE or Pb – gas mixture, H_2/H_2O equilibrium or solid PbO – should always be reported. The knowledge of the oxygen concentration in the LBE or Pb is mandatory. This value, along with temperature, will give the valid area of operation.

6.7.3 Post-test analysis

The development of common criteria to quantify LBE or Pb effects on materials is essential for comparison of results from different laboratories and to reach conclusions. In general, the corrosion damage and the oxidation observed are heterogeneous, with simultaneous existence of dissolution areas and oxidation protected areas. In these cases, weight change measurements alone could lead to erroneous interpretation. There is not a single method reliable for all the cases. For comparison, metallographic examination, weight change measurements and an attempt to measure the remaining unaffected thickness of interior bulk should be undertaken. The weight change measurement method requires that an appropriate procedure for removing the oxide scale from the steel surface be performed.

Metallographic examination

Cross-sections of the tested steels without removal of the remaining LBE or Pb should be used for the analysis of the oxide layer formed on the surface or the morphology of dissolution and its depth. Measurements of the thickness of distinguishable components (layers) of the oxide scale and the determination of the dimensions of a sub-surface zone affected by corrosion are a mandatory part of the characterisation of the corrosion processes and, therefore, generally performed in connection with the microscopic examination of metallographic cross-sections. Parameters such as porosity, adherence, hardness, enrichment or depletion of the main steel elements, etc., of the oxide layer should be reported.

Methods routinely applied to material specimens after exposure to a corrosive environment are light and scanning electron microscopy (SEM) supplemented by semi-quantitative energy-dispersive X-ray analyses (EDX), in order to characterise the mode of material degradation, the structure and composition of the corrosion (oxide) scale that may have formed on the material surface and changes in structure and composition of the material in a near-surface zone. For this purpose, metallographic cross-sections of the corroded specimens have to be prepared using standard metallographic techniques. Emphasising structural changes in the material may require etching of the cross-section.

In the case of thin corrosion scales, the analysis of the scale surface by means of Auger electron spectroscopy (AES) in combination with depth profiling by ion sputtering is more appropriate. An alternative method is X-ray photoelectron spectroscopy (XPS) which gives additional information on the chemical bonding of the constituents of the scale. Considering material specimens which were exposed to HLM, remnants of the liquid metal adhering to the specimen surface have to be removed, before AES and XPS can be applied. The same is true for the analysis of the compounds of the scale or phase transitions in the material by X-ray diffraction (XRD).

Quantification of the material degradation

Procedures most commonly used to quantify the material degradation due to high-temperature corrosion processes rely on the measurement of either the change in geometric dimensions or the mass change of the specimens after a certain exposure time to the corrosive environment.

Regarding the structural integrity, the parameter to be determined is the loss of the sound material, i.e. the thickness of the sound material which is no longer capable of bearing the mechanical loads to which the material is subjected under service conditions. On the other hand, the thickness of the oxide scale forming on the material surface is an important parameter for the efficiency of heat transfer surfaces.

Three different methods can be considered to quantify the degradation of materials exposed to HLM (Schroer, 2006b). To measure oxide scale thickness and to determine the depth of a subsurface zone affected by corrosion, metallographic preparation of the tested specimens should be performed.

- *Method A*: Metallographic method to determine the geometric dimensions of sound metal. The loss of sound material relies on the measurement of the thickness of the specimen not affected by corrosion and the initial thickness of the specimens before exposure to the corrosive environment. Both light microscope and scanning electron microscope are suitable for this determination.
- *Method B:* Metallographic method to determine the thickness of different parts of the oxide scale on the steel surface. The determination of the oxide scale thickness and the depth of the sub-surface corrosion area are not enough to calculate the overall material loss, since dissolution of the main elements of materials may be significant. As heterogeneous oxide layers can be found on materials tested in

HLM, a sufficient number of measurements should be done in order to obtain representative values of the oxide layers thickness. Both light microscope and scanning electron microscope are suitable for this determination.

- *Method C:* Method to determine the mass change after exposure and removal of adherent oxides. Change of mass per area unit provides a higher accuracy against metallographic methods when local corrosion and sub-surface corrosion are of minor importance. The challenge of this method is the adequate removal of the liquid metal deposited on the specimen.

Experimental protocol for oxide layer thickness measurements

Martinelli (2007) generated a paper which provides an experimental protocol for oxide layer thickness measurements. The oxidation process of T91 in LBE leads to the formation of a duplex oxide scale at the steel surface. This duplex layer is constituted of an external magnetite scale and an internal Fe-Cr spinel scale. For the quantification of the oxide layer thickness, the most important measurement error comes from the localisation of the oxide1/oxide2 interface inside the duplex oxide scale.

An experimental protocol, based on SEM/EDX analyses, is given in order to measure the oxide layer thicknesses. Considering an EDX profile, perpendicular to the oxide surface, in which first points are in the Pb-Bi and last one in the steel; it is proposed that the magnetite/Pb-Bi interface is localised at the first point of inflexion on the iron concentration graph, the Fe-Cr spinel/magnetite interface is localised at the first point of inflexion on the chromium concentration graph, and the Fe-Cr spinel/T91 interface is localised at the second point of inflexion on the oxygen concentration graph. A scale measurement method is proposed: several (from three to five) SEM/EDS profiles are performed on the T91 sample cross-section in order to localise the Fe-Cr spinel/magnetite interface. When this interface is localised some measurements are performed directly on the SEM pictures. As the oxide layers thicknesses are not exactly the same on the whole cross-section, the mean of ten measurements for each oxide layer is given as the thickness value. In order to obtain the most representative mean value, the oxide layer measurements are performed all around the sample cross-section.

According to this protocol, the most important uncertainty is due to: *i)* the interface localisation when the oxide thickness is thinner than 10 μm, in which case the thickness measurement error is equal to ±1 μm; *ii)* heterogeneity of the oxide scale thicknesses. This heterogeneity is, in most cases, lower than 10% of the oxide scale thickness. Each oxide layer thickness is thus given by the mean of ten measurements with a 10% uncertainty for oxide scales thicker than 10 μm and with ±1 μm error on oxide scales lower than 10 μm.

Reduction of thickness through metallographic measurements, Δl_m

Babayan (DEMETRA, 2009a) proposed this method for post-exposure examinations. The specimen prepared for metallographic examination is cut into two parts: one half is cleaned in a fresh solution of CH_3COOH:H_2O_2:C_2H_5OH = 1:1:1, to remove the residual deposits of LBE and in the other half the deposit is left on the specimen. Both halves of the same specimen are embedded in resin and polished to 1 μm finish for metallographic examination. The embedded specimens are used for the measurements of the thickness loss and for the observation of the damaged areas with the scanning electron microscopy (SEM).

The average thickness of specimens after the exposure to LBE is measured on each sample according to the schematic representation in Figure 6.7.1. The software attached to the optical microscope for image analyses (LUCIA G 5.20) calculates the extent of the area (red area) of sound metal (by colour contrast, the metal can be separated from the corrosion products), which, divided by the initial length (b) is used to calculate the change in the thickness of specimens (Δl_m).

Figure 6.7.1: Schematic of the measurement of area of residual metal, which divided by the length, b, generated an average value of the residual thickness

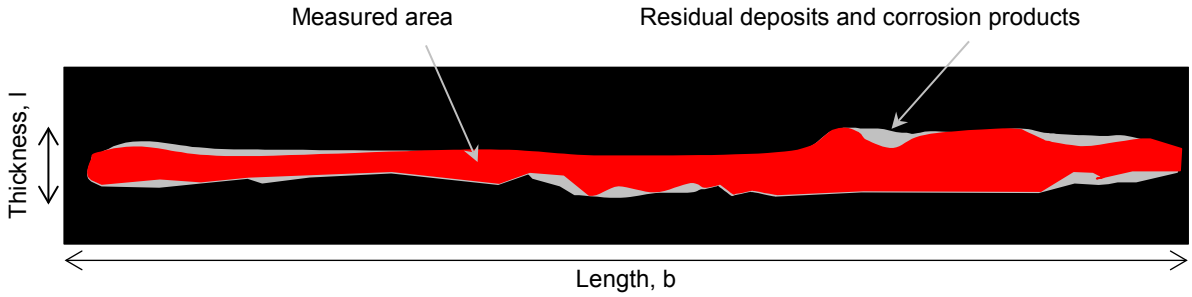

Source: DEMETRA (2009a).

Reduction of thickness through weight loss measurements, Δl_m

Almost three specimens from each set of samples are cleaned in a fresh solution of $CH_3COOH:H_2O_2:C_2H_5OH$ = 1:1:1, to remove the residual deposits of LBE. After the weight measurements, average values are calculated and used for the extrapolation of the reduction of thickness. In fact, Δl_w can be calculated from the mass change, Δw, where, the absolute amount of Δw has to be divided by the total initial exposed surface area (A) of the cross-section and the density of the steel (ρ_{steel}). In this specific case, this formula is valid assuming that only one dimension changed after exposure, the thickness, l (while the other two dimensions are not affected by the dissolution process):

$$\Delta l_w = \frac{\Delta w}{A \cdot \rho_{steel}} [\mu m] \tag{6.5}$$

Subsequently, the corrosion rate, V_{corr} is evaluated by extrapolating the exposure time, t, to one year and assuming that the correlation between the weight loss and the time was linear:

$$V_{corr} = \frac{\Delta l_w}{t} \left[\mu m \cdot y^{-1}\right] \tag{6.6}$$

6.8 Tables

Table 6.8.1: Composition of Fe-Cr Steels

	Manet II	56T5	12Cr	ODS	EP823	HT9	HCM 12A	HCM 12	410ss	T410	430ss	TMK1
C	0.11	0.20	0.11		0.14-0.18	0.22			0.067		0.08	0.15
Cr	10.3	10.51	10.54	11.72	10.97-12	12	12	12.1	12.21	12.5	16.24	10.
Ni	0.68	0.66	0.33		0.75-0.89	0.59			0.12	0.34	0.15	0.6
Mo	0.61	0.65	0.34		0.7-0.73	1.11	0.3	1.1	0.02		0.02	0.5
W			1.76	1.99	0.64-1.2	0.5	1.9	1				
Mn	0.78	0.61	0.64		0.59-0.67	0.58	0.5	0.5	0.80	1	0.23	0.5

Table 6.8.1: Composition of Fe-Cr Steels (*cont.*)

	SCM 420	2,25Cr-1Mo	F82H	STBA 28	T91	NF 616	ODS-M	Eurofer 97	STBA 26	Optifer IVc	EM10
C		0.100-11	0.10-0.095	0.10	0.1-0.11		0.13	0.12		0.13	0.1-0.097
Cr	1.2	2.18-2.25	7.70-7.75	8.41-8.6	8.26-8.63	8.8-9	8.85	8.93	9	9.05	8.8-9.15
Ni		0.02	0.015	0.06	0.13-0.23		0.01	0.022			0.04-0.2
Mo	0.2	0.92-1.00	0.010	0.88-1	0.91-0.95	0.3-0.5		0.0015	1		0.97-1
W			1.94-2.10		<0.01	1.8-1.9	1.94	1.07		1	0.005
Mn		0.44-0.55	0.01-0.16	0.40	0.43-0.78	0.5	<0.01	0.47	0.3-0.43	0.52	0.5
Si	0.2	0.34	0.1-0.23	0.30-0.40	0.31-0.43	0.3	<0.005	0.06	0.20-0.43		0.37-0.44
P		<0.035			0.01-0.02		0.001	0.005			0.0042
S		<0.030	0.003		0.003-0.006		0.003	0.004			<0.001
Cu			0.01-0.03		0.19-0.05			0.0036			0.055
Al		0.002	0.004		<0.01			0.008			<0.005
Nb			<0.01	0.08	0.07-0.09	0.07		0.0022			0.01
Co			3×10^{-3}		0.02			0.0036			0.03
V		0.01	0.14-0.18	0.20	0.20-0.23	0.2		0.20		0.25	0.032
Ti		<0.01	0.004-0.01	0.033	0.003		0.2				0.01
N		0.009	0.010	0.047	0.04		0.011	0.018			0.014
B			4×10^{-4}		<0.0005						<0.001
Y							0.27				
Zr											

	Manet II	56T5	12Cr	ODS	EP823	HT9	HCM 12A	HCM 12	410ss	T410	430ss	TMK1
Si		0.22	0.27		1.21-1.8	0.30	0.3	0.3	0.31	1	0.52	0.1
P	0.003		0.016									
S			0.002									
Cu			1									
Al			0.001						0.002		0.007	
Nb	0.14	0.48	0.048		0.34-0.4		0.05	0.09				
Co												
V	0.20	0.18	0.19		0.33-0.43		0.2	0.3	0.07		0.10	0.2
Ti				0.29					<0.01		<0.01	
N			0.071						0.013		0.024	
B			0.034									
Y				0.4								
Zr												

Table 6.8.1: Composition of Fe-Cr Steels (*cont.*)

	17-5PH	RECLOY	SUH3	MA957	12YWT	14YWT	NTK04L	420	P122	9Cr-2W ODS
C	0.01	0.01	0.42	0.01	0.2	0.2	0.002	0.15	0.11	0.13
Cr	16.0	17.69	10.39	14	12	14	17.84	14.72	10.54	8.85
Ni	4.5		<0.6					0.44	0.33	
Mo			0.72						0.34	
W					0.8	0.6			1.72	1.94
Mn	0.5	0.68	0.49				0.14	0.56	0.64	
Si	1.0	0.99	1.90				0.41	0.33	0.27	
P		0.24	0.023				0.022			
S		0.003	0.002				0.001			
Cu									1.00	
Al		0.89					3.34			
Nb	0.2								0.048	
Co										
V									0.19	
Ti				0.9	0.4	0.3				0.20
N									0.071	0.011
B										
Y				0.25	0.25	0.25				0.27
Zr										

Table 6.8.2: Composition of Fe-Cr-Ni steels

	D9	14Cr-16Ni-2Mo	1.4970	316L	1.4984	304L	JPCA	316 (2Mo)	316 (3Mo)	321	EI 211
C	0.04	0.058	0.46	0.012-0.02	0.06	0.020	0.06	0.06	0.08	0.07	0.08
Cr	13.6	14.14	16.5	16-18	17-19	18.50	15	17.64	17.56	1.26	21.26
Ni	13.6	15.85	13.8	10-17.392	10-12	8.31	15	13.15	13.02	8.19	13.09
Mo	1.67	2.29	0.66	2-2.75		0.39	2	2.57	3.53		
Mn	2.1	1.54	1.91	0.2-2	0-2	1.67		1.06	1.62	1.79	0.7
Si	0.85	0.50	0.89	0.1-1	0-0.75	0.49		0.45	0.48	0.62	2.62
P			0.012	0.024-0.19		0.026					
S			0.009	0.0005-0.03		0.003					
Co				0.06-0.14							
N		0.003		0.02-0.1		0.069					
Ti	0.30	0.22	0.43				0.25			1.00	
V		0.03									
W		0.010									
Al		0.012									

References

Aiello, A. et al. (2004), "Corrosion Behaviour of Stainless Steels in Flowing LBE at Low and High Oxygen Concentration", *Journal of Nuclear Materials*, 335, pp. 169-173.

Atkinson, A. and D.W. Smart (1988), "Transport of Nickel and Oxygen During the Oxidation of Nickel and Dilute Nickel/Chromium Alloy", *J. Electrochem. Soc*, 135-11, pp. 2886-2893.

Backhaus-Ricoult, M. and R. Dieckmann (1986), "Defects and Cation Diffusion in Magnetite (VII): Diffusion Controlled Formation of Magnetite During Reactions in the Iron-Oxygen System", *Ber Bunsenges Phys. Chem*, 90 (8), pp. 690-698.

Bagnall, C. et al. (1995), *Liquid Metals, Corrosion Tests and Standards*, p. 387, R. Baboian (ed.).

Barbier-Célérier, F. and A. Rusanov (2001), "Corrosion Behavior of Steels in Flowing Lead-Bismuth", *Journal of Nuclear Materials*, 296, p. 23.

Balbaud-Célérier, F. and F. Barbier (2001b), "Investigation of Models to Predict the Corrosion of Steels in Flowing Liquid Lead Alloys", *Journal of Nuclear Material*, 289, p. 227.

Balbaud-Célérier F. et al. (2002), "Corrosion of Metallic Materials in Flowing Liquid Lead-Bismuth", *Journal de Physique IV (Proceedings)*, France, 12, pp. 177-190.

Balbaud-Célérier, F. et al. (2003), *Corrosion of Steels in Liquid Lead Alloys Protected by an Oxide Layer Application to the MEGAPIE Target and to the Russian Reactor Concept BREST 300*, Report Technique RT-SCCME 630, CEA Report.

Balbaud-Célérier, F. and A. Terlain (2004), "Influence of the Pb-Bi Hydrodynamics on the Corrosion of T91 Martensitic Steel and Pure Iron", *Journal of Nuclear Materials*, Vol. 335, 2, pp. 204-209.

Balbaud-Célérier, F. and L. Martinelli (2010), "Modeling of Fe-Cr Martensitic Steels Corrosion in Liquid Lead Alloys", *Journal of Engineering for Gas Turbines and Power*, Vol. 132, No. 10, 102912.

Barbier, F. et al. (2001c) "Compatibility Tests of Steels in Flowing Liquid Lead-bismuth", *Journal of Nuclear Material*, 295, p. 149.

Benamati, G. et al. (2000), "Behaviour of Materials for Accelerator Driven Systems in Stagnant Molten Lead", *Journal of Nuclear Materials*, 279, p. 308.

Benamati, G. et al. (2002), "Temperature Effect on the Corrosion Mechanism of Austenitic and Martensitic Steels in Lead-bismuth", *Journal of Nuclear Materials*, 301, p. 23.

Brückman, A. and J. Romanski (1965), "On the Mechanism of Sulphide Scale Formation on Iron", *Corrosion Science*, Vol. 5, pp. 185-191.

Chang, S.L., F.S. Pettit and N. Birks (1990), "Some Interactions in the Erosion-Oxidation of Alloys", *Oxidation of Metals*, Vol. 34, N° 1/2, pp. 71-100.

Cory, N.J. and T.M. Herrington (1987), "Kinetics of Oxidation of Ferrous Alloys by Superheated Steam", *Oxidation of Metals*, Vol. 28, No. 5/6, pp. 237-258.

Cory, N.J. and T.M. Herrington (1988), "The Location of Hydrogen in the Kinetics of Oxidation of Ferrous Alloys by Superheated Steam", *Oxidation of Metals*, Vol. 29, No. 1/2, pp. 135-152.

Cox, M.G.C., B. McEnaney and V.D. Scott (1972), "A Chemical Diffusion Model for Partitioning of Transition Elements in Oxide Scales on Alloys", *Philosophical Magazine*, Vol. 26, pp. 839-851.

DEMETRA (2009a), *Final Report on Long-Term Corrosion of Reference Steels in Flowing LBE and Pb, Including Fast Flowing at CICLAD and Abnormal Operation Conditions after Exposure of FeAl Surface Layer to LBE at 550°C*, DEMETRA Deliverable D4.62, FZK, IPPE/FZK, CIEMAT, ENEA, CEA, NRI.

DEMETRA (2009b), *Modeling of Mass Transport Processes and Corrosion in Loop-Type LBE Systems*, DEMETRA Deliverable D4.52, FZK.

Del Giaccio, M.A. Weisenburger and G. Müller (2012), *Investigation of Fretting Wear of Cladding Materials in Liquid Lead*, dissertation at KIT, 978-3-86644-960-2, J. Jelonek (ed.), KIT Scientific Publishing, Karlsruhe.

Del Giaccio, M.A. Weisenburger and G. Müller (2012b), "Fretting Corrosion in Liquid Lead of Structural Steels for Lead-Cooled Nuclear Systems: Preliminary Study of the Influence of Temperature and Time", *Journal of Nuclear Materials*, 423, pp. 79.

Deloffre, Ph., A. Terlain and F. Barbier (2002), "Corrosion and Deposition of Ferrous Alloys in Molten Lead-Bismuth", *Journal of Nuclear Materials*, 301, pp. 35.

Doubkova, A. et al. (2008), "Corrosion Behavior of Steels in Flowing Lead-bismuth Under Abnormal Conditions", *Journal of Nuclear Materials*, Vol. 376, 3, pp. 260-264.

Efanov, D. et al. (2001), "Study of Lead Coolant Technology", *ANS Winter Meeting*, Reno, Nevada, 11-15 November.

Evans, U.R. (1948), "An Outline of Corrosion Mechanisms, Including the Electrochemical Theory", *Cotroszon Handbook,* H.J. Uhlig (ed.), Wiley, New York.

Fazio, C. et al. (2001), "Compatibility Tests on Steels in Molten Lead and Lead-bismuth", *Journal of Nuclear Materials*, 296, p. 243.

Fazio, C. et al. (2003), "Corrosion Behaviour of Steels and Refracto Metals and Tensile Features of Steels Exposed to Flowing PbBi in the LECOR Loop", *Journal of Nuclear Materials*, 318, p. 325.

Furukawa, T. et al.(2004), "Corrosion Behavior of FBR Candidate Materials in Stagnant Pb–Bi at Elevated Temperature", *Journal of Nuclear Science and Technology*, 41, 3, pp. 265-270.

Furukawa, T. et al. (2004b), "Effect of Oxygen Concentration and Temperature on Compatibility of ODS Steel with Liquid, Stagnant $Pb_{45}Bi_{55}$", *Journal of Nuclear Materials*, 335, pp. 189-193.

Gerasimov, V. and A. Monakhov (1983), *Nuclear Engineering Materials*, Mir Publishers.

Gessi, A. and G. Benamati (2008), "Corrosion Experiments of Steels in Flowing Pb at 500°C and in Flowing LBE at 450°C", *Journal of Nuclear Materials*, Vol. 376, 3, pp. 269-273.

Gibbs, G.B. (1973), "A Model for Mild Steel Oxidation in CO_2", *Oxidation of Metals*, Vol. 7, No. 3, pp. 173-184.

Glasbrenner, H. et al. (2001), "Corrosion Investigation of Steels in Flowing Lead at 400°C and 550°C", *Journal of Nuclear Materials*, 296, p. 237.

Gnecco, F. et al. (2004), "Corrosion Behaviour of Steels in Lead-bismuth at 823 K", *Journal of Nuclear Materials*, 335, pp. 185-188.

Gómez-Briceño, D. et al. (2001), "Behaviour of F82Hmod. Stainless Steel in Lead-bismuth under Temperature Gradient", *Journal of Nuclear Materials*, 296, p. 265.

Gómez-Briceño, D. et al. (2002), "Influence of Temperature on the Oxidation/Corrosion Process of F82Hmod. Martensitic Steel in Lead-bismuth", *Journal of Nuclear Materials*, 303, p. 137.

Gómez-Briceño, D. et al. (2004), *Oxide Formation Efficiency in Stagnant Lead-bismuth*, TECLA report, Deliverable 8, CIEMAT, Madrid, Spain.

Gómez-Briceño, D. (2008), *Critical Review of Materials Corrosion and Experimental Procedures in HLM*, VELLA D22, Deliverable NA D22A, CIEMAT, Madrid, Spain.

Gómez-Briceño, D. (2009), *Guideline Document for HLM Technology*, VELLA D25, Deliverable NA D25, CIEMAT, Madrid, Spain.

Gorynin, V. et al. (1998), "Structural Materials for Power Plants with Heavy Liquid Metals as Coolants", *Proceedings of the Conference Heavy Liquid Metals Coolants in Nuclear Technologie (HCLM-98)*, Vol. 1, p. 120, Obninsk, Russian Federation.

Gorynin, V. et al. (1999), "Structural Materials for Atomic Reactors with Liquid Metal Heat-transfer Agents in the Form of Lead or Lead-bismuth Alloy", *Metal Science and Heat Treatment*, Vol. 41, No. 9-10, pp. 384-388.

Gromov, B.F. et al. (1998), "Designing the Reactor Installation with Lead-bismuth Coolant for Nuclear Submarines: The Brief History - Summarised Operations Results", *Proceedings of the Conference Heavy Liquid Metals Coolants in Nuclear Technologies (HCLM-98)*, Vol. 1, p. 14, Obninsk, Russian Federation..

Gullevsky, V.A. et al. (1998), "Application of Hydrogen/Water Vapor Mixtures in Heavy Coolant Technology", *Proceedings of the Conference Heavy Liquid Metals Coolants in Nuclear Technologies (HCLM-98)*, Volume 2, p. 668, Obninsk.

Hata, K., K. Hara and M. Takahashi (2005), "Experimental Studies on Steel Corrosion in Pb-Bi with Steam Injection", *Progress in Nuclear Energy*, Vol. 47, No. 1-4, pp. 596-603.

Heinzel, A., M. Kondo and M. Takahashi (2006), "Corrosion of Steels with Surface Treatment and Al-Alloying by GESA Exposed in Lead-Bismuth", *Journal of Nuclear Materials*, Vol. 350, pp. 264-270.

Heinzel, A., G. Müller and A. Weisenburger (2013), "Corrosion Behavior of Austenitic Steels in Liquid Lead Containing 10^{-6} wt% and 10^{-8} wt% Oxygen at 400-500°C", *Journal of Nuclear Materials*, Vol. 448,1-3, pp.163-171

Hoseman, P. et al. (2008), "Corrosion of ODS Steels in Lead-bismuth Eutectic", *Journal of Nuclear Materials*, Vol. 373, 1-3, pp. 246-253.

Hosemann, P. et al. (2008b), "Characterization of Oxide Layers Grown on D9 Austenitic Stainless Steel in Lead Bismuth Eutectic", *Journal of Nuclear Materials*, Vol. 375, pp. 323-330.

Hosemann, P. et al. (2008c), "AFM and MFM Characterization of Oxide Layers Grown on Stainless Steels in Lead Bismuth Eutectic", *Journal of Nuclear Materials*, Vol. 376 (3), pp. 289-92.

Hosemann, P. et al. (2008d), "Nano-Indentation Measurement of Oxide Layers Formed in LBE on F/M Steels", *Journal of Nuclear Materials*. Vol. 377, 1, pp. 201-205.

Hosemann, P. et al. (2008e), "Nanoscale Characterisation of HT9 Exposed to Lead Bismuth Eutectic at 550°C for 3 000 h", *Journal of Nuclear Materials*. Vol. 381, pp. 211-215.

Hussey, R.J. and M.J. Graham (1981), "Some Observations on Void Formation in Fe_3O_4 Layers on Fe", *Corrosion Science*, Vol. 21, No. 3, pp. 255-258.

Johnson, A.L. et al. (2006), "Spectroscopic and Microscopic Study of the Corrosion of Iron-Silicon Steel by Lead-bismuth Eutectic (LBE) at Elevated Temperatures", *Journal of Nuclear Materials*, Vol. 350, 3, pp. 221-231.

Kikuchi, K. et al. (2008), "Corrosion Rate of Parent and Weld Materials of F82H and JPCA Steels Under LBE Flow with Active Oxygen Control at 450 and 500°C", *Journal of Nuclear Materials*, Vol. 377, 1, pp. 232-242.

Knebel, J.U., G. Müller and G. Schumacher (1999), "Gas-Phase Oxygen Control Processes for Lead/Bismuth Loops and Accelerator-Driven Systems (ADS)", *Jahrestagung Kerntechnik*.

Kofstad, P. (1987), *High Temperature Corrosion*, Elsevier Applied Science Publishers, Ltd., p. 413.

Kondo, M. et al. (2005), "Metallurgical Study on Erosion and Corrosion Behaviors of Steels Exposed to Liquid Lead-bismuth Flow", *Journal of Nuclear Materials*, Vol. 343, pp. 349-359.

Kondo, M. et al. (2006), "Corrosion of Steels in Lead-bismuth Flow", *Journal Nuclear Science and Technology*, Vol. 43, 2, pp. 107-116.

Kondo, M. and M. Takahashi (2006b), "Corrosion Resistance of Al- and Si-Rich Steels in Lead Bismuth Flow", *Journal of Nuclear Materials*, Vol. 356, pp. 203-212.

Kurata, Y. et al. (2002), "Corrosion Studies in Liquid Pb-Bi Alloy at JAERI: R&D Program and First Experimental Results", *Journal of Nuclear Materials*, 301, p. 28.

Kurata, Y., M. Futakawa and S. Saito (2005), "Comparison of the Corrosion Behavior of Austenitic and Ferritic/Martensitic Steels Exposed to Static Liquid Pb-Bi at 450 and 550°C", *Journal of Nuclear Materials*, 343, pp. 335-340.

Kurata, Y., M. Futakawa and S. Saito (2008), "Corrosion Behavior of Steels in Liquid Lead-Bismuth with Low Oxygen Concentrations", *Journal of Nuclear Materials*, Vol. 373, 1-3, pp. 164-178.

Li, N. et al. (2001), *Corrosion Tests of US Steels in Lead-bismuth Eutectic (LBE) and Kinetic Modelling of Corrosion in LBE Systems*, LA-UR-01-5241, Los Alamos National Laboratory, Los Alamos, New Mexico.

Li, N. (2002), "Active Control of Oxygen in Molten Lead-bismuth Eutectic System to Prevent Steel Corrosion and Coolant Contamination", *Journal of Nuclear Materials*, Vol. 300, pp. 73-81.

Lim, J. et al. (2010), "A Study of Early Corrosion Behaviors of FeCrAl Alloys in Liquid Lead-Bismuth Eutectic Environments", *Journal of Nuclear Materials*, Vol. 407, pp. 205-210.

Long, B. (2003), *International Workshop on Materials for Heavy Liquid Metal Cooled Reactors and Related Technologies (IWMHR)*, Rome.

Machut, M. et al. (2007), "Time Dependence of Corrosion in Steels for Use in Lead-Alloy Cooled Reactors", *Journal of Nuclear Materials*, Vol. 371, pp. 134-144.

Mansani, L., B. Arien and A. Woaye-Hune (2009), "XT-ADS: Feedback to the Designers from Research and from Safety", *International Topical Meeting on Nuclear Research Applications and Utilization of Accelerators (AccApp09)*, Vienna.

Martín-Muñoz, F.J. et al. (2004), "Oxide Layer Stability in Lead-bismuth at High Temperature", *Journal of Nuclear Materials*, 335, pp. 194-198.

Martín-Muñoz, F.J., L. Soler-Crespo and D. Gómez-Briceño (2011), "Assessment of the Influence of Surface Finishing and Weld Joints on the Corrosion/Oxidation Behaviour of Stainless Steels in Lead Bismuth Eutectic", *Journal of Nuclear Materials*, Vol. 416, Issues 1-2, pp. 80-86.

Martinelli, L. et al. (2005), "High Temperature Oxidation of Fe-9Cr Steel in Stagnant Liquid Lead-Bismuth", *Eurocorr2005*, Lisbon.

Martinelli, L. (2007), *Experimental Protocol for Oxide Layers Thickness Measurements*, CEA/DEN/DANS report, NE DPC/SCCME 07-028-A.

Martinelli, L. et al. (2008), "Oxidation Mechanism of a Fe-9Cr-1Mo Steel by Liquid Pb-Bi Eutectic Alloy (Part I)", *Corrosion Science*, Vol. 50 (9), pp. 2523-2536.

Martinelli, L. et al. (2008b), "Oxidation Mechanism of an Fe-9C-1Mo Steel by Liquid Pb-Bi Eutectic Alloy at 470°C (Part II)", *Corrosion Science*, Vol. 50 (9), pp. 2537-2548.

Martinelli, L. et al. (2008c), "Oxidation Mechanism of a Fe-9Cr-1Mo Steel by Liquid Pb-Bi Eutectic Alloy (Part III)", *Corrosion Science*, Vol. 50 (9), pp. 2549-2559.

Martinelli, L. et al. (2008d), "High Temperature Oxidation of Fe-9Cr-1Mo Steel in Liquid Metal", *Materials Science Forum*, Vols. 595-598, p. 519.

Martinelli, L. et al. (2008e), "High Temperature Oxidation of Fe-9Cr-1Mo Steel in Stagnant Liquid Lead-Bismuth at Several Temperatures and for Different Lead Contents in the Liquid Alloy", *Journal of Nuclear Materials*, 376, 3, pp. 282-288.

Martinelli, L. and F. Balbaud-Célérier (2011), "Modelling of the Oxide Scale Formation on Fe-Cr Steel During Exposure in Liquid Lead-bismuth Eutectic in the 450-600°C Temperature Range", *Materials and Corrosion*, 62 (5), pp. 531-542.

Maruyama, T. et al. (2004), "Chemical Potential Distribution and Void Formation in Magnetite Scale Formed in Oxidation of Iron at 823 K", *Materials Science Forum*, Vols. 461-464, pp. 807-814.

Müller, G., G. Schumacher and F. Zimmermann (2000), "Investigation on Oxygen Controlled Liquid Lead Corrosion of Surface Treated Steels", *Journal of Nuclear Materials*, 278, p. 85.

Müller, G. et al. (2002), "Results of Steel Corrosion Tests in Flowing Liquid Pb/Bi at 420-600°C After 2 000 h", *Journal of Nuclear Materials*, 301, p. 40.

Müller, G. et al. (2003), "Control of Oxygen Concentration in Liquid Lead and Lead-bismuth", *Journal of Nuclear Materials*, Vol. 321, p. 256.

Müller, G. et al. (2004a), "Behavior of Steels in Flowing Liquid PbBi Eutectic Alloy at 420-600°C After 4 000-7 200 h", *Journal of Nuclear Materials*, 335, p. 163.

Müller, G. et al. (2004b), *Protection by Restructuring and Alloying Surface Layer by Pulsed Electron Beam Facility*, TECLA report, Deliverable 11.

Rishel, D.M., F.S. Pettit and N. Birks (1991), "Some Principle Mechanisms in the Simultaneous Erosion and Corrosion Attack of Metals at High Temperatures", *Materials Science and Engineering A*, 143, p. 197.

Rivai, A.K. and M. Takahashi (2008), "Compatibility of Surface-Coated Steels, Refractory Metals and Ceramics to High Temperature Lead-bismuth Eutectic", *Progress in Nuclear Energy*, Vol. 50, pp. 560-560.

Rivai, A.K. and M. Takahashi (2010), "Corrosion Characteristics of Materials in Pb-Bi Under Transient Temperature Conditions", *Journal of Nuclear Materials*, Vol. 398, 1-3, pp. 139-145.

Rivai, A.K. and M. Takahashi (2010b), "Corrosion Investigations of Al-Fe-Coated Steels, High Cr Steels, Refractory Metals and Ceramics in Lead Alloys at 700°C", *Journal of Nuclear Materials*, Vol. 398, 1-3, pp. 146-152.

Robertson, J. (1991), "The Mechanism of High Temperature Aqueous Corrosion of Stainless Steels", *Corrosion Science*, 32, No. 4, p. 443.

Sapundjiev, D., S. Van Dyck and W. Bogaerts, (2006), "Liquid Metal Corrosion of T91 and A316L Materials in Pb-Bi Eutectic at Temperatures 400-600°C", *Corrosion Science*, Vol. 48, pp. 577-594.

Schroer, C. et al. (2006), "Oxidation of Steel T91 in Flowing Lead-bismuth Eutectic (LBE) at 550°C", *Journal of Nuclear Materials*, Vol. 356, 1-3, pp. 189-197.

Schroer, C. et al. (2006b), *Quantification of the Degradation of Steels Exposed to Liquid Lead-Bismuth Eutectic*, FZKA Report 7224, Forschungszentrum Karlsruhe, Karlsruhe.

Schroer, C. et al. (2010), "Oxidation Behaviour of P122 and a 9Cr-2W ODS steel at 550°C in Oxygen-Containing Flowing Lead-Bismuth Eutectic", *Journal of Nuclear Materials*, Vol. 398, 1-3, pp. 109-115.

Schroer C. and J. Konys (2010b), "Quantification of the Long-Term Performance of Steels T91 and 316L in Oxygen-Containing Flowing Lead-bismuth Eutectic at 550°C", *Journal of Engineering for Gas Turbines and Power*, 132 (8), pp. 082901-082908.

Shamatko, B.A. and A. Rusanov (2000), "Oxide Protection of Materials in Melts of Lead and Bismuth", *Materials Science*, Vol. 36, No. 5, pp. 689-700.

Sheir, L.L., R.A. Jarman and G.T. Burstein (eds.) (1994), "Metal/Environment Reactions", *Corrosion*, Chapter 2.9, Butterworth-Heinemann, Oxford, Vol. 1, 3rd edition.

Soler, L., F.J. Martín and D. Gómez-Briceño (2001), "Short-Term Static Corrosion Tests in Lead-bismuth", *Journal of Nuclear Materials*, 296, p. 273.

Soler-Crespo, L. et al. (2004), "Corrosion of Stainless Steels in Lead-bismuth Eutectic Up to 600°C", *Journal of Nuclear Materials*, 335, pp. 174-179.

Song, Y. et al. (2008), "The Lead and LBE Corrosion Research at KAERI", *Proceedings of the Workshop on Structural Materials for Innovative Nuclear Systems (SMINS)*, Karlsruhe, Germany, pp. 371-379, OECD/NEA, Paris.

Staudhammer, P.K. (1992), *Materials Compatibility and Corrosion Issues for Accelerator Transmutation of Waste*, LA-1227-MS, Los Alamos National Laboratory, Los Alamos, New Mexico.

Steiner, H. et al. (2008), "Modeling of Oxidation of Structural Materials in LBE Systems", *Journal of Nuclear Materials,* Vol. 374, 1-2, pp. 211-219.

Stott, F.H. (1987), "The Protective Action of Oxide Scales in Gaseous Environments at High Temperature", *Reports on Progress in Physics*, 50, p. 861.

Takaya, S. et al.(2009), "Corrosion Behavior of Al-Alloying High Cr-ODS Steels in Lead-Bismuth Eutectic", *Journal of Nuclear Materials,* Vol. 386-388, pp. 507-510.

Takaya, S. et al.(2010), "Corrosion Resistance of Al-Alloying High Cr-ODS Steels in Stagnant Lead-Bismuth", *Journal of Nuclear Materials*, Vol. 398, 1-3, pp. 132-138.

Taylor, M.R. et al.(1980), "The Mechanism of Corrosion of Fe-9%Cr Alloys in Carbon Dioxide", *Oxidation of Metals*, Vol. 14, No. 6, p. 499.

Takahashi, M. et al. (2002), "Experimental Study on Flow Technology and Steel Corrosion of Lead-bismuth", *Proceedings of the 10th International Conference on Nuclear Engineering (ICONE10)*, Arlington, Virginia.

Tedmon, C.S., Jr. (1966), "The Effect of Oxide Volatilization on the Oxidation Kinetics of Cr and Fe-Cr Alloys", *Journal of the Electrochemical Society*, 113, pp. 766-768.

Tomlinson, L. (1981), "Mechanism of Corrosion of Carbon and Low Alloy Ferritic Steels by High Temperature Water", *Corrosion-NACE*, Vol. 37, No. 10, pp. 591-596.

Töpfer, J., S. Aggarwal and R. Dieckmann (1995), "Point Defects and Cation Tracer Diffusion in $(Cr_xFe_{1-x})_{3-\delta}O_4$ Spinels", *Solid State Ionics*, 81 (2), pp. 251-266.

Tortorelli, P.F. et al. (1987), "Metals Handbook", *Corrosion*, 9th Edition, Vol. 13.

Tortorelli P.F. and Pawel S.J. (2003), "Corrosion by Liquid Metals", *Corrosion: Fundamentals, Testing and Protection*, ASM Handbook Vol. 13A, ASM International, pp. 129-134.

VELLA (2008a), *Experimental Results on Corrosion Behaviour of Al, ODS and Structural Steels in Pb as a Function of Temperature and Oxygen Concentration*, VELLA Deliverable D33, FZK, CIEMAT, CNR-IENI.

VELLA (2008b), *The Experimental Results on Candidate Steels Corrosion Rate and Cracking Sensitivity in Liquid Lead*, VELLA Deliverable D37, A. Kobzová, UJV.

VELLA (2009a), *Corrosion Behaviour of the T91 Martensitic Steel and PM2000 ODS Steel in Lead Analysis of the Results Obtained in the frame of The European Project "VELLA"*, VELLA Deliverable D36, L.A. Pichard, CEA.

VELLA (2009b), *Final Report on the Experimental Results on Corrosion Behaviour of Al, ODS and Structural Steels in Pb as a Function of Temperature and Oxygen Concentration*, VELLA Deliverable D34, F.J. Martín-Muñoz, CIEMAT.

Vogt, J.B. et al. (2007), "Understanding the Liquid Metal Assisted Damage Sources in the T91 Martensitic Steel for Safer Use of ADS", *Engineering Failure Analysis*, Vol. 14, 6, pp. 1185-1193.

Wagner, C. (1933), "Beitrag zur Theorie des Anlaufvorgangs", *Zeitschrift für Physikalische Chemie B*, 21, p. 25.

Weeks, J.R. and D.H. Gurinsky (1958), *Liquid Metals and Solidification*, American Society for Metals, pp. 106-161.

Weeks, J.R. and H.S. Isaacs (1973), "Corrosion and Deposition of Steels and Nickel-Base Alloys in Liquid Sodium, Advances in Corrosion Science and Technology", M.G. Fontana and R.W. Staehle (eds.), Vol. 3, pp. 1-67.

Weeks, J.R. (1997), "Compatibility of Structural Materials with Liquid Lead-bismuth and Mercury", *Proceedings of the Symposium on Materials for Spallation Neutron Sources*, Orlando, FL.

Weisenburger, A. et al. (2006), "Behaviour of Chromium Steels in Liquid Pb-55.5Bi with Changing Oxygen Content and Temperature", *Journal of Nuclear Materials*, Vol. 358, 1, pp. 69-76.

Weisenburger, A. et al. (2008), "T91 Cladding Tubes with and Without Modified FeCrAlY Coatings Exposed in LBE at Different Flow, Stress and Temperature Conditions", *Journal of Nuclear Materials*, Vol. 376, 3, pp. 274-281.

Weisenburger, A., L. Mansani, G. Schumacher and G. Müller (2014) "Oxygen for protective oxide scale formation on pins and structural material surfaces in lead-alloy cooled reactors", *Nuclear Engineering and Design*, Vol. 273, pp.584-594.

Weisenburger, A. et al. (2011), "Long Term Corrosion on T91 and AISI1 316L Steel in Flowing Lead Alloy and Corrosion Protection Barrier Development: Experiments and Models", *Journal of Nuclear Materials*, Vol. 415, Issue 3, pp. 260-269.

Yachmenyov, G.S. et al. (1998), "Problems of Structural Materials. Corrosion in Lead-Bismuth Coolant. The Problem of Technology of the Heavy Liquid Metal Coolants (Lead, Lead-bismuth)", *HLMC-98*, pp. 133.

Yeliseyeva, O., V. Tsisar and G. Benamati (2008), "Influence of Temperature on the Interaction Mode of T91 and AISI 316L Steels with Pb-Bi Melt Saturated by Oxygen", *Corrosion Science*, Vol. 50, 6, pp. 1672-1683.

Zhang, J. and N. Li (2005), "Oxidation Mechanism of Steels in Liquid-Lead Alloys", *Oxidation of Metals*, 63, pp. 353-381.

Zhang, J., N. Li and Y. Chen (2005b), "Dynamics of High-Temperature Oxidation Accompanied by Scale Removal and Implications for Technological Applications", *Journal of Nuclear Materials*, Vol. 342, 1-3, pp. 1-7.

Zhang, J. and N. Li (2007), "Analysis on Liquid Metal Corrosion-Oxidation Interaction", *Corrosion Science*, 49, pp. 4154-4184.

Zhang, J., R. Kapernick and T.F. Marcille (2008), "Corrosion of Materials by Liquid NaK Coolant in a Nuclear Power Systems", *Nuclear Science and Engineering*, 160, pp. 75-97.

Zhang, J. (2009), "A Review of Steel Corrosion by Liquid Lead and Lead-bismuth", *Corrosion Science*, Vol. 51, pp. 1207-1227.

7. Effect of lead-bismuth eutectic and lead on mechanical properties of martensitic and austenitic steels*

7.1 Introduction

The use of heavy liquid metals (HLM), and especially of lead-bismuth eutectic (LBE) or lead for accelerator-driven systems (ADS) and lead-cooled (Pb) or lead-alloy-cooled (primarily Pb-Bi) fast reactor (FR) concepts of generation IV requires an assessment of their compatibility with structural materials. Their deployment requires that the materials' compatibility issue be resolved, with and without irradiation, either under the mixed proton-neutron spectrum typical of the spallation source of an ADS in the one case, or under the fast neutron spectrum typical of an FR in the other case. The irradiation effects on structural materials in contact with HLM are the subject of a dedicated chapter.

The experience gained with liquid metal-cooled FRs in industrialised countries should not be ignored; however, practically all these reactors have used sodium as their coolant, with the exception of some of the Russian fast reactors. Therefore and unfortunately, the expertise on compatibility of stainless steels with sodium is not transferable to lead and lead alloys, due to the significant differences in their physics and metallurgical properties (Gorse-Pomonti, 2007).[1]

Certainly, the older literature dedicated to the mechanical properties of steels, from carbon steels to high Cr steels, in contact with lead and lead alloys is essentially of Russian origin: the research on HLM technology will soon cover one century, early on oriented toward developing a fundamental understanding of the liquid metal embrittlement (LME) mechanisms since the Rebinder discovery (1928), then largely R&D oriented at the beginning of the fifties with the development of submarine propulsion reactors in parallel with two full scale ground test reactor facilities, using LBE as a coolant (Gromov, 1997).

In a European country like France, that opted early for the sodium-cooled FR concept with Rapsodie, Phénix, then Superphénix, the R&D continued in parallel on other reactor concepts, for example the molten salt reactor (MSR) concept between 1970 and 1983, using a cooling system operated by direct contact between the salt and the molten lead. In this context, a harmful effect of reducing lead[2] on the tensile properties of Chromesco 3 and EM12 ferritic steels was noticed between 300 and 350°C (Broc, 1983), corroborating an earlier Japanese study (Tanaka, 1969). The possible influence of lead on the fatigue strength of these steels remained unknown. In the United States, a Pb-Bi cooled reactor was considered in the early fifties, and then abandoned in favour of sodium cooling (Manly, 1954). In Japan, as in Europe and in the United States, the sodium-cooled FR option was selected, with the related R&D for JOYO and MONJU. In Japan, as in many

* Chapter leads: J-B. Vogt and I. Proriol-Serre. Thanks are expressed to D. Gorse, author of the first version and who should be considered as co-lead due to her meaningful contribution.

1. Voluntarily omitting the difference in the nuclear (activation) and neutronic properties between Na and Pb or LBE, which is well outside the scope of the present chapter.
2. Lead made with reduced oxygen by introduction of a deoxidising agent (Zr, Ti, etc.) and bubbling of an Ar-5%H_2 mixture, since the OCS technology developed in USSR was not yet redeveloped in Europe.

other countries, studies dedicated to specific solid/liquid model systems (Mae, 1991) can also be found in the literature, with the aim of improving the understanding of LME, or of solving various industrial problems.[3] The Japanese literature on mechanical resistance of materials in contact with LMs is thus varied, ranging from basic papers directed toward the understanding of LME (Ina, 2004) to patents related to materials resistant to LME (Kanetani, 1992), to the evaluation of the resistance to embrittlement of metals in the environment (Funaki, 1993).

It is a fact that, in R&D devoted to nuclear systems using corrosive lead or LBE as a coolant, compatibility is generally associated with reduced or controlled corrosiveness (Loewen, 2003). Lead- or LBE-induced corrosion must be investigated in detail to understand mechanisms and evaluate kinetics. This allows one to assess predictive models and provide research routes for surface treatment in order to ensure long-term safe operation of a future reactor.

In this context, the present chapter is an update of that written by D. Gorse for the first edition of the handbook. It contains a review of the published research on the effect of LBE or lead on the mechanical behaviour of T91 martensitic steel and to some extent of the 316L austenitic stainless steel, which seem to be the most suitable materials for such systems as revealed in the framework of the EUROTRANS[4] programmes FP6 and FP7.

To provide information that is as complete as possible on ferritic/martensitic steels in contact with lead or lead alloys, the results of some studies carried out as part of the fusion programmes on related steel grades like MANET, OPTIFER and 1.4914 in contact with Pb-17Li or even lithium and also in contact with LBE, are also included when available. Since information on 316L in contact with lead or LBE is lacking in some areas, the results of some studies conducted either as part of liquid metal fast breeder reactor (LMFBR) programmes on type 316 steel in contact with sodium, or as part of the spallation neutron source projects on type 316 steel in contact with mercury, and if possible on 316 type steel in contact with lead or LBE, are also included when available. The main difference between the present chapter and the previous one is the determination of mechanical properties in low oxygen LBE.

In this chapter, mechanical properties on smooth and notched specimens are presented and discussed. We start first with the monotonic behaviour investigated by tensile tests and by small punch tests, mainly to point out the factor promoting LME. We then document the effects of toughness, creep and fatigue which are properties necessary to assess the durability and reliability of materials. The focus will be on T91 steels and 316L stainless steels, as base materials or in the welded form, in contact with LBE or lead. Some results on coated materials are also presented. This chapter is organised as follows:

- Section 7.2 focuses on the different manifestations of liquid metals on mechanical properties. It is subdivided into four parts. Section 7.2.1 is dedicated to wetting, which is one of the two main requirements for occurrence of LME, and today the only one for which there is some data available on *real* systems, in addition to an abundant theoretical literature. Sections 7.2.2, 7.2.3 and 7.2.4 are devoted respectively to the definition of LME, of liquid metal-assisted damage and of environment-assisted cracking.
- Section 7.3 is a short and introductive section that mentions the origin of the study of LME of T91 steel in contact with LBE or lead. It includes the list of chemical compositions of the steels mentioned in this chapter.

3. For steel makers, LME studies are conducted to improve the machinability of steels, to understand the crack failure of hot-dip galvanised steel structures, or to develop weldability of metallic alloys.
4. EUROTRANS: European Research Programme for Transmutation of High-Level Nuclear Waste in an Accelerator-Driven System, Contract No. FI6W-CT-2004-516520.

- The effect of lead or LBE on the tensile properties of T91 is now very well documented, thanks to the European TECLA and MEGAPIE-TEST[5] programmes of FP5 and to the DEMETRA programme of FP6.[6] The results are summarised in Section 7.4. The tensile behaviour of 316 type stainless steel in contact with LBE or lead is less documented.
- Section 7.5 reports the results of the mechanical behaviour of steels in contact with LBE obtained by the small punch test (SPT). This technique is popular in the nuclear field, especially for irradiated materials because it requires a small amount of material. In addition, the stress field is a little bit different to that in tensile test.
- Fracture toughness data were missing. But now, a great amount of effort has been made to determine toughness values. This will be presented in Section 7.6.
- The effect of lead or LBE on the creep properties of both T91 and 316L were also scarce. Now, fresh data presented in Section 7.7 are available as well secondary creep rate values such as creep to fracture times.
- Section 7.8 is devoted to fatigue behaviour in LBE. Both crack initiation and crack propagation tests provide information on low cycle fatigue resistance and fatigue crack growth rate. The notion of increasing fatigue resistance by coating is included.
- Section 7.9 is dedicated to recommendations for testing procedures.
- A short conclusion is provided in Section 7.10.

List of abbreviations

ADS	Accelerator-driven systems
CGR	Crack growth rate
EAC	Environmentally assisted cracking
EPMA	Electron probe microscopy analysis
FR	Fast reactor
HLM	Heavy liquid metal
LCF	Low cycle fatigue
LMAD	Liquid metal-assisted damage
LME	Liquid metal embrittlement
OCS	Oxygen control system
LMFBR	Liquid metal fast breeder reactor
MSR	Molten salt reactor
PVD	Physical vapour deposition
SPT	Small punch test
SMIE	Solid-metal-induced embrittlement
UHV	Ultra-high vacuum
XPS	X-ray photoelectron spectrometry

5. TECLA: Technology, Thermal-hydraulics for Lead Alloys, European programme funded by the EU 5th Framework Programme.
6. DEMETRA: Development and Assessment of Structural Materials and Heavy Liquid Metal Technologies for Transmutation Systems, is one of five technical domains of the EUROTRANS programme funded by FP6.

7.2 The different manifestations of liquid metals on mechanical properties

The degradation of mechanical properties by liquid metals can be classified as liquid metal embrittlement (LME), liquid metal-assisted damage (LMAD) and environmentally assisted cracking (EAC). It implies a physico-chemical and mechanical process, the interpretation of which is largely based on the wetting concept. For this reason a discussion of the wetting process is presented first in this section. Then LME, LMAD and EAC are discussed individually, respectively in Sections 7.2.2, 7.2.3 and 7.2.4.

7.2.1 Wetting: From ideal to real metallic systems

The study of the wetting, i.e. of the spreading of a liquid on a solid was first reported at the beginning of the 19th century with Laplace and Young (1805). From the theoretical point of view, a renewal of interest was initiated by de Gennes in the early 1980s (Leger, 1992; de Gennes, 2002). From the practical point of view, there are a number of applications,[7] which largely benefit from an improved understanding of the wetting phenomena, allowing for predictions of the interface reactions when a liquid is put into contact with a solid phase.

While theoretical understanding has improved since Young, it is worth emphasising that *real* solid/liquid (S/L) metal systems remain too complex to allow for predictions of the spreading of one oxidisable metal alloy onto another metal alloy of different electronic and physico-chemical properties, thus exhibiting differing oxidation properties (see Chapters 2, 3 and 4). Consequently, in most cases, experimental work is required in conditions that mimic the *real* situation of interest.

In the following, we shall first consider ideal S/L systems, then non-interacting metal-metal systems, followed by interacting S/L systems, including ceramic-metal systems. Finally we conclude with a discussion of the wettability of steels by HLM.

Ideal solid/liquid systems

Ideally, for a homogeneous and smooth surface, only partially wetted by a "simple" liquid, a liquid drop, small enough to neglect the gravity effects, does not spread and therefore retains a spherical shape characterised by the contact angle between the liquid-vapour interface and the solid-liquid interface at the contact line where these two interfaces merge. The equilibrium contact angle θ_E is determined by the values of the surface tensions between the three phases. Each of these surface tensions is a force per unit length of the contact line, tangential to the interface, tending to retract the interface. At mechanical equilibrium, the horizontal components of these forces balance (Figure 7.2.1, left). This is the Young law:

$$\cos\theta_E = \left(\gamma_{sv} - \gamma_{sl}\right)/\gamma_{lv} \tag{7.1}$$

with γ_{sv}, γ_{sl}, γ_{lv} being respectively the solid-gas, solid-liquid and liquid-gas surface tensions. Eq. (7.1) can be rewritten in terms of the spreading coefficient $S = \gamma_{sv} - (\gamma_{sl} + \gamma_{lv})$, as:

$$S = \gamma_{lv}\left(\cos\theta_E - 1\right) \tag{7.2}$$

showing that θ_E can be defined only in case of partial wetting with $S < 0$.

Total wetting is characterised by $S > 0$ with the drop spontaneously spreading and tending to cover the solid surface (Figure 7.2.1, right).

7. Such as paints, lubrication, gluing, cosmetology, without forgetting metallurgical processes like hot dip coating (Ebrill, 2000).

Figure 7.2.1: The mechanical equilibrium of the solid-liquid-vapour triple line determines the value of θ_E (left); liquid metal drop spreading completely on a solid substrate ($S > 0$) or not ($S < 0$) until attainment of the equilibrium contact angle θ_E (right)

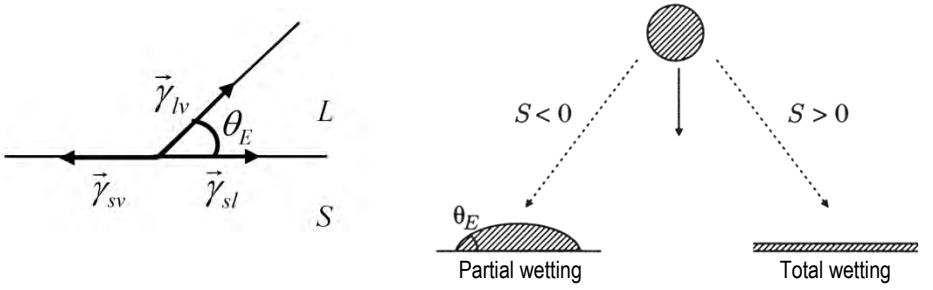

In less ideal situations, taking into account the heterogeneities, the chemical contamination and the roughness of the solid surface, one does not measure the equilibrium contact angle θ_E of Young's law, but at best a steady-state contact angle depending on the history of the system. If the liquid-vapour interface has been obtained by advancing the liquid (after spreading of a drop), the contact angle has a value, θ_A, larger than the equilibrium value θ_E. The advancing contact angle θ_A is defined as the threshold value beyond which the contact line begins to move when the liquid advances (Figure 7.2.2). If, on the contrary, the liquid-vapour interface has been obtained by receding the liquid (by aspiration or retraction of the drop), the measured contact angle θ_R is smaller than the equilibrium contact angle $\theta_E \cdot \theta_R$ is defined as the limit value without moving the contact line by aspiration of the drop (Figure 7.2.2). Intuitively, the advancing contact angle θ_A is larger than the equilibrium contact angle θ_E, which is again larger than the receding contact angle θ_R: $\theta_R < \theta_E < \theta_A$.

Figure 7.2.2: Advancing θ_A and receding θ_R contact angles

The difference $\theta_A - \theta_R$ (> 0) informs on how far the surface state is from ideal. The hysteresis $|\theta_A - \theta_R|$ can reach tens of degrees depending on the surface conditions, whether it is contamination or roughness. The prediction of the wetting hysteresis of a randomly rough *real* surface will always be difficult due to the lack of determination of the relevant size of defects on/in the surface. Note that one knows today that the triple line can stick at very small defects of micrometric size (Jonghe, 1995). This suggests that if one wants to classify the wettability of *real* surfaces by a given liquid, the experimental procedure must be extremely rigorous (de Gennes, 2002).

Non-interacting metal-metal systems

This condition is idealised by ignoring the potential influence of impurities and especially oxygen at the interface, *after* de Gennes (2002). The spreading coefficient S is determined by the respective Van der Waals interactions in both phases in contact and at the interface.

S can thus be re-written as:

$$S = V_{sl} - V_{ll} \tag{7.3}$$

with V_{sl} and V_{ll} being respectively the Van der Waals energy at the S/L interface and in the liquid phase. Wetting will be generally good and even complete if the liquid is less polarisable than the solid. Note that Eq. (7.3) describes a scenario with no electronic and ionic charge transfer at the S/L interface. At the macroscopic scale, this means no mass transfer between two immiscible phases (no oxidation, no corrosion reactions).

For interacting S/L systems (e.g. ceramic-metal)

In this case, so-called reactive wetting occurs by successive stages accompanied by interfacial reactions, changing the *de facto* nature of the interface. Dynamic non-equilibrium wetting occurs with the spreading rate of the initially non-interacting system, leading to determination of a first quasi-equilibrium contact angle, followed by a modification of the spreading rate due to interfacial reactions, until attainment of an equilibrium contact angle at the interface between new phases of *a priori* different composition, structure and properties (Nakae, 1992). In case of reactive wetting, the contact angle obeys the empirical law:

$$\cos\theta_{\min} = \cos\theta - \frac{\Delta\gamma_r}{\gamma_{lv}} - \frac{\Delta G_r}{\gamma_{lv}} \tag{7.4}$$

with $\Delta\gamma_r$ and ΔG_r being respectively the change of interfacial energy brought about by the interfacial reaction(s) and the change in free energy per unit area released by the reaction of the material contained in the immediate vicinity of the metal substrate interface (Espié, 1994). It has been proposed that spreading occurs because ΔG_r is at least partially transformed to interfacial energy (Naidich, 1981). Note that until now there is no generally accepted theory capable of describing reactive wetting satisfactorily. As noted above, experimental work is necessary for each interacting S/L system of interest. However, as far as ceramic-metal model systems are concerned, equilibrium phase diagrams are available and although they do not predict the wetting behaviour they at least help to explain the observed wetting behaviour.

Interacting steel/HLM systems

For interacting steel/HLM systems, like T91-LBE and T91-lead, or 316L-LBE and 316L-lead couples, the following points are immediately noticeable:

1) It is very difficult to predict the wettability of a Cr-containing steel (like T91, 316L…) by molten HLMs (Pb, Pb-55Bi, Pb-17Li, Hg…) and to verify *a posteriori* that a wetting angle, if measurable (Chatain, 1993), is acceptable, since research on the equilibrium phase diagram for such multi-component systems is very new. The reader should consult the studies on the Bi-Fe-Hg-O-Pb quinary systems or on the Bi_2O_3-Fe_2O_3 pseudo-binary system performed by Maitre (2002, 2004, 2005). To be more precise, it is impossible, today, to predict whether lead and/or bismuth will form stable phases with one of the components of the T91 steel substrate (essentially Fe and/or Cr), if and how reactive wetting will occur. However, XPS analysis of the oxidised T91-lead interface has revealed the presence of lead at the steel/oxide interface (Gamaoun, 2003).

2) Being unpredictable, the wettability of steels (T91, 316L) by lead, LBE and other liquid metals must be determined in each experimental situation, as a function of the composition and structure of the interfacial oxide film (Medina, 2008). It is once again worth emphasising that a meaningful steady-state contact angle will not be obtained if the surface state and overall experimental procedure are not rigorously controlled, according to the recommendations of Section 7.8.[8]

8. See e.g. the influence of microscopic defects on the pinning of the triple line (Leger, 1992).

3) It is generally observed that an oxidised metal or metal alloy is at most partially wetted ($\theta_E < 90°$) or poorly wetted ($90° \leq \theta_E \leq 130°$) by a liquid metal. The tendency to spreading can be estimated if one knows the value of the liquid-vapour surface tension of the LM of interest in contact with the steel surface. Several measured values for the surface tension of liquid metals are listed in Table 7.2.1.

   For example, considering T91 steel or, more specifically, some Russian steel grades with a significant Si content (from 0.4 to 1.3 wt.%), a plausible hypothesis is that for some temperatures and oxygen activities, the uppermost surface layers of the oxidised steel will be essentially a silicon oxide. Considering that the surface tension of SiO_2 should be of the order of 150 mN/m, no wetting of the steel by Bi, Pb or Hg is expected based on the high values of surface tensions reported in Table 7.2.1.

4) As of this date, there are few reliable studies concerning the wetting of lead or LBE on T91 steel. On a diamond-polished T91 steel specimen, a contact angle of 126±5° was found at 380°C with 99.9999% pure lead by using a sessile drop set-up installed in an ultra-high vacuum (UHV) chamber (Lesueur, 2002). This contact angle did not change whatsoever with the annealing time or the volume of the lead drop. This result is consistent with the presence of a $FeCr_2O_4$ oxide film onto the T91 steel surface. These results have been corroborated by other research performed on the T91-lead system at 450°C by Ghetta (2001) (see Figure 7.2.3).

Table 7.2.1: Surface tension of some liquid metals at the melting point or just above in vacuum or under rare gas (He, Ar, etc.), with exception of Pb-55%Bi for which the temperature of the measurement is indicated

The surface tension is given in mN/m (= dyne/cm)

Potassium	118	Passerone (1998)
Sodium	$191 \leq \gamma_{Na} \leq 205$	Handbook (1966)
Bismuth	$376 \leq \gamma_{Bi} \leq 390$	Handbook (1966)
Bismuth	$370 \leq \gamma_{Bi} \leq 410$	Novakovic (2002)
Bismuth	389	Passerone (1998)
Lithium	399	Passerone (1998)
Lead	$450 \leq \gamma_{Pb} \leq 480$	Handbook (1966)
Lead	471	Passerone (1998)
Lead	$443 \leq \gamma_{Pb} \leq 480$	Novakovic (2002)
Lead-55%Bismuth	406 at 350°C	Novakovic (2002)
Lead-55%Bismuth	391 at 500°C	Pokrovskii (1969)
Mercury	$435 \leq \gamma_{Hg} \leq 485$	Handbook (1966)
Mercury	498	Passerone (1998)
Magnesium	577	Passerone (1998)

As shown above, the oxidised T91 steel is poorly wetted by lead in the 380-450°C range. Certainly, wetting studies of T91 and 316L steel in either "reducing" or "oxidising" lead and LBE, covering the 450-600°C temperature range would be of interest in the future.

Long-term ageing in flowing and even stagnant HLM may modify the surface state, with successive phases of stability/instability of the surface oxide. Correlatively a non-wetting to wetting "transition" could occur, with consequences on the potential damages due to the HLMs.

Figure 7.2.3: Lead drops on T91 steel after 15 days exposure to a reducing stagnant lead bath under OCS at 450°C

Note that the contact angles θ_E are larger than 90°, and approach 130°

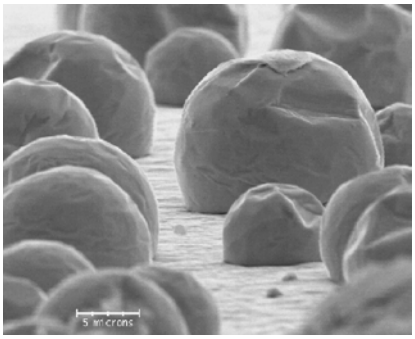

7.2.2 Definition and criteria of occurrence of LME

Slight differences between the definitions of LME can be found in the literature. The reader should return to the review papers on LME by Rostoker (1960), Westwood (1963), Kamdar (1973), Nicholas (1979) and Gordon (1982), to the recent models reviewed by Joseph (1999), and to the point of view of Glickman (2000). The very important former USSR literature was stimulated by Academician P.A. Rebinder, since its discovery in 1928. A new field of research, referred to as "physico-chemical mechanics", headed by Rebinder, was started in 1954 and lasted until the end of the twentieth century… (Likhtman, 1954, 1958, 1962; Shchukin, 1977, 1999).

The following definition is proposed: LME is the loss of ductility of a normally ductile metal or metallic alloy when stressed in contact with a liquid metal that can result in brittle fracture.

LME is considered as a particular type of case of brittle fracture, intergranular (IG) or transgranular (TG), by cleavage that occurs in the absence of an inert environment and at low temperature.[9] LME is accompanied by little or no penetration of the embrittling atomic species into the solid metal (Kamdar, 1973). In other words, strictly speaking a time and temperature-dependent fracture process will not be considered as a manifestation of LME.

In this line, corrosion or diffusion-controlled grain boundary penetration of a solid metal by a liquid metal that occurs under tensile stress tending to zero or even stress independent,[10] which characterises a limited number of well-known metallic couples like Al-Ga or Zn-Hg, is considered as liquid-metal-induced damage, irrelevant in the present chapter.

LME failure occurs by nucleation of a crack at the wetted surface of a solid and its subsequent propagation into the bulk until ultimate failure. Work is still strongly needed to clarify this very old and tricky problem in physical metallurgy. Single crystals can be susceptible to LME (Likhtman, 1962). In this case, a model including all physico-chemical and metallurgical aspects, from initiation to intermittent crack growth (Goryunov, 1978) until final rupture, is still strongly missing. This is also the case of *real* materials, in spite of the potentially pre-existing crack embryos. Today, for *real* materials prone to LME, the main issue is why and how some micrometric or nanometric cracks remain stable whereas others (at least one), made unstable, will develop under the influence of the embrittling metal atoms filling the crack until the crack tip (Clegg, 2001; Ina, 2004). In some cases,

9. High-temperature liquid metal embrittlement is not considered here.
10. And the related macroscopic phenomenon of grain separation and decohesion.

crack propagation is also found spasmodic in polycrystals (Abramov, 1994). A crucial issue is why and how the presence of embrittling metal atoms accelerates the crack kinetics (Glickman, 2000). Note that the embrittling metal phase, often considered as a macroscopic liquid controlling the crack propagation (Robertson, 1966) is also sometimes considered as a "quasi-liquid" when approaching the crack tip area (Rabkin, 2000). In short, this means that, in the future, a multi-scale modelling approach will be necessary to account for all LME failures. This is not the scope of this chapter. However, this had to be emphasised here, as one of the aims of this chapter is to examine the susceptibility to LME of some new systems with respect to the currently available literature reviews (Nicholas, 1979, 1981, 1982).

The prerequisites for LME are listed below:

1) Intimate or direct contact at the atomic scale between the solid and liquid metal phases, a concept classically interpreted as wetting.
2) Applied stress sufficient to produce plastic deformation, even if the required deformation may be produced, on a microscopic scale, at stresses much below the engineering yield point.
3) The existence of stress concentrators or pre-existing obstacles to the dislocations motion. This requirement is a matter of controversy, and is not considered as important as the two criteria mentioned above.

In the discussion, we shall come back to the concept of wetting, in general considered macroscopically and thermodynamically. It will appear that the behaviour of structural materials in contact with liquid metals can be rationalised only if the notions of reactive and non-reactive wetting are properly discriminated. Most often, assumptions will be made to produce consistency between the various literature sources.

A widely accepted explanation of the LME failure is based on the Griffith criterion establishing the fracture stress σ_F for crack propagation (Griffith, 1920), modified to take into account the Rebinder effect, i.e. the reduction of the surface free energy, γ_{sl}, by adsorption of a liquid metal with respect to an inert environment (Rebinder, 1928). σ_F is written as follows:

$$\sigma_F = \sqrt{\frac{E\,\gamma_{sl}}{2c}} \tag{7.5}$$

where E is the Young modulus, and c is the crack dimension or its radius in case of an internal flaw as shown in Figure 7.2.4 (Griffith, 1920). Eq. (7.5) supposes that the change in stored elastic strain energy is entirely used in the fracture process to create fresh fracture surfaces.

Figure 7.2.4: Flat crack, of length 2c and width 2r, in a sheet, subject to a tensile stress σ, perpendicular to the crack length

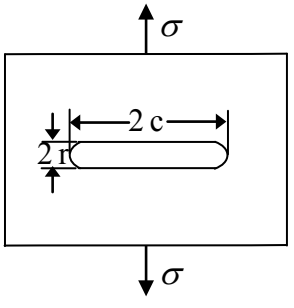

In *real* situations, rupture does not proceed as a result of the development of an elastic microcrack since a crack cannot be stable in an ideal lattice; as soon as it appears, it will develop at a rate of the order of the sound velocity throughout the whole crystal, if there is no barrier to its development. Assuming that a stable crack serves as a stress concentrator, this crack already exists in the deformed lattice. Thus plastic deformation first occurs, and only after a stable crack may appear and survive at the so-called subcritical stage, so long as the stress intensity factor *K*, written $K = Y\,\sigma\sqrt{\pi c}$ with *Y* being a geometric correction factor and *c* the crack length, does not attain the threshold $K_{C,LME}$.

In *real* situations, Rebinder and Shchukin (1972) proposed to include the plastic deformation of the material accompanying crack growth, and to write a critical fracture stress as:

$$\sigma_c = \mu\left(E/c\right)^{1/2}\left(\gamma_p + \gamma_{sl}\right)^{1/2} \tag{7.6}$$

where μ, *E*, γ_p and γ_{sl} are respectively a proportionality coefficient, the Young modulus, a contribution to the plastic deformation and the solid-liquid interfacial free energy defined above. This expression is still the central point of all Russian models of LME. The correctness of Eq. (7.6) was previously questioned by Popovich (1979). At this point it is worth recalling that, until now, in the literature, there has been no analytical expression of the fracture stress, accounting for the energy to create a new, fresh surface wetted by a liquid metal and the plastic energy to form the plastic zone around the crack tip.

The consequences of metal adsorption on softening or strengthening of the surface layers is still a matter of discussion in metallurgy in the absence of a universal modelling of dislocation-atomic impurities interactions and consequences on plastic flow.

It should be noted that the necessary condition for LME to occur of "intimate contact at the atomic scale between the solid and liquid metal phases", which can be reformulated as the metal adsorption condition due to Rebinder, implicates various physic-chemical macroscopic processes that include: *i)* dissolution and formation of de-alloyed layers possibly brittle (as in SCC modelling) in the case of corrosive LM; *ii)* inter-atomic mixing and formation of surface alloys whose consequences depend on the SM/LM system in case of limited solubility between the two metallic phases, a concept that may be interpreted diversely; *iii)* no exchange, at the atomic scale, between the two solid and liquid phases, considered immiscible, which is rigorously impossible to prove experimentally.

7.2.3 Liquid-metal-assisted damage (LMAD)

As opposed to LME, LMAD refers to an effect of liquid metal that accelerates the fracture without any change in the fracture mode. No corrosive effect occurs during LMAD.

The prerequisites for LMAD are the same for those listed previously for LME.

7.2.4 Environment-assisted cracking

Environmentally assisted cracking refers to the premature and catastrophic failure of a material in the simultaneous presence of a tensile stress and an even possibly an only mildly corrosive environment.

The prerequisites for EAC are the following:

1) Liquid-metal-induced corrosion (LMC), that may be localised, intergranular or uniform, or to the contrary that may lead to the growth of an oxide film at the solid metal surface, is considered as a main requirement for occurrence of EAC. As indicated above, the corrosiveness of the LM may be very limited, affecting only the superficial solid layers.
2) Plastic deformation, interacting with corrosion, characterises EAC at all stages of the process.

It is worth recalling that corrosion and consequently EAC are time-dependent. Therefore a liquid-metal-induced degradation of the mechanical properties that will be indubitably a function of the ageing time in the LM will be considered as a case of EAC in the following discussion of the data in Section 7.4. Let us note that the crack velocity in EAC never attains the values reported in LME, which may attain 10^{-1} m/s for some embrittling couples (Glickman, 2000).

Nevertheless, so long as LME, LMAD and EAC are not totally understood, which is the situation today, and as long as the wetting concept intervening in LME is defined macroscopically, and in case there is some doubt about the fracture surface, corroded or not, wetted or not, it may be that the fracture of a material in contact with a liquid metal will be considered as a manifestation of LME, LMAD or EAC depending on the author.

In order to discriminate properly between these related phenomena, EAC, LMAD and LME, it is essential to properly characterise the surface state in contact with the LM phase, at the appropriate scale. Once past this crucial phase, the metallurgical and mechanical parameters for either LME, LMAD or EAC failure could be better defined (Glickman, 2000; Gorse, 2000).

7.3 Experimental results that point out LME effects: Case of T91 in contact with LBE or lead

When the French, European (TECLA, MEGAPIE-TEST…) and international (MEGAPIE…) programmes on ADS began, there was little information about the compatibility of 9-12%Cr-containing steels with lead and lead-bismuth alloys. The publications in Russian journals dedicated to the compatibility of structural materials with liquid lead or lead alloys were largely unknown, untranslated or poorly translated. This is for example the case for all studies dealing with the liquid-metal-induced failure of steels before 1955, which was the subject of a monograph by Potak (1955). It would also have been interesting to be aware of the research related to the mechanical properties of austenitic and ferritic/martensitic steels in contact with lead which were proposed for the main components of the BREST-OD-300 reactor, and especially that liquid lead has practically no effect on the tensile properties of austenitic steels between 420 and 550°C, or that the lead effect on the tensile properties of the selected 9Cr ferritic/martensitic steels simply consists of a decrease in elongation near the melting point at 350°C, and disappears at higher temperatures (Abramov, 2003). It would also have been interesting to know that research to optimise the composition and structure of steels for Pb-cooled, Pb-Bi-cooled reactors was performed in Russia (Gorynin, 2000; Solonin, 2001). In this line, all information on the influence of HLMs on the mechanical properties of steels obtained to design and build the Russian reactor facilities by a very active scientific community was fully missing at the outset of the European Union, United States and Asian programmes on ADS and LMFBRs.

Last, it would have been of primary importance to know that Popovich noted as early as 1978 that wetting of iron and iron-based alloys by lead or bismuth is not so easily achieved, even when using the efficient method of soldering fluxes and, consequently, that Pb or Bi should not be strong embrittlers of steels.

Thus, initially, T91 was pre-selected as a structural material for the European ADS project and for the MEGAPIE spallation target, due to its excellent mechanical properties under irradiation by fast neutrons. As mentioned above, it was a challenge to prove that contact with molten lead or LBE could produce LME effects. Now, after more than ten years, it is known that T91 can be embrittled by LBE and it is possible to undertake a review, at least partial, of the metallurgical conditions producing LME effects. It is also possible to propose solutions to protect T91 steel against LME.

Table 7.3.1: Chemical compositions of the above-mentioned steels (wt.%, balance Fe)

	Cr	W	Ni	Mn	V	Nb	Mo	Ta	Ti	Al	Cu	C	N	P	S	B	Si	As	Sn	Co	Ref.
Chromesco 3	2.09	–	–	0.50	–	–	1.09					0.085					0.30				Sannier (1982)
EM 12	9.65	–	–	1.03	0.32	0.46	2.04					0.105					0.37				Sannier (1982)
T91	8.26		0.13	0.38	0.2	0.08	0.95			0.024	0.08	0.105	0.055	0.009	0.003		0.43				*
T91	8.5	–	0.12	0.47	0.21	0.6	0.95	–	–	–	–	0.1	–	–	–	–	0.22				Vogt (2011, 2013) Serre (2007)
T91	8.8		0.17	0.38	0.25	0.07	1.00					0.11					0.41				Ye (2013)
T91	8.63		0.23	0.43	0.21	0.09	0.95		0.003		0.046	0.1	0.03	0.02	0.006		0.31				Long (2008)
T91	8.76		0.099	0.597	0.186	0.073	0.862				0.054	0.088		0.019			0.317			0.019	Long (2008)
T91	8.99	0.01	0.11	0.38	0.21	0.06	0.89		0.003	0.015	0.06	0.1	0.042	0.021	0.0004		0.22	0.008	0.004		**
T91	8.32	<0.01	0.24	0.43	0.24	0.06	0.96	–				0.10	0.03	0.02		<0.0005	0.32				van den Bosch (2008)
T91	8.87		0.12	0.39	0.20	0.08	0.87			0.01	0.08	0.10	0.04	0.02			0.22				Hojna (2011)
MANET	10.37	–	0.657	0.76	0.21	0.16	0.5B	–	–	0.007	0.01	0.10	0.032	0.004	0.005	0.0075	0.18				Glasbrenner (2003)
1.4914	10.6		0.82	0.54	0.24	0.19	0.49	–	–	0.05	0.01	0.172		0.005	0.005	0.002	0.34				Borgstedt (1986)
HT9	11.8	0.52	0.51	0.50	0.33	–	1.03	–	–	–	–	0.21	–	–	–	–	0.21				Chopra (1986)
F82H-mod	7.66	2.0	–	0.16	0.16	–	–	0.02	–	–		0.09	0.005				0.11				Sample (2000)
OPTFER IVb	8.3	1.4	–	0.34	0.22	–	–	0.06	–	–		0.12	0.03								Sample (2000)
EUROFER 97	8.8	1.15	–	0.44	0.2	0.002	0.003	–	–	–		0.10	–				0.05				Benamati (2002)
E97	8.96	1.1	0.007	0.43	0.19	<0.001	<0.001	0.13				0.12	0.016	<0.005		<0.001	0.07				van den Bosch (2008)
P92	8.99	1.75	0.12	0.43	0.2	0.06	0.49			0.016		0.11	0.043	0.018	0.003	0.002	0.26				Yurechko (2013)
316L	16.69		10.26	1.842			2.075					0.015		0.027	0.0028		0.643				Serre (2009)
316L	16.73	0.02	9.97	1.81	0.07		2.05		0.06	0.018	0.23	0.02	0.0293	0.032	0.0035		0.67				Coen (2010)

* Legris (2000, 2002), Nicaise (2001), Vogt (2002), Pastol (2002), Gamaoun (2002, 2003), Guérin (2003), Auger (2004, 2005), Verleene (2006) and Auger (2008), as the T91 steel whose composition is reported above was supplied by Creusot Loire Industrie in the framework of the French GEDEON programme on structural materials for ADS.

** van den Bosch (2009, 2010), Coen (2010), Di Gabriele (2008), Weisenburger (2008, 2012), Yurechko (2011) and Auger (2011) used the material of the DEMETRA project provided by Arcelor.

With the DEMETRA programme of FP6 and with the GETMAT project of FP7,[11] the question of the susceptibility to LME of both the T91-LBE and T91-lead couples has been much more documented as tensile tests (reported in Tables 7.4.1 to 7.4.8 [see annex]) have been completed by fatigue and fracture mechanics tests that were conducted in strictly controlled environmental conditions.

In the following, we successively consider the role of the different parameters, which demonstrate an LME effect.

The chemical composition of the different steels to which the different papers refer to are listed in Table 7.3.1.

7.4 Tensile behaviour of austenitic and ferritic/martensitic steels in contact with lead and LBE

7.4.1 Description of the test

The tensile test consists of the application of an increasing load on a specimen which will progressively deform and fracture. Tensile tests are usually displacement controlled, but they can also be load controlled. Cylindrical or plate specimens with a specified gauge-length have an extremely useful and convenient test geometry for studying the constitutive behaviour of materials. An ongoing application of tensile tests is the study of fracture processes in metals. They are used in the following sections to assess the susceptibility to LME, LMAD and EAC of the T91-LBE or T91-lead couples, and to a lesser extent 316L-LBE couples, T91/T91 welds, T91/316L welds and enriched Si steels.

During a tensile test, load (N)-displacement (mm) data are recorded which are then calculated into engineering stress (MPa)-engineering strain (%) data (load divided by the initial section area versus elongation normalised by the initial length L_0). After plotting the engineering stress-strain curve, the following data can be obtained (see Figure 7.4.1 for the position of the values described below):

1) Young modulus (E), slope of the linear part of the curve characterising the elasticity of the material (available if an extensometer has been used).
2) Yield strength (YS), the engineering stress at the transition from elastic to plastic behaviour, generally defined for a given value of the plastic strain, conventionally 0.2%.
3) Ultimate tensile strength (UTS), the maximum value of engineering stress.
4) Total elongation (A%), the strain of the specimen at fracture: $100 \times (L_f - L_0)/L_0$, where L_f is the length of the gauge length after fracture.
5) Uniform elongation (A_u): the strain of the specimen at the maximum value of engineering stress.
6) Reduction of area (Z), $Z = 100 \times (S_0 - S_u)/S_0$ where S_u is the section area after fracture (circular or elliptical if anisotropy).

7.4.2 Tensile behaviour of T91 in LBE

7.4.2.1 Tensile behaviour of T91 steel in its standard heat treatment in lead and LBE

The standard heat treatment of T91 consists in an austenisation at 1 040-1 050°C followed by water quench or air cooling and then in a tempering at 750-770°C followed by air cooling.

11. GETMAT: Generation IV and Materials Transmutation.

Figure 7.4.1: Schematic showing the positions of the values described in Section 7.4.1

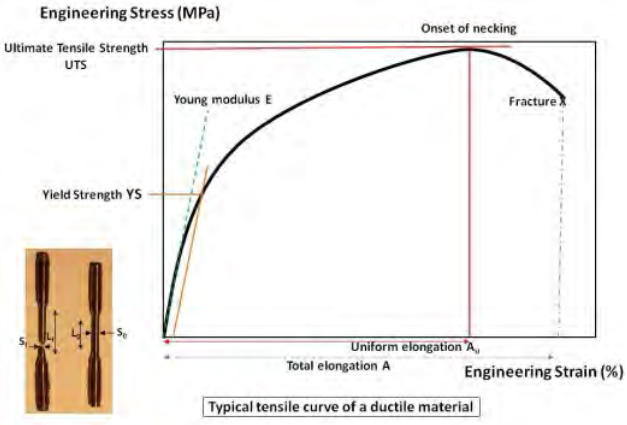

The first tests were conducted on standard heat-treated T91 steel (normalised at 1 050°C/1 h, then air-cooled, followed by tempering at 750°C/1 h and air cooling) on electro-polished specimens at 350°C in oxygen-saturated lead. Tests performed on cylindrical specimens (4 mm in diameter and 20 mm in gauge length) at an average strain rate of 10^{-4} s^{-1} showed a ductile behaviour and fracture of T91 (Legris 2000, 2002; Verleene, 2006). Similar results have been obtained more recently (Di Gabriele, 2008; Long, 2008a; Van den Bosch, 2006, 2008) in which the effect of strain rate, the effect of purity of LBE and the effect of temperature were additionally investigated. It is sometimes mentioned that after testing at 300°C, lateral cracks around the fracture surface had a cleavage-like aspect but the main feature of the surface remains ductile.

In low oxygen content LBE (less than 1 wppm), a ductility trough in the temperature range 300°C-450°C has been pointed out, see Figure 7.4.2 (Long, 2008a). The tensile curves of the specimens tested in this temperature range show fast failure of the specimens after necking began. In this temperature range, the specimens tested in Ar broke in a typical ductile fracture mode, while the specimens tested in LBE ruptured in a brittle cleavage fracture mode.

Thus, the main conclusion is that *LBE can modify the behaviour of T91 but mainly after large deformation, at the moment of necking* where cracks form at the surface, suggesting that LBE promoted crack propagation.

Figure 7.4.2: Total elongation versus test temperature for 760°C tempered T91 tested in Ar and LBE (O < 1 wppm) at a strain rate of $1{\cdot}10^{-5}$ s^{-1}

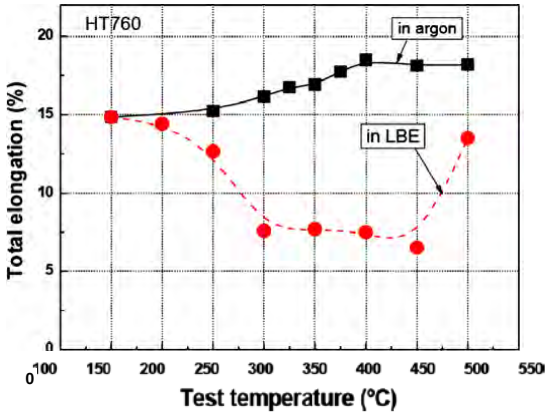

Source: Long (2008a).

7.4.2.2 *Effect of heat treatment and effect of presence of flaws on the tensile behaviour of T91 steel in LBE*

At the outset, the role of flaws had been pointed out at the same time that attention was turned toward the effect of heat treatment.

The first studies taking into account the effect of heat treatment were based on changing the tempering temperature (Legris, 2000; Nicaise, 2001; Legris, 2002). Application of a hardening heat treatment to smooth cylindrical specimens of T91 steel consisting in tempering the steel at 500°C instead of 750°C was not sufficient to produce an embrittling effect in contact with stagnant lead under air at 350°C, according to Vogt (Nicaise, 2001). No change was found after 1 h of tempering at 500°C. LME was then however observed when the authors employed a notched specimen, the root of which contained a very hard layer susceptible to cracking during loading. Combining the effect of a notch and of a hardening thermal treatment was apparently required to obtain a brittle failure in a variety of liquid metals (Pb at 350°C, LBE and Sn at 260°C) (Figure 7.4.3). A ductility trough was estimated between 350-425°C for hardened T91 in oxygen-saturated lead (Vogt, 2002).

These results were later confirmed by Glasbrenner (2004) on U-bent T91 specimens, hardened by means of the same hardening heat treatment applied above by Vogt (one hour tempering at 500°C, air cooling).

Figure 7.4.3: (a) Tensile test results of notched specimens of hardened T91 steel obtained at 260°C in liquid Sn, LBE, air and at 350°C in liquid lead and air; (b) SEM micrograph of the fracture surface obtained in LBE at 260°C

Black squares – Sn; black circles – LBE; white triangles – air;
black diamonds – 350°C in liquid lead; white squares – 350°C in air

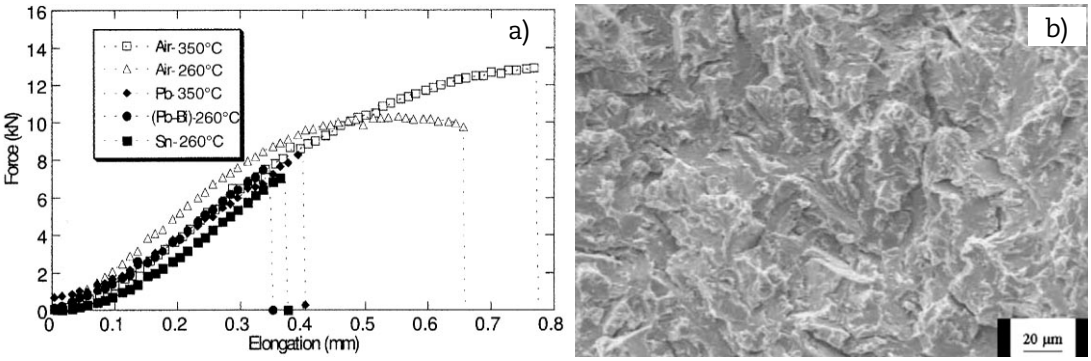

Dai (2006a) noticed that EDM-cutting could lead to surface flaws at the surface flat of tensile specimens of T91 (normalised at 1 040°C for 1 h and followed by air cooling, and then tempered at 760°C for 1 h followed by air cooling). This resulted in a deleterious effect over a wide temperature range extending from 300 to 425°C, in oxygen-saturated LBE under argon, as illustrated in Figure 7.4.4 at 325 and 375°C. Some scattering in the results (particularly the elongation to rupture) is unavoidable with an uncontrolled distribution of micro-cracks, filled or not by LBE, which is absolutely unpredictable. Moreover, the advance of the cracks filled with LBE is always competing with the oxide film formation on crack walls and at crack tip, which is also unpredictable.

Glasbrenner (2003) performed tensile tests during the commissioning phase of the LiSoR loop, using flat specimens of MANET II, at a strain rate of 10^{-4} mm s^{-1}. Ductile behaviour was observed under argon over the whole temperature range tested (T_{room} to 250°C), whereas some embrittling effect is apparently observed in flowing (1 m.s^{-1}) oxygen-saturated or at least "close to saturation" LBE, once reached 250 and 300°C. The results of these tests are shown in Figure 7.4.5.

Figure 7.4.4: Micro-cracks due to EDM-cutting (top); tensile test results of mechanically polished EDM-cut specimens obtained (bottom)

Before (left) and after (right) tensile testing in LBE; note that all pre-cracks are not filled by LBE. The exposure time to LBE prior testing is indicated. The propagation of the micro-cracks filled by LBE is revealed during tensile testing.

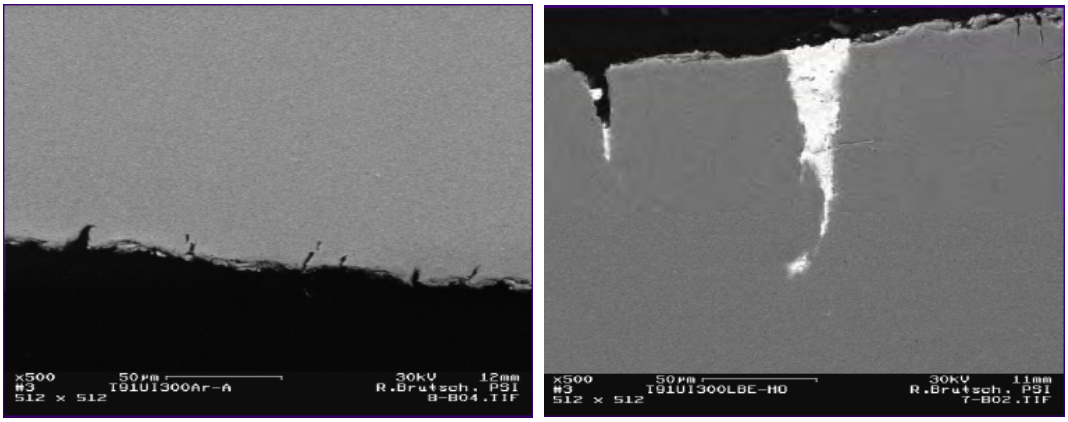

At 325°C in oxygen-saturated LBE under argon (left) and at 375°C in oxygen-saturated LBE under argon (right)

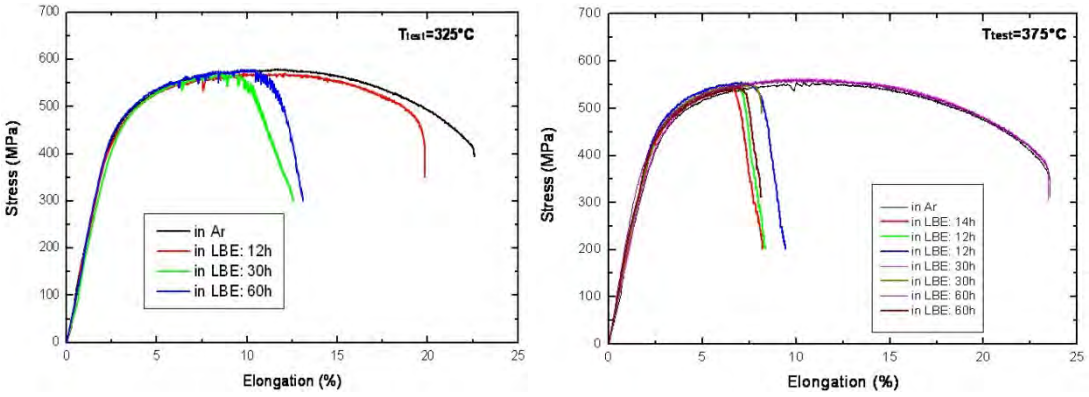

Figure 7.4.5: (a) Comparison of stress-strain curves obtained in argon and in oxygen-saturated LBE (no OCS) in LiSoR loop at 250 and 300°C. (b) SEM micrograph showing the mixed fracture surface obtained with MANET II after tensile testing at 300°C in LBE

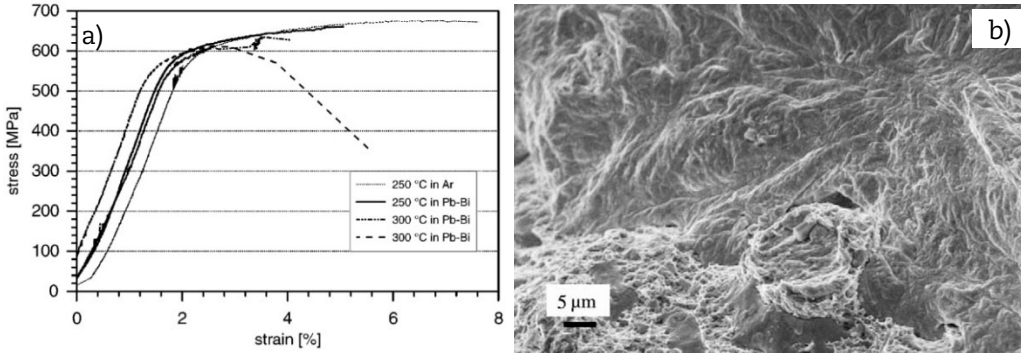

Under the LiSoR loop conditions, a mixed fracture surface was obtained with both flat and ductile areas. The final surface preparation of the tensile specimen was not specified. However, the presence of small cracks initially present on the specimen surface, propagating under the influence of liquid Pb-Bi, and more specifically bismuth as indicated by the authors, is a plausible hypothesis, possibly more plausible than the suggestion that the specimens of MANET II could be wetted by LBE under these conditions at 250 or 300°C after a two hour pre-exposure to oxidising LBE before tensile testing. Note that ductile failure was always obtained for MANET II in LBE at the lower temperatures tested of 180 and 200°C.

The effect of heat treatment has been revisited more recently (Long, 2008a). The experimental details differed slightly, notably as concerns apparently un-notched specimens (0.75 × 1.5 × 5 mm), low oxygen LBE (> 1 wppm) and lower strain rate ($1{\cdot}10^{-5}$ s^{-1}).

T91 was studied after the following heat treatment conditions (HT760, HT600 and HT500 respectively):

1) normalised at 1 040°C in high vacuum for 60 min, followed by air cooling;

2) tempered at 760°C, 600°C and 500°C in high vacuum for 2 h, followed by air cooling.

As a consequence of increasing the strength of the steel by lowering the tempering temperature, specimens tempered at 600°C and 500°C (Figure 7.4.6) demonstrated more pronounced embrittlement effects, reflected by wider and deeper ductility troughs, indicating clearly that they became more susceptible to the LBE embrittlement. The authors believe that the fracture of the specimens resulted from the propagation of micro-cracks on the transverse surfaces, which were produced during EDM cutting. All specimens tested in Ar environment ruptured in a ductile fracture mode.

In this way, they confirm the deleterious effect of flaws on the tensile behaviour (Dai, 2006a; Glasbrenner, 2003), and the role of hardness.

Figure 7.4.6: Tensile stress-strain curves of T91 steel tempered at 500°C tested in LBE and in Ar

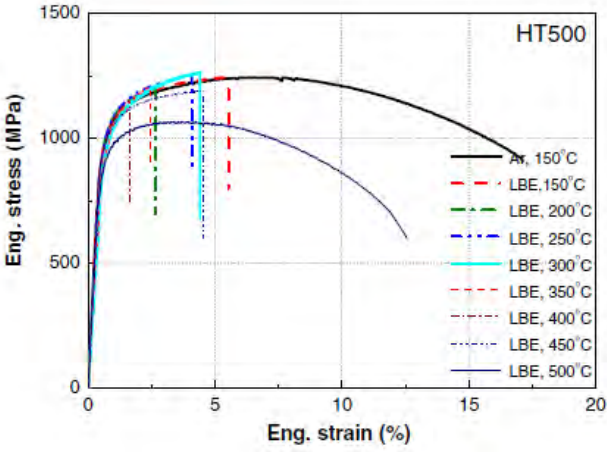

Source: Long (2008a).

7.4.3 *Effect of pre-exposure in LBE on tensile behaviour of T91*

In the framework of the TECLA and MEGAPIE-TEST programmes, Benamati and Fazio studied the T91-LBE couple after a long-term exposure of T91 to flowing and reducing Pb-55Bi at 400°C in the LECOR loop (1 500-4 500 h) by tensile test under argon at the same temperature (Fazio, 2003; Aiello, 2004).

The oxygen level in the melt, ranging from $3{\cdot}10^{-10}$ to 10^{-7} wt.ppm was lowered by the addition of Mg and bubbling under pure H_2. The results are: *i)* a net reduction of the elongation; *ii)* a decrease of the ultimate tensile strength; *iii)* with mixed ductile (at the centre) and brittle (at the periphery) fracture surfaces (Figure 7.4.7).

Figure 7.4.7(a): Stress-strain curves obtained at 400°C in argon at strain rate of 3 10^{-3} s^{-1} after long-term exposure of T91 to LBE at 400°C in LECOR loop

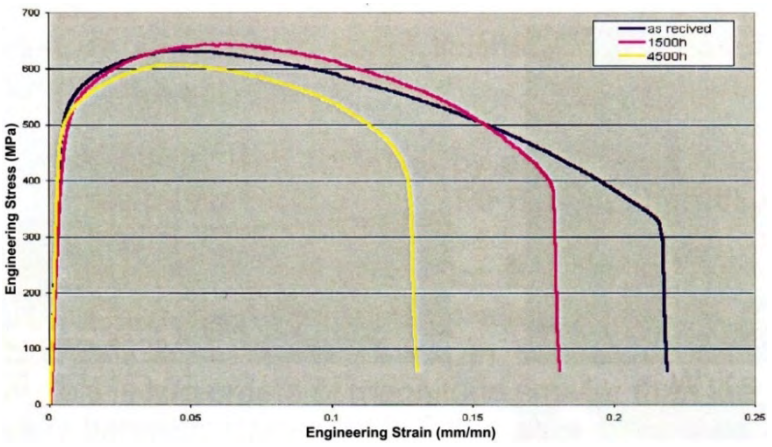

Figure 7.4.7(b): Morphology of T91 specimens after 4 500 h in LECOR loop at 400°C followed by tensile testing in argon at 400°C

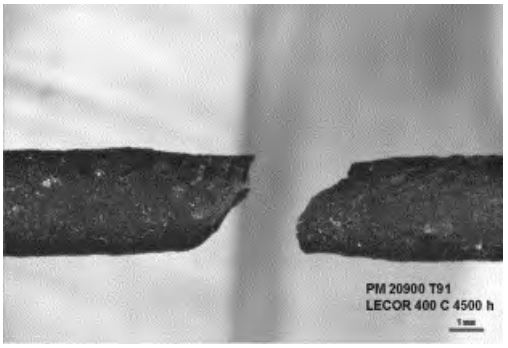

Figure 7.4.7(c): SEM micrograph showing a zone at the periphery of the fracture surface of the T91 tensile specimen

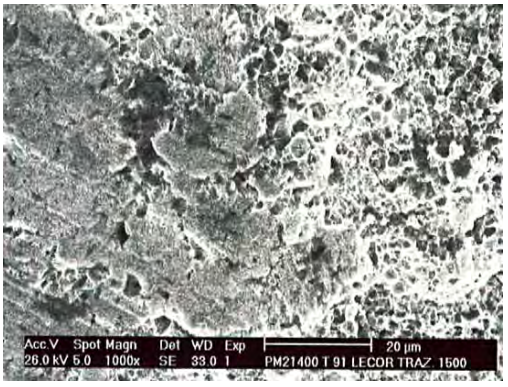

Source: Aiello (2004).

A detrimental effect of long-term exposure (4 000 h) to oxygen-poor LBE (the oxygen content is not mentioned) on the tensile properties of T91 was also observed by Van den Bosch (2006). This work also shows an effect of the ageing temperature, clear at 450°C but undetectable at 300°C (Figure 7.4.8). The results of this study are not in so good agreement with those described at the beginning of this chapter. This could be explained by the conditions of specimen preparation (mechanical grinding not followed by any surface treatment to minimise the roughness of the tensile specimens) and testing procedures, differing from those applied in the previously cited research.

Figure 7.4.8: Tensile curves from tests at 300°C (dashed) and 450°C (solid) for samples of T91 that were pre-exposed to Pb-Bi at 450°C for 4 000 h (grey curves)

The black curves result from tensile testing T91
without pre-exposure to Pb-Bi under the same conditions

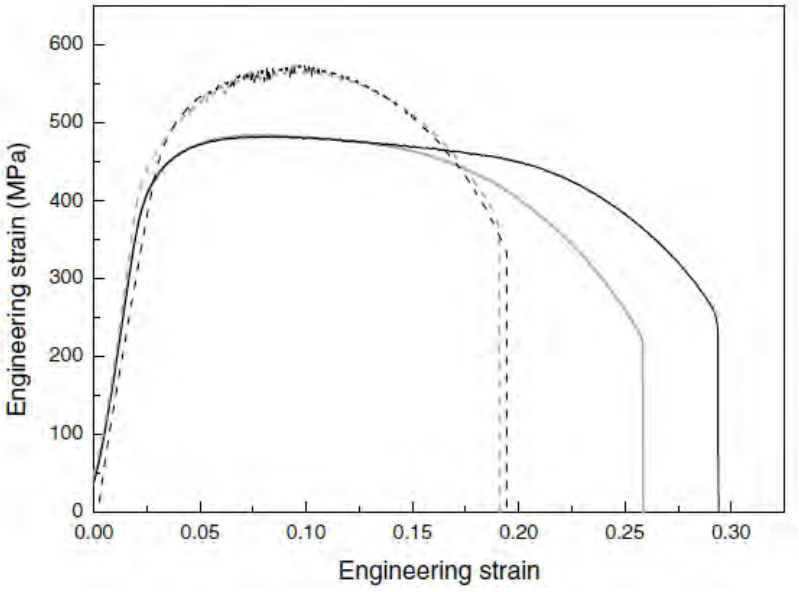

7.4.4 *Role of oxide layer*

T91 steel is highly oxidisable and passivating, due to its 9% chromium content. As a result, its native oxide film is stabilised after a few hours of ageing in the laboratory environment. It has been shown that the native oxide film on T91 does not dissolve in high purity (99.9999%) lead at 380°C after prolonged ageing (Lesueur, 2002). At the same time, it has also been shown that T91 is poorly wetted by lead over the 380-450°C range, even in the presence of active OCS in the melt. In the following, the role of oxide is discussed on the basis of former tensile tests, but new results have been obtained using the small punch test. The reader is thus invited to consult Section 7.5.2.1 for more information on this topic.

Indirect contact via an oxide film

First, the hypothesis was made that short ageing in LBE, which is more corrosive than pure lead, would allow for a partial gentle removal of the thin oxide film grown after 12 hours in LBE, avoiding surface roughening and permitting some (localised) wetting of T91 by LBE:

- As long as un-notched specimens were tested, no effect of LBE was detected over the 200-450°C temperature range, neither under vacuum nor under hydrogenated helium.

- When notched specimens were tensile tested, after standard heat treatment and careful surface preparation (see Section 7.8), a damaging effect of LBE was found, strongly dependent on the liquid and gas phases in contact as is shown in Figure 7.4.9. The reduction in strength and ductility, undetectable at 200°C, passes through a maximum at 350°C before beginning ductility recovery at 400°C. The effect of LBE (exposure in stagnant LBE for 12 h at 350°C with a He-4%H_2 cover gas, oxygen content not measured) was shown in ductility and energy to rupture, with a clear dependence on the deformation rate against oxidation rate (Guérin, 2003).

However, in the above experiment (Guérin, 2003), the surface state was not rigorously controlled, smooth at submicroscopic scale and wetted, as compared to the experiment that will be described below (Auger, 2004).

Figure 7.4.9: Load versus cross-head displacement curves obtained with notched T91 specimens, after standard heat treatment at 350°C for a cross-head displacement rate of 6.7 10^{-4} mm/s, showing the environmental effects: vacuum (V), LBE under vacuum (V+LBE), He-4%H_2, LBE under He-4%H_2 (He-4%H_2 + LBE)

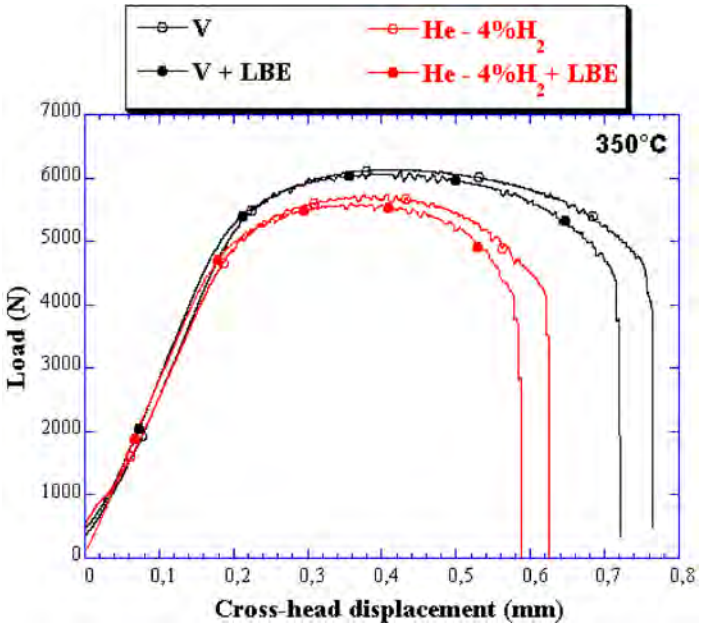

In order to remove the oxide film so as to wet the T91 steel and check whether the T91-LBE couple is embrittling, there are different methods of surface preparation. We focus on the more efficient ones.

Direct contact via physical vapour deposition

To deoxidise the T91 steel, without roughening, corroding and contaminating the steel surface, it is necessary to proceed under UHV. The oxide film is removed by argon ion sputtering in an UHV chamber, followed by physical vapour deposition of Pb-Bi layers with thickness of the order of a few hundred of nanometres. After tensile testing at 340°C under helium at a strain rate of 10^{-4} s^{-1}, a decrease in strength and elongation to rupture were measured. In addition, a mixed ductile/brittle fracture is observed with a number of small cracks on the gauge length of the T91 specimen as shown in Figure 7.4.10, after Auger (2004, 2005). The fracture process is controlled by the reservoir of embrittling atoms at the specimen surface.

Figure 7.4.10: In case of direct T91-LBE contact obtained by ion beam sputtering in an UHV chamber prior to deposition of Pb-Bi by PVD, LME effects are produced at 340°C under He (top). SEM micrograph (SE2) of the multi-cracked gauge length of the T91 specimen (bottom left). SEM micrograph (SE2) of an initiation site close to the surface showing a quasi-cleavage fracture surface (bottom right)

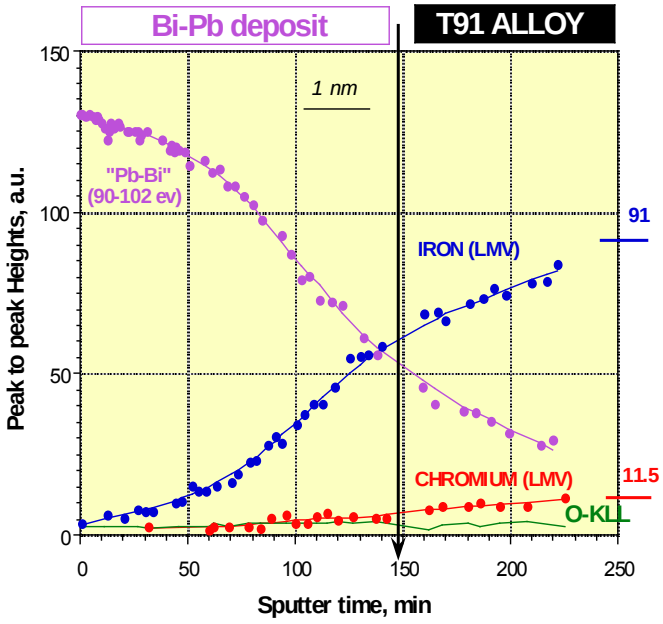

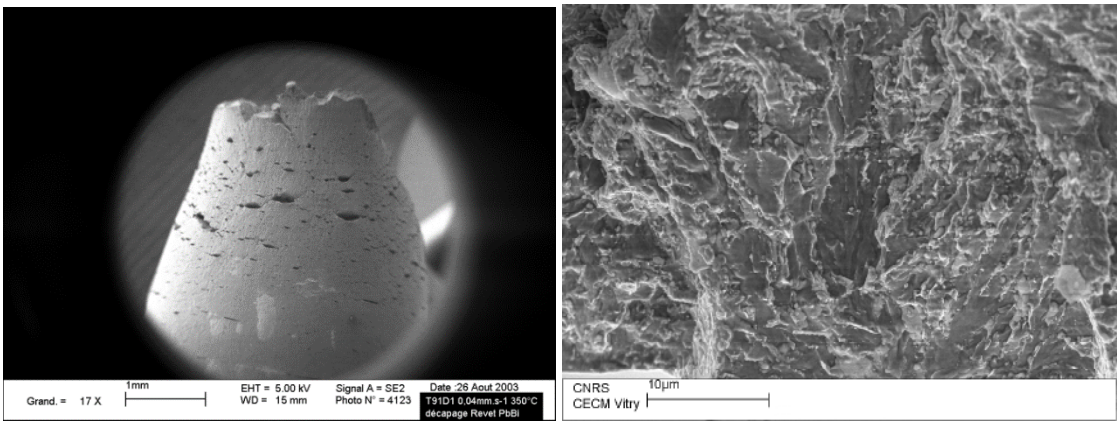

This method was largely employed in the former USSR. In almost all reported research (Abramov, 1994; Antipenkov, 1991; Balandin, 1970; Bichuya, 1969; Chaevskii, 1962, 1969; Dmukhovs'ka, 1993a, 1993b; Gorynin, 1999; Nikolin, 1968; Popovich, 1978, 1979, 1983; Soldatchenkova, 1972), the intimate contact between Armco iron or other Russian steel grades and a potentially embrittling metal (Cd, Ga, Bi, Pb, Sn… or their alloys) is forced by using the method of the soldering fluxes.

De facto, the hypothesis is made that the flux does not perturb the experiment with residual impurities at the steel/LM interface. This drawback, inherent to the method, was minimised by the Russian scientists. For pre-tinning steel specimens with LBE, the employed soldering flux contains zinc, known as a strong embrittler. Balandin (1970) tested the mechanical properties of steel specimens in liquid Pb-Bi containing 0.05 to 0.1% Zn and found results comparable to those obtained with pre-tinned specimens tested in pure Pb-Bi. This does not constitute proof that Zn does not affect the results of the mechanical tests.

Intimate contact by means of chemical fluxes

Wetting of T91 steel by LBE has also been achieved by the method of soldering fluxes. However, the LME effects obtained under these conditions are not reproduced here, because of the embrittling influence of the chemical impurities, and especially zinc, at the steel-LBE interface. In fact, brittle failure of T91 in stagnant LBE containing traces of zinc was observed by Gamaoun (2003). To give another example in a different context, a harmful effect of zinc as an impurity in flowing sodium on the creep life of a type 304 SS at 550°C was noted by Huthmann (1980).

Once again, it appears that the surface preparation is a crucial phase to determine the susceptibility to LME of a given solid-liquid couple.

Last, let us note that de-wetting of Armco iron (0.37%C), initially coated with Pb, Bi or LBE by the method of soldering fluxes, may occur due to interfacial oxidation caused by atmospheric oxygen inward diffusion, throughout the embrittling metal layers (Popovich, 1978). At this point, it should be mentioned that the inward diffusion of oxygen toward the interface could affect the results of the mechanical tests before de-wetting becomes macroscopically observable. However, the remarkable efficiency of the method of soldering fluxes was proved by Balandin (1970) in a study of a 12 KhM pearlitic steel in contact with LBE: the author has shown that, after exposure to oxygen-saturated LBE for durations ranging from 2.5 to 25 hours at 500°C, re-tinning with LBE restores its embrittling effect.

7.4.5 *Role of traces of impurities*

An example of the embrittling effect of zinc, even at trace levels, was demonstrated by Gamaoun in his PhD thesis (2003). Cylindrical, smooth specimens of T91, diamond polished, were first exposed for one month at 525°C in reducing LBE. The specimens were then submitted to a relaxation test in LBE at 380°C for a few days, and finally ruptured by tensile testing at the same temperature. The main characteristics of the test results were: *i)* a significant reduction of the elongation to rupture; *ii)* a brittle fracture; *iii)* a surface completely covered with LBE, adherent over the whole gauge length.

A reasonable assumption is that the thus-obtained surface state and the brittle failure obtained during tensile testing were promoted by traces of zinc in the liquid LBE, as previously mentioned.

The embrittling effect of zinc, antimony and tin, alloyed to lead, was emphasised by Warke in a 1970 review paper. However, these authors were considering their role as alloying elements, not at the level of trace elements as is the case here. Note that the influence of trace elements on mechanical properties in metallurgy remains a matter of debate.

7.4.6 *Mechanical behaviour of welds in LBE*

The only studies devoted to the mechanical behaviour of homogeneous and heterogeneous welds of 316L and T91 steels in LBE have been conducted by Van den Bosch (2009a, 2010a) using tensile tests and by Serre (2009) using the small punch test (see Section 7.5).

7.4.6.1 Description of the weld procedure

Van den Bosch considered two types of weld. The first weld was obtained by tungsten inert gas (TIG) welding in combination with shielded metal arc welding (SMAW) and submerged arc welding (SAW). The second weld type was obtained by electron beam (EB) welding. T91/T91 TIG and EB welds and T91/316L TIG and EB welds were investigated:

- T91/T91 TIG weld comprised a total of 10 weld passes as shown Figure 7.4.11. The first two passes were performed using manual gas tungsten inert gas welding

(GTAW) while applying a minimal pre-heating temperature of 220°C. Passes 3-6 were performed by manual shielded metal arc welding (SMAW) with a minimal pre-heating temperature of 220°C and weld passes 7-10 were done by submerged arc welding (SAW) under a bed of Marathon 543 flux, the chemical composition of which is given Table 7.4.1 with a minimum pre-heating temperature of 230°C. The post-welding heat treatment (PWHT) consisted of a maximum heating rate of 105°C.h^{-1} up to 750°C where the material was kept for 1 h and 10 min. The applied cooling rate was 100°C.h^{-1} down to a temperature of 80°C. At that moment, the welded plate was removed from the furnace and cooled down to ambient temperature without temperature control. The TIG weld filler material Thermanit MTS 3 had a chemical composition very close to T91.

- The T91/316L TIG weld was performed in two phases. At first a high-alloyed 309 alloy was welded by SAW onto the T91 in five passes using an Arosta 309S (see chemical composition in Table 7.4.1) electrode of ∅ 2.5-3.2 mm while the T91 steel was pre-heated to a minimal temperature of 250°C. This procedure is called "beurrage" or "buttering". After buttering, a PWHT was performed in order to relieve stresses by heating up the plate starting from room temperature at a maximum heating rate of 100°C.h^{-1} up to 740°C and holding it for 45 min. Cooling was performed at a controlled rate of maximum 95°C.h^{-1} down to 50°C when the plate was removed from the furnace. In a second phase, the actual connection weld was made between the 316L plate and the over-alloyed 309 side of the T91 plate by using the filler material in 316L alloy (NERTALINOX). This weld comprised 11 passes in total (see Figure 7.4.11).
- The T91/T91 electron beam weld was performed by KIT (Germany) in a single pass using an EBW 1001/10-60 CNC from PTR Präzisiontechnik, Maintal, Germany. Prior to EB welding, the plates to be welded were degreased and fixed together at a few points by manual TIG welding. When placed in the vacuum chamber, the chamber was pumped down to about 6·10^{-5} Pa and an applied electrical tension of 60 kV at a current of 62 A was applied during EB welding. The welding travel speed was 10 mm.s^{-1}.
- The T91/316L electron beam weld was performed in a similar way as for T91/T91, except the parts to be welded were degreased and fixed together by one single pass of TIG welding prior to EB welding. The EB weld was given a PWHT of 740°C for 45 min with a maximum heating and cooling rate of 10°C.h^{-1}.

Table 7.4.1: Chemical composition of the SAW flux material (Marathon 543), wt.%

Material	CaF_2	$SiO_2 + TiO_2$	$CaO + MgO$	$Al_2O_3 + MnO$	$K_2O + Na_2O$
Marathon 543	31.0	14.0	32.0	18.0	2.6

Figure 7.4.11: Schematic representation and microstructure of the T91/T91 (left) and 316L/T91 (right) TIG weld joints

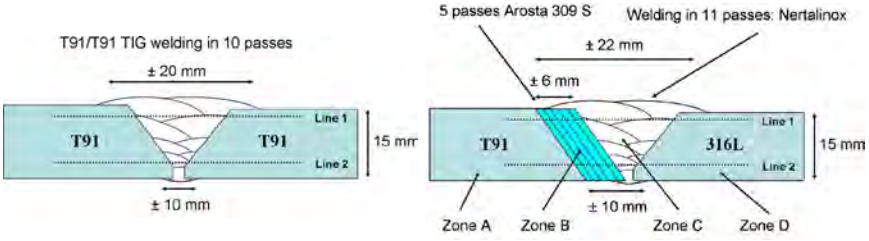

7.4.6.2 Mechanical response of the weld in LBE

Cylindrical tensile specimens with a total length of 24 mm, a gauge length of 12 mm and a diameter of 2.4 mm were machined from the weld joints. The specimen's gauges were polished up to a P4000 fine grit.

Tensile tests were performed using a strain rate of $5{\cdot}10^{-6}$ s^{-1} at 350°C in both gas (argon and 5% hydrogen mixture) and LBE purged with an argon and 5% hydrogen gas mixture. The samples tested in LBE were pre-exposed in LBE with low oxygen concentration, following a thermal cycling pattern. This thermal cycling procedure involved exposure to six periods of approximately one month each at about 350°C separated by periods of about one month at room temperature.

T91/T91 TIG and EG weld

Cylindrical tensile specimens were taken along different orientations of the T91/T91 TIG weld (across the weld with the weld deposit in the centre of the specimen gauge, across the weld with the HAZ in the centre of the gauge and parallel to the weld inside the weld deposit) and across the T91/T91 EB weld (weld zone in centre of gauge).

Figure 7.4.12 shows that both the T91/T91 TIG and EB welds have good mechanical behaviour when tested in gas environment.

Figure 7.4.12: Engineering stress-strain curves of (a) T91/T91 TIG weld; (b) T91/T91 EB weld along various orientations of the welds

Welds tested in argon and hydrogen gas mixture (dashed curves) and in LBE (solid curves) at 350°C, using a strain rate of $5{\cdot}10^{-6}$ s^{-1}. The tensile curve of the T91 base material tested in gas environment under the same conditions was added to the EB weld data for comparison

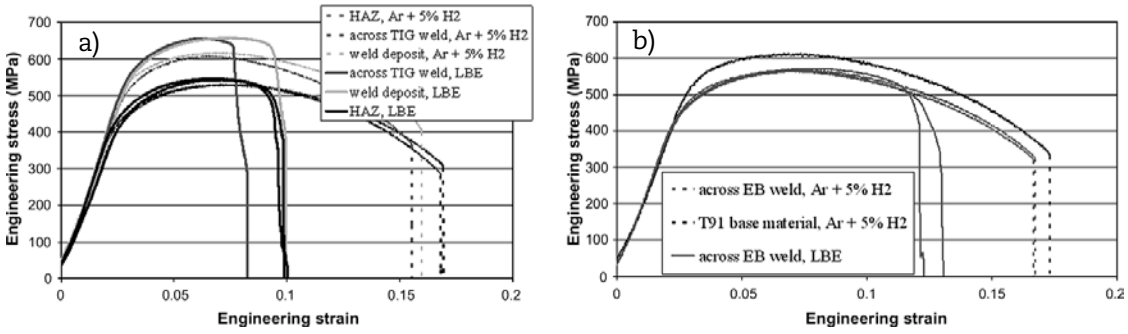

When tested in LBE however, all welds showed significantly decreased total elongation. The elastic behaviour and yield point of both the T91/T91 TIG and EB welds were unaffected by the environment, indicating no significant penetration of the LBE into the weld or matrix during pre-exposure. The plastic behaviour of both weld types also remains the same up to the point of fracture. In the case of the T91/T91 TIG weld tested in liquid LBE, fracture followed shortly after reaching the ultimate tensile strength. The T91/T91 EB weld displayed reduced elongation to fracture when tested in liquid LBE compared to that of the T91/T91 EB weld tested in a gas environment.

Detailed SEM examination of the fracture surfaces revealed that all T91/T91 weld samples tested in gas environment (see left column in Figure 7.4.13) were fully dimpled and showed the cup and cone shape characteristic of ductile failure. The SEM fracture surface images of the T91/T91 weld samples tested in liquid LBE are depicted in the middle column of Figure 7.4.13. Detailed fracture surface images from the brittle regions of the specimens tested in LBE and indicated by a box in the overview SEM images are depicted on the right in Figure 7.4.13. The weld specimens tested in liquid LBE showed very limited necking with the fracture surface perpendicular to the load line. All fracture

surfaces of T91/T91 weld samples tested in liquid LBE show at least one initiation site of LME characterised by the semi-circular flower pattern as seen in LME studies of T91 base material (Van den Bosch, 2009a; Di Gabriele, 2008).

Figure 7.4.13: SEM fracture surface images of T91/T91 TIG and T91/T91 EB weld samples along various orientations of the welds (indicated on the right)

Welds tested in argon and hydrogen gas mixture (left column)
and in LBE (right column) at 350°C, using a strain rate of $5 \cdot 10^{-6}$ s^{-1}

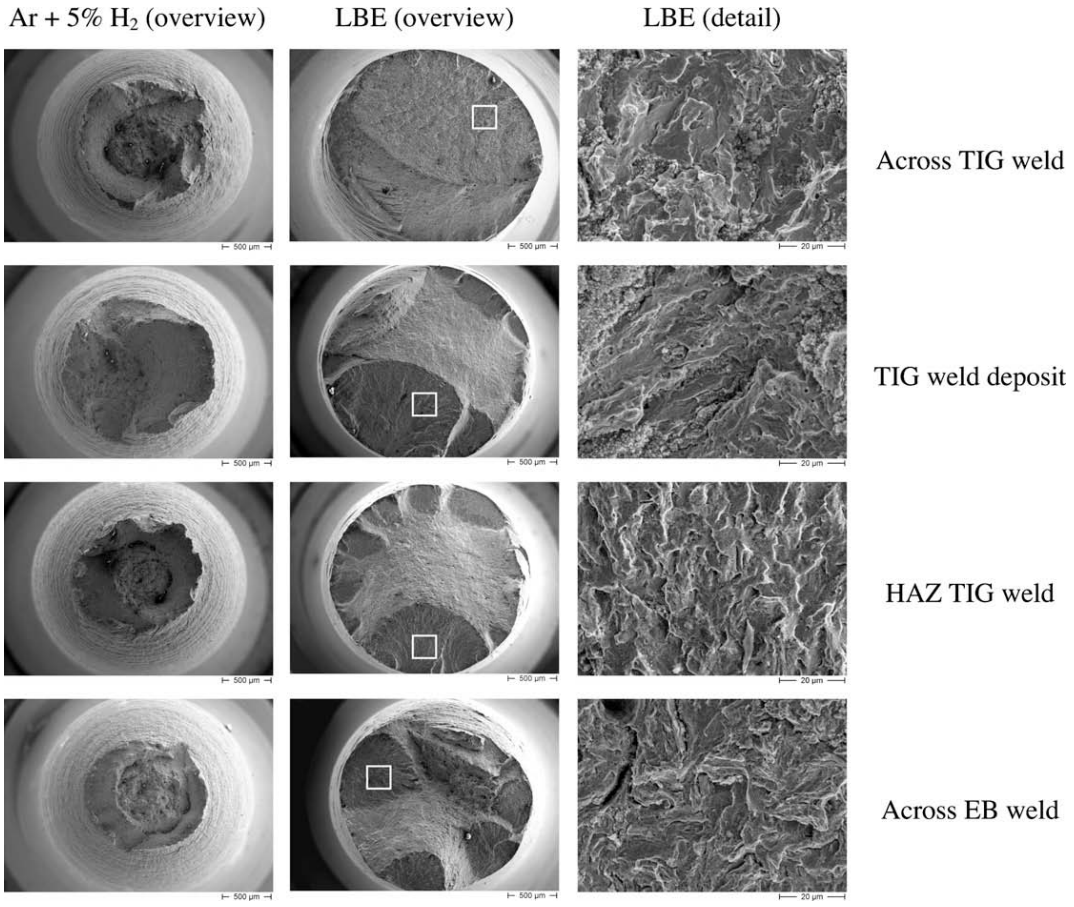

T91/316L TIG weld

Cylindrical small size tensile samples were taken across the weld with either the HAZ on the T91 side (Figure 7.4.14, middle left) or the HAZ on the 316L side in the middle of the gauge (Figure 7.4.14, middle centre) and inside the 316L weld material (Figure 7.4.14, middle right).

The T91/316L EB weld however, was sufficiently narrow to machine samples across the weld, halving the area that had been molten in the middle of the gauge.

The sample with the HAZ on the 316L side in the middle of the gauge exhibited the same ductile behaviour in Ar-H2 as in LBE (Figure 7.4.14, top centre) without any sign of LME and a marked necking (Figure 7.4.14, bottom centre).

The sample inside the 316L weld deposit exhibited a reduction in total elongation (Figure 7.4.14, top right).when deformed in LBE instead of Ar-H2. However, this does not represent a dramatic problem since sufficient ductility remains (Figure 7.4.14, bottom right).

Figure 7.4.14: Tensile results of T91/316L TIG weld tested in Ar + 5% H2 and LBE

Schematic representation of sample orientation indicated below the stress-strain curves. Picture of the broken sample after testing in LBE depicted below the schematic representation of sample orientation

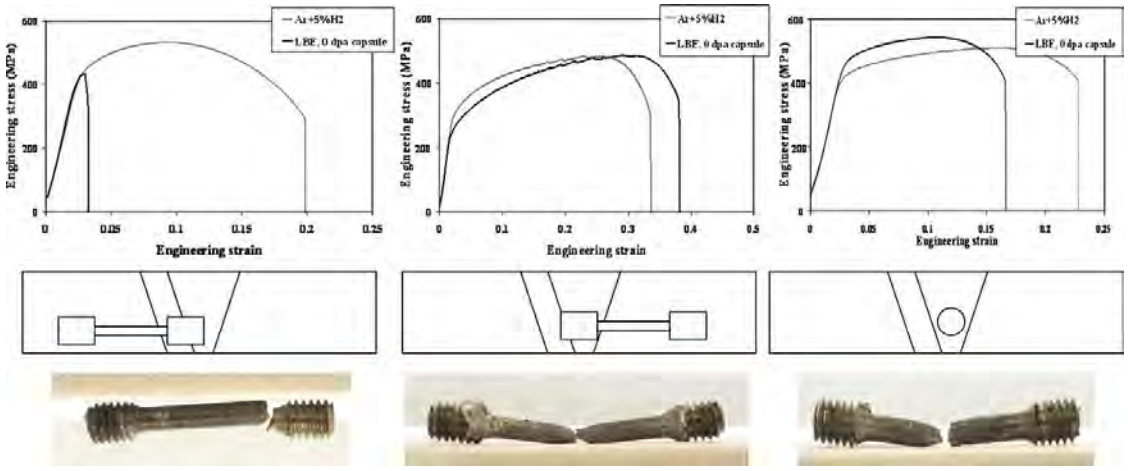

The sample with the HAZ on the T91 side in the middle of the gauge however, broke in a very brittle manner displaying very little elongation (Figure 7.4.14, top left) and no necking at all (Figure 7.4.14, bottom left). In this case, on the fracture surface of the broken sample, LME occurred at several sites. Metallurgical investigation shows that the specimen broke in a brittle manner at the interface between the T91 and the 309 steel. The crack path partly goes through the 309 buttering in a ductile manner, however the brittle fracture is at the interface of the T91 base material with the 309 buttering. This severity of LME is probably due to the increased hardness at this location of the weld. Increased hardness of the T91 base material obtained by reducing the tempering temperature is known to increase the susceptibility of T91 steel to LME (Long 2008a; Legris 2000).

T91/316L EG weld

The stress-strain curve of the T91/316L EB weld is similar to that of 316L but has much less elongation (Figure 7.4.15, top). This was to be expected since the yield and tensile strength of 316L are lower than that of T91 steel. Tests in Ar + 5% H2 show good mechanical properties. When the EB weld is tested in LBE without pre-exposure however, the specimen was broken in the weld without any necking. The fracture surface has aspects of both brittle and ductile behaviour (Figure 7.4.15, bottom right). After thermal cycling the embrittlement is much worse and the sample broke in the weld after very little plastic deformation. The fracture surface is predominantly brittle (Figure 7.4.15, bottom left). Again here, the increased susceptibility to LME in the weld is attributed to the locally increased hardness of the weld.

7.4.7 Mechanical behaviour of silicon-enriched steels in LBE

The literature (Yachmenyov, 1999; Kondo, 2006; Kurata, 2004, 2008) points out that the corrosion resistance of steels in LBE is improved with silicon addition. This does not imply that the sensitivity to LM is also improved. In this context, Van den Bosch (2012) studied the mechanical behaviour of silicon-enriched steel.

The chemical composition of the investigated steels and their heat treatment are reported in Tables 7.4.2 and 7.4.3, respectively.

Figure 7.4.15: Tensile results of T91/316L EB weld tested in Ar + 5%H2 and LBE without pre-exposure and after thermal cycling in low oxygen

SEM fracture surface images show mixed fracture surface when tested in LBE without pre-exposure and fully brittle fracture after thermal cycling in low oxygen LBE

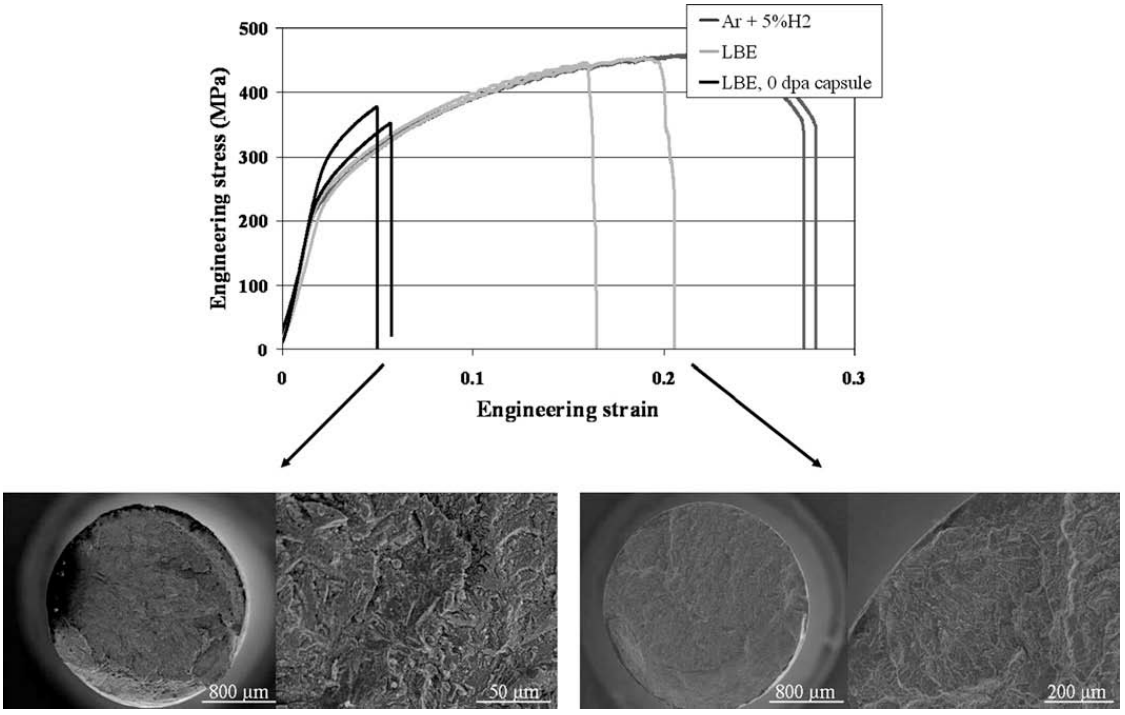

Table 7.4.2: Chemical composition of elevated Si steels (wt.%)

	C	Cr	Ni	Si	Mo	Mn	Al	V	W	Nb	P	S	N
T91	0.1	8.99	0.11	0.22	0.89	0.38	0.01	0.21	–	0.06	0.02	0.004	0.044
T91-Si	0.13	8.10	0.99	1.45	0.86	0.52	0.003	0.20	–	0.074	–		0.054
EP-823	0.16	11.70	0.66	1.09	0.74	0.55	–	0.30	0.60	–	0.014	0.004	–
2439	0.19	11.58	0.48	2.75	1.03	0.37	0.042	0.31	0.48	–	0.004	0.004	–
2440	0.19	13.52	0.51	4.83	1.00	0.38	0.043	0.31	0.45	–	0.004	0.004	–

Table 7.4.3: Heat treatment applied to the investigated steels

	Normalisation	Cooling	Tempering	Cooling
T91	1 040°C – 60 min	Air cool	760°C – 60 min	Air cool
T91-Si	1 050°C – 30 min	Air cool	750°C – 30 min	Air cool
EP-823	1 010°C – 60 min	Oil quench	620°C – 75 min	Air cool
2439	1 050°C – 60 min	Air cool	760°C – 60 min	Air cool
2440	1 050°C – 60 min	Air cool	760°C – 60 min	Air cool

T91, T91-Si and EP823 are all ferritic-martensitic steels with very similar prior austenite grain sizes and martensite lath sizes. S2439 has a bainitic microstructure and S2440 is fully ferritic with rather large grains.

The addition of silicon increases the DBTT. The S2439 and S2440 materials had a DBTT of 93°C and 227°C, respectively, with an upper shelf energy of 3.6 J, while the T91-Si had a DBTT of 48°C.

These measured DBTT values are considerably higher and the upper shelf energy is lower than that of e.g. conventional HT9 or standard T91 steel (T91 used in this study had a DBTT of -92°C).

Small size cylindrical tensile samples were used with a total length of 24 mm, a gauge length of 12 mm and a diameter of 2.4 mm. These samples were manufactured in the rolling direction. Prior to testing, the samples were degreased by ultrasonic cleaning in methanol and dried in air.

Slow strain rate tensile (SSRT) tests were performed at strain rates between $5{\cdot}10^{-7}$ s^{-1} and $1{\cdot}10^{-3}$ s^{-1} at a constant test temperature. Test temperatures were ranging between 150°C and 500°C for a given strain rate. Ar + H_2 was bubbling in LBE but the dissolved oxygen content is not given.

The effect of test temperature for a strain rate of $5{\cdot}10^{-6}$ s^{-1} and the effect of strain rate for a test temperature of 350°C are reported in Figures 7.4.16 and 7.4.17, respectively, for T91-Si, EP823, S2439 and S2440.

The uniform and total elongations are the two indicators to study the effect of LBE on the tensile behaviour.

Figure 7.4.16: Total and uniform elongation of T91, T91-Si, EP823, S2439 and S2440 vs. temperature (strain rate: $5{\cdot}10^{-6}$ s^{-1})

Full symbols for tests performed in liquid LBE while bubbling with Ar + 5% H_2; empty symbols for tests performed in controlled gas atmosphere (Ar + 5% H_2)

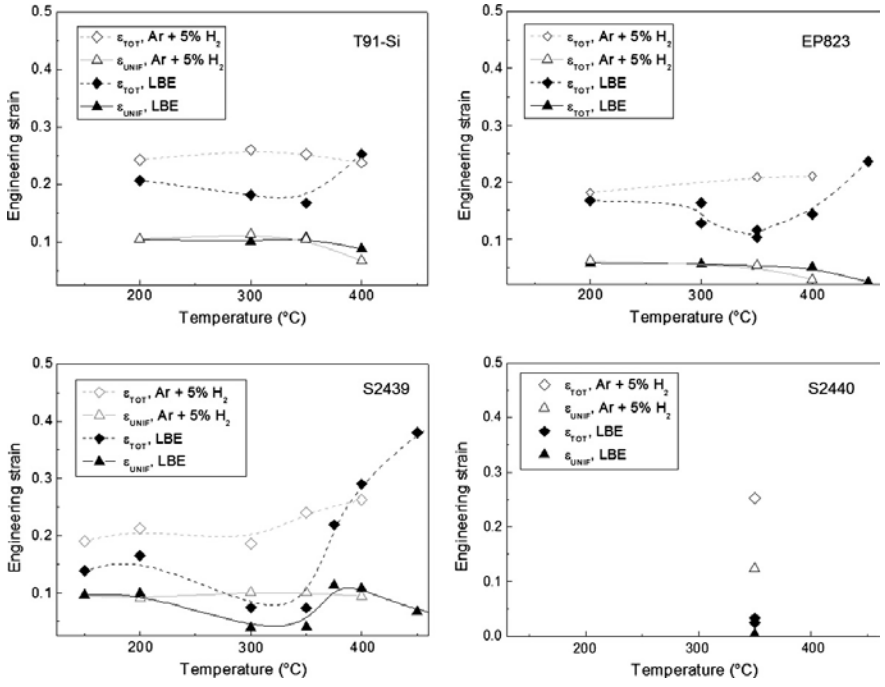

Figure 7.4.17: Total and uniform elongation of T91, T91-Si, EP823, S2439 and S2440 as function of strain rate (temperature 350°C)

Full symbols for tests performed in LBE while bubbling with Ar + 5% H_2;
empty symbols for tests performed in controlled gas atmosphere (Ar + 5% H_2)

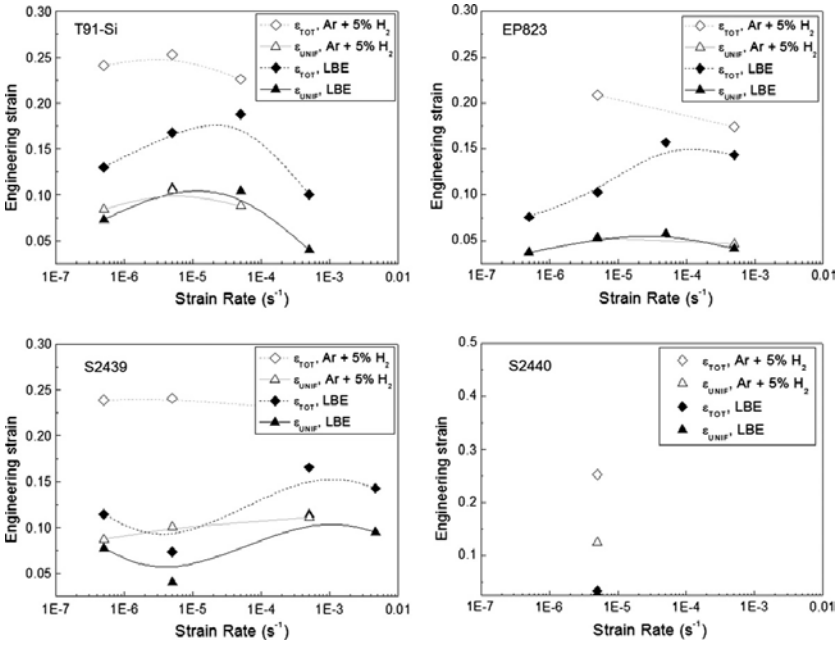

The tensile behaviour of all four Si-enriched steels is significantly different in liquid LBE environment than in gas. The main mechanical characteristic affected by LBE is the total elongation. This type of behaviour, where the uniform elongation remains the same while the total elongation is reduced, has been shown in the previous paragraph for the martensitic steel T91 tested in LBE.

For S2440, which was only tested at 350°C, fracture occurred at the onset of yielding when tested in LBE and therefore strongly reduced both total and uniform elongation when compared to the test results in gas.

For T91-Si, EP823 and S2439, the ductility seems to fully recover between 400 and 450°C. Based on Figure 7.4.16, the ductility trough of the examined Si-enriched steels seems to be between 200 and 400°C. Compared to the LME observed in ferritic-martensitic steels such as T91 and Eurofer97, the effect of the liquid metal environment is more severe for the bainitic elevated Si steel S2439 and the ferritic S2440 and the observed decrease in total elongation when testing in LBE for T91-Si and EP823 is slightly worse and more reproducible under the same testing conditions than for T91.

Although the addition of Si to the matrix is known to promote the formation of SiO_2 at the surface and decreases the wettability of the oxidised Si-enriched steel surface by LBE as observed by Zaïdi (2008), Si addition also influences the mechanical properties of the native oxide layer as discussed further below.

Figure 7.4.18 provides a visual representation of the different mechanical behaviours of ferritic-martensitic steels T91, T91-Si, EP823, bainitic steel S2439 and ferritic steel S2440 when tested in different environments by comparing the fracture surfaces after testing in Ar + 5% H_2 gas and liquid LBE at 350°C and a strain rate of $5{\cdot}10^{-6}$ s^{-1}. The images of T91 correspond to the SSRT test results reported in the previous paragraph after testing in Ar + 5% H_2 gas and liquid LBE at 350°C and a strain rate of $1{\cdot}10^{-6}$ s^{-1}.

Figure 7.4.18: Fracture surfaces of T91 tested in LBE and Ar + 5% H_2 at 350°C and $5 \cdot 10^{-6}$ s^{-1}, T91-Si, EP-823, S2439 and S2440, tested in LBE and in Ar + 5% H_2 gas mixture at 350°C and $5 \cdot 10^{-6}$ s^{-1}

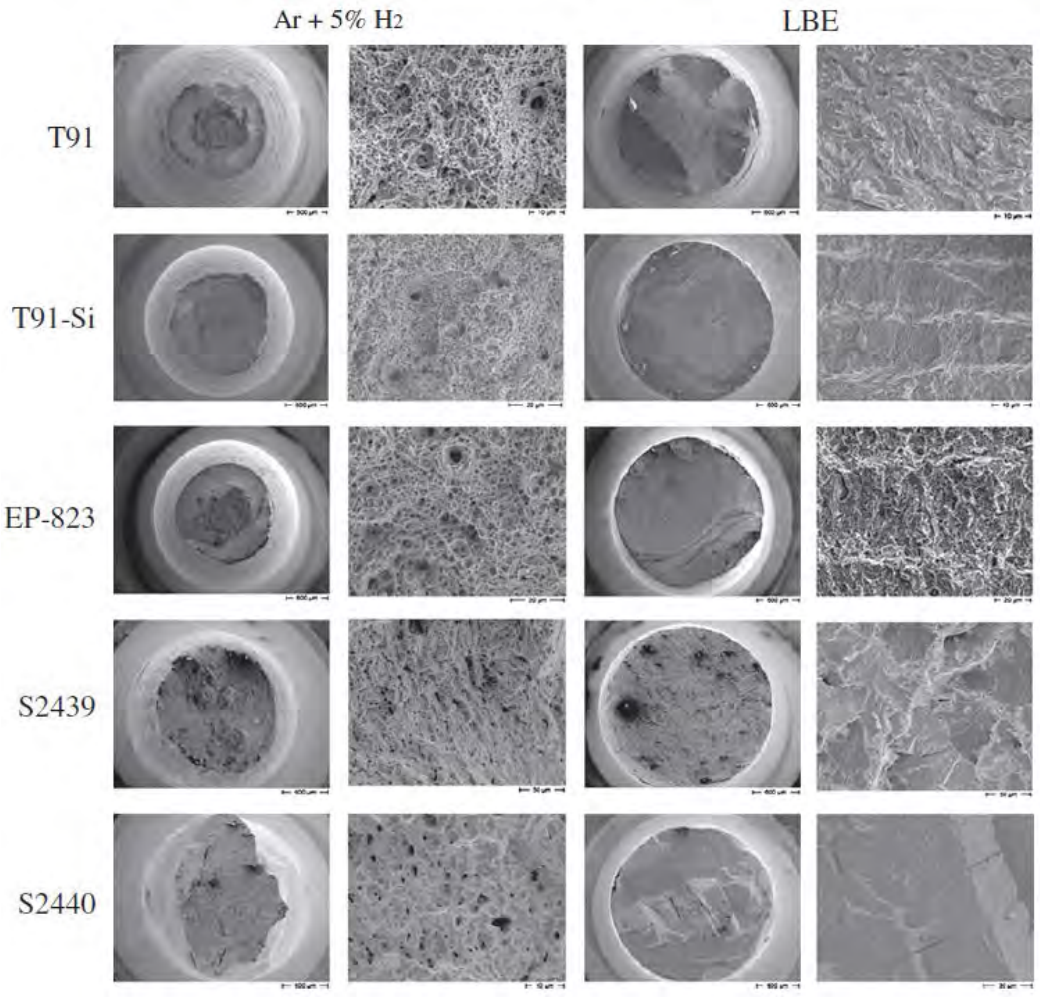

All investigated steels tested in gas environment have a dimpled fracture surface, thus indicating fully ductile fracture, with significant necking (Figure 7.4.18, left column).

After testing in liquid LBE however, there is absolutely no necking visible for S2439 and S2440, and there is hardly any necking for the ferritic-martensitic steels tested in LBE. For T91, T91-Si and EP823 there are several regions near the surface that have a fully brittle, transgranular cleavage fracture surface showing a semi-circular pattern while the centre of the specimen and/or parts of the edges are dimpled. This indicates that LME brittle fracture is initiated at the surface and grows inward while the competing ductile fracture is known to initiate internally and grows by microvoid coalescence thus creating dimples. The S2439 and S2440 steels show a fully brittle transgranular cleavage fracture surface after testing in liquid LBE at 350°C without any dimples. No intergranular fracture was observed.

Elevated Si steels have better corrosion resistance in LBE while their mechanical properties in LBE at an oxygen concentration of 10^{-5}-10^{-6} wt.% are very bad. The author explained the LME of Si-enriched steel by the mechanical properties of the native oxide layers. By using nano-indentation, they found that the oxide layer formed on EP823 while in contact with LBE was found to be slightly stiffer and significantly harder than that

formed on T91 under the same conditions. After nano-indentation, cracking was observed in EP823 along the inner oxide-bulk interface while no cracking was observed in the T91 oxide layer or along the interface. This difference in mechanical response of the Si-enriched oxide layer is thought to be related to improve wetting by penetration of the liquid through the cracked oxide when the material is stressed while in contact with LBE.

7.4.8 Main requirements to prevent LME effects

The following conditions must be fulfilled to prevent LME effects:

1) Excellent surface finish of the steel surface, which must be free of surface defects such as pre-cracks, scratches as a result of the surface preparation, and also free of inclusions or precipitates which could act as stress concentrators and initiate cracks in service conditions.

2) The presence of a protective oxide film on the steel surface prior to and during contact with the liquid metal, and self-healing in service conditions. This can be achieved by OCS implementation in the system. However, no OCS is required in the case of oxygen-saturated HLM during the entire life of the installation of interest.

3) No specific recommendation on the oxide film thickness, provided that the film remains adherent to the steel surface, with sufficient plasticity. This supposes an adapted oxide film composition and structure, which must be determined and controlled over the test duration, in each experimental situation of interest (Bichuya, 1969).

4) The temperature must be chosen outside the ductility trough, above the upper temperature limit, which means, for example:

   – $T \geq 425°C$ for T91, after hardening heat treatment and using notched specimens in oxygen-saturated lead (Nicaise, 2001; Vogt, 2002);

   – $T \geq 400°C$ for T91, after standard heat treatment, and using notched specimens in oxygen-saturated LBE (Guérin, 2003).

   There is no rigorous proof that the range of the lower temperature limit, close to the melting point or below the melting point of the embrittling metal, must be avoided. However, besides LME, solid-metal-induced embrittlement (SMIE) is a well-known phenomenon. Some manifestations of SMIE are famous in the literature (Gordon, 1982), which strongly suggests that one keeps the system above the upper limit of the ductility trough. This supposes a systematic study of the influence of the temperature and strain rate to determine the ductility trough of each new steel-HLM system, if no reliable data are available. This also supposes that the metallurgical state of the steel and the chemistry of the HLM be controlled over the entire testing procedure.

5) Control of the presence of impurities; attention must be paid to metallic embrittling impurities like zinc, antimony, tin, and to metalloid impurities and also to chloride and fluoride species not only in the liquid metal phase but also at all stages of the specimen preparation, especially if one uses the method of the soldering fluxes to wet the steel under study. Their presence, even as trace elements, may significantly affect the mechanical properties (Huthmann, 1980).

7.5 Small punch test

7.5.1 Description of the test

The small punch test (SPT) is a mechanical test approved in the 1980s for testing the irradiated materials because the test requires small quantities of materials.

It was suitable to characterise the plastic deformation behaviour and to point out the ductile to brittle transition treated by several authors (Lucas, 1990; Mao, 1991; Misawa, 1987; Ule, 1999; Finarelli, 2004; Jia, 2003). Another particularity of the SPT together with the small size of the specimen is that biaxial stress occurs at the surface of the specimen at the beginning of loading.

Recently, the SPT has been employed for the characterisation of the behaviour of materials in liquid metals by CNRS Lille (Serre, 2008, 2009). The set-up was designed to perform tests in air and in liquid metals (Pb, LBE, Na, Ga, etc.) at temperatures up to 550°C. It consists of a specimen holder, a pushing rod and a ball. The specimen holder includes a lower die, an upper die which is also used as the tank for the liquid sodium and four clamping screws. The load is transferred onto the specimen by means of a pushing rod and a 2.5 mm diameter tungsten carbide ball in contact with the lower surface of the specimen. In this way, the puncher being under the specimen (unlike usual small punch test set-up), the upper surface of the specimen is in contact with the liquid metal and is submitted to tensile loading (Figure 7.5.1). A typical response of a ductile material is shown in Figure 7.5.2 and comprises four stages. The first stage, noted as "1" on the curve in Figure 7.5.2, corresponds to the elastic bending. While the entire sample undergoes an elastic deformation, the ball-sample contact area, which is very small in size, is plastically deformed. The second stage (noted as "2") corresponds to a plastic bending state: the volume of the sample which is plastically deformed progressively increases spreading from the ball-sample contact area through the overall thickness and in a radial direction. Then a stretching of the membrane occurs in the third stage (noted as "3"). At this point, the deformation of the sample is not caused by bending but by stretching around the contact area between the ball and the sample. Micro-cracks are generated during this stage. Finally, during the fourth stage where the load reaches its highest value (noted as "4"), the main crack forms and propagates.

This technique, mainly used by the CNRS Lille team (Serre, 2008, 2009), allowed evidencing the sensitivity to LME using a smooth specimen with slightly more severe conditions than the tensile test did. Before testing, the sample surfaces were mechanically polished with SiC paper up to 1 200 grade and then electro-polished, in order to avoid effects due to the roughness of the surface and residual stresses developed during the mechanical polishing. The final thickness was 500 (±20) μm.

Figure 7.5.1: Small punch test (SPT) set-up

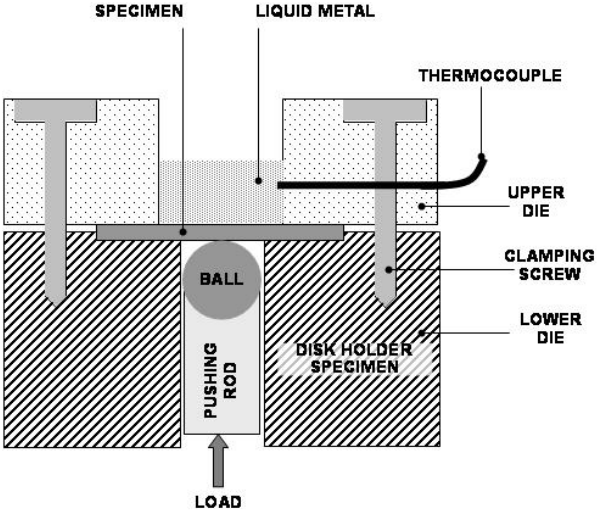

Figure 7.5.2: Typical SPT curve of a ductile material

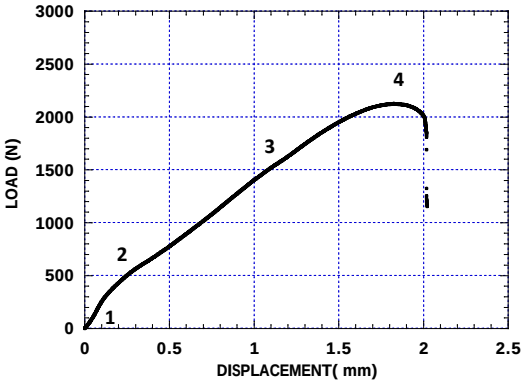

7.5.2 *T91 response in saturated oxygen LBE*

SPT were performed at 300°C for the T91 steel and in addition at 380°C for the 316L stainless steel in air and in saturated LBE (45 wt.% Pb and 55 wt.% Bi) at a controlled cross-head speed of 0.5 mm/min.

7.5.2.1 Behaviour of T91 steel: Role of heat treatment

LME was investigated through the effect of heat treatment as has been done for tensile testing (Serre, 2008). The effect of tempering temperature was investigated: 750°C (the recommended temperature), 500°C (giving rise to increased hardness) and absence of tempering. This corresponds respectively to materials TR750, TR500 and T.

Figure 7.5.3 shows the load displacement curves obtained at 300°C in air and in LBE. Tables 7.5.1 and Table 7.5.2 contain the mechanical data obtained from SPT carried out at 300°C in air and in oxygen-saturated LBE respectively.

One can see that the major difference is between T and TR500 materials tested in LBE with all the other materials. The load displacement curve of the TR500 material is quasi-linear up to failure, exhibits very little plastic bending and zero plastic membrane stretching. This is typical of brittle material. The tests performed on the T material in LBE at 300°C give rise to two kinds of curve. The first kind of curve, noted as T1, has all the features (quasi-linear response, weak maximum force), suggesting a brittle behaviour as for the TR500 material. The second one noted as T2, not linear right to failure and with a rather large maximum load, does not exhibit the character for brittle or clear ductile behaviour.

Figure 7.5.3: Load displacement curves of T91 steel according to the heat treatment and tested at 300°C in air (left) and in LBE (right)

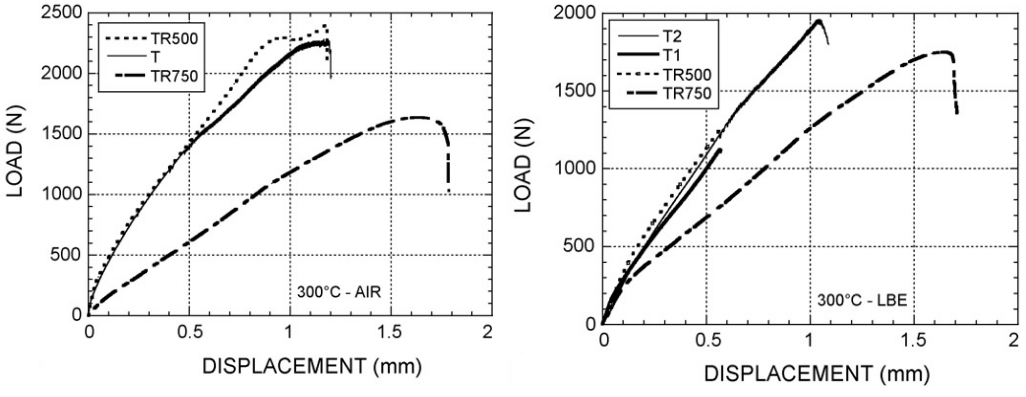

Table 7.5.1: Average values of key points measured in the small punch tests at 300°C in air

Tests in air at 300°C			
Heat treatment	T	TR500	TR750
F_m (N)	2 311±150	2 185±150	1 655±45
F_e (N)	530±50	592±80	345±40
J_f (J)	1.79±0.17	1.67±0.20	1.66±0.10
d_f (mm)	1.22±0.07	1.18±0.10	1.67±0.09
Fracture surface	Ductile	Ductile	Ductile

Table 7.5.2: Average values of key points measured in the small punch tests at 300°C in LBE

Tests in oxygen-saturated LBE at 300°C				
Heat treatment	T1	T2	TR500	TR750
F_m (N)	1 105±150	2 014±100	1 295±200	1 762±100
F_e (N)	Not measured	530±40	571±80	369±40
J_f (J)	0.33±0.07	1.27±0.25	0.39±0.09	1.8±0.15
d_f (mm)	0.5±0.06	1.04±0.10	0.54±0.08	1.66±0.11
Fracture surface	Brittle	Brittle	Brittle	Ductile

The suggested ductile to brittle transition has been confirmed from macro observation of deformed specimen and by SEM fractography (Figure 7.5.4). Low magnification SEM observations show that the specimen dome of TR750 contained a circular crack after test in LBE while radial cracks were observed on T and TR500 on the specimen domes of T and TR500 materials. For the latter materials, transgranular brittle fracture was mostly observed and intergranular brittle fracture occasionally observed.

Figure 7.5.4: SEM macrographs and SEM fracture surface

The SEM macrographs on the left show circular and radial cracks (a) TR750 material and (b) T material with only radial cracks at the surface of the samples tested at 300°C in LBE (c) TR500 material and (d) T material. The SEM fracture surface (set of three right images) after tests in LBE at 300°C showing transgranular brittle fracture (a and b) and intergranular brittle fracture (c)

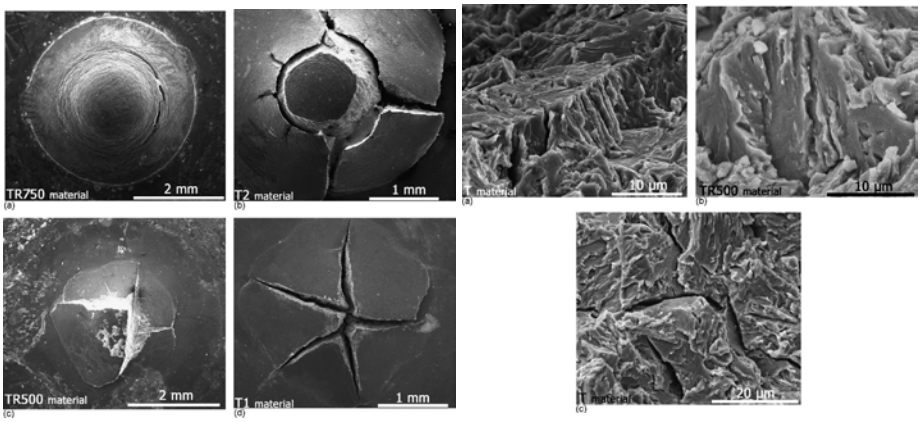

So, the main conclusion was that a clear LME embrittlement in T91 can occur without the pre-existing flaws at the surface of the specimen. The SPT experiments contrast with tensile test experiments where pre-existing flaws were at the origin of brittle fracture.

7.5.2.2 Behaviour of T91 steel: Role of oxide layer

The experiments where the oxide layer was controlled were performed by Auger (2008).

Flat discs of 8.9 mm diameter and 500 μm thickness of T91 martensitic steel were machined from the as-received alloy (tempered at 750°C). The surface of the disc to be prepared under ultra-high vacuum (UHV) was diamond-polished down to 1 μm. The samples were taken to an Auger/XPS set-up equipped with an ion gun and an Auger/XPS analysis set-up. Before sputtering, the native oxide is composed of a mixture of external iron oxide and internal chromium oxide typical for a Fe-Cr alloy. The surface of the disc was ion beam etched with krypton ions at an energy of 3 keV up to the disappearance of the O-KLL transition on Auger spectra (<1% monolayer surface coverage). After this cleaning step, four conditions were investigated:

- DNO2 is an oxygen free interface.
- D0.5O2 and D4O2: *In situ* re-oxidation has also been performed according to two different conditions. At once, the clean samples were brought back after ion etching in the sample transfer chamber. The chamber was then filled with oxygen at 20 mbar pressure and the samples were re-oxidised during 0.5 h and from 4 to 8 h at room temperature (D0.5O2 and D4O2, respectively).
- DAO2: Specimen was air oxidised in the transfer chamber at a 210 mbar O_2 pressure for 250 h.

Finally, the oxide thickness and the composition of the thin oxide film formed were characterised by XPS. After the alloy surface was re-oxidised and analytically characterised to a given level, a solid Pb-Bi coating is deposited by physical vapour deposition (PVD). As this deposit solidifies in UHV, it is enough to protect the interface from re-oxidation and to allow one to transfer in air without special care the sample to a SPT testing apparatus. Samples in the DAO2 condition were also coated by PVD after having been re-introduced in the UHV set-up.

The load displacement curves of the SPT of D4O2, D0.5O2 and DNO2 performed at 250°C and 300°C have shown that, if taking as reference the SPT curve of the air-oxidised specimen (DAO2), the load displacement curves of the other specimens are systematically below. The behaviours of the DNO2 specimens were very remarkable in their lower values of the yield point values, suggesting a strong LME effect. Interestingly, there is also a tendency to measure decreasing load values (at a given displacement value) with decreasing oxide layer thickness. The effect of oxide layer thickness appears to be correlated to the fracture energy values (see Table 7.5.3) calculated from the load displacement integral. Indeed, the total energy for final fracture increases as a function of the oxide thickness. It indicates an effect on crack initiation and crack propagation linked with the oxide type.

Table 7.5.3: Fracture energy evaluated from SPT curves according the oxidising conditions and tests temperatures

Test temperature (°C)	DAO2 (J)	DNO2 (J)	D0.5O2 (J)	D4O2 (J)
250	1.91	1.44	1.34	1.46
300	1.79	0.87[a]	1.40	1.52

SEM macro top view of the DNO2 (non-oxidised condition) sample after being tested at 300°C in LBE revealed a lot of circular cracks. The SEM scans presented taken near the crack initiation site showed a difference in the fracture modes as a function of the oxidising condition. It can be seen that the DNO2 specimen (non-oxidised condition) exhibits a fully transgranular brittle fracture surface (Figure 7.5.5[a]). On the other hand, a ductile fracture was observed in the DAO2 specimen (native oxide condition) without any sign of brittleness (Figure 7.5.5[d]). For the two other samples, D0.5O2 and D4O2, intermediate situations were obtained. In the D0.5O2 specimen (low oxidation condition) multiple cracking on the disc top did not occur. The fracture near the external surface looks fully ductile without any brittle fracture. Surprisingly, the D4O2 specimen (medium oxidation condition) exhibits multiple cracking, as in the DNO2 specimen (non-oxidised condition). The fracture surfaces near the external surface of most cracks were found to be of brittle transgranular type. In this case, however, the brittle zone extended at most up to a few tens of microns. SEM BSE views taken before LBE dissolution showed that LBE is found on the brittle fracture surfaces overcoming the wetting barrier of the oxide. This clearly shows that in spite of the presence of the oxide, a brittle fracture promoted by the liquid LBE is possible and that not any type of oxide layer can guarantee a protection against LME. The small area concerned with the brittle fracture is most likely linked with the limited amount of LBE deposited on the surface by the PVD technique. However, the size of the affected zone is large enough to be considered as being a definite proof that LME can occur in spite of the development of an already quite thick oxide.

Figure 7.5.5: SEM images of the fracture surface

a) DNO2 at 300°C, b) D0.5O2 at 300°C, c) D4O2 at 300°C, d) DAO2 at 250°C

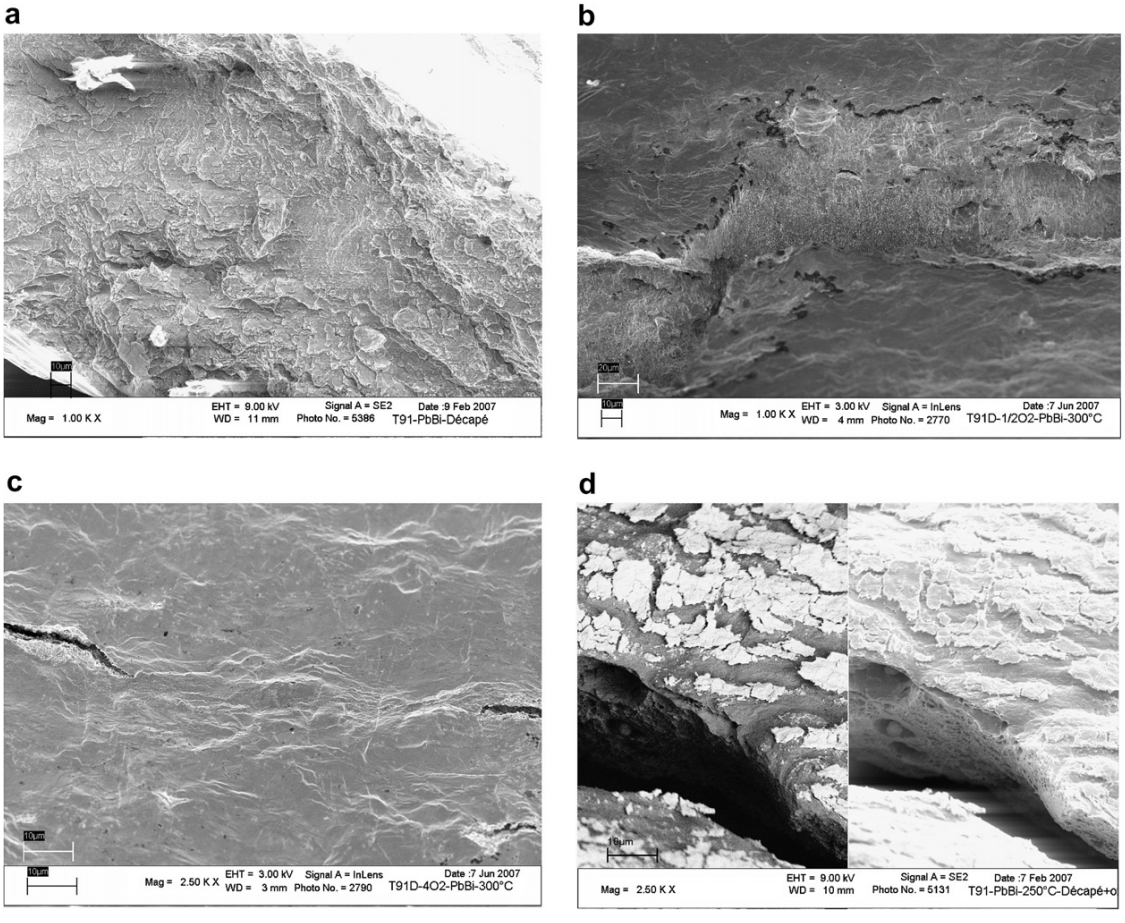

7.5.3 316L stainless steel response in saturated oxygen LBE

The behaviour of 316L austenitic stainless steel in air and in saturated oxygen LBE has been investigated at 300°C and 380°C.

The load displacement curves were nearly the same for all conditions, with the same key point values and the fracture surfaces were always ductile with dimples (Figure 7.5.6).

No evidence of LBE embrittlement has been observed for these conditions.

Figure 7.5.6: Load displacement curves (left) of 316L tested at 300°C and 380°C in air and in saturated LBE and ductile fracture (right)

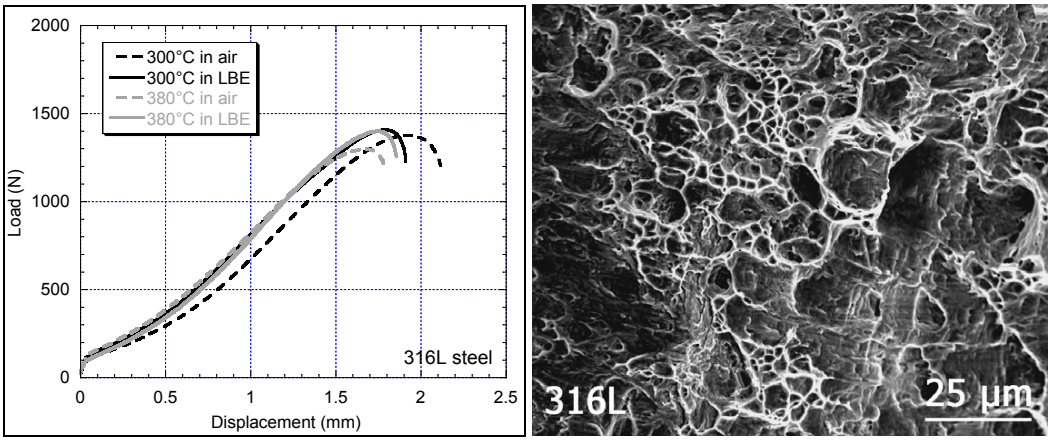

7.5.4 Effect of temperature and of variable strain rate tests in low oxygen LBE

SPT were performed at 200°C, 300°C and 400°C on the T91 steel (tempered at 750°C) in air, in oxygen-saturated LBE and in low oxygen LBE (10^{-8} wt.%). SPT were performed at controlled cross-head speed of 0.5 mm/min, 0.05 mm/min and 0.005 mm/min (Ye, 2014).

At a displacement speed of 0.5 mm/min, the load displacement curves of TR750 SPT specimens tested at 200°C, 300°C and 400°C in purified liquid LBE and in oxygen-saturated LBE exhibited the same behaviour for a given test temperature (Figure 7.5.7).

Figure 7.5.7: Load displacement curves of T91 steel tested at 200, 300 and 400°C in saturated and low oxygen LBE

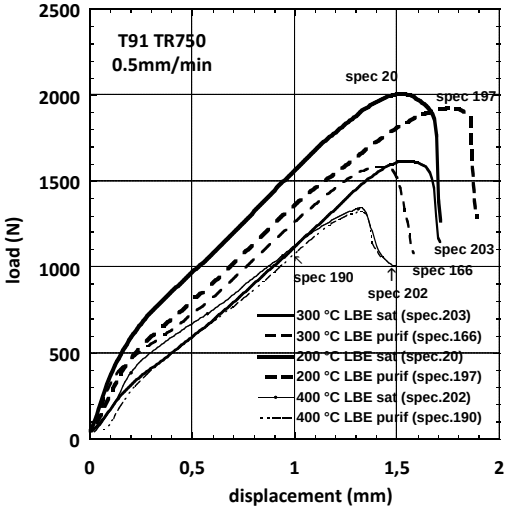

SEM observations of TR750 SPT specimens in oxygen-saturated LBE and in low oxygen LBE revealed that the shape of the cracks was circular with some small radial cracks.

At a test temperature of 300°C, the load displacement curves of TR750 SPT specimens tested material in low oxygen LBE at 300°C at a displacement speed of 0.5 mm/min and 0.005 mm/min exhibited a pronounced difference. First, for the lowest displacement speed, the maximum load was strongly reduced as compared to the other tests performed at high speed by a factor of two-thirds. Second, the displacement at maximum load was decreased in the same way (Figure 7.5.8).

Figure 7.5.8: Load displacement curves of T91 steel tested at 0.5 and 0.005 mm/min in low oxygen LBE

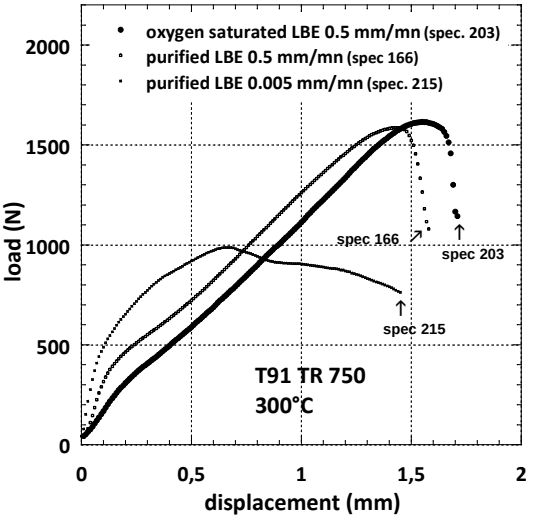

Analysis of the fractured specimen also pointed out an effect of the displacement velocity as well at the macroscopic and microscopic scales. All SPT specimens exhibited circular and radial cracks but the decrease in the displacement velocity promoted radial cracking. For the lowest displacement velocity, the number of radial cracks was much reduced as compared to the other tests but the radial cracks were also much longer (Figure 7.5.9). In addition, transgranular brittle fracture was observed (Figure 7.5.10).

Figure 7.5.9: SEM image of the dome of the TR750-T91 after testing in low oxygen LBE at 300°C at a displacement speed of 0.005 mm/min

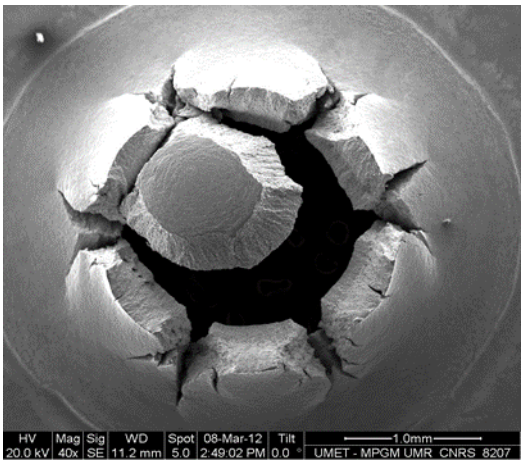

Figure 7.5.10: SEM image of brittle fracture in the TR750-T91 after testing in low oxygen LBE at 300°C at a displacement speed of 0.005 mm/min

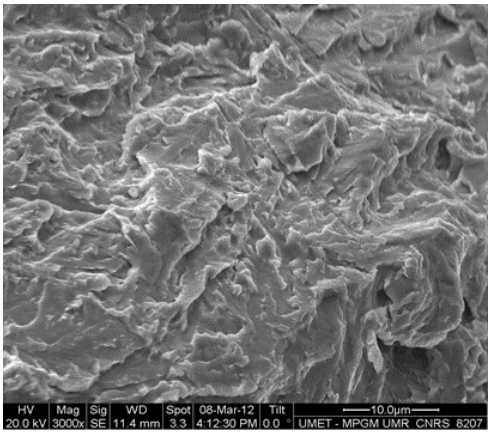

7.5.5 316L/T91 EB weld joint response in saturated oxygen LBE

The EB welding of T91 with 316L was carried out at KIT (Germany) as described in Section 7.4. Before welding, each material received its own heat treatment. A voltage of 60 kV at a current of 62 A and a welding speed of 10 mm/s were controlled. After welding, the welded plate was subjected to a post-welding heat treatment (PWHT) under argon which consisted in heating up the material from room temperature to 740°C at a heating rate of 100°C /h, holding it for 45 mn, and then cooling at a rate of 100°C/h down to room temperature.

The molten material zone is about 1 mm wide and comprises two parts. The first one, referred to as ZA, was the largest and was characterised by an acicular microstructure. In the second part, referred to as ZD, a mixture of dendrites and needles was observed. The ZD part has a higher quantity of chromium (15 wt.%) as well as a higher quantity of nickel (7.5 wt.%) as compared to the ZA part (respectively 12 wt.% and 4.5%).The chromium and nickel contents appear as the average values between those of T91 and of 316L base materials.

Cylindrical bars 8.9 mm in diameter were extracted from the 316L/T91 weld joint to obtain samples from the three different zones: T91, 316L and weld (see Figure 7.5.11). For reasons of dimensions, the sample used for SPT did not contain the ZD part. Tests were carried at 300°C and at 380°C, in laboratory air or in LBE.

Figure 7.5.11: Schematic representation of the weld metal

The circles indicate the location where SPT were extracted

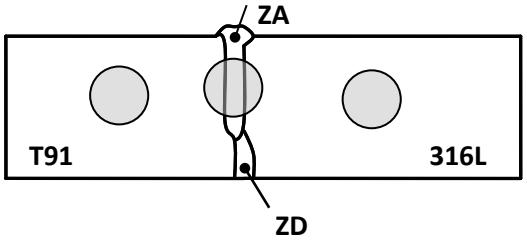

The load displacement curves (Figure 7.5.12) related to the weld joints tested in air and LBE at 300°C and 380°C also exhibit a typical shape of a ductile response. However, for a given temperature, they strongly differ from air to LBE by the maximum load values

and its associated displacement values which are smaller in LBE test than in air test. This is also associated with a reduction of about 30% of the normalised fracture energy. The normalised fracture energy of the T91/316L weld joint specimen was comparable to that of the 316L specimen for tests in air. For tests in LBE, the fracture energy of the T91/316L weld joint specimen was 25% and 30% lower, respectively at 300°C and 380°C, in comparison with the values obtained in 316L material.

Figure 7.5.12: Load displacement curves of T91/316L weld tested at 300°C and 380°C in air and in oxygen-saturated LBE

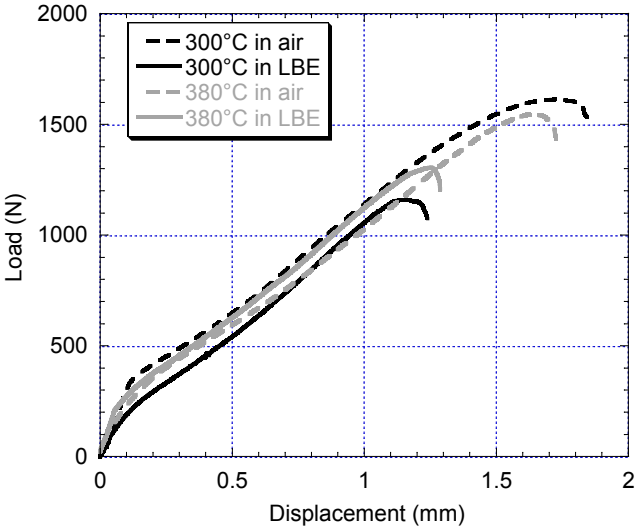

The general aspect of the weld joint fractured in air is that cracking is circular or semi-circular with a ductile fracture surface and therefore behaves as a homogeneous material (Figure 7.5.13[a]). But, in some samples, though the cracking is circular and the fracture ductile, cracking tends to propagate outwards in a linear direction, which was identified by EDX analyses as the interface between the weld and the T91 steel. The fracture surface of the circular crack is ductile whereas the linear crack at the interface is flat and looks more like decohesion rather than a brittle fracture. It was noted that generally the semi-circular crack was located largely in the T91 steel (Figure 7.5.13[b]).

Figure 7.5.13(a): General aspect of the weld joint fractured in air at 300°C with circular or semi-circular cracking

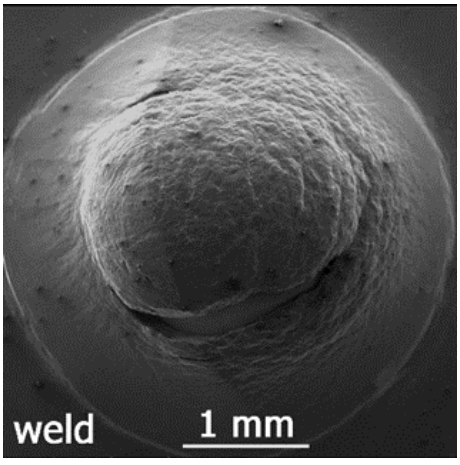

Figure 7.5.13(b): Macroview of the T91/316L weld with a semi-circular crack accompanied with a linear crack at the interface T91/ weld after test in air at 300°C, and fractographs showing ductile fracture in T91 and decohesion of the linear crack

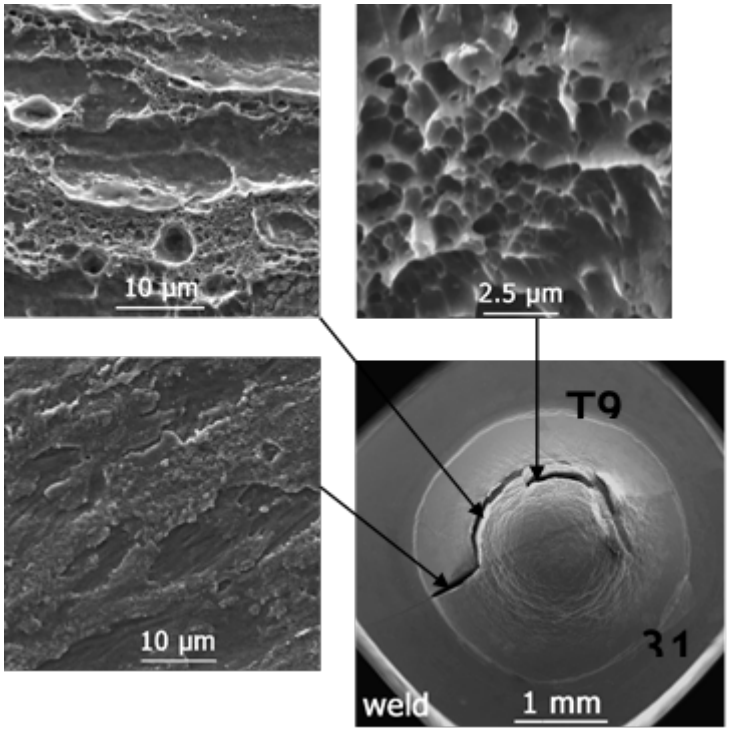

In LBE, two types of cracking were observed. The first one consists of an initial semi-circular crack localised for a large part in the T91 steel, which tends to propagate in a linear direction at the interface between the weld and the T91 steel. In this case, the semi-circular crack is ductile and the interfacial crack has the same aspect of decohesion as in air (Figure 7.5.17[a]). The second type of cracking was characterised by a semi-circular crack widely open and developed in the T91 steel but also to a lesser extent in the 316L steel and in the weld. In this case, the interface between the weld and the T91 steel also cracked but was less open. In addition, short radial cracks were observed in the T91 steel. The fracture surface of the circular crack is ductile in T91 steel, 316L steel and the weld, while a decohesion-like fracture was observed at the interfacial crack. However, the radial cracks are brittle and transgranular (Figure 7.5.14[b]).

Figure 7.5.14(a): Macroview of the T91/316L weld with a semi-circular crack along with a linear crack at the T91/ weld interface after testing in LBE at 380°C

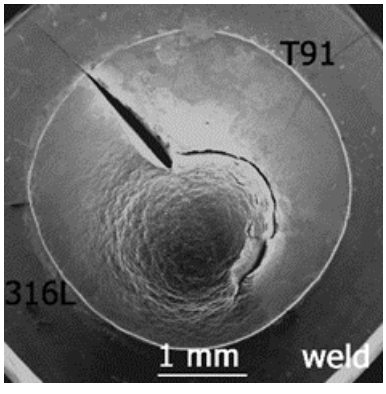

Figure 7.5.14(b): Macroview of the T91/316L weld with a semi-circular crack accompanied with short radial cracks after testing in LBE at 300°C, and fractographs showing ductile fracture (upper images) and brittle fracture (lower micrographs)

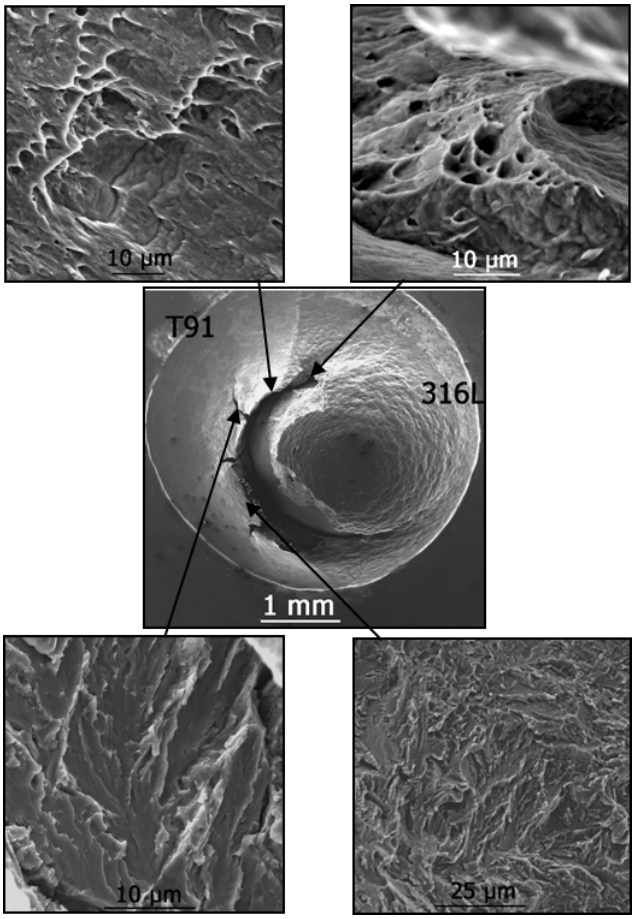

7.6 Fracture toughness

7.6.1 *Definition*

Fracture toughness is defined as the resistance of a material to unstable crack propagation at elastic stresses. Mode I fracture is the condition in which the crack plane is normal to the direction of largest tensile loading. This is the most commonly encountered mode. It is a very important material property since the manifestation of flaws is not completely avoidable in the processing, fabrication or service of a material/component. Flaws may appear as cracks, voids, metallurgical inclusions, weld defects, design discontinuities or some combination of these. The linear elastic fracture mechanics (LEFM) approach is often employed to design critical components. This approach uses the flaw size and features, component geometry, loading conditions and the material property called fracture toughness to evaluate the ability of a flawed component to resist fracture. Several parameters can be employed to characterise the toughness of materials:

- A parameter called the stress intensity factor (K) is used to determine the fracture toughness of most materials. K is a function of crack length, average stress and geometrical factor. Cracks propagate when the applied stress intensity factor reaches a critical value for the material. When K exceeds the critical value K_{IC}, then the crack suddenly advances.

- The *J* parameter is a measure of energy needed to drive a crack under monotonic loading conditions. This value is calculated at several points along a loading curve. The load line compliance and the area under the load vs. clip gauge opening displacement curve are used in calculating the crack length and *J* values. A plot of *J* versus the change in crack length is then plotted. A least-squares curve is then plotted through the valid data set. Where this regression line crosses an offset line, a qualification *J* is chosen and called J_q. A series of validity checks are then run. If these checks pass, the qualification J_q is then termed J_{IC}.

When a material with a crack is loaded in tension, the materials develop plastic strains as the yield stress is exceeded in the region near the crack tip. Material within the crack tip stress field, situated close to a free surface, can deform laterally because there can be no stresses normal to the free surface. The state of stress tends to be biaxial and the material fractures in a characteristic ductile manner, with a 45° shear lip being formed at each free surface. This condition is called "plane stress" and it occurs in relatively thin bodies where the stress through the thickness cannot vary appreciably due to the thin section. However, material away from the free surfaces of a relatively thick component is not free to deform laterally as it is constrained by the surrounding material. The stress state under these conditions tends to triaxial and there is zero strain perpendicular to both the stress axis and the direction of crack propagation when a material is loaded in tension. This condition is called "plane strain" and is found in thick plates. Under plane strain conditions, materials behave essentially elastic until the fracture stress is reached and then rapid fracture occurs.

7.6.2 Available data

Fracture toughness experiments of T91 steels and 316L stainless steels in LBE have mainly been performed at SCK•CEN (Belgium) (Van den Bosch, 2009b; Coen, 2010) on disk-shaped compact test (DCT) specimens, at Ustav Jaderneho Vyzkumu Rez a.s. (Czech Republic) (Hojna, 2011) on round compact test (RCT), at PSI (Switzerland) (Long, 2008b) on three-point bending test (TPBT) specimen and at CNRS (France) (Auger, 2011) on Centre cracked in tension (CCT). Most of the experiments were performed at 300°C but additional results at 160, 200, 250, 350, 400 and 500°C have also been obtained.

Because the number of investigations is small, we recall the chemical composition and the heat treatment of the tested materials. The chemical composition of T91 is provided in Table 7.6.1, and the thermal treatment applied to the material by each laboratory is reported in Table 7.6.2.

Table 7.6.1: Chemical composition of T91 tested according to the testing laboratory

	Cr	Ni	Mn	V	Nb	Mo	Ti	Al	Cu	C	N	P	S	Si	Co
SCK, CNRS	8.99	0.11	0.38	0.21	0.06	0.89	0.03	0.015	0.06	0.10	0.042	0.021	0.0004	0.22	
PSI	8.76	0.099	0.597	0.186	0.073	0.862	–	–	0.054	0.088		0.019		0.317	0.019
Ustav	8.87	0.12	0.39	0.20	0.08	0.87	–	0.01	0.08	0.10	0.01	0.02		0.22	

Table 7.6.2: Heat treatment performed on T91 according to the testing laboratory

	Normalising	Tempering
SCK	1 050°C – Water quench	770°C – Air cooling
PSI	1 040°C – Air cooling	500°C, 600°C or 750°C – Air cooling
Ustav	1 050°C – Water quench	770°C – Air cooling

7.6.3 Fracture toughness of T91 martensitic steel in LBE at 200 °C and 300 °C

Two methodologies were considered for the toughness measurement. The first is based on a CCT sample geometry involving plane stress loading and is more relevant for thin wall applications such as cladding tubes. The other is based on DCT and RCT sample geometry and allows approaching a plain-strain fracture toughness measurement.

7.6.3.1 Toughness assessment by DCT specimen

The experimental procedure employed at SCK•CEN consisted of loading T91 at a displacement rate of 0.25 mm/min in air and in a LBE bath saturated in oxygen. DCT specimens (Figure 7.6.1) were employed and pre-cracked in fatigue to a crack length of $a = 1/2W$, where a is the crack length and W is the width of the specimen. The force displacement data, consisting of the deformation of the load line and the crack mouth opening displacement (CMOD), which is the crack displacement due to elastic and plastic deformation measured by the clip gauge extensometer at the mouth of the crack, were employed for fracture toughness measurements. Figure 7.6.2 shows an experimental load displacement curve for T91 in air and in LBE at 200°C.

Figure 7.6.1: Shape and dimensions of DCT employed for toughness measurement

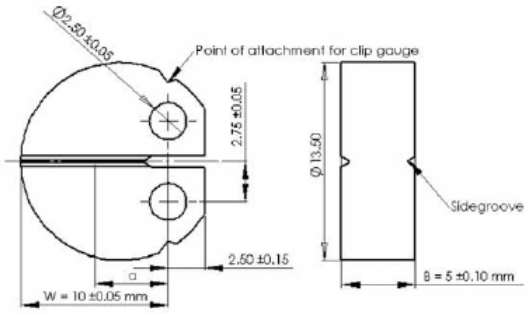

Figure 7.6.2: Force displacement curves of T91 steels at 200°C and 0.25 mm/min

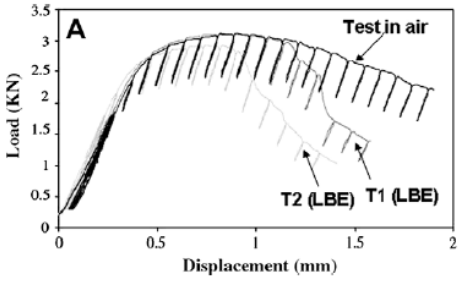

The average J_q value at 200°C is 223 kJ.m^{-2} for the test in air and 174 kJ.m^{-2} for the test in LBE, a difference of about 30% with the average value of the tests in air. In air, the specimen fractured due to a ductile fracture mechanism (void nucleation, growth and coalescence) resulting in the dimpled fracture surface while in LBE a mixed ductile-brittle fracture surface was observed with several grains cracked in cleavage mode (Figure 7.6.3).

A decrease in J_q due to LBE is still observed at 300°C. In air, the J_q value of 222 kJ.m^{-2} moved to 185 kJ.m^{-2}. The embrittlement was confirmed by SEM observations. However, although there is embrittlement of the T91 steel by the LBE, there is still sufficient ductility to prevent brittle failure.

Note: SCK•CEN mentioned that though the values are not valid as J_{Ic} values, they give a clear indication of the decrease of the plain-strain fracture toughness when tested in LBE.

Figure 7.6.3: Fracture surfaces of T91 steel tested at 200°C

Mixed ductile and brittle fracture surface in LBE (left)
and dimpled ductile fracture surface in air (right)

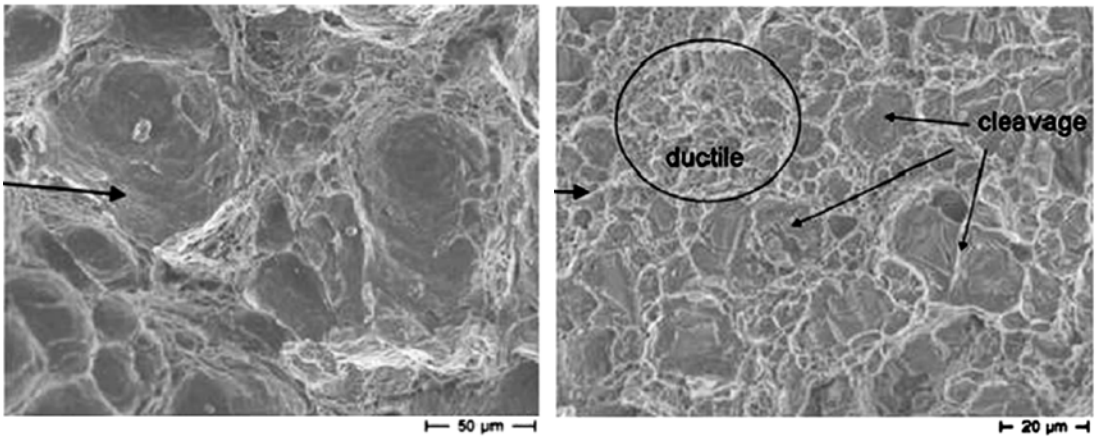

For TPB test the specimens (Long, 2008b) were fatigue pre-cracked to a ratio of the crack length to specimen width of about 0.5. The reference medium was argon and the oxygen content in the LBE should have been below 1 wppm. The same reduction in toughness was observed between tests in Ar and tests in LBE.

7.6.3.2 Toughness assessment by CCT specimen

The experiments performed by Auger (Hamouche, 2008; Auger, 2011) involved a pre-wetting of the CCT specimen performed by chemical fluxing. This is done on the flat blank of a notch machined in a thin T91 CCT specimen. The notch surfaces were hand polished (using 1 200 grade SiC paper) and the CCT specimen is heated at 200°C. The chemical flux (Castolin FP4201 composed of $ZnCl_2$, NH_4Cl, $SnCl_2$, HCl and water) is applied to dissolve the oxides at the notch that is filled immediately with a small drop of liquid LBE. After cooling, each sample is thoroughly cleaned in distilled water. The absence of chemical contamination by flux elements (Zn, Cl, Sn) has been checked by EPMA. No pre-cracking was performed. Subsequent testing was performed in a quartz cell under a reducing cover gas (He-4%H_2). Heating of the sample was achieved through the Joule effect using a high intensity and low voltage internal current loop. No pre-exposure was performed, the crack propagation was studied after the desired temperature and thermal equilibrium was reached (measured by an on-line pyrometer). The loading rate in the experiment was constant and was measured by the cross-head speed (set to $6{\cdot}10^{-6}$ m s^{-1}). The CCT specimen had the dimensions given in Figure 7.6.4.

The fracture toughness results for the CCT geometry are plotted in Figure 7.6.5 for four test temperatures (160, 250, 300 and 350°C). At 350°C in contact with LBE, there is a ductility recovery (Hamouche-Hadjem, 2009). The fracture toughness is plotted for comparison with the reference one obtained at 160°C. For the other test temperatures, this was not possible with the employed specimen geometry due to the side effect of dynamic strain ageing. Only the reference T91 toughness at 160°C associated with a ductile fracture has been found measurable even if it is still limited to small crack length. Notwithstanding these difficulties, fracture toughness in the ductile case does not vary much within the investigated temperature range and these two cases (160°C and 350°C in LBE) represent the reference fracture toughness to be compared to. The *J-R* curves of T91 in contact with LBE at 300°C show a marked reduction compared with the reference ones (160°C in argon and 350°C in LBE). The toughness reduction is of the order of 20% by comparison with that measured at 350°C where a ductility recovery occurs. The toughness

reduction is slightly higher at 160°C than at 250°C and 300°C (of the order of 30%). The effect of temperature could be due to a difference in the crack initiation process at the different temperatures. The slope of the *J-R* curve is the same once a stable subcritical crack has been generated.

Figure 7.6.4: Shape of CCT employed for toughness measurement width

W = 50 mm, thickness *B* = 1.5 mm, *a* = 5 mm

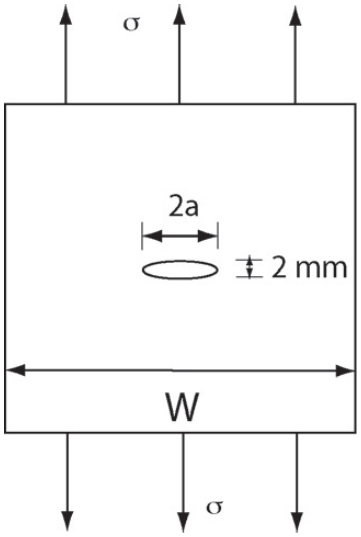

Figure 7.6.5: *J-R* curves for T91 in contact with LBE in the CCT geometry

Ductile cases: T91 in Ar at 160°C and T91/LBE at 350°C
Brittle cases: T91/LBE at 160°C, 250°C and 300°C

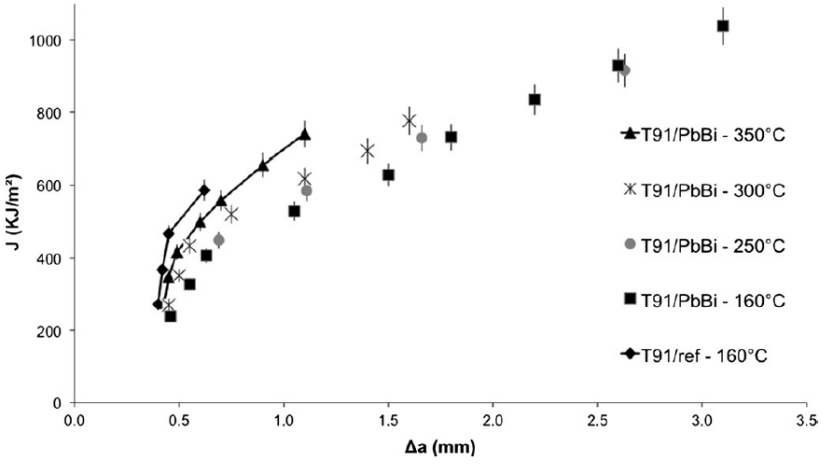

For the CCT specimen broken in LBE at 300°C, crack initiation occurs after a large amount of plastic deformation localised at the tip of the notch (Figure 7.6.6[a]). The cleavage or pseudo-cleavage fracture mode is observed at the crack initiation site (Figure 7.6.6[b]). Brittle cracking in this fracture mode runs over approximately 100 μm. Then the fracture mode switches to shear cracking over more than 10 mm with a fracture plane macroscopically in the transverse plane relative to the tensile axis (Figure 7.6.6[c]).

Figure 7.6.6: (a) Top view of the fracture surface of T91 in the CCT geometry tested at 300°C with LBE; (b) view of crack initiation site; (c) view of a shear fracture area (crack propagation proceeds as indicated by the white arrow)

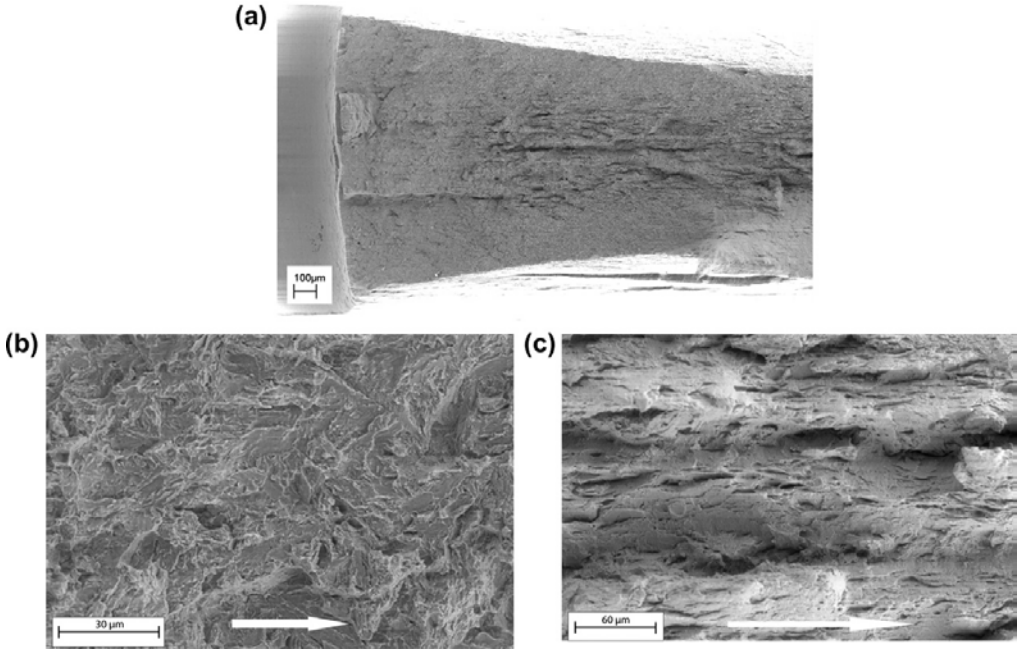

7.6.4 Effect of pre-exposure

The effect of pre-exposure has been taken into account by maintaining the material at 500°C for 1 000 h in LBE with an oxygen content of less than 10^{-6} wt.% and with a flow rate of about 1 cm/s (Hojna, 2011). The influence of LBE on the crack growth rate (CGR) was studied using a two-phase loading method: during the first pre-cracking phase, a cyclic load under load control was applied at a frequency of about 1 Hz; the number of cycles was different for each experiment. Afterwards, the specimen was unloaded and a slow rising displacement at a constant cross-head speed was applied.

It was found that 8 (out of 14) specimens underwent fast rupture during the first phase loading in LBE. Amongst these ruptured specimens: four were RCT (6 mm thick) pre-exposed in LBE, four were RCT and RCT (8 and 6 mm thick) in the as-received state. This fast rupture was due to both environment and loading mode. The failures of the pre-exposed specimens in LBE were extremely fast. This will be discussed in Section 7.8.

The average CGR measured during the slow rising displacement phase is plotted vs. the test displacement rate (Figure 7.6.7). Clearly, all data points of LBE were slightly above the ''no environment effect'' line, meaning that the environment slightly increased the CGR. The effect was stronger at lower displacement rates. However, the one data point of the pre-exposed specimen showed four times higher CGR together with a complete change in the fracture mode.

For tests in air a ductile dimple fracture mechanism of the crack growth during monotonic loading was observed. In LBE, there was no change of fracture mode if the as-received specimen was pre-cycled in air or in LBE. However, for pre-exposed in LBE and pre-cycled in LBE specimens, transgranular cleavage-like fracture was the single fracture mode examined for the slow rising displacement in LBE (Figure 7.6.8).

Figure 7.6.7: Average measured CGR vs. displacement rate of the constant displacement rate stage

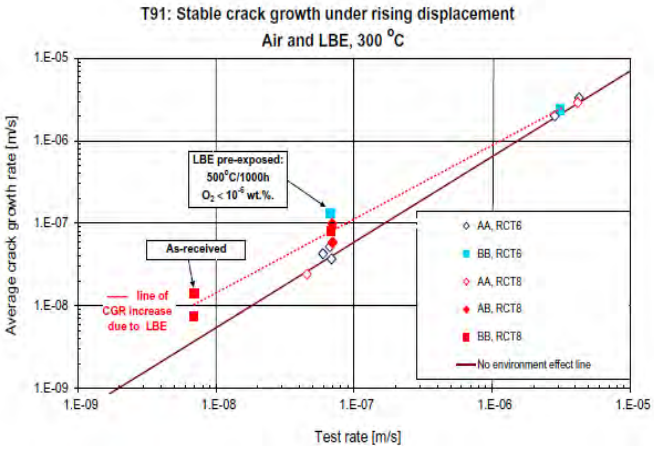

Test condition	Number of specimens		Media/environment	
	RCT6	RCT8	1. Phase: cyclic load	2. Phase: rising displacement
AA	5	2	Air	Air
AB	–	4	Air	LBE
BB	1	7 (3)[a]	LBE	LBE
BB pre-exp	6 (5)[a]	–	LBE	LBE

[a] Number of specimens failed during 1st cyclic load phase

Figure 7.6.8: Details of fracture morphology of the pre-exposed in LBE and pre-cycled in LBE specimen subjected to the slow rising displacement in LBE

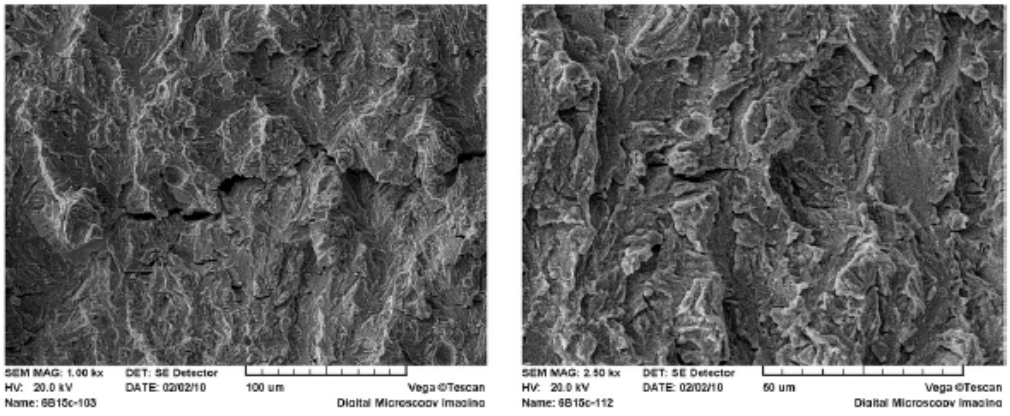

7.6.5 *Effect of heat treatment on T91*

The standard heat treatment of T91 comprises a tempering step for which the temperature is of prime interest. The standard heat treatment recommends a tempering temperature in the range 750-770°C.

The role of tempering temperature has been studied by tempering the T91 at 500°C and at 600°C instead of 750°C (Long, 2008b).

TPB test on a pre-fatigued specimen to a ratio of the crack length to specimen width of about 0.5 were carried out. The reference medium was argon and the oxygen content in the LBE should have been below 1 wppm. Tests were performed at 200, 300, 400 and 500°C.

The evolution of the J_q value with test temperature and environment is reported in Figure 7.6.9 for the material tempered at 500°C, 600°C and 750°C.

The results demonstrate that hardening of the T91 steel has a significant influence on its susceptibility to LBE-induced embrittlement. The 500°C tempered specimens with the highest hardening were the most sensitive to LBE embrittlement, which resulted in brittle fracture at lower temperatures and substantial reduction of fracture toughness up to 400°C. The 600°C tempered specimens with medium hardening appeared quite sensitive

to LBE embrittlement as well. The *J* values reduced more than 50% in a temperature range of 200-400°C. The specimens of non-hardened normal T91 steel also illustrated embrittlement effect. The *J* values reduced 20-30% in the presence of LBE.

Figure 7.6.9: Evolution of the J_q value with test temperature and environment for T91 tempered at 500°C (left), 600°C (middle) and 750°C (right)

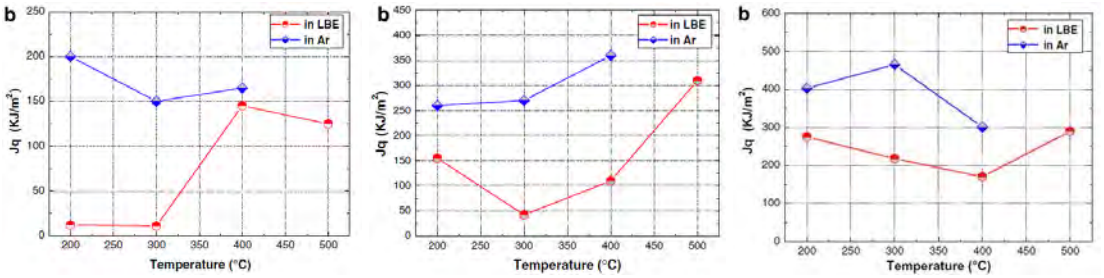

The SEM observation illustrated that almost all specimens tested in Ar and some the 750°C tempered specimen tested in LBE ruptured in ductile fracture mode. Most of the 600°C tempered specimens tested in LBE ruptured in a mixed ductile-brittle fracture mode. Only the 500°C tempered specimens tested at 200°C and 300°C in LBE showed nearly pure cleavage fracture.

7.6.6 *Fracture toughness of 316L austenitic steel in LBE at 200°C and 300°C*

With the same procedure employed for characterisation of the T91 steel by Coen (2010), 316L austenitic stainless steel appeared to be almost insensitive (Figure 7.6.10). The J_q values of 316L steel in air were 258 kJm^{-2} at 200°C and 199 kJm^{-2} at 300°C. In LBE, these values were respectively 232 kJm^{-2} and 175 kJ m^{-2}.

A difference of 10% is within the normal scatter range found in fracture toughness tests, so the J_q values for 316L austenitic stainless steel showed no clear signs of LME.

Figure 7.6.10: Force displacement curves of tests on austenitic stainless steel 316L in air and in oxygen-saturated LBE

Tests performed at 200°C (A) and 300°C (B)

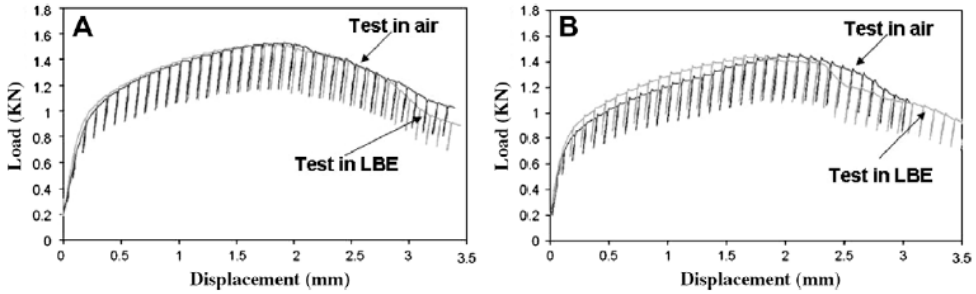

7.7 Creep

7.7.1 *Definition*

Creep of a material refers to its increasing elongation under constant loading. The phenomenon is associated with time-dependent plasticity at elevated temperature, often larger than roughly 0.5 T_m (T_m = absolute melting temperature). The micro-mechanisms controlling creep deformation involve dislocation glide and also climb and at low stresses, diffusion-controlled mass transport along grains boundaries.

The easiest creep test consists of applying a constant load while recording the elongation of the specimen. In general, the load value is changed from one test to another while keeping the test temperature constant. Constant stress or constant strain rate tests can be performed but require a loop-controlled machine. The creep data include the stress vs. time to rupture, the total elongation vs. time to rupture, the reduction of area vs. time to rupture as function of temperature, and also the evolution of the creep rate as function of temperature, under various applied stresses. Classically, the creep rate varies in between 10^{-7} h^{-1} and 10^{-1} h^{-1}, depending on applied stress (from tens to a few hundred MPa) and temperature.

The creep test is a long and time consuming test, and under low loading and/or low temperature, the fracture can take several years to occur. Therefore the time to fracture value is not necessarily a suitable parameter to characterise the creep property of a material. The creep strength is approached in terms of stress versus creep rate. The measurement of the creep rate is then performed when a linear evolution of the strain with time is obtained under a given applied load. Another criterion is the time required to obtain a predefined strain value under a given applied load.

7.7.2 Liquid-metal-accelerated creep (LMAC)

An increase in the secondary creep rate, by a factor of 2 to 100 was reported for single and polycrystals of Zn, Cd, Cu, Fe and Fe-Ni alloy, tested under tensile or compressive stress in experiments performed in the former USSR (Glickman, 1976, 1978; Nikitin, 1967). LMs simultaneously accelerate creep and the nucleation growth of vacancy voids near the metal surface in traction or compression.

7.7.3 Creep properties of martensitic and austenitic stainless steels in air or liquid metals other than lead or LBE

There is a substantial amount of creep data on air in the literature on commercial heats of modified 9Cr-1Mo steels over a wide temperature range, from 425°C to ~700°C. These data were required to establish the effect of a number of metallurgical parameters like heat treatment, cold work, notch sensitivity, thermal ageing and applied stress. Irradiation creep of ferritic/martensitic steels was also thoroughly investigated using different reactors or in laboratory irradiation facilities (Klueh, 2001; Toloczko, 1996). The (interrupted) tests are followed by micro-structural investigations.

Today, the tempered martensitic Cr steels are reputed for their quite stable microstructures and good mechanical properties at elevated temperatures thanks to the pinning of dislocations and lath interfaces by fine precipitates and elements in solid solution (Cr, Mo, C…) (Guttmann, 1997; Hättestrand, 2001). Since creep behaviour in lead or LBE of T91 and P92 steels will be presented in the following, let us take a look at the experimental stress-rupture curves revisited by Yurechko (2011, 2013) of T91 and P92 respectively in Figures 7.7.1 and 7.7.2.

The creep behaviour of both martensitic and austenitic stainless steels in contact with Pb-17Li, lithium and sodium were studied in parallel with the studies on fatigue and creep-fatigue behaviour, in the framework of the fast breeder reactors and fusion projects. Perhaps it could be an element of information to recall that there is no evidence of a deleterious influence of sodium on the creep properties of type 316 austenitic stainless steels. As concerns the influence of Pb-17Li on the creep properties of martensitic steels, one should refer to the review papers by Borgstedt (1986, 1991); once again a slight reduction of creep life was obtained in a number of experimental conditions.

7.7.4 Creep of austenitic and ferritic/martensitic steels in lead or LBE

The availability of information on the creep strength, creep damage and creep crack growth rates of both T91 and 316L in contact with lead or LBE is slowly increasing. Glickman was the first to mention a detrimental effect of liquid metals on creep (1976, 1977, 1985, 2000). At the end of the 70s, the author proposed an explanation, considering that liquid-metal-accelerated creep (LMAC) is one more manifestation of the Rebinder effect, besides LME. At the same period, in Russia, in the context of the BREST-0D-300 reactor system, creep tests were performed on a chromium steel 10Kh9NSMFB (containing 1.2%Si) in flowing liquid lead under 70, 100 MPa between 420 and 550°C, showing an earlier transition into the third stage of creep and a decrease of the duration of the steady creep stage, explained by the authors as a consequence of the lead corrosiveness (Kashtanov, 2004). More detailed information about the test conditions and composition and structure of the steel/lead interface would be of interest at all stages of the test. This includes easier access to past and present Russian literature on structural materials in contact with liquid metals for nuclear applications (Balandin, 1961; Bryant, 1988).

Uniaxial creep test results were recently obtained by KIT (Germany) (Jianu, 2009; Yurechko, 2011; Weisenburger, 2012).

Figure 7.7.1: Experimental stress-rupture curves of T91 in air

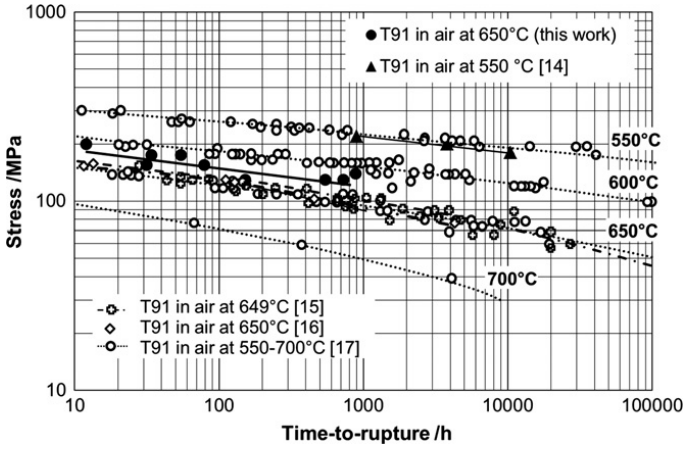

Source: Yurechko (2013).

Figure 7.7.2: Experimental stress-rupture curves of P92 in air

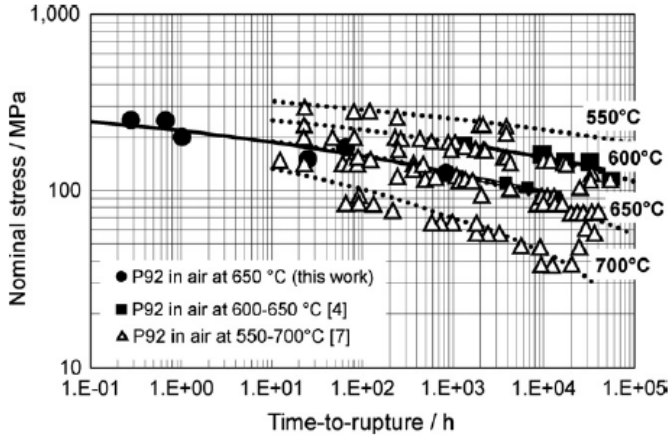

Source: Yurechko (2013).

7.7.4.1 *Qualitative investigation of creep behaviour of T91 steel in contact with lead*

In 2002, Gamaoun (2002, 2003, 2004) reported LMAC effects on T91 steel plates in contact with lead and LBE under OCS, using the two COXCIMEL[12] and FLEXIMEL[13] set-ups for control of the oxygen activity in molten lead and LBE developed by Ghetta (2001, 2002).

The FLEXIMEL specimens are 4 mm × 50 mm × 1 mm plates inserted into an alumina specimen holder, which applies a fixed symmetric four-point bending. They can be annealed either in a liquid LM bath under OCS, or in gas atmosphere (air or pure H_2). A constant deflection of 0.2 mm is imposed to the platelets between the central and outer bearings, which corresponds to an initial maximum stress of 135 MPa, about 25% of the yield stress at the imposed temperature of 525°C. During annealing in lead, LBE or in air at elevated temperature, the elastic energy stored is relaxed and activates plastic deformation mechanisms.

The test results are shown in Figures 7.7.3 and 7.7.4. The authors observed the formation of cavities and an acceleration of plastic strain in the T91 steel specimens under fixed four-point bending at 525°C in both reducing (oxygen activity: $a_0 = 2.7 \cdot 10^{-16}$) and oxidising (oxygen activity: $a_0 = 3.1 \cdot 10^{-10}$) lead or LBE, which is never observed at same temperature in air.

Apparently no such LMAC effect is detected at 380°C, in otherwise identical conditions (Gamaoun, 2003). The threshold temperature for appearance of an LMAC effect is still missing.

Figure 7.7.3: SEM micrographs of the FLEXIMEL specimen central cross-section after one month annealing in stagnant liquid lead bath at 525°C under Ln(a_0) = -16 oxygen activity

Tensile zone (left); compressive zone (right)

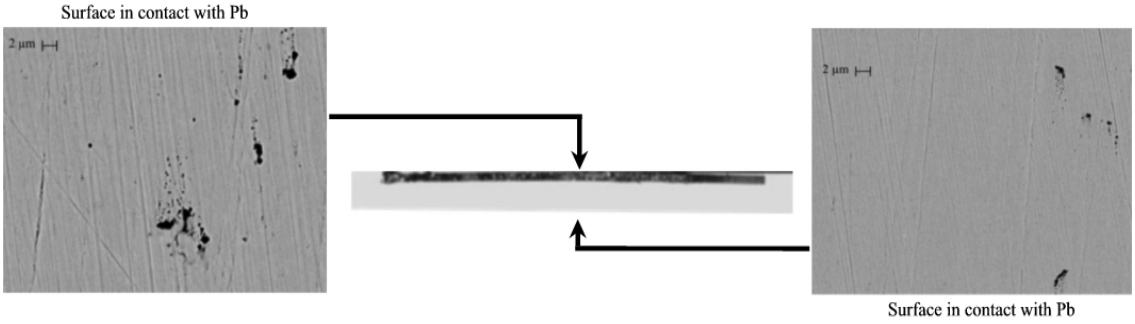

12. COXCIMEL: in French, "Corrosion sous oxygène contrôlé et interaction avec les métaux liquides", refers to an original oxygen control system (OCS) developed by Ghetta (2001), which permitted to determine the values of the oxygen solubility in lead and LBE over the 250-700°C temperature range, in very good agreement with the results obtained by Courouau using a CEA-made OCS device (2002, 2004).

13. FLEXIMEL: in French, "Flexion sous oxygène contrôlé et interaction avec les métaux liquides", refers to an experimental set-up allowing for four-point bending test under the OCS developed earlier by Ghetta (2002).

Figure 7.7.4: Volume fraction of cavities in the central cross-section of a FLEXIMEL specimen after one month annealing in stagnant liquid lead bath under flowing H_2 at 525°C (image analysis)

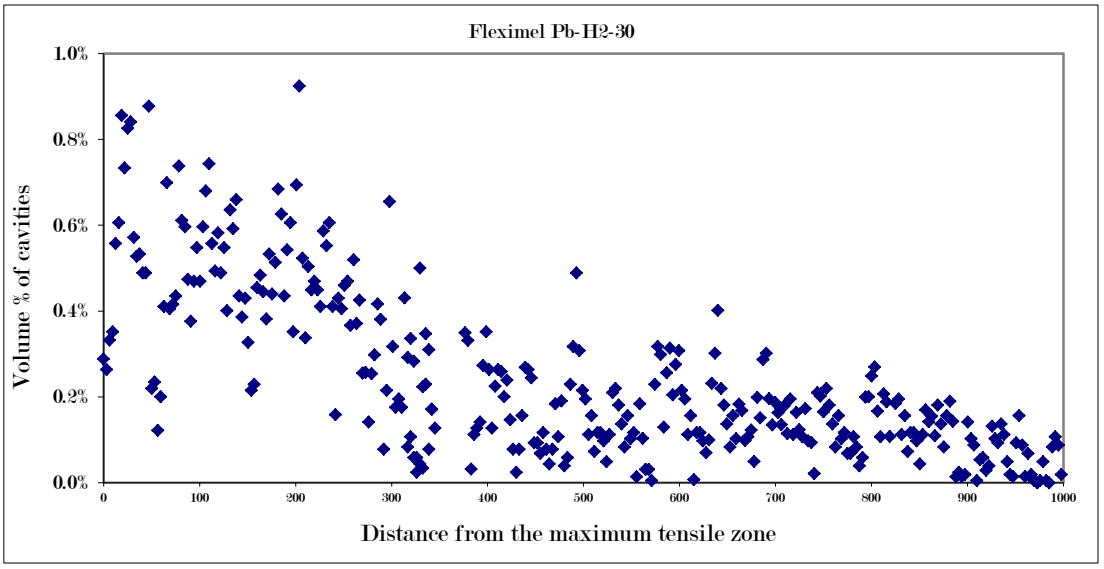

7.7.4.2 *Quantitative assessment of creep behaviour of T91 steel in contact with LBE*

Recently, unixial creep interrupted tests (up to 2 000 h) and uniaxial creep-to-rupture investigations were carried out by CRISM and KIT (Jianu, 2009; Weisenburger, 2012) on T91 in air and in flowing LBE at a flow rate of 0.5 m/s. The LBE contained 10^{-6} wt.% oxygen. Before applying the stress, the specimens were kept for 100 h at 550°C to pre-oxidise the surfaces and to release stresses. Tests were performed in both environments at 550°C with some tests at 500°C, at uniaxial tensile stress levels of 140, 160, 180, 200 and 220 MPa. For stress levels of 60, 80, 100 and 120 MPa, tests were done only in LBE. The experimental strain-time diagrams are shown in Figure 7.7.5.

Figure 7.7.5: Creep-to-rupture diagrams of T91 in LBE and in air at 550°C for stresses ranging between 60 and 200 MPa

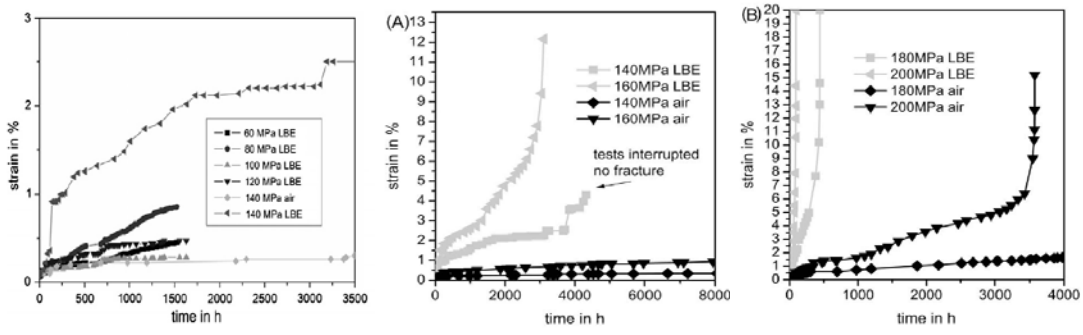

The strain rates of secondary creep stages for tests in LBE were in the range of 10^{-4} s^{-1} for applied stress levels less 140 MPa which was the same order as for tests performed in air at a stress level of 140 MPa. Increasing stress level resulted in an increase of the strain rate and of the strain. Compared to specimens tested in air, the specimens tested in LBE at high stress levels (above 140 MPa) exhibited marked differences: *i)* strain increase (Figure 7.7.5); *ii)* secondary strain rate increase up to a factor of about 50 (strain rate)

(Table 7.7.1); *iii)* time-to-rupture decrease (Figure 7.7.5); *iv)* rapid transition into the third creep stage at high stress, above 180 MPa (Figure 7.4.5).

The change in the behaviour with the applied stress appears as a consequence of the integrity of the oxide layer. When T91 is loaded under a low stress level, the oxide layer avoids and delays direct contact between the steel and LBE even if few cracks form in the oxide layer. At high stress, cracks are more numerous and widely opened, allowing direct contact of LBE and the steel.

Table 7.7.1: Ratio of second creep rates for T91 at 550°C tested in air and LBE

Stress (MPa)	Ratio of second creep rates, LBE/air
140	27
160	35
180	44
200	53

7.7.4.3 Role of GESA treatment on creep behaviour of T91 steel in contact with LBE

An improvement in creep resistance in LBE is possible by alloying the specimen surface with Al (Weisenbuger, 2012). The GESA treatment which involves pulsed electron beams for coating has been employed. Secondary creep rates and times to rupture of GESA treated T91 loaded at 550°C in LBE were similar to those obtained in air, and much better than those obtained in LBE, as can be seen in Figure 7.7.6.

Figure 7.7.6: Comparison of original T91 at 550°C in air and LBE and surface-alloyed T91 in LBE

Secondary creep rates versus applied stress (a) and stress versus rupture times (b)

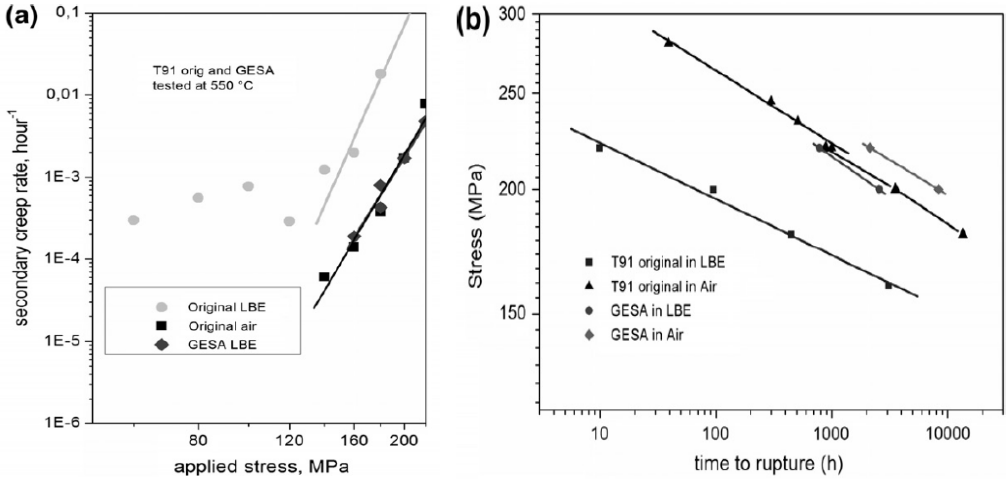

7.7.4.4 Quantitative assessment of creep behaviour of T91 steel in contact with lead

Uniaxial creep-to-rupture have been recently measured at KIT (Yurechko, 2011) in the CRISLA facility on T91 at 650°C in stagnant air and in stagnant lead with 10^{-6} wt.% dissolved oxygen. Nominal applied stresses ranged between 100 and 200 MPa. The influence of pre-exposure for up to 200 h to oxygen-containing lead has been investigated at a stress level of 160 MPa.

The authors compared the performance in Pb and air on the basis of time to rupture at given stress and found that the lifetime in Pb is at the lower end of the scatter band obtained in the case of air (Figure 7.7.7). The experimental creep exponent in Pb, n_{Pb} = 13, is slightly higher in comparison to air (n_{air} = 9). They conclude to an insignificant effect of Pb on creep performance which is contrary to observations for flowing LBE (Jianu, 2009). In addition, no effect of pre-exposure has been noticed.

The fracture surfaces were also very similar for creep-to-rupture in Pb and air, cup and cone, ductile fracture with dimples.

Figure 7.7.7: Comparison of time to rupture-vs. stress curves of T91 in stagnant air and Pb (Co = 10^{-6} mass%) at 650°C

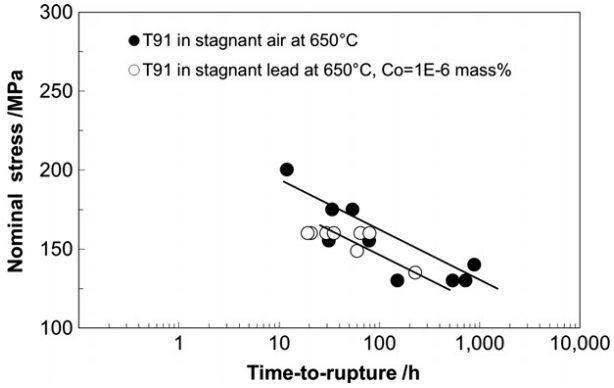

7.7.5 *Creep–to-rupture of P92 steel in lead*

P92 is a martensitic steel with improved creep resistance. The main difference with T91 is the addition of tungsten (near 2 wt.%). The uniaxial creep-to-rupture has been investigated at KIT (Yurechko, 2013) in the CRISLA facility at 650°C in stagnant air and in stagnant lead with 10^{-6} wt.% dissolved oxygen. Nominal applied stresses were ranging between 75 and 325 MPa.

From the creep curves of the P92 loaded at 100-200 MPa in oxygen-controlled lead at 650°C and in air, no difference was found. For tests in lead, the strain at rupture, $\varepsilon_{c;R}$, and reduction of load-bearing cross-section, Z, are close to the values observed in air. The secondary creep rates at > 100 MPa are also similar for stagnant lead (n = 14), and air (Figure 7.7.9). The same holds for the time-to-rupture t_R (Figure 7.7.8). This is similar to what has been observed for T91 steel.

Figure 7.7.8: Stress-rupture curves for P92 in stagnant lead and air

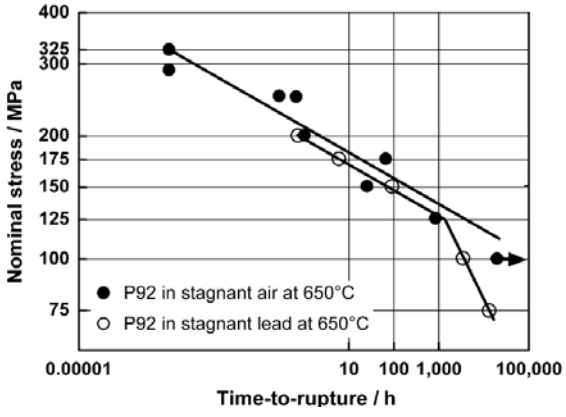

Figure 7.7.9: Secondary creep rate for P92 in air and Pb at 650°C

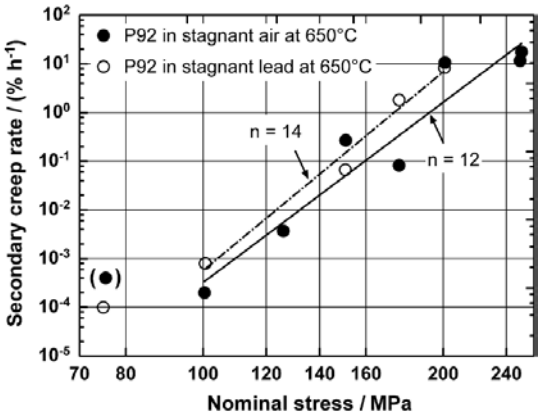

Creep-to-rupture behaviour of P92 at 75 MPa, however, differs from the performance at higher stress. $\varepsilon_{c;R}$ and Z are significantly lower, indicating brittle fracture. Secondary creep rate at 75 MPa in lead is lower than estimated for air from the interrupted experiment and still conforms to n ~14 as at > 100 MPa. Accordingly, the reduced t_R at 75 MPa in lead (Figure 7.7.8), in comparison to the expectation from the data for air, mostly results from a decrease in plasticity of the steel rather than increase in creep rate. The latter would imply the weakening of a near-surface zone by interactions between the steel and liquid lead, which does apparently not occur. Reduced plasticity of P92 becomes noticeable in t_R at around 100 MPa or exposure time 3 442 h.

Creep-to-rupture in stagnant lead and air generally resulted in a cup and cone fracture. At 75 MPa in Pb, brittle fracture occurred. The macroscopic appearance of the failure surface is reminiscent of shear fracture at an angle of approximately 45° (Figure 7.7.10). The failure origin is close to the crack seen in the oxide scale shown with an arrow in the micrograph (a). The failure started in a point where several rupture-plane surfaces are crossed shown with arrow in micrographs (b), (c) and (d), developing with a formation of the plane surfaces and step(s) in between and then turned out with shear lips as a residual fracture.

Figure 7.7.10: P92 ruptured in stagnant lead at 75 MPa after 13 090 h

Crack in oxide scale (a) and failure origin (b-d) are marked with arrows

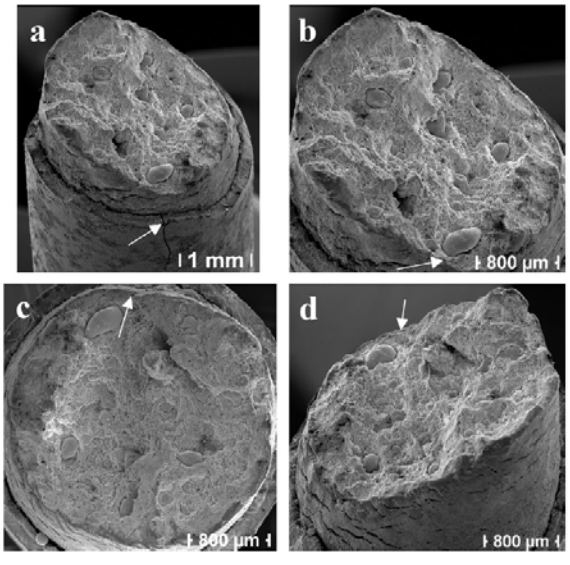

On the contrary, for T91 tested at 650°C and 100 MPa in stagnant lead in the same facility as P92, a ductile fracture (modified cup and cone fracture) dominates accompanied by slightly reduced $\varepsilon_{c;R}$ and Z in comparison to higher stress.

t_R = 19 500 h at 100 MPa corresponds to the trend of the nominal stress–time-to-rupture curve observed at high stresses slightly reduced $\varepsilon_{c;R}$ and Z in comparison to higher stress.

The long exposure time resulting from slow secondary creep at low stresses favours LME of P92 due to cracks that form in the oxide scale. LME may not be only the factor that reduced t_R in comparison to exposure to air. The loss of load-bearing cross-section in Pb is higher, but cannot explain brittle fracture during the long-term test. LME after long exposure time is probably not specific to P92, but might occur for other ferritic-martensitic steels (e.g. T91) as well. In addition, long-term exposure modifies the characteristics of precipitates such as Laves phase.

7.8 Fatigue

7.8.1 Definition

Fatigue is the progressive, localised, permanent structural change that occurs in materials subjected to fluctuating stresses or strains; this may result in cracks or fracture after a sufficient number of fluctuations. The different steps of fatigue damage include:

- cyclic accommodation;
- short crack initiation;
- short crack growth at the surface and formation of the long crack;
- long crack propagation in the bulk;
- final fracture of tensile type.

The procedures of fatigue testing can be classified into four groups:

- the stress life approach;
- the strain life approach;
- the fatigue crack propagation approach;
- the component test model approach.

Corrosion fatigue is one of the environmentally assisted cracking phenomena.

The strain life and fatigue crack propagation approaches have been investigated in the framework of the French GEDEPEON programme, TECLA, MEGAPIE-TEST, DEMETRA European programmes on ADS by Vogt (2004, 2006, 2013; Verleene, 2006) and by Weisenbuerger (2008) in the frame of DEMETRA project. This was motivated by the fact that information on the resistance to crack initiation, the behaviour of small cracks and the crack velocity under cyclic loading in contact with LBE were extremely sparse. The only existing data on nearly similar steel were those published by Kalkhof (2003) on MANET II. Consequently, low-cycle fatigue (LCF) as well as fatigue crack propagation (FCP) tests in HLMS were developed:

- LCF tests inform about the cyclic accommodation of a material and characterise the resistance to crack initiation under cyclic loading. It is performed with smooth specimens (cylindrical, or hourglass shape gauge length, plates). LCF tests are conducted under total or plastic strain control, with $\Delta\varepsilon_t$ ranging from 0.4% to 2.5%, generally with a triangular waveform and constant strain rate (in the range of 10^{-2} to 10^{-4} s^{-1}). Stress-strain hysteresis loops are periodically recorded during cycling allowing for the measurement of the stress range $\Delta\sigma$. The LCF life is equal to the number of cycles required to initiate surface cracks, and the propagation of at least one of them to failure.

- FCP tests inform about the velocity of long cracks. Pre-cracked specimens, of CT or four-point bend type, are used. The test is generally performed under load control and requires the measurement of the single crack advance that propagates throughout the specimen. The results are compiled into a relationship of type $da/dN = f(\Delta K)$ where da/dN is the crack velocity expressed in mm/cycle and ΔK the cyclic stress intensity factor range.

Fatigue testing began at first on T91 in contact with LBE at 300°C in the framework of the MEGAPIE target project. There were at least two motivations. Design of the target window has to ensure that cyclic loading imposed to the target window by the beam trips is less than the critical load leading to crack initiation after about 10^4 load cycles, i.e. the expected lifetime foreseen for the LBE liquid metal target. Besides the beam trips, the structural materials of an ADS, especially the target container, will be subjected to a variety of loading conditions in service, thermo-mechanical or not. Then attention has been paid to see if the modified surface layer (FeCrAlY coating) had any influence on the LCF behaviour at test temperature of 550°C.

In some aspects, the situation is different as concerns the fatigue behaviour of 316-type austenitic stainless steels:

- In the framework of the fusion programme, the compatibility of 316L type SS with lithium or Pb-17Li, its corrosion and mechanical behaviour including low cycle fatigue (LCF) have been extensively studied for decades (Borgstedt, 1991; Chopra, 1983; Benamati, 1994).
- In the framework of the LMFBR project, the fatigue behaviour of 316L type SS in contact with alkali metals, particularly sodium and lithium, has also been thoroughly studied for years now (Borgstedt, 1991; Mishra, 1997; Kalkhof, 2003).
- Recently, in the framework of the Japanese or United States projects of spallation neutron sources, the compatibility of type 316LN stainless steel with mercury has been the subject of a number of works, since a type 316LN SS was selected for the vessel containing mercury (Strizak, 2001, 2003; Tian, 2003).

However, to our knowledge, besides the former USSR literature concerning carbon steels and various Russian steel grades pre-tinned with LBE, tin or tin-lead eutectic (Bichuya, 1969; Nikolin, 1968; Chaevskii, 1969; Popovich, 1979; Dmukhovs'ka, 1995), the effects of lead or LBE on the fatigue behaviour of 316 type SS are largely unknown. In the following, we briefly comment on recent results (Kalkhof, 2003; Vogt, 2004, 2006, 2013; Verleene, 2006; Weisenbuerger, 2008). One can find some of these results in the paper written by Gorse (2011).

7.8.2 Low cycle fatigue behaviour of ferritic/martensitic steels in contact with oxygen-saturated LBE

We first recall the conditions of the study of Kalkhof (2003): Fully reversed ($R = -1$) strain-controlled LCF tests were performed on a Schenck servo-hydraulic machine with a load capacity of 250 kN, at total strain amplitude (ε_{at}) varying from 0.2% to 1% (i.e. total strain range $\Delta\varepsilon_t$ varying from 0.4% to 2%) at 1 Hz cycle frequency, with some tests conducted at $\Delta\varepsilon_t = 0.3\%$ and 0.1 Hz frequency. The environmental conditions are air or stagnant LBE at 260°C, with no indication of the oxidising or reducing power of LBE. Some tests were also carried out in air at room temperature.

The conditions of the study of Vogt are based on the ASTM standard E 606 (Annual book of ASTM standards – 1991, Section 3, Vol. 03.01) (Vogt, 2004, 2006; Verleene, 2006): LCF tests were carried out at 300°C in air and in oxygen-saturated LBE under air, using a hydraulic MTS closed loop servo-controlled machine with a load capacity of 100 kN. A cylindrical vessel containing the HLM surrounded the specimen. Tests were total axial

strain controlled using a strain gauge extensometer set outside the HLM vessel. They were conducted in a fully push-pull mode (R = -1) at different imposed total strain ranges: $0.4\% \leq \Delta\varepsilon_t \leq 2.5\%$, using a triangular waveform and a control of the strain rate ($4{\cdot}10^{-3}$ s^{-1}). Hence, the cyclic frequency ranged from 0.25 Hz to 0.08 Hz for the smallest and highest strain tests respectively. During cycling, hysteresis loops were periodically recorded to allow measurement of the stress variation $\Delta\sigma$ at each cycle. The fatigue life is defined as the number of cycles for which a 25% drop in the quasi-stabilised tensile stress occurs.

In all cases, attention was paid to the surface state of the specimens, carefully manually polished (Kalkhof, 2003), or electro-polished (Vogt, 2004, 2006, 2013) depending on the authors.

The LCF behaviour of MANET II and T91 in contact with LBE or lead at $\Delta\varepsilon_t < 0.3\%$, i.e. in the high cycle fatigue regime, is unknown.

7.8.2.1 Role of LBE on cyclic accommodation

Cyclic softening was observed for both MANET II (Kalkhof, 2003) and T91 (Vogt, 2004), independent of the environment, air or stagnant LBE, in the previously described experimental conditions. This point is illustrated for the T91-LBE couple in Figure 7.8.1. These results suggest that LBE affects only the surface but not the bulk properties.

Figure 7.8.1: Evolution of the stress amplitude with the number of cycles for tests carried out at $\Delta\varepsilon_t$ ranging from 0.4% to about 2.5% at 300°C in air and in LBE for the T91 steel

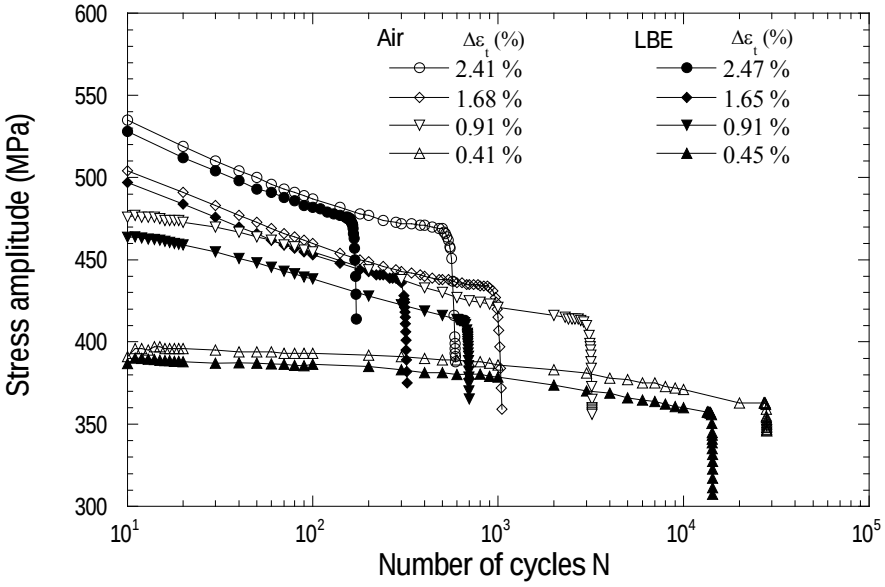

7.8.2.2 Role of LBE on fatigue resistance

A marked effect of LBE on the fatigue resistance has been observed on MANET II (Kalkhof, 2003) and T91 (Vogt, 2004, 2013; Verleene, 2006), whose fatigue life is reduced in contact with LBE as shown in Figure 7.8.2. Test carried out at 200°C and 300°C in LBE resulted in similar fatigue lives.

Figure 7.8.2: Fatigue resistance of T91 at 300°C and 200°C in air and in LBE in oxygen-saturated LBE

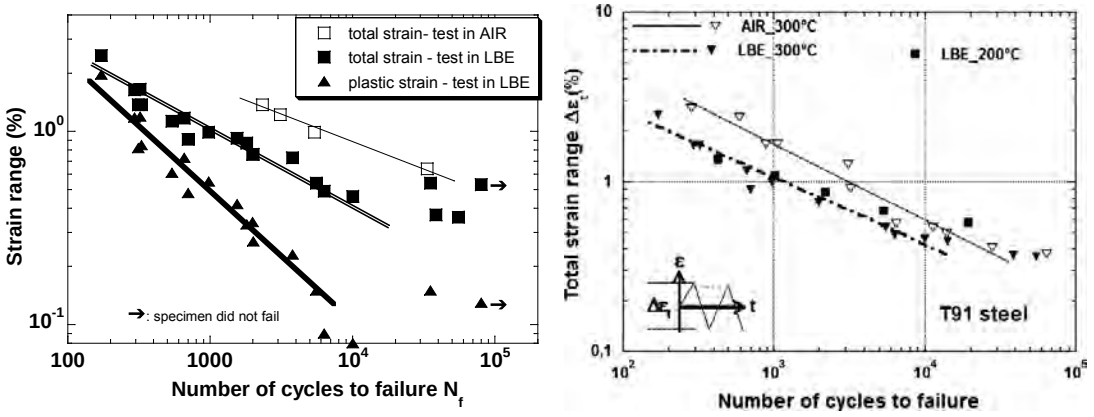

7.8.2.3 Role of LBE on fatigue crack density

Metallographic investigations on T91 and MANET II have been carried out to explain the difference in fatigue resistance due to the presence of LBE.

For both MANET II and T91, LBE modifies the short crack density, in comparison with air, as reported in Kalkhof (2003), Vogt (2004) and Verleene (2006). Figure 7.8.3 shows a transversal cut of a specimen cycled in air and in LBE. Short cracks can be seen only in the specimen fatigued in air:

- In air as in LBE, the short cracks are generated by a classical extrusion-intrusion process.
- In air, the grain-sized cracks are stopped by the grain boundaries, which can be overcome after a certain number of cycles. Additional cycles are necessary to overcome these micro-structural barriers, crack extension therefore occurs by crystallographic growth but cracks are then stopped again by the next grain boundaries and during that time, new short cracks can initiate. The crack length attains now three or four grain sizes and again additional cycles allow their growth. Longer micro-cracks can form by coalescence of smaller ones. Finally, only very few of them propagate in a plane perpendicular to the stress axis into the bulk. The role of the microstructure in a martensitc steel on crack growth in air has already been published (Vogt, 1988).
- In LBE, Vogt suggests that once a microcrack is formed inside a grain, the grain boundary resistance to crystallographic growth vanishes in contact with the liquid metal, allowing for crack extension throughout the neighbouring grains until final rupture. Grain boundaries are non-efficient micro-structural barriers in the presence of LBE.

All these steps described for fatigue in air are cycle consuming, which is not the case for fatigue in LBE. This explains the large difference in fatigue resistance between tests performed in air and in LBE.

7.8.3 Influence of hold time on fatigue behaviour of T91 in LBE

Data as a function of hold time are presented in Figure 7.8.4 (Vogt, 2006). The tests were performed under strain control, using a trapezoidal waveform, with 10 min. tension hold time. The environmental conditions were 300°C in air or oxygen-saturated LBE.

Figure 7.8.3: Micrographs of MANET II specimens after LCF (top) in air and (bottom) in LBE

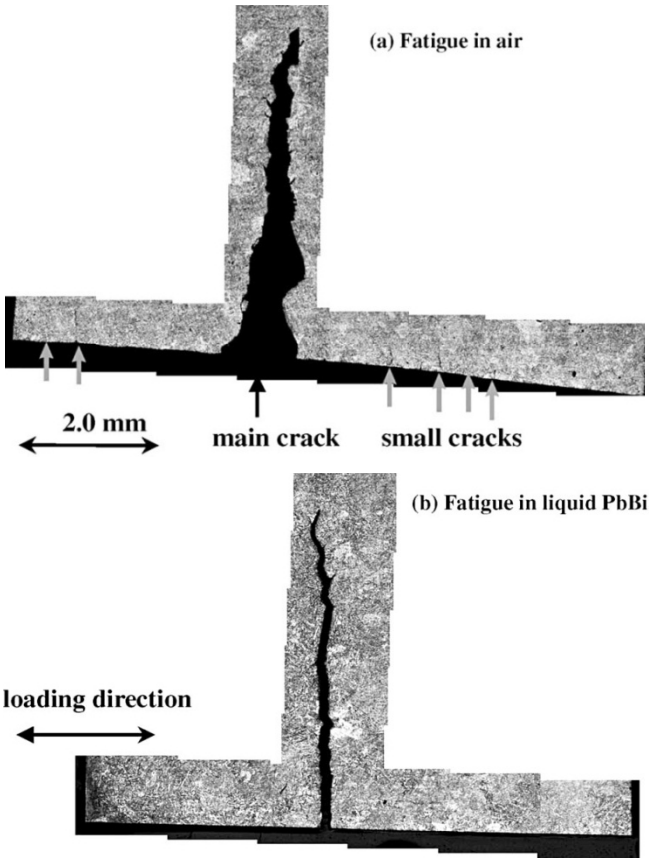

Figure 7.8.4: Fatigue resistance of T91 in air and in LBE, with and without 10 min hold time in tension

As an example, for $\Delta\varepsilon_t$ = 0.7%, the fatigue life is reduced of a factor ~2 at 300°C in oxygen-saturated LBE and by a factor of ~4 if a hold time is introduced

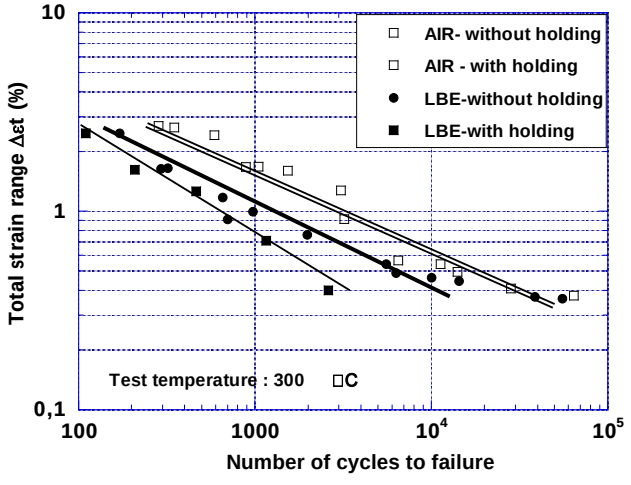

The stress response to strain cycling is unmodified by the introduction of a hold time, either in air or in LBE. No stress relaxation was recorded at this temperature. On the contrary, for all tests performed at imposed total strain ranges in between 0.4% and 2.5%, the fatigue life of T91 decreases with application of a hold time in tension, contributing to the modification of the surface state in contact with LBE at 300°C. A synergistic effect of the environment and the mechanical test conditions may explain this decrease of LCF life. No such effect was observed in air.

7.8.4 Influence of preliminary exposure to LBE on fatigue behaviour of T91

A first batch of specimens was exposed in a LBE loop for 613 h at 600°C under reducing conditions (oxygen content less than 10^{-10} wt.%). Another batch was exposed to oxygen-saturated LBE (air overpressure of 200 mbar) at 470°C for 502 hours. They were then fatigued in LBE at 300°C with the mechanical testing conditions reported in Table 7.5.2: strain control, symmetrical triangular waveform (R = -1) (Vogt, 2006). The stress responses to strain cycling of T91 steel in LBE at 300°C after pre-exposure to LBE in either oxidising or reducing conditions, under OCS, were similar to those of non-exposed specimens.

The results of LCF tests are shown in Figure 7.8.5. The following results were observed:

- Cyclic softening was unaffected by pre-exposure in LBE, whatever the conditions.
- Fatigue life was significantly decreased by pre-exposure in reducing LBE.
- Fatigue life was unmodified or slightly increased by pre-exposure in oxidising LBE.

Figure 7.8.5: Influence of pre-exposure of T91 in LBE under reducing or oxidising conditions (under OCS, in collaboration with Terlain, CEA Saclay) on the fatigue resistance at 300°C in oxygen-saturated LBE

Note that the fatigue life of T91 pre-exposed in oxidising LBE is similar to that of the reference in air (as-received), but larger than the fatigue life of T91 aged in reducing LBE for $\Delta\varepsilon_t$ ~ 0.4%, the effect being less marked for $\Delta\varepsilon_t$ ~ 0.9%

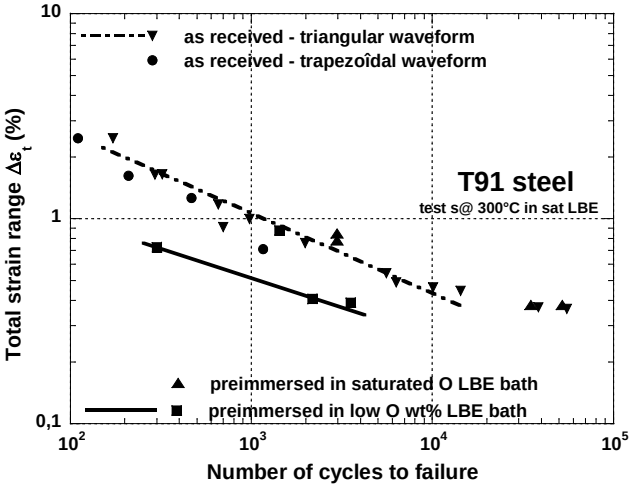

Preliminary exposure to reducing LBE leads to intergranular defects. When the pre-exposed specimens are fatigued in saturated oxygen LBE, these defects behave as short fatigue cracks and some of them will propagate during LCF testing, depending locally on the chemical and metallurgical conditions (Figure 7.8.6). In others, the fatigue crack initiation step did not occur, which reduces the number of cycles to failure.

Figure 7.8.6: SEM micrographs of cross-sections of T91 specimens 613 h ageing in reducing LBE (<10^{-10} wt.% oxygen)

Before LCF testing (a) and after LCF testing (b) in LBE at 300°C, $\Delta\varepsilon_t$ = 2.2%

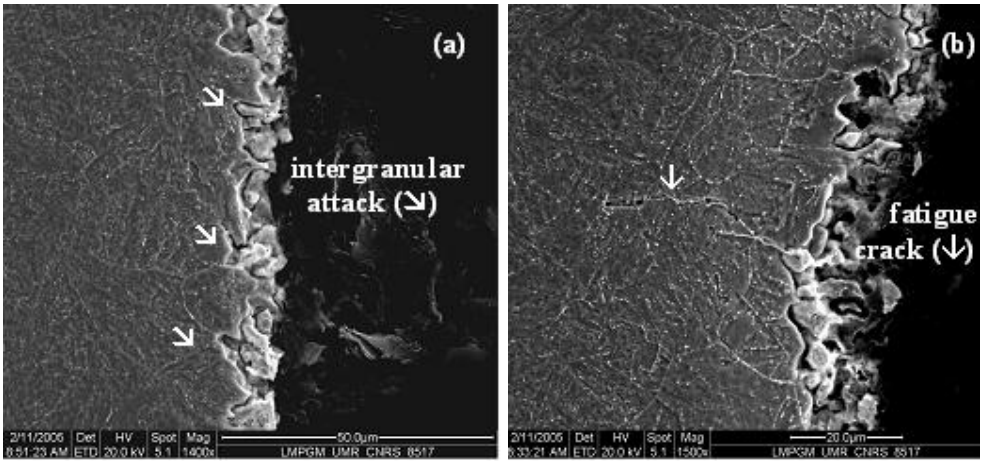

7.8.5 *Low cycle fatigue behaviour of T91 steel in contact with low oxygen LBE*

The LCF tests were carried out at CRISM in St. Petersburg (Weisenburger, 2008). Before the fatigue experiment, the specimen was maintained for 100 h at 550°C under controlled oxygen content of 10^{-6} wt% LBE, of which the flow velocity was about 1.3 m/s. Fatigue tests were performed under total axial strain control $\Delta\varepsilon_t/2$ from 0.3% to 2% using a triangular waveform, a constant frequency of 0.5 s^{-1} and a fully push-pull mode (R = -1). Tests were conducted at 550°C in air and in LBE containing 10^{-6} wt.% dissolved oxygen. The oxygen activity was not controlled during the test, but due to the test procedure and duration no change in oxygen content was expected. T91 steel has been tested with and without surface treatment of the GESA type.

Contrary to tests performed at 300°C by Vogt (Verleene, 2006) and Kalkhof (2003), LBE showed no influence on the LCF properties, as well for the fatigue lives (Figure 7.8.7) as for the stress response to strain cycling behaviour. Besides, the GESA treatment did not bring any strong marked influence as it can do creep resistance, for instance.

Figure 7.8.7: Fatigue life (Coffin-Manson plot) as a function of elastic and plastic strain

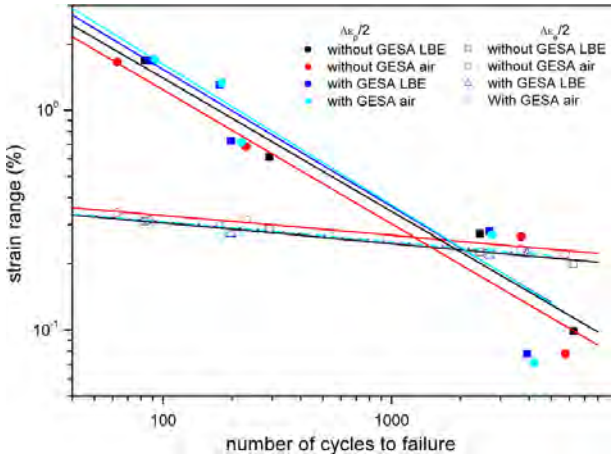

7.8.6 *Low cycle fatigue resistance of 316L austenitic stainless steel in saturated oxygen LBE*

For 316L (Kalkhof, 2003; Vogt, 2013), the fatigue lives in LBE were much less affected than for the T91 steel. The difference in fatigue lives between air and LBE increases with the imposed total strain range. At low strain amplitudes, taking into account scattering, the fatigue lives were similar in air and in LBE. At higher strain amplitudes (ε_{at} = 0.5, 0.6%), the influence of LBE on the fatigue resistance starts occurring as is shown in Figure 7.8.6. Moreover, it seems that the tests performed at 300°C by Vogt were more harmful than those performed at 260°C by Kalkhof.

However, after pre-exposure in LBE (oxygen content = 10^{-11} wt.%) at 500°C for 1 000 h, austenitic stainless steel 316L had the same fatigue resistance as in the as-received condition (Figure 7.8.8) even though defects have been produced by corrosion.

Figure 7.8.8: Total strain vs. number of cycles to failure curves for 316L stainless steel in air and LBE at 260°C (left) and at 300°C (right)

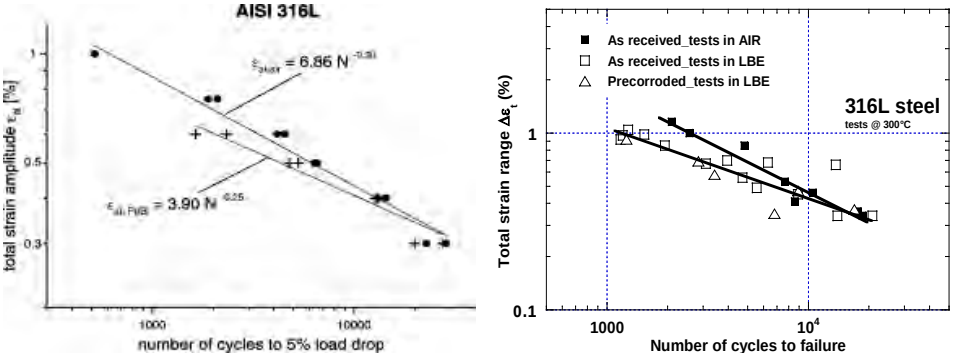

Source: Left image from Kalkhof (2003), right image from Vogt (2013).

7.8.7 *Role of coating on fatigue crack initiation resistance of T91 steel*

Because fatigue crack initiation occurs at material surface where the liquid metal is in contact, coating the material surface can modify the fatigue resistance:

- FeCrAlY coating is the surface treatment developed at KIT (Germany) The Al surface-alloyed specimens are produced in a two-step process: *i*) deposition of the Al-containing layer; *ii*) post-treatment using pulsed electron beams (GESA treatment). GESA is a pulsed electron beam facility consisting of a high voltage generator with a pulse duration control unit, a multi-point explosive emission cathode, a controlling grid and an anode which forms a triode system. More details can be found in the paper by Engelko (2001). GESA treatment involves fusion of the material surface and therefore no visible interface between the modified layer and the substrate can be detected. An alloying of the layer with the substrate led to an almost perfect intermixing, especially at the former interface. Therefore, after GESA treatment the term "coating" is no longer correct. As mentioned in Section 7.8.5, no effect of the treatment, positive or negative, is observed on the fatigue resistance of T91 at 550°C in air and in LBE containing 10^{-6} wt.% dissolved oxygen (see Figure 7.8.7).
- Oxide coating has been considered after pre-exposure in saturated LBE. T91 fatigue specimens were exposed in a saturated oxygen (air overpressure of 200 mbar) LBE bath at 470°C for 502 h at CEA Saclay (France). This led to the formation of an oxide film 8 μm in thickness and with a morphology of double layer. Then fatigue tests

were performed at 300°C in saturated oxygen LBE. The number of tests is rather small, the fatigue lives of the pre-oxided T91 specimen cycled in LBE approached those of the as-received cycled in air.

- Carbide coating obtained by pack cementation, the chemical vapour deposition (CVD) coating technique, is the treatment developed at Institut Jean Lamour, Nancy (France). In the cementation process, the part to be coated is heated in a powder mixture comprising an inert material (usually Al_2O_3), the powder of the element to be deposited (Al, Cr or Si for example), and a halide salt activator. At the process temperature and under low pressure (P_{total} = 10^{-1} Pa), a volatile metal halide forms, diffuses in the gaseous phase and reacts with the substrate to form a coating, the growth of which is governed by solid diffusion. The pack cementation process was applied on the T91 fatigue specimen at 980°C for four hours. The cement consisted of a mixture of 75% $Fe_{30}Cr_{70}$, 25% of Al_2O_3 and 17 mg of $CrCl_{3(s)}$. Then, after deposition, the conventional heat treatment, austenitisation at 1 050°C and tempering at 750°C, was performed. The coating consists of a superficial $M_{23}C_6$ (M = Cr + Fe) compound covering a thick layer of $Cr_{1-y}Fe_y$ (0 < y < wt.%) solid solution. A beneficial effect of the coating is pointed out as can be seen in Figure 7.8.9(a) (Vogt, 2011). Observations of the transversal cut of pack cemented specimens fatigued in LBE show that the coating was adherent to the substrate. Fatigue cracks were observed in the coating as well as in the substrate. In the coating, the cracks appeared to be branched in the $Cr_{1-y}Fe_y$ solid solution layer. A crack in the substrate was always associated with a crack in the coating and no isolated crack in the T91 steel substrate was observed (Figure 7.8.9[b]).

Figure 7.8.9(a): Effect of pack cementation coating on the fatigue resistance of T91 steel

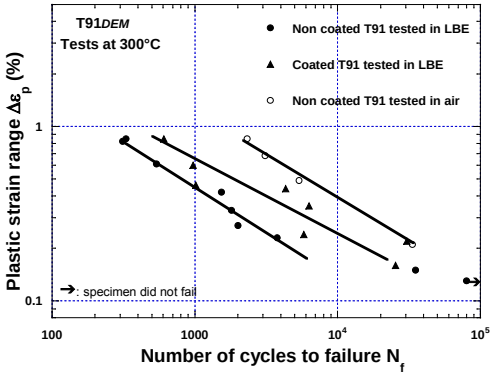

Figure 7.8.9(b): Pack cemented specimen after fatigue in LBE at 300° at $\Delta\varepsilon_t$ = 0.97% (transversal cut) at 300°C in LBE and comparison with fatigue resistance in air

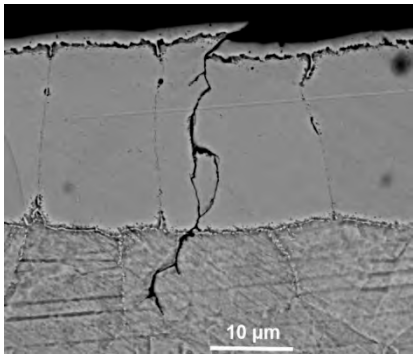

7.8.8 Influence of LBE on (long) fatigue crack growth of T91 and MANET II

Strictly speaking, only fatigue crack growth rate tests using pre-cracked specimens can provide quantitative information on the effect of LBE.

7.8.8.1 Qualitative analysis of the effect of LBE on fatigue crack propagation

However, a qualitative behaviour or tendency can be obtained from LCF tests. Indeed, the final decrease of the stress amplitude (see Figure 7.8.1) is related to crack propagation in the bulk. It was found that the stress decrease was more abrupt in LBE than in air suggesting that the crack growth rate is accelerated by LBE for both 316L (Kalkhof, 2003) and T91 (Kalkhof, 2003; Verleene, 2006).

The influence of LBE on the macroscopic fracture surface morphology is illustrated in Figure 7.8.10. The following characteristics are observed:

- After LCF test of T91 in air (Figure 7.8.10[a]), the fracture surfaces are rather tortuous with a fracture surface at about 45° with respect to the loading axis. The specimen exhibits several fatigue propagation zones (indicated by the star on the micrograph) into the bulk. The fracture surface results from the junction of the various propagation planes, which entails a macroscopically inclined fracture.
- After LCF test of T91 in contact with LBE, without preliminary exposure to LBE, the fracture surface was rather flat with a single fatigue crack propagation zone (Figure 7.8.10[b]).
- Fatigue striations on the fracture surface of the specimen fatigued in LBE appear visible to the naked eye due to their very high inter-distance, possibly attaining a few hundred micrometres (Figure 7.8.10[b]). For the specimen fatigued in air, fatigue striations were distinguished by SEM which could be observed at high magnification.

Figure 7.8.10: Macroscopic view of typical fatigue fracture surfaces of T91 after LCF tests conducted on specimens tested in air, and on as-received specimens directly immersed in LBE for LCF testing (right)

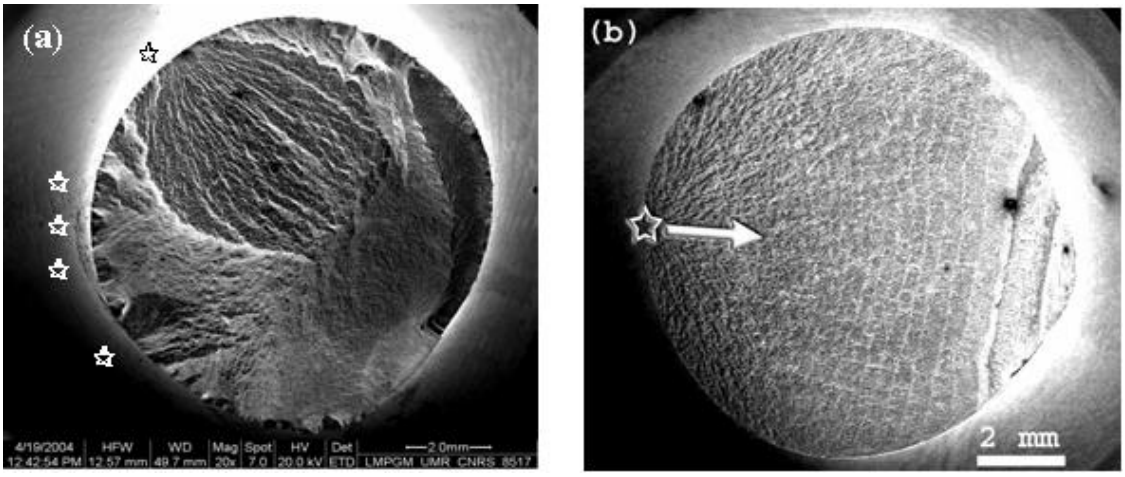

7.8.8.2 Quantitative analysis of the effect of LBE on fatigue crack propagation

Fatigue crack growth measurements (Verleene, 2006) were performed according to a specific experimental procedure of the AFNOR standard A03.404 (1991). Tests were carried out using four-point bend specimens (10 mm × 10 mm × 55 mm) under load control. The crack opening displacement (COD) was measured using a strain gauge extensometer. The COD was converted into crack length using a calibration procedure, which allowed

the calculation of both the crack growth rate *da/dN* (mm/cycle) and the cyclic stress intensity factor ΔK (MPa.√m). Pre-cracking was performed in air at room temperature at 15 Hz using the step down procedure starting at 20 MPa.√m and decreasing load to attain about 5 MPa.√m. Then the FCG tests started from 5 MPa.√m at a frequency of 5 Hz and a stress ratio R = 0.5, at 300°C in air and in LBE.

The results shown in Figure 7.8.11 reveal a net increase in the fatigue crack growth rate for T91 in contact with LBE, in comparison with air.

A change in the fracture mode was observed in the FCGR specimens, with a transition from ductile striations with small distances between them in air (Figure 7.8.12[a]) to a mixed brittle inter- and transgranular fracture in LBE (Figure 7.8.12[b]).

Figure 7.8.11: *da/dN* vs. ΔK curves for T91 at 300°C in air and in LBE (5 Hz, R = 0.5)

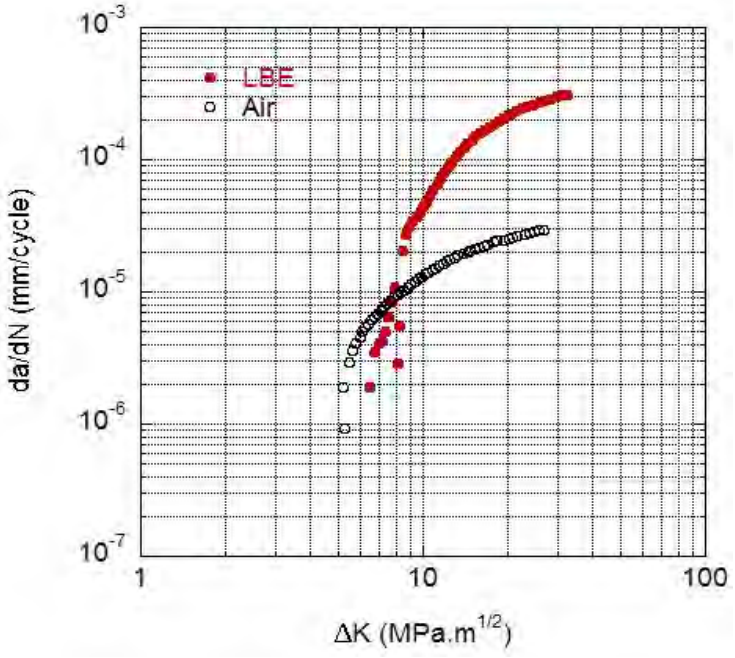

Figure 7.8.12: SEM micrographs of typical fatigue fracture surfaces, as a result of FCP tests of T91 in air (left) and in LBE (right)

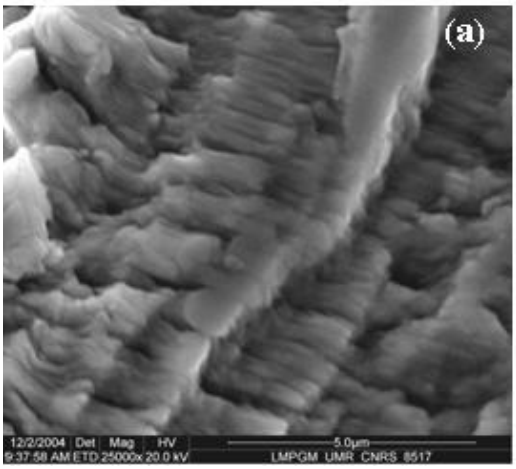

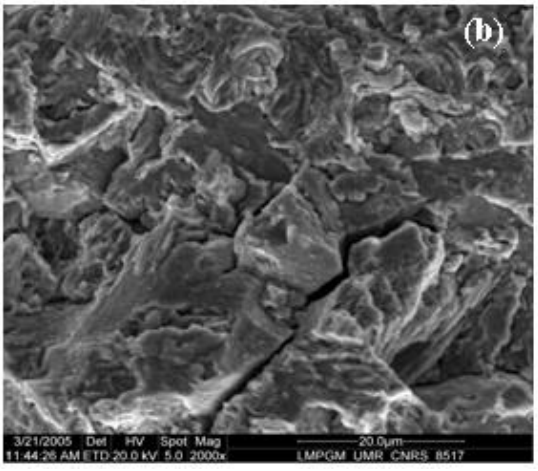

The above results are remarkable, owing to the common observation that LBE does not easily reach the crack tip. Intergranular penetration of the liquid metal is not a characteristic of the T91-LBE couple. In this system, crack opening is not immediately followed by filling with liquid metal, contrary to model systems like Cu-Bi or Ni-Bi (Wolski, 2002).

7.8.8.3 *Influence of pre-exposure on fatigue crack propagation*

During their work on toughness measurements, Hojna (2011) observed fracture of some specimens of T91 during the step of pre-cracking by fatigue a frequency of about 1 Hz. Eight (out of 14) specimens underwent fast rupture during cyclic loading in LBE. Amongst these ruptured specimens: four specimens were RCT (8 and 6 mm thick) in the as-received state, four were RCT (6 mm thick) pre-exposed in LBE. The pre-exposure consisted in maintaining the specimen at 500°C for 1 000 h in LBE containing less than 10^{-6} wt.% oxygen with a flow rate of about 1 cm/s.

This fast rupture of specimens was due to both environment and loading mode. The failures of the pre-exposed specimens in LBE were extremely fast. The average FCGR data, measured in environment, plotted vs. the calculated air crack growth rates is reported in Figure 7.8.13. In spite of the scatter, a clear significant shift of measured data points between as-received and pre-exposed specimens can be observed. In fact, all the data points of the pre-exposed RCT (6 mm thick) specimens fell well above the line. In this case, the LBE increased the CGR for more than one order of magnitude.

Figure 7.8.13: Average measured FCGR vs. calculated air crack growth rate

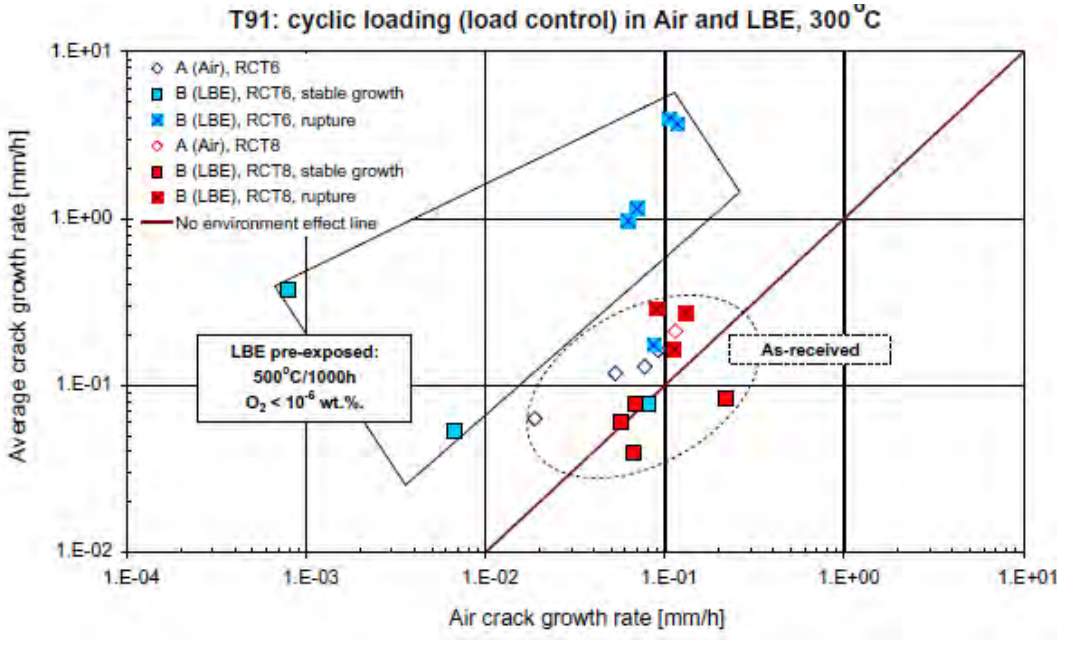

SEM observation on fracture morphology showed identical features for as-received specimens loaded in air and in LBE, with transgranular fatigue fracture. The characteristic striations were observed (see Figures 7.8.14[a] and 7.8.14[b]). On the other hand, only transgranular cleavage-like and intergranular fractures, with no evidence of striations at the same magnifications, were observed on the fracture surface of the pre-exposed specimens (Figure 7.8.14[c]) loaded in LBE.

Figure 7.8.14: Details of fracture morphology

As-received tested in air (a), as-received tested in LBE (b) and pre-exposed tested in LBE (c)

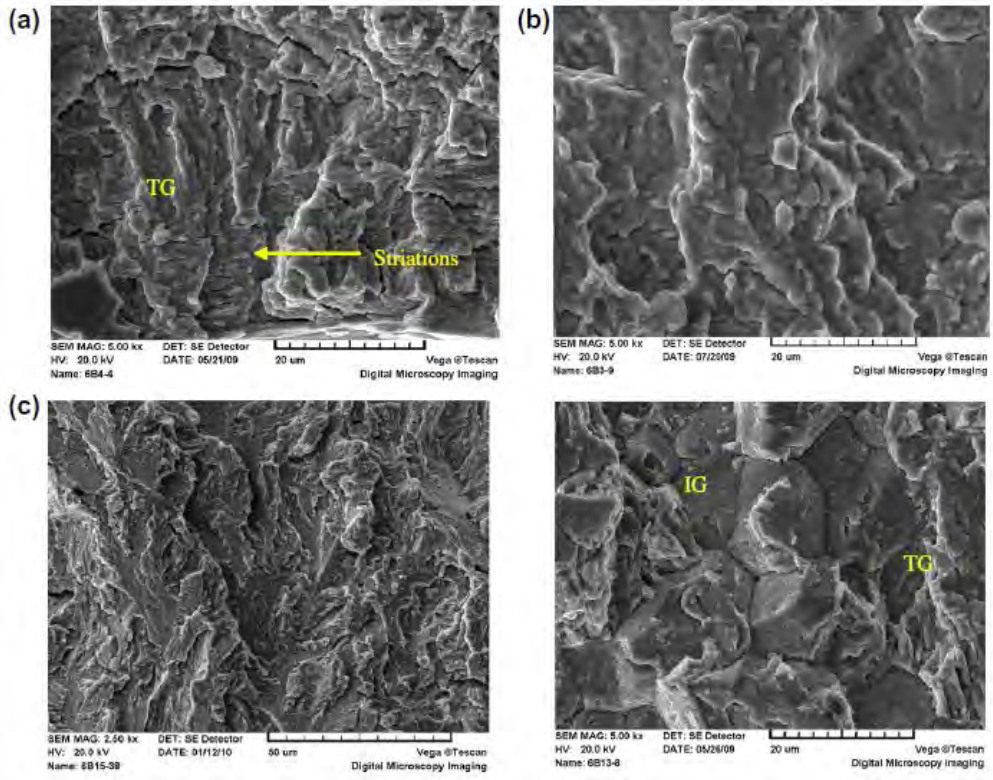

7.9 Recommendations for testing procedures

We begin by listing some of the ASTM standards, which could be useful for mechanical tests in HLMs, in spite of the fact that none of them are valid in such an LM environment. We continue with a brief summary of the possible experimental installations, pointing out the drawbacks of each. We then present recommendations for the mechanical testing procedures, emphasising all that concerns the surface state.

7.9.1 ASTM standards useful for mechanical tests in LBE

Strictly speaking, there is no ASTM standard rigorously applicable in an HLM environment. However, we shall recall those that provide some useful information for our activities.

7.9.1.1 ASTM E 1457-98

Standard test method for measurement of creep crack growth rates in metals.

Aim: Determination of creep crack growth rates in metals at elevated temperature using compact type $C(T)$ specimens subjected to static loading. The crack growth rate da/dt is expressed in terms of the magnitude of a crack tip parameter $C^*(t)$. For definitions of $C^*(T)$, see Test.

Note that the surface crack length measurement by optical means is not, in principle, considered reliable as a primary but only as an auxiliary method, because of the possibly non-uniform crack extension across the thickness of the specimen.

Concluding remarks: *Stricto sensu*, the ASTM E1457-98 test is not applicable to quantify creep crack growth rates in case of structural materials in contact with corroding heavy liquid metals like lead and *a fortiori* corroding LBE. Nevertheless, the recommendations mentioned in the test method E 1457 will be useful to determine qualitatively the creep crack growth rates of T91 steel wetted/corroded by lead or LBE, under various temperature and loading conditions.

Table I: Some specifications and conditions of application of ASTM E 1457-98

Applicable	Restricted to materials in which crack growth is accompanied by accumulation of substantial time-dependent creep strains at crack tip.
Not applicable	If crack growth controlled by high temperature corrosion. In case of transition creep behaviour leading to transient crack growth behaviour. In case of wide spread creep damage at crack tip.
Specimens	$C(T)$, $M(T)$[1] *possibly* required: fatigue pre-cracking.
Referenced documents	E 139: Test method for conducting creep, creep-rupture and stress-rupture tests of metallic materials. E 399:Test method for fracture toughness of metallic materials.[2] E 616: Terminology related to fracture testing.[3] E 647: Test method to measure fatigue crack growth rates.

1 $M(T)$ = centre cracked tension specimens.

2 ΔK, the stress intensity factor range, can be calculated using equations in test method E 399.

3 *J*-integral = line or surface integral describing the local stress-strain field around the crack front, as described in test method E 616.

7.9.1.2 ASTM E 813-89 (discontinued 1998)

Standard test method for J_{IC}, a measure of fracture toughness.

Aim: Determination of J_{IC},[14] which can be used as an engineering estimate of fracture toughness near the initiation of slow stable crack growth for metallic materials.

Concluding remarks: Stricto sensu, the ASTM E813-98 test is not applicable to determine the fracture toughness of structural materials in contact with heavy liquid metals like lead or LBE, especially in case wetting could cause sudden brittle failure. Nevertheless, the recommendations mentioned in the test method E 813 will be useful to determine qualitatively the resistance to crack growth of T91 steel wetted/corroded by lead or LBE, under various temperature and loading conditions.

Table II: Some specifications and conditions of application of ASTM E 813-89

Applicable	To sufficiently ductile material. Lacking sufficient thickness to be tested for K_{IC} according to test method E 399. Displaying ductile slow stable crack growth at test temperature. To evaluate the effects of metallurgical variables, heat treatments and weldments.

14. J_{IC} designates the line or surface integral characterising the local stress-strain field around the crack tip, near the onset of stable crack growth.

Table II: Some specifications and conditions of application of ASTM E 813-89 (*cont.*)

Not applicable	In case of predominant environmentally assisted cracking.[4] In case of fast fracture, and especially brittle (cleavage) fracture of steels.
Specimens	Containing notches or flaws, sharpened by fatigue cracks. Recommended: three-point bend specimen *SE* (*B*),[1] or *C* (*T*) with slow loading rate.
Referenced documents	E 399: Test method for fracture toughness of metallic materials.[2] E 616: Terminology relating to fracture testing.[3] E 1152: Test method for determining *J-R* curves.

1 *SE* (*B*) = single edge-cracked specimens of length $0.5 \leq a0/W \leq 0.75$.

2 ΔK, the stress intensity factor range, can be calculated using equations in test method E 399.

3 *J*-integral = line or surface integral describing the local stress-strain field around the crack front, as described in test method E 616. The *JIC* value is in principle independent of the testing speed in quasi-static regime. Its value becomes a function of testing speed in the dynamic regime.

4 Environmental attack under sustained stress or cyclic loading can cause crack extension at *J* values less than J_{IC}.

7.9.1.3 ASTM E 1820-99

Standard test method for measurement of fracture toughness, combination of ASTM E 813 for J_{IC} evaluation and ASTM E 1152 for *J-R* curve evaluation.

Aim: Determination of fracture toughness of metallic materials using the parameters *K*, *J* and crack tip opening displacement *(CTOD)* (δ).

Assuming the presence of a pre-existing sharp fatigue crack, the fracture toughness values identified by this method characterises its resistance to: *i)* fracture of a stationary crack; *ii)* fracture after some stable tearing; *iii)* stable tearing onset; *iv)* sustained stable tearing.

Concluding remarks: See those for test method E 813.

Table III: Some specifications and conditions of application of ASTM E 1820-99

Applicable	"When the material response cannot be anticipated before the test". Useful as a basis for material comparison, selection and quality assurance. Useful as a basis for structural flaw tolerance assessment.
Specimens	*C* (*T*), *SE* (*B*), *DC* (*T*).[1] Required: notches sharpened by fatigue cracks.
Referenced documents	E 399: Test method for plain-strain fracture toughness of metallic materials.[2] E 813: Test method for J_{1c}, a measure of fracture toughness.[3] E 1152: Test method to determine *J-R* curves. E 1290: Test method for crack tip opening displacement (CTOD) fracture toughness measurement. E 1737: Test method for *J*-integral fracture toughness determination. E 1823: Terminology relating to fatigue and fracture testing.

1 *SE* (*B*) = single edge bend; *DC* (*T*) = disk-shaped compact.

2 ΔK, the stress intensity factor range, can be calculated using equations in test method E 399.

3 *J*-integral = line or surface integral describing the local stress-strain field around the crack front, as described in test method E 616.

7.9.1.4 ASTM E 1921-05

Standard test method for measurement of reference temperature T_0, which characterises the fracture toughness of a steel that experiences onset of cleavage cracking at elastic, or elastic-plastic *KJc* instabilities, or both.

Aim: Determination of fracture toughness of metallic materials using the parameter *J* in the transition temperature region.

Table IV: Some specifications and conditions of application of ASTM E 1921-05

Applicability	To steel that fails by cleavage.
Specimens	*C* (*T*), *SE* (*B*), *DC* (*T*). Required: notches sharpened by fatigue cracks.
Referenced documents	E 399: Test method for plain-strain fracture toughness of metallic materials. E 1823: Terminology relating to fatigue and fracture testing.

7.9.2 Adaptation of experimental installations for HLMs

1) Use an open crucible, containing the test specimen immersed in stagnant LM, which is located within an inert gas cell or glove box. Advantage: Inexpensive to build and operate. Drawback: Exposure to contaminants.

2) Use a circulating loop; CT and three-point bend specimens can be studied in such an installation. The advantage is obvious in case of *in situ* testing; tests are generally conducted *post mortem*; this procedure is convenient provided the tests are conducted at the temperature of exposure to the flowing LM, with layers of liquid metal present on the specimen surface. Otherwise, one should be careful for interpretation of results obtained at room temperature.

3) Use sealed environmental chamber attached to the specimen that completely surrounds the notch and crack extension plane for compact type specimens, which contains the LM but does not extend to the region of the loading holes. Advantage: Simple and low cost. Drawback: Static LM…hence the characteristics of large heat-transport systems (e.g. mass transport due to non-isothermal operation) cannot be studied.

4) Controlled specimen preparation, using surface physics techniques, in order to wet, oxidise, protect or corrode the specimens, particularly notch or pre-cracked area. Advantage: Possibility to follow (optically…) the damage evolution, well adapted to understand damage mechanisms. Drawback: Impossible to reproduce the conditions of a liquid metal cooling system.

One other additional difficulty in case of testing with conductive liquid metals in contact with conductive structure materials, electric potential methods cannot be adapted for crack propagation studies. The ultrasonic techniques recently developed to investigate the LM/steel interfaces would be of great interest (Lesueur, 2008; Paumel, 2009).

7.9.3 Recommendations for testing procedures

The details of the recommendations concerned each step of the LME study: prior, during and after mechanical testing. Note that contrary to what is considered mandatory for corrosion studies, OCS is not required for mechanical tests.

Prior to mechanical testing

1) Polishing conditions must be made precise: diamond-polishing should be preferred, knowing that electro-polishing is an efficient passivating treatment, which is not the case of manual polishing (SiC or diamond); coarse mechanical grinding should be avoided.
2) Topography of gauge part of specimen must be controlled: shiny if possible; in case of roughness the presence of metallurgical defects like inclusions, scratches, and presence, distribution and size of superficial pre-cracks must be flagged.
3) Ageing time and conditions (air, cover gas, LBE…) prior testing must be noted:
   - In case of air ageing, it is important to know precisely the ageing time, even if a few hours, since the native oxide on Cr-containing steels evolves very rapidly during the first 24 hours and the first week of ageing, which may have non-negligible consequences on the mechanical resistance.
   - In case of direct immersion and ageing in liquid LBE, the oxygen activity in LBE and temperature must be known if possible, if different from that applied during testing.

During mechanical testing

Except in some specific cases, in an opaque LM, it is not generally possible to follow the surface state. However, all accessible parameters must be known: temperature, duration of the different test phases, and oxygen content in LM, depending on the test (for slow strain rate tensile test if possible, for creep test and creep crack growth testing…).

During the mechanical test, once a crack initiated, it would be important, ideally, to know how LBE fills the crack. It could be of interest to analyse some specimens obtained during interrupted tests. It should be important for creep, fatigue and creep-fatigue testing. This is a hard task, but which could be really helpful in order to interpret the obtained mechanical data, as far as LME or EAC effects are concerned.

Post-test analysis

Surface state analysis is very important for all tests:

1) general aspect including roughness, porosity of surface layers;
2) distribution of cracks (if possible);
3) chemical and (if possible) structural analysis of surface layers (top view and cross-sections).

For Charpy impact testing, this is mandatory, especially if one wants to determine a DBTT shift due to contact with LBE, since we can already infer that the DBTT shift should strongly depend on the contact conditions. Moreover, it could help to quantify the data since the DBTT shift due to LBE is unpredictable, and will be strongly dependent on the contact conditions between the steel and the embrittling species. In case of a wide scattering of data, it could help to determine reliable ones. Moreover, it would help to compare the DBTT shift that could be obtained *in fine* by different laboratories and teams.

In any case, whatever the applied experimental procedure (with tests carried out: *i)* in LM; *ii)* in air after exposure to LM at same temperature; *iii)* always in air but at room temperature), information on the evolution of fracture toughness or ductile to brittle transition temperature will be of primary importance since there is no data available in the literature, for either T91 or 316L.

For fatigue, creep and tensile tests, post-test surface state analysis is also requested. Analysis of specimens after interrupted tests is requested and could be helpful to improve understanding of LME or EAC.

7.10 Conclusions

The study of the compatibility of structural materials with heavy liquid metals (lead, lead-bismuth eutectic…) represents a non-negligible contribution to the international research effort dedicated to the development of accelerator-driven systems and other innovative concepts of LM-cooled fast reactors concepts of generation IV. It is worth recalling *that compatibility means both corrosion and mechanical resistance*, possibly in a radiation environment which should be the more representative of the nuclear facilities in project. Therefore a chapter devoted to mechanical properties of martenstic and stainless steel is totally justified.

The present chapter, which is an update of the version edited in 2007, clearly shows that this topic is of great interest in light of the papers published during this last period. It incorporates new results, new data and new, improved understanding of the effect of lead or lead-bismuth on mechanical properties on T91 and 316L which were not only selected as structural materials for the European ADS project and MEGAPIE target but are also of interest for the MYRRHA project.[15] MYRRHA, a flexible fast spectrum research reactor (50-100 MW_{th}) to be built at Mol (Belgium) is conceived as an accelerator-driven system (ADS), able to operate in subcritical and critical modes. It contains a proton accelerator of 600 MeV, a spallation target and a multiplying core with MOX fuel, cooled by liquid lead-bismuth (Pb-Bi). As compared to the previous version of this chapter, the tensile properties have been extensively documented and additional techniques such as the small punch test allowed to better outline the parameters promoting LME. Fracture toughness values are now available, as is more information on creep and fatigue. A lot of experiments have been conducted by controlling and lowering the dissolved oxygen in the LBE. At the end of this chapter, a certain number of points are noticeable.

From the study of the monotonic properties of T91 in lead and LBE in various experimental conditions, it turns out that T91 can be embrittled by LBE or lead but *the risk is better managed*. Even in its standard heat treatment, T91 can be embrittled and this depends on temperature, strain rate, oxygen content in LBE and the quality of the surface state. If any defects are present at the surface prior to use, as for instance the presence of flaws resulting from machining, then the risk of embrittlement increases. Nevertheless, a smooth surface can be degraded during the in-service use of the material; slip-band-induced roughness, oxide cracking and this can be site initiation for liquid metal embrittlement. It is also shown that the presence of an oxide layer is not a full guarantee of protection against LME. For long or very long exposure in LBE, the problem can be more complicated because the oxide layer at the material surface will evolve, as will the microstructure of the bulk material. Creep performances can be affected by the presence of LBE or Pb. Secondary creep rate is increased and time to rupture is decreased. Fracture toughness can be reduced by 30% in the presence of LBE.

Fatigue is inherent to any structural component in service. The more significant effect of LBE on the fatigue behaviour of T91 is a detrimental effect of LBE on the fatigue crack initiation resistance, especially in the LCF regime. Fatigue crack growth rate is increased by a factor of ten in the presence of LBE.

For mechanical loading where the exposure is suspected to be long (creep, fatigue), coating can be interesting and those studied (pack cementation, GESA) show that this field should be more thoroughly investigated.

On the contrary, 316L has been less investigated but the results suggest that this alloy is less sensitive to LME. Nevertheless, LMAD is observed as the low cycle fatigue of 316L stainless steel is nevertheless a little bit affected by LBE.

15. MYRRHA: Multi-Purpose Hybrid Research Reactor for High-Tech Applications.

Researches, experiments, collection of data on mechanical properties of structural steels in contact with LBE continue. The MatiSSE[16] project of FP7 should produce a certain amount of this new information.

Due to the very numerous factors promoting LME and LMAD, it seems difficult to accept that one single theory on LME could explain the practical cases encountered in the industry. Of course, basic ideas and basic concepts must be kept in mind and should be taught at universities. Consequently, to solve practical problems, it is necessary to conduct investigations under conditions imitating or at least approaching those of service together with more fundamental ones. In all cases, it is recommended to investigate in more detail the relationship between the physico-chemical processes occurring at the interface, the deformation and failure of the material, and to be open-minded to the possibility of new structural materials. Indeed, new modified grades such as P92 (containing tungsten), ODS steels, welded materials, coated materials have not yet been sufficiently investigated.

16. MatISSE: Materials Innovations for a Safe and Sustainable Nuclear in Europe.

References

Abramov, V.Y. et al. (1994), "Influence of Lead Melt on Plastic Deformation of High-alloyed Heat-resistant Steels", *Materials Science*, 30, pp. 465-469.

Abramov, V.Y. et al. (2004), "Corrosion and Mechanical Properties of BREST-OD-300 Reactor Structural Materials", *Proceedings of the 11th International Conference on Nuclear Engineering (ICONE11 – 36413)*, Tokyo, Japan, 20-23 April 2003, published in JSME International Journal B (2003), Vol. 47.

Aiello, A. et al. (2004), "Mechanical Properties of Martensitic Steels after Exposure to Flowing Liquid Metals", *Journal of Nuclear Materials*, 335, pp. 217-221

Antipenkov, A. et al. (1991), "Compatibility of Eutectic with Structural Materials", *Fusion Engineering and Design*, 14, pp. 347-351.

Auger, T. et al. (2004), "Effect of Contact Conditions on Embrittlement of T91 Steel by Lead-bismuth", *Journal of Nuclear Materials,* 335, pp. 227-231.

Auger, T. and G. Lorang (2005), "Liquid Metal Embrittlement Susceptibility of T91 Steel by Lead-bismuth", *Scripta Materialia*, 52, pp. 1323-1328.

Auger, T., et al. (2008), "Role of Oxidation on LME of T91 Steel Studied by Small Punch Test", *Journal of Nuclear Materials*, 376, pp. 336-340.

Auger, T. et al. (2011), "Fracture Mechanics Behavior of the T91 Martensitic Steel in Contact with Liquid Lead-bismuth Eutectic for Application in an Accelerator Driven System", *Journal of Nuclear Materials.,* 415, pp. 293-301.

Balandin, Yu.F. and V.G. Markov (1961), "Structural Materials for Systems with Liquid Metal Coolants", *Sudpromgiz*, Saint-Petersburg.

Balandin, Yu.F. and I.F. Divisenko (1970), "Strength and Ductility of a Type 12 Khm Heat-resistant Steel in Contact with Liquid Pb-Bi Eutectic", *Fiz. Khim. Mekh. Mater.*, 6, pp. 85-89.

Benamati, G. et al. (1994), "Corrosion and Low-cycle Fatigue Properties of AISI 316L in Flowing Pb-17Li", *Journal of Nuclear Materials*, 212, pp. 1515-1518.

Bichuya, A.L. (1969), "Effect of Oxide Films on the Corrosion-Fatigue Strength of 1Cr18Ni9Ti Steel in Liquid Pb-Bi Eutectic", *Sov. Mater. Sci.*, 5, pp.352-354.

Borgstedt, H.U. and M. Grundmann (1986), "The Fracture of Austenitic and Martensitic Steels in Liquid Lithium", *Nuclear Engineering and Design/Fusion*, 3, pp. 273-286.

Borgstedt, H.U., et al. (1991), "Corrosion and Mechanical Properties of the Martensitic Steel X18CrMoVNb 12 1 in Flowing Pb-17Li", *Fusion Engineering and Design*, 14, pp. 329-334.

Bryant, K. and S. Benerjie (1988), "Embrittlement of Structural Steels and Alloys", *Metallurgiya*, Moscow (Russian translation).

Broc, M., J. Sannier and G. Santarini (1983), "Experimental Studies on the Use of Liquid Lead in a Molten Salt Nuclear Reactor", *Nuclear Technology*, 63, pp. 197-208.

Chatain, D., F. Chabert and V. Ghetta (1993), "New Experimental Setup for Wettability Characterization Under Monitored Oxygen Activity: I. Role of Oxidation State and Defect Concentration on Oxide Wettability by Gold", *J. Am. Ceram. Soc.*, 76, pp. 1568-1576.

Chaevskii, M.I. and V.I. Likhtman (1962), "The Effect of the Rate of Deformation on the Strength and Plasticity of Carbon Steel in Contact with a Melt of a Low-melting Metal", *Soviet Physics Doklady*, 6, pp. 914-916.

Chaevskii, M.I. and A.L. Bichuya (1969), "Eliminating the Weakening Effect of Lead-bismuth Eutectic on Steel by Reducing the Strain Rate", *Sov. Mater. Sci.*, 5, pp. 82-84.

Chopra, O.K. and D.L. Smith (1983a), "Compatibility of Ferrous Alloys in a Forced Circulation Pb-17Li System", *Journal of Nuclear Materials*, 141-143, pp. 566-570.

Chopra, O.K. (1983b), "Effects of Sodium and Lithium Environments on Mechanical Properties of Ferrous Alloys", *Journal of Nuclear Materials*, 115, pp. 223-238.

Clegg, R.E. (2001), "A Fluid Flow Based Model to Predict Liquid Metal Induced Embrittlement Crack Propagation Rates", *Eng. Fracture Mechanics*, 68, pp. 1777-1790.

Coen, G. et al. (2010), "Investigation of the Effect of Lead-bismuth Eutectic on the Fracture Properties of T91 and 316L", *Journal of Nuclear Materials*, 385, pp. 122-128.

Courouau, J-L., P. Deloffre and R. Adriano (2002), "Oxygen Control in Lead-bismuth Eutectic: First Validation of Electrochemical Oxygen Sensors in Static Conditions", *J. Phys. IV*, 12, Pr8-141-153.

Courouau, J-L. (2004), "Electrochemical Oxygen Sensors for On-line Monitoring in Lead-bismuth Alloys: Status of Development", *Journal of Nuclear Materials*, 335, pp. 254-259.

Dai, Y., B. Long and F. Gröschel (2006a), "Slow Strain Rate Tensile Tests on T91 in Static Lead-Bismuth Eutectic", *Journal of Nuclear Materials*, 356, pp. 222-228.

Dai, Y. et al. (2006b), "Summary of the Preliminary Assessment of the T91 Window Performance in the MEGAPIE Conditions", *Nuclear Instruments and Methods A,* 562, pp. 698-701.

Di Gabriele, F., A. Doubkova and A. Hojna (2008), "Investigation of the Sensitivity to EAC of Steel T91 in Contact with Liquid LBE", *Journal of Nuclear Materials*, 376, pp. 307-311.

Dmukhovs'ka, I.H. and V.V. Popovich (1993a), "Influence of Stress Concentrators on the Temperature Dependence of the Liquid Metal Embrittlement of Armco Iron", *Materials Science*, Vol. 29, pp. 501-506.

Dmukhovs'ka, I.H. (1993b), "Embrittlement of Armco Iron by Indium at High Temperatures", *Materials Science*, Vol. 29, pp. 596-599.

Dmukhovs'ka, I.H. and V.V. Popovich (1995), "Effect of Lithium-lead Eutectic and Hydrogen on the Fatigue Behavior of some Austenitic Alloys", *Materials Science*, 31, pp. 99-104.

Ebrill, N., Y. Durandet and L. Strezov (2000), "Dynamic Reactive Wetting and its Role in Hot Dip Coating of Steel Sheet with an Al-Zn-Si Alloy", *Metallurgical and Mater. Trans.*, 31B, pp.1069-1079.

Engelko, V. et al. (2001), "Pulsed Electron Beam Facility (GESA) for Surface Treatment of Materials", *Vacuum,* 62, pp. 211-216.

Espié, L., B. Drevet and N. Eustathopoulos (1994), "Experimental Study of the Influence of Interfacial Energies and Reactivity on Wetting in Metal/Oxide Systems", *Metallurgical and Materials Trans.*, 25A, pp. 599-605.

Fazio, C. et al. (2003), "Corrosion Behavior of Steels and Refractory Metals and Tensile Features of Steels Exposed to Flowing PbBi in the LECOR Loop", *Journal of Nuclear Materials,* 318, pp. 325-332.

Finarelli, D., M. Roedig and F. Carsughi (2004), "Small Punch Tests on Austenitic and Martensitic Steels Irradiated in a Spallation Environment with 530 MeV Protons", *Journal of Nuclear Materials*, 328, 146-150.

Funaki, S. (Nippon Steel Corp., Japan) (1993), "Environment Embrittlement Evaluation of Metals", Jpn. Kokai Tokkyo Koho, patent written in Japanese, Application: JP 92-80793 19920402. Priority: CAN 120:83053 AN 1994:83053.

Gamaoun, F. et al. (2002), "Influence of Long Term Exposure to Molten Lead on the Microstructure & Mechanical Behavior of T91 Steel", *J. Phys. IV*, 12, Pr8-191-202.

Gamaoun, F. (2003), "Effet de maintiens de longue durée en bain de plomb ou d'eutectique plomb-bismuth liquide sur un acier martensitique à 9%Cr", PhD Thesis, Institut National Polytechnique, Grenoble.

Gamaoun, F. et al. (2004), "Cavity Formation and Accelerated Plastic Strain in T91 Steel in Contact with Liquid Lead", *Scripta Materialia*, 50, pp. 619-623.

Ghetta, V. et al. (2001), "Experimental Setup for Steel Corrosion Characterization in Lead Bath", *Journal of Nuclear Materials*, 296, pp. 295-300.

Ghetta, V. et al. (2002), "Control and Monitoring of Oxygen Content in Molten Metals. Applications to Lead and Lead-bismuth Melts", *J. Phys. IV*, Vol. 12, Pr8-123-140.

Glasbrenner, H., F. Gröschel and T. Kirchner (2003), "Tensile Tests on MANET II Steel in Circulating Pb-Bi Eutectic", *Journal of Nuclear Materials*, 318, pp. 333-338.

Glasbrenner, H. and F. Gröschel (2004), "Bending Tests on T91 Steel in Pb-Bi Eutectic, Bi and Pb-Li Eutectic", *Journal of Nuclear Materials*, 335, pp. 239-243.

de Gennes, P-G., F. Brochard-Wiart and D. Quéré (2002), "Gouttes, bulles, perles et ondes", *Collection échelles*, Belin, Paris.

Glickman, E.E. et al. (1976), "Kinetics and Mechanism of Copper Fracture During Deformation in Surface-Active Baths", *Sov. Phys. Journal*, 19, pp.844-849.

Glickman, E.E. and Yu.V. Goryunov (1978), "Mechanisms of Embrittlement by Liquid Metals and Other Manifestations of the Rebinder Effect in Metal Systems", *Fiz. Khim. Mek. Mater*, 14, pp. 20-30.

Glickman, E.E., Yu.V. Goryunov and V.M. Denim (1985), "The Effect of Intercrystalline Internal Absorption of Bismuth on the Intergranular Fracture of Copper in Liquid Bismuth and the Mechanism of Liquid Metal Embrittlement", *Phys. Chem. Mech. Surf.*, 2, pp. 3041-3052.

Glickman, E.E. (2000), "Mechanism of Liquid Metal Embrittlement by Simple Experiments: From Atomistics to Life-Time", in *Multiscale Phenomena in Plasticity*, J. Lepinoux et al. (eds.), Kluwer Academic Publishers, Dordrecht, the Netherlands, pp. 383-401.

Gordon, P. and H.H. An (1982), "The Mechanisms of Crack Initiation and Crack Propagation in Metal-induced Embrittlement of Metals", *Metal. Trans.*, 13A, pp.457-472.

Gorse, D. (2000), "Stress Corrosion Cracking: An Electrochemist Point of View", in *Multiscale Phenomena in Plasticity*, J. Lepinoux et al. (eds.), Kluwer Academic Publishers, Dordrecht, The Netherlands, pp. 425-439.

Gorse-Pomonti, D. and V. Russier (2007), "Liquid Metals for Nuclear Applications", *Journal of Non-Crystalline Solids*, 353, pp. 3600-3614.

Gorse, D. et al. (2011) "Influence of Liquid Lead and Lead-bismuth Eutectic on Tensile, Fatigue and Creep Properties of Ferritic/Martensitic and Austenitic Steels for Transmutation Systems", *Journal of Nuclear Materials*, 415, pp. 284-292.

Gorynin, I.V. et al. (1999), "Structural Materials for Power Plants with Heavy Metals as Coolants", *Proceedings of the Conference on Heavy Liquid Metal Coolants in Nuclear Technology*, Obninsk, Russian Federation, B.F. Gromov (ed.), Vol. 1, pp. 120-132.

Gorynin, I.V. et al. (2000), "Structural Materials for Atomic Reactors with Liquid Metal Heat-transfer Agents in the Form of Lead or Lead-bismuth Alloy", *Metal Science and Heat Treatment*, Vol. 41, pp. 384-388.

Goryunov, Yu.V. et al. (1978), "The Intermittent Growth of Cracks in Single Crystals of Zinc During Strain at a Contact with Mercury and Gallium", *Sov. Phys. Dokl.*, 23, pp. 683-684.

Griffith, A.A. (1920), *Phil. Trans. Roy. Soc.*, A 221, pp. 163-168.

Gromov, B.F. et al. (1997), "Use of Lead-bismuth Coolant in Nuclear Reactors and Accelerator-Driven Systems", *Nuclear Engineering and Design*, 173, pp.207-217.

Guérin, S. et al. (2003), "Synergy Effect of LBE and Hydrogenated Helium on Resistance to LME of T91 Steel Grade", *Journal of Nuclear Materials*, 318, pp. 339-347.

Guttmann, M. (1997), "Metallurgy, Properties and Ageing Behaviour of High-Cr Steels for Potential Use in Hybrid Nuclear Reactors", *GEDEON Workshop on Materials for Hybrid Systems*, Paris, 24 September 1997.

Hamouche-Hadjem, Z., T. Auger and I. Guillot (2009), "Temperature Effect in the Maximum Propagation Rate of a Liquid Metal Filled Crack: The T91 Martensitic Steel/Lead-bismuth Eutectic System", *Corros. Sci.*, 51, pp. 2580-2587.

Hamouche-Hadjem, Z. et al. (2008), "Susceptibility to LME of 316L and T91 Steels by LBE: Effect of Strain Rate", *Journal of Nuclear Materials*, 376, pp. 317-321.

Handbook of Chemistry and Physics, 46th Edition, R.C. Weast, S.M. Selby and C.D. Hodgman (eds.), The Chemical Rubber Co., Cleveland, 1965-1966.

Hättestrand, M. and H-O. Andrén (2001), "Influence of Strain on Precipitation Reactions During Creep of an Advanced 9% Chromium Steel", *Acta Materialia*, 49, pp. 2123-2128.

Hojna, A. and F. Di Gabriele (2011), "On the Kinetics of LME for the Ferritic-martenstic Steel T91 Immersed in Liquid PbBi Eutectic", *J. Nuclear Mat.*, 413, pp. 21-29.

Huthmann, H. et al. (1980), "Influence of Flowing Sodium on the Creep Rupture and Fatigue Behaviour of Type 304 SS at 550°C", *Proceedings of the 2nd International Conference on Liquid Metal Technology in Energy Production*, Richland, Washington, 20-24 April, pp. 19-33.

Ina, K. and H. Koizumi (2004), "Penetration of Liquid Metals into Solid Metals and Liquid Metal Embrittlement", *Mater. Sci. Eng.*, A 387-389, pp. 390-394.

Jia, X. and Y. Dai (2003), "Small Punch Tests on Martensitic/Ferritic Steels F82H, T91 and Optimax-A Irradiated in SINQ Target-3", *Journal of Nuclear Materials*, 323, 360-367.

Jianu, A., et al. (2009), "Creep-to-Rupture Tests of T91 Steel in Flowing Pb-Bi Eutectic Melt at 550°C", *Journal of Nuclear Materials*, 394, pp. 102-108.

Jonghe, V. de and D. Chatain (1995), "Experimental Study of Wetting Hysteresis on Surfaces with Controlled Geometrical and/or Chemical Defects", *Acta Mater.*, 43, 1505-1515.

Joseph, B., M. Picat and F. Barbier (1999), "Liquid Metal Embrittlement: A State-of-the-art Appraisal", *Eur. Phys. J. AP.*, 5, pp. 19-31.

Kalkhof, D. and M. Grosse (2003), "Influence of PbBi Environment on the Low-Cycle Fatigue Behavior of SNS Target Container Materials", *Journal of Nuclear Materials*, 318, pp. 143-150.

Kamdar, M.H. (1973), "Embrittlement by Liquid Metals", *Prog. Mater. Sci.*, 15, pp. 289-372.

Kanetani, K. and H. Inoue (Nippon Steel Corp., Japan) (1992), "Steels Resistant to Brittle Fracture in Molten Lead", Jpn. Kokai Tokkyo Koho, patent written in Japanese, Application: JP 90-280039 19901018. Priority: CAN 117:237822 AN 1992:637822.

Kashtanov, A.D. et al. (2004), "Corrosion-Mechanical Strength of Structural Materials in Contact with Liquid Lead", *Atomic Energy*, 97, pp. 538-542.

Klueh, R.L. and D.R. Harries (2001), "Irradiation Creep", Chapter 8 of *High-Chromium Ferritic and Martensitic Steels for Nuclear Applications*, ASTM MONO3, ASTM, West Conshohocken, PA, pp. 113-121.

Kondo, M. and M. Takahashi (2006), "Corrosion Resistance of Si- and Al-Rich Steels in Flowing Lead-Bismuth", *Journal of Nuclear Materials*, 356, 203-212.

Kurata, Y., M. Futakawa and S. Saito (2008), "Corrosion Behavior of Steels in Liquid Lead-Bismuth with Low Oxygen Concentrations", *Journal of Nuclear Materials*, 373, 164-178.

Leger, L. and F.J. Joanny (1992), "Liquid Spreading", *Rep. Prog. Phys.*, pp. 431-486.

Legris, A. et al. (2000), "Embrittlement of a Martensitic Steel by Liquid Lead", *Scripta Mater.*, 43, pp. 997-1001.

Legris, A. et al. (2002), "Liquid Metal Embrittlement of the Martensitic Steel T91: Influence of the Chemical Composition of the Liquid Metal; Experiments and Electronic Structure Calculations", *Journal of Nuclear Materials*, 301, pp. 70-76.

Lesueur, C. et al. (2002), "Analysis of the Stability of Native Oxide Films at Liquid Lead/Metal Surfaces", *J. Phys. IV*, Vol. 12, Pr8-155.

Lesueur, C., et al. (2008), "Experimental Study of Ultrasound Propagation at a Liquid-Solid Composite Interface for Inspection of Liquid-Metal Cooled Nuclear Reactors", *NDT&E International*, 41, pp. 217-222.

Likhtman, V.I., P.A. Rebinder and G.V. Karpenko (1954), "Influence of Surface-Active Media on Deformation of Metals", *Akad. Nauk SSSR*, Moscow (in Russian).

Likhtman, V.I. and E.D. Shchukin (1958), "Physico-Chemical Phenomena in the Deformation of Metals", *Usp. Fiz. Nauk*, 66, pp. 213-245.

Likhtman, V.I., E.D. Shchukin and P.A. Rebinder (1962), "The Physico-Chemical Mechanics of Metals", *Izd. Akad. Nauk SSSR*, Moscow.

Long, B. et al. (2008a), "Liquid Pb-Bi Embrittlement Effects on the T91 Steel After Heat Treatments", *J. Nuclear Mat.*, 377, pp. 219-224.

Long, B. and Y. Dai (2008b), "Investigation of LBE Embrittlement Effects on the Fracture Properties of T91", *Journal of Nuclear Materials*, 376, pp. 341-345

Loewen, E.P. and A.T. Tokuhiro (2003), "Status of Research and Development of the Lead-Alloy-Cooled Fast Reactor", *J. Nuclear Science and Technology*, 40, pp. 614-627.

Lucas, G.E. (1990), *Metall. Trans.* A, 21 A, pp.1105-1119.

Mae, T. and S. Hori (1991), "Liquid-Metal Embrittlement of Aluminium by Several Eutectic Alloys Containing Zinc", *J. Mater. Sci.*, 26, pp. 479-483.

Maitre, A. et al. (2002), "Preliminary Study of Some Parts of the Quinary System Bi-Fe-Hg-O-Pb", *J. Phys IV*, Vol. 12, Pr8-163-174.

Maitre, A., M. François and J-C. Gachon (2004), "Experimental Study of the Bi_2O_3-Fe_2O_3 Pseudo-Binary System", *J. Phase Equilibria and Diffusion*, 25, pp. 59-67.

Maitre, A. (2005), "Transformations de phases dans quelques systèmes réactifs métalliques et céramiques: aspects thermodynamiques et cinétiques", Habilitation à Diriger les Recherches de l'Université Henri Poincaré, Nancy I, 24 January 2005.

Manly, W.D. and A. Brasunas (1954), *Interim Report on Static Liquid-Metal Corrosion*, ORNL Report, Metallurgy Division, Oak Ridge National Laboratory, Oak Ridge, Tennessee.

Mao, X. and Kameda, J. (1991), "Small-Punch Technique for Measurement of Material Degradation of Irradiated Ferritic Alloys", *J. Mater. Sci.*, 26, 9, pp. 2436-2440.

Medina-Almazán, L., T. Auger and D. Gorse (2008), "Liquid Metal Embrittlement of an Austenitic 316L Type and a Ferritic-Martensitic T91 Type Steel by Mercury", *Journal of Nuclear Materials*, 376, pp. 312-316.

Misawa, T. et al. (1987), "Small Punch Tests for Evaluating Ductile-Brittle Transition Behavior of Irradiated Ferritic Steels", *Journal of Nuclear Materials*, 150, pp. 194-202.

Mishra, M.P. et al. (1997), "Influence of Sodium Environment and Load Ratio (r) on Fatigue Crack Growth Behaviour of a Type 316LN Stainless Steel at 813 K", *Int. J. Pres. Ves. & Piping*, 70, pp. 77-82.

Naidich, Ju.V. (1981), "The Wettability of Solids by Liquid Metals", *Progress in Surface and Membrane Science*, Vol. 14, pp. 353-484.

Nakae, H., H. Fujii and K. Sato (1992), "Reactive Wetting of Ceramics by Liquid Metals", *Materials Transactions JIM*, 33, pp. 400-406.

Nicaise, G. et al. (2001), "Embrittlement of the Martensitic Steel T91 Tested in Liquid Lead", *Journal of Nuclear Materials*, 296, 256-264.

Nicholas, M.G. and C.F. Old (1979), "Review Liquid Metal Embrittlement", *J. Mater. Sci.*, 14, pp. 1-18.

Nicholas, M.G., C.F. Old and B.C. Edwards (1981), "A Summary of the Literature Describing Liquid Metal Embrittlement", Materials Development and Metallurgy Division, AERE Harwell, AERE – 9199 (Revised).

Nicholas, M.G. (1982), "A Survey of Literature on Liquid Metal Embrittlement of Metals and Alloys", in *Embrittlement by Liquid and Solid Metals*, M.H. Kamdar (ed.), St. Louis, *TMS-AIME*, pp. 27-50.

Nikitin, V.I. (1967), "Physicochemical Phenomena in the Interaction of Liquid and Solid Metals", *Atomizdat*, Moscow (in Russian).

Nikolin, E.S. and G.V. Karpenko (1968), "Effect of Liquid Low-Melting Metals on the Fatigue Strength of Carbon Steel in Relation to the Stress Frequency", *Sov. Mater. Sci.*, 4, pp. 15-17.

Novakovic, R. et al. (2002), "Surface Properties of Bi-Pb Liquid Alloys", *Surface Sci.*, 515, pp. 377-389.

Passerone, A. and E. Ricci (1998), "High Temperature Tensiometry", in *Drops and Bubbles in Interfacial Research*, D. Möbius and R. Miller (eds.), Elsevier, Amsterdam, pp. 475-524.

Paumel, K. et al. (2009), **"**Visualization of the Ultrasound-induced Behaviour of Gas Pockets Entrapped on a Patterned Surface. Application to Inspection of Sodium-cooled Fast Reactors", *Nuclear Engineering and Design,* 239, pp. 2272-2278.

Pokrovskii, N.L., P.P. Pugachevich and N.A. Golubev (1969), *Russian J. Phys. Chem.*, 43, pp. 1212.

Popovich, V.V. and I.G. Dmukhovskaya (1978), "Rebinder Effect in the Fracture of Armco Iron in Liquid Metals", *Sov. Mater. Sci.*, 14, pp. 365-370.

Popovich, V.V. (1979), "Mechanisms of Liquid Metal Embrittlement", *Sov. Mater. Sci.*, 15, pp. 438-445.

Popovich, V.V. and I.G. Dmukhovskaya (1983), "Liquid Metal Embrittlement of Deformable Metals", Preprint N°69, Karpenko Physico-Mechanical Institute, Ukrainian Academy of Sciences, L'viv.

Potak, Y.M. (1955), "The Brittle Failure of Steels and Steel Parts", *Oborongiz* (in Russian).

Protsenko, P. and N. Eustathopoulos (2005), "Surface and Grain Boundary Wetting of Fe-Based Solids by Molten Pb and Pb-Bi Eutectic", *J. Mater. Sci.*, 40, pp. 2383-2387.

Rabkin, E. (2000), "Grain Boundary Embrittlement by Liquid Metals", in *Multiscale Phenomena in Plasticity*, J. Lepinoux, et al. (eds.), Kluwer Academic Publishers, Dordrecht, Netherlands, pp. 403-413.

Rebinder, P.A. (1928), "Investigation of the Influence of the Surface Energy of a Crystal on its Mechanical Properties when the Surface Tension of its Faces is Lowered by the Introduction of Surface-Active Substances into the Working Medium", *Proceedings of the 6th Conference of Russian Physicists*, compendium of lectures, *Gosizdat*, Moscow, pp. 29-30 (in Russian).

Rebinder, P.A. and E.D. Shchukin (1972), "Surface Phenomena in Solids in the Processes of Their Deformation and Failure", *Usp. Fiz. Nauk*, 108, pp. 3-42.

Rebinder, P.A. and E.D. Shchukin (1972), *Progress in Surface Science*, Vol. 3, No. 2, S.G. Davison (ed.), Pergamon Press, Oxford, p. 97.

Robertson, W.M. (1966), "Propagation of a Crack Filled with Liquid Metal", *Trans. Met. Soc. AIME*, 236, pp. 1478-1482.

Rostoker, W., J.M. McCaughey and H. Markus (1960), *Embrittlement by Liquid Metals*, Reinhold Publishing Corporation, New York.

Saltsman, J.F. and G.R. Halford (1988), "An Update of the Total-Strain Version of Strainrange Partitioning", *Low Cycle Fatigue*, ASTM-STP 942, H.D. Solomon, *et al.* (eds.), ASTM, Philadelphia, PA, pp. 329-341.

Serre, I. and J-B. Vogt (2008), "Heat Treatment Effect of T91 Martensitic Steel on Liquid Metal Embrittlement", *Journal of Nuclear Materials*, 376, pp. 330-335.

Serre, I. and J-B. Vogt (2009), "Mechanical Properties of a 316L/T91 Weld Joint Tested in Lead-bismuth Liquid", *Materials and Design*, 30, pp. 3776-3783.

Shchukin, E.D. (1977), "Environmentally Induced Lowering of Surface Energy and the Mechanical Behavior of Solids", in *Surface Effects in Crystal Plasticity*, R. Latanision, J. Fourie (eds.), *NATO ASI Series E 317*, Nordhoff, Leyden, pp. 701-736.

Shchukin, E.D. (1999), "Physical-Chemical Mechanics in the Studies of P.A. Rehbinder and His School", *Colloids and Surfaces A*, 149, pp. 529-537.

Soldatchenkova, L.S. et al. (1972), "Effect of an Artificial Defect in a Layer Near the Surface on the Ductility of Zinc Single Crystals in the Presence of Mercury", *Soviet Physics Doklady*, 17, pp. 253-256.

Solonin, M.I., *et al.* (2001), "Problems in the Development and Modification of Stainless Steels for Components of Cores of Fast Neutron Nuclear Reactors and a Fusion Reactor", *Fizika i Khimiya Obrabotki Materialov*, 5, pp. 5-13 (in Russian).

Strizak, J.P. et al. (2001), "The Effect of Mercury on the Fatigue Behavior of 316 LN Stainless Steel", *Journal of Nuclear Materials*, 296, pp. 225-230.

Strizak, J.P. and L.K. Mansur (2003), "The Effect of Mean Stress on the Fatigue Behavior of 316LN Stainless Steel in Air and Mercury", *Journal of Nuclear Materials*, 318, pp. 151-156.

Tanaka, M. and H. Fukunaga (1969), "Fatigue Strength of Mild Steel, 13 Cr Steel and 18 Cr-8 Ni Steel Subjected to Elevated Temperatures and to Contact with Liquid Pb and Sn", *J. Soc. Material Sci. Jpn.*, 18, 186.

Tian, H. et al. (2003), "Effects of Mercury on Fatigue Behavior of Type 316LN Stainless Steel: Application in the Spallation Neutron Source", *Journal of Nuclear Materials*, 318, pp. 157-166.

Toloczko, M.B. and F.A. Garner (1996), "Radiation Creep, Related to Void Swelling, is Apparently Independent of the Crystal Structure (b.c.c or f.c.c) in Iron-Base Alloys", *Journal of Nuclear Materials*, 233, pp. 289.

Ule, B. et al. (1999), "Small Punch Test Method Assessment for the Determination of the Residual Creep Life of Service Exposed Components: Outcomes from an Interlaboratory Exercise", *Nucl. Eng. Des.*, 192, pp. 1-11.

Van den Bosch, J., D. Sapundjiev and A. Almazouzi (2006), "Effects of Temperature and Strain Rate on the Mechanical Properties of T91 Material Tested in Liquid Lead Bismuth Eutectic", *Journal of Nuclear Materials*, 356, pp. 237-246.

Van den Bosch, J. et al. (2008), "Liquid Metal Embrittlement Susceptibility of Ferritic-martensitic Steel in Liquid Lead Alloys", *Journal of Nuclear Materials*, 376, pp. 322-329.

Van den Bosch, J. et al. (2009a), "Compatibility of Martensitic/Austenitic Steel Welds with Liquid Lead Bismuth Eutectic Environment", *Journal of Nuclear Materials,* 385, pp. 504-509.

Van den Bosch, J. et al. (2009b), "Fracture Toughness Assessment of Ferritic-martensitic Steel in Liquid Lead-bismuth Eutectic", *Journal of Nuclear Materials*, 385, pp. 250-257.

Van den Bosch, J. et al. (2010a), "Compatibility of Ferritic-Martensitic Steel T91 Welds with Liquid Lead-Bismuth Eutectic: Comparison between TIG and EB Welds", *Journal of Nuclear Materials*, 396, pp. 57-64.

Van den Bosch, J. et al. (2010b), "Liquid Metal Embrittlement of Silicon Enriched Steel for Nuclear Applications", *Journal of Nuclear Materials*, 398, pp. 116-121.

Van den Bosch, J. et al. (2012), "On the LME Susceptibility of Si Enriched Steels", *Journal of Nuclear Materials*, 429, pp. 105-112.

Verleene, A. et al. (2006), "Low Cycle Fatigue Behaviour of T91 Martensitic Steel at 300°C in Air and Liquid Lead Bismuth Eutectic", *Int. J. Fatigue*, 28, pp. 843-851.

Vogt, J-B., G. Degallaix and J. Foct (1988), "Cyclic Mechanical Behavior and Microstructure of a 12Cr-Mo-V Martensitic Stainless Steel", *Fatigue Fract. Eng. Mater. Struct.*, 11, pp. 435-446.

Vogt, J-B. et al. (2002), "The Risk of Liquid Metal Embrittlement of the Z10CDNbV 9-1 Martensitic Steel", *J. Phys. IV*, Vol. 12, Pr8-217-225.

Vogt, J-B. et al. (2004), "Mechanical Behaviour of the T91 Martensitic Steel under Monotonic and Cyclic Loadings in Liquid Metals", *Journal of Nuclear Materials*, 335, pp. 222-226.

Vogt, J-B. et al. (2006), "Coupling Effects Between Corrosion and Fatigue in Liquid Pb-Bi of T91 Martensitic Steel", *Proceedings of EUROCORR 2005*, Lisbon.

Vogt, J-B. and I. Proriol Serre (2013), "Fatigue Behaviour of a Martensitic and an Austenitic Steel in Heavy Liquid Metals", *Procedia. Engng.*, 55, pp. 812-818.

Vogt, J-B. et al. (2011), "Fatigue Resistance in Liquid Lead-bismuth Eutectic Alloy of T91", *Proceedings of ICAPP 2011*, Nice, France, paper 11328, pp. 2411-2417.

Warke, W.R., K.L. Johnson and N.N. Breyer (1970), "Liquid Metal Embrittlement of Steel by Lead and Lead Alloys", *Corrosion by Liquid Metals*, J.E. Draley, J.R. Weeks (eds.), Plenum Press, pp. 417-439.

Weisenburger, A. et al. (2008), "Low Cycle Fatigue Tests of Surface Modified T91 Steel in 10^{-6} wt% Oxygen Containing $Pb_{45}Bi_{55}$ at 550°C", *Journal of Nuclear Materials*, 377, pp. 261-267.

Weisenburger, A. et al. (2012), "Creep, Creep-to-rupture Tests of Al-Surface-Alloyed T91 Steel in Liquid Lead Bismuth at 500 and 550°C", *Journal of Nuclear Materials*, 431, pp. 77-84.

Westwood, A.R.C. and M.H. Kamdar (1963), "Concerning Liquid Metal Embrittlement, Particularly of Zinc Monocrystals by Mercury", *Phil. Mag.*, 8, pp. 787-803.

Wolski, K. et al. (2002), "Liquid Metal Embrittlement Studies on Model Systems with Respect to the Spallation Target Technology: The Importance of Nanometer-Thick Films", *J. Phys IV*, Pr8-249-261.

Yachmenyov, G.S. et al. (1999), "The Problems of Structural Materials Corrosion in Lead-bismuth Coolants", *Proceedings of the Conference on Heavy Liquid Metal Coolants in Nuclear Technology*, Obninsk, Russian Federation, B.F. Gromov (ed.), Vol. 1, pp. 133-140.

Ye, C., J-B. Vogt and I. Proriol Serre (2014), "Liquid Metal Embrittlement of the T91 Steel in Lead Bismuth Eutectic: The Role of Loading Rate and of the Oxygen Content in the Liquid Metal", *Mater. Sci. Eng.*, A680, pp. 2424-248.

Young, T. (1805), *Phil. Trans. Soc. London*, 95, pp. 65.

Yurechko, M. et al. (2011), "Creep-to-rupture of 9%Cr Steel T91 in Air and Oxygen-Controlled Lead at 650°C", *Journal of Nuclear Materials*, 419, pp. 320-328.

Yurechko, M. et al. (2013), "Creep-to-Rupture of the Steel P92 at 650°C in Oxygen-Controlled Stagnant Lead in Comparison to Air", *Journal of Nuclear Materials*, 432, pp. 78-86.

Zaïdi, M. et al. (2008), "Spreading of Liquid Lead Droplets on Metallic Iron Covered by Silicon Oxide Particles or Films", *Mat. Sci. Eng.*, A 495, pp. 90-95.

8. Irradiation effects on compatibility of structural materials with lead-bismuth eutectic*

8.1 Introduction

One of the key issues for the R&D of ADS and LFRs which use liquid Pb or LBE as coolant material is the understanding of the behaviour of structural materials in severe service environments. Besides irradiation-induced degradation of mechanical properties, the corrosion (Chapter 6) and embrittlement (Chapter 7) effects of liquid Pb or LBE can also significantly reduce the performances of structural materials. The synergistic effect of irradiation and liquid Pb or LBE is believed to be even more detrimental to structural materials. Systematic study of this hypothesis was not undertaken until the 5th Framework Programme MEGAPIE test programme, where the so-called LiSoR experiments were conducted at PSI (Switzerland) by irradiating specimens of T91 steel with 72 MeV protons in flowing LBE. The LiSoR experiments were continued in the 6th Framework Programme VELLA. In the 6th Framework Programme EUROTRANS/DEMETRA, ferritic/martensitic (FM) steels and austenitic steel SS 316L were irradiated in the presence of LBE in the BR2 reactor at SCK•CEN (Belgium) and in BOR60 (Russia). In parallel, many specimens were irradiated in the presence of LBE in Swiss Spallation Neutron Source (SINQ) targets with a mixed spectrum of high-energy protons and spallation neutrons. In the 7th Framework Programme GETMAT, the post-irradiation examinations (PIE) on the irradiated MEGAPIE (Mega-watt Pilot Experiment) target were included. However, it should be noted that, due to great difficulties with regard to handling highly activated specimens, particularly with alpha-contamination from irradiated LBE, the results thus far obtained are still rather limited. On the other hand, some specimens irradiated within the framework of the SINQ Target Irradiation Programme (STIP) and in BR2 and BOR60 were tested in an LBE environment to evaluate the LBE embrittlement effect on irradiated materials.

The contents of this chapter are organised as follows: Section 8.2 describes results of LiSoR experiments; Section 8.3 presents the results obtained from the irradiation experiments in fission reactors BR2 and BOR60; in Section 8.4, the results of specimens irradiated in STIP and tested in LBE are given; and in Section 8.5 the preliminary results obtained from the PIE of the MEGAPIE target are discussed.

8.2 LiSoR: Irradiation of T91 steel with 72 MeV protons in flowing LBE

Liquid-metal/solid-metal reaction (LiSoR) experiments were performed with the aim of supporting the development and operation of the MEGAPIE target. LiSoR was a unique facility used to simultaneously investigate the influence of flowing LBE, static mechanical stress and additional fluctuating thermal stress of a steel probe under irradiation. The facility was actually an LBE loop installed at a proton beam line of Injector-I at PSI. The energy of the proton beam is 72 MeV. Protons with this energy can penetrate about 10 cm in steels or LBE (Kirchner, 2003). Since the material used for the LBE container of the MEGAPIE target was T91 steel, it was used in the LiSoR experiments. The LBE flow rate was about 1 m/s, slightly higher than that of the LBE flow at the proton beam window of the MEGAPIE target, ~0.6 m/s.

* Chapter lead: Y. Dai. For additional contributors please see Appendix 1.

8.2.1 *Irradiation experiments*

The T91 steel used in LiSoR was supplied by the company CLI-FAFER (France) and had a composition in wt.% of 8.41 Cr, 0.08 Ni, 0.95 Mo, 0.44 Mn, 0.31 Si, 0.1 C, 0.25 V, 0.08 Nb, 0.24 Si, 0.035 Cu, 0.002 S with Fe in balance. The material was normalised at 1 070°C for 1 h followed by air cooling, and then tempered at 765°C for 1 h followed by air cooling.

Samples of interest are the test-section tube (TS tube) and inner tensile-stressed specimen (TS specimen) in the test section. The wall of both the TS tube and the TS specimen are 1 mm thick. Figure 8.2.1 illustrates the geometry of the specimen, and in Figure 8.2.2 the schema shows the test tube made of T91 and the cross-section, including the specimen and the flowing LBE.

Figure 8.2.1: Nominal dimensions of the specimen irradiated in test section Nos. 2 to 5

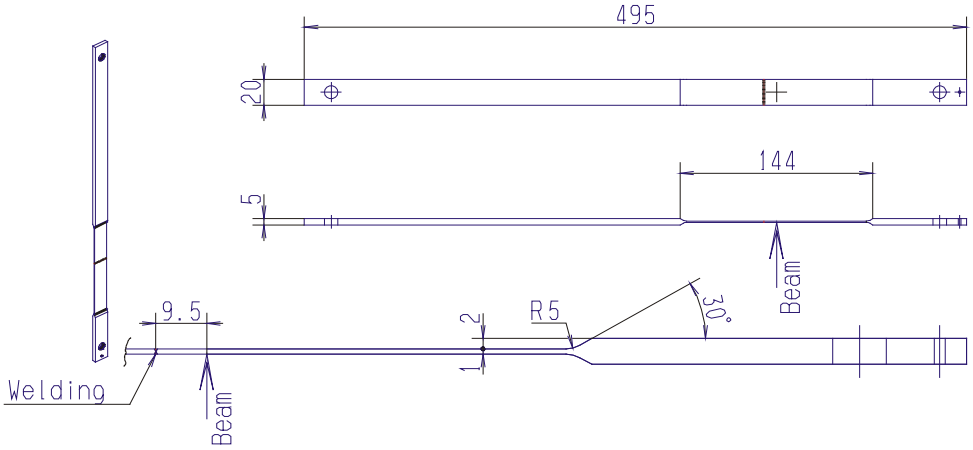

Figure 8.2.2: Sketches show the test tube and its cross-section, including the specimen and flowing LBE

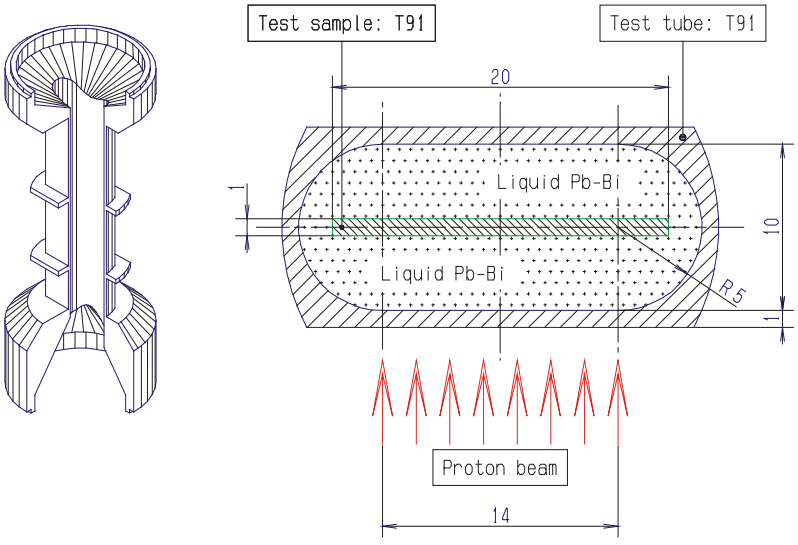

During irradiation (including beam off time) a constant mechanical load was applied upon the tensile specimen and the temperature of inlet LBE was constantly controlled at 300°C. In the TS tube and TS specimen the irradiation areas were about 5.5×14 mm^2. In the irradiation areas the proton beam induced a localised temperature increase and thermal stress oscillated with the wobbled proton beam at a frequency of about 2 Hz. The materials and irradiation parameters are listed in Table 8.2.1 for the five irradiation campaigns, LiSoR-2 to LiSoR-6. The details of the experiments and the temperature and stress distributions are given in Kirchner (2003), Glasbrenner (2005a), Samec (2005) and Dai (2012). As an example, Figure 8.2.3 shows the calculated temperature, stresses in longitudinal/transversal directions and shear stress changing with time at a point in the irradiation area of the TS specimen LiSoR-5 (Samec, 2005). In LiSoR-6, the surface of the TS tube was coated with TiN (Glasbrenner, 2006a) and one of the major surfaces of the TS specimen was coated with FeCrAlY (Weisenburger, 2008) to investigate the behaviour of coating under such experimental conditions (Dai, 2012).

It should be noted that there were no oxygen control or measurement devices installed in the LiSoR LBE loop. Therefore, the oxygen content in LBE was not known. But, it should be lower than the saturated level at 300°C (the operation temperature).

Table 8.2.1: Materials and irradiation conditions of the TS tubes and TS specimens of LiSoR-2 to LiSoR-6

		LiSoR-2	LiSoR-3	LiSoR-4	LiSoR-5	LiSoR-6
Irradiation time		34 h	264 h	144 h	724 h	900 h
Material	TS tube TS specimen	T91-A[1] T91-B[2]	T91-A T91-B	T91-A T91-B	T91-A T91-C[3]	T91-TiN coating T91-FeCrAlY coating
Averaged proton energy[4]	TS tube TS specimen	70 MeV 40 MeV	70 MeV 40 MeV	70 MeV 40 MeV	70 MeV 40 MeV	70 MeV 20 MeV
Beam current		50 μA	15 μA	30 μA	30 μA	25-28 μA
Peak oscillating temp. LBE-surf.[5]	TS tube TS specimen	650°C 580°C	330°C 324°C	400°C 380°C	400°C 380°C	390°C 395°C
Peak oscillating. temp. maximum[6]	TS tube TS specimen	– –	380°C 345°C	550°C 440°C	550°C 440°C	525°C 425°C
Maximum stress[7]	TS tube TS specimen	– 200 MPa	25 MPa 200 MPa	75 MPa 200 MPa	75 MPa 200 MPa	70 MPa 200 MPa
Irradiation dose	TS tube TS specimen	0.19 0.23	0.39 0.48	0.39 0.48	1.9 2.3	1.8 2.5
He concentration[8]	TS tube TS specimen	3.6 appm 2.6 appm	7.2 appm 5.2 appm	7.2 appm 5.2 appm	36 appm 26 appm	35 appm 20 appm

1 T91-A, the material of the tube produced by Creusot Loire Industrie (France) and has a composition in wt.% of 8.26 Cr, 0.13 Ni, 0.95 Mo, 0.43 Si, 0.38 Mn, 0.1 C, 0.2 V, 0.017 P, 0.065 Nb and with Fe in balance.

2 T91-B, the TS specimen material, originates from the SPIRE programme supplied by Ugine (France) and has a composition in wt.% of 8.63 Cr, 0.23 Ni, 0.95 Mo, 0.31 Si, 0.43 Mn, 0.1 C, 0.21 V, 0.02 P, 0.09 Nb and with Fe as balance. The material was normalised at 1 040°C for 1 h followed by air cooling, and then tempered at 760°C for 1 h followed by air cooling.

3 T91-C, the material of the TS-specimen of LiSoR-5.

4 Kirchner (2003), Figure 8.

5 Samec (2005).

6 Samec (2005). The maximum temperature in the TS specimen is in the central position (0.5 mm depth) while for the tube it is at the outer surface.

7 Samec (2005). For the TS tube it is the maximum shear stress. In fact the TS tube has a maximum compression stress which is six times larger than the shear stress.

8 The helium concentration of LiSoR-2 was measured (Dai, 2006b). The others were calculated using LiSoR-2 data.

Figure 8.2.3: The time dependence of temperature, stresses in longitudinal/ transversal directions and shear stress at a point in the irradiation area of the TS specimen LiSoR-5 calculated with the ANSYS code

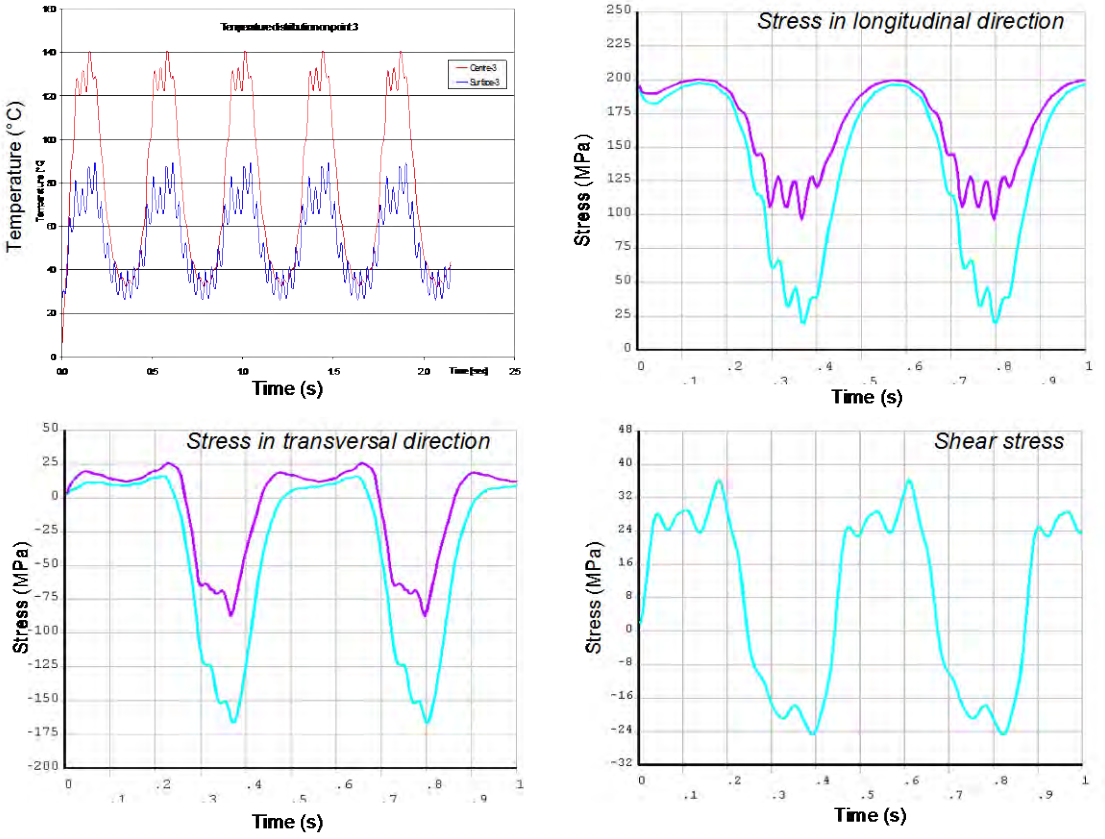

Source: Samec (2005).

8.2.2 *Surface analyses*

The surface analyses of LiSoR samples were performed in different ways: visual inspection (photography), SEM and EPMA.

The photos of the visual inspection were taken from the irradiation areas of both the TS tubes and the TS specimens of the five irradiations, as shown in Figure 8.2.4. In the upper photos the beam foot print on each TS tube can be clearly seen. In the LiSoR-2 TS tube, a crack was formed due to high temperature and high thermal stress induced by small proton beam size (Dai, 2004). No other evident damages were observed in other TS tubes. The LBE on the LiSoR-2 TS tube was leaking out from the crack. On the surfaces of the TS specimens one can see some remaining LBE. On the TS specimens of LiSoR-2 and -5 a significant amount of adherent LBE is visible, which could be attributed to either higher temperature (LiSoR-2) or longer exposure time (LiSoR-5) as compared to LiSoR-3 and -4. The irradiation areas in LiSoR-2 and -5 specimens are quite easy to recognise, while those of LiSoR-3 and -4 are more difficult to discern. There are some deposits on the surfaces of LiSoR-2 and -5 specimens below the irradiation areas. The irradiation area on the TS tube of LiSoR-6 is not so clear, but it can clearly be seen on the TS specimen of LiSoR-6, particularly on the bare (non-coated) surface. On both coated and bare surfaces of the TS specimen there was only little LBE.

Figure 8.2.4: Upper photos show the TS tubes of LiSoR-2 to -6 after irradiation; lower photos show the TS specimens of LiSoR-2 to -6 after irradiation

The arrows indicate the irradiation areas; the LBE flow direction is always upwards

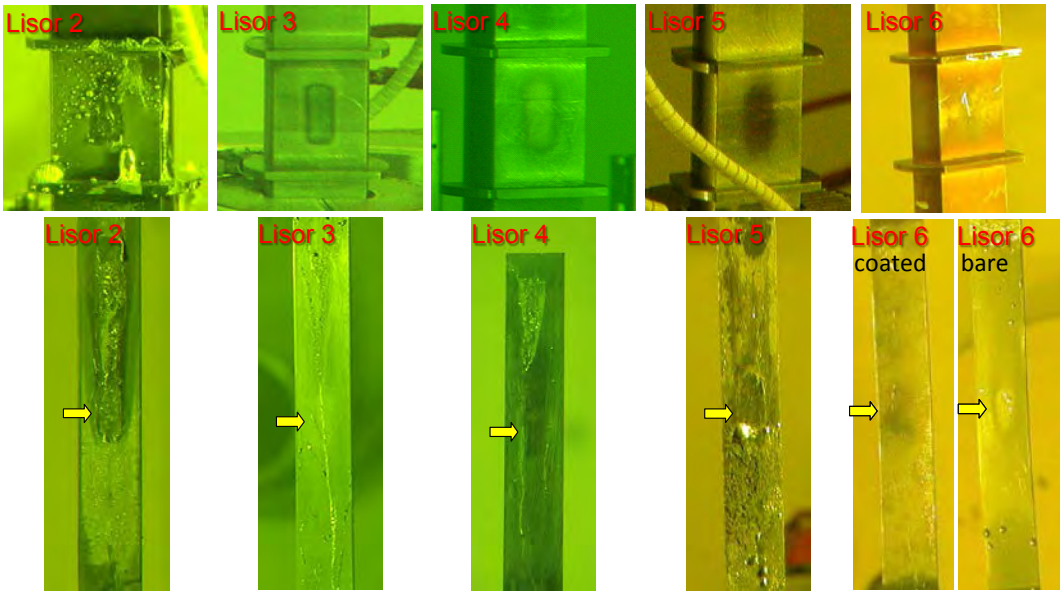

After visual inspection, the TS tubes and TS specimens were cut with an EDM machine into small dog-bone shaped tensile samples for tensile testing or small straight bars for bend testing. The remaining pieces between the tensile samples were saved for TEM, SEM, etc., analyses. In some cases, gamma-mapping was performed on the irradiation area to determine the distribution of the proton fluence (Dai, 2012).

SEM (for low activity samples) or EPMA (for high activity samples) analyses were carried out to inspect the surface irradiated in contact with LBE. As of this date samples from LiSoR-2, -3, -5 and -6 have been analysed (Dai, 2004, 2012; Glasbrenner, 2005a, 2005b, 2006).

The general feature is the formation of an oxide scale of up to a few microns thickness on the surface in the irradiated areas, as illustrated in Figure 8.2.5. One can see that the oxide layer of LiSoR-2 is the thickest while that of LiSoR-3 is thinnest. From the irradiation conditions given in Table 8.2.1 one can conclude that the variation of the thickness of the oxide scale depends mainly on the irradiation temperature, but that the irradiation time may play a role as well. The difference between LiSoR-2 and the others suggests that the temperature effect is much more pronounced than the time effect. Further, the oxygen content in LBE was neither controlled nor measured. It should be slightly different for the five tests.

The inner surface of the LiSoR-2 TS tubes was not polished after EDM wire cutting and before irradiation. After the leakage incident of LiSoR-2, the TS tubes for the following LiSoR irradiations were polished on the inner surfaces to remove the microcracked layer. The three micrographs in Figure 8.2.6 show the inner surface of the LiSoR-2 TS tube and the cross-sections of the LiSoR-2 and LiSoR-3 TS tubes, respectively. It can be seen that the surface after EDM cutting is very rough (micrograph a) and cracks of a depth of about 10 μm were introduced in the surface layer (micrograph b). Mechanical polishing removed the damaged layer with micro-cracks of the inner surface layers of the LiSoR-3 to -5 TS tubes (micrograph c).

Figure 8.2.5: SEM (a and b) and EPMA (c) micrographs showing the cross-sections in the irradiation areas of (a) LiSoR-2, (b) LiSoR-3 and (c) LiSoR-5 TS specimens

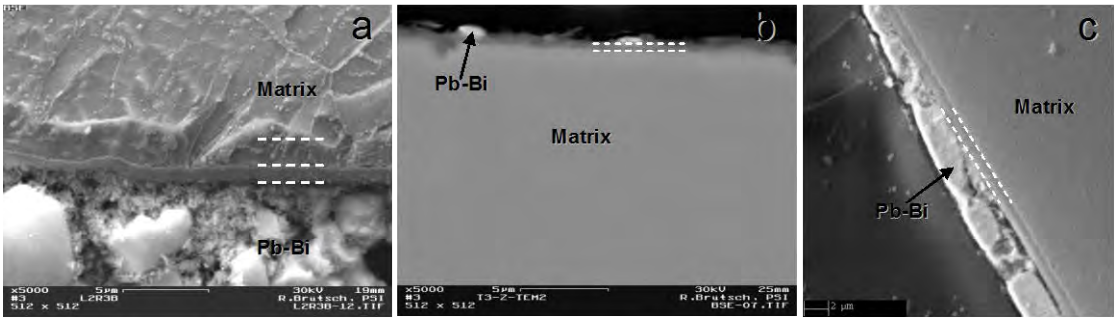

Figure 8.2.6: Graphs show (a) the inner surface of LiSoR-2 TS tube, (b) the cross-sections of LiSoR-2 TS tube and (c) the cross-sections of LiSoR-3 TS-tube

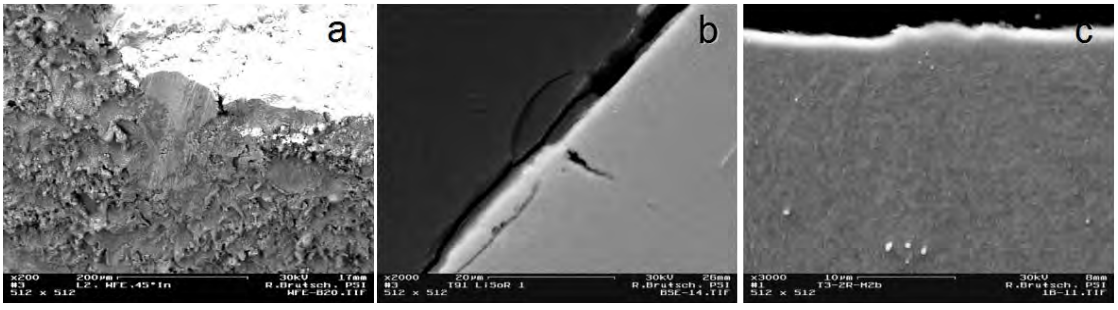

Figure 8.2.7: SEM micrographs showing the appearance of the FeCrAlY coated surface of (a) an unirradiated specimen, (b, c) after irradiation to 2.5 dpa, and (d) the cross-section of the FeCrAlY coated surface irradiated to 2.5 dpa

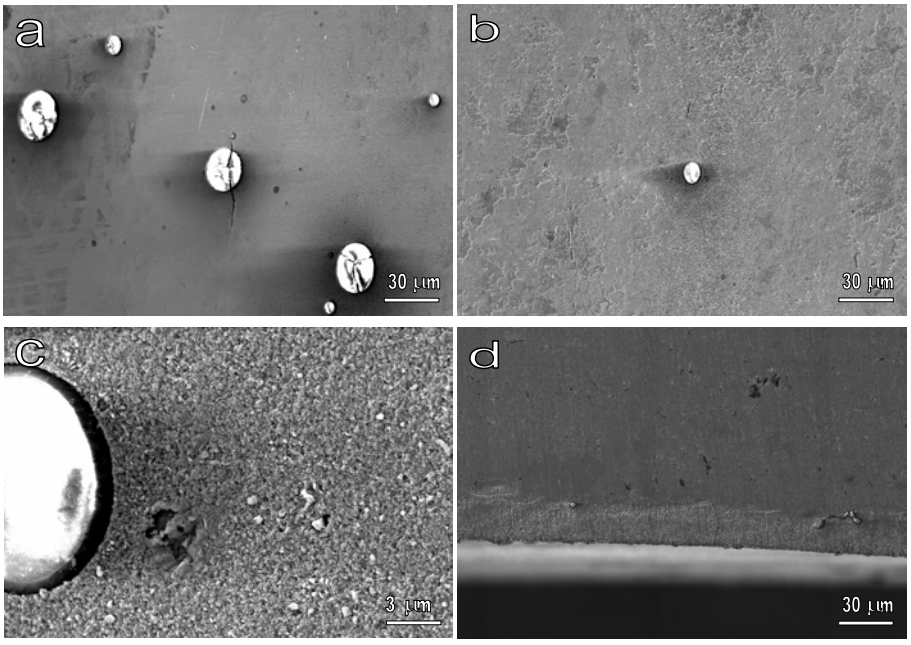

In LiSoR-6, the FeCrAlY coating on the TS specimen did not show any evidence of damage such as corrosion pits and cracks at the interface between the coating layer and the steel matrix, as shown in Figure 8.2.7 (Dai, 2012). Only a thin (<1 μm) oxide layer formed on the surface (micrographs b-d), which almost fully covered the surface in the irradiation area. Outside the irradiation area the oxide layer also existed, but thinner. The surface and the cross-section of the TiN coating before and after irradiation in contact with flowing LBE are shown in Figure 8.2.8. Compared to the unirradiated specimen (micrograph a), the coated surface became slightly smoother subsequent to irradiation (micrograph b). The view of the cross-section (micrograph d) shows the same features as such in the unirradiated case (micrograph c). The irradiated coating looks thinner than the unirradiated, but it is not clear whether both specimens are of the same initial thickness. In Figures 8.2.7(a) and 8.2.8(a) micro-cracks can be seen on the coated surface before irradiation.

The LBE on the surfaces of the TS specimens was analysed. Figure 8.2.9 shows an example of LiSoR-5. The region observed is below the irradiation area where a lot of precipitation adhered on the surface. The element analysis indicates Pb and Bi mostly separated due to re-crystallisation.

Figure 8.2.8: SEM micrographs showing the appearance of the TiN coated surface of (a) an unirradiated specimen (b) after irradiation to 1.8 dpa, and (c and d) the cross-section view of the TiN coated surfaces corresponding to (a) and (b)

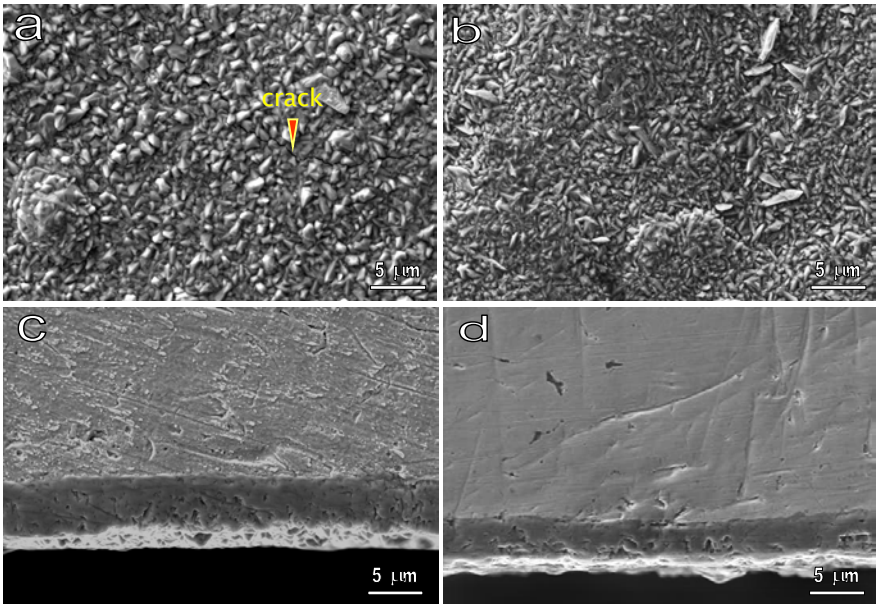

Figure 8.2.9: Wave dispersive spectrometer (WDS) analysis of LBE on the surface of the TS specimen of LiSoR-5

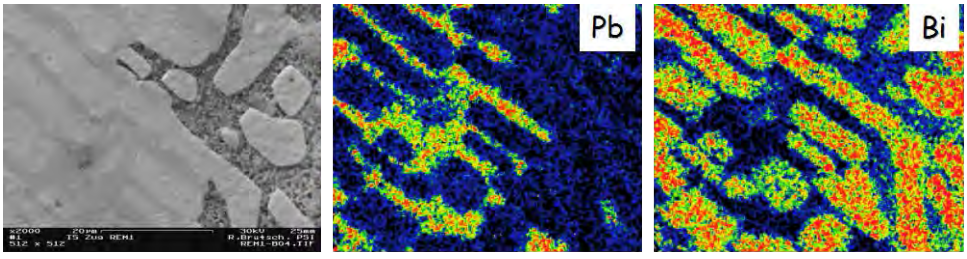

An important point to note is that, except for the LiSoR-2 TS tube, no other micro-cracks were observed either in the TS specimens or in the TS tubes, even in the LiSoR-2 TS specimen where the material of the irradiation area experienced about 120 000 cycles of fatigue deformation at a relatively high stress and temperature (Glasbrenner, 2005a).

8.2.3 *Tensile tests*

As mentioned above, one of the main purposes of LiSoR experiments is to investigate the LBE embrittlement effect on T91 steel under irradiation. All the inner TS specimens from LiSoR-2 to -5 were not broken during irradiation, although a mechanical loading of 200 MPa was always applied. This is at least a good indication that shows the material can withstand such a mechanical load while being irradiated to a radiation damage level of about 2.5 dpa. To analyse the actual degradation of mechanical properties induced by LBE and irradiation, tensile tests were performed. The samples were divided into two groups. The first group included a part of the samples from LiSoR-2 TS specimens and all samples from the TS tubes and TS specimens of LiSoR-3 and LiSoR-5. They were tested in Ar (+2%H_2) atmosphere. The results of these tests should represent the original status of the T91 steel after irradiation in LiSoR. The second group included the rest of LiSoR-2 samples and the samples from LiSoR-4 which has almost the same irradiation dose as LiSoR-3. These samples were tested in LBE. These tests were intended to show additional effects from the testing environment in LBE. All the tests were performed at 300°C. The oxygen content in the LBE was less than 1 wppm (Dai, 2006c).

Figure 8.2.10 presents the tensile results of some LiSoR-3 and LiSoR-5 samples tested in Ar. The samples from the irradiation area of the TS specimens demonstrate slight hardening induced by irradiation as expected (a and c). However, the hardening in the samples from the irradiation area of the TS tubes is much less (b and d). This is due to the fact that the temperature in the irradiation area of the TS tubes was higher ≥350°C, where

Figure 8.2.10: Tensile results of some LiSoR-3 and LiSoR-5 samples performed in Ar

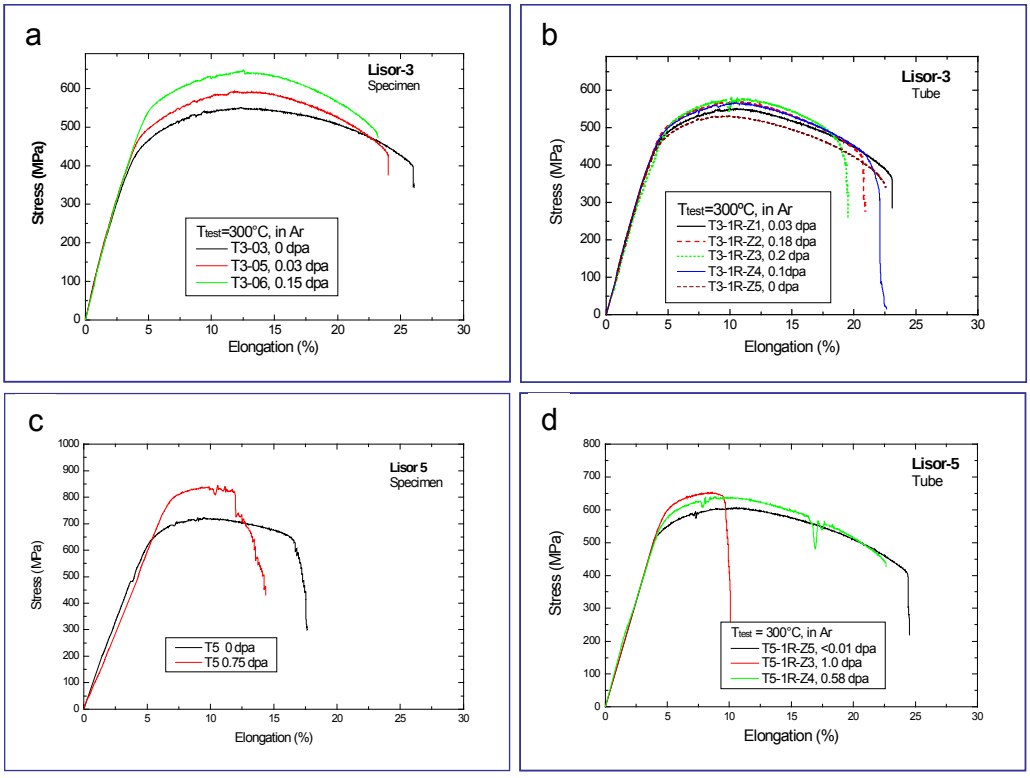

irradiation hardening effects in martensitic steels are not significant. The ductility is only slightly reduced in samples of LiSoR-3, and more strongly in LiSoR-5. It is clear that the strong reduction of the ductility in LiSoR-5 samples is mostly due to the embrittlement of LBE. As can be seen in Figure 8.2.4, some LBE adhered on the surface of the TS specimen of LiSoR-5. During EDM cutting or testing, the LBE could enter the micro-cracks on the side surfaces of the samples, which were produced by EDM cutting, and finally induced the embrittlement effect. For LiSoR-3 samples, as very little LBE adhered on the TS specimen and TS tube surfaces, the effect was not pronounced. On the other hand, the irradiation should have a synergetic effect. One can see that the embrittlement is more serious at higher doses in each individual case (a to d). Unfortunately, the present results are compromised by the effect the micro-cracks on the side surfaces, and therefore do not separate the original irradiation and LBE embrittlement effect.

Figure 8.2.11 shows the results of tensile tests performed in LBE of some samples from the TS specimens of LiSoR-2 and LiSoR-4 tested in oxygen-saturated LBE. For comparison, the result of one LiSoR-2 sample tested in Ar is also included. The embrittlement effect of LBE is clearly demonstrated by the significant reduction of ductility. For the irradiation effect, the results also indicate a trend that the embrittlement effect is more evident at higher doses.

Figure 8.2.11: Tensile results of the some samples from the TS specimens of LiSoR-2 and -4 tested at 300°C in oxygen-saturated LBE

The numbers indicate the irradiation doses

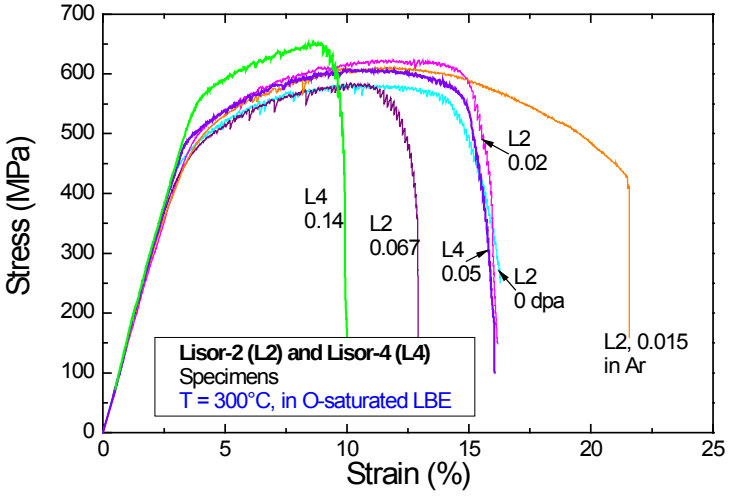

8.2.4 *Bend tests on LiSoR-6 samples*

The behaviour of the coatings under deformation and after irradiation was studied by performing a series of SEM observations in the course of bending the samples to various surface strain values between 0.7% to 9% for most of the tested samples and up to 16% for an unirradiated sample with the FeCrAlY coating (Dai, 2012).

8.2.4.1 The FeCrAlY coating

The behaviours of the unirradiated FeCrAlY coating at various deformation levels between 1.2% and 16% are presented in Figure 8.2.12. At 1.2% surface strain only very few fine cracks were observed. The original micro-cracks on the surface (Figure 8.2.7[a]) were not affected. After strain increased to 7%, the original cracks opened and new cracks formed. New cracks preferentially formed at the Al-Y-O particles on the surface, probably due to the brittleness of such particles. At a high strain level of 16%, many more cracks

were observed. It is interesting to note that many cracks were widely opened but did not propagate much (Figure 8.2.12[c]). Dense slip bands appeared on the surface and in cross-section, as shown in Figures 8.2.12(c) and (d).

Figure 8.2.12: SEM observation on the unirradiated FeCrAlY coating at 1.2%, 7% and 16% surface strain levels (a-c) plan view, (d) side view

The scale is the same for all graphs

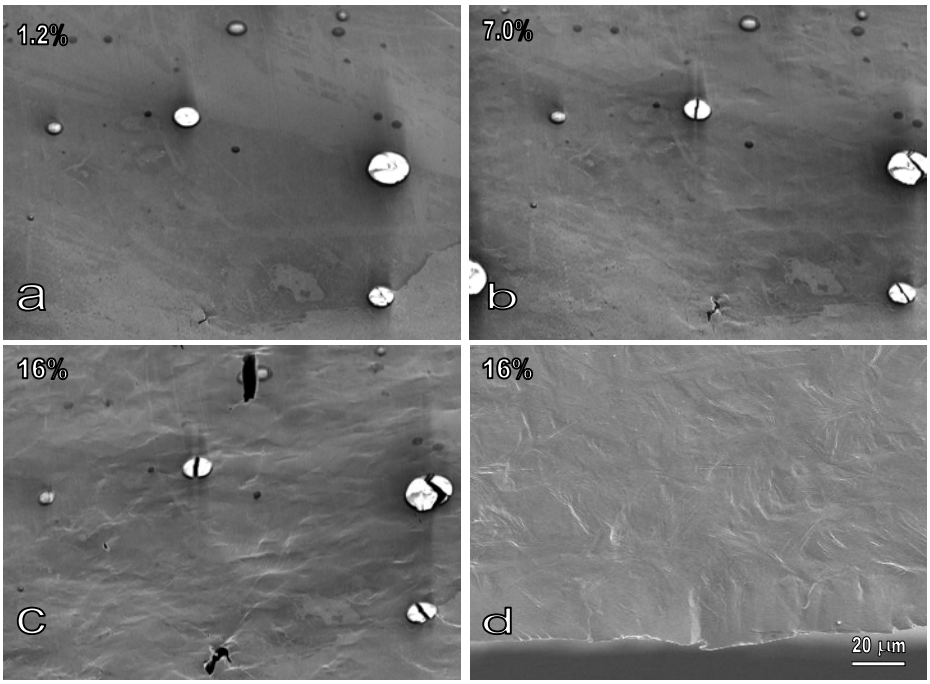

Figures 8.2.13 and 14 present the results of the FeCrAlY coating irradiated to 0.48 dpa and 2.5 dpa, respectively. In both samples, fine cracks were observed at low strain ~0.7%, as shown in Figures 8.2.13(a) and 8.2.14(a). After increasing strain to ~2.7%, many cracks of a few microns in width and hundreds of microns in length were formed. Some of them looked to be along grain boundaries. As strain was further increased strain to about 9%, the crack width and number density increased, though the crack length did not increase much. This can be seen by comparing Figure 8.2.13(b) with 13(c) or Figure 8.2.14(b) with 14(c). In Figures 8.2.13 and 8.2.14 one can also see that cracks in the sample with a dose of 0.48 dpa is denser than that in the sample of 2.5 dpa. On the other hand, the width of the cracks is slightly smaller in the 0.48 dpa sample. This is reasonable, because the higher dose sample should be more brittle than the lower dose sample. In brittle materials, high stress concentration induces larger but fewer cracks as compared to ductile materials.

It is interesting to note that, at least on the cross-sections of the samples, the propagation cracks mostly stopped at the interface of the coating and the matrix. This observation indicates that the interface is a strong barrier for the crack propagation from the coating layer to the matrix.

The behaviours of the TiN coating are shown in Figure 8.2.15 for the unirradiated case and in Figure 8.2.16 for a sample irradiated to 1.8 dpa. In the unirradiated case, nearly no cracks could be observed at a strain of 0.58% (Figure 8.2.15[a]). Many fine but long cracks were formed after strained to 4% (Figure 8.2.15[b]). As was observed for the FeCrAlY coating, the crack length did not increase with increasing strain to 8.8%, but the width of the cracks became larger, as shown in Figure 8.2.15(c). The features shown in Figure 8.2.15 clearly demonstrate that the TiN coating is rather brittle even in the unirradiated condition.

Figure 8.2.13: SEM observation on the FeCrAlY coating irradiated to 0.48 dpa at 0.72%, 2.7% and 8.7% surface strain levels (a-c) plan view, (d) side view

The scale is the same for all graphs

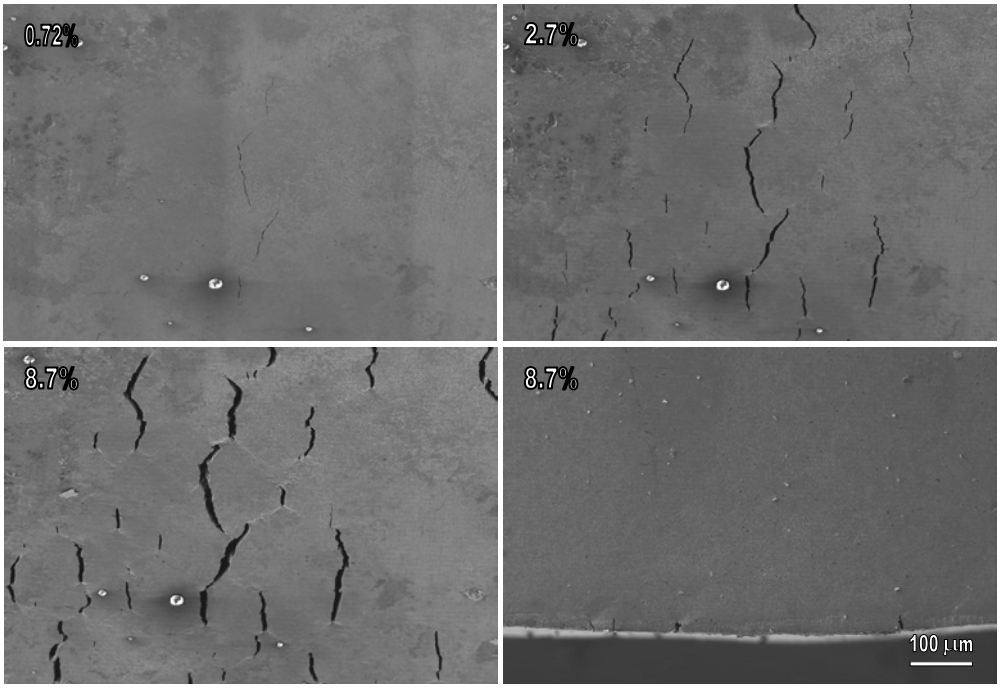

Figure 8.2.14: SEM observation on the FeCrAlY coating irradiated to 2.5 dpa at 0.66%, 2.8% and 8.8% surface strain levels (a-c) plan view, (d) side view

The scale is the same for all graphs

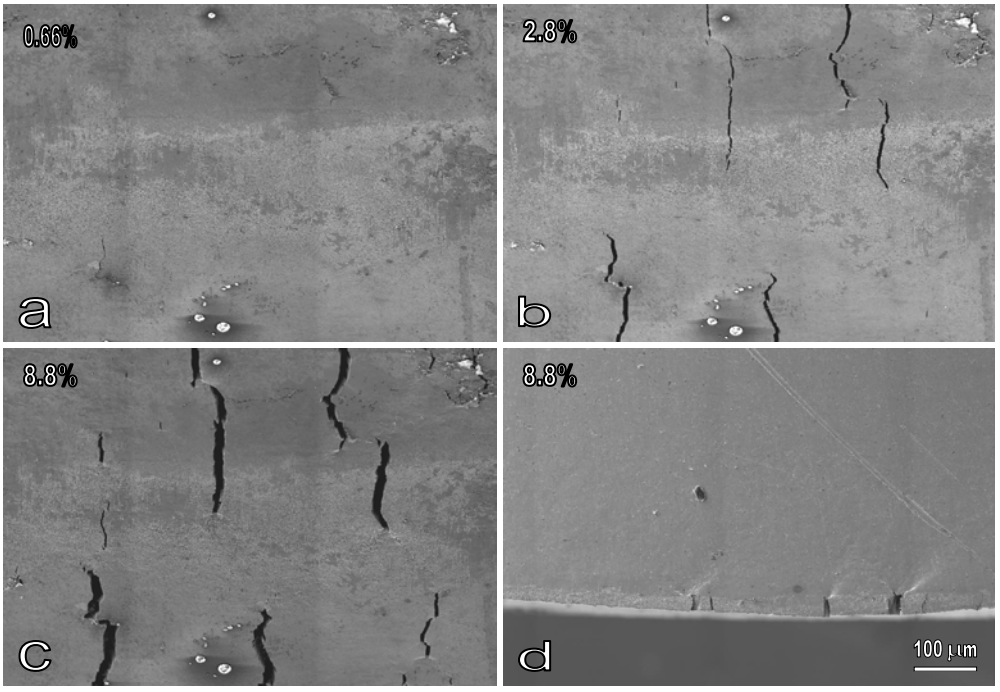

Figure 8.2.15: SEM observation on the unirradiated TiN coating at 0.58%, 3.4% and 8.8% surface strain levels (a-c) plan view, (d) side view

The scale is the same for all graphs

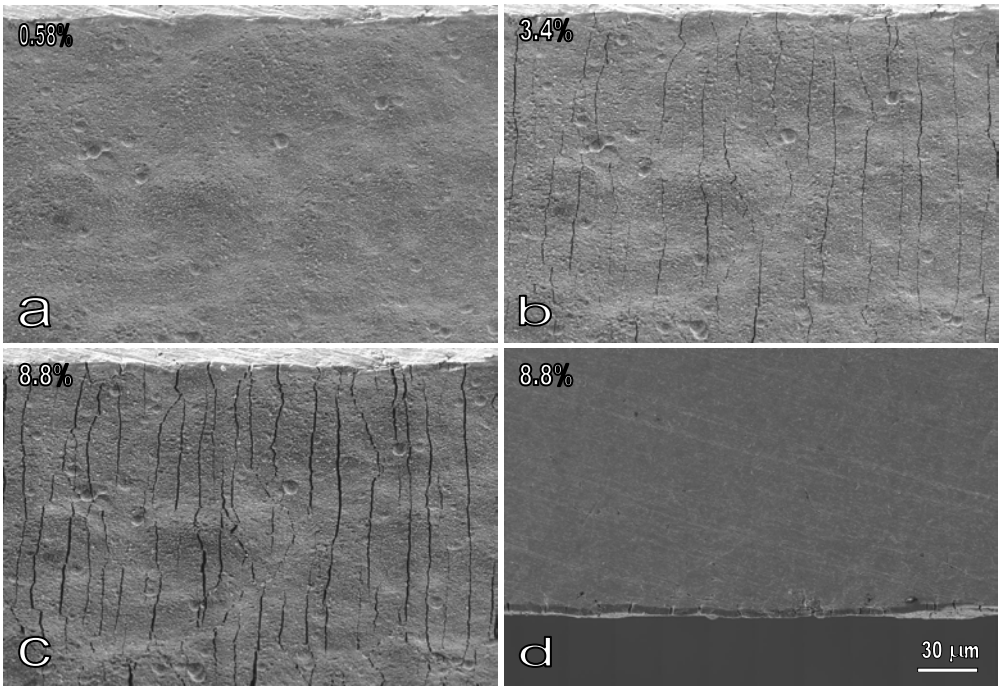

Figure 8.2.16: SEM observation on the TiN coating irradiated to 1.8 dpa at 0.71%, 4.0% and 9.1% surface strain levels (a-c) plan view, (d) side view

The scale is the same for all graphs

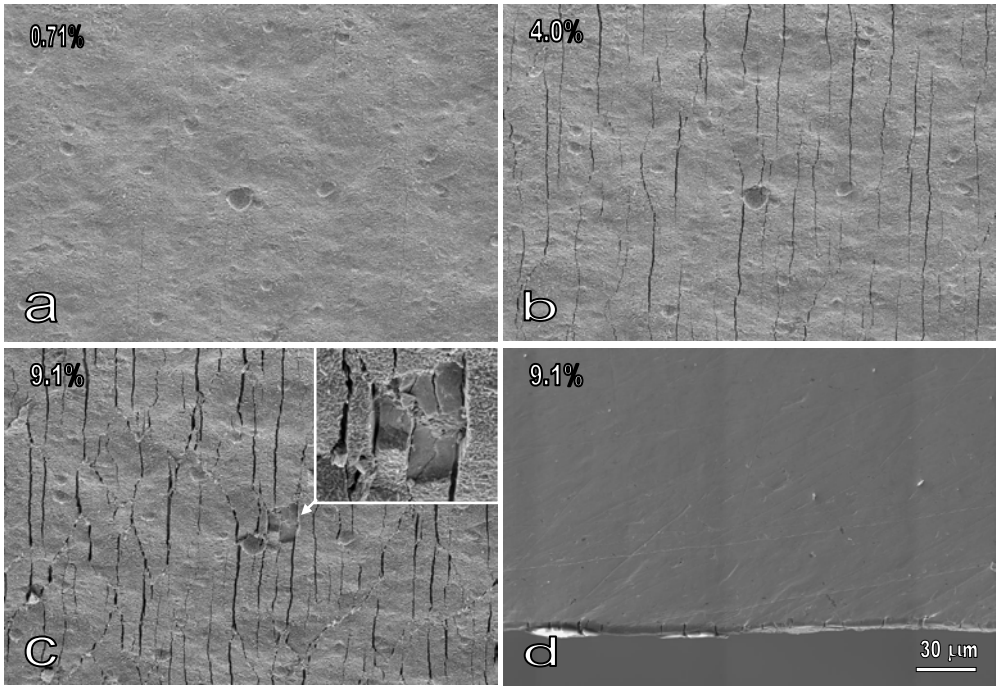

After irradiation to 1.8 dpa, the TiN became more brittle. Compared to the unirradiated TiN coating, cracks were clearly observed at low deformation of about 0.7% (Figure 8.2.16[a]), and the coating started to delaminate at high deformation of about 9% (Figure 8.2.16[c]). However, the delaminating phenomenon was not detected in the case with a surface strain of 4% (Figure 8.2.16[b]).

The results of this study clearly demonstrate that both the FeCrAlY and TiN coatings manifest good resistance to LBE corrosion under intensive irradiation. In the unirradiated condition, the FrCrAlY coating is more ductile than that of TiN. In principle the FrCrAlY is better than the TiN coating for this application. However, attention should be paid to irradiations at temperatures below about 400°C where embrittlement can be induced by irradiation. The FeCrAlY becomes brittle at relatively low irradiation doses, which may result in large cracks after deformation. The formation of large cracks may greatly increase the susceptibility T91 base material to LBE-induced embrittlement effect (Dai, 2006d).

8.3 Irradiation with fission neutrons

To investigate the combined effect of neutron irradiation and exposure to liquid lead-bismuth eutectic environment on the mechanical properties and corrosion resistance of steels selected as candidate materials for structural components and fuel assemblies of the future experimental accelerator-driven system MYRRHA, irradiation experiments, including ASTIR and LEXUR-II-LBE, have been conducted in fission reactors BR2 (SCK•CEN, Belgium) (Gavrilov, 2013a) and BOR-60 (Russia) (Gavrilov, 2013b), respectively. In addition, copies of the irradiation capsules were heat-treated for the same time as the irradiation lasted. The latter was done to distinguish between the effects of exposure to LBE and the combined effect of exposure and neutron irradiation.

The samples were irradiated in the BR-2 reactor at Mol and experimental details and the results of these experiments are taken from Sapundjiev (2005). The irradiation was performed at the Multipurpose Irradiation System for Testing of Reactor Alloys (MISTRAL) in-pile sections (MIPS).

8.3.1 Material and irradiation conditions

The materials tested were austenitic steel AISI 316L, 15-15Ti and ferritic-martensitic steels T91, HT9 and EM10. The materials' chemical compositions are given in Table 8.3.1.

Table 8.3.1: Chemical composition (wt.%) of AISI 316L, T91, EM10, and HT9 materials tested in liquid Pb-Bi eutectic

Material	Cr	Ni	Mo	Mn	V	Nb	S	Si	N	C	P	W
AISI 316L (I)	16	10.1	2.1	1.58	–	–	0.016	0.51	–	0.022	0.029	–
AISI 316L (II)	16.8	10.2	2.1	1.8	–	–	0.003	0.6	–	0.02	0.026	–
15-15Ti [1] (for pres. tubes)	14.9	15.1	1.4	1.6	–	–	0.002	0.8	–	0.08	0.04	–
15-15Ti [2] (for others)	15.5	12.8	1.2	1.6	–	–	0.007	0.6	–	0.09	0.044	–
T91 (I)	8.3	0.13	0.95	0.4	0.2	0.08	–	0.4	0.02	0.11	–	<0.01
T91 (II)	8.9	0.1	0.9	0.4	0.2	0.08	0.0007	0.235	0.048	0.1	0.019	–
EM10	8.97	0.07	1.06	0.49	0.013	<0.002	<0.003	0.46	0.014	0.099	0.013	0.01
HT9	11.68	0.66	1.06	0.63	0.29	0.03	<0.003	0.45		0.204	0.020	0.47

1. With 0.4Ti.

2. With 0.5Ti.

The materials were received in the following conditions:

- AISI 316L(I): Two heats of this material have been used for specimen fabrication. The first heat irradiated in was supplied by SIDERO STAAL, Belgium, n.v., heat number 744060 in the shape of bars 6 mm in diameter and 500 mm in length, from which the specimens were manufactured. The material is solution annealed with some cold work.
- AISI 316L (II): In accordance with ASTM A240-Ed02, the austenitic stainless steel 316L (S31603) was delivered as a hot-rolled and heat-treated plate with a thickness of 15 mm by Industeel (ArcelorMittal group).
- 15-15Ti (for pressurised tubes): Delivered as tubes with 23-24% CW and external/ internal diameters 6.55/5.65 mm.
- 15-15Ti (others): Experimental heats provided by KIT.
- T91 (I): Supplied by Ugine, France, heat 36224 normalised at 1 040°C for 60 min. and tempered at 760°C for 60 min.
- T91 (II): This ferritic-martensitic steel was delivered by Industeel (ArcelorMittal group) in the form of a 15-mm thick hot-rolled and heat-treated plate. This plate was normalised at 1 323 K for 15 minutes followed by a water quench to room temperature. The normalised plate was then tempered by heating to 1 043 K for 45 minutes followed by air cooling to room temperature.
- EM10: Supplied by CEA France, normalised at 990°C for 50 min., tempered at 750°C for 60 min.
- HT9: Normalised at 1 050°C for 30 min., tempered at 700°C for 2 h.

Two types of sub-size tensile samples were used. Most tests were done with specimens of 12 mm gage length and 2.4 mm diameter, though in the LEXUR II experiment the tensile specimens irradiated had a 15 mm gage length and 3 mm diameter. Other specimens irradiated in LEXUR II include: corrosion samples of 5 mm diameter and 2 mm in thickness, DCT samples of 13.5 mm diameter and 5 mm in thickness, and pressurised tubes of 40 mm length and with 6.56/5.65 mm outer and inner diameter, as shown in Figure 8.3.1.

Figure 8.3.1: Types and geometries of specimens irradiated in the LEXUR II programme

a) Corrosion sample, b) tensile sample type I (RIAR design), c) DCT sample, d) tensile sample type II (SCK design) and e) pressurised tube

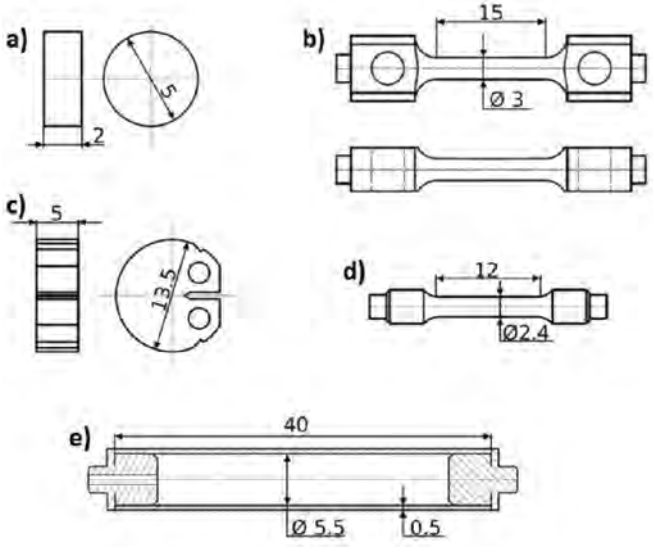

A summary of irradiation experiments described in this section is given in Table 8.3.2.

The PIEs in the framework of the ASTIR and LEXUR II programmes are ongoing and the results described in this section are thus not fully complete.

Table 8.3.2: Irradiation doses and specimen designations of AISI 316L, T91, EM10 and HT9

Irradiation programme	Reactor	Material	Specimen	Dose (dpa)	Temp. (°C)	Environment	Reference
MISTRAL	BR2	316L	Tensile (I)	1.46-1.72	200°C	PWR water	Sapundjiev (2004)
MISTRAL		EM10	Tensile (I)	2.93-4.36	200°C	PWR water	Sapundjiev (2004)
MISTRAL		HT9	Tensile (I)	2.53-4.36	200°C	PWR water	Sapundjiev (2004)
MISTRAL		T91	Tensile (I)	1.14-4.36	200°C	PWR water	Sapundjiev (2004)
ASTIR		316L, T91	Tensile (I) + corrosion	2.59	460-490	LBE	Gavrilov (2013)
ASTIR		316L, T91	DCT	2.59	350-70	LBE	Gavrilov (2013)
ASTIR		316L, T91	DCT, tensile (I)	2.59	300-320	PWR water	Gavrilov (2013)
LEXUR-II	BOR60	T91	Tensile (I&II), DCT, corrosion	6÷8.5 28÷29	350±20	LBE	Gavrilov (2013)
LBE		316L	Tensile (I&II), DCT, corrosion	6÷8.5 28÷29	350±20	LBE	Gavrilov (2013)
		15-15Ti	Tensile (I&II), DCT, corrosion	6÷8.5 28÷29	350±20	LBE	Gavrilov (2013)
		15-15Ti	Press. tubes	9.1 34.5	350±20	LBE	Gavrilov (2013)

8.3.2 Testing conditions

Slow strain rate tensile (SSRT) tests of samples Type I were performed in an autoclave in conjunction with a gas conditioning system. Tests were performed at a strain rate of $0.5\text{-}50 \times 10^{-6}$ s^{-1} and irradiation temperatures in either LBE or air environment. After a sample was broken in LBE, it was removed from the autoclave and cleaned by hot oil or by chemical solutions.

SSRT tests of samples Type II were performed in small open crucibles, which can be filled with LBE and mounted in the oven of loading machine. Due to contact of LBE with air during the test oxygen concentration most probably was at the level of saturation for corresponding temperatures. The tests were performed at strain rate of 5×10^{-5} s^{-1} and at a temperature of 350°C in either LBE or air environment.

Lead-bismuth eutectic alloy (44.8% Pb, 55.2% Bi) was supplied by Hetzel Metalle GmbH, Germany, with reported purity: Pb 99.985% minimum and Bi 99.99% minimum.

It remains very challenging to maintain precise control of oxygen dissolved in LBE in mechanical testing set-ups. At earlier stages, when the first tests of irradiated specimens were performed it was equally difficult to monitor oxygen concentration at testing temperatures below 400°C. Therefore the results reported in this section were obtained

sometimes without monitoring oxygen concentration during the tests. In those cases when oxygen concentration was successfully measured during the tests it is reported in the text. To reach low oxygen conditions, the liquid metal was constantly purged with 5% H_2 in Ar gas mixture before and during the experiment.

8.3.3 *Effect of irradiation and LBE on austenitic steels 316L and 15-15Ti*

The curves from the SSRT tests of the irradiated 316L and 15-15Ti steels are plotted in Figures 8.3.2-8.3.4. In the same figures the SSRT curves of non-irradiated specimens tested under the same conditions are given for comparison.

Irradiation at 200°C resulted in significant hardening and loss of ductility in the steels. Figure 8.3.2 presents the SSRT curves of 316L samples irradiated to 1.46 and 1.72 dpa at 200°C (Sapundjiev, 2004). The uniform elongation is nearly zero. The stress-strain curves are almost the same after irradiation to 1.46 and 1.72 dpa. Irradiation hardening resulted in an increase of the yield (σ_{02}) and tensile (σ_{UTS}) strengths of about 27% and 23%. Regarding the strain to failure, the irradiation resulted in a reduction of total elongation of about 27%. Testing in LBE has essentially no influence on the total elongation of the irradiated samples.

Figure 8.3.2: Strain stress curves of 316 L (MISTRAL) tested in liquid Pb-Bi at 200°C and strain rate 5×10^{-6} s^{-1}, oxygen concentration was not monitored

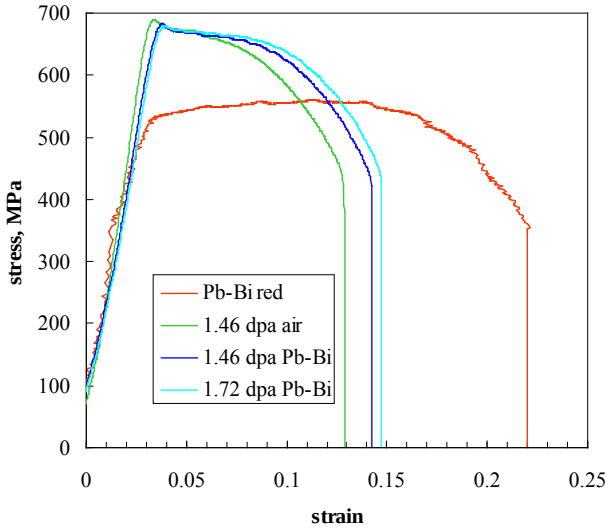

Figure 8.3.3 shows the SSRT curves of the 316L specimens irradiated to 2.59 dpa and tested either in LBE or in inert environment at two different strain rates, 5×10^{-5} s^{-1} and 5×10^{-7} s^{-1} to investigate strain rate effect on the tensile properties (Gavrilov, 2013). As one can see there is no reduction in ductility of the tests performed in LBE in comparison with the tests in inert environment. One may notice that yield strength of the specimens tested in LBE is slightly lower. But looking at all the results of tensile tests obtained from the 316L steel one can conclude that it is just scatter and not the effect of testing in LBE environment. The fractography also did not show any difference between a fractured surfaced obtained in an inert environment and in LBE.

SSRT tests were also performed on the 316L and 15-15Ti samples irradiated in BOR60 to 6.1 dpa at about 350°C. The stress-strain curves of the SSRT tests are given in Figure 8.3.4. Again no reduction of ductility for irradiated austenitic stainless steels tested in LBE was found. The fracture surfaces of the specimens tested in both air and in LBE shows a near fully dimpled fracture surface, having the well-known cup and cone shape, as shown in Figure 8.3.5.

Figure 8.3.3: The stress-strain curves of 316L irradiated to 2.59 dpa (ASTIR) and tested in either argon or LBE at 300°C with the strain rate of 5×10^{-5} s^{-1} and 5×10^{-7} s^{-1}, oxygen concentration in LBE was $10^{-8} \div 10^{-6}$ wt.%

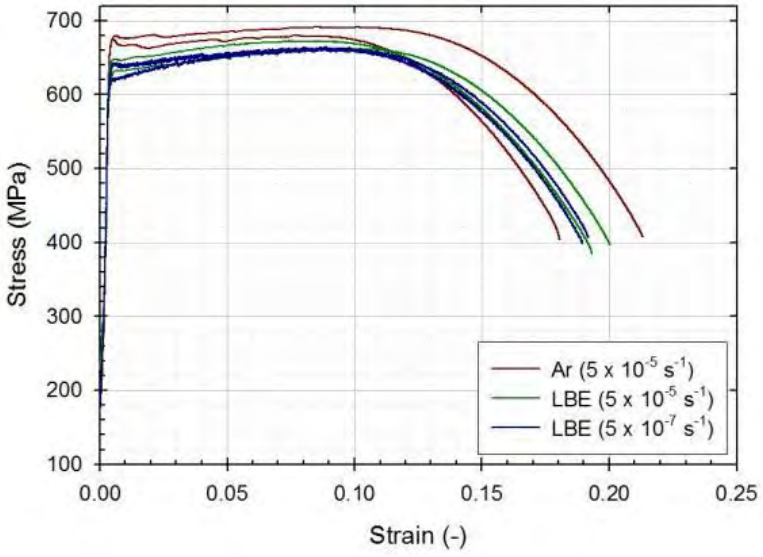

Figure 8.3.4: The stress-strain curves of 316L and 15-15Ti steels irradiated to 6.1 dpa (LEXUR II) and tested in either air or LBE at 350°C with a strain rate of 5×10^{-5} s^{-1}, oxygen concentration was not monitored

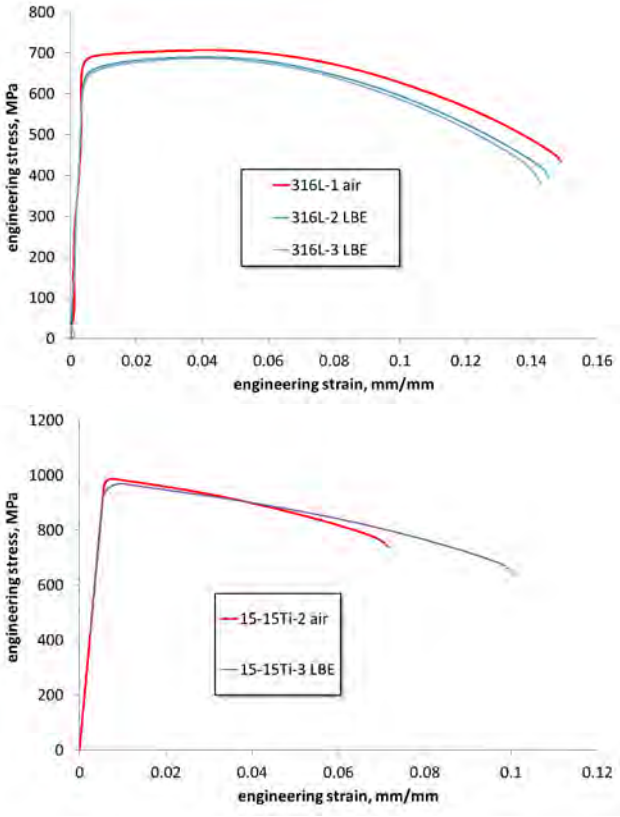

Figure 8.3.5: Fractography of 316L and 15-15Ti specimens irradiated to 6.1 dpa and tested at 350°C in either air or LBE

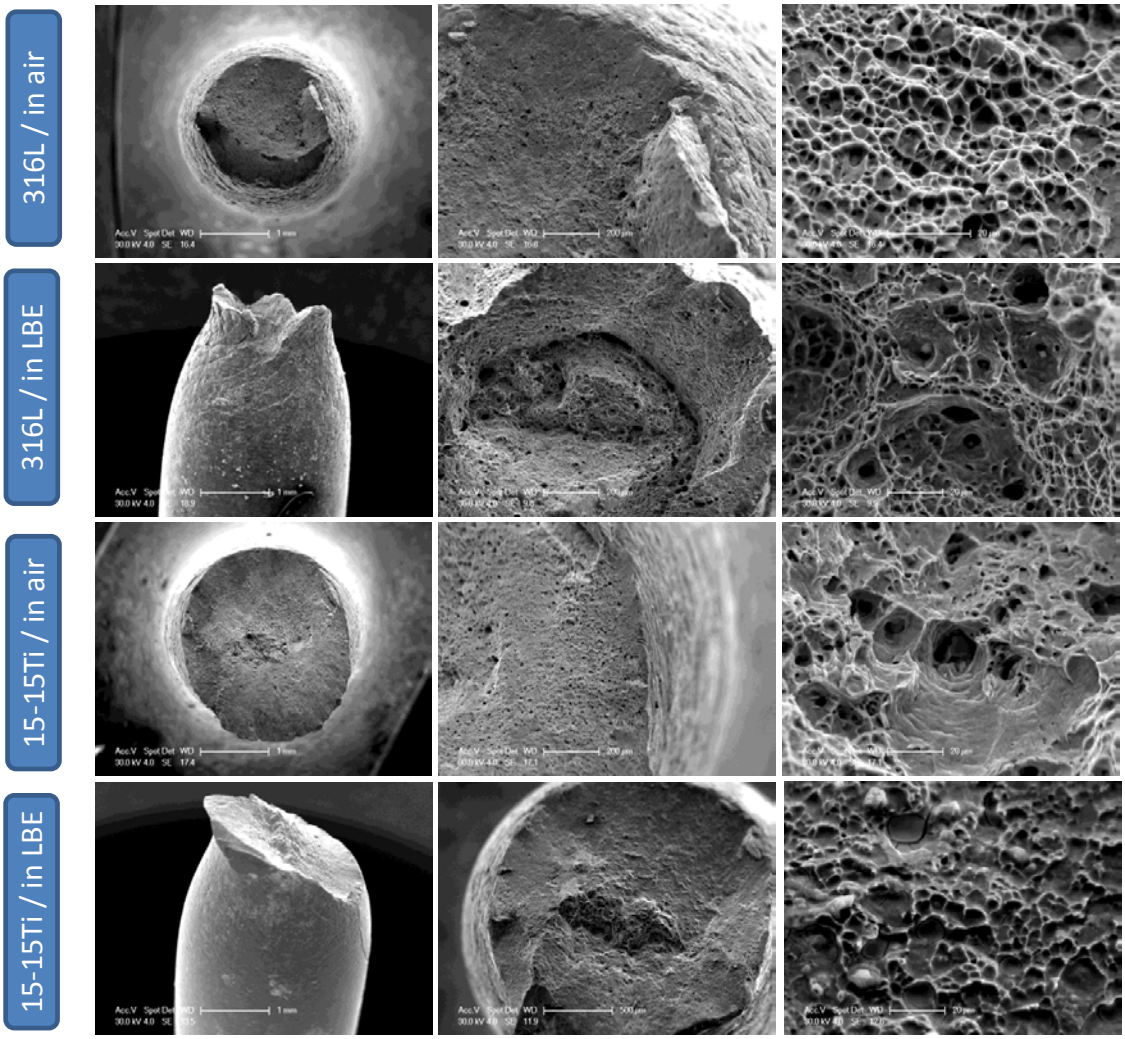

8.3.4 *Effect of irradiation and LBE on FM steels T91, EM10 and HT9*

8.3.4.1 *T91 steel*

In this section, the results of T91 irradiated in BR2 and BOR60 to different doses between 1.15 and 6.1 dpa and tested in air and in LBE are presented. The results of the non-irradiated samples are also provided for comparison.

The stress-strain curves of the irradiated T91 specimens are plotted in Figures 8.3.6 through 8.3.9. Similar to that observed from the austenitic steel specimens, the irradiated T91 specimens demonstrated significant hardening and embrittlement in the present irradiation conditions. The difference between the T91 results and the 316L/15-15Ti results is that the irradiated T91 specimens manifest additional embrittlement effect when they are tested in LBE at 300 and 350°C (Figures 8.3.8 and 8.3.9). However, it is interesting to note that the LBE effect was not detected in the testing at 200°C.

The fractography of specimens irradiated 2.59 dpa and tested at 300°C illustrated ductile fracture for the specimens tested in air and partially cleavage fracture for the specimens tested in LBE, as shown in Figure 8.3.10.

Figure 8.3.6: Strain-stress curves of T91 tested in liquid Pb-Bi at 200°C and strain rate 5 × 10^{-6} s^{-1}, oxygen concentration was not monitored

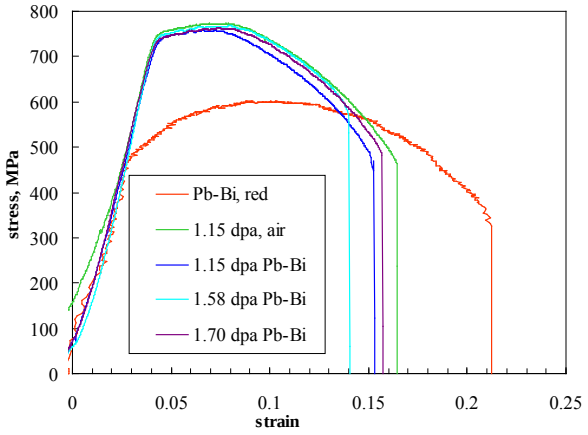

Figure 8.3.7: Tensile curves of irradiated and un-irradiated T91 material tested in liquid Pb-Bi at 200°C at strain rate 5 × 10^{-6} s^{-1} in Pb-Bi and 3 × 10^{-4} s^{-1} in air, oxygen concentration was not monitored

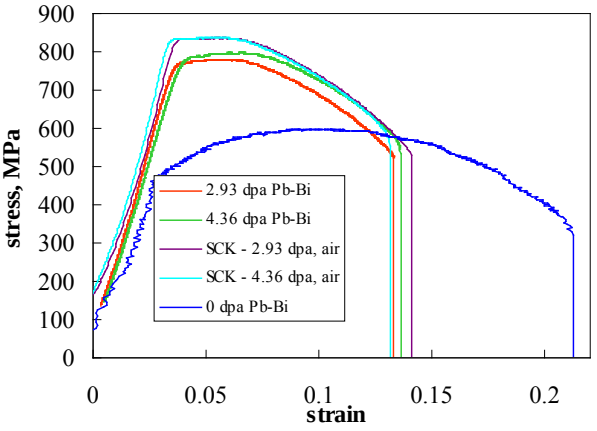

Figure 8.3.8: Tensile curves of T91 irradiated to 2.59 dpa and tested in LBE at 300°C at strain rate 5 × 10^{-5} s^{-1}, oxygen concentration in LBE was 10^{-8}÷10^{-6} wt.%

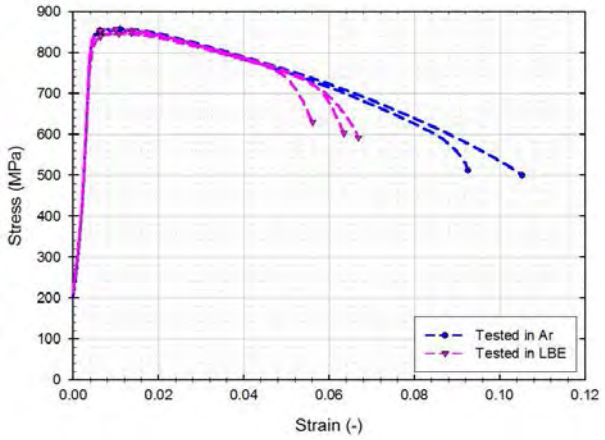

Figure 8.3.9: Tensile curves of T91 irradiated to 6.1 dpa and tested in LBE at 350°C at strain rate 5 × 10^{-5} s^{-1}, oxygen concentration was not monitored

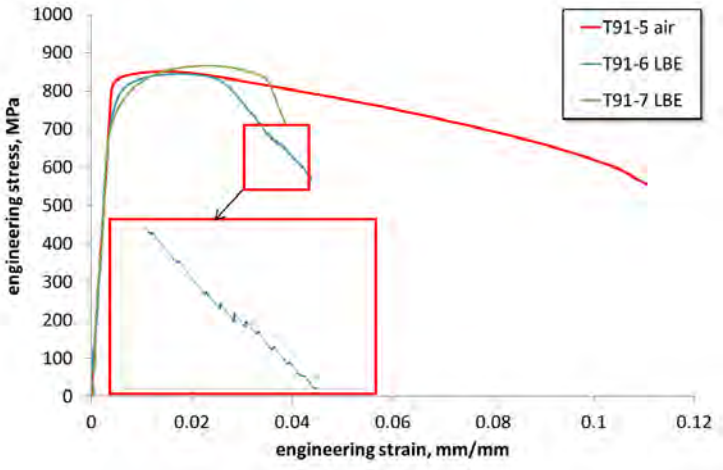

Figure 8.3.10: Fractography of T91 specimens irradiated to 2.59 dpa and tested at 300°C in either air or LBE

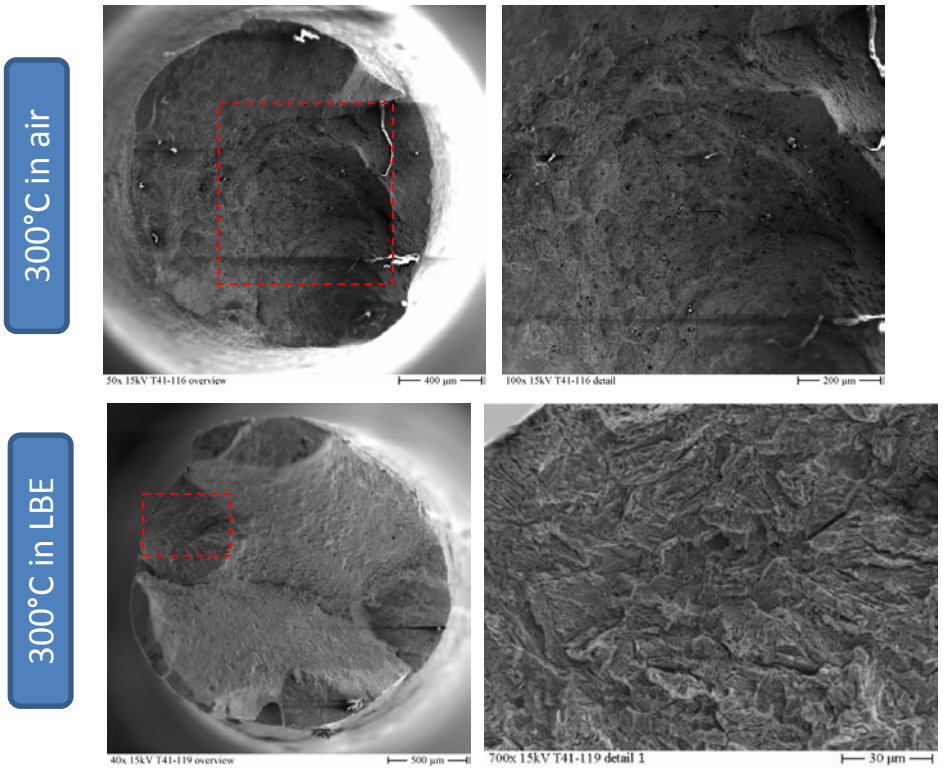

8.3.4.2 *EM10 steel*

The stress-strain curves of the EM10 specimens tested in air and in LBE eutectic after irradiation to 2.93 and 4.36 dpa are plotted in Figure 8.3.11. The material has very similar irradiation behaviour to that of T91 under the same irradiation conditions (Figure 8.3.7). Furthermore, the testing at 200°C did not show LBE embrittlement either.

Figure 8.3.11: Strain-stress curves of EM10 specimens irradiated to 2.93 and 4.36 dpa tested at 200°C and strain rate 5 × 10^{-6} s^{-1} in LBE and 3 × 10^{-4} s^{-1} in air

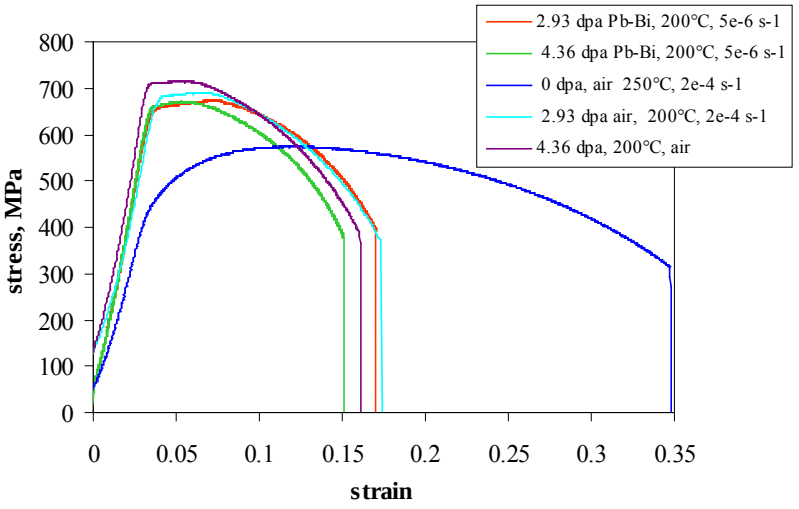

8.3.4.3 *HT9 steel*

The stress-strain curves of the HT9 specimens tested in air and in LBE after irradiation to 2.53 and 4.36 dpa are plotted in Figure 8.3.12. Compared to the T91 and EM10 steels, the HT9 steel shows slightly stronger irradiation hardening and embrittlement effect. But, HT9 specimens possess greater uniform elongation in the present irradiation and test conditions. The two specimens tested in LBE did not indicate any LBE effect as compared to those tested in air at 200°C.

Figure 8.3.12: Strain-stress curves of HT9 material tested in liquid Pb-Bi at 200°C and strain rate 5 × 10^{-6} s^{-1} in Pb-Bi and 3 × 10^{-4} s^{-1} in air

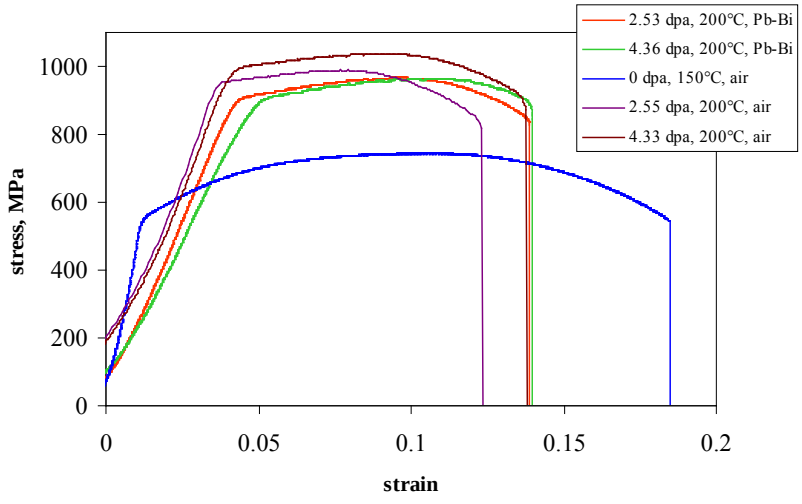

It should be noted that some samples of T91 and 316L steels and their welds irradiated in the BR2 reactor up to 2.5 dpa in contact with LBE at 460-490°C (TWIN ASTIR experiment) do not show any irradiation hardening effect. Further, no clear evidence of additional LBE embrittlement was observed when they were tested in LBE (Van den Bosch, 2008, 2010).

8.3.5 *Corrosion specimens irradiated in BOR60*

Specimens of 316L and T91 steels were irradiated in capsules filled with LBE in BOR60 to 9.1 dpa at about 350°C. The extracted corrosion specimens were embedded in resin and ground to obtain cross-sections for microstructural and microchemical examination. The specimens were examined using the techniques of both scanning electron microscopy (SEM) and electron probe microanalysis (EPMA) (Gavrilov, 2013).

Figure 8.3.13 presents SEM micrographs of the cross-section of the 316L, T91 and 15-15T specimens. No evidence of corrosion damage could be detected on these specimens. There is neither depletion of alloying elements nor penetration of LBE. A small quantity of oxygen measured on the specimen surfaces suggests the formation of a very thin oxide layer, which, however, is not so visible with SEM. From analysis of results obtained on all analysed specimens one can conclude that there is no visible corrosion damage of the surfaces except for the thin submicron scale oxide layer formed.

Figure 8.3.13: SEM micrographs of 316L, T91 and 15-15Ti specimens irradiated to 9.1 dpa at 350°C in contact with LBE

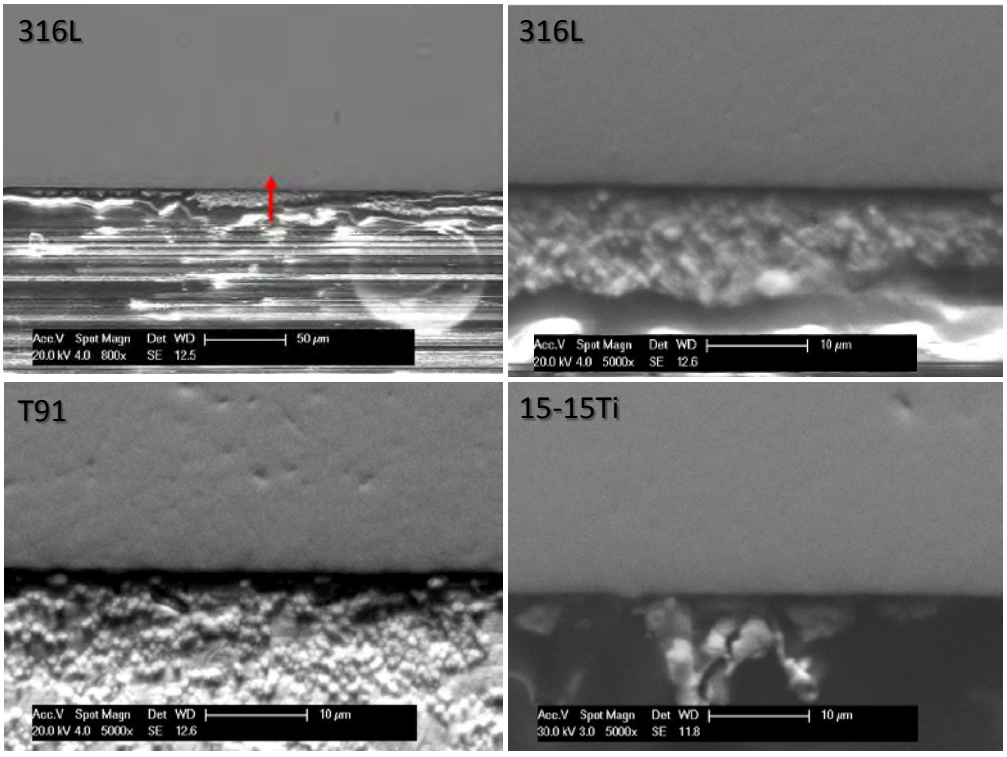

8.4 Irradiation with proton and neutron spectrum in SINQ targets at PSI

In the SINQ target irradiation programme (STIP) many samples have been irradiated in the presence of LBE and pure Pb as well. In STIP-II (Dai, 2005), which was performed in 2000 and 2001, about 150 samples of different types such as tensile, bend-fatigue, TEM and stressed capsules from more than ten kinds of ferritic/martensitic (FM) and austenitic steels were irradiated to doses up to 19 dpa in the temperature range of 100 to 400°C. Unfortunately, due the difficult PIE work and limited hot-cell availability, only two stressed capsules were investigated (Dai, 2008). On the other hand, in the R&D programme of MEGAPIE, some FM steel specimens irradiated in STIP were tested in an LBE environment to understand the LBE effect on irradiated FM steels (Long, 2009, 2012).

8.4.1 *Stressed capsules of EC316LN and 9Cr2WVTa irradiated in LBE*

8.4.1.1 Materials and specimens

Four capsules were supplied by Oak Ridge National Laboratory (ORNL, United States). They were fabricated from 9Cr2WVTa and EC316LN steels which were taken to be representative of FM and austenitic steels, respectively (Dai, 2008). The compositions of the materials are given in Table 8.4.1.

Table 8.4.1: Compositions (wt.%) of the 9Cr2WVTa and EC316LN steels

Steel	Fe	Cr	Ni	Mo	Mn	C	Si	N	W	V	Ta
9Cr2WVTa	Bal	8.71	0.02	<0.01	0.39	0.098	0.19	0.016	2.17	0.23	0.06
EC316LN	Bal	17.45	12.2	2.5	1.81	0.024	0.39	0.067			

Capsules with dimensions of 10 mm length, 3.3 mm outer diameter and 2.8 mm inner diameter were shrink-fit with Al rods exact fit to the inner volume. The end plug was sealed with electron beam (EB) welding. Four such capsules, two 9Cr2WVTa and two of EC316LN were irradiated in STIP-II along with some other specimens. All the specimens were packed in a specially designed sample holder, and then submerged into liquid LBE at about 150°C. After taking out the filled holder from the LBE bath and cooling down to room temperature, a rod with LBE, specimens and sample fixtures (of the T91 steel) was cast. This rod was then inserted into a capsule of T91 steel, sealed with laser welding in helium gas of 1 bar, and finally inserted into a SS 316L tube and sealed with EB welding. Since the LBE filling was conducted at about 150°C, the oxygen content in LBE should be relatively low. The irradiation dose at the middle position of the EC316LN capsule was 16.7 dpa and at the 9Cr2WVTa capsule was 12.2 dpa; the corresponding He concentrations were about 1 695 and 1 050 appm, respectively. The irradiation temperature was 315°C for the EC316LN capsule (middle position) and 225°C for the 9Cr2WVTa capsule (middle position). The temperature varied about ±15% around the mean value during the two-year irradiation period (Dai, 2005). The stress distribution in the walls of the capsules was rather complicated due to the inhomogeneous temperature distribution inside the capsules. The difference of thermal expansion between the Al filler and the steels stressed the walls of steel capsules mainly in the longitudinal direction, while the hoop stress was much smaller. The stress level of the EC316LN capsule was about 160 MPa. The 9Cr2WVTa capsule was stressed at about 540 MPa in the beginning of irradiation. The high stresses should be gradually relaxed by irradiation creep afterwards.

8.4.1.2 The EC316LN capsule

An overview of the capsule indicated that there was a large gap of about 50 μm in width located at the top between the Al filler and the steel wall, and a small gap of 5-10 μm at the bottom but almost no gap at the side. This suggests that the capsule underwent quite a large deformation, probably resulting from both the plastic deformation and irradiation creep. No cracks and no severe corrosion damage were observed in the wall of the capsule. Figure 8.4.1 shows the view of the cross-section of the capsule wall: (a the most evident damage observed on the surface, (b) an area with adherent LBE, and (c) a view of an area almost LBE-free. The large roughness in (a) is suspected to be produced by fabrication, while the view shown in (b) is considered as representative of the surface slightly corroded by LBE. The view in (c) indicates that some areas were not wetted by the LBE. Elemental analysis suggests that no or a very thin (<1 μm) oxide layer was on the surface.

Figure 8.4.1: Micrographs showing views of three areas of the EC316LN capsule

The largest damage observed on the surface (a), a view of an area with adherent Pb-Bi (b) and a view of an area almost free of Pb-Bi(c); the scale is the same for all three images

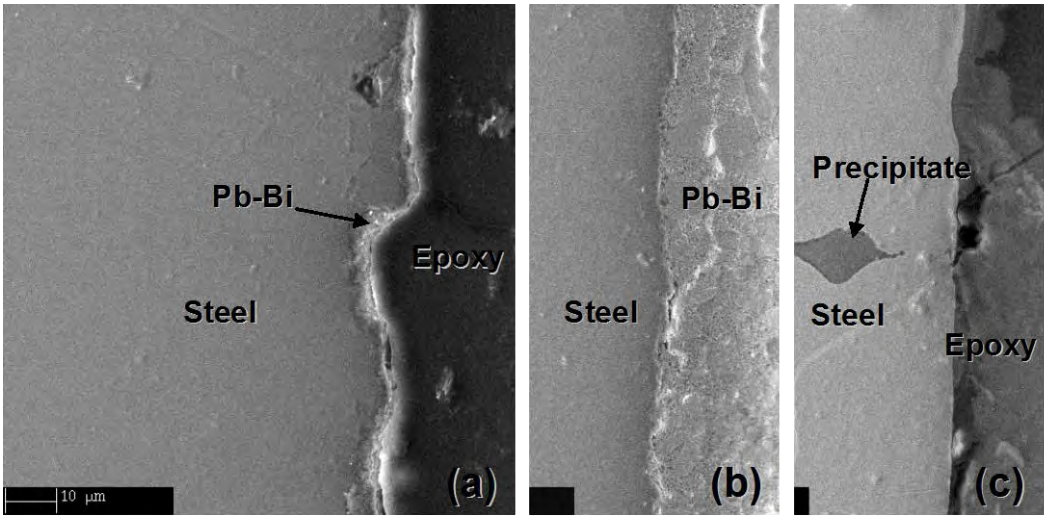

8.4.1.3 *The 9Cr2WVTa capsule*

The situation of the 9Cr2WVTa capsule is quite different from that of the EC316LN capsule. The first evidence is the observation of cracks in the EBW and its vicinity of the capsule, as shown in Figure 8.4.2. Unfortunately, no similar capsules were available for checking cracks in as-received condition. But cracks in an EBW of an FM steel are seldom observed. Therefore, it is believed that the cracks could essentially be attributed to two reasons: the high stress level and the brittleness of the material.

Figure 8.4.2: Micrograph showing cracks observed in the 9Cr2WVTa capsule in different areas of (a) the EBW and (b) and (c) the vicinity of the EBW

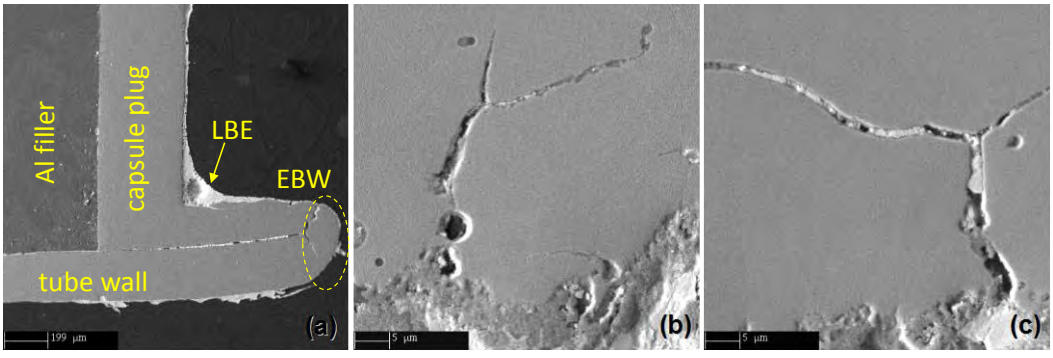

As mentioned in the previous section, the stress in this capsule was about 540 MPa at the beginning of the irradiation. Since the temperature was low, the thermal creep could be negligible. Based on published irradiation creep data of FM steels (Ando, 2007), it was estimated that it would take about three months of irradiation time to reduce the stress level from 540 MPa to about 100 MPa. During this time period, a displacement damage level of about 3 dpa was reached.

On the other hand, it is expected that after welding heat treatment was not performed on this capsule in order to avoid any deformation before irradiation induced by thermal stress. Hence, like non-tempered FM steels, in the EBW region the material was very hard and brittle. The large crack in the EBW (Figure 8.4.2[a]) could initiate and propagate from inside at the tip of the gap between the walls of the plug and the capsule tube. The micro-cracks shown in Figures 8.4.2(b) and 8.4.2(c), on the other hand, propagated from the outer surface, which could be due to the embrittlement effect of LBE. Studies on liquid metal embrittlement effects of LBE on the T91 steel demonstrated that hardened specimens presented much higher susceptibility of embrittlement when high stress and surface flaws existed in the specimens (see Chapter 7) (Long, 2008). The material in the region where the micro-cracks were observed could be hardened by welding in or very close to the heat-affected zone. Micro-cracks could be readily initiated at sites of precipitates on the surface or fabrication flaws, and their propagation would be driven by the embrittlement effect of LBE.

The observations show some evidence of corrosion even though the irradiation temperature was low. The roughness of the surface observed on the 9Cr2WVTa capsule (Figure 8.4.3[a]) indicates slightly higher corrosion rate than in the EC316LN capsule (Figure 8.4.1[b]). Element mapping images (b) to (f) indicate that a thin oxide layer formed on the surface. There were some other interesting observations, as shown in Figure 8.4.4. The micrographs in Figure 8.4.4(a) and (b) present features that are considered as a combined effect of corrosion and fabrication. The rough surface was most likely produced by fabrication. During irradiation some small pieces (e.g. the small island in Pb-Bi at the upper-left corner of Figure 8.4.4[a]) were spalled from the surface by corrosion. Figure 8.4.4(c) and (d) and also Figure 8.4.2(b) demonstrate that precipitates at the surface or in the surface layer may enhance corrosion penetration into the steel matrix.

Last, but not least, the observation showed that the surface was mostly covered by Pb-Bi, which indicates the wetting of LBE to the 9Cr2WVTa steel at quite low temperatures (195-255°C) under irradiation.

Figure 8.4.3: Micrograph and element mapping of the surface of the 9Cr2WVTa capsule

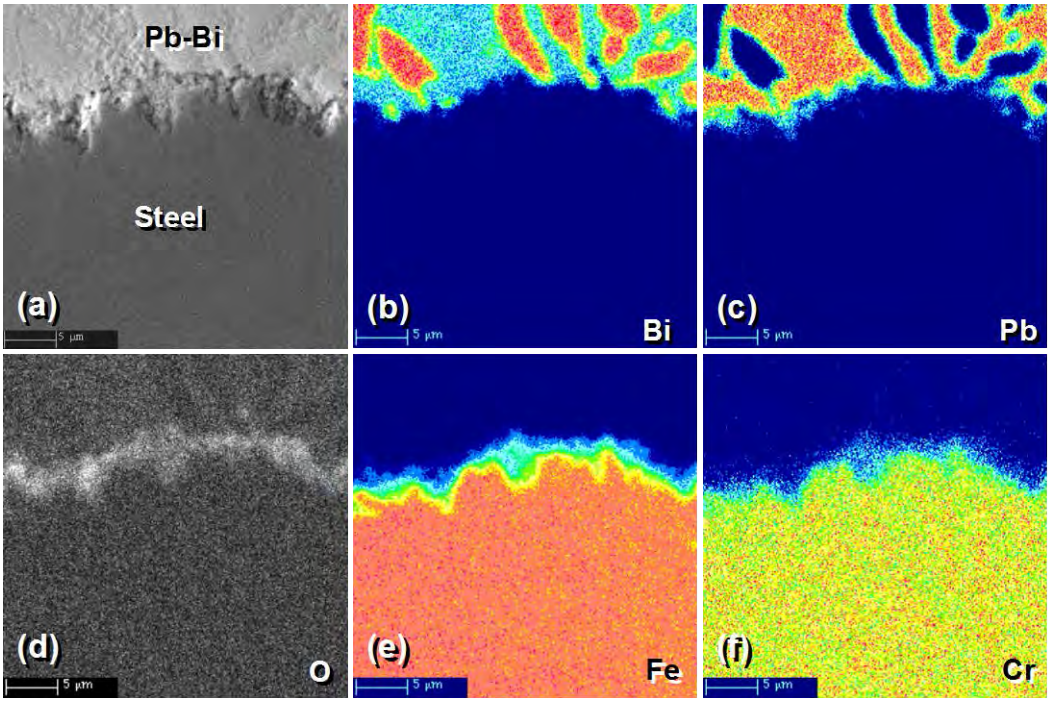

Figure 8.4.4: Micrographs showing some interesting morphology features on the 9Cr2WVTa capsule

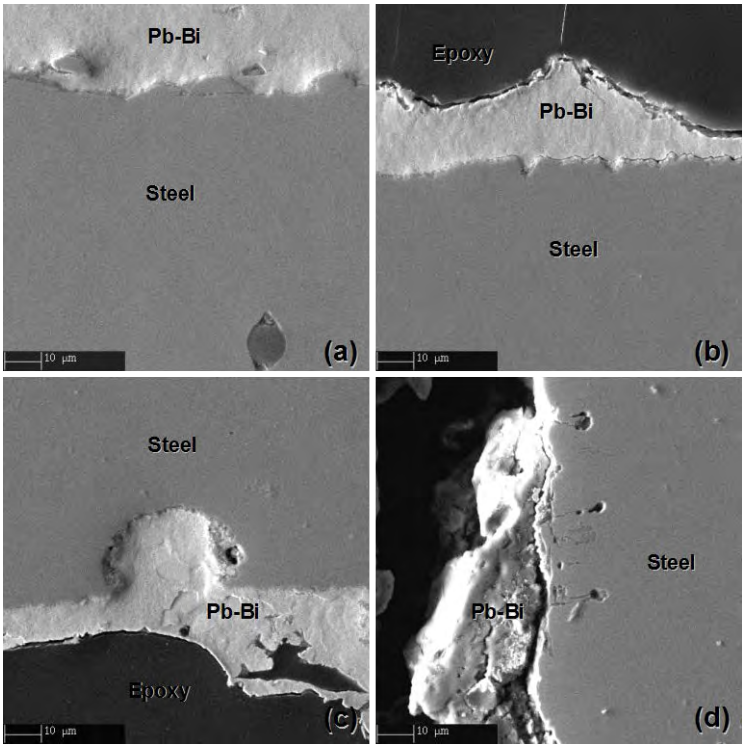

8.4.2 SSRT tests on irradiated FM steels in LBE

8.4.2.1 Materials and specimens

FM steels T91 and F82H were used. The T91 steel Heat-36224 was supplied by Ugine (France) for the EU FP5 SPIRE project. The steel was normalised at 1 040°C for 1 h, followed by air cooling, and then tempered at 760°C for 1 h, followed by air cooling. Specimens of this material were irradiated in the STIP-II and STIP-III experiments. The F82H was obtained from the fusion materials community in the form of a 15 mm thick plate from the IEA Heat 9741. The steel was normalised at 1 040°C for 38 min and tempered at 750°C for 1 h. The chemical composition of the T91 and F82H steels is listed in Table 8.4.2.

Table 8.4.2: Chemical compositions of the T91 and F82H steels (wt.%, Fe for the balance)

Material	Cr	Ni	Mn	Mo	Ti	V	Si	P	Nb	W	Ta	C
T91	8.76	0.10	0.60	0.86	–	0.19	0.32	0.019	0.07	–	–	0.09
F82H	7.65	0.02	0.10	0.003	0.004	0.19	0.07	0.003	0.002	1.98	0.03	0.09

Dog-bone shaped flat specimens were cut out from the as-received plates with an electrical-discharging machining (EDM). Two kinds of specimens were prepared: *i)* large tensile (LT) specimens, $16 \times 4 \times 0.75$ mm^3 with a gauge section of $5 \times 1.5 \times 0.75$ mm^3; *ii)* small tensile (ST) specimens, $12 \times 2.5 \times 0.4$ mm^3 with a gauge section of $5 \times 1.0 \times 0.4$ mm^3. The specimens were finely polished with 1 000 grit abrasive papers before irradiation. The specimens used in this work were irradiated in a helium gas environment to doses between 7.8 and 19.3 dpa with helium concentrations of 620 and 1 800 appm, respectively.

8.4.2.2 *SSRT tests*

SSRT tests were conducted at a constant cross-head speed of 3 μm/min, which corresponds to a nominal strain rate of 1×10^{-5} s^{-1} (Long, 2009, 2012). This strain rate was selected because it was previously shown that it allowed evidencing LBE embrittlement effects in tests performed at 300°C (Dai, 2006d). There was no special control on the oxygen content in LBE. The oxygen content was as much as that saturated at 250°C in LBE, because the LBE was kept in a tank at 250°C.

Figure 8.4.5 shows the tensile stress-strain curves obtained for the irradiated T91 specimens tested either in Ar or in LBE at 250, 400, 450 and 500°C, i.e. close to their average irradiation temperature. All the irradiated specimens exhibit a significant hardening as compared to the unirradiated ones. Meanwhile, the ductility decreases significantly. Nevertheless, all the specimens tested in Ar possess a total elongation of 5% or greater. The specimens tested in LBE at 250, 400 and 450°C show no or little necking at fracture (Figure 8.4.5 [a-c]). The stress-strain curve of the 10.9 dpa specimen tested in LBE at 500°C is nearly the same as that of the specimen tested in Ar at 500°C, which means that additional embrittlement by LBE does not occur at 500°C.

Figure 8.4.5: Tensile engineering stress-strain curves of the T91 specimens irradiated in STIP-III and tested either in Ar or in LBE at temperatures close to their irradiation temperatures

(a) 250°C, (b) 400°C, (c) 450°C, (d) 500°C; the unirradiated specimens were tested in Ar

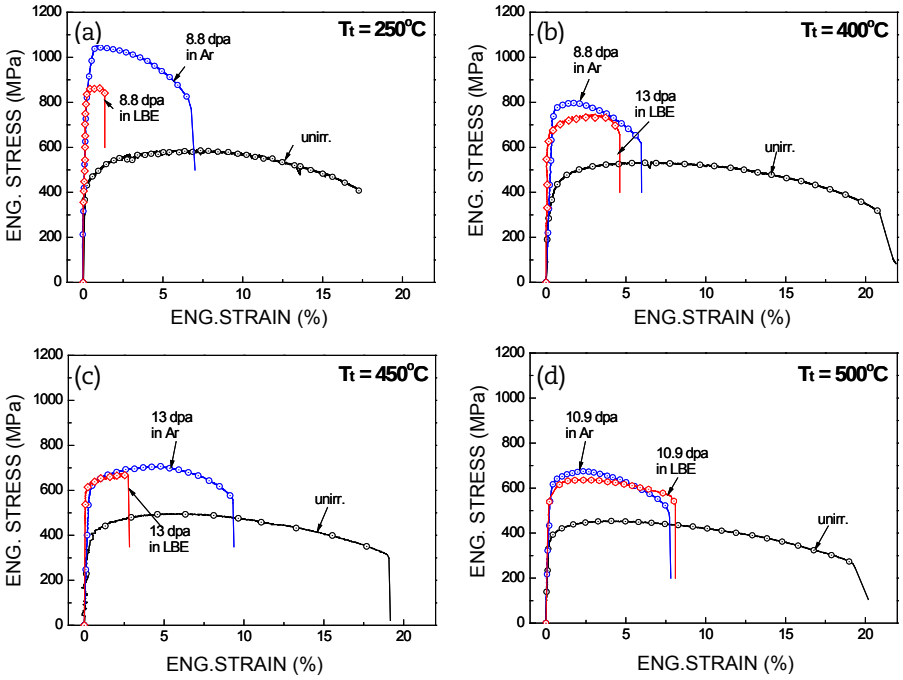

Similar results were obtained for the F82H specimens. Figure 8.4.6 presents the results of SSRT tests on the irradiated F82H specimens tested either in Ar or in LBE environment. As in the case of the irradiated T91 specimens, the F82H specimens exhibit significant irradiation-induced hardening in the temperature range 150-350°C. LBE embrittlement can be seen in the tests performed at 200, 250 and 300°C, but not in the test at 150°C. In the test at 350°C, the sample of 19.5 dpa was found very brittle, even when tested in Ar. The sample tested at 350°C in LBE also shows very brittle fracture, but perhaps mainly due to the irradiation-induced embrittlement effect.

Figure 8.4.6: Tensile engineering stress-strain curves of irradiated F82H specimens tested either in Ar or in LBE

The irradiation dose and irradiation temperature/test temperature are indicated on each curve

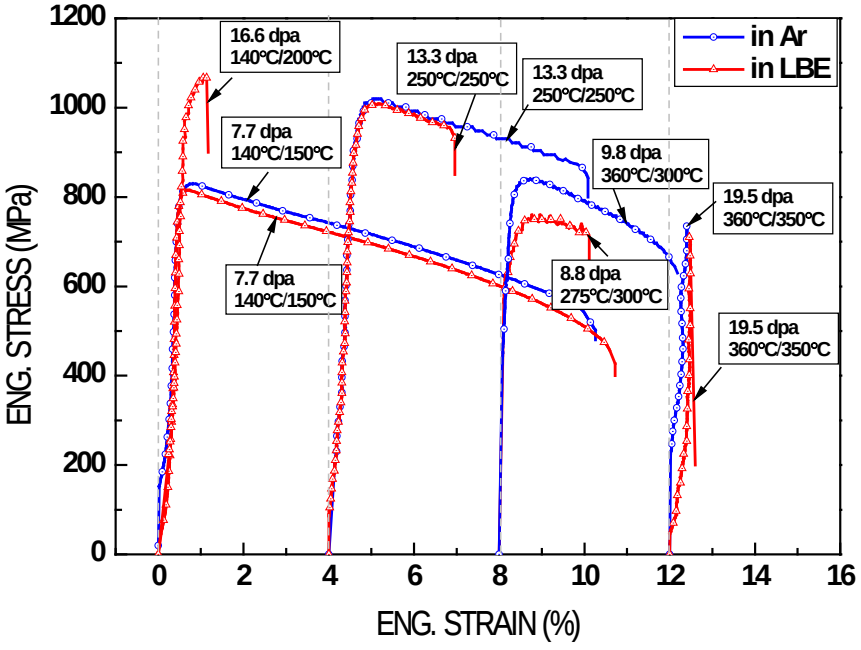

SEM micrographs of the fracture surfaces of two irradiated T91 specimens tested in LBE at 250 and 450°C are shown in Figure 8.4.7. Both specimens failed without necking and in a transgranular cleavage fracture mode. The rest of the specimens tested in LBE were found to exhibit the same fracture characteristics. In the case of the irradiated F82H specimens, the fracture surfaces of some specimens were observed to exhibit a very brittle fracture mode, almost fully intergranular. As an example, Figure 8.4.8 presents the surfaces of the specimens irradiated to 13.3 dpa and tested either in Ar or in LBE. Although the specimen tested in Ar illustrates a transgranular cleavage dominant fracture mode, the specimen tested in LBE displays a very brittle and almost fully intergranular fracture mode.

Figure 8.4.7: Fracture surfaces of the irradiated T91 specimens tested in LBE

a) Specimen 3-ST-B25 irradiated at 253°C to 8.8 dpa/615 appm He and tested at 250°C

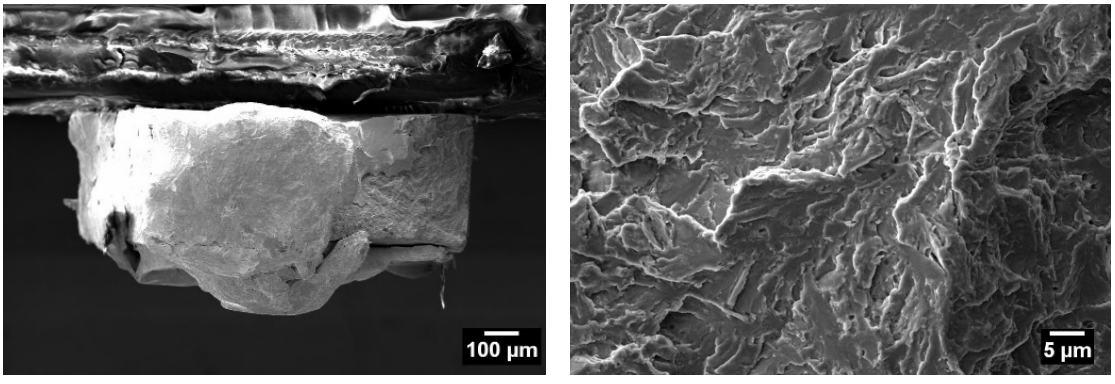

Figure 8.4.7: Fracture surfaces of the irradiated T91 specimens tested in LBE (*cont.*)

b) Specimen 3-ST-B06 irradiated at 451°C to 13 dpa/985 appm He and tested at 450°C

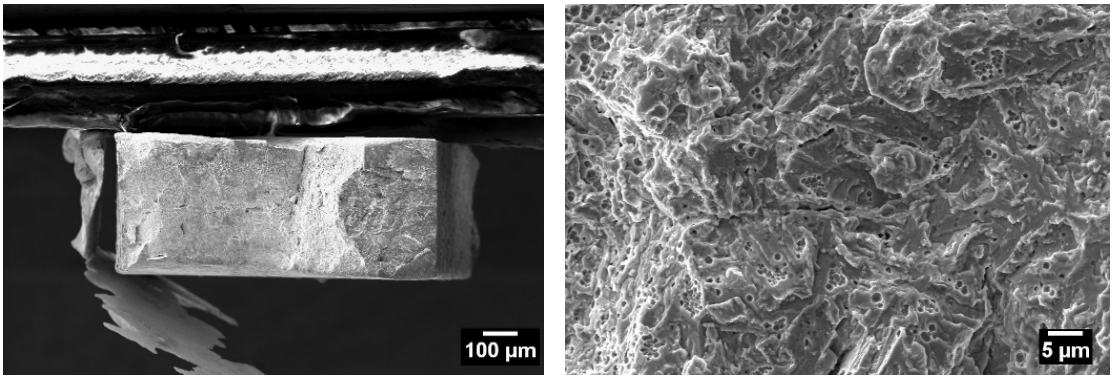

Figure 8.4.8: Fracture surfaces of irradiated F82H specimens after SSRT tests either in Ar or in LBE environment

a) 13.3 dpa/Tirr 250°C, in Ar at 250°C

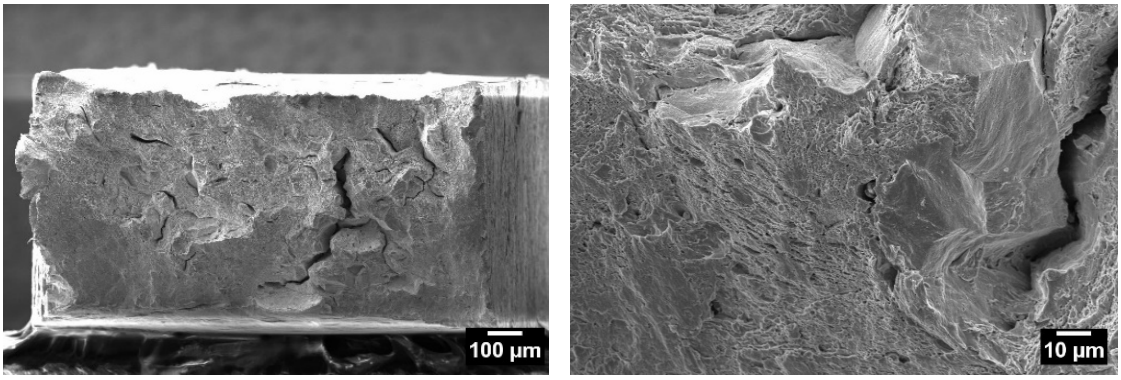

b) 13.3 dpa/Tirr 250°C, in LBE at 250°C

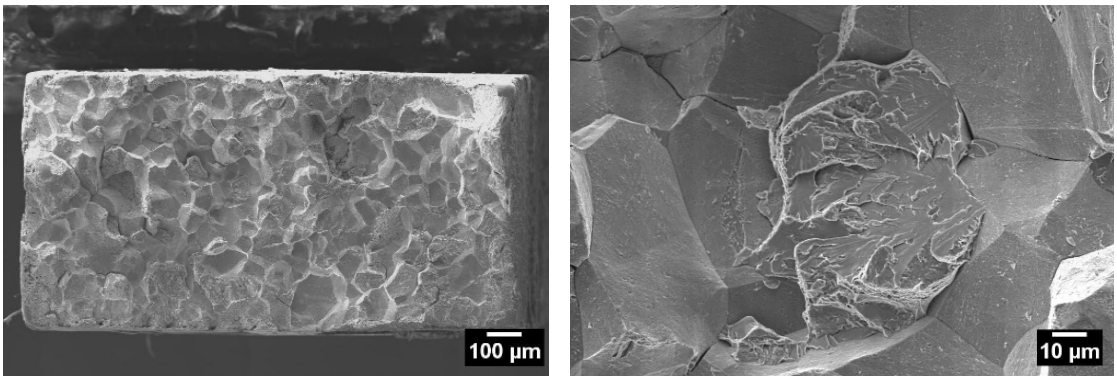

Figure 8.4.9: Test temperature dependence of the total elongations of the T91 and F82H specimens irradiated in STIP-2 and 3 experiments and tested either in argon or in LBE

The "ductility trough" of unirradiated T91 in LBE is added for comparison

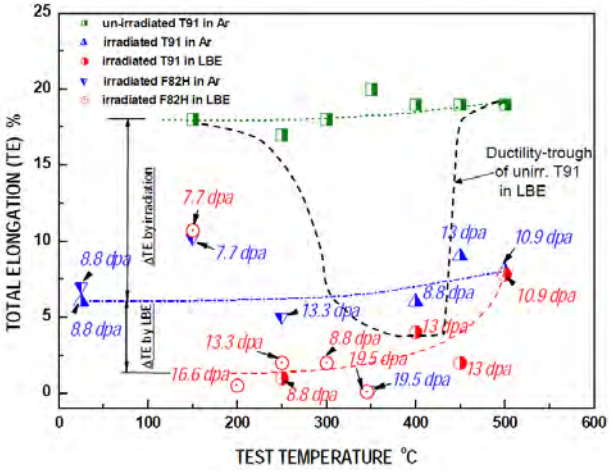

8.4.3 *LBE effect on fracture toughness of irradiated T91 steel*

Due to the limited availability and high radioactivity of irradiated bend bar specimens for fracture toughness evaluation, to date only few specimens irradiated in STIP have been tested in an LBE environment. Similar to the STIP specimens used for SSRT tests, the bend bar specimens were irradiated to different doses between 7.1 and 15.3 dpa at different temperatures between 150 and 415°C (Table 8.4.3). In order to study annealing effect on eventual recovery of the mechanical properties of the irradiated T91 steel, four specimens in two irradiation conditions were tested after annealing at 600°C for two hours. Figure 8.4.9 presents the load displacement curves of the specimens irradiated to 7.1, 8.2 and 9.1 dpa and tested at the temperatures of 200, 150 and 250°C, corresponding to the irradiation temperatures of the specimens. It can be seen that the irradiated specimens tested in LBE failed much earlier as compared to the specimens tested in Ar, which indicates the additional LBE embrittlement effect on the irradiated specimens. It should be noted that, in Figure 8.4.10(a), the strength of the 8.2 dpa specimen is much higher than that of the 9.1 specimen, because the a_0/W value of the 8.2 specimen is 0.48 and 0.54 for the 9.1 dpa specimen (Table 8.4.3).

Table 8.4.3: Irradiation and test parameters for bending bars

Sample ID	$T_{irr.}$[3] (°C)	Dose (dpa)	He (appm)	T_{test} (°C)	Test envir.	Anneal at 600°C	a_0/W	J_Q (kJ/m²)	K_Q (MPa√m)
1-BB-I01[1]	240	9.1	532	250	Ar		0.51	140	177
1-BB-I02[1]	240	9.1	532	250	LBE		0.51	40	95
1-BB-I03[1]	185	7.1	398	200	LBE		0.49	175	198
1-BB-I04[1]	185	7.1	398	250	Ar		0.50	250	237
3-BB-B01[2]	154	9.1	590	150	Ar	Yes	0.54	450	318
3-BB-B02[2]	154	9.1	590	150	Ar		0.54	220	222
3-BB-B10[2]	155	8.2	515	150	LBE		0.48	85	138

See notes on page 601.

Table 8.4.3: Irradiation and test parameters for bending bars (*cont.*)

Sample ID	$T_{irr.}$[3] (°C)	Dose (dpa)	He (appm)	T_{test} (°C)	Test envir.	Anneal at 600°C	a_0/W	J_Q (kJ/m²)	K_Q (MPa√m)
3-BB-B11[2]	155	8.2	515	150	LBE	Yes	0.54	310	264
3-BB-B03[2]	329	15.3	1 110	250	Ar	Yes	0.51	220	218
3-BB-B04[2]	329	15.3	1 110	250	Ar		0.51	3	25
3-BB-B09[2]	290	14.9	1 110	300	Ar	Yes	0.48	8	42
3-BB-B07[2]	290	14.9	1 110	300	LBE	Yes	0.49	9	44
3-BB-B05[2]	417	19.5	1 550	400	Ar	Yes	0.49	5	32
3-BB-B06[2]	417	19.5	1 550	400	Ar		0.49	2	20

1. Samples from STIP-I.

2. Samples from STIP-III.

3. The mean irradiation temperature values, with variation of about ±15% during irradiation.

Figure 8.4.10: Load displacement curves of irradiated specimens tested in either Ar or LBE at (a) 150, (b) 200 and (c) 250°C

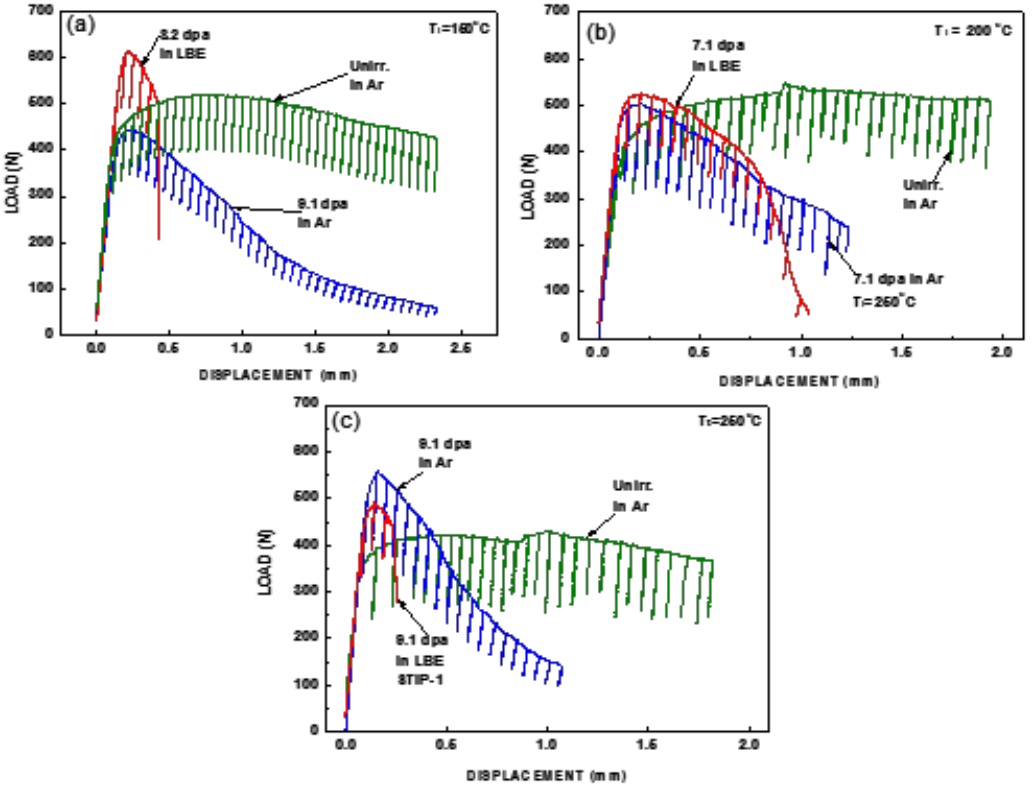

The load displacement curves of the irradiated specimens after annealing at 600°C for two hours and then tested either in Ar or in LBE at 150 and 300°C are presented in Figure 8.4.11. For comparison purposes, the results of the as-irradiated specimens tested at 150°C in both Ar and LBE are included. Figure 8.4.11(a) illustrates that for the specimens

of 8.2 dpa and 515 appm He and irradiated at about 155°C, the load displacement curves changed significantly after annealing at 600°C for two hours. For the tests in Ar, the curve of the annealed specimen looks quite similar to that of unirradiated one, which indicates that the irradiation embrittlement effect is significantly reduced. For the tests in LBE, the LBE embrittlement is also evidently reduced after annealing as compared that of as-irradiated specimen. In the case of the specimens of 15.3 dpa and 1 110 appm He and irradiated at about 290°C, the specimens are still very brittle after annealing and tested at 300°C. The specimen tested in Ar shows large crack jumps during propagation until breaking through the ligament. For the specimen tested in LBE, the crack simply propagated through the ligament in one step, which indicates the LBE embrittlement effect once again.

Figure 8.4.11: Load displacement curves of the irradiated specimens after annealing at 600°C for 2 hours and tested both in Ar and LBE at 150°C (a) and 300°C (b)

For comparison the results of the as-irradiated specimens tested 150°C in Ar and LBE are included

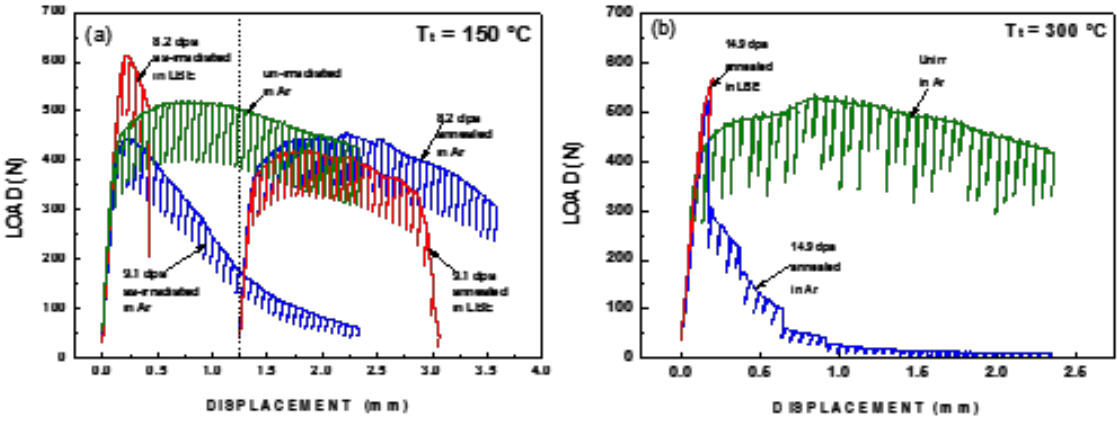

The J_Q values obtained for the six irradiated specimens are equal to 150, 120 and 90 kJ/m^2 for the 7.1, 8.2 and 9.1 dpa specimens tested in Ar and equal to 100, 80 and 40 kJ/m^2 for the 7.1, 8.2 and 9.1 dpa specimens tested in LBE (Table 8.4.1), while for the unirradiated T91 (HT760) specimens the J_Q values are above 450 kJ/m^2 in this temperature range (150-250°C). Therefore, the J_Q value was significantly reduced by the irradiation and further reduced by the LBE embrittlement effect.

The *J*-*R* curves of the annealed specimens tested at 150°C in both Ar and LBE are given in Table 8.4.1. It is clear that the *J* values of the annealed specimens are greatly recovered. The J_Q value of the annealed specimen tested in Ar is about 340 kJ/m^2, and for that tested in LBE about 90 kJ/m^2. In the brittle fracture cases of the specimens of 15.3 dpa, J_{1C} is about 10 kJ/m^2 for both specimens independent of test environments.

8.5 MEGAPIE experiment

The Megawatt Pilot Experiment (MEGAPIE) is a joint initiative by six European research institutions (SCK•CEN [Belgium], CEA [France], CNRS [France], ENEA [Italy], FZK [Germany], PSI [Switzerland]), the European Union, JAEA (Japan), the DOE (United States), and KAERI (Korea) to design, build, operate and explore a liquid lead-bismuth spallation target for 1 MW of beam power (Bauer, 2001; Wagner, 2008). The goal of this experiment is to explore the conditions under which such a target system can be licensed, to accrue relevant materials data for a design database for liquid metal targets, to gain experience in operating such a system under realistic beam conditions, and to ascertain the neutronic performance of such a target for use in SINQ and other (future) accelerator-driven systems

(e.g. ADS). Taking advantage of the existing spallation facility SINQ, a target was developed through the effort of all partners from 1999-2005, and was successfully operated for about four months in 2005.

The PIE of the target components exposed to high fluxes of high-energy protons and spallation neutrons in flowing LBE environment is one of most important tasks of the MEGAPIE project. The PIE of MEGAPIE can provide important information for R&D of future ADS for nuclear waste transmutation. The PIE mainly includes four parts: *i)* non-destructive tests (NDT); *ii)* radiochemical analysis of the radionuclide inventory in LBE; *iii)* analysis of corrosion effect on structural components; *iv)* mechanical testing of materials exposed to high proton and neutron fluxes. In this report, some results of parts *i)*, *ii)* and *iv)* obtained in the GETMAT time frame will be described.

8.5.1 *Target structure and irradiation*

Since MEGAPIE was using the existing conditions of SINQ, the target has to match the given opening in the target block shielding. Therefore, the shape and external dimensions of the MEGAPIE target are nearly the same as a normal SINQ solid target. Figure 8.5.1 shows the fully assembled MEGAPIE target lifted before being inserted into the SINQ operation position. It has a length of about 5 m, a diameter of about 40 cm in the upper part and a diameter of about 22 cm in the lower part. Detailed information about the structure of the MEGAPIE target can be found in Wagner (2008).

Figure 8.5.1: MEGAPIE target before being inserted into the SINQ target station and sketches showing the main components of the target

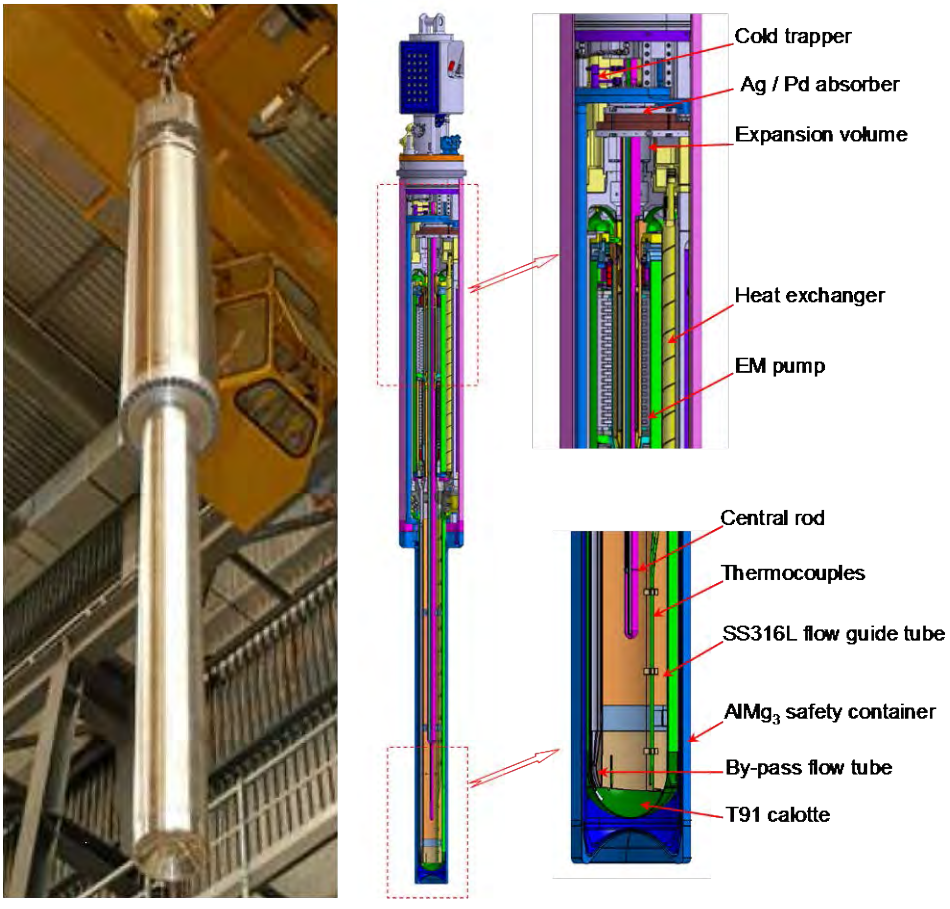

The operation of MEGAPIE was started on 14 August 2006 and completed on 2 December 2006. Figure 8.5.2 presents the proton beam history of the irradiation period (Wagner, 2008). It shows that the proton beam current was about 1 mA in the first three weeks and was then kept at a level between 1.2 mA and 1.4 mA. The corresponding power for 1.3 mA beam current is about 750 kW. A proton charge of 2.78 Ah was received after the four-month irradiation.

Figure 8.5.2: Proton beam history during the irradiation period of MEGAPIE

In the figure, the time interval is 20 minutes between the data points

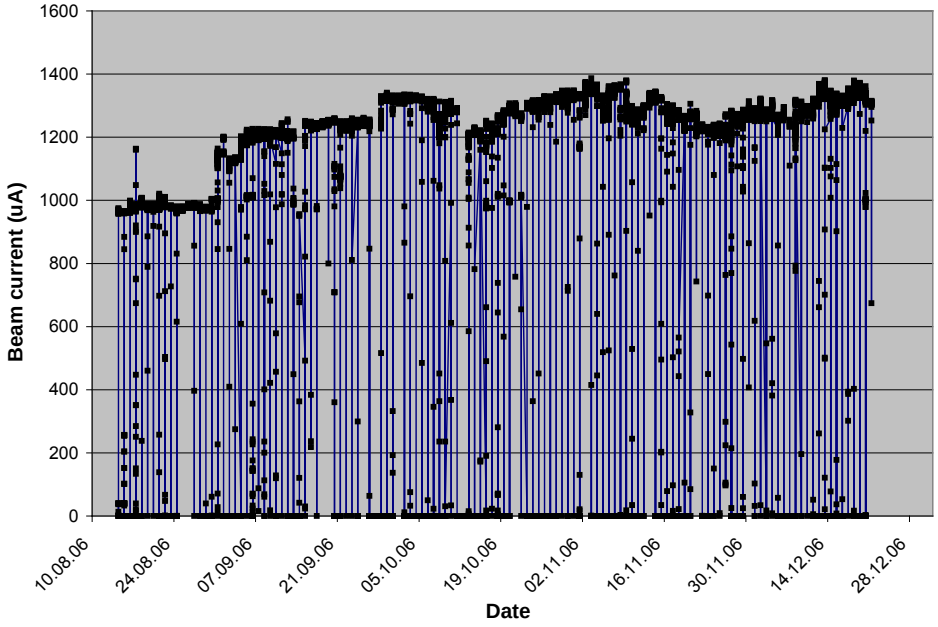

The accumulated proton fluence distribution profile was evaluated by conducting gamma mapping on the proton beam window area of the AlMg3 safety-container, which gave the maximum proton fluence of 1.9E+25 p/m^2 (Dai, 2011, 2013). Using the proton fluence distribution profile, irradiation dose distribution was calculated, which indicated the maximum irradiation dose of 7.1 dpa of the T91 calotte (Donegani, 2011).

Temperature distribution in the target was monitored by more than 80 thermocouples during irradiation (Wagner, 2008). Since no thermocouples were installed in the beam window area of the T91 calotte, the temperature distribution in the wall of the T91 calotte has to be calculated. Figure 8.5.3 presents the calculated temperature distribution across the wall thickness in the bypass flow direction, namely the major axis of the proton beam ellipse print. The calculation was done using the CFD code and compared with the measurements in the lower part of the flow guide tube (Roubin, 2008; Dai, 2014).

In 2009 the MEGAPIE target was transferred from SINQ target storage to the hot cell of the central Swiss interim storage facility (ZWILAG). The target was sawed into segments (Wohlmuther, 2012). Nine segments, H01 to H09, were selected and transferred to PSI's hot laboratory for extracting PIE samples. In a hot cell of PSI's hot lab, the LBE in the selected segments was removed by melting it in a specially designed oven. The melting was done in an Ar atmosphere at below 180°C. After removing most of the LBE, the tubes in these segments were cut into slices of 25-35 mm width for the next cutting steps with an electron discharge machine (EDM). Since the specimens shipped to the MEGAPIE partner laboratories should be nearly free of contamination, the slices were cleaned in diluted nitric acid to remove the remaining LBE on the surface before EDM cutting.

Figure 8.5.3: Calculated temperature distribution cross-wall thickness of the T91 calotte in the bypass flow direction

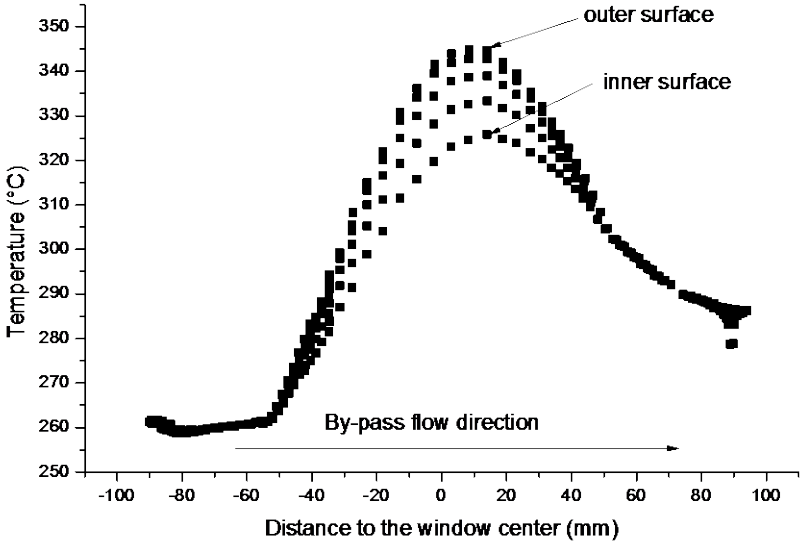

Figure 8.5.4: Sketches showing specimen groups used for MEGAPIE PIE

The left two groups were used from specimens cut along electron beam weld (EBW) lines

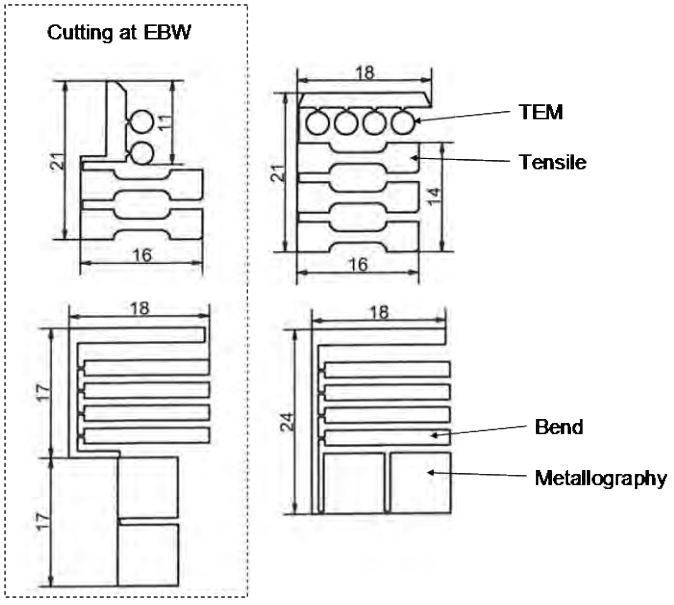

8.5.2 *Visual inspection*

The lower part of the target was inspected with a high-resolution video camera installed in a hot cell. Figure 8.5.5(a) shows the beam window area of the T91 calotte. The central part was covered by the black material sticking on the surface of the calotte. Figure 8.5.5(b) shows the appearance of the T91 calotte after removing the deposited material and slightly polished with sandpaper. With the exception of some scratches produced by polishing, no visible failure was observed in the beam window area.

After melting LBE, the selected pieces were inspected again. Figure 8.5.6 shows the appearance of the inner surface of the T91 calotte after melting out LBE. It can be seen that the inner surface of the calotte was only partially covered by LBE. The same is true for the other pieces. This means that the surface components were not well wet by LBE during irradiation, particularly in the lower temperature regions. Again, no evident failure was found.

Figure 8.5.5: Pictures taken through the glass window of a hot cell

The T91 calotte after irradiation (a), the T91 calotte after removing the deposited material (b)

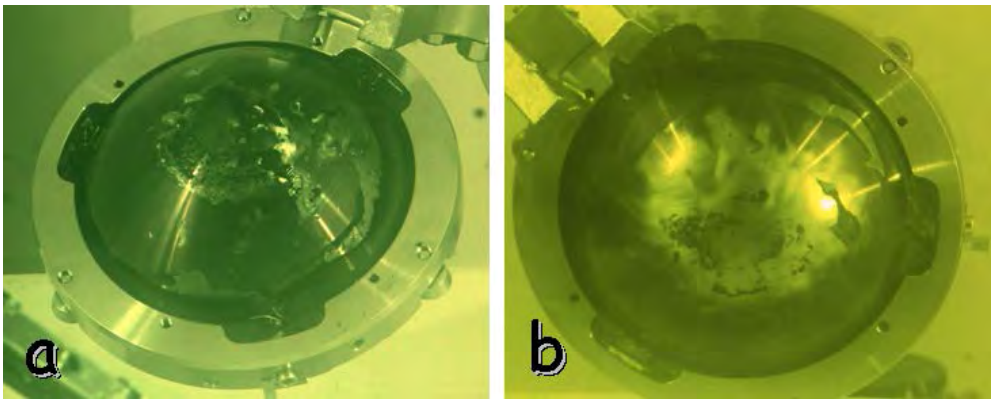

Figure 8.5.6: A picture showing the inner surface of the T91 calotte after melting out LBE

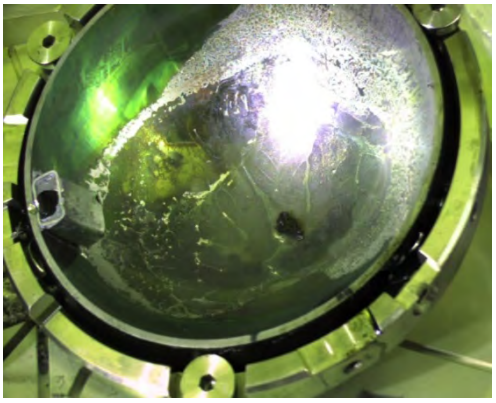

8.5.3 *Ultrasonic measurement*

Ultrasonic measurement was conducted on the proton beam window of the T91 calotte before and after irradiation. Before irradiation, the measurement was conducted on the T91 calotte without filling LBE. After irradiation, the measurement was done on the T91 calotte fully filled with solidified LBE. The measurement was performed at the exact same positions before and after irradiation. The results are presented in Table 8.5.1. One can see that the thickness value measured after irradiation is systematically lower than that measured before irradiation. The difference is 20-25 microns. A measurement test was conducted on a steel tube of about 2 mm wall thickness. It was found that a similar difference value was given by the measurement before and after filling PbBi. Therefore, it could be concluded that, within the precision of the measurement of about 5 μm, no change in the wall thickness in the proton beam window area was induced by LBE corrosion after four-month operation (Dai, 2013).

Table 8.5.1: Thickness measured in the beam window area of the T91 calotte before and after irradiation (upper) and the difference between the two sets of measurement (lower)

Thickness before and after irradiation										
Conf. angle	0°		30°		60°		90°		120°	
Vert. angle	Bef. irr. thickness (mm)	After irr. thickness (mm)	Bef. irr. thickness (mm)	After irr. thickness (mm)	Bef. irr. thickness (mm)	After irr. thickness (mm)	Bef. irr. thickness (mm)	After irr. thickness (mm)	Bef. irr. thickness (mm)	After irr. thickness (mm)
0	1.428	1.408	1.432	1.409						
6	1.452	1.438	1.452	1.436	1.451	1.431	1.451	1.438	1.452	1.435
12	1.501	1.479	1.500	1.482	1.501	1.475	1.501	1.475	1.505	1.463
18	1.530	1.508	1.526	1.507	1.526	1.497	1.526	1.498	1.525	1.501
24	1.545	1.519	1.541	1.527	1.539	1.529	1.539	1.511	1.537	1.519
30	1.572	1.551	1.578	1.561	1.575	1.553	1.575	1.547	1.571	1.548
36	1.598	1.575	1.607	1.589	1.603	1.589	1.603	1.571	1.602	1.581
42	1.641	1.621	1.656	1.635	1.650	1.627	1.650	1.618	1.643	1.621
48	1.680	1.661	1.697	1.662	1.682	1.662	1.682	1.652	1.681	1.665

Difference before and after irradiation					
Vert. angle	Difference (mm)	Difference (mm)	Difference (mm)	Difference (mm)	Difference (mm)
0	0.020	0.023			
6	0.014	0.016	0.020	0.013	0.017
12	0.022	0.018	0.026	0.026	0.042
18	0.022	0.019	0.029	0.028	0.024
24	0.026	0.014	0.010	0.028	0.018
30	0.021	0.017	0.022	0.028	0.023
36	0.023	0.018	0.014	0.032	0.021
42	0.020	0.021	0.023	0.032	0.022
48	0.019	0.035	0.020	0.030	0.016
Average	0.021	0.020	0.021	0.027	0.023

8.5.4 Analysis of LBE corrosion and erosion effects

Some specimens without cleaning LBE were reserved to investigate the corrosion effect of LBE on steels at PSI. Specimens were cut from slices of the T91 calotte (H02-1-9), lower liquid metal container (H03-1-L, made of T91 steel) and flow guide tube (H03-2-B1, made of SS 316L steel), which received high proton and neutron fluxes.

8.5.4.1 Analysis of the T91 calotte

LBE corrosion effect was investigated at two positions: Sample A1 in the central part of the T91 calotte with an irradiation dose of about 6.5 dpa and irradiation temperature of about 315°C on the inner surface, and Sample A3 at the edge of the proton beam footprint with an irradiation dose of about 0.8 dpa and irradiation temperature of about 250°C on the inner surface. Figures 8.5.7 to 8.5.9 present the results of A1. It was observed that only a part of the surface was covered by LBE, as shown in Figure 8.5.7. An oxide layer formed on the surface, but it was very thin (0.2-0.4 μm). The surface was smooth and without features such as corrosion pits, grooves, etc. Figure 8.5.8 presents the element mapping in

an area with LBE sticking on the surface. It can be seen that the thin layer on the surface is rich in Cr and Mn. Beneath the surface exists a Cr and Mn depleted zone of 2-3 μm depth. However, this feature was also observed in a reference T91 sample. Therefore, it should not be induced by irradiation or corrosion. Further, no LBE penetration into the steel matrix was detected. Quantitative results of line scan (Figure 8.5.9) confirm this conclusion as well.

The analyses of Sample A3 and samples from the lower liquid metal container tube show essentially the same features. No evidence of corrosion damage was detected.

Figure 8.5.7: SEM image showing the inner surface in the central part of the T91 calotte

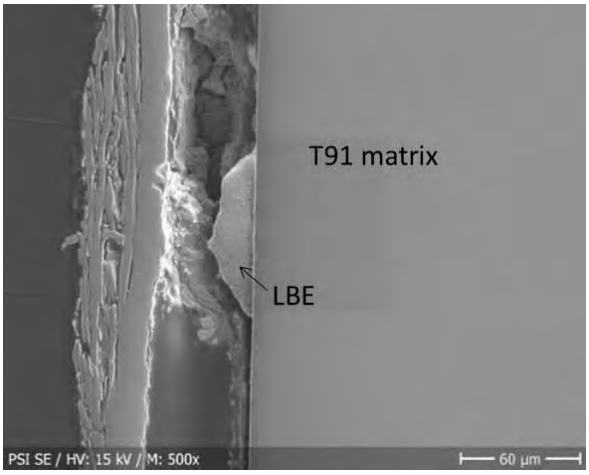

Figure 8.5.8: Element mapping in an area with LBE one surface in the central part of the T91 calotte

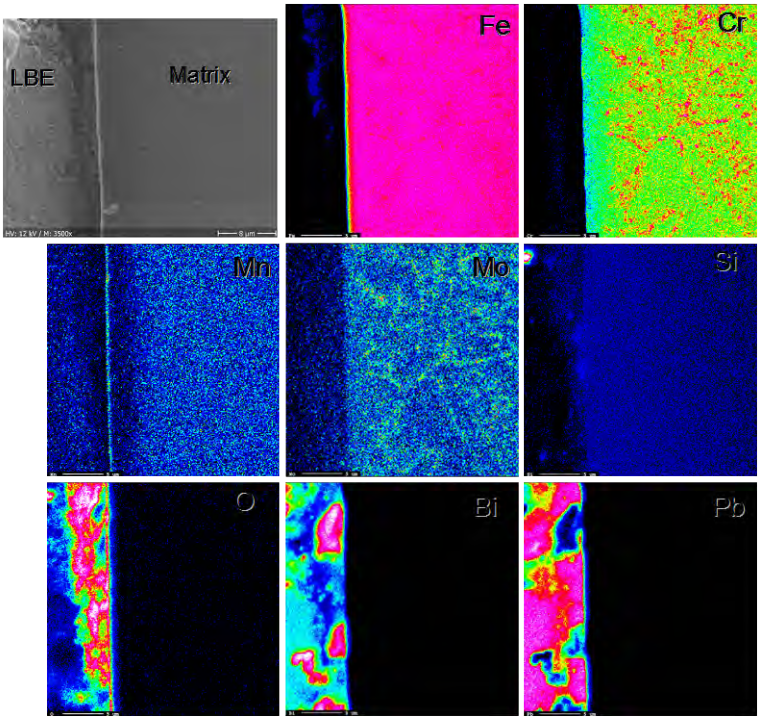

Figure 8.5.9: Quantitative line scan on Sample A1 across the inner surface and LBE on the surface

Cr and Mn enriched in the oxide layer

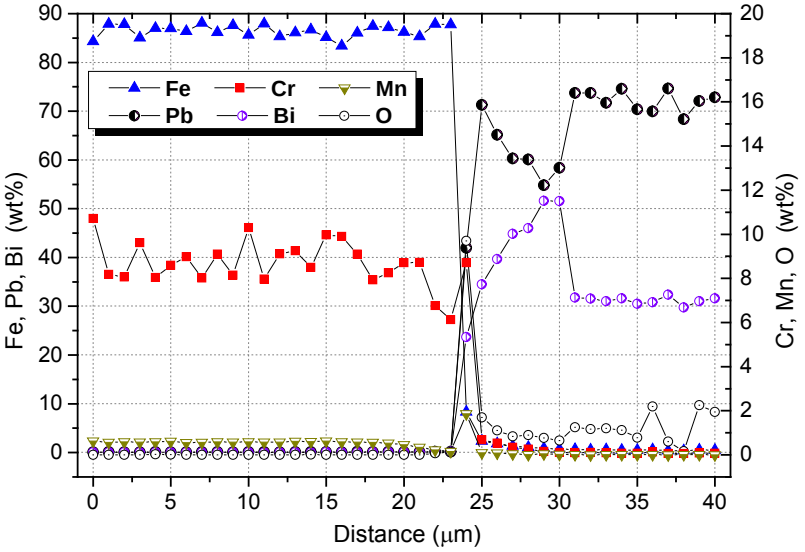

8.5.4.2 *Analysis of the flow guide tube (FGT)*

On the inner surface of FGT quite deep traces or grooves were produced by manufacturing (Figure 8.5.10). Except for these traces, no clear corrosion damage could be identified. Element mapping did not show either an oxide layer (too thin) on the surface or penetration of PbBi into the steel matrix (Figure 8.5.11).

Figure 8.5.10: SEM image showing the cross-section of the flow guide tube

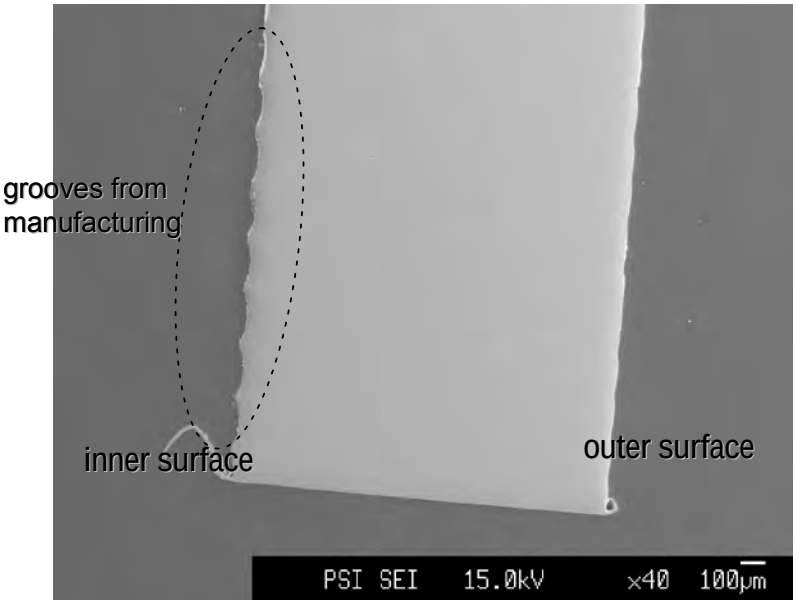

Figure 8.5.11: Element mapping in an area of the inner surface of FGT with LBE on the surface

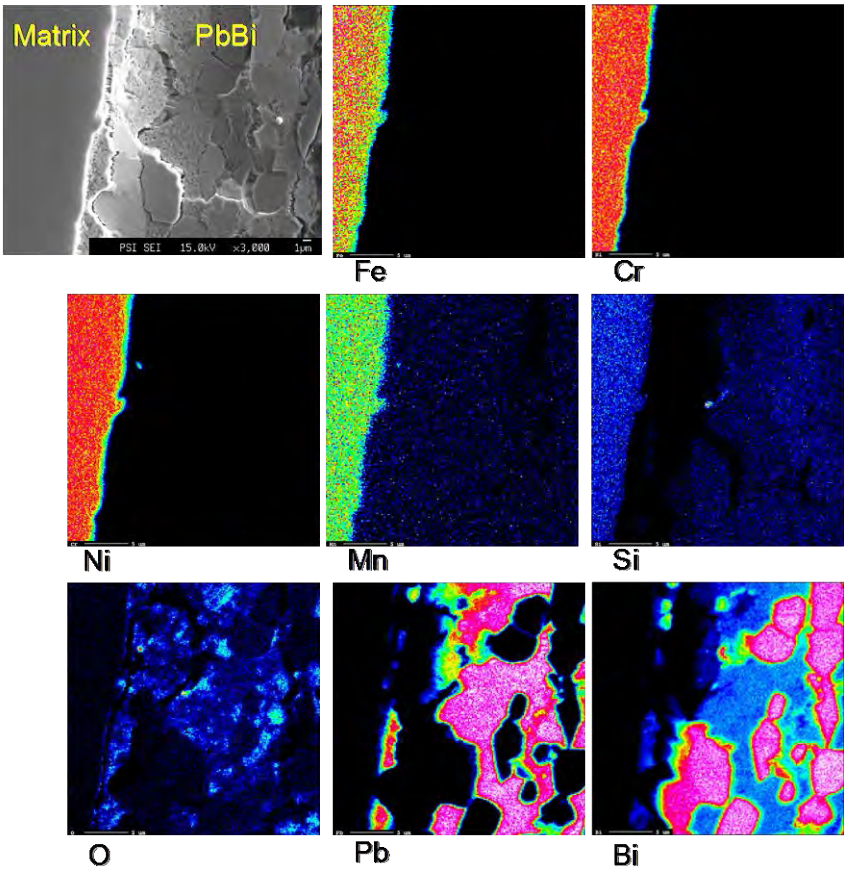

8.5.5 *Mechanical testing*

Mechanical testing includes tensile and bend tests and hardness measurements were planned for evaluating the changes in the mechanical properties of the T91 and SS 316L steels in the intensive irradiation region of the lower part of the target. To date, only preliminary results have been obtained. One of the main difficulties encountered is the heavy contamination of the samples even after cleaning in a hot cell at PSI. In this section, only the tensile results of the T91 calotte obtained by PSI are presented.

The tensile specimens shown in Figure 8.5.4 have a gauge length of 5 mm and a width of 1.5 mm. Since the wall thickness of the T91 calotte varies from about 1.45 mm to about 1.7 mm (Table 2), specimens have different thickness values. Further, the specimens are slightly curved. Considering the curvature in the 5 mm gauge length is not much, the specimens were tested without removing the curvature. Figure 8.5.12 presents the results of the specimens cut from the T91 calotte. It should be noted that all the specimens were cleaned before testing. The specimens were tested in air at room temperature (23°C), 250 and 300°C, according to the irradiation temperature of the specimens. The results manifest similar irradiation-induced hardening and embrittlement effect as shown in previous Sections 8.3 and 8.4.

There are a large amount of tensile results obtained from ferritic/martensitic steels irradiated in the STIP (Dai, 2003, 2008; Henry, 2003, 2008; Chen, 2005; Maloy 2006). However, the irradiation condition of the MEGAPIE specimens is different from that of STIP specimens. The irradiation temperature of the MEGAPIE tensile specimens is in the

range of 250 to 320°C and irradiation dose is in the range of 0.7 to 6.1 dpa. The irradiation temperature of STIP-I and STIP-II specimens is in the range of 80 to 350°C and the irradiation dose is in the range of 3 to 20 dpa. For STIP specimens at low doses, the irradiation temperature is lower than that of the MEGAPIE specimens. Compared to STIP specimens, the MEGAPIE specimens possess greater elongation values at similar irradiation doses. For example, the total elongation of the T91 specimens irradiated in STIP at ≤6 dpa is less than 10% (Dai, 2003). This difference should be greatly attributed to the geometry of the specimens. STIP small tensile specimens have a cross-section of 0.4×1.0 mm^2, while those for MEGAPIE have a cross-section of about 1.5×15 mm^2.

Figure 8.5.12: Tensile curves of specimens cut from the T91 calotte tested in air at RT, 250 and 300°C

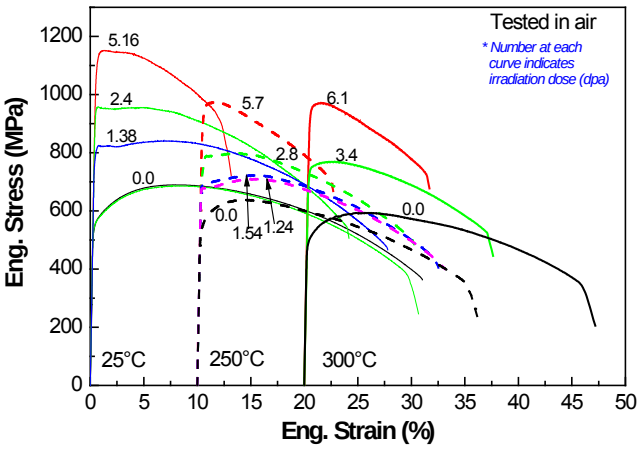

8.6 Conclusions

Irradiation effect on the compatibility of ferritic/martensitic and austenitic steels with LBE has been extensively studied up to the present day. Experiments have been carried out utilising irradiation possibilities of proton accelerators, fission reactors and spallation targets. Understanding of this specific materials issue has been greatly improved.

In LiSoR experiments, specimens of T91 steel were irradiated with 72 MeV protons in contact with flowing LBE. Except for the second LiSoR experiment with unexpected high temperature and high thermal stress, no clear corrosion evidence was observed on the T91 specimens irradiated up to about 2.5 dpa at temperatures up to about 400°C (on surfaces) for a duration of about 725 hours. The same is true for the specimens with coatings irradiated for 900 hours. Only slight irradiation hardening and embrittlement effect was observed from the specimens cut from the irradiation areas. However, for the coatings very clear embrittlement effect was detected during bend testing at ambient temperature. It should be mainly attributed to the irradiation rather than LBE attack, at least for the FeCrAlY coating, because the surface was slightly oxidised.

Similarly, the results obtained on all analysed specimens of T91, SS 316L and 15-15Ti steels irradiated in the BOR60 reactor to 9.1 dpa at 350°C in contact with static LBE do not show visible corrosion damages of the surfaces except for a thin submicron scale oxide layer formed on the surfaces. Further, no corrosion attack could be identified on the MEGAPIE samples of both T91 and SS 316L steels after irradiated to 6-7 dpa at 300-340°C for four months, although no oxide layer on the surface could be seen (a very thin oxide layer existed before irradiation).

Only gentle dissolution attack was observed on stressed capsules of 316LN and 9CrWVTa steels irradiated in STIP to doses of 12-17 dpa at temperatures of 200-315°C. The attack could be due to low oxygen content in the LBE, because hydrogen was produced in irradiation inside the capsules and could not be released from the LBE. However in the MEGAPIE case, the hydrogen produced during irradiation could be released from LBE to cover gas (Wagner, 2008).

LBE effect on irradiated steels is indicated by further reduction in ductility when irradiated steel specimens tested in an LBE environment. MEGAPIE specimens after cleaning the LBE on the surface did not show such an effect when they were tested in air. The additional embrittlement effect of LBE on irradiated steel specimens should be largely attributed to the high strength of steels resulting from the irradiation-induced hardening, which is similar to that observed from T91 specimens hardened by heat treatment and tested in LBE (see Chapter 7) (Long, 2008). Great attention should be reserved for steel components irradiated in LBE environment, although no failure occurred in the MEGAPIE target. At higher irradiation doses, the LBE effect becomes more pronounced, as shown in Section 8.4.

References

Ando, M. et al. (2007), "Creep Behavior of Reduced Activation Ferritic/Martensitic Steels Irradiated at 573 and 773 K Up to 5 dpa", *Journal of Nuclear Materials,* Vol. 367, pp. 122-126.

Bauer G.S., M. Salvatores and G. Heusener (2001), "MEGAPIE, a 1 MW Pilot Experiment for a Liquid Metal Spallation Target", *Journal of Nuclear Materials*, Vol. 296, pp. 17-33.

Chen, J. et al. (2005), "The Tensile Properties of AISI 316L and OPTIFER in Various Conditions Irradiated in a Spallation Environment", *Journal of Nuclear Materials*, Vol. 343, pp. 236-240.

Dai, Y. and G.S. Bauer (2001), "Status of the First SINQ Irradiation Experiment, STIP-I", *Journal of Nuclear Materials,* Vol. 296, pp. 43-53.

Dai, Y., X. Jia and K. Farrell (2003), "Mechanical Properties of Modified 9Cr-1Mo (T91) Irradiated at ≤300°C in SINQ Target 3", *Journal of Nuclear Materials*, Vol. 318, pp. 192-199.

Dai, Y. et al. (2004), "Preliminary Results of Post-Irradiation Examinations on LiSoR-2 Test Section", *Journal of Nuclear Materials*, Vol. 335, pp. 232-238.

Dai, Y. et al. (2005), "The Second SINQ Target Irradiation Program, STIP-II", *Journal of Nuclear Materials*, Vol. 343, pp. 33-44.

Dai, Y. et al. (2006a), "An Assessment of the Window Lifetime of MEGAPIE Target Liquid Metal Container", *Journal of Nuclear Materials*, Vol. 356, pp. 308-320.

Dai, Y. and B. Oliver (2006b), "A Comparison Between Calculated and Measured He and H Contents of STIP Samples", *7th International Workshop on Spallation Materials Technology*, 29 May-3 June 2005, Thun, Switzerland.

Dai, Y. et al. (2006c), "Tensile Tests and TEM Investigations on LiSoR-2 to -4", *Journal of Nuclear Materials*, Vol. 356, pp. 256-263.

Dai, Y., B. Long and F. Groeschel (2006d), "Slow Strain Rate Tensile Tests on T91 in Static Lead-bismuth Eutectic", *Journal of Nuclear Materials*, Vol. 356, p. 222.

Dai, Y, D. Gavillet and R. Restani (2008), "Stressed Capsules of Austenitic and Martensitic Steels Irradiated in SINQ Target-4 in Contact with Liquid Lead-bismuth Eutectic", *Journal of Nuclear Materials*, Vol. 377, p. 225.

Dai, Y. et al. (2011), MEGAPIE Technical Report, MPR-11-DY34-003-1.

Dai, Y. et al. (2012), "FeCrAlY and TiN Coatings on T91 Steel after Irradiation with 72 MeV Protons in Flowing LBE", *Journal of Nuclear Materials*, Vol. 431, pp. 66-76.

Dai, Y. et al. (2013), "Non-Destructive Test and Proton Distribution Profile Determination of the MEGAPIE Target", PSI Highlight 2012.

Dai Y. et al. (2014), "PIE of MEGAPIE Target", 7th Framework Programme GETMAT Deliverable D3.5.

Donegani E., L. Zanini and M. Wohlmuther (2011), MEGAPIE Technical Report.

Fazio, C., J.U. Knebel and G. Benamati (eds.) (2004), "Proceedings of the 3rd International Workshop on Materials for Hybrid Reactors and Related Technologies", *Journal of Nuclear Materials*, Vol. 335, 2, pp.147-298

Fazio, C. et al. (2005), "Assessment of Reference Structural Materials, Heavy Liquid Metal Technology and Thermal-Hydraulics for European Waste Transmutation ADS", *Proceedings of GLOBAL 2005,* Tsukuba, Japan, 9-13 October.

Glasbrenner, H., Y. Dai and F. Groeschel (2005a), "LiSoR Irradiation Experiments and Preliminary Post-Irradiation Examinations", *Journal of Nuclear Materials*, Vol. 343, pp. 267-274.

Glasbrenner, H., Y. Dai and F. Groeschel (2005b), "LiSoR Experiment: Overview and Relevant Results for MEGAPIE", *TRM-MEGAPIE Meeting*, Mol, Belgium.

Glasbrenner, H. et al. (2006), "Post-Irradiation Examination on LiSoR-3 Experiment", *IWSMT-7*, Thun, Switzerland, 2005, *Journal of Nuclear Materials*, Vol. 356, pp. 247-255.

Glasbrenner, H. and F. Gröschel (2006a), "Exposure of Pre-Stressed T91 Coated with TiN, CrN and DLC to Pb-55.5Bi", *Journal of Nuclear Materials*, Vol. 356, pp. 213-221.

Gavrilov, S. et al. (2013a), *Report on the Full Set of Results of Tests on Irradiated and Non-Irradiated Specimens*, 7th Framework Programme GETMAT DELIVERABLE D3.7 PIE of ASTIR.

Gavrilov, S. et al. (2013b), *PIE of LEXUR II LBE Capsules*, 7th Framework Programme GETMAT DELIVERABLE D3.9a.

Henry, J. et al. (2003), "Tensile Properties of 9Cr-1Mo Martensitic Steel Irradiated with High Energy Protons and Neutrons", *Journal of Nuclear Materials*, Vol. 318, pp. 215-227.

Henry, J. et al. (2008), "Tensile Behaviour of 9Cr-1Mo Martensitic Steel Irradiated up to 20 dpa in a Spallation Environment", *Journal of Nuclear Materials*, Vol. 377, pp. 80-93.

Howlader, M.M.R. et al. (1999), "*In-Situ* Measurement of Electrical Conductivity of Zircaloy Oxides and Their Formation Mechanism under Electron Irradiation", *Journal of Nuclear Materials*, Vol. 265, pp. 100-107.

Hunn, J.D., R.E. Stoller and S.J. Zinkle (1995), "*In-situ* Measurement of Radiation-Induced Conductivity of Thin Film Ceramics", *Journal of Nuclear Materials*, Vol. 219, pp. 169-175.

Jung, P. (2002), "Radiation Effects in Structural Materials of Spallation Targets", *Journal of Nuclear Materials*, Vol. 301, pp. 15-22.

Long, B. et al. (2008), "Liquid Pb-Bi Embrittlement Effects on the T91 Steel after Different Heat Treatments", *Journal of Nuclear Materials*, Vol. 377, pp. 219-224.

Long, B. (2009), *Liquid Lead-Bismuth Embrittlement Effects on Unirradiated and Irradiated Ferritic/Martensitic Steels for Nuclear Applications*, PhD Thesis No. 4355, École Polytechnique Fédérale de Lausanne.

Long, B., Y. Dai and N. Baluc (2012), "Investigation of Liquid LBE Embrittlement Effects on Irradiated Ferritic/Martensitic Steels by Slow-Strain-Rate Tensile Tests", *Journal of Nuclear Materials,* Vol. 431, pp. 85-90.

Kirchner, T. et al. (2003), "LiSoR, a Liquid Metal Loop for Material Investigation Under Irradiation", *Journal of Nuclear Materials*, Vol. 318, pp. 70-83.

Jacquet, P. (2003), *Irradiation Achieved in BR2 during Cycle 05/2002 from 26 November 2002 to 17 December 2002*, SCK•CEN Internal Memo, MI.57/D089010/02/PJ, 10 February 2003.

Lillard, R.S., M. Paciotti and V. Tcharnotskaia (2004), "The Influence of Proton Irradiation on the Corrosion of HT-9 during Immersion in Lead Bismuth Eutectic", *Journal of Nuclear Materials*, Vol. 335, pp. 487-492.

Maloy, S.A. et al. (2006), "Tensile Testing of EP-823 and HT-9 After Irradiation in STIP II", *Journal of Nuclear Materials*, Vol. 356, pp. 56-61.

Robin, P. (2008), MEGAPIE TRM 2008.

Samec, K. (2005), *Temperature Calculations of the LiSoR Experiment*, PSI Technical Report, TM-34-05-02, Paul Scherrer Institut, Villigen, Switzerland.

Sapundjiev, D., A. Al Mazouzi and S. Van Dyck (2004), *Synergetic Effects Between Neutron Irradiation and LME: PIE Tests in Lead-Bismuth Eutectic, Part I: Tests on Non-Irradiated Samples*, SCK•CEN Report R-3847, SCK•CEN, Mol, Belgium.

Sapundjiev, D. et al. (2005), "Mechanical Behaviour of Candidate Steels in LBE after Irradiation in BR2 at 200°C", *Journal of Nuclear Materials*, Vol. 356, pp. 229-236.

Sato, F. et al. (2004), "Impedance Measurements of Thin Film Ceramics under Ion Beam Irradiation", *Journal of Nuclear Materials*, Vol. 329-333, pp. 1034-1037.

Shikama, T. et al. (1998), "Electrical Properties of Ceramic during Reactor Irradiation", *Journal of Nuclear Materials*, Vol. 258-263, pp. 1867-1872.

Tanifuj, T. et al. (1998), "Electrical Conductivity Change in Single Crystal Al_2O_3 and MgO under Neutron and Gamma-Ray Irradiation", *Journal of Nuclear Materials*, Vol. 253, pp. 156-166.

Van den Bosch, J. et al. (2008), "Twin Astir: An Irradiation Experiment in Liquid Pb-Bi Eutectic Environment", *Journal of Nuclear Materials,* Vol. 377, pp. 206-212.

Van den Bosch, J. et al. (2010), "TWIN ASTIR: First Tensile Results of T91 and 316L Steel After Neutron Irradiation in Contact with Liquid Lead-bismuth Eutectic", *Journal of Nuclear Materials,* Vol. 398, pp. 68-72.

Vila, R. and E.R. Hodgson (2000), "In-Beam Dielectric Properties of Alumina at Low Frequencies", *Journal of Nuclear Materials*, Vol. 283-287, pp. 903-906.

Wagner, W. et al. (2008), "MEGAPIE at SINQ – The First Liquid Metal Target Driven by a Megawatt Class Proton Beam", *Journal of Nuclear Materials*, Vol. 377, pp. 12-16.

Weisenburger, A. et al. (2008), "T91 Cladding Tubes with and without Modified FeCrAlY Coatings Exposed in LBE at Different Flow, Stress and Temperature Conditions", *Journal of Nuclear Materials*, Vol. 376, pp. 274-281.

Willekens, M. (2004), *Neutron Dosimetry – Experiment SPIRE*, Technical Note RF&M/VWi/vwi 32.D049011-205/04-01, 14/01/2004.

Wohlmuther, M. and W. Wagner (2012), "PIE Preparation of the MEGAPIE Target", *Journal of Nuclear Materials*, Vol. 431, pp. 10-15.

9. Corrosion protection in lead and lead-bismuth eutectic at elevated temperatures*

9.1 Introduction

Compatibility of materials with liquid LBE is a key problem for Pb- and LBE-cooled systems. Steels are attacked by dissolution of their components in Pb and LBE. Dissolution has to be minimised or, even better, entirely prevented for the structural cladding and target materials in contact with Pb and LBE. One measure that is widely being used for temperatures in the range up to 500°C is dissolution of oxygen in Pb and LBE up to a concentration that allows oxidation of the structural material but not oxidation of the LBE (Gromov, 2004; Müller, 2000; Benamati, 2000). This method is described in Chapters 4 and 6 of this handbook and will not be considered here. Nevertheless, the protection measures described in this chapter also work in most cases at oxygen potentials in the ranges considered before or may also be effective at much lower potentials. In this chapter we deal with surface alloys that develop slowly growing protective oxide scales by reaction of oxygen with the alloyed elements at the surface. These scales are suitable for protection of highly loaded parts like claddings, wrappers and spacers, and heat exchangers at elevated temperatures above 500 up to 650°C (Asher, 1977; Gorynin, 1999, Müller, 2000; Deloffre, 2004; Hosemann, 2008). Other coatings or alloys that are based on refractory low soluble elements or on nitrides and carbides would require very low oxygen potentials to prevent oxidation of the coating material (Seifert, 1961; Block, 1977; Asher, 1977; Benamati, 2004). The following materials and modifications are discussed in this chapter for a successful application in liquid Pb and LBE systems:

1) surface alloying with Al, Si or FeCrAlY, which forms thin stable oxide layers in Pb and LBE containing appropriate oxygen concentrations;
2) coatings containing Al and Si, which form protective oxide layers in Pb and LBE containing oxygen;
3) coatings of refractory metals, such as W, Mo, Nb, and coatings of nitrides, carbides and ceramics, which require low oxygen potentials in Pb and LBE;
4) inhibitors like Zr, dissolved in Pb and LBE, which cause formation of a protective surface layer on the structural material.

The methods presented in points 1 and 2 above require an oxygen concentration in Pb and LBE, which allows the formation of oxide scales at the surface of the structural material. The oxygen concentration must be high enough to prevent dissociation of the oxide scale. The methods described in points 3 and 4 require an oxygen concentration low enough to prevent extensive oxidation of protective layers like nitrides, carbides and refractory metals and also inhibitors dissolved in Pb and LBE. The self-healing requirement of the protective layers has to be considered in this case.

The material surface that contacts LBE should comply with the following criteria:

- durability under irradiation;

* Chapter leads: G. Müller, G. Schumacher, A. Heinzel, A. Jianu, A. Weisenburger.

- prevention of dissolution attack;
- tolerable oxidation rate during and after oxide scale formation;
- long-term stability under normal and temporarily abnormal conditions;
- self-healing ability;
- long-term mechanical stability;
- tolerable influence on the mechanical properties of the structural material;
- feasibility on an industrial level.

The requirements concerning the material properties depend on the reactor components. The critical values of different requirements to be fulfilled by materials have to be adapted on this basis.

9.2 Methods of surface protection

9.2.1 *Alloying with stable oxide formers*

It is known from several examinations that Al and Si, alloyed into steel within appropriate concentration ranges, develop thin, stable and protective oxide scales by diffusion into the surface where they react with oxygen dissolved in LBE or lead (Asher, 1977; Gorynin, 1999; Müller, 2000; Deloffre, 2004; Hosemann, 2008). These protective scales are an effective barrier against diffusion of cations, as well as of anions, and therefore prevent a fast oxide growth that is often observed with the magnetite and spinel layers on FeCr steels. The slow-growing oxide scale ensures a long-term protection function without extensive steel oxidation. Even if scale breach happens, self-healing occurs by diffusion of the scale forming cations to defect positions, on condition that sufficient oxygen is contained in the liquid lead or lead-bismuth. Examinations of the nature of alumina scales on PM2000 ODS steel, alloyed with 5.5 wt.% Al, show that these scales are very thin, e.g. 120 nm after 400 h at 535°C exposure to LBE containing 10^{-6} wt.% oxygen (Hosemann, 2008). Considerable improvement of the corrosion resistance was also attained with Si alloyed into steel by an industrial production process (Gorynin, 1999; Kurata, 2005; Lim, 2006). An example is the Russian steel EI 852 containing 2 wt.% Si (Yachmenyor, 1999).

Improvement of the compatibility by alloying Al or Si into the steel bulk has the disadvantage of a negative influence on the mechanical and nuclear properties. This disadvantage can be avoided by alloying Al or Si just into a thin surface layer, creating a kind of functionally graded material with no influence on the mechanical properties of the bulk material. There are some examinations reported on the suitability of Al-alloyed into the surface of ferritic and austenitic steels for their protection against dissolution attack of LBE (Asher, 1977; Müller, 2000; Deloffre, 2004). Surface layers containing an alloy with Si should in principle work as protective oxide scale formers as well as described in recently published articles dealing with the development of a functional graded coating based on Fe12Cr2Si (Short, 2010a, 2012, 2013).

The procedures for alloying Al into a steel surface layer reported up to date are:

- Surface alloying by melting of a metal surface covered with an Al foil or with precipitated Al by pulsed electron beams of large diameters (GESA process) (Müller, 2005).
- Diffusion alloying which is achieved using three different procedures. The first is hot dipping of the steel into an Al melt with subsequent annealing (Glasbrenner, 1998). The second is heating of the steel covered by an Al foil beyond the melting point of Al (Heinzel, 2003). The third is calorising or pack cementation (Asher, 1977; Deloffre, 2004).

9.2.1.1 *Surface alloying by the GESA process*

GESA is a pulsed electron beam facility that is driven by a high voltage generator with a pulse duration control unit. It contains a multi-point explosive emission cathode, a controlling grid and an anode which form a triode (Engelko, 2001). The kinetic energy of the beam electrons can be varied in the range of 50 up to 150 keV, with a beam power density up to 2 MW/cm^2 at the target and pulse durations up to 40 μs. The important parameters for the melting process, the electron energy, power density and pulse duration can be chosen independently of each other. The energy density absorption at the surface of the target is up to 80 J/cm^2, which is sufficient to melt metallic materials adiabatically down to a depth of 10-50 μm. The beam diameter is 6-10 cm and this is the area of surface melting by applying one single pulse. Due to the high cooling rate of about 10^7 K/s, very fine-grained or even amorphous structures develop during solidification of the molten surface layer. This is a suitable basis for the formation of protective oxide scales with good adhesion (Müller, 2005; Engelko, 2001). The new GESA IV facility allows surface alloying of cladding tubes with small diameters by employing a cylindrical cathode (Engelko, 2001). A tube length of 32 cm can be surface-alloyed by employing one single pulse on the whole circumference.

Surface alloying of steel specimens was achieved by applying the electron pulse to the surface covered with an 18 μm thick Al foil (Müller, 2005). During melting a thin steel surface layer together with the aluminium foil, 20-25% of the Al is dissolved in the steel melt, the other part of the Al evaporates. The micrographic cross-section and the Al concentration profile perpendicular to the surface of an alloy layer are shown in Figure 9.2.1. The micrographic cross-section on the left shows the dense alloyed layer with a smooth surface and perfect bonding to the steel bulk. EDX analysis along the layer cross-section reveals that Al penetrates into the steel within the molten surface layer. Profile A was obtained with an 18 μm Al foil by applying just one electron pulse and Profile B with a second pulse after attaching a new Al foil. When an additional pulse is applied to the surface having Profile B without replacing the Al foil, Profile C is obtained, which has an almost constant concentration down to a depth of 15 μm. The concentration profiles are not typical for a diffusion process, but for a distribution by turbulences in the melt. The obtained structure consists of two phases, which contain different Al concentrations (4-10 wt.%) but having the same Cr content. One phase corresponds to Al dissolved in Fe, α-Fe(Al), the other is FeAl (Müller, 2000).

Figure 9.2.1: Micrographic cross-section (corresponding to Profile C) and EDX-Al concentration profiles after alloying Al into an OPTIFER IVc surface with 0.45 MJ/m^2

A: One pulse with 18 μm Al foil; B: Two pulses, each one with 18 μm Al foil;
C: One additional pulse onto the surface layer containing Al with B profile

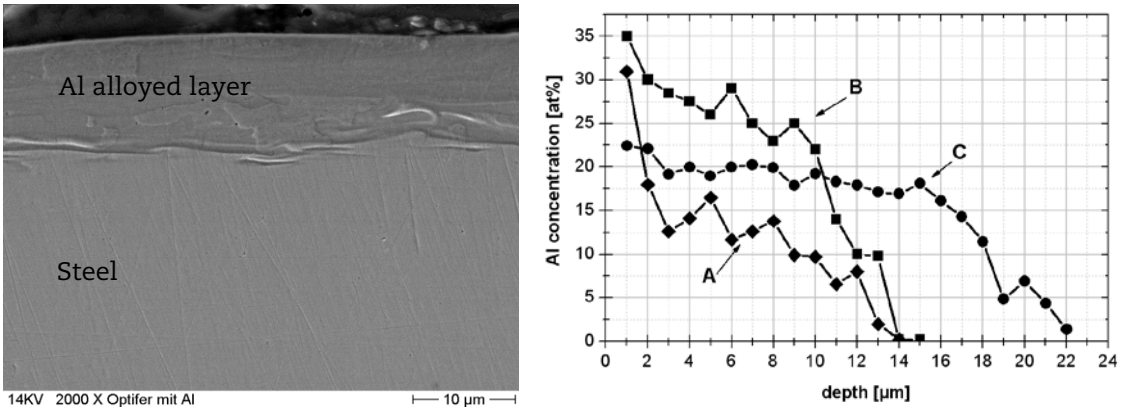

Source: Müller (2005).

Work reported on corrosion experiments with alloyed steels show that a concentration of 4 wt.% Al should be high enough to achieve selective alumina scale formation (Asher, 1977). Other examinations lead to the conclusion that 5 wt.% Al is necessary to reach that goal (Hosemann, 2008). For concentrations above 24 wt.%, however, the Al activity gets too high and dissolution attack may occur (Müller, 2002).

For a complete protection of the surface it is necessary to avoid areas in which the Al content drops below the concentration at which an effective protection by the alumina scale is expected. Therefore, insufficient overlapping of the electron beam areas during the alloying process should not happen. Applying the new GESA IV, which has a cylindrical cathode, avoids such imperfections on cylindrical surfaces (Weisenburger, 2005).

MCrAlY coatings (M=Fe, Ni, Co or NiCo) are widely applied for first and second stage turbine blades as corrosion-resistant overlays or as bond-coats for use with thermal barrier coatings (Nicholls, 2003). The corrosion resistance is based on its ability to form alumina layers on the surface due to selective Al oxidation. The coating could be applied by a number of processes like physical vapour deposition (PVD), air plasma spraying (APS) or vacuum plasma spraying (VPS), but the most common process is the low pressure plasma spraying (LPPS). To achieve a homogeneous thin 20-30 μm coating, conventional LPPS processes with ca. 60 μm particle size are not applicable. The powders are sieved to a maximal particle size below 38 μm. In addition the spray distance, powder feeding rate and number of layers are optimised. Like in a conventional LPPS process the coating head swings above the substrate surface resulting in a coating composed of several layers. Figure 9.2.2 shows a cross-section of a cladding tube wall with a ~20 μm LPPS FeCrAlY coating.[1] Coatings with Co could not be used because of its activation in a reactor, nor could those with Ni because of the high solubility of Ni in Pb and PbBi.

Figure 9.2.2: FeCrAlY LPPS coating on austenitic steel tube wall

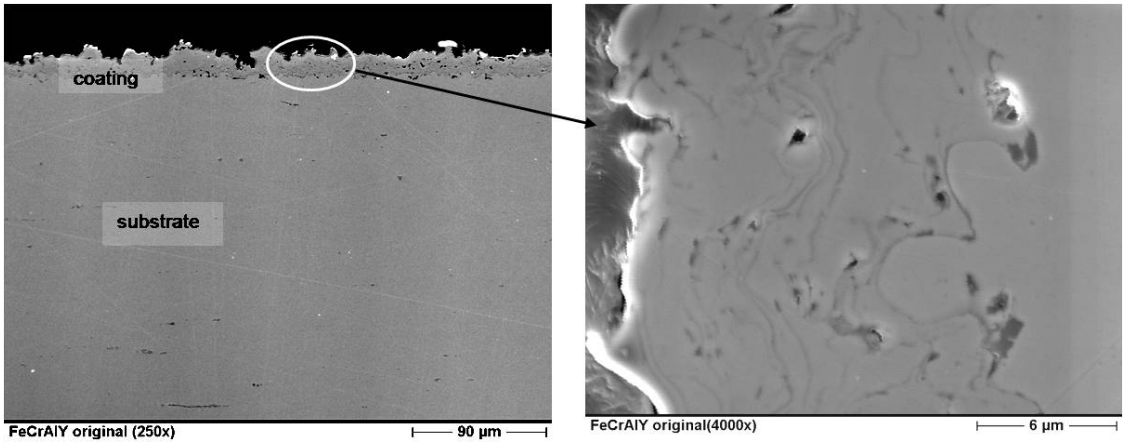

Source: Weisenburger (2005).

The coating has a rough surface because of the relatively large spray droplets, contains pores and also the adhesion on the bulk material is not perfect. To exclude these uncertainties, the coatings are treated using the GESA melting process. Experiments with GESA show that a GESA treatment smooths the surface and removes pores. Another important effect of the GESA treatment is that because of the small layer thickness the coating is "welded" to the bulk material. Figure 9.2.3 shows such a GESA-treated sample with LPPS FeCrAlY coating (Weisenburger, 2005).

1. Coating by Sulzer (Wohlen, Switzerland).

Figure 9.2.3: Cross-section of 1.4970 cladding tube wall with FeCrAlY coating after melt treatment by GESA (left); EDX analysis perpendicular to surface of coating (right)

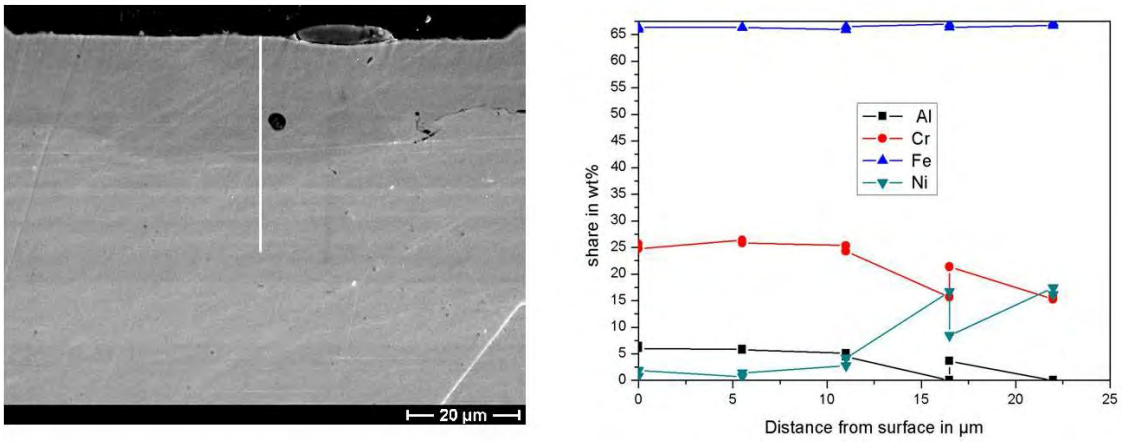

Source: Weisenburger (2005).

Looking at the microstructure of the GESA-treated FeCrAlY (24.8% Cr, 8.7% Al, 0.49% Y, Fe balance) coating after remelting together with a small surface layer by GESA in Figure 9.2.3, it could be argued that the coating attained properties like a surface-alloyed layer and can be classified as such a type of surface protection. This is because the melting zone reaches beyond the coating substrate interface and causes a mixing of both materials at this place as shown in the EDX analysis of the concentration profile.

9.2.1.2 Surface alloying by diffusion processes

As opposed to the GESA process the diffusion alloying processes cause surface Al alloys by interdiffusion between the steel matrix and the Al at the surface, which is in most cases in a liquid state. The time for interdiffusion should be long enough to lower the Al concentration at the surface to a value for which no rapid dissolution in LBE takes place that occurs with too-high Al activity. We refer here to three processes: hot dipping, pack cementation and liquefying of an Al foil at the surface.

In the hot dipping process austenitic steel specimens are dipped into liquid AlSi12(at.%) contained in an alumina crucible under an Ar5%H_2 atmosphere (Glasbrenner, 1998). The temperature of the Al is 700°C and the dipping time around 30 sec. Annealing follows at 500°C for 2 h and finally air cooling to room temperature. The Al layer is typically 50 µm thick with an interdiffusion zone of <10 µm thickness, Figure 9.2.4 (left). This is expected to lead to dissolution reactions in contact with LBE because of the high Al activity at the surface.

On martensitic steel the hot dipping procedure leads to a very thick surface layer of Al and interdiffusion zones of >100 µm, Figure 9.2.4 (right), because of the rapid diffusion of Al into the steel matrix (Glasbrenner, 1998). Therefore, hot dipping followed by annealing is not a suitable protection method for this type of steel.

An alternative method for alloying aluminium into the steel surface was also proposed (Heinzel, 2003). During the first step pure Al foil is wrapped around the steel sample and fixed with Al spray. After a drying time of 12 h at 180°C a heat treatment follows at 1 050°C for 0.5 h, when aluminium melts and an interdiffusion phenomenon occurs. A typical cross-section of an Al alloy layer obtained by wrapping the tube sample and annealing is shown in Figure 9.2.5.

Figure 9.2.4: Austenitic 1.4970 steel (left) and martensitic MANET steel (right) after hot dipping at 700°C in AlSi12 and subsequent annealing, at 500°C for 2 h and 1 050°C for 0.5 h, respectively

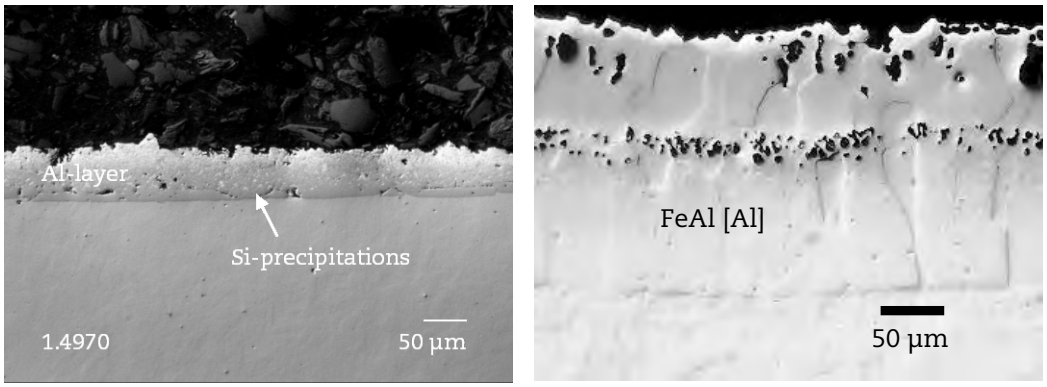

Source: Glasbrenner (1998).

Figure 9.2.5: Scanning electron microscopy (SEM) micrograph of the surface cross-section and Al concentration profile of the austenitic 1.4970 steel after melting an Al foil at the surface and subsequent diffusion annealing

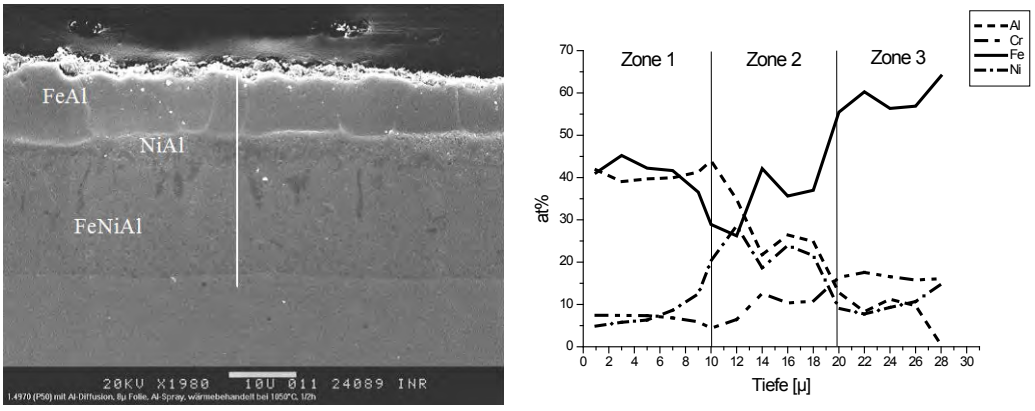

Source: Heinzel (2003).

On top of the original surface there is a FeAl layer which forms by diffusion of iron into the liquid Al layer during annealing. This zone has an Al concentration of around 40 at.% which corresponds to about 24 wt.%.The diffusion zone of 25 µm depth below the surface contains Al dissolved in Fe and in NiAl precipitations (dark), while the interface of some µm thickness contains a zone of NiAl created by Ni diffusion. The Al content can be controlled by the thickness of the Al foil, but simple specimen geometry like a tube is a precondition for this procedure. It is not suitable for martensitic steels because of the high temperature during the heat treatment and the high Al diffusion coefficient in these steels.

Another method to precipitate Al at the steel surface is by calorising or pack cementation (Asher, 1977; Deloffre, 2004). The pack cementation process described by Deloffre (2004) is industrially available for austenitic steels (ASTM B875-96 [2003]). In this process, the components to be coated are immersed in a powder mixture containing Al (source), a halide salt like NaF (activator) and an inert diluent such as alumina. When the mixture is heated at 750°C the Al source reacts with the activator to a gaseous compound which carries Al to the substrate. The gas decomposes at the substrate surface depositing Al and releasing the halogen activator. The activator returns to the powder mixture and reacts again with the Al source. A period of several hours is needed to produce such a

coating. Afterwards the Al is alloyed into the steel surface by a heat treatment at 900°C for 6 h under an argon atmosphere. On austenitic steels such a treatment leads to a 60-70 μm thick alloyed surface layer. The layer contains Fe, Al, Cr, Ni and O, with higher concentrations of Cr in the inner and of Al in the outer part. In between there are precipitates rich in Ni and Al. The alloyed layer is similarly structured like that obtained with a liquefied foil (see Figure 9.2.5).

No industrial process is available for pack cementation of martensitic steels like T91 because the tempering temperature of the pack cementation process is too high for such steels. It should be below 750°C. To accomplish this process for martensitic steels a 70Fe30Al donor with an NH_4Cl activator and Al_2O_3 inert filler was used to allow application of lower temperatures at a laboratory scale (Deloffre, 2004). The protective oxide scale was created either by *in situ* or air oxidation or by Pyrosol Al_2O_3 deposition. The thickness of the alloyed zone was 40-120 μm.

As compared to the GESA surface alloying, the diffusion alloying processes result in a concentration distribution that corresponds to an exponential profile below the original steel surface and to a surface layer which is formed by iron diffusion into the liquid Al. GESA-alloyed surface layers have a relatively even Al distribution in the whole melt region of about 20 μm. The GESA process can be applied to any steel whilst diffusion alloying processes are mainly suitable for austenitic steels. The hot-dipped steels have thick Al layers, which also after annealing have a high Al activity that leads to dissolution attack in LBE. Alloying by a liquefied Al foil and pack cementation has, compared to hot-dipping, the advantage that the thickness of the Al layer can be controlled by the thickness of the foil or the duration of the reaction process.

9.2.2 Corrosion-resistant coatings

Instead of employing the surface alloying process, refractory metals, alloys or compounds can be precipitated onto the steel surface (Ballinger, 2004).

Refractory metals like W, Mo, Nb or alloys of these metals need a clean environment with very low oxygen activity to prevent their oxidation. This is a strong requirement for a liquid metal loop. Such metals have a low solubility and are stable in LBE at low oxygen activities.

Al- or Si-containing alloys gain protective behaviour by forming a stable, dense oxide scale on the surface. These alloys require an oxygen activity that causes oxide scale formation, keeps the scales stable and allows their self-healing.

Coatings consisting of resistant compounds like carbides or nitrides need again a low oxygen activity in LBE, while oxide coatings require a higher activity to stabilise the oxide scale. Both will, however, generally not possess self-healing properties. Furthermore, long time stability and good adhesion to the steel surface is not easily being achieved.

9.2.2.1 Al- or Si-containing coatings

Al- or Si-containing coatings require oxygen in the LBE, because the protective mechanism of such coatings relies on its slowly growing thin oxide scales that are formed in the liquid LBE. An Al alloy coating that was employed for surface protection of T91 steel is Fe65Al35. The coating represented in Figure 9.2.6 precipitated by VPS is compact and has a good adherence to the substrate material. The thickness is around 6.2 μm and stays quite constant throughout the whole specimen surface area.

Good corrosion behaviours were also obtained with FeAl coatings (20 μm thickness) deposed by physical vapour deposition (PVD) exposed to stagnant LBE and Pb at 700°C with oxygen concentration of 10^{-6} and 10^{-7} wt.% (Rivai, 2010). A weakness of FeAl coatings is their brittle behaviour. Under loading the coating cracked, which leads to a corrosion attack at the 316 SS base material (Yamaki-Irisawa, 2011).

Figure 9.2.6: Fe65Al35 coating on T91 steel

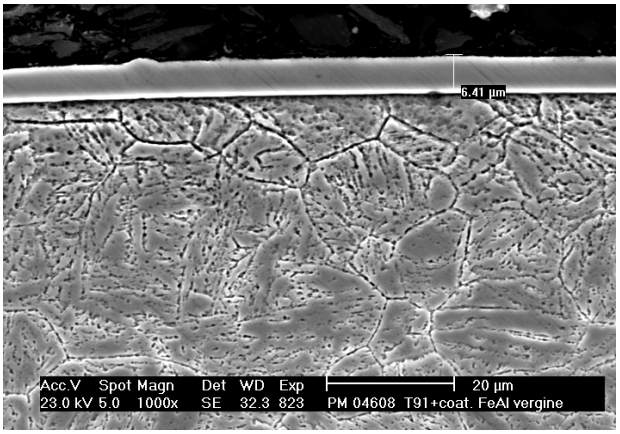

Source: Gessi (2010).

Since Si as an alloying element has a protective function like Al, a corrosion-resistant layer of the composite Fe-12Cr-2Si is proposed for T91 steel (Short, 2010). Experiments and calculations are currently being conducted on the long-term stability of the alloy with respect to Si migration into the T91 steel. Corrosion experiments are also currently being conducted.

9.2.2.2 Coatings with refractory metals

Early experiments on the compatibility of Bi with Ta, Mo and Be were carried out to explore suitable materials for the containment for liquid Bi in a liquid metal fuel reactor (Seifert, 1961). Up to this time several experiments are reported in which no appreciable attack of Bi at temperatures of up to 1 000°C was observed after several 100 h. Bi containing 5%U at 800-1 000°C had an average corrosion rate of only 0.025 mm after 5 000 h. Later, such experiments were also conducted with LBE (Romano, 1963). The results are more or less expected if one looks at the low solubilities of these metals in Bi and LBE. Low solubilities are also observed with W and Nb. These metals are all candidates for a coating to protect structural steels against the attack of LBE (Benamati, 2004). However, there are studies (Hosemannn, 2008) that come to the conclusion that Ta is not compatible with technical LBE melts because it gets embrittled by the oxygen impurities.

Several coatings with the above-mentioned metals were produced by plasma spraying (Block, 1977). However, only the Mo coating was successful because Mo was the only metal with which a satisfying coating could be achieved. This is because of the high access of oxygen to the plasma beam in which in this case MoO_3 evaporates and is not precipitated on the target. There are other possibilities to coat the surface of metals without oxide formation such as employing PVD and CVD processes and electrochemical deposition (Asher, 1977). However, cracks and spalling occur within the coatings during temperature changes. An exception was Mo on Croloy. More development work is necessary to explore the potential of such coatings.

It is obvious that dense coatings with metals of low solubility offer a good protection against LBE especially if the oxygen potential of the LBE is below that of the metal oxide formation. If this is not the case, stable oxide layer formation on the metal surface is necessary for an effective protection.

9.2.2.3 Oxide-, carbide- and nitride-based coatings

Oxide, carbide and nitride coatings are widely used in industrial applications and the technique of their precipitation on metal surfaces is well developed e.g. for the hot

sections of gas turbines for numerous cases of corrosion protection and wear resistance. These materials isolate the steel from aggressive media but have poor strength and ductility and cannot be used as a structural material. As a protective coating, however, they allow application of steels with high strength and ductility which, if unprotected, are exposed to strong dissolution attack by LBE.

There were some early attempts to employ ceramic coatings for the protection of steels against LBE. They include nitrides and borides of Ti and Zr, carbides of W, aluminium-magnesium spinel (Romano, 1963) and ZrO_2 + Y_2O_3 (Asher, 1977). The layers were, however, not dense enough to inhibit cation and anion diffusion. Lifting, cracking and spalling often occurred.

Later on it was possible to produce coatings of high density and good adherence to the steel surface. Two examples produced by CVD (Gessi, 2010) are shown in Figure 9.2.7.

Figure 9.2.7: AlTiN (left) and TiZrC (right) coating on T91 steel

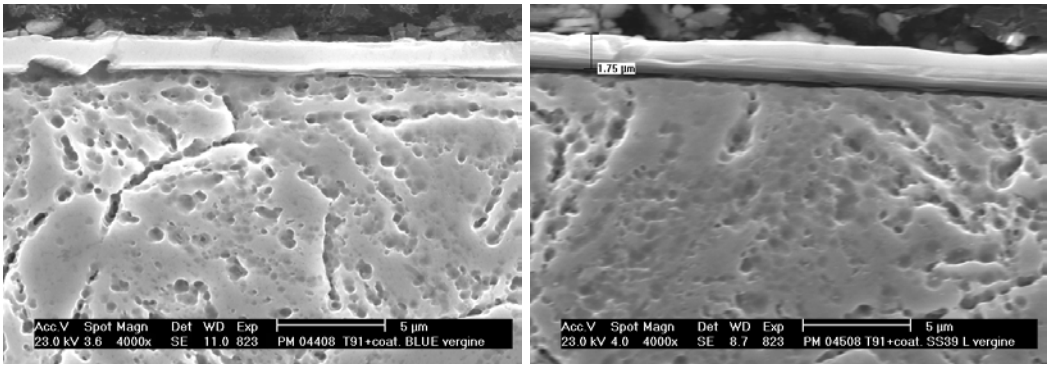

Source: Gessi (2010).

The disadvantage of this coating concept is, however, that the coatings are brittle and have no self-healing ability and a fracturing or spallation of the coating would lead to a direct dissolution attack on the uncovered part of the steel by LBE. This is the main problem with oxide, carbide and nitride coatings and it is enhanced by the fact that bad adherence may exist as well as stresses because of the differences in thermal expansion.

Examples of brittle ceramic behaviour are SiC and Si_3N_4, which were tested in flowing LBE up to 2 000 h at 550°C and an oxygen concentration of 10^{-6} wt.%. They showed good corrosion resistance but the observed cracking of the coating, probably during cutting of the specimens before the exposure, was its major drawback (Takahashi, 2011).

TiN, (CVD) CrN (PVD, see Figure 9.2.8), and diamond-like carbon coatings (DLC) of good adherence were obtained from Ion Bond AG (Olten, Switzerland) and employed for examination in the LBE of the CORWETT loop (PSI, Villigen, Switzerland) under stress at a temperature of 350°C (Glasbrenner, 2006b).

9.2.3 Corrosion inhibitors in LBE

By definition inhibitors are substances which, when added to a chemical system in small amounts (in the order of only 10^{-3} wt.%), interact with the reactants to reduce the reaction rate. By this definition oxygen dissolved in LBE acts as such an inhibitor through the formation of a stable oxide film which reduces the dissolution rate. Additions of other elements such as Zr or Ti and Mg to low oxygen LBE may also provide an inhibitive effect (Hodge, 1970; Asher, 1977; Shmatko, 1998). The mechanism assumed is first reduction of the oxides at the surface by Mg then formation of nitrides of Zr and Ti, which are insoluble in LBE and form a protective surface layer (Hodge, 1970). If enough nitrogen is present in the steel, protective TiN or ZrN films will form at first. After consuming all the

nitrogen (most structural steels contain nitrogen in the order of several ppms) TiC and ZrC films start to grow (Ilincev, 2002). The existence of such films was experimentally proofed. Synergetic effects have not been reported. An indirect proof of the TiC, TiN or ZrC, ZrN role is that inhibition is most effective on steels which are rich in both C and N and are characterised by a low content of Cr, Mo, V and other carbide and nitride-forming elements (Ilincev, 2002).

Figure 9.2.8: CrN coating on T91 steel obtained by PVD

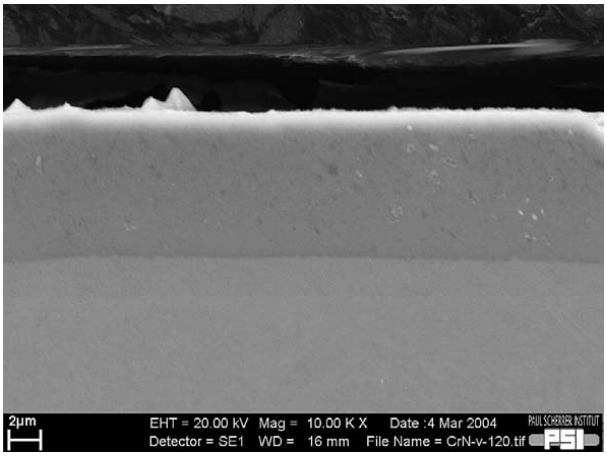

Source: Glasbrenner (2006a).

Inhibited corrosion rates of low-alloyed steels were examined as a function of temperature (Weeks, 1958) in comparison to reference tests without an inhibitor, postulating that Zr/Ti solubilities in LBE are the most important factors affecting inhibition. Diffusion is of secondary importance. Stainless chrome, chrome-nickel and low-alloyed steels stabilised with strong carbide- and nitride-forming elements do not form protective films and corrode as in LBE without an inhibitor (tests with reference samples).

To determine an optimal (in any case: low) concentration of the inhibitive additives and maintaining it at this low level during the whole loop operation and to explain the role of particular alloying elements in steels on the formation and mechanical stability of protective inhibitive films is still an obvious need. Long-term tests in large devices are required before the inhibition method could be utilised on a large scale (Park, 2000).

Proper mixing procedures, which assure a homogenous distribution of the inhibitor within the LM as well as maintaining its amount at a constant level during the whole loop operation, are a crucial demand.

9.3 Corrosion resistance of alloyed surfaces and coatings

9.3.1 *Alloyed surfaces*

Early corrosion experiments at 720°C with calorised (pack cementation) Croloy steel (Asher, 1977) resulted in no attack after 56 days in lead. It was assumed that traces of oxygen in the lead caused a self-healing protective alumina scale. The concentration of oxygen was not specified. It was assumed to be very low because the melt was blanketed with Ar+2%H_2.

During the last two decades, several experiments with surface-alloyed steel have been conducted in stagnant and flowing LBE with oxygen concentrations in the range of 10^{-4}-10^{-13} wt.%. The experimental conditions and results are listed in Tables 9.3.1 and 9.3.2. Most of the experiments were conducted with Al surface alloys produced by surface alloying with the GESA process and by pack cementation.

Table 9.3.1: Experimental evaluation of the surface alloys compatibility with stagnant LBE

Surface alloying method	Pb/ PbBi	Test facility	Temp. (°C)	Oxygen conc. (wt.%)	Time (h)	Material	Results	Ref.
Calorising	Pb	Lab. 0.13 m/s	720	Low, Ar_2H_2	1 340	Croloy	Protective alumina scale.	Asher (1977)
Al + GESA	Pb	COSTA	550	10^{-6}	1 500 2 500	1.4970, OPTIFER IVc	Thin protective layers.	Müller (2000, 2003)
Hot-dipped Al 12 at.% Si	PbBi	Prometey (0.5 m/s); IPPE (1.3 m/s)	420, 550, 600	10^{-6}	4 000 7 500	316L, 1.4970	Dissolution of Al layer starts at 420°C and is completed at 600°C (pure Al on surface).	Müller, (2002, 2004a)
FeAl by pack cementation + *in situ* ox	PbBi	COLIMESTA	350, 500, 600	10^{-9}-10^{-8}	3 000	316L, T91	Protective layers up to 500°C; at 600°C partial destruction of the alloyed layer occurred with consequent steel oxidation and dissolution attack.	Deloffre (2004)
Pack cementation + oxidation								
Pack cementation + pyrosol Al_2O_3 deposition								
Pack cementation	PbBi	COLIMESTA	350, 500, 600	10^{-9}-10^{-8}	3 000 10 000	316L		
Pack cementation, industrial	PbBi	IPPE facilities	470, 600	$2.5 \cdot 10^{-4}$ $9 \cdot 10^{-4}$ $4 \cdot 10^{-9}$ $4.3 \cdot 10^{-13}$	1 000	316L	Protective at 10^{-4} wt.%, deep cracks at low oxygen concentrations.	Deloffre (2004)
FeAl by pack cementation	PbBi	JAERI facility	450, 550	Saturated	3 000	F82H, 9Cr- JPCA, 410SS, 430SS, 2,25Cr-1Mo	Layer produced by pack cementation showed corrosion resistance, while hot-dipped samples had severe corrosion attack.	Kurata (2004)
Hot-dipped Al								
9Cr-ODS + GESA Al	PbBi	COSTA	650	10^{-6}	10 000	9Cr ODS	Good corrosion resistance, some local oxide nodules.	Takaya (2012)

Table 9.3.2: Experimental evaluation of surface alloys' compatibility with flowing LBE

Surface alloying method	Pb/ PbBi	Test facility	Temp. (°C)	Oxygen conc. (wt.%)	Time (h)	Material	Results	Ref.
Al-foil diff.	PbBi	Prometey (0.5 m/s); IPPE (1.3 m/s)	420, 550, 600	10^{-6}	4 000 7 500	316L, 1.4970	FeAl on the surface forms stable, thin alumina layer.	Müller (2004a)
Pack cementation, industrial performed	PbBi	CICLAD (2.3 m/s)	400	10^{-11}-10^{-12}	500	316L	Localised attacks on the coating, but only at external parts.	Deloffre (2004)
Pack cementation, industrial performed	PbBi	IPPE (1.3 m/s)	470, 600	10^{-6} 10^{-7}-10^{-8}	1 000	316L	Protected up to 600°C, near sample holder some local corrosion problems because of PbBi turbulences.	Deloffre (2004)
Al-GESA	PbBi	CORRIDA	550	10^{-6}	5 000	ODS, P122	No reaction, thin alumina scales.	Schroer (2004)
Al-GESA	PbBi	Tokyo Inst. of Technol.	550	10^{-6}	2 000	T91, E911, ODS	Thin protective alumina. scale, oxide growth in places with too low Al concentration.	Heinzel (2006)
FeCrAlY GESA-alloyed	PbBi	IPPE loop	500, 550, 600	10^{-6}	5 000	1.4970	No dissolution attack, no spallation of the surface layer.	Weisenburger (2008a, 2009)
FeCrAlY GESA-alloyed (Al < 4 wt.%)	PbBi	CORRIDA	550	10^{-6}	11 000	T91	Only some surface parts with thin scale otherwise thick oxide layers.	Weisenburger (2010a)

In all GESA-alloyed specimens stable protective oxide scales with no attack of LBE up to 650°C and 10 000 h are observed. This concerns the austenitic AISI-316, 1.4970, P122 and ODS steels as well as martensitic OPTIFER IVc steel exposed to stagnant LBE with 10^{-4}, 10^{-6} and 10^{-8} wt.% oxygen in the COSTA device. The alumina scales also stay very thin (below 2 μm) after 10 000 h of exposure (Müller, 2000, 2003).

Al surface alloys on T91 and 316L produced by pack cementation (Section 9.2.1.2) were tested in the COLIMESTA facility (CEA Saclay, France). The specimens were exposed to stagnant LBE with oxygen concentrations of 10^{-9}-10^{-8} wt.% for 3 000 h at temperatures of 350, 500 and 600°C. No dissolution attack of LBE was observed up to 500°C. For the alloyed 316L steel the exposure was extended to 10 000 h without LBE attack at temperatures up to 500°C. Above 500°C, however, the experiments caused a measurable dissolution attack as early as 1 000 and 3 000 h (Deloffre, 2004). Static experiments performed at IPPE (Obninsk, Russia) at 470 and 600°C, on the other hand, resulted in formation of protective, stable oxide scales on surface-alloyed (Al) AISI-316 at high oxygen concentration (9×10^{-4} wt.%) after exposure for 1 000 h. Decreasing the oxygen concentration to 4.3×10^{-13} wt.%, however, led to unsatisfying corrosion behaviour with deep cracks in the coating.

Six Japanese austenitic steels, surface-alloyed by pack cementation, also showed corrosion resistance in stagnant LBE (saturated in oxygen) at a JAERI facility. After 3 000 h no attack took place on the steel at 450 and 550°C (Kurata, 2004). The same steels, with the surface-alloyed by hot dipping, suffered, however, from severe dissolution attack under the same conditions. The tested steels were: F52H, JPCA, 410SS, 430SS, 2.25Cr-1Mo and Mod9Cr-1Mo.[2]

Experiments performed on hot-dipped austenitic AISI-316 and 1.4970 steels in flowing LBE at Prometey (St. Petersburg, Russia) (0.5 m/s) and IPPE (1.3 m/s) loops showed also a reduced corrosion resistance: dissolution of the Al layer started at 420°C and became heavy at 600°C after 4 000 h of exposure (Müller, 2002). The Al activity on the surface of the hot-dipped steels was so high that Al dissolution proceeded even before oxide scale formation occurred.

Looking at other IPPE loop experiments (1.9 m/s) performed at 470 and 600°C in LBE with 10^{-8}-10^{-7} and 10^{-6} wt.% oxygen, successful protection is observed after 1 000 h in case of AISI-316 steel surface-alloyed with Al by pack cementation. Exceptional corrosion probably initiated by erosion due to turbulences near one specific sample holder, however, led to severe corrosion phenomena at this place. Experiments with this type of specimen in the CICLAD device (rotating flow speed 2.3 m/s) at 400°C and very low oxygen concentrations (10^{-12}-10^{-11} wt.% O) also resulted in localised attack by LBE (Deloffre, 2004).

The formation of a continuous, protective oxide scale was observed on AISI-316 and 1.4970 steels alloyed by melting an Al foil at the surface using the GESA process (Section 9.2.1.2). The specimens exposed at 420, 550 and 600°C to flowing LBE (10^{-6} wt.% O) in the IPPE (1.3 m/s) and Prometey (0.5 m/s) loops developed a thin alumina scale with no signs of LBE attack after 7 500 h (Müller, 2002, 2004a). Simultaneous experiments under these conditions performed on two unalloyed steels led to the formation of thick oxide layers at 550°C and severe dissolution attack by LBE at 600°C on both steels. Other experiments, conducted with ODS, P122, T91 and E911 steels after alloying Al into the surface using the GESA process, also showed positive protection properties. They were carried out in the CORRIDA loop (KIT, Germany) at 2 m/s and in the loop of Tokyo Institute of Technology at 1 m/s, in LBE with 10^{-6} wt.% oxygen. Thin alumina scales protected the steels and no attack of LBE was observed (Schroer, 2004; Heinzel, 2006).

Good protection behaviour was observed with FeCrAlY surface-alloyed 1.4970 cladding tubes (GESA melting treatment of FeCrAlY coating) (compare Figures 9.2.2 and 9.2.3) exposed up to 10 000 h to flowing LBE containing 10^{-6} wt.% oxygen at 500-600°C in the IPPE loop (Weisenburger, 2005). The melting treatment was performed with the GESA IV device. The microstructure of the modified FeCrAlY coating shows columnar grains, grown perpendicularly to the surface (Figure 9.3.1[a]).

Other GESA-modified FeCrAlY coatings on T91 cladding tubes were successfully tested for 2 000 h in flowing LBE with 10^{-6} wt.% oxygen at 480, 550 and 600°C (Weisenburger, 2008a). Irrespective of the flow velocity, adjusted at 1, 2 and 3 m/s, the alumina scale grown on the surface was very thin (below 1 μm in all cases), protecting the steels against interaction with the LBE melt. The EDX line scan performed on the cross-sections of the exposed specimens clearly demonstrated the presence of Al-rich oxide at the surface (Figure 9.3.1[b]). The chromium peak, appearing immediately beneath the Al and O peaks, drives to the conclusion that a Cr-rich oxide layer was formed, most probably during the initial stage of the oxidation process. (Weisenburger, 2013). Some regions with Fe-rich oxide were also observed in the scale, which is in accordance with the analysis performed by Hosemann (2008) on a bulk FeCrAlY alloy (Section 9.3.3).

2. See Chapter 6 for the chemical composition of the steels.

Figure 9.3.1: (a) SEM of etched cross-section of a FeCrAlY coated T91 after GESA melt treatment; (b) SEM and EDX of the cross-section of a FeCrAlY coated T91 cladding tube wall after 2 000 h exposure to flowing LBE (10^{-6} wt.% oxygen) in a liquid metal loop of IPPE Obninsk

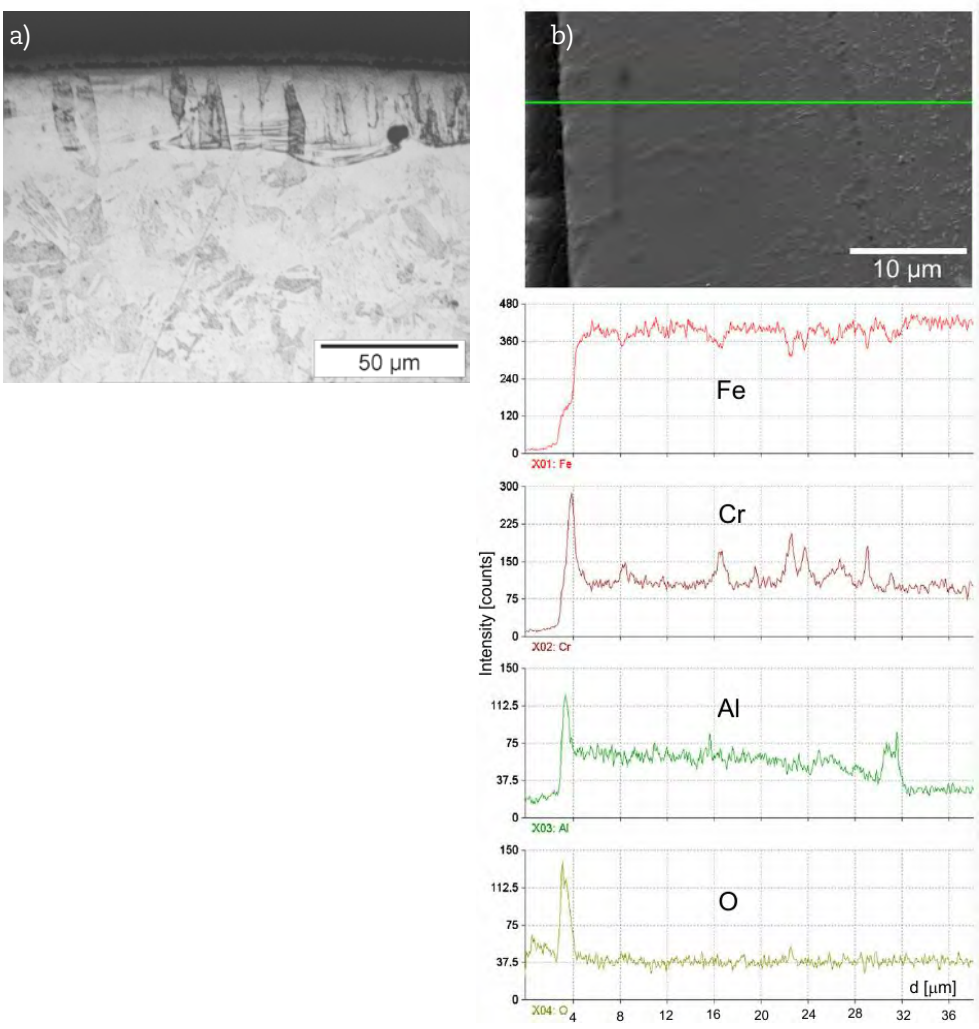

Source: Weisenburger (2008a).

The alumina layers protect the steel not only against LBE attack but also strongly diminish oxygen diffusion into the coating and bulk material up to 600°C which was the highest temperature in these experiments. Specimens of T91 without coating exposed in the same loop under the same conditions suffered from oxide scale growth of more than 20 µm thickness and loss of the outer magnetite layer by erosion after only 2 000 h (Weisenburger, 2008a).

Successful methods of alloying Al into the steel surface are:

- surface alloying by GESA, as well as pack cementation for austenitic steels;
- FeCrAlY coating with subsequent modification by GESA process.

The temperature range, in which surface-alloyed austenitic (pack cementation) and austenitic and ferritic/martensitic steels (GESA process) were tested in Pb or LBE, showing corrosion resistance by forming a thin Al-rich scale, was between 470-480 and 600°C.

In these experiments the oxygen concentration was between 10^{-8} and 10^{-4} wt.%. The maximum exposure time of 10 000 h and the maximum velocity of 3 m/s were achieved in case of GESA surface-alloyed FeCrAlY.

9.3.2 *Coatings*

A comprehensive list of the corrosion experiments conducted on ceramic and metallic coatings in Pb and LBE is provided in Tables 9.3.3 and 9.3.4.

Aluminium-containing coatings are developing protective and stable alumina layers, through Al selective oxidation process, when exposed to Pb and LBE containing small amounts of oxygen. Experiments which were conducted with a FeAl coating on Manet steel which was oxidised before exposure resulted in no attack in a Pb-17Li loop after 10 000 h at 450°C (Borgstedt, 1994) Experiments in LBE with FeAl coatings on T91 in the CORWETT loop (Glasbrenner, 2006a) at 350°C for 6 000 h showed also successful protection of the steel.

Also, a positive behaviour showed AlTiFe coating with Al content of 2.8 and 4.2 wt.%, which were produced by Al powder alloy coating with a laser beam. While at 2.8 wt.% oxide nodes of Fe and Cr were possible, a thin Al oxide scale was formed at the specimen with 4.2wt.%Al. The specimens were exposed at 10^{-6}wt oxygen in LBE at 550°C, 1 000-3 000 h. At Al contents of 17.8 wt.% cracks occurred during the coating process (Kurata, 2011, 2012).

Table 9.3.3: Experimental evaluation of coatings compatibility with stagnant LBE

Type of coating	Pb/ PbBi	Test facility	Temp. (°C)	Oxygen conc. (wt.%)	Time (h)	Material	Results	Ref.
Mo plasma sprayed-on	Pb		720	Not known	1 344	Croloy	No visible attack.	Asher (1977)
Nb by galvanic deposition Nb_2O_5/Nb	PbBi	ENEA, Brasimone Laboratory	480	Mg in LBE, H_2 bubbling	1 000	EUROFER97, T91	No visible reaction.	Benamati (2004)
Nb by magnetron sputtering Nb_2O_5/Nb								
Nb by galvanic deposition + oxidation Nb_2O_5/Nb								
Nb by magnetron sputtering + oxidation Nb_2O_5/Nb								
AlTiFe (A: 2.8Al, B: 4.2Al; 3Ti, C: 17.8Al)	PbBi	JAEA	550	10^{-4}-10^{-6}	1 000 3 000	316SS	2.8 Al oxide nodes of Fe and Cr, 4.2 Al thin Al oxide, 17.8 Al cracks during coating.	Kurata (2011, 2012)
Al-Fe (UBMS/PVD)	LBE Pb	TIT	700	$5{\cdot}10^{-6}$ $4.5{\cdot}10^{-7}$	1 000 500		Very thin oxide layer, layer crack under loading.	Rivai (2010); Yamaki-Irisawa (2011)

Table 9.3.4: Experimental evaluation of coatings compatibility with flowing LBE

Type of coating	Pb/ PbBi	Test facility	Temp. (°C)	Oxygen conc. (wt.%)	Time (h)	Material	Results	Ref.
Mo flame spraying	Pb		700-720	Reduced	Up to 1 344	Croloy	Coatings did not remain intact; the bad performance of most coatings seems to be independent of the production process, but Mo (plasma sprayed) and Al show some promise.	Asher (1977)
Mo and $ZrO + Y_2O_3$ plasma spraying								
Mo chemical deposition						Croloy		
Ta electro-chemical								
Ta vapour phase						Croloy, stainless steel		
Al pack cementation						Croloy		
WC, Al_2O_3, Mo, Ti plasma and flame spraying	Pb		Up to 1 127	Reduced	100-120	Incolloy 800, X15Cr-NiSi 25 20	All coatings except Ti protected the steels; because of the different expansion coefficient of steel and protective layer, no tight interlocking and some cracks were observed.	Block (1977)
FeAl (CVD)	PbBi	CORRWETT	350	Sat.	6 000	T91	No dissolution attack, no spallation of the surface layer.	Glasbrenner (2004)
TiN (CVD)								
CrN (PVD)								
DLC (low temp. coating process)								
SiC, Si_3N_4	PbBi	TIT loop	550	10^{-6}	2 000	Ceramic	No chemical segregation, but cracks at the surface due to the cutting of the specimens before exposure.	Takahashi (2011)
Nb by magnetron sputtering, Nb by electron sputtering	PbBi	LECCOR		10^{-10}		T91	No visible reaction.	Benamati (2004)

In the last decade coatings, consisting of ceramics and refractory metals obtained by different methods, have been also tested for their compatibility with Pb and LBE. Two nitride coatings, TiN and CrN, and one diamond-like carbon (DLC) coating deposed on T91 steel were exposed to LBE at 350°C in the CORWETT loop for 6 000 h. The experiments were conducted to examine the influence of the stresses on the integrity and on the protection capacity of the coatings (see also Chapter 4). The regions located outside the stressed zones did not show any deteriorations caused by the flowing LBE for all three coatings (Glasbrenner, 2006b).

Niobium coated on the surface of EUROFER97 and T91 steel did not react with LBE under strongly reducing conditions at 480°C during 1 000 h of exposure (Benamati, 2004). This is due to the very low solubility of Nb in LBE. Nb coating with an Nb_2O_5 oxide scale produced by Nb anodisation is also resistant against attack by LBE in the temperature range of 450-500°C. Appropriate oxygen potential control is required in this case to prevent Nb_2O_5 decomposition. Experiments with tungsten coating in LBE indicate that the coating is not compatible if the LBE is saturated with oxygen. A 50 μm thick reaction layer of WO_3 and Pb-W complex oxide covers the surface after 2 000 h at 520°C (Benamati, 2004).

Useful information concerning the behaviour of refractory metals like W, Mo and Ta, when exposed to Pb and LBE, were obtained during corrosion tests performed on bulk samples (Fazio, 2003; Benamati, 2005). After exposure in flowing LBE with low oxygen content all refractory metals exhibited smooth surfaces even after 4 500 h. The weight loss was measured and, in the cases of W and Mo, it could be associated with the uniform dissolution, due to the low solubility of W and Mo in LBE at 673 K. Ta exhibited a different behaviour, showing a weight gain due to a presumable formation of a very thin oxide layer.

Early experiments in molten Pb performed on coatings with refractory elements (Asher, 1977), have shown that, in case of W and Ta, cracks and spalling of the coating occur due to the expansion coefficient mismatch between coating and substrate. However, molybdenum coating, thermal sprayed-on Croloy (low chromium steel), did not show cracks or spalled regions.

In conclusion, coatings based on ceramics and refractory metals have raised concerns related to crack susceptibility, dissolution attack and lack of self-healing, which are diminishing their possibility to be used in Pb and LBE environments.

9.3.3 Bulk alloys

Although the focus of this chapter is on surface alloys and coatings, useful information can be obtained from the evaluation of corrosion behaviour of bulk alloys containing slowly growing oxide formers like Al and Si, during their exposure to Pb and LBE, containing small amounts of oxygen.

A review on the experiments conducted with bulk alloys containing Al or Si is given in Table 9.3.5.

Screening experiments on bulk FeCrAlY (Fe-based alloy with 15 wt.% Cr, 4.0 wt.% Al) and Tantiron (Fe-based alloy with 13.5 wt.% Si) were carried out at 700°C in flowing lead (0.13 m/s) at low oxygen potentials (Asher, 1977). No signs of dissolution attack of the liquid lead were observed on both steels, after 551 and 56 days of exposure, respectively. More recently, a very thin Al-based oxide layer was detected on FeCrAlY (22 wt.% Cr, 5 wt.% Al) as the corrosion protection barrier, after exposure to oxygen-saturated LBE at 550°C and 3 600 h (Chen, 2012).

Numerous experiments were conducted on steels alloyed with Si, especially in the low concentration region up to 3 wt.%. The first experiments reported on austenitic steels, containing up to 3 wt.% Si, resulted in formation of a relatively thin oxide scale. The thickness of the protective oxide scale reaches levels up to 20 μm, after 12 000 h of exposure to LBE in a narrow region around 10^{-6} wt.% oxygen at 550°C (Gorynin, 1999). The same steel, without Si addition, formed an oxide scale higher than 80 μm thick under similar conditions. Another experiment, performed on SX steel (17.6Cr, 4.8Si) at 450 and 550°C, showed the formation of a thin protective SiO_2 scale at the surface, after 3 000 h exposure in LBE with saturated oxygen content (Kurata, 2005).

Table 9.3.5: Experimental evaluation of Si/Al alloyed bulk steels compatibility with LBE

Material	Si/Al conc. (wt.%)	Pb/ PbBi	Temp. (°C)	Oxygen conc. (wt.%)	Time (h)	Stag. or flow.	Results	Test facility	Ref.
FeCrAlY Tantiron	4 Al 13.5 Si	Pb	720	Low, $Ar2H_2$	13 000 1 340	Stag.	No attack on both steels.		Asher (1977)
EP823 ODS Fe20Cr	1.8 Si 5.5 Al	PbBi	300-470 535	10^{-6}	3 116	2 m/s	Si reduces oxide growth.	CU-1M (IPPE)	Barbier (2001)
JPCA 316 SS SX	0.5 Si 0.69 Si 4.8 Si	PbBi	450 + 550	Sat.	3 000	Stag.	450°C: All steels are protected. 550°C: JPCA, 316SS dissolution attack. SX is protected by a thin SiO_2 scale.	No name	Kurata (2004)
SUH3 (11Cr) NTK04L (18Cr)	2 Si 3.34 Al	PbBi	550	$2{\cdot}10^{-8}$	1 000	1 m/s	In general the weight loss decreases with increasing Cr content.		Kondo (2004)
Fe-Si alloys	1.24/ 2.55/ 3.82	PbBi	400, 500, 600, 700	Below Fe/Fe_3O/ FeO form.	100-1 000	0.2 m/s	No effect of Si on surface protection.	Forced con-vection corrosion cell	Loewen (2004, 2005)
Fe12Cr Fe2.25Cr Fe18Cr Fe18Cr Fe18Cr	0.5 Si 1.25 0.5 1.25 2.55	PbBi	600	Below Fe/Fe_3O_4/ FeO form.	100-300	Stag.	Reduction of oxide layer thickness with increasing Si content.		Lim (2006)
Fe20Cr	5.5 Al 4.5 Al	PbBi	535	10^{-6}	600	2 m/s	Protective thin alumina scale at 5.5 wt.%, pitting at 4.5 wt.%.	LANL	Hosemann (2008)
ODS Fe17.3Cr Fe13.7 & 16.1Cr Fe15.8Cr	3.5 Al 3.4 Al 1.9 Al	PbBi	550-650	$10^{-6}/10^{-8}$	3 000	Stag.	Protective thin alumina scale (3.5Al), protective scale + internal oxidation (3.4Al), protective scale at 10^{-6} + dissolution at 10^{-8}, (1.9 Al).	COSTA FZK	Takaya (2009)
Kanthal-D 22 Cr Kanth.-AF 22 Cr Kanth.APM 20-23 Cr Kanthal-Alkrothal 15 Cr	4.8 Al 5.3 Al 5.8 Al 4.3 Al	LBE Pb	500-750	$10^{-6}/10^{-8}$	1 000		500°C: Thin scale on D & AF; at 10^{-6} & 10^{-8} + IOZ on APM & ALK. 600°C: Thin scale at 10^{-8}; scale + IOZ in Pb at 10^{-6}. 750°C: Thin scale at 10^{-6}, dissol. at 10^{-8} in LBE.	COSTA FZK	Del Giacco (2012)

Table 9.3.5: Experimental evaluation of Si/Al alloyed bulk steels compatibility with LBE (*cont.*)

Material	Si/Al conc. (wt.%)	Pb/ PbBi	Temp. (°C)	Oxygen conc. (wt.%)	Time (h)	Stag. or flow.	Results	Test facility	Ref.
Fe12Cr2Si (to be used as a functionally graded composite)	2 Si	LBE	600-715	$10^{-9}/10^{-6}$	506	Stag.	Oxide scale of Cr_2O_3 with SiO_2 underneath.		Short (2012, 2013)
316SS-Si T91-Si	2.5 Si 1.5 Si	LBE	550	10^{-5} 10^{-8}	1 372 1 200	Stag.	10^{-5}: 316Si oxide nodes, T91Si oxide layer more than half thinner in comparison to T91. 10^{-8}: Dissolution.	JAEA with oxygen sensor	Kurata (2013)
Fe22Cr5Al	5 Al	LBE	550	Sat.	3 600	Stag.	Thin alumina layer (837 nm).		Chen (2012)
ODS Fe14.7CrAl0.51Zr Fe14.7CrAl0.46Hf	3.3 3.8	PbBi	650 700	10^{-6}	Up to 10 000	Stag.	3.3 Al: at 650°C IOZ with a thickness of 10-100 μm, at 700°C large alumina nodules underneath the surface oxide scale. 3.8 Al: Dense Al oxide layer at 650 and 700°C.	COSTA	Takaya (2012)
FeCrAl	4-8	Pb	400-600	10^{-6}	1 000	Stag.	Formation of alumina at all temperatures at Cr content between 15.5 and 17 wt.% and Al between 6 and 7.5 wt.%.		Weisenburger (2013)

Although these are desired results, this method cannot be followed because, above 1.5-2 wt.% of Si, the steel impact strength decreases rapidly due to embrittlement (Gorynin, 1999) and to the decrease of the resistance against radiation damage. In case of low Si concentrations, such as 0.5 and 0.69 wt.%, experimented in JPCA and 366 steels, respectively, thick stratified oxide scales were developed and dissolution attack appeared at 550°C.

Systematic investigations of the influence of Si on surface protection in LBE with oxygen activities below that for the $Fe/Fe_3O_4/FeO$ stability range showed the importance of Cr concentrations in steel (Ballinger, 2003; Lim, 2006). While Si concentrations of up to 3.8 wt.% have no positive effect on protection of low Cr martensitic steel, in case of martensitic steels with 12-18 wt.% Cr, the thickness of the protective spinel oxide scale is drastically decreased by increasing Si concentration up to 2.25 wt.%. It is believed that a network of precipitated SiO_2 and Fe_2SiO_4 localised beneath the Cr-rich oxide layer forms a barrier for diffusion of oxygen into the steel matrix (Lim, 2006). Based on these results Short (2010a, 2012, 2013) tested Fe12Cr2Si material, which should be used as a functional graded composite. At an oxygen concentration of approximately 10^{-9} and 10^{-6} wt.% in LBE, after 506 h at 600°C and 715°C, a Cr_2O_3 layer with SiO_2 underneath was detected at the surface of the specimens.

Steels EI 852 and EP 823 containing 1.5-2 wt.% Si were exposed to LBE with oxygen concentrations around 10^{-6} wt.% in IPPE (Obninsk, Russia) loops with a flow velocity of 1.2-2 m/s at temperatures of 560 and 620°C. A thin oxide layer of 3-5 μm protected the steels after 2 300-2 598 h at 620°C and after 8 000-12 000 h at 560°C (Yachmenyov, 1999).

The formation of thin alumina oxide scales on two ODS steels containing 20 wt.% Cr and 5.5 (P2000) and 4.5 (MA965) wt.% Al was observed after exposure for 600 h at 535°C to flowing LBE (2 m/sec) containing 10^{-6} wt.% oxygen (Hosemann, 2008). Scale analysis was conducted by X-ray photoelectron spectroscopy sputter depth profiling (XPS-SDP). Figure 9.3.2 presents the measured amount of oxygen at the surface and the amount of oxygen, calculated for oxidised marked elements (Cr_2O_3, Fe_3O_4, Al_2O_3 and Y_2O_3). They show good agreement up to a depth of 190 nm.

Figure 9.3.2: Composition (estimated) of the thin protective oxide scale on the surface of ODS steel P2000 (5.5 wt.% Al)

Solid line: measured oxygen concentration in the oxide layer; dashed line: oxygen concentration calculated from the oxides with the lowest oxygen potential in the respective region

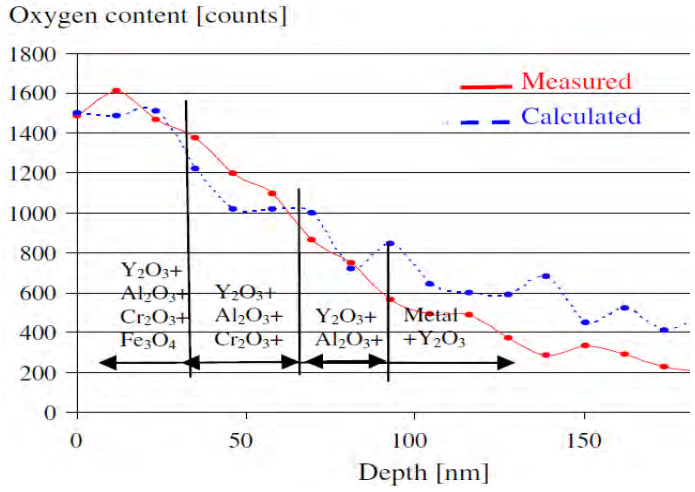

Source: Hosemann (2008).

The scales on the surface of the P2000 steel have a multi-layer structure, as shown in Figure 9.3.2. The elemental concentration within the first two zones below the surface is 20-30 wt.% Al, 10-15 wt.% Fe, 5-6 wt.% Cr and 0.17 wt.% Y. The oxide scale has an outer 0.35 μm thick layer consisting mainly of alumina containing a much smaller amount of Fe and Cr oxides and some Y_2O_3. It is followed by a 0.35 μm layer containing Cr, Al, Y oxides, again with high alumina concentration. The innermost layer of 0.25 μm contains Al, Y oxides with diminishing alumina share. The oxides noted within the marked zones are estimated by comparison of the measured oxygen concentration with that calculated for the formation of the oxides with the lowest oxygen potentials. Once the oxide scale has been built up, the oxygen supply to the bulk material below the scale gets so low that only the strong oxide formers are oxidised. Furthermore, the scale keeps ion migration so low that oxide scale growth cannot be considered a problem (Hosemann, 2008).

The second steel, MA956 containing 4.5 wt.% Al, also develops a thin alumina scale on the surface under the same conditions of exposure. However, analysis by XPS-SPD reveals a much deeper oxygen penetration, which is the outcome of some areas with pitting. The fact that XPS-SDP averages the data of the whole surface can be the explanation for this result. The conclusion was that Al concentrations higher than 4.5 wt.% will be necessary to ensure formation of effective protection scales (Hosemann, 2008).

Other corrosion tests with Al-alloyed ODS steels were conducted with samples containing 13.7-17.3 wt.% Cr and 1.9-3.5 wt.% Al (Takaya, 2009). They were exposed to stagnant LBE with 10^{-6} and 10^{-8} wt.% oxygen at 550 and 650°C for 3 000 h. The best result was obtained by the 17.3 Cr steel alloyed with 3.5 wt.% Al. There was no sign of dissolution attack at both oxygen concentrations and temperatures applied. The oxide scale was very thin and a good barrier against further oxygen diffusion into the bulk material. Specimens containing less than 17.3 wt.% Cr and 3.5 wt.% Al also formed thin protective oxide scales but these scales allowed enough oxygen diffusion to build up some internal oxidation of Cr and Fe below the surface. The specimens with 15.8 wt.% Cr and 1.9 wt.% Al formed protective scales in LBE with 10^{-6} wt.% oxygen on the major part of the surface, but suffered from dissolution attack at some places. Internal oxidation was also observed. The conclusion is that in high Cr steels, the addition of 3.5 wt.% Al or more improves the compatibility of ODS steel because it allows the development of stable, slowly growing protective oxide scales.

Corrosion tests with different Kanthal alloys were conducted because these steels were considered as structural material of pumps for liquid Pb and PbBi. The Kanthal materials are: D (22 wt.% Cr, 2.8 wt.% Al), AF (22 wt.% Cr, 5.3 wt.% Al), APM (20-23 wt.% Cr, 5.8 wt.% Al), Alkrothal (15 wt.% Cr, 4.3 wt.% Al). Tests conditions were 500, 600 and 750°C in stagnant LBE and Pb with 10^{-8} and 10^{-6} wt.% oxygen and 1 000 h exposure time (Weisenburger 2010b). All Kanthal alloys were resistant against dissolution attack at 500°C in LBE and Pb by formation of oxide scales consisting of thin alumina on D and AF alloys and on stratified $Fe_3O_4/(AlCr)_2O_3$/IOZ oxide layer at 10^{-6} wt.%. All alloys developed a protective, thin alumina scale at 10^{-8} wt.% oxygen. Protective oxide scale formation prevented dissolution attack once again at 600°C. The scale consists of alumina in LBE. Only D had additionally an IOZ. In case of Pb a protective, thin alumina scale developed on all alloys at 10^{-8} wt.% oxygen, but stratified layers with IOZ at 10^{-6} wt.%. Dissolution attack occurred at 750°C in LBE with 10^{-8} wt.% oxygen. No attack took place at 10^{-6} wt.% in LBE and Pb because a thin alumina scale was formed, with the exception of AF, which had a stratified oxide layer.

An oxide map illustrating the stability domain of alumina, grown on FeCrAl model alloys when exposed to molten, oxygen-containing lead, over a temperature range of 400-600°C is shown in Figure 9.3.3 (Weisenburger, 2013). Ten FeCrAl bulk alloys were prepared by arc-melting in argon atmosphere starting from high purity elements. Their nominal compositions were: Fe-6Cr-6Al (P1), Fe-8Cr-6Al, Fe-10Cr-5Al, Fe-12Cr-5Al, Fe-14Cr-4Al, Fe-16Cr-4Al, Fe-6Cr-8Al, Fe-10Cr-7Al, Fe-12Cr-7Al, Fe-16Cr-6Al (numbers in wt.%). The evaluation of the specimens was performed using scanning electron microscopy (SEM), energy dispersive X-ray spectroscopy (EDX), X-ray diffraction using conventional and synchrotron radiation (XRD), and, for some selected samples, X-ray photoelectron spectroscopy sputter depth profiling (XPS-SDP).

The map also includes additional points corresponding to alumina-forming coatings (R1s) and alloys (R2: Kanthal AF, R3: Al-containing ODS) that fit very well with experiments performed on model alloys. Cr and Al contents of 12.5-17 wt.% and 6-7.5 wt.%, respectively, are high enough to obtain thin, stable and protective alumina scales on FeCrAl-based model alloys exposed in such conditions. For the temperature range and exposure times used during the current evaluation, the growth rate of the alumina scale was low.

The borderline, defining the critical concentration of Al and Cr required for the growth of a protective alumina scale on FeCrAl alloys' surface during their exposure in oxygen-containing Pb at temperatures between 400-600°C, was established based on experimental results. No calculated criteria have been defined up to now.

The influence of the model alloys' grain size, of the addition of reactive elements and of longer exposure time on the alumina scale polymorphs type, growth, stability and properties is currently under evaluation.

This map can be also used to define the critical Al concentration in FeCrAl surface alloys proposed as corrosion barriers for cladding tubes.

Figure 9.3.3: Oxide "map" for the oxidation of FeCrAl-based model alloys exposed to oxygen-containing molten lead, in the temperature range 400-600°C from Weisenburger (2013), also containing data from literature

Line at 800°C (Tomaszewicz, 1983), line at 1 000°C in oxygen atmosphere (Zhang, 2009), R1s (Fetzer, 2012), R2 (Del Giacco, 2012) and R3 (Takaya, 2012) (in lead and lead-bismuth, respectively)

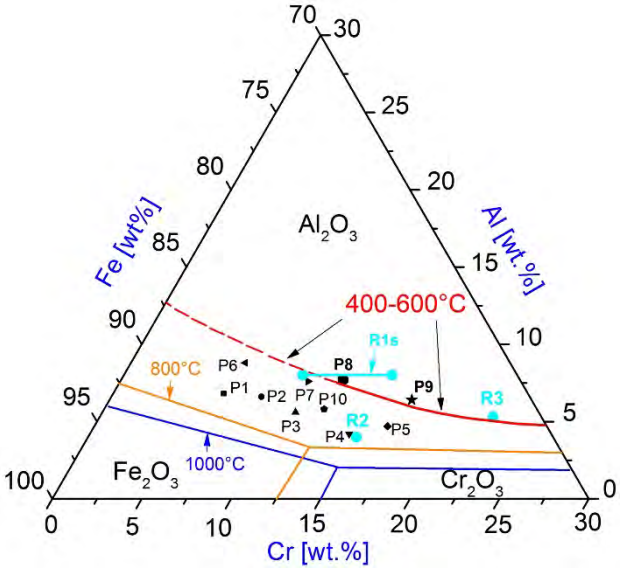

9.4 Mechanical properties

The main goal in applying a thin coating or alloying Al into the steel surface is to attain an effective corrosion protection by elements that form a stable oxide layer without impacting the mechanical properties of the substrate. It is known that the mechanical properties of the steels would be negatively influenced if elements like Al or Si were alloyed into the bulk of the steel in an amount that could improve protective oxide scales. This chapter describes mechanical tests that were conducted to examine the influence of mechanical loads on the protection layer and the underlying bulk steels. Results of the tests are listed in Table 9.4.1.

Experiments have been carried out at the relatively low temperature of 350°C to examine the influence of stresses on TiN, DLC and CrN coatings on T91 steel. Specimens pre-stressed with static stresses of 70, 150 MPa, exerted by three-point bending in a sample holder, were inserted in the CORWETT loop and exposed to flowing LBE for 6 000 h. They show diminishing of the protection behaviour in the stressed as compared to the unstressed regions. Only TiN was not influenced by stresses and showed neither dissolution attack nor formation of cracks (Glasbrenner, 2006b). The results obtained in the experiments can be described as follows: Static load on CrN caused corrosion attack by LBE. This was not the case when the exposure tests were carried out without any static pressure. Hence, the stress has a negative influence on the compatibility of this layer. There seems to be no chemical interaction between LBE and the unstressed DLC layer, but there is one at a static stress of 150 MPa. Compression causes more deterioration than tension. The steel was attacked by LBE in areas with damaged scale. Exposure of TiN-coated specimens up to 6 000 h in LBE revealed the most promising results. This coating is not influenced by LBE without static stresses and with up to 200 MPa.

Table 9.4.1: Influence of coatings on mechanical properties

Material	Pb/ PbBi	Test facility	Temp. (°C)	Oxygen conc. (wt.%)	Conditions	Steel	Results	Ref.
TiN (CVD) CrN (PVD) DLC	PbBi	CORRWETT	350	10^{-6}	Stressed with 150 MPa before expos.	T91	No cracking, no LBE attack on TiN-coated steel cracked CrN + DLC coating with LBE attack on steel.	Glasbrenner (2006b)
FeCrAlY (GESA)	PbBi	CRISM, Prometey	550	10^{-6}	Creep, creep to rupture tests, stress 160-220 MPa	T91	Surface alloying acts as an effective protection against LBE influenced creep strength reduction; thin Al oxide at the surface.	Weisenburger (2012)
FeCrAlY GESA-alloyed	PbBi	IPPE	500	10^{-6}	Stress	T91	No infl. of 0.7% strain on oxide scale.	Weisenburger (2008a)
FeCrAlY GESA-alloyed	PbBi	Prometey	550	10^{-6}	LCF	T91	No influence of coating.	Weisenburger (2008b, 2009)
FeCrAlY GESA-alloyed	PbBi	IPPE	500 550 650	10^{-6}	Creep, creep to rupture	T91 T91	Prolonged second creep stage with coating in air and in LBE, prolonged time to rupture of coated specimens in LBE; values approaching those obtained in air.	Weisenburger (2012)

The behaviour of the FeCrAlY surface-alloyed T91 steel was studied by conducting three mechanical tests. The first one was a pressurised tube test in which a stress was applied to a coated tube wall. The second test was a low cycle fatigue test (LCF) and the third one a creep to rupture test (Weisenburger, 2008a, 2008b, 2009).

The cladding tubes under internal pressure were exposed to flowing LBE with 10^{-6} wt.% oxygen and 550°C at IPPE (Obninsk, Russia) (Weisenburger, 2008a). The internal pressure of 15 MPa (tangential stress of 112.5 MPa) in these experiments resulted in a strain of 0.7%. The FeCrAlY surface-alloyed tubes did not show any changes of oxide scale thickness and integrity, while the T91 tube without surface alloying underwent enhanced oxide scale growth by a factor of about 2 caused under the influence of the internal pressure.

The LCF test was performed in the loop at Prometey, St. Petersburg, in LBE with 10^{-6} wt.% oxygen at 550°C. Cycling was conducted at 0.5 Hz with elongations $\Delta\varepsilon_t$ between 0.3-2%. There was no influence on the surface-alloyed FeCrAlY layer and on the corrosion protection during the test. Summarising the results, under test conditions (in LBE and air), the GESA-modified layer did not change the low-cycle fatigue behaviour of T91 steel (Figure 9.4.1) (Weisenburger, 2008b).

The first creep-to-rupture tests on T91 steel in flowing LBE with 10^{-6} wt.% oxygen at 550°C of the Prometey loop show significant reduction of creep-to-rupture compared to the experiments in air, both at stresses of 160 and 220 MPa. However, a threshold below these high stresses was expected at which deviation between behaviour in air and in LBE can be neglected (Jianu, 2009).

Figure 9.4.1: Mechanical properties of T91 steel with and without FeCrAlY alloyed into the surface

Fatigue life as a function of strain in air and LBE (left); creep-to-rupture test (right)

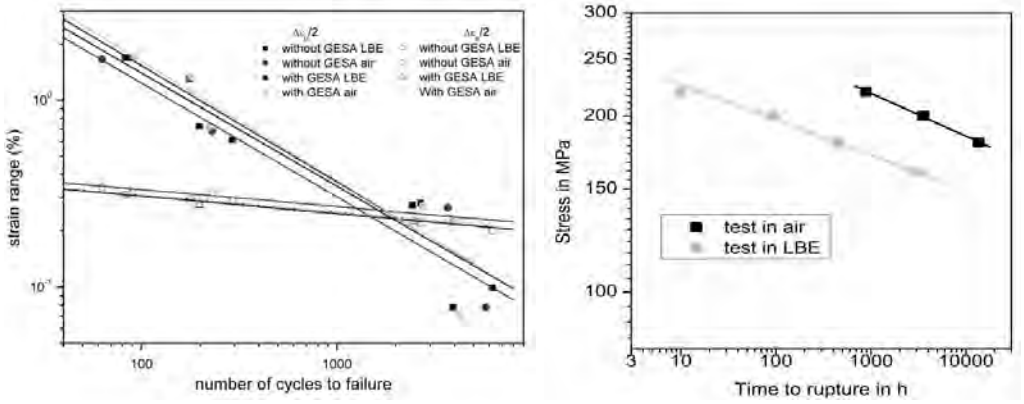

Source: Left image from Weisenburger (2008b), right image from Jianu (2009).

It was assumed from the first judgement of experiments with FeCrAlY surface-alloyed specimens that the protection layer drastically reduces the negative influence of the LBE (Weisenburger, 2012). Experiments were conducted with the goal to explore the influence of surface-alloyed FeCrAlY protection layer on the creep properties of T91 steel. It is important to mention that the FeCrAlY after precipitation by LPPS was melt-treated by applying the electron beam of the GESA device. The melting process caused a smooth surface and dense, homogeneous coating structure and was also deep enough to enhance the bonding, by alloying with a thin layer of the metal surface. The results of the experiments depicted in Figure 9.4.2 (left) show a marked difference in creep properties of T91 steel with FeCrAlY alloyed and unalloyed surface when exposed in air. The coating, modified with GESA, improves the creep properties when exposed in air. It is obvious from the diagram depicted in Figure 9.4.2 (left) that the second creep stage of the FeCrAlY surface-alloyed specimen in air extends to longer time – 5 000 h at 200 MPa and 2 000 h at 220 MPa – while that of the surface-unalloyed specimen is shorter: 3 000 at 200 MPa and a few hours at 220 MPa.

The estimation of the time to rupture under different loads depicted in Figure 9.4.2 (right) also shows improved performance in case of FeCrAlY surface-alloyed specimens. The rupture time of surface-alloyed specimens creep tested in PbBi are close to those of surface-unalloyed specimens in air, while the surface-unalloyed specimens in PbBi end up at much lower rupture times. This is certainly the advantage of the thin alumina protective layer on the FeCrAlY alloyed surface which is much more stable when exposed to stress than it is the brittle multi-layer oxide scale on unalloyed steel.

The mechanical behaviour of Si-enriched (between 1.45-4.83 wt.% Si) high Cr steels (between 8.1-13.52 wt.% Cr) in contact with LBE and the stability and strength of the formed oxide layer by nano-indentation measurements were estimated (Van den Bosch, 2012). Slow strain rate tensile (SSRT) tests were conducted between 150-500°C at a constant strain rate of 5×10^{-6} s^{-1}. The effect of strain rate was estimated by varying the strain rate between 5×10^{-7} s^{-1} and 1×10^{-3} s^{-1} at a constant test temperature. The result showed that steels with a high Cr and Si content were very prone to liquid metal embrittlement between 300 and 375°C. The materials broke by brittle transgranular cleavage fracture with nearly any prior plastic deformation. The uniform elongation remained unaffected under all tested conditions for the Si ferritic-martensitic steels EP 823 and T91-Si (1.45 wt.% Si) but the total elongation was strongly reduced between 200 and 400°C with a maximum at 350°C. At slower strain rates and larger grain size the LME effect was found to be worse.

Slightly worse and more reproducible than for T91 was the LME effect for martensitic steels enriched in Si. Concerning the oxide layer it was found that oxide layer formed on EP 823 was slightly stiffer and considerable harder than that formed on T91.

Figure 9.4.2: Creep tests of original and FeCrAlY alloyed (GESA-treated) specimens in air and LBE

Creep in air at 550°C with 200 MPa and 220 MPa (left);
time to rupture at 550 and 600°C with 140-290 MPa (right)

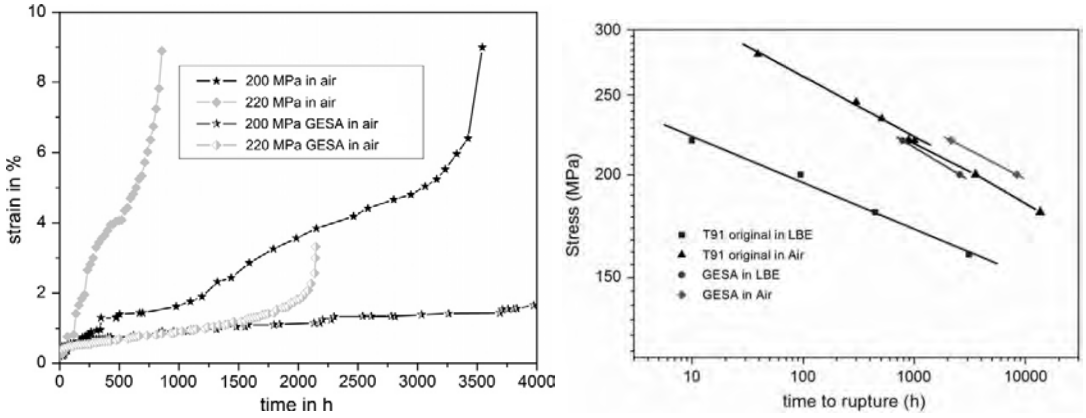

Source: Weisenburger (2012).

9.5 Concluding remarks

Lead and lead-bismuth eutectic alloys with low oxygen concentration that ensures formation of an oxide scale on an unprotected steel surface are the first choice for realisation of an LBE-cooled nuclear installation. The concentration of oxygen must be lower than that at which precipitation of PbO takes place. This would provide protective conditions especially for the low temperature parts.

However at elevated temperatures, above 450°C in the case of austenitic steels and 480°C in the case of ferritic/martensitic steels, this method for steel protection fails due to the insufficient prevention of dissolution attack by Pb or LBE and extensive steel corrosion by oxidation, respectively. As an example, after long exposure periods, oxide scales become intolerably thick, preventing, in the case of the cladding tubes, the heat transfer from fuel to coolant. Therefore, structural parts exposed to high thermal loads such as cladding tubes, which could reach temperatures above 450/480°C, require additional protection measures.

It can be concluded that the austenitic and martensitic steel surface-alloyed with Al though the GESA process and also austenitic steels surface-alloyed with Al by the pack cementation process or by foil melting fulfil the requirements for corrosion protection in molten Pb and LBE up to 600°C, if the oxygen concentration is between 10^{-4} and 10^{-8} wt.%. These parameters might also be valid for steels alloyed with Si.

However, based on the results obtained on samples made of pack-cemented steels exposed in LBE containing less than 10^{-8} wt.%, it can be concluded that the oxygen activity above 500°C is sufficiently low to allow dissolution attack before a stable alumina scale is developed. The explanation resides in the strong dependence of alumina scale formation on the Al activity at the sample surface and the oxygen concentration in the liquid Pb or LBE. A very promising measure for corrosion protection is alloying of FeCrAlY into the steel surface using the GESA process, which provides the best compatibility with Pb and LBE.

The addition of a small quantity of oxygen in Pb and LBE and the surface alloying with aluminium led to the formation of very thin, slowly growing oxide scales that prevent steel oxidation and dissolution attack. Additionally, self-healing in case of oxide scale detachments, which may occur during thermos-cycling, is ensured.

Successful methods of alloying Al into the steel surface are:

- surface alloying by GESA as well as pack cementation for austenitic steels;
- FeCrAlY coating with subsequent modification using the GESA process.

It can be considered an advantage that the pack cementation and FeCrAlY coating processes are already performed on an industrial level. Therefore, these processes should be favoured on condition that the surface concentration of Al is kept below 24 wt.% to prevent dissolution attack at low oxygen potentials. This holds for steels alloyed with Si during fabrication as well.

Coatings with refractory metals and low solubility in Pb and LBE, e.g. Mo, as well as the nitrides and carbides should be excluded because they would require very low oxygen activities and would leave uncoated low temperature parts unprotected. However, for a correct judgement of their compatibility with Pb and LBE, reliable experimental data are still lacking.

The use of oxide coatings, e.g. alumina, which would allow application of Pb and LBE over a wide range of oxygen concentrations, must be excluded because of expected adhesion problems and due to the absence of a self-healing of defects.

Several tests showed that there are no problems with the influence of FeCrAlY alloyed into the surface on relevant mechanical properties. The LCF behaviour is not changed and stresses that cause enhanced growth of the oxide scale thickness on unalloyed steel have no effect on the corrosion protection at least up to a strain of 0.7%. A positive influence of FeCrAlY surface alloying was also observed on the creep rate and the creep-to-rupture time. The second creep stage was much more extended and the negative influence of LBE on the creep-to-rupture time was largely diminished. The general conclusion is that FeCrAlY surface alloying improves the mechanical properties of the steel especially when it is exposed to Pb or LBE up to temperatures of 650°C. Thus, besides the improvement of corrosion resistance, the better mechanical properties are another important reason for applying a protective FeCrAlY alloying to the steel surface.

Answers were approached to some of the open questions concerning the protective layers like long-term behaviour, self-healing and mechanical properties, behaviour under irradiation and the influence of fretting. Long-term experiments of up to 10 000 h showed successful protection of surfaces alloyed by aluminium and also of those surface-alloyed with FeCrAlY. This may be an indication that these protection layers fulfil the conditions for long time use in nuclear reactor loops. Self-healing of defects like fissures in the oxide scale has also been observed as well as a positive influence of the alloyed surface layers on the mechanical properties. The only remaining questions that have not been investigated up to now are the behaviour under irradiation and the influence of fretting on the protection layers.

However, irradiation experiments have already been conducted in the PHENIX reactor and await evaluation. Also, experiments on the influence of fretting are ongoing. For the prediction of the long-term behaviour of the alloyed surfaces and coatings, models and calculation criteria have to be developed in order to improve the confidence in such solutions concerning the protection of structural materials at temperatures above 500°C.

References

Asher, R.C., D. Davies and S.A. Beetham (1977), "Some Observations on the Compatibility of Structural Materials with Molten Lead", *Corrosion Science*, Vol. 17, No. 7, pp. 545-557.

Ballinger, R.G. and J. Lim (2004), "An Overview of Corrosion Issues for the Design and Operation of High-temperature Lead- and Lead-bismuth-cooled Reactor Systems", *Nuclear Technology*, 147 (3), pp. 418-435.

Barbier, F. and A. Rusanov (2001), "Corrosion Behavior of Steels in Flowing Lead-bismuth", *Journal of Nuclear Materials,* 296, pp. 231-236.

Benamati, G. et al. (2000), "Behaviour of Materials for Accelerator Driven Systems in Stagnant Molten Lead", *Journal of Nuclear Materials*, Vol. 279, pp. 308-316.

Benamati, G. (ed.) (2004), *Final Scientific Technical Report TECLA*, European Community, 5th R&D Framework Programme.

Benamati, G., A. Gessi and G. Scaddozzo (2005), "Corrosion Behaviour of Steels and Refractory Metals in Flowing Lead-bismuth Eutectic at Low Oxygen Activity", *Journal of Materials Science*, 40, pp. 2465-2470.

Block, F.R., J. Schneider and G. Stolzenberg (1977), *Archiv Eisenhüttenwesen*, 48, No. 6 June, pp. 359-364.

Borgstedt, H.U., H. Glasbrenner and Z. Peric (1994), "Corrosion of Insulating Layers on MANET Steel in Flowing Pb-17Li", *Journal of Nuclear Materials,* 212-215, pp. 1501-1503.

Chen, X., R. Haasch and J.F. Stubbins (2012), "Impedance Spectroscopy and Microstructural Characterization of the Corrosion Behavior of FeCrAl Alloy in Lead-bismuth Eutectic", *Journal of Nuclear Materials*, 431, pp. 125-132.

Deloffre, P.H. et al. (2003), *Behavior of the Aluminized T91 Martensitic Steel and 316 Austenitic Steel on Contact with Static and Dynamic Pb-Bi*, Technical Report SCCME, RT-SCCME 584.

Deloffre, Ph., F. Balbaud-Célérier and A. Terlain (2004), "Corrosion Behaviour of Aluminized Martensitic and Austenitic Steels in Liquid Pb-Bi", *Journal of Nuclear Materials*, Vol. 335, pp. 180-184.

Del Giacco, M. et al. (2012), "Influence of Composition and Microstructure on the Corrosion Behavior of Different Fe-Cr-Al Alloys in Molten LBE", *Journal of Nuclear Materials*., 421, pp. 39-46.

Engelko, V. et al. (2001), "Pulsed Electron Beam Facility (GESA) for Surface Treatment of Materials", *Vacuum*, Vol. 62, pp. 211-216.

Fazio, C. et al. (2003), "Corrosion Behaviour of Steels and Refractory Metals and Tensile Features of Steels Exposed to Flowing PbBi in the LECOR Loop", *Journal of Nuclear Materials*, 318, pp. 325-332.

Fetzer, R. et al. (2012), "Oxide Scale Formation of Modified FeCrAl Coatings Exposed to Liquid Lead", *Corros. Sci*., 55, pp. 213-218.

Gessi, A. and A. Weisenburger (2010), Deliverable D38 of 6th Framework Programme Project ELSY FI6W – 036439.

Glasbrenner, H. et al. (1998), "Comparison of Microstructure and Formation of Intermetallic Phases on F82H-mod. and MANET II", *Journal of Nuclear Materials*, Vol. 258, pp. 1173-1177.

Glasbrenner, H. and F. Gröschel (2006a), "Exposure of Pre-Stressed T91 Coated with TiN, CrN and DLC to Pb–55.5Bi", *7th International Workshop on Spallation Materials Technology (IWSMT-7)*, Thun, Switzerland, 29 May-03 June 2005, *Journal of Nuclear Materials*, Vol. 356, Issues 1-3, pp. 213-221.

Glasbrenner, H. and F. Gröschel (2006b), "Exposure of Pre-Stressed T91 Coated with TiN, CrN and DLC to Pb-55.5Bi", *Journal of Nuclear Materials*, Vol. 356, No. 1-3, pp. 213-221.

Gorynin, I.V. et al. (1998), "Structural Materials for Power Plants with Heavy Liquid Metals as Coolants", *Proceedings of Heavy Liquid Metal Coolants in Nuclear Technology*, Obninsk, Russian Federation, Vol. 1, pp. 120-132.

Gromov, B.F. et al. (1999), *Proceedings of Heavy Liquid Metal Coolants in Nuclear Technology*, Obninsk, Russian Federation, Vol. 1, p. 87.

Heinzel, A. (2003), *Korrosionsverhalten von Stählen in sauerstoffbeladenem, flüssigem Pb55,5%Bi unter Berücksichtigung von Oberflächenmodifikationen*, Dissertation Universität Karlsruhe, Report FZKA 6823.

Heinzel, A., M. Kondo and M. Takahashi (2006), "Corrosion of Steels with Surface Treatment and Al-Alloying by GESA Exposed in Lead-bismuth", *Journal of Nuclear Materials*., Vol. 350, pp. 264-270.

Hodge, R.I., R.B. Turner and J.L. Platten (1970), "A 5 000 h Test of a Lead-bismuth Circuit Constructed in Steel and Niobium", *Corrosion by Liquid Metals*, AIME Proc. 1969, J.E. Draley and J.R. Weeks (eds.), Plenum Press, New York.

Hosemann, P. et al. (2008), "Corrosion of ODS Steels in Lead-bismuth Eutectic", *Journal of Nuclear Materials*, Vol. 373, pp. 246-253.

Ilincev, G. (2002), "Research Results on the Corrosion Effects of Liquid Heavy Metals Pb, Bi and Pb-Bi on Structural Materials with and Without Corrosion Inhibitors", *Nuclear Engineering and Design*, Vol. 217**,** Issues 1-2, pp. 167-177.

Jianu, A. et al. (2009), "Creep-to-Rupture Tests of T91 Steel in Flowing Pb-Bi Eutectic Melt at 550°", *Journal of Nuclear Materials*, Vol. 394, Issue 1, pp. 102-108.

Knebel, J.U. et al. (2000), "Design and Corrosion Study of a Closed Spallation Target Module of an Accelerator-Driven System (ADS)", *Nuclear Engineering and Design*, 202, pp. 279-296.

Kondo, M. et al., "Experimental Studies on Pb-Bi Flow Technology and Steel Compatibility with Pb-Bi", ICONE 12-49285.

Kurata, Y. and M. Furukawa (2004), "Excellent Corrosion Resistance of 18Cr-20Ni-5Si Steel in Liquid Pb-Bi", *Journal of Nuclear Materials*, Vol. 325, pp. 217-222.

Kurata, Y., M. Furukawa and S. Saito (2004), "Corrosion Behavior of Al Surface-Treated Steels in Liquid Pb-Bi in a Pot", *Journal of Nuclear Materials*, Vol. 335, pp. 501-507.

Kurata, Y. et al. (2011), "Applicability of Al-Powder-Alloy Coating to Corrosion Barriers of 316SS in Liquid Lead-bismuth Eutectic", *Materials Transactions*, Vol. 52, No. 5, pp. 1033-1040.

Kurata, Y., H. Yokota and T. Suzuki (2012), "Development of Al-Alloy Coating for Advanced Nuclear Systems Using Lead Alloys", *J. of Engineering for Gas Turbines and Power*, Vol. 134, Issue 6.

Kurata, Y. (2013), "Corrosion Behavior of Si-Enriched Steels for Nuclear Applications in Liquid Lead-bismuth", *Journal of Nuclear Materials*, Vol. 437, pp. 401-408.

Lim, J. (2006), PhD Thesis (MIT 2005), Massachusetts Institute of Technology, Cambridge, MA.

Loewen, E.P. (2005), "Corrosion Studies in Support of Lead-bismuth Cooled FBRs", *Progress in Nuclear Energy*, Vol. 47, No. 1-4, pp. 561-586.

Loewen, E.P., R. Ballinger and J. Lim (2004), "Corrosion Studies in Support of a Medium-power Lead-alloy-cooled Reactor", *Nucl. Tech.*, Vol. 147, pp. 436-456.

Müller, G., G. Schumacher and F. Zimmermann (2000), "Investigation on Oxygen Controlled Liquid Lead Corrosion of Surface Treated Steels", *Journal of Nuclear Materials*, Vol. 278, pp. 85-95.

Müller, G. et al. (2002), "Results of Steel Corrosion Tests in Flowing Liquid Pb/Bi at 420-600°C After 2 000 h", *Journal of Nuclear Materials*, Vol. 301, pp. 40-46.

Müller, G. et al. (2003), *Study on Pb-Bi Corrosion of Structural and Fuel Cladding Materials for Nuclear Applications Part III*, JNC TY9400 2003-026, Japan Nuclear Cycle Development Institute.

Müller, G. et al. (2004a), "Behavior of Steels in Flowing Liquid PbBi Eutectic Alloy at 420-600°C After 4 000-7 200 h", *Journal of Nuclear Materials*, Vol. 335, pp. 163-168.

Müller, G. et al. (2004b), *Study on Pb-Bi Corrosion of Structural and Fuel Cladding Materials for Nuclear Applications. Part IV. Corrosion Investigation of Steels at 550 and 650°C After 800, 2000 and 5000 h of Exposure to Stagnant Liquid Pb-Bi Containing 10^{-4} and 10^{-8} wt.% of Oxygen*, JNC TY9400 2003-028, Japan Nuclear Cycle Development Institute.

Müller, G et al. (2005), "Surface Alloying by Pulsed Intense Electron Beams", *Vacuum*, Vol. 77, pp. 469-474.

Müller, G. et al. (2008), *7th Meeting of the Expert Group on LBE Technology*, 29 October 2008, OECD/NEA, Paris.

Nicholls, J.R. (2003), "Advances in Coating Design for High-Performance Gas Turbines", *MRS Bulletin*, Vol. 28, No. 9, pp. 659-670.

Park, J.J., D.P. Butt and C.A. Beard (2000), "Review of Liquid Metal Corrosion Issues for Potential Containment Materials for Liquid Lead and Lead-bismuth Eutectic Spallation Targets as a Neutron Source", *Nuclear Engineering and Design*, Vol. 196, pp. 315-325.

Rivai, A.K. and M. Takahashi (2010), "Corrosion Investigations of Al-Fe-Coated Steels, High Cr Steels, Refractory Metals and Ceramics in Lead Alloys at 700°C", *Journal of Nuclear Materials*, Vol. 398, pp. 146-152.

Romano, A.J., C.J. Klamut and D.H. Gurinsky (1963), *The Investigation of Container Materials for Bi and Pb Alloys, Part I, Thermal Convection Loops*, Brookhaven National Laboratory Report BNL-811 (T-313), BNL, Upton, New York.

Schroer, C. et al. (2004), JNC TY9400 2004-023, Japan Nuclear Cycle Development Institute.

Seifert, J.W. and A.L. Loewe (1961), *Corrosion*, Vol. 17, p. 97.

Shmatko, B.A. et al. (1998), "Concept of Heavy Coolant Technology Without Oxygen", *HLMC-98*, Obninsk, Russian Federation, 5-9 October 1998, pp. 683-685.

Short, M.P. et al. (2010), "Diffusional Stability of Ferritic-Martensitic Steel Composite for Service in Advanced Lead-bismuth Cooled Nuclear Reactors", *Int. Heat Treatment and Surface Engineering*, Vol. 4, No. 2, pp. 74-80.

Short, M.P. (2010a), *The Design of a Functionally Graded Composite for Service in High Temperature Lead and Lead-bismuth Cooled Nuclear Reactor*, Thesis, Massachusetts Insitute of Technology, Dept. Nuclear Science and Engineering, Cambridge, Massachusetts.

Short, M.P. and R.G. Ballinger (2012), "A Functionally Graded Composite for Service in High-temperature Lead- and Lead-bismuth-cooled Nuclear Reactors – I: Design", *Nuclear Technology*, Vol. 177, pp. 366-381.

Short, M.P., R.C. Ballinger and H.E. Hänninen (2013), "Corrosion Resistance of Alloys F91 and Fe-12Cr-2Si in Lead-bismuth Eutectic Up to 715°C", *Journal of Nuclear Materials*, Vol. 434, pp. 259-281.

Takahashi, M. and M. Kondo (2011), "Corrosion Resistance of Ceramics SiC and Si_3N_4 in Flowing Lead-bismuth Eutectic", *Progress in Nuclear Energy*, Vol. 53, pp. 1061-1065.

Takaya, S. et al. (2009), "Corrosion Behavior of Al-Alloying High Cr-ODS Steels in Lead-Bismuth Eutectic", *Journal of Nuclear Materials*, Vol. 386-388, pp. 507-510.

Takaya, S. et al. (2012), "Al-Containing ODS Steels with Improved Corrosion Resistance to Liquid Lead–bismuth", *Journal of Nuclear Materials*, Vol. 428, pp. 125-130.

Terlain, A. et al. (1990), *Technol.*, 1, 916.

Tomaszewicz, P. and G.R. Wallwork (1983), "The Oxidation of High-Purity Iron-Chromium-Aluminum Alloys at 800°C", *Oxid. Met.*, Vol. 20, pp. 75-109.

Van den Bosch, J. et al. (2012), "On the LME Susceptibility of Si Enriched Steels", *Journal of Nuclear Materials*, Vol. 429, pp. 105-112.

Weeks, J.R. and D.H. Gurinsky (1958), *Liquid Metals and Solidification*, ASM, pp. 106-161.

Weisenburger, A. et al. (2005), "Corrosion of Modified FeCrAlY Coated Cladding Tubes in Liquid PbBi", *Proc. of EUROCORR 2005*, Lisbon, Portugal, 4-8 September, ISBN 972-95921-2-8.

Weisenburger, A. et al. (2008a), "T91 Cladding Tubes with and without Modified FeCrAlY Coatings Exposed in LBE at Different Flow, Stress and Temperature Conditions", *Journal of Nuclear Materials*, Vol. 376, pp. 274-281.

Weisenburger, A. et al. (2008b), "Low Cycle Fatigue Tests of Surface Modified T91 Steel in 10^{-6} wt.% Oxygen Containing $Pb_{45}Bi_{55}$ at 550°C", *Journal of Nuclear Materials*, Vol. 377, pp. 261-267.

Weisenburger, A. et al. (2009), *Proc. 17th Int. Conf. Nucl. Eng. ICONE17*, Brussels, Belgium, 12-16 July 2009.

Weisenburger, A. et al. (2012), "Creep, Creep-Rupture Tests of Al-Surface-Alloyed T91 Steel in Liquid Lead Bismuth at 500 and 550°C", *Journal of Nuclear Materials*, Vol. 431, Issues 1-3, pp. 77-84.

Weisenburger, A. et al. (2013), "Oxide Scales Formed on Fe-Cr-Al-Based Model Alloys Exposed to Oxygen Containing Molten Lead", *Journal of Nuclear Materials*, Vol. 437, pp. 282-292.

Yachmenyov, G.S. et al. (1999), "Problems of Structural Materials Corrosion in Lead-bismuth Coolant", *Proceedings of Heavy Liquid Metal Coolants in Nuclear Technology*, Vol. 1, Obninsk, Russian Federation, pp. 133-140.

Yamaki-Irisawa, E., S. Numata and M. Takahashi (2011), "Corrosion Behavior of Heat-Treated Fe-Al Coated Steel in Lead-bismuth Eutectic Under Loading", *Progress in Nuclear Energy*, Vol. 53, Issue 7, pp. 1066-1072.

Zhang, Z.G. et al. (2009), "The Effect of the Third Element Cr on Oxidation Behavior of Fe-xCr-10Al (at.%) Alloys at 900°C", *Open Corros. J.*, Vol. 2, pp. 37-44.

10. Low Prandtl number thermal-hydraulics*

This chapter is an introduction to the field of momentum and heat transfer in liquid metals, characterised by their low Prandtl number. To fully grasp the concepts discussed, a basic knowledge of fluid dynamics and thermodynamics is recommended, although some background information is included. For the sake of compactness and readability, only selected formulas for the relevant technical configurations are listed and the extent of the descriptions is limited, emphasising the main particular features of liquid metals as compared to other fluids. If further knowledge is desired concerning specific topics, the reader is directed to the cited bibliography. A further caveat: this topic is currently being intensively investigated in the framework of national and international research programmes. Thus, the state of knowledge is continuously evolving and it is recommended to the reader to be aware of additional literature that might have become available.

A collection of background information is presented in Section 10.1, including a derivation of the conservation equations, focusing on the relevant assumptions applicable for liquid metal flows. Different flow scenarios commonly found in heavy liquid metal systems are presented. Additionally, the main specific features of liquid metals, including their physical properties and experimental conditions, are discussed. Rather specific low Prandtl number fluids like ferromagnetic fluids or metal/oil suspensions are not considered in this context, as the scope of this chapter is restricted to the single-phase thermal-hydraulics of liquid metals obeying the Newtonian law.

An analysis of momentum and heat transfer in laminar flows is briefly presented in Section 10.2. Although laminar conditions are rarely found in liquid metal flows, this analysis is considered for an understanding of the underlying physical mechanisms under relatively simple circumstances. The modelling of turbulence, as one of the major parts of the study of thermal-hydraulics, is described in Section 10.3. Liquid metals behave differently from other fluids regarding the turbulent heat flux, and thus common analogies for the turbulent Prandtl number in particular cannot be applied. Practical approximations are presented in connection with experimental findings and different closure methods for the numerical solution of these models are discussed. The available literature on the modelling of turbulent duct and pool flows, as well as direct numerical simulations, is reviewed, highlighting recent developments.

Engineering correlations and experimental observations for heat transfer in common technical applications are analysed in Section 10.4. An extensive analysis is presented for the round-tube geometry, comparing the available experimental data and proposed model, and best-estimate correlations are recommended. Furthermore, the available literature for other relevant geometries, such as flat and annular channels, as well as in triangular rod bundles, is reviewed in this section. The effects of the turbulent flow-developing region and over-imposed buoyancy are discussed. Moreover, additional flow scenarios specifically found in heavy liquid metal systems are analysed.

Final comments and remarks are summarised in Section 10.5. In general this chapter provides a comprehensive overview of reported models and experiences in liquid metal flow systems, which exhibited considerable progress over the last decade. Considering the great efforts currently devoted to this field of study, remarkable progress is expected in the years to come.

* Chapter lead: J. Pacio. For additional contributors please see Appendix 1.

10.1 Background

Liquid metals (LM) represent a particular category of fluids, characterised among others by their low Prandtl number (see Section 10.1.3). In this context, the study of LM flows can greatly benefit from the much broader field of fluid mechanics, covering an enormous range of engineering applications. This discipline involves in most cases the combination of theory and experiment. On the one hand, a general theory, applicable to arbitrary geometries and flow conditions, has been developed based only on a small set of basic laws. On the other hand, this general description is found to be too complex to represent some flow scenarios of engineering relevance and some simplifying assumptions are often needed in practice. Experimental observations must complement the theory, confirming the validity of these assumptions, as well as providing information on specific flow parameters, such as drag, lift and heat transfer coefficients.

This section does not intend to give a complete description of the available theory for fluid dynamics and heat transfer, as plenty of literature is already dedicated to these topics. For further reference, the textbooks by Kakaç (1987) and Bird (2007) are recommended. For the sake of completeness, the main governing equations, in their simplified form applicable to most LM flow scenarios, are presented in Section 10.1.1. An overview on the different flow scenarios typically find in LM systems is given in Section 10.1.2. The main specific features of LM affecting the thermal-hydraulics of these flows are described in Section 10.1.3.

10.1.1 *The governing equations*

In general, describing the flow behaviour involves accounting for the transport of three quantities: mass, momentum and energy. Modelling each individual transport mechanism as well as the external sources or sinks, the problem is governed by a set of equations dictating the balance (or conservation) of these quantities. Within the context of this chapter we restrict ourselves to the consideration of flows in channels or closed cavities without the entrainment of an additional mass source or a mass transfer between different species. In that case, these equations must be solved in the complete domain, subject to given initial and boundary conditions, described in the following paragraphs.

Consider the flow of a single-phase and single-component fluid throughout a fixed differential control volume. The rate of change of an intensive property c (per unit mass) expressed using a fixed co-ordinate system (that is, in an Eulerian representation) is given by its material derivative Dc/Dt, given by Eq. (10.1) (Chorin, 1979). The first term in the right-hand side indicates the rate of change observed at this position and, in steady-state flows, it is zero. The second term indicates the rate at which the quantity c is transported by the fluid moving at a velocity $\vec{u}$.

$$\frac{Dc}{Dt} = \frac{\partial c}{\partial t} + \vec{u} \cdot \nabla c \tag{10.1}$$

Thus, the expression for the conservation of the intensive property c within a given control volume (and throughout its borders) considers the balance given by Eq. (10.2). The left-hand side indicates the material derivative of the quantity ρc, and the right-hand side includes the contributions of additional surface-transport mechanisms ($\nabla \cdot \vec{J}$) and volumetric sources ($\rho\Phi$):

$$\frac{\partial}{\partial t}(\rho c) + \nabla \cdot (\rho c \vec{u}) = \nabla \cdot \vec{J} + \rho\Phi \tag{10.2}$$

Equation (10.2) expresses the general balance for the quantity c. In the following paragraphs, it is applied to the particular cases of the conservation of mass, momentum and energy. The main variables considered for each case are listed in Table 10.1.1.

Table 10.1.1: Main variables considered for applying the general balance Eq. (10.2) to the conservation of mass, momentum and energy

	Symbol	Mass	Momentum	Energy
Intensive property	c	1	$\vec{u}$	$e_0 = e + \frac{u^2}{2}$
Surface-transport flux	$\vec{J}$	0	$\overline{\overline{\tau}} - p\overline{\overline{I}}$	$\left(\overline{\overline{\tau}} - p\overline{\overline{I}}\right)\cdot\vec{u} - \vec{q}'''$
External source (per unit of mass)	Φ	0	$\vec{f}$	$\frac{q'''}{\rho} + \vec{u}\cdot\vec{f}$
Balance equation (general)	Eq.	(10.3)	(10.5)	(10.7)
Balance equation (simplified with assumptions applicable to engineering liquid metal flows)	Eq.	(10.4)	(10.6)	(10.8)

Source: Todreas (2012).

10.1.1.1 *Mass balance (continuity equation)*

In the absence of mass sources or sinks, the mass is only transported by the flow velocity field $\vec{u}$. Thus, with $c = 1$, $\vec{J} = 0$, and $\Phi = 0$, Eq. (10.3) is obtained:

$$\frac{\partial \rho}{\partial t} + \nabla \cdot \left(\rho \vec{u}\right) = 0 \tag{10.3}$$

Because liquid metals below their boiling point are almost incompressible (constant density) Eq. (10.3) can be approximated by Eq. (10.4), where u, v and w are the components of $\vec{u}$ in the x, y and z directions, respectively:

$$\nabla \cdot \vec{u} = 0 \Rightarrow \frac{\partial u}{\partial x} + \frac{\partial v}{\partial y} + \frac{\partial w}{\partial z} = 0 \tag{10.4}$$

In this context, the changes in density (for example in the x direction) are considered small if:

$$u\frac{\partial \rho}{\partial x} \ll \rho\frac{\partial u}{\partial x}$$

These changes are given by the thermodynamic relation $\rho = \rho(p,T)$. On the one hand, considering the changes due to pressure, this condition is fulfilled when the Mach number is much smaller than unity, with a threshold value of $Ma < 0.3$ being normally accepted, and valid for all studied LM flows. On the other hand, however, considering the changes due to temperature, the density and velocity are affected in equal proportions and thus this condition is not strictly fulfilled. Nevertheless, in all engineering applications of liquid-metal flows, the divergence of the velocity due to changes in density would be very small, and Eq. (10.4) can be assumed to hold true in practice.

10.1.1.2 *Momentum balance (Navier-Stokes equations)*

This balance is derived from the basic law of mechanics dictating that the sum of acting forces is equal to the product of mass and acceleration. In this context, the source of momentum Φ is given by an acting external force per unit mass $\vec{f}$. In most practical cases, the dominant acting body force is the gravity $\vec{g}$, although additional forces of electrical or magnetic origin can be found in some LM applications. The acting surface

forces are represented by the symmetric viscous shear-stress tensor ($\bar{\bar{\tau}}$) and the pressure acting in the normal direction ($-p\bar{\bar{I}}$).

Ultimately, the relation between the state of stress (given by $\bar{\bar{\tau}}$) and the state of deformation (given by the velocity field $\vec{u}$) can only be empirical (Schlichting, 2003). Experimental observations indicate that in most cases the shear stress is proportional to the velocity gradient, and the dynamic viscosity μ is the proportionality constant. The list of fluids following this so-called Newtonian law (and thus called Newtonian fluids) is very extensive and it includes liquid metals, as well as air, water and oils, among others. With this consideration, the momentum balance is given by the Navier-Stokes Eq. (10.5):

$$\frac{\partial}{\partial t}\left(\rho\vec{u}\right)+\nabla\cdot\left(\rho\vec{u}\vec{u}\right)=-\nabla p-\nabla\cdot\left(\mu\nabla\vec{u}\right)+\frac{1}{3}\nabla\left(\mu\nabla\cdot\vec{v}\right)+\rho\vec{f} \tag{10.5}$$

For incompressible fluids such as that of LM, Eq. (10.4) holds and, considering as well the changes in μ to be negligibly small, the simplified momentum balance reads as in Eq. (10.6), where $\nu = \mu/\rho$ is the kinematic viscosity:

$$\frac{\partial\vec{u}}{\partial t}+\vec{u}\nabla\vec{u}=-\frac{\nabla p}{\rho}+\vec{f}+\nu\nabla^2\vec{u} \tag{10.6}$$

10.1.1.3 *Energy balance*

This balance is derived from the first law of thermodynamics, dictating that the changes in energy are equal to the net sum of heat sources and work performed by the acting forces. In that context, the stagnation internal energy e_0 as the sum of the internal energy e and the kinetic energy $u^2/2$ is considered as the intensive quantity being transported by the fluid. The heat sources in a given control volume are the surface flux $\vec{q}''$ and, eventually, a volumetric heat generation q'''. The work of all forces studied in the development of the momentum balance is considered. Thus, a balance equation for e_0 can be obtained by replacing c, $\vec{J}$ and Φ from Table 10.1.1 into Eq. (10.2). Furthermore, a transport equation for $u^2/2$ can be derived from algebraic operations on the momentum balance equation. Subtracting both expressions, the generic energy balance for e is given by Eq. (10.7):

$$\frac{\partial}{\partial t}\left(\rho e\vec{u}\right)+\nabla\cdot\left(\rho e\vec{u}\right)=-\nabla\cdot\vec{q}''+q'''-p\nabla\cdot\vec{u}+\left[\nabla\cdot\left(\bar{\bar{\tau}}\cdot\vec{u}\right)-\vec{u}\cdot\left(\nabla\cdot\bar{\bar{\tau}}\right)\right] \tag{10.7}$$

Several simplifications can be applied for LM flows. First, as they are incompressible, $\nabla\cdot\vec{u}=0$ and the changes in energy at a constant pressure are given by $\delta e = \delta h = c_p\delta T$. Second, neglecting radiation, the heat flux is given by the Fourier law of conduction $\vec{q}''=-\lambda\nabla T$, where λ is the thermal conductivity. Third, usually there are no external heat sources/sinks within the fluid, i.e. $q''' = 0$. Fourth, the production of heat by friction, expressed by the last term in brackets, is generally small and can be neglected. With all these considerations, the simplified energy balance is given by Eq. (10.8):

$$\frac{\partial T}{\partial t}+\vec{u}\nabla T=\frac{\lambda}{\rho c_p}\nabla^2 T \tag{10.8}$$

10.1.1.4 *Boundary conditions*

A complete description of the flow behaviour involves the solution of Eqs. (10.4), (10.6) and (10.8), coupled by the temperature-dependence of the physical properties, subject to proper initial and boundary conditions. In particular, given the nature of these

differential equations, one boundary condition is needed for the pressure $p(\vec{x})$, two for the velocity $\vec{u}(\vec{x})$ and two for the temperature $T(\vec{x})$.

For flows in a duct or closed cavity as studied in this chapter, the boundary conditions are given at the wall. This geometry sets the following constraints on the flow variables:

- A non-slip condition indicates that the fluid remains in direct contact with the wall and thus they both move locally at the same velocity. For all practical applications where the geometry itself is not moving, this means that $\vec{u}(\vec{x}) = 0$ at the wall. For certain geometries, additional conditions can be obtained from symmetry considerations, e.g. at the centreline of a circular pipe.
- A similar condition of continuity at the wall can be set up for the temperature. Thus, the local fluid temperature is the same as that of the wall. Furthermore, two representative boundary conditions are commonly found in stationary engineering applications: a known distribution of the wall temperature T_w or of the imposed heat flux q''_w, of which an adiabatic wall is just a special case ($q''_w = 0$). In steady state, the continuity condition indicates that the heat flux across the wall must be the same as that into the fluid. For the transient case, as well as for stationary condition where neither T_w nor q''_w are known *a priori*, it is necessary to solve the energy balance within the wall, leading to a conjugate heat transfer problem. A more detailed systematic exposition of thermal boundary conditions is provided by Shah (1978) and Reed (1987).
- For most liquid-metal flows, the effects of pressure on the physical properties (ρ, μ, λ, c_p) can be neglected. Thus, the pressure variable is floated, as only its gradient operates in Eq. (10.6) and thus a reference value is normally assumed at a given position, normally at the duct outlet.

10.1.2 Flow scenarios commonly found in HLM systems

In large systems cooled by (heavy) liquid metals, such as fast reactors and accelerator-driven systems (ADS), many different flow scenarios can be found. Although they are all indeed governed by the conservation equations described in Section 10.1.1, it is worth classifying them at an early stage in the following broad categories.

10.1.2.1 Geometry: Wall-confined, free-surface or two-phase flows

Most flow scenarios consist of a duct or wall-confined cavity filled with a single-phase LM. These include among others the flow throughout the core and steam generator, as well as in the lower and upper plena. In those cases, the boundary conditions are given at the wall as described in Section 10.1.1. This chapter is mainly focused on this type of flow. Turbulent flow in liquid-metal pools and jets are analysed in Section 10.3.6.

Free-surface flow can be found at the interface with the cover gas, as well as in some proposed concepts for windowless beam targets for ADS. These flows are subject to different boundary conditions, and surface tension effects can play a major role. Two-phase flows involving the transport of gas pockets (e.g. bubbles) must be considered for the safety analysis, given the neutronic void feedback in the core. Liquid-metal boiling is of major interest for sodium systems, see for example Kottowski-Dümenil (1994), but not for HLM due to their high boiling point (see Chapter 2). These more complex geometries and flow scenarios are the main topic of Section 10.4.7.

10.1.2.2 Steady-state duct flows: Fully developed or developing

Consider a flow in a very long duct. In steady state all time derivatives in Eqs. (10.4), (10.6) and (10.8) vanish. Further, the boundary conditions at the wall diffuse towards the centre following the momentum and energy balance equations, and eventually they affect the

complete cross-section. The flow is said to be fully developed at the axial position (called the developing length) where the cross-sectional profiles are observed to be constant or in practice, when a representative value falls below a given threshold.

Regarding the transport of momentum, the flow is hydrodynamically developed if the profile of the axial velocity u becomes independent of the axial co-ordinate x. Such a strict condition cannot be established for the temperature, due to the continuous heat transfer at the wall. Instead, the flow is said to be thermally developed if the profile for a non-dimensional temperature T^* remains unchanged. This variable is given by Eq. (10.9) (Seban, 1951), where $\overline{T}_w$ is the mean wall temperature and T_b is the bulk or mean fluid temperature, defined by Eq. (10.10):

$$T^* = \frac{\overline{T}_w - T}{\overline{T}_w - T_b} \tag{10.9}$$

$$T_b(x) = \frac{\int_{A(x)} \rho c_p u T dA}{\int_{A(x)} \rho c_p u dA} \tag{10.10}$$

In the developing region, the evolving cross-sectional profiles are usually accompanied by increased pressure-drop and heat-transfer rates. Thus, the knowledge of the developing length is essential for comparing the results from theoretical predictions and experimental observations.

10.1.2.3 Laminar or turbulent

In the year 1883, Osborne Reynolds presented a groundbreaking experiment where dye filaments were transported by a water flow, following Eq. (10.4). He observed that at low velocities, the dye followed the streamlines, parallel to the axial direction. That is a characteristic of well-structured laminar flow with clearly developed velocity profiles. At higher velocities, however, the dye patterns are completely mixed and the entire cross-section is colored. The flow thus changed its behaviour and became turbulent, and the visual observation provides no further information.

This transition is a consequence of an instability problem, on which plenty of literature is available, see e.g. Lin (1955), Betchov (1967), White (1991) and Schlichting (2003). Within the scope of this chapter, it shall only be noted that it occurs when the inertial forces are much larger than the viscous forces. This concept is represented in non-dimensional terms by a large Reynolds number Re, given by Eq. (10.11), where U and L are a reference velocity and length, respectively, accordingly defined for each geometry:

$$Re = \frac{\rho U L}{\mu} \tag{10.11}$$

For each geometry, a threshold value of Re is found to exist (around 2 300 for a circular pipe), above which the flow becomes turbulent, and essentially transient and three-dimensional in nature. This leads to an increased diffusion of momentum and energy transported by eddy fluid pockets. The modelling of turbulence represents a major part of fluid mechanics in general. In Section 10.3 the main characteristics as applicable to liquid metal flows are presented. Furthermore, given the low kinematic viscosity $\nu = \mu/\rho$ of heavy liquid metals, laminar flows are rarely found in practice.

10.1.2.4 Forced, mixed or natural convection

The transport equations make no distinctions regarding which is the force actually driving the flow and compensating viscous losses. In many engineering problems, this is given by an externally imposed pressure gradient or total mass flow rate coming in and out of the domain. This case, where the driving force is externally imposed by the

boundary conditions, is called of forced convection and is the normal operating regime of many liquid metal systems.

In the absence of such imposed boundary conditions, the flow is driven by the external unit force $\vec{f}$, which in most practical cases is the gravity $\vec{g}$. At a constant temperature, this force brings the fluid at rest ($\vec{u} = 0$) and a constant pressure gradient (hydrostatic pressure) is formed in the vertical direction z. For non-isothermal cases, the differences in temperature δT produce differences in density $\delta\rho$ and thus in the acting force $\delta\rho\vec{g}$. Thus, the fluid is moved by buoyancy alone. This regime is called natural convection or free convection and is relevant for the analysis of situations without an external active driving force (e.g. a pump), such as postulated design-basis accident scenarios.

If these changes are small, the approximation given by Boussinesq (1872) can be applied. In that case, the flow is still considered to be incompressible, with a constant reference density ρ_0 corresponding to the temperature T_0, and the changes in density are only considered to affect the buoyancy term in the momentum equation (10.6). Thus, this equation can still be used for representing the flow behaviour, using a modified gravity ($\vec{g}'$) and pressure (p') variables as in Eq. (10.12), where β [K^{-1}] is the volumetric expansion coefficient:

$$\beta = \frac{1}{\rho_0}\frac{\partial\rho}{\partial T}\bigg|_{T_0} \; ; \; \vec{g}' = \vec{g}\,\beta\left(T - T_0\right) \; ; \; p' = p - \rho_0\vec{g}\cdot\vec{x} \tag{10.12}$$

In this context, the main non-dimensional parameter characterising the flow is the Grashof number *Gr*, given by Eq. (10.13), where ΔT is a reference temperature difference. For problems with a heat flux boundary condition, several modified Grashof numbers can be defined. In particular, Gr^* considers $\Delta T^* = q''_w L/\lambda$ as the reference temperature difference, and Gr' is based on the axial temperature gradient, with $\Delta T' = \partial T/\partial x L$ as a reference:

$$Gr = \frac{g\beta\Delta T L^3}{\nu^2} \tag{10.13}$$

An intermediate regime is found when an external component drives the flow (forced convection) but buoyancy effects cannot be neglected. This case is called mixed convection or aided flow. It is particularly relevant when the temperature difference is large or the velocity is low. This transition is thus related to both the Grashof and Reynolds numbers. In particular, from non-dimensionalising the governing equations, a criterion based on Gr/Re^2 can be established (Sparrow, 1959). If this ratio is much lower than unity ($Gr/Re^2 \ll 1$) buoyancy effects can be ignored and a pure natural convection analysis can be applied for $Gr/Re^2 \gg 1$. The intermediate region is covered by the mixed-convective regime, and although exact values are difficult to define, some transition criteria have been proposed for liquid-metal flows, as discussed in Section 10.4.6.

10.1.3 Specific features of liquid metals

Compared to other fluids such as air and water, liquid metals present two main specific features. These are given by their physical properties and the experimental conditions, as well as particular consideration for the extrapolation of experimental results, as detailed in the following sections.

10.1.3.1 Physical properties

The main difference between the metals and the other media is that they have a significantly higher thermal conductivity λ [W m^{-1} K^{-1}] and lower specific heat capacity c_p

[J kg^{-1} K^{-1}]. Furthermore, the kinematic viscosity ν [m^2 s^{-1}] of HLM like lead, lead-bismuth eutectic (LBE) or mercury is often smaller than that of air or water, thus leading to a larger *Re* for the same velocity. These properties can be combined to form a characteristic quantity, the so-called Prandtl number *Pr*, given by Eq. (10.14). In a physical sense, this number weights the transport coefficients of momentum (ν) and thermal energy (α), and is thus an essential non-dimensional parameter in convective heat transfer problems:

$$Pr = \frac{c_p \mu}{\lambda} = \frac{\nu}{\alpha}, \text{with} \, \alpha = \frac{\lambda}{\rho c_p} \tag{10.14}$$

It should be noted that *Pr* is based solely on physical properties of the fluid and it does not include the velocity or the geometry. Thus, it becomes difficult to replicate these conditions in an experiment with another fluid. While for engine oils *Pr* is usually of the order O(10^2-10^6) and for "conventional" media like air or water in the order of O(1), liquid metals are located in the much lower range $0.003 \leq Pr \leq 0.06$ (Reed, 1987). For comparison, the Prandtl numbers of several fluids are listed in Table 10.1.2.

Table 10.1.2: Typical Prandtl number for different fluids at 1 bar and different temperatures

Temperature	Mercury	$Na^{22}K^{78}$	Air	Water	Engine oil
000°C	0.0288	0.0517	0.7110	13.61	$4.7 \cdot 10^4$
020°C	0.0249	0.0411	0.7081	7.009	$1.0 \cdot 10^4$
100°C	0.0162	0.0179	0.7003	1.761	$2.6 \cdot 10^2$

Source: Foust (1976), Grote (2012), VDI (2013).

In this context, consider the flow a Newtonian fluid with the temperature T_0 over a semi-infinite plate with the constant temperature T_w. Figure 10.1.1 shows representative velocity and temperature profiles for three cases (a) $Pr \ll 1$ (e.g. liquid metals), (b) $Pr \sim 1$ (e.g. air) and (c) $Pr \gg 1$ (e.g. oils).

For liquid metals (Case [a]), the diffusion of thermal energy from the wall is larger than that of momentum. Thus, the thickness of the thermal boundary layer (δ_{th}) is larger than that of the viscous layer (δ_v) near the wall. This means that there is a large difference between the temperature and velocity profiles in that region (as would also be the case for $Pr \gg 1$) and concepts of similarity between the transport of momentum and of energy cannot be applied.

Figure 10.1.1: Illustration of the influence of *Pr* on the magnitude of the viscous and thermal boundary layers in a two-dimensional flow with inlet temperature T_0 over a plate with a constant wall temperature $T_w > T_0$

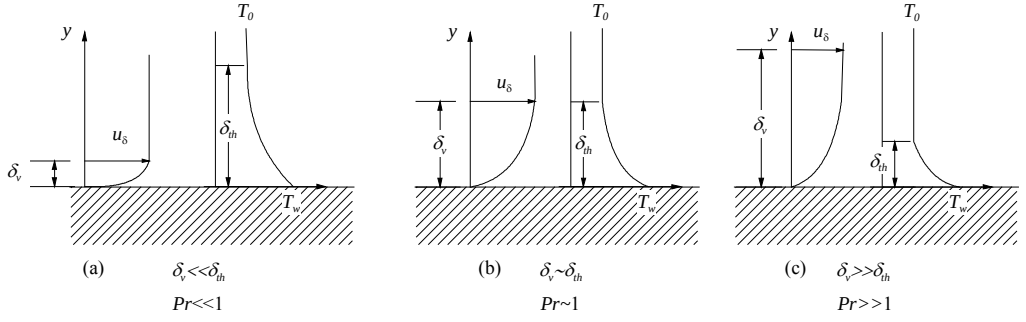

In forced-convective laminar flows, where the thermal transport is dominated by molecular conduction and is not influenced by the velocity profile, this situation does not lead to any fundamental difference with other fluids. Accordingly, non-dimensional correlations developed to describe the heat transfer performance under those conditions, studied in Section 10.2, can be generally applied equally well to liquid metals in spite of their low Prandtl number.

Under turbulent flow conditions, however, eddy conduction of heat becomes important and the process of heat transfer is determined by both transport mechanisms over the various flow regions in the fluid stream. Indeed in turbulent flows of ordinary fluids like air and water, the heat transport is dominated by eddy conduction, except near the wall (in the viscous sublayer). In LM, on the other hand, the eddy transport of heat only exceeds the molecular one for large Reynolds numbers beyond 60 000 for $Pr = 0.025$ (LBE) and beyond 214 000 for $Pr = 0.007$ (Na) (Grötzbach, 2013). Thus, the molecular conduction is felt by the flow not only in the boundary layer but also to a significant extent in the turbulent core of the fluid stream. Due to this fundamental difference in the underlying heat transfer mechanisms, relationships (or correlations) developed to determine the heat transfer coefficients for turbulent flows obtained in other fluids cannot be used for the analysis of LM flows.

10.1.3.2 Experimental conditions and extrapolation of results

An additional challenge for the development of reliable predicting models applicable to liquidmetal flows is the scatter of the available experimental data, particularly for the older data sets. This situation is the result of several conditions related to the experiments, including the following:

- The fluid-to-wall interface can be affected by several phenomena and thus deviate from the ideal case covered by the theory. First, for several combinations of liquid and solid, only partial or no-wetting conditions have been obtained, leading to a reduced heat transfer (Stromquist, 1953). In contact with stainless steel, alkali metals normally show a more complete wetting behaviour than mercury and lead or LBE (MacDonald, 1954). Second, the presence of entrained gas trapped in the wall cavities has been observed for non-wetting conditions by Mizushina (1964), Yovanovich (1970), Winterton (1974) and Bishop (1979), among others. Third, a layer formed by oxides and impurities deposited on the heated wall results in fouling (Kirillov, 1960; Beznosov, 2004; Niu, 2007). Furthermore, these processes can occur simultaneously and interact with each other. In particular, the degree of wetting alone does not have a large impact for clean systems, although non-wetted surfaces are more prone to trap gas bubbles or impurities (Dwyer, 1969). This scenario can lead to a reduction of heat transfer rates as large as 40% (Subbotin, 1963c).
- As well as for other flow conditions, see e.g. Shah (1978), the reliability of the reported data cannot always be easily judged. For many LM experiments a detailed description of the thermal and viscous boundary conditions, as well as of the evaluation methods and physical properties considered, is incomplete. Furthermore, the experimental uncertainty when measuring small temperature differences (for a description of challenges in the instrumentation of LM flows, see Chapter 11 of this book) has not always been reported.
- Buoyancy effects can distort the velocity profiles at large heat fluxes, even at high Reynolds numbers, where pure forced convection is normally expected to occur. Thus, it should be checked whether some results that were reported as for forced convection were not actually measured in the mixed-convective regime. Some criteria for this transition have been proposed, for example, by Buhr (1968) and Jackson (1983).

Taking into account these considerations, extensive knowledge can be derived from previous experiments. In particular for heavy LM, valuable lessons can be learned from experiences in alkali metals, in the framework of sodium breeder and fusion reactor development programmes. For the extrapolation of these results, the geometry and the main non-dimensional flow parameters (*Re*, *Pr*, *Gr*) must be respected. In strict terms, this would mean repeating the exact same experiment, which is impractical and some approximations are possible. In that context, it should be recalled that the range of *Pr* is generally smaller for alkali metals than for heavy LM such as lead and LBE (see Figure 10.1.2).

Figure 10.1.2: Molecular Prandtl number as a function of temperature in °C for different fluids

The thermo-physical data for lead and lead-bismuth are taken from this book, while the data for sodium, the eutectic sodium-potassium alloy ($Na^{22}K^{78}$) are from Foust (1976), mercury (Hg) from Lyon (1954), lithium from Addison (1984), lead-lithium ($Pb^{83}Li^{17}$) from Jauch (1986) and gallium-indium-tin from Barleon (1996)

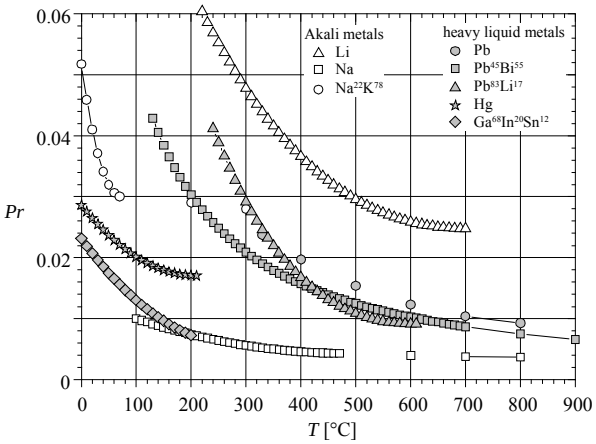

Given the differences in density (and thus in the kinematic viscosity ν) it is normally not possible to match simultaneously both *Re* and *Pr* for alkali and heavy LM. In that case, a compromise can be found by keeping *Re* and *Pr* within the same range (i.e. respecting the flow regime) and matching the Péclet number *Pe*, given by Eq. (10.15):

$$Pe = Re\,Pr = \frac{\rho U c_p L}{\lambda} = \frac{UL}{\kappa} \tag{10.15}$$

As the product of *Re* and *Pr*, *Pe* represents the ratio of thermal energy transported by convection ($\rho U c_p$) and by molecular conduction (λ/L). Thus, for a given geometry and boundary conditions, experimental results for alkali and heavy liquid metals can be compared by means of the Péclet number, as long as both *Re* and *Pr* are not substantially different.

In the absence of detailed information for a specific geometry, the heat transfer rates are generally estimated using correlations developed for a more generic geometry (e.g. a circular tube) and the concept of the hydraulic diameter d_h, expressing the ratio of surface to perimeter. For liquid metal flows, this approach provides an accurate description only in limited scenarios. One example is the flow along widely spaced rod bundles, which can be well approximated by correlations developed for an annular flow (Rehme, 1987; Ma, 2012). In the general case, however, the distortion between temperature and velocity profiles as a consequence of the low Prandtl number results in a large influence of the geometry and the boundary conditions on the flow thermal behaviour. Thus, the concept of hydraulic diameter cannot be used to compare arbitrary geometries in liquid-metal flows with heat transfer (Dwyer, 1976; Reed, 1987; Kirillov, 2001; Kays, 2007).

10.2 Laminar flow and heat transfer in ducts

As discussed in Section 10.1.2.3, laminar flows at Reynolds numbers present a stable structure and analytical solutions for the governing equations can be obtained for simple geometries and boundary conditions. Since a deep mathematical description is possible, laminar flows have been widely investigated for over a century. A vast amount of literature has been published on this topic, already compiled elsewhere; as a remarkable example, see the book by Shah (1978).

It should be noted, however, that liquid-metal flows are rarely laminar. Although the threshold Reynolds number leading to the onset of turbulence (Re_{crit}) strongly depends on the geometry and particularly, on the wall roughness, see e.g. Schlichting (2003), it is generally too low for common applications of liquid metals in nuclear engineering systems. For example, for a circular duct (Re_{crit} = 2 300), mean velocities of only a few centimetres per seconds would be required. In the current section, some representative solutions of laminar flows are presented for the sake of completeness. It shall be observed that for fully developed duct flows (see Section 10.2.1) the Nusselt number is only governed by the geometry and boundary conditions. The molecular Prandtl number *Pr* (main specific feature of liquid metals, see Section 10.1.3) plays a role in the flow-developing region. The solutions presented in this section shall also provide the basis for the analysis of turbulent flows in Section 10.3, as laminar conditions normally represent upper or lower limits for technical set-ups.

10.2.1 Fully developed flow in circular ducts

As discussed in Section 10.1.2.2, a stationary flow is fully developed when axially constant cross-sectional profiles are achieved. For the transfer of momentum, this means that $\partial u/\partial x = 0$. Inserting this condition into the continuity equation (10.4) immediately yields $v = 0$. Thus, the Navier-Stokes equation (10.6) can be directly integrated (considering a constant pressure gradient and neglecting body forces) and the velocity profile is given by Eq. (10.16), where u_m is the mean axial velocity:

$$u(r) = 2u_m\left[1-\left(\frac{r}{R}\right)^2\right] \tag{10.16}$$

For these conditions, the energy balance reads as in Eq. (10.17). Postulating a variable separation for the temperature as in Eq. (10.18) led to the eigenvalue problem given by Eq. (10.19), where all the eigenfunctions $\theta_{r,n}$ and $\theta_{x,n}$ must fulfil the boundary conditions:

$$\rho c_p u(r)\frac{\partial T}{\partial x} = \frac{1}{r}\frac{\partial}{\partial r}\left(\lambda r\frac{\partial T}{\partial r}\right) \tag{10.17}$$

$$T(x,r) = \sum_{n=0}^{\infty} c_n \theta_{r,n}(r)\theta_{x,n}(x) \tag{10.18}$$

$$\frac{1}{\theta_{x,n}}\frac{d\theta_{x,n}}{dx} = \frac{1}{\rho c_p u(r)\theta_{r,n}}\frac{1}{r}\frac{d}{dr}\left(r\frac{d\theta_{r,n}}{dr}\right) = -\lambda_n^2 = constant \tag{10.19}$$

This eigenvalue problem, postulated over 125 years ago, see Graetz (1882, 1885), is known as the Graetz problem and it represents the basis for the analytical study of hydrodynamically developed laminar flows. In its general expression, unfortunately, an infinite number of eigenvalues and eigenfunctions are required, as observed in Eq. (10.18). Nevertheless, practical engineering solutions have been developed for different boundary conditions, as detailed below.

For a uniform wall heat flux boundary condition, the axial temperature gradient $\partial T/\partial x$ is a constant and Eq. (10.17) can be directly integrated. Expressing this result in terms of the non-dimensional temperature T^* (see Eq. [10.9]) reads as in Eq. (10.20):

$$T^*(r) = \frac{T_w - T(r)}{T_w - T_b} = \frac{6}{11}\left[1 - \left(\frac{r}{R}\right)^2\right]\left[r - \left(\frac{r}{R}\right)^2\right] \tag{10.20}$$

This temperature profile leads to a constant heat transfer coefficient α and its corresponding non-dimensional Nusselt number Nu. It can be calculated as in Eq. (10.21):

$$Nu = \alpha\frac{D}{\lambda} = \frac{q''_w}{T_w - T_b}\frac{D}{\lambda} = \frac{48}{11} \approx 4.364 \tag{10.21}$$

For a uniform wall temperature boundary condition, an analytical integration is not possible and the full series expansion as in Eq. (10.18) is suitable. Nevertheless, it can be observed that the axial dependence is of exponential type, and thus the contribution of the different modes $\theta_{x,n}(x)$ vanishes faster for higher values of n and only a limited number of fundamental solutions are needed for a given precision. The interested reader can find a solution based on ten eigenvalues in Sellars (1956). An asymptotic expression for the bulk temperature T_b as a function of the dimensionless axial position $x^* = x/D\,1/RePr$, based only on the first eigenvalue and valid for $x^* > 0.0335$ can be obtained as in Eq. (10.22), where T_0 is the inlet temperature, see e.g. Shah (1987):

$$\frac{T_w - T_b}{T_w - T_0} = 0.8198048\exp\left(-2\lambda_0^2 x^*\right), \text{ with } \lambda_0 \approx 2.70436442 \tag{10.22}$$

An expression for the heat transfer coefficient can be derived from the energy balance expressed in Eq. (10.23). Operating on both equations leads to a constant Nusselt number as in Eq. (10.24):

$$\rho u_m \frac{\pi}{4} c_p \frac{\partial T_b}{\partial x} = \alpha\left(T_w - T_b\right) \tag{10.23}$$

$$Nu = \frac{\lambda_0^2}{2} \approx 3.6568 \tag{10.24}$$

It can be observed that the Nusselt number for a uniform wall temperature boundary condition is lower than for a uniform heat flux. This is a consequence of the different temperature profiles, in particular of the lower temperature gradient in the near-wall region (Kays, 2007). For most turbulent flows (Section 10.3), this situation is not observed because the flow mixing dominates the heat transfer and this process is independent of the thermal boundary condition. In liquid-metal turbulent flows, however, molecular conduction plays a major role due to the low Pr and this influence of the boundary condition is again observed (Section 10.4). Due to the large influence of molecular thermal conduction (which is the only mechanism in laminar flows), liquid-metal flows retain some of the characteristics of laminar heat transfer problems.

As discussed in Section 10.1.1.4, the two idealised thermal boundary conditions considered in this section (constant T_w or q''_w) are the most relevant ones for engineering applications. For a more detailed description of possible thermal boundary conditions and their effect on the laminar fully developed Nusselt number, the reader is referred to Shah (1978). An overview of other phenomena relevant for liquid metal applications for laminar flow is given in Section 10.2.3.

10.2.2 Developing flows in circular ducts

For the analysis presented in Section 10.2.1 it was assumed that the duct was sufficiently long for axially constant cross-sectional profiles to be achieved. In practice, as the effect of

the boundary conditions diffuses from the wall to the centreline, a certain duct length is required for these profiles to develop. This is called the developing length and is denoted by l_{hy} and l_{th} for the hydrodynamic and thermal cases, respectively. As the flow development is asymptotic, these lengths are defined when a certain threshold value is achieved. In particular, for symmetrical ducts the hydrodynamic entrance length l_{hy} is considered when the maximum duct section velocity is 99% of the fully developed value. Similarly, the thermal length l_{th} is defined when the local Nusselt number Nu_x reaches 1.05 times the fully developed value (see Section 10.2.2.1).

Figure 10.2.1: Types of developing laminar duct flow for a constant wall temperature boundary condition

Top – Hydrodynamically developing flow followed by thermally developing (and hydrodynamically developed) flow

Bottom – Simultaneously developing flow in liquid metals ($Pr \ll 1$)

Solid and dotted lines denote the velocity and temperature distributions, respectively

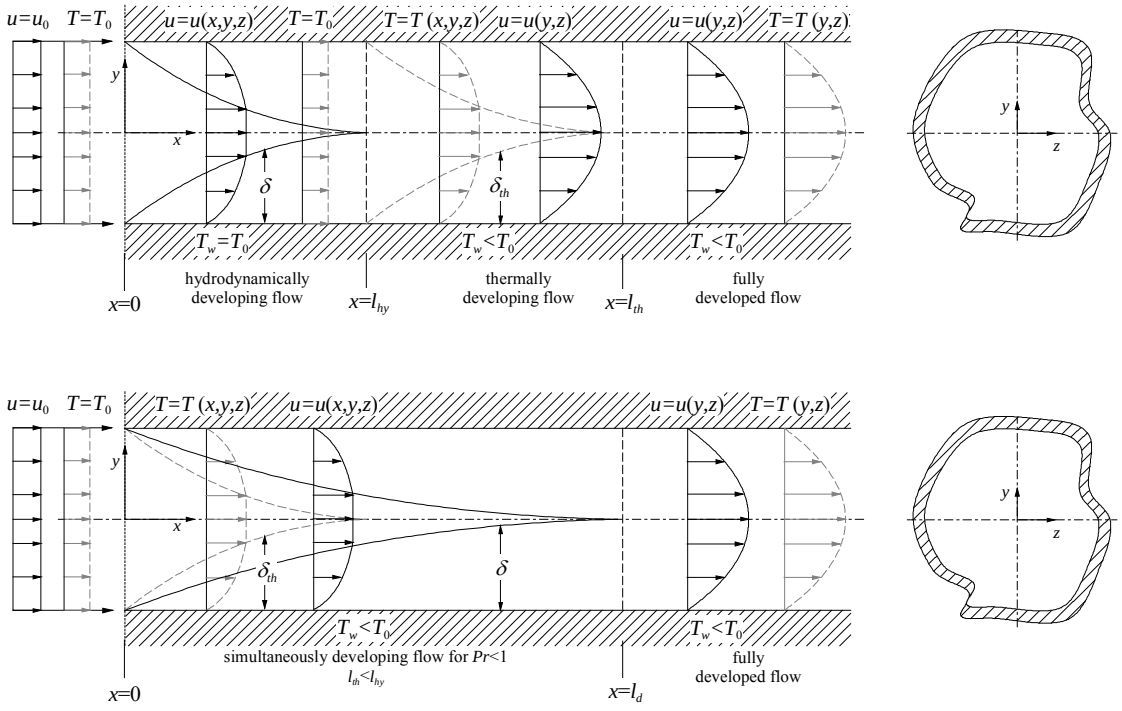

The developing region is characterised by a cross-sectional diffusion of momentum and temperature, reflected in increased heat transfer rates and pressure gradients. In principle we can distinguish between a hydrodynamically developing region, a thermally developing region and a simultaneously developing region, as depicted in Figure 10.2.1, for the particular case of a constant wall temperature boundary condition.

In the general case, the development of momentum and energy do not necessarily behave similarly, and this phenomenon is dominated by the Prandtl number. In the following sub-sections, the three most representative scenarios for developing laminar flows in circular ducts are presented.

10.2.2.1 Thermally developing flow

In this case, it is assumed that the velocity profile is already developed, though not yet the temperature profile. In practice, these conditions are achieved in experiments with a

relatively long isothermal length, followed by a heated or cooled section. As the flow is already hydrodynamically developed, the velocity profile $u(r)$ from Eq. (10.16) can be assumed throughout the heated section, where the eigenvalue problem given by Eq. (10.19) still holds. In this case, its solutions (assuming a uniform inlet temperature profile) are normally presented in terms of the non-dimensional axial position x^*, defined as in Eq. (10.25). The non-dimensional developing length l_{th}^* is defined accordingly as $l_{th}^* = l_{th}/(DPe)$:

$$x^* = \frac{x}{D}\frac{1}{Re\,Pr} = \frac{x}{D}\frac{1}{Pe} \tag{10.25}$$

Furthermore, as the temperature profile evolves, a local heat transfer coefficient α_x and Nusselt number Nu_x can be defined as in Eq. (10.26). Furthermore, an axially mean Nusselt number Nu_m is defined as in Eq. (10.27). As the flow develops, i.e. as $x \to \infty$, both values of the Nusselt number shall tend to the fully developed conditions presented in Section 10.2.1. With these considerations, the solutions for the thermally developing region are given for different thermal boundary conditions:

$$Nu_x(x) = \alpha_x(x)\frac{D}{\lambda} = \frac{q''w(x)}{T_w(x) - T_b(x)}\frac{D}{\lambda} \tag{10.26}$$

$$Nu_m(x) = \frac{1}{x}\int_0^x Nu_x(x)\,dx \tag{10.27}$$

For a uniform q''_w, numerical values for the first seven eigenvalues, eigenfunctions and constants of the series expansion given by Eq. (10.17) were given by Siegel (1958). This work was later extended by Hsu (1965), who presented accurate values up to $n = 20$, and approximate formulas for higher-order parameters. Replacing these solutions in the temperature profile, the developing length can be calculated, yielding the result given in Eq. (10.28):

$$l^*_{th,q''_w} = \frac{l_{th,q''_w}}{D}\frac{1}{Re\;Pr} = 0.0430527 \tag{10.28}$$

It should be noted that liquid metals have shorter thermal developing lengths than other fluids at the same Re, due to the low Pr. Thus, under laminar conditions of, for example $Re = 2\,000$ and $Pr = 0.03$, this length is less than three times the tube diameter.

Similarly, the local and mean Nusselt numbers (Nu_x and Nu_m, respectively), can be obtained. Although in general, the complete series expansion must be calculated, approximate formulas have been derived. Among them the expressions in Eqs. (10.29) and (10.30) by Grigull (1965) and Shah (1975) are recommended as the best fit of numerical calculations. In both cases, the asymptotic value $Nu(x \to \infty) = 4.364$ as in Eq. (10.21) is obtained. More detailed tabulated values can be found in the book by Shah (1978).

$$Nu_{x,q''_w} = \begin{cases} 1.302\left(x^*\right)^{-\frac{1}{3}} - 1 & \text{for } x^* \le 5.10^{-3} \\ 1.302\left(x^*\right)^{-\frac{1}{3}} - 0.5 & \text{for } 5.10^{-5} < x^* \le 1.510^{-3} \\ 4.364 + 8.68\left(10^3 x^*\right)^{-0.506}\exp\left(-41x^*\right) & \text{for } x^* > 1.510^{-3} \end{cases} \tag{10.29}$$

$$Nu_{m,q''_w} = \begin{cases} 1.953\left(x^*\right)^{-\frac{1}{3}} & \text{for } x^* \le 0.03 \\ 4.364 + \dfrac{0.0722}{x^*} & \text{for } x^* > 0.03 \end{cases} \tag{10.30}$$

For a uniform T_w, a detailed solution can be obtained based on the first ten eigenvalues and eigenfunctions of the Graetz problem derived by Brown (1960) and the formulas for higher-order contributions postulated by Newman (1973). Based on these results, the entry length $l_{th,Tw}$, local and mean Nusselt numbers can be approximated by Eqs. (10.31), (10.32) and (10.33), respectively as recommended by Shah (1975):

$$l^*_{th,T_w} = \frac{l_{th,T_w}}{D}\frac{1}{Re\ Pr} = 0.0334654 \tag{10.31}$$

$$Nu_{x,T_w} = \begin{cases} 1077\left(x^*\right)^{-\frac{1}{3}} - 0.7 & \text{for} \quad x^* \le 0.01 \\ 3.657 + 6.874\left(10^3 x^*\right)^{-0.488}\exp\left(-57.2x^*\right) & \text{for} \quad x^* > 0.01 \end{cases} \tag{10.32}$$

$$Nu_{m,T_w} = \begin{cases} 1.615\left(x^*\right)^{-\frac{1}{3}} - 0.7 & \text{for} \quad x^* \le 5.10^{-3} \\ 1.615\left(x^*\right)^{-\frac{1}{3}} - 0.2 & \text{for} \quad 5.10^{-3} < x^* \le 0.03 \\ 3.657 + \dfrac{0.0499}{x^*} & \text{for} \quad x^* > 0.03 \end{cases} \tag{10.33}$$

Furthermore, following this solution, the dimensionless temperature distribution $T^*(x,r)$ as a function of r/R and x^* is depicted in Figure 10.2.2(a) and the mean local Nusselt number Nu_x and the mean Nusselt number Nu_m are shown in Figure 10.2.3(a). In both cases, the asymptotic value $Nu_{Tw}(x \to \infty) = 3.6568$ as in Eq. (10.24) is obtained.

A convective boundary condition is commonly found in heat exchangers. In this case, the wall is externally cooled (or heated) by a fluid at a temperature T_e and with a heat transfer coefficient α_e. The thermal resistance of the wall R_w can be represented by the Biot number Bi given by Eq. (10.34):

$$\frac{1}{Bi} = R_w = \frac{\lambda}{\lambda_w}\frac{t_w}{D} + \frac{\lambda}{\alpha_e D} \tag{10.34}$$

This number can be conceived as a ratio of the thermal resistance of the fluid and that of the wall. On the one hand, for large thermal resistance, i.e. $Bi \to 0$, this condition can be represented by a uniform q''_w and the solution if given by Eqs. (10.28) to (10.30).

Figure 10.2.2: Dimensionless temperature distribution for thermally developing laminar flows in a circular duct along the axial direction (x^*) with constant wall temperature (a) and constant heat flux (b)

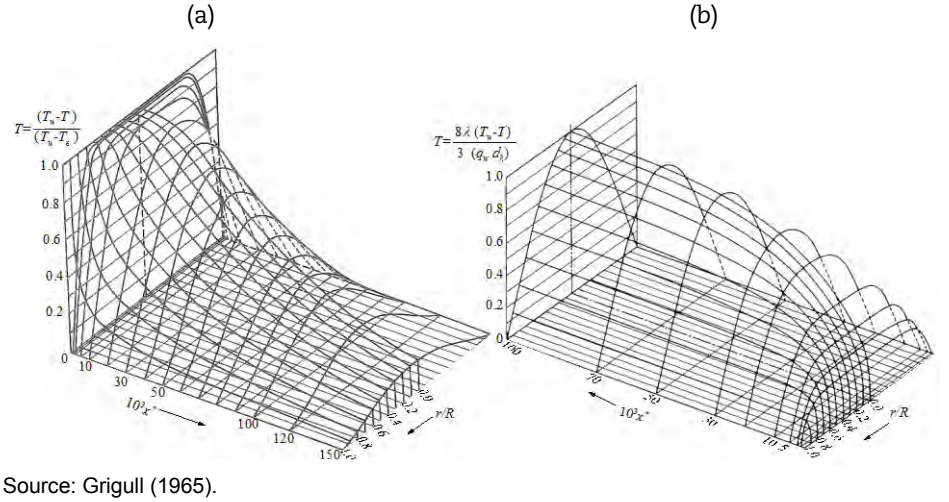

Source: Grigull (1965).

Figure 10.2.3: Nusselt number as a function of the dimensionless entrance length x^* for a hydraulically developed and thermally developing laminar flow in a circular tube

a) Local and mean Nusselt numbers Nu_x and Nu_m for T_w = constant and q''_w = constant

b) Local Nusselt number Nu_x for mixed-convective thermal boundary conditions expressed by the Biot number

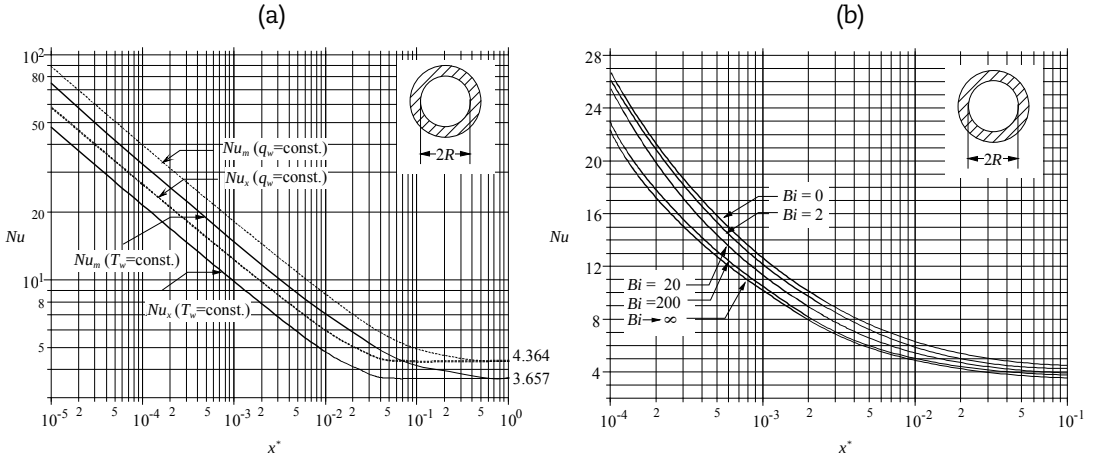

On the other hand, if $Bi \to \infty$, the resistance is very low and a constant wall temperature $T_w \approx T_e$ can be assumed, and the solutions given by Eqs. (10.31) to (10.33) above applies. For intermediate values of Bi, a problem of conjugated convective and conductive heat transfer is obtained. A numerical solution to the series expansion for this problem can be found for example in Hsu (1968). Based on these results, the local Nusselt numbers Nu_x as a function of the dimensionless distance x^* for different Biot numbers are shown in Figure 10.2.3(b). It is important to notice that the extreme cases of $Bi = 0$ (equivalent to q''_w = const.) and $Bi \to \infty$ (equivalent to T_w = const.) are the same as in Figure 10.2.3(a), as discussed above.

10.2.2.2 Hydrodynamically developing flow

In this case, it is assumed that the temperature profile is already developed and the velocity profile evolves. Due to the coupling between the momentum and energy equations, such a scenario can be found in practice only in the case of isothermal adiabatic flow, i.e. $q''_w = 0$ and $T = T_w$. In the absence of heat transfer, this problem is governed by the Reynolds number, and the axial position can be non-dimensionalised as in Eq. (10.35) and many theoretical models have been developed for predicting the developing length l_{hy}:

$$x^+ = \frac{x}{D}\frac{1}{Re} \tag{10.35}$$

For $Re > 400$, an approximation with linearised conservation equations has been widely used, as reviewed in detail in the book of Shah (1978). Among them, the numerical solution of Hornbeck (1964) given by Eq. (10.36) is recommended. For $Re < 400$, Eq. (10.37) was obtained by Chen (1973) by a numerical solution of the Navier-Stokes equations:

$$l_{hy}^+ = \frac{l_{hy}}{D}\frac{1}{Re} = 0.0565 \tag{10.36}$$

$$l_{hy}^+ = \frac{l_{hy}}{D}\frac{1}{Re} = 0.056 + \frac{0.6}{Re\left(1 + 0.035Re\right)} \tag{10.37}$$

Comparing these results with those in Section 10.2.2.1, it can be observed that l_{hy}^{+} and l_{th}^{*} have the same order of magnitude. Thus, the ratio of the developing lengths is approximately the Prandtl number, in particular $l_{th}/l_{hy} \approx Pr$. This mean that in liquid-metal flows the temperature profiles develop much faster than the velocity profile, see Section 10.2.2.3.

In the limiting case $Pr = 0$, corresponding to $\mu = 0$ or $\lambda/c_p \to \infty$, the temperature profile is always developed, while the velocity profile remains flat (plug flow). This means that the non-modified velocity profile has a relatively large flow rate close to the wall, yielding considerably larger heat transfer. Consequently, the Nusselt number results larger than for other fluids with finite Prandtl numbers which follow Eqs. (10.21) and (10.24). The solutions for this limiting case were already obtained by Graetz (1882) and rediscovered by Lévêque (1928), leading to the asymptotic values given by Eqs. (10.38) and (10.39). Although this is an idealised assumption, in practice liquid-metal flows are closer to the asymptotic case of $Pr = 0$ than to the other fluids, such as air ($Pr \approx 0.7$). This fact has led some authors to consider a fully developed value of $Nu = 7.0$ for a constant wall heat flux, see Section 10.4.1. Such value, however, does not find its origin in the solution of the laminar Graetz problem, but rather on empirical observations.

$$Nu_{q_w''}\left(Pr = 0, x \to \infty\right) = 8.0 \tag{10.38}$$

$$Nu_{T_w}\left(Pr = 0, x \to \infty\right) = 5.7832 \tag{10.39}$$

10.2.2.3 Simultaneously developing flow

In contrast to the previous cases, the analysis of a simultaneously developing flow depends inherently on the Prandtl number, and thus results from water and/or air experiments cannot be directly implemented into liquid-metal flows. Two extreme cases can be identified as follows:

- $Pr \to \infty$, in which case the flow is hydrodynamically developed, as described in Section 10.2.2.1.
- $Pr = 0$, meaning that the flow is thermally developed, and falls in the analysis of Section 10.2.2.2.

For any other finite values of the Prandtl number, a complete numerical solution of the eigenvalue problem is required. Some results are presented below for both uniform wall heat flux and uniform wall temperature boundary conditions. A detailed analysis of the convective boundary condition case exceeds the scope of this section. Numerical results for that case for different Biot and Prandtl numbers can be found in Javeri (1976). The dependence of the Nusselt number as it develops in the axial direction for the constant q_w'' and constant T_w are shown in Figure 10.2.4 and Figure 10.2.5, respectively. It is important to notice that the cases with $Pr = 0$ converge towards asymptotic values larger than for other conditions, as discussed in Section 10.2.2.2.

The combined developing length should combine both criteria, i.e. maximum velocity at 99% of its final value and Nusselt value at 1.05 times the fully developed conditions. Several non-dimensional values for this combined entry length have been proposed for $Pr \geq 0.7$, see e.g. Shah (1978). For liquid metals, however, the thermal developing length l_{th} is rather short. Thus, if both the velocity and profiles develop simultaneously (i.e. no previous unheated length), the analysis described in Section 10.2.2.2 is most relevant, as the hydrodynamic entry length is much larger than the thermal one.

Figure 10.2.4: Local Nusselt numbers Nu_x as a function of the dimensionless entrance length x^* for a simultaneously developing flow in a circular tube with the thermal boundary condition q''_w = constant and for different Prandtl numbers

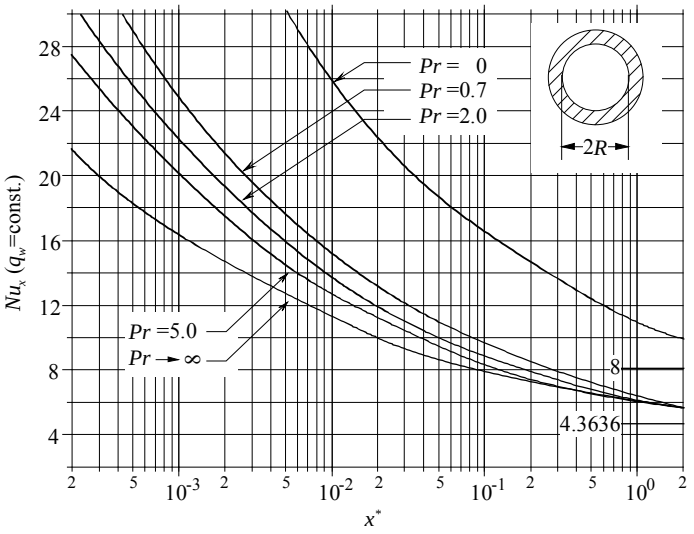

Figure 10.2.5: Local and mean Nusselt numbers Nu_x (a) and Nu_m (b) as a function of the dimensionless entrance length x^* for a simultaneously developing flow in a circular tube with the thermal boundary condition T_w = constant and for different Prandtl numbers

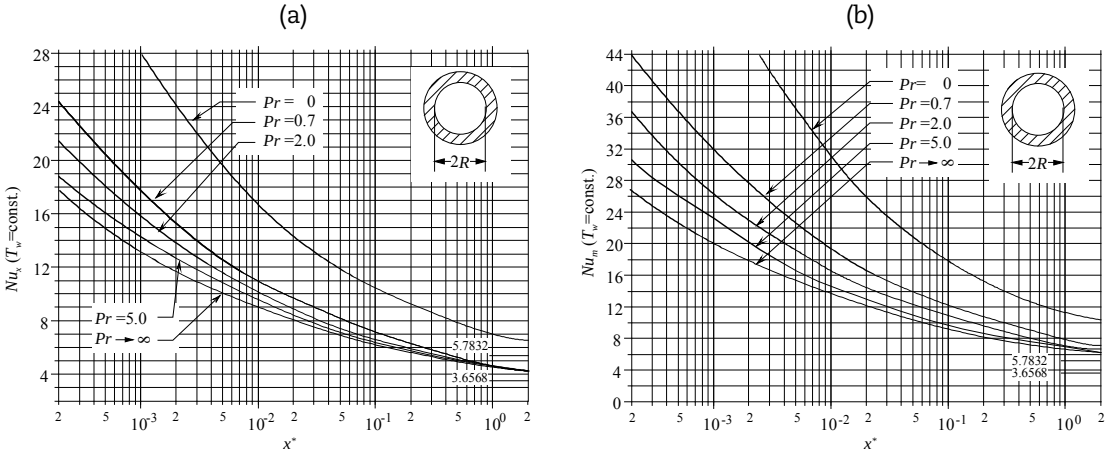

10.2.3 Additional effects: Other geometries and axial thermal conduction

Some additional phenomena which were not included in the previous description and that can be relevant for laminar liquid-metal flows are shortly reviewed in the following paragraphs.

10.2.3.1 Non-circular geometries

In the previous sub-sections, the behaviour of laminar flows in circular ducts has been presented. For other ducts with a constant cross-section, the hydraulic diameter d_h is defined as in Eq. (10.40) for representing a circular pipe with the same area-to-perimeter ratio (= $d_h/4$).

$$d_h = 4\frac{\text{Cross-sectional area}}{\text{Wetted perimeter}} = 4\frac{A}{\Pi} \tag{10.40}$$

Nevertheless, the correlations developed in Section 10.2.1 and 10.2.2 for circular ducts cannot be directly applied to other geometries simply relying on the hydraulic diameter d_h. Instead, the governing equations must be integrated for each geometry and boundary condition. Furthermore, for doubly connected ducts, such as annuli, asymmetric boundary conditions are also relevant. Extensive lists of fully developed Nusselt numbers under conditions of uniform q''_w or T_w for a large number of duct geometries can be found in Shah (1978, 1987). Moreover, solutions in the developing region were reported for flat channels and concentric annuli. For fully developed flow along triangular rod bundles Dwyer (1970) predicted very large azimuthal variations in the wall temperature, thus making the mean Nusselt number representative of the complete geometry only for $P/D \geq 1.4$.

10.2.3.2 Axial thermal conduction

Several authors have studied the extended Graetz problem including the effects of axial conduction in the fluid, which was neglected in the previous sections. In general, it should be noted that, except in the immediate neighbourhood of $x^* = 0$, this phenomenon is only relevant for $Pe < 50$. (Shah, 1978). Such conditions can be achieved, for example, in laminar flow of sodium ($Pr = 0.005$-0.007) or LBE ($Pr = 0.01$-0.04) at low velocities.

Consider a hydrodynamically developed and thermally developing laminar flow heated from the wall ($T < T_w$) with non-negligible axial conduction. In that case, some of the energy transferred from the wall to the fluid is diffused upstream and the local temperature gradient (and consequently the heat transfer coefficient) is increased. Thus, in thermally developing flows, axial heat conduction results in a larger Nu_x and also a longer developing length. According to the calculations presented by Hennecke (1968) l^*_{th} increases considerably from 0.033 for $Pe \geq 50$ to 0.5 for $Pe = 1$.

For a fully developed laminar flow, axial conduction has no effects for a constant q''_w condition, because in that case $\partial^2 T/\partial x^2 = 0$. For a constant T_w boundary condition, on the other hand, the situation described above holds. An asymptotic expression given by Eq. (10.41) was recommended by Michelsen (1974). It should be noticed that the Nusselt number decreases from 4.1807 at $Pe = 0$ until 3.6568 for $Pe \to \infty$. Moreover, this effect is less than 1% for $Pe > 10$.

$$Nu_{\infty,T} = \begin{cases} 3.6568\left(1 + \dfrac{1.227}{Pe^2}\right) & \text{for } Pe > 5 \\ 4.1807\left(1 - 0.0439Pe\right) & \text{for } Pe < 1.5 \end{cases} \tag{10.41}$$

10.3 Turbulent flow modelling

As discussed in Section 10.1.2.3, the transition from laminar to turbulent flow regimes is the outcome of a stability problem. From an experimental perspective, turbulent flows are more complex, always unsteady, diffusive and three-dimensional. In the Reynolds experiment, as the dye covers the entire cross-section, the motion of an individual fluid particle cannot be tracked.

From a strictly mathematical perspective, on the other hand, the governing equations described in Section 10.1.1 also hold for turbulent flow conditions. Although they become more complex, given a complete set of initial and boundary conditions, they can be solved without further assumptions. This first-principles approach is known as direct numerical simulation (DNS) and, with sufficient computational capability, it can potentially describe any flow scenario, based only on the transport equations at a molecular scale.

In practice, due to its large computational requirements, this approach is still restricted to heat transfer problems in rather simple geometries and at low Reynolds numbers, and cannot be applied to many engineering flow problems found in LM systems. In this context, DNS can be considered as a powerful tool with large potential, which can currently be used for the validation of different turbulent models (which are the main topic of this section) under simple conditions. An overview of the application of DNS to LM problems is given in Section 10.3.7.

In this section, existing models for representing the stationary behaviour of a turbulent flow are presented. Thus, although all variables depend on the spatial co-ordinates $x_i = (x,y,z)$ and the time t, they can be represented according to their stochastic nature. In particular, a time-averaged mean value can be defined, as Eq. (10.42) shows for the velocity vector $u_i = (u,v,w)$. For transient cases, it should be recalled that the time interval Δt must be sufficiently large to be statistically representative, but also shorter than the characteristic time of the flow, e.g. L/U. In this context, each variable can be decomposed in this time-averaged mean value plus the fluctuations around it. This so-called Reynolds decomposition reads for the velocity as in Eq. (10.43):

$$\overline{u_i(x_i)} = \frac{1}{\Delta t}\int_t^{t+\Delta t} u_i(x_i,t)\,dt \tag{10.42}$$

$$u_i(x_i,t) = \overline{u_i(x_i)} + u_i'(x_i,t) \tag{10.43}$$

Similar definitions as in Eqs. (10.42) and (10.43) can be given for the pressure $p = \bar{p} + p'$, and the temperature $T = \bar{T} + T'$. These fluctuations, in principle, affect all the thermodynamic and thermo-physical properties of the fluid which depend on the state (p, T). However, these effects shall be neglected in this chapter as they are not relevant for incompressible flows. When suitable, the effects of buoyancy shall be represented by the Boussinesq approximation, see Section 10.1.2.4. In this context, steady-state transport equations for the mean values of stationary flows can be obtained by averaging the Navier-Stokes equations, as described in Section 10.3.1.

By definition, the time average of the fluctuations u_i' is identically zero. The magnitude of these fluctuations is then best represented by the mean value of their squares. This turbulence intensity or root-mean-square (RMS) value is given by Eq. (10.44). Its relative value, defined as in Eq. (10.45) is called the turbulence intensity Tu.

$$\sqrt{\overline{u_i'^2}} = \sqrt{\overline{u'^2} + \overline{v'^2} + \overline{w'^2}} \tag{10.44}$$

$$Tu = \frac{\sqrt{\overline{u_i'^2}}}{\left|\overline{u_i}\right|} \tag{10.45}$$

According to Jischa (1982), common turbulence intensities are 1% downstream of a sieve, 10% close to a wall and above 10% in a free jet. Generally, according to the directionality of the fluctuations, turbulent flows can be divided into three classes, as follows:

- *Isotropic turbulence*. The statistical properties in the whole flow field are the same and are independent of the direction, that is ($\overline{u'^2} = \overline{v'^2} = \overline{w'^2}$). They are invariant against any translation and rotation of the co-ordinate system.
- *Homogeneous turbulence*. All statistical properties depend only on the direction and not on the location. They are translational invariant.

- *Anisotropic or shear turbulence*. This is of practical interest in technical applications, since it appears in boundary layer flows, free jets, duct flows, etc.

10.3.1 *Reynolds equations for turbulent flows*

Most of the present-day prediction methods for turbulent flows are based on the time-averaged Navier-Stokes equations. These are referred to as the Reynolds equations. In the following, the general balance equations for mass (10.3), momentum (10.5) and energy (10.7) are time-averaged, considering the Reynolds decomposition as in Eq. (10.43). Furthermore, a set of assumptions generally applicable to LM flows are considered, similarly as in Section 10.1.1. In particular, the flow is considered incompressible and the buoyancy included by means of the Boussinesq approximation. Furthermore, it is assumed that the molecular heat flux is governed by the Fourier law of conduction and that there are no sources nor sinks of mass, momentum and energy. With all these considerations, the following Reynolds transport equations, as applicable to liquid-metal flows, are obtained:

- Reynolds form of the continuity equation:

$$\frac{\partial \overline{u_i}}{\partial x_i} = 0 = \frac{\partial \overline{u}}{\partial x} + \frac{\partial \overline{v}}{\partial y} + \frac{\partial \overline{w}}{\partial z} \tag{10.46}$$

- Reynolds form of the momentum equation:

$$\rho \overline{u_j} \frac{\partial \overline{u_i}}{\partial x_j} = -\frac{\partial \overline{p}}{\partial x_i} + \frac{\partial}{\partial x_j}\left(\mu \frac{\partial \overline{u_i}}{\partial x_j} - \rho \overline{u_i' u_j'} \right) + \rho g_i \left(1 - \beta\left(T - T_{ref}\right)\right) \tag{10.47}$$

- Reynolds form of the energy equation:

$$\overline{u_i} \frac{\partial \overline{T}}{\partial x_i} = \frac{\partial}{\partial x_i}\left(\frac{\nu}{\mathrm{Pr}} \frac{\partial \overline{T}}{\partial x_i} - \overline{u_i' T'} \right) \tag{10.48}$$

It can be observed that the continuity equation in its time-averaged (Reynolds) form (10.46) is essentially similar to the stationary case (10.4). In other words, as there are no additional mechanisms for the transport of mass (it is only transported by the velocity field u_i), the fluctuations in the velocity field do not affect the stationary mass balance. On the other hand, additional terms appear in the momentum and energy balances by time-averaging them. These new quantities, related to the turbulent motion are:

- the apparent or virtual Reynolds stress tensor $\tau_{ij}^{R} = -\rho \overline{u_i' u_j'}$;
- the turbulent heat flux $q_i'' = \overline{u_i' T'}$.

The major task in solving the turbulence problem is to correlate the Reynolds stress tensor and the turbulent heat flux vector with the temporal mean velocity and temperature fields by means of appropriate turbulence models. Following an analogy proposed by Boussinesq (1897), these additional terms can be represented in terms of turbulent momentum (ν_t, also called ε_M) and thermal (α_t, also called ε_H) diffusivities, as in Eqs. (10.49) and (10.50), where $k = 1/2 \overline{u_i' u'}$ is the turbulent kinetic energy and δ_{ij} is the Kronecker delta function:

$$R_{ij} = -\overline{u_i' u_j'} = \frac{2}{3} k \delta_{ij} - 2\nu_t \left(\frac{\partial \overline{u_i}}{\partial x_j} + \frac{\partial \overline{u_j}}{\partial x_i} \right) \tag{10.49}$$

$$q_i = \overline{u_i T'} = -\alpha_t \frac{\partial \bar{T}}{\partial x_i} \tag{10.50}$$

In this context, the turbulence fluctuations result in an increased diffusivity of both momentum and heat, as ν_t and α_t are directly added to ν and α, respectively, in the time-averaged balance equations. A turbulent Prandtl number Pr_t can then be defined as in Eq. (10.51).

$$Pr_t = \frac{\nu_t}{\alpha_t} = \frac{\varepsilon_M}{\varepsilon_H} \tag{10.51}$$

It should be noted that, while ν, α and Pr are physical properties, their corresponding turbulent parameters ν_t, α_t and Pr_t depend on the local flow velocity and temperature. As this dependence cannot be found in the transport, closure laws are needed. The most relevant proposed models for both the turbulent momentum and thermal transport, as per their application to liquid metal problems, are described in the following sections.

10.3.2 *Laws of the wall: Universal profiles in the boundary layers*

One of the most common engineering problems is computing turbulent flows that are influenced by an adjacent wall. As already discussed, the velocity and temperature gradients are largest close to the solid boundaries. Because both heat transfer and friction are computed using gradients of the dependent variable, it is very important to accurately capture this near-wall variation.

The procedure for deriving boundary layer equations for turbulent flows is similar to that for laminar flows and the details may be taken from the textbooks of Burmeister (1983) and Anderson (1984). Assuming a near-wall fully developed 2-D turbulent flow with negligible pressure gradient in the streamwise direction all statistical properties depend only upon the distance to the wall, represented by the co-ordinate y. The continuity equation is then automatically satisfied with $\bar{v} = 0$. Applying the Boussinesq assumption of eddy diffusivities as in Eqs. (10.49) and (10.50), the momentum and energy equations reduce to Eqs. (10.52) and (10.53), respectively:

$$0 = \frac{\partial}{\partial y}\left[\left(\nu + \nu_t\right)\frac{\partial \bar{u}}{\partial y}\right] \tag{10.52}$$

$$0 = \frac{\partial}{\partial y}\left[\left(\frac{\nu}{Pr} + \frac{\nu_t}{Pr_t}\right)\frac{\partial \bar{T}}{\partial y}\right] \tag{10.53}$$

According to Eqs. (10.52) and (10.53), a fluid with turbulent Prandtl number and molecular Prandtl number equal unity, i.e. $Pr_t = 1$ and $Pr = 1$, has identical temperature and velocity profiles. The first of the preceding conditions is known as Reynolds analogy. Both approximations are generally good for gases, but not for liquid metals. In any case, in the presence of a non-negligible pressure gradient in the momentum equation, much of the similarity between the two above equations would be lost. For the definition of universal profiles near the wall, the following reference variables are defined. A shear velocity u_τ is given by Eq. (10.54), where τ_w is the shear stress at the wall, and a reference temperature difference T^* is defined as in Eq. (10.55):

$$u_\tau = \sqrt{\frac{\tau_W}{\rho}} \tag{10.54}$$

$$T^* = \frac{q''_w}{\rho c_p u_\tau} \tag{10.55}$$

Thus, normalised variables are defined as in Eqs. (10.56) to (10.58):

$$u^+ = \frac{u}{u_\tau} \tag{10.56}$$

$$y^+ = \frac{u_\tau y}{\nu} \tag{10.57}$$

$$T^+ = \frac{T_w - T}{T^*} \tag{10.58}$$

By dividing the near-wall region at $y^+ = 5$ in a laminar and turbulent layer and for a smooth wall, integration of Eqs. (10.52) and (10.53) leads to Eqs. (10.59) and (10.60), as derived by Kader (1972):

$$u^+ = \begin{cases} y^+ & \text{for } 0 \le y^+ \le 5 \\ \dfrac{1}{0.41}\ln y^+ + 5.25 & \text{for } 5 < y^+ < y^*(Re) \end{cases} \tag{10.59}$$

$$T^+ = \begin{cases} y^+ Pr & \text{for } 0 \le y^+ < y_T^+(Pr) \\ \alpha \ln y^+ + \beta(Pr) & \text{for } y_T^+(Pr) < y^+ < y_T^*(Re, Pr) \end{cases} \tag{10.60}$$

It should be noted that the both the extent of the laminar thermal boundary layer and the profile in the turbulent layer depend strongly on the Prandtl number. These parameters must be determined based on experimental information. For the liquid metal regime in circular tubes, the coefficients $\alpha = 2.12$, $\beta(Pr) = 3.85Pr^{0.33} - 1.3)^2 + 2.12 \ln Pr$ and $y_T^+ = 2Pr^{-1}$ were proposed by Kader (1981). A narrower laminar boundary layer $y_T^+ = Pr^{-1}$ is recommended by Kirillov (2001).

The values of the upper limits for the log-law region of velocity and temperature depend on the Reynolds and both Reynolds and Prandtl number, respectively. Actually, the laminar sublayer is continuously transformed into the fully turbulent layer. A transition region exists between the two, known as the buffer layer. The wall laws of velocity and temperature can then be split into three areas, the boundaries of which are set by experimentation. The different extensions of the thermal and velocity viscous sublayer by varying the Prandtl number is known as the separation of scales. Liquid metals, which have a $Pr \ll 1$, are characterised by a thickness of the thermal viscous sublayer ($y^+ \le Pr^{-1}$), much greater than the thickness of the velocity laminar layer ($y^+ \le 5$), as discussed above. An overview on the different definitions between viscous sublayers and fully developed boundary layers may be taken from Shah (1978).

For the transition from the anisotropic turbulent boundary layer towards the isotropic core flow, the logarithmic laws lose their applicability. Within this region the so-called "wake laws" are introduced. There exist numerous articles regarding the description of the velocity profile in pipe flows, which mainly differ only by the constants chosen for the wake profile. A comprehensive picture of the dimensionless velocity distribution in liquid-metal flows can be found in the PhD thesis by Fuchs (1974). Newer results can be taken from Zagarola (1996, 1997), Barenblatt (1998) and Guo (2003).

10.3.3 *Analytical Nusselt number correlations for turbulent parallel flow*

Consider a fully developed turbulent flow in a channel. The resulting shear stress τ and heat flux q'' assume the form as in Eqs. (10.61) and (10.62), respectively combining both molecular and turbulent diffusion mechanisms:

$$\frac{\tau}{\rho} = (\nu + \nu_t)\frac{d\bar{u}}{dy} \tag{10.61}$$

$$\frac{q''}{\rho c_p} = (\alpha + \alpha_t)\frac{d\bar{T}}{dy} \tag{10.62}$$

Considering fully turbulent flows with $\nu \ll \nu_t$, $\alpha \ll \alpha_t$ and $Pr_t = 1$ (Reynolds analogy), the temperature can be integrated as a function of the velocity, since $c_p d\bar{T} = -(q''/\tau)d\bar{u}$. Thus, the non-transfer coefficient and friction factors are directly related, as expressed by Eq. (10.63). The Fanning friction factor (c_f) for fully developed turbulent flows is given in Eq. (10.64):

$$St = \frac{Nu}{Pe} = \frac{c_f}{2} \tag{10.63}$$

$$c_f = 0.0592 Re^{-0.2} \quad \text{for} \quad 5.10^5 < Re < 10^7 \tag{10.64}$$

The Reynolds analogy yields good results for molecular Prandtl numbers larger than $Pr \geq 0.7$. It is also embedded in many commercial computational fluid dynamics (CFD) codes. It definitely fails in describing the heat transport in liquid metals because the assumption of a constant $Pr_t \approx 1$ is not fulfilled for this type of fluid. This problem has been known since Martinelli (1947), and over the last two decades it has been critically reviewed by several authors such as Grötzbach (1992, 2013), Kays (1994), Carteciano (2003) and Arien (2004).

A better analytically derived equation valid for a wide range of Prandtl numbers for a steady turbulent parallel flow with vanishing pressure gradient, $Pr_t = 1$, $u = u(y)$ and $T = T(y)$, can be obtained by separating the boundary layer into a viscous sublayer and a fully turbulent layer (*Prandtl analogy*), see e.g. Baher (2011) leading to Eq. (10.65):

$$St = \frac{Nu}{Pe} = \frac{c_f}{2}\frac{1}{1 + (Pr - 1)5\sqrt{\frac{c_f}{2}}} \tag{10.65}$$

It can be observed that, for $Pr = 1$, Eq. (10.65) is identically equal to Eq. (10.63). However, the increase of Pr_t with decreasing Pr, as observed in numerous experiments (see Section 10.3.5), invalidates the applicability of Prandtl analogy to liquid-metal flows.

Following the ideas of Prandtl, von Kármán divided the flow field into three layers, the viscous sublayer ($y^+ < 5$) a transition layer ($5 < y^+ < 30$) and a fully turbulent region ($y^+ > 30$). He assumed an identity of the molecular and the turbulent quantities, i.e. $\nu = \nu_t$ and $\alpha = \alpha_t$, in the intermediate transition layer. Integration of these profiles leads to Eq. (10.66):

$$St = \frac{Nu}{Pe} = \frac{c_f}{2}\frac{1}{\left[Pr - 1 + \ln\left(\frac{5Pr + 1}{6}\right)\right]5\sqrt{\frac{c_f}{2}}} \tag{10.66}$$

The exact derivation may be taken from the book by Gebhardt (1971). Again for $Pr = 1$, the Reynolds analogy is obtained. This three-layer model of von Kármán was extended by Martinelli (1947) considering both the molecular heat diffusivity and the eddy diffusivity in the fully turbulent range. Using this approach his analogy is also applicable to liquid metals. The considerations of Martinelli (1947) and especially its restrictions are extensively discussed in the books of Rohsenow (1961) as well as in Knudsen (1958). The results obtained consist of a number of tables. Martinelli's ideas were extended by Rohsenow (1961) by implementing a relation of $Pr_t = f(Pr)$. However, a comparison of the results with experiments only shows satisfactory results for $Pe > 700$. Moreover, the turbulent Prandtl number remains space-independent, which does not hold for liquid metals, as discussed in Section 10.3.5.

10.3.4 *Closure methods for the turbulent transport of momentum*

As discussed in Section 10.1.1, the main specific features of liquid metals are related to the turbulent transport of heat. Regarding the transport of momentum, their behaviour is similar to other Newtonian fluids. In this context, this section does not intend to provide an exhaustive description of available models, as this topic is not specific to liquid metals and is extensively examined in literature, see e.g. Pletcher (1987) and Schlichting (2003).

Nevertheless, it is important to recall that the transport of momentum has a strong influence in the energy balance.[1] Thus, the modelling of the turbulent heat flux, described in Section 10.3.5, is always coupled to a model for the turbulent transport of momentum. For that reason, an overview of proposed closure laws is given in the following sub-sections. Most are based on the concept of an eddy viscosity ν_t as defined in Section 10.3.1, while the Reynolds stress models described in Section 10.3.3.4 do not rely on this assumption.

10.3.4.1 *Algebraic models (zero or one-half equations)*

The simplest approach consists of representing the eddy viscosity as a known function of the mean velocity, without need for additional balance equations. The most representative model in this category is the mixing-length theory postulated by Prandtl (1925). From a physical point of view, this theory considers that in a turbulent flow, individual fluid particles maintain their original momentum over a certain mean free path, prior to colliding to other particles and mixing, thus transporting the momentum. Following this approach, the turbulent fluctuations in the velocity u_i' are given by the scale of the mixing length l and the velocity gradients. This can be translated into the turbulent viscosity for a planar flow as in Eq. (10.67):

$$\nu_t = l^2 \left| \frac{\partial \bar{u}}{\partial y} \right| \tag{10.67}$$

There remains the problem of determining the mixing length l, which cannot be measured directly, but by means of inverting the shear stress, see e.g. Andersen (1975). Several extensions of this model, e.g. von Kármán (1930), van Driest (1956), Cebeci (1974) and Baldwin (1978), have proven to be reasonably adequate for plain two-dimensional flows, particularly in the near-wall region.

It should be noted that Eq. (10.67) considers that the turbulent viscosity is scalar, and thus uniform in all directions. Furthermore, it yields a zero turbulent viscosity in the locations of zero gradient of the mean axial velocity, such as the centreline of a round pipe. This defies both intuition and experimental observations, although in this region the turbulent stress given by Eq. (10.49) is small and thus the error is not that large (Malik, 1981). Nevertheless, for the general case of three-dimensional flows, higher-order turbulence models, as described below, are required.

10.3.4.2 *One-equation models*

More advanced models employ the single partial differential equation for the turbulent kinetic energy:

$$k = \frac{1}{2}\overline{u_i' u_i'} = \frac{1}{2}\overline{u'^2 + v'^2 + w'^2}$$

1. Considering the temperature dependence of the physical properties, the opposite is also true.

A transport equation for k can be derived directly from the Navier-Stokes equations, as in Eq. (10.68), see the derivation e.g. in Rotta (1972):

$$\frac{Dk}{Dt} = P_k + G_k - \varepsilon + \frac{\partial}{\partial x_j}\left(D_j + D_j^{\nu}\right) \tag{10.68a}$$

$$\frac{Dk}{Dt} = \overline{u_i}\frac{\partial k}{\partial x_i} \qquad \text{Convection} \tag{10.68b}$$

$$P_k = -\overline{u_i' u_j'}\frac{\partial \overline{u_i}}{\partial x_j} \qquad \text{Production} \tag{10.68c}$$

$$G_k = -\beta g_i \overline{u_i' T'} \qquad \text{Generation by buoyancy} \tag{10.68d}$$

$$\varepsilon = \nu\overline{\frac{\partial u_i'}{\partial x_j}\frac{\partial u_i'}{\partial x_j}} \qquad \text{Dissipation} \tag{10.68e}$$

$$D_j = -\left(\frac{\overline{u_j' p'}}{\rho} + \frac{1}{2}\overline{u_j' u_i' u_i'}\right) \qquad \text{Diffusion} \tag{10.68f}$$

$$D_j^{\nu} = -\nu\frac{\partial k}{\partial x_j} \qquad \text{Viscous diffusion} \tag{10.68g}$$

Those models considering Eq. (10.68) in conjunction with the algebraic expression for the turbulence length scale (e.g. Prandtl mixing length l) are referred to as one-equation models or $k - l$ models. Several models of this type have been developed, e.g. Schlichting (2003). Among them, the model of Spalart (1994) appears to be the most accurate for practical turbulent flow applications.

10.3.4.3 Two-equation models

These models consider Eq. (10.68) as well as another transport equation for a second turbulent quantity. The most famous and widely used is the $k - \varepsilon$ model, which was initially proposed by Harlow (1968) and modified by Jones (1972) and Launder (1974). The near-wall region is typically treated using a wall-function approach (Bredberg, 2000). Modifications to the $k - \varepsilon$ model to include the effect of buoyancy and streamline curvature on the turbulence structure have also been proposed. Moreover, additional terms have been added to the k and ε equations by Jones (1972) or Chien (1982) to extend their applicability to the viscous sublayer. In this connection the viscous sublayer is often referred to as the region of low turbulent Reynolds number ($k^{0.5} L/\nu$). The inner model is crucial for complex turbulent flows, as for example those containing flow separation or severe property variations. The uncertainty of such inner-region modelling for complex flows appears to limit the range of the applicability of the $k - \varepsilon$ models. The modified $k - \varepsilon$ models by Jones (1972) or Rodi (1980) applicable all the way down to the wall without the need of wall functions are known as low Reynolds number (LRN) $k - \varepsilon$ models. Details of such models are beyond the scope of this work.

Numerous other two-equation models have been suggested. The main difference between these models is the choice of the secondary turbulent quantity, from which the length scale is determined. The most frequently used is the $k - \omega$ model (Wilcox, 1976), where ω is the reciprocal to the time scale or vorticity. This secondary quantity is however more commonly referred to as the specific dissipation rate of turbulent kinetic energy.

Often two-equation models coexist; a famous example is the so-called Shear Stress Transport (SST) turbulence model of Menter (1993, 1994). It combines the advantages of the $k-\varepsilon$ model with those of the $k-\omega$ model. The latter is used in the near-wall region, because, as for LRN models, it can be integrated all the way down to the wall (Wilcox, 2006). The matching of the $k-\omega$ model close to the walls to the $k-\varepsilon$ model in the rest of the fluid domain is performed by means of blending functions.

10.3.4.4 Reynolds stress models (RSM)

These models do not rely on the eddy-viscosity concept. Instead, they solve one equation for each Reynolds stress term. Since only terms in the transport equations for the Reynolds stress (third or higher moments) are modelled, RSM are referred to as *second-moment closures*. RSM naturally include effects of streamline curvature, sudden changes in strain rate and secondary motions. Therefore, they are more strictly related to the underlying physics of the flow than eddy-viscosity-models (EVM) based on the Boussinesq assumption. Nevertheless, RSM are numerically demanding and generally a converged solution is more difficult to obtain. The most widely used RSM are those of Hanjalic (1972), Launder (1975) and Donaldson (1972). A brief description of RSM turbulence models, together with pertinent references, can be found in Reynolds (1976).

A simplification of the RSM is known as algebraic Reynolds stress models (ARSM). This approach is discussed in detail in Rodi (1981). The idea is to simplify the description of the Reynolds stress transport equations, in order to reduce them to algebraic relations that are successively solved iteratively. Unfortunately, ARSM are even more numerically unstable then RSM and hence are rarely used.

10.3.5 Closure methods for the turbulent heat flux

For all theoretical considerations concerning turbulent heat transfer, a central problem is given by the evaluation of the turbulent heat flux $\overline{u_i' T'}$. This quantity is intimately coupled to the turbulent transport of momentum, on which extensive information can be obtained from isothermal problems, see Section 10.3.4. For that reason, the turbulent heat flux is often modelled using the concept of the eddy diffusivity (α_t) and the corresponding turbulent Prandtl number (Pr_t), as described in the following sub-sections. In addition, models based on the transport equations at different levels (Section 10.3.5.4) and direct numerical simulations (DNS, Section 10.3.7) are also available.

A large number of models have been published in the past which address the prediction of Pr_t for two-dimensional boundary layers and duct flows. There is a very strong influence of the molecular Prandtl number on the value of Pr_t, particularly in liquid-metal flows. Additionally, Pr_t varies with the distance from the wall, being higher close to the solid boundary. The increase of Pr_t near the wall is especially important for high Prandtl number fluids because of the very thin thermal boundary layer. Outside this small region the turbulent Prandtl number seems to be constant for fluids with $Pr > 1$. A great amount of effort has been made in the past to develop prediction models which are able to account for the dependence of Pr_t on Pr, as well on the distance from the wall.

The currently massive use of numerical simulation tools to design critical components of liquid metal cooled devices in many technical fields requires a principle understanding of what is modelled in the individual closure assumptions for the turbulent heat fluxes. The type of this modelling plays a decisive role in the analysis of the results. It is clear that not all the details of the modelling can be described within this context. However, the main ideas, the assumptions and the approaches yielding specific results for the different types of closure methods are flash-lighted. Moreover, their range of validity is given as far as known to the authors. To the best knowledge of the authors, a list of the most relevant literature is cited in this context.

10.3.5.1 *Experimental observations*

Bearing in mind the definition of the turbulent Prandtl number, its experimental determination necessitates the measuring of four quantities: the turbulent shear stress ($\overline{u'v'}$), the turbulent heat flux ($\overline{u'T'}$), the velocity gradient ($d\bar{u}/dy$) and the temperature gradient ($d\bar{T}/dy$), as in Eq. (10.69):

$$Pr_t = \frac{\nu_t}{\alpha_t} = \frac{\overline{u'v'}}{\overline{u'T'}} \frac{\partial \bar{T}/\partial y}{\partial \bar{u}/\partial y} \tag{10.69}$$

This is why direct measurements of turbulent Prandtl numbers in confined flows are relatively scarce and hardly available in boundary layers. Experiments on Pr_t in circular tubes indicate its dependency on the Reynolds number Re, the molecular Prandtl number Pr and the distance from the wall expressed by (y/R), i.e. $Pr_t = f(Re,Pr,y/R)$. Eckert (1972) collected measurements of the turbulent Prandtl number for various fluids including heavy liquid metals. He wrote, "The experimental difficulties are obviously so large, that no satisfying coherence between the individual data sets can be established for the liquid metals." A more detailed description of the problem was given by Fuchs (1974), pointing out the following as the main sources of errors:

- determination of temperature and velocity gradients from measured distributions;
- determination of normal turbulent heat flux $\overline{u'T'}$, which is very complex to obtain in liquid metals due to the lack of adequate measurement techniques applicable to these types of fluids.

Although the measuring techniques for liquid-metal systems have greatly evolved since (see Chapter 11), this situation endures. Despite the large experimental difficulties it is clear that the turbulent Prandtl number is larger than unity ($Pr_t > 1$) in LM flows, because of its large molecular thermal conductivity compared to its molecular viscosity. Thus, a turbulence parcel travelling into these fluids transfers more energy than momentum to the adjacent parcels.

There is an influence of the wall distance (y/R) on the turbulent Prandtl number in fully developed flows. In the majority of the experimental investigations Pr_t seems to decrease with increasing distance from the wall, see Azer (1960) or Davies (1969). For the fully developed turbulent flow in circular ducts, the local turbulent Prandtl number was evaluated in detail by Fuchs (1974) for sodium ($Pr = 0.007$) as a function of y/R, with the results depicted in Figure 10.3.1(a). This general tendency is also supported by the measurements of Brown (1957) and Sleicher (1973). Furthermore, the dependence of the measured mean turbulent Prandtl number Pr_{tm} depends strongly on the molecular Prandtl, as shown in Figure 10.3.1(b).

In the liquid-metals range, a large scatter in the experimental data is observed, related to the reasons explained above. From experimental observations the following statements on the mean turbulent Prandtl number Pr_{tm} can be made:

- For $Pr \geq 1$ (air, water, oil, etc.) the turbulent Prandtl number seems to be constant and independent of the Reynolds number and molecular Prandtl number.
- The influence of the Prandtl number and the Reynolds number increases both with decreasing Prandtl number and decreasing Reynolds number.
- The turbulent Prandtl number increases with decreasing Pr and decreasing Re.

An exact formulation for circular ducts was postulated in an integral form by Lyon (1949). Some authors tried to derive formulas for the mean turbulent Prandtl number, based on different assumptions. This aspect will be discussed in the following sub-sections.

Figure 10.3.1: (a) Measured Pr_t as a function of the dimensionless distance y/R in a fully developed turbulent circular duct flow with a constant wall heat flux and Pr = 0.007 (Fuchs, 1974). (b) Measured mean turbulent Prandtl number Pr_{tm} for different Pr for a fully developed turbulent circular duct flow with a constant wall heat flux for two different Reynolds numbers $Re = 2{\cdot}10^4$ (open symbols) and $Re = 10^5$

Experimental data from Fuchs (1974) for Na (□), Buhr (1968) for NaK (○) and Hg (△), Subbotin (1963a) for Na (▽) and PbBi (◊), Sleicher (1958) for air (★), Allen & Eckert (1964) for water (+)

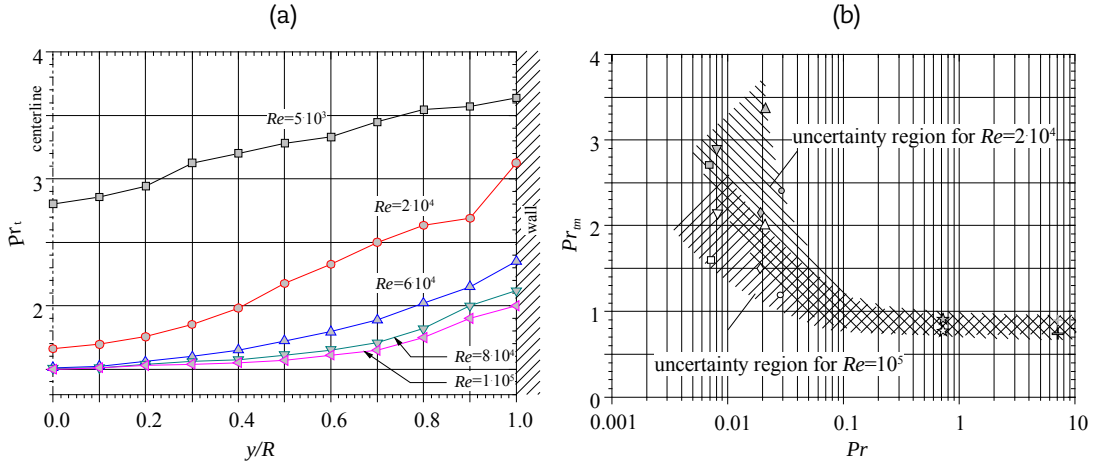

10.3.5.2 *Semi-empirical methods of zero and first order*

Independently of their order, all semi-empirical closures for the turbulent heat flux, do not give detailed insight of the turbulent exchange mechanisms between the velocity fluctuations and the temperature oscillations. For engineering purposes some of them can be applied to assess the heat exchange, but the selected model, its validity and the relative empirical constants chosen often apply only for one fluid in a rather limited range of the dependent parameters. Assuming a constant turbulent Prandtl number close to unity, typically $Pr_t = 0.9$, can give reliable results only for large Reynolds numbers, in which the thermal boundary layer remains small and the turbulent Prandtl number tends to unity. For lower Reynolds number flows, this analogy leads to inaccurate results in liquid-metal flows. This fact should be also considered for numerical simulations using two-equation models without an additional turbulent heat flux modelling, as shown for example in the benchmark studies of Arien (2004).

Extensive work has been devoted to developing predicting models for the turbulent Prandtl number in liquid-metal flows based on experimental observations. Successive reviews of the existing works of these types of closure methods can be found in Reynolds (1976), Kays (1994), Churchill (2002) and Grötzbach (2013). It should be noted that within these types of models, normally a whole branch of assumptions is hidden.

The simplest ones are purely empirical correlations, in which Pr_t is mainly fitted to various experimental data. For example Notter (1969) and Kunz (1969) adopted Eq. (10.70) for LM flows in circular ducts, accepting deviations of ±0.5 from the experiments they considered. In an independent analysis, Quarmby (1972, 1974) concluded that, in view of the scatter of the measurements, it was impossible to isolate the dependence of Pr_t on Pr and Re. Nevertheless, they found an important variation across the pipe and formulated Eq. (10.71) for their individual experiment:

$$Pr_t = \frac{2}{3}\exp\left[0.9\left(\frac{\nu_t}{\nu}\right)^{0.64}\right] \qquad (10.70)$$

$$Pr_t = \left(1 + 400^{-\frac{y}{R}}\right)^{-1} \tag{10.71}$$

This yields $Pr_t = 0.5$ at the wall (which is considerably too low for liquid-metal flows, see Figure 10.3.1) and $Pr_t \approx 1$ at the centreline (which is acceptable for $Re > 5{\cdot}10^4$). These purely empirical results offer neither practical nor fundamental advantages. In fact, the effort spent on these methods ended around the late 1970s.

A more theoretical approach is offered by the individual mixing length models that account for the exchange of momentum and heat transfer between the instantaneous surroundings and a lump of fluid which moves across the gradients of velocities and temperature within the flow. At the end of its journey the lump (mostly considered to be a sphere) is assumed to mix instantaneously with the surrounding fluid; the transfer rate is calculated using the terminal properties of the moving element. This implies more or less a proportional relation between turbulent heat and turbulent momentum flux known from the Reynolds analogy. Clearly, these types of models are physically inconsistent because heat and momentum are continuously exchanged while the parcel moves into the fluid. Nevertheless, several types of mixing length models were proposed ranging from the beginning of the 1950s up to the end of the 1960s. The most famous are the Jenkins-type mixing models (1951), with their several modifications, as summarised in Table 10.3.1. They basically yield the turbulent Prandtl number as a function of the molecular Prandtl number and the turbulent viscosity ratio ν_t/ν with only a marginal dependence on y/R.

Table 10.3.1: Different types of Jenkins mixing length models for Pr_t and their range of validity

Author(s), year	Functional form	Empirical constants	Validity
Jenkins (1951)	$f(Pr,\nu_t/\nu)$	0	All Pr
Sleicher (1957)	$f(Pr,\nu_t/\nu)$	1	All Pr
Rohsenow (1960)	$f(Pr)$	1	$Pr \ll 1$
Tien (1961)	$f(Pr,\nu_t/\nu)$	1	All Pr
Senechal (1968)	$f(y^2\nu/(l\kappa))$	1	$Pr \ll 1$

The other class of mixing length models is formed by the Deissler-type models (1952), which are focused mainly on low Prandtl number fluids like liquid metals. They take into account only the heat transfer from the moving element and relate the length scale of an imaginary fluid sphere in the temperature gradient field to the mixing length. On this scale only molecular diffusion is assumed. These types of models are listed in Table 10.3.2 with their range of validity. The same problem arises as for the Jenkins models, in that the velocity field here is directly coupled to the temperature field, although there is experimental evidence that the statistical features of both fields are different (Kader, 1981; Grötzbach, 2013).

Table 10.3.2: Different types of Deissler mixing length models for Pr_t and their range of validity

Author(s), year	Functional form	Empirical constants	Validity
Deissler (1952)	$f(Pe)$	1	$Pr \ll 1$
Lykoudis (1958)	$f(Pr)$	1	$Pr \ll 1$
Aoki (1963)	$f(Pr\,Re^{2.25})$	1	$Pr \ll 1$
Mizuhina (1963)	$f(Pr,\nu_t/\nu)$	3	$Pr < 1$
Mizushina (1969)	$f(Pr,\nu_t/\nu, all)$	3	$Pr < 1$
Wassel (1973)	$f(Pr,\nu_t/\nu)$	3	All Pr

The advanced mixing length models adopt a more sophisticated picture of the turbulent activity. The defining feature of this category is not the use of an immutable mixing length but the introduction of a discrete element, which gains or loses heat and momentum as it moves through the bulk of the fluid. Nevertheless, this analysis is also constrained by the assumption of a basic analogy between momentum and heat transfer, at least in its statistical behaviour. In the article by Reynolds (1976) the individual aspects of these types of models are discussed as well as their advantages and disadvantages. They seem to fit quite well for the turbulent Prandtl number in duct and parallel plate flows but do not generally account for the temporal behaviour of the temperature and flow field. These more advanced models are listed in Table 10.3.3.

Table 10.3.3: Different types of varied mixing length models for Pr_t and their range of validity

Author(s), year	Functional form	Empirical constants	Validity
Azer (1960)	$f(Pe,Pr,y/R)$	1+	$Pr \ll 1$
Buleev (1962)	$f(Pr,Re,\text{geometry})$	5	All Pr
Dwyer (1963a)	$f(Pr,\nu_t/\nu)$	2	$Pr \ll 1$
Tyldesley (1968)	$f(Pr)$	1	All Pr
Tyldesley (1969)	$f(Pr)$	2	All Pr
Ramm (1973)	$f(Pr,Re,\text{geometry})$	5+	All Pr

These semi-empirical types of closure methods contain also another group of models which is based on the analysis of the Reynolds equations without the direct formulation of transport equations. Additionally, Kays (1993) developed a prediction model for Pr_t, later extended by Weigand (1997), based on the thermal molecular conduction from an eddy during the mixing length. This model is given by Eq. (10.72), where $Pe_t = Pr_t\,(\nu_t/\nu)$, and it can be used for all molecular Prandtl numbers. It contains two empirical constants (C and $Pr_{t\infty}$) which must be determined from available experimental data, and some recommended values for circular ducts are given in Weigand (1997). A functional relation for $Pr_{t\infty} = f\,(Re,Pr)$ was proposed, adjusting some constant in the model from Jischa (1979) for pipe and channel flows:

$$Pr_t = \frac{1}{\dfrac{1}{2Pr_{t\infty}} + CPe_t\sqrt{\dfrac{1}{2Pr_{t\infty}}} - \left(CPe_t\right)^2\left[1-\exp\left(-\dfrac{1}{CPe_t\sqrt{Pr_{t\infty}}}\right)\right]} \tag{10.72}$$

The idea of near-wall damping of the mixing length from van Driest (1956) was adopted by Cebeci (1973), who proposed a turbulent Prandtl number concept, later extended by Chen (1981) for liquid-metal flows in pipes by incorporating the enthalpy thickness, δ_T, in Pr_t. Although the predictions of this model agree well with measured Nusselt numbers for liquid-metal flows, it has the disadvantage that an additional non-linearity is introduced into the energy equation through the enthalpy thickness in Pr_t. This restricts the possibility of analytical solutions of the energy equation for hydrodynamically fully developed flows. Furthermore, the von Kármán constant is changed in the mixing length expression for their calculation. This can derive in misleading results for larger molecular Prandtl numbers.

10.3.5.3 Turbulent Prandtl number from analytical solutions

It should be noted that the analytic class of solutions for the turbulent Prandtl number is not well suited for implementation in a numerical commercial code package.

Nevertheless, they give important information on the near-wall behaviour of the heat flux and thus contribute considerably to the treatment of the thermal wall functions. Moreover, the temporal behaviour of the temperature field is still a part of the final result. This allows verifying the validity of direct numerical simulations (DNS), which are in principle exact but may use a too-coarse grid. Only the analytic solutions are able to provide near-wall data of the kinetic and thermal energy spectrum, because current measurement technologies are still at a stage where they can hardly resolve the viscous and thermal boundary layers simultaneously. The analytic solutions could be used in complex geometries, which are currently not accessible to a DNS. Unfortunately, for the engineering applications these analyses are time consuming and require a lot of effort.

Based on a renormalisation group analysis (Yakhot, 1986), Eq. (10.73) was developed by Yakhot (1987). It is however not clear whether this result is expected to be valid over the entire boundary layer or only in the region where the logarithmic law holds (see Section 10.3.2):

$$\left[\frac{\left(Pr_{eff}^{-1}-1.1793\right)}{\left(Pr^{-1}-1.1793\right)}\right]^{0.65}\left[\frac{\left(Pr_{eff}^{-1}-2.1793\right)}{\left(Pr^{-1}-2.1793\right)}\right]^{0.35}=\frac{1}{1+\frac{\nu_t}{\nu}}\text{ with }Pr_{eff}=\frac{1+\nu_t/\nu}{\frac{\nu_t/\nu}{Pr_t}+\frac{1}{Pr}} \tag{10.73}$$

It is remarkable that nearly all experimental observations match quite well with the above relationship. An asymptotic curve for this expression was given by Kays (1994) as in Eq. (10.74), where Pe_t is the turbulent Péclet number. It looks similar to one previously suggested by Reynolds (1975) but in that case Pr_t is an average throughout the whole boundary layer:

$$Pr_t=\frac{0.7}{Pe_t}+0.85 \tag{10.74}$$

This renormalisation group analysis was later modified by Lin (2000). Within this model a quasi-normal approximation is assumed for the statistical correlation between the velocity and temperature fields. Due to the statistical approach the different time scales of the temperature fluctuations and the velocity fluctuations remain in the model and are coupled together by the wave number k. A differential argument leads to derivation of the turbulent Prandtl number as a function of the turbulent Péclet number, which in turn depends on the turbulent eddy diffusivity ν_t, leading to Eq. (10.75). The functional relationship is comparable to that of Yakhot (1987) but it also contains the spectral properties of both oscillating fields:

$$\left[\frac{\left(Pr_{eff}^{-1}-1\right)}{\left(Pr^{-1}-1\right)}\right]^{2/3}\left[\frac{\left(Pr_{eff}^{-1}+2\right)}{\left(Pr^{-1}+2\right)}\right]^{1/3}=\frac{1}{1+\frac{\nu_t}{\nu}}\text{ with }Pr_{eff}=\frac{1+\nu_t/\nu}{\frac{\nu_t/\nu}{Pr_t}+\frac{1}{Pr}} \tag{10.75}$$

The apparent resemblance between both equations is quite remarkable not only because of the similarity in the mathematical structure, but also because the results are basically derived entirely from different approaches to the renormalisation group analysis of turbulence. Pr_t can be represented in terms of for any given molecular Prandtl number Pr.

A comparison with the direct numerical simulation results of Kasagi (1993) and Kim (1989) shows excellent agreement for $Pr = 0.1$. Excellent agreement with experimental data in sodium at the pipe centreline is also obtained, as shown in Figure 10.3.2(a). They observed that Pe_t is a thermal analogy of the Reynolds number. The reason why Pr_t always tends to 1 as Pe_t becomes sufficiently large would rely on the fact that for $Pe_t \to \infty$ the thermal flow turbulence is completely convection dominated and the temperature field T responds immediately to any change of the velocity field.

Figure 10.3.2: (a) Pr_t vs. Pe_t plotted based on Eq. (10.75) for liquid sodium (Pr = 0.007) in comparison with experimental data by Bremhorst (1992) (□), Sheriff (1981) (Δ) and Fuchs (1974) (O). (b) Scaling law of the thermal energy spectrum $E_{Htur}(k)$ versus the normalised wave number k/k_0 for $Pr \ll 1$ after Lin (2000) in comparison with experiments by Boston (1972)

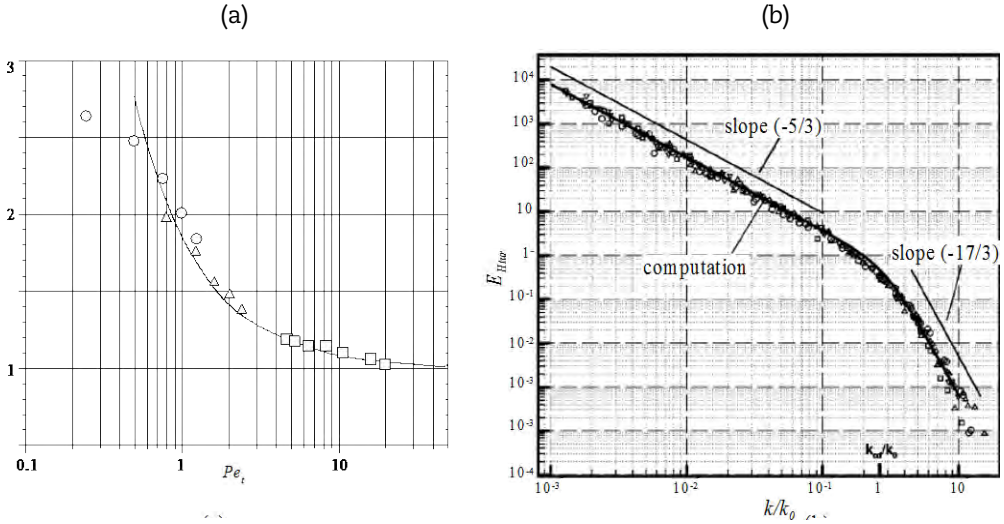

For the thermal energy spectrum, scaling laws have been proposed for $Pr \gg 1$ and $Pr \ll 1$ (Batchelor, 1959a, 1959b). They left undetermined a proportionality constant C_B, which was later estimated or measured by several authors under various flow conditions. For example, based on theoretical reasoning, C_B = 0.208 was obtained by Kraichnan (1971) and C_B = 0.9 by Gibson (1963a). According to their ε-based renormalisation group analysis, C_B = 1.16 was obtained by Yakhot (1987), while independent numerical calculations by Kerr (1990) led to C_B = 0.6. Based on experimental data C_B = 0.35 was estimated by Gibson (1963b); C_B = 0.31 by Grant (1968) and C_B = 0.81 by Boston (1972). In summary, no concern has yet been reached.

Due to the retaining of the spectral information in the model by Lin (2000) the scaling laws for the thermal energy spectrum (E_{Htur}) versus the wave number k can be obtained. Such a thermal energy spectrum, as a function of the normalised wave number, is depicted in Figure 10.3.2(b). It can be observed that in the inertial-convective range the thermal energy spectrum follows a power law of -5/3, while in the inertial conductive range a slope of -17/3 is obtained. The latter value is different from that obtained for large Prandtl number fluids, where in the inertial conductive domain a slope of -1 is observed, see experiments by Grant (1968). Thus, an essential result of the renormalisation group analysis is that the Batchelor constant is not universal, but depends on the shape of the actual thermal energy spectrum.

10.3.5.4 Modelling by transport equations at different levels

In a sense, these models are also semi-empirical methods, because the development of each additional transport equation generates a set of constants *a priori* unknown. These can be either determined experimentally or calculated from exact solutions (analytic or from DNS). The modelling of the turbulent heat flux transport equations follows the same systematic scheme as shown in the section of the turbulent momentum exchange (Section 10.3.4).

A first proposal to model turbulent heat fluxes using transport equations was made by Jischa (1979). Generally, all types of turbulent transport equations exhibit the same structure previously illustrated in Section 10.3.4 and consisting of convective terms,

turbulence production, dissipation, redistribution and diffusion. Every newly modelled transport equation contains unknown correlations and/or time-averaged products, which represent the most challenging part of those models. This can be accomplished with a gradient approach, like Boussinesq approximation for the shear stress, i.e. $\overline{u'v'} \approx \nu_t \, \partial\overline{u}/\partial y$, or even by introducing an additional transport equation if the simple gradient hypothesis gives unsatisfactory results.

In the work of Jischa (1979, 1982) the turbulent fluctuations $\overline{v'^2}$ are assumed to be proportional to the turbulent kinetic energy k. The Prandtl mixing length approach has been used for the dissipation of the turbulent kinetic energy, which in principle is not adequate for liquid metals, since the molecular heat conduction is not negligible for this type of fluid. In the resulting simplified transport equation, the turbulent heat flux is a function of the temperature gradient. Although this model is rather crude, it exhibits the dependence of the turbulent Prandtl number on the distance from the wall and on the Reynolds number. As a disadvantage it should be clearly noted that the thermal eddy diffusivity α_T is still linked to the eddy momentum diffusivity ν_T, thus assuming similar statistical turbulence behaviour. Furthermore the validity of the model is restricted to high Péclet numbers in purely forced-convective flows. Thus, it is not suitable for the simulation of any kind of mixed or buoyant flows, see Section 10.4.6.

Considerable efforts have been devoted in the last two decades to the development of a detailed modelling of the turbulent temperature variance $\overline{T'^2}$ and its dissipation rate:

$$\varepsilon_T = 2\alpha \overline{\frac{\partial T'}{\partial x_i} \frac{\partial T'}{\partial x_i}}$$

A first order four-equation type model has been proposed by Nagano (1988, 1994, 1995). This model proved to be able to represent the physics in more detail, but required of course data for the unknown constants appearing in the new transport equations as well as information on the statistical behaviour of the fluctuations near the boundaries, especially close to the walls. In this region, and in mixed or even more in buoyant convective flows, the turbulence field is strongly anisotropic, which does not allow matching the turbulent normal stresses $\overline{v'^2}$ to the turbulent kinetic energy k, see Durbin (1993b). The details of the more advanced shear stress modelling close to the walls may be taken from Durbin (1993a), Manceau (2000), Ooi (2002) or Speziale (1998).

Also the modelling of the turbulent heat flux equations is still problematic and the reported results are only slightly better than those obtained with lower order closure models based on the eddy diffusivity (Nagano, 1988). Thus, in many forced-convective flows two-equation approaches accounting for the temperature variance $\overline{T'^2}$ and its dissipation rate ε_T are currently the state-of-the-art (Grötzbach, 2004; Karcz, 2005). The details of the different approaches in modelling ε_T may be taken from Sommer (1992), Abe (1995), Shikazono (1996), Deng (2001), or a comprehensive study by Nagano (2002).

Buoyancy-influenced flows exhibit strong heat flux anisotropy close to the walls. A second-order description of the turbulent transport of heat should therefore be applied, (Grötzbach, 2004). This means using an independent transport equation for each of the three components of the turbulent heat flux vector, as in the turbulent model for buoyant flow mixing (TMBF) proposed by Carteciano (1997, 2003).

In purely forced-convective flows, which may even not appear for values of the Reynolds number based on hydraulic diameter beyond $Re > 10^5$ (see Section 10.4.6) a two-equation model, for example the $k - \varepsilon$, may give good results for the mean Nusselt number provided that the appropriate thermal wall function formulation is selected. For this type of problem, only marginal benefits are obtained by implementing higher-order turbulence models (Chandra, 2009; Thiele, 2013). In strongly anisotropic liquid-metal flows

with heat transfer, two-equation models using a constant turbulent Prandtl number (Reynolds analogy) yield unphysical results. In such situations higher-order closure approaches are necessary, in which the turbulent heat fluxes are modelled with transport equations containing the statistical features of the thermal field, introducing unknown constants and triple correlations. These can hardly be determined experimentally due to difficulties with currently available measurement techniques; they are often evaluated by comparison with data from DNS, as described in the following section.

10.3.6 Pool thermal-hydraulics

Throughout Section 10.3, mostly flows along ducts, with a strong influence of the surrounding wall, have been considered. In liquid-metal pool-reactor systems, however, there are large regions where the effect of the wall is minimal, namely in the lower and upper plena. These types of flows are in principle governed by the same balance equations, but the closure methods for their modelling (e.g. the turbulent Prandtl number) must be accordingly verified with specific experiments. Recent reviews on this topic have been published by Tenchine (2010) and Roelofs (2013). In the following paragraphs, an overview of the main challenges for modelling liquid-metal pool flows is given, with the main focus placed on the specific features of low Prandtl number flows.

This configuration leads to several thermal-hydraulic challenges, recently compiled by Tenchine (2010) and Velusamy (2010), as shown in Figure 10.3.3. This list includes the fluctuations near the walls which can lead to thermal fatigue, stratification and stripping and their consequences in the overall natural circulation and the flow behaviour in non-symmetric scenarios, e.g. following the shutdown of some but not all secondary circuits. Moreover, the entrainment of gas by fluctuations of the free surface has been extensively studied as recently reviewed by Tenchine (2014) due to the safety concern of positive void feedback if they are transported to the core.

Figure 10.3.3: Main thermal-hydraulic challenges found in the upper (a) and lower (b) plena of liquid-metal pool reactors

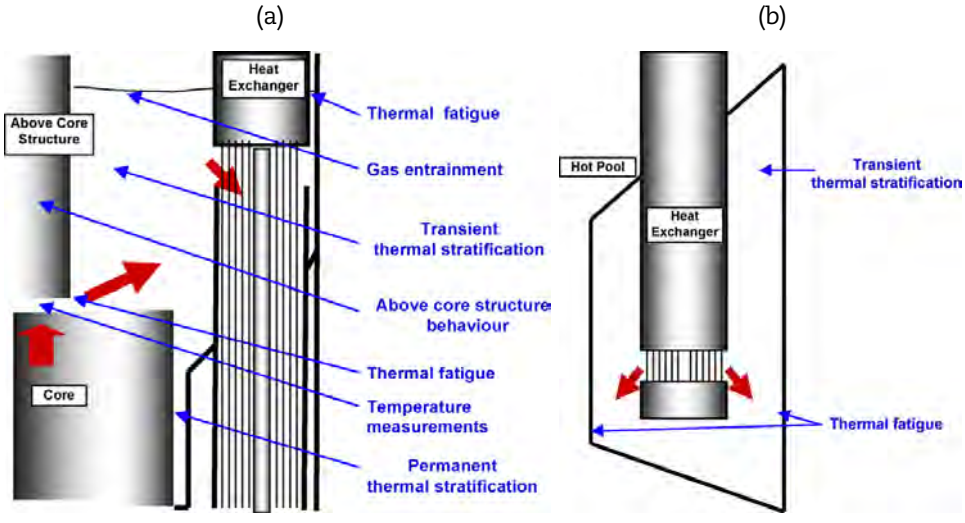

Source: Tenchine (2010).

From a modelling perspective, the most complex feature in this flow configuration is the turbulent mixing both of momentum and temperature. In this geometry the wall effects, which are dominant in duct flows (for which the closure methods described in Sections 10.3.4 and 10.3.5 were mostly developed and validated) play only a marginal role.

In this context, fundamental information for understanding the underlying physics can be obtained by study the mixing of jets at different temperatures.

The effect of the molecular Prandtl number on the mixing of two coaxial (hot and cold) forced-convective jets flowing into a large vessel was studied by Tenchine (1997) in two similar test sections using air and sodium, respectively. In general, reasonable agreement of the mean temperature and temperature fluctuations between both fluids can be obtained at the same *Re*, despite the differences in *Pr* (and *Pe*). The air experiments indicated larger high-frequency fluctuations which gives then a conservative estimation of thermal fatigue for sodium systems (Tenchine, 2013). For a buoyant sodium jet discharging into a slowly moving ambient, Knebel (1993, 1998) observed that the evolution of velocity profiles are similar to the ones observed in air and water, while the temperature fluctuations were found to vary more rapidly in both the axial and radial directions. It was inferred then that the temperature heterogeneities are lower in sodium due to its larger thermal diffusivity α. The low *Pr* results in a large molecular diffusion of heat, thus reducing the turbulent heat flux compared to the turbulent transport of momentum (Carteciano, 2003), i.e. $Pr_t > 1$.

A more complex experiment, considering the interaction of three parallel jets (two hot and the central one cold) in sodium was presented by Kimura (2007), using a similar configuration as experiments in water previously reported by Tokuhiro (1999). Single-jet experiments were also performed, and it was observed that the interaction of the jets largely enhances the mixing. Special emphasis in these experiments was placed on the transfer of thermal fluctuations to the solid walls. The best agreement with the sodium experimental data is given by the LES simulations reported by Tenchine (2013) considering $Pr_t = f(\nu_t)$.

Moreover, experimental set-ups considering a scaled mock-up of the reactor geometry have been performed in water and sodium, and a facility using LBE is currently under construction. For details on these experiments and the corresponding numerical simulations, see Tenchine (2012) and Roelofs (2013). In general, as these investigations are design-specific, they provide relevant information for the feasibility and safety assessment of such systems, while a more accurate validation of turbulent models can be obtained from the mixing-jet problem.

10.3.7 Direct numerical simulation (DNS)

In principle, the direct numerical solution of the time-dependent Navier-Stokes equations represents an exact solution of the problem. Although the computational capabilities considerably increased over the past decade the application of a DNS is still limited to heat transfer problems in rather simple geometries and for low Reynolds numbers. While the current section is focused on the modelling of turbulence for liquid-metal flows, it should be noted that the developments of numerical techniques and computational capabilities have expanded the (yet limited) extent of DNS and more complex problems are expected to be tackled in the upcoming years.

The DNS performed in the last years for low *Pr* fluids were focused on the influence of the Prandtl number in isotropic turbulence (Kasagi, 1993), in near wall flows (Kawamura, 1998, 1999; Piller, 2002; Redjem-Saad, 2007; Ould-Rouiss, 2010) and in buoyancy-governed flows (Otic, 2005). A result of these computations, which is not achievable experimentally, is the spatial and temporal dependence of the statistical properties of the thermal and momentum fields on the different boundary conditions. Thus, the DNS is currently the only available tool to qualify and verify the completeness and quality of computer codes based on transport equations modelling. It reveals their deficits and allows determining more accurate higher-order closures. DNS can thus be perceived as a complementary tool for a more advanced turbulence modelling for technical and engineering applications.

Recently Bricteux (2012) and Duponcheel (2013) adopted a hybrid LES/DNS approach to study the turbulent forced-convective flow of LBE in a channel up to $Re_t = 2\,000$. Due to the reduced temperature fluctuations they could perform with the same grid an LES for the flow and a DNS for the temperature field. Among the different correlations for Pr_t (see Section 10.3.5), they found the one from Kays (1994) to give the best performance. A similar approach was used by Otic (2007) for studying a buoyant sodium jet. An extensive database of DNS solutions has been compiled and made available by Japanese researchers (Kawamura, 1999; Abe, 2004), including some results for $Pr = 0.025$, which is representative of LBE. This database is widely used for the validation of turbulence models, see e.g. Manservisi (2014) and references therein.

10.4 Engineering correlations, models and experiences for liquid-metal flows

A thorough description of theoretical considerations for the analysis of liquid-metal channel flows was presented in Sections 10.1 to 10.3. This complete description consists of a set of governing equations indicating the conservation of mass, momentum and energy, in combination with proper turbulence models. In principle, the solution of this problem allows determining the flow velocity, pressure and temperature profiles. Such fully three-dimensional representation can indeed allow for a very detailed description of the flow. However, such solutions are often not practical due to the complexity of the problem, leading to overwhelming numerical calculations and, despite the remarkable advances in computational capabilities, computational fluids dynamics (CFD) is still restricted in its applicability.

Moreover, such detailed results are often not necessary, as sometimes only the overall changes in temperature and pressure are sufficient. Many technical configurations consist of several devices and each of them acts as a heat sink (cooler) or heat sources (e.g. by viscous dissipation as a valve or mechanical pump, by direct electric heating like an electro-magnetic pump, or the fluid flow through the reactor core). The component interaction is mainly performed by one-dimensional models taking into account relevant correlations for the heat transfer and friction factor in the flow components, to predict the temporal system performance in dependence of normal and abnormal operation cases. This task performed by system thermal-hydraulic codes cannot be replaced by experiments or full CFD representations, and thus engineering correlations continue to play a significant role for the design and operation of complex systems. As engineering correlations are intended for replacing experiments (within a given context), a key issue for determining their applicability is given by the accuracy with which they represent reality.

The present section is focused on Nusselt number correlations for steady-state liquid-metal duct flows under forced-convective and fully developed conditions. Special emphasis is placed on experimental observations and relations derived for representing them accurately. Different duct geometries and, when suitable, varying thermal boundary conditions are studied. Additional comments on the effects of flow-developing and buoyancy on the heat transfer are also included. Pressure-drop correlations are not included in this section, as liquid metals behave similarly to other fluids regarding the transport of momentum. Since the pressure drop is governed by the geometry and the Reynolds number, non-dimensional correlations for the friction factor from the much more extensive database of investigations using e.g. water or air can be directly applied to the analysis of liquid-metal flow.

10.4.1 *Circular ducts*

For both forced-convective in general and liquid-metal flows in particular, the round-tube geometry is the most widely studied configuration for heat transfer. A relatively vast amount of literature has been published on both experimental and theoretical investigation for this particular arrangement since the 1940s. However, a common agreement is not yet available, as often different authors reach contradictory conclusions.

A critical review of the available literature is presented in the following sub-sections for the experimental data (Section 10.4.1.1) and proposed correlations (Section 10.4.1.2). It will be shown that, despite considerable scatter, suitable correlations can be used for predicting heat transfer coefficients (Nusselt numbers) within acceptable accuracies.

10.4.1.1 Survey of experimental data in the open literature

Most of the available data for this configuration correspond to experiments performed before 1970. In this period, a large number of researchers in several countries studied the heat transfer of liquid metals for different geometries and operating conditions. Extensive lists of these early investigations can be found, for example, in the works by Lubarsky (1955), Kutateladze (1958) and Fuchs (1974).

It should be noted, however, that these reported results are not always directly comparable to each other for several reasons related to the experimental conditions, and therefore, they must be properly filtered. For example, while some authors report locally measured heat transfer coefficients, others only presented average values and many researchers do not even indicate to which type their values correspond, thus failing to make their experiments reproducible. In this section, only those locally measured values for fully developed conditions are considered.

An important distinction must be made according to the thermal boundary condition in the test section. Only two cases shall be considered in this analysis, as they are the most relevant from a modelling perspective. First, a uniform heat flux in the wall can be rather well established by means of electric heating. Second, an axially constant wall temperature can be obtained by surrounding the test section with a temperature-controlled solid or liquid jacket. These two thermal boundary conditions can be well reproduced and they reliably represent common theoretical considerations. In addition, several experiments, such as those of Seban (1950a) and Lyon (1951), were performed with a short heat-exchanger-type test section. These results are not included in the present survey because they rely on far-fetched assumptions on the temperature profiles for their evaluation of the heat transfer coefficients and only average values can be reported.

Furthermore, for the purpose of this analysis, the available experiments shall be divided into three groups according to the particular fluid used as follows:

- sodium (Na) and sodium-potassium (NaK) alloys of several compositions;
- pure lead (Pb) and LBE;
- pure mercury (Hg), excluding cases with alkali additives.

Uniform wall heat flux

With the considerations described in the above introduction to this section, this survey is restricted to the experimental data for uniform wall heat flux as summarised in Table 10.4.1. In total, over 1 100 data points from 21 different sources are considered, covering wide ranges of operating conditions (velocity, heat flux, diameter, among others) for both alkali and heavy-liquid metals. In all cases, a vertical upward flow direction has been considered. The large extent of the considered data set allows for a statistical analysis.

In general, all these authors agree in representing their results in terms of the dimensionless Nusselt (Nu) and Péclet (Pe) numbers. Following this reasoning, the complete data set is represented in those terms in Figure 10.4.1(a). Furthermore, in order to identify whether the Prandtl number has any particular effect, the results for each of the three categories of fluids defined above are represented individually in Figures 10.4.1(b) to (d).

Table 10.4.1: Summary of available experimental data in the open literature for fully developed liquid-metal flow in round tubes with uniform wall heat flux

Ref.	Author, year	Fluid	Points	Remarks
1	Styrikovich (1940)	Hg	35	
2	English (1951)	Hg	13	From Lubarsky (1955)
3	Isakoff (1951)	Hg	9	From Lubarsky (1955)
4	Johnson (1952)	LBE	92	From Johnson (1953a)
5	Johnson (1953b)	LBE	127	From Johnson (1953a)
6	Johnson (1953a)	Hg	98	Laminar and transition
6	Johnson (1953a)	LBE	21	Laminar and transition
7	MacDonald (1954)	Na	42	
8	Stromquist (1953)	Hg	15	From Lubarsky (1955)
9	Brown (1957)	Hg	10	
10	Kuczen (1957)	NaK	23	
11	Novikov (1957)	Na	65	
12	Ibragimov (1960)	LBE	21	
12	Ibragimov (1960)	Hg	65	
12	Ibragimov (1960)	Pb	14	
13	Kirillov (1960)	Hg	45	
13	Kirillov (1960)	NaK	109	
14	Subbotin (1963b)	Hg	7	From Fuchs (1974)
15	Holtz (1965)	NaK	89	
16	Skupinski (1965)	NaK	89	
17	Emery (1967)	NaK	18	
18	Buhr (1968)	NaK	4	
19	Borishanskii (1969c)	Na	79	From Fuchs (1974)
20	Borishanskii (1969a)	Hg	35	From Fuchs (1974)
21	Kinoshita (2013)	Hg	63	

A detailed observation of Figure 10.4.1 provides the following conclusions:

- In terms of the Péclet number, a wide range of operating conditions is covered by the data. At a minimum value of $Pe = 10$ and maximum of $Pe = 20 \cdot 10^3$, the laminar, transition and turbulent flow regimes are included in this survey.
- For the three categories of fluids, some experimental results are observed below the theoretical limit for laminar flow $Nu = 48/11 = 4.36$. These results have been categorised by the experimenters themselves and other authors as the consequence of erroneous measurements. In particular, this means that the experimental conditions do not fit to the assumptions of single-phase fully developed flow due to different practical reasons, as discussed below.
- Even neglecting those points below the laminar limit, a relatively large scatter is observed in the data. For comparable values of the Péclet numbers, differences up to ±50% (from a mean value) in the measured Nusselt numbers can be observed.

Some possible causes for the scatter of the experimental data have been discussed in Section 10.1.3.2, as well as by Cheng (2006). These include, among others, the fluid-wall interaction (wetting, entrained gas), and the use of different evaluating procedures for reporting the results only in non-dimensional terms.

- It should also be noted that the differences between fluids (Figure 10.4.1[a]) are not larger than within a single fluid by different authors (Figures [b] to [d]) or even by a single author, e.g. MacDonald (1954) (Ref. 7 in Table 10.4.1). Furthermore, the relative magnitude of this scatter follows the number of authors investigating those particular fluids, that is LBE and Pb < Na and NaK < Hg, as can be observed in Figures 10.4.1(b) to (d) and Table 10.4.1.

Figure 10.4.1: Experimental *Nu* vs. *Pe* data for fully developed liquid metal flow in round tubes under uniform wall heat flux conditions

The numbered legend (1 to 21) assigned to each symbol in the plots (b) to (d) indicate the sources for these data points, as listed in Table 10.4.1

(a) Complete data for all liquid metals

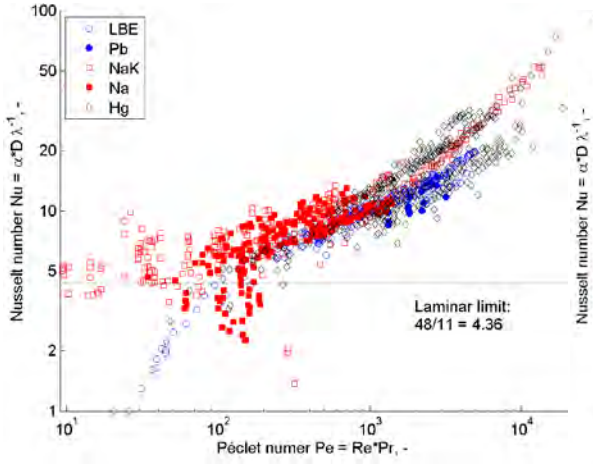

(b) Data for Na and NaK by different authors

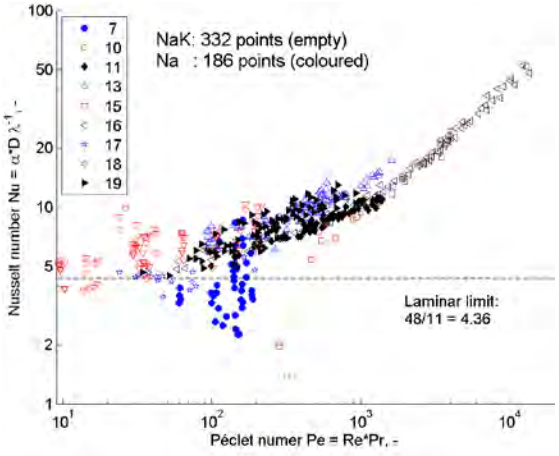

(c) Data for LBE and Pb by different authors

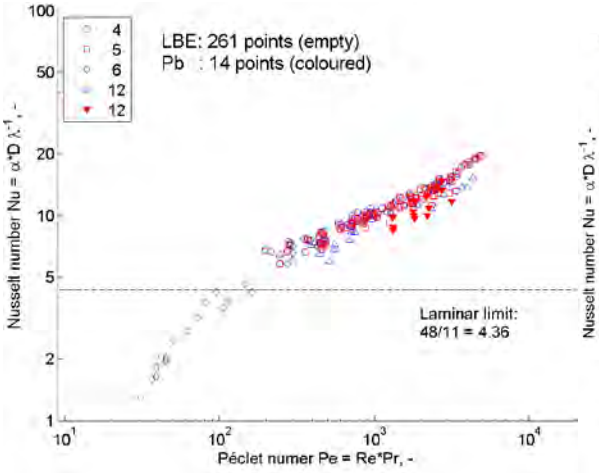

(d) Data for Hg by different authors

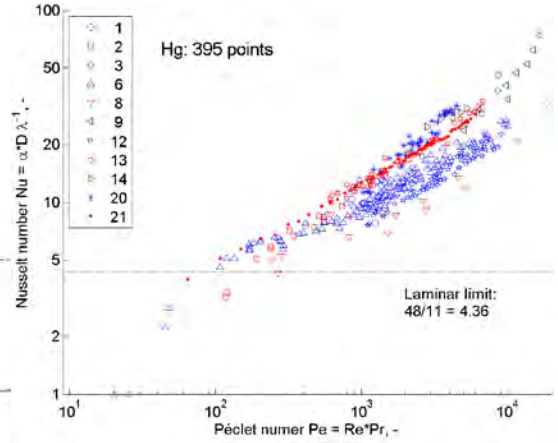

Some previous authors have indicated that the Nusselt number in alkali metal flows is usually larger than for corresponding heavy-liquid metals. This affirmation, however, was based on smaller databases and it is not supported by the data presented here. On the contrary, it can be observed in Figure 10.4.1(a) that, within the uncertainties of the experiments, all liquid metals present similar heat transfer behaviour as represented by the dimensionless Nusselt and Péclet numbers.

Uniform wall temperature

For this thermal boundary condition, there are few reliable experimental data. In particular, only the data sets by Gilliland (1951) and Sleicher (1973), i.e. 22 data points in total, are evaluated and displayed in Figure 10.4.2.

Figure 10.4.2: Experimental *Nu* vs. *Pe* data for fully developed liquid metal flow in round tubes under uniform wall temperature conditions

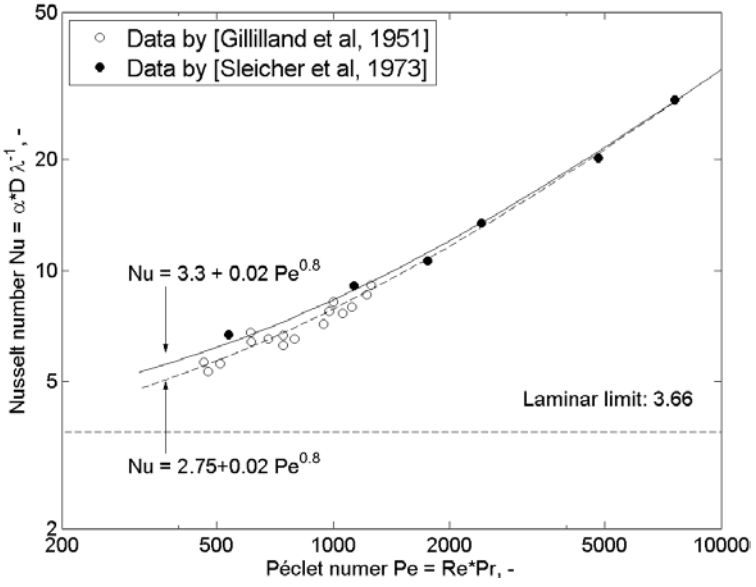

The relatively small number of data points does not allow for a thorough statistical analysis. In general, it can be observed that the measured Nusselt numbers for a uniform wall temperature condition are lower than for a uniform heat flux. Assuming a functional dependence of the type $Nu = a + bPe^{0.8}$ (see Section 10.4.1.2), Reed (1987) proposed Eq. (10.76) as the best fit for the data of Sleicher (1973). However, this correlation slightly overestimates the data by Gilliland (1951). Including both data sets in the analysis, Eq. (10.77) is developed in the present work as a best fit of the complete data:

$$Nu = 3.3 + 0.02\,Pe^{0.8} \tag{10.76}$$

$$Nu = 2.75 + 0.02\,Pe^{0.8} \tag{10.77}$$

All the experimental observations in Figure 10.4.2 correspond to the turbulent regime, within the Péclet range 450-8 000. Therefore, the existence of measured Nusselt numbers below the laminar limit for $Pe < 300$ (as observed for the uniform wall heat flux condition, see Figure 10.4.1) can be neither confirmed nor denied for this boundary condition.

10.4.1.2 Evaluation of analytical, empirical and semi-empirical correlations

Early experiments, e.g. those by Styrikovich (1940) indicated that heat transfer coefficients for liquid-metal flows are not well represented by correlations developed for

other fluids (e.g. water or air), such as the Dittus-Boelter model. Therefore, specific models for these liquids were required and large research efforts were devoted to their development in several countries. Those by Martinelli (1947) and Lyon (1949) are among the pioneer works dealing with the theoretical background explaining the experimental observations. Based on this Lyon-Martinelli model, successive authors have developed empirical and semi-empirical correlations, improving the agreement between measured and predicted values.

In this section, the different available correlations are presented and compared for both: (a) uniform wall heat flux; (b) uniform wall temperature boundary conditions. While several have been already compiled by Reed (1987), that list is extended with further developments, and a critical review of their predicting performance is included.

Uniform wall heat flux

As discussed in Section 10.1.3 the low Prandtl number of liquid metals leads to a scale separation between the thermal and viscous boundary layers. In particular, the role of molecular heat conductivity in the turbulent core is not negligible. In his pioneering work, Martinelli (1947) indicated that the correlations developed for other fluids fail to predict heat transfer in liquid metals precisely due to the different temperature profiles given by this molecular conduction effects. Based on this consideration, Lyon (1949) proposed an integral expression for the fully developed heat transfer coefficient, valid for $Pr < 0.1$. Assuming constant physical and eddy properties along the radial direction, it leads to the Lyon-Martinelli equation (10.78), where Pr_t is the mean turbulent Prandtl number:

$$Nu = 7.0 + 0.025\left(\frac{Pe}{Pr_t}\right)^{0.8} \tag{10.78}$$

The first term in Eq. (10.78) represents the contribution from molecular conduction alone and corresponds to laminar conditions with $Pe \to 0$. According to the laminar theory (Section 10.2), this value should be $48/11 = 4.36$ for common fluids with a developed parabolic velocity profile and 8.0 in the limiting case of $Pr = 0$, where the convective transport of heat would be negligible and the same results as with a flat velocity profile (plug flow) would be obtained. Lyon (1949, 1951) selected the value of 7.0 as the most representative one for turbulent conditions of alkali metal flows. In the second term, which expresses the contribution of turbulent convection, the exponent 0.8 was derived from the assumed velocity and temperature profiles, and it was later found to satisfactorily represent experimental values.

Furthermore, a constant value of $Pr_t = 1$ was assumed by Lyon (1949). As discussed in Section 10.3.5, it has been noticed that $Pr_t > 1$ for liquid metals, thus leading to lower Nusselt numbers. Several empirical and semi-empirical models have been developed for Pr_t, specifically to be used in the Lyon-Martinelli correlation. A recent review, with particular emphasis in LBE, can be found in Chen (2013). Among them, the model by Dwyer (1963a), given by Eq. (10.79), was used by several authors. However, these results are not backed by experimental observations and, according to his own sub-model for (ε_M/ν), it leads to negative values of Pr_t for $Re < 104$:

$$\frac{1}{Pr_t} = 1 - \frac{1.82}{Pr\left(\varepsilon_M/\nu\right)_{max}^{1.4}} \tag{10.79}$$

For that reason, Nusselt correlations relying on empirical models for the turbulent Prandtl number (Pr_t) in addition to the Lyon-Martinelli equation are not considered in this survey, as they depend on too many empirically determined parameters. Instead, only those with the functional relations as expressed in Eq. (10.80) shall be considered:

$$Nu = a + bPe^{c}Pr^{d} \tag{10.80}$$

This type of functional relation is basically an extension of the Lyon-Martinelli model. With few exceptions, the parameter c is close to the value of 0.8 recommended by Lyon (1949). A few authors added a dependence on the Prandtl number, given by the coefficient d, in order to represent the difference between alkali and heavy-liquid metals. While this distinction might be justified by theoretical considerations, it is not observed in the experiments, as discussed in Section 10.4.1.1. This dependence is only slight, as the values of d are rather small, for example, $d = 0.01$ (Chen, 1981). This exponent indicates that a tenfold change in the Prandtl number only results in a 2% difference in the Nusselt number. Therefore, in principle, this dependence can be neglected (that is, assume $d = 0$). In this context, the available correlations reported in the open literature are summarised in Table 10.4.2.

Table 10.4.2: Survey of heat transfer correlations for liquid metals flows with a uniform heat flux

The coefficients a to d correspond to those used in Eq. (10.80)

#	Author, year	a	b	c	d	Remarks
1	Lyon (1949, 1951)	7	0.025	0.8	0	Semi-analytical
2	Stromquist (1953)	3.6	0.018	0.8	0	Fitting Hg data
3	Lubarsky (1955)	0	0.625	0.4	0	Best fit of all data
4	Hartnett (1957)	5.33	0.015	0.8	0	Assuming a slug velocity profile
5	Sleicher (1957)	6.3	0.016	0.91	0.3	
6	Kutateladze (1959)	3.3	0.014	0.8	0	As a lower limit
7	Kutateladze (1959)	5	0.0021	1.0	0	As a lower limit
8	Kutateladze (1959)	5.9	0.015	0.8	0	Developed for Na
9	Ibragimov (1960)	4.5	0.014	0.8	0	
10	Subbotin (1963a)	5	0.025	0.8	0	Developed for Na
11	Skupinski (1965)	4.82	0.0185	0.827	0	Developed for NaK
12	Notter (1972)	6.3	0.0167	0.85	0.08	Based on NaK (T,u) profiles
13	Chen (1981)	5.6	0.0165	0.85	0.01	Developed for Na and NaK eutectic
14	Siman-Tov (1997)	0	0.685	0.3726	0	Developed for Hg
15	Kirillov (2001)	4.5	0.018	0.8	0	Developed for LBE

Furthermore, Cheng (2006) proposed, as a best fit to the LBE data of Johnson (1953a), a broken model, where correlation 14 is recommended for $Pe < 1\,000$ and number 15 for $Pe > 2\,000$, with a linear interpolation for the coefficient a in the intermediate range. However, such transition is not justified when the data from other authors are also considered; see Figure 10.4.1(c). Therefore, it is not included in the present survey.

In order to distinguish between these correlations, they shall be compared in the following analysis with the experimental data presented in Section 10.4.1.1. It should be noted, however, that all these correlations have been developed for fully developed turbulent flow conditions, with Reynolds numbers in the broad range between 104 and 106. Therefore, the complete data set listed in Table 10.4.1 must be filtered in order to provide a fair comparison. In particular, only those experimental data points above the laminar limit ($Nu > 48/11$) and in the Péclet range $Pe > 300$ are taken into account. With this consideration, the database is reduced roughly by 30%. Nevertheless, it remains large enough (855 data points) to allow for a statistical description.

For this analysis, the relative error ε as defined in Eq. (10.81) is considered. In particular, the statistical results are presented in terms of the mean and root-mean-square (RMS) values of ε, defined for a set of *N* data points as in Eqs. (10.82) and (10.83), respectively. On the one hand, the mean value $\overline{\varepsilon}$ gives an indication of directionality, that is if the model over- or under-predicts the measured values. On the other hand, an absolute measure of negative and positive errors is the RMS error $\overline{\varepsilon}_{RMS}$. For that reason, a complete statistical description as given below shall include both indicators:

$$\varepsilon_i = \frac{Nu_{predicted,i}}{Nu_{measured,i}} \tag{10.81}$$

$$\text{Mean value: } \overline{\varepsilon} = \frac{1}{N}\sum_{i=1}^{N}\varepsilon_i \tag{10.82}$$

$$\text{RMS value: } \overline{\varepsilon}_{RMS} = \sqrt{\frac{1}{N}\sum_{i=1}^{N}\varepsilon_i^2} \tag{10.83}$$

A few general conclusions can be derived from Figure 10.4.3, such as the following:

- A clear over-prediction (+ 10%) is observed in all cases (a) to (d) for the correlation number 1 (Lyon-Martinelli with $Pr_t = 1$), which was long used as a reference model. Due to its large mean relative errors up to 40%, its use is not recommended and it shall only be considered as an upper limit for the Nusselt numbers.
- The opposite trend, i.e. an under-prediction, is given by the correlations 2, 4, 6, 7, 9 and 14. Similarly, these models shall only be considered as lower limits for the Nusselt numbers, although the under-predictions are relatively lower for LBE and Pb, see Figure 10.4.3(c).
- Some correlations developed for alkali metals (in particular, those numbered 10 to 12) tend to over-predict the heat transfer rates in heavy-liquid metals. This circumstance, added to the above-mentioned over-prediction of the Lyon-Martinelli equation, has been long understood as alkali metals yielding larger Nusselt numbers than mercury and lead alloys. However, as discussed in Section 10.4.1.1, the cloud of points in Figure 10.4.1(a) does not support this conclusion. On the contrary, this over-prediction is a specific feature only of those correlations. For example, the correlation by Kutateladze (1959) (No. 8 in Table 10.4.2), although developed for sodium, gives similar results for all liquid metals.

Furthermore, the correlations which give the best results for each specific liquid metal can be selected based on the individual results in Figure 10.4.3(a) to (d) as follows:

- Because the three subcategories (Na and NaK; LBE and Pb; Hg) are evenly represented in this database, generic conclusions can be derived. In that context, the best general results are given by the correlation number 12, by Notter (1972), while correlations 3 and 8 also present a good performance. It should be noted, however, that the RMS error for all these models is roughly 20%. Therefore, it might be convenient to use individual models for each specific liquid metal, instead of one unique generic correlation.
- Not surprisingly, the experimental data for alkali metals (Na and NaK) are best predicted by those models developed specifically for them. In particular, correlations 10 and 13 show the best performance, followed by 11 and 12. In this analysis, because the slight dependence on the Prandtl number postulated by Chen (1981) is not justified by the experimental observations, correlation No. 10

(Subbotin, 1963a) is recommended as the most suitable for alkali liquid-metal flows.

- Lead and lead-bismuth measurements are well predicted by correlations No. 3 and No. 8, although they propose rather different functional relations. In particular, correlation No. 8, although it was developed for sodium flows, is rather similar to a best fit of the LBE and Pb data. For example, a least-squares analysis assuming $c = 0.8$ and $d = 0$ in Eq. (10.80) would lead to $a = 5.89$ and $b = 0.0145$, i.e. very similar values to those given by Kutateladze (1959).
- In general, the results for mercury follow the same trend as for Pb and LBE. Nevertheless, in all cases, a relatively large RMS error in excess of 20% is observed. This circumstance is a consequence of the large scatter of the experimental data by different authors, as can be seen in Figure 10.4.1(d). In that context, the best results are obtained by correlation No. 8, followed closely by 3 and 15. It should be noted that these models perform better than others developed specifically for mercury. This is probably a consequence of the limited data sets considered by previous authors for developing their empirically fitted models.

Figure 10.4.3: Statistical evaluation of the predicting performance of several correlations for liquid-metal flow with uniform wall heat flux, in terms of the mean and root-mean-square (RMS) relative errors

The correlations are numbered as listed in Table 10.4.2

(a) Complete data for all liquid metals

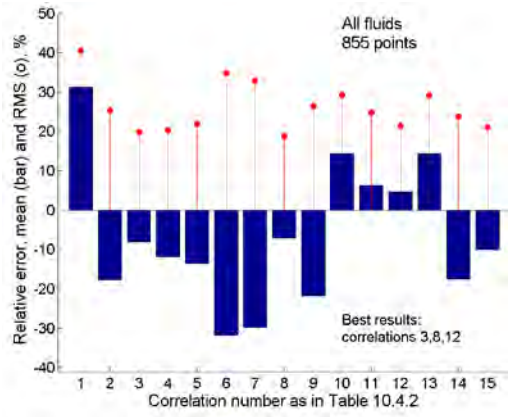

(b) Data for Na and NaK by different authors

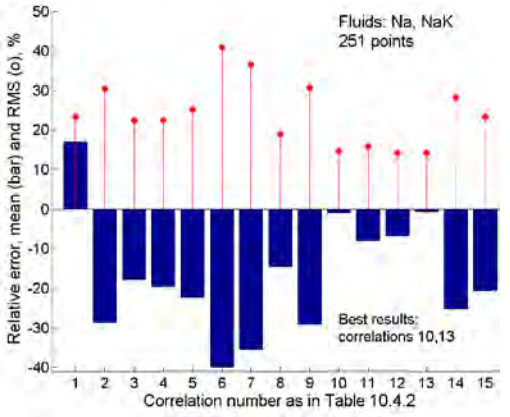

(c) Data for LBE and Pb by different authors

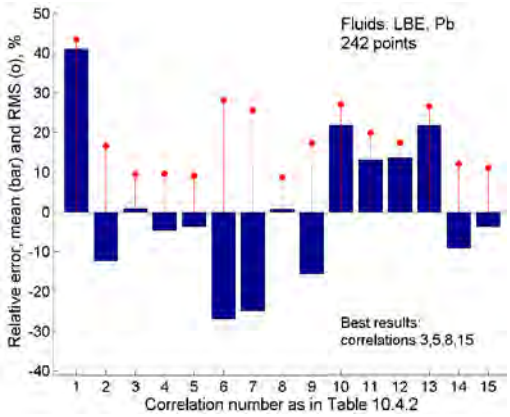

(d) Data for Hg by different authors

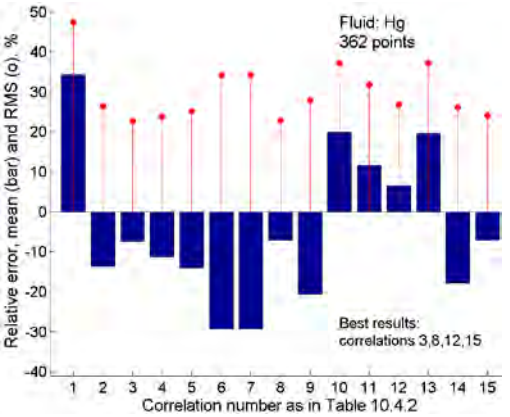

Following these observations, individual correlations for each specific group of liquid metals can be recommended as summarised in Table 10.4.3. It can be concluded from this analysis that for this specific geometry and boundary condition, extensive experimental data as well as empirical models are available. Thus, following such a statistical treatment of the data, suitable recommendations can be made. This is not the case, however, for other geometries and/or boundary conditions.

Table 10.4.3: Recommended correlations and their statistical performance for predicting heat transfer coefficient in liquid metals flow in round tubes with uniform wall heat flux

Fluid(s)	Author(s), year	Equation	$\overline{\varepsilon}$ (%)	$\overline{\varepsilon}_{RMS}$ (%)
All	Notter (1972)	$Nu = 6.3 + 0.0167\, Pe^{0.85} Pr^{0.08}$	+4.7	21.3
Na and NaK	Subbotin (1963a)	$Nu = 5.0 + 0.0125\, Pe^{0.8}$	-0.9	14.7
LBE and Pb	Kutateladze (1959)	$Nu = 5.9 + 0.015\, Pe^{0.8}$	+0.7	8.7
Hg	Kutateladze (1959)	$Nu = 5.9 + 0.015\, Pe^{0.8}$	-7.1	22.9

Uniform wall temperature

As discussed in Section 10.4.1.1, few experimental data for this case are available in the open literature. Nevertheless, this issue has been widely investigated both analytically and numerically by several authors. Based on these investigations, several correlations with the functional dependence as in Eq. (10.80) have been proposed, as summarised in Table 10.4.4.

Due to the limited number of experimental data points, a critical statistical evaluation of the performance of these correlations as for the uniform heat flux case is not suitable. Therefore, few generic conclusions can be derived. In particular, the lower and upper limits are given by the models of Sleicher (1957) and Seban (1951), respectively. The best performance is obtained by models fitting the available data points, i.e. the correlation by Reed (1987) or that derived in this work as in Eq. (10.77). However, as they are purely empirical and do not have a theoretical basis, their extension beyond the exact range of the data is not recommended.

An alternative description has been proposed by Tricoli (1999), based on a surface renewal concept. He postulated that, for incompressible high Péclet and low Prandtl numbers flows, the ratio of local temperature gradients at the wall for uniform wall temperature to that of uniform heat flux remains constant. Following this observation, Eq. (10.84) was proposed and verified with the few available liquid-metal heat transfer data presented above:

$$\frac{\mathrm{Nu}\big|_{T_w = constant}}{\mathrm{Nu}\big|_{q''_w = constant}} = \frac{\pi^2}{12} \tag{10.84}$$

The strong influence of the thermal boundary conditions on the Nusselt number for LM flows has been known since Sleicher (1957). For $Pr = 0.7$ and higher this influence is only a few perc ent, it can be more than 30% for $Pr < 0.01$ (e.g. sodium). Although a dependence on the Reynolds number is to be expected, this constant number ($\pi^2/12$) can be assumed as a first approximation. With these considerations, the Nusselt numbers for uniform wall temperature boundary conditions can be estimated using the correlations recommended in Table 10.4.3 and the correction recommended by Tricoli (1999), expressed as in Eq. (10.84).

Table 10.4.4: Survey of heat transfer correlations for liquid-metal flows with a uniform wall temperature

The coefficients *a* to *d* correspond to those used in Eq. (10.80)

#	Author, year	*a*	*b*	*c*	*d*	Remarks
1	Seban (1951)	5.0	0.025	0.8	0	Assuming a slug velocity profile
2	Harnett (1957)	3.85	0.015	0.8	0	
3	Sleicher (1957)	4.8	0.015	0.91	0.3	
4	Azer (1961)	5.0	0.05	0.77	0.25	
5	Notter (1972)	4.8	0.0156	0.85	0.08	
6	Chen (1981)	4.5	0.0156	0.85	0.01	
7	Reed (1987)	3.3	0.02	0.8	0	Best fit of data by Sleicher (1973)

10.4.2 *Flat channels (flow between parallel plates)*

The flat duct heat transfer problem has been studied quite extensively by many authors in the past, as this type of duct constitutes the limiting geometry for the family of rectangular and concentric annular ducts. In this context a duct is considered to be flat if its height ($2a$) to width ($2b$) ratio is smaller than 0.1, i.e. $a/b \leq 0.1$.

The first detailed analytical study of heat transfer coefficients for liquid-metal flows in non-circular ducts was presented by Hartnett (1957). In their analysis, they presented a generic correlation following the functional dependence as in Eq. (10.80). They considered that only the direct contribution from molecular conduction (coefficient a) is directly related to both the duct geometry and the thermal boundary conditions, while the other coefficients remain constant. This is expressed in terms of the Nusselt number corresponding to a slug flow (Nu_{slug}), in addition to a correction factor (2/3) for the actual velocity profile, as in Eq. (10.85):

$$Nu = \frac{2}{3} Nu_{slug} + 0.015 Pe^{0.8} \tag{10.85}$$

They recommended values of Nu_{slug} for several common duct geometries and wall conditions (constant temperature or heat flux). They recommended the values $Nu_{slug} = \pi^2$ and $Nu_{slug} = 12$ for a uniform-wall-temperature and uniform wall heat flux on both walls, respectively. This condition was later generalised by Tricoli (1999) as in Eq. (10.84) for generic flow conditions, as discussed above. In the asymmetric case, that is with one wall heated and the other one insulated, the slug Nusselt numbers (always based on the hydraulic diameter) are reduced by half.

A further comprehensive analysis of turbulent heat transfer results for arbitrarily prescribed heat fluxes at both walls was presented by Kays (1963). Based on this analysis, the fully developed Nusselt number for the constant wall heat flux under arbitrary conditions at constant heat flux conditions case can be represented by Eq. (10.86):

$$Nu\big|_{q_w = constant} = \frac{Nu_0}{1 - \gamma\varphi} \tag{10.86}$$

In this case, γ is the ratio of the prescribed heat fluxes at the two duct walls, Nu_0 is the value corresponding to $\gamma = 0$, and φ is a correction factor. In that context, $\gamma = 0$ represents the case with one wall heat and the other one insulated, for $\gamma = 1$ are both heated with the same heat flux and $\gamma = -1$ is heated and the other cooled at the same rate. The parameters Nu_0 and φ were obtained by means of numerical integration for different values of the Reynolds number. The relevant results for the range $Pr \leq 0.03$ are summarised in Table 10.4.5.

Table 10.4.5: Parameters for evaluating the Nusselt number as in Eq. (10.86) for turbulent flow in a smooth flat duct with uniform heat flux

Pr	*Re* = 10^4		*Re* = $3{\cdot}10^4$		*Re* = 10^5		*Re* = $3{\cdot}10^5$		*Re* = 10^6	
	Nu_0	φ	Nu_0	φ	Nu_0	φ	Nu_0	φ	Nu_0	φ
0	5.7	0.428	5.78	0.445	5.80	0.456	5.80	0.460	5.80	0.468
0.001	5.7	0.428	5.78	0.445	5.80	0.456	5.88	0.460	6.23	0.460
0.003	5.7	0.428	5.80	0.445	5.90	0.450	6.32	0.450	8.62	0.422
0.01	5.8	0.428	5.92	0.445	6.70	0.440	9.80	0.407	21.5	0.333
0.03	6.1	0.428	6.90	0.428	11.00	0.390	23.00	0.330	61.2	0.255

Source: Kays (1963).

This analysis was in principle developed and validated for $Pr = 0.7$ (representative of air and other gases). Asymptotic solutions were also proposed for wider ranges of *Re* and *Pr* and, in the liquid-metal range, it is the only description available for predicting the heat transfer performance under generic asymmetric thermal boundary conditions.

For the specific case of one wall heated with a uniform heat flux and the other adiabatic ($\gamma = 0$), Duchatelle (1964) correlated their experimental observation by Eq. (10.87) and Dwyer (1965a) developed a theoretical model for the turbulent heat transport, represented by Eq. (10.88). Both models, only differing in the empirical constants, are claimed to be valid of $0 \leq Pr \leq 0.04$ and $10^4 \leq Re \leq 10^5$:

$$Nu = 5.85 + 0.00341 Pe^{1.29} \tag{10.87}$$

$$Nu = 5.60 + 0.01905 Pe^{0.775} \tag{10.88}$$

The best agreement with both the predictions by Kays (1963) and the few available experimental data is given by Eq. (10.87), which is recommended for use within the above-mentioned ranges. In the experiments by Duchatelle (1964), it was noticed that for $Pe < 300$, the Nusselt number remains roughly constant at $Nu = 6.0$, within the accuracy of the measurements. This result was later confirmed by DNS calculations, such as that of Kasagi (1993).

For the case of a uniform wall temperature, only one relevant experiment by Seban (1950b) is available. These experimental observations yield the correlation expressed as in Eq. (10.89). It should be noted that it predicts Nusselt values comparable or larger than those from Eqs. (10.87) and (10.88), which is in contradiction with the considerations by Hartnett (1957), who postulated that the heat transfer coefficients for a uniform wall temperature are roughly 20% lower than for a uniform wall heat flux condition. Without further experimental evidence, Eq. (10.89) should be used with caution:

$$Nu = 5.8 + 0.02 Pe^{0.8} \tag{10.89}$$

For the case of both walls equally heated ($\gamma = 1$), Eq. (10.90) was proposed by Dwyer (1965a) for uniform wall heat flux conditions in the range $Pr < 0.03$ and $10^4 < Re < 10^5$. Experiments with mercury flowing in a narrow channel (2 mm × 40 mm), which can be approximated as flow between parallel plates, for this thermal boundary condition were reported by Crye (2002):

$$Nu = 9.49 + 0.0596 Pe^{0.688} \tag{10.90}$$

10.4.3 *Concentric annulus*

This geometry has been widely studied mainly in two contexts. First, as a simple tube-in-tube heat exchanger geometry, where the two flow channels are the inner pipe and the annular region between both tubes. Second, in nuclear fuel assemblies and tube bundles, where the flow channel is surrounded by cylindrical tubes in a specific arrangement and the concentric annulus is often considered as a representative solution for the single problem (Ma, 2012). In general, several different thermal boundary conditions can be defined for this geometry and they cannot all be covered by one single correlation.

In this section, only concentric annuli shall be considered. It has been observed that eccentricity in general tends to reduce the mean Nusselt, particularly at low Péclet numbers (Snyder, 1963; Yu, 1966, 1967). This effect is not included in this analysis, and the concentric annulus geometry can be represented by the ratio of the inner (r_i) and outer (r_o) radii r^*, defined as in Eq. (10.91). Following this definition, the limiting cases $r^* = 0$ and $r^* = 1$ represent the round tubes and flat channel cases discussed in Sections 10.4.1 and 10.4.2, respectively:

$$r^* = r_i / r_o \tag{10.91}$$

As this geometry is a double-connected duct (as well as the case of a flat channel), several symmetric and asymmetric boundary conditions can be found. A list of published experimental data for this geometry and different thermal boundary conditions is given in Table 10.4.6.

Table 10.4.6: List of published experimental heat transfer data for the flow of alkali and heavy-liquid metals in concentric annuli

#	Author, year	Fluid	r^*	Pe	Thermal boundary condition
1	Trefethen (1951)	Hg	0.4325; 0.5721; 0.7174; 0.7197; 0.8558; 0.8570	100-2 000	Heat exchanger: cooled at the inner wall and adiabatic at the outer wall
2	Khabakhpasheva (1961)	NaK	0.4762; 0.5882; 0.7143	300-1 100	Two-sided and one-sided heat supply [sic]
3	Petrovichev (1961)	Hg	0.4833; 0.6431	700-5 000	Either wall cooled by counter-flow water
4	Subbotin (1961)	Hg	0.9174; 0.9524	200-3 500	Two-way and one-way heating [sic]
5	Baker (1962)	NaK-44	0.4762	60-1 500	Heat exchanger: cooled at the inner wall and adiabatic at the outer wall
6	Dwyer (1966)	Hg	0.3597	Not available	Inner wall heated only
7	Borishanskii (1969d)	n.a.	0.65; 0.734	400-4 000	Two-sided and one-sided heat supply [sic]
8	Rensen (1982)	Na	0.5409	30-350	Inner wall heated only
9	Lefhalm (2004) Zeiniger (2009) Marocco (2012)	LBE	0.1367	450-7 000	Inner wall heated only
10	Ma (2011)	LBE	0.4316	Not available	Inner wall heated only

These experimental works can be divided into two groups or generations. The first generation, until the end of the 1960s, was focused on finding the differences between the round and annular geometries, and in particular the effect of the different thermal boundary conditions. These authors highlighted the fact that correlations developed for

round pipes are not applicable for annuli following the hydraulic diameter concept and specific models are required. Some of these models, reviewed below, were found to give sufficiently accurate representations of the fully developed heat transfer coefficients. Thus, the next generation of experimental works focused on the developing flows. Recent experiments in LBE also included local temperature velocity measurements and observed that these profiles differ from those obtained in e.g. water (Kays, 1963), as expected for turbulent heat transfer problems in liquid metals, see Section 10.3. The behaviour of the flow in the developing region observed in these experiments is presented in Section 10.4.5.

In Section 10.4.2 the model by Hartnett (1957) for non-circular ducts was introduced, as expressed by Eq. (10.85). For a concentric annulus, the slug Nusselt values presented in Figure 10.4.4 were proposed for both or only one wall being heated. It should be noted that these results are purely analytical and are not particularly backed by empirical evidence.

Figure 10.4.4: Slug flow Nusselt numbers for smooth concentric annular ducts

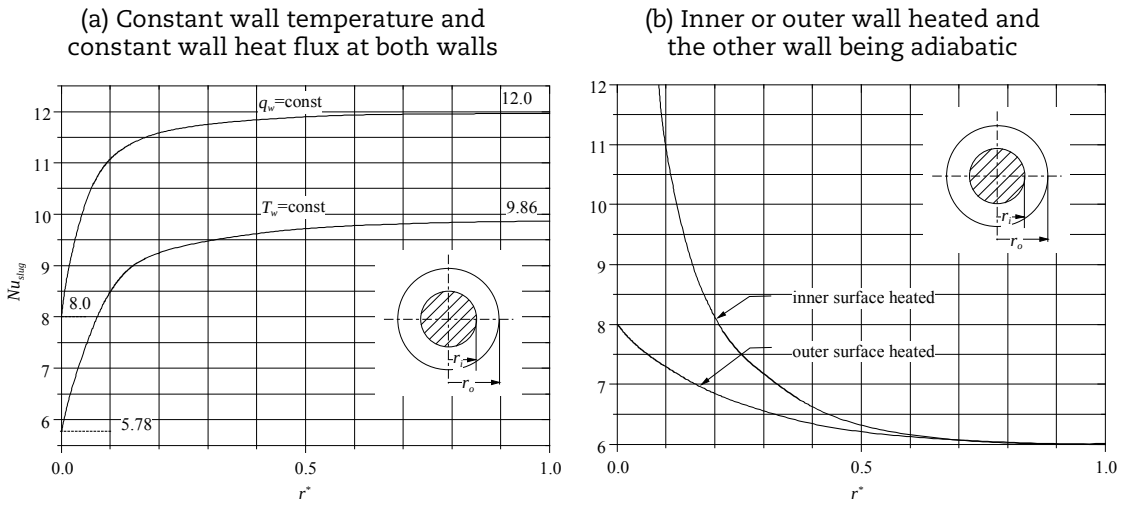

Source: Hartnett (1957).

These predictions can be compared with the sodium ($Pr \approx 0.005$) experiments by Rensen (1982) in a test section with $r^* = 0.5409$, under conditions of the inner wall subjected to a uniform q''_w and the outer tube thermally insulated. For this particular set-up, he obtained the empirical correlation given by Eq. (10.92), valid for the Reynolds number range $6{\cdot}10^3$-$6{\cdot}10^4$, while the model by Hartnett (1957) results in Eq. (10.93).

$$Nu = 5.75 + 0.022\,Pe^{0.8} \tag{10.92}$$

$$Nu = 4.2 + 0.015\,Pe^{0.8} \tag{10.93}$$

It can then be observed that predictions of the analytical Eq. (10.93) are up to 32% lower than the empirical Eq. (10.92). Although this difference is relatively significant, it should be noted that the correlations by Hartnett (1957), developed at such an early stage, provide conservative predictions of the Nusselt numbers.

Naturally, the design engineer is interested in a general correlation for an arbitrary ratio r^*. Due to the large differences in the conditions of the experiments listed in Table 10.4.6, it is not possible to derive a general empirical formula from them. Kays (1963) extended their model for flat channels given by Eq. (10.86) and provided parameters as those listed in Table 10.4.5 for discrete values of $r^* = 0.1$; 0.2; 0.5; and 0.8.

A semi-analytical correlation for liquid-metal flows was developed by Dwyer (1966) as in Eq. (10.94), where α, β and γ are constants which depend on the ratio r^* and thermal boundary conditions and $1/Pr_t$ is given by Eq. (10.79):

$$Nu = \alpha + \beta\left(\frac{Pe}{Pr_t}\right)^{\gamma} \tag{10.94}$$

Based on the velocity profile proposed by Rothfus (1958), empirical expressions for α, β and γ as a function of r^*. For the two boundary conditions with one side heated and the other adiabatic, these coefficients were first reported by Dwyer (1963c). Shortly afterwards, an improved calculation was presented by Dwyer (1963b) and these two sets are sometimes confused. In the following, the updated coefficients given by Dwyer (1963b) are detailed.

For the case with the inner wall heated and the outer wall insulated (boundary condition No. 1), these coefficients are given by Eq. (10.95):

$$\alpha_1 = 4.82 + \frac{0.697}{r^*};\ \beta_1 = 0.0222;\ \gamma_1 = 0.758 r^{*-0.053} \tag{10.95}$$

The validity of this model was demonstrated in the ranges $0.005 < Pr < 0.03$ and $3{\cdot}10^2 < Pe < 10^5$, with an accuracy between 10 and 15% compared to the measurements by Rensen (1982). More recently, Marocco (2012) observed that their experimental data is well predicted by this model. They also observed that the correlation developed by Chen (1981) for round tubes (No. 13 in Table 10.4.2) also gives good results when applied to an annular geometry. The model derived by Yu (2005) based on DNS calculations and free of any empirical parameters, was not found to be in good agreement with the experimental data reported by Marocco (2012). Some buoyancy effects which can affect the overall heat transfer were also observed, see Section 10.4.6.

For the opposite case, with the outer wall heated and the inner wall insulated (boundary condition No. 2), these coefficients read as in Eq. (10.96):

$$\alpha_2 = 5.54 - \frac{0.023}{r^*};\ \beta_2 = 0.0189 + \frac{3.1610^{-3}}{r^*} + \frac{8.6710^{-5}}{r^{*2}};\ \gamma_2 = 0.758 r^{*0.0204} \tag{10.96}$$

This model is in very good agreement with the data by Petrovichev (1961) in experiments with Hg. The NaK data of Baker (1962) exhibit about 15% higher Nusselt numbers, although the flow in that experiment was probably not fully developed.

The same analysis was applied to the case of bilateral heat transfer (both walls heated). For this boundary conditions, these coefficients depend both on the geometry (r^*) and the ratio of heat flux at each wall, represented by $\xi = q_i/(q_i + q_o)q_o$. Tabulated values of α, β and γ for discrete values of r^* and ξ were presented by Dwyer (1965b), although not compared with experiments.

Semi-empirical correlations have been developed by Yu (2005) for a wide range of Prandtl numbers and several thermal boundary conditions. Based on empirical models for Pr_t and assuming a given velocity profile, they presented tabulated values of Nusselt for fully developed flows for this geometry, as previously Yu (2001) has for round tubes. These correlations, however, do not offer significant advantage and are rather complex to implement.

10.4.4 *Rod bundles*

Engineering correlations for the mean heat transfer coefficient in rod bundles have been developed for the feasibility analysis of fast breeder reactors since the 1960s, based on many experimental investigations in several countries. Most of them considered bare rod bundles (Section 10.4.4.1). As the presence of spacers tends to enhance the heat transfer

and pressure drop these correlations can be considered conservative for actual fuel assemblies. Additionally, experiments with grid or wire spacers were focused on other specific features, such as flow mixing and hot spots. These three-dimensional effects are analysed in Section 10.4.4.2.

10.4.4.1 Bare rod bundles

Successive reviews on experiments and predictions for this scenario were given by Dwyer (1969), Weinberg (1975), Bobkov (1988), Pfrang (2007) and Mikityuk (2009). Most of the experiments were performed in triangular or hexagonal arrays or bundles, which arise from the most common design of fuel assemblies for fast breeder reactors and are the main topic of this section. Only few experiments are available in the open literature for square arrays with some heated rods in a cluster of 25 by Ushakov (1963) and Zhukov (2002), who proposed Eq. (10.97), where P/D is the pitch-to-diameter ratio, as a best fit of the data, valid for $1.2 \le P/D \le 1.5$ and $10 \le Pe \le 2\,500$.

$$Nu = 7.55\frac{P}{D} - 14\left(\frac{P}{D}\right)^5 + 0.007Pe^{0.64+0.246\frac{P}{D}} \tag{10.97}$$

For triangular (or hexagonal) arrays, much more experimental information is available, as listed in Table 10.4.7. These data sets cover the ranges from $1.0 \le P/D \le 1.95$ and $20 \le Pe \le 4\,500$, with rod bundles from 7 to 37 pins being investigated.

Based on the data sets listed in Table 10.4.7, several empirical and theory-based correlations have been proposed. Most of them follow the functional relation expressed by Eq. (10.98), where the coefficients a, b and c are empirical functions of the pitch-to-diameter ratio P/D. The most relevant correlations, as well as their validity range, are listed in Table 10.4.8.

$$Nu\left(\frac{P}{D}, Pe\right) = a\left(\frac{P}{D}\right) + b\left(\frac{P}{D}\right)Pe^{c\left(\frac{P}{D}\right)} \tag{10.98}$$

$$Nu = 7.0 + 3.8\left(\frac{P}{D}\right)^{1.52} + 0.027\left(\frac{P}{D}\right)^{0.27}\left(\frac{Pe}{Pr_t}\right)^{0.8} \tag{10.99}$$

$$Nu = 6.66 + 3.126\frac{P}{D} + 1.184\left(\frac{P}{D}\right)^2 + 0.0155\left(\frac{Pe}{Pr_t}\right)^{0.86} \tag{10.100}$$

$$Nu = \begin{cases} Nu_1 & \text{for} \quad Pe < 200 \\ Nu_1 + Nu_2 & \text{for} \quad Pe > 200 \end{cases} \tag{10.101}$$

$$Nu_1 = 24.15\log\left[-8.12 + 12.75\frac{P}{D} - 3.65\left(\frac{P}{D}\right)^2\right]$$

$$Nu_2 = 0.0174\left\{1 - \exp\left[-6\left(\frac{P}{D} - 1\right)\right]\right\}(Pe - 200)^{0.9}$$

$$Nu = 0.25 + 6.2\frac{P}{D} + \left(0.32\frac{P}{D} - 0.007\right)Pe^{0.8-0.024\frac{P}{D}} \tag{10.102}$$

$$Nu = 4.0 + 0.16\left(\frac{P}{D}\right)^{5.0} + 0.33\left(\frac{P}{D}\right)^{0.38}\left(\frac{Pe}{100}\right)^{0.86} \tag{10.103}$$

$$Nu = 7.55\frac{P}{D} - 20\left(\frac{P}{D}\right)^{-13} + \frac{3.67}{90}\left(\frac{P}{D}\right)^{-2} Pe^{0.19\frac{P}{D}+0.56} \tag{10.104}$$

$$Nu = 0.047\left\{1 - \exp\left[-3.8\left(\frac{P}{D} - 1\right)\right]\right\}\left(Pe^{0.77} + 250\right) \tag{10.105}$$

Table 10.4.7: List of published Nusselt number experimental data for the flow of alkali metals and mercury along a bare bundle of rods in a triangular array of rods, without spacers

Only those cases with $P/D \geq 1.1$ are listed, for lower P/D see e.g. Marchese (1972)

#	Author, year	Fluid	Rods	P/D	Pe	Temperature measurements
1	Friedland (1961a)	Hg	19	1.38; 1.75	190-4 000	Central rod, at several axial and azimuthal locations
2	Borishanskii (1963)	Na	7	1.2	30-345	Central rod only
3	Borishanskii (1964)	Na	7	1.5	28-172	Central rod only
4	Maresca (1964) Nimmo (1965)	Hg	13	1.75	150-4 000	As in No. 1
5	Kalish (1967)	NaK-44/56	19	1.75	250-1 200	As in No. 1
6	Pashek (1967)	Na	7	1.2	20-120	Central rod only
7	Zhukov (1967)	Hg	7	1.1; 1.2; 1.3; 1.4; 1.5	150-3 000	Central rod; it could be rotated to any arbitrary azimuthal position
8	Hlavac (1969)	Hg	13	1.75	550-3 800	As in No. 1
9	Borishanskii (1969b)	Na; ? (Pr = 0.03)	7	1.1; 1.3; 1.4	65-2 200	This information was not provided by the authors
10	Subbotin (1971)	Na	37	1.1	20-1 800	One central, edge and corner rod; they could be rotated
11	Gräber (1972)	NaK-44/56	31	1.25; 1.60; 1.95	106-4 300	In 11 different rods, at several azimuthal positions each

Table 10.4.8: List of engineering heat transfer correlations for liquid-metal flows along triangular rod bundles, at constant q''_w

#	Author, year	Type	Eq.	*P/D*	*Pe*
1	Friedland (1961b)	Theoretical	(10.99); (10.79)	1.375-10	10-100 000
2	Maresca (1964) Nimmo (1965) Dwyer (1969)	Empirical	(10.100); (10.79)	1.3-3.0	70-10 000
3	Borishanskii (1969c)	Empirical	(10.101)	1.1-1.5	1-2 000
4	Gräber (1972)	Empirical	(10.102)	1.2-2.0	150-4 000
5	Kazimi (1976)	Empirical	(10.103)	1.1-1.4	10-5 000
6	Ushakov (1977)	Empirical, simplified	(10.104)	1.3-2.0	1-4 000
7	Mikityuk (2009)	Empirical	(10.105)	1.1.-1.95	30-5 000

It should be noted that in most cases the coefficients *a*, *b* and *c* are linear functions of *P*/*D* and thus they are in good agreement with those experiments upon which they are based, but not necessarily with others outside their validity range. Considering the specifics of liquid metal experiments (Section 10.1.3.2) and that temperatures were not always measured at the same positions, it is not recommended to use a correlation based on a relatively small data set and lacking additional theoretical basis other than the generic Eq. (10.98).

In this context, a general correlation was derived at the Institute of Physics and Power Engineering (IPPE) in Obninsk, considering the case of vanishing Prandtl number and a uniform heat flux density at the inner wall of the rod cladding. In particular, it is observed that the mean Nusselt number for this problem is affected by the azimuthal variations in temperature and heat flux. This variation is represented by the parameter ϵ_K, defined by Eq. (10.106), where the sub-indices 1, 2 and 3 represent the fuel, cladding and liquid, respectively. The non-dimensional factor Λ_0 expresses the ratio of thermal conductivities of the solids, as in Eq. (10.107):

$$\epsilon_K = \frac{\lambda_2}{\lambda_3}\frac{1-\Lambda_0\left(\frac{r_1}{r_2}\right)}{1+\Lambda_0\left(\frac{r_1}{r_2}\right)} \tag{10.106}$$

$$\Lambda_0 = \frac{\lambda_2-\lambda_1}{\lambda_2+\lambda_1} \tag{10.107}$$

A low value of $\epsilon_K \to 0$ indicates that the thermal conductivity of the cladding is much lower than that of the liquid and a situation similar to a uniform heat flux density is achieved. The opposite case $\epsilon_K \to \infty$. With these considerations, Eqs. (10.108), (10.109) and (10.110) were reported by Ushakov (1977) to be valid in the wide ranges $1.0 \le P/D \le 2.0$, $1 \le Pe \le 4\,000$ and $0.01 \le \epsilon_K \le \infty$. Comparing these predictions with their own experiments, the authors reported that the expected accuracy of this model is ±15%.

$$Nu = Nu_{lam} + \frac{3.67}{90}\left(\frac{P}{D}\right)^{-2}\left\{1-\frac{1}{\frac{1}{6}\left[\left(\frac{P}{D}\right)^{30}-1\right]-\sqrt{1.24\epsilon_K+1.15}}\right\}Pe^m \tag{10.108}$$

$$Nu_{lam} = \left[7.55\frac{P}{D}-6.3\left(\frac{P}{D}\right)^{-17\frac{P}{D}\left(\frac{P}{D}-0.81\right)}\right]\left[1-\frac{3.6\frac{P}{D}}{\left(\frac{P}{D}\right)^{20}\left(1+2.5\epsilon_K^{0.86}\right)+3.2}\right] \tag{10.109}$$

$$m = 0.56+0.19\frac{P}{D}-0.1\left(\frac{P}{D}\right)^{-80} \tag{10.110}$$

For increasing values of *P*/*D*, the effect of the boundary condition (given by ϵ_K) vanishes. For $P/D \ge 1.3$, this expression can be greatly simplified and is reduced to Eq. (10.104), listed in Table 10.4.8 above. This model is recommended here to be used in the range specified by the authors. The behaviour of *Nu* as a function of *Pe* and *P*/*D* as predicted by this model is shown in Figure 10.4.5. It can be observed that at increasing *P*/*D* the laminar contribution increases significantly, while the exponent on *Pe* remains rather constant, close to the value of 0.8 also commonly used in other geometries.

Figure 10.4.5: Nusselt numbers in fully developed flow in rod bundles arranged in a triangular array as a function of the Péclet number *Pe* and *P/D* for constant wall heat flux, according to Eqs. (10.108), (10.109) and (10.110)

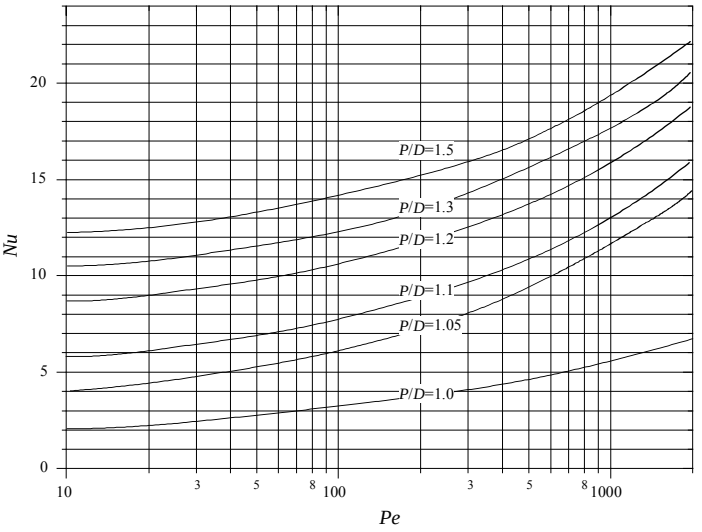

The predictions of the correlations listed in Table 10.4.8 with an extensive data set (658 point in total, from four authors, including the square bundles from Zhukov [2002]) were analysed by Mikityuk (2009). In this comparison, he observed that both Eqs. (10.102) by Gräber (1972) and (10.104) by Ushakov (1977) presented good statistical results. However, both are found to over-predict the Nusselt number at low values of $P/D \leq 1.2$, which is actually outside their range of validity. Under these circumstances, Eq. (10.104) is preferred due to its more solid theoretical basis.

Mikityuk (2009) observed that the Ushakov (1977) model tends to slightly over-predict *Nu* at low values of *Pe* and *P/D* and under-predict it at high values of *Pe* and *P/D*. Thus, he postulated a model with a constant exponent for the Péclet number and non-linear coefficients, as in Eq. (10.105). Indeed, this model yielded the best statistical results, with similar behaviour at low and high values of both *Pe* and *P/D*.

It should be noted that in the range $Pe > 500$ (relevant for forced convection in HLM) and $1.3 \leq P/D \leq 1.8$, both models differ in less than 5%. Thus, considering its wider range of validity $1.1 \leq P/D \leq 1.95$ and $30 \leq Pe \leq 5\,000$, Eq. (10.105) by Mikityuk (2009) is recommended here for design purposes. For the comparison of new experimental data, on the other hand, it must be recalled that several correlations have been proposed as listed in Table 10.4.8 and some of them, in particular that given by Eq. (10.104) also present good results within their narrower range of validity.

10.4.4.2 Temperature profiles and the effects of spacers

Further caution should be taken regarding the practical relevance of the correlations presented above, which predict average Nusselt numbers and are thus useful for the analysis of bundled cores under design conditions. In the case of transients and accident scenarios, the most relevant variable is the highest local temperature. Therefore, it is important to know the peripheral variations of the rod surface temperatures superimposed on the average temperature. The dimensionless peripheral variation of the surface temperature have been correlated by Subbotin (1974) and co-workers who proposed Eq. (10.111) for calculating the wall maximum temperature:

$$T_w^{max} - T_w^{min} = \frac{q''_w D}{2\lambda} \frac{\Delta\theta_{max,lam}}{1 + \gamma Pe^{\beta}} \tag{10.111}$$

$$\Delta\theta_{max,lam} = \frac{0.022}{\left(\frac{P}{D}\right)^{3\left(\frac{P}{D}-1\right)^{0.4}}} - 0.99\left\{1-\tanh\left[\frac{1.2\exp\left(-26.4\left(\frac{P}{D}-1\right)\right)+\ln\dot{\alpha}_K}{0.84+0.2\left(\frac{\frac{P}{D}-1.06}{0.06}\right)^2}\right]\right\} \quad (10.112)$$

$$\gamma = 0.008\left(1+0.03\varepsilon_K\right) \quad (10.113)$$

$$\beta = 0.65 + 51\frac{\log_{10}\left(P/D\right)}{\left(P/D\right)^{20}} \quad (10.114)$$

This model, valid in the ranges $1.0 < P/D \leq 1.15$ and $1.0 < Pe \leq 2.10^3$, considers the maximum ΔT to be proportional to the applied heat flux, non-dimensionalised as $q''_w/(2\lambda D^{-1})$, where D is the rod outer diameter. The proportionality constant is related to a non-dimensional laminar maximum temperature difference $\Delta\theta_{max,lam}$ given by Eq. (10.112), obtained by integration of the laminar velocity and temperature profiles. The effect of increased turbulent mixing, given by the Péclet number, is to reduce the temperature differences. This effect is modelled by two parameters γ and β, for which Eqs. (10.113) and (10.114), respectively, were developed based on a best-fit of available empirical data.

In a reactor fuel assembly, spacers are used for keeping the distance between the fuel pins constant and thus avoid serious distortions of the geometry. Two main types of spacers have been proposed and used for fuel assembly cooled liquid metals, as detailed below. In general, they induce additional turbulent mixing and thus the mean heat transfer coefficients are enhanced. The use of the correlations described in Section 10.4.4.1 for the mean Nusselt number is thus a conservative approach.

On the one hand, grid spacers as those used in LWR have also considered for LMFBR. Temperature profiles for such geometry obtained in a sodium experiment were reported by Möller (1980). Moreover, the Nusselt number data in NaK reported by Gräber (1972) and considered in Section 10.4.4.1 for the bare-bundle geometry were actually obtained in a test section including three grid spacers. Similarly, experimental data in a 19-pin bundle with three grid spacers cooled by LBE were recently presented by Pacio (2014) and compared to the correlations for bare bundles. In this case it should be noted that the effects of grid spacers are only local and are restricted to a few hydraulic diameters upstream and downstream of these perturbations to the flow, as predicted numerically e.g. by Jäger (2013) and observed in air by Krett (1971).

On the other hand, a more compact arrangement (smaller P/D) can be obtained using wire spacers. Their effects are not local, but rather distributed along the complete bundle and are characterised by one additional parameter, namely the wire longitudinal pitch H. Experimental temperature profiles for sodium have been presented by Falzetti (1979), Collingham (1970) and Yatabe (1970) in 7-pin bundles and by Baumann (1968), Fontana (1974) and Wantland (1976) in 19-pin bundles. Larger geometries with non-uniform heating were also studied by Namekawa (1984) and Engel (1980) in 37- and 61-pin bundles, respectively.

No general correlation could be derived from these experiments. Instead, this problem is often studied by sub-channel analysis (Kim, 2002; Memmott, 2010; Wu, 2013; Pramuditya, 2013). Alternatively, it is represented by a complete three-dimensional CFD, (Chandra, 2009; Natesan, 2010; Merzari, 2012; Rolfo, 2012; Fricano, 2014), including some lower-resolution approaches such as those presented by Hu (2010) and Roelofs (2012).

In general, these simulations present some marked differences related to the underlying turbulence models discussed in Section 10.3 and detailed and accurate experimental data are required for their validation (Roelofs, 2013). For heavy liquid metals, this topic is currently being investigated in the framework of ongoing European research projects, with experiments in LBE under development.

10.4.5 *Some comments about the turbulent developing region*

In this section, a few general comments about the entrance lengths and local Nusselt number correlations are presented for the geometries discussed above. Only for the round-tube and annular geometries, proper correlations for the local Nusselt number Nu_x are available. In the case of the other geometries, only the developing length l_{th} can be studied.

10.4.5.1 Round tube

As for laminar flows (Section 10.2.2), a solution to the developing flow can be obtained by means of variable separation and a corresponding eigenvalue problem. For the numerical integration of these equations, some values for the turbulent diffusion parameters ν_t and α_t must be assumed. This approach was followed by Notter (1972), who presented tabulated and graphical values of Nu_x for several Prandtl numbers, including the liquid-metal range. For a hydrodynamically developed flow with a constant q''_w they observed that the thermal entry length l_{th} increased with Re and showed a marked dependency with Pr, reaching up to $l_{th}/D = 35$. At low Re (104) a lower Prandtl number (0.01) leads to a shorter developing length than for a larger Pr (up to 0.06), and the situation is reversed for large Re (106). This behaviour (although not yet confirmed by experiments), indicates that this problem cannot be represented by a constant non-dimensional developing length l^*_{th}.

The experimental results reported by Johnson (1953b) at constant q''_w and Sleicher (1973) at constant T_w indicate that in the developing region the ratio of local to fully developed Nusselt numbers Nu_x/Nu_∞ is insensitive to changes in the Reynolds number. Based on this analytical and experimental information, Chen (1981) presented a comprehensive analysis for the entrance region of liquid-metal flows. In the study, several correlations presented for Nu_x referred to the fully developed values Nu_∞ proposed by Notter (1972). For the thermally developing (and hydrodynamically developed) flow under uniform wall temperature conditions, they recommended Eq. (10.115), valid for $Pe > 500$. For a simultaneously developing flow, they proposed Eqs. (10.116) and (10.117), valid for $2 \le x/D \le 35$, $Pe > 500^2$ and $Pr \le 0.03$, for a uniform wall heat flux and a uniform wall temperature, respectively, considering a flat inlet velocity profile:

$$\frac{Nu_x}{Nu_\infty} = 1 + \frac{2.4}{x/D} - \frac{1}{(x/D)^2} \tag{10.115}$$

$$\frac{Nu_x}{Nu_\infty} = 0.88 + \frac{2.4}{x/D} - \frac{1.25}{(x/D)^2} \tag{10.116}$$

$$\frac{Nu_x}{Nu_\infty} = 0.88 + \frac{2.4}{x/D} - \frac{1.25}{(x/D)^2} - \frac{40 - x/D}{190} \tag{10.117}$$

10.4.5.2 Flat channels

The experiment by Duchatelle (1964) provides the few available data for this geometry. In their set-up, one wall was insulated and a constant wall heat flux was supplied to the opposite one, i.e. $\gamma = 0$ (Section 10.4.2). The ratio of the local Nusselt number Nu_x to the fully developed flow Nusselt number Nu_∞ observed in these experiments for a simultaneously developing flow (Section 10.2.2.3) is shown in Figure 10.4.6.

Figure 10.4.6: Normalised local Nusselt number for simultaneously developing turbulent flow of NaK (*Pr* ≈ 0.02) in a smooth flat duct, with one wall heated and the other insulated

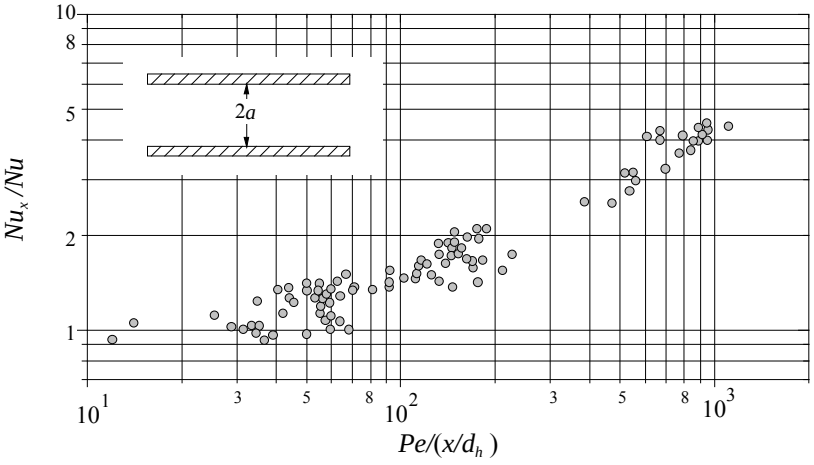

Source: Duchatelle (1964).

It can be noted that this ratio attains unity at $Pe/(x/d_h) \approx 25$. Thus the thermal entrance length l_{th} for the simultaneously developing flow can be estimated to be $l^*_{th} \approx 1/25 = 0.04$. They also observed that for hydrodynamically developed flows, the thermal entrance length is substantially reduced, $l^*_{th} \approx 1/80 = 0.0125$. Thus, turbulent flows retain this feature from laminar flows observed in Section 10.2.2: the temperature profiles develop much faster than the velocity profile, due to the low $Pr \ll 1$.

10.4.5.3 Concentric annulus

For this geometry the flow-developing region (hydrodynamically developed, after an unheated region) has only been studied experimentally for the boundary condition of the inner wall being heated at a constant q''_w and the outer one adiabatic (see the last three set-ups listed in Table 10.4.6). A detailed measurement of the thermal entrance length l_{th} of sodium flow ($Pr = 0.0054$) was reported by Rensen (1982). A strong dependence of the thermal entrance length on the Reynolds number was observed, as listed in Table 10.4.9 and in agreement with the theory by Chen (1970).

It can be observed that while l_{th}/d_h increases with the Reynolds and Péclet numbers, the dimensionless developing length l^*_{th} decreases significantly. The laminar value of $l_{th}/d_h = 2$ agrees with the theoretical predictions by Hsu (1968). Local values of Nu_x were also reported by Rensen (1982), although no empirical correlations was developed.

Table 10.4.9: Thermal entrance length l_{th} for thermally developing flow in a smooth concentric annulus with $r^* = 0.5409$ for sodium ($Pr = 0.0054$) with the inner wall heated and the outer one adiabatic

Re	*Pe*	l_{th}/d_h	$l^*_{th} = l_{th}/(Pe\ d_h)$
6 000	32.4	02.0	0.0648
8 000	43.2	02.7	0.0625
10 000	54	03.2	0.0593
20 000	108	06.0	0.0555
50 000	270	13.0	0.0481
60 000	324	13.5	0.0416

Source: Rensen (1982).

Recently Marocco (2012) proposed a correlation as in Eq. (10.118) for the Nusselt number in the thermal entrance region, based on the LBE data of Zeiniger (2009) and considering that the fully developed Nusselt value Nu_∞ is well represented by Eq. (10.94) by Dwyer (1966). This correlation is valid in the range $400 < Pe < 6\,000$:

$$\frac{Nu_x}{Nu_\infty} = 1 + \frac{1.14}{\left(x/d_h\right)^{0.5}} \tag{10.118}$$

Radial temperature profiles at selected axial positions have also been reported for these three experimental set-ups. Furthermore, radial velocity profiles were also obtained in the LBE experiments by Zeiniger (2009). This local information is most relevant for the validation of numerical tools, as in the simulation results recently presented (Chandra, 2009; Litfin, 2011; Thiele, 2013; Wang, 2013). In general, it is very challenging for the turbulence models to represent the experimental observations.

10.4.5.4 Rod bundles

For the case of the thermally developing flows along bare rod bundles the Nusselt number values may significantly deviate from those in a circular duct, because of the strong geometric non-uniformity of the sub-channels. In particular, the entrance regions for rod bundles are substantially larger. In the only reported experiment of its kind, Subbotin (1975) observed that thermally developed conditions cannot be reached below 200 diameters for $Pe > 10^2$ and $P/D = 1.15$ in sodium. For lower P/D ratios the thermal developing length is even larger, because the heat transfer between the sub-channels is reduced. This large entrance length has been confirmed by the measurement of Möller (1980) obtained in a 19-rod bundle with $P/D = 1.3$, observing $l_{th}/d_h = 70$ for $Pe = 150$ in a corner sub-channel. Numerical simulations for this geometry also result in large developing lengths (Rasu, 2013, 2014).

The use of fins or spacers reduces the thermal entrance length considerably, since they lead to a better lateral mixing. For example, LBE flow in a 19-pin bundle downstream of a grid spacer was observed to be already fully developed (constant Nusselt number) after ~$30d_h$ (Pacio, 2014), thus yielding the same order of magnitude as in circular tubes and annuli.

10.4.6 Buoyancy effects

As discussed in Section 10.1.2.4, even under conditions of forced convection, the differences in local density given by the temperature profiles result in buoyant forces, which influence the momentum equation and thus affect the velocity profiles. The main special feature of liquid-metal flows in that context is that, due to the low Pr, the temperature gradients are less steep than in other fluids, and the thermal boundary layer is relatively thick. Thus, the buoyancy effects on the velocity are not restricted only close to the wall, but extend over the scale of the thermal boundary layer δ_{th}. Thus, free convection distortions in forced-convective liquid-metal flows occur generally over a wider range of the flow parameters than in other fluids.

In horizontal flow, these distortions had already been observed by Schrock (1964) in sodium-potassium (NaK) for Reynolds number up to $1.6{\cdot}10^4$ and by Gardner (1969) in mercury for $Re = 3{\cdot}10^5$. In vertical circular tubes with upward flows Kowalski (1974) detected free convection distortion up to of $Re = 9{\cdot}10^4$ and Lefhalm (2004) in LBE up to $Re = 1.1{\cdot}10^5$.

The experimental data indicate that the velocity profile rapidly distorts as the heat flux is increased. At high heat flux a limiting profile shape with the centreline velocity well below the mean velocity u_0 develops. As a matter of this fact the experimentally determined Nusselt number, even in a "fully developed pipe flow", depends on several parameters, such as whether the pipe flow is upwards or downwards, the pipe is horizontal or vertical, the direction of the heat flux (cooled or heated) and the value of the Rayleigh

number. Figure 10.4.7(a) shows the measured Nusselt number variations dependent on the angle of the perimeter for a horizontal turbulent mercury pipe flow with free convection distortion. In an order of magnitude estimation the parameter Z given by Eq. (10.119) was introduced by Buhr (1968), representing the ratio of buoyancy to inertia forces.

$$Z = \frac{Ra}{Re}\frac{d_h}{L};\ \text{with}\ Ra = Gr\,Pr\ ;\ Gr = \frac{d_h^3 \beta g \Delta T}{\nu^2}\ \text{and}\ \Delta T = \frac{\partial T}{\partial x} d_h \tag{10.119}$$

After analysing a series of vertical and horizontal heat transfer experiments in pipe flow, Buhr (1968) concluded that if $Z > 2{\cdot}10^{-3}$ free convection affects the forced-convective measured Nusselt number *Nu*. It should be noted that the fluid properties in Eq. (10.119) should be evaluated at the bulk mean temperature $T_m = T_{in} + T_{out}/2$, especially for larger temperature differences.

Figure 10.4.7: (a) Measured local Nusselt number at several angles of the perimeter in a turbulent mercury in a horizontal pipe with convection distortion effects; (b) Nusselt number dependence on the Z parameter from Eq. (10.111), in a vertically upward directed turbulent mercury pipe flow exhibiting free convection effects

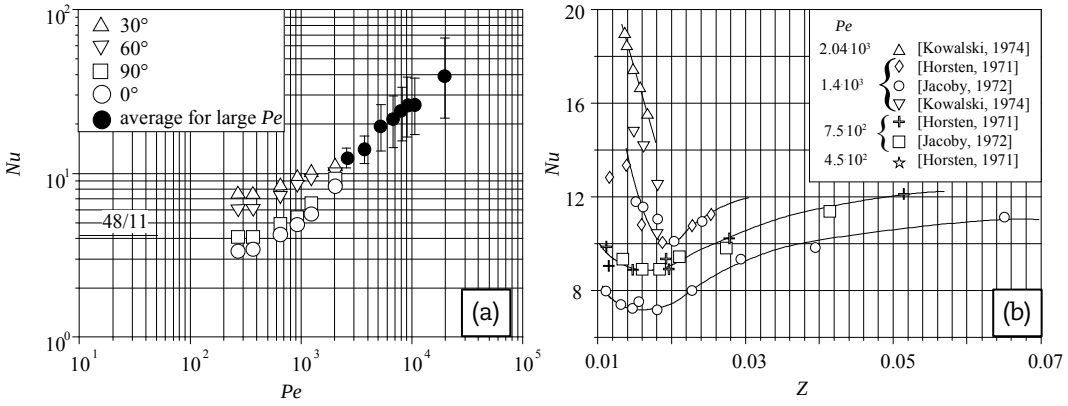

Source: Gardner (1969).

The Nusslet number is a function of the parameter Z as shown qualitatively in Figure 10.4.7(b) – initially decreasing, then growing as Z increases. It should be noted that the parameter Z is essentially proportional to the applied heat flux. As the buoyancy forces become comparable to the inertia forces of the flow the Nusselt number reaches a minimum, begins to increase, and finally appears to reach a limiting value. It can be seen that the effects of free convection distortion can affect the measured value of the Nusselt number and could, therefore, explain some of the well-known scatter in the Nusselt number data for the liquid-metal heat transfer.

A similar, though theoretical and not empirical, criterion for sodium in upward flow was developed by Jackson (1983) as in Eq. (10.120), based on the assumption that for liquid metals the ratio of viscous to thermal boundary layer being equal to $Pr^{0.8}$:

$$Y = \frac{Gr}{Re^2} > 2.10^{-3};\ \text{with}\ Gr = \frac{d_h^3 \beta g \left(T_w - T_b\right)}{\nu^2} \tag{10.120}$$

It should be noted that this criterion is very similar to the one by Buhr (1968), because with these definitions $Z/Y = 4Nu\,d_h/L$ is close to unity in the experiments considered. Furthermore, the threshold in Eq. (10.120) for sodium is two orders of magnitude lower than the well-accepted value of 0.3 proposed by Sparrow (1959) for $Pr = 0.7$.

In mixed convection of ordinary fluids, the following qualitative picture is observed. Buoyancy forces influence the convective heat transfer indirectly through their effect on shear-stress distribution in the liquid metal. In vertically downward flow, the buoyancy

forces operate against the mean flow direction and increase the isothermal shear stress near the heated surface. In contrast to the upwards flow the shear stress is reduced by the buoyancy. The increase in shear stress in the downwards flowing case leads to an increase of the turbulence production and hence will enhance the heat transfer, and the opposite holds for the upward flow. This model was also proposed to be valid for sodium by Jackson (1983). However, in later sodium experiments Jackson (1994) noticed that the heat transfer is indeed enhanced by buoyancy-aided flow (upward) and impeded by buoyancy-opposing flow (downward), thus contradicting the previous predictions.

It can thus be observed that a general agreement between theory and experiments has not yet been reached. Some discrepancies between the mercury experimental data by Kowalski (1974) on the one hand and that in mercury and NaK (Buhr, 1968; Jacoby, 1972) on the other were observed by Jackson (1994). Based on their own experimental observations, they concluded that sodium behaves differently from other fluids, including mercury and NaK, which in principle is not backed by theoretical considerations.

Recently, Marocco (2012) presented experimental data for LBE in the mixed-convective flow regime. The velocity profiles were largely affected by the heat flux density q''_w. They observed that at a low value of $Re \approx 1.5 \cdot 10^4$ the Nusselt number in upward flow was more than doubled when the effects of buoyancy were large. These effects were correlated to a non-dimensional parameter $c^* = Ra^{0.833}/(Re^{0.8}Pr^{0.4})$. In any case, it can be concluded that further development of both experimental information and theoretical models are required for achieving a general agreement.

For the case of purely buoyant (free convective) liquid-metal flows along plane surfaces, extensive experimental information and correlations have been reported at an early stage for sodium and mercury, as compiled by Sheriff (1979). In general, the agreement for upward flow is satisfactory, although not for horizontal surfaces. For heavy-liquid metals, this topic is currently being investigated under the framework of several collaborative European research projects. Integral circulation experimental results have been reported (Ma, 2007; Tarantino, 2011).

10.4.7 Investigations on additional flow scenarios found in HLM systems

In Sections 10.4.1 to 10.4.6, previous investigations of single-phase flow of liquid metals in straight ducts were reviewed. These configurations have been widely studied and, although additional experimental data is required for validating the evolving turbulence models presented in Sections 10.3, some simple models with good engineering accuracy have been developed for some of the most representative geometries and boundary conditions.

The present section is focused on additional flow scenarios found in HLM systems, such as ADS and fast reactors. Despite extensive investigation, these scenarios are generally too complex to be represented by simple correlations and usually a complete three-dimensional simulation is required. In that context, the main lessons learned from both experiments and simulations are briefly summarised in the following paragraphs. For more detailed information on this topic, the interested reader is referred to the cited bibliography. Many of these studies have been published in recent years and, as these topics continue to be the subject of intensive investigation, additional experiences shall be gained in the upcoming years.

10.4.7.1 Beam-entrance windows in spallation targets, e.g. for ADS

The spallation reaction of a proton beam onto a target allows producing fast neutrons in a subcritical system. Spallation targets are thus key components of fast neutron sources and accelerator-driven systems. A general overview of different target concepts, including a summary of previous, operating and planned large-scale facilities, was given by Bauer (2010).

As opposed to solid targets, heavy liquid metals offer the significant advantages of allowing to easily transport the generated heat elsewhere and being less susceptible to radiation damage. Thus, they also present the largest potential for upscaling. In any case, a physical barrier is required for separating the target material (in this case the HLM itself) from the vacuum required for the proton beam line. Most existing and planned spallation targets consider a beam-entrance window geometry. This list includes some systems using Hg as the working fluid and target material, such as currently in operation in the SNS (McManamy, 2008) and JSN (Ikeda, 2005), and under investigation for application in the ESS (Lengeler, 1998) and EURISOL (Samec, 2011) plants, while LBE or Pb would be the fluid of choice for ADS. A prototypical target using LBE was irradiated in the Megawatt Pilot Experiment (MEGAPIE) test in 2006. The main R&D lessons learned from this international venture were summarised by Fazio (2008), and more information can be found in the references therein.

From a thermal-hydraulic perspective both fluids behave similarly, as they both have $Pr \approx 0.025$ in the design operating temperature ranges. Thus, in principle, generic conclusions could be obtained from both experiences, although it should be noted that the design of the window and target geometry is to a great extent influenced by the desired neutronic characteristics of the spallation source. As a representative example, the MEGAPIE target is illustrated in Figure 10.4.8, with special focus on the lower part, where the BEW is located (beam incoming from below).

Figure 10.4.8: Schematic of the MEGAPIE target

(a) MEGAPIE target; (b) the lower shell; (c) geometric dimensions of the lower target shell (heated jet experiment) and zones of different heat transfer problems occurring in MEGAPIE

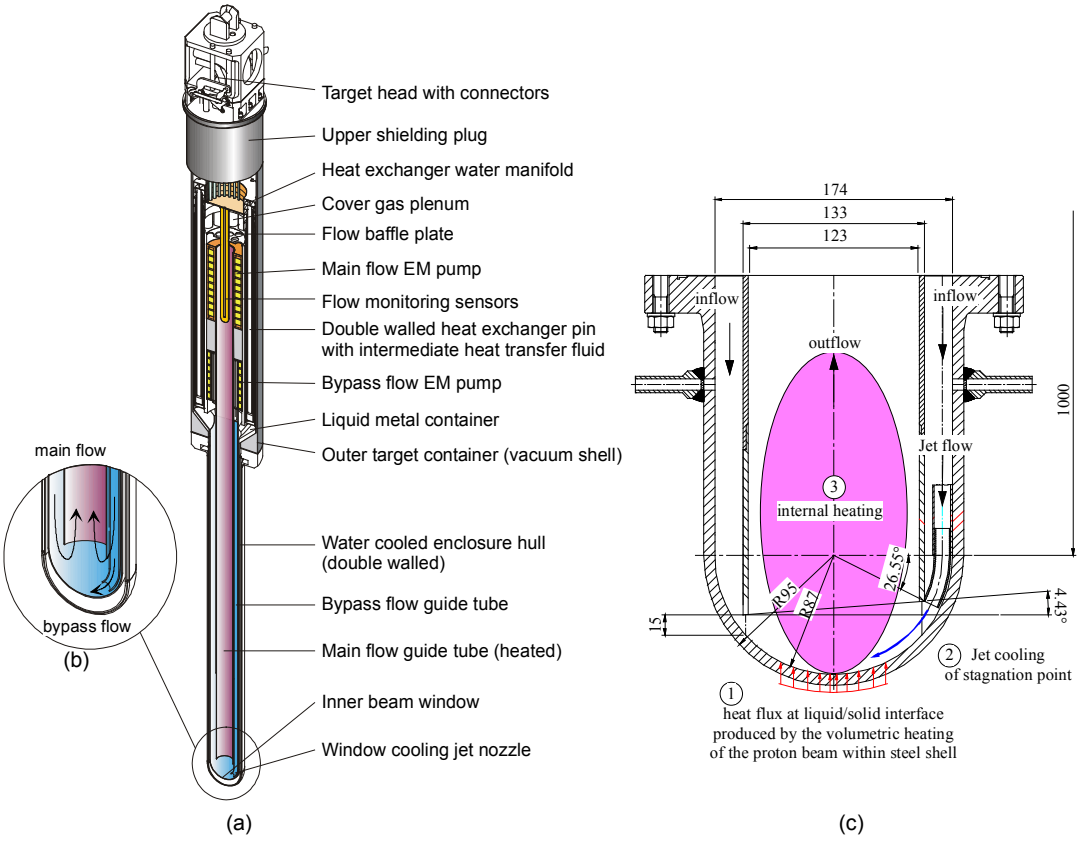

Source: Stieglitz (2007).

In this beam window geometry, the main flow is guided downwards in an annular gap downwards and then u-turned close to a hemispherical shell into a slanted riser tube. This configuration might lead to stagnation points and thus to unacceptably high window temperatures. In order to avoid this phenomenon, a lateral hotter jet flow is injected. This thermal-hydraulic problem involves the interaction of several phenomena and it must be simplified in order to validate the numerical tools aiming to predict the complete flow scenario (Smith, 2007).

To that purpose, several experiments tackling each individual phenomenon have been performed (Gnieser, 2003; Daubner, 2004, 2005; Patorski, 2006; Stieglitz, 2007). Large recirculation zones were observed in a water mock-up under nominal flow conditions. This was also tested in LBE, where a heated jet was injected and thus the temperature was transported as a passive scalar by the flow. Different flow patterns were observed according to the ratio of main-flow to jet-flow and stability domains, where the jet reaches the centreline and thus disrupts the stagnation zones, could be defined. Numerical simulations for this geometry, compiled by Smith (2008), capture in principle the different flow patterns but differ quantitatively with the domains observed in the experiments. Furthermore, although only a small fraction of the heat is deposited on the window, it can lead to large heat flux, in the range $q''_w \geq 1.4$ MW m^{-2}. Thus, the appropriate cooling of the window, within acceptable wall temperatures, is a key issue which was verified in the above-mentioned experiments. The problem of internal heat generation is difficult to represent in out-of-pile experiments, although it can be well implemented into a model given that the velocity and temperature profiles were validated for the simpler case (Smith, 2009).

In this section, the MEGAPIE target is presented as a flagship example, having completed all the stages ranging from design, preliminary tests, beam irradiation and undergoing post-irradiation evaluations (Zanini, 2011). Nevertheless, it should be noted that this thermal-hydraulic problem is strongly dependent on the geometry. Moreover, experimental data on a mock-up of the envisaged J-PARC target window (Sugawara, 2010), cooled by LBE have been presented by Kikuchi (2006), Obayashi (2006) and Obayashi (2008).

10.4.7.2 Free-surface and two-phase flows

Throughout this chapter, single-phase liquid-metal flow and heat transfer problems were analysed. Indeed they represent the most widely found flow scenarios in HLM systems. Moreover, some free-surface and two-phase flows are also relevant for the operation safety analysis of such systems. These include the design of windowless spallation targets, transport of gas bubbles in the liquid-metal pool and sloshing at the free-surface level. The main investigations on these topics are briefly reviewed in the following paragraphs. In general, these flows are hardly affected by the Prandtl number, but they have nevertheless been specifically studied for heavy-liquid metal systems.

Considering the challenges for cooling the beam windows described in Section 10.4.7.1, as well as radiation damage concerns, windowless liquid metal targets have also been proposed and studied by several research institutions. This concept considers the confluence of falling vertical coaxial flow, forming a conical free surface which can be subjected to the proton beam. Thus, the liquid metal directly transports the heat generated in that region. In order to obtain acceptable fluid temperature stagnation zones (which can occur at high flow rates) leading to excessive residence times in the target region must be avoided. The main challenges for the modelling of this free-surface problem and approaches followed by several research groups have been summarised by Class (2011), who also derived a set of design rules for obtaining a stable surface, based on the lessons learned from the numerical simulations. These rules were verified in experimental observations in water by Jeanmart (2011), Su (2012), as well as in LBE by Litfin (2012). Additionally, rectangular free-surface targets are being evaluated for fusion applications (Nakamura, 2008). An overview of the main challenges for that geometry and the results of a mock-up test were given by Gordeev (2009).

The transport of gas bubbles plays a significant role in the safety evaluation of HLM systems because they can lead to a reactivity increase if they enter the core (Tuček, 2004). Gas-lift solutions have also been proposed and tested for aiding natural circulation (Benamati, 2007). This section does not consider boiling, because it is not relevant in the temperature range of HLM (Pb and LBE). An overview of boiling studies for sodium systems can be found e.g. in Kottowski-Dümenil (1994). In principle, for the evaluation of momentum transport, those models developed e.g. for air-water flows could also be applied for the analysis of liquid metal-gas systems. However, a review of the few specific experimental data presented by Mikityuk (2005) indicate that specific correlations for the drag coefficient might be required, considering the large difference in the ranges of density ratios. In any case, large research efforts have been devoted to the evaluation of the source terms for bubbles in a liquid-metal pool.

In that context, a major concern is the scenario of a steam generator tube rupture (SGTR). The two most serious consequences of a SGTR event are the potential of a postulated steam explosion and the entrapment of bubbles in the primary coolant flow, which could be transported into the core (Dinh, 2007). For that reason, the direct-contact interaction between liquid and heavy liquid metals has been widely studied. Experimental results injecting a jet of sub-cooled or saturated water into a vessel with molten lead or LBE have been reported (Beznosov, 2005; Sibamoto, 2002, 2005, 2007; Ciampichetti, 2009, 2011). These experimental observations indicate that a large fraction of the water does not boil directly upon contact due to the formation of a vapour film. Transient simulations, such as reported by Wang (2008) and Flad (2010), present good agreement with the experiments regarding the evolution of pressure, flow rate and penetration depth. In principle, sloshing at the free surface can also result in the entrainment of some gas bubbles (Okamoto, 1998), although their transport into the core is less feasible. In fact, this topic is mainly studied for its consequences regarding fluid-structure interactions and the mechanical stability of the vessel (Buongiorno, 2004; Frano, 2012), which exceed the scope of this chapter.

10.5 Summary and conclusions

For the further development of advanced liquid metal (LM) systems, one of the major areas which requires further investigation is the study of low Prandtl number thermal-hydraulics. Due to their specific features (among others, low *Pr*, Section 10.1.3), turbulence heat transfer models developed for other common fluids, such as air and water, are not directly applicable for liquid-metal systems. Moreover, it is frequently challenging to accurately assess a LM flow scenario by means of a mock-up experiment using a model fluid. In that context, specific experiments and models are often needed.

This chapter deals with the analysis of liquid-metal flow and heat transfer in steady state. Although transient scenarios are also found in LM systems, stationary conditions are usually considered in both experiments and simulations for understanding the underlying physical mechanisms leading to the transport of momentum and energy, which is the main topic of this chapter. Special emphasis is placed on two issues, namely that of turbulence modelling and of engineering correlations and empirical models based on experiences.

Closure methods for the turbulent transport of momentum derived for other fluids can also be applied to liquid metals, as this process is governed by the Reynolds number alone. For the turbulent transport of energy, the scales separation results in an increased influence of molecular thermal conduction for liquid metals, and thus a lower contribution of turbulence to the diffusion of energy than to the diffusion of momentum, i.e. $Pr_t > 1$. Moreover, the turbulent Prandtl number is found to depend on the position, as well as *Re* and *Pr*. A major challenge for the evaluation of this key parameter is the lack of sufficient experimental data, particularly considering the strong influence of the geometry. Direct numerical simulations are a prominent source of detailed information on turbulent flows

for the validation of turbulence models, although yet restricted to simple flow scenarios. Moreover, caution should be taken when considering turbulent convection in heavy-liquid metals with large heat fluxes, as the effects of buoyancy might not be negligible.

Despite recent efforts, the databases in some cases continue to be too sparse to allow for a comprehensive and detailed analysis. This fact is reflected, for example, by different researchers proposing sometimes contradicting models and yet claiming agreement with experimental observations. To a certain extent, this can be explained by the reasonable scatter of the data, in addition to the limited data basis considered by individual authors. Furthermore, some early publications in the open literature failed to include all required data for making their results reproducible, and relevant information on their experimental condition is sometimes missing. Nevertheless, for the most common geometries and thermal boundary conditions, reliable heat transfer correlations with sufficient engineering accuracy have been developed and are recommended for design purposes in Section 10.4. More complex scenarios found in heavy-liquid metal systems, such as beam window geometries, cannot be treated by such simple analysis and a three-dimensional representation is often required. The main experiences are summarised here.

During the last decade, the field of low *Pr* thermal-hydraulic has progressed substantially. As large research efforts are currently devoted to this topic in the framework of national and international programmes, extensive progress is foreseen in the upcoming year. In that context, this chapter intends to provide an overview of the state-of-the-art regarding both modelling and experiences, and a comprehensive exploration of the available literature for further reading. As this field continues to evolve, this literature is expected to expand significantly in the next decade.

References

Abe, H., H. Kawamura and Y. Matsuo (2004), "Surface Heat-Flux Fluctuations in a Turbulent Channel Flow Up to Re_τ = 1020 with Pr = 0.025 and 0.71", *International Journal of Heat and Fluid Flow*, 25 (3), pp. 404-419.

Abe, K., T. Kondoh and Y. Nagano (1995), "A New Turbulence Model for Predicting Fluid Flow and Heat Transfer in Separating and Reattaching Flows – II. Thermal Field Calculations", *International Journal of Heat and Mass Transfer*, 38 (8), pp. 1467-1481.

Addison, C. C. (1984), *The Chemistry of the Liquid Alkali Metals*, Wiley, Chichester.

Allen, R.W. and E.R.G. Eckert (1964), "Friction and Heat-transfer Measurements to Turbulent Pipe Flow of Water (Pr = 7 and 8) at Uniform Wall Heat Flux", *Journal of Heat Transfer*, 86 (3), pp. 301-310.

Andersen, P.S., W.M. Kays and R.J. Moffat (1975), "Experimental Results for the Transpired Turbulent Boundary Layer in an Adverse Pressure Gradient", *Journal of Fluid Mechanics*, Vol. 69, pp. 353-375.

Anderson, D.A., J.C. Tannehill and R.H. Pletcher (1984), *Computational Fluid Mechanics and Heat Transfer*, Hemisphere, Washington.

Aoki, S. (1963), "A Consideration on the Heat Transfer in Liquid Metals", *Bulletin of the Tokyo Institute of Technology*, September, Vol. 54, pp. 63-73.

Arien, B. (2004), *Assessment of Computational Fluid Dynamic Codes for Heavy Liquid Metals – ASCHLIM*, Final Report, EC-Con. FIKW-CT-2001-80121-.

Azer, N. and B. Chao (1960), "A Mechanism of Turbulent Heat Transfer in Liquid Metals", *International Journal of Heat and Mass Transfer*, 1 (2-3), pp. 121-138.

Azer, N. and B. Chao (1961), "Turbulent Heat Transfer in Liquid Metals – Fully Developed Pipe Flow with Constant Wall Temperature", *International Journal of Heat and Mass Transfer*, 3 (2), pp. 77-83.

Baher, H. D. and K. Stephan (2011), *Heat and Mass Transfer*, 3rd Edition, Springer, Berlin.

Baker, R. and A. Sesonske (1962), "Heat Transfer in a Sodium-potassium Alloy", *Nuclear Science and Engineering*, Vol. 13, pp. 283-288.

Baldwin, B.S. and H. Lomax (1978), "Thin Layer Approximation and Algebraic Model for Separated Turbulent Flows", *AIAA 16th Aeropsace Sciences Meeting*, Huntsville, AL, 16-18 January, Paper 78-257.

Barenblatt, G. and A. Chorin (1998), "Turbulence: An Old Challenge and New Perspectives", *Meccanica*, 33 (5), pp. 445-468.

Barleon, L., K.J. Mack and R. Stieglitz (1996), *The MEKKA-Facility – A Flexible Tool to Investigate MHD-flow Phenomena*, Forschungszentrum Karlsruhe GmbH, Karlsruhe.

Batchelor, G.K. (1959a), "Small-Scale Variation of Convected Quantities Like Temperature in Turbulent Fluid Part 1. General Discussion and the Case of Small Conductivity", *Journal of Fluid Mechanics*, Volume 5, pp. 113-133.

Batchelor, G.K., I.D. Howells and A.A. Townsend (1959b), "Small-Scale Variation of Convected Quantities like Temperature in Turbulent Fluid Part 2. The Case of Large Conductivity", *Journal of Fluid Mechanics*, Vol. 5, pp. 134-139.

Bauer, G. (2010), "Overview on Spallation Target Design Concepts and Related Materials Issues", *Journal of Nuclear Materials*, 398 (1-3), pp. 19-27.

Baumann, W. et al. (1968), *Brennelemente mit wendelföormigen Abstandshaltern für Schnelle Brutreaktoren*, Kernforschungszentrum Karlsruhe, Karlsruhe.

Benamati, G. et al. (2007), "Experimental Study on Gas-injection Enhanced Circulation Performed with the CIRCE Facility", *Nuclear Engineering and Design*, 237 (7), pp. 768-777.

Betchov, R. and W.O. Criminale (1967), *Stability of Parallel Flows*, Academic Press, New York.

Beznosov, A. et al. (2004), "Experimental Investigation of Heat Transfer from a Circular Pipe to Lead Coolant with Controlled Oxygen Content", *Atomic Energy*, 97 (5), pp. 757-760.

Beznosov, A.V. et al. (2005), "Experimental Studies of the Characteristics of Contact Heat Exchange Between Lead Coolant and the Working Body", *Atomic Energy*, Vol. 98, pp. 170-176.

Bird, R.B., W.E. Stewart and E.N. Lightfoot (2007), *Transport Phenomena*, 2nd Edition, John Wiley & Sons Inc., New York.

Bishop, A., F. Engel and R. Markley (1979), "Heat Transfer Effect of Entrained Gas in Liquid Sodium Systems", *Nuclear Engineering and Design*, 52 (1), pp. 1-13.

Bobkov, V., V. Vinogradov and N. Kozina (1988), "Analysis of Data and Recommendations on Heat Transfer by Liquid Metals in Rod Bundles", *Soviet Atomic Energy*, 65 (6), pp. 1007-1011.

Borishanskii, V. and E.V. Firsova (1963), "Heat Exchange in the Longitudinal Flow of Metallic Sodium Past a Tube Bank", *Soviet Atomic Energy*, 14 (6), pp. 614-615.

Borishanskii, V. and E.V. Firsova (1964), "Heat Exchange in Separated Bundles of Rods with Metallic Sodium Flowing Longitudinally", *Soviet Atomic Energy*, 16 (5), pp. 562-563.

Borishanskii, V.M. et al. (1969a), "Heat Transfer During Flow of Mercury in Horizontal and Vertical Tubes", *Convective Heat Transfer in Two-Phase and One-Phase Flows*, Technical Report AEC-6877, s.l.:s.n.

Borishanskii, V.M., M.A. Gotovskii and E.V. Firsova (1969b), "Heat Transfer to Liquid Metals in Longitudinally Wetted Bundles of Rods", *Soviet Atomic Energy*, 27 (6), pp. 1347-1350.

Borishanskii, V.M., T.V. Zablotskaya and N.I. Ivsashchenko (1969c), "Heat Transfer and Temperature Fields During Turbulent Flow of Metallic Sodium in Tubes", *Convective Heat Transfer in Two-Phase and One-Phase Flows*, Technical Report AEC-6877, s.l.:s.n.

Borishanskii, V.M. et al. (1969d), "Heat Transfer to Liquid Metals Flowing Through an Annular Duct", *Heat Transfer – Soviet Research*, 1 (1), pp. 1-5.

Boston, N.E.J. and R.W. Burling (1972), "An Investigation of High-Wavenumber Temperature and Velocity Spectra in Air", *Journal of Fluid Mechanics*, Vol. 55, 10, pp. 473-492.

Boussinesq, J. (1872), *Essai sur la théorie des eaux courantes*, Thesis presented at the French Academy of Sciences, Paris.

Boussinesq, J. (1897), *Théorie d'écoulement tourbillant et tumultueux des liquides*, Thesis presented at the French Academy of Sciences, Paris.

Bredberg, J. (2000), *On the Wall Boundary Condition for Turbulence Models*, Internal report 00/4, Chalmers University of Technology, Göteborg.

Bremhorst, K. and L. Krebs (1992), "Experimentally Determined Turbulent Prandtl Numbers in Liquid Sodium at Low Reynolds Numbers", *International Journal of Heat and Mass Transfer*, 35 (2), pp. 351-359.

Bricteux, L. et al. (2012), "Direct and Large Eddy Simulation of Turbulent Heat Transfer at Very Low Prandtl Number: Application to Lead-bismuth Flows", *Nuclear Engineering and Design*, Vol. 246, pp. 91-97.

Brown, G. M. (1960), "Heat or Mass Transfer in a Fluid in Laminar Flow in a Circular or Flat Conduit", *AIChE Journal*, 6 (2), pp. 179-183.

Brown, H.E., B.H. Amstead, B.E. Short (1957), "Temperature and Velocity Distribution and Transfer of Heat in a Liquid Metal", *Transactions of the American Society of Mechanical Engineers*, Vol. 79, pp. 279-285.

Buhr, H., A. Carr and R. Balzhiser (1968), "Temperature Profiles in Liquid Metals and the Effect of Superimposed Free Convection in Turbulent Flow", *International Journal of Heat and Mass Transfer*, 11 (4), pp. 641-654.

Buongiorno, J. and B. Hawkes (2004), "Seismic Analysis of Heavy Liquid Metal Cooled Reactor Vessels", *Nuclear Engineering and Design*, 228 (1-3), pp. 305-317.

Burmeister, L.C. (1983), *Convective Heat Transfer*, Wiley, New York.

Carteciano, L.N. and G. Grötzbach (2003), *Validation of Turbulence Models in the Computer Code FLUTAN for a Free Hot Sodium Jet in Different Buoyancy Flow Regimes*, Forschungszentrum Karlsruhe, Karlsruhe.

Carteciano, L.N., D. Weinberg and U. Müller (1997), "Development and Analysis of a Turbulence Model for Buoyant Flows", *Proceedings of the 4th World Conference on Experimental Heat Transfer, Fluid Mechanics and Thermodynamics*, Brussels, Belgium, 2-6 June, pp. 1339-1347.

Cebeci, T. (1973), "A Model for Eddy Conductivity and Turbulent Prandtl Number", *Journal of Heat Transfer*, Vol. 95, pp. 2227-234.

Cebeci, T. and A.M. Smith (1974), *Analysis of Turbulent Boundary Layers*, Academic Press, New York.

Chandra, L. et al. (2009), "A Stepwise Development and Validation of a RANS Based CFD Modelling Approach for the Hydraulic and Thermal-Hydraulic Analyses of Liquid Metal Flow in a Fuel Assembly", *Nuclear Engineering and Design*, 239 (10), pp. 1988-2003.

Chen, C.J. and J.S. Chiou (1981), "Laminar and Turbulent Heat Transfer in the Pipe Entrance Region for Liquid Metals", *International Journal of Heat and Mass Transfer*, 24 (7), pp. 1179-1189.

Chen, F. et al. (2013), "Investigation on the Applicability of Turbulent-Prandtl-number Models for Liquid Lead-Bismuth Eutectic", *Nuclear Engineering and Design*, Vol. 257, pp. 128-133.

Chen, J.C. and W. Yu (1970), "Entrance Region and Variable Heat Flux Effects in Turbulent Heat Transfer to Liquid Metals Flowing in Concentric Annuli", *International Journal of Heat and Mass Transfer*, 13 (4), pp. 667-680.

Chen, R.Y. (1973), "Flow in the Entrance Regio at Low Reynolds Number", *Journal of Fluids Engineering*, 95 (1), pp. 153-158.

Cheng, X. and N. Tak (2006), "Investigation on Turbulent Heat Transfer to Lead-bismuth Eutectic Flows in Circular Tubes for Nuclear Applications", *Nuclear Engineering and Design*, 236 (4), pp. 385-393.

Chien, K.Y. (1982), "Predictions of Channel and Boundary-layer Flows with a Low-Reynolds-number Turbulence Model", *AIAA Journal*, 20 (1), pp. 33-38.

Chorin, A.J. and J.E. Marsden (1979), *A Mathematical Introduction to Fluid Mechanics*, Springer, New York.

Churchill, S.W. (2002), "A Reinterpretation of the Turbulent Prandtl Number", *Industrial & Engineering Chemistry Research*, 41 (25), pp. 6393-6401.

Ciampichetti, A. et al. (2009), "Experimental and Computational Investigation of LBE-Water Interaction in LIFUS 5 Facility", *Nuclear Engineering and Design*, 239 (11), pp. 2468-2478.

Ciampichetti, A. et al. (2011), "LBE-Water Interaction in LIFUS 5 Facility Under Different Operating Conditions", *Journal of Nuclear Materials*, 415 (3), pp. 449-459.

Class, A. et al. (2011), "XT-ADS Windowless Spallation Target Thermohydraulic Design and Experimental Setup", *Journal of Nuclear Materials*, 415 (3), pp. 378-384.

Collingham, R. E. et al. (1970), "Development and Results of an Electrically-heated Seven-Pin Bundle Assembly for Thermal-hydraulic Testing in Liquid Metals", *Liquid-Metal Heat Transfer and Fluid Dynamics*, J.C. Chen and A.A. Bishop (eds.), American Society of Mechanical Engineers, New York, pp. 41-49.

Crye, J.M. et al. (2002), "Measurement of the Heat Transfer Coefficient for Mercury Flowing in a Narrow Channel", *Journal of Heat Transfer*, 124 (6), pp. 1034-1038.

Daubner, M. et al. (2004), "Turbulent Heat Mixing of a Heavy Liquid Metal Flow Within the MEGAPIE Window Geometry: The Heated Jet Experiments", *Journal of Nuclear Materials*, 335 (2), pp. 286-292.

Daubner, M. et al. (2005), *Turbulent Thermal Mixing of a Heavy Liqud Metal Flow in a Target Window Geometry – The Heated Jet Experiment*, Forschungszentrum Karlsruhe, Gmbh, Karlsruhe.

Davies, F. (1969), *Eddy Viscosity and Eddy Conductivity: A Statistical Approach and Experimental Verification*, Eidgenössische Technische Hochschule, Zurich.

Deissler, R.G. (1952), *Analysis of Fully-Developed Turbulent Heat Transfer at Low Péclet Numbers with Application to Liquid Metals*, National Advisory Committee for Aeronautics, Washington.

Deng, B., W. Wu and S. Xi (2001), "A Near-wall Two-Equation Heat Transfer Model for Wall Turbulent Flows", *International Journal of Heat and Mass Transfer*, 44 (4), pp. 691-698.

Dinh, T-N. (2007), "Multiphase Flow Phenomena of Steam Generator Tube Rupture in a Lead-cooled Reactor System: A Scoping Analysis", *International Congress on Advances in Nuclear Power Plants (ICAPP)*, Nice, France, pp. 2765-2775.

Donaldson, C. (1972), "Calculation of Turbulent Shear Flows for Atmospheric and Vortex Motions", *AIAA Journal*, 10 (1), pp. 4-12.

Duchatelle, L. and L. Vautrey (1964), "Determination des coefficients de convection d'un alliage nak en ecoulement turbulent entre plaques planes paralleles", *International Journal of Heat and Mass Transfer*, 7 (9), pp. 1017-1031.

Duponcheel, M. et al. (2013), "Numerical Simulation of Liquid Metal Turbulent Heat Transfer in a Channel Flow at $Re_\tau = 2\,000$", *Proceedings of the 15th International Topical Meeting on Nuclear Reactor Thermal-Hydraulics (NURETH-15)*, Pisa, Paper 38.

Durbin, P.A. (1993a), "Application of a Near-Wall Turbulence Model to Boundary Layers and Heat Transfer", *International Journal of Heat and Fluid Flow*, 14 (4), pp. 316-323.

Durbin, P.A. (1993b), "A Reynolds Stress Model for Near-wall Turbulence", *Journal of Fluid Mechanics*, 4, Vol. 249, pp. 465-498.

Dwyer, O.E. (1963a), "Eddy Transport in Liquid-metal Heat Transfer", *AIChE Journal*, 9 (2), pp. 261-268.

Dwyer, O.E. (1963b), "On the Transfer of Heat to Fluids Flowing Through Pipes, Annuli, and Parallel Plates", *Nuclear Science and Engineering*, 17 (3), pp. 336-344.

Dwyer, O.E. and P.S. Tu (1963c), "Unilateral Heat Transfer to Liquid Metals Flowing in Annuli", *Nuclear Science and Engineering*, 15 (1), pp. 58-68.

Dwyer, O.E. (1965a), "Heat Transfer to Liquid Metals Flowing Turbulently Between Parallel Plates", *Nuclear Science and Engineering*, Vol. 21, pp. 79-85.

Dwyer, O.E. and P.S. Tu (1965b), "Bilateral Heat Transfer to Liquid Metals Flowing Turbulently Through Annuli", *Nuclear Science and Engineering*, 21 (1), pp. 90-105.

Dwyer, O.E. (1966), "Recent Development in Liquid Metal Heat Transfer", *Atomic Energy Review*, Vol. 4, pp. 3-92.

Dwyer, O.E. (1969), "Heat Transfer to Liquid Metals Flowing in-line through Unbaffled Rod Bundles: A Review", *Nuclear Engineering and Design*, 10 (1), pp. 3-20.

Dwyer, O.E. and H.C. Berry (1970), "Laminar-Flow Heat Transfer for In-line Flow through Unbaffled Rod Bundles", *Nuclear Science and Engineering*, Vol. 42, pp. 81-88.

Dwyer, O.E. (1976), "Liquid Metal Heat Transfer", *Sodium-NaK Engineering Handbook*, O.J. Foust (ed.), New York, Gordon and Breach Science Publishers, pp. 73-191.

Eckert, E.R.G. and R.M. Drake (1972), *Analysis of Heat and Mass Transfer*, New York, McGraw-Hill.

Emery, A. and D. Bailey (1967), "Heat Transfer to Fully Developed Liquid Metal Flow in Tubes", *Journal of Heat Transfer*, Vol. 89, pp. 272-273.

Engel, F. et al. (1980), "Characterization of Heat Transfer and Temperature Distributions in an Electrically Heated Model of an LMFBR Blanket Assembly", *Nuclear Engineering and Design*, 62 (1-3), pp. 335-347.

English, D. and T. Barrett (1951), *Heat-Transfer Properties of Mercury*, Institute of Mechanical Engineers, London, pp. 458-460.

Falzetti, L., S. Meneghello and M. Pezzilli (1979), "Steady-State Thermohydraulic Studies in Seven-pin Bundle Out-of-pile Experiments: Nominal and Distorted Geometry Tests", *International Working Group on Fast Reactors. Vienna: Specialists' Meeting on Thermodynamics of FBR Fuel Subassemblies Under Nominal and Non-Nominal Operating Conditions*; Karlsruhe, Germany, 5-7 February 1978, IAEA, Vienna, pp. 261-270.

Fazio, C. et al. (2008), "The MEGAPIE-TEST Project: Supporting Research and Lessons Learned in First-of-a-Kind Spallation Target Technology", *Nuclear Engineering and Design*, 238 (6), pp. 1471-1495.

Flad, M., S. Wang and W. Maschek (2010), "Simulation of a Steam Generator Tube Rupture Accident in a Lead-cooled Accelerator Driven System", *ASME Conference Proceedings* (49347), pp. 241-249.

Fontana, M.H. et al. (1974), "Temperature Distribution in the Duct Wall and at the Exit of a 19-Rod Simulated LMFBR Fuel Assembly (FFM Bundle 2A)", *Nuclear Technology*, 24 (2), pp. 176-200.

Foust, O.J. (ed.) (1976), *Sodium-NaK Engineering Handbook*, Gordon & Breach, New York.

Frano, R.L. and G. Forasassi (2012), "Preliminary Evaluation of the Seismic Response of the ELSY LFR", *Nuclear Engineering and Design*, Vol. 242, pp. 361-368.

Fricano, J. and E. Baglietto (2014), "A Quantitative CFD Benchmark for Sodium Fast Reactor Fuel Assembly Modeling", *Annals of Nuclear Energy*, Vol. 64, pp. 32-42.

Friedland, A. et al. (1961a), "Heat Transfer to Mercury in Parallel Flow through Bundles of Circular Rods", *International Heat Transfer Conference*, Boulder, Colorado.

Friedland, A.J. and C.F. Bonilla (1961b), "Analytical Study of Heat Transfer Rates for Parallel Flow of Liquid Metals through Tube Bundles: II", *AIChE Journal*, 7 (1), pp. 107-112.

Fuchs, H. (1974), *Wärmeübergang an strömendes Natrium. theoretische und experimentelle Untersuchungen über Temperaturprofile und turbulente Temperaturschwankungen bei Rohrgeometrie*, Eidgenossische Technische Hoschule, Zurich.

Gardner, R.A. and P.S. Lykoudis (1969), "Magneto-fluid-mechanic Pipe Flow in a Transverse Magnetic Field with and Without Heat Transfer", *AIAA*, San Francisco.

Gebhardt, B. (1971), *Heat Transfer*, McGraw Hill Book Corporation, New York.

Gibson, C.H. and W.H. Schwarz (1963a), "Detection of Conductivity Fluctuations in a Turbulent Flow Field", *Journal of Fluid Mechanics*, Vol. 16, 7, pp. 357-364.

Gibson, C.H. and W.H. Schwarz (1963b), "The Universal Equilibrium Spectra of Turbulent Velocity and Scalar Fields", *Journal of Fluid Mechanics*, Vol. 16, 7, pp. 365-384.

Gilliland, E.R., R.J. Musser and W.R. Page (1951), *Heat Transfer to Mercury*, *The Institution of Mechanical Engineers*, London, pp. 402-404.

Gnieser, S. et al. (2003), *Thermohydraulic Investigations for MEGAPIE: The HYTAS-KILOPIE and Heated Jet Experiments*, Forschungszentrum Karlsruhe GmbH, Karlsruhe, pp. 134-143.

Gordeev, S., L. Stoppel and R. Stieglitz (2009), "Turbulent Liquid Metal Flow in Rectangular Shaped Contraction Nozzles for Target Applications", *International Journal of Computational Fluid Dynamics*, 23 (6), pp. 477-493.

Gräber, H. and M. Rieger (1972), "Experimentelle Untersuchung des Wärmeübergangs an Flüssigmetalle (NaK) in parallel durchströmten Rohrbündeln bei konstanter und exponentieller Wärmeflußdichteverteilung", *Atomkernenergie*, 19 (1), pp. 23-40.

Graetz, L. (1882), "Über die Wärmeleitungsfähigkeit von Flüssigkeiten", *Annalen der Physik*, 254 (1), pp. 79-94.

Graetz, L. (1885), "Über die Wärmeleitungsfähigkeit von Flüssigkeiten", *Annalen der Physik*, 261 (7), pp. 337-357.

Grant, H.L. et al. (1968), "The Spectrum of Temperature Fluctuations in Turbulent Flow", *Journal of Fluid Mechanics*, Vol. 34, 12, pp. 423-442.

Grigull, U. and H. Tratz (1965), "Thermischer Einlauf in ausgebildeter laminarer Rohrströmung", *International Journal of Heat and Mass Transfer*, 8 (5), pp. 669-678.

Grote, K.-H. and J. Feldhusen (eds.) (2012), Dubbel : Taschenbuch für den Maschinenbau, 23rd ed., Springer, Berlin, Heidelberg.

Grötzbach, G. and M. Wörner (1992), *Analysis of Second Order Transport Equations by Numerical Simulations of Turbulent Convection in Liquid Metals*, American Nuclear Society, Salt Lake City, pp. 358-365.

Grötzbach, G. et al. (2004), "Challenges in Thermal and Hydraulic Analyses of ADS Target Systems", *Proceedings of the 6th International Conference on Nuclear Thermal Hydraulics, Operation and Safety (NUTHOS-6)*, Nara, Japan, Paper N6P005.

Grötzbach, G. (2013), "Challenges in Low-Prandtl Number Heat Transfer Simulation and Modelling", *Nuclear Engineering and Design*, Vol. 264, pp. 41-55.

Guo, J. and P.Y. Julien (2003), "Modified Log-wake Law for Turbulent Flow in Smooth Pipes", *Journal of Hydraulic Research*, 41 (5), pp. 493-501.

Hanjalic, K. and B.E. Launder (1972), "A Reynolds Stress Model of Turbulence and Its Application to Thin Shear Flows", *Journal of Fluid Mechanics*, Vol. 52, 4, pp. 609-638.

Harlow, F.H. and P.I. Nakayama (1968), *Transport of Turbulence Energy Decay Rate*, Los Alamos Scientific Laboratory of the University of California, Los Alamos, NM.

Hartnett, J.P. and T.F. Irvine (1957), "Nusselt Values for Estimating Turbulent Liquid Metal Heat Transfer in Noncircular Ducts", *AIChE Journal*, 3 (3), pp. 313-317.

Hennecke, D. (1968), "Heat Transfer by Hagen-Poiseuille Flow in the Thermal Development Region with Axial Conduction", *Wärme - und Stoffübertragung*, 1 (3), pp. 177-184.

Hlavac, P., O. Dwyer and M. Helfant (1969), "Heat Transfer to Mercury Flowing in Line Through an Unbaffled Rod Bundle: Experimental Study of the Effects of Rod Displacement on Rod-average Heat Transfer Coefficients", *Journal of Heat Transfer*, Vol. 91, pp. 568-580.

Holtz, R. (1965), *A Liquid-Metal Heat Transfer Experiment*, Argonne National Laboratory, Argonne, IL.

Hornbeck, R.W. (1964), "Laminar Flow in the Entrance Region of a Pipe", *Applied Scientific Research, Section A*, 13 (1), pp. 224-232.

Horsten, E.A. (1971), *Combined Free and Forced Convection on Turbulent Flow of Mercury*, University of Cape Town, Cape Town, South Africa.

Hsu, C-J. (1965), "Heat Transfer in a Round Tube with Sinusoidal Wall Heat Flux Distribution", *AIChE Journal*, 11 (4), pp. 690-695.

Hsu, C-J. (1968), "Exact Solution to Entry-Region Laminar Heat Transfer with Axial Conduction and the Boundary Condition of the Third Kind", *Chemical Engineering Science*, 23 (5), pp. 457-468.

Hu, R. and T.H. Fanning (2010), "Intermediate-Resolution Method for Thermal-Hydraulic Modeling of a Wire-Wrapped Pin Bundle", *Transactions of the American Nuclear Society*, Vol. 103, pp. 1003-1005.

Ibragimov, M., V. Subbotin and P. Ushakov (1960), "Investigation of Heat Transfer in the Turbulent Flow of Liquid Metals in Tubes", *The Soviet Journal of Atomic Energy*, 8 (1), pp. 48-50.

Ikeda, Y. (2005), "Current Status of 1 MW Pulse Spallation Neutron Source (JSNS) of J-PARC", *Journal of Nuclear Materials*, 343 (1-3), pp. 7-13.

Isakoff, S.E. and T.B. Drew (1951), *Heat and Momentum Transfer in Turbulent Flow of Mercury*, The Institution of Mechanical Engineers, London.

Jackson, J. (1983), "Turbulent Mixed Convection Heat Transfer to Liquid Sodium", *International Journal of Heat and Fluid Flow*, 4 (2), pp. 107-111.

Jackson, J.D., B.P. Axcell and A. Walton (1994), "Mixed Convection Heat Transfer to Sodium in a Vertical Pipe", *Experimental Heat Transfer*, 7 (1), pp. 71-90.

Jacoby, J.K. (1972), *Free-Convection Distortion and Eddy-Diffusivity Effects in Turbulent Mercury Heat Transfer*, Purdue University, West Lafayette, Illinois.

Jäger, W. and V. Sánchez (2013), "Validation of the Heat Transfer Enhancement Models for Spacer Grids in the System Code TRACE", *Nuclear Engineering and Design*, Vol. 265, pp. 272-287.

Jauch, U. et al. (1986), *Thermophysical Properties in the System Li-Pb*, Kernforschungszentrum Karlsruhe, Karlsruhe.

Javeri, V. (1976), "Simultaneous Development of the Laminar Velocity and Temperature Fields in a Circular Duct for the Temperature Boundary Condition of the Third Kind", *International Journal of Heat and Mass Transfer*, 19 (8), pp. 943-949.

Jeanmart, H. et al. (2011), "Characterisation in Water Experiments of a 'Detached Flow' Free Surface Spallation Target", *Journal of Nuclear Materials*, 415 (3), pp. 385-395.

Jenkins, R. (1951), "Variation of the Eddy Conductivity with Prandtl Modulus and Its Use in Prediction of Turbulent Heat Transfer Coefficients", *Proceedings of the Heat Transfer and Fluid Mechanics Institute*, Stanford.

Jischa, M. and H.B. Rieke (1979), "About the Prediction of Turbulent Prandtl and Schmidt Numbers from Modeled Transport Equations", *International Journal of Heat and Mass Transfer*, 22 (11), pp. 1547-1555.

Jischa, M. (1982), *Konvektiver Impuls-, Wärme- und Stoffaustausch*, Vieweg, Braunschweig.

Johnson, H.A., W.J. Clabaugh and J. Hartnett (1952), *Heat Transfer to Mercury in Turbulent Pipe Flow*, Institute of Energy Research, University of California, Berkeley, California.

Johnson, H.A., J. Hartnett and W. Clabaugh (1953a), *Heat Transfer to Lead-bismuth and Mercury in Laminar and Transition Pipe Flow*, Institute of Energy Research, University of California, Berkeley, CA.

Johnson, H.A., J. Hartnett and W.J. Clabaug (1953b), "Heat Transfer to Molten Lead-bismuth Eutectic in Turbulent Pipe Flow", *Transactions of the American Society of Mechanical Engineers*, 75 (6), pp. 1191-1198.

Jones, W. and B. Launder (1972), "The Prediction of Laminarization with a Two-equation Model of Turbulence", *International Journal of Heat and Mass Transfer*, 15 (2), pp. 301-314.

Kader, B. (1981), "Temperature and Concentration Profiles in Fully Turbulent Boundary Layers", *International Journal of Heat and Mass Transfer*, 24 (9), pp. 1541-1544.

Kader, B. and A. Yaglom (1972), "Heat and Mass Transfer Laws for Fully Turbulent Wall Flows", *International Journal of Heat and Mass Transfer*, 15 (12), pp. 2329-2351.

Kakaç, S., R.K. Shah and W. Aung (eds.) (1987), *Handbook of Single-Phase Convective Heat Transfer*, John Wiley & Sons, Inc., New York.

Kalish, S. and O.E. Dwyer (1967), "Heat Transfer to NaK Flowing Through Unbaffled Rod Bundles", *International Journal of Heat and Mass Transfer*, 10 (11), pp. 1533-1558.

Karcz, M. and J. Badur (2005), "An Alternative Two-Equation Turbulent Heat Diffusivity Closure", *International Journal of Heat and Mass Transfer*, 48 (10), pp. 2013-2022.

Kasagi, N. and Y. Ohtsubo (1993), "Direct Numerical Simulation of Low Prandtl Number Thermal Field in a Turbulent Channel Flow", *Turbulent Shear Flows 8*, F. Durst et al. (eds.), Springer, Berlin, pp. 97-119.

Kawamura, H. (1998), "DNS of Turbulent Heat Transfer in Channel Flow with Low to Medium-High Prandtl Number Fluid", *International Journal of Heat and Fluid Flow*, 19 (5), pp. 482-491.

Kawamura, H., H. Abe and Y. Matsuo (1999), "DNS of Turbulent Heat Transfer in Channel Flow with Respect to Reynolds and Prandtl Number Effects", *International Journal of Heat and Fluid Flow*, 20 (3), pp. 196-207.

Kays, W. and E. Leung (1963), "Heat Transfer in Annular Passages – Hydrodynamically Developed Turbulent Flow with Arbitrarily Prescribed Heat Flux", *International Journal of Heat and Mass Transfer*, 6 (7), pp. 537-557.

Kays, W.M. and M.E. Crawford (1993), *Convective Heat and Mass Transfer*, 3rd edition, McGraw-Hill, New York.

Kays, W.M. (1994), "Turbulent Prandtl Number – Where Are We?", *Journal of Heat Transfer*, Vol. 116, pp. 284-295.

Kays, W.M., M.E. Crawford and B. Weigand (2007), *Convective Heat and Mass Transfer*, 4th edition, McGraw-Hill, Boston.

Kazimi, M.S. and M.D. Carelli (1976), *Clinch River Breeder Reactor Plant – Heat Transfer Correlation for Analysis of CRBRP Assemblies*, Westinghouse Electric Power Corporation, s.l.

Kerr, R.M. (1990), "Velocity, Scalar and Transfer Spectra in Numerical Turbulence", *Journal of Fluid Mechanics*, Vol. 211, 2, pp. 309-332.

Khabakhpasheva, E. and Y. Il'in (1961), "Heat Transfer to a Melt of Sodium and Potassium in Annular Clearances", *The Soviet Journal of Atomic Energy*, 9 (6), pp. 1038-1040.

Kikuchi, K. et al. (2006), "Measurement of LBE Flow Velocity Profile by UDVP", *Journal of Nuclear Materials*, 356 (1-3), pp. 273-279.

Kim, J. and P. Moin (1989), "Transport of Passive Scalars in a Turbulent Channel Flow", *Turbulent Shear Flows 6*, J. André et al. (eds.), Springer, Berlin, pp. 85-96.

Kim, W-S., Y-G. Kim and Y-J. Kim (2002), "A Subchannel Analysis Code MATRA-LMR for Wire Wrapped LMR Subassembly", *Annals of Nuclear Energy*, 29 (3), pp. 303-321.

Kimura, N., H. Miyakoshi and H. Kamide (2007), "Experimental Investigation on Transfer Characteristics of Temperature Fluctuation from Liquid Sodium to Wall in Parallel Triple-jet", *International Journal of Heat and Mass Transfer*, 50 (9-10), pp. 2024-2036.

Kinoshita, H. et al. (2013), "Experimental Study on Heat Transfer and Pressure Drop in Mercury Flow System for Spallation Neutron Source", *Journal of Nuclear Science and Technology*, 50 (4), pp. 400-408.

Kirillov, P. et al. (1960), "Heat-transfer in a Tube to Sodium-potassium Alloy and to Mercury", *The Soviet Journal of Atomic Energy*, 6 (4), pp. 253-260.

Kirillov, P.L. and P.A. Ushakov (2001), "Heat Transfer to Liquid Metals: Specific Features, Methods of Investigation, and Main Relationships", *Thermal Engineering*, 48 (1), pp. 50-59.

Knebel, J.U. (1993), *Experimentelle Untersuchungen in turbulenten Auftriebstrahlen in Natrium*, Kernforschungszentrum Karlsruhe, Karlsruhe.

Knebel, J.U. et al. (1998), "Experimental Investigation of a Confined Heated Sodium Jet in a Co-flow", *Journal of Fluid Mechanics*, Vol. 368, 7, pp. 51-79.

Knudsen, J.G. and D.L. Katz (1958), *Fluid Dynamics and Heat Transfer*, McGraw-Hill, New York.

Kottowski-Dümenil, H.M. (ed.) (1994), *Liquid Metal Thermal-Hydraulics*, Inforum-Verl, Bonn.

Kowalski, D.K. (1974), *Free Convection Distortion in Turbulent Mercury Pipe Flow*, Purdue University, West Lafayette, Illinois.

Kraichnan, R.H. (1971), "Inertial-Range Transfer in Two- and Three-dimensional Turbulence", *Journal of Fluid Mechanics*, Vol. 47, 6, pp. 525-535.

Krett, V. and J. Majer (1971), *Temperature Field Measurement in the Region of Spacing Elements*, Skoda Works, Plzen.

Kuczen, K.D. and T.R. Bump (1957), "Measurement of Local Heat Transfer Coefficients with Sodium-potassium Eutectic in Turbulent Flow", *Nuclear Science and Engineering*, Vol. 2, pp. 181-198.

Kunz, H.R. and S. Yerazunis (1969), "An Analysis of Film Condensation, Film Evaporation, and Single-phase Heat Transfer for Liquid Prandtl Numbers from 10^{-3} to 10^{4}", *Journal of Heat Transfer*, 91 (3), pp. 413-420.

Kutateladze, S., V. Borishanskii and I. Novikov (1958), "Heat Transfer in Liquid Metals", *The Soviet Journal of Atomic Energy*, 4 (5), pp. 555-571.

Kutateladze, S., V. Borishanskii and I. Novikov (1959), "Heat Transfer in Liquid Metals", *Journal of Nuclear Energy, Part B, Reactor Technology*, 9 (1-4), pp. 214-229.

Launder, B.E. and D. Spalding (1974), "The Numerical Computation of Turbulent Flows", *Computer Methods in Applied Mechanics and Engineering*, 3 (2), pp. 269-289.

Launder, B.E., G.J. Reece and W. Rodi (1975), "Progress in the Development of a Reynolds-stress Turbulence Closure", *Journal of Fluid Mechanics*, Vol. 68, 4, pp. 537-566.

Lefhalm, C-H. et al. (2004), "Turbulent Heavy Liquid Metal Heat Transfer Along a Heated Rod in an Annular Cavity", *Journal of Nuclear Materials*, 335 (2), pp. 280-285.

Lengeler, H. (1998), "The European Spallation Source Study", *Nuclear Instruments and Methods in Physics Research Section B: Beam Interactions with Materials and Atoms*, 139 (1-4), pp. 82-90.

Lévêque, A.M. (1928), "Les lois de la transmission de chaleur par convection", *Annales des Mines*, Vol. 13, pp. 201-415.

Lin, B.S., C.C. Chang and C.T. Wang (2000), "Renormalization Group Analysis for Thermal Turbulent Transport", *Physical Review E*, Vol. 63, pp. 016304-1/11.

Lin, C-C. (1955), *The Theory of Hydrodynamic Stability*, University Press, Cambridge.

Litfin, K. et al. (2011), "Investigation on Heavy Liquid Metal Cooling of ADS Fuel Pin Assemblies", *Journal of Nuclear Materials*, 415 (3), pp. 425-432.

Litfin, K. et al. (2012), "Investigation of a Heavy-Liquid Metal Surface Target Experiment", *Proceedings of the 20th International Conference on Nuclear Engineering*, Anaheim, CA, p. 54460.

Lubarsky, B. and S.J. Kaufman (1955), *Review of Experimental Investigations of Liquid-Metal Heat Transfer*, Lewis Flight Propulsion Laboratory – National Advistory Comitee for Aeronautics, Cleveland, OH.

Lykoudis, P.S. and Y.S. Touloukian (1958), "Heat Transfer in Liquid Metals", *Transactions of the American Society of Mechanical Engineers*, Vol. 80, pp. 653-666.

Lyon, R. (1949), *Forced Convection Heat Transfer Theory and Experiments with Liquid Metals*, Oak Ridge National Laboratory, Oak Ridge, Tennessee.

Lyon, R. (1951), "Liquid Metal Heat-Transfer Coefficients", *Chemical Engineering Progress*, 47 (2), pp. 75-79.

Lyon, R.N. (ed.) (1954), *Liquid-Metals Handbook*, 2nd rev. ed., Atomic Energy Commission, Department for the Navy, Washington, DC.

MacDonald, W.C. and R.C. Quittenton (1954), "A Critical Analysis of Metal Wetting and Gas Entrainment in Heat Transfer to Molten Metals", *Chemical Engineering Progress Symposium Series*, 50 (9), pp. 59-67.

Malik, M.R. and R.H. Pletcher (1981), "A Study of Some Turbulence Models for Flow and Heat Transfer in Ducts of Annular Cross-Section", *Journal of Heat Transfer*, 103 (1), pp. 146-152.

Manceau, R., S. Parneix and D. Laurence (2000), "Turbulent Heat Transfer Predictions Using the v2-f Model on Unstructured Meshes", *International Journal of Heat and Fluid Flow*, 21 (3), pp. 320-328.

Manservisi, S. and F. Menghini (2014), "A CFD Four Parameter Heat Transfer Turbulence Model for Engineering Applications in Heavy Liquid Metals", *International Journal of Heat and Mass Transfer*, Vol. 69, pp. 312-326.

Marchese, A.R. (1972), *Experimental Study of Heat Transfer to NaK Flowing In-Line through Tightly Packed Rod Bundles*, Atomics International, Canoga Park, California.

Maresca, M.W. and O.E. Dwyer (1964), "Heat Transfer to Mercury Flowing in-line through a Bundle of Circular Rods", *Journal of Heat Transfer*, 86 (2), pp. 180-186.

Marocco, L. et al. (2012), "Experimental Investigation of the Turbulent Heavy Liquid Metal Heat Transfer in the Thermal Entry Region of a Vertical Annulus with Constant Heat Flux on the Inner Surface", *International Journal of Heat and Mass Transfer*, 55 (23-24), pp. 6435-6445.

Martinelli, R.C. (1947), "Heat Transfer to Molten Metals", *Transactions of the American Society of Mechanical Engineers*, Vol. 69, pp. 947-959.

Ma, W., A. Karbojian and B.R. Sehgal (2007), Experimental Study on Natural Circulation and Its Stability in a Heavy Liquid Metal Loop", *Nuclear Engineering and Design*, Vol. 237, pp. 1838-1847.

Ma, W. et al. (2011), "Experimental and Numerical Study on Lead-bismuth Heat Transfer in a Fuel Rod Simulator", *Journal of Nuclear Materials*, 415 (3), pp. 415-424.

Ma, Z. et al. (2012), "An Innovative Method for Prediction of Liquid Metal Heat Transfer Rate for Rod Bundles Based on Annuli", *Annals of Nuclear Energy*, Vol. 47, pp. 91-97.

McManamy, T. et al. (2008), "Overview of the SNS Target System Testing and Initial Beam Operation Experience", *Journal of Nuclear Materials*, 377 (1), pp. 1-11.

Memmott, M., J. Buongiorno and P. Hejzlar (2010), "On the Use of RELAP5-3D as a Subchannel Analysis Code", *Nuclear Engineering and Design*, 240 (4), pp. 807-815.

Menter, F.R. (1993), "Zonal Two-Equation k-w Turbulence Models for Aerodynamic Flows", *AIAA 24th Fluid Dynamics Conference*, Orlando, FL.

Menter, F.R. (1994), "Two-equation Eddy-Viscosity Turbulence Models for Engineering Applications", *AIAA Journal*, 32 (8), pp. 1598-1605.

Merzari, E. et al. (2012), "Numerical Simulation of the Flow in Wire-wrapped Pin Bundles: Effect of Pin-Wire Contact Modeling", *Nuclear Engineering and Design*, Vol. 253, pp. 374-386.

Michelsen, M. and J. Villadsen (1974), "The Graetz Problem with Axial Heat Conduction", *International Journal of Heat and Mass Transfer*, 17 (11), pp. 1391-1402.

Mikityuk, K., P. Coddington and R. Chawla (2005), "Development of a Drift-Flux Model for Heavy Liquid Metal/Gas Flow", *Journal of Nuclear Science and Technology*, 42 (7), pp. 600-607.

Mikityuk, K. (2009), "Heat Transfer to Liquid Metal: Review of Data and Correlations for Tube Bundles", *Nuclear Engineering and Design*, 239 (4), pp. 680-687.

Mizuhina, T. and T. Sasano (1963), "The Ratio of the Eddy Diffusivities of Heat and Momentum and Its Effect on the Liquid Metal Heat Transfer", *International Developments in Heat Transfer*, Boulder, Colorado, pp. 662-668.

Mizushina, T. et al. (1964), "Effect of Gas Entrainment on Liquid Metal Heat Transfer", *International Journal of Heat and Mass Transfer*, 7 (12), pp. 1419-1425.

Mizushina, T. et al. (1969), "Eddy Diffusivities for Heat in the Region Near the Wall", *Memoires of the Faculty of Engineering*, Kyoto University, Vol. 31, pp. 169-181.

Möller, R. and H. Tschöke (1980), "Steady-State, Local Temperature Fields with Turbulent Liquid Sodium Flow in Nominal and Disturbed Bundle Geometries with Spacer Grids", *Nuclear Engineering and Design*, 62 (1-3), pp. 69-80.

Nagano, Y. and C. Kim (1988), "A Two-equation Model for Heat Transport in Wall Turbulent Shear Flows", *Journal of Heat Transfer*, 110 (3), pp. 583-589.

Nagano, Y., M. Shimada and M.S. Youssef (1994), "Progress in the Development of a Two-equation Heat Transfer Model Based on DNS Data Bases", *Proceedings of the International Symposium on Turbulence, Heat and Mass Transfer*, Lisbon, Portugal, pp. 3.2.1-3.2.6.

Nagano, Y. and M. Shimada (1995), "Rigorous Modeling of Dissipation-rate Equation Using Direct Simulations", *JSME International Journal Serie B, Fluids and Thermal Engineering*, 38-B (1), pp. 51-59.

Nagano, Y. (2002), "Modeling Heat Transfer in Near-wall Flows", *Closure Strategies for Modeling Turbulent and Transitional Flows*, B.E. Launder and N.D. Sandham (eds.) Cambridge University Press, Cambridge.

Nakamura, H. et al. (2008), "Latest Design of Liquid Lithium Target in IFMIF", *Fusion Engineering and Design*, 83 (7-9), pp. 1007-1014.

Namekawa, F., K. Mawatari and A. Ito (1984), "Buoyancy Effects on Wire-wrapped Rod Bundle Heat Transfer in a LMFBR Fuel Assembly", *AIChE*, Niagara Falls, New York, pp. 128-133.

Natesan, K. et al. (2010), "Turbulent Flow Simulation in a Wire-wrap Rod Bundle of an LMFBR", *Nuclear Engineering and Design*, Vol.240, 5, pp. 1063-1072.

Newman, J. (1973), "The Graetz Problem", *The Fundamental Principles of Current Distribution and Mass Transport in Electrochemical Cells*, A.J. Bard (ed.), Dekker, New York, pp. 187-352.

Nimmo, B. and O. Dwyer (1965), "Heat Transfer to Mercury Flowing Inline through a Rod Bundle", *Journal of Heat Transfer*, Vol. 87, pp. 312-313.

Niu, F., R. Candalino and N. Li (2007), "Effect of Oxygen on Fouling Behavior in Lead-bismuth Coolant Systems", *Journal of Nuclear Materials*, Vol. 366, 1-2, pp. 216-222.

Notter, R. (1969), *Two Problems in Turbulence: A. A Theoretical and Empirical Study of the Limiting Form of the Eddy Diffusivity Near a Wall. B. Matched Asymptotic Expansions Applied to the Turbulent Graetz Problem*, University of Washington, Seattle.

Notter, R. and C. Sleicher (1972), "A Solution to the Turbulent Graetz Problem III. Fully Developed and Entry Region Heat Transfer Rates", *Chemical Engineering Science*, Vol. 27, 11, pp. 2073-2093.

Novikov, I. et al. (1957), "The Heat-Transfer and High-Temperature Properties of Liquid Alkali Metals", *Journal of Nuclear Energy*, Vol. 4,3, pp. 387-408.

Obayashi, H., K. Kikuchi and Y. Takeda (2006), "Flow Measurement of Lead Bismuth Eutectic in Spallation Target Model Loop", *Proceedings of the 5th International Symposium on Ultrasonic Doppler Methods for Fluid Mechanics and Fluid Engineering*, Zurich.

Obayashi, H. and K. Kikuchi (2008), "Experimental Study for Thermal Striping in LBE Loop by Using UVP with High-Temperature Ultrasonic Transducer", *Proceedings of the 6th International Symposium on Ultrasonic Doppler Methods for Fluid Mechanics and Fluid Engineering*, Prague.

Okamoto, K. and H. Madarame (1998), "Fluid Dynamics of a Free Surface in Liquid Metal Fast Breeder Reactors", *Progress in Nuclear Energy*, Vol. 32,1-2, pp. 195-207.

Ooi, A. et al. (2002), "Reynolds Averaged Simulation of Flow and Heat Transfer in Ribbed Ducts", *International Journal of Heat and Fluid Flow*, Vol. 23, 6, pp. 750-757.

Otic, I., G. Grötzbach and M. Wörner (2005), "Analysis and Modelling of the Temperature Variance Equation in Turbulent Natural Convection for Low-Prandtl-number Fluids", *Journal of Fluid Mechanics*, Vol. 525, 1, pp. 237-261.

Otic, I. and A.G. Class (2007), *Numerical Investigation of a Heated Sodium Jet in Co-flow*, American Society of Mechanical Engineers, San Diego, CA, pp. 225-231.

Ould-Rouiss, M. et al. (2010), "Effect of Prandtl Number on the Turbulent Thermal Field in Annular Pipe Flow", *International Communications in Heat and Mass Transfer*, Vol. 37, 8, pp. 958-963.

Pacio, J. et al. (2014), "Heavy-Liquid Metal Heat Transfer Experiment in a 19-Rod Bundle with Grid Spacers", *Nuclear Engineering and Design*, forthcoming.

Pashek, M. (1967), *Study of Local Heat Transfer and Thermal Fields in a Seven-rod Bundle with Axial Flow of Sodium*, s.n., s.l.

Patorski, J.A. and F. Groeschel (2006), *Experimental Determination of Local Convection Heat Transfer Coefficient Field Using Two-Dimensional and Dynamic Infrared Thermography (2DD-IRT) Method*, s.n., s.l., pp. 62050T-62050T-12.

Petrovichev, V. (1961), "Heat Transfer in Mercury Flow Through Annular Channels", *The Soviet Journal of Atomic Energy*, Vol. 7, 4, pp. 844-847.

Pfrang, W. and D. Struwe (2007), *Assessment of Correlations for Heat Transfer to the Coolant for Heavy Liquid Metal Cooled Core Designs*, Forschunszentrum Karlsruhe GmbH, Karlsruhe.

Piller, M., E. Nobile and T.J. Hanratty (2002), "DNS Study of Turbulent Transport at Low Prandtl Numbers in a Channel Flow", *Journal of Fluid Mechanics*, Vol. 458, 4, pp. 419-441.

Pletcher, R.H. (1987), "External Flow Forced Convection", *Handbook of Single-Phase Convective Heat Transfer*, S. Kakaç, R.K. Shah and W. Aung (eds.), John Wiley & Sons, Inc., New York.

Pramuditya, S. and M. Takahashi (2013), "Thermal-hydraulic Analysis of Wire-wrapped SFR Test Subassemblies by Subchannel Analysis Method", *Annals of Nuclear Energy*, Vol. 54, pp. 109-119.

Prandtl, L. (1925), "Bericht über Untersuchungen zur ausgebildeten Turbulenz", *Zeitschirft für angewandte Mathematik und Mechanik*, Vol. 5, pp. 136-139.

Quarmby, A. and R. Quirk (1972), "Measurements of the Radial and Tangential Eddy Diffusivities of Heat and Mass in Turbulent Flow in a Plain Tube", *International Journal of Heat and Mass Transfer*, Vol.15, 11, pp. 2309-2327.

Quarmby, A. and R. Quirk (1974), "Axisymmetric and Non-Axisymmetric Turbulent Diffusion in a Plain Circular Tube at High Schmidt Number", *International Journal of Heat and Mass Transfer*, Vol.17, 1, pp. 143-147.

Ramm, H. and K. Johannsen (1973), "Radial and Tangential Turbulent Diffusivities of Heat and Momentum in Liquid Metals", *Progress in Heat and Mass Transfer*, Vol. 7, pp. 45-58.

Rasu, N.G. et al. (2013), "Investigations of Flow and Temperature Field Development in Bare and Wire-Wrapped Reactor Fuel Pin Bundles Cooled by Sodium", *Annals of Nuclear Energy*, Vol. 55, pp. 29-41.

Rasu, N.G. et al. (2014), "Simultaneous Development of Flow and Temperature Fields in Wire-wrapped Fuel Pin Bundles of Sodium Cooled Fast Reactor", *Nuclear Engineering and Design*, Vol. 267, pp. 44-60.

Redjem-Saad, L., M. Ould-Rouiss and G. Lauriat (2007), "Direct Numerical Simulation of Turbulent Heat Transfer in Pipe Flows: Effect of Prandtl Number", *International Journal of Heat and Fluid Flow*, Vol.28,5, pp. 847-861.

Reed, C. (1987), "Convective Heat Transfer in Liquid Metals", *Handbook of Single-Phase Convective Heat Transfer*, S. Kakaç, R.K. Shah and W. Aung (eds.), John Wiley & Sons, Inc., New York.

Rehme, K. (1987), "Convective Heat Transfer Over Rod Bundles", *Handbook of Single-Phase Convective Heat Transfer*, S. Kakaç, R.K. Shah and W. Aung (eds.), John Wiley & Sons, New York, p. 62.

Rensen, Q. (1982), "Experimental Investigation of Turbulent Heat Transfer to Liquid Sodium in the Thermal Entrance Region of an Annulus", *Nuclear Engineering and Design*, Vol.68, 3, pp. 397-404.

Reynolds, A. (1975), "The Prediction of Turbulent Prandtl and Schmidt Numbers", *International Journal of Heat and Mass Transfer*, Vol.18, 9, pp. 1055-1069.

Reynolds, W.C. (1976), "Computation of Turbulent Flows", *Annual Review of Fluid Mechanics*, Vol.8,1, pp. 183-208.

Rodi, W. (1980), *Turbulence Models and Their Application in Hydraulics: A State of the Art Review*, IAHR, Delft.

Rodi, W. (1981), "Progress in Turbulence Modeling for Incompressible Flows", *AIAA 19th Aerospace Sciences Meeting*, M. St. Louis (ed.), s.l.

Roelofs, F. et al. (2012), "Simulating Fuel Assemblies with Low Resolution CFD Approaches", *Nuclear Engineering and Design*, Vol. 250, pp. 548-559.

Roelofs, F. et al. (2013), "Review of Fuel Assembly and Pool Thermal Hydraulics for Fast Reactors", *Nuclear Engineering and Design*, Vol. 265, pp. 1205-1222.

Rohsenow, W.M. and L.S. Cohen (1960), *Turbulent Transfer of Heat*, MIT Heat Transfer Laboratory, Cambridge, MA.

Rohsenow, W.M. and H.Y. Choi (1961), *Heat, Mass, and Momentum Transfer*, Prentice-Hall, Englewood Cliffs, NJ.

Rolfo, S. et al. (2012), "Thermal-Hydraulic Study of a Wire Spacer Fuel Assembly", *Nuclear Engineering and Design*, Vol. 243, pp. 251-262.

Rothfus, R.R., J.E. Walker and G.A. Whan (1958), "Correlation of Local Velocities in Tubes, Annuli, and Parallel Plates", *AIChE Journal*, Vol.4, 2, pp. 240-245.

Rotta, J.C. (1972), *Turbulente Strömungen : eine Einführung in die Theorie und ihre Anwendung*, Teubner, Stuttgart.

Samec, K. et al. (2011), "Measurement and Analysis of Turbulent Liquid Metal Flow in a High-power Spallation Neutron Source – EURISOL", *Nuclear Instruments and Methods in Physics Research Section A: Accelerators, Spectrometers, Detectors and Associated Equipment*, Vol.638, 1, pp. 1-10.

Schlichting, H. and K. Gersten (2003), *Boundary Layer Theory 8*, revised and English translation edition, Springer, Berlin.

Schrock, S.L. (1964), *Eddy Diffusivity Ratios in Liquid Metals*, Purdue University, West Lafayette, IN.

Seban, R.A. (1950a), *Heat Transfer Measurements on Lead Bismuth Eutectic in Turbulent Pipe Flow*, Institute of Engineering Research, University of California, Berkeley, California.

Seban, R.A. (1950b), "Heat Transfer through a Fluid Flowing Turbulently between Parallel Walls with Asymmetric Wall Temperatures", *Transactions of the American Society of Mechanical Engineers*, Vol. 72, pp. 789-795.

Seban, R.A. and T.T. Shimazaki (1951), "Heat Transfer to a Fluid Flowing Turbulently in a Smooth Pipe with Walls at Constant Temperature", *Transactions of the American Society of Mechanical Engineers*, Vol. 73, pp. 803-809.

Sellars, J., M. Tribus and J. Klein (1956), "Heat Transfer to Laminar Flow in a Round Tube or Flat Conduit. The Graetz Problem Extended", *Transactions of the American Society of Mechanical Engineers*, Vol. 78, pp. 441-448.

Senechal, M. (1968), *Contribution to Convection Theory for Liquid Metals*, University Press, Paris.

Shah, R.K. (1975), "Thermal Entry Length Solutions for the Circular Tube and Parallel Plates", *Proceedings of the 3rd National Heat Mass Transfer Conference*, Mumbai.

Shah, R.K. and A.L. London (1978), *Laminar Flow Forced Convection in Ducts: A Source Book for Compact Heat Exchanger Analytical Data*, Academic Press, New York.

Shah, R.K. and M.S. Bhatti (1987), "Laminar Convective Heat Transfer in Ducts", *Handbook of Single-Phase Convective Heat Transfer*, S. Kakaç, R.K. Shah and W. Aung (eds.), John Wiley & Sons, Inc., New York.

Sheriff, N. and N. Davies (1979), "Liquid Metal Natural Convection from Plane Surfaces: A Review Including Recent Sodium Measurements", *International Journal of Heat and Fluid Flow*, Vol.1, 4, pp. 149-154.

Sheriff, N. and D. O'Kane (1981), "Sodium Eddy Diffusivity of Heat Measurements in a Circular Duct", *International Journal of Heat and Mass Transfer*, 24 (2), pp. 205-211.

Shikazono, N. and N. Kasagi (1996), "Second-moment Closure for Turbulent Scalar Transport at Various Prandtl Numbers", *International Journal of Heat and Mass Transfer*, Vol.39,14, pp. 2977-2987.

Sibamoto, Y., Y. Kukita and H. Nakamura (2002), "Visualization and Measurement of Subcooled Water Jet Injection into High-temperature Melt by Using High-frame-rate Neutron Radiography", *Nuclear Technology*, Vol.139, 3, pp. 205-220.

Sibamoto, Y., Y. Kukita and H. Nakamura (2005), "Simultaneous Measurement of Fluid Temperature and Phase during Water Jet Injection into High Temperature Melt", *Proceedings of the 11th International Topical Meeting on Nuclear Thermal-Hydraulics (NURETH-11)*, Avignon, France, 2-5 October.

Sibamoto, Y., Y. Kukita and H. Nakamura (2007), "Small-Scale Experiment on Subcooled Water Jet Injection into Molten Alloy by Using Fluid Temperature-phase Coupled Measurement and Visualization", *Journal of Nuclear Science and Technology*, Vol.44,8, pp. 1059-1069.

Siegel, R., E. Sparrow and T. Hallman (1958), "Steady Laminar Heat Transfer in a Circular Tube with Prescribed Wall Heat Flux", *Applied Scientific Research, Section A*, Vol.7,5, pp. 386-392.

Siman-Tov, M. et al. (1997), "Thermal-hydraulic Analysis of the Liquid Mercury Target for the National Spallation Neutron Source", *Proceedings of the International Topical Meeting on Advanced Reactor Safety*, Orlando, Florida.

Skupinski, E., J. Tortel and L. Vautrey (1965), "Détermination des coefficients de convection d'un alliage sodium-potassium dans un tube circulaire", *International Journal of Heat and Mass Transfer*, Vol.8,6, pp. 937-951.

Sleicher, C.A. (1958), "Experimental Velocity and Temperature Profiles for Air in a Turbulent Pipe Flow", *Transactions of the American Society of Mechanical Engineers*, Vol. 80, pp. 789-797.

Sleicher, C. and M. Tribus, Jr. (1957), "Heat Transfer in a Pipe with Turbulent Flow and Arbitrary Wall Temperature Distribution", *Transactions of the American Society of Mechanical Engineers*, Vol. 79, pp. 788-797.

Sleicher, C., A. Awad and R. Notter (1973), "Temperature and Eddy Diffusivity Profiles in NaK", *International Journal of Heat and Mass Transfer*, Vol.16, 8, pp. 1565-1575.

Smith, B.L. (2007), "Novel Heat Transfer Issues Associated with the Design and Safe Operation of the MEGAPIE Spallation Source Target", *Journal of Thermal Science*, Vol.16, 1, pp. 63-78.

Smith, B.L. et al. (2008), "Computational Fluid Dynamic Studies of the MEGAPIE Spallation Source Target and Safety Vessel", *Journal of Nuclear Science and Technology*, Vol.45,12, pp. 1334-1346.

Smith, B.L. (2009), "Adaptation of the Law of the Wall Boundary Treatment to Include Volumetric Heating Effects", *Applied Mathematical Modelling*, Vol.33, 3, pp. 1306-1322.

Snyder, W.T. (1963), "An Analysis of Slug Flow Heat Transfer in an Eccentric Annulus", *AIChE Journal*, Vol.9,4, pp. 503-506.

Sommer, T., R.M.C. So and Y. Lai (1992), "A Near-wall Two-equation Model for Turbulent Heat Fluxes", *International Journal of Heat and Mass Transfer*, Vol.35,12, pp. 3375-3387.

Spalart, P. and S. Allmaras (1994), "One-equation Turbulence Model for Aerodynamic Flows", *Recherche aerospatiale*, Issue 1, pp. 5-21.

Sparrow, E.M., R. Eichhorn and J.L. Gregg (1959), "Combined Forced and Free Convection in a Boundary Layer Flow", *Physics of Fluids*, Vol.2, 3, pp. 319-328.

Speziale, C.G. and R.M.C. So (1998), "Turbulence Modeling and Simulation", *The Handbook of Fluid Dynamics*, R.E. Johnson (ed.), CRC Press LLC, Boca Raton, FL, pp. 1-111.

Stieglitz, R. et al. (2007), "Turbulent Heat Mixing of a Heavy Liquid Metal Flow in the MEGAPIE Target Geometry – The Heated Jet Experiment", *Nuclear Engineering and Design*, Vol.237,15-17, pp. 1765-1785.

Stromquist, W. and R. Boarts (1953), *Effect of Wetting on Heat Transfer Characteristics of Liquid Metals*, United States Atomic Energy Commission, Technical Information Service, s.l.

Styrikovich, M. and I. Semenovker (1940), "Heat Exchange at Very Low Prandtl Numbers", *Žurnal techničeskoj fiziki - Journal of Technical Physics* (USSR), Vol.10, 16, pp. 1324-1330.

Subbotin, V., P. Ushakov and I. Sviridenko (1961), "Investigation of Heat Exchange in Connection with a Turbulent Flow of Mercury in an Annular Duct", *The Soviet Journal of Atomic Energy*, Vol.9,4, pp. 851-854.

Subbotin, V. et al. (1963a), "A Study of Heat Transfer to Molten Sodium in Tubes", *Soviet Atomic Energy*, Vol.13,4, pp. 991-994.

Subbotin, V.I., M. Ibragimov and E. Nomofilov (1963b), "Measurement of Temperature Profiles in Turbulent Pipe Flow of Mercury", *Teplotnergetika*, Vol. 10, p. 70.

Subbotin, V.I., F.A. Kozlov and N.N. Ivanovsky (1963c), "Heat Transfer to Sodium Under Conditions of Free- and Forced-convection and when Oxides are Deposited on the Transfer Surface", *High Temperature*, Vol. 1, pp. 368-372.

Subbotin, V.I. et al. (1971), "Experimental Study on Models of the Operating Temperature Regimes of the Fuel Elements of a BOR-60 Reactor", *Heat Transfer – Soviet Research*, Vol.3,5, pp. 15-26.

Subbotin, V.I. (1974), "Heat Exchange and Hydrodynamics in Channels of Complex Geometry", *Proceedings of the 5th International Heat Transfer Conference*, Tokyo.

Subbotin, V.I. et al. (1975), "Heat Transfer in Cores and Blankets of Fast Breeder Reactors – A Collection of Reports", *Symposium of CMEA Countries: Present and Future Work on Creating AES with Fast Reactors*, Obninsk.

Sugawara, T. et al. (2010), "Conceptual Design Study of Beam Window for Accelerator-Driven System", *Journal of Nuclear Science and Technology*, Vol.47, 10, pp. 953-962.

Su, G., H. Gu and X. Cheng (2012), "Experimental and Numerical Studies on Free-Surface Flow of Windowless Target", *Annals of Nuclear Energy*, Vol. 43, pp. 142-149.

Tarantino, M. et al. (2011), "Integral Circulation Experiment: Thermal-Hydraulic Simulator of a Heavy-Liquid Metal Reactor", *Journal of Nuclear Materials*, Vol.415,3, pp. 433-448.

Tenchine, D. and J. Moro (1997), *Experimental and Numerical Study of Coaxial Jets*, Atomic Energy Society of Japan, Kyoto, pp. 1381-1387.

Tenchine, D. (2010), "Some Thermal Hydraulic Challenges in Sodium Cooled Fast Reactors", *Nuclear Engineering and Design*, Vol. 240,5, pp. 1195-1217.

Tenchine, D. et al. (2012), "Natural Convection Test in Phenix Reactor and Associated CATHARE Calculation", *Nuclear Engineering and Design*, Vol. 253, pp. 23-31.

Tenchine, D. et al. (2013), "Experimental and Numerical Studies on Mixing Jets for Sodium Cooled Fast Reactors", *Nuclear Engineering and Design*, Vol. 263, pp. 263-272.

Tenchine, D., C. Fournier and Y. Dolias (2014), "Gas Entrainment Issues in Sodium Cooled Fast Reactors", *Nuclear Engineering and Design*, Vol. 270, pp. 302-311.

Thiele, R. and H. Anglart (2013), "Numerical Modeling of Forced-Convection Heat Transfer to Lead-bismuth Eutectic Flowing in Vertical Annuli", *Nuclear Engineering and Design*, Vol. 254, pp. 111-119.

Tien, C.L. (1961), "On Jenkins Model of Eddy Diffusivities for Momentum and Heat", *Journal of Heat Transfer*, Vol. 83, pp. 389-390.

Todreas, N.A. and M.S. Kazimi (2012), *Nuclear Systems*, 2nd edition, Taylor & Francis, Boca Raton, FL.

Tokuhiro, A. and N. Kimura (1999), "An Experimental Investigation on Thermal Striping: Mixing Phenomena of a Vertical Non-Buoyant Jet with Two Adjacent Buoyant Jets as Measured by Ultrasound Doppler Velocimetry", *Nuclear Engineering and Design*, Vol.188,1, pp. 49-73.

Trefethen, L.M. (1951), *Liquid Metal Heat Transfer in Circular Tubes and Annuli*, The Institution of Mechanical Engineers, London, pp. 436-438.

Tricoli, V. (1999), "Heat Transfer in Turbulent Pipe Flow Revisited: Similarity Law for Heat and Momentum Transport in Low-Prandtl-number Fluids", *International Journal of Heat and Mass Transfer*, Vol. 42, 8, pp. 1535-1540.

Tuček, K., J. Wallenius and W. Gudowski (2004), "Coolant Void Worth in Fast Breeder Reactors and Accelerator-Driven Transuranium and Minor-actinide Burners", *Annals of Nuclear Energy*, Vol.31, 15, pp. 1783-1801.

Tyldesley, J. and R. Silver (1968), "The Prediction of the Transport Properties of a Turbulent Fluid", *International Journal of Heat and Mass Transfer*, Vol.11, 9, pp. 1325-1340.

Tyldesley, J. (1969), "Transport Phenomena in Free Turbulent Flows", *International Journal of Heat and Mass Transfer*, Vol.12,4, pp. 489-496.

Ushakov, P.A. et al. (1963), "Heat Transfer and Hydraulic Resistance in Tightly Packed Corridor Bundle of Rods", *Soviet Atomic Energy*, Vol.13, 2, pp. 761-768.

Ushakov, P., A. Zhukov and N. Matyukhin (1977), "Heat Transfer to Liquid Metals in Regular Arrays of Fuel Elements", *High Temperature (USSR)*, Vol.15, 10, pp. 1027-1033.

van Driest, E.R. (1956), "On Turbulent Flow Near a Wall", *Journal of the Aeronautical Sciences*, Vol.23, 11, pp. 1007-1011.

VDI (ed.) (2013), *VDI-Wärmeatlas*, Springer Vieweg, Berlin, Heidelberg.

Velusamy, K. et al. (2010), "Overview of Pool Hydraulic Design of Indian Prototype Fast Breeder Reactor", *Sadhana*, Vol.35, 2, pp. 97-128.

von Kármán, T. (1930), "Mechanische Änlischkeit und Turbulenz", *Nachrichten von der Gesselschaft der Wissenschaften zu Göttingen*, Vol. 1, pp. 58-76.

Wang, M. et al. (2013), "Numerical Research on Local Heat Transfer Distribution of Liquid Sodium Turbulent Flow in an Annulus", *Progress in Nuclear Energy*, Vol. 65, pp. 70-80.

Wang, S. et al. (2008), "Evaluation of a Steam Generator Tube Rupture Accident in an Accelerator-driven System with Lead Cooling", *Progress in Nuclear Energy*, Vol. 50, 2-6, pp. 363-369.

Wantland, J. et al. (1976), "Effects of Duct Configuration on Flow and Temperature Structure in Sodium-cooled 19-rod Simulated LMFBR Fuel Bundles with Helical Wire-wrap Spacers", *National Heat Transfer Conference*, St. Louis, MO.

Wassel, A. and I. Catton (1973), "Calculation of Turbulent Boundary Layers over Flat Plates with Different Phenomenological Theories of Turbulence and Variable Turbulent Prandtl Number", *International Journal of Heat and Mass Transfer*, Vol.16, 8, pp. 1547-1563.

Weigand, B., J. Ferguson and M. Crawford (1997), "An Extended Kays and Crawford Turbulent Prandtl Number Model", *International Journal of Heat and Mass Transfer*, Vol.40, 17, pp. 4191-4196.

Weinberg, D. (1975), "Temperaturfelder in Bündeln mit Na-Kühlung", *Thermo- und fluiddynymische Unterkanalanalyse der Schnellbrüter-Brennelemente und ihre Relation zur Brennstabmechanik*, P. Voj (ed.), Gesselschaft für Kernforschung m.b.H., Karlsruhe, pp. 167-202.

White, F.M. (1991), *Viscous Fluid Flow*, 2nd edition, McGraw-Hill, New York.

Wilcox, D.C. and R.M. Traci (1976), "A Complete Model of Turbulence", *Proceedings of the American Institute of Aeronautics and Astronautics, Fluid and Plasma Dynamics Conference*, San Diego, CA, p. 30.

Wilcox, D.C. (2006), *Turbulence Modeling for CFD*, 3rd edition, DCW Industries, La Cañada, California.

Winterton, R. (1974), "Effect of Gas Bubbles on Liquid Metal Heat Transfer", *International Journal of Heat and Mass Transfer*, Vol.17, 5, pp. 549-554.

Wu, Y. et al. (2013), "Subchannel Thermal-hydraulic Analysis of the Fuel Assembly for Liquid Sodium Cooled Fast Reactor", *Progress in Nuclear Energy*, Vol. 68, pp. 65-78.

Yakhot, V. and S.A. Orszag (1986), "Renormalization Group Analysis of Turbulence. I. Basic Theory", *Journal of Scientific Computing*, Vol.1,1, pp. 3-51.

Yakhot, V., S.A. Orszag and A. Yakhot (1987), "Heat Transfer in Turbulent Fluids – I. Pipe Flow", *International Journal of Heat and Mass Transfer*, Vol.30, (1), pp. 15-22.

Yatabe, J. et al. (1970), "Fast Reactor Fuel Asembly Thermalhydraulic Development", Program: Sodium Heat Transfer, Pacific Northwest Laboratories, Richland, Washington.

Yovanovich, M. (1970), "An Analysis of Thermal Resistance at a Solid-Stationary Liquid Metal Interface Due to the Presence of Gas Cavities", *International Journal of Heat and Mass Transfer*, Vol.13,1, pp. 93-103.

Yu, B., H. Ozoe and S.W. Churchill (2001), "The Characteristics of Fully Developed Turbulent Convection in a Round Tube", *Chemical Engineering Science*, Vol.56,5, pp. 1781-1800.

Yu, B. et al. (2005), "The Computed Characteristics of Turbulent Flow and Convection in Concentric Circular Annuli. Part II. Uniform Heating on the Inner Surface", *International Journal of Heat and Mass Transfer*, Vol 48, 3-4, pp. 621-634.

Yu, W-S. and O. Dwyer (1966), "Heat Transfer to Liquid Metals Flowing Turbulently in Eccentric Annuli – I", *Nuclear Science and Engineering*, Vol.24, 2, pp. 105-117.

Yu, W-S. and O. Dwyer (1967), "Heat Transfer to Liquid Metals Flowing Turbulently in Eccentric Annuli – II", *Nuclear Science and Engineering*, Vol.27, 1, pp. 1-9.

Zagarola, M.V. and A.J. Smits (1997), "Scaling of the Mean Velocity Profile for Turbulent Pipe Flow", *Physical Review Letters*, Vol. 78, pp. 239-242.

Zagarola, M.V. (1996), *Mean-Flow Scaling of Turbulent Pipe Flow*, Princeton University, New Jersey.

Zanini, L. et al. (2011), "Experience from the Post-test Analysis of MEGAPIE", *Journal of Nuclear Materials*, Vol.415, 3, pp. 367-377.

Zeiniger, J. (2009), "Turbulenter Wärmetransport in flüssigem Blei-Wismut an einem vertikalen Heizstab im Ringspalt", Karlsruhe Institute of Technology, Karlsruhe.

Zhukov, A.V., V.I. Subbotin and P.A. Ushakov (1967), "Heat Transfer from Loosely-Spacer [Fuel] Rod Clusters to Liquid Metal Flowing in the Axial Direction", *Liquid Metals*, P.L. Kirillov, V.I. Subbotin and P.A. Ushakov (eds.), National Aeronautic and Space Administration, n.l., pp. 149-169 (translated from *Atomizdat*).

Zhukov, A. et al. (2002), "An Experimental Study of Heat Transfer in the Core of a BREST-OD-300 Reactor with Lead Cooling on Models", *Thermal Engineering*, Vol.49,3, pp. 175-184.

11. Instrumentation*

11.1 Background of the measurement technique development

Accelerator-driven systems (ADS) – and any fast neutron system using lead (Pb) or eutectic lead-bismuth (PbBi) alloys as primary coolants – require especially adapted measurement technologies. Besides their relatively high density, corrosivity and opacity, the sensors in contact with these liquid metals face elevated temperatures in the range of 200-550°C or higher. Although in the past decades much progress has been achieved in developing liquid-metal-adapted measurement devices in the context of sodium-operated fast breeder reactors, due to their specific properties only a portion of this knowledge can be transferred to lead or lead-alloy-cooled systems.

While using measurement devices, one has to distinguish clearly between operational and maintenance purposes and scientific ones. A list of topics for the different requirement profiles are given in Table 11.1.1.

Table 11.1.1: Requirement profiles of measurement technologies for operational and scientific purposes

Operation and maintenance	Scientific use
Reliable component and reactor operation	High spatial and temporal resolution
Safe system monitoring	Negligible impact on measured quantity/effect
Sufficiently fast response time to abnormal conditions (shutdown)	Applicability in the specific environment (temperature, pressure magnetic fields, etc.)
Long life time	Repeatability and accuracy
Simple replacement	Calibration effort can be higher
Calibration effort should be limited	

Measurement devices for fluid flows are in principle divided into two classes of system. One is the measurement of global quantities, which are mostly scalars like the flow rate, the pressure in the system or mean temperatures. The other class is represented by measurement devices for local quantities like the velocity and void distribution, the heat flux, the surface structure and shape. The detection of these particular effects in benchmark problems allows the development of new physical models or e.g. the validation of computational fluid dynamic (CFD) simulations. Naturally, the border between the two classes is not sharply defined. For example Pitot or Prandtl tubes can be enabled to detect the smallest velocities by miniaturisation of the utilised pressure measurement devices.

Of course, this handbook cannot cover the whole range of measurement devices currently available or under development. In this context we limit ourselves to the presentation of flow rate, local flow velocity and pressure measurement devices, discuss some temperature measurement technologies and typical mistakes often made therein.

* Chapter lead: T. Wetzel. For additional contributors please see Appendix 1.

These chapters are very specific to liquid metal applications. Methodologies to measure local velocity and void fraction distributions, surface structures and filling level detection techniques complement the first part, however, there we also describe techniques that have not yet been largely (or at all) applied to liquid metals, but seem to be promising approaches in our eyes. For the individual devices, the physical operation principles are explained, and often an example for the application in heavy liquid metals is described and appropriate literature sources are cited. As far as known to the authors, the advantages and disadvantages are mentioned and discussed.

Since the instrumentation technology for lead and its alloys is still in its infancy, some examples of the application of techniques in other heavy liquid metals are described, which offer a potential transferability to lead/lead alloys and their applications. Among the quite large amount of instrumentation literature textbooks, there are only a few related to liquid metal, e.g. Drowden (1972) or Foust (1978).

11.2 Flow meters

Many physical principles can be used to determine the flow rate of fluids in pipes (Goldstein, 1983), but the physical and chemical properties of lead-bismuth exclude some of these right from the start. The opacity, which all liquid metals have in common, disables all optical methods, not only for a quantitative but also for a qualitative characterisation of the flow. A summary of liquid metal measurement techniques applied in the casting industry is given in the overview article by Argyropoulos (2001). In the following sections, physical principles of methods used in recent years, application examples and contributions from several authors as well as from the authors' personal experience are described, with special emphasis on techniques that make use of the electric conductivity of liquid metals.

11.2.1 *Electromagnetic flow meters*

11.2.1.1 DC electromagnetic flow meters

Permanent magnet flow meters (PMF) are mostly used if the installation volume is rather small or where low flow rates have to be resolved. According to the Faraday law, an electrically conducting fluid flowing perpendicular to a magnetic field induces an electric field. The strength of this electric field is proportional to the flow velocity and can be measured with diametrically opposed electrodes on the pipe walls perpendicular to flow direction and magnetic field vector. A compilation of the theoretical concepts concerning electromagnetic flow measurements is given by Shercliff (1962). From the Maxwell equations the Poisson equation for an electromagnetic flow meter can be derived:

$$\nabla^2 \varphi = \nabla \cdot (u \times B) \tag{11.1}$$

with the electric potential ϕ and the vector quantities velocity u and magnetic field B. The partial differential Eq. (11.1) cannot be solved in general, but with simplified boundary conditions and with the aid of the Green function, a transformation can be made and a solution can be given for a finite region of a flow meter with point electrodes. For the voltage at the electrodes, derived from the electric potential difference $\Delta\phi$, one obtains:

$$\Delta\varphi = \int_{x,y,z} W\,(u \times B)\,dx\,dy\,dz \tag{11.2}$$

with a weighting vector W, which indicates the contribution of the flow in a single volumetric element to the effective measurable voltage. For an axially symmetric flow profile and an infinite, homogenous magnetic field, the simple dependency:

$$\Delta\phi = c \cdot u_m B d \tag{11.3}$$

follows, showing the proportionality between the measured electrode voltage $\Delta\phi$ and the mean flow velocity u_m depending on the mean magnetic field strength B and the pipe diameter d. The weighting vector introduced in Eq. (11.2) was evaluated by Shercliff (1962, 1987) for an infinitely long, homogeneous magnetic flow meter field (2-D problem), see Figure 11.2.1 below. A theoretical consideration of the influence of inhomogeneous conductivity profiles and pulsating flow velocities has been presented by Rutkevich (1981). Applicability of the single-velocity approximation in the averaged Ohm's law is examined there. On the basis of the solution of an electrodynamic boundary value problem, an expression is obtained for the flow meter sensitivity for arbitrary axisymmetric velocity profile and different conductivities of the core of the flow, the wall layer and the wall. If the amplitude of oscillations in the flow rate is comparable with the constant component, the instantaneous sensitivity of the flow meter changes rapidly with the time and the characteristic of the instrument becomes essentially non-linear.

Potential error sources of the PMF sensor and the correct installation

With the weighting distribution shown in Figure 11.2.1, the influence of an asymmetric flow profile on the measurement accuracy of an electromagnetic flow meter can be estimated. Due to higher gradients in the weighting field, the use of point electrodes should introduce higher uncertainties in magnetic flow meter systems than line electrodes. In reality this can be observed, but the deviations are always small compared to the signal amplitude, normally lower than 1% (Bonfig, 2002). A different situation occurs when impurities accumulate in the vicinity of the electrodes. In this case a massive change of the signal voltage arises and destroys the linearity of the flow meter system. Hence, Eq. (11.3) no longer holds and the flow meter becomes useless. Vel't and Mikhailova (2007) propose improvements concerning these boundary condition problems, i.e. minimising the influence of wall and liquid conductivity and particularly contact resistances by means of an extraneous current fed to the measurement electrodes.

Figure 11.2.1: Evaluation of the weighting vector function based on Shercliff (1962) for point and line electrodes

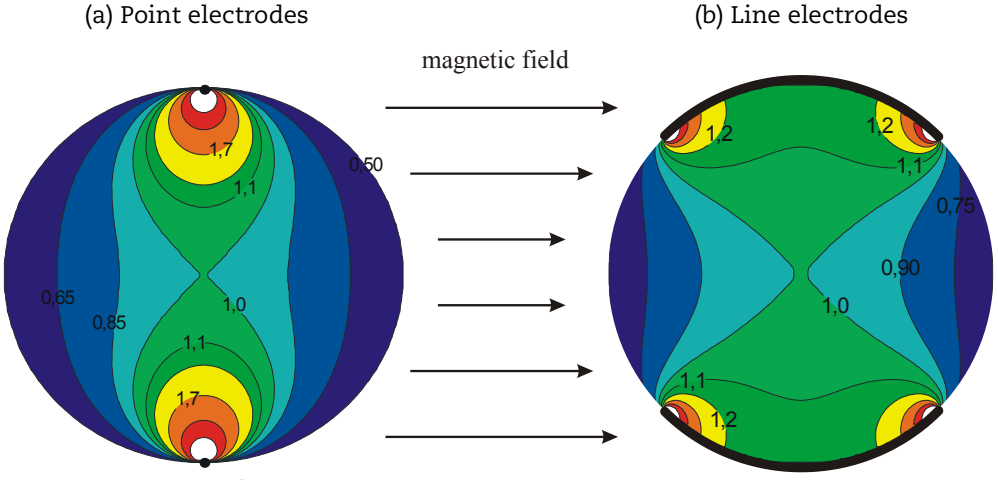

Furthermore, the pipe walls at the electrodes and the fluid form a galvanic element, which produces an additional voltage depending on temperature, flow, pressure, the chemical properties of the fluid and the surface conditions of the (e.g. steel) walls. Consequently this voltage is different at both electrodes and contributes as a perturbation to the signal, which cannot solely be determined theoretically, but has to be compensated for by means of a calibration.

Another problem is varying boundary conditions during operation, which make it necessary to perform this calibration at regular intervals. Especially the unreliable wetting behaviour of liquid lead-bismuth with regard to the electrically conducting structure material can lead to misreadings even during one measurement day. The fluid may be wetting the wall in the adhesive sense, so that the pressure drop in the piping shows a wetting of the surface. However, there may still exist an electric contact resistance between the wall and the fluid. Due to this contact resistance part of the current induced in the fluid by the permanent magnetic field B short-circuits in the fluid and the other one in the duct walls. This effect is important since the specific electric conductivity of liquid metals σ_{LM} like lead or the eutectic alloy $Pb^{45}Bi^{55}$ is of the same order as that of the most structure materials like steel σ_{wall}. For use in sodium or sodium potassium, most of the current is confined to the liquid, because there $\sigma_{LM}/\sigma_{wall} \gg 1$, so this problem is less pronounced there.

A further issue as pertains to the use of PMF and its set-up in piping systems should be mentioned. Since large permanent magnets penetrating the whole ducts cross-section in which the flow rate is measured are expensive, smaller magnets are sometimes used. However, this can lead to misreadings, particularly at low flow rates. If the flow is laminar in the duct and the magnetic field is penetrating only a part of the cross-section, the non-homogeneous magnetic field modifies the laminar flow profile in the duct. This leads to induction of small electric potentials transverse to the mean magnetic field und thus to an underestimation of the flow rate. This non-linearity at low flow velocities has to be considered by means of a Reynolds number analysis and can be taken into account by inserting Venturi nozzles upstream of the PMF.

If the applied magnetic field is disturbed by another steady magnetic field, the magnetic field lines are bent (Figure 11.2.2[b]). As a result, the flow rate measured is no longer correct. However, if a magnetic shield in the form of a ferromagnetic plate (with a high magnetic permeability $\mu r \ll 1$) is placed between the flow meter and the scattering field, the field lines of the scattering field are guided in the plate and hence the measurement field remains unchanged (Figure 11.2.2[c]). The thickness of the plate can be calculated using the magnetic potential equation. In general, a few millimetres are enough to compensate for a field of nearly one Tesla. The shown method of magnetic shielding works only for DC magnetic fields. In the case of AC fields the flow meter has to be fully capsuled with ferromagnetic materials.

Figure 11.2.2: Electromagnetic flow meter

(a) Measurement principle of a DC electromagnetic flow meter

(b) Influence of a scattering magnetic field on the magnetic field of a permanent electromagnetic flow meter

(c) Protection of the electromagnetic flow meter from a DC magnetic scattering field using a ferromagnetic shielding

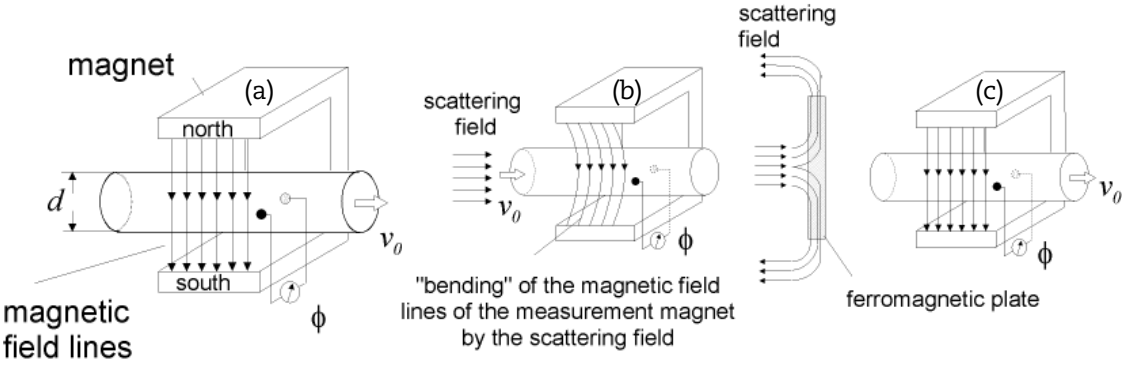

In Figure 11.2.3 a typical calibration curve of the electromagnetic flow meter in the technology loop THESYS of the KALLA laboratory is given (Knebel, 2001). There is a perfect linear relationship between induced potential and power supply to the pump. Due to the temperature dependence of the magnetic field, such a calibration has to be done for each operating temperature of the magnet.

Figure 11.2.3: Calibration curve of the DC electromagnetic flow meter (measured DC voltage as a function of the pump supply current) in the technology loop THESYS

Here the induced potential PMF is shown as a function of the pump power

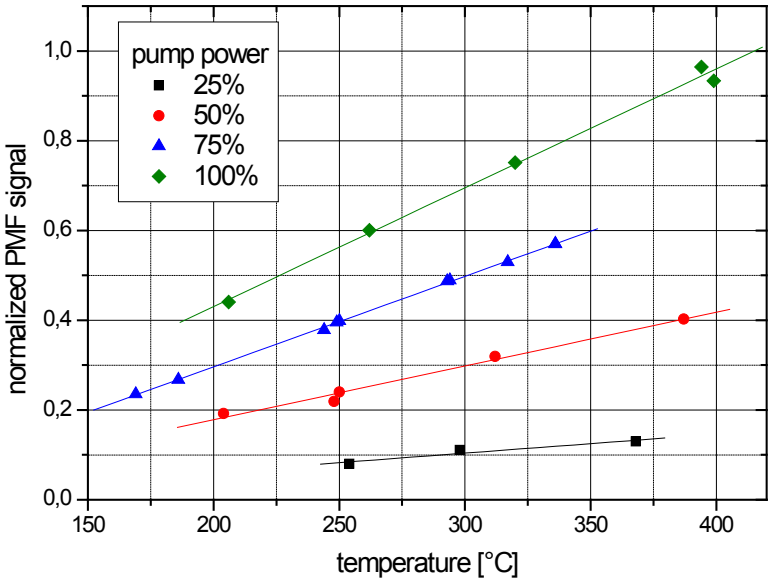

Operational characteristics

Figure 11.2.3 shows the normalised PMF signal plotted against temperature. Here, a clear linear dependency is observed for the four selected pump power stages. The slope of the four lines obviously varies linearly with the flow rate. Since a linear dependency between flow rate and PMF signal is expected, one can construct a linear equation with temperature-dependent slope:

$$V\left(U_{PMF}\right) = \frac{U_{PMF} - b}{m_T \cdot T + c} \tag{11.4}$$

In Eq. (11.4) V is the flow rate, U_{PMF} the PMF signal, T the temperature, m_T the temperature-dependent slope (sensitivity) of the PMF and b and c temperature-dependent offsets, which will be determined from the calibration against the heat balance. From the change of the slope of the lines in Figure 11.2.3, m_T can be calculated and Eq. (11.4) gives the flow rate for a measured PMF signal.

On the left side of Figure 11.2.4 the results of the temperature correction are plotted in terms of the calculated flow rate against the pump power. From an error propagation analysis the uncertainty is calculated to 2% at a linear regression coefficient of 99.84%. The disadvantage of this method is the necessity of measurements at every point in the whole parameter range of the flow rate and temperature to perform the described calibration. This is a great effort and an isothermal operation is recommended, because this would require only two calibration measurements.

Another argument against a protracted calibration process is the instable long-term behaviour of the investigated PMF systems in lead-bismuth. In the section of the PMF signal time series on the right in Figure 11.2.4 an example of the observed discontinuities is shown. The jumps in the signal, which was taken at constant flow rate, can easily reach 20 times the actual value. These annoyances are produced by galvanic reaction at the interface between the pipe wall and liquid metal close to the electrodes and are worsened by accumulating impurities at these positions. Additionally, the corrosion of the pipe material (liquid metal corrosion and/or oxidation) changes the liquid-solid interface properties and causes a drift of the PMF signal. A favourable positioning and the use of line electrodes can work against these problems, but a recalibration at regular intervals is still necessary. The aspect of calibration effort is tackled by Gramolin (1983), addressing particularly the above-mentioned effects of inhomogeneous field distribution and corrosion layers at the tube walls, and providing a potential solution by means of calculated calibration.

Figure 11.2.4: Flow rate calculated from temperature-corrected PMF data according to Eq. (11.4) (left); outliers of the PMF signal in a section of the time series (right)

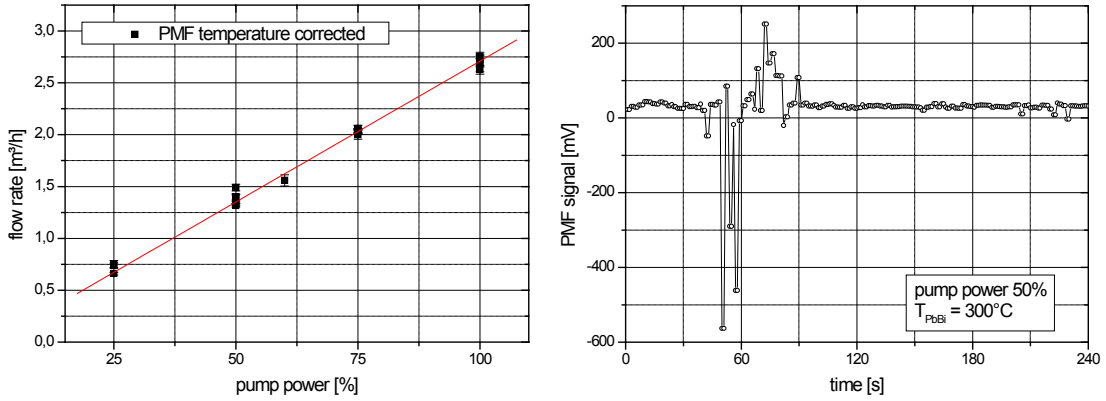

11.2.1.2 *Lorentz force velocimetry*

Lorentz force velocimetry (LFV) utilises the well-known breaking effect of a conducting medium when moving through a static magnetic field. In this case, the magnetic field, typically created using a strong permanent magnet, penetrates the flowing liquid metal. The interaction of the eddy currents induced within the fluid and their accompanying magnetic field with the original field of the permanent magnet creates a force acting on the magnet, which has exactly the same magnitude as the breaking force itself (reciprocity principle), i.e. it depends linearly on the flow velocity. The determination of the flow velocity can thus be achieved by measuring the force acting on the magnet. Figure 11.2.5 illustrates the principle for a longitudinal and transverse flux flow meter (taken from Thess [2007]). This paper also contains a comprehensive description and application of the theory to the specific cases shown in Figure 11.2.5, derivation of the governing equations, including a verification of the reciprocity principle as well as an analysis about the influence of the measurement on the measured flow itself by solving the full magneto-hydrodynamic problem. The latter is necessary, as though LFV is a contactless measurement technique, it still interacts with the flow. The authors state that this back-reaction causes only small errors in the considered laminar and turbulent pipe flows. For the case neglecting the back-reaction, referred to as the kinematic case, i.e. with prescribed velocity field and not modified by the magnetic field, they formulate the general theory which holds for arbitrary distributions of magnetic material or electric currents and for any velocity distribution, and which therefore provides a rational framework for the prediction of the sensitivity of Lorentz force flow meters in practice.

Figure 11.2.5: Principle of Lorentz force velocimetry for duct flows based on coils or permanent magnets

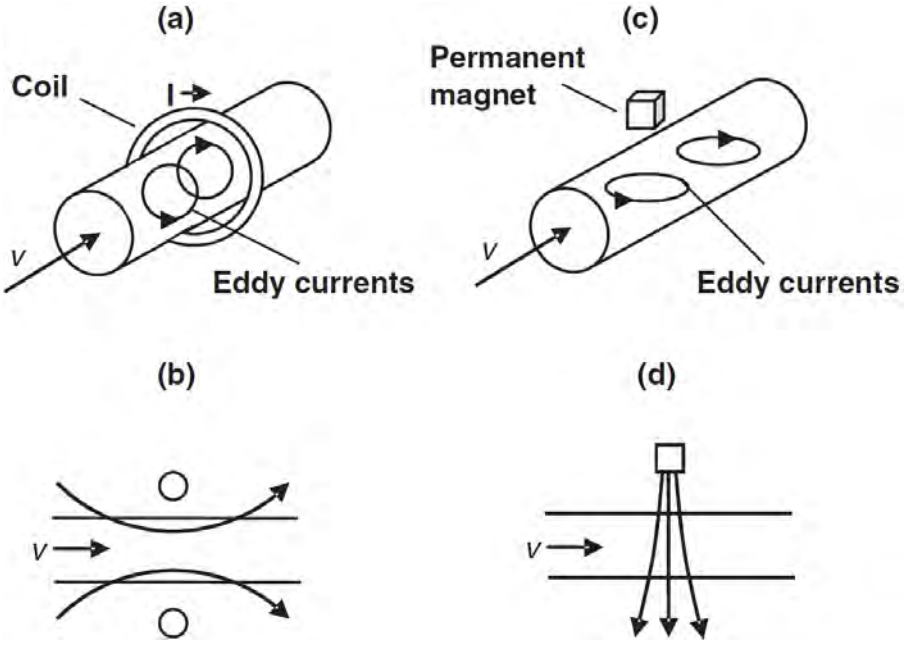

Source: Thess (2007).

In a more recent paper, Kolesnikov (2011) describes the application of the principle in laboratory and industrial measurements of liquid metal flow. While the laboratory experiments were conducted at a closed channel and with InGaSn flow, the industrial measurements were made at an open channel with liquid aluminium. In both cases, the measurement device is based on calibration rather than calculation and decent accuracy of the industrial open channel measurements is achieved, as the relative error is estimated with 2.34%. For the closed channel laboratory experiments the linear dependence between Lorentz force and velocity was proven, as predicted by the kinematic theory. It is concluded that applying the principle to fluids with lower electric conductivity like lead requires stronger magnetic fields and parallel magnet poles. Viré (2010) proposes and describes the use of a two-coil Lorentz force velocimeter arrangement and correlation between the signals to make the measurement independent from the electric conductivity of the fluid. The principle behind this approach is the "time-of-flight" methodology, exploited e.g. in hot wire anemometry for two-point velocity correlations. Through simulations, it is also proven that the back-reaction of the magnetic field on the flow and thus the error of the measurement is small.

In a more recent publication, Jian (2012) presents experimental results on time-of-flight LFV for a duct flow, accompanied by simulation results. Also presented is the idea of extending the method to the measurement of surface velocities in free surface flows, which could be extremely valuable in liquid metal free surface flows. However, the first results indicate a strong influence of the probe magnets on the surface flow, with unknown effect on the applicability of the method. Further investigations are planned.

11.2.1.3 AC electromagnetic flow meters

11.2.1.3.1 Electromagnetic frequency flow meters (EMFM)

The induction effect of dynamic electromagnetic fields is utilised in electromagnetic frequency flow meters (EMFM). The general measurement principle of such an induction

flow meter is that the motion of an electrically conducting fluid in an imposed field B produces an induced field B' which is proportional to the flow rate in the first order. The attraction of the EMFM is that its indication is directly electrical and no transducer is required, which allows a large temporal resolution. Moreover, no direct contact of the sensor with the operation fluid is necessary for the acquisition, such that material compatibility issues play a minor role. For a more detailed description of the measurement principle refer to e.g. Buchenau (2011) or Schulenberg (2010).

The earliest proposal for an EMFM has been made by Lehde (1948), the scheme of which is illustrated in Figure 11.2.6. The two coils A and C are energised in series opposition so as to produce an AC magnetic field of the form illustrated in Figure 11.2.6 at the bottom. In the absence of a fluid motion the field is symmetrical and induces no signal in the sensing coil B according to the induction equation. As soon as flow occurs, the magnetic field lines are dragged downstream by $(u\nabla B)$ and a signal appears in coil B, which is proportional to the flow rate to the first order. But great care is necessary that there be no output signal in case of zero flow and in practice it is hardly feasible to produce a geometrically exact symmetric arrangement. A precise fabrication is thus required; otherwise the genuine signal, which is quite often small, will be lost among stray signals.

Figure 11.2.6: Operation principle of an electromagnetic frequency flow meter (EMFM)

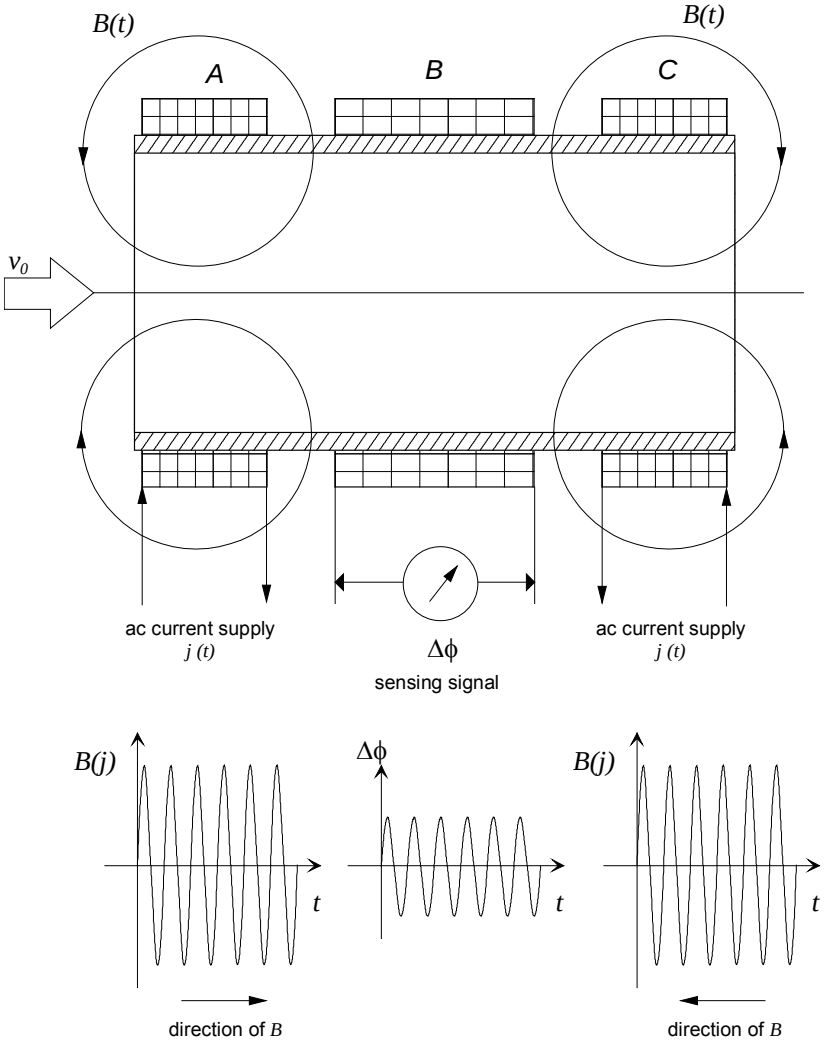

Source: Adapted from Lehde (1948).

The flow direction can be detected by the sign of the RMS value of the sensing coil. The magnitude of the RMS value in the sensing coil is proportional to the magnetic Reynolds number of the fluid flow Re_m, where Re_m is calculated according to Eq. (11.5):

$$Re_m = \mu_0 \sigma(T) u_m d \tag{11.5}$$

where μ_0 is the magnetic permeability of vacuum, given as $4\pi\ 10^{-7}$ As/(V·m), σ the specific electric conductivity of the fluid as a function of the temperature T, u_m the mean flow velocity within the duct and d its diameter. The magnetic Reynolds number weights the induced magnetic field to the applied magnetic field. If the temperature remains constant the measured RMS value of $\Delta\phi$ is proportional to the mean fluid velocity u_m.

Potential error sources of the EMFM sensor and the correct installation

However, this linear increase of the signal with the velocity and hence this operation principle is only valid if the magnetic Reynolds number Re_m is significantly smaller than unity. Only then can the induced potential ($u_m x B$) and the associated Lorentz force ($j x B$) be approximated by the ($u_m x B_{imposed}$) and ($j x B_{imposed}$). But, if Re_m is of O(1) the non-linear contributions ($u_m x B_{induced}$) and ($j x B_{induced}$) become important. Other non-linear behaviour will occur if the imposed magnetic field $B(t)$ is strong enough to perturb the flow pattern. This effect is expressed by the Hartmann number Ha or (M), which weights the electromagnetic forces versus the viscous ones, and the Stewart number St, (often called interaction parameter). The latter can be interpreted as the ratio of the electromagnetic forces versus the inertial forces within the fluid. Both quantities are calculated according to Eq. (11.6). They have to be smaller than unity (Shercliff, 1987) throughout the operation range of the electromagnetic induction flow meter:

$$Ha = dB_{\max}\sqrt{\frac{\sigma(T)}{\rho(T)\cdot\nu(T)}} \text{ and } St = \frac{d\,\sigma(T)B_{\max}^2}{\rho(T)u_m} \tag{11.6}$$

In Eq. (11.6) ρ is the fluid density, B_{max} the peak magnetic induction and ν the kinematic viscosity of the fluid.

Also for the sensing coil counteracting demands exits. On the one hand a lot of wire turns are required in order to detect the smallest flow rate changes without using sophisticated AC amplifiers. On the other hand, the more wire turns the coil has the more enforced the problem of pick-up effects. Pick-up effects refers to the occurrence of stray AC signals superimposed on the flow-dependent signal. The main source of pick-up is stray alternating fields from equipment placed nearby, such as electromagnetic pumps and AC powered equipment like ventilators, personal computers, etc. They can never be entirely suppressed and a large effort has to be directed into separating the wanted from the stray signals. As a rule, separation of the signals is achieved by exploiting the fact that the flow-dependent signal and the pick-up are in quadrature, the first being proportional to the magnetic field strength, and the second to its time derivative (Davidson, 2001). This calibration necessitates elaborate electronic equipment.

Another complication is caused by phase shifts due to eddy currents in nearby solid and fluid conductors, because of the generation of harmonics through the non-linearity of the material or because of capacitive pick-up. Another source of trouble can be resonance or beats when the flow contains slight periodic fluctuations due, for instance, to the use of electromagnetic or mechanical pumps running at or near synchronous speed. A technically feasible solution to minimise pick-up effects is a complete enclosure of the EMFM device by means of a ferromagnetic foil, thick enough not to run into saturation of external DC and AC magnetic fields. This foil has to be grounded through the liquid flow far away from any eddy currents.

Finally, some limitations concerning the AC current feed $j(t)$ must be considered, which are also of contradictory nature. A minimisation of pick-up effects is achieved if a low frequency of $j(t)$ is used but if it is necessary to study the instantaneous of transient or pulsating flows the frequency must be at least three times higher than the highest frequency of interest occurring in the flow. Also, in order to avoid the generation of sub- and super-harmonics in the sensing signal frequencies have to be omitted which are a factor of the environmental power supply. Of course, a definite upper limit of the acceptable frequency exists. If the fluid is a good conductor the frequency must not be so high as to cause a skin effect, while if the fluid is a poor conductor the frequency ω, which is $\omega = 2\pi f$, must not be so high that dielectric relaxation is not virtually instantaneous. The condition for there to be no skin effect is:

$$\omega d^2 \mu \sigma(T) \ll 1 \tag{11.7}$$

and for immediate dielectric relaxation, which means a negligible displacement current, is given by:

$$\frac{\omega \varepsilon \varepsilon_0}{\sigma(T)} \ll 1 \tag{11.8}$$

with fluid permittivity ε and the electric field constant $\varepsilon_0 = 8.85419\ 10^{-12}$ $As/(V{\cdot}m)$. In case of liquid metals the permittivity ε is closely over unity, i.e. 1.01 (Siemens, 1969). A photograph of an EMFM flow meter taken during the fabrication (a) and its installation in the THESYS loop of KALLA (b) is shown in Figure 11.2.7. For the calculation of the magnetic peak induction Eq. (11.9) is used:

$$B_{\max} = \frac{I_{\max} \cdot R}{n(Lf)\pi d_{m,Coils,A}} \tag{11.9}$$

where, R is the ohmic resistance of the coils, L the coil width, n the number of current turns and $d_{m,Coils,A}$ the mean diameter of the feeding coils. As long as the Stewart number and the magnetic Reynolds number are significantly lower than unity a linear behaviour of the flow meter with respect to the temperature can be expected. The linear dependence of the signal induced in a typical EMFM flow meter for heavy liquid metals as a function of the pumping power for a constant temperature of 300°C and different feeding currents and frequencies is shown in Figure 11.2.8.

An exact theoretical analysis of the EMFM is usually difficult and an empirical calibration for each device is inevitable.

Figure 11.2.7: (a) EMFM fabrication at the KALLA laboratory; (b) Installation of the EMFM in the technology loop THESYS of KALLA

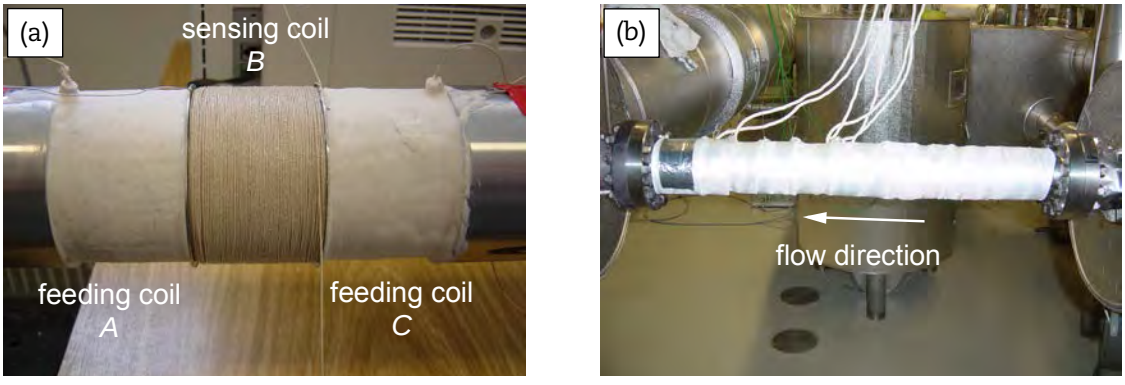

Figure 11.2.8: Measured EMFM signal as a function of the pumping power for different feeding currents and feeding frequencies of the pump at a constant temperature of T = 300°C in the THESYS loop of KALLA

Characteristics (left) and calculated flow rate (right)

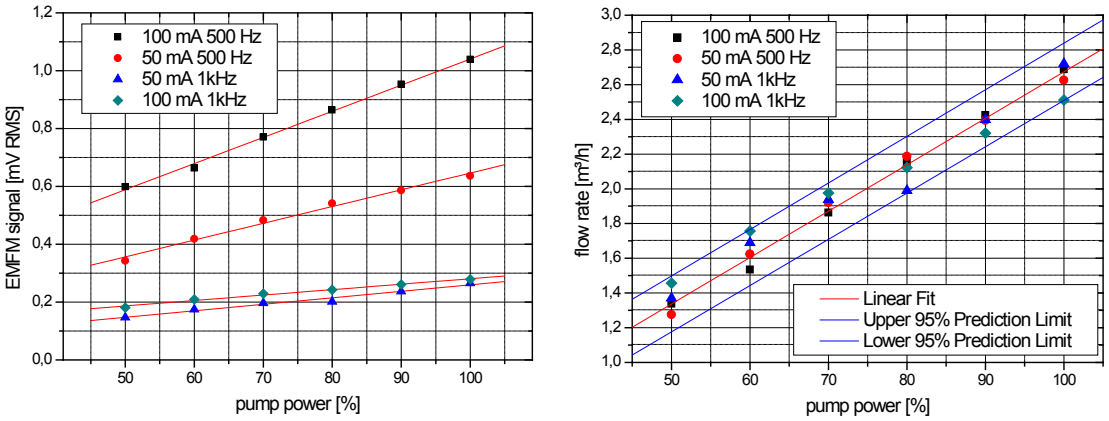

Operational characteristics

For a frequency of 500 Hz an increase of the EMFM signal with higher feeding current is obvious, but there is hardly an effect at a frequency of 1 kHz. This is a clear indicator for the occurrence of the skin effect. The magnetic field can penetrate just a thin boundary layer where the fluid moves so slowly that a change of the induced field strength causes only a marginal change of the output signal. Consequently the performance of the EMFM flow meter increases with lower frequency and the best is found for 100 mA feeding current at 500 Hz. Higher feeding currents are not feasible because the strong magnetic field would cause MHD effects which change the flow pattern in the duct.

To verify the linearity of the characteristics, the flow rate was calculated using the result of a heat balance at 100% pump power. The results are plotted against the pump power shown in the right diagram in Figure 11.2.8. All values are found to lie inside the 95% prediction limit of their linear regression regardless of the parameter used for the feeding current. If a reliable calibration can be made, the EMFM is a very stable and robust flow rate measurement device for lead-bismuth loops.

11.2.1.3.2 Phase-shift sensor

An alternative realisation of a contactless AC flow rate sensor is based on an electromagnetic transformer principle operating without any locomotive parts (Priede, 2009, 2011; Buchenau 2011). The detector head of the phase shift sensor (cf. Figure 11.2.9[a] and [b]) consists of two receiving coils and an emitter coil, placed on opposite sides of the duct containing the liquid metal flow.

The emitter coil (L_S) is fed by a temperature-stabilised alternating current (I_0) of constant angular frequency (Ω). In order to concentrate the magnetic field the coils are interspersed with laminated mild iron providing a low magnetic resistance of the sensor arrangement. An alternating magnetic flux is provided by the emitter coil aligned perpendicularly with respect to the direction of the electrically conducting flow. Considering a symmetrical arrangement between the emitter coil (L_S) and the receiving coils (L_{E1} and L_{E2}) the equal distribution of the alternating magnetic flux is disturbed by the flow.

**Figure 11.2.9: (a) Set-up of the phase-shift sensor;
(b) Sketch of the phase-shift sensor in an asymmetric adjustment**

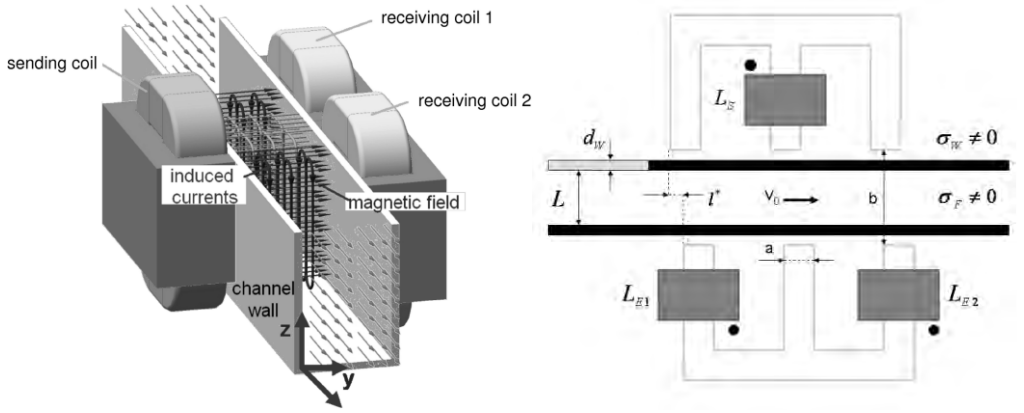

The information about the averaged velocity or flow rate is provided by a voltage difference or phase shift ($\Delta\phi_p$) between the receiver coils:

$$\Delta\phi_p = \arctan\left(\frac{\Omega_0 \pi^{-1} Rm K}{1 + \Omega_0^2\left(1 + \pi^{-1} Rm K\right)}\right) \tag{11.10}$$

The flow-induced phase-shift ($\Delta\phi_p$) is proportional to the non-dimensional magnetic Reynolds number ($Rm = \mu_0 \sigma v_0 D$) describing the magnitude of the measurement effect in the first order. Further contributing parameters are: the absolute permeability (μ_0), the electrical conductivity (σ) and averaged velocity (v_0) of the flow and the diameter of the pipe or width of the channel (D) in the direction of the magnetic field. The dimensionless exciting frequency ($\Omega_0 = \Omega L_E / R_E$) of the flow rate sensor contributes to the magnitude of a measurable phase shift which is composed of the angular frequency of the electrical current ($\Omega = 2\pi f$) and the ratio of the inductance of the receiver coils (L_E) to the resistance (R_E) of the same. The flow rate sensor has to be calibrated implied as indicated by the factor K in Eq. (11.10). Emitter and receiver coils can be placed either directly against each other or shifted by some offset (l^*). From this point on we refer to these arrangements as symmetric and asymmetric, respectively. The calibration factor ($K = K_b K_{l^*}$) can be considered as a product of the contributions related to variations of the channel width ($K_b = 1 + \Delta b/b$) and the sensitivity factor related to the choice of an asymmetric adjustment ($K_{l^*} = 1 + 2l^*/a$), in which (l^*) denotes the displacement length and (a) the width of the laminated mild iron poles (cf. Figure 11.2.9[b]). The principle of the phase shift sensor turned out to be very resistant against electromagnetic distortions. During experimental investigations lock-in amplifiers were used in order to measure the phase shifts. These narrow band pass filters offer an angle resolution of (0.001-0.01)° combined with a high drift stability.

The expansion of Eq. (11.10) comprises two important effects induced by the presence of electrically conducting channel or pipe walls, described by the conductance (σ_W) and the thickness of the wall (d_W). Assuming a perfect wetting between the walls and the melt, the effective magnetic Reynolds number ($Rm' = RmK_\sigma$) is significantly increased due to a higher effective electrical conductivity in the measurement volume:

$$\sigma' = \sigma + \sigma_W\left(\frac{d_W}{R_i}\right) \tag{11.11}$$

in which ($R_i = D/2$) denotes the length scale in the magnetic field direction. The introduced sensitivity factor ($K_\sigma = 1 + c_\sigma$) considers the enhanced electrical conductivity in presence of electrically conducting walls. Thereby, the factor:

$$\left(c_\sigma = \left(\frac{\sigma_W}{\sigma} \right) \left(\frac{d_W}{R_i} \right) \right)$$

denotes the so-called wall-conductance ratio. The skin effect is considered by the subsequent relation:

$$\Omega_0' = \Omega_0 K_\sigma^{-1} \tag{11.12}$$

Incorporating both effects into Eq. (11.10) the flow-induced phase shift between the receiver coils is described by:

$$\Delta\phi_P = \arctan\left(\frac{\Omega_0' \pi^{-1} Rm K}{1 + \Omega_0'^2 \left(1 + \pi^{-1} Rm K \right)} \right) \tag{11.13}$$

The sensitivity factor (K) has to be supplemented by the factor of (K_σ) to: ($K = K_b K_l \cdot K_\sigma$). An increase of ($K$) caused by electrically conducting walls implies the possibility to shift the frequency optimum to lower frequencies at higher magnitudes of the phase. For the limitation $Rm \leq 1$, the principle provides a linear dependence between the flow and the measurable phase shift.

Referring to Figure 11.2.10(a) the evaluable frequency range of the flow-induced phase shift exhibits an optimum determined by the electrical characteristics of the receiver coils (L_{E1} and L_{E2}) and (R_{E1} and R_{E2}) as well as the skin effect. The evaluable frequency range was measured for different sensitivity factors (K_b) (cf. Figure 11.2.10[a]) at a constant flow rate in dependence of the width of the measurement gap (b) (Buchenau, 2011). In this particular case an optimum frequency of about $\hat{f} = 68\,\text{Hz}$ becomes obvious. The optimum frequency can be computed by the first derivative of Eq. (11.10) or (11.13). As predicted by the theory the optimum shifts slightly to lower frequencies due to the increase of the sensitivity factors (K). The measurements of the flow-induced phase shift in dependence of the emitter frequency of $\hat{f} = 68\,\text{Hz}$ result in a linear dependence as shown in Figure 11.2.10(b).

Figure 11.2.10: (a) Frequency response of the phase shift flow meter measured in a sodium loop; (b) Linear dependence of the phase shift from the averaged velocity of the liquid sodium

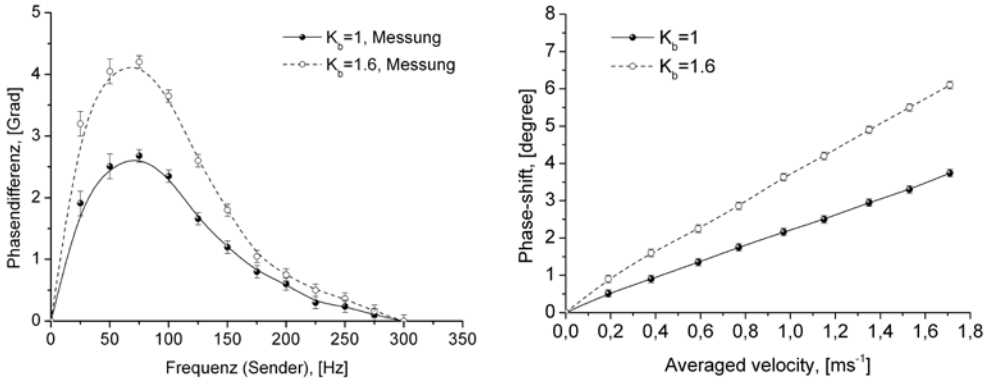

Source: Buchenau (2011).

According to an evaluation of the experiments depicted by Figure 11.2.10(a), 11.2.10(b) and corresponding computations using Eq. (11.13) the velocity resolution of the phase shift sensor can be determined to $v_{Min.} = 1\ cms^{-1}$ based on a minimal angle resolution of the lock-in amplifiers of $\Delta\phi_{Min.} = 0.01°$. Based on the analysis of 100 phase shift measurements at $\hat{f} = 68\ Hz$ the temporal resolution of the principle was determined to $t_{Min.} = 1.4\ s$.

11.2.1.3.3 Magnetic flywheel

The so-called magnetic flywheel operates on the basis of the mechanical force ($F_L \propto \sigma v_0 B^2$) which is exerted by a moving liquid metal on a permanent magnet placed outside the flow. It is an arrangement of a couple of permanent magnets which are equidistantly spaced on the circumference of a soft iron plate (Bucenieks, 2002; 2014). The peripheral speed of the iron plate (v_ϕ) follows the flow rate (Q) in a pipe or duct of a determined cross-section (A) as a linear function:

$$v_\phi = f(N) Q A^{-1} \tag{11.14}$$

The function $f(N)$ expresses the dependence of the peripheral speed (v_ϕ) on the number of magnetic pole pairs (N) of the flywheel according to:

$$f(N) = \frac{N\left(N^2 - 4\right)}{\left(N + 1\right)\left(N^2 - 1\right)} \tag{11.15}$$

The influence of an electrically conducting channel or pipe wall results in a decrease of the peripheral speed of the flywheel. In such a case, the calculation of the flow rate (Q) from the measured peripheral speed (v_ϕ) has to take into account a sensitivity factor (K_σ):

$$v_\phi = f(N) Q A^{-1} K_\sigma^{-1} \tag{11.16}$$

The sensitivity factor (K_σ) can be separated into two parts:

$$K_\sigma = 1 + c_\sigma G \tag{11.17}$$

in which (c_ϕ) denotes the so-called wall-conductance parameter and (G) stands for a function, describing the influence of the distance between the permanent magnets and the flow channel (Buchenau, 2014).

Figure 11.2.11 shows an embodiment of a magnetic flywheel using *SmCo*-magnets which provide an induction of $B_S = 0.33T$ at their surface (Buchenau, 2014). The magnets are placed equidistantly spaced on the circumference of a soft iron plate with a diameter of 124 mm diameter. The soft iron plate is rotatable due to a bearing with a low mechanical friction.

Figure 11.2.11: (a) Embodiment of the magnetic flywheel with four magnetic pole pairs (N); (b) Principle of the magnetic flywheel flow meter

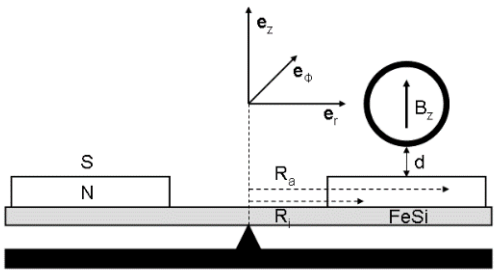

The functionality of the sensor was tested at a pipe flow (inner diameter D = 27 mm) of GaInSn (Buchenau, 2014). Typical dependencies between the rotary frequency of the magnetic flywheel and the flow rate of the liquid metal are depicted in Figures 11.2.12(a) and 11.2.12(b) for electrically conducting and non-conducting walls, respectively. An increase of the distance between the permanent magnets and the pipe wall results in a reduction of the rotary frequency of the magnetic flywheel for both cases. Experiments in the electrically conducting pipe reveal a distinct decrease of the rotary frequency in comparison to the situation of the non-conducting walls.

Figure 11.2.12: (a) Linear dependence of the rotary frequency from the averaged GaInSn velocity in an insulating pipe; (b) Linear dependence of the rotary frequency from the averaged GaInSn velocity in a brass pipe

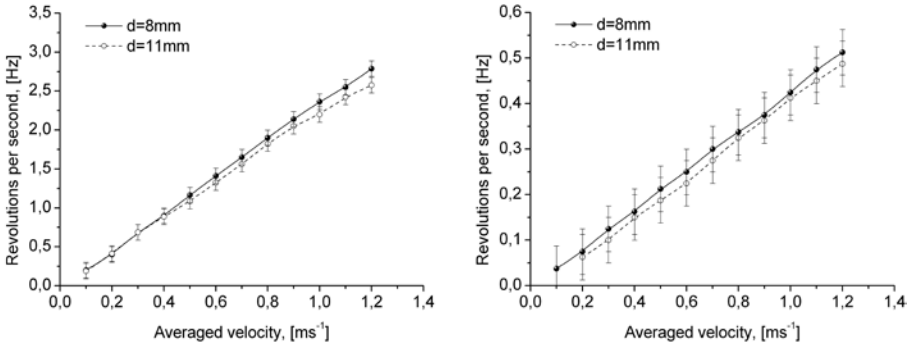

Source: Buchenau (2014).

11.2.1.3.4 Rotating magnet

Another permanent magnet-based principle, the so-called rotating magnet, uses a single cylindrical permanent magnet magnetised perpendicularly to its axis (Priede, 2007; 2009; 2011). An almost frictionless bearing allows free rotation of the magnet. The equilibrium rotation rate is determined by a vanishing total electromagnetic torque and depends only on the flow rate and the geometry of the system while it is independent of the electromagnetic torque itself. In case of negligible friction losses, the rotation rate is not affected either by the strength of the magnet or by the conductivity of the liquid metal (Priede, 2009, 2011). The arrangement of the sensor components is depicted in Figures 11.2.13(a) and 11.2.13(b).

Figure 11.2.13(a): Single magnet rotary flow meter; (b) Principle of the single magnet rotary flow meter

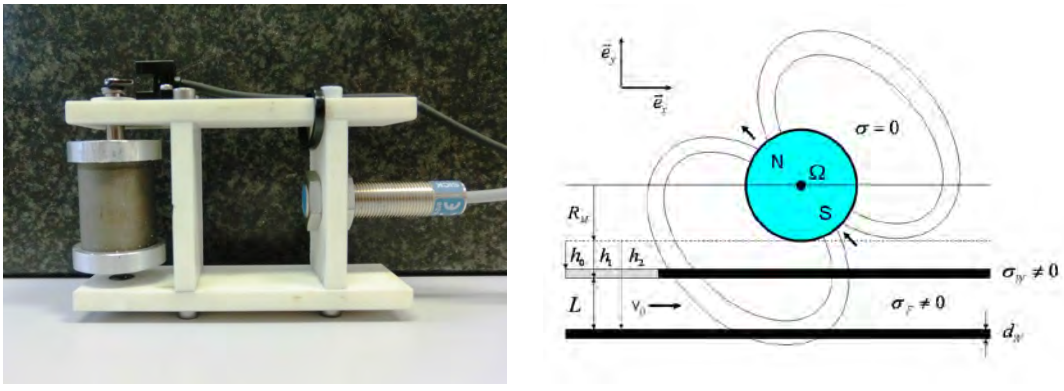

The direction of the axial velocity component (v_0), the rotation axis of the magnet and the direction of the magnetisation are perpendicularly aligned to each other. The equilibrium rotation rate of the rotating magnet is directly proportional to the flow rate ($Q \sim v_0$) in the channel or pipe:

$$\Omega = \frac{v_0}{2}\left(\frac{1}{h_1} - \frac{1}{h_2}\right)\ln\left(\frac{h_2}{h_1}\right) \tag{11.18}$$

whereas the rotation rate is further determined by the geometric parameters of the arrangement (h_1) and (h_2), cf. Figure 11.2.13(b). The linear dependence between (v_0) and (Ω) is limited by the condition $Rm \leq 1$.

The influence of an electrically conducting channel or pipe wall causes an additionally appearing moment which acts counter-clockwise to the moment driving the magnet. Inserting this moment in the law of momentum conservation ($M = 0$) and neglecting the frictional losses leads to:

$$\frac{v_0}{2}\left(\frac{1}{h_1} - \frac{1}{h_2}\right) = \Omega\left\{\ln\left(\frac{h_2}{h_1}\right) + \left(\frac{\sigma_W}{\sigma}\right)\ln\left(\frac{h_1}{h_0}\right)\right\} \tag{11.19}$$

According to Eq. (11.19) the equilibrium rotation rate of the flow meter shows a dependency on the electrical conductivity of the melt (σ), the conductivity of the wall (σ_W), as well as on (h_0) and (h_1) standing for the distances from the outer periphery of the magnet to the outer wall and the inner wall. A sensitivity factor (K_σ) can be defined:

$$K_\sigma = 1 + \left(\frac{\sigma_W}{\sigma}\right)\ln\left(\frac{h_1}{h_0}\right)\ln^{-1}\left(\frac{h_2}{h_1}\right) \tag{11.20}$$

describing the reduction of the rotation rate in the situation of an electrically conducting wall. The linearity of the measurement principle is limited by the condition $Rm \leq 1$.

Figure 11.2.14(a) displays a measurement of a sodium channel flow. The graph presents the linear relation between the equilibrium rotation rate of the rotating magnet in dependence of the sodium flow (Priede, 2011). Residual magnetism of the channel walls consisting of stainless steel causes a shift of the characteristics out of the origin of the co-ordinate system. Because of the inertia of the system velocities less than $v_0 = 0.3$ ms^{-1} were not measurable. The distance between the periphery of the magnet and the outer stainless steel channel wall was adjusted to $d = 8$ mm as well as $d = 11$ mm (cf. Figures 11.2.14[a] and 11.2.14[b]).

Figure 11.2.14: (a) Linear dependence of the rotation rate from the averaged velocity of the sodium (Priede, 2011); (b) Rotating magnet installed at a sodium loop

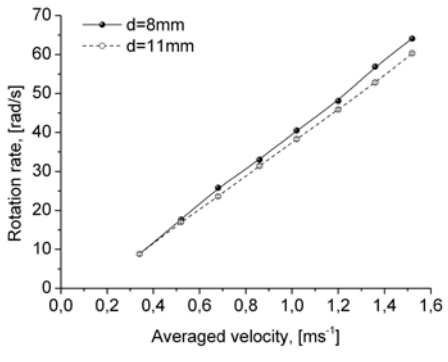

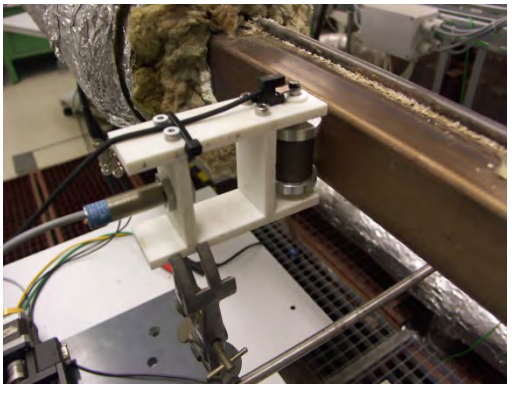

11.2.2 *Momentum-based flow meters*

11.2.2.1 Turbine flow meter

In a turbine flow meter the measuring element is an axial rotor, turned by the force generated by the flowing fluid pushing onto the turbine blades. In most applications this rotation will be picked up by a magnetic sensing coil placed onto the housing in the immediate vicinity of the interiorly passing blades. The measured rotation frequency is direct proportional to the volumetric flow rate. In reality bearing friction and dependencies on the flow profile, the viscosity of the fluid and eddy production in the turbine cause a disturbance of the linear characteristics. These influences are compensated by means of integrated flow straighteners and factory calibrations with a model fluid of the same viscosity as the future working fluid. Turbine flow meters like that shown in Figure 11.2.15 are commercially available for different pipe diameters (Natec Schultheiß, 1999). They are used for flow rate measurements of gases and turbulent flowing, low viscosity fluids and feature a high measurement accuracy.

Figure 11.2.15: Construction sketch of a turbine flow meter

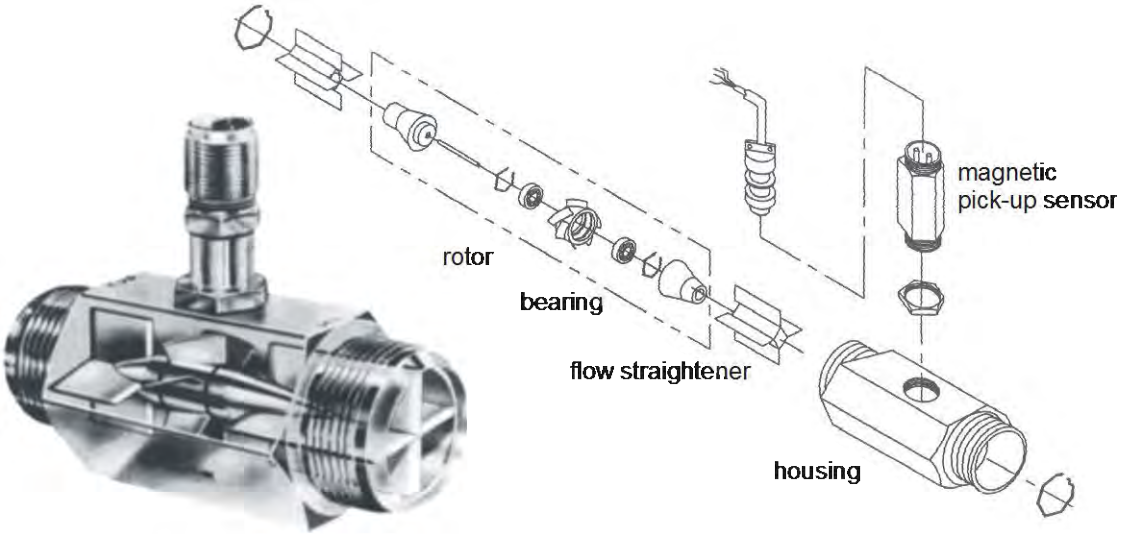

Source: Natec Schultheiß (1999).

For application in liquid metals the question of compatible materials arises. Rotor and bearing have to withstand the corrosive environment and high temperature of the fluid. Because of their relatively wide conduit turbines are rather unsusceptible against floating particles, but in heavy liquid metals impurities are buoying upwards and can accumulate in the top region of the rotor housing. Hence, the narrow gap between rotor and housing can plug up and destroy the turbine.

An advantage of the turbine flow meter is the possibility to use it as a measurement standard, because its mechanical measurement principle depends only on a few very well-known parameters and calibrations can be done with model fluids. Thus the turbine flow meter was selected for qualification in lead-bismuth flows in the KALLA laboratory, namely in its THESYS loop.

Operational characteristics

For the tests of a turbine flow meter a device from the company Natec Schultheiß was purchased. The selected model FT-1600-YBBLED-6108 is a measurement turbine for liquids with a magnetic inductive pick-up system. Housing and rotor consist of stainless steel,

journal, axis and bearing of carbide. As specified, fluid temperatures up to 600°C are allowed with this material combination, but the magnetic inductive pick-up has to be cooled (Natec Schultheiß, 1999). The turbine was calibrated in a company laboratory with an oil mixture, which acts as a model fluid for lead-bismuth at low temperature by adjusting its viscosity. Figure 11.2.16 shows a photograph of the used turbine flow meter and a view into its duct with the rotor.

Figure 11.2.16: Photographs of the Natec Schultheiß turbine flow meter installed in the THESYS loop of KALLA

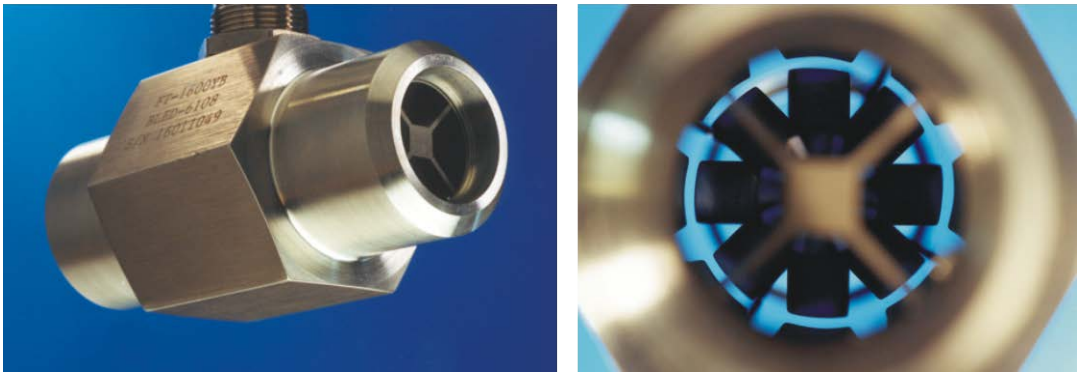

To evaluate the performance of the turbine flow meter, a heat balance calibration was conducted. Measurements were made at lead-bismuth temperatures from 200 to 250°C. Figure 2.17 shows the flow rate as a function of pump power measured by means of the turbine flow meter in comparison with the values derived from the heat balance. A systematic error between the two independent measurement methods was found, but the uncertainties in the heat balance are higher due to the difficult evaluation of heat losses. Therefore, the results of the turbine flow meter are preferred and the linear regression coefficient amounts to 98.7%. For further considerations in the analysis of the heat balance the heat losses were corrected by 2.1% to achieve consistency between the measurements of turbine and heat balance.

Figure 11.2.17: Flow rate measured by turbine and calculated from a heat balance as a function of pump power at lead-bismuth temperatures between 200 and 250°C in the THESYS loop of KALLA

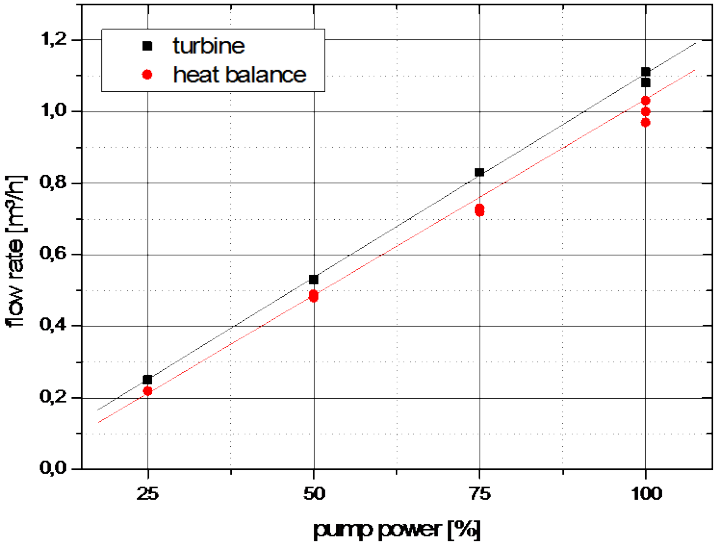

Figure 11.2.18 shows slices out of the time series from turbine and heat balance at a lead-bismuth temperature of 375°C and 100% pump power. In the left chart the deviation between the signals is lower than 1% and the limit of variation is ±0.02 m³/h, which is in the range of the expected flow rate fluctuation in the THESYS loop.

After two weeks of correct continuous operation repeated collapses of the turbine flow meter signal were observed as shown in Figure 11.2.18 (right image). The assumption that a problem with the bearing of the rotor is responsible for the signal losses was confirmed a few days later by a post-failure analysis of the turbine: corrosion had destroyed the journal and bearing material at the heavily loaded spots, which were at the top of the bearing, because the rotor swam up in the heavy liquid metal. The turbine flow meter provides reliable data with a high accuracy, repeatability and linearity, but materials have to be found to assure a long-term stability of the mechanical components in the liquid metal flow. Then, a turbine flow meter could be used as a calibration device for PMF or EMFM systems.

Figure 11.2.18: Time series of flow rate acquired by turbine and heat balance before (left) and after (right) turbines bearing damage at 100% pump power at THESYS, KALLA

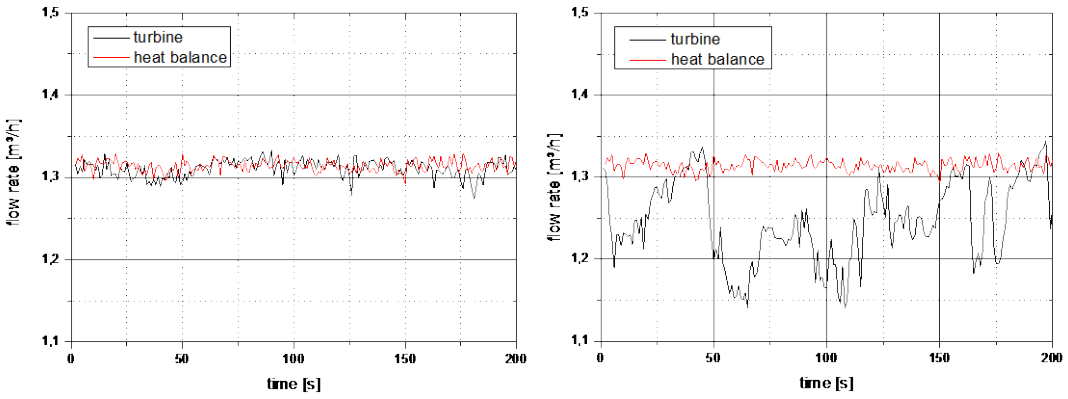

11.2.2.2 *Coriolis flow meters*

The Coriolis or gyrostatic flow meter directly measures the mass flow in a tube. The measurement is based on the Coriolis force, generated if a liquid flows through a U-tube oscillating on the axis A, see Figure 11.2.19. In both branches of the U-tube Coriolis forces of opposite direction appear. They lead to an oscillation around the axis B. The magnitude of the angle χ around axis B is directly proportional to the mass flow through the U-tube.

Figure 11.2.19: Measurement principle of a gyrostatic mass flow meter

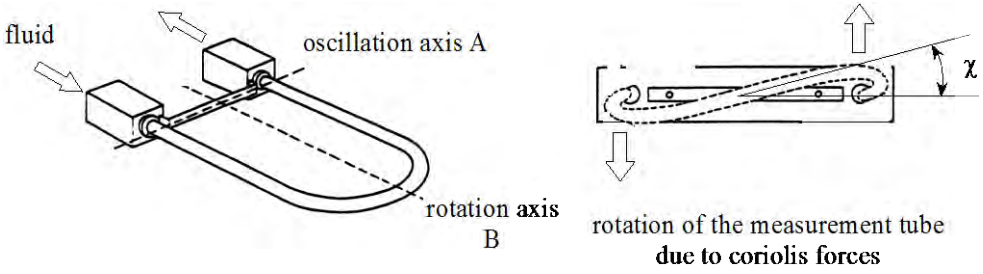

There has been a dynamic development of Coriolis flow meters throughout recent years, therefore the reader should refer to commercial suppliers when considering such instruments in a heavy liquid metal application. This section only briefly summarises slightly older experience with Coriolis flow meters in liquid metal systems.

The measurement method is independent of the kinematic viscosity, temperature, flow profile and gas content in the fluid. The used mass flow meter can – dependent on the model – be adjusted stepless in its measurement range via a remote control from the operation room. Moreover, the instruments offer the option to perform a self-calibration. For calibration the fluid in the measurement tube has to be at rest. This can be done via two valves interconnected in the line at inlet and outlet of the mass flow meter. The uncertainty of the mass flow meter is less than ±1% of the chosen scale, depending on the specific model.

The temperature and pressure operation range of the instruments is limited, however, successful runs with sodium and sodium potassium alloys have shown its applicability to liquid metal systems, see e.g. Barleon (1996) or Stieglitz (1996). The temperature restriction is one of the most critical parts for the use in liquid metal systems. The component should not be installed close to magnetic fields due to the electronics in the instrument in order to avoid disturbances in the electronics.

11.2.3 Pressure- and counter-based flow meters

11.2.3.1 Von Kármán vortex street flow meter

The measurement principle of so-called vortex flow meters is based on the Kármán vortex street where counter-rotating vortices are periodically formed downstream to an obstacle as depicted in Figure 11.2.20.

Figure 11.2.20: Principle of the formation of a Kármán vortex street behind a cylindrical obstacle

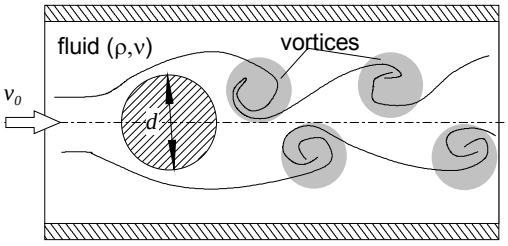

The frequency at which these vortices alternate sides is essentially proportional to the fluid velocity u_m. The frequency of the vortices f in a liquid metal flow can be detected e.g. by a simple pressure transducer or any other mechanical device. In commercial vortex flow meters piezoelectric crystals are often used, which produce a small voltage pulse every time a vortex is created. Then an electronic signal processing is done to eliminate noise, for instance, thus providing vibration immunity and stable measurements.

The two dimensionless physical numbers describing this simple problem are the Strouhal number *Str* and the hydraulic Reynolds number *Re* built with the characteristic length of the obstacle, e.g. the diameter *d* of a cylinder:

$$Str = \frac{f\,d}{v_0} \tag{11.21}$$

and:

$$Re = \frac{u_m\,d}{\nu} \tag{11.22}$$

Since the Strouhal number is not constant in every range of the Reynolds number it is necessary to choose the right diameter for the vortex flow meter to obtain a constant calibration factor. A linear operating range starts typically at a minimum Reynolds number of 10^4 for an inner diameter up to 100 mm. Below the minimum flow rate the device sets the output signal to zero. With such a flow rate measurement system a conflict of flow meter diameter and the nominal pipe size can easily arise. In order to obtain proper measurement conditions it is necessary to design or substitute an appropriate length of the pipe system, about 15-20 diameters for the inlet and 5 diameters for the outlet pipe between the transition pieces.

Besides the proper flow conditions, the rate of impurities plays a role for the accuracy of this type of flow meter as well as huge vibrations leading to a disproportion of flow signal and noise and therefore producing an error in the signal processing.

However this technique provides an easy and reliable measurement system including the large benefit of temperature independence and operation at high process temperatures up to 450°C.

Operational characteristics

In the THEADES loop at KALLA a vortex flow meter as depicted in Figure 11.2.21 operates with an inner diameter of 54 mm, supplied by a pipe length of 1 100 mm at temperatures up to 450°C, achieving an accuracy of ±0.5%.

Figure 11.2.21: High temperature version and schematic view of vortex flow meter

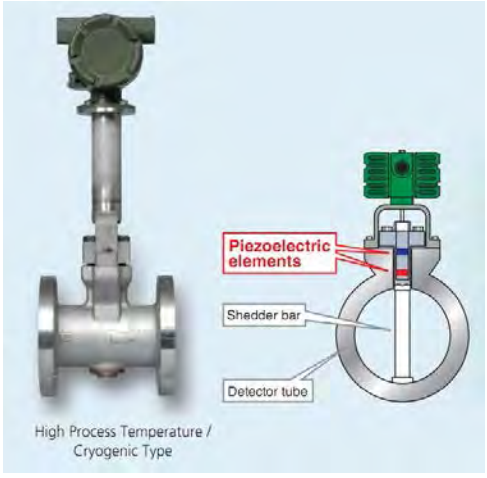

11.2.3.2 Obstacle flow meters, nozzle and orifice flow meters

Orifices, nozzles or Venturi nozzles as illustrated in Figures 11.2.23(a) are commonly used flow meters and a broad overview is given in the DIN tables (1982). The pressure loss coefficients ξ_2 related to the smallest cross-section d_2 are shown in Figure 11.2.23(b) as a function of different diameter ratios d_2/d_1. The data have been collected from Herning (1966) and White (1986). Using the continuity condition the pressure drop coefficient ξ_1 is obtained from Eq. (11.23):

$$\xi_1 = \left(\frac{d_1}{d_2}\right)^2 \cdot \xi_2 \qquad (11.23)$$

Knowing ξ_1, the mean velocity u_m and hence the flow rate can be calculated using Eq. (11.24):

$$u_m = \sqrt{\frac{2\Delta p}{\rho \xi_1}} \tag{11.24}$$

where the pressure difference Δp is measured between the positions indicated in Figure 11.2.23(a). Using special obstacles as is done for instance at the Annubar flow meter can deliver an improvement in accuracy compared to nozzle flow meters but greater sensitivity to impurities. In Figure 11.2.22 the technical set-up of the pressure difference flow meter type being installed in THESYS is illustrated. With this set-up and a developing length of 20 diameters an accuracy of ±0.8-1% was achieved.

Figure 11.2.22: (a) Pressure difference flow meter as it is used in THESYS; (b) Flow straightener being installed upstream the flow meter; (c) Flange for insertion of flow meter

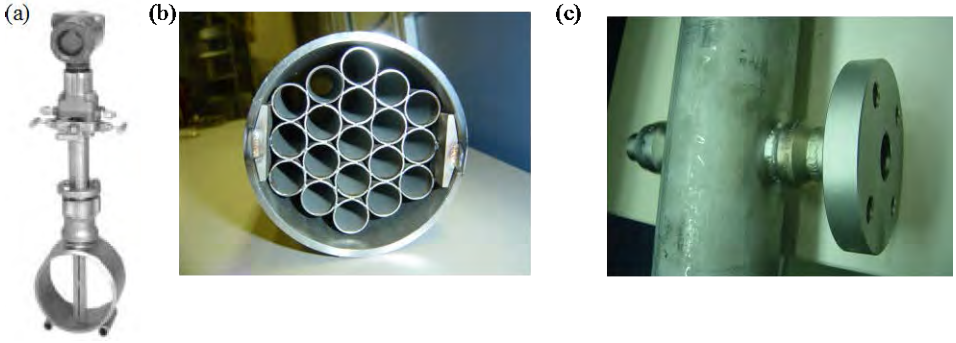

Figure 11.2.23: (a) Orifice designs used for flow rate measurements; (b) Pressure drop coefficient ξ_2 as a function of the diameter ratio d_2/d_1 for the different orifice geometries from (a)

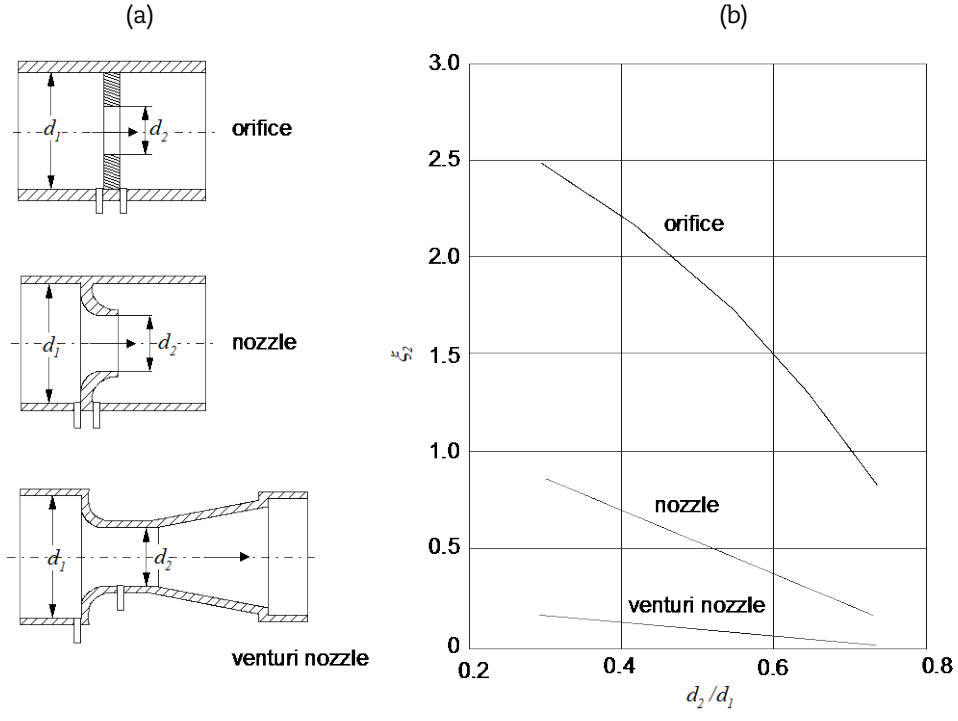

Pitot and Prandtl tubes also rely on the measurement of pressure differences. By means of positioning the tube as depicted in Figures 11.2.24(a) and 11.2.24(b) in the flow the total pressure p_0 can be measured by:

$$p_0 = p_1 + \rho_{meas}\, g\, h \tag{11.25}$$

where p_0 is the absolute outer pressure and ρ_{meas} the density of the measurement fluid.

Using Pitot tubes an absolute pressure transducer is connected at the end of the line so that p_r is given for $u = 0$. The dynamic pressure p_{dyn} can be calculated from the difference of the total pressure p_0 and the static pressure p_{stat} using a Prandtl tube.

Figure 11.2.24: (a) Local flow velocity measurements using Pitot tubes; (b) Local flow velocity using Prandtl tubes; (c) Local axial velocity normalised by the mean velocity as a function of the dimensionless radius *r/D* at different Reynolds numbers *Re*; (d) Schematic set-up of the Pitot flow meter

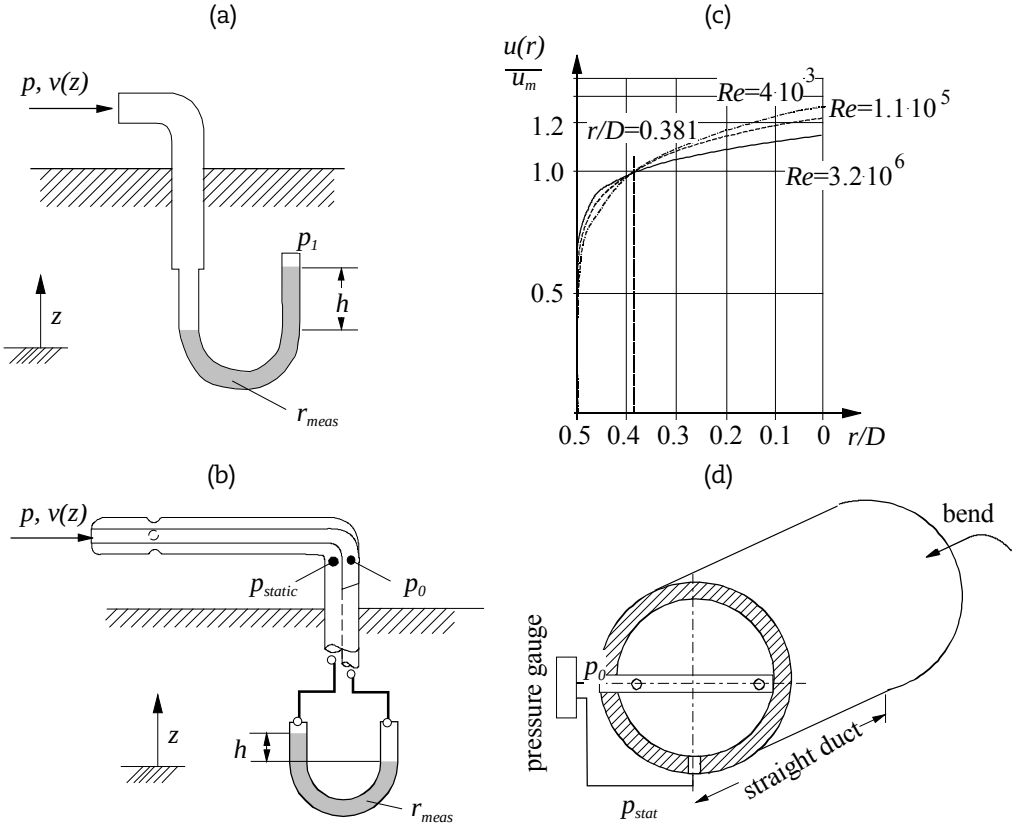

By measuring $p_{dyn} = p_0 - p_{stat} = \rho_{meas} g h$ the local velocity $u(z)$ can be calculated using Eq. (11.26):

$$u(z) = \sqrt{\frac{2\, p_{dyn}}{\rho}} \tag{11.26}$$

While using Pitot tubes as flow rate measurement devices, at least two sensors have to be located within the tube according to ISO 3966-1977, see Figure 11.2.24(d). Since the velocity profile varies as a function of dimensionless radius r/D the Pitot tubes have to be

placed in positions such that this deviation is minimal. In Figure 11.2.24(c) the dimensionless velocity is depicted as a function of the radius (VDI, 2001). It shows that at $r/D = 0.381$ in a Reynolds number range $Re = 4{\cdot}10^3$-$3.2{\cdot}10^6$ the deviation is less than 3%. Another error source while using Pitot tube flow meters is that they require a developing length of at least 25 tube diameters after a 90° bend. For developing lengths of more than 35 diameters the systematic error is minimised to less than ±0.5%.

11.2.4 *Ultrasound transit time method (UTT)*

The velocity of propagation of sound waves in moving fluids changes with the flow velocity of the transmitting medium. An ultrasound wave is sent through a fluid under an angle α to the flow direction from a sender A to a receiver B as shown in Figure 11.2.25 (Gaetke, 1991; Millner, 1987).

Figure 11.2.25: Principle of ultrasound transit time measurement

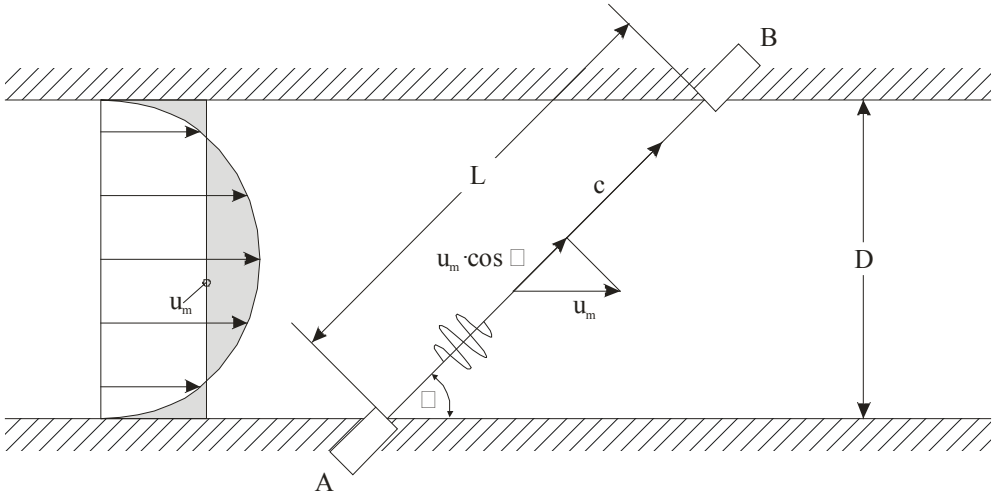

Source: Adapted from Gaetke (1991).

If the fluid is not moving the signal travels with the sound speed c from A to B from which the transit time is calculated to $t_0 = L/c$. But if the fluid flows with the mean velocity u_m the signal is accelerated by the portion of the projection of this velocity to the measurement line. Accordingly the signal is decelerated by the same amount on its way from B to A. The transit times of the signals can then be calculated by:

$$t_{AB} = \frac{L}{c + u_m \cos\alpha} \quad \text{and} \quad t_{BA} = \frac{L}{c - u_m \cos\alpha} \tag{11.27}$$

Transformation yields to an expression for the mean flow velocity:

$$u_m = \frac{L}{2\cos\alpha}\left(\frac{1}{t_{AB}} - \frac{1}{t_{BA}}\right) \tag{11.28}$$

In practice determining the transit time difference from the phase shift between the two signals $\Delta t = t_{AB} - t_{BA}$ is common; with the postulate $(u_m/c)^2 \ll 1$ one obtains:

$$u_m = \frac{c^2}{2L\cos\alpha}\Delta t \tag{11.29}$$

Compared to Eq. (11.28), in Eq. (11.29) the mean velocity depends on the sound speed. This disadvantage is accepted because the determination of the usually very short transit times appearing in Eq. (11.27) is technically difficult and less accurate than the identification of its difference. Due to the fact that besides the sound speed only geometric measures occur in the equation, the ultrasound transit time method can be used for calibration of other measurement methods if the sound speed in the fluid is known and a fully developed flow profile is present.

To generate ultrasound, mainly piezoelectric materials are used (quartz, lead zirconate, barium titanate) whose Curie temperature, above which they get instable and irreversibly destroyed, limits the applicable temperature range to a maximum of about 150°C. For measurements in high temperature fluids like liquid metals, wave guides are required. Liu (1998) developed bundled wave guides at the company Panametrics for ultrasound transit time measurements in fluids and gases for temperatures up to 450°C. They describe wetted and clamp-on systems and show results of their application for flow rate measurements at temperatures between 200 and 300°C. The fact that ultrasound is also transported as a longitudinal pressure fluctuation in opaque media renders it a promising method for measurements in liquid metals.

In order to transport a significant energy through the structure into the fluid, the material thickness of the emitter has to be adapted to the fluid. Here, the impedance Z, which is the product of the sound speed c and the density ρ, has to be taken into account. The permittance D of an acoustic wave through a solid-fluid interface can be expressed as a function of the thickness of the material d, the wavelength λ of the sound wave and the impedance of the fluid and the liquid Z_1 according to Eq. (11.30):

$$D = \frac{1}{\sqrt{1 + \frac{1}{4}\left(m - \frac{1}{m}\right)^2 \sin^2 \frac{2\pi d}{\lambda}}} \quad \text{and} \quad m = \frac{Z_1}{Z_2} \tag{11.30}$$

The permittance of a steel plate for a longitudinal wave at a frequency of 4 MHz towards water and lead-bismuth as a function of the thickness is shown in Figure 11.2.26. This permittance is only achieved if the interface is perfectly physically wetted and no mode transitions of the wave at the interface appear.

Figure 11.2.26: Permittance *D* of steel at a frequency of 4 MHz as a function of the plate thickness *d* for the interface steel-water and steel-PbBi

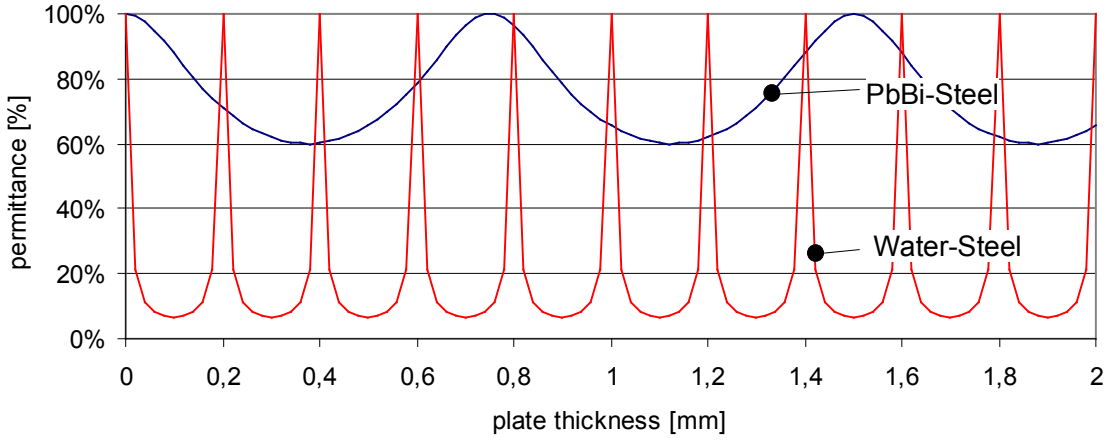

Other sources of uncertainty using the ultrasound technique are the absorption and the sound scattering. Finally, the anisotropy of the sound speed has to be taken into account. In case of measuring flows containing a temperature gradient, the sound speed varies with the square root of the temperature and thus the temperature (distribution) has to be known and adequate countermeasures must be foreseen.

A fundamental uncertainty analysis for UTT flow rate measurements according to the GUM standard has been presented by Furuichi (2012).

The mode transition problem at the interface leading to a significant decrease of the signal magnitude is solved by a specific sensor design. The mode transitions can in principle occur due to:

- longitudinal to transverse wave transitions;
- surface waves like Rayleigh waves;
- creep waves;
- ring sound.

Operational characteristics

Crucial for the coupling of ultrasound is an adhesive wetting of the wave guide ends to transmit the oscillation energy into and out of the fluid. Hence, to guarantee the wetting, a 2 μm thick sacrificial nickel layer can be applied on the wave guides in a galvanic bath. Due to the high solubility of nickel in lead-bismuth the wetting can be preserved for the duration of the application, which results in 60% of the senders' signal amplitude at the receiver.

Figure 11.2.27 shows the flow rate over pump power measured by means of the USTT and the PMF methods at two temperature levels. The PMF was calibrated at 70% pump power as described above and shows a good agreement with the USTT values at the other settings. The flow rates measured at a temperature of 376.5°C are about 5% higher than the ones at a temperature of 208.4°C, which is caused by a slightly better performance of the EM pump at higher temperatures due to a lower contact resistance between the liquid metal and the pump channel.

Figure 11.2.27: Flow rate measured by USTT and PMF at temperatures of 208.4°C and 376.5°C as a function of the pump power

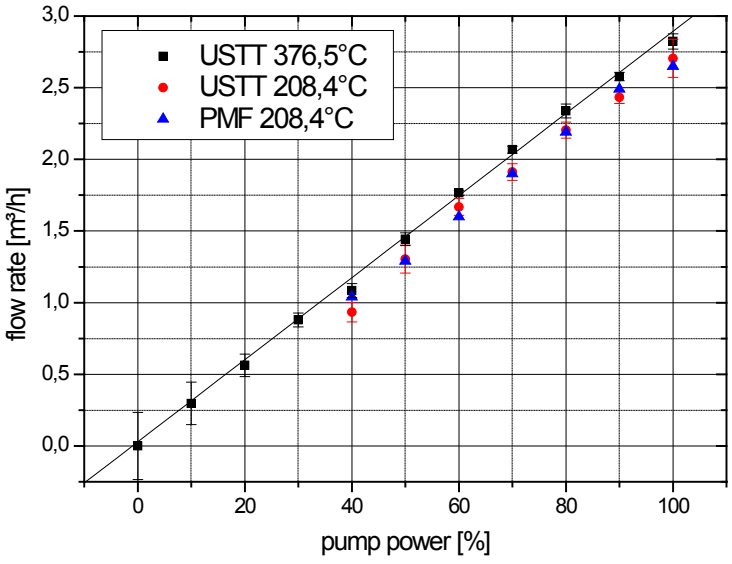

The nickel coating of the wave guides results in a stable coupling and therefore a small uncertainty of lower than 1% for flow rates of more than 0.5 m³/h. The linear regression coefficient is calculated from the measurements at 376.5°C to 99.8%. Systematic errors occur in consequence of the test sections' thermal elongation, which changes the length of the sound path appearing in Eq. (11.18). This error can be calculated to ~3% so that the complete uncertainty sums up to ~4%. For the Panametrics XMT868 a measuring range of ±12.2 m/s at an uncertainty of ±2-5% of the reading is given and coincides with the ascertained value. In principle bigger pipe diameters and higher flow rates reducing the errors and improving signal to noise ratio for the USTT method, because the transit time differences increase. In addition multiple ultrasound paths circumferentially arranged around the pipe can also increase the accuracy.

11.3 Pressure sensors

11.3.1 *Types of pressure gauges and operation experience*

Generally two types of pressure measurement devices are available in more or less direct contact with lead-bismuth. These types of sensors are also capable of measuring local velocity distributions if they are used in the context of a Pitot or Prandtl tube. Additionally, they can be used as flow meters of different principles in case an elevated pressure drop in the piping can be accepted by the individual user.

The first are capacitive transducers illustrated in Figure 11.3.1, which measure the pressure difference (Δp) between two discrete points in a piping system.

Figure 11.3.1: Capacitive transducers

(a) Schematical set-up of a capacitive pressure difference transducer using a coupling medium

(b) Photograph of an absolute pressure transducer using a fast Wheatstone bridge

(c) Test stand to measure liquid levels and pressure differences erected at ENEA/Brasimone

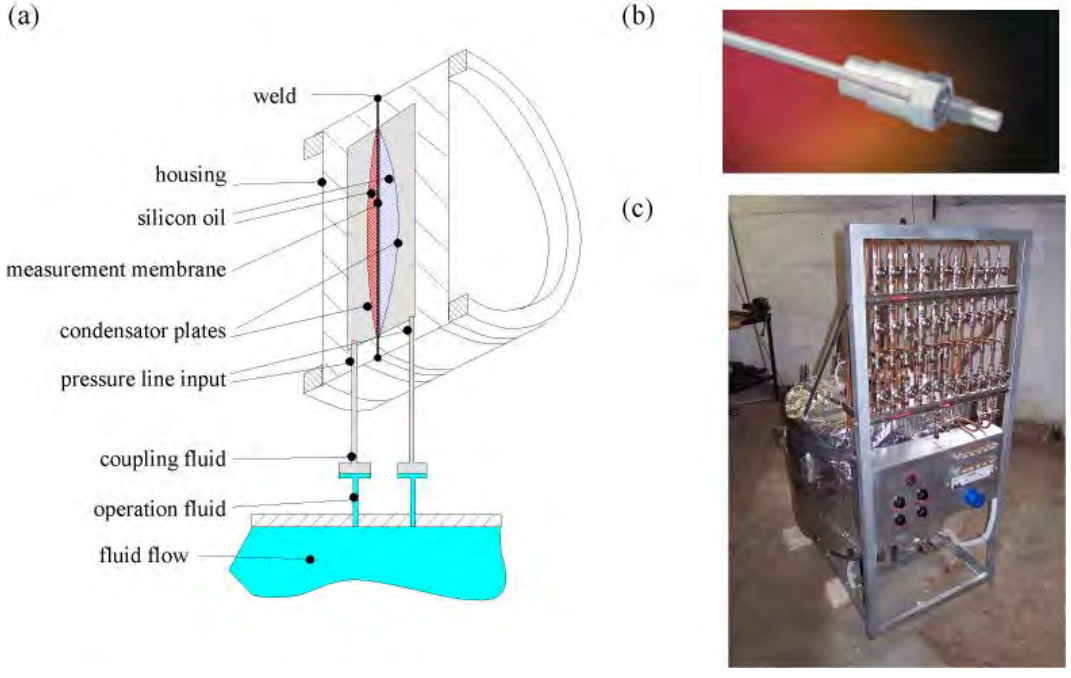

The differential pressure signal is obtained by an electric capacity change between two plates, filled with silicon oil. Since the transducer medium is only capable to withstand temperatures less than 200°C the connection between the liquid PbBi and the transducer itself is realised by an incompressible coupling medium. The eutectic sodium-potassium alloy $Na^{78}K^{22}$ is often used here, with a melting point of -11°C. The use of a coupling medium limits the temporal resolution. The frequency response time of the transducer is typically limited to 5 Hz, which does not allow to measure fast fluctuations of the velocity or flow rate oscillations. A technical sketch of the differential pressure measurement sensor used in the Karlsruhe Lead Laboratory (KALLA) is depicted in Figure 11.3.1(a). Nevertheless, the major advantage of the capacitive methods is their excellent stability and accuracy. They offer a high resolution (±12.5 Pascal), a differential as well as an absolute pressure signal if one chamber is evacuated, and additionally the zero point can be easily determined. But, they require a complex set-up of heating elements in the transmission line up to the coupling clutch, a precise fill and drain strategy to avoid bubbles and they are actually expensive.

Another method to measure absolute pressures p is to use pressure gauges based on semiconductor technology. The sensor holds a diaphragm with strain gauges, taking use of the piezo resistive effect in a fast Wheatstone bridge. This kind of sensor is compact and can be screwed directly into any tap of the liquid containing piping. Due to their small dimension they have a negligible inertia and hence allow detection of fast oscillations of the order of several hundred Hz. A photograph of such a sensor is shown in Figure 11.3.1(b). Due to the fabrication principle the maximal span is given and a calibration before each experimental run must be performed. Then, the pressure resolution reaches nearly the range of the capacitive units. Nevertheless, this technique, which can sustain up to 480°C liquid temperature, is the preferred option for use in the Pitot and Prandtl tubes later described and used for recording local velocities and their fast fluctuations.

A third option to measure pressures, differential pressures, liquid levels or flow rates is offered by the bubbling technique, successfully performed in the lead-bismuth loop CIRCE of ENEA. Here, bubbles of inert gas are injected via Venturi tubes into the liquid. While measuring the gas pressure in the bubble tubes, levels and pressures can be recorded at several locations simultaneously using only one sensor, which is not in direct contact with the liquid and thus temperature limitations for this kind of use do not exist. The technical realisation of a test stand proofing this principle at ENEA is illustrated in Figure 11.3.1(c). Beside the simple set-up of the pressure cells operating at room temperature and the simultaneous recording at several positions, the low price is rather attractive. Nevertheless, all results depend on the nozzle shape, the detailed positioning in the system and an extensive calibration. Also, the temporal resolution is rather limited and a temperature correction has to be performed because the surface tension of the liquid depends on it.

11.3.2 *Pressure correction in fully developed turbulent pipe flow*

Particularly in very fine resolution measurements, say e.g. in benchmark experiments, it may appear that misreadings of the wall static pressure occur, which are related due to the finite size of the pressure tapping. This effect was observed over a wide range of Reynolds numbers by numerous authors some time ago, as shown in the papers by Allen (1932), Ray (1956), Thom (1957), Rayle (1959), Livesey (1962), but also by Franklin (1970) and Ducruet (1984). A summary of the complete literature dealing with this problem is given by Chue (1975).

All results indicate that the correction term as a fraction of the wall stress continues to increase as the hole's Reynolds number $d^+ = (u_\tau d)/\nu$ increases. For small holes relative to the pipe diameter the results follow a single curve, but for larger holes the data diverge from this universal behaviour at a point that depends on the ratio of the holes' diameter

to the pipe diameter. This effect becomes pronounced especially for large Reynolds numbers, which appear easily in heavy liquid metals because of their low kinematic viscosity ν. A flow structure within a pressure tapping yielding the pressure error is schematically shown in Figure 11.3.2.

Figure 11.3.2: Flow structure

(a) Flow structure within the static pressure tapping

(b) Variation of the non-dimensional pressure error Π as a function of the holes' Reynolds number d^+ for different d/D after McKeon (2002)

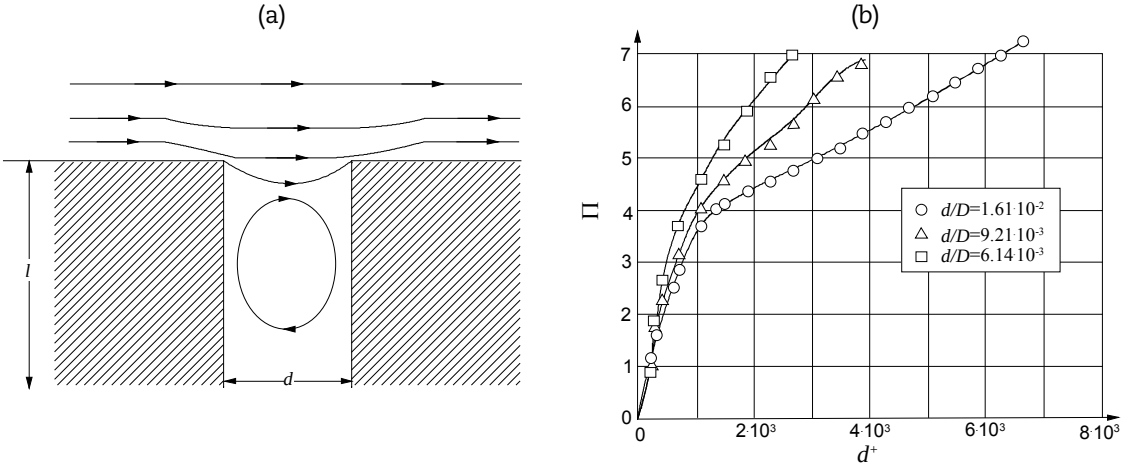

A dimensionless analysis performed by McKeon (2002) shows that the pressure error Δp depends on the hole diameter d, the hole depth l, the diameter of the connection to the transducer d_c, the wall shear stress τ_W, the fluid density ρ and the kinematic viscosity ν. Within this context the characteristic length scale of the facility where the experiment is conducted, namely the pipe diameter D, is important especially considering large holes. Then the non-dimensional error Π can be expressed by a dimensionless parameter group of the form:

$$\Pi = \frac{\Delta p}{\tau_W} = f\left(\frac{d\,u_\tau}{\nu}, \frac{d}{D}, \frac{l}{d}, \frac{d_c}{d}\right) \text{ with } u_\tau = \sqrt{\frac{\tau_w}{\rho}} \tag{11.31}$$

where u_τ is the friction velocity. Assume first that d/D, l/d and d_c/d are constant, then the pressure error Π depends only on d^+. With a decreasing hole Reynolds number d^+ (namely $d \to 0$) Δp tends to zero. Far from the wall dynamic and turbulent effects dominate the flow behaviour and thus for large d the ratio d/D becomes important. Shaw (1960) investigated the hole Reynolds number d^+ effect in a 50 mm diameter tube for flow Reynolds number up to $Re = 1.7 \cdot 10^5$. He found that the non-dimensional error Π increases with increasing d^+ but reaches an asymptotic limit of 3 for $d^+ = 750$. But he dismissed the effect d/D, because as d increases not only the hole's Reynolds number increases but also d/D. Shaw suggested that the hole must become large enough to change the flow field itself and postulated this occurrence to appear at $d/D \sim 0.1$. For $d/D > 0.1$ the global flow patter in the pipe and – even more important – the flow over the tapping is changed, leading to a miscellaneous pressure reading. In this case a correction due to the secondary flows affecting the pressure tap has to be performed. Further literature treating this topic may be taken from Pozrikidis (1994), McKeon (2002) or Ligrani (2001).

The depth to diameter also plays a role in the pressure error, since it dictates the eddy system set-up within the cavity. Even the Allen (1932) investigations show that the error increases with l/d, but if l/d exceeds the value 2, Chue (1975) demonstrated through a compilation of all previous experiments that an asymptotic value is reached, which represents the "deep" limit for all Reynolds numbers. Consequently, a wide cavity behind the tapping reduces the error, while a contraction in diameter from the tapping to the pressure gauge can increase the error, see e.g. Livesey (1962).

As a practical guide, it is suggested that if a Pitot tube and static tapping are used to make pressure measurements within a pipe flow, the static tapping should have a large and constant l/d, at least $l/d > 2$ to ensure that the flow structure within the cavity is fully developed and not changing with the Reynolds number. Second, a small ratio of tapping to pipe diameter has to be set up, to prevent the tapping fundamentally altering the external flow.

11.4 Local velocity measurements

The development of technical units like beam windows or fuel bundles requires sophisticated information on the local velocity distribution (and local heat fluxes) in the complex flow, which often cannot be simulated numerically or where numerical simulation needs local validation data. The opacity of liquid metals excludes the use of optical methods which are commonly used in thermal-hydraulics. The intention to develop new measurement techniques to determine the local velocities in liquid metals arises from the following requirements:

- Although there is a growing interest in measuring the local velocities in opaque fluids at high temperatures, most of the currently developed techniques only exist at laboratory scale and show no reasonable accuracy over a sufficiently long time period.
- The measuring conditions in liquid metal facilities are often characterised by external magnetic fields or strong electric noise caused by heating elements, pumps or high power supplies.
- Disturbances of the flow caused by the presence of the sensor should be prevented as much as possible.
- The measurement range should cover low (mm/s) as well as high values of the velocity in terms of several metres per second.

This chapter presents a few velocity measurement principles successfully applied in past decades to liquid metal flows. Moreover, the operation principle, the necessary calibration methods and correction factors are described or the appropriate literature sources are cited.

For intrusive methods like e.g. reaction probes, fibre mechanical probes, permanent magnetic probes or Pitot tubes, corrections are necessary accounting for the impact of the probe on the velocity field to be measured experimentally. This effect is discussed extensively in the section concerning the Pitot tube, but it can be generally applied to all other intrusive methods.

11.4.1 *Ultrasound Doppler velocimetry*

A non-intrusive method to instantaneously measure whole velocity profiles is offered by the ultrasound Doppler velocimetry (UDV). The UDV technique is based on sending ultrasound pulses through the liquid instead of a continuous wave. The echoes from particles immersed in the fluid (which requires a flow seeding) are sampled. The related velocity information is obtained from the shift in position of scatters between ultrasound pulses and not from the Doppler frequency shift of the echoes. Hence, the velocity

information is yielded from a correlation function. One of the major advantages of UDV is that it is a non-intrusive method, with which the velocity is scanned not only at one exclusive position as in a laser Doppler anemometer. Rather, it samples velocity information instantaneously at several positions along the ultrasound wave path. The operation principle is shortly explained below. A more comprehensive overview of principles and development status of ultrasonic velocity measurements can be found in the review article of Kaatze (2008). The text below contains some experience of UDV application specifically in liquid metals.

The location of the measurement volume is given by Eq. (11.32a), in which c is the sound speed and t_d the actual traveling time of the pulse. The spatial shift of the position ΔP between two pulses applying a pulse repetition time t_{prf} is given by Eq. (11.32b):

$$P = \frac{c\, t_d}{2} \quad \text{and} \quad \Delta P = \left(P_2 - P_1\right) = u\left(z\right) t_{prf} \cos\theta = \frac{c\,\left(t_2 - t_1\right)}{2} \tag{11.32a,b}$$

The time difference $(t_2 - t_1)$ is recorded by means of the phase shift of the echoed signals and can be expressed by Eq. (11.33a), where f_e is the echo velocity. Finally, the velocity $u(z)$ at a discrete co-ordinate z can be evaluated by Eq. (11.33b):

$$\Delta d = 2\pi f_e \left(t_2 - t_1\right) \quad \text{and} \quad u\left(z\right) = \frac{c\,\Delta d}{2 f_e \cos\theta t_{prf}} = \frac{c\, f_d}{2 f_e \cos\theta} \tag{11.33a,b}$$

with f_d representing the Doppler shift. Of course, an upper limit of the maximum measurable velocity and the maximum measurement depth exists. This constraint is expressed by Eqs. (11.34a,b).

$$u_{\max} = \frac{c}{4 t_{prf} f_e \cos\theta} \;\; ; \;\; y_{\max} = \frac{c\, t_{prf}}{2} \tag{11.34a,b}$$

The UDV technique allows the instantaneous acquisition of whole velocity profiles. This is performed by a reconstruction of the velocity information in the following way. First, the length of the acquired echoes reflected from the particles within in fluid is divided into intervals of the temporal length $\Delta\tau_i$. The run time τ_i is associated with a measurement position in the duct y_i via the relation:

$$y_i = \frac{c\, \tau_i}{2} \tag{11.35}$$

Then the velocity within a discrete interval u_i can be calculated. This procedure determines the local resolution and the size of the measurement volume, which is given by the Eqs. (11.36):

$$\Delta y_i = \frac{c\, \Delta\tau_i}{2} \;\; \text{and} \;\; \Delta y_e = \frac{c\, \Delta\tau_e}{2} \tag{11.36}$$

The entire process of the acquisition of a velocity profile is sketched in Figure 11.4.1.

Another feature of the UDV technique is that it allows to measure even deep into the boundary layer close to the duct wall and thus is able to measure velocities only a few microns away from the wall. For this purpose wall correction functions have to be applied, which account for the fact that a part of the measurement volume is located within the wall. In order to get the correct velocity contribution from the fluid domain only echoes from the fluid region are sensed. In a next step the mass centre of the fluid/wall interval is calculated. The deviation of the mass centre of the fluid/wall interval from the distance centre yields a displacement of acquisition point. A detailed description of this procedure may be taken from Wunderlich (2000), Nowak (2002) or Lefhalm (2004a).

Figure 11.4.1: Operation principle of the ultrasound Doppler velocimetry (UDV) to acquire local velocities in heavy liquid metal flows

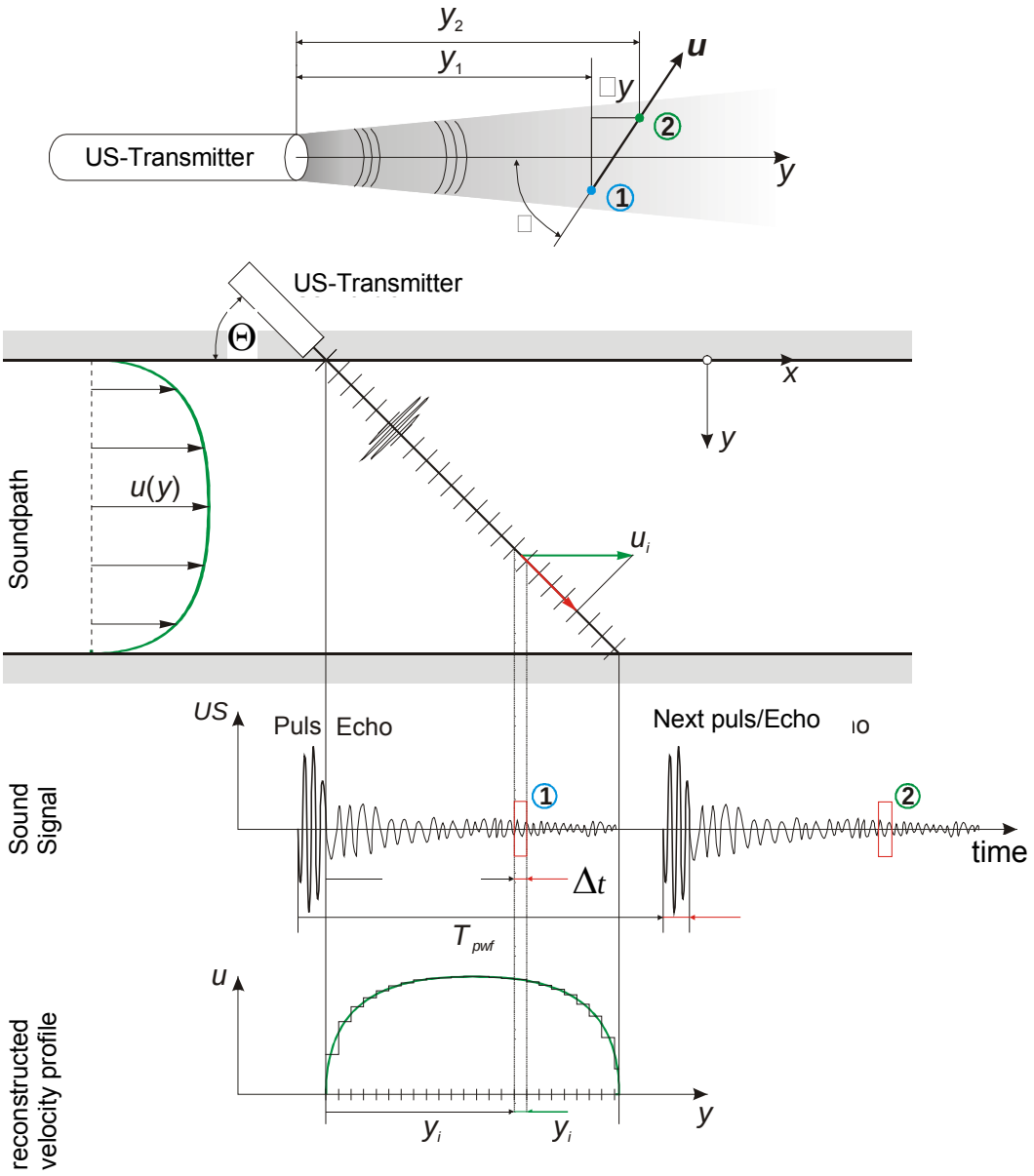

Source: Lefhalm (2004a).

The measurements of the velocity profiles within the turbulent boundary layer of an annular duct performed by Lefhalm (2004a), which are shown in Figure 11.4.2(a), illustrate that by means of correction functions the velocity can be acquired. The measured velocities coincide with the literature data of Reichhardt (1951) almost perfectly. The deviations found are less than 5%. Moreover, it was possible to measure into the viscous sublayer up to values of $y^+ \approx 3$. In his experimental configuration this corresponded to a wall distance of 46 μm. The measurement of the turbulent fluctuations within the boundary layer are also possible using the wall correction procedure. Only for $y^+ < 10$ the RMS resolution rapidly dropped.

Figure 11.4.2: Measurements of the velocity profiles

(a) Measured turbulent velocity profiles in the boundary layer in an annular duct of ∅ = 60 mm at $Re = 8.1 \cdot 10^4$ and comparison with Reichardt (1951)

(b) Comparison of the velocity fluctuations (RMS) with Durst (1996)

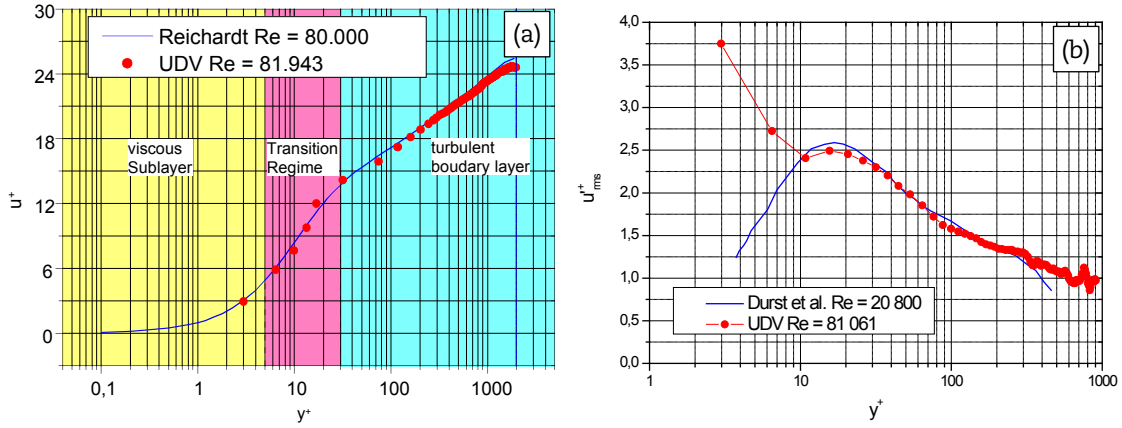

From the procedure explained above it is clear that numerous effects contribute to the acquisition of a proper signal and in fact about 100 parameters are necessary to define the measurement process. The enormous sound speed of heavy liquid metals like PbBi requires extremely fast acquisition and data processing systems to obtain reliable velocity information. Besides these quite sophisticated demands on the data transmission recording and processing units (which are depicted in Figure 11.4.3[d]) several constraints regarding the environmental conditions have to be fulfilled. One of the most crucial problems is the elevated temperature of more than 200°C in typical liquid metal applications, which cannot be sustained by commercially available barium titanate ($BaTiO_3$) sensors. Thus, wave guides have been developed to decouple the temperature from the sensor. Such an integrated probe consisting of a wave guide and a sensor is shown in Figure 11.4.3(b). It was initially developed by the Forschungszentrum Rossendorf (now Helmholtz Zentrum Dresden-Rossendorf) and is in principle applicable to liquid metal temperatures up to 620°C, see Eckert (2003). Secondly, an acoustic coupling of the sensor and the fluid has to be ensured, which in principle means that the probe has to be physically wetted. This is partially achieved by applying a sacrificial nickel layer on the probe surface before inserting it through the fluid. Within the lead-bismuth this nickel layer is dissolved and ensures for a certain time the wetting of the surface. However, after a few days of operation the wetting of the sensor surface gets lost.

The study of the wetting behaviour of lead-bismuth on steel surfaces is a task which has to be solved not only for this application. Another problem is the long-term stability of the probe and the flow seeding. By means of conditioning the oxygen content within liquid lead bismuth a certain long-term stability of the probe was achieved and a sampling of velocity profiles was successfully performed without any additional artificial flow seeding. Artificial flow seedings with particles of a density like the ones in lead-bismuth are hardly available and stable within the operational conditions typically used.

Nevertheless, it is a question to be clarified, whether lead-bismuth clusters or other impurities are responsible for the generation of the echoes. If temperature gradients are present in the flow being studied, traveling time corrections have to be applied, because the sound speed depends on the square root of the temperature. Thus, either the temperature field of the studied flow has to be known or temperature correlations have to be used. Besides the numerous difficulties using UDV within the THESYS loop KALLA velocity measurements have been successfully performed in a turbulent PbBi pipe flow at temperatures up to 400°C. In Figure 11.4.3(e) the measured mean velocities are shown as

a function of the pipe depth for different pump power levels (here given in per cent). Within this campaign velocity fluctuations of frequencies up to 15 Hz were recorded. If appropriate wall correction functions are used even the velocity distribution in the wall near boundary layers can be detected, as shown in Lefhalm (2004a).

Figure 11.4.3: Measured mean velocities

(a) Measurement principle of the ultrasound Doppler velocimetry (UDV)
(b) Integrated probes consisting of a sensor and a wave guide
(c) Application of a UDV sensor in PbBi in KALLA
(d) Corresponding data acquisition and processing unit for the UDV probe
(e) Measured mean velocity in PbBi as a function of the pipe depth at several power levels of the pump

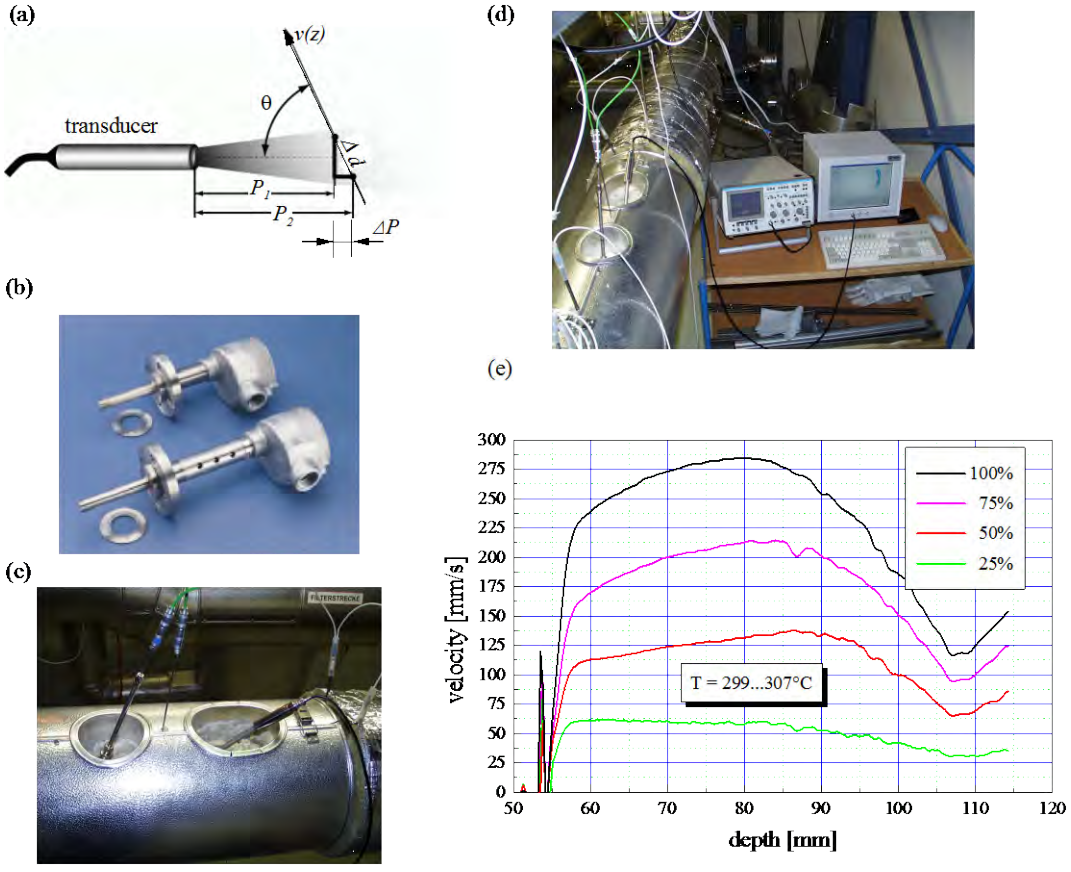

Lenz (2012) recently presented a novel approach for measuring the speed of sound in fluids with scattering particles. The method also works non-invasively and uses the echo signals from scattering particles suspended in the fluid directly, relying on the fact that the stray echo is strongest for the scattering particles located in the sound focus. Results are shown for different homogeneous fluids, including eutectic GaInSn.

11.4.2 *Permanent magnet probes (PMP)*

Another method to measure fluid velocity within an electrically conducting fluid is given by permanent magnet probes (PMP). This probe, developed by Vives, is shown schematically in Figure 11.4.4. Analogous to the permanent magnet flow meter, it is based on the principle that a conductor moving within a magnetic field will generate a

corresponding electric field. Referring to Figure 11.4.4, when immersed in a conducting liquid, a potential difference develops between the tips A and B of the probe leads connected to a voltmeter. The potential difference is proportional to the magnitude of the velocity vector perpendicular to the line AB. A second pair of probes CD thus provides information on the orthogonal velocity component. Operation up to the Curie point is possible, and Ricou and Vives have reported on the use of this device to measure velocities in aluminium. Lee (1984) describes the use of the probe for measurements in Wood's metal. More references on the early development of this probe can also be taken from that paper.

Figure 11.4.4: Vives (PMP) probe classical principle

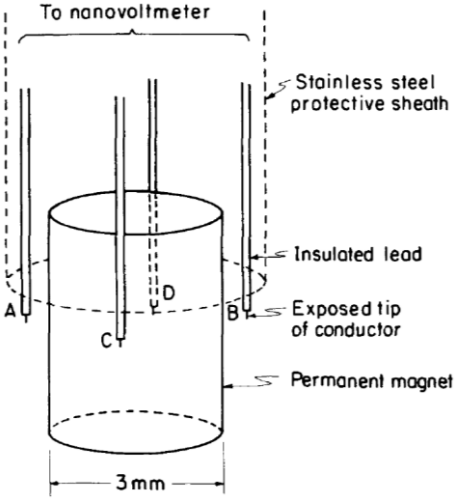

Source: Lee (1984).

The PMP has been continuously further developed and miniaturised. Newer PMP probes allow to simultaneously measure the velocity and the temperature, similar to the combined Pitot tube presented in Section 11.4.1. The turbulent heat fluxes can be determined from the cross-correlation of both signals (temperature and velocity fluctuations, see Figure 11.4.5).

Figure 11.4.5: PMP-probe with thermocouples

(a) Photograph of a miniaturised PMP-probe with thermocouples from Kapulla (2000)

(b) Side and top view of the arrangement of the thermocouples within a PMP probe

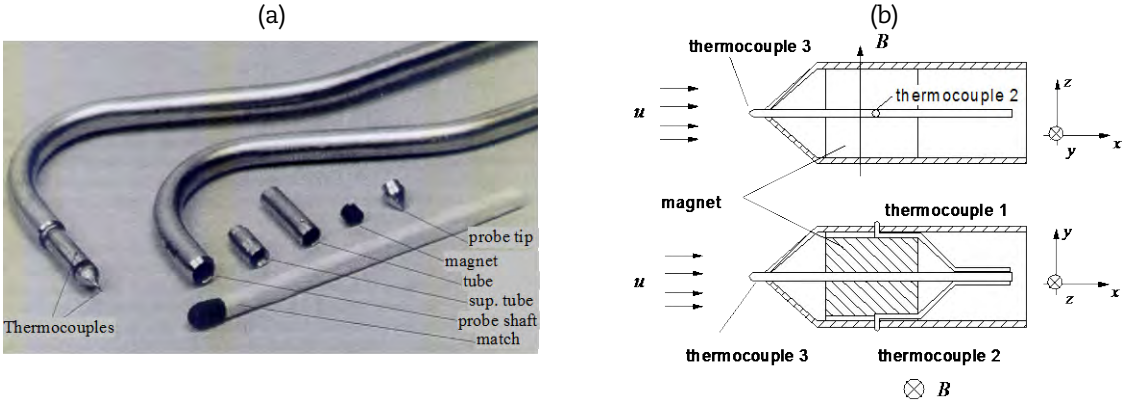

The PMP probe signal is obtained as low ohmic electric potential $\Delta\phi$ arising from the interaction of the flow field u with the magnetic field B. The simplified Ohm's law for moving electric conductors and temporal steady magnetic fields reads to:

$$j = \sigma\left(E_e + E_{th} + u \times B\right) \tag{11.37}$$

where j is the current density, σ the specific electric conductivity of the fluid, E_e the electro-static field, E_{th} the thermo-electric field, u the integrated velocity of the probe dimension and B the magnetic induction.

Generally, there are two main disturbances affecting the induced electric potential. If one takes into account the Maxwell equations (Eqs. [11.38a-c]) and the simplified Ohm's law (Eq. [11.37]) one obtains Eq. (11.39):

$$\nabla \times B = \mu j; \quad \nabla \times E = 0; \quad E = -\nabla\varphi; \quad \nabla \cdot B = 0 \tag{11.38}$$

where μ is the magnetic permeability given by $4\pi \cdot 10^{-7}\, As/Vm$:

$$E_{th} = -S\,\nabla T - Q\left(\nabla T \times B\right) \tag{11.39}$$

in which S is the thermoelectric coefficient in $V/°K$ and Q the Nernst-Ettinghausen coefficient in $V/°K{\cdot}Tesla$. Thus, in order to calibrate the probe isothermal measurements are required in a flow with a defined velocity field. A detailed description of this procedure may be taken from Ricou (1982), Weissenfluh (1986) and Kapulla (2000). The calibration yields the specific Seebeck coefficient of the individual probe. Additional care has to be taken if external magnetic fields are present in the domain of interest as e.g. near electromagnetic pumps or close to DC electromagnetic flow meters. Under such circumstances an even more complicated effort has to be made to determine the coefficients of the probe. The methodology necessary in this case is exhaustively treated in the work of Ricou (1982) and more precisely in Müller (2006).

In the absence of external magnetic fields the PMP probe allows to detect liquid metal velocities in the range from 0-10 m/s with an extreme high sensitivity of about 1 mm/s (Horanyi, 1988; Knebel, 1994; Ricou, 1982; Weissenfluh, 1988). The sensitivity and the velocity range is not restricted and scopes several decades, which is not possible with other techniques. Generally this technique is applicable up to temperatures of 720°C as the paper by Ricou (1982) shows with measurements in mercury, aluminium, tin, zinc and some alkali metals. The upper limit of the temperature is given by the Curie temperature of the magnet, which is e.g. for nickel-based permanent magnets about 860°C, see e.g. Eringen (1980). Due to responses that are steady, instantaneous and proportional to the velocity of the liquid metal flow high temporal resolutions can be resolved, which is necessary for the study of turbulent flows.

Although an intrusive method, modern fabrication technologies allow to miniaturise the PMP probe down to diameters less than 2-3 millimetres and thus to minimise the impact of the probe on the flow.

One of the most crucial problems of the PMP is the wetting behaviour in the sense of an electro-chemical wetting without any contact resistance between the fluid and the probe. Regarding the alkali metals this is not a problem. However, lead and its alloys show a poor electro-chemical wetting behaviour of steel surfaces. Similarly as for the UDV probe the PMP has been plated with nickel or silver as a sacrificial layer, which is dissolved immediately by the lead-bismuth in order to ensure a proper wetting of the sensor. Nevertheless, after two weeks exposure of the probe to lead-bismuth in the composition $Pb^{45}Bi^{55}$ at 400°C the wetting got lost even in an oxygen controlled atmosphere. Also within a reducing atmosphere by means of hydrogen input into the loop the wetting of the probe could not be recovered again (Knebel, 2001). This wetting problem is an issue

which is currently not fully understood and requires a detailed investigation in order to develop HLM adapted sensors.

Hayachi (1999) demonstrated the potential of replacing the permanent magnet by an electromagnet. The principle is proven up to an environment temperature of 970 K. Miralles (2011) proposed a modification of the PMP principle by introducing integrated Hall-effect sensors as magnetic sensors for the induced magnetic field. Advantages claimed include no sealing at the electrode location, no concern of chemical compatibility or wetting issues between the fluid and the electrodes and no electrode contamination. The probes were used in gallium.

11.4.3 *Electric-potential difference probes (EPDP)*

In liquid metal flows with applied external magnetic fields, local velocity components might be determined measuring local potential differences, basically guided by Ohm's law. However, this technique requires careful considerations, specific for the set-up of the experiment, the flow structure and the magnetic field arrangement. Examples for such measurements can be found in Bojarevics (2006). There, possibilities of flow and free surface control by means of a superimposed DC magnetic field have been investigated experimentally at an inductively stirred melt contained in a rectangular crucible. Cramer (2012) reports about turbulence measurements in a rotating magnetic field-driven flow, based on potential difference measurements. Gallet (2009) reports an experimental investigation on the influence of an external magnetic field on forced three-dimensional turbulence of liquid gallium in a closed vessel.

11.4.4 *Mechanical-based techniques*

11.4.4.1 Reaction probes (RP)

Especially in steel and aluminium casting or in molten salts where the liquid is highly corrosive, reaction probes are used, which are based on the measuring of the force exerted on a submerged body by the flowing liquid. The submerged bodies used in different studies could be discs, plates or spheres. The operation principle of a reaction probe sensor is akin that of a Pitot tube, in that the device responds to the stagnation pressure developed when the fluid impacts the disc. The flow velocity u can be easily calculated using Bernoulli's equation:

$$u = \sqrt{\frac{2F}{A}} \tag{11.40}$$

where F is the force on the disc and A its area. A sketch of such a reaction probe is shown in Figure 11.4.6(a). Here the flow faces the disc and the connected wire compresses a spring. By measuring the compression using a triangulation method the mean velocity can be calculated. The fluctuations are captured by a strain gauge. Even in this simple set-up the measurements of Szekely (1977) showed quite sensible and reproducible results. The temporal resolution of the probe was particularly fine. The disc probe also requires a specific calibration procedure and it can only be used in a limited velocity range, due to the secondary flow, which is induced by the disc. Moreover, this simple sensor is only capable of detecting one velocity component. Due to the decoupling of the sensor element from the liquid with its elevated temperatures, conventional and reliable technology can be used.

A more sophisticated design of a reaction probe was developed by Moore (1982), in which the drag force acting on a sphere is utilised to deduce the velocity. This probe type is depicted in Figure 11.4.6(b). A perforated sphere was used to effectively eliminate the vortex shedding and to increase the drag. In this set-up the sphere was made of tantalum with a diameter of 5 mm. Strain gauges were bonded to either sides of the steel strip, which was connected to the sphere via a 1 mm wire.

The signals from the drag reaction probe can measure the drag experienced by the shell and the connecting wire. The mean drag force D integrated over the sphere facing the flow is related to the velocity by:

$$D = \frac{1}{2}\rho A' C_D u^2 \tag{11.41}$$

where ρ is the specific density, A' the cross-sectional area normal to the flow and C_D the drag coefficient, which depends in most cases on the Reynolds number. According to Schlichting (1979) the drag coefficient of a sphere, however, is in the Reynolds number range from $2{\cdot}10^3 < Re < 2{\cdot}10^5$ almost constant. In the study performed by Moore (1982) this was accomplished by the proper selection of the dimensions of the tantalum sphere. After a calibration in an annular duct flow the probe showed an excellent performance regarding the mean velocity fields, see El-Kadah (1984). Because of the high temporal resolution of the strain gauges a large bandwidth of oscillations of the turbulent flow could be captured so that fast Fourier transforms up to 2-3 kHz could be performed. A comparison of the duct flow data with numerical studies computed by Evans (1983) demonstrated that the precision achieved with this type of reaction probe was the best compared to similar probe types and matched the model better than 5%.

Figure 11.4.6: Reaction probes

(a) Disc reaction probe used by Szekeli (1977)

(b) Drag force reaction probe by Moore (1982)

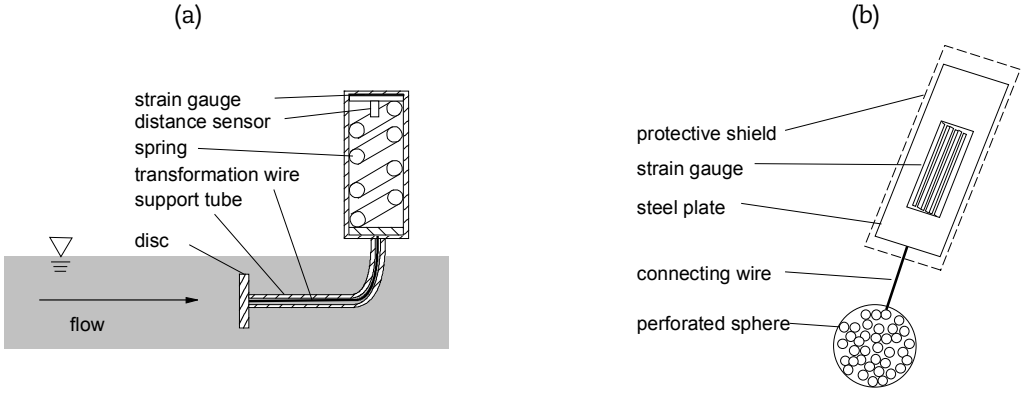

The initial probe designed by Moore was modified by Moros (1985) in such a way as to simultaneously measure the vertical and one of the horizontal velocity components. A sketch of the Moros (1985) reaction probe type is shown in Figure 11.4.7.

Figure 11.4.7: Modified two-component drag reaction probe designed by Moros (1985)

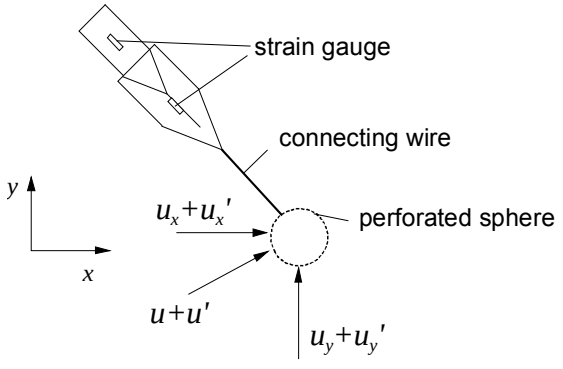

Eckert (2000) presented an improvement of RP called the mechano-optical technique, based on the separation of the mechanical interaction between fluid and sensor tip and the optical acquisition and processing of the signal. The probe can be used at high temperatures, and is insensitive to electrical noise and external magnetic fields. The probe has been tested in an InGaSn eutectic melt at room temperature, as well as at higher temperatures (350°C) in PbBi and SnBi. Cramer (2004) reports on local velocity measurements in electrically driven vertical flows using the mechano-optical probes, where the flow structures are in the same dimension as the probe.

Since all reaction probe types are intrusive methods they suffer from various shortcomings, which are:

- *Mechanical oscillations*. The oscillation of the suspended probe has to be kept within an acceptable range in order to resolve the desired velocity value. The sensor has to be mechanically decoupled from the piping to avoid miscellaneous readings (which gives an advantage to the mechano-optical probe mentioned above). The design of the drag element and the connection wire predefines the damping of the sensors and thus its temporal resolution.
- *Dimension of the drag body*. The dimension of drag body and wire must be chosen in such a way to keep the drag coefficient in the velocity range of interest most insensitive to the Reynolds number. Otherwise a time-consuming calibration over the whole velocity range to be expected in the individual geometrical experimental set-up must be performed in a reference experiment to measure $C_D(Re)$.
- *Probe impact on the flow*. Since the body of the reaction probe induces secondary flows it impacts and modifies the flow to be measured. The pressure waves may have an upstream effect and the secondary flows induced by the drag body may change the flow in such a way that the effect to be measured can be hidden behind the artificial flow modifications. Thus, the flow field in the experimental set-up to be investigated should be identified before the use of reaction probes.

Aside from these shortcomings the reaction probes offer the opportunity to measure in liquid steel baths with temperatures of more than 1 500°C, which is currently not accessible with any other technique.

11.4.4.2 Fibre mechanics systems (FMS)

The measuring apparatus of FMS is based, like the reaction probe, on simple mechanics in the way that a mechanical sensor, which is in direct contact with the hot liquid, is mounted rigidly on an optical system used to acquire the measuring data. The thin tip of the probe shaped by a special glass manufacturing technique in the form of a cone acts as the sensitive part. A small glass rod, the so-called pointer, having a length of the order of 10-50 mm depending on the desired sensitivity of the probe, is positioned inside this glass tube and connected with the sensor tip ideally only at the front point. Technically it is bonded mostly over a length of 1 mm. The initial position of the free end of the pointer is approximately located in the centre of the glass tube. In the presence of a fluid motion around the tip the sensor reacts in the form of an elastic deformation as shown in Figure 11.4.8(a). Consequently, at the opposite end a resulting spatial shift of the pointer can be observed by optical means in the opposite direction of the displacement of the sensor tip. The deflection of the tip is a function of the fluid velocity at the tip. The evaluation of the direction and the amplitude of the pointer displacement allows to determine the two velocity components perpendicular to the sensor. Therefore, an endoscope combined with a lens system connected to a CCD array is used to observe the pointer image. The information is stored by digitalisation and analysing of the images using a frame grabber.

Figure 11.4.8: Mechano-optical probe

(a) Measurement principle of a mechano-optical probe
b) Stereo-microscopic photograph of a mechano-optical probe with an attached sphere by Eckert (2003)
(c) Mechanic model of the displacement of the probe tip by the flow to evaluate the flow velocity

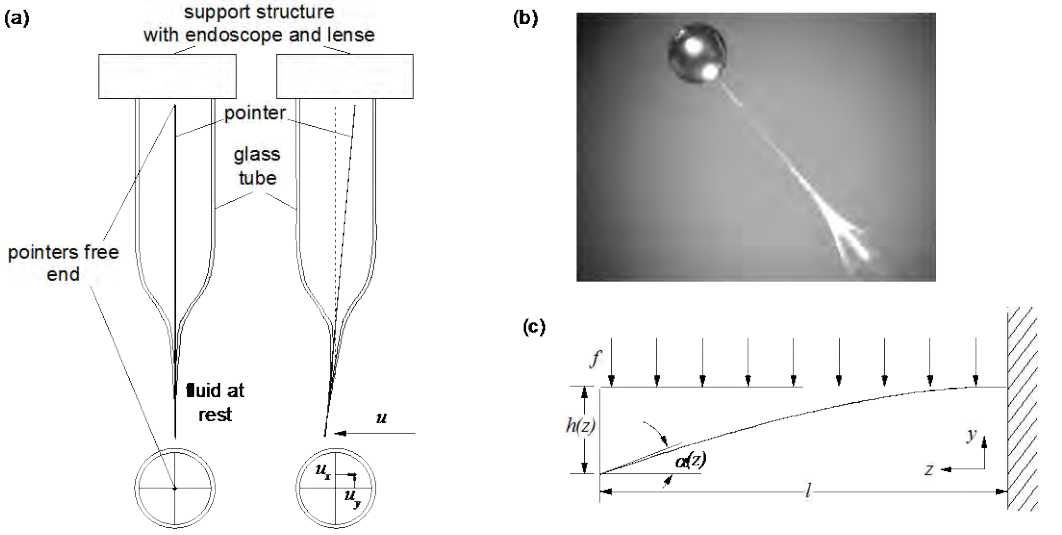

Initially such systems were invented by Zhilin (1987, 1989) and Boyarevich (1990). However, higher resolution, successful miniaturisation and implementation to higher melting point liquids were reached by Eckert (2000). Probe tips with diameters around 50 μm were fabricated and pointers with a length of 30-40 mm were embedded. The bonding of tip and sensor was only 1 mm, which represents the integration length scale of the sensor in the flow.

A critical point is the choice of sensor material. The material has to obey Hook's law and must be temperature and chemical resistant to the fluid of interest, e.g. boron silicate glass is favourable for applications up to 350°C in sodium, gallium but also InGaSn, SnPb, SnBi or PbBi. It exhibits a constant elastic modulus E up to 400°C (Scholze, 1965) and is even stable against sodium (compare Eckert [1997]). Moreover, the fabrication technology and handling of this glass type is simple. For higher temperatures quartz-glass tips can be used, which operate up to temperatures of 800°C (Eckert, 2003).

In order to calculate the pointer displacement the sensor tip is considered as a mechanical element in the configuration shown in Figure 11.4.8(c). A flow around the tube causes a more or less constant force per unit length $f = \rho r u^2 \cdot C_W$ leading to a deformation of the sensor, where r is the radius of the tube and l its length, ρ the specific fluid density, u the velocity and C_W the drag coefficient. The displacement of the tube from the equilibrium position is described by the parameter $h(z)$.

Assuming that the tube is bent by a torque M_x in x direction the displacement is expected parallel to the y direction. The original x-z sections are not deformed and remain transverse to the y axis. If we consider only small displacements $h(z)$ and the wall thickness δ is small compared to r then the moment of inertia transverse to the tube I_x can be approximated by $I_x = \pi \cdot \delta \cdot r^3$. Thus, one gets an ordinary differential equation for the force f in the form:

$$f = \frac{d^2 M_x(z)}{dz^2} = E \cdot I_x \cdot \frac{d^4 h(z)}{dz^4} \qquad (11.42)$$

where the elastic modulus E and the moment of inertia in x direction I_x are assumed to be constant. Imposing the boundary conditions $h = (dh/dz) = 0$ at $z = 0$ and $M_x = (dM_x/dz) = 0$ at $z = l$ one obtains:

$$h(z = l) = \frac{C_W \rho u^2 l^4}{8E\pi r^2 \delta} \tag{11.43}$$

According to the drag curve for a flow around a cylinder (Brauer, 1971) the C_W value can be considered as constant in a wide range such that a parabolic dependence of the measured quantity $h(z)$ can be expected. A significant influence of the probe geometry in terms of r, l and δ becomes obvious, which allows a defined adjustment of the sensor with respect to the desired velocity range.

An enhancement of the sensitivity can be obtained by attaching a sphere to the sensor tip (Section 11.4.3). If the radius of the sphere r_s is significantly larger than the fibre shaft the bending is mainly governed by the sphere at the end of the fibre. Thus, the boundary conditions applied to Eq. (11.44) are $h = (dh/dz) = 0$ at $z = 0$ and $M_x = 0$, $(dM_x/dz) = -F_s$ at $z = l$, where F_s is the force acting on the sphere, which yields:

$$h(z = l) = \frac{C_D \rho r_s^2 u^2 l^3}{6E\pi r^3 \delta} \quad \text{with} \quad F_s = \frac{\pi}{2} C_D \rho r_s^2 u^2 \tag{11.44}$$

Since the drag coefficient of a sphere C_D is even less sensitive to the Reynolds number than that of the tube, i.e. it is almost constant for $10^2 < Re < 3 \cdot 10^5$, an increase of the sensitivity by a factor three can be attained. Such a sensor type is shown in Figure 11.4.8(b).

To extract the actual velocity from the measurements each sensor tip has to be calibrated separately. Due to the dependence of the pointer displacement on the fluid density the calibration procedure has to be performed with the same liquid as the experiment conducted later on.

11.4.5 *Hot wire anemometry (HWA)*

Quite a lot of problems arise when using hot film anemometers in liquid metal flows. The main question is the chemical compatibility of the liquid metal and the hot wire, in which surface tension and heat transfer aspects have to be considered. If alkali or earth alkali metals are used for the loop the compatibility of the wire with the liquid may become a killing issue, due to the low electro-chemical potential of these liquids. Up to now only silicon oxide plated wires of hot wire anemometers show no degradation in connection with NaK at temperatures up to 100°C (Reed, 1986, 1987, 1989). Murthy (1983) went with Wood's metal up 120°C, but nearly all other hot film measurements were restricted to mercury, gallium or other low melting liquid metals or alloys (Malcolm, 1969; Hill, 1971; Platnieks, 1971; Sleicher, 1975). Only one example of an application reaching a temperature of 250°C in $Na^{44}K^{56}$ was found (Hochreiter, 1969); this is also the case for an example for sodium up to 300°C (Platnieks, 1984).

Surface effects which occur due to impurities in the liquid metal lead to reaction and change the characteristics of the probe. Only by an appropriate cleaning of the probe can such an effect be avoided. Another issue related to MHD that has to be considered is the use of hot wire probes. In principle, the hot wire probe measures the heat transfer from the wire. The heat transfer in an MHD flow, however, is different from that of an ordinary hydrodynamic flow. The measurements of Lykoudis (1973) show that the Nusselt number Nu strongly depends on the Hartmann number M or Ha (see Eq. [11.6]) and the hydraulic Reynolds number, see Figure 11.4.9. Thus, a calibration measurement of the hot wire anemometer for each measured magnetic field strength has to be performed.

Figure 11.4.9: Dependence of the Nusselt number *Nu* on the Reynolds number *Re* and the Hartmann number *M* (or *Ha*) in a hot wire calibration measurement performed by Lykoudis (1973)

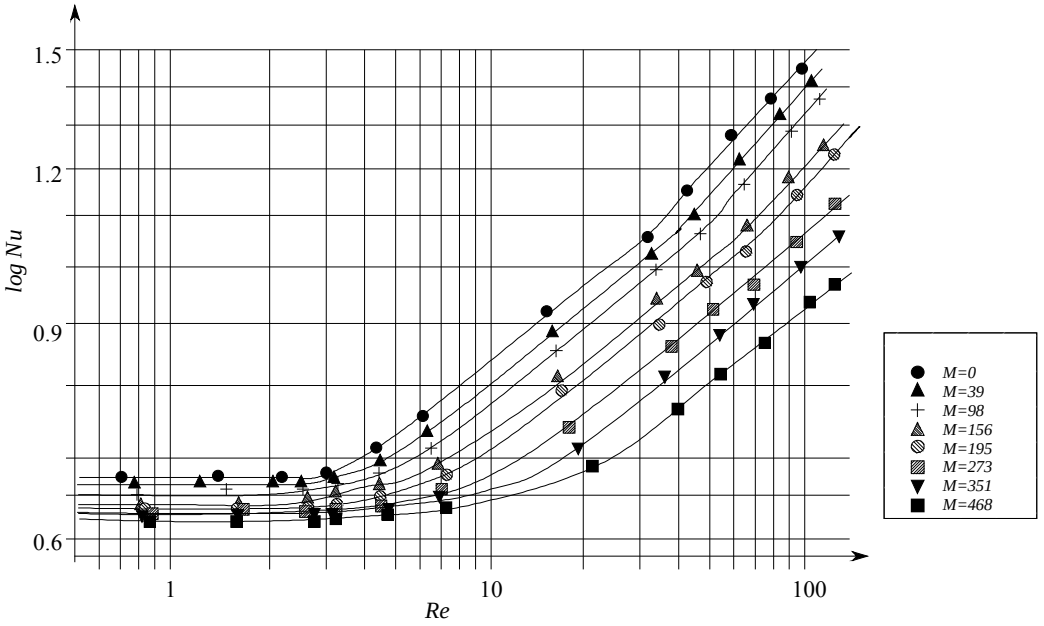

Contrary to the potential probe, the hot wire anemometer is not capable of detecting the direction of the flow, because it measures the integral heat transfer at the wire (Hill, 1971). Therefore correlation measurements, which are necessary to determine vortex structures in turbulent flows, cannot be performed using this probe type. Another disadvantage of the hot film probes originates from the low Prandtl numbers of the liquid metal leading to a drastic reduction of the probe resolution, because the conductive heat transfer in liquid metals is favoured compared to that of convective heat transfer. Hot wire-type probes exhibit interesting features with a crucial advantage compared to reaction probes and PMP sensors. They are rather small; the wires are only some microns thin and thus hardly affect the flow. On the other hand, the probe is not very robust. A schematic drawing of an HWA probe is shown in Figure 11.4.10.

Figure 11.4.10: Schematic drawing of hot wire anemometer

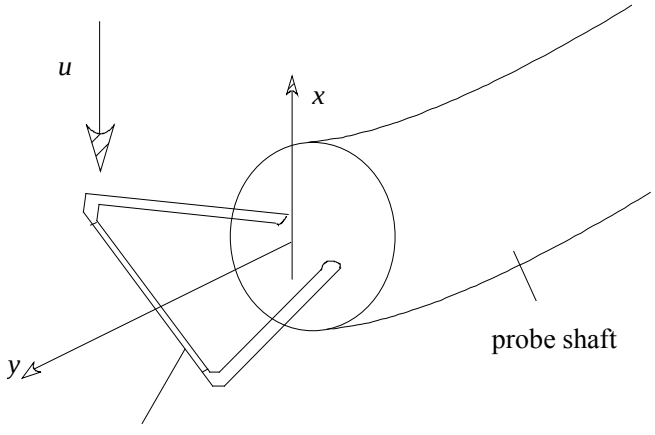

The high thermal conductivity of liquid metals plus the necessity of keeping a nearly constant temperature makes the use of HWA probes difficult. Another problem is a drift that may occur in the signal because of the disposition of oxide in metals. In Szekeli (1988) it is reported that despite protective blankets of inert gas it is common to encounter drift in the signal due to fouling of the probe by oxide in both mercury and Wood's metal.

Another issue related to HWA probes is that the sensitivity of the probe is inhibited at low Peclet numbers. Here, even at quite low flow frequency oscillations the low Prandtl number of the liquid metals yields to a reduction of the signal (Malcolm, 1981). The Peclet number is defined by the product of the Reynolds number with the Prandtl number:

$$Pe = Re \cdot Pr \quad \text{with} \quad Pr = \frac{\nu \rho c_p}{\lambda} \tag{11.45}$$

where ν is the kinematic viscosity (m^2/s), ρ the specific density (kg/m^3), c_p is the heat capacity (J/[kg K]) and λ is the heat conductivity (W/[m K]). For the observed decreasing sensitivity at low Peclet numbers two effects are responsible:

- The amplitude of fluctuation is attenuated and the degree of attenuation depends upon a non-dimensional quantity $\kappa f/u^2$ in the range of Peclet numbers up to 10, where κ is the thermal diffusivity given by $\kappa = l/(rc_p)$, f the frequency of the fluctuations and u the mean flow velocity. The amplitude is attenuated by 10% and 90% at $\kappa f/u^2$ values of 0.02 and 4.0 respectively.
- There is a phase lag in the HWA signal with respect to the true velocity of the fluctuation which is about the same as that in potential flow at low frequencies, but is considerably higher than that in potential flow at higher frequencies. The measured lag does not level off asymptotically at high frequencies.

11.4.6 Transition time methods

11.4.6.1 Temperature pulse method

The temperature pulse method is based on the measurement of the decay time of temperature pulses in a medium. The fluid velocity can be calculated from the propagation time of the temperature pulse. The temperature waves are produced by a miniaturised heater, which is surrounded in defined positions by thermocouples. The propagation of a temperature pulse in a fluid at rest is shown in Figure 11.4.11(a). A drawing of the measurement instrument is shown in Figure 11.4.11(b). A problem may arise with this measurement method in fluids with extremely low Prandtl numbers like in liquid metals, because there a temperature pulse diffuses rather fast. Therefore, high temperature pulses have to be brought in the liquid metal in order to enable a resolvable measurement of temperature changes in small distances from the miniaturised heater. A determination of the velocity vector is only possible if a grid of thermocouples is placed next to the heater. However, such a grid affects the flow in a non-negligible manner. A second aspect which should be also considered is the choice of the thermocouples for this method (see Section 11.6). Casal (1988) demonstrated the viability of this measurement method in water and also in liquid metals. Nevertheless, the resolution of this method in liquid metals is rather poor (around ±25%) and the technical effort high. Another assessment of the error connected with this method can be found in Adamovskii (1986).

Figure 11.4.11: (a) Temperature propagation of a temperature pulse as a function of the time t; (b) Schematic drawing of a temperature pulse measurement instrument to detect velocity vectors in sodium-potassium $Na^{22}K^{78}$ by Casal (1988)

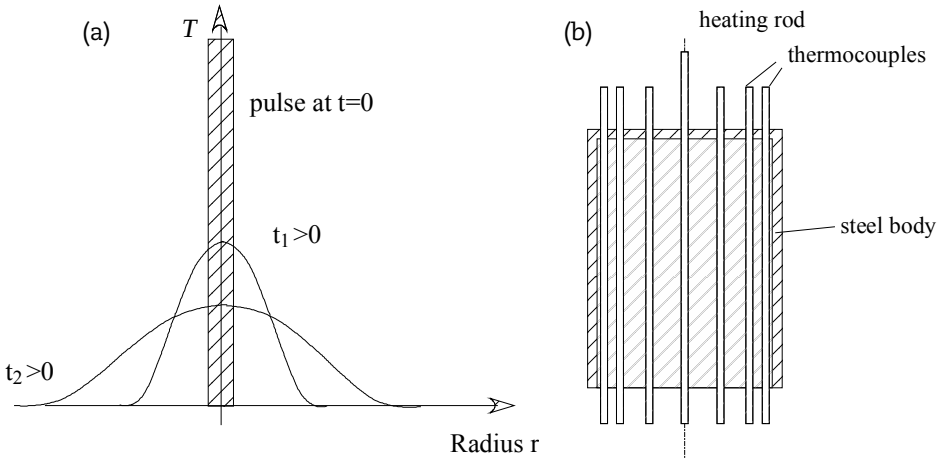

11.4.6.2 Tracer studies

Tracer studies were initially developed for velocity and diffusivity measurements in molten salts. In using this technique a small amount of tracers is introduced at a defined time *t* at a discrete point of the flow field, while downstream the liquid is sampled periodically. A simple representation of this technique is sketched in Figure 11.4.12(a). If the integrity of the tracer is ensured for the duration of the experiment and assuming isotropic conditions, the tracer concentration *C* in a radial co-ordinate system is given by Eq. (11.46):

$$\frac{\partial C}{\partial t} = \frac{D_t}{r^2}\frac{\partial}{\partial r}\left(r^2\frac{\partial C}{\partial r}\right) \tag{11.46}$$

where D_t is the molecular diffusivity in case of laminar flows or the effective diffusivity considering turbulent flows. In principle the tracer studies are a coupled initial and boundary problem for which the following conditions are assumed:

$$C = 0 \quad \text{at} \quad r \to \infty; \quad C \quad \text{finite for } t > 0, \text{ at } t = 0 \quad C = \delta(t = 0) \tag{11.47}$$

The solution of Eq. (11.46) under the conditions in Eq. (11.47) is given by:

$$C = \frac{A}{2\sqrt{\pi D_t t^3}}\exp\left(-\frac{r^2}{4D_t t}\right) \tag{11.48}$$

where *A* is a constant. However, for a moving co-ordinate system the location r_{Sensor} of the sampling sensor is given by $r_{sensor} = d - u \cdot t$, where *u* is the probe flow velocity such that Eq. (11.48) mutates to:

$$C = \frac{A}{2\sqrt{\pi D_t t^3}}\exp\left(-\frac{(d - u \cdot t)^2}{4D_t t}\right) \tag{11.49}$$

By fitting the measured concentration curve (Figure 11.4.11[b]) to Eq. (11.46) the quantities *u* and D_t can be determined. There are problems arising from the above interpretation with the path pursued by the fluid between the point where the tracer was introduced and the sampling point, the tracer decay, while the velocities measured in

this way are average values over a relatively large region. Velocity and diffusivity measurements are reported by Grjotheim (1970, 1971) and Berge (1973) for aluminium reduction cells. Tracers may not only be oxides of the fluid investigated but radionuclides can also be used (Szekely, 1964, 1977a, 1977b).

The tracer methods allow to measure even in steel and iron bath but their accuracy is rather poor and a great deal of pre-knowledge of the velocity in the domain of interest is required. In all cases measurements and theoretical predictions agreed within a factor of ±50%.

Figure 11.4.12: (a) Schematic representation of the tracer technique; (b) Tracer concentration at a downstream sampling point as a function of time

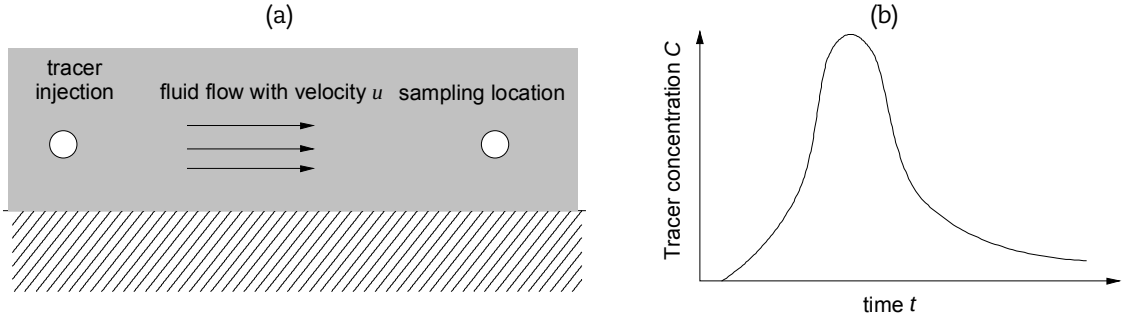

11.4.6.3 Dissolution and melting studies

Measurements of metal velocities from the mass lost of iron rods introduced in liquid aluminium were initially developed by Johnson (1978) and subsequently improved Taberaux (1984). The latter derived calibration curves correlating mass loss with liquid metal velocity by measuring the iron rod mass lost in a stirred tank using a load cell. Here the following correlations are used:

$$Sh = A + B \cdot Re^{n} Sc^{m} \tag{11.50}$$

where *Sh* is the Sherwood number, *Re* the Reynolds number, *Sc* the Schmidt number and *A, B, n* and *m* are constants. The characteristic numbers are defined as:

$$Sh = \frac{\beta \cdot d}{D_t}, \mathrm{Re} = \frac{u \cdot d}{\nu} \text{ and } Sc = \frac{\nu}{D_t} \tag{11.51}$$

β is the mass transfer coefficient and is not a material property. It depends on the concentration, velocity and temperature field and has the dimension of the velocity.

Due to the dependence of the mass transfer coefficient β on flow, concentration and temperature field, a sophisticated calibration procedure is required which is described in detail by Bradley (1984). Besides aluminium this method has been also applied to steel melts by El-Kaddah (1984). By determining the extend of dissolution for specific time intervals, the local mass transfer coefficients are calculated and compared to the predicted ones using both laminar (Eq. [11.52a]) and turbulent correlations (Eq. [11.52b]), which were found experimentally by Grevet (1982) and Szekely (1984):

$$Sh = 0.683 \cdot Re^{0.466} \cdot Sc^{\frac{1}{3}} \;;\; Sh = 0.338 \cdot \left(Re \times Tu\right)^{0.8} \cdot Sc^{\frac{1}{3}} \tag{11.52a,b}$$

Herein, *Tu* is the turbulence intensity. *Tu* and *Re* were an input to the above-named correlations from a numerical simulation. A clear analysis of the Eqs. (11.52a,b) rapidly exhibits that both of them have an error of about ±25% (Jischa, 1982).

A comprehensive elaboration on local velocity measurements using melting probes in an aluminium induction furnace is given by Mikrovas (1993). The apparatus is shown, the probe and measurement principle and the realisation are explained in a detailed manner, a careful error estimation is made and detailed results are shown. It is claimed that a measurement accuracy of 10% can be achieved if certain conditions are fulfilled, particularly careful and extensive calibration. A similarly comprehensive elaboration on a melting technique for aluminium has been presented by Melissari (2005), who went so far as to test sphere probes with three thermocouples to detect local velocity direction.

11.4.7 *Neutron radiography*

The attenuation of neutron rays for heavy liquid metals is small. Therefore, the flow in these liquid metals can be seen by neutron rays. An initial method to visualise the flow of a liquid metal by tracer and dye injection using neutron radiography has been made by Takenaka (1994a) using an accelerator-based real-time neutron radiography. In these first studies a fluorinated hydrocarbon, which is transparent for neutrons, was used. For use in heavy liquid metals, however, particles having a similar density are required. Takenaka (1996) reports that for use in eutectic lead-bismuth gold cadmium ($AuCd_3$) intermetallic alloy particles were successfully applied, since they wet well by this liquid and its density is close to that of the metal. The flow can be visualised by watching the movement of the individual particles by real-time radiography and a digital image post-processing procedure.

The image post-processing method used is the same as for particle image velocimetry (PIV), in which the acquired images of the moving tracers are obtained by subtracting the time-averaged image from the original one. With two consecutive images of the moving tracer, pattern matching is carried out at each point to obtain the flow vector by calculating the spatial correlations. Since the tracers are much larger than one image element, i.e. that of noises in the experiment, the tracers' image can easily be obtained by using a spatial filter in the image processing programme. Because the noise is random and has no correlations, the noise does not affect the spatial correlation of the tracer signals. The spatial correlation function $\Psi(u,v)$ between the data of two consecutive images $f_1(x,y)$ and $f_2(x,y)$ is defined as:

$$\Psi(u,v) = \iint f_1(x-u, y-v) \cdot f_2(x,y) \quad dx\,dy \tag{11.53}$$

Takenaka achieved temporal resolution of 30 Hz using this method. The most probable movement of the tracers' pattern is indicated by (u,v) at the peak of the function, and the flow vector can be determined. Since the noises are random, the spatial correlation method is applicable to the images where the tracer and the noise cannot be divided by any spatial filters. Reasonable vector fields with an uncertainty of less than 10% could be obtained in lead-bismuth eutectics, the thickness of which is 25 mm, i.e. the attenuation rate is about $1/e$, by the spatial correlation method even if the tracer sizes were the same order as those of the image noises. Since the attenuation coefficients of sodium and sodium-potassium are much smaller than that of lead-bismuth, flow in thick liquid metal layers of alkali metals can be visualised.

11.4.8 *Pitot and Prandtl tubes*

11.4.8.1 *General features and application*

The measurement principle of Pitot and Prandtl tubes was previously discussed in Section 11.2.3.2 in the context of flow rate measurement. Thus only a few remarks on the operational experience for local velocity measurements are made here. Via miniaturisation of the sensors local velocities and – if thermocouples are embedded – heat fluxes can be measured. The resolution of this local measurement technique is given by the resolution of the pressure gauges used.

Within the THESYS loop of KALLA, which uses Kulite pressure transducers, the local velocity could be determined with an accuracy of ±5 mm/s (Schulenberg, 2010). The Pitot tube used there is sketched in Figure 11.4.13(a) and is capable of resolving a pressure of 12.5 Pa. Higher resolutions may be obtained by more sensitive sensors. A typical turbulent velocity profile and the corresponding temperature profile which has been measured by means of a combined Pitot tube with two thermocouples in a circular tube at a temperature of 300°C is depicted in Figure 11.4.13(b).

Figure 11.4.13: Measured velocity and temperature in the Pitot tube

(a) Pitot tube with small thermocouples to measure local velocities $u(z)$ and temperatures $T(z)$ and their fluctuations developed at KALLA (Schulenberg, 2010)

(b) Measured mean velocity and temperature in a turbulent lead bismuth pipe flow at 300°C with the Pitot tube depicted in (a)

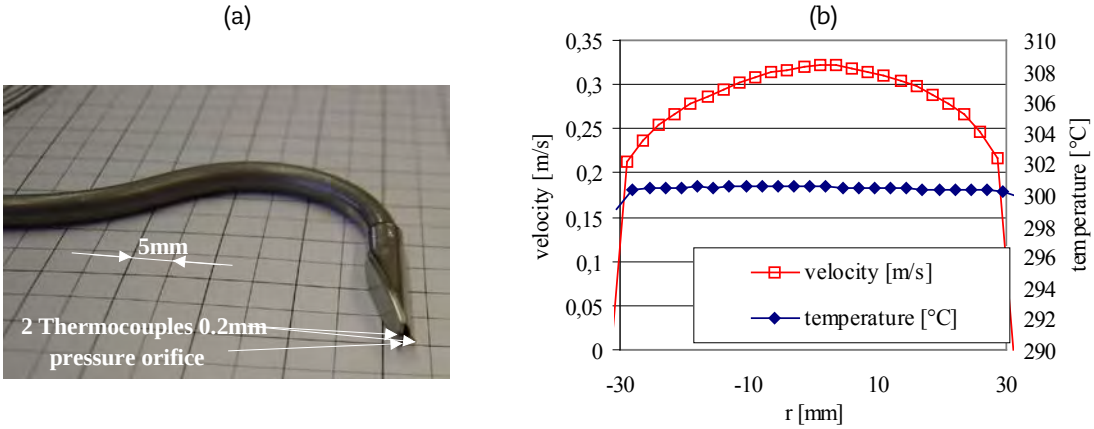

The smallest spatial dimension over which the velocity is integrated is given by the size of the orifice of the Pitot tube. Since the surface tension of heavy liquid metals like lead or lead-bismuth is quite large and of the order O(10^2 mN/m) the pressure difference required to fill the tube orifices significantly increases with the degree of miniaturisation. A reliably operating Pitot tube system is only obtained for a gas-free tube. Thus, drain tubes to ensure a complete filling of the sensor are required. Due to the large Reynolds numbers appearing in HLM flows the boundary layers appearing there are relatively thin and thus only near to the region towards the main flow resolvable with Pitot tubes. An experimental example of the flow field measurement using a Pitot tube near a heated rod in an annular cavity is shown in Figure 11.4.14. In order to acquire the flow distribution within the boundary non-intrusive methods such as UDV are required.

In order to obtain accurate mean velocity profiles using a Pitot tube many corrections need to be made to account for the effects of viscosity, turbulence, velocity gradients and the presence of a wall. Measurements by Zagarola (1998) in a turbulent pipe flow in a Reynolds number regime from $3.1 \cdot 10^3 < Re < 3.5 \cdot 10^7$ have raised questions regarding the accuracy and applicability of the current correction methods, which are summarised in the work of Perry (2001). In pipe flows with Reynolds numbers around 10^5-10^6, which easily appear in heavy liquid metal applications, there is a difference of greater than 5% in the slope of the logarithmic region between data with and without wall correction (McKeon, 2003).

Figure 11.4.14: Measured mean velocity u_z (m/s) near a rod in an annular cavity as a function of the radius r (mm) at T_{in} = 300°C for different Reynolds numbers Re at z/d = 13.9

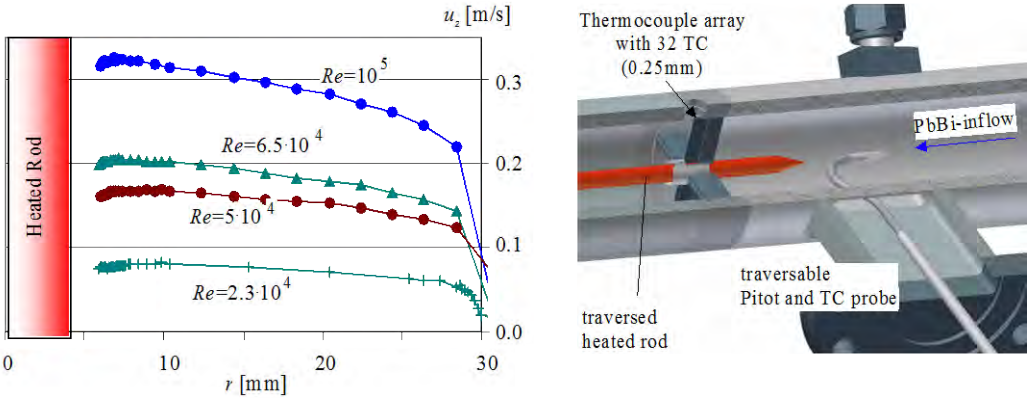

Source: Lefhalm (2004b).

11.4.8.2 *Viscous corrections for Pitot tubes*

Viscous corrections are important if the Reynolds number based on the probe diameter, Re_d, falls below 10^3. This is one of the most important and most often forgotten corrections while using Pitot tubes. If the Reynolds number Re_d is larger than 10^2 the viscous correction is in the range of 0.5% (Zagarola, 1996); for smaller values of Re_d, however, it can reach several per cent. Using earlier pipe flow results (Barker, 1922; Reichardt, 1951; Hurd, 1953), MacMillan (1954, 1956), Chue (1975) and Zagarola (1996) suggested that for $Re_d > 30$ the following relation should be applied:

$$C_P = 1 + \frac{10}{(\mathrm{Re}_d)^{3/2}} \tag{11.54}$$

where C_P is the measured pressure coefficient. Due to the numerous experimental data Eq. (11.54) can be considered as a true representation of the viscous effects on the Pitot tube data.

11.4.8.3 *Turbulence correction for Pitot tubes*

The effects of turbulence on the Pitot tube reading are twofold. First, the velocity fluctuations increase the measured pressure. Second, when measurements are taken using a pressure tapping at the wall to measure the static pressure, the radial gradient in static pressure due to velocity fluctuations must be taken into account. The combined effect of these two phenomena is given by Ozarapoglu (1972) by:

$$\frac{u - u_m}{u_m} = -\frac{\overline{u^2} - (1 + K_t)\overline{v^2} + (1 + K_t)\overline{w^2}}{2u_m^2} \tag{11.55}$$

where u is the true mean velocity, u_m is the measured mean velocity and $\overline{u^2}$, $\overline{v^2}$ and $\overline{w^2}$ are the mean square velocity fluctuations in the streamwise, radial and circumferential directions. K_t is a coefficient that accounts for the directional sensitivity of the Pitot probe and is for circular taps around 0.3. While measuring close to the wall, Dickinson (1975) suggested that for $y^+ > 50$ Eq. (11.55) could be simplified as:

$$\frac{u - u_m}{u_m} = -\frac{\overline{u^2}}{2u_m^2} \tag{11.56}$$

accepting errors of ±0.5%. Here, the dimensionless wall distance y^+ is defined as:

$$y^+ = \frac{\Delta y \cdot u_\tau}{\nu} \quad \text{where} \quad u_\tau = \sqrt{\frac{\tau_\omega}{\rho}} \tag{11.57}$$

where u_τ is the friction velocity, Δy is the wall normal distance from the wall, τ_ω the wall shear stress and ρ and ν the specific fluid density and kinematic viscosity.

11.4.8.4 Velocity gradient correction for Pitot tubes

In a shear flow the presence of the probe deflects the streamlines so that the probe registers a velocity that is higher than the velocity at the geometric centre of the probe. In order to account for this interference effect, which usually dominates all other Pitot tube errors, a correction is made which can be expressed as an error in the measured velocity or as an apparent shift in the probe location. The origin of this error is shown schematically in Figure 11.4.15.

Figure 11.4.15: The effect of a Pitot tube on the streamline pattern

In a shear flow (left) and in a uniform flow (right) near a wall without adhesive wetting

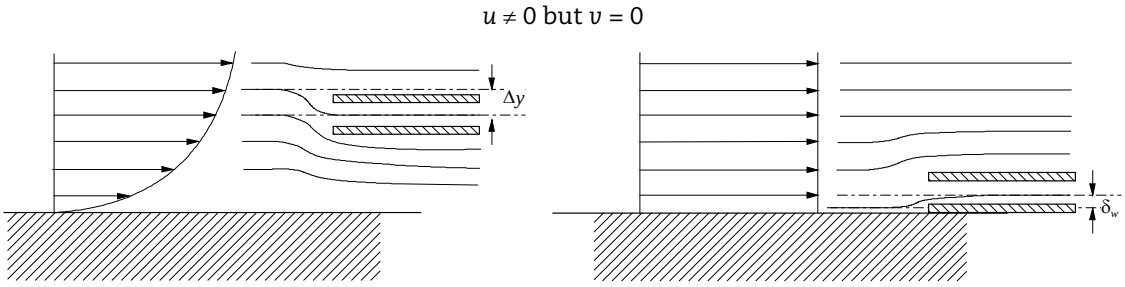

If the velocity gradient across the Pitot tube is small compared to its mean value and additionally if we assume that the mean velocity is a function of y only then one can deduce:

$$\frac{\Delta u}{u(y_c)} = \frac{u(y_c + \Delta y) - u(y_c)}{u(y_c)} = 2\alpha\frac{\Delta y}{d} - \beta\frac{(\Delta y)^2}{d^2} + \ldots. \tag{11.58}$$

where y_c is the position of the centre of the Pitot tube, $u(y_c)$ is the true velocity at y_c, Δy is the correction in the position due to the streamline displacement and the velocity gradients are evaluated at the centre of the probe. The probe's diameter is d. The coefficients α and β are defined by:

$$\alpha = \frac{d}{2u(y_c)}\left.\frac{du}{dy}\right|_{y=y_c}, \beta = -\frac{1}{2}\frac{d^2}{u(y_c)}\left.\frac{d^2u}{dy^2}\right|_{y=y_c} \tag{11.59}$$

Eq. (11.58) exhibits that the correction in the velocity and the apparent shift of probe position $\Delta y/d$ are directly connected. In fact, the velocity gradient correction is usually implemented by correcting the probe position rather than by correcting the velocity itself. This form is often called the displacement correction and several authors (MacMillan, 1954; Livesey, 1956; Patel, 1965; Tavoularis, 1989) have suggested that:

$$\frac{\Delta y}{d} = \varepsilon \tag{11.60}$$

where $0.08 < \varepsilon < 0.16$. Other correction correlations for individual applications can be found in works by Chue (1975), Patel (1965) or Zagarola (1998).

In the presence of a wall, an additional mechanism for streamline displacement exists. Consider a Pitot tube resting on the wall in a uniform flow, as shown in Figure 11.4.15 (right). Since it resembles a forward-facing step, it may be expected that the streamlines would be displaced away from the wall, i.e. towards the region of higher velocity (rather than towards the region of lower velocity as in free shear). Therefore, the true correction close to the wall must be some combination of these two effects. MacMillan (1956) had earlier observed this trend and suggested that a wall correction was necessary in addition to the displacement correction for $y/d < 2$. He proposed that it be represented by:

$$\frac{\Delta u}{u} = 0.015 \exp\left[-3.5\left(\frac{y}{d} - 0.5\right)\right] \tag{11.61}$$

It should be noted in this context that the MacMillan corrections were not corrected for the effects of turbulence intensity and velocity gradient. In other words, implementing an additional turbulence correction when using MacMillan's method is not appropriate.

11.4.8.5 Displacement correction for Pitot tubes

The displacement correction is another type of velocity gradient correction, which is more accurate. The best results have been obtained by McKeon (2003) using the following relation:

$$\frac{\Delta y}{d} = 0.15 \cdot \tanh\left(4 \cdot \sqrt{\alpha}\right) \tag{11.62}$$

where α is defined by Eq. (11.59). This form is based on the analysis by Hall (1956) and Lighthill (1957), who found that the displacement correction for a sphere in a velocity gradient could be expressed by a hyperbolic tangent function of the non-dimensional shear. The constants described by McKeon (2003) match experimental data based on the analytical derivation of Hall (1956) in such a way that both collapse identically. Note that this type of correction gives zero displacement for zero shear and asymptotes the MacMillan (1956) correction for large shear, i.e. $\alpha \to 1$.

11.4.8.6 Wall correction of Pitot tubes

The wall correction based on the Preston tube data of Patel (1965) was made under the condition where the probe is under maximum influence of the wall as well as shear, where a Preston tube is simply a Pitot tube resting on the wall. If one assumes that the Preston tube reads the true pressure at:

$$y = 0.5 \cdot d\left(1 + \frac{\delta_w}{d}\right) \tag{11.63}$$

then a definition of the wall displacement correction δ_w is obtained. If the form of the velocity profile is known, $\Delta p_0 = \frac{1}{2}\rho u^2$ may be formulated and substituted in the expression of the logarithmic low for the boundary layer velocity distribution.

Especially for $8 < d^+ < 110$ viscous effects are undoubtedly important, and it is known that α changes significantly, so that one can expect that δ_w will vary with d^+. McKeon (2003) elaborated the following wall corrections applicable for $y/d < 2$:

$$\frac{\delta_w}{d} = \begin{cases} 0.150 \; for \; d^+ < 8 \\ 0.120 \; for \; 8 < d^+ < 110 \\ 0.085 \; for \; 110 < d^+ < 1600 \end{cases} \tag{11.64}$$

11.4.8.7 *Comments on displacement and corrections*

To evaluate displacement and wall corrections it would be convenient if the true velocity profile were known. Unfortunately, the nature of the true profile is still a source of debate, specifically as to what role geometry and/or Reynolds number play, particularly in the buffer region. To clarify this aspect, experimentally non-intrusive methods like LDA in transparent fluids and UDV in opaque ones as well as direct numerical simulations (Eggels, 1994) lead to further insight.

11.4.9 *Flow field mapping*

11.4.9.1 *Contactless inductive flow tomography (CIFT)*

While the measurement of integral values such as the mass flow rate is more or less sufficient in many liquid metal technologies, there are some applications for which knowledge of the entire flow structure would be highly desirable. This applies in particular to the two- or three-dimensional flow fields in the various moulds of liquid steel casting facilities, to the liquid silicon flow in the crucible of Czochralski crystal growth pullers, and also to the heavy liquid metal flow in the lower plenum of accelerator-driven systems such as MYRRHA. In this rather spacious volume the on-line monitoring of the flow pattern would be very valuable, with particular emphasis on the occurrence of recirculation zones and stagnant zones, which could influence the cooling and the physico-chemistry of the lead-bismuth eutectic that is corrosive against the steel.

Contactless inductive flow tomography (CIFT) is intended to provide full two- or three-dimensional pictures of the flow of electrically conducting liquids. When an electrically conducting medium, moving with the velocity $\mathbf{u}$, comes under the influence of an imposed steady magnetic field $\mathbf{B}_0$, an electromotive force (emf) $\mathbf{u} \times \mathbf{B}_0$ is induced that drives an electric current:

$$\mathbf{j}_0 = \sigma\left(\mathbf{E}_0 + \mathbf{u} \times \mathbf{B}_0\right) \tag{11.65}$$

where σ is the electrical conductivity of the fluid, and $\mathbf{E}_0$ is the electric field which results from the emf. The current $\mathbf{j}_0$, in turn, produces an additional magnetic field $\mathbf{b}$, so that the total current $\mathbf{j}$ also becomes dependent on the total magnetic field $\mathbf{B} = \mathbf{B}_0 + \mathbf{b}$:

$$\mathbf{j} = \sigma\left(\mathbf{E} + \mathbf{u} \times \mathbf{B}\right) \tag{11.66}$$

The ratio of the induced magnetic field $\mathbf{b}$ to the imposed magnetic field $\mathbf{B}_0$ is governed by the magnetic Reynolds number:

$$Re_m = \mu\sigma LU \tag{11.67}$$

where μ is the magnetic permeability of the fluid, and L and U are typical length and velocity scales of the flow, respectively. This dimensionless number is, in the most relevant technical applications, smaller than one.

Starting from Eq. (11.66) one can employ Biot-Savart's law for the magnetic field and Green's theorem for the electric potential (Stefani, 1999). In the following, we will only consider the quasi-stationary case, in which the electric field can be expressed by the gradient of the electric potential, $\mathbf{E} = -\nabla\phi$. The resulting integral equation system consists then of one equation for the induced magnetic field:

$$\mathbf{b}(\mathbf{r}) = \frac{\sigma\mu_0}{4\pi}\int_D \frac{\left(\mathbf{u}(\mathbf{r}') \times \mathbf{B}(\mathbf{r}')\right) \times (\mathbf{r} - \mathbf{r}')}{|\mathbf{r} - \mathbf{r}'|^3} dV' - \frac{\sigma\mu_0}{4\pi}\iint_S \phi(\mathbf{s}') d\mathbf{S}' \times \frac{\mathbf{r} - \mathbf{s}'}{|\mathbf{r} - \mathbf{s}'|^3} \tag{11.68}$$

and one equation for the electric potential at the fluid boundary S:

$$\phi(\mathbf{s}) = \frac{1}{2\pi}\int_D \frac{\left(\mathbf{u}(\mathbf{r}')\times\mathbf{B}(\mathbf{r}')\right)\times(\mathbf{s}-\mathbf{r}')}{|\mathbf{s}-\mathbf{r}'|^3} dV' - \frac{1}{2\pi}\iint_S \phi(\mathbf{s}')d\mathbf{S}'\times\frac{\mathbf{s}-\mathbf{s}'}{|\mathbf{s}-\mathbf{s}'|^3} \tag{11.69}$$

From Eq. (11.68) it is evident that the induced magnetic field **b** depends on both the induced primary currents in the volume D and the induced electric potential ϕ at the fluid boundary S. The second term must not be forgotten (as in earlier attempts, e.g. Baumgartl, 1993) since it can be of the same order as the first term. The equation system (11.68) and (11.69) is in principle valid for arbitrary values of Re_m, and provides a suitable mathematical set-up to treat dynamo problems in arbitrary domains (Xu, 2004). For small Rm, however, the induced magnetic field **b** under the volume integrals on the r.h.s. of Eqs. (11.68) and (11.69) can be neglected and the total **B** can be replaced by $\mathbf{B}_0$.

Stefani (1999, 2000a) had shown that the velocity structure of a three-dimensional flow can be reconstructed from the external measurement of an appropriate component of the induced magnetic field and the induced electric potential at the fluid boundary. However, there remains a non-uniqueness concerning the radial distribution of the flow, a fact that can be made plausible by representing the fluid velocity by two scalars living in the whole fluid volume (e.g. the toroidal and poloidal parts). Then it is clear that two quantities measured on a two-dimensional covering of the fluid do not provide enough information for the reconstruction of the two desired 3-D quantities.

Later, Stefani (2000b) developed a general method to avoid the inconvenient electric potential measurement at the fluid boundary. The main idea is to apply the external magnetic field in two different, e.g. orthogonal, directions and measure both corresponding sets of induced magnetic fields. An obstacle to applying this method is the electric potential term at the boundary, the measurement of which is just to be avoided. This problem is solved in the following way: Assume, for a given $\mathbf{B}_0$, all measured induced magnetic field components are collected into an NB-dimensional vector with the entries $b_i^{(B_0)}$. Assume further a certain discretisation of the electric potential at the surface, denoted by an NP-dimensional vector with the entries $\phi_m^{(B_0)}$. The velocity in the domain D is discretised as an NV-dimensional vector with the entries u_k. Then, Eqs. (11.68) and (11.69) can be written in the form:

$$b_i^{(B_0)} = K_{ik}^{(B_0)} u_k + L_{im}\phi \tag{11.70}$$

$$\phi_m^{(B_0)} = M_{mk}^{(B_0)} u_k + N_{mn}\phi \tag{11.71}$$

With $\mathbf{K}^{(B_0)}$ being a matrix of type (NB,NV), **L**a a matrix of type (NB,NP), $\mathbf{M}^{(B_0)}$ a matrix of type (NP,NV), and **N** a matrix of type (NP,NP). Note that only the matrices $\mathbf{K}^{(B_0)}$ and $\mathbf{M}^{(B_0)}$ depend on the applied magnetic field $\mathbf{B}_0$, whereas the matrices **L** and **N** are independent of $\mathbf{B}_0$.

As is well-known from magnetoencephalography (Hämäläinen, 1993), the inversion of Eq. (11.71) is non-trivial due to the singularity of the matrix (**I** – **N**). However, by applying the so-called deflation method, one ends up with a single linear relation between the desired velocity field and the measured magnetic field in the form:

$$b_i^{(B_0)} = K_{ik}^{(B_0)} u_k + L_{im}\left(I-N\right)_{mn}^{-1,delf} M_{nk}^{(B_0)} u_k \tag{11.72}$$

where the superscript "*defl*" denotes the deflation method for the inversion of the matrix (**I** – **N**).

Despite this far-reaching similarity, CIFT maintains one essential difference as compared to magnetoencephalography. While in the latter method one has to determine a neuronal current distribution from one set of magnetic field data, in CIFT one is free to produce *quite different induced current distributions from the same flow field* just by applying various external magnetic fields $\mathbf{B}_0$ subsequently. For each applied magnetic field $\mathbf{B}_0$ the corresponding induced fields $b_i^{(B_0)}$ can be measured and utilised together for the reconstruction of the flow.

For many technological applications in which a rough knowledge of the flow field would be sufficient, the remaining non-uniqueness of the inversion can be circumvented by the use of Tikhonov regularisation and the method of Tikhonov's L-curve (Hansen, 1992). Note that the inversion of Eq. (11.72) is equivalent to the minimisation of the mean quadratic deviation of the measured fields $b_{i,meas}^{(B_0)}$ from the fields $b_i^{(B_0)}[\mathbf{u}]$ that are modelled according to Eq. (11.72). For the regularisation one adds to the functional of mean quadratic residual one or more penalty functions which are chosen, for convenience, as quadratic functionals of the velocity. The normal equations that follow from the minimisation of this total functional are solved by Cholesky decomposition. By scaling the penalty parameter one can derive the so-called Tikhonov's L curve, i.e. the mean squared residual in dependence on the penalty function (Stefani, 2004). At the point of highest bending (the "knee") one obtains a good compromise between the fit of the modelled magnetic fields to the measured ones and the minimum kinetic energy demand.

In order to demonstrate the feasibility of CIFT an experiment was conducted in which the propeller-driven flow of a liquid metal had to be reconstructed solely from externally measured magnetic field data (Stefani, 2004). Figure 11.4.16(a) shows the sketch of this experiment with 4.4 litres of the eutectic alloy GaInSn. The flow is produced by a motor-driven propeller with a diameter of 6 cm inside a polypropylene vessel with 18.0 cm diameter. The height of the liquid metal is 17.2 cm, giving an aspect ratio close to 1. The propeller can rotate in both directions, resulting either in upward or downward pumping. The rotation rate can reach 2 000 rpm producing a mean velocity of 1 m/s, which corresponds to a magnetic Reynolds number of 0.4. Note that the flow structure for the two directions is not symmetric. The downward pumping produces, in addition to the main poloidal roll, a considerable toroidal motion as well. For the upward pumping, this toroidal motion is to a large extent inhibited by guiding blades installed above the propeller. One of the tasks of the experiment was to discriminate between those different flow structures. For the case of upward pumping, Figures 11.4.16(b) and 11.4.16(c) show the induced magnetic fields for applied axial ($\mathbf{B}_{0,z}$) and transverse ($\mathbf{B}_{0,x}$) field, respectively. The velocity structure (Figure 11.4.16[d]), inferred from these two sets of induced fields, clearly exhibits an upward flow in the centre of the cylinder and a downward flow at the rim. It is worth noting that not only the structure of the flow, but also the range of the velocity scale is correctly reproduced by the inversion. This has been validated by comparison with UDV measurements at different positions (Stefani, 2004).

Recently, a reduced version of the CIFT technique has been successfully applied to the basically two-dimensional flow in a small mock-up of a continuous steel caster (Wondrak, 2010, 2011). Applying only a single, vertically directed magnetic field and using a few magnetic field sensors positioned at the narrow face of the mould it was possible to clearly discriminate between the desired double role and the undesired single role structure, both of which are typical for the two-phase flow of liquid metal and gas in the continuous casting process. This was done in connection with the simultaneous measurement of the argon distribution in the submerged entry nozzle by means of mutual inductance tomography (Terzija, 2011a, 2011b). In a slightly modified version, the effect of a magnetic stirrer at the submerged entry nozzle on the flow in the mould was studied (Wondrak, 2012).

Figure 11.4.16: CIFT demonstration experiment

(a) Schematic view: The motor M drives a propeller P that can pump the liquid eutectic GaInSn either in the upward or downward direction. In the case of upward pumping, the rotation of the flow is strongly reduced by the guiding blades G. The transverse and axial external fields are produced by two pairs of Helmholtz-like coils C. The induced fields are measured using 48 Hall sensors H, which cover the cylindrical vessel rather uniformly

(b) Induced magnetic fields at 48 positions for the case of upward pumping, and axial applied magnetic field

(c) Same as (b), but for applied transverse magnetic field

(d) Velocity structure as inferred by CIFT from (b) and (c)

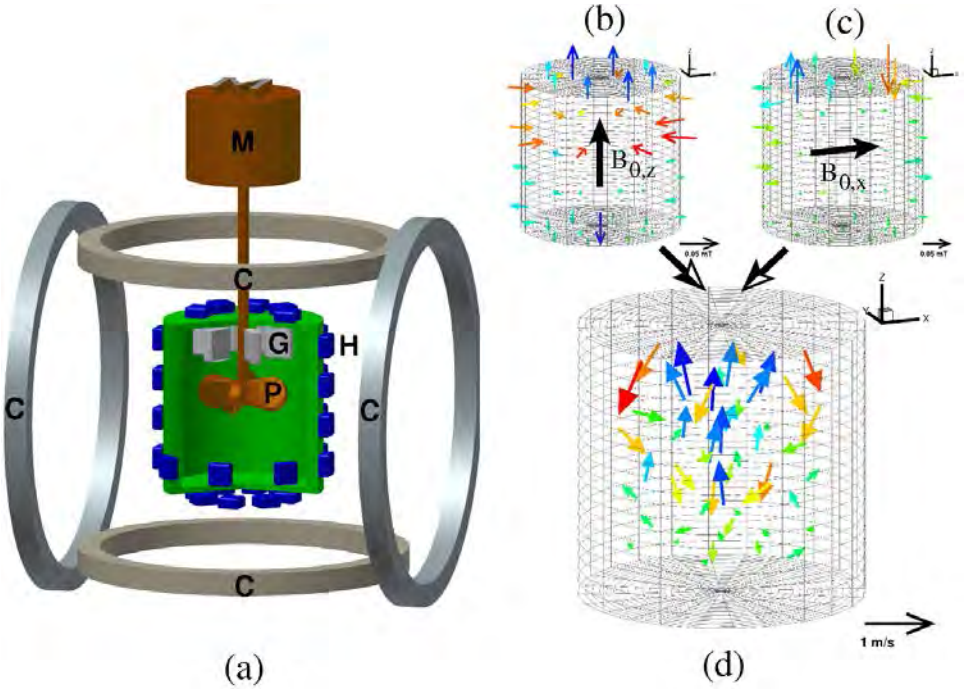

11.4.9.2 Radioscopic visualisation

Radioscopic visualisation techniques reveal a high potential for the investigation of dynamic phenomena in materials processing. The visualisation of flow and transport processes and solidification in metallic melts relies on local differences of the density inside the sample. Such uneven density distributions arise from temperature and/or concentration gradients or occur in multi-phase systems. In particular, radioscopic techniques operating with short wavelength radiation, such as X-ray or gamma radiation, can be employed for *in situ* investigations of kinetics and morphology of solid-liquid interfaces during solidification. Respective X-ray visualisations of the density field in liquid and solidifying alloys were proposed by Campbell (1994), Koster (1997) and Derebail (1998). The authors developed a real-time X-ray radioscopic density visualisation system based on a sealed X-ray tube and a fluorescent image detector achieving a highest resolution in detection of local density changes of 0.02%. Recent developments of more powerful synchrotron sources have led to vast improvements in the performance of X-ray imaging. Mathiesen (1999) presented the first experimental study where intense and coherent synchrotron X-ray radiation was used for *in situ* studies of interfacial and phase-specific spatio-temporal structures which appear during non-equilibrium growth in binary alloys. Nowadays, synchrotron X-ray imaging has been established as a method of choice for *in situ* and real-time studies of solidification microstructure formation in

metallic alloys, with excellent temporal and spatial resolution down to 0.25 s and 1 μm, respectively (Nguyen-Thi, 2012). Restrictions arise from small observation windows having a typical size of view of 1.5 × 1.5 mm^2. Such dimensions allow for the depiction of microscopic dendritic structures; however, it is too small to capture the mesoscopic pattern of the melt flow ahead of the solidification front. Micro-focus X-ray tubes offer a good compromise, achieving a spatial resolution of about 5 μm in a field of view with an edge length up to several cm. The X-ray facility provides a two-dimensional visualisation showing transient modifications of the local composition in the solidifying melt. An estimate of the flow field ahead of the solidification front can be obtained by analysing the motion of brightness contours corresponding to gradients of solute distribution (Boden, 2008) using the optical flow approach. Optical flow is a concept for determining the motion of objects within a visual depiction. Horn (1981) defines the optical flow as a distribution of apparent velocities describing the movement of brightness pattern in a digital image sequence. This definition gives the velocities of objects projected onto the image plane. The solidification process creates differences of the local composition within the melt leading to a characteristic pattern of the transmitted light intensity. The velocity measurement relies on the local information concerning the temporal and spatial gradients of the brightness distribution at each pixel. Assuming a solely two-dimensional motion parallel to the image plane, that analysis delivers in a first step the velocity component in the direction of the brightness gradient. Further constraints derived from physical considerations have to be imposed to compute the two-dimensional velocity field. The brightness of a particular point P can be assumed as constant:

$$\frac{dP}{dt} = \frac{\partial P}{\partial t} + \frac{\partial P}{\partial x} \cdot u + \frac{\partial P}{\partial y} \cdot v = 0 \tag{11.73}$$

with $u = dx/dt$ and $v = dy/dt$. The validity of this so-called brightness constancy equation (BCE) with respect to the captured X-ray image sequence is often violated. In the particular case of solidification the brightness of the objects within the images is not constant by nature. On one hand, the crystallisation of the primary dendrites and the corresponding rejection of the solute generate the brightness contrast, which is the basis for the optical flow analysis. On the other hand, diffusion effects may cause perceptible deformations of the brightness pattern. Such deformations of the flow pattern occurring between two time steps can be neglected for flows at high Peclet numbers. Instead of fulfilling the strict requirements of the BCE a solution to the flow field can be found by minimising the residual error of the brightness constraint, which we denote as $c_c^2 = (dP/dt)^2$. Another physical constraint coming from fluid mechanics is the assumption that the neighbouring points in the image should have similar velocities. This so-called smoothness constraint of the velocity field can be enforced by minimising the square of the gradient of the optical flow velocity c_s:

$$c_s^{\,2} = \left(\frac{\partial u}{\partial x}\right)^2 + \left(\frac{\partial u}{\partial y}\right)^2 + \left(\frac{\partial v}{\partial x}\right)^2 + \left(\frac{\partial v}{\partial y}\right)^2 \tag{11.74}$$

The flow field can be assessed by minimising the following cost function:

$$\int_{\Omega} \left(c_c^{\,2} + \lambda c_s^{\,2}\right) dx dy \tag{11.75}$$

in the measuring domain Ω, whereas λ weights the influence of the regularisation term. Figure 11.4.17 shows a reconstruction of the melt flow in a solidifying Ga-In alloy.

The utilisation of radioactive tracers can be considered as another approach to determine the flow field. Szekely (1964) introduced capsules containing radioactive gold into the bulk of liquid steel. The radioactive content was measured from samples which were periodically extracted from certain positions. A similar procedure was applied by Stewart (1972) to reproduce the flow pattern in liquid tin infiltrated with radioactive

tracers. At a certain stage of the experiment the position of the tracers was frozen by a rapid quenching of the melt. The interpretation of the distribution of the frozen tracers gives a rough estimation of the melt flow. A really non-invasive and *in situ* monitoring of the tracer movement in the melt was successfully performed by Kakimoto (1988) in silicon. The authors used small tungsten cylinders covered by a SiO_2 layer in order to wet the tracer with the molten silicon. The actual positions of these tungsten particles can be localised in the X-ray images because tungsten shows a significantly larger absorption coefficient compared to the circumambient silicon. The same principle is exploited for high frame-rate neutron radiography at nuclear reactor providing high neutron fluxes (Saito, 2005). The motion of gold-cadmium particles inside a lead-bismuth melt was monitored and corresponding 2-D velocity fields were reconstructed by means of particle tracking velocimetry.

Figure 11.4.17: Flow pattern in a solidifying Ga-In alloy reconstructed from X-ray images using the optical flow method

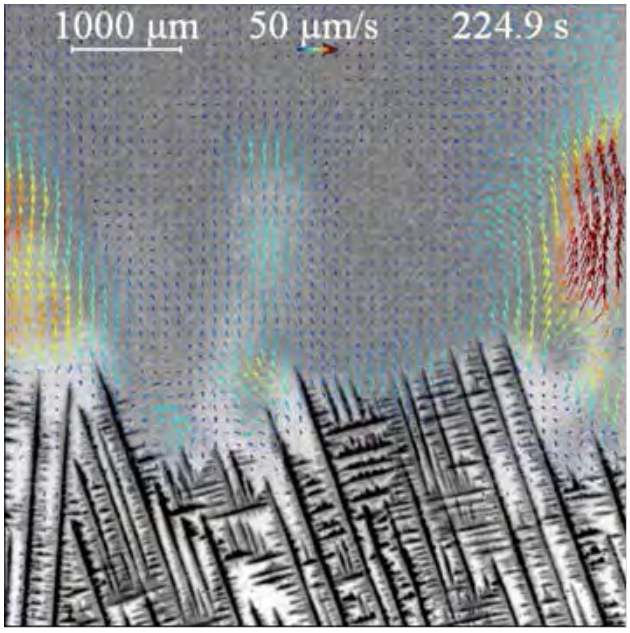

Source: Boden (2008).

11.5 Two-phase flow measurement

In the concept for an ADS the injection of gas is considered as one method to generate a forced convection inside the liquid metal loop. In order to control the flow rate of the liquid metal and the resulting pressure drop the structure of the two-phase flow in the riser has to be known. On the other hand, ingress of gas bubbles into the reactor core following an accidental scenario like steam generator tube rupture (SGTR) must be prevented. This requires experimental investigations which do give insights into the flow paths of gas in the HLM, both with good local resolution as well as covering a wide measurement area.

Beside the description of the integral state of a two-phase flow, which is described by the void fraction, the local conditions are of interest. Therefore, measurement equipment is required to locally measure the void fraction, the bubble size and the individual transport velocities.

As for one-phase flow measurement methods, intrusive and non-intrusive methods can be applied for two-phase flow measurements in liquid metals. Intrusive methods are e.g. the local resistive probes, while a non-intrusive sensing can be achieved by means of X-ray (γ-ray) techniques, neutron radiography (NR) or UDV. Due to the opacity of the fluid, optical or fibre optical methods cannot be used. The high specific electric conductivity of liquid metals does not allow to use impedance probes, because hardly any electric field of significant size can be built up within the fluid, (Cho, 2005). In poorly electrically conducting media sometimes magnetic resonance imaging (MRI) is used, which requires strong permanent magnets (Daidzic, 2005). However, the interaction of the magnetic field with the fluid motion yields Lorentz forces altering the flow pattern and void distribution within the duct in such a way that the intended measuring quantity is hidden behind the magneto-hydrodynamic effects.

The consecutive sections describe the techniques successfully applied to liquid metals thus far, their operation principles and their deficits. We starts with the global methods that acquire the void fraction within a defined cross-section and continue with individual devices measuring local effects. In contrast to single-phase investigations, information about two-phase liquid metal flow instrumentation is rather sparse. Nevertheless, we attempt to present the currently available technologies and discuss their limitations.

Many of the methods described above for single-phase flows might also be used for two-phase flows, particularly the flow field mapping techniques like radiography and CIFT. They are not described in detail here; the reader might refer back to Section 11.4.

11.5.1 *Electromagnetic sensors*

An exact description of the characteristics of two-phase flow is required for better performance and safety design of power plant and air conditioning machinery. In general, it is not easy to simultaneously measure the liquid volume flow rate and the void fraction under the existence of a gas phase. The electromagnetic flow meter has been used successfully and accurately to measure the mean liquid velocity in various industries for about 40 years.

The electromagnetic flow meter is a device for detecting the potential difference between electrodes that is induced when a conducting fluid flows through a magnetic field, see e.g. Section 11.2.1. The feasibility of using the electromagnetic flow meter for measuring the characteristics of two-phase flow has been continuously considered. The reasons for this are that it causes no pressure drop, it has fast response for the change of flow, and it can effectively use the sharp difference between conductivities of two phases. There are many potential applications for the electromagnetic flow meter in two-phase flow, but there is also uncertainty due to the effects of the non-conducting phase. As for the electromagnetic flow meters, generally two types of electromagnetic void fraction sensors can be used, the DC permanent magnetic sensors and the AC sensor types. Both are described below.

11.5.1.1 DC permanent magnet void fraction sensors (PMVS)

The permanent magnet void fraction sensors (PMVS) rely on the same principle as the DC permanent magnetic flow meter (PMF) presented in Section 11.2.1.1. The experimental set-up is also the same, consisting of a permanent magnet imposing a steady magnetic field B, penetrating the geometry to be investigated. The electrodes are arranged both perpendicular to flow u with u_f and u_g and the magnetic field B, where u_f is the mean fluid velocity and u_g the mean velocity of the gas. Further on the subscripts f and g denote the fluid and the gas, respectively. Since liquid metals possess a high specific electrical conductivity an order of magnitude larger than that of its vapour or that of other gases one can assume that to the leading order the signal output of a PMVS will be a linear function of the liquid velocity alone up to a high value of vapour volume fraction. This

postulation, however, assumes that – at least for the temporal mean – a uniform current path is maintained normal to the liquid metal flow.

The flow of a two-phase stream may be expressed as:

$$m_f = \rho_f A \left(1-\alpha\right) u_f \tag{11.76}$$

where α represents the gas volume fraction, m_f the mass flux and A the ducts cross-section. The ratio u_f/u is obtained from Eq. (11.77a) and the total mass flow m is equal to sum of the gas and liquid flows as in Eq. (11.77b):

$$\frac{u_f}{u} = \frac{m_f}{m}\ \left(1-\alpha\right)\ ,\ m = m_f + m_g \tag{11.77a,b}$$

Defining the quality x as $x = m_g/m$ one gets:

$$\frac{u_f}{u} = \frac{\left(1-x\right)}{\left(1-\alpha\right)} \tag{11.78}$$

Considering now only low qualities in the range $0 < x < 0.02$ Eq. (5.3) mutates to:

$$\alpha = 1 - \frac{u}{u_f} \tag{11.79}$$

in which u and u_f can be independently measured by permanent electromagnetic flow meters; one in the two-phase domain as $\Delta\phi$ and the second in the single-phase flow $\Delta\phi_f$. Connecting both readings one gets directly the void fraction from:

$$\alpha = 1 - \frac{k_f \Delta\varphi_0}{k\,\Delta\varphi_{f\,0}} \tag{11.80}$$

where k_f and k are the calibration constants of the single and two-phase electromagnetic flow meters. In alkali liquid metals this technique has been successfully proofed by Heinemann (1962). The PMVS experimental data was compared in tests with γ-ray measurements; an accuracy of ±5% up to void fractions of 66% and temperatures of 600°C was obtained. However, it was noted that a high temperature wetting procedure was necessary to ensure constant thermal-electric properties at the fluid wall interface, otherwise a reliable reading could not be achieved. Hori (1966) successfully demonstrated this technique with mercury, a high density liquid metal. In case of well electrically wetting fluids this technique has been improved by Ochiai (1971).

Additional correction factors for a more accurate detection of the void fraction value were made by Murakami (1990). Correlation techniques to acquire high temporal resolutions were made by Velt (1982). However, these latter works concentrated mainly on use in alkali metals.

11.5.1.2 *AC electromagnetic void fraction sensors (EMVS)*

A method to overcome the problems of direct wetting of the surface is given by AC sensors, similarly as for flow meters. In Figure 11.5.1 an EMVS invented and successfully tested by Cha (2002) is shown.

Within this device the electromagnet of the electromagnetic flow meter is sinussoidally excited and controlled by a frequency converter and an uninterruptible power system. The flow meter is composed of a signal detector and a signal processor. A pair of corrosion-resistive and non-magnetic electrodes is mounted along the inner wall of the test tube. Lead wires to draw out the signal are connected at both electrodes, and shielded for noise proofing, with the shield lines being grounded at one end. One of the greatest difficulties in electromagnetic flow meter design is that the amplitude of the

voltage across the electrodes is of the order of a few millivolts, which is relatively small compared with extraneous voltages and noise. The main noise sources of electromagnetic flow meters, excited by AC power, are as follows:

- the transformer signal from the alternating magnetic field (including the effect of eddy current in the flow tube);
- noise from the capacitive and resistive coupling between signal and power circuits.

The following effects that distort the signal (flow signal) corresponding to flow rate should also be noted:

- fluctuation of the magnetic field due to fluctuation of the power input;
- iron loss and hysteresis effects of the electromagnet;
- amplifier loading effect from the impedance of measuring devices.

Figure 11.5.1: Schematic drawing of the EMVS (left) and normalised output of electromagnetic flow meter considering the ratio of correction factor with void fraction α (right)

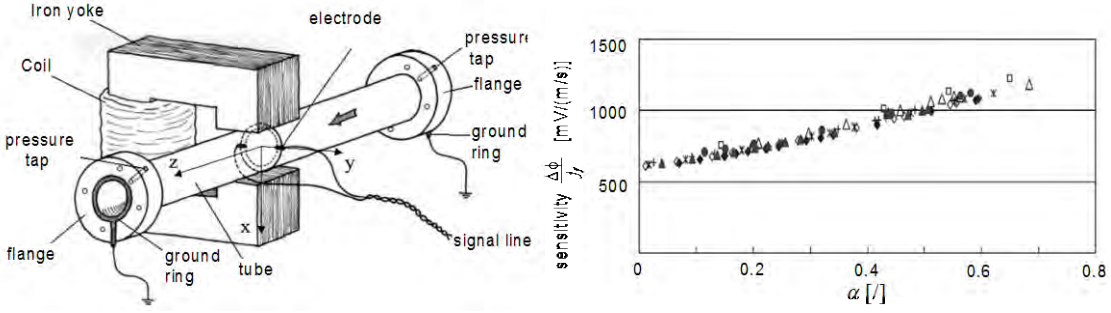

Source: Cha (2003).

To avoid the difficulties stated above, a somewhat complex signal processing unit was needed. The signal processor has an input stage with voltage followers, a filtering stage and an amplifying stage with large gain (> 10^2). To cancel out the differential noise (transformer signal), a counter differential noise is generated intentionally before the voltage followers with a kind of pick-up coil and variable resistor. Low-frequency excitation using a frequency converter enables to reduce the noise by capacitive and resistive coupling between the signal and power circuits. Using these procedures, noise can be reduced considerably, and zero-flow tuning is possible. A reference resistor is used to ensure that the reference voltage has the same phase as the excitation current. From the reference voltage, information about the characteristics of the magnetic field can be inferred, and the comparison between flow signal and noise is possible.

The EMVS also requires a single-phase calibration procedure to determine the calibration constants. In fact, the void fraction cannot be measured directly with one device in the liquid metal-gas system. By using two EMVS an artificial void fraction can be calculated from the signals of the two electromagnetic flow meters under the assumption that the ratio of correction factors of both flow meters is unity, similar as for the DC flow meters. For the single-phase flow calibration of each of the devices, the correction factors can be determined. As a result from both calibrations one gets a linear dependence of the signal ratio versus the void fraction for low void fractions up to $\alpha = 0.3$. However, this signal ratio is not the actual real void fraction value since the ratio of correction factor is not unity: It is a function of fluid conductivity and hence is coupled to the void fraction. The effective conductivity σ_{eff}, however, can be calculated by the correlation experimentally determined by Petrick (1964) and thus the signal ratio can be

corrected to obtain the real void fraction. The result obtained by Cha (2003) for a sodium-nitrogen system showed an uncertainty of less than 2%. The result is shown in Figure 11.5.1.

$$\sigma_{eff} = \frac{(1-\alpha)^2}{1+\alpha}\sigma_f \text{ for } 0 \le \alpha \le 0.7 \tag{11.81}$$

11.5.2 *Local void determination*

11.5.2.1 Resistive or conductance probes

The resistive probes are local sensors with an electrically conducting tip (Cr/Ni wires, tungsten, stainless steel or platinum, with diameters ∅ 0.1 mm) in direct contact with the liquid. These kinds of probes are usually supplied with an AC current typically operating at frequencies in the range 1-25 kHz. The AC source induces an electric current flowing from the probe tip to an opposite electrode (e.g. the probe support or the channel wall). The gas contact at the sensitive wire is detected by an interrupt of the electrical current. Due to the huge differences in the electrical conductivity between the gas and the metal, one obtains sharp signals easy to evaluate by a threshold method.

The measuring quantity is the ratio of the gas contact time to the total sampling time. This ratio yields a time-averaged local void fraction. Using this method the number of bubbles during the total sampling time is also known and hence the bubble frequency. The measurement principle of resistive probes is shown in Figure 11.5.2.

Figure 11.5.2: Measuring principle of the resistive probes (left); typical signal delivered by a single-wire resistive probe in a sodium/argon bubbly flow (right)

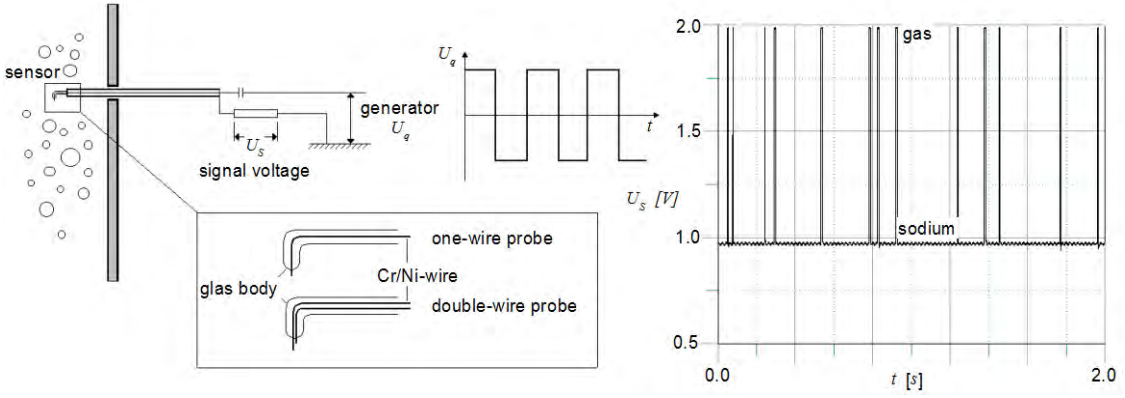

The electrical resistive probe method is attractive for bubbly flow measurements because of its relative simplicity and wide applicability. It detects the passage of interfaces at the tip of each sensor, and uses this data to determine void fraction and bubble size and velocity (Delhaye, 1983; Serizawa, 1975; Kocamustafaogullari, 1991). Optic fibre has a faster response, but besides the opacity of liquid metals, the commercial probes found are both expensive and too fragile to use in heavy liquid metals and in typical large bubble column experiments.

Early versions involved only one needle, which gave two different signals depending upon whether the needle tip was in a bubble or in liquid. Hills (1974) used a short needle with a single 90° bend and investigated the radial variation of gas hold-up in a vertical bubble column. Neal (1963) also used the single 90° bend configuration and analysed bubble signals in terms of autocorrelation functions to obtain local values of gas fraction, bubble frequencies and bubble size.

Serizawa (1975) developed the method further and presented a double-sensor probe for measuring local values of air-water bubbly flows. This probe had the advantage that it was capable of measuring bubble velocity from the time lag between a pair of upstream/downstream signals. It consisted of two identical electrically insulated needles placed side-by-side with their tips about 5.0 mm apart. Kocamustafagullari (1991) recommended a 2.5 mm separation to account for possible bubble size and velocity. A comprehensive list of previous probe designs is given in Sanaullah (2001). The problem with the two-point probe is the difficulty of matching the signals from the two needles which correspond to the same bubble, especially since bubbles do not always rise vertically, and often strike the probe with a glancing blow.

One attempt to improve the situation is to use a five-point probe (Burgess, 1975; Buchholz, 1984) with a leading needle surrounded by four needle tips in the same horizontal plane a few millimetres downstream of the central tip. The extra complexity involved has meant that these devices have not been used as much as the simpler two-point probe. One of the major concerns with multiple probes is that the leading needle may interfere with the bubble, and so disturb the reading of the downstream needle(s). The Burgess-Calderbank algorithm (1975) for analysing data from a five-point probe rejected any bubble not seen simultaneously by three equi-spaced downstream needles, thus ensuring that only "head-on" collisions, least likely to be affected, were analysed. This, however, meant that only a very small sample of the bubble population was included, raising doubts about whether the sample was representative.

The resistive probe needles are commonly oriented either horizontal (perpendicular to the bubble path) or vertical. In the horizontal configuration, the ability of the probe to withstand the lateral drag of the fluid becomes an important factor; in the double needle probe, this leads to uncertainty about the exact vertical positions, and hence the separation, of the tips. However, with any double sensor probe, the two tips must be vertically one above the other, which is impossible if both needles are vertical. Most recent workers have used two very fine needles touching each other. However, the use of touching needles means that there is a danger of the liquid meniscus in the channel between them affecting the behaviour of the downstream needle tip. A common orientation in commercial two-point optic fibre probes is to separate the two needles, but to bend the upstream one so that the two tips are aligned, but this raises the question as to whether the different orientations of the two probes influences the result.

Probe design

Designs of a two-needle and a four-needle probe used in liquid metal experiments are shown in Figure 11.5.3 (Saito, 2005). The wires have usually a distance of 2-5 mm from each other and are aligned with respect to the main flow direction. Too large a separation can introduce errors in the detected signals as multi-bubble contact may occur between two signals originating from the same bubble, whereas too small a separation will lead to errors in the estimation of velocity. The two sensors are electrically insulated from the probe body, except their tips, which are made by simply cutting the ends off the insulated wires. The other ends of the wires are soldered to two coaxial cables. The soldered connections are carefully electrically insulated using air-dried insulating varnish, and as an additional measure for safe insulation soldered connections are wrapped by heat shrinking plastic tubes. The other ends of the coaxial cables are connected to the bubble signal processor. The screens of these cables are joined to a lead whose other end touches the liquid metal in the column as the "ground". The signal processor mainly compares the resistance between the probe tip and the ground. A constant potential of several volts DC is applied across each needle and the potential across a series resistor is amplified to provide the output signal.

Figure 11.5.3: Schematic illustration of an inclined dual-sensor resistive probe (left); sketch of a four-needle resistive sensor used in PbBi (right)

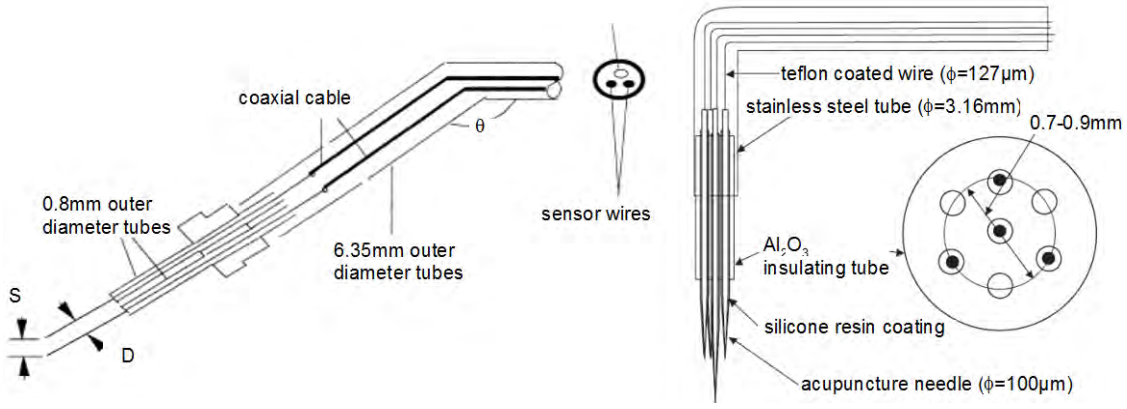

Source: Left image from Sanaullah (2001), right image from Saito (2005).

Data processing

The raw signals obtained by the probe are not square waves as to ideal contact or not. This is due to the relatively slow drainage of liquid film formed around the sensor tip, which leads to a slow rise time as compared to the sharp fall time when the sensor re-enters the water. To obtain bubble properties, it is necessary to have data in terms of perfect square waves with the rise and fall corresponding to the precise moment when the needle enters and leaves the gas phase. For this purpose, the raw data are differentiated, and the moment when the value of the derivative crosses a certain threshold is used as the interface contact time. This processing can be implemented via software algorithms. A detailed description is given in the thesis of Cheng (1997).

The local void fraction α can be calculated from the sum of duration time t_g for bubbles at the upstream probe for the sample time T:

$$\alpha = \frac{\Sigma t_g}{T} \tag{11.82}$$

Using the time lag between the signals for the two sensors and the vertical distance L between them, the velocity of the i-th bubble, u_{Bi}, can be determined by:

$$u_{Bi} = \frac{L}{t_{di}} \tag{11.83}$$

where the average displacement time of liquid-gas interface and gas-liquid interface for a bubble travelling between the two sensors is given as:

$$t_{di} = \frac{1}{2}\left(t_{dri} - t_{uri}\right) + \frac{1}{2}\left(t_{dfi} - t_{ufi}\right) \tag{11.84}$$

where subscripts d and u correspond to downstream and upstream, respectively, and r and f correspond to rise and fall signals, respectively. The bubble chord length L_{Bi} is then obtained as:

$$L_{Bi} = u_{Bi}\left(t_{uri} - t_{ufi}\right) \tag{11.85}$$

where the upstream contact time is used, as explained above, for its greater reliability.

Estimating bubble size distribution from the bubble chord length distribution is not easy, and even estimating the mean bubble size and velocity is not without problems. Since the probe is more likely to see a large bubble than a small one, complicated weighting factors are needed. In order to use the resistive probe for two-phase studies, it is most important to establish a statistical model that relates the local interfacial area concentration to the measured quantities. Over the past twenty years, different statistical models for local interfacial area concentration measurement using a double-sensor probe have been developed. In this context only the four most common models are described. The evaluation of multi-tip probes is more sophisticated and requires several estimates, which would expand the scope of this presentation. Detailed descriptions of the methods required are given by Dias (2000), Kim (2001) and Shen (2005). Here, only the different methods for two-tip arrangements are described.

Statistical methods to evaluate the local interfacial area concentration

Kataoka's statistical model (1986)

According to the definition of the local interfacial area concentration by Ishii (1975), Kataoka (1986) carried out derivations and established a statistical model that related the local time-averaged interfacial area concentration a_i to the harmonic mean of the interfacial velocity. Consider the main flow is in z-direction. Assume that the bubbles are spherical, the probe passes every part of the bubbles with an equal probability, and there is no statistical relation between interfacial velocity and the angle between the interfacial velocity and the normal vector of the interface. With this statistical model the time-averaged interfacial are concentration can be expressed as:

$$\overrightarrow{a_i}^{t} = 4N_t \cdot \left(\overline{\frac{1}{u_{szj}}}\right) \cdot \frac{1}{1-\cot\left(\frac{\alpha_0}{2}\right)\ln\left(\cos\frac{\alpha_0}{2}\right)-\tan\frac{\alpha_0}{2}\ln\left(\sin\frac{\alpha_0}{2}\right)} \tag{11.86}$$

where u_{szi}, α_0 and N_r denote the z component of the interfacial velocity, the maximum angle between the interfacial velocity and the mean flow direction, and the number of bubbles measured per unit time, respectively. On the derivation of Eq. (11.86), it is also assumed that the angle between the bubble interfacial velocity and the main flow direction, α, is random with an equal probability within some maximum angle α_0. The value of α_0 is determined from the statistical parameters of the measured interfacial velocity. Assuming that the interfacial velocity fluctuations in three directions are equilateral, Kataoka (1986) derived the relationship between the maximum angle α_0 and the standard deviation of bubble velocity fluctuation in the main flow direction with the following form:

$$\frac{\sin 2\alpha_0}{2\alpha_0} = \frac{1-\sigma_z^2/\overline{u_{szj}^2}}{1+3\sigma_z^2/\overline{u_{szj}^2}} \tag{11.87}$$

where σ_z denotes the root mean square of the interface velocity fluctuation. For more details on the mathematical modelling of this measurement method, one can refer to Kataoka (1986). The interfacial area a_i can then be used to estimate the Sauter mean diameter d_s, using:

$$d_s = \frac{6\alpha}{\overline{a_i}} \tag{11.88}$$

Kalkach-Navarro's statistical model (1993)

Kalkach-Navarro (1993) assumed that the bubbles were spherical and the bubble sizes were represented by a probability distribution function, $f(V_j)$, where $f(V_j)\Delta V$ was the number of bubbles per unit volume having a volume between V_j and $V_j + DV$. From the geometrical consideration, they proposed the following statistical model for local interfacial area concentration measurement:

$$\overrightarrow{a}_i^t = (36\pi)^{\frac{1}{3}} \sum_j f\left(V_j\right) V_j^{2/3} \Delta V_j \tag{11.89}$$

where V_j is the volume of the group-j bubbles and calculated from the chord length measured by a double-sensor probe. In order to determine $f(V_j)$, the maximum chord length measured is divided into equal partitions, then a probability of each partition of chord length is obtained. Assuming the bubbles can be penetrated at any point with equal probability by the sensor tips, a triangular matrix, which represents the relationship between the probability of the chord length cut by sensors and the probability of bubble radius, is established. Then, the bubble size probability distribution function $f(V_j)$ can be derived from the probability distribution of the bubble radius. In this model, however, the authors derive straightway the relations for local measurement from the chord length distributions, and take no account of the effect of bubble lateral motions.

Hibiki's statistical model (1998)

Hibiki (1998) conducted a similar derivation to Kataoka (1986) based on basically the same assumptions, except for the probability density function of α, the angle between the bubble interfacial velocity and the main flow direction. Of the view that the probability density function of α has a peak in the main flow direction from the experimental data, they replaced the equal probability within a maximum angle of α, using the following relations:

$$g(\alpha) = \begin{cases} \dfrac{1}{\alpha_0^3}\left(\alpha - \alpha_0\right)^2 \text{ for } 0 \le \alpha \le \alpha_0 \\ 0 \text{ for } \alpha_0 \le \alpha \le \pi/2 \end{cases} \tag{11.90}$$

The following relations were derived between the maximum angle, α_0, and the standard deviation of bubble velocity fluctuation in the main flow direction:

$$\frac{3}{\alpha_0^2}\left(1 - \frac{\sin 2\alpha_0}{2\alpha_0}\right) = \frac{1 - \sigma_z^2/\overline{u_{sz}^2}}{1 + 3\sigma_z^2/\overline{u_{sz}^2}} \tag{11.91}$$

Wu's statistical model (1999)

Wu (1999) carried out a sensitivity study using a numerical method on double-sensor conductivity probes measuring local interfacial area concentration. It is assumed that the bubble velocity fluctuation is isotropic and the bubble is spherical. Considering the effects of bubble lateral motions and the distance between the two tips of the double-sensor probe, and taking the contribution of the missed bubbles into account, a statistical model is also obtained from the definition by Ishii (1975) as:

$$\overrightarrow{a}_i^t = \frac{2N_b}{\Delta T\left(N_b - N_{miss}\right)} \cdot \left(\overline{\frac{1}{u_{szj}}}\right) \cdot \left[2 + \left(\frac{u_b'}{u_b}\right)^{2.25}\right] \tag{11.92}$$

where ΔT, N_b, N_{miss} and u_b'/u_b denote the sampling time, the total number of measured bubbles, the number of the missed bubbles, and relative bubble velocity fluctuation, respectively. The missed bubbles referred to those that are touched by the first sensor but not by the second sensor, or those that pass the second sensor ahead of the first sensor in view of the bubble lateral motions. The number of missed bubbles can be obtained from the double-sensor probe signals directly. From the numerical method, Wu (1999) suggests the relative standard deviation of the inverse of the measured interfacial velocity to characterise the relative bubble velocity fluctuation with the following form:

$$\frac{u_b'}{u_b} = 0.85 \cdot \frac{\sqrt{\overline{1/u_{szj}} - \left(\overline{1/u_{szj}}\right)^2}}{\left(\overline{1/u_{szj}}\right)} \tag{11.93}$$

where 0.85 has been determined by their numerical analysis. When the bubble diameters are in the range from $1.2\Delta s$ to $3\Delta s$, the authors report that the error of the above relation is in the range of ±10%, where Δs denoted the distance between the two tips of the double-sensor probe.

Experimental experience and accuracy

The impact of inclination of the probe with respect to the main flow is a critical issue. Here in particular, the effect of the interaction between the two needles by calculating bubble frequency or void fraction from the upstream or the downstream needle makes this obvious. The accuracy of the double-tip probes can be checked by comparing the calculated values of the void fraction and the gas superficial velocities with those determined manometrically. The agreement is of course not better than the statistical methods used for the signal processing and is thus around ±10%.

A better agreement is only obtained for more advanced statistical methods. If e.g. the bubbles are categorised into two groups, such that group one includes spherical and distorted bubbles and group two includes cap and slug bubbles, then correction methods in calculating the local a_i for missing and non-effective bubble signals can be formulated accounting for different contributions from various bubble interfaces. Such a procedure was successfully tested by Kim (2001). The deviation between experiment and numerical simulations shrinks to only a few per cent.

11.5.3 *Ultrasound Doppler velocimetry (UDV) for two-phase flows*

Detection of bubbles or particles in a dominant liquid two-phase flow inside pipes or vessels is important in research and industries. The ultrasonic pulse-echo method allows by means of liquid-metal-adapted waveguides to measure up to temperatures of 620°C, (Eckert, 2003), and dense media with a high sound velocity such as gallium (~2 600 m/s, compare Brito [2001]). Use of the ultrasound technique for two-phase flow determination, however, is quite new. Hofmann (1996) made a first attempt to analyse a two-phase flow using this technique. A straight beam transmitting-receiving probe transmits short bursts at regular intervals in the range 0.1-4 kHz and more, having an ultrasonic frequency in the range 1-10 MHz. The ultrasonic waves penetrate the wall and the two-phase flow. They will be directly reflected by the bubbles or particles and by the inner back wall of the vessel. The back wall echo is more intense in comparison with the direct echo in most cases. Reflected waves are received partially by the same probe and displayed on the screen of an ultrasonic echo detector as an echogram, as shown in Figure 11.5.4(a).

If the sizes of objects (bubbles) and arrangements (structure elements like the pipe or an immersed body) are much greater than the ultrasonic wavelength the behaviour of ultrasonic waves can be considered as similar to optics in the following. If the inclination of the reference object (the bubble) with respect to the emitter/sensor cross-section is too

large, the intensity of the received echo goes to zero. Assuming a homogeneous cylindrical sound field and neglecting any changes in wave mode, the largest inclination angle α_{R0} of a plane reflector (bubble) to be allowed can be calculated as follows:

$$\alpha_{R0} = \frac{1}{2} a\tan\left(\frac{d_p c_l}{2c_s l_s\left(1+\frac{c_l l_l}{c_s L_s}\right)}\right) \tag{11.94}$$

where c_s, c_l are the sound velocities of the wave guide and the liquid metal, l_s and l_l the length of the waveguide and that of the fluid in the sound direction, respectively. Having a probe transducer diameter d_p = 10 mm, l_l = 40 mm, l_s = 135 mm, c_l = 1 730 ms^{-1} (liquid lead-bismuth), c_s = 5 730 ms^{-1} (stainless steel), this angle has a value of only α_{R0} = 0.21°. This means that an echo cannot be received by the probe if $\alpha_R > 0.21°$.

Great progress for the use of UDV in two-phase flows was achieved by Suzuki (2000, 2002). When the ultrasound probe UVP is applied to bubbly flows, the system records velocities of both phases together. In their studies, the phase discrimination is made using pattern recognition. All stored instantaneous velocity profiles are classified into two groups with regard to the existence of bubble data. If no bubble crosses the measuring line when an ultrasonic pulse is emitted, the instantaneous velocity profile obtained should give only negative values at all the measuring points in the channel. Such instantaneous velocity profiles are stored as Group A (ensemble averaged local liquid velocity profile distant from bubbles). On the other hand, if a bubble exists on the ultrasonic beam path, the obtained velocity profile has positive values near the gas-liquid interface. These profiles are stored as Group B (velocity profile around a bubble). The Group B profiles are rearranged according to the distance from the bubble's surface. Furthermore, in relation to the influence of wakes behind leading bubbles, instantaneous velocity profiles of Group B are subdivided into two groups, Groups B1 and B2. Group B1 includes velocity profiles that contain effects of leading bubbles. When the instantaneous velocity profile is not affected by leading bubbles, the profile is categorised into Group B2. The presence of the wake effect is determined by another pattern recognition. If a positive small peak exists between the transducer and the bubble's surface in an instantaneous velocity profile, that small peak is considered as the effect of the leading bubbles, or the wake. As a result of this pattern recognition and conditional sampling of data, the ensemble-averaged velocity is obtained at each relative distance from a bubble's surface.

Figure 11.5.4: The principle of ultrasonic pulse-echo technique for two-phase flow measurement (left); experimental scheme of the PbBi bubbly flow facility from Eckert (2003)

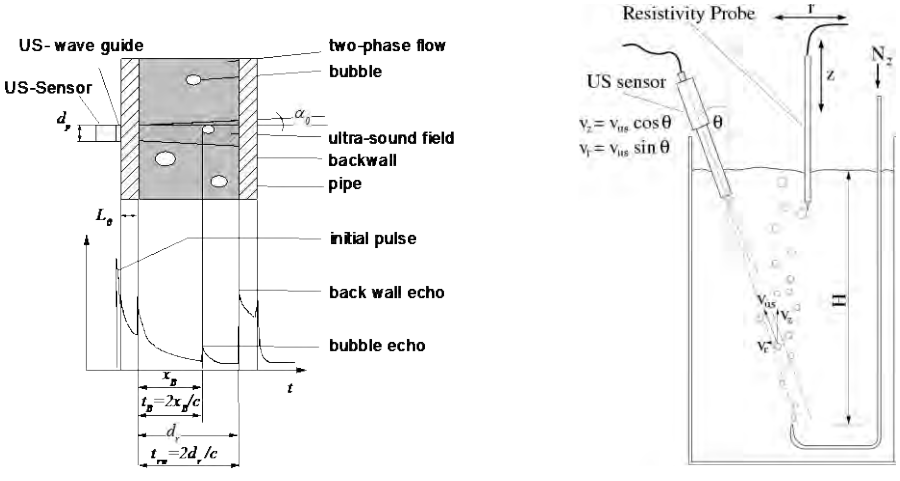

Eckert (2003) improved Suzuki's technique and applied it to PbBi melts up to 300°C and CuSn melts with up to 620°C using nitrogen as gas. A sketch of their experimental set-up, which they referenced against a resistivity probe, is shown in Figure 11.5.4(right).

An example for a typical velocity profile obtained from the bubbly flow is shown in Figure 11.5.5(left). The lower velocity at the small measuring depths corresponds to the flow of the liquid metal that is driven by the rising bubbles. Since the ultrasonic pulse is reflected at the bubble interface, the velocity measured can be interpreted as an interfacial velocity. If the entire ultrasonic energy is reflected by the bubble as demonstrated in this example, no information can be received from measuring depths behind the bubble position, which is called the shadow effect. Measurements of the phase velocities and the bubble frequency can be obtained only for low void fractions ($\alpha < 0.1$), unless tomographic systems consisting of several transmitters and receivers are used (Xu, 1997; Beckord, 1998). However, such systems were not applied to liquid metal two-phase flows at the time.

Figure 11.5.5: Typical measured velocity profile of a single bubble case from, Eckert (2003) (right); example of a calculated probability density function to separate both phase velocities (left)

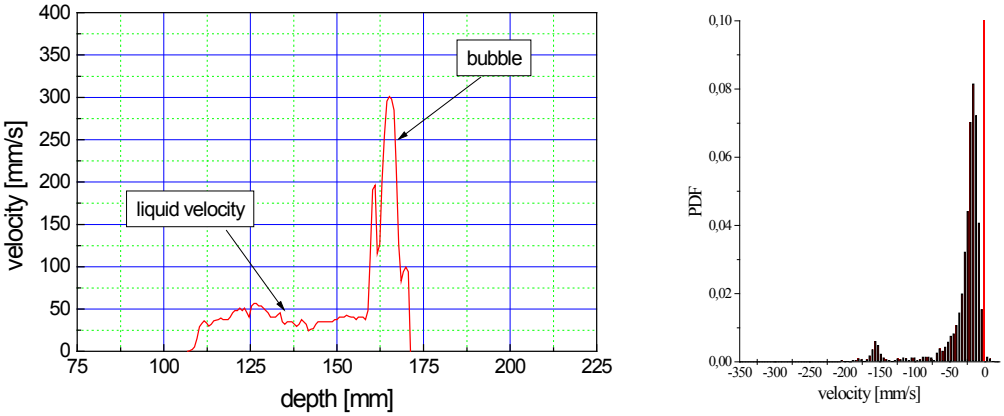

A phase separation of the measured velocities of the liquid and gas can be performed by calculating the corresponding probability density functions (PDF). Here, the assumption is made that the PDF of both phases can be expressed by a normal distribution, as shown for example in Figure 11.5.5. The PDF were calculated by Eckert (2003) on the basis of 4.096 velocity profiles.

More recent application experience as well as the fundamentals can be found in Kikura (2006) and particularly in Zhang (2009). The simultaneous acquisition of void and liquid velocity using multi-wave sensors has been described by Biddinika (2009) and Ito (2010).

11.5.3.1 Further probe principles

Iguchi (1997) describes a combined probe for velocity of the liquid phase and the void fraction, using a two-needle electro-resistivity probe and a magnet probe.

Schneider (2006) describes a probe that uses pressure fluctuations caused by a stream of tiny auxiliary bubbles, but it seems that this is not very mature.

Marcolongo (2007) suggests a bubble probe where accelerations and decelerations of the gas-liquid interface of the probe are the basis of the measurement, rather than surface tension effects. That has been substantiated by experiments in which the pressure trace generated by the probe has been matched to high-speed digital movies of bubble behaviour at the probe. It is shown that the sensor merely detects the wake of the bubble. The investigation was obviously using cap bubbles in water; work for other regimes and fluids was announced.

11.5.4 *Tomographic flow mapping for multiphase flows*

11.5.4.1 *Electromagnetic inductance tomography*

Electromagnetic inductance tomography (EMT), otherwise known as mutual inductance tomography (MIT), employs inductance measurements to extract tomographic data related to permeability and/or conductivity distributions in a melt (Peyton, 1996). A typical example is the inference of gas bubbles in liquid metal pipe flows, by positioning some N coils around the pipe and determining the $N(N-1)/2$ mutual inductances between them. A specific system with eight coils has been successfully applied to gas bubble detection in a low melting point liquid metal mock-up of continuous steel casting (Terzija, 2011a, 2011b) as well as in hot pilot plant trials (Ma, 2008).

11.5.4.2 *X-ray, γ-ray and neutron radiography (NR)*

The attenuation of various radiations has been used quite successfully by different experimenters since the late fifties (Hooker, 1958; Petrick 1958). Nearly all of them have been applied to light metals previously considered for fast breeder research. The growing interest of the metal casting industry as well as the transmutation of minor actinides put the focus on heavy liquid metals, which require a strong source due to considerable absorption. These sometimes continuously operating high power sources became available over the past decade (Baker, 1998; Satyamurthy, 1998; Mishima, 1999; Saito, 2005). Additional advances in using the techniques described below stemmed from improved computer technologies and the progress in image-processing algorithms.

11.5.4.2.1 X-ray absorption

This subsection describes the technique developed for visualisation of the multi-phase mixture and the transient measurement of the two-dimensional distribution of chordal averaged void fraction applicable to liquid metal gas two-phase systems. X-rays have been successfully used in the visualisation of vapour explosion phenomena and the measurement of void fraction by several authors. One example of the use of a flash X-ray source is the visualisation of the fragmentation process in single droplet vapour explosions by Ciccarelli (1994). A recent use of flash X-rays to measure void fraction was the study of hot particles plunging into water by Theofanus (1994). But the use of a continuous source of X-rays for the measurement of void fraction in molten metal systems with gas is still rare. First successful attempts in the system tin gas were made by Baker (1998). Since this is still the standard it is described more extensively.

The imaging through a layer of heavy liquid metal and an additional structural material e.g. steel requires a high-energy beam and a high dose rate to get data that can be used in quantitative analysis. For a 100 mm tin layer ($\rho_{tin} \sim 7{\cdot}10^3$ kg/m^3) and 25 mm steel walls, Baker (1998) used a continuous spectrum X-ray source with a peak energy of 9 MeV and an on-axis dose rate, one meter from the source, of 30 Gy/min to image the test section. The X-ray source pulses at approximately 275 Hz at this dose rate. The pulse frequency may be synchronised with the imaging system so that a constant number of one to nine pulses is collected for each frame. In most cases the X-ray and imaging systems are left unsynchronised to avoid a serious noise component introduced in the video signal.

The focal spot for the Baker-Bonazza (1998) X-ray source is less than 2 mm. The X-ray head is mounted on a scissor lift table that allows it to be moved vertically and aligned with the image collection system. Images are collected using an X-ray sensitive glass screen. The conversion screen is imaged through a mirror and a lens onto an inverting image intensifier which is coupled to one of two CCD cameras by means of a relay lens. Then the images are digitised and stored with a frame grabber. The signal path is shown in Figure 11.5.2.

The first step to obtain a digital image is to eliminate the effect of the CCD camera's dark current. In a next step the images are normalised against any spatial non-uniformity

of the X-ray source output. In the third step the images have to be normalised against any spatial non-uniformity originating from the structure of the test section. All these steps are achieved by means of subtracting a dark current constant D from each pixel value $P(x,y)$, and by dividing this difference by the difference between the corresponding pixel value of an image of the empty test section (obtained immediately prior to the pouring of molten liquid metal into the test section), $P_0(x,y)$, and the same dark current constant, D. The logarithm of this ratio is a grey level from here on indicated as $P_{liquid}(x,y)$.

$$P_{liquid}(x,y) = \ln\left[\frac{P(x,y)-D}{P_0(x,y)-D}\right] \tag{11.95}$$

Due to the exponential nature of the interaction of the X-rays with material, $P_{liquid}(x,y)$ is directly proportional to the thickness of the absorbing material in the test section as described below. Since the production of secondary radiation from the test section structure is small, this technique also accounts for the attenuation that occurs in the structure of the test section. The value of each pixel in the subtracted image is dependent on the material; the X-ray beam must traverse when travelling from the source to the X-ray sensitive glass screen. At an average energy of approximately 3 MeV, water, water vapour and nitrogen gas are undetectable and the intensity I of the pixel (grey level) is only dependent on the amount of liquid metal in the beam path and the magnitude of scatter present in the imaging plane. This relationship, where the liquid metal thickness, z_{liquid}, is the product of the liquid metal density and the portion of the chordal path length comprised of the liquid metal, is:

$$\frac{I}{I_{empty}} = B\exp\left[-\left(\frac{\mu}{\rho}\right)_{liquid} z_{liquid}\right] \tag{11.96}$$

where I is the X-ray fluence intensity in photons per square centimetre, B the built-up factor, μ the magnetic permeability $4\cdot\pi\cdot10^{-7}$ As/Vm and ρ the density of the fluid.

Since the pixel values are linearly proportional to the intensity of the light reaching the CCD sensor, the image can be thought of as a two-dimensional mapping of the chordal average amount of liquid metal, along the beam path. If one assumes that the liquid vapour or the injected gas are void within the liquid metal, then the liquid metal chordal average can be related to the void fraction as:

$$\alpha(x,y) = 1 - \frac{z_{liquid}(x,y)}{z_0(x,y)} \tag{11.97}$$

in which $z_0(x,y)$ is the amount of liquid metal along the beam path for zero void at the individual test conditions. Running an arbitrary experiment at different temperatures the thermal expansions both of the liquid metal and the test sections has to be taken into account, since both quantities modify the density the X-ray beam faces.

The difficulty in the data reduction is in determining how to compensate for the scatter of X-rays. This is frequently neglected in studies with much thinner test sections and low energy X-rays. But our test section is several mean free paths thick, and therefore produces a significant amount of scatter when high energy X-rays are used. If the scattered X-rays are distributed homogeneously in the plane of the glass screen, the previously mentioned linear relationship between the chordal average amount of tin and the grey level is maintained and each individual image may be calibrated using two known points to define the relationship between the grey level and liquid metal thickness. These two points allow the slope, m, and intercept, b, to be calculated and a calibration line may be defined as:

$$P_{liquid}(x,y) = b - m\cdot z_{liquid}(x,y) \tag{11.98}$$

In order to check for this linear relationship a solid liquid metal piece is inserted into the test section and a large amount of images has to be taken. Through an averaging procedure one single image is obtained. This procedure substantially reduces the noise in the image and is the preferred method of quantitative imaging of static objects. The mean grey level for the pixels in the image of each step can then be measured. Repeating this procedure with liquid metal pieces of different thickness a linear relation between grey level and liquid metal thickness should be obtained. If the secondary radiation is not as assumed above, the void distribution in the test section would affect the calibration. A series of performance experiments conducted by Baker (1996) in which the void fraction distribution within a test box was artificially changed by means of Styrofoam balls demonstrated that there is little to no effect on the measurement of void fraction due to void distribution.

Once established that a linear relationship between grey level and liquid metal chordal average thickness exists, the calibration of each individual image in an experimental run can be accomplished with two points to define the calibration line. The grey level associated with 0% void is determined from the darkest pixel value. Typically this region is in the bottom corners of the test section or between the two injection ports for gas lifting. Depending on the height of the liquid metal within the test section, the grey level associated with 100% void is determined from either the region above the level of the liquid surface; or from the image of a hollow steel tube, sealed at both ends, of the same chordal length as the test section, placed at the upper right corner of the field of view. The linear relationship between these two points is used to relate the spectrum of grey levels to the chordal average amount of the liquid metal. Figure 11.5.6 shows an example of a two-dimensional map of void fraction for an experiment by Bonazza (1998) that involved only gas injection into 11 kg of molten tin. The 12 grey levels in the image represent equal bands of void fraction between 0% and 100%. For example, the darkest grey level represents a void fraction band of 0-8.3% void while the next grey level represents 8.4-16.6% void and so on. The integral (volume averaged) void fraction for the image can be obtained by calculating an average grey level weighted by the number of pixels in each band in the image, N_i, as follows:

$$\alpha = \frac{\sum_i N_i \alpha_i}{\sum_i N_i} \tag{11.99}$$

where α_i represents the average void fraction for the i-th band with N_i pixels. The conditions exhibited in Figure 11.5.6 represent an average void fraction of 25.9% for the entire volume.

Figure 11.5.6: Arrangement of a void fraction measurement using the X-ray technique and the associated image recording (left); X-ray image of gas injection at a rate of 9.2 cm/s into 11 kg of molten tin at 421°C (right)

Top edge of the molten tin pool is clearly visible (Baker, 1998)

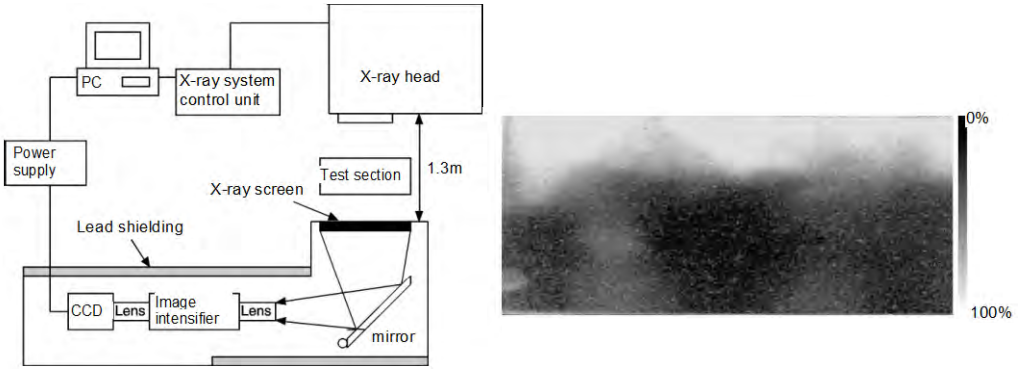

Noise and unsharpness

Although image quality is frequently discussed on the basis of sharpness and contrast, these are poor measures for a quantitative analysis of the errors involved in void fraction measurement. As suggested by Macovski (1983), a better measure is the signal-to-noise ratio (SNR) defined as:

$$SNR = \frac{(I_2 - I_1)}{SD} \tag{11.100}$$

where I_1 is the background or 100% void signal, I_2 is the signal of interest, and SD is the standard deviation of I_2. The processes that must be considered to estimate the signal-to-noise ratio are photon generation, photon interaction with the test section and metal, photon to light conversion in the glass screen, light collection through two lenses, the light photon conversion to electrons in the image intensifier and the CCD sensor, and the signal digitisation. If one assumes that the energy of the X-ray source is either constant or Poisson distributed, then the photons that are emitted from the source are Poisson distributed with parameter N, the number of photons emitted. The transmission of the beam through the test section is accounted for by modelling the beam absorption in the structural steel and liquid metal as a series of binomial processes. The beam that exits the test section is therefore still Poisson distributed, but with parameter M given by:

$$M = N \cdot \exp\left[-\left(\frac{\mu_{steel}}{\rho_{steel}}\right) z_{steel}\right] \exp\left[-\left(\frac{\mu_{metal}}{\rho_{metal}}\right) z_{metal}\right] \tag{11.101}$$

assuming the test section to be made of steel and the subscript *metal* indicating the liquid metal to be investigated. As for any Poisson distributed random variable with parameter M, the standard deviation is just the square root of M.

To account for the glass screen, intensifier and camera, several processes must be included. First, the screen must absorb or interact with an incoming photon. This process may also be modelled as a binomial process. Second, the production of light photons following X-ray absorption is modelled as a Poisson process. Then, the intensifier and CCD camera are modelled as additional Poisson-distributed amplification stages that account for photon to electron and electron to photon conversions in the intensifier as well as the light collection efficiency of the camera. As derived by several authors, including Macovski (1983), this results in the following expression for SNR:

$$SNR = \left(\frac{I_1 - I_2}{I_1}\right) \cdot \frac{\sqrt{1 - \exp\left(\mu_g x_g\right) M}}{\sqrt{1 + \frac{1}{g_1} + \frac{1}{g_1 g_2} + \frac{1}{g_1 g_2 g_3}}} \tag{11.102}$$

where g_1, g_2 and g_3 are the gains of the glass screen, image intensifier and camera respectively.

The last step in the imaging chain is the digitisation that occurs in the CCD camera. This increases the noise in the image by the Factor F_d, derived by Swindell (1991):

$$F_D = \left[1 + \frac{1}{12}\left(\frac{N_m \cdot SD}{2^8}\right)\right]^{\frac{1}{2}} \tag{11.103}$$

where N_m is the number of electrons required to produce a maximum video signal and SD is the standard deviation of the signal prior to digitisation. The final factor which must be accounted for is the effect of X-ray scatter on the SNR. Scatter produces an additive noise to that of the primary photons already accounted for. The scatter reduces the SNR by a

factor F_s, which depends on the number of photons in the primary beam, N_p, the number of photons at the imaging plane due to scatter, N_s, and the ratio, q, of the glass screen X-ray to light conversion efficiencies for scatter and primary photons. F_s was shown by Jaffray (1994) to be:

$$F_s = \frac{1}{\sqrt{1 + \left(q \cdot \frac{N_s}{N_p} \right)}} \tag{11.104}$$

Scattered photons are at a lower energy than the primary photons so they have a lower absorption probability but a higher light production per absorbed photon. Using the correction for the parameters discussed, one can estimate the maximum error in the void fraction determination.

To illustrate the effect of noise, one can determine the minimum size void that would be detectable in a liquid metal pool. A common method to determine the size of a void that is detectable by a human observer, is to assume that contrast must be at least five times the noise in the system. The void detectability and image quality are also limited by the image unsharpness which can be attributed to three sources. First, the finite size of the X-ray source focal spot creates a geometric distortion or penumbra. Second, the inherent characteristics of the glass screen limit resolution as does the requirement that the size of an area imaged by a single pixel of the camera must be at least half of the detectable void size. Overall, it is evident that noise considerations will limit void detectability to a much larger extent than the image unsharpness produced in the digital imaging system.

Errors due to mixture dynamics

In addition to the effects of system noise, scatter and image unsharpness on the visualisation and measurement of void fraction, the effects of the multi-phase system dynamics on the measurement accuracy must be analysed. The most significant source of error is the motion of the liquid metal and gases and the consequent void fraction fluctuations during the time required to obtain an image. The fluctuations in the amount of void along the beam path increase the transmission of X-rays through the mixture as shown by Harms (1973) and Oyedele (1991). Examples of phenomena that could result in these fluctuations are bubble growth or movement in the test section as shown in Figure 11.5.7. This effect will result in the present measurements overestimating the actual void fraction. If one models the void fluctuations as variations about a mean, $\alpha + \Delta\alpha$, then the transmittance of X-rays is increased by a factor F_T, derived by:

$$F_T = 1 + \frac{\lambda^2 \langle \Delta\alpha \rangle^2}{2} \;,\; \Delta\alpha = \frac{1}{\lambda} \ln \left[\frac{1}{\tau} \int_{t=0}^{t=\tau} \exp\left(\lambda\alpha(t)\right) dt \right] - \frac{1}{\tau} \int_{t=0}^{t=\tau} \alpha(t)\, dt \tag{11.105a,b}$$

where λ is the number of mean free paths along the beam direction through the test section. An expression for this dynamic error was subsequently derived by Harms (1973) as Eq. (11.105b). In this equation t is the time required to collect one image frame. A detailed knowledge of the void fluctuation with time is required to estimate the error. Since this information is mostly unavailable, reasonable estimates of the largest possible fluctuations must be made from the rise velocity of bubbles in the multi-phase mixture.

Regan (1997) reports on X-ray reflectivity studies of liquid metal and alloy surfaces. They observe a mono-atomic layering of the liquid phase at the surface, connected with reflection of X-rays, potentially opening up possibilities to measure the surface structure. On the other hand, they might also have to be considered in the evaluation of other X-ray measurement results.

Figure 11.5.7: Illustration of the void dynamics that increase X-ray transmission

Void growth or the increase in the number of voids along the beam path as illustrated in Case 1 will increase transmission. Void movement or change in distribution without a change in the total void along the beam path, as illustrated in Case 2 will not result in a transient change in X-ray transmission

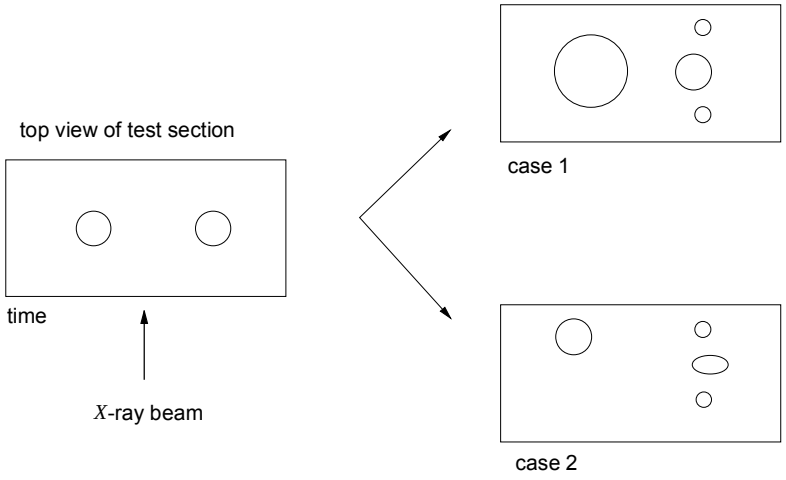

11.5.4.2.2 γ-ray absorption

Because of extreme complexity of two-phase flows, most of the well-known empirical relations and models give area-averaged void fractions. Since void fraction varies across the cross-section of the pipe, to determine averaged void fraction, void fraction profiles as a function of radial distance should be determined. This can be done two-dimensionally through one cross-section by means of the γ-ray absorption technique.

For this purpose the cross-section of the two-phase flow in the pipe is assumed to have a number of circular zones having a uniform void fraction in each zone. This is schematically depicted in Figure 11.5.8. Consider now m circular zones having the void fractions α_1, α_2,..., α_j,..., α_m to be determined and additionally let β_1, β_2,..., β_i,..., β_n be the measured void fractions at the various chord lengths, then one gets:

$$\beta_i = \sum_{j=1}^{m} \frac{d_{ij}}{c_i} \alpha_j$$

where c_i is the total path length for the gamma ray at the i-th chord length and d_{ij} is the length of the j-th zone intercepted by the gamma ray bean at the i-th chord length. β_i are obtained from measured gamma ray intensities at the i-th chord with gas alone ($I_{i,g}$), with liquid metal alone ($I_{i,l}$) and when two-phase-flow is present ($I_{i,t}$) and are given by:

$$\beta_i = \frac{\ln\left[\frac{I_{i,t}}{I_{i,l}}\right]}{\ln\left[\frac{I_{i,g}}{I_{i,l}}\right]} \tag{11.106}$$

Let E be the error function defined as follows:

$$E^2 = \left(\sum_{i=1}^{n} \beta_i - \sum_{j=1}^{m} \frac{d_{ij}}{c_i} \alpha_j\right)^2 \tag{11.107}$$

The minimisation of E with respect to the m parameters of α_1, α_2,..., α_j,..., α_m gives a set of of m linear equations. Using the measured values of β_1, β_2,..., β_i,..., β_n the values of α are obtained.

Figure 11.5.8: Scheme for the cross-sectional measurement of the two-dimensional void fraction profile using γ-ray absorption

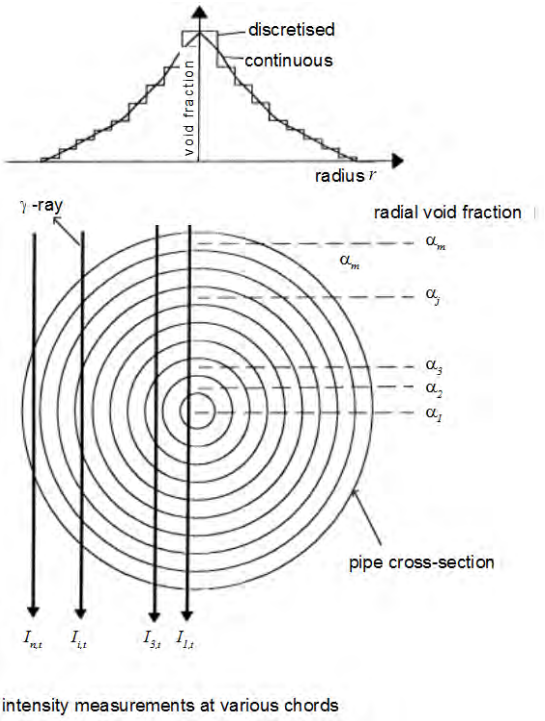

Source: Satyamurthy (1998).

In the experiment performed by Satyamurthy (1998) in a mercury nitrogen mixture, the number of chords chosen was 38 with 2.0 mm spacing. Seven zones were assumed. From the void fraction profiles, the area averaged void fraction was determined. The beam diameter (3 mm) was chosen so that finite beam errors were negligible (Satyamurthy, 1994) besides obtaining a large number of zones. Number of counts were taken in excess of 6 000 for every measurement so that statistical fluctuations were negligible (<1.5%) (Munshi, 1993). In addition, dynamic void fluctuation corrections were estimated to determine the error range in the analysis (Thiyagarajan, 1991).

Corrections for the void fraction measurements

In a two-phase flow, void fraction fluctuation increases the radiation transmittance. Because of this the measured void fraction from the transmitted radiation intensity will be greater than the time-averaged void fraction (Harms, 1971). The effect of these fluctuations with respect to the attenuation parameter λ (= $\mu \cdot l/M$) is studied in detail by Thiyagarajan (1991). If the fluctuation magnitude (maximum deviation from average) is known, then the exact error due to the fluctuation can be determined. Corrections for two types of fluctuations – large (±100% deviation from the average) and medium (±50% deviation from the average) – have been worked out for a given attenuation parameter. Due to the non-availability of data on the degree of fluctuation in the experiment, the required correction for dynamic fluctuation is applied by the following procedure. The fluctuation correction for maximum possible fluctuation magnitude (±100% deviation from average) is applied to the measured data β', and the corrected value β'' is obtained.

The exact dynamic fluctuation-corrected void fraction lies between β′ and β″. Radial void fraction profiles are obtained separately with the uncorrected data (β′) and the corrected data (β″). The average of the two profiles is considered the dynamic fluctuation-corrected void fraction profile.

Statistical fluctuation correction

Radioactive decay obeys Poisson's distribution law and is prone to random statistical fluctuations in the gamma-ray emission. It is well known from counting statistics that the maximum error involved in any intensity counts N is equal to $N^{1/2}$. Since the measured void fraction is related to three intensities as given in Eq. (11.108), the effect of statistical fluctuation has to be determined. In this method, it can be shown that the error due to statistical fluctuation is described by Eq. (11.109):

$$\varepsilon_i = \beta_i - \sum_{j=1}^{m} \frac{d_{ij}}{c_i} \alpha_j \tag{11.108}$$

$$\frac{\Delta\alpha}{\alpha} = \frac{1}{\alpha}\left(\frac{1}{\ln\left(I_g / I_l I\right)}\right) \cdot \left[\frac{1}{I} + \frac{\alpha^2}{I_g} + \frac{(\alpha-1)^2}{I_l}\right]^{\frac{1}{2}} \tag{11.109}$$

Herein, ε_i is the dimensionless error in one particular measurement.

Calibration, effort and accuracy

Due to the high density especially of the heavy liquid metals quite strong γ-sources are required. Satyamurthy (1998) used a Cobalt-60 emitter with an activity of 2 775 MBq as the γ-ray source. Moreover, for the measurements 1.33 MeV photons were used which expands the capabilities of most of the liquid metal laboratories.

To determine the overall accuracy in measuring the void fraction profile, a static simulation system of gas and liquid metal is required similarly as for the X-ray technique in order to determine the individual levels corresponding to a specific void fraction value. The output of this process which must be performed with the liquids later used in the experiment is a calibration curve. If this is properly done void fraction profiles with an accuracy of about ±5% can be measured with the γ-ray absorption.

11.5.4.2.3 Neutron radiography (NR)

Neutron radiography (NR) is one of radiographic techniques which make use of the difference in attenuation characteristics of neutrons in materials (von der Hardt, 1981). Since thermal neutrons easily penetrate heavy materials like dense metals and are attenuated well by light materials as those containing hydrogen, NR was developed as a technique for non-destructive inspection which is complementary to X-ray radiography in the automobile and aerospace industries (Barton, 1993). Recently, the application has spread to various scientific fields such as agricultural, medical and dental sciences, as well as application to porous materials like concrete and brick. Moreover, fluid research with use of the dynamic method of NR, i.e. real-time NR, has been a great hit because this technique is suitable for visualisation of a multi-phase flow in a metallic casing (Mishima, 1992; Hibiki, 1994a) and a liquid metal (Takenaka, 1994b). With ever-widening fields of application, it is thought that the research trend is evolving from qualitative to quantitative applications. Some attempts have been made to use NR not only as a tool for visualisation but also as a tool for quantitative measurement. Quantitative utilisation can be classified into two categories.

The first is to use the geometrical information extracted from NR images, for example, measurement of particle trajectory and velocity (Ogino, 1994), and hold up in a fluidised

bed (Chiba, 1989). The second is to use the attenuation characteristics of neutrons in materials, for instance, measurement of void fraction in multi-phase flow (Mishima, 1993; Hibiki, 1993). For this purpose a quantification method, namely the Σ-scaling method, was developed (Hibiki, 1996).

Basic concept of neutron radiography

The mass attenuation coefficient of X-rays increases monotonically with the atomic number. Conversely, thermal neutrons easily penetrate most metals, and are attenuated well by materials such as hydrogen, water, boron, gadolinium and cadmium. In other words, X-ray radiography takes advantage of the difference in densities, while NR takes advantage of the difference in neutron absorption cross-sections. It is thus clear that NR is more suitable for observing the fluid behaviour in a metallic duct and liquid metals.

A block diagram of the imaging system for high-frame-rate NR with a steady neutron beam is shown in Figure 11.5.5. Here, the test section is set up in front (right) of the scintillator. When the neutron beam penetrates two-phase flow in the test section, the beam is attenuated in proportion to the liquid layer thickness along its path. Thus, the neutron beam projects the image of two-phase flow. The neutron beam is changed into an optical image by the scintillator. The luminous intensity of the optical image is then increased by an image intensifier to obtain a better image. After the image is enlarged with a telephotographic lens, it is detected with a high-speed video camera. The quality of the image obtained can be improved by using an image processing system consisting of an image memory and image processor. The conditions necessary to achieve a high-frame-rate NR for liquid metal two-phase flows are listed directly following Figure 11.5.9.

Figure 11.5.9: Schematic view of the neutron components falling on the converter screen and the subsequent path for processing the data for the void fraction measurement using neutron radiography (NR)

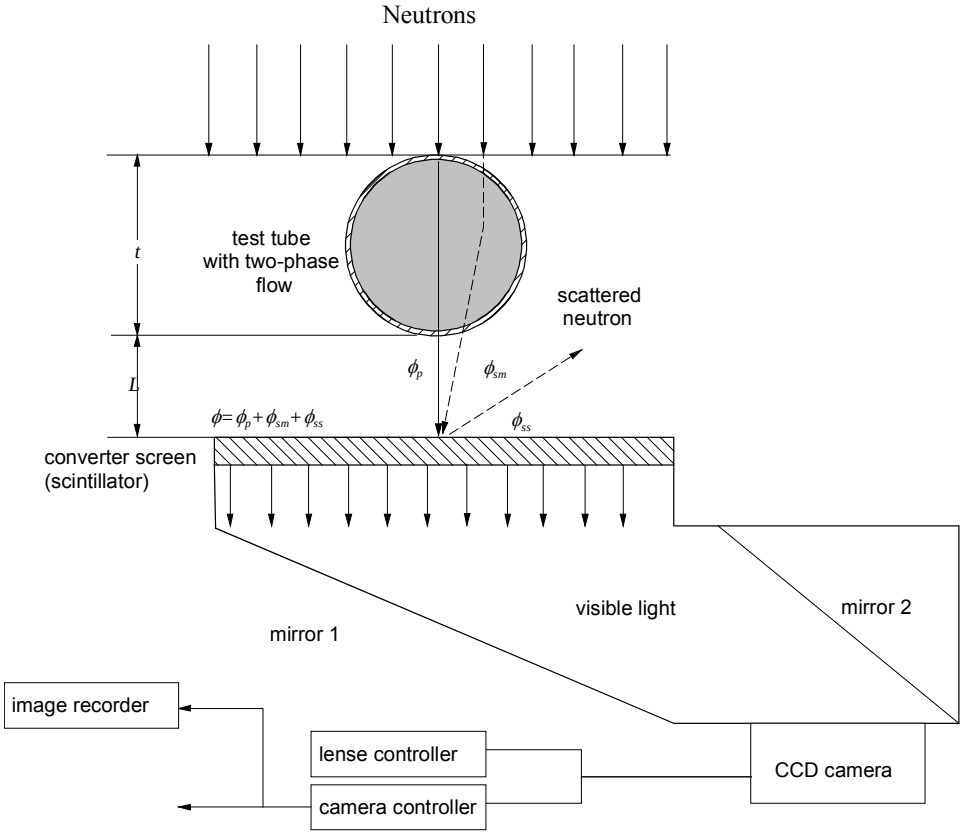

- *Considerable large high flux neutron source (nuclear reactor):*

  The neutron beam of thermal reactors is not monoenergetic. The spectrum has a Maxwellian distribution in the thermal region, a distribution proportional to 1/E above 0.5 eV, and a bump in the fast region around 2 MeV. Above 10 MeV, the distribution drops rapidly. In sample materials this leads to beam hardening. As the sample becomes thicker, the lower energy parts of the spectrum are depleted at a faster rate than the higher energy parts because of the larger cross-section at low energy, decreasing the effective attenuation coefficient for thicker samples. Thus, a correction for beam hardening is inevitable.

  Fast neutron radiography (FNR) is attractive as a non-destructive inspection technique due to the excellent matter penetration characteristics of fast neutrons. FNR is especially suitable for non-destructive inspection of industrial products that are too thick or dense to be inspected by conventional thermal neutron radiography (NR). Despite the availability of various fast neutron sources such as nuclear reactors, radioisotopes and accelerators without a neutron moderator, FNR is not in widespread use. One of the reasons for this is the difficulties in clearly discriminating γ-rays associated with the neutron beam. These problems were overcome by the use of imaging plates with γ–ray discrimination (Matsubayashi, 2001) and an FNR converter using wavelength-shifting fibres (Matsubayashi, 2003).

- *A high sensitivity scintillator:*

  The scintillator to be used in high-frame-rate NR should have characteristics of a high light yield, high resolution and short light decay time. Since rare earth scintillators of gadolinium compounds have a long light decay time and glass scintillators have a low light yield, these are not applicable to high-frame-rate NR. Only zinc sulphide scintillators mixed with lithium fluoride currently meets the above three conditions.

- *A high-speed video system with high reliability and long recording time*:

  The purpose of developing high-frame-rate NR with a steady neutron beam is to visualise rapid phenomena for a long time period. Therefore, a high-speed video with a long recording time should be used, although the sensitivity is also important.

- *A high performance image intensifier or a high sensitivity camera*:

  Regarding the image intensifier a high amplification rate of the order of 105 with a high frame rate and a high resolution in terms of line pairs per millimetres is required to capture oscillations. The image intensifier has to be matched to the high-speed camera.

Due to the oscillations of the neutron spectrum in a reactor, spatial variations of the beam and varying random noise a lot of effort has to be spent in the pre-processing of images to correct systematic noise errors. A detailed description of this procedure can be found in Richards (2004). Once the pre-processing is done and the reference measurements to obtain the flat field images for a single-phase only (gas/liquid), no duct inside are conducted in order to correct for scattering, etc., the void fraction measurement can start.

The principle of the void fraction measurement

The flux of incident neutron ϕ_{th} is attenuated in the liquid and the structure material of the test section, thus:

$$\phi = \phi_{th} \cdot \exp\left[-\Sigma_G \delta_G - \Sigma_L \delta_{ML} - \Sigma_t \delta_t\right] + \phi_S \tag{11.110}$$

where ϕ and ϕ_S denote the total neutron flux falling on the converter and scattered neutron component, respectively. Ignoring the neutron absorption in the gas phase, the

measured grey levels G are given by the following equations for the gas-filled (subscript G), liquid-filled (subscript L), and two-phase-mixture-filled (subscript ML) test sections.

$$\begin{aligned}\tilde{G}_G^0 &= C\,\phi_{th}\cdot\exp\left[-\Sigma_t\,\delta_t\right]+G_0\\ \tilde{G}_L^0 &= C\,\phi_{th}\cdot\exp\left[-\Sigma_L\,\delta_L-\Sigma_t\,\delta_t\right]+G_0\\ \tilde{G}_M^0 &= C\,\phi_{th}\cdot\exp\left[-\Sigma_L\,\delta_{ML}-\Sigma_t\,\delta_t\right]+G_0\end{aligned} \tag{11.111}$$

where G_0 is the offset term which consists of scattered neutron component G_S and dark current G_D; $G_0 = G_S + G_D$. The tilde (~) denotes that the grey levels among the images were normalised, i.e. by matching the reference brightness at some point outside the test section where neutron attenuation is negligible. Usually the dark current term G_D is uniform and can be treated as an offset. On the other hand the scattered neutron component G_S is not always uniform. To treat G_0 as an offset, the scattered neutron component G_S should be spatially uniform. The scattered neutron component G_S consists of neutrons scattered in the test section G_{SM} and those scattered in the surrounding background objects G_{SS}:

$$G_S = G_{SM} + G_{SS} = C\left(\phi_{SM} + \phi_{SS}\right) \tag{11.112}$$

Since ϕ_{SS} is, in most cases, spatially uniform, the scattered neutron component G_S could be made spatially uniform if ϕ_{SM} is spatially uniform or negligible. This condition can be achieved by taking a sufficiently large distance L' between the test section and the converter. The minimum of this distance is currently being estimated experimentally to be about the width of the test section. With this uniform G_S, the term G_0 can be treated as a constant offset. Then, from Eq. (11.111), the offset term G_0 can be determined using the grey levels obtained from the liquid-filled and gas-filled test sections by:

$$G_0 = G_S + G_D = \frac{\tilde{G}_L^0 - \tilde{G}_G^0\exp\left(\Sigma_L\delta_L\right)}{1-\exp\left(\Sigma_L\delta_L\right)} \tag{11.113}$$

Finally, the void fraction α is obtained by:

$$\alpha_0 = 1-\frac{\delta_{ML}}{\delta_L} = \frac{\ln\left(\tilde{G}_L/\tilde{G}_M\right)}{\ln\left(\tilde{G}_L/\tilde{G}_G\right)} = \frac{\ln\left(\tilde{G}_L^0 - G_0/\tilde{G}_M^0 - -G_0\right)}{\ln\left(\tilde{G}_L^0 - G_0/\tilde{G}_G^0 - -G_0\right)} \tag{11.114}$$

In this method, the offset term G_0 is determined based upon the total macroscopic cross-section Σ_L, and quantitative information is derived from grey levels which are relative quantities by nature. In this sense, this is called the Σ-scaling method. As discussed above, this method assumes that the offset term G_0 can be made spatially uniform by taking a large distance L'. It should be noted here that the un-parallelness of the incident neutron beam causes image blur, especially in the vicinity of material boundary. The spatial resolution is given by the distance L' and the L/D ratio of the NR facilities follows:

$$R = \frac{L'}{\left(L/D\right)} \tag{11.115}$$

Therefore the appropriate range of L' to be used in the Σ-scaling method should be an optimum value taking into account the above two requirements. This method was tested with a known void profile (Matsubayashi, 2004).

Moreover, to confirm this method for the void fraction of two-phase flow in a rectangular duct gas velocities calculated from the void fractions measured by the NR method are compared with those by calculated by conductance probe methods (Mishima, 1993; Saito, 2005) as shown in Figure 11.5.10 (left).

Figure 11.5.10: Comparison of the measured void fractions taken by real-time NR, optical and conductance probe methods with the drift correlation (left); simultaneous time series of void fraction and resistive (conductance) probe signals in a lead-bismuth nitrogen two-phase flow (right)

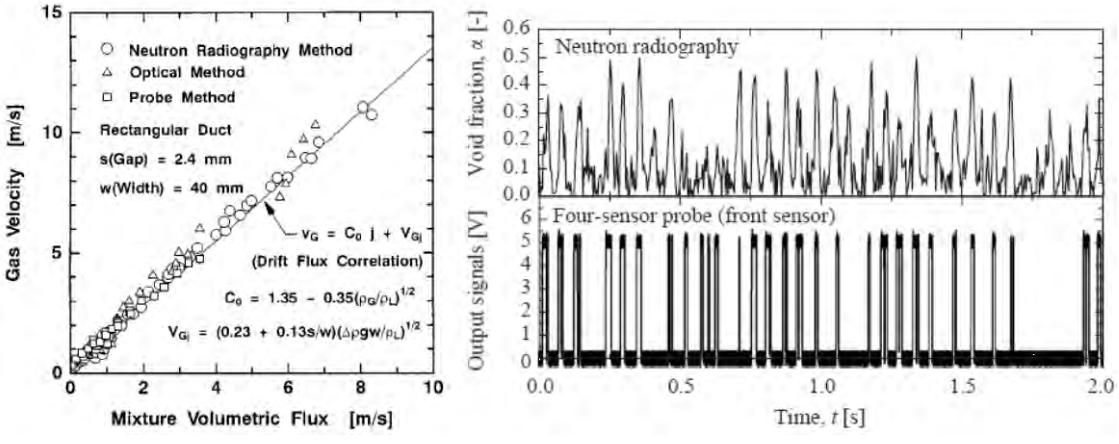

Source: Left image from Mishima (1997), right image from Saito (2005).

Since the measured values by high-frame-rate NR are particularly affected by neutrons' statistical variation, the integrated image of the images obtained by the real-time NR with a recording speed of 30 frames per second instead of the high-frame-rate NR was used here. It is shown that the measured values are consistent with each other and correlated well by Mishima's (1997) drift flux correlation. The measurement error by the NR method is estimated to be less than 5%. The sensitivity of the high-speed NR compared to intrusive methods like resistive (or conductance) probes is orders of magnitude larger than the latter. They are not affected by local effects close to a probe tip, wetting effects or material compatibility. With one scan consisting of several frames a complete void fraction profile along a tube can be acquired. Using an Abel integration, which implicitly assumes axis symmetry, even the two-dimensional void fraction profiles can be reconstructed (Saito, 2004, 2005). A comparison of the NR performance and its resolution to a conductance probe is shown in Figure 11.5.6 (right) on the example of a time series of the measured void fraction.

11.6 Temperature measurement

11.6.1 Thermocouples

The measurement of the liquid lead-bismuth temperature is usually performed using NiCr-Ni thermocouples being mantled by a stainless steel tubing. A careful determination of the temperature is necessary to determine the thermophysical data of the fluid. The diameter of the elements used varies between 0.25 mm and 3.0 mm depending on the time scales to be resolved at the desired location. Because of the high heat transfer coefficients that are characteristic of a liquid metal the frequency response of thermocouples is far higher than in conventional fluids. According to Krebs (1983) a 0.25 mm sheathed thermocouple with an insulated junction gives undamped signals in sodium in excess of at maximum 40 Hz.

The temperature signal coming from a thermocouple arises from the thermo-electric effect. The connection of two different materials is called "thermocouple". If two different types of metals are connected together by welding, soldering or only by twisting, a voltage is generated. This can be measured at the end of the two materials. At the connection of two different metals the electrons are changing from one metal into the other. The key

parameter for this process is the escape work of the electrons. The metal with the lower escape work delivers electrons and becomes positive. Thereby an electric field ϕ arises in the interface.

The contact voltage $\Delta\phi$ which is generated in the contact surface is proportional to the Boltzmann distribution of the temperature T and also to the relation of the free electron densities n_A and n_B. This is the so-called Seebeck effect:

$$\Delta\phi = \frac{kT}{e_0} \ln\left(\frac{n_A}{n_B}\right) \tag{11.116}$$

where k is the Boltzmann constant and e_0 the elementary charge. The terms in the right side can be combined with the material constant k_{AB}. Then the equation reduces to:

$$\Delta\phi = k_{AB} \cdot T \tag{11.117}$$

About 13 "standard" thermocouple types are commonly used. Eight have been given internationally recognised letter type designators. The letter type designator refers to the electromotive force (emf) table, not the composition of the metals, so any thermocouple that matches the emf table within the defined tolerances may receive that table's letter designator. Some of the non-recognised thermocouples may excel in particular niche applications and have gained a degree of acceptance for this reason, as well as due to effective marketing by the alloy manufacturer. Some of these have been given letter type designators by their manufacturers that have been partially accepted by industry. Each thermocouple type has characteristics that can be matched to applications. Industry generally prefers *K* and *N* types because of their suitability to high temperatures, while others often prefer the *T* type due to its sensitivity, low cost and ease of use. The standard thermocouple types are presented in Table 11.6.1. The table also shows the temperature range for extension grade wire in brackets.

The dependence of the measurement signal against a reference ice point (T = 0°C) is shown in Table 11.6.2 for Ni-CrNi and Cu-CuNi (copper-constantan) thermocouples as examples.

Table 11.6.1: ANSI registered thermocouple groups containing the accuracy, range and composition

Type	Positive material	Negative material	Accuracy*** Class 2	Range °C (extension)	Comments
B	Pt, 30%Rh	Pt, 6%Rh	0.5% > 800°C	50 to 1 820 (1 to 100)	Good at high temperatures, no reference junction compensation required
C**	W, 5%Re	W, 26%Re	1% > 425°C	0 to 2 315 (0 to 870)	Very high temperature use, brittle
D**	W, 3%Re	W, 25%Re	1% > 425°C	0 to 2 315 (0 to 260)	Very high temperature use, brittle
E	Ni, 10%Cr	Cu, 45%Ni	0.5% or 1.7°C	-270 to 1 000 (0 to 200)	General purpose, low and medium temperatures
G**	W	W, 26%Re	1% > 425°C	0 to 2 315 (0 to 260)	Very high temperature use, brittle
J	Fe	Cu, 45%Ni	0.75% or 2.2°C	-210 to 1 200 (0 to 200)	High temperature, reducing environment
K*	Ni, 10%Cr	Ni, 2%Al 2%Mn 1%Si	0.75% or 2.2°C	-270 to 1 372 (0 to 80)	General purpose high temperature, oxidising environment

See notes on page 811.

Table 11.6.1: ANSI registered thermocouple groups containing the accuracy, range and composition *(cont.)*

Type	Positive material	Negative material	Accuracy*** Class 2	Range °C (extension)	Comments
L**	Fe	Cu, 45%Ni	0.4% or 1.5°C	0 to 900	Similar to J type; obsolete – not for new designs
M**	Ni	Ni, 18%Mo	0.75% or 2.2°C	-50 to 1 410	
N*	Ni, 14%Cr 1.5%Si	Ni, 4.5%Si 0.1%Mg	0.75% or 2.2°C	-270 to 1 300 (0 to 200)	Relatively new type as a superior replacement for K type
P**	Platinel II	Platinel II	1.0%	0 to 1 395	A more stable but expensive substitute for K & N types
R	Pt, 13%Rh	Pt	0.25% or 1.5°C	-50 to 1 768 (0 to 50)	Precision, high temperature
S	Pt, 10%Rh	Pt	0.25% or 1.5°C	-50 to 1 768 (0 to 50)	Precision, high temperature
T*	Cu	Cu, 45%Ni	0.75% or 1.0°C	-270 to 400 (-60 to 100)	Good general purpose, low temperature, tolerant to moisture
U**	Cu	Cu, 45%Ni	0.4% or 1.5°C	0 to 600	Similar to T type; obsolete, not for new designs

* Most commonly used thermocouple types.

** Not ANSI recognised types.

*** See IEC 584-2 for more details.

Material codes: Al – aluminium, Cr – chromium, Cu – copper, Mg – magnesium, Mo – molybdenum, Ni – nickel, Pt – platinum, Re – rhenium, Rh – rhodium, Si – silicon, W – tungsten.

Table 11.6.2: Electric voltage of the thermocouples Cu-CuNi and Ni-NiCr in millivolts as a function of the temperature in the range 0-400°C

The temperature function is calculated from the electric voltage produced by the thermocouple with the following polynom $T\,(°C) = A_0 + A_1 \cdot U(mV) + A_2 \cdot U^2(mV)$

Temperature	Cu-CuNi	Ni-CrNi	Temperature	Cu-CuNi	Ni-CrNi
0°	0.00	0.00	210°	9.74	8.54
10°	0.40	0.40	220°	10.29	8.94
20°	0.80	0.80	230°	10.85	9.34
30°	1.21	1.20	240°	11.41	9.75
40°	1.63	1.61	250°	11.98	10.16
50°	2.05	2.02	260°	12.55	10.57
60°	2.48	2.43	270°	13.13	10.98
70°	2.91	2.85	280°	13.71	11.39
80°	3.35	3.26	290°	14.30	11.80
90°	3.80	3.68	300°	14.90	12.21
100°	4.25	4.10	310°	15.50	12.63
110°	4.71	4.51	320°	16.10	13.04
120°	5.18	4.92	330°	16.70	13.46

Table 11.6.2: Electric voltage of the thermocouples Cu-CuNi and Ni-NiCr in millivolts as a function of the temperature in the range 0-400°C *(cont.)*

The temperature function is calculated from the electric voltage produced by the thermocouple with the following polynom T (°C) = $A_0 + A_1 \cdot U(mV) + A_2 \cdot U^2(mV)$

Temperature	Cu-CuNi	Ni-CrNi	Temperature	Cu-CuNi	Ni-CrNi
130°	5.65	5.33	340°	17.31	13.88
140°	6.13	5.73	350°	17.92	14.29
150°	6.62	6.13	360°	18.53	14.71
160°	7.12	6.53	370°	19.14	15.13
170°	7.63	6.93	380°	19.76	15.55
180°	8.15	7.33	390°	20.38	15.98
190°	8.67	7.73	400°	21.00	16.40
200°	9.20	8.13	410°	21.62	16.82
Fitfunction polynom	A_0	A_1	A_2	Temperature range	
Cu-CuNi	3.4834965	23.22235	-0.21285	0-410°C	
Ni-CrNi	-0.4179542	24.79475	-0.0201893	0-380°C	

There are four common ways in which thermocouples are mounted within a stainless steel or Inconel sheath and electrically insulated with mineral oxides (Figure 11.6.1). Each of the methods has its advantages and disadvantages. A relatively robust arrangement is the sheath mounted thermocouple, due to the sealing and insulation effect of the sheath. The principal reason for not using this arrangement for all applications is its sluggish response time – the typical time constant is 75 seconds. The sealed mounting, grounded to the sheath, can cause ground loops and other noise injection. But, it provides a reasonable time constant (40 seconds) and a sealed enclosure. A faster response time constant (typically 15 seconds) is given by the exposed bead mounting. It lacks mechanical and chemical protection, however, as well as electrical isolation from material being measured. The porous insulating mineral oxides must be sealed.

The fastest response time constant is represented by the exposed fast response type. Typically for this arrangement this is 2 seconds, but with fine gauge junction wire the time constant can be 1-100 ms, depending on their diameter. In addition to problems of associated with exposed beads, protrusion and light construction render this type of thermocouple more prone to physical damage.

Because of their physical characteristics, thermocouples are the preferred method of temperature measurement in many applications. They can be very rugged, are immune to shock and vibration, are useful over a wide temperature range, are simple to manufacture, require no excitation power, there is no self-heating and they can be made very small. No other temperature sensor provides this degree of versatility. Thermocouples are wonderful sensors to experiment with in liquid metals because of their robustness, wide temperature range and unique properties.

On the down side, the thermocouple produces a relative low output signal that is non-linear. These characteristics require a sensitive and stable measuring device that is able to provide reference junction compensation and linearisation. The low signal level also demands that a higher level of care be taken when installing to minimise potential noise sources. The measuring hardware requires good noise rejection capability. Ground loops can be a problem with non-isolated systems, unless the common mode range and rejection is adequate.

Figure 11.6.1: Sheath options of thermocouples

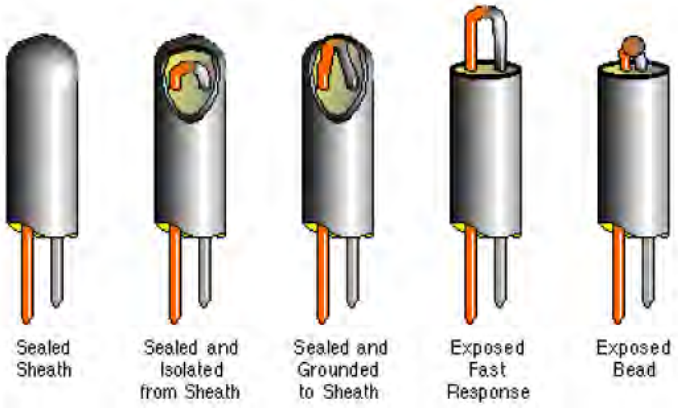

Source: Ni (2003).

If temperature is monitored with electromagnetic flow meters or electromagnetic pumps, misreadings may occur due to the ferromagnetic properties of the Ni-NiCr thermocouple. This effect increases dramatically if temperature gradients or gradients of the magnetic field exist. Numerous effects listed afterwards can lead to misreadings and as a consequence to misinterpretations during the operation.

In principle six thermo-magnetic effects exist which can influence the temperature measurement. An overview and detailed description of these effects is given by Kollie (1977) and Eringen (1980). The effects can be categorised as:

(a) transverse effects, Righi-Leduc effect and Nernst-Ettingshausen effect;

(b) longitudinal effects in a transverse field;

(c) longitudinal effects in a longitudinal field.

Both (b) and (c) cause changes in the thermal conductivity and the Seebeck coefficient of a material. Of all the effects, the Righi-Leduc and the two longitudinal effects of the Seebeck coefficient are – beside the Nernst-Ettingshausen effect – the most important in thermocouple thermometry in a magnetic field. In general appropriate design considerations and material choices have to be made before instrumenting a test section. Only the consideration of the afterwards-named effects and order of magnitude estimations prevent an exhaustive calibration effort. For example: temperature control some distance from the magnets of a pump might be performed by Ni-NiCr thermocouples. The temperature measurements within the magnetic field should rather be carried out using Cu-CuNi (copper-constantan) thermocouples.

The Nernst-Ettingshausen effect

If a temperature gradient ∇T is perpendicular to a magnetic field $\vec{\boldsymbol{B}}$ an electric field $\vec{\boldsymbol{E}}$ will be produced perpendicular to both according to Eq. (11.118). The magnitude of the electric field is determined by the Nernst-Ettingshausen coefficient Q, which is a material property.

$$\vec{\boldsymbol{E}} = \mathrm{Q}\left(\nabla T \times \vec{\boldsymbol{B}}\right) \tag{11.118}$$

The electromotive force (EMF) produced is given by the integral along the wire from zero to the length l:

$$EMF = \int_{s=0}^{s=l} \left[\mathrm{Q}\left(\nabla T \times \vec{\boldsymbol{B}}\right)\right] ds \tag{11.119}$$

The Nernst-Ettingshausen factor Q for the four compounds appearing in thermocouples Ni-NiCr and Cu-CuNi are shown in Table 11.6.3.

Table 11.6.3: Nernst-Ettingshausen coefficient Q and magnetic permeability μr of different thermocouple materials

Material	Q (10^{-11} V/[°C gauss])	μr magnetic permeability
Copper (Cu)	0.27	1
Copper-nickel (CuNi)	0.71	1
Ni (Alumel)	5.25	5
NiCr (Chromel)	27.00	1

Let us consider a configuration in which a temperature gradient of 50°C per mm exists, the thermocouple has a diameter of 0.5 mm and the magnetic field strength is 2 Tesla (2.104 gauss). The thermocouple wires may have a length of 30 mm perpendicular to the temperature gradient and the magnetic field and they are insulated from each other by magnesium oxide ceramics. A calculation which includes the heat conduction in the thermocouple yields the following astonishing result. The measurement error for a copper-constantan thermocouple for this set-up yields 1.015 K; for Ni-NiCr, however, on such a short length an error of 33.2 K is measured. Of course, the assumed temperature gradient has been chosen to exemplify the measurement errors.

The Righi-Leduc effect

If a temperature gradient ∇T is oriented perpendicular to a magnetic field $\vec{\boldsymbol{B}}$ a temperature gradient ∇T_t will develop transverse to ∇T and $\vec{\boldsymbol{B}}$ according to Eq. (11.120):

$$\nabla T_t = S\left(\vec{\boldsymbol{B}} \times \nabla T\right) \tag{11.120}$$

where S is the Righi-Leduc coefficient. However, Eq. (11.120) applies only if no heat flow occurs in direction of ∇T_t which is under adiabatic conditions. A line integral for the temperature difference ∇T can be formulated, similar to the Nernst-Ettingshausen effect, which reads to:

$$\Delta T = \int_{s=0}^{s=l} \left[S\left(\vec{\boldsymbol{B}} \times \nabla T\right)\right] ds \tag{11.121}$$

The Righi-Leduc effect results finally in an indicated temperature in a magnetic field that is different from that indicated without a magnetic field. However, for a 1 m long Ni-NiCr wire in a magnesium oxide mantle exposed to a magnetic field of 2 Tesla and a transverse temperature gradient of 50°C/1 mm the error would be 45°C. The Righi-Leduc coefficient of nickel is 10^{-7} gauss whereas the NiCr value was assumed to be infinitely small, as no according data is available.

The Seebeck effect

The Seebeck effect is of course the basis for thermocouple temperature measurement. However, the Seebeck coefficient of metals is changed in the presence of magnetic fields. Such changes cause errors in the temperature measurement because the thermal electromotive force of a thermocouple E_t is defined as a line integral:

$$E_t = \int_{s=0}^{s=l_p} \left[Se_p \nabla T \right] ds - \int_{s=0}^{s=l_n} \left[Se_n \nabla T \right] ds \tag{11.122}$$

along the length of the positive (l_p) and negative branches (l_n) of the thermocouple. The positive and negative Seebeck coefficients Se_p and Se_n of non-ferromagnetic materials usually changes rather weakly with the magnetic field (Kollie, 1977). For ferromagnetic materials the change is more pronounced. The Seebeck coefficients for the two thermocouple pairs considered are shown in Table 11.6.4.

Table 11.6.4: Seebeck coefficients *Se* from Kollie (1977) and Powell (1974)

Material	*Se* (10^{-9} V/[°C])
Copper (Cu)	±1
Copper-nickel (CuNi)	3±1
Ni (Alumel)	37±1
NiCr (Chromel)	2±1

Galvano-magnetic effects

Up to now only thermomagnetic effects have been discussed. However, where magnetic fields appear, galvano-magnetic effects may also appear due to the interaction of electric and magnetic fields and lead to a miscellaneous reading of a temperature signal. For example the Ettingshausen galvano-magnetic effect, with the coefficient *Pg*, produces a transverse temperature gradient in a transverse magnetic field $\vec{\boldsymbol{B}}$ and a current density *j* according to Eq. (11.123):

$$\nabla T = Pg\left(\vec{\boldsymbol{j}} \times \vec{\boldsymbol{B}}\right) \tag{11.123}$$

The coefficients *Pg* and the Nernst-Ettingshausen coefficient Q are related through the absolute temperature *T* and the thermal conductivity λ by Eq. (11.124):

$$\lambda Pg = T \cdot \mathrm{Q} \tag{11.124}$$

11.6.2 Heat-emitting temperature sensing surfaces (HETSS)

A technology to determine the heat flux transferred from a liquid metal flow through a thin-walled structure is given by the heat-emitting temperature sensing surface (HETSS) technique (Platnieks, 1998; Patorski, 2000).

The active element of the method is a simple surface which allows a well-defined heat flux density to be generated in selected areas and the resulting temperature distribution to be recorded simultaneously. A HETSS represents the boundary between the solid and liquid flow to be measured. Technically, the surface is an ensemble of electrically heated ohmic resistors whose electrical resistance and power dissipation can be measured with a definite spatial resolution. Measuring the potential difference $\Delta\phi$ and the electric current *I* in each HETSS unit, the dissipated power can be determined from the product ($\Delta\phi \cdot I$) of the two locations, while their ratio ($\Delta\phi/I$) is the resistance between them, which depends on the temperature. The measured power release and the detected local resistance correspond in principle to the local heat transfer coefficient α, which is detected using this method. In order to measure this quantity several aspects have to be fulfilled. The surface resistor must be thin enough to ensure a large heat resistance in longitudinal direction and it must be backed by a thermal insulation in order to direct most of the heat through the liquid via the structural material.

The local heat transfer coefficient α not only depends on the local cooling capabilities of the flow, but also strongly on the distribution of the heat flux density. Therefore, a sophisticated design of the foil shape is required in order to attain the desired heat flux distribution. Figure 11.6.2 illustrates the operation principle of a HETSS element.

Figure 11.6.2: Technical sketch of a HETSS element used in the KILOPIE-MEGAPIE experiment (left); measurement principle of a HETSS element (right)

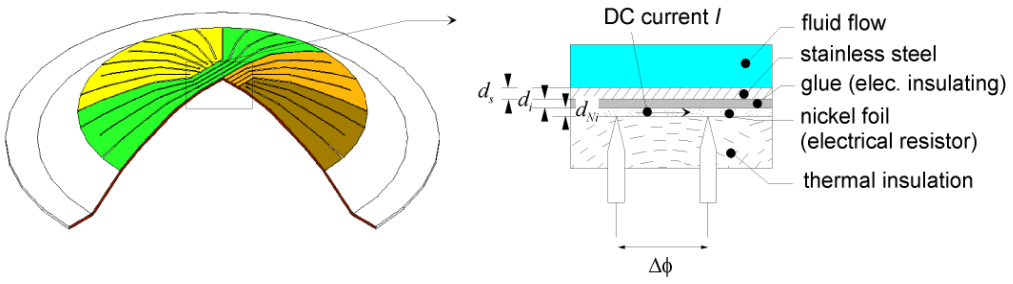

Source: Platnieks (2000).

The time-dependent temperature $T(t)$ between two discrete points m and n of a segment of a HETSS element can be calculated:

$$T_{m,n}(t) = \frac{\dfrac{\phi_{m,n}}{\phi_m / k_m} - r_{m,n} \cdot \dfrac{T}{T_0}}{\alpha\, r_{m,n} \dfrac{T}{T_0}} - \frac{\phi_{m,n} \cdot \phi_m}{A_{m,n} \cdot k_m} \cdot \left(\frac{d_i}{\lambda_i} + \frac{d_S}{\lambda_S} \right) \tag{11.125}$$

Herein, $\phi_{m,n}$ is the measured potential difference between the discrete points m and n, ϕ_m the potential at m, k_m the instrument resistance, $r_{m,n}$ the unheated HETSS unit resistance between the points m and n, T/T_0 the ratio of the bulk temperature and the temperature of the unheated HETSS, $A_{m,n}$ the surface of the HETSS unit between the points m and n, d_i the thickness of the insulation and λ_i its heat conductivity and finally d_s is the thickness of the steel and its corresponding heat conductivity λ_s. The unheated HETSS unit resistance and the reference temperature are given by the following time integration:

$$r_{m,n} = \frac{1}{\tau} \int_{t=0}^{t=\tau} \left[\left(\frac{\overline{\phi_m}}{\phi_m(t)} \right)^2 \cdot \left(\frac{\phi_{m,n}(t)}{\phi_m(t)/k_m} - \frac{\overline{\phi_{m,n}}}{\overline{\phi_m}/k_m} \right) \Bigg/ \left(\left(\frac{\overline{\phi_m}}{\phi_m(t)} \right)^2 - 1 \right) \right] d\tau \; ;$$

$$T_0 = \frac{1}{\tau} \int_{t=0}^{t=\tau} T(t)\, d\tau \tag{11.126a,b}$$

Eqs. (11.125) and (11.126) drastically reveal the difficulties using the HETSS technology as a measurement tool. Besides the tremendous effort needed for the calibration of the device and the rather exact fabrication know-how, the following uncertainties have to be quantified:

- accuracy of the measurement chain;
- detailed knowledge of the heat transport trough the glue and the steel;
- heat losses through the environment and tangential to the foil (electric, convective and radiation losses;
- wetting behaviour of the liquid through the steel wall.

Despite these difficulties HETSS technology represents a non-intrusive method to measure local temperatures and, moreover, allows to simulate various heat loading scenarios of surfaces as they may appear in nuclear or chemical engineering applications (Patorski, 2001).

A challenge in the context of HETSS is the fabrication technology. In order to attain sufficiently high heat fluxes (up to 50 W/cm^2) a thin nickel foil (around 50 μm thick) is glued to a 0.5 mm thick steel dish and is heated electrically by a DC current. The nickel heating foil can be specifically tailored, which allows to simulate different heat release scenarios. In order to get accurate results from the HETSS the element should employ adiabatic conditions to the ambient except for the test port. This can be achieved by a vacuum chamber or by an appropriate thermal insulation. The electric signals from the HETSS are obtained by pin-contacts touching the nickel foil at discrete positions delivering a potential to the data acquisition. From these values the local heat flux can be calculated and the local temperature can be determined. Finally, the estimation of local convection heat transfer coefficient α is a result of the ratio of the local heat flux to the difference of local surface temperature to the bulk temperature of the adjacent fluid. The spatial resolution perpendicular to the strips in the central part of the foil is equal to the width of the strip. For a typical digital (16 bit, 1 digit = 40 μV) measurement equipment and appropriate integration time, the accuracy of the measurement in the middle can be predicted to approximately ±1% and at the periphery of the nickel foil to about ±10%.

11.7 Level meters

11.7.1 *Direct contact sensors*

The simplest system to detect a level in a container is a simple electrode contact switch. Two states can be measured using this system, namely if the contact height is arrived or not.

This kind of system is mostly realised using simple self-made constructions. The contact electrode technique takes advantage of the good electrical conductivity of the liquid metal. If an initially open electric circuit stressed by a voltage of 24 V is closed, the potential decreases at the moment when the liquid metal surface contacts the spike of the electrode. This can be captured by a reference circuit and gives the digital signal. In order to gather more information about the actual liquid level, it is necessary to install an array of these filling level meters or to traverse the level meter. A sketch of such a level meter and a photograph of a spark electrode are shown in Figure 11.7.1.

Figure 11.7.1: Sketch of a spark electrode to detect a defined liquid metal level within a container and photograph of a level electrode used in the KALLA laboratory of FZK (left, centre); swimmer arrangement to detect the level height using an electric potentiometer (right)

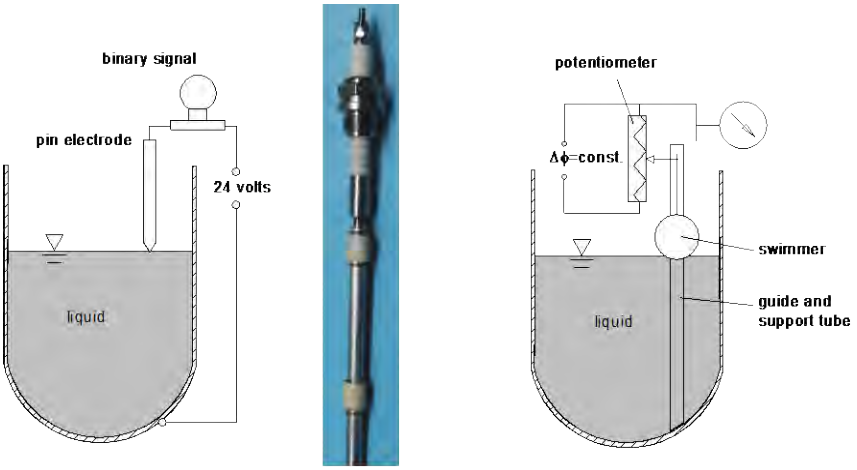

Other direct contact systems are swimmers, in which a lighter body is immersed in the container. Due to the high density of heavy liquid metals like lead and its alloys, mercury, InGaSn and others different solutions are possible. The swimmer may be directly attached to a shaft connected with resistive electronics or it may contain a magnet transmitting the level to a sensor outside. The output of such systems shows a continuous signal which is proportional to the height of the liquid metal level within the container. A schematic drawing of a swimmer arrangement is shown in Figure 11.7.1 (right). The advantage of the swimmer and the electrode systems is that they are cheap and reliable, because in such arrangements the detection system is decoupled from the high temperatures and the corrosive properties of the liquid.

Other direct level measurement methods are differential pressure gauges mounted to the container in such a way that one bore is connected to the bottom and the other branch is in the gas atmosphere above the liquid level. The liquid level corresponds to the measured pressure difference Δp in the way:

$$\Delta p = \rho \cdot g \cdot \Delta h \tag{11.127}$$

where ρ is the fluid density, g the gravity constant and Δh the liquid level height. This method is especially preferred for heavy liquid metals which have high density. A principal sketch is shown in Figure 11.7.2.

Figure 11.7.2: Level measurement using differential pressure gauges

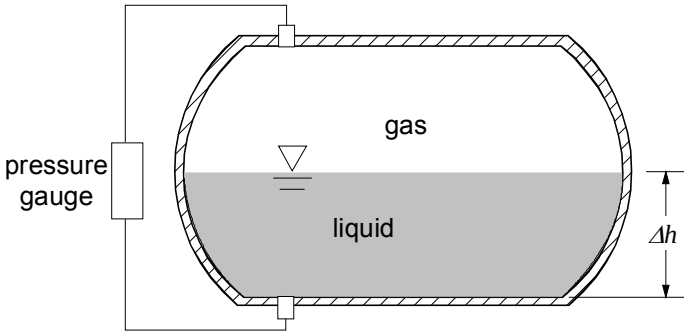

Another option to measure the liquid level in a container offers the bubbling technique, successfully performed in the CIRCE loop of ENEA. Here, bubbles of inert gas are injected via a Venturi tube into the liquid. While measuring the gas pressure in the bubble tube, the level can be recorded at the discrete position using only one sensor, which is not in direct contact with the liquid and thus for which temperature limitations do not exist. However, this type of level meter requires a calibration for the specific type of orifice at the outlet of the venture tube. Moreover, a simultaneously measuring thermocouple at the outlet of the tube is required accounting for the surface tension difference between the gas and the liquid at the different temperature levels.

Other direct contact sensor types are ultrasonic sensors connected to the volume of interest from underneath. For heavy liquid metals melting at temperatures above 120°C wave guides are necessary to decouple the ultrasonic sensor from the hot medium. Generally for this purpose two types of level and distance instrument are used in process industries: continuous and binary instruments. Both can be realised with ultrasound reflection techniques applying Eq. (11.128):

$$c = \lambda \cdot f = \frac{\Delta x}{\Delta t} \tag{11.128}$$

where c is the sound speed, λ the wave length, f the frequency, Δx the path length and Δt the transit time. The time of flight (TOF) Δt of a pulse sent by the device and reflected

from the surface (or object) is measured and c is known. Often the propagation of ultrasonic waves in air or inert gas is used. Then compensations for temperature and speed of sound changes due to vapours are needed. In dependence on the ultrasonic frequency (most devices work with ultrasonic frequencies from around ten to a few hundred kilohertz) a measurement range from millimetres to a few metres can be realised. Distance sensors operating in gas and using broadband ultrasonic transducers achieve a high local resolution in the direction of sound propagation. Accurate measurements down to a resolution of 0.25% can be expected. In latest developments of distance sensors with extremely high resolution, techniques of scanning acoustic microscopy are exploited (Kim, 1999).

In many conventional ultrasonic distance sensors simple comparator circuits are used to detect the arrival of the reflected signal in a specific time window. Such distance sensor are employed in the automation of industrial processes, for example the positioning of work pieces, as well as in the chemical industry. Level measurement becomes difficult when more than one object creates echoes or the surface is rapidly changing its level, e.g. in case of a draining. For this reason intelligent ultrasonic sensors have been developed in the past, which have the capability to evaluate partial echoes in complex echo profiles. In Eccardt (1995) a concept of signal processing for an intelligent distance sensor and its realisation is described. The main point is to separate real target echoes from misleading echoes by evaluating a set of suitable rules. Fuzzy logic techniques are used. The results are very important for level measurements. The spectrum of ultrasonic distance or level sensors ranges from relatively simple configurations to intelligent sensor systems. Endress & Hauser (Switzerland) has a large variety of continuous liquid/solid level instruments and limit switches on the market with the Prosonic system. Milltronics (Canada) offers a wide spectrum of level instruments; Honeywell (United States) offers distance and proximity sensors. Lundahl (United States) sells programmable ultrasonic sensors, which can be used for most level and presence detection applications. Many other producers are also on the market. Continuous ultrasonic level instruments compete with hydrostatic, radar and float technologies. About 20% of the level instruments are based on ultrasound. It is expected that the market share of ultrasonic instruments will increase since ultrasound is non-intrusive and the technology is well accepted. However, in the future radar techniques will gain more importance for the reasons of higher accuracy and dropping costs (Hauptmann, 2002).

In the context of liquid metal application for level detection the ultrasound technique was put in the direct contact sensor class, since especially in heavy liquid metal systems a very clean atmosphere is frequently used. In order to achieve this the loop systems are often filled against vacuum. In vacuum, however, no acoustic signal can be transmitted and thus here a direct coupling to the medium via a waveguide is required (Zhmylew, 2003).

11.7.2 Non-intrusive level sensors

Non-intrusive methods for level detection in a container can be principally based on optic, acoustic, electromagnetic or nuclear methods. Since nuclear methods in terms of X-ray, γ-ray or neutron tomography are extremely expensive due to the high attenuation especially of heavy liquid metals, they are mostly not used to acquire the level height within a container. The relations to detect the surface height with these techniques are given in principle in Section 11.5.2 for void measurement systems. Measurement principles based on electromagnetic waves and radar waves are described in this section. The optic sensors to detect surface waves are presented in the context of surface shape detection.

11.7.2.1 Electromagnetic level sensors

One of the simplest electromagnetic level sensing tools is based on electromagnetic induction. Assume two plane, parallel arranged coils, in which one is AC powered by a constant sinusoidal voltage supply, while the adjacent passive coil detects the sinusoidal

excitation with a certain amplitude, depending on the distance between active and passive coil. The detection amplitude rapidly decreases if a well electrically conducting fluid rises in the container. The amplitude decrease is directly proportional to the height of the liquid level in the vessel. Such a system is schematically depicted in Figure 11.7.3, in which two coils are inserted in an open tube. For level detection purposes the support tube configuration is mostly used, but the support tube can also be placed directly in the neighbourhood of the container. Then, however, the sensitivity of the device has to be calibrated anew, and is of course less than in the support tube configuration. Typically excitation frequencies of 45-400 Hz are used. Due to the decoupling of the sending and sensor device from the medium it can be used for arbitrary temperature ranges. In sodium such level meters worked up to 700°C (GEC Energy Systems, 1981). They were recently put into operation in the THESYS loop of KALLA for LBE.

Figure 11.7.3: Sketch of an electromagnetic level meter used for sodium and lead bismuth application in KALLA

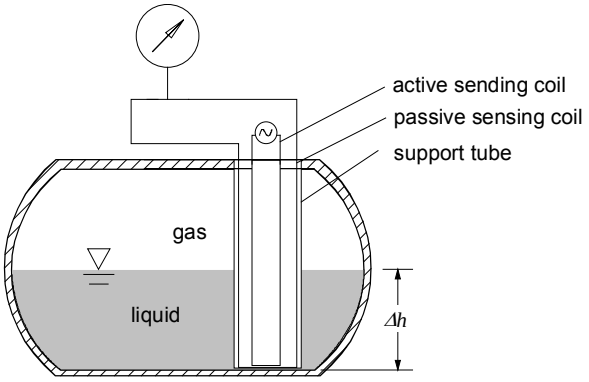

11.7.2.2 Light detection and ranging (LIDAR)

Light detection and ranging (LIDAR) is an optical method using laser pulses and their reflections from a surface to determine distance using the measured time of flight. It is closely related to the TOF methodology described in Chapter 7. Commercial systems today are robust and relatively cheap and therefore an attractive option for level detection, particularly in a hot, closed environment like liquid-metal-filled pools, etc. Kupschus (2003) proposed a LIDAR system for determining the filling level or upper free surface position in a windowless PbBi neutron spallation target prototype for the MYRHHA facility in Mol, Belgium (Class, 2011).

The system has been successfully applied in a prototype test in the THEADES loop at the KALLA laboratory. General recommendations however cannot be given, as:

- The application is highly dependent on the accessibility and geometry of the level to be determined.
- The development of commercial LIDAR systems has been extremely fast recently, such that the available systems should be evaluated at the time of application.

For more considerations on the theory of optical TOF systems please also refer to the following section.

11.8 Free surface measurements

Methods for surface recognition – both optical and acoustic – have undergone tremendous development during recent years for all kinds of applications. Development for liquid metals and even the application of new methods have not been as rapid. Therefore, this section merely has the

character of a brief overview of potential methods, but is by far not as comprehensive as the other sections of the instrumentation chapter of the HLM handbook.

Free liquid metal surfaces are present in any pool-type HLM-cooled reactor. Surface flow structures, particularly surface waves, can be generated in such reactors, particularly under abnormal operation conditions. Research on such effects requires measurement techniques, which allow the reconstruction of the surface, preferably with high spatial and temporal resolution. Another type of free liquid metal surface can be found in windowless spallation targets. A prominent example of this is the development of the free surface target for the planned international material irradiation facility IFMIF, where accelerated neutrons (>14 MeV) are shot directly on a lithium target (Ida, 2002, 2005; Jameson, 2004). Another example also using a free lithium target is the SUPER FRS target planned to be put into operation at GSI (Geissel, 2003). There, a pulsed uranium ion beam is accelerated and fragmented in a gravity-driven vertical lithium jet. Regarding the nuclear heavy liquid metal application for waste transmutation the windowless target prototype for the MYRRHA concept is one of the examples of a free surface lead-bismuth cooled target (Abderrahim, 2001).

Since liquid metals are opaque, corrosive and mostly operated at relatively high temperatures, we concentrate our discussion in this section mainly on non-intrusive optic or acoustic measurement devices.

The optical reflection coefficient of liquid metals is close to one, which means that they are almost totally reflecting for light. In most cases this causes difficulties in using highly sensitive optical distance measurement methods. In particular, the commercially available photomultipliers are too sensitive for a totally reflecting material. But, some of the liquid metals show wave length regimes, in which the reflectivity is significantly reduced. For example liquid lead has a reflectivity of 0.94 at a wave length of $\lambda = 900$ nm. At $\lambda = 584$ nm corresponding to yellow light the reflectivity is decreased to 0.62, but it increases to 0.92 at $\lambda = 500$ nm (Blaskett, 1990). Making use of this behaviour e.g. by means of using a yellow filter, triangulation methods can be used. Consequently, before any optic method is used a detailed literature study or pre-experiments should be performed to take advantage of the individual properties of the metal used in the experiment.

The basic principle of active non-contact range-finding devices is to project a signal (radio, ultrasonic or optical) onto an object and to process the reflected or scattered signal to determine the distance. If a high resolution range-finder is needed, an optical source must be chosen, as radio and ultrasonic waves cannot be focused adequately. In addition to absolute distance measurement, laser range-finding devices are traditionally used for 3-D vision, dimensional control, positioning or level control.

11.8.1 *Optical methods*

Optical distance measurement methods can technically be placed into three categories: interferometry, time-of-flight and triangulation methods. Considerable progress has been achieved in recent years by understanding the basic physical and information theoretical principles of range sensing. It appears certain that advances in the design of lasers, integrated optics devices, emitter and receiver electronics will lead to further interesting developments.

Many applications do not allow contact or alterations to an object or its surroundings to suit the measurement system, e.g. by changing the reflectivity of the surface with paint. Thus, non-contact measurement techniques have found widespread use in heritage, environment modelling, virtual reality, robotics and many industrial fields. The true problem of these methods remains the fast and precise acquisition of the depth map with a large volume and in a natural environment. The most critical parameters of such systems are depth measuring range z and depth resolutions δz. Figure 11.8.1 illustrates the measuring and resolution ranges that are covered by existing industrial measuring

systems. The highest absolute resolutions are achieved by interferometry, which reaches accuracies of λ/100 and can measure ranges up to 10 m using multi-wavelength techniques. Active triangulation can be used with high resolution from the millimetre range up to several metres. Here the accuracy depends mainly on depth of field and can be as high as 10 μm for small depths.

Figure 11.8.1: Relative resolution of methods for optical shape and distance measurements

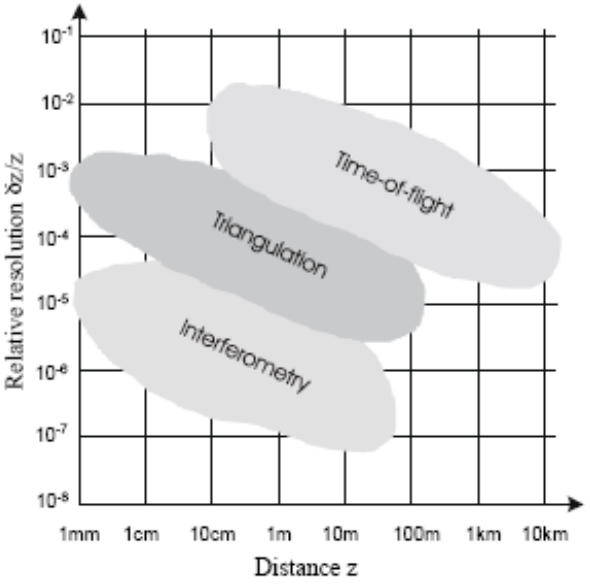

Source: Simoni (2002).

Time-of-flight techniques allow depth measurements in the range of tens of mm up to tens of km (Simoni, 2002). Here the depth estimation is an extreme challenge for time measurement and accuracy, being mainly dependent on mechanical and electronic drifts and independent of distance, and is of the order of some mm.

Optical distance measurement with the optical radar technique, often called the FMCW (frequency modulated continuous wave) technique, has been used in various applications such as non-contact surface profiling, fibre optic sensing, reflectometry, positioning and tomography. Interest in the FMCW technique is due to its large dynamic range and high resolution, particularly as regards short range sensing. Because of the recent progress in the area of laser diode technology, high performance FMCW ranging systems can currently be realised with electronically tuneable laser diodes.

The demand of the automobile industry to manufacture precise reflecting surfaces in order to allow for a fully automatic production process controlled by manipulators led to the development of rapid 3-D surface detection techniques in the past two decades. Most of these techniques are based on projection of the object on an observing CCD camera. An overview and the related literature on new developments in fast 3-D surface quality control can be found in Leopold (2003). In general, several reflection techniques can be used such as structured lighting reflection, coded lighting or colour lighting. Most of these techniques can only be used on objects at rest. Flowing heavy liquid metals, however, reveal a spectrum of motion on different time and length scales, which requires a fast acquisition technique. Thus the information to describe the surface is not only a function of the geometry but also of the time. Due to this fact mostly fringe projection systems are used for acquiring three-dimensional information on rapidly changing surfaces. These systems are robust against surface texture and reliable. Using fringe projection even

objects with large surface gradients and large extensions in the direction of recording can be captured. The fringe projection also allows to measure shapes or films without any gradients, which is impossible using stereo-matching (Böhm, 2001).

If a laser beam illuminates a continuous deformation of a surface, it will lead to a temporal speckle pattern on the observation plane. Recording this time-dependent speckle pattern the deformation of the surface of an object can be obtained. In general two methods, the scanning phase method (SPM) and the time sequence phase method (TSPM), are used for measuring the displacement caused by the deformation in temporal speckle pattern interferometry (TSPI). Their principle is that by capturing a series of speckle interference patterns related to the object deformations, the fluctuations in the intensity of the interference patterns can be obtained. Through scanning these fluctuations and estimating both the average intensity and modulation of the temporal speckle interference patterns, the phase maps for whole-field displacements are calculated. In this way it is possible to quantitatively measure continual displacements simply by using a conventional electronic speckle pattern interferometry (ESPI) system without phase shifting or a carrier. These methods are elaborated on by Li (2001) and Toh (2001). The data reduction of the acquired images and the subsequent image processing is similar to that of fringe projection. The speckle interferometry also requires a significant mathematical and computational effort. Due to the use of a more sophisticated optical system as compared to fringe projection, image processing is more time consuming. However, the attainable spatial resolutions using speckle interferometry are an order of magnitude larger than that of the fringe projection.

Hillenbrand (2012) presented a technique specifically developed to detect fast-moving liquid-metal-free surfaces. The measurement principle is based on the enhancement of a basic trigonometric distance measurement technique by using a pair of transparent screens. Within this double-layer projection (DLP) technique, a laser beam is projected through a glass plate of prescribed thickness to the reflecting liquid metal surface from which it is back-reflected again to the plate. The upper and lower sides of the plate act as screens on which the laser beams are diffusively scattered, rendering them visible to a high-speed camera, which maps these projected beam cross-sections on images. The use of a scanner allows, in addition to point measurements, line and area tracing of the surface. In order to reconstruct a surface distribution from the two-dimensional image, artificial information must be filtered out by introducing primary and secondary evaluation criteria. The major parameters impacting the accuracy of the DLP technique are addressed, and the limitations are discussed in this context. The validation of the DLP technique using mirrors and complex, well-defined objects is shown with the objective of demonstrating the accuracy as well as the temporal and spatial resolution of the system. Along with showing its capability to measure reflecting, curved and moving surfaces, two important constraints are identified. One is attributed to the DLP functional principle, which is given by the aspect ratio of the surface, while the second is given by the technical limitation of DLP determined by the user-specified accuracy and temporal resolution. In the latter case, the selection of strict criteria leads to a rapidly increasing effort in terms of calibration, costs for set-up and the computational resources required for post-processing.

11.8.2 Ultrasonic methods

Ultrasonic measurement methods – particularly ultrasonic Doppler velocimetry – were described in Section 11.4.1. The fact that ultrasound totally reflects at the gas-liquid interface at any incident angle provides a simple technique to detect the liquid-gas interface. However, beside measuring local distances of liquid metal surfaces from a single sensor through the gas volume above the surface, no application to HLM for areal measurements has been reported so far.

Generally, two possibilities to acquire the surface shape of a wavy liquid metal surface might be possible. The first is to install an ultrasound sensor in the gas phase and transport the sound waves through the gas. This technique first requires a gas filling as transport medium and a detailed knowledge of the temperature layering within the gas, which determines the sound velocity; but, it has the advantage of the temperature decoupling of the sensor from the liquid and further, both the wetting problem and sensor corrosion are avoided. However, in most problems the free liquid metal surface is shaped by the pressure field and the velocity distribution within the flow. Hence, for a detailed analysis of the problem at least two quantities must be known. Applying an ultrasound sensor directly in the fluid gives the opportunity to capture the velocity field and the surface height, but faces the challenges outlined above.

11.9 Summary and final comments

The 2007 edition of this chapter ended with these remarks by Robert Stieglitz:

> *Instrumentation development for special liquid metal adapted techniques has increased its speed in the past decade significantly. This observation can be seen from the attached literature list and it is triggered by many aspects, which arise from nuclear technology both in fission (fast breeder, accelerator-driven systems to transmute nuclear waste or high power density systems) and in fusion (liquid metal-cooled blankets or diverters) but also in conventional engineering as steel or aluminium casting, metal refinery or crystal growth for computer technology. In all of these fields liquid metal adapted instrumentation is required to control the process, ensure the safety and reliability of the individual facility.*
>
> *The realisation of different nuclear and industrial facilities operating with liquid metals pushed the speed of innovation, since increasing energy costs enforce the demand of a simultaneously economic operation and safe operation.*
>
> *Of course, the author of this chapter cannot cover the whole development process currently underway. This chapter is restricted to the description of the techniques and methods known from the literature or tested by colleagues or by myself. In some cases measurement techniques are described, which were up to now not tested for liquid metals, but show from their principle the feasibility of application to it. I tried to explain the measurement principle, to describe the algorithms to reduce the measurement data and to sketch the experimental effort to obtain the required quantities property adequately. Of course, many of the techniques described in this context reveal numerous error sources or require model assumptions. I tried to quantify the potential error sources and methodologies to avoid systematic errors. Regarding the model assumptions in some cases necessary to interpret the measured raw data I hopefully mentioned the main ideas completely to the gracious reader and gave the adequate literature sources.*
>
> *In this context I have to thank my colleagues from the Karlsruhe Lead Laboratory (KALLA), the programme NUKLEAR at the research centre Karlsruhe and many other unnamed persons for supplying me information on this compression.*

For this 2014 edition I can only join Robert in his statement, as it still is fully valid. One major change however has been made: Numerous colleagues from the Helmholtz Centre Dresden-Rossendorf, truly leading experts in liquid metal measurement techniques worldwide, acted as co-authors for this edition. I am sure this has further significantly improved the quality of the elaboration and it was an extremely valuable help to me in leading this chapter. Thank you very much for this, I am already looking forward to the next edition.

Karlsruhe Institute of Technology, January 2014

Thomas Wetzel

References

Abderrahim, H.A et al. (2001), "MYRRHA: A Multipurpose Accelerator Driven System for Research and Development", *Nuclear Instruments and Methods in Physics Research* A, 463, pp. 487-494.

Adamovskii, L.A et al. (1986), "The Error of a Correlation Method of Measuring Liquid Metal Flow Rate", Translated from *Izmeritel'naya Tekhnika*, 4, pp. 29-31.

Adamovskii, L.A. (2007), "Vortex Electro-Magnetic Flow Meters for Liquid Metal Coolants", *Measurement Techniques*, 50 (1), pp.58-65.

Allen, C.M. and L.J. Hooper (1932), "Piezometer Investigation", *ASME Trans*., 54, p. 54ff.

Argyropoulos, S.A. (2001), "Measuring Velocity in High-Temperature Liquid Metals: A Review", *Scandinavian Journal of Metallurgy*, 30, pp. 273-285.

Baker, M.C. and R. Bonazza (1998), "Visualization and Measurements of Void Fraction in a Gas-Molten Tin Multiphase System by X-ray Absorption", *Exp. in Fluids*, 25, pp. 61-68.

Barleon, L., K.J. Mack and R. Stieglitz (1996), *The MEKKA Facility: A Flexible Tool to Investigate MHD Flow Phenomena*, FZKA-Report FZKA-5826, Forschungszentrum Karlsruhe, Karlsruhe.

Barker, M. (1922), "On the Use of Very Small Pitot-Tubes for Measuring Wind Velocities", *Proc. R. Soc. A*, 101, pp. 435-445.

Barton, J.P. (1993), "Neutron Radiography – Status and International Prospects", *Proc. of the* 5th *Int. Symp. Advanced Nuclear Energy Research – Neutrons as Microscopic Probes*, Mito, Japan, 10-12 March, JAERI-M93-228, 1, p. 125ff.

Baumgartl, J., A. Hubert and G. Müller (1993), "The Use of Magnetohydrodynamic Effects to Investigate Fluid Flow in Electrically Conducting Melts", *Phys. Fluids*, 5, pp. 3280-3289.

Beckord, P et al. (1998), "Temperature and Velocity Field Measurements Using Ultrasonic Computer Tomography", *Heat and Mass Transfer*, 33, pp. 395-403.

Beitz, W. and K.H. Küttner (1986), *Dubbel-Taschenbuch des Maschinenbaus*, 15th edition, Springer-Verlag, ISBN 3-540-12418-7, p. 1211 ff (in German).

Berge, B et al. (1973), *Met. Trans*., 4, pp. 1945-1952.

Biddinika, M.K et al. (2009), "Velocity Profile Measurements in Two-Phase Flow Using Multi-Wave Sensors", *Journal of Physics: Conference Series*, 147 (012006), pp. 1-6.

Bissessur, Y. and A.J. Peyton (2006), "Computation of Forward and Inverse Problems in Electromagnetic Inductance Tomography (EMT) for Compact Scattering Objects", *Int. J. of Information and System Sciences*, 2 (4), pp. 557-574.

Blaskett, D.R. (1990), *Lead and Its Alloys*, Ellis Horwood Limited, Chichester, England.

Boden, S et al. (2008), "X-ray Radioscopic Visualization of the Solutal Convection During Solidification of a Ga-30 Wt Pct in Alloy", *Met. And Materials Transactions* A, 39A, pp. 613-623.

Bojarevics, A et al. (2006), "Experiments on the Magnetic Damping of an Inductively Stirred Liquid Metal Flow", *Experiments in Fluids*, 40, pp. 257-266.

Bonfig, K.W. (2002), *Technische Durchflußmessung*, 3, Auflage, Vulkan Verlag Essen.

Boyarevich, A.V. (1990), **"**Measurement of Averaged Local Velocities in Magneto-hydrodynamic Experiments", *Magnetohydrodynamics*, 26, p. 133.

Bradley, B.E., E.W. Dewing and J.N. Rogers (1984), *Light Metals*, 1, pp. 541-552.

Brauer, H. (1971), *Grundlagen der Ein- und Mehrphasenströmungen*, Sauerländer Verlag (in German).

Brito, D et al. (2001), "Ultrasonic Doppler Velocimetry in Liquid Gallium", *Experiments in Fluids*, 31, pp. 653-663.

Buchenau, D et al. (2011), "Measurement Techniques for LBE Flows", *Journal of Nuclear Materials*, 415, pp. 396-403.

Buchenau, D. and V. Galindo (2014), "The Magnetic Flywheel in Theory and Experiment", *Journal of Applied Physics Letters* (submitted).

Bucenieks, I. (2002), 5th *Int. Pamir Conference*, Proc. II, pp. 103-105.

Buchholz, J. and R. Steinemann (1984), "Application of an Electrical Conductivity Microprobe for the Characterisation of Bubble Behaviour in Gas-Liquid Bubble Flow", *Part. Charact.*, 1.

Burgess, J.M. and P.H. Calderbank (1975), "The Measurement of Bubble Parameters in Two-Phase Dispersions. I. The Development of an Improved Probe Technique", *Chem. Eng. Sci.*, 30, pp. 743-750.

Campbell, T.A. and J.N. Koster (1994), "Visualization of Liquid/Solid Interface Morphologies in Gallium Subject to Natural Convection", *Journal of Crystal Growth*, 140, pp. 414-425.

Casal, V. and G. Arnold (1988), **"**Velocimeter for Local Measurement in Liquid Metals", 1st *World Conf. on Experimental Heat Transfer in Fluid Mech. and Thermodyn.*, Dubrovnik, Yugoslavia, 4-9 September.

Cha, J.E., Y.C. Ahn and M.H. Kim (2002), "Flow Measurement with an Electro-Magnetic Flow Meter in Two-Phase Bubbly and Slug Flow Regimes", *Flow Meas. Instrum.*, 12, pp. 329-339.

Cha, J.E et al. (2003), "An Experimental Study on the Characteristics of Electro-Magnetic Flow Meters in the Liquid Metal Two-Phase Flow", *Flow Meas. Instrum.*, 14, pp. 201-209.

Cha, J.E et al. (2003), "The Performance of Electromagnetic Flowmeters in a Liquid Metal Two-Phase Flow", *Journal of Nucl. Sci. and Tech.*, 40 (10), pp. 744-753.

Cheng, H. (1997), *The Bubble-to-Slug Flow Pattern Transition in Vertical Columns*, PhD Thesis, Department of Chemical Engineering, University of Nottingham, UK.

Cherry, E. and D. Hooper (1968), *Amplifying Devices and Low-Pass Amplifier Design*, Wiley, New York.

Cho, J., M. Perlin and S.L. Ceccio (2005), "Measurement of Near Wall Stratified Bubbly Flows Using Electrical Impedance", *Meas. Science Techn.*, 16, pp. 1021-1029.

Chiba, S et al. (1989), "Neutron Radiographic Observation of High Pressure Three-Phase Fluidization", *Proceedings Int. Conf. Fluidization*, Banff, Alberta, Canada, 7-12 May, J.R. Grace, L.W. Shemilt and M.A. Bergougnon (eds.), Fluidization VI, AIChE, p. 523ff.

Chue, S.H. (1975), "Pressure Probes for Fluid Measurements", *Prog. Aerosp. Science*, 16, pp. 147-223.

Ciccarelli, G. and D. Frost (1994), "Fragmentation Mechanisms Based on Single Drop Steam Explosion Experiments Using Flash X-ray Radiography", *Nuc Engng. Des.*, 146, pp. 109-132.

Class, A.G et al. (2011), "XT-ADS Windowless Spallation Target Thermohydraulic Design and Experimental Setup", *Journal of Nuclear Materials*, Vol. 415, Issue 3, pp. 378-384.

Cramer, A., J. Pal and G. Gerbeth (2012), "Turbulence Measurements in a Rotating Magnetic Field Driven Flow", *Physics of Fluids*, 24, 045105, pp. 1-23.

Daidzic, N.E et al. (2005), "Gas-Liquid Phase Distribution and Void Fraction Measurements Using MRI", *Nuc. Engng. Des.*, 235, pp. 1163-1178.

Davidson, P. (2001), *An Introduction to Magnetohydrodynamics*, Cambridge University Press, ISBN 0521 791 499.

Delhaye, J.M. (1983), "Two Phase Pipe Flow", *Int. Chem. Eng.*, 23 (3), pp. 395-410.

Derebail, R. and J.N. Koster (1998), "Visualization Study of Melting and Solidification in Convecting Hypoeutectic Ga-In Alloy", *International Journal of Heat and Mass Transfer*, 41, pp. 2537-2548.

Dias, S.G., F.A. Franca and E.S. Rosa (2000), "Statistical Method to Calculate Local Interfacial Variables in Two-Phase Bubbly Flows Using Intrusive Crossing Probes", *International Journal of Multiphase Flow*, 26, pp. 1797-1830.

Dieckmann, A. (1994), "FMCW-LIDAR with Tunable Twin-Guide Laser Diode", *Electron. Lett.*, 30, pp. 308-309.

Dieckmann, A. and M. Amann (1995), "FMCW-LIDAR with Tunable Twin-Guide Laser Diode", *Trends in Optical Fibre Metrology and Standards*, O.D.D. Soares (ed.), pp. 791-802, Kluwer Academic Publishers, Dordrecht.

Dickinson, J. (1975), *Turbulent Skin Fraction Techniques*, Internal Report, Laval University, Quebec, Canada.

DIN (1952, 1982) *Druchflußmessung mit Blenden, Düsen und Venturirohren in voll durchströmten Rohren mit Kreisquerschnitt*, DIN Blätter (in German).

Drowden, R.R. (1972), *Fluid Flow Measurement – A Bibliography*, The British Hydromechanics Research Association, Cranfield Bedford, BHRA-10-1972.

Ducruet, C. and A. Dyment (1984), "The Pressure Hole Problem", *J. Fluid Mech.*, 142, pp. 251-267.

Durst, F et al. (1996), "Wall Shear Stress Determination from Near-Wall Mean Velocity Data in Turbulent Pipe and Channel Flows", *Experiments in Fluids*, 20, pp. 417-428.

Eccardt, P-C., M. Vossiek and V. Magori (1995), "Fuzzy Logic Applied to an Intelligent Ultrasonic Distance Sensor", *Proc. EUFIT '95,* Aachen, pp. 1-5.

Eckert, S. (1997), *Exp. Untersuchungen turbulenter Flüssigmetall-Gas-Strömungen in einem äußeren Magnetfeld*, PhD Thesis, Technical Univ. Dresden and FZR-Report FZR-219 (1998).

Eckert, S., W. Witke and W. Gerbeth (2000), "A New Mechano-Optical Technique to Measure Local Velocities in Opaque Fluids", *Flow Measurement and Instrumentation*, 11, pp. 71-78.

Eckert, S et al. (2003), "Measurement Techniques for Liquid Metal Velocity Measurements", *Proc. 5th Int. Symp. on Liquid Metal Processing and Casting*, Nancy, France, pp. 261-271.

Eckert, S., G. Gerbeth and V.I. Melnikov (2003), "Velocity Measurements at High Temperatures by Ultra-Sound Doppler Velocimetry Using an Acoustic Wave Guide", *Experiments in Fluids*, 35, pp. 381-388.

Eggels, J.G.M et al. (1994), "Fully Developed Turbulent Pipe Flow: A Comparison Between Direct Numerical Simulation and Experiment", *J. Fluid Mech.*, 268, pp. 175-209.

El-Kaddah, N. and J. Szekely (1983), "The Turbulent Recirculating Flow Field in a Coreless Induction Furnace, a Comparison of Theoretical Predictions with Measurements", *J. Fluid Mech.*, 133, pp. 37-46.

El-Kaddah, N., J. Szekely and G. Carlsson (1984), *Met. Trans.*, 14, pp. 633-640.

Eringen, C.A. (1980), *Mechanics of Continua*, Robert E. Krieger Publishing Comp., New York, pp. 459ff.

Evans, J.W. and S.D. Lympany (1983), *Met. Trans.*, 14B, pp. 306-308.

Foust, O.J. (1978), *Sodium-NaK Engineering Handbook*, Vol. 3, Gordon & Breach Science Publishers Inc., Philadelphia, PA, ISBN-0-677-03040-1.

Franklin, R.E. and J.M. Wallace (1970), "Absolute Measurements of Static Hole Error Using Flush Transducers", *J. Fluid Mech.*, 42, pp. 33-48.

Furuichi, N. (2012), "Uncertainty Analysis of Flowrate Measurement Using UVP", *Proc. 8th Int. Symp. on Ultra Sonic Doppler Methods for Fluid Mechanics and Fluid Engineering*, pp. 133-136.

Gaetke, J. (1991), *Akkustische Strömungs- und Durchflussmessung*, Akademischer Verlag, Berlin (in German).

GEC Energy Systems (1981), *Level Meter for Liquid Metals*, Cambridge Road, Leicester, LE8 3LH, United Kingdom.

Gallet, B., M. Berhanu and N. Mordant (2009), "Influence of an External Magnetic Field on Forced Turbulence in a Swirling Flow of Liquid Metal", *Physics of Fluids*, 21, 085107, pp. 1-13.

Geissel, H et al. (2003), "The Super-FRS Project at GSI", *Nuclear Instruments and Methods in Physics Research B*, 204, pp. 71-85.

Goldstein, R.J. (1983), *Fluid Mechanics Measurement*, Hemisphere Publishing, Springer Verlag, Berlin.

Goldstein, R.M., H.A. Zebker and C.L. Werner (1988), "Satellite Radar Interferometry: Two-Dimensional Phase Unwrapping", *Radio Sci.*, 23, pp. 713-720.

Gramolin, V.L et al. (1983), "Electro-Magnetic Flow Meters with Elevated Calibration Stability", Translated from *Izmeritel'naya Tekhnika*, 11, pp. 32-34.

Grevet, J.H., J. Szekely and N. El-Kaddah (1982), *Int. J. Heat and Mass Transfer*, 25, pp. 487-492.

Griffith, P. (1963), *The Prediction of Low Quality Boiling Void*, ASME Preprint 63-HT-20.

Grjotheim, K et al. (1970), *Met. Trans.*, 1, pp. 3133-3141.

Grjotheim, K et al. (1971), *Met. Trans.*, 2, pp. 199-204.

Hall, I. (1956), "Displacement Effect of a Sphere in a Two-Dimensional Shear Flow", *J. Fluid Mech.*, 1, pp. 142-162.

Hämäläinen, M et al. (1993), "Magnetoencephalography – Theory, Instrumentation, and Applications to Noninvasive Studies of the Working Human Brain", *Rev. Mod. Phys.*, 65, pp. 413-497.

Hansen, P.C. (1992), "Analysis of Discrete Ill-Posed Problems by Means of the L-Curve", *SIAM Review*, 34, pp. 561-580.

Harms, A. and C.F. Forrest (1971), "Dynamic Effects in Radiation Diagnosis of Fluctuating Voids", *Nucl. Sci. Eng.*, 46, pp. 408-413.

Harms, A. and A. Laratta (1973), "The Dynamic Bias in Radiation Interrogation of Two-Phase Flow", *Int. J. Heat Mass Transfer*, 16, pp. 1459-1465.

Harvel, G.D et al. (1996), "Real-Time Cross-Sectional Averaged Void Fraction Measurements in Vertical Annulus Gas-Liquid Two-Phase Flow by Neutron Radiography and X-ray Tomography Techniques", *Nuclear Instruments and Methods in Physics Research*, A 371, pp. 544-552.

Hauptmann, P., N. Hoppe and A. Püttmer (2002), "Application of Ultrasonic Sensors in the Process Industry", *Meas. Sci. Technol.*, 13, pp. 73-83.

Hayachi, H., A. Becker and J.W. Ewans (1999), "Toward a Probe for Velocity Measurement in Molten Metals at High Temperatures", *Met. and Mat. Trans. B*, 30, pp. 623-630.

Heinemann, J.B., J.F. Marchaterre and S. Mehta (1962), "Electro-Magnetic Flow Meters for Void Fraction Measurement in Two-Phase Liquid Metal Flow", *Rev. Sci. Instr.*, 34 (4), pp. 399-401.

Herning, F. (1966), *Stoffströme in Rohrleitungen*, VDI Verlag, Düsseldorf (in German).

Hibiki, T et al. (1993), "Study on Air-Water Two-Phase Flow in a Small Diameter Tube", *Annu. Rep. Res. Reactor Inst. Kyoto Univ.*, 36, pp. 34-44.

Hibiki, T et al. (1994b), "Visualization of Fluid Phenomena Using a High Frame-Rate Neutron Radiography with a Steady Thermal Neutron Beam", *Nucl. Instrum. Methods Phys. Res.*, A351, pp. 423-436.

Hibiki, T. and K. Mishima (1996), "Visualization and Measurements of Two-Phase Flow in Metallic Ducts Using Neutrons as Microscopic Process", 3rd Report, Quantitative Measurement of Neutron Radiography Image, *Trans. Jpn. Soc. Mech. Engrs. Ser. B*, 62 (595), pp. 919-926 (original paper in Japanese).

Hibiki, T., H. Hogsett and M. Ishii (1998), "Local Measurement of Interfacial Area, Interfacial Velocity and Liquid Turbulence in Two-Phase Flow", *Nucl. Engng. Des.*, 184, pp. 287-304.

Hill, J.C. and C.A. Sleicher (1971), "Directional Sensitivity of Hot Film Sensors in Liquid Metals", *Rev. Science Instr.*, 42, pp. 1461-1468.

Hillenbrand, M.P., R. Stieglitz and G.P. Neitzel (2012), "Detection of Flowing Liquid Metal Surface Using the DLP Measurement Technique", *Exp. Fluids*, 52, pp. 179-192.

Hills, J.H. (1974), "Radial Non-Uniformity of Velocity and Voidage in a Bubble Column", *Trans. Inst. Chem. Engrs.*, 52, p. 1ff.

Hochreiter, L.E. and A. Sesonske (1969), "Thermal Turbulence Characteristics in Sodium-Potassium", *Int. J. Heat and Mass Transfer*, 12, pp. 114-118.

Hofmann, B. and M. Rockstroh (1996), "Study on Acoustic Waveguides and Reflectors for Use in Ultrasonic Two-Phase Flow Measurement", *Ultrasonics*, 34, pp. 431-434.

Hooker, H.H. and G.F. Popper (1958), *A Gamma Ray Attenuation Method for Void Fraction Measurement in Steam-Water Mixtures*, ANL-5766, Argonne National Laboratory, Argonne, IL.

Horanyi, S. and L. Krebs (1988), "Temperature Compensated Miniature Permanent Magnetic Flow Meter for Liquid Metal. Experimental Heat Transfer", *Proc. 1st World Conf. on Experimental Heat Transfer, Fluid Mechanics and Thermodynamics*, Dubrovnik, Yugoslavia, pp. 279-285.

Hori, M., T. Kobori and Y. Ouichi (1966), *Method for Measuring Void Fraction by Electromagnetic Flowmeters*, Nippon Genshiryoku Kenkyuho (Rep.), JAERI 1111, Elsevier.

Horn, B.K.P. and B.G. Schunck (1981), "Determining Optical Flow", *Artificial Intelligence*, 17, pp. 185-203.

Hurd, C.W., K.P. Chesky and A.H. Shapiro (1953), "Influence of Viscous Effects on Impact Tubes", *J. Appl. Mech.*, 248, pp. 253-256.

Ida, M et al. (2002), "Thermal-Hydraulic Characteristics of IFMIF Liquid Lithium Target", *Fusion Engineering and Design*, 63-64, pp. 333-342.

Ida, M et al. (2005), "Thermal and Thermal-Stress Analyses of IFMIF Liquid Lithium Target Assembly", *Fusion Engineering and Design*, Vols. 75-79, pp. 847-851.

Imbeni, V et al. (1999), *Properties of the Eutectic Alloys Pb55.5Bi and Pb17Li*, BoMet Institute of Metallurgy, University of Bologna, ENEA Report DT-EUB-00001, Part 2 (1999).

Iguchi, M., H. Tokunaga and H. Tatemichi (1997), "Bubble and Liquid Flow Characteristics in a Wood's Metal Bath Stirred by Bottom Helium Gas Injection", *Met. and Mat. Trans. B*, 28, pp. 1053-1061.

Ishii, M. (1975), *Thermo-Fluid Dynamic Theory of Two-Phase Flow*, Eyerolles, France, Paris.

Ishii, M. (1977), *One-Dimensional Drift-Flux Model and Constitutive Equations for Relative Motion Between Phases in Various Two-Phase Flow Regimes*, ANL-77-47, Argonne National Laboratory, Argonne, IL.

ISO (International Organization for Standardization) (1977), *Measurement of Fluid Flow in Closed Conduits – Velocity Area Method Using Pitot Static Tubes*, ISO 3966-1977, Edition 1999, ISO, Geneva, Switzerland.

Ito, D., H. Kikura and M. Aritomi (2010), "Two-Phase Flow Monitoring Using Ultrasonic Multi-Wave Technique", *7th International Symposium on Ultrasonic Doppler Methods for Fluid Mechanics and Fluid Engineering*, Gothenburg, Sweden, 7-9 April, pp. 75-79.

Jaffray, D et al. (1994), "X-ray Scatter in Megavoltage Transmission Radiography: Physical Characteristics and Influence on Image Quality", *Med. Phys.*, 2, pp. 45-60.

Jameson, R.A et al. (2004), "IFMIF Accelerator Facility", *Journal of Nuclear Materials*, 329-333, pp. 193-197.

Jian, D. and Ch. Karcher (2012), "Electromagnetic Flow Measurement in Liquid Metals Using Time-of-Flight Lorentz Force Velocimetry", *Measurement Science and Technology*, 23.

Jiang, Y., J. Ma and R.R. Saddi (2007), "Thermal Transient Flow Rate Sensor for High Temperature Liquid Metal Cooled Nuclear Reactor", University of Nevada, Las Vegas, *Faculty Rep. Mech. Engng.*, 1-1-2007, pp. 2-9.

Jischa, M. (1982), *Konvektiver Impuls- Wärme und Stoffaustausch*, Vieweg Verlag, ISBN 3-528-08144-9, p. 137ff and p. 254ff (in German).

Johnson, A.R. (1978), *Light Metals*, 1, pp. 45-58.

Kaatze, U., F. Eggers and K. Lautscham (2008), "Ultrasonic Velocity Measurements in Liquids with High Resolution – Techniques, Selected Applications and Perspectives", *Meas. Sci. Technol.*, 19.

Kakimoto, K et al. (1988), "Direct Observation by X-ray Radiography of Convection of Molten Silicon in the Czochralski Growth Method", *Journal of Crystal Growth*, 88, pp. 365-370.

Kalkach-Navarro, S et al. (1993), "Interfacial Area Density, Mean Radius and Number Density Measurements in Bubbly Two-Phase Flow", *Nucl. Eng. Des.*, 142, pp. 341-351.

Kapulla, R. (2000), *Experimentelle Untersuchung von thermisch stratifizierten und unstratifizierten Mischungsschichten in Natrium und Wasser*, Dissertation 13430, Eidgenössische Technische Hochschule, Zurich, Switzerland (in German).

Kataoka, I., M. Ishii and A. Serizawa (1986), "Local Formulation and Measurement of Interfacial Area Concentration in Two-Phase Flow", *Int. J. Multiphase Flow*, 12 (4), pp. 505-529.

Kikura, H et al. (2006), "Application of Linear Ultrasonic Array Transducer to Two-Phase Flow Measurements", *6th International Symposium on Ultrasonic Doppler Methods for Fluid Mechanics and Fluid Engineering*, pp. 95-98.

Kim, T.J et al. (1999), "Confocal Scanning Acoustic Microscopy in Air at Normal Conditions at Frequencies Close to the Phonon Cut-Off Regime", *Physica B*, 263-264, pp. 558-94.

Kim, S et al. (2001), "Study on Interfacial Structures in Slug Flows Using a Miniaturized Four-Sensor Conductivity Probe", *Nuclear Eng. Design*, 204, pp. 45-55.

Kocamustafaogullari, G. and Z. Wang (1991), "An Experimental Study on Local Interfacial Parameters in a Horizontal Bubbly Two-Phase Flow", *Int. J. Multiphase Flow*, 17 (5), pp. 553-572.

Kolesnikov, Y., C. Karcher and A. Thess (2011), "Lorentz Force Flowmeter for Liquid Aluminum: Laboratory Experiments and Plant Tests", *Metallurgical and Materials Transactions B*, 42, pp. 441-450.

Kollie, T.G et al. (1977), "Large Thermocouple Thermometry Errors Caused by Magnetic Fields", *Rev. Science Instrum.*, 48 (5), pp. 501-511.

Knebel, J.U. and L. Krebs (1994), "Calibration of a Miniature Permanent Magnetic Flow Meter Probe and Its Application to Velocity Measurements in Liquid Sodium", *Experimental Thermal and Fluid Science*, 8, pp. 135-148.

Knebel, J.U et al. (1998), "A Confined Sodium Jet in a Co-Flow", *J. Fluid Mech.*, 368, pp. 51-80.

Knebel, J.U et al. (2001), *Thermalhydraulic and Material Specific Investigations into the Realization of an Accelerator Driven System (ADS) to Transmute Minor Actinides*, Wissenschaftliche Berichte, FZKA 6618, Forschungszentrum Karlsruhe, Karlsruhe.

Krebs, L. and K. Bremhorst (1983), "Verification of the Extended Gradient Diffusion Model by Measurement of the Mean and Fluctuating Temperature Fields in Sodium Flow Downstream of a Multi-Bore Jet Block", *Proc. 4th Symp. Turbulent Shear Flows*, Karlsruhe, Germany.

Koster, J.N., T. Seidel and R. Derebail (1997), "A Radioscopic Technique to Study Convective Fluid Dynamics in Opaque Liquid Metals", *Journal of Fluid Mechanics*, 343, pp. 29-41.

Kupschus, P et al. (2003), "MYRRHA Spallation Loop Design", *Proceedings of the International Workshop on P&T and ADS Development*, Mol, Belgium, pp. 6-8.

Lee, H.C., J.W. Evans and C. Vives (1984), "Velocity Measurement in Wood's Metal Using an Incorporated Magnet Probe", *Metallurgical Transactions B*, 15B, pp. 734-736.

Lefhalm, C-H. (2004a), *Qualifikation von Meßtechniken in schweren Flüssigmetallströ-mungen*, Dissertation, University of Karlsruhe (in German).

Lefhalm, C-H et al. (2004b), "Turbulent Heavy Liquid Metal Heat Transfer Along a Heated Rod in an Annular Cavity", *Journal of Nuclear Materials*, 335, pp. 280-285.

Lefhalm, C-H., M. Daubner and R. Stieglitz (2005), "Development and Assessment of Flow Rate Measurement Techniques for Lead Bismuth", *11th International Topical Meeting on Nuclear Reactor Thermal-Hydraulics (NURETH-11)*, Avignon, France, 2-6 October, Paper 394.

Lehde, H. and W. Lang (1948), *AC Electromagnetic Induction Flow Meter*, US Patent 1948, Patent No. 2.435.045.

Lenz, M et al. (2012), "Sound Velocity Measurements in Fluids Using Echo Signals from Scattering Particles", *8th Int. Symp. on Ultrasonic Doppler Methods for Fluid Mechanics and Fluid Engng.*, pp. 129-133.

Leopold, J., H. Günther and R. Leopold (2003), "New Developments in Fast 3D-Surface Quality Control", *Measurement*, 33, pp. 179-187.

Lighthill, M.J. (1957), "Contributions to the Theory of the Pitot Tube Displacement Effect", *J. Fluid Mech.*, 1, pp. 493-512.

Ligrani, P.M et al. (2001), "Flow Structure Due to Dimple Depressions on a Channel Surface", *Phys. Fluids*, 13, pp. 3442-3451.

Lillicrap, D.C and D.J. Moore (1982a), "Electromagnetic Stirring in Core Induction Furnaces", *Proc. Electroheat and Metals Conf.*, University of Cambridge.

Lillicrap, D.C (1982b), "A Technique for Velocity Measurements in Coreless Induction Furnaces", *Proc. of the Symp. Int. Union of Theoretical and Applied Mechanics*, H.K. Moffat and M.R.E. Proctor (eds.), pp. 46-56.

Liu, Y., L.C. Lynnworth and M.A. Zimmermann (1998), "Buffer Waveguides for Flow Measurement in Hot Fluids", *Ultrasonics*, 36, pp. 305-315.

Livesey, H.J.L. (1956), "The Behaviour of Transverse Cylindrical and Forward Facing Total Pressure Tubes in Transverse Total Pressure Gradient", *J. Basic. Eng.*, 23, pp. 949-955.

Livesey, J.L., J.D. Jackson and C.J. Southern (1962), "The Static Hole Error Problem: An Experimental Investigation of Error for Holes of Varying Diameter and Depth", *Aircr. Eng.*, 34, p. 43ff.

Lykoudis, P.S. and P.F. Dunn (1973), "Magneto Fluid Mechanic Heat Transfer from Hot Film Probes", *Int. Journal Heat and Mass Transfer*, 16, p. 1439ff.

Ma, X et al. (2008), "Development of Multiple Frequency Electromagnetic Induction Systems for Steel Flow Visualization", *Meas. Sci. Technol.*, 19, 094008, pp. 1-9.

MacMillan, F.A. (1954), "Viscous Effects on Pitot Tubes at Low Speeds", *J. R. Aero. Soc.*, 58, pp. 837-839.

MacMillan, F.A. (1956), "Experiments on Pitot Tubes in Shear Flow", Ministry of Supply, Aero. Res. Council, R&M 3028.

Macovski, A. (1983), "Noise Considerations in Radiography and Fluoroscopy", *Medical Imaging Systems*, Prentice-Hall.

Malcolm, D.J. (1969), "Some Aspects of Turbulence Measurement in Liquid Mercury Using Cylindrical Quartz-Insulated Hot-Film Sensors", *J. Fluid Mech.*, 37, p.701-714.

Malcolm, D.G. and V. Verma (1981), "Dynamic Response of Forced Convective Heat Transfer from Hot-Film Sensors to Mercury. Part 2: Experiment", *J. Fluid Mech.*, 112, pp. 475-485.

McKeon, B.J. and A.J. Smits (2002), "Static Pressure Correction in High Reynolds Number Fully Developed Pipe Flow", *Meas. Sci. Techn.*, 13, pp. 1608-1614.

McKeon, B.J et al. (2003), "Pitot Probe Correction in Fully Developed Turbulent Pipe Flow", *Meas. Science and Instrumentation*, 14, pp. 1449-1458.

Marcolongo, P., J.W. Evans and D.A. Steingart (2007), "A Novel, Inexpensive, and Rugged Probe for Measuring Gas Bubbles in Liquid Metals: Part I. Mathematical Modeling and Laboratory Experiments", *Met. and Mat. Trans. B*, 38, pp. 389-399.

Mishima, K et al. (1999), "Visualization and Measurement of Gas-Liquid Metal Two-Phase Flow with Large Density Difference Using Thermal Neutrons as Microscopic Probes", *Nuc. Instr. Meth. in Phys. Res.*, A 424, pp. 229-234.

Matsubayashi, M et al. (2001), "Preliminary Examination of the Applicability of Imaging Plates to Fast Neutron Radiography", *Nucl. Instr. and Meth.*, A 463, pp. 324-330.

Matsubayashi, M et al. (2003), "Development of a Fast Neutron Radiography Converter Using Wavelength-Shifting Fibers", *Nucl. Instr. and Meth.*, A 510, pp. 325-333.

Matsubayashi, M et al. (2004), "An Improved Fast Neutron Radiography Quantitative Measurement Method", *Nuclear Instruments and Methods,* A 533, pp. 481-490.

Melissari, B. and S.A. Argyropoulos (2005), "Measurement of Magnitude and Direction of Velocity in High-Temperature Liquid Metals. Part II: Experimental Measurements", *Metallurgical and Materials Transactions*, 36B, pp. 639-649.

Mikrovas, A.C. and S.A. Argyropoulos (1993), "Measurement of Velocity in High-Temperature Liquid Metals", *Metallurgical and Materials Transactions*, 24B, pp. 1009-1021.

Miralles, S et al. (2011), "The Magnetic-Distortion Probe: Velocimetry in Conducting Fluids", *Rev. of Scientific Instruments*, 82 (095112), pp. 1-10.

Mishima, K et al. (1992), *A Study of Air-Water Flow in a Narrow Rectangular Duct Using an Image Processing Technique, Dynamics of Two-Phase Flow*, O.C. Jones and I. Michiyos (eds.), CRC Press, Boca Raton, FL, pp. 141-160.

Mishima, K., T. Hibiki and H. Nishihara (1993), "Some Characteristics of Gas-Liquid Flow in Narrow Rectangular Ducts", *Int. J. Multiphase Flow*, 19, pp. 115-124.

Mishima, K., T. Hibiki and H. Nishihara (1997), "Visualization and Measurement of Two-Phase Flow by Using Neutron Radiography", *Nuclear Engineering and Design*, 175, pp. 25-35.

Moazzeni, T et al. (2008), "Algorithms for the Measurement of Liquid Metal Coolant Flow Velocity with Correlated Thermal Signals", *ICSP2008 Proceedings*, pp. 2702-2706.

Moore, D.J. (1982), *Magnetohydrodynamics of the Coreless Induction Furnace*, PhD Dissertation, University of Cambridge.

Moore, D.J. and J.C.R. Hunt (1983), "Electromagnetic Stirring in the Coreless Induction Furnace", *Liquid-Metal Flows and Magnetohydrodynamics*, *Prog. in Astronautics and Aeronautics*, 83, p. 359-373.

Moros, A., J.C.R. Hunt and D.C. Lillicrap (1985), "Study of the Electromagnetic Features in Channel Induction Furnaces", *Single- and Multi-Phase Flows in an Electromagnetic Field: Energy, Metallurgical, and Solar Applications*, *Prog. in Astronautics and Aeronautics*, 100, pp. 706-715.

Müller, U., R. Stieglitz and S. Horanyi (2006), "Experiments at a Two-Scale Dynamo Test Facility", *J. Fluid Mechanics*, Vol. 552, pp. 419-440.

Munshi, P. and M.S. Vaidya (1993), "A Sensitivity Study of Poisson's Corruption in Tomographic Measurements for Air-Water Flows", *Trans. American Nuclear Society*, 68, pp. 234-236.

Murakami, M., M. Maruo and T. Yoshiki (1990), "Development of an Electromagnetic Flowmeter for Studying Gas-Liquid Two-Phase Flow", *International Chemical Engineering*, 30 (4), pp. 699-702.

Murthy, A. and J. Szekely (1983), *Met. Trans.*, 14B, pp. 499-502.

Nakamura, H., M. Kondo and Y. Kukita (1998), "Simultaneous Measurement of Liquid Velocity and Interface Profiles of Horizontal Duct Wavy Flow by Ultrasonic Velocity Profile Meter", *Nuclear Engineering and Design*, 184, pp. 339-348.

Natec Schultheiß GmbH (1999), *FT Series Turbine Flowmeter – Installation, Operation and Maintenance Manual*, Flow Technology, Inc. Phoenix, Arizona.

Neal, L.G. and S.G. Bankoff (1963), "A High Resolution Resistivity Probe for Determination of Local Void Properties in Gas-Liquid Flow", *AIChE J.*, 9 (4), pp. 490-494.

Nguyen-Thi, H et al. (2012), "On the Interest of Synchrotron X-ray Imaging for the Study of Solidification in Metallic Alloys", *C. R. Physique*, 13, pp. 237-245.

Nowak, M. (2002), "Wall Shear Stress Measurement in a Turbulent Pipe Flow Using Ultrasound Doppler Velocimetry", *Experiments in Fluids*, 33, pp. 249-255.

Ochiai, M et al. (1971), "Void Fraction and Heat Transfer Coefficient of Sodium-Argon Two-Phase Flow in Vertical Channel", *J. Atomic Energy Society of Japan*, 13, pp. 566-573.

Ogino, F et al. (1994), "Application of Neutron Radiography to the Study of Liquid-Solid Two-Phase Flow", *Exp. Therm. Fluid Sci.*, 12, p. 339ff.

Oyedele, J. and T. Akintola (1991), "Void Fluctuation Effects in Radiation Interrogation of Voided Liquids", *Applied Radiation and Isotopes*, 42, pp. 341-346.

Ozarapoglu, V. (1972), PhD Thesis, Laval University, Quebec, Canada.

Panametrics (1998), *Handbuch Ultraschalldurchflußmessgerät XMT868 mit IDM-Software*, Version 10/98 (in German).

Parrilla, M., J.J. Anaya and C. Fritsch (1991), *IEEE Trans. Instrum. Meas.*, 40, p. 759ff.

Patel, V.C. (1965), "Calibration of the Preston Tube and Limitations on Its Use in Pressure Gradients", *J. Fluid Mech.*, 23, pp. 185-208.

Patorski, A et al. (2000), *Experimental Estimation of Optimum Bypass-Jet-Flow Conditions for the Cooling of the Window of the SINQ Liquid Metal Target*, PSI Report 2000, ISSN 1423-7350, Vol. VI, pp. 42-44, Paul Scherrer Institut, Villigen, Switzerland.

Patorski, J., G.S. Bauer and S. Dementjev (2001), "Two-Dimensional and Dynamic Method of Visualization of the Flow Characteristics in a Convection Boundary Layer Using Infrared Thermography", *Journal of Theoretical and Applied Mechanics*, Vol. 39, 2.

Perry, A.E., S. Hafez and M.S. Chong (2001), "A Possible Reinterpretation of the Princeton Superpipe Data", *J. Fluid Mech.*, 439, pp. 395-401.

Petrick, M. and B.S. Swanson (1958), *Rev. Sci. Instr.*, 29, p. 1079ff.

Petrick, M. and K.Y. Lee (1964), *Performance Characteristics of a Liquid Metal Generator*, ANL-6870, Argonne National Laboratory, Argonne, IL.

Peyton, A.J et al. (1996), "An Overview of Electromagnetic Inductance Tomography: Description of Three Different Systems", *Meas. Sci. Technol.*, 7, pp. 261-271.

Platnieks, I. (1971), "Comparison of the Hot-Wire Anemometric and Conduction Methods of Measuring Velocity Characteristics of a Flow of Mercury in a Transverse Magnetic Field", *Magnetohydrodynamics*, 7, pp. 140-143.

Platnieks, I. and G. Ulmann (1984), "Hot Wire Sensor for Liquid Sodium", *J. Phys. E., Sci. Intrum.*, 17, pp. 862-863.

Platnieks, I et al. (1998), "Measurements of Heat Transfer at the Beam Window in a Mockup Target for SINQ Using Mercury", *14th Meeting of the Intern. Collaboration on Adv. Neutron Sources*, Utica, IL, 14-19 June.

Platnieks, I. (2000), "Heat Transfer Experiments Using HETSS", *4th MEGAPIE Coordination Meeting* (WP X4/5/6), 5 October, ENEA Research Centre Brasimone, Italy.

Poornapushpakala, S et al. (2010), "An Analysis on Eddy Current Flowmeter – A Review", *IEEE Transactions*, pp. 185-188.

Powell, R.L et al. (1974), *Thermocouple Reference Tables*, IPTS-68, United States Department of Commerce.

Pozrikidis, C. (1994), "Shear Flow over a Plane Wall with an Axis-Symmetric Cavity or a Circular Orifice of Finite Thickness", *Phys. Fluids*, 6, pp. 68-79.

Priede, J et al. (2007), Patent DE 102007 046 881 A1 2009.04.16, EP 2045581A1.

Priede, J et al. (2009), *Verfahren und Anordnung zur kontaktlosen Messung des Durchflusses elektrisch leitfähiger Medien*, Patent DE 10 2006 018 623 B4, EP 1847813 B1.

Priede, J., D. Buchenau and G. Gerbeth (2009), "Force-Free and Contactless Sensor for Electromagnetic Flow-Rate Measurements", *MHD*, Vol. 45, pp. 451-458.

Priede, J., D. Buchenau and G. Gerbeth (2011), "Contactless Electromagnetic Phase-Shift Flowmeter for Liquid Metals", *Meas. Sci. Technol.*, 22.

Priede, J., D. Buchenau and G. Gerbeth (2011), "Single-Magnet Rotary Flowmeter for Liquid Metals", *J. Appl. Phys.*, 110.

Ray, A.K. (1956), "On the Effect of Orifice Size on Static Pressure Reading at Different Reynolds Numbers", *Img.-Arch.*, 24, p. 3ff.

Rayle, R.J., Jr. (1959), *An Investigation of the Influence of Orifice Geometry on Static Pressure Measurements*, MS Thesis, Massachusetts Institute for Technology, Cambridge, MA.

Reed, C.B. and B.F. Picologlou (1986), "Techniques for Measurements of Velocity in Liquid Metal MHD-Flows", *7th Top. Meeting on Fusion Technology*, Nevada.

Reed, C.B., B.F. Picologlou and J.S. Walker (1987), "ALEX-Results – A Comparison of Measurements from a Round and a Rectangular Duct with 3D-Code Predictions", *IEEE*, No. 87CH2507-2, Vol. 2, pp. 1267-1270.

Reed, C.B. and B.F. Picologlou (1989), "Side Wall Flow Instabilities in a Liquid Metal MHD-Flow Under Blanket Relevant Conditions", *Fusion Technology*, 15, pp. 705-715.

Regan, M.J et al. (1997), "X-ray Reflectivity Studies of Liquid Metal and Alloy Surfaces", *Phys. Rev. B*, 55 (23), pp. 15874-15884.

Reichardt, V.H. (1951), "Vollständige Darstellung der turbulenten Geschwindigkeitsverteilung in glatten Leitungen", *Zeitschrift für Angewandte Mathematik und Mechanik*, 31 (7) (in German).

Richards, W.J., M.R. Gibbons and K.C. Shields (2004), "Neutron Tomography Developments and Applications", *Applied Radiation and Isotopes*, 61, pp. 551-559.

Ricoud, R. and Ch. Vives (1982), "Local Velocity and Mass Transfer Measurements in Molten Metals Using an Incorporated Magnet Probe", *Int. J. Heat and Mass Transfer*, 25 (10), pp. 1579-1588.

Rohrbacher, H.A. and R. Bartholomay (1975), *Ultraschallmesstechnik in Natrium-Systemen,* Gesellschaft für Kernforschung mbH, Karlsruhe (in German).

Rutkevich, M. (1981), "Theory of Electro-Magnetic Flow Measurement", Translated from *Izvestiya Akademii Nauk SSSR, Mechanica Zhidkoski I Gaza*, 3, pp. 114-199.

Saito, Y et al. (2004), "Velocity Field Measurement in Gas-Liquid Metal Two-Phase Flow with Use of PIV and Neutron Radiography Techniques", *Applied Radiation and Isotopes*, 61, pp. 683-691.

Saito, Y et al. (2005), "Application of High Frame-Rate Neutron Radiography to Liquid-Metal Two-Phase Flow Research", *Nuclear Instruments and Methods in Physics Research A*, 542, pp. 168-174.

Saito, Y et al. (2005), "Measurements of Liquid-Metal Two-Phase Flow by Using Neutron Radiography and Electrical Conductivity Probe", *Experimental Thermal & Fluid Science*, 29, pp. 323-330.

Sanaullah, K., S.H. Zaidi, and J.H. Hills (2001), "A Study of Bubbly Flow Using Resistivity Probes in a Novel Configuration", *Chemical Engineering Journal*, 83, pp. 45-53.

Satyamurthy, P., T.K. Thiyagarajan and N. Venkatramani (1994), "Void Fraction Profile Measurement in Two-Phase Liquid Metal Flows Correction for Finite Beam Size of the Gamma-Rays", *2nd Int. Conference on Energy Transfer in Magnetohydrodynamic Flows*, France.

Satyamurthy, P et al. (1998), "Two-Fluid Model Studies for High Density Two-Phase Liquid Metal Vertical Flows", *Int. J. Multiphase Flows*, 24, pp. 721-737.

Schlichting, H. (1979), *Boundary Layer Theory*, 7th edition, McGraw-Hill.

Schneider, M. and J.W. Ewans, (2006), "A Novel Probe for Detecting Gas Bubbles in Liquid Metals", *Met. and Mat. Trans. B*, 37, pp. 333-337.

Schulenberg, Th. and R. Stieglitz (2010), "Flow Measurement Techniques in Heavy Liquid Metals", *Nuclear Engineering and Design*, 240, pp. 2077-2087.

Scholze, H. (1965), *Glas-Natur, Struktur und Eigenschaft*, F. Viehweg Verlag (in German).

Shoenwald, J.S. and C.V. Smith, Jr. (1984), *Proc. of the IEEE Ultrasonic Symposium*, p. 469ff.

Serizawa, A., I. Kataoka and I. Michiyoshi (1975), "Turbulence Structure of Air-Water Bubbly Flow. 1. Measuring Techniques", *Int. J. Multiphase Flow*, 2, p. 221-223.

Shaw, R. (1960), "The Influence of Hole Dimensions on Static Pressure Measurements", *J. Fluid Mech.*, 7, pp. 550-564.

Shen, X et al. (2005), "Methodological Improvement of an Intrusive Four-Sensor Probe for the Multi-Dimensional Two-Phase Flow Measurement", *International Journal of Multiphase Flow*, 31, pp. 593-617.

Shercliff, J.A. (1962), *The Theory of Electromagnetic Flow-Measurement*, Cambridge University Press.

Shercliff, J.A. (1987), *The Theory of Electromagnetic Flow-Measurement – Induction Devices*, Cambridge University Press, ISBN 0521 335 54X.

Shevchenko, N et al. (2013), "Chimney Formation in Solidifying Ga-25wt pct in Alloys Under the Influence of Thermosolutal Convection", *Metallurgical and Materials Transactions A*, 44, pp. 3797-3808.

Siemens (1969), *Formel und Tabellenhandbuch für Starkstromingenieure*; 4th edition (in German).

Simoni, A., L. Gonzo and M. Gottardi (2002), "Integrated Optical Sensors for 3-D Vision", *Trans. IEEE*, 78, pp. 745-748.

Sleicher, C.A. and G.B. Lim (1975), "Dynamic Behaviour of Hot Film Anemometers in Liquid Metals", *Proc. Symp. on Turbulence in Liquids*, University of Missouri, Rolla, pp. 563-570.

Soleimani, M et al. (2006), "A Three-Dimensional Inverse Finite-Element Method Applied to Experimental Eddy-Current Imaging Data", *IEEE Trans. on Magnetics*, 42 (5), pp. 1560-1567.

Stefani, F. and G. Gerbeth (1999), "Velocity Reconstruction in Conducting Fluids from Magnetic Fields and Electric Potential Measurements", *Inverse Problems*, 15, pp. 771-786.

Stefani, F. and G. Gerbeth (2000a), "On the Uniqueness of Velocity Reconstruction in Conducting Fluids from Measurements of Induced Electromagnetic Fields", *Inverse Problems*, 16, pp. 1-9.

Stefani, F. and G. Gerbeth (2000b), "A Contactless Method for Velocity Reconstruction in Electrically Conducting Fluids", *Meas. Sci. Technol.*, 11, p. 758.

Stefani, F., Th. Gundrum and G. Gerbeth (2004), "Contactless Inductive Flow Tomography", *Physical Review E*, 70, 056306, pp. 1-7.

Stewart, M.J. and F. Weinberg (1972), "Fluid Flow in Liquid Metals: Experimental Observations", *Journal of Crystal Growth*, 12, pp. 228-238.

Stieglitz, R. and U. Müller (1996), *Der Geodynamo, eine Versuchsanlage zum Nachweis des homogenen Dynamoeffektes*, FZKA-5716, Forschungszentrum Karlsruhe, Karlsruhe.

Suzuki, Y., M. Aritomi and H. Kikura (2000), "Measurement of the Flow Around Bubbles Using the Ultrasonic Velocity Profile Monitor", *Bull. Res. Lab. Nucl. Reactors* (Tokyo Inst. Technol.), 3, pp. 93-99.

Suzuki, Y et al. (2002), "Microstructure of the Flow Field Around a Bubble in Counter-Current Bubbly Flow", *Experimental Thermal and Fluid Science*, 26, pp. 221-227.

Swindell, W et al. (1991), "The Design of Megavoltage Projection Imaging Systems: Some Theoretical Aspects", *Med. Phys.*, 18, pp. 855-866.

Szekely, J. (1964), *ISI Journal*, 202, pp. 505-508.

Szekely, J., C.W. Chang and R.E. Ryan (1977), *Met. Trans.*, 8B, pp. 333-338.

Szekely, J. and C.W. Chang (1977a), *Ironmaking and Steelmaking*, 3, pp. 196-204.

Szekely, J., and C.W. Chang (1977b), *Ironmaking and Steelmaking*, 3, pp. 190-195.

Szekely, J, J.H. Grevet and N. El-Kaddah (1984), *Int. J. Heat and Mass Transfer*, 27, pp. 1116-1121.

Szekely, J., J.W. Evans and J.K. Brimacombe (1988), *The Mathematical and Physical Modelling of Primary Metals Processing Operation*, John Wiley & Sons, pp. 117-120.

Taberaux, A.T. and R.B. Hester (1984), *Light Metals*, 11, pp. 519-539.

Takeda, Y. and H. Kikura (1997), "Measurement of Liquid Metal Flow in a SINQ Target Geometry", *PSI Annual Report 1997*, Annex IIIA, pp. 20-21.

Takenaka, N et al. (1994a), *Nondestr. Test. Eval.*, 11, p. 107ff.

Takenaka, N et al. (1994b), "Visualization of Streak Lines in Liquid Metal by Neutron Radiography", *Exp. Therm. Fluid Sci.*, 12, p. 355.

Takenaka, N et al. (1996), "Liquid Metal Flow Measurement by Neutron Tomography", *Nuc. Inst. and Methods in Phys. Res.*, A377, pp. 156-160.

Tavoularis, S. and M. Szymczak (1989), "Displacement Effects of Square Ended Pitot Tubes in Shear Flows", *Exp. in Fluids*, 7, pp. 33-37.

Terzija, N et al. (2011a), "Use of Electromagnetic Induction Tomography for Monitoring Liquid Metal/Gas Flow Regimes on a Model of an Industrial Steel Caster", *Meas. Sci. Techn.*, 22, 015501.

Terzija, N et al. (2011b), "Electromagnetic Inspection of a Two-Phase Flow of GaInSn and Argon", *Flow Meas. Instrum.*, 22, pp. 10-16.

Theofanus, T et al. (1994), *Steam Explosions: Fundamentals and Energetic Behaviour*, NUREG/CR-5960, Nuclear Regulatory Commission, Washington, DC.

Thess, A et al. (2007), "Theory of the Lorentz Force Flowmeter", *New J. Phys.*, 9 (299), pp. 1-21.

Thiyagarajan, T.K et al. (1991), "Gamma-Ray Attenuation Method for Void Fraction Measurement in Fluctuating Two-Phase Liquid Metal Flows", *Measurement Science and Technology*, 2, pp. 69-74.

Thom, A. and C.J. Appelt (1957), "The Pressure in a Two-Dimensional Static Hole at Low Reynolds Numbers", *Aero. Res. Counc. R&M* 3090.

Toh, S.L et al. (2001), "Whole Field Surface Roughness Measurement by Laser Speckle Correlation Technique", *Optics Laser Technology*, 33, pp. 427-434.

Tsubayashi, M., M. Sobajima and S. Ohtomo (1994a), *Proceedings 4th World Conference Neutron Radiography*, San Francisco, CA, 10-16 May, *Neutron Radiography*, 4th edition, J.P. Barton Gordon and Breach, Yverdon, Switzerland, p. 317ff.

VDI-Wissensforum (2001), "Durchfluss und Mengenmessungen in Rohrleitungen", *VDI-Seminar 361624*, University of Stuttgart (in German).

von der Hardt, P. and H. Röttger (eds.) (1981), *Neutron Radiography Handbook*, D. Reidel (ed.), Dordrecht, Holland.

Velt, I.D et al. (1982), *Correlation Technique for Flow Rate Measurement of Electro-Conductive Fluids and Two-Phase Media and a Device for Its Implementation*, Int. Patent No. 30.01.82.

Velt, I.D. and Yu.V. Mikhailov (2007), "Magnetic Flow Meters with Controlled Boundary Conditions", *Measurement Techniques*, 50 (5), pp. 560-564.

Viré, A., B. Knaepen and A. Thess (2010), "Lorentz Force Velocimetry Based on Time-of-Flight Measurements", *J. Appl. Physics*, 22.

Webster, D. (1994), *IEEE Trans. Instrum. Meas.*, 43, p. 578.

Weissenfluh, Th. (1985), "Probes for Local Velocity and Temperature Measurements in Liquid Metal Flow", *Int. J. Heat and Mass Transfer*, 28 (8), pp. 1563-1574.

Weissenfluh, Th. and B. Sigg (1988), "Experience with Permanent Magnetic Probes for the Measurement of Local Velocities in Liquid Metals", *Prog. in Astronautics and Aeronautics*, 111, pp. 61-81.

White, F.M. (1986), *Fluid Mechanics*, 2nd edition, McGraw-Hill, New York.

Wondrak, T et al. (2009), "Some Methodological Improvements of the Contactless Inductive Flow Tomography", *Int. J. Appl. Electromagn. Mech.*, 30, pp. 255-64.

Wondrak, T et al. (2010), "Contactless Inductive Flow Tomography for a Model of Continuous Steel Casting", *Meas. Sci. Techn.*, 21, 045402.

Wondrak, T et al. (2011), "Combined Electromagnetic Tomography for Determining Two-Phase Flow Characteristics in the Submerged Entry Nozzle and in the Mold of a Continuous Casting Model", *Met. and Materials Trans. B*, 42, pp. 1201-1210.

Wondrak, T et al. (2012), "Liquid Metal Experiments with a Swirling-Flow Submerged Entry Nozzle", *Ironmaking and Steelmaking*, 39, pp. 1-9.

Wu, Q. and M. Ishii (1999), "Sensitivity Study on Double-Sensor Conductivity Probe for the Measurement of Interfacial Area Concentration in Bubbly Flow", *Int. J. Multiphase Flow*, 25 (1), pp. 155-173.

Wunderlich, Th. and P.O. Brunn (2000), "A Wall Layer Correction for Ultrasound Measurement in Tube Flow: Comparison Between Theory and Experiment", *Flow Measurement and Instrumentation*, 11, pp. 63-69.

Xu, L et al. (1997), "Application of Ultra-Sonic Tomography to Monitoring of Two-Phase Flow", *Chem. Engng. Science*, 52 (13), pp. 2171-2183.

Xu, M., F. Stefani and G. Gerbeth (2004), "The Integral Equation Method for a Steady Kinematic Dynamo Problem", *J. Comp. Phys.*, 196, pp. 102-105.

Zagarola, M.V. (1996), *Mean Flow Scaling in Turbulent Pipe Flow*, PhD Thesis, Princeton University, Princeton, NJ.

Zagarola, M.V. and A.J. Smits (1998), "Mean Flow Scaling of Turbulent Pipe Flow", *J. Fluid Mech.*, 373, pp. 33-79.

Zhilin, V.G., K.V. Zvyagin and Y.P. Ivochkin (1987), "Dynamic Response and Spectral Resolution in Fibre-Optics Liquid Metal Velocity Sensors", Plenum Publishing, Paper 0018-151X/86/2405-0729, pp. 729-736.

Zhilin, V.G et al. (1989), "Liquid Metal Magnetohydrodynamics, Diagnostics of Liquid Metal Flows Using Fibre-Optic Velocity Sensor", J. Lielpetris and R. Moreau (eds.), Kluwer Academic Publishers, pp. 373-379.

Zhmylev, A., L. Lisitsinskii and A. Topunov (2003), "Testing the New VZLET UR Ultrasonic Level Meter", *Measurement Techniques*, 46 (2), pp. 212-215.

12. Existing heavy liquid metal facilities for experimental applications*

12.1 Introduction

The use of the heavy liquid metals (HLM), lead-bismuth eutectic (LBE) and lead (Pb) as cooling mediums and spallation material has been envisaged for accelerator-driven systems (ADS), which are devoted to transmutation, thus reducing the burden of nuclear waste. An increasing interest in HLM has also been identified in other research and industrial fields, for instance energy production with advanced nuclear systems, e.g. the lead-cooled fast reactor (LFR), hydrogen production and the development of spallation neutron sources for medical applications and materials studies. Moreover, HLM might also play a future role in the development of concentrated solar power plants. Therefore, scientific and technological activities focused on materials compatibility, thermal fluid dynamics characterisation and technology issues have been launched. In this framework a great effort has been made in Europe, Japan, Korea and the United States since the late 1990s to build and operate HLM test facilities in support of the previously mentioned applications. In the following paragraphs updated descriptions of the HLM facilities available at the laboratories of the expert groups participating in the realisation of this handbook are given. An updated list of the facilities is also given in Table 12.4.1 at the end of this chapter. The update has been done with respect to the 2007 version of the HLM handbook, as new facilities have been built and existing facilities have been refurbished or dismantled. In particular, the new and existing facilities built in Europe as well as the future needs have been analysed within the Advanced Reactor Initiative and Network Arrangement (ADRIANA) project. The outcomes of this project and the input received from the experts have been used to update the chapter. As far as the dismantled facilities are concerned, these have been removed from this edition of the handbook.

The available facilities cover almost all basic studies needed to design HLM nuclear systems working at temperatures up to 550°C; in a few new facilities declared operating temperature can reach 700°C. However, further needs can be envisaged for specific analysis concerning safety aspects in representative conditions, i.e. simulating selected transients, where higher temperatures can be reached for a short time period. These experiments might be considered valuable for code validation. Moreover, for specific component testing in prototypical conditions (e.g. dedicated heat exchanger, pump, etc.) and in-service inspection and repair (ISI&R) further needs might be declared in future.

Additionally, the need to characterise and validate specific measurement techniques (e.g. oxygen sensors) and operational techniques (e.g. pumps, flow meters) for reactor applications in a combined neutron field and HLM environment can be also envisaged as a topic for future study.

In the following sections the available facilities are listed, and the objectives and the operational parameters are reported. Contact data have been provided in the summary tables at the end of the chapter. In terms of organisation, technological facilities are discussed first, followed by materials testing facilities and finally facilities related to thermal-hydraulics studies.

* Chapter lead: C. Fazio, with special thanks to K. Litfin for his collaboration on the update.

12.2 Technological facilities and their applications

Technological facilities comprise two areas of research, on the one hand techniques relevant to thermal-hydraulics and on the other techniques which are implemented to control the chemistry of the liquid metal. These two types of facility are grouped together, as the purpose is to highlight the technological aspect. However, one can also treat the two classes of facility in a separated way. Technological and liquid metal chemistry experiments performed in this field are aimed at the development of measurement tools and devices to realise and execute thermal-hydraulics benchmark experiments with well-known and measurable initial and boundary conditions. Moreover, these facilities aim to validate specific procedures for large circuit operation. The relevant measurement tools and devices to be applied for thermal-hydraulics experiments are:

- heat flux simulation tools;
- flow meter devices;
- pressure measuring systems;
- local velocity measurement systems;
- development of tools to measure locally and globally free surfaces.

A second item is the study of liquid metal chemistry, where the development and validation of oxygen monitoring and control systems is one of the most important tasks. Three types of oxygen control methods are currently analysed, which make use of a mixture of hydrogen/moisture, oxygen and hydrogen gases, and PbO pellets, respectively. Concerning the measurement of the oxygen content in the liquid metal, electrochemical oxygen probes are presently being developed. Activities are focused on the definition of a standardised calibration procedure to assess the probes for reliability, an imperative requirement for nuclear use. Key variables include dose, dose rate, thermal transients, pressure variations, etc.

Facility: Technologies of Heavy Liquid Metal Systems (THESYS) loop

KIT, Germany (Figure 12.2.1)

- Objectives:
  - Optimisation of Karlsruhe OCS for loop applications.
  - Development of thermal-hydraulic measurement techniques.
  - Heat transfer and turbulence experiments.
  - Development of high performance Inconel heaters (fuel rod simulator).
  - Set-up of thermal-hydraulic database for physical model development and code validation.
- Operational parameters:
  - Maximum temperature: 400°C.
  - Maximum flow rate: 14 m³/h.
  - LBE volume: 220 l.

Figure 12.2.1: Schematic of THESYS

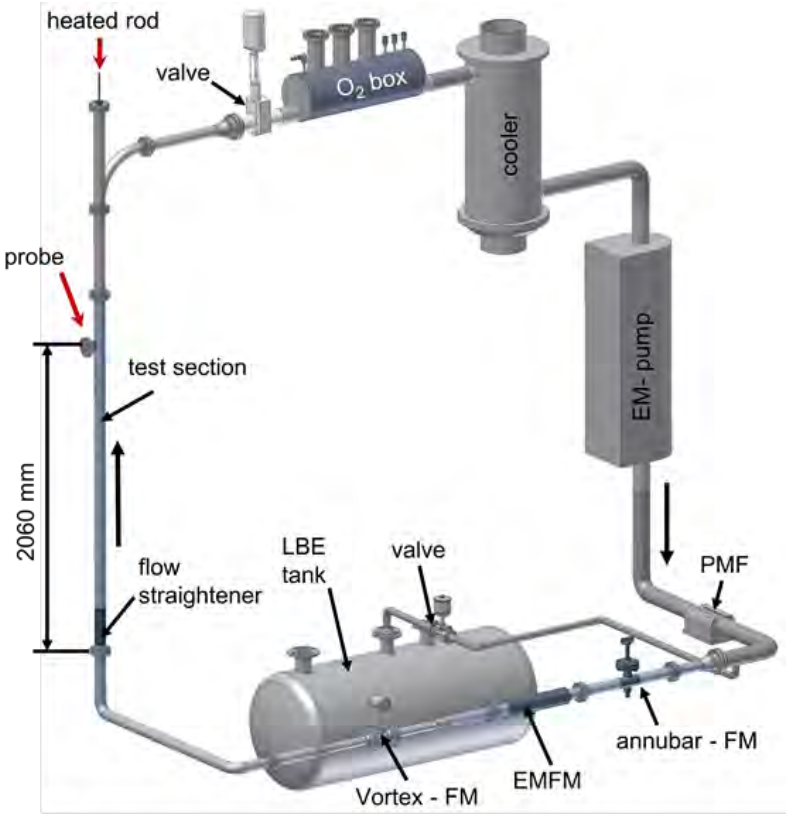

Facility: Karlsruhe Oxygen Control System (KOCOS)

KIT, Germany (Figure 12.2.2)

- Objectives:
  - Development of the Karlsruhe Oxygen Control System (OCS).
  - Measurement of diffusion coefficients of oxygen in LBE.
  - Measurement of oxygen mass exchange rates.

Figure 12.2.2: Diagram sketch of KOCOS experiment

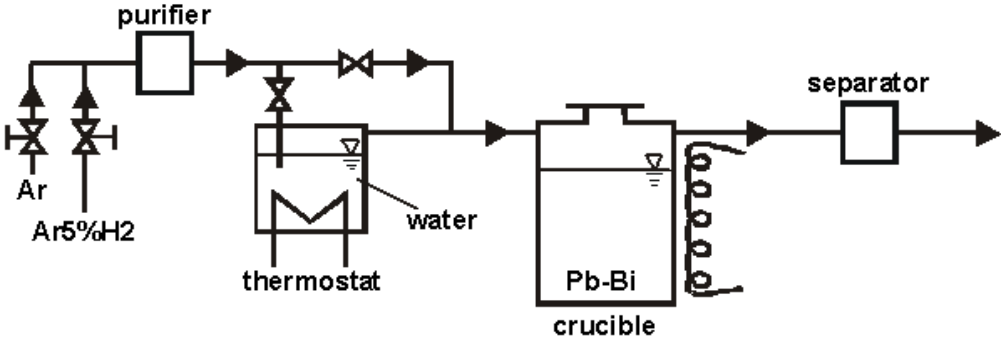

Facility: Heavy Liquid Metals Interaction with Water (LIFUS 5)

ENEA, Italy (Figure 12.2.3)

- Objectives:
  - To study the interaction between heavy liquid metals and pressurised water.
  - To simulate LOCA accidents in water-cooled HLM reactors operating under a wide range of conditions.
  - To start the water injection though an impulsive increase of pressure at the water side.
- Operational parameters:
  - Maximum temperature: 500°C.
  - Maximum diameter for free water injection: 1 inch.
  - Maximum water pressure: 200 bar.
  - Volume of HLM/water interaction: 110 litres.
  - Heavy liquid metal: LBE.

Figure 12.2.3: Photo of LIFUS 5

Facility: SOLDIF

CEA, France (Figure 12.2.4)

- Objectives:
  - Determination of solubility and diffusivity of dissolved species in molten lead or lead alloys by means of electrochemical techniques using a molten salt electrolyte.
  - Characterisation of the oxide layer on a metallic material immersed in molten lead or lead alloys by means of electrochemical techniques.

- Operational parameters:
  - Maximum temperature: 500°C.
  - Maximum flow rate: Static.
  - Number of electrochemical cells: One.
  - Heavy liquid metal: LBE or Pb.

Figure 12.2.4: Schematic and photo of SOLDIF

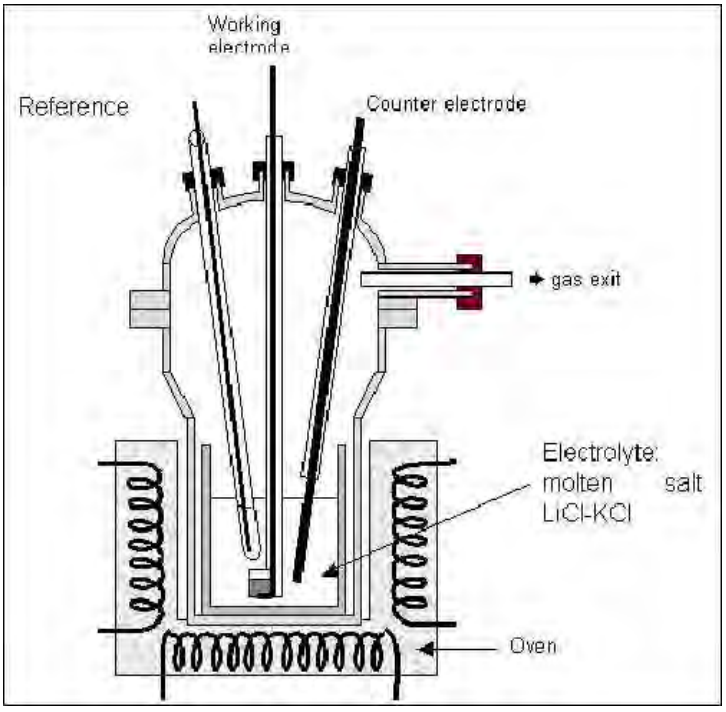

Facility: Mass Exchanger in Continuous Operation (MEXICO)

SCK•CEN, Belgium (Figure 12.2.5)

In operation: January 2014

- Objectives:
  - Investigations on the applicability of solid (PbO) oxygen control systems (OCS) in large LBE loops.
  - Long-term testing of oxygen sensors in LBE as part of the OCS.
  - Oxygen mass transfer modelling and monitoring.
  - Particles filter testing.
  - Cold trap testing.
- Operational parameters:
  - Maximum temperature: 500°C.
  - Minimum temperature: 200°C.
  - Maximum (typical) flowrate: 1.8 (< 1) l/s.
  - Electrical power: 160 kW.
  - Oxygen control system (OCS): Via solid PbO mass exchanger.
  - Oxygen sensors: 20 in LBE.
  - Flow meters: 3.
  - Filter units: 2 in parallel.
  - Heavy liquid metal: LBE.

Figure 12.2.5: Flow schematic of MEXICO

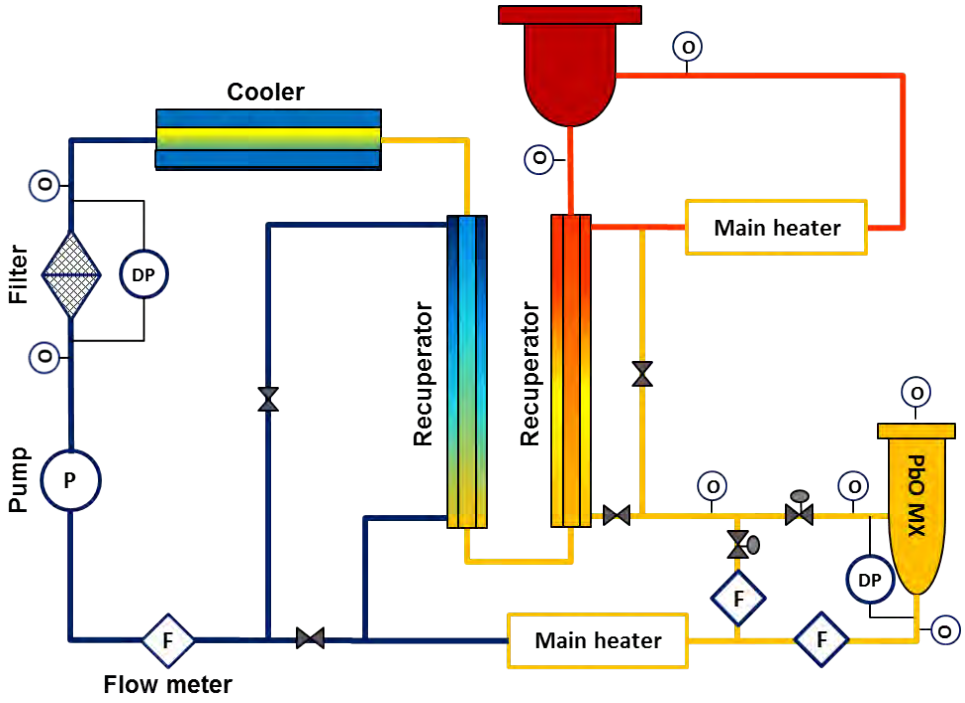

Facility: Heavy Liquid Metal Oxygen Conditioning System (HELIOS 3)

SCK•CEN, Belgium (Figures 12.2.6[a] and 12.2.6[b])

In operation: August 2012

- Objectives:
  - Investigations on the optimisation of LBE oxygen reduction.
  - Investigations on feasibility of gas recycling.
  - Investigations on calamity recovery.
  - Component testing.
- Operational parameters:
  - Maximum temperature: 450°C.
  - Minimum temperature: 200°C.
  - Maximum gas flow rate: $1.7 \cdot 10^{-3}$ mol/s.
  - Electrical power: 12 kW.
  - Oxygen control system (OCS): H_2/H_2O ratio.
  - Oxygen sensors: 3 in LBE, 1 in gas.
  - LBE volume: 20 l (× 2).
  - Heavy liquid metal: LBE.

Figure 12.2.6(a): Schematic of HELIOS 3

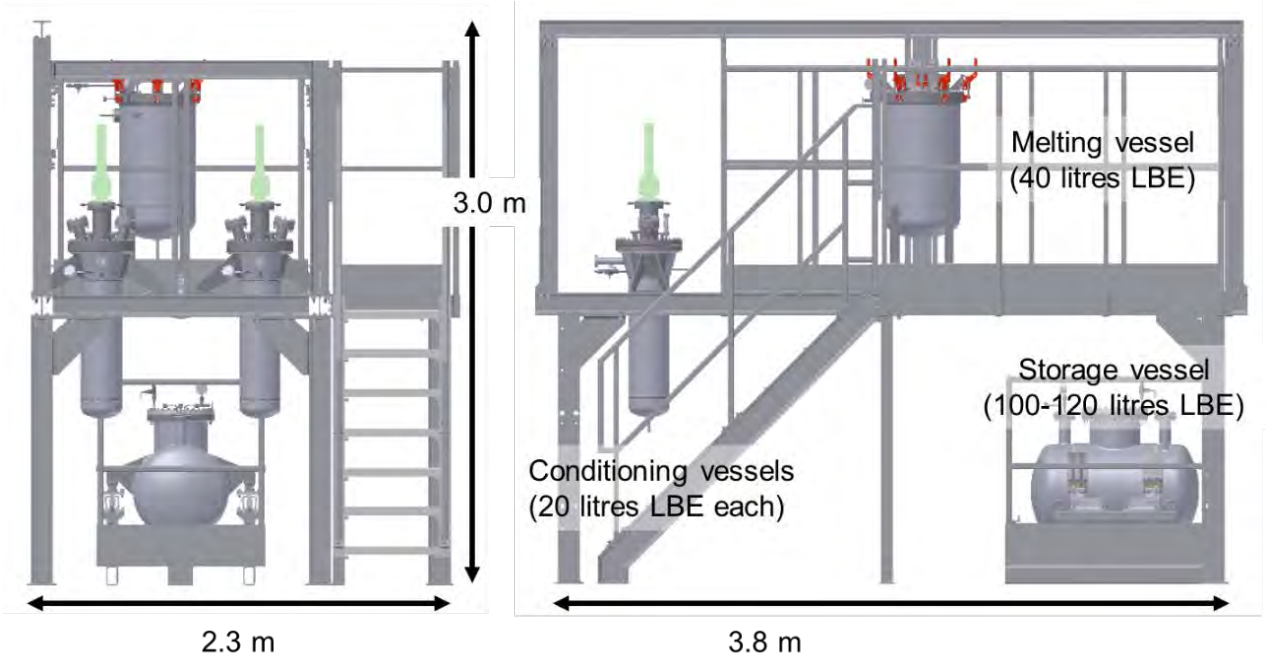

Figure 12.2.6(b): Photo of HELIOS 3

Facility: Liliputter 2

SCK•CEN, Belgium (Figure 12.2.7)

In operation: April 2013

- Objectives:
  - Investigations on filtration.
  - Investigations on mass transfer of impurities.
  - Component testing.
- Operational parameters:
  - Maximum temperature: 450°C (250°C of main loop).
  - Minimum temperature: 200°C.
  - Nominal flow rate: 0.5 l/s.
  - Electrical power: 10 kW.
  - Flow meter: 1.
  - Oxygen sensors: 1 in LBE.
  - Heavy liquid metal: LBE.

Figure 12.2.7: Schematic of Liliputter 2

Facility: Remote Handling Parts Test Rig (RHAPTER)

SCK•CEN, Belgium (Figure 12.2.8)

In operation: September 2011

- Objectives:
  - Investigations on moving mechanical components for robotics in LBE.
- Operational parameters:
  - Heavy liquid metal: Lead-bismuth eutectic (LBE).
  - Maximum temperature: 450°C.
  - Minimum temperature: 200°C.
  - Oxygen control system: Via H_2/H_2O ratio in gas phase.
  - Oxygen sensors: 1 in LBE.
  - LBE volume: 50 l.
  - Fast shaft: 1 000 rpm-10 Nm.
  - Slow shaft: 10 rpm-1 000 Nm.
  - Instrumentation: torque sensor, position encoder, accelerometer, thermocouples, pressure gauges.

Figure 12.2.8: Schematic and photo of RHAPTER

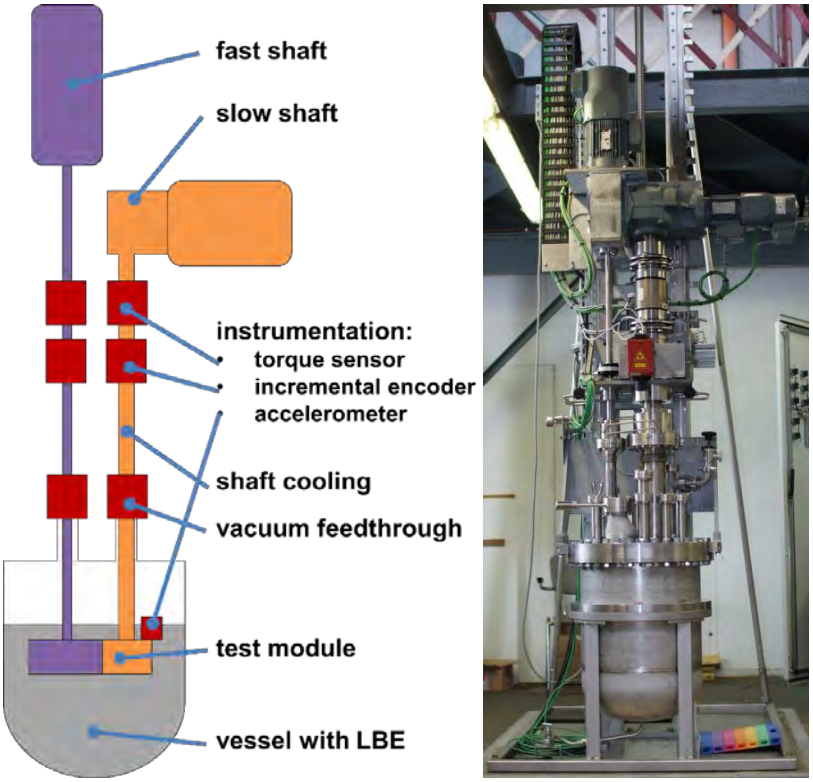

Facility: Steam Injection and Oxygen Concentration Control Apparatus

Research Laboratory for Nuclear Reactors, Tokyo Institute of Technology, Japan (Figure 12.2.9)

- Objectives:
  - Performance of oxygen sensor.
  - Control of oxygen potentials in LBE.
  - Material corrosion and corrosion product in LBE.
  - Carry-over of LBE mist and impurities into steam flow.
  - Dissolved H_2 in steam and water.
  - Chemistry and transport of metal elements in LBE.
- Operational parameters:
  - Maximum temperature: 500°C.
  - Maximum pressure: 0.5 MPa.
  - LBE inventory: 70 kg.
  - Water/steam inventory: 30 kg.
  - Maximum water/steam flow rate: 25 g/min., 250°C.
  - LBE flow system: Steam gas lift pump.
  - Maximum electrical power LBE: 6 KW.

– Maximum electrical power water/steam: 4 KW.
– LBE test vessel number: 1.

  Size: ϕ260 × 760 mm.

  Material: Cr-Mo steel.
– Maximum apparatus height: 3.2 m.
– Oxygen control system (OCS): Yes (hydrogen-dissolved water).
– Heavy liquid metal: LBE.

Figure 12.2.9: Flow diagram and photo of the Steam Injection and Oxygen Concentration Control Apparatus

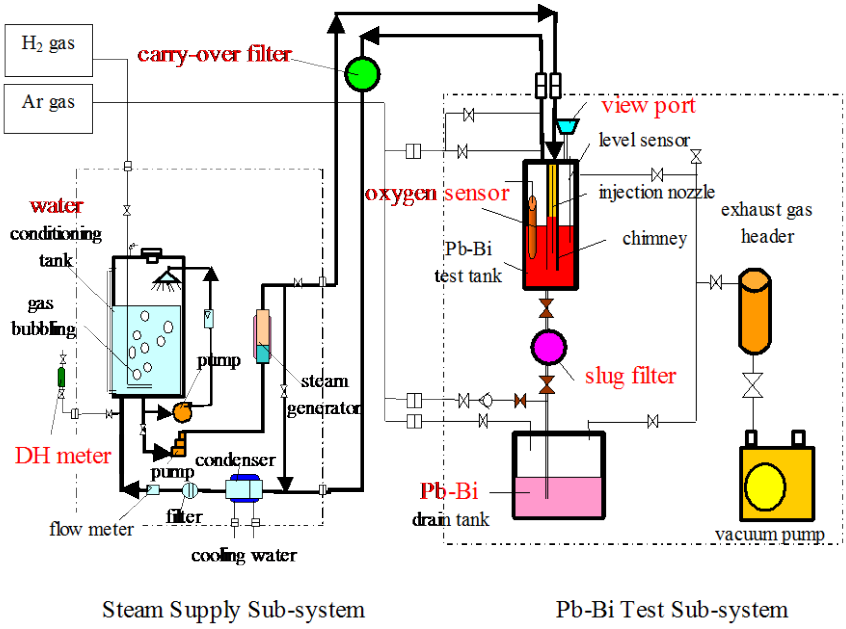

12.3 Materials testing facilities and their applications

In materials testing, the facilities used to characterise materials behaviour in the liquid metal are principally of two types. One are static tests facilities, which are used for materials screening tests and for basic corrosion mechanism investigations. Usually on these static devices an oxygen control and monitoring system is installed in order to evaluate the basic corrosion mechanism in well controlled oxygen conditions. Some of these static devices are also devoted to the mechanical testing of non-irradiated and irradiated materials in the liquid metal. The second type of materials testing facilities are loops. The tests performed with the loops are of importance for the evaluation of the long-term corrosion resistance of the materials. The tests were typically performed under well-known conditions in terms of oxygen concentration, temperature, HLM flow rate. The database produced with the loop tests can be employed for the development and validation of corrosion prediction models.

Facility: Corrosion Test Stand for Stagnant Liquid Lead Alloys (COSTA)

KIT, Germany (Figures 12.3.1[a] and 12.3.1[b])

- Objectives:
  - Investigation of corrosion mechanisms.
  - Influence of protection layers and coatings on corrosion.
  - Investigation of GESA (Gepulste Electronen Strahlanlage) treated surfaces (alloyed surfaces with a pulsed electron beam).
  - Influence of surface alloying on corrosion.

Figure 12.3.1(a): Sketch of the COSTA facility

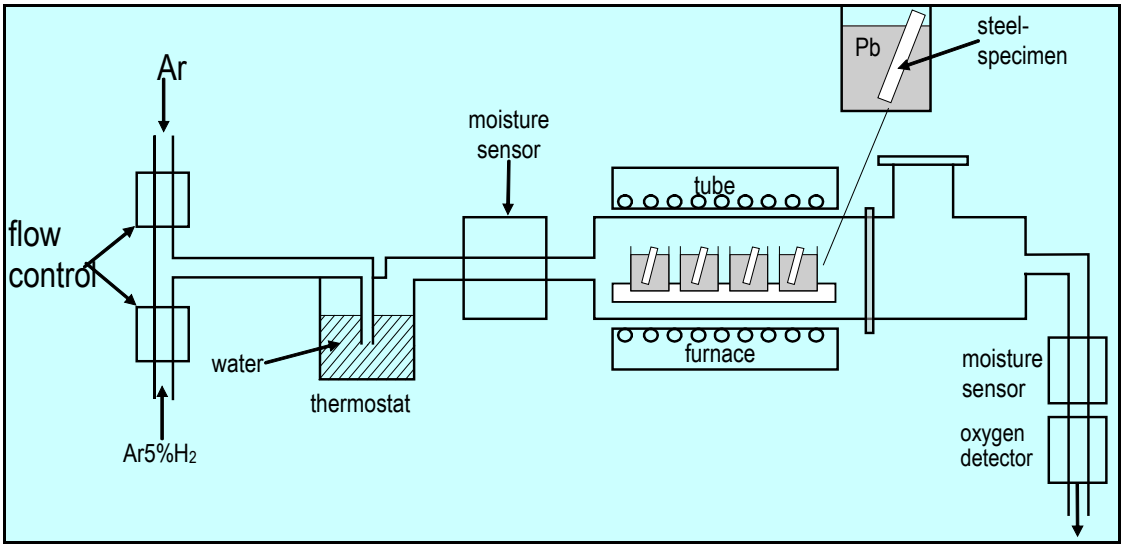

Figure 12.3.1(b): Photo of the COSTA facility

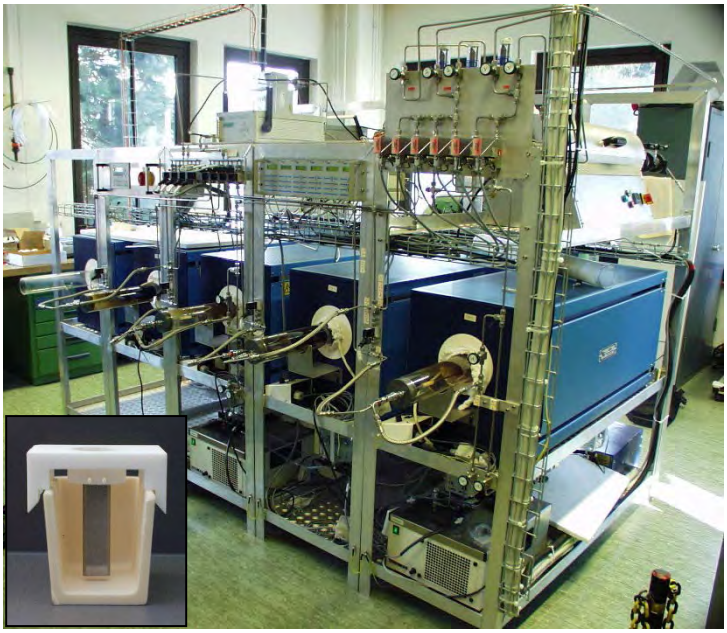

Facility: Corrosion in Dynamic Alloys (CORRIDA)

KIT, Germany (Figure 12.3.2)

- Objectives:
  - Long-term corrosion investigations of structural materials in flowing LBE.
  - Long-term corrosion investigations of coated materials in flowing LBE.
  - Investigations on the mechanisms and the kinetics of material/LBE interactions.
  - Modelling of corrosion/precipitation behaviour in LBE.
  - Investigations on the applicability of oxygen control systems (OCS) in large LBE loops.
  - Testing of appropriate zirconia-based oxygen sensors in LBE as part of the OCS.
- Operational parameters:
  - Maximum temperature: 550°C.
  - Minimum temperature: 400°C.
  - Maximum (typical) flow rate: 4 (2) m/s.
  - Electrical power: 170 kW.
  - Number of test sections: 2.
  - Number of samples: Ca. 32.
  - Oxygen control system (OCS): Via H_2/H_2O ratio in gas phase.
  - Oxygen sensors: 3 in LBE, 1 in gas phase.
  - Heavy liquid metal: LBE.

Figure 12.3.2: Schematic and photo of CORRIDA

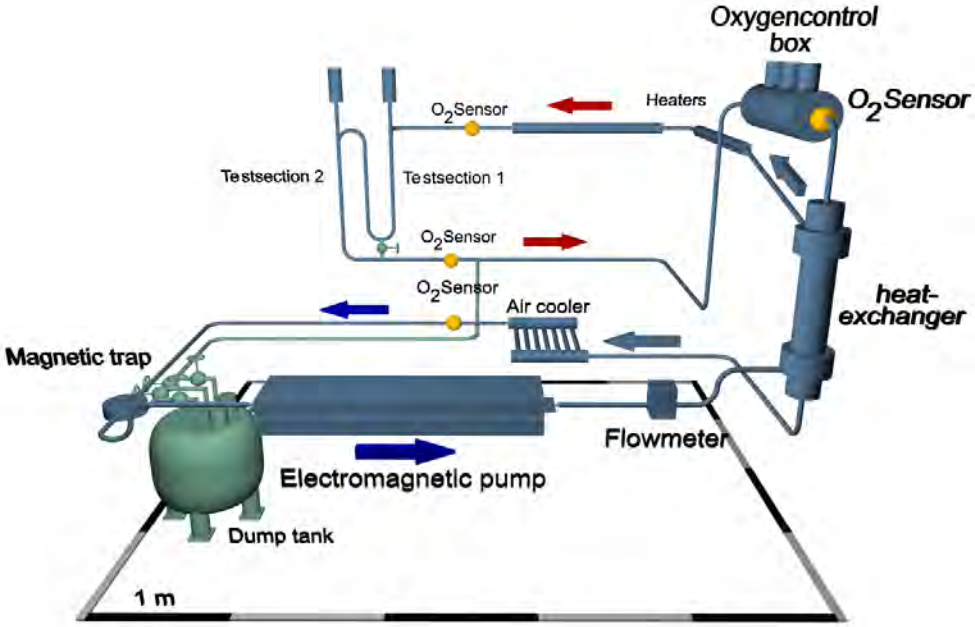

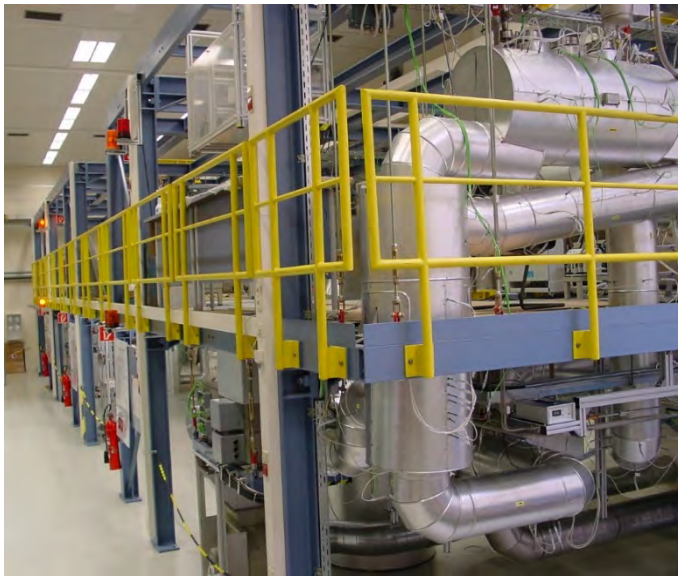

Facility: Test Loop for Lead Material Testing (TELEMAT)

KIT, Germany (Figure 12.3.3)

- Objectives:
  - Long-term corrosion investigations of structural materials in high temperature flowing lead.
  - Long-term corrosion investigations of coated materials in high temperature flowing lead.
  - Modelling of corrosion/precipitation behaviour in high temperature flowing lead.

- Operational parameters:
  - Maximum temperature: 750°C.
  - Diameter of pipes: 18.9 mm.
  - Mean velocity of the lead in the test section: Up to 2 m/s.
  - Lead inventory: 150 litres.
  - Heavy liquid metal: Pb.

Figure 12.3.3: Schematic and photo of TELEMAT

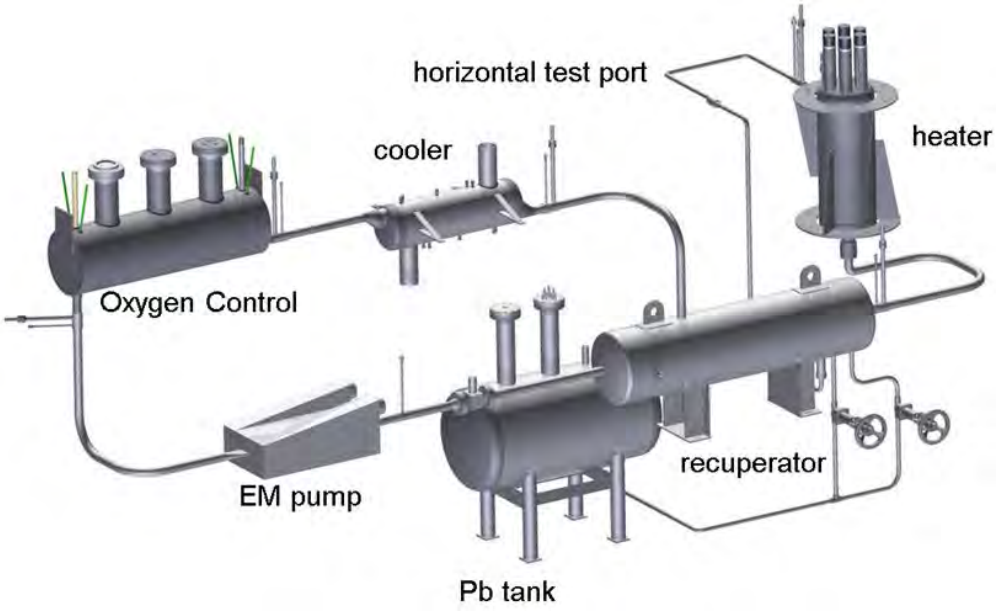

Facility: Creep-to-Rupture Tests in Stagnant Lead Alloys (CRISLA)

KIT, Germany (Figure 12.3.4)

- Objectives:
  - Effects of Pb/LBE on the creep-to-rupture behaviour of un-coated and coated materials.
  - Effects of oxide layers on the creep strength of the structural materials.
- Operational parameters:
  - Maximum temperature: 650°C.
  - Minimum temperature: 400°C.
  - Number of test sections: 4-5.
  - Number of test sections for reference tests in air: 3.
  - Volume of the liquid metal: ~1 l.
  - Oxygen control system (OCS): Computer-controlled
  - Oxygen sensors: 1 per stand in LBE, 2 in gas phase (in gas inlet and outlet).
  - Heavy liquid metal: Pb and LBE.

Figure 12.3.4: Photo of CRISLA

Facility: Corrosion Erosion Test Facility for Liquid Lead Alloy (CORELLA)

KIT, Germany (Figure 12.3.5)

- Objectives:
  - Corrosion studies also in stagnant Pb.
  - Effects of hydrodynamic on corrosion using a rotating inner cylinder – erosion corrosion phenomena.
  - Test of selected pump materials.

- Operational parameters:
  - Maximum temperature: 650°C.
  - Minimum temperature: Tm of LBE or Pb.
  - Maximum speed: 20 m/s – corresponding to 1 200 rpm highly turbulent flow – flow impact directed to surface.
  - Oxygen-control system (OCS): Via gas phase.
  - Oxygen sensors: One in each chamber.
  - Heavy liquid metal: Pb and LBE.

Figure 12.3.5: Photo of CORELLA

Facility: Fretting Tests in Heavy Liquid Metal (FRETHME)

KIT, Germany (Figure 12.3.6)

- Objectives:
  - Fretting corrosion of cladding materials in stagnant Pb.
  - Effects of frequency, amplitude, temperature, oxygen content, load on fretting corrosion.
- Operational parameters:
  - Maximum temperature: 650°C.
  - Maximum applied load: 500 N.
  - Maximum frequency: 40 Hz.
  - Range of amplitudes: 5-500 μm.
  - Minimum temperature: Tm of LBE or Pb.
  - Maximum number of coupled specimens: 3 couples.
  - Oxygen control system (OCS): Via gas phase.

– Oxygen sensors: One in each chamber.
– Heavy liquid metal: LBE.

Figure 12.3.6: Photos of FRETHME

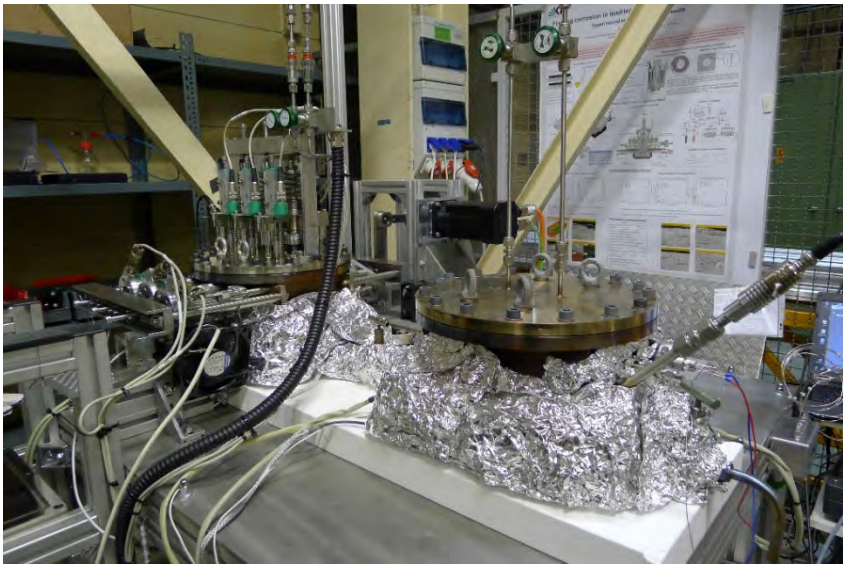

Facility: Lead Corrosion (LECOR)

ENEA, Italy (Figure 12.3.7)

- Objectives:
  – Corrosion investigation in lead alloys.
  – Component test and development.
  – Physico-chemistry.
- Operational parameters:

- Maximum temperature hot leg: 500°C.
- Maximum flow rate: 4.5 m³/h.
- Maximum electrical power: 4 MW.
- Number of test sections: 3.
- Oxygen meter: Yes.
- Oxygen control system (OCS): Separate addition of hydrogen and oxygen.
- Heavy liquid metal: LBE.

Figure 12.3.7: Schematic and photo of LECOR

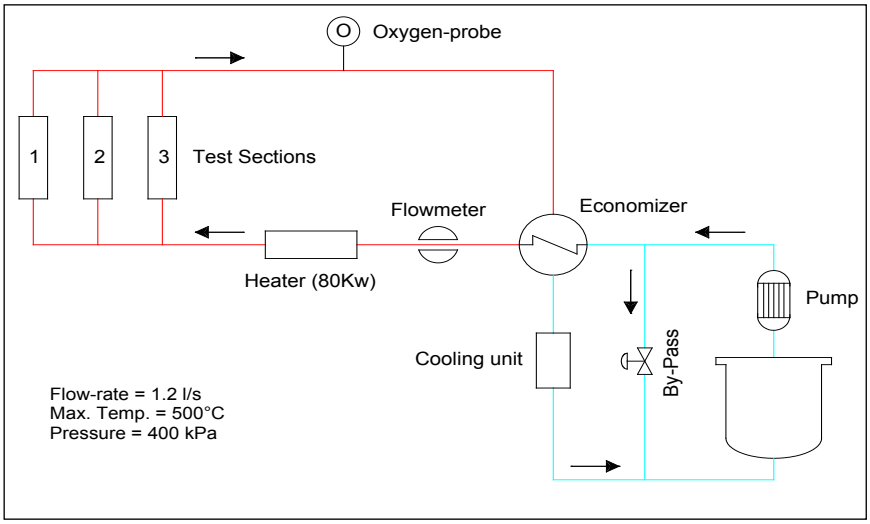

Facility: Development of Lead-Alloy Technology and Applications (DELTA)

LANL, United States (Figures 12.3.8[a] and 12.3.8[b])

- Objectives:
  - Corrosion tests of structural and surface treated materials in flowing LBE.
  - Investigations on mechanisms of material/LBE interactions.
  - Investigations and benchmarking of corrosion/precipitation and system kinetics models.
  - Implementation, testing and improvement of oxygen sensors and control systems in large LBE loops.
  - Thermal-hydraulics experiments (e.g. natural convection) and system modelling (e.g. TRAC) and benchmarking.
  - Development and testing of components, data acquisition and control systems.
- Operational parameters:
  - Maximum temperature: 550°C.
  - Minimum temperature: 400°C.
  - Maximum (typical) flow rate: 5 (2) m/s.
  - Electrical power: 65 kW (main heater).
  - Number of test sections: 2 (corrosion, scc).
  - Number of samples: 186 (in 32/holder batches).
  - Oxygen control system (OCS): Direct injection of O_2/He and H_2/He.
  - Oxygen sensors: 4 in LBE, 1 in gas phase.
  - Heavy liquid metal: LBE.

Figure 12.3.8(a): Schematic of DELTA loop

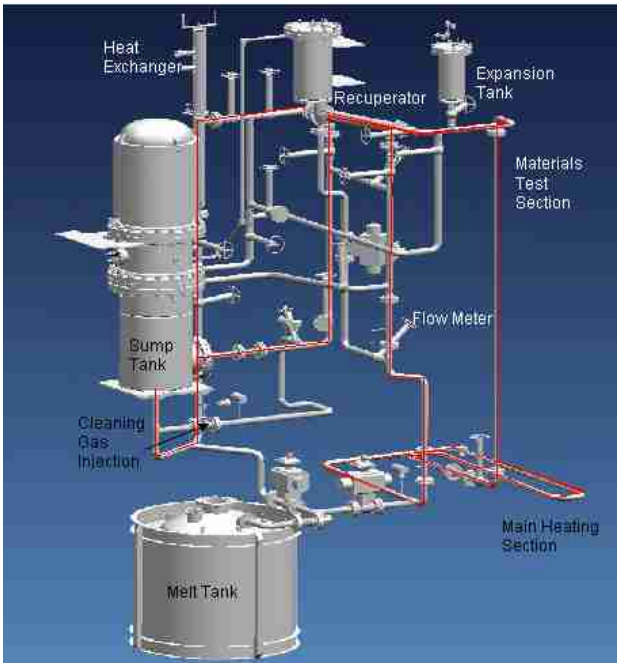

Figure 12.3.8(b): Photo of DELTA loop

Facility: Lead Correlation Stand (LCS)

LANL/UNLV, United States (Figure 12.3.9)

- Objectives:
  - Transfer and extend LBE coolant technology to high temperature Pb systems.
  - Corrosion tests of structural and surface treated materials in flowing Pb.
  - Thermal-hydraulics experiments (e.g. natural convection and flow stability).
  - Adapting and testing of sensors, components, data acquisition and control systems to use in Pb at higher temperatures.
  - Test ODS steel (MA956) welding and construction for the loop.
- Operational parameters:
  - Maximum temperature: 700°C.
  - Minimum temperature: 400°C.
  - Maximum flow rate: 0.25 m/s.
  - Electrical power: 15 kW (main heater).
  - Number of test sections: 1 (corrosion).
  - Number of samples: TBD.
  - Oxygen control system (OCS): Direct injection of O_2/He and H_2/He.
  - Oxygen sensors: 2.
  - Heavy liquid metal: Pb.

Figure 12.3.9: Schematic of the LCS

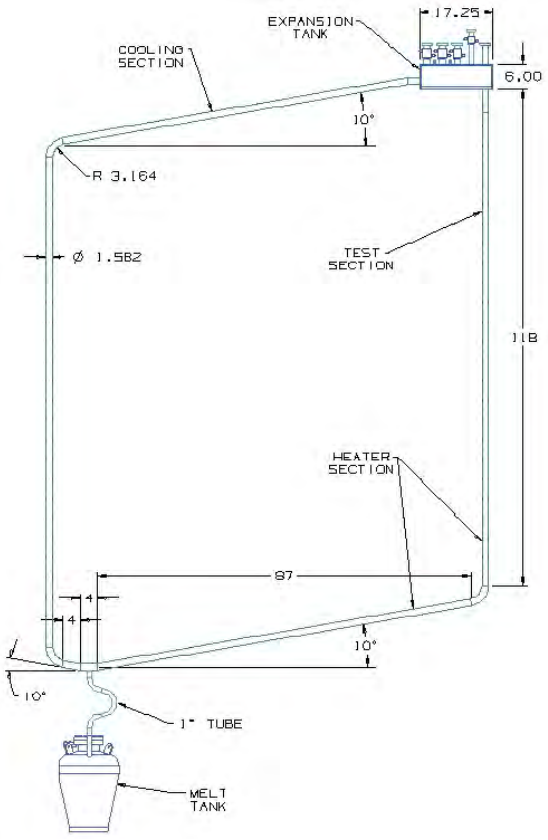

Facility: COLIMESTA

CEA, France (Figure 12.3.10)

- Objectives:
  - Corrosion studies of materials (including welds) and coatings.
  - Corrosion mechanisms.
  - Effect of oxygen content on corrosion processes.
  - Corrosion kinetics.
  - Development of corrosion models.
- Operational parameters:
  - Maximum temperature: 500°C.
  - Maximum flow rate: Static.
  - Number of test sections: 2.
  - Oxygen control system (OCS): Yes.
  - Heavy liquid metal: LBE.
  - Corrosion protection: Aluminisation by pack cementation max.

Figure 12.3.10: Schematic and photo of COLIMESTA

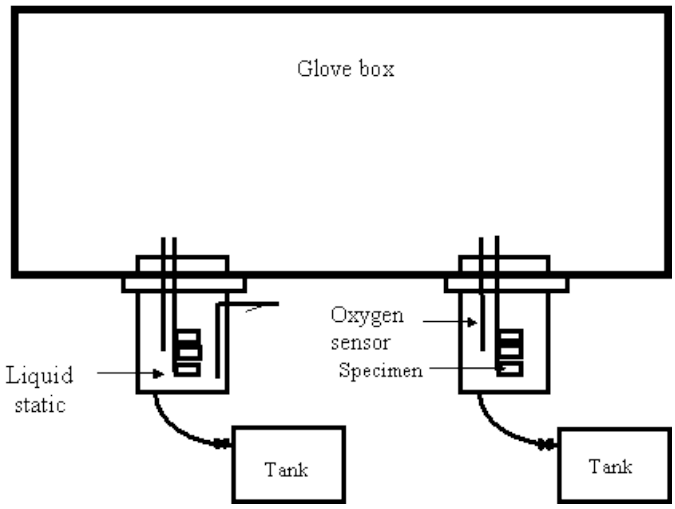

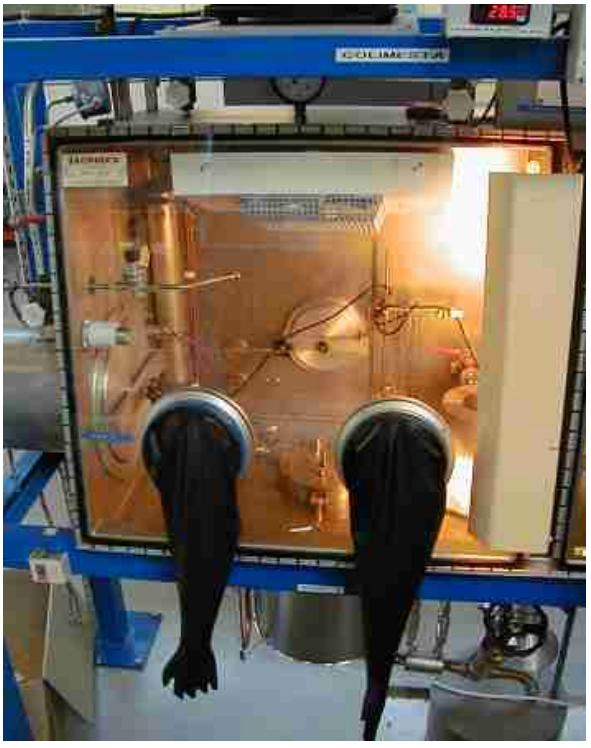

Facility: CICLAD

CEA, France (Figure 12.3.11)

- Objectives:
  - Corrosion studies of materials (including welds) and coatings.
  - Effect of hydrodynamic on corrosion by means of a rotating cylinder (especially at high velocity and including erosion phenomena).
  - Effect of oxygen content on corrosion processes.

  - Corrosion kinetics.
  - Development of corrosion models.
- Operational parameters:
  - Maximum temperature: 500°C.
  - Maximum flow rate: 5 m s^{-1} corresponding to 5 000 rev.min^{-1}.
  - Number of test sections: 1 with the rotating specimens, 1 with in-pipe specimens.
  - Oxygen control system (OCS): Yes.
  - Heavy liquid metal: LBE.
  - Corrosion protection: Aluminisation by pack cementation max.
  - Oxygen control system (OCS): Yes.

Figure 12.3.11: Scheme and photo of CICLAD

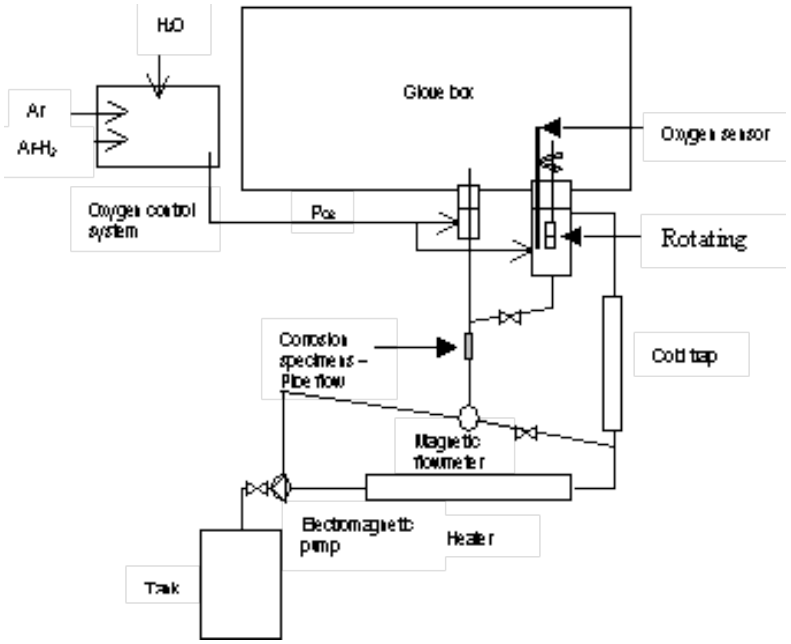

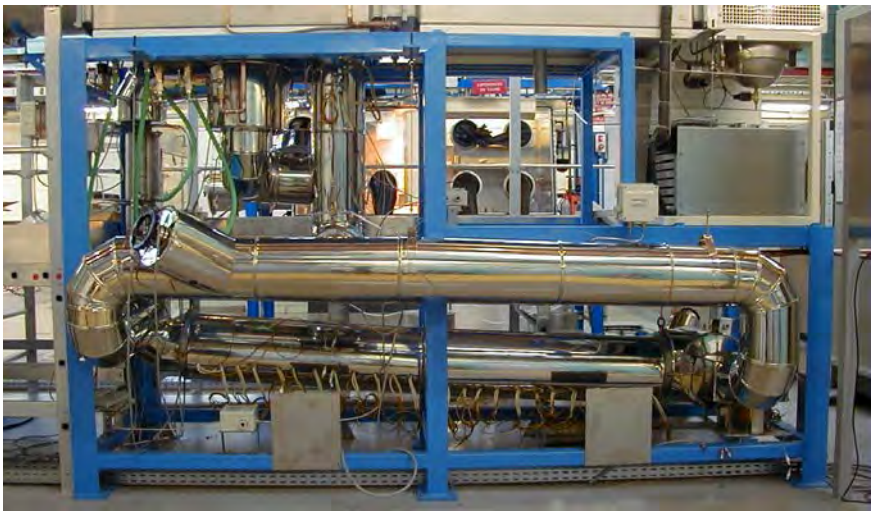

Facility: FELIX

CIEMAT, Spain (Figure 12.3.12)

- Objectives:
  - Materials screening test in stagnant conditions.
- Operational parameters:
  - Different gas atmospheres are used.
  - Oxygen content is measured.
  - Maximum temperature is 600°C.

Figure 12.3.12: Scheme and photo of FELIX

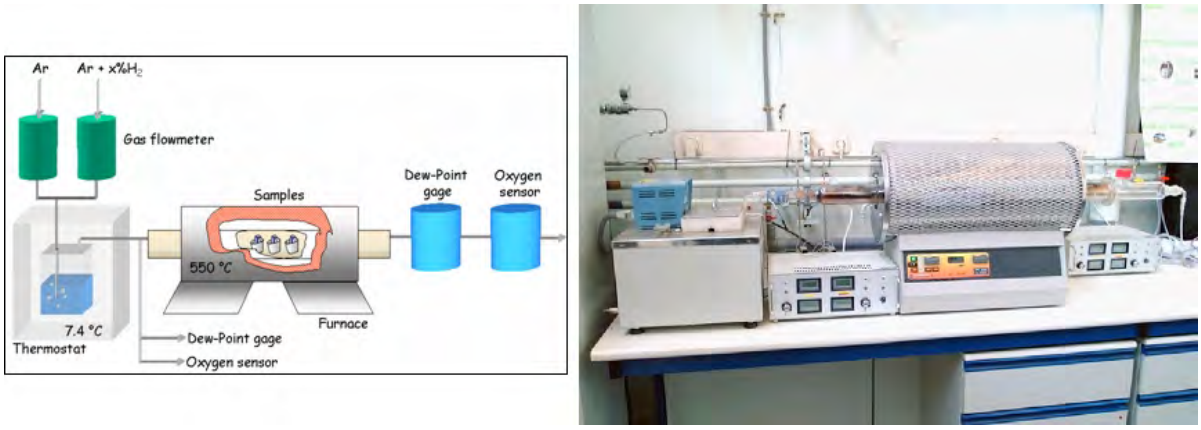

Facility: LINCE (forced convection loop)

CIEMAT, Spain (Figure 12.3.13)

- Objectives:
  - Long-term corrosion experiments in LBE.
  - Oxygen control systems in flowing LBE.
- Operational parameters:
  - Maximum temperature: 500°C.
  - Maximum flow rate: 2.5 m^3/h.
  - Number of test sections: 2.
  - Lead-bismuth inventory: 170 L.
  - Electrical power: 80 kW.
  - Oxygen control system installed.

Figure 12.3.13: Scheme and photo of LINCE

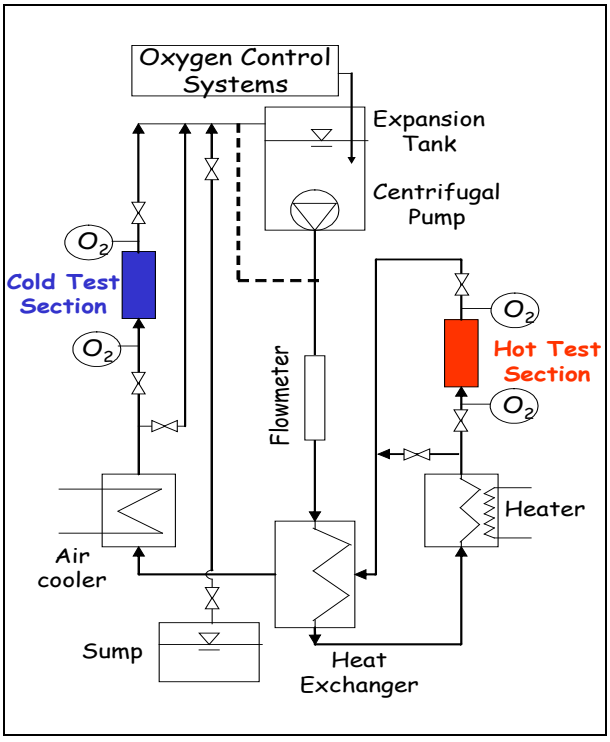

Facility: JAEA Lead-Bismuth Static Corrosion Facility (JLBS)

JAEA, Japan (Figure 12.3.14)

- Objectives:
  - Corrosion of materials for ADS components under static condition.
  - Screening tests of materials for ADS components.

  - Corrosion mechanism of various materials in LBE.
  - Corrosion of surface treated materials.
  - Effect of alloying elements and stress on corrosion in LBE.
  - Effect of impurities in LBE.
- Operational parameters:
  - Maximum temperature: 600°C.
  - Number of pots: 4.
  - Number of test pieces: 10/pot.
  - Diameter of pot: 100 mm.
  - Heavy metal weight: 7 kg/pot.
  - Oxygen control system (OCS): Yes (partially).
  - Heavy liquid metal: LBE.

Figure 12.3.14: Photo of JLBS

Facility: JAEA Lead-Bismuth Flow Loop (JLBL-1)

JAEA, Japan (Figure 12.3.15)

- Objectives:
  - Corrosion study of ADS components in flowing LBE.
  - Development of LBE flow control.
  - Material corrosion-proof test for ADS target test facility at JAEA.
- Operational parameters:
  - Maximum temperature: 450°C.
  - Maximum pressure: 5 bar.
  - Maximum flow rate: 18 L/min.
  - Maximum electrical power: 15 kW heaters.

- Number of test sections: 2.
- Oxygen control system (OCS): Under preparation.
- Heavy liquid metal: LBE.

Figure 12.3.15: Schematic and photo of JLBL-1

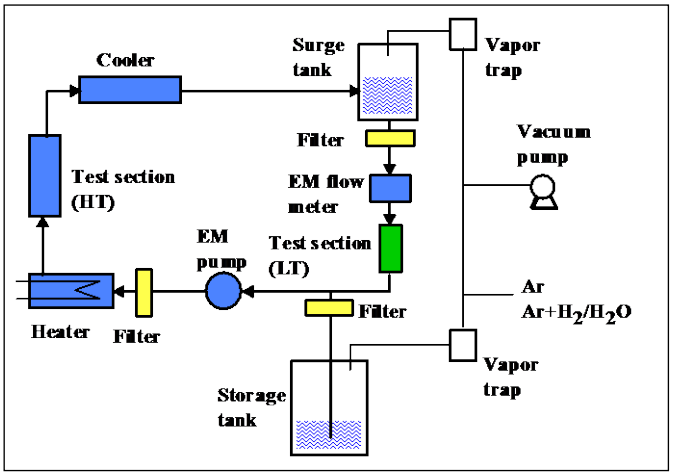

Facility: KPAL-I

KAERI, Korea (Figure 12.3.16)

- Objectives:
  - Database for LBE corrosion.
  - Development of oxygen control technique.
  - Development of oxygen sensor.
  - Development of thermal-hydraulic device for LBE loop.
  - Enhancement of LBE loop operation technique.

- Operational parameters:
  - Maximum temperature: 550°C.
  - Maximum flow rate: 3.6 m³/h at 4.0 m NPSH.
  - Maximum electrical power: 120 kW.
  - Number of test sections: 1.
  - Maximum test section height: 0.9 m.
  - Oxygen control system (OCS): Yes.
  - Heavy liquid metal: LBE.

Figure 12.3.16: KAERI Pb-Bi loop

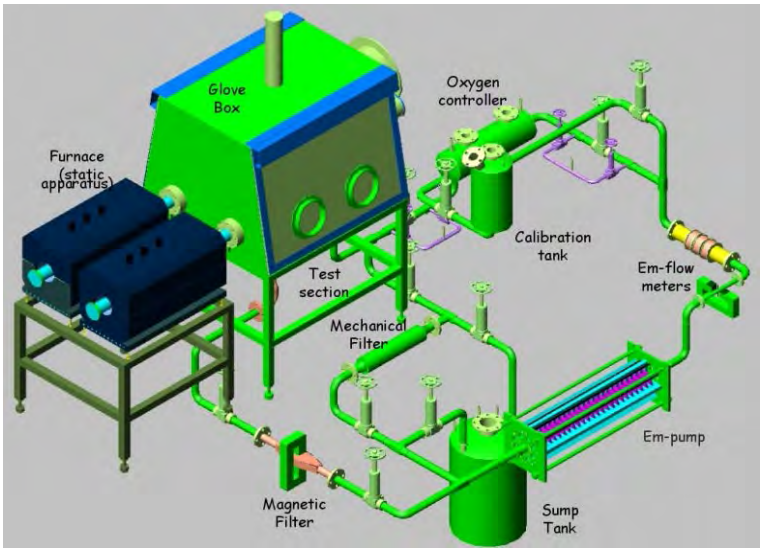

Facility: Convectional Loop, COLONRI I

Nuclear Research Institute Rež, Czech Republic (Figures 12.3.17[a] and 12.3.17[b])

- Objectives:
  - Evaluation of corrosion resistance of structural materials in lead-bismuth under different conditions.
  - Impact of oxygen content (oxygen technology).
- Operational parameters:
  - Maximum temperature: 700°C.
  - Maximum flow rate: 1-2 cm/s.
  - Maximum electrical power: 4 KW.
  - Number of test sections: 2.
  - Maximum test section height: 2.5 m.
  - Oxygen control system (OCS): Yes – indirectly.
  - Heavy liquid metal: LBE.

Figure 12.3.17(a): Schematic of COLONRI I

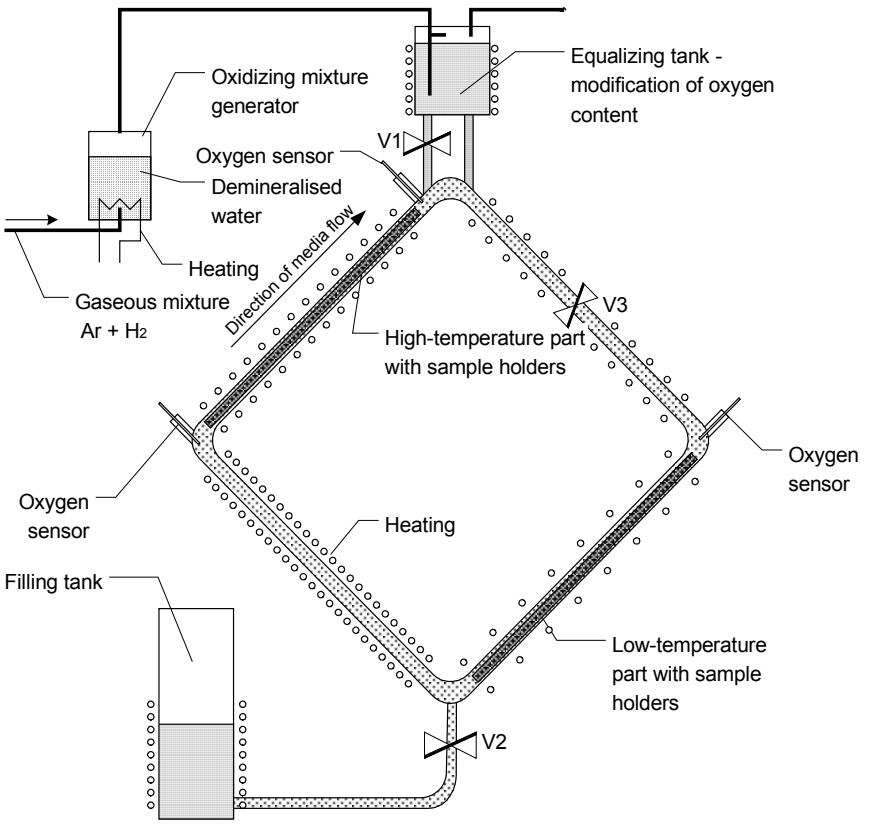

Figure 12.3.17(b): Photo of COLONRI I

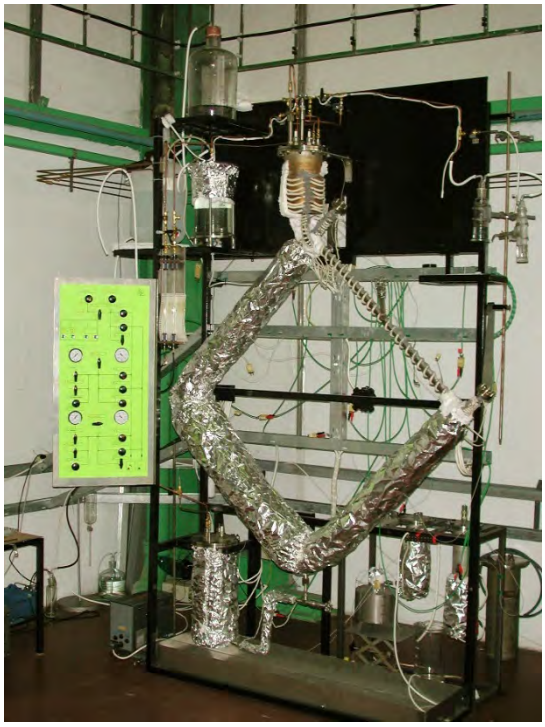

Facility: Quartz Convection Harp

ANL, United States (Figure 12.3.18)

Natural Convection Quartz Harps based on J.V. Cathcart and W.D. Manley (1954), *Corrosion*, 10, 432.

- Objectives:
  - Long-term corrosion investigations of structural materials in flowing Pb or LBE.
  - Long-term corrosion investigations of coated materials in flowing Pb or LBE.
  - Investigations on corrosion mechanisms and thermo-mechanical behaviour between materials and Pb or LBE.
- Operational parameters:
  - Maximum temperature: 800°C.
  - Minimum temperature: 375°C (LBE), 500°C (Pb).
  - Typical flow rate: ~0.01 m/s.
  - Electrical power: Low.
  - Number of test sections: 2.
  - Number of samples: 2.
  - Oxygen control system (OCS): Via H_2/H_2O ratio in gas phase.
  - Oxygen sensors: None.
  - Heavy liquid metal: Pb or LBE.

Figure 12.3.18: Schematic and photo of quartz convection harp

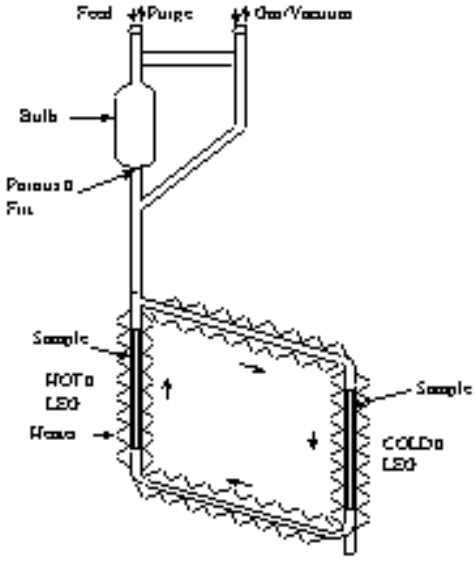

Facility: H.H. Uhlig Corrosion Laboratory

MIT, United States (Figure 12.3.19)

- Objectives:
  - Corrosion tests of structural and surface treated materials in LBE.
  - Investigations on fundamental mechanisms of material/LBE interactions.
  - Investigations and benchmarking of corrosion/precipitation and system kinetics models.
  - Implementation, testing and improvement of oxygen sensors.
- Operational parameters:
  - Maximum temperature: 800°C.
  - Minimum temperature: 400°C.
  - Maximum/minimum flow velocity: 3/0 m/s.
  - Electrical power: 15 kW/test station (heater).
  - Number of test stations: 2 (corrosion, scc, rotating electrode).
  - Number of samples (immersion): 15/test station (individual crucibles).
  - Number of samples (rotating): 1/test station.
  - Oxygen control system (OCS): Direct injection of O_2/He and H_2/He, H_2/H_2O.
  - Oxygen sensors: 1 in LBE, 1 in gas phase.
  - Heavy liquid metal: LBE/Pb.

Figure 12.3.19: Schematic of rotating electrode system and photograph of various components of the system

Facility: Mechanical Properties in Liquid Metals

University of Lille – UMR CNRS 8517, France (Figure 12.3.20)

- Objectives:
  - Determination of mechanical behaviour and mechanical resistance of structural metallic alloys in liquid metals.
  - Monotonic tensile behaviour:
    - Standard tensile test (STT) using cylindrical specimen.
    - Small punch test (SPT) using 9 mm diameter, 0.5 mm thickness disk.
  - Cyclic behaviour:
    - Low cycle fatigue (LCF) on smooth specimen.
    - Fatigue crack growth gate (FCGR) on notched specimen.
- Operational parameters:
  - Maximum temperature: 350°C for LCF, FCGR and SPT, 600°C for STT.
  - Maximum flow rate: Static.
  - Oxygen control system (OCS): No.
  - Heavy liquid metals: Pb, Bi, Sn,…
  - Machine for STT and SPT: 20 kN load capacity strain rate 10^{-2} to 10^{-5} s^{-1}.
  - Machine for LCF: 100 kN load capacity – strain control, strain range $\Delta\varepsilon_t$: $0.5 \cdot 10^{-2}$ to $2.5 \cdot 10^{-2}$ strain rate 10^{-2} to 10^{-4} s^{-1}.
  - Machine for FCGR: 100 kN load capacity – load control, four-point bending specimen frequency 15 Hz maxi COD measurement.

Figure 12.3.20: Photo of fatigue propagation set-up

Facility: Lead-Bismuth Corrosion Test Loop

Research Laboratory for Nuclear Reactors, Tokyo Institute of Technology, Japan (Figure 12.3.21)

- Objectives:
  - Material corrosion in flowing LBE.
  - Oxygen control technique.
  - Performance of oxygen sensor.
  - Performance of electromagnetic flow meter.
  - Performance of ultrasonic flow meter.
- Operational parameters:
  - Maximum temperature: 550°C.
  - Maximum system pressure: 0.4 MPa.
  - Maximum flow rate: 0.36 m^3/h.
  - Maximum electrical power: 22 kW.
  - Number of test sections: 1.
  - Maximum test section height: 1.5 m.
  - Oxygen control system (OCS): Yes (PbO tablets).
  - Heavy liquid metal: Pb-Bi eutectic.
  - LBE inventory: 450 kg.

Figure 12.3.21: Flow diagram and photo of the Lead-Bismuth Corrosion Test Loop at TIT

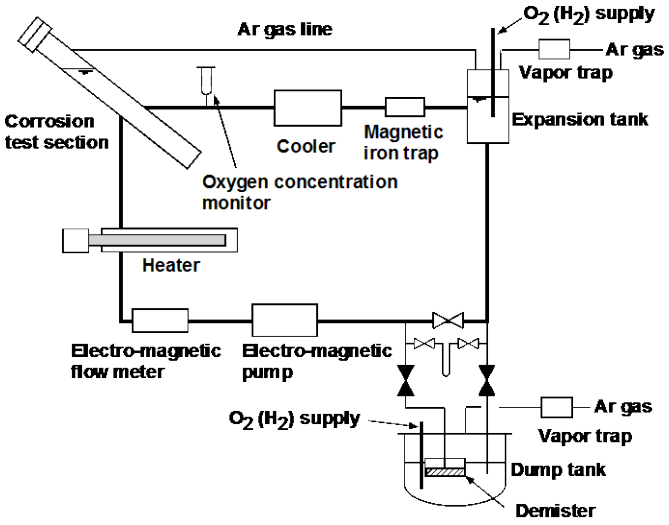

Facility: Liquid Metal Test Station 1 (LIMETS 1)

SCK•CEN, Belgium (Figure 12.3.22)

In operation: August 2004.

- Objectives:
  - Mechanical testing of materials in order to investigate mechanisms and kinetics of material/liquid metal interactions influencing mechanical material properties.
  - Tensile tests of structural materials in stagnant LBE.
  - Fracture toughness tests of structural materials in stagnant LBE.
  - Slow strain rate tests.
  - Crack growth rate.
  - Constant load tests.
- Operational parameters:

- Maximum temperature: 550°C.
- Minimum temperature: Room temperature.
- Oxygen control: Gas flow.
- Oxygen sensors: Bi/BiO_2 sensors; 2 in dump tank, 2 in autoclave.
- Heavy liquid metal: LBE.
- Load capacity 20 kN.
- Displacement rates: $3{\cdot}10^{-6}$-$9{\cdot}10^{-2}$ mm/s.
- Conditioning gases: Ar, Ar+5% H_2, Ar+20% H_2.

Figure 12.3.22: Photo of the LIMETS 1 facility

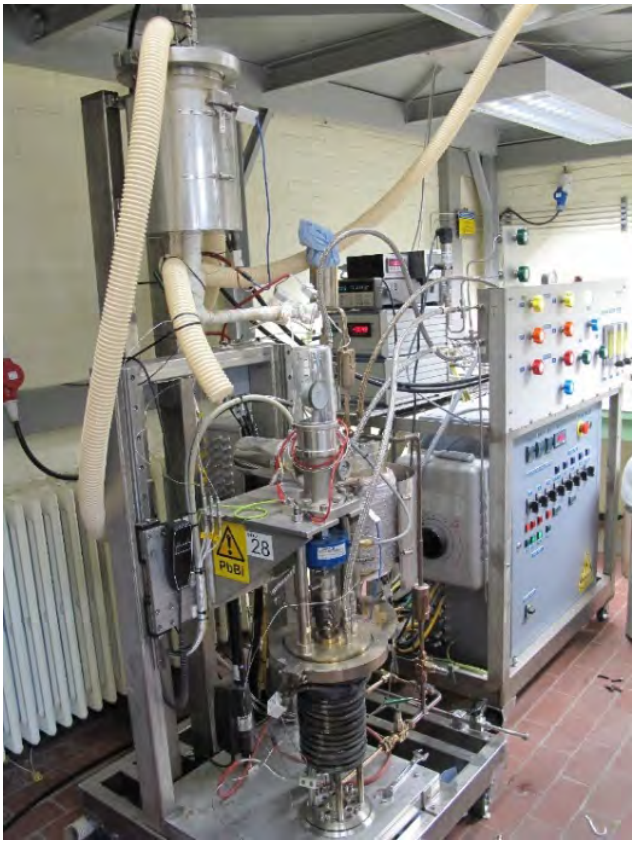

Facility: Liquid Metal Test Station 2 (LIMETS 2)

SCK•CEN, Belgium (Figure 12.3.23)

- Objectives:
  - Mechanical testing of irradiated materials in order to investigate mechanisms and kinetics of material/liquid metal interactions influencing mechanical material properties.
  - Tensile tests of structural materials in stagnant LBE.
  - Fracture toughness tests of structural materials in stagnant LBE.

  - Slow strain rate tests.
  - Crack growth rate.
  - Constant load tests.
- Operational parameters:
  - Maximum temperature: 550°C.
  - Minimum temperature: Room temperature.
  - Oxygen control: Gas flow.
  - Oxygen sensors: Bi/BiO_2 sensors; 2 in dump tank, 2 in autoclave.
  - Heavy liquid metal: LBE.
  - Load capacity: 20 kN.
  - Displacement rates: $9{\cdot}10^{-6}$-$3{\cdot}10^{-2}$ mm/s.
  - Conditioning gases: Ar, Ar+5% H_2, Ar+20% H_2.

Figure 12.3.23: Schematic of LIMETS 2

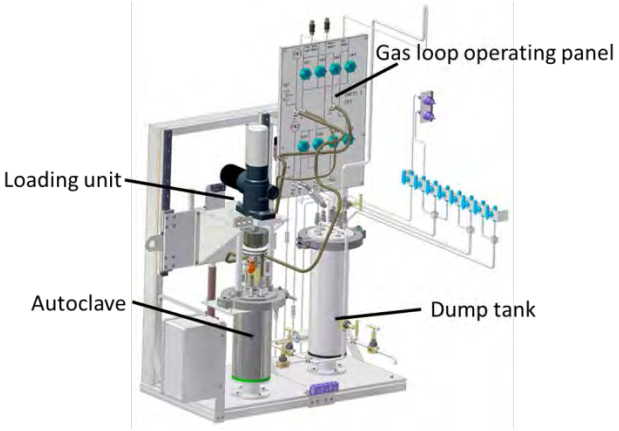

Facility: Liquid Metal Test Station 3 (LIMETS 3)

SCK•CEN, Belgium (Figures 12.3.24[a] and 12.3.24[b])

- Objectives:
  - Fatigue testing of materials in order to investigate mechanisms and kinetics of material/liquid metal interactions influencing mechanical material properties.
  - Fatigue tests in LBE with extensometer on the sample.
  - Tensile/compression tests in LBE with extensometer on the sample.
- Operational parameters:
  - Maximum temperature: 500°C.
  - Minimum temperature: Room temperature.
  - Oxygen control: Via gas flow.
  - Oxygen sensors: Bi/iO_2 oxygen sensors; 2 in dump tank, 2 in autoclave.

- Heavy liquid metal: LBE.
- Load capacity: 15 kN.
- Frequency: ~0.3 Hz
- Conditioning gas: Ar, Ar+5% H_2, Ar+20% H_2.

Figure 12.3.24(a): Schematic of LIMETS 3

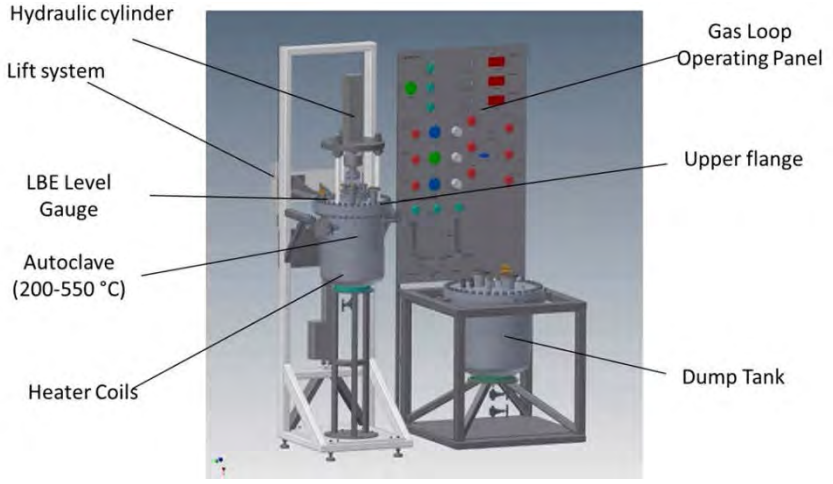

Figure 12.3.24(b): Photo of LIMETS 3

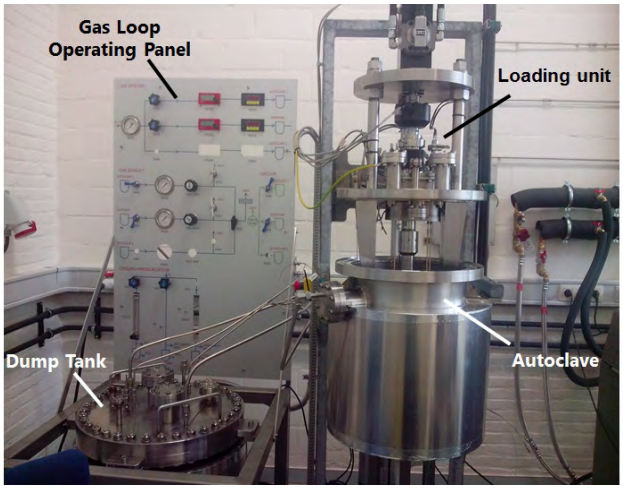

Facility: Liquid Metal Test Station 4 (LIMETS 4)

SCK•CEN, Belgium (Figure 12.3.25)

- Objectives:
  - Mechanical testing of materials to investigate mechanisms and kinetics of material/liquid metal interactions influencing mechanical material properties.
  - Tensile tests of structural materials in stagnant LBE.
  - Fracture toughness tests of structural materials in stagnant LBE.

  - Slow strain rate tests.
  - Crack growth rate.
  - Constant load tests.
- Operational parameters:
  - Maximum temperature: 550°C.
  - Minimum temperature: Room temperature.
  - Oxygen control: Via gas flow.
  - Oxygen sensors: Bi/BiO_2 oxygen sensors; 2 in dump tank, 2 in autoclave.
  - Heavy liquid metal: LBE.
  - Load capacity: 25 kN.
  - Displacement rates: $1.9 \cdot 10^{-6}$-$1.3 \cdot 10^{-1}$ mm/s.
  - Conditioning gases: Ar, Ar+5% H_2, Ar+20% H_2.

Figure 12.3.25: Scheme and photo of LIMETS 4

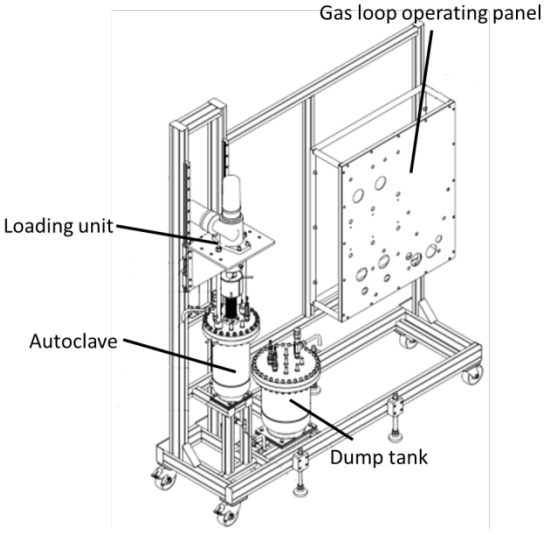

Facility: Corrosion Research for Advanced Fast Reactor Technology (CRAFT)

SCK•CEN, Belgium (Figures 12.3.26[a] and 12.3.26[b])

Planned operation: September 2013

- Objectives:
  - Long-term corrosion investigations of structural materials in flowing LBE.
  - Long-term corrosion investigations of coated materials in flowing LBE.
  - Investigations on the mechanisms and the kinetics of material/LBE interactions.
  - Modelling of corrosion/precipitation behaviour in LBE.
  - Investigations on the applicability of gas – liquid-based oxygen control system (OCS) in large LBE loops.
  - Long-term testing of oxygen sensors in LBE as part of the OCS.
- Operational parameters:
  - Maximum temperature: 550°C.
  - Minimum temperature: 250°C.
  - Maximum (typical) flow rate: 5 (2) m/s.
  - Electrical power: 180 kW.
  - Number of test sections: 2.
  - Number of samples: Ca. 32.
  - Oxygen control system (OCS): Via gas phase.
  - Oxygen sensors: 3 in cold leg, 9 in hot leg, 1 in gas phase.
  - Heavy liquid metal: LBE.

Figure 12.3.26(a): Flow scheme of CRAFT

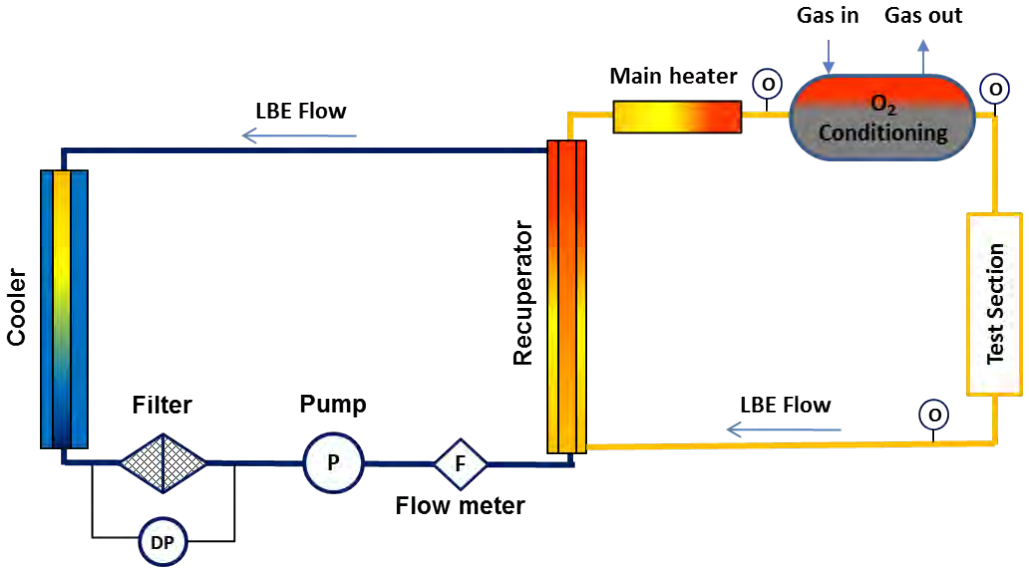

Figure 12.3.26(b): Photo of CRAFT

12.4 Thermal-hydraulics facilities and their applications

Thermal-hydraulics facilities are aimed at the study of basic phenomena as well as the execution of integral tests. Basic phenomena e.g. turbulent heat transfer, free surface flow and two-phase flows can be studied by performing experiments with simple geometries. In addition, a very challenging activity is the execution of design-oriented experiments, for instance experiments devoted to the characterisation of a spallation target or a fuel bundle. Integral tests are related to e.g. the investigation of functionalities of different types of decay heat removal systems in pool type configuration. experimental activities are normally prepared with the help of computational analysis (CFD calculations) in the case of basic phenomena as well as with the help of system codes for integral tests. One important aim of thermal-hydraulics experiments is to improve physical models and validate codes. The importance of these activities can be recognised by the fact that these codes are regularly used for the design layout of an HLM system.

Facility: Thermal-Hydraulics and ADS Design (THEADES)

KIT, Germany (Figure 12.4.1)

- Objectives:
  - Thermal-hydraulic single-effect investigations of ADS components.
  - Cooling of the beam window.
  - Flow field of a windowless target configuration.
  - Cooling of fuel element(s).
  - Heat transfer characteristics of an LBE/LBE heat exchanger.

  - Heat transfer characteristics of a steam generator.
  - Heat transfer characteristics of an LBE/air heat exchanger.
  - Set-up of thermal-hydraulic database for physical model and code validation.
- Operational parameters:
  - Maximum temperature: 450°C.
  - Maximum flow rate: 100 m³/h at 4.5 m NPSH.
  - Maximum electrical power: 4 MW.
  - Number of test sections: 4.
  - Maximum test section height: 3.4 m.
  - Oxygen control system (OCS): Yes.
  - Heavy liquid metal: LBE.

Figure 12.4.1: Scheme and photo of THEADES

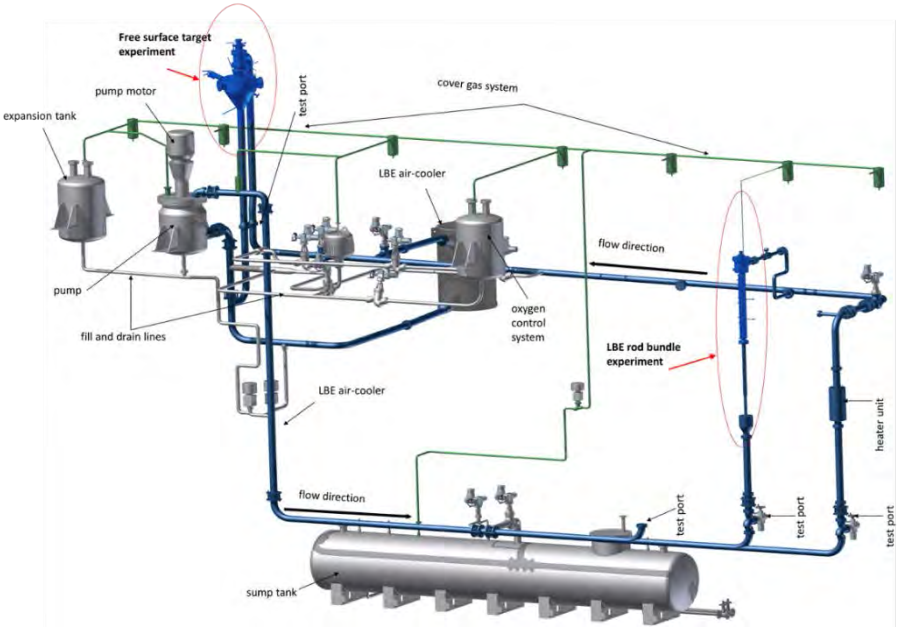

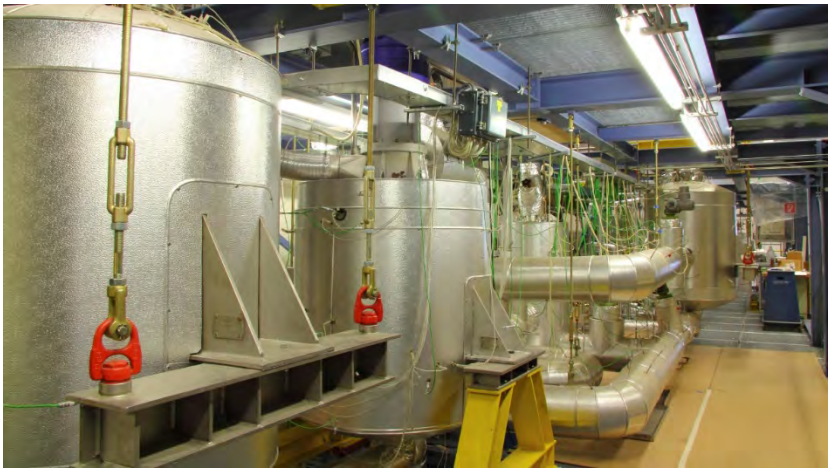

Facility: Circolazione Eutettico (CIRCE)

ENEA, Italy (Figures 12.4.2[a] and 12.4.2[b])

- Objectives:
  - Thermal-hydraulic experiments.
  - Component development.
  - Large scale experiments in pool configuration.
  - Liquid metal chemistry in pool configuration.
- Operational parameters:
  - Maximum temperature: 450°C.
  - Volume test section: 9 480 l.
  - Volume storage tank: 9 250 l.
  - Volume pumping tank: 924 l.
  - Oxygen meter: No.
  - Oxygen control: Yes (controlling the cover gas).
  - Heavy liquid metal: LBE.

Figure 12.4.2(a): Schematic of CIRCE

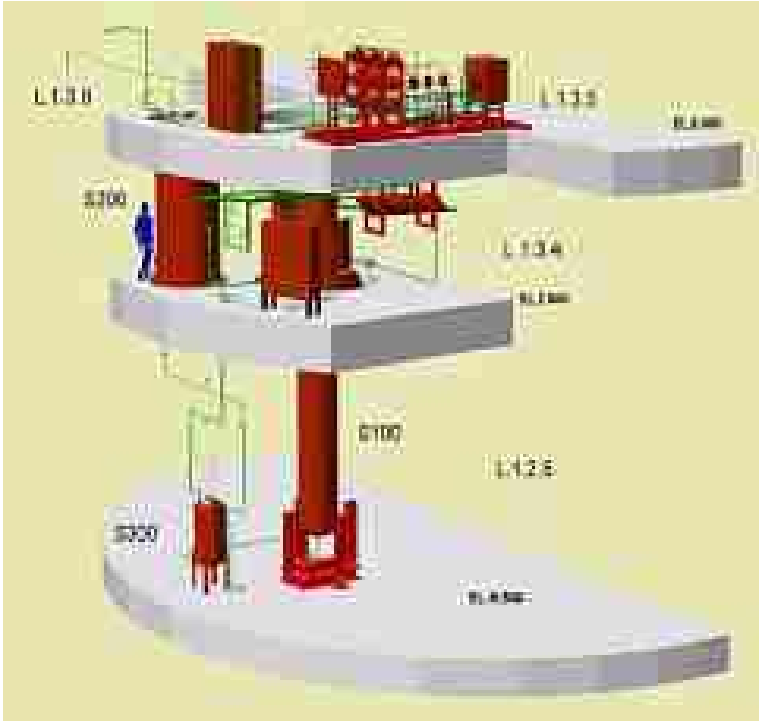

Figure 12.4.2(b): Photo of CIRCE

Facility: Heavy Liquid Metal Experimental Loop for Advanced Nuclear Applications (HELENA)

ENEA, Italy (Figure 12.4.3)

- Objectives:
  - Investigate the thermal-hydraulic behaviour of heavy liquid metal coolant (i.e. heat exchange under forced convection).
  - Characterise structural material when working in lead (i.e. AISI 316L, T91, 15-15 Ti, 14 Cr-ODS, 9 Cr-ODS, coated steels).
  - Qualify prototypical components (i.e. centrifugal pump with MAXTHAL impeller, prototypical ball valve).
  - Develop and test suitable instrumentations for HLM applications (i.e. OCS).
  - Support the CFD and system code validation when employed in a lead-cooled system.
- Operational parameters:
  - Working fluid: Pure lead.
  - Design pressure/temperature: 10 bar/500°C.
  - Circulation pump: Centrifugal with coated impeller.
  - Pump performance (BEP): 35 kg/s, 3.5 bar.
  - Piping material: AISI 316L (2.5" – extra strong).
  - Power heating section: 250 kW.
  - Main length/height: 8 000/4 000 mm.

  - Lead inventory: 1.6 tonnes.
  - Heat exchanger: Tube in tube doubled wall, counter flow type.
  - Secondary fluid: Pressurised water (100 bar).
- International contacts:
  - EU Projects: LEADER, MATISSE.
  - Programme agreement (ADP) between MSE and ENEA.
- Additional information:
  - www.brasimone.enea.it.

Figure 12.4.3: Flow scheme and photo of HELENA

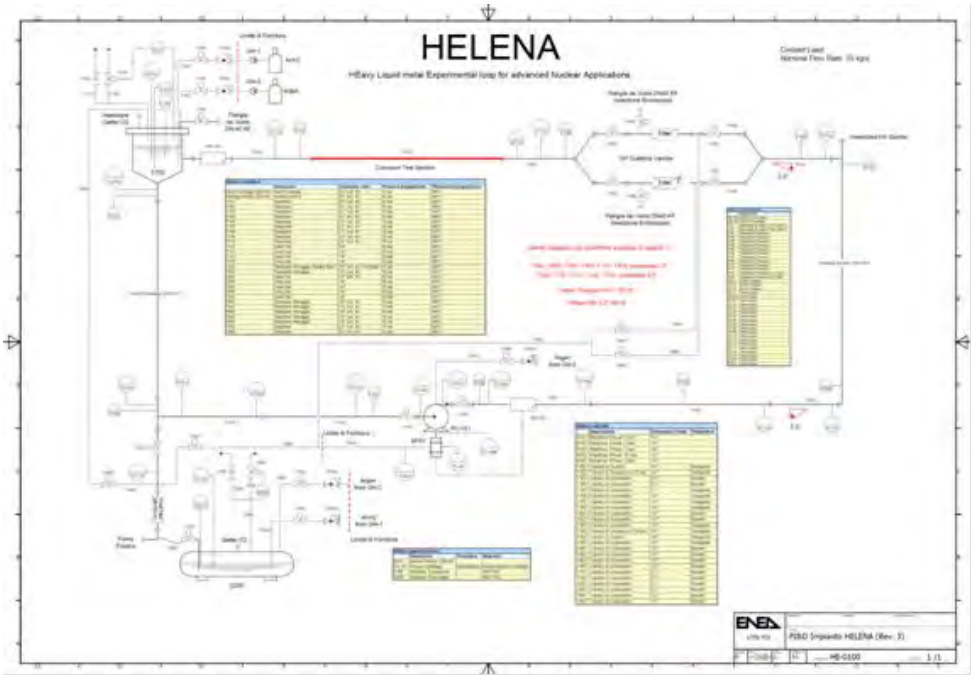

Facility: Thermal-Hydraulic ADS Lead-Bismuth Loop (TALL)

KTH, Sweden (Figures 12.4.4[a] and 12.4.4[b])

- Objectives:
  - To perform medium-scale heat transfer experiments of TECLA on different heat exchangers.
  - Investigation on LBE flow and heat transfer with prototypic thermal-hydraulic conditions (as in conceptual ADS design).
  - Thermal-hydraulic characteristics of natural and forced circulation under steady and transient conditions.
  - To perform tests representative of accident scenarios and to strengthen the database for code validation in support of the EU's PDS-XADS project.
  - Set-up of thermal-hydraulic database for physical model and code validation.
- Operational parameters:
  - Maximum temperature: 500°C.
  - Maximum flow rate: 2.5 m³/h.
  - Maximum electrical power: 55 kW.
  - Electromagnetic pump: 5.5 kW.
  - Maximum test section height: 6.8 m.
  - Oxygen control system (OCS): No.
  - Oxygen control sensors: Yes.
  - Heavy liquid metal: LBE.
  - Secondary loop coolant: Glycerol.

Figure 12.4.4(a): Schematic and photo of TALL

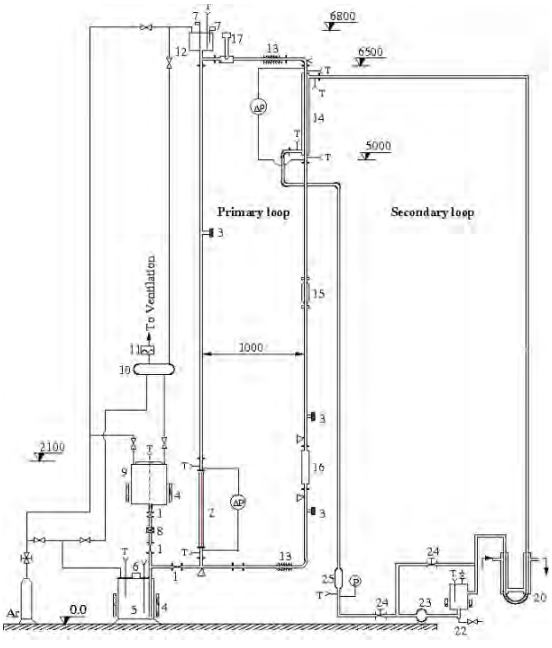

Figure 12.4.4(b): Photo of TALL

Facility: JAEA Lead-Bismuth Flow Loop (JLBL-2)

JAEA, Japan (Figure 12.4.5)

- Objectives:
  - Flow study in horizontal LBE target.
  - Proof test of I-target.
- Operational parameters:
  - Maximum temperature: <450°C.
  - Maximum pressure: 2 bar.
  - Maximum flow rate: 50 L/min.
  - Maximum electrical power: 5 kW heaters.
  - Number of test sections: None.
  - Oxygen control system (OCS): No.
  - Heavy liquid metal: LBE.

Figure 12.4.5: Schematic and photo of JLBL-2

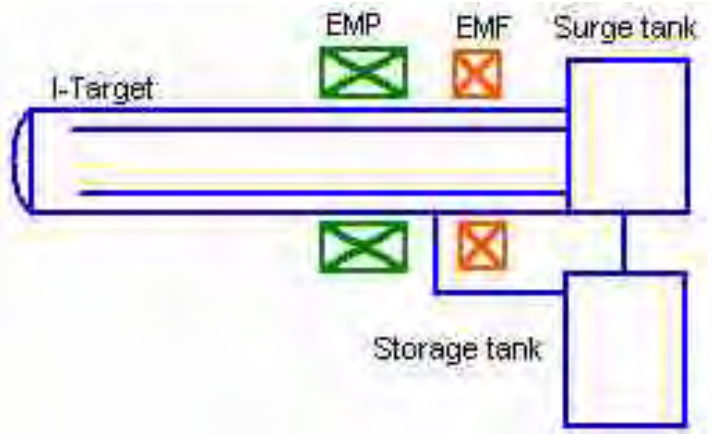

Facility: JAEA Lead-Bismuth Flow Loop-3 (JLBL-3)

JAEA, Japan (Figure 12.4.6)

- Objectives:
  - Thermal fluid test of beam window.
  - Proof test of mechanical pump and massive LBE flow.
- Operational parameters:
  - Maximum temperature: 450°C.
  - Maximum pressure: 7 bar.
  - Maximum flow rate: 500 L/min.
  - Maximum electrical power: 6 kW heaters.
  - Number of test sections: 1.
  - Oxygen control system (OCS): Yes
  - Heavy liquid metal: LBE.
  - Total inventory: 450 litres.

Figure 12.4.6: Flow diagram and photo of JBL3 loop

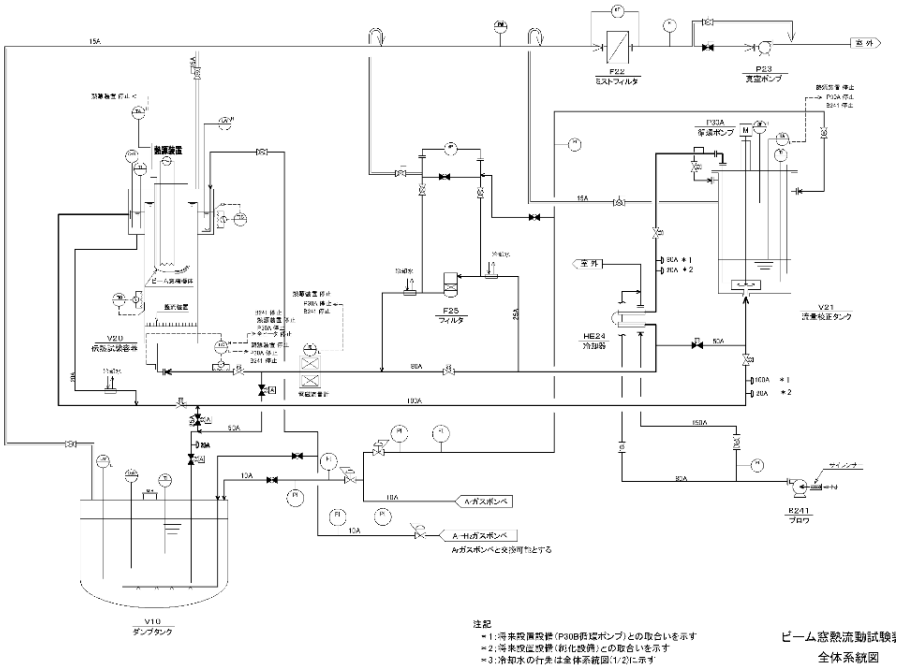

Facility: Wisconsin Tantalus Facility

UW, United States (Figure 12.4.7)

- Objectives:
  - Multi-phase flow, heat transfer and flow stability/oscillations of steam/water injection into liquid metal.
- Operational parameters:
  - Maximum temperature: 550°C.
  - Minimum temperature: 400°C.
  - Maximum (typical) flow rate: 1-10 gram/sec.

- Electrical power: 30 kW.
- Number of test sections: 2 with multiple injectors.
- Heavy liquid metal: Pb and LBE.

Figure 12.4.7: Schematic and photo of the Wisconsin Tantalus Facility

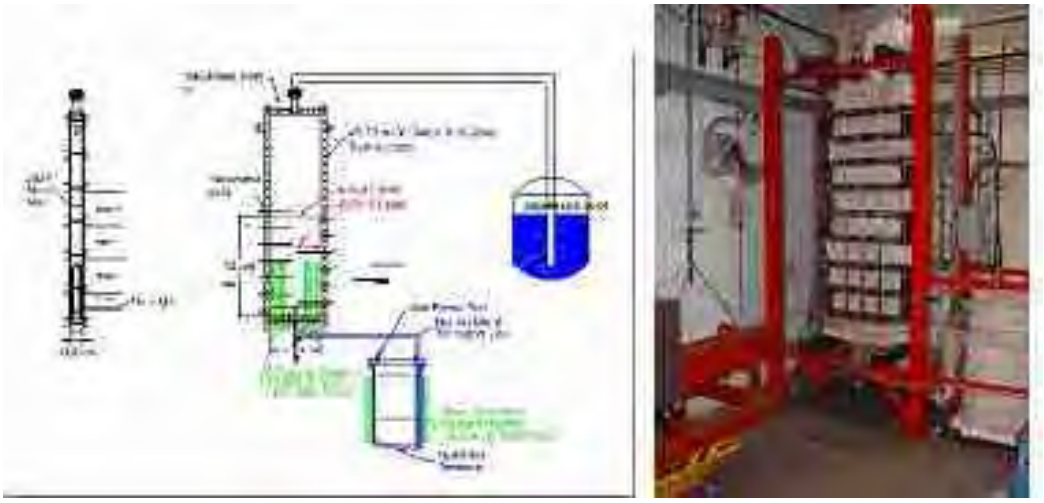

Facility: Heavy Eutectic Liquid Metal Loop for Investigation of Operability and Safety (HELIOS)

Seoul National University (SNU), Korea (Figure 12.4.8)

- Objectives:
  - Verification of operability and safety characteristics of PEACER-300 design with applicability for thermo-hydraulic experiments materials corrosion testing and on-line condition monitoring under either forced or natural circulation mode.
  - HELIOS is going to be completed at the end of 2004. Materials corrosion tests are planned for 2005 and the natural circulation tests for 2006.
- Operational parameters:
  - Features: Ability to test multiple components.
  - Dimensions: 8 feet long, 6 feet tall.
  - Volume loop: 1.5 gal loop, system 6.5 gal.
  - Temperature: 100-650°C.
  - Pressure: 0-55 psi at 250°C, 0-25 psi at 650°C.
  - Flow rate: 0-35 gpm a 250°C.
  - Current test velocity: 0-10 m/s.
  - Oxygen concentrations: <C0 ~ 2 wppm.

Figure 12.4.8: 3-D CAD drawing and front view photograph of HELIOS at Seoul National University, Republic of Korea

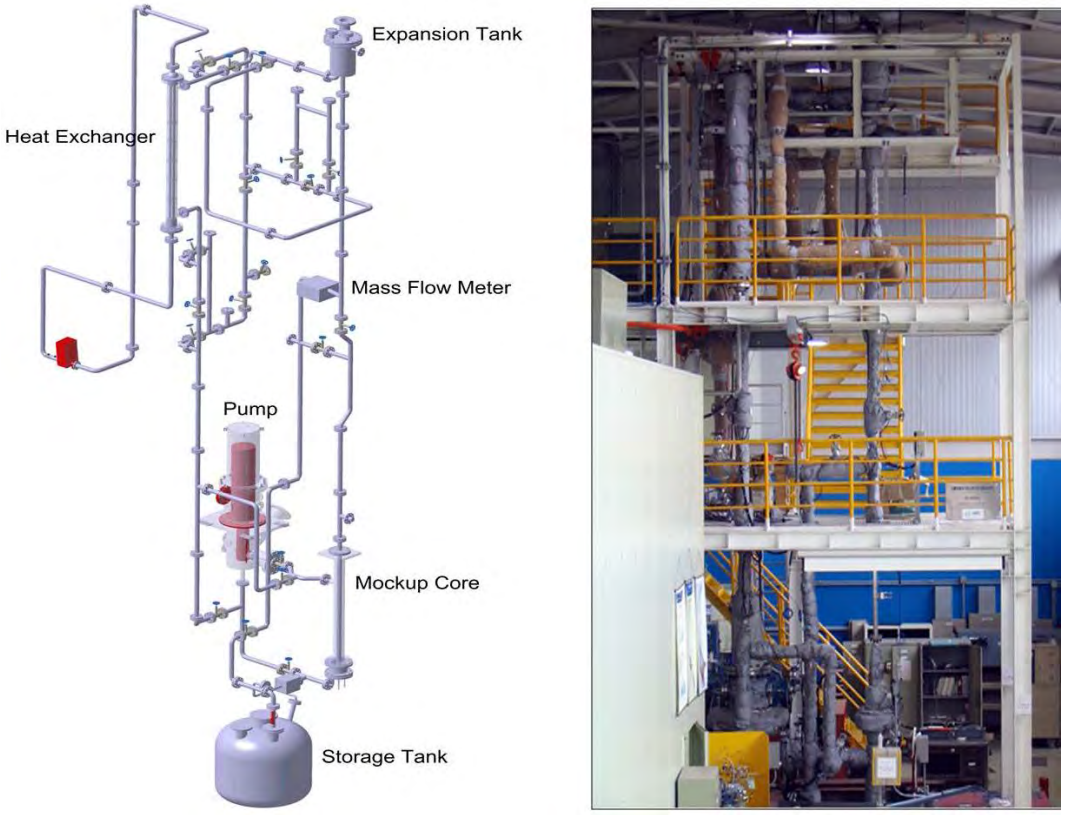

Facility: Lead-Bismuth-Water Direct Contact Boiling Two-Phase Flow Apparatus

Research Laboratory for Nuclear Reactors, Tokyo Institute of Technology, Japan (Figure 12.4.9)

- Objectives:
  - Operation technique of steam gas lift pump-type LBE-cooled fast reactor.
  - Thermal-hydraulics of LBE-water direct contact boiling flow.
- Operational parameters:
  - Maximum LBE temperature: 460°C.
  - Steam temperature: 296°C.
  - System pressure: 7 MPa.
  - LBE flow rate: 33 840 kg/h.
  - Steam-water flow rate: 250 kg/h.
  - Heater bundle power: 133 kW.
  - Number of test sections: 1.
  - Length of test section: 7 m.
  - Oxygen control system (OCS): Yes (hydrogen-dissolved water).

– Heavy liquid metal: LBE.
– LBE inventory: 1 000 kg.
– Water inventory: 50 kg.

Figure 12.4.9: Flow diagram and photo of the Lead-Bismuth-Water Direct Contact Boiling Two-Phase Flow Apparatus at TIT

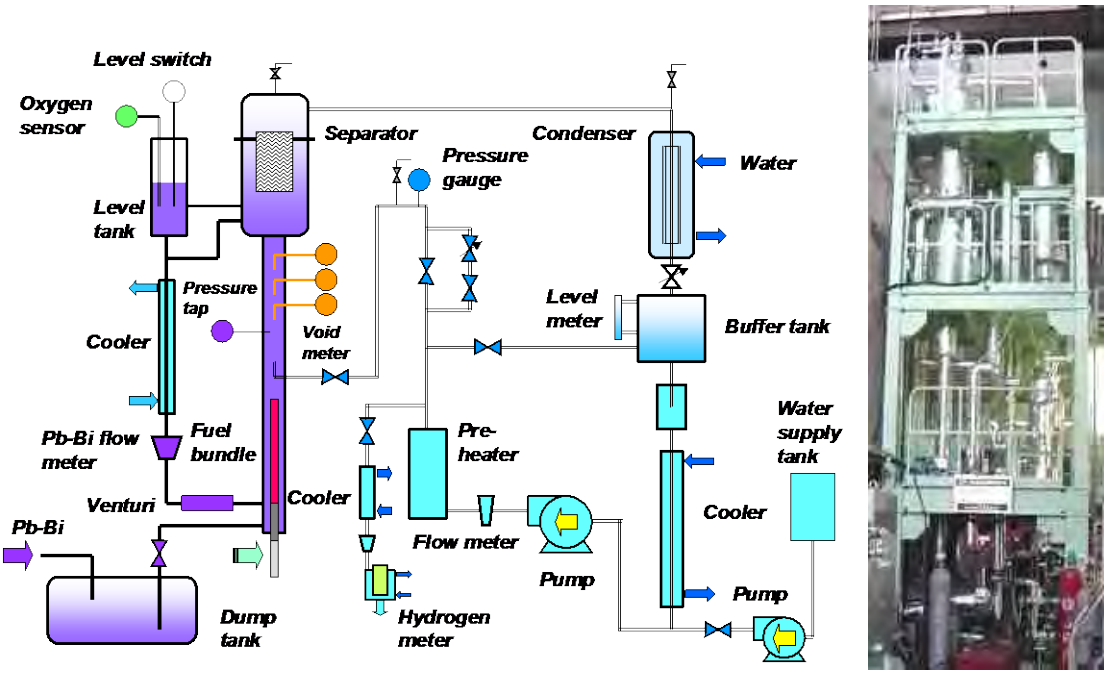

Facility: Lead Loop ELEFANT

HZDR, Germany (Figure 12.4.10)

- Objectives:
  – Thermo-hydraulic studies with pure lead.
  – Long-term tests of electromagnetic pumps.
  – Development and test of instrumentation, e.g. contactless flow rate sensors.
  – Development and test of a well-adjustable heat exchanger with an intermediate liquid metal.
  – Use of such a Pb target for a pulsed neutron source. Long-term operational experience with a lead target for such a neutron source.
- Operational parameters:
  – Liquid metal: Pb.
  – Lead inventory: 10 litres.
  – Maximum temperature: 550°C.
  – Maximum pressure: 6 bar.
  – Maximum flow rate: 0.3 l/s.
  – Heat exchanger: Pb – GaInSn – water adjustable within 0…25 kW.

Figure 12.4.10: Photo of ELEFANT

Facility: Component Loop Testing (COMPLOT)

SCK•CEN, Belgium (Figure 12.4.11)

Planned operation: May 2014

- Objectives:
  - Investigations on hydraulics and hydrodynamics of MYRRHA components at full scale: fuel assembly, spallation target, control rod and safety rod.
- Operational parameters:
  - Heavy liquid metal: Lead-bismuth eutectic (LBE).
  - Maximum temperature: 400°C.
  - Minimum temperature: 150°C.
  - Oxygen control system: Via H_2/H_2O ratio in gas phase.
  - LBE volume: 770 l.
  - Flow rate: 1.24-36 m³/h.
  - Number of test sections: 2.
  - Instrumentation: Flow and velocity measurements, static and dynamic pressure measurements, vibration analysis, temperature measurements.

Figure 12.4.11: Schematic of COMPLOT

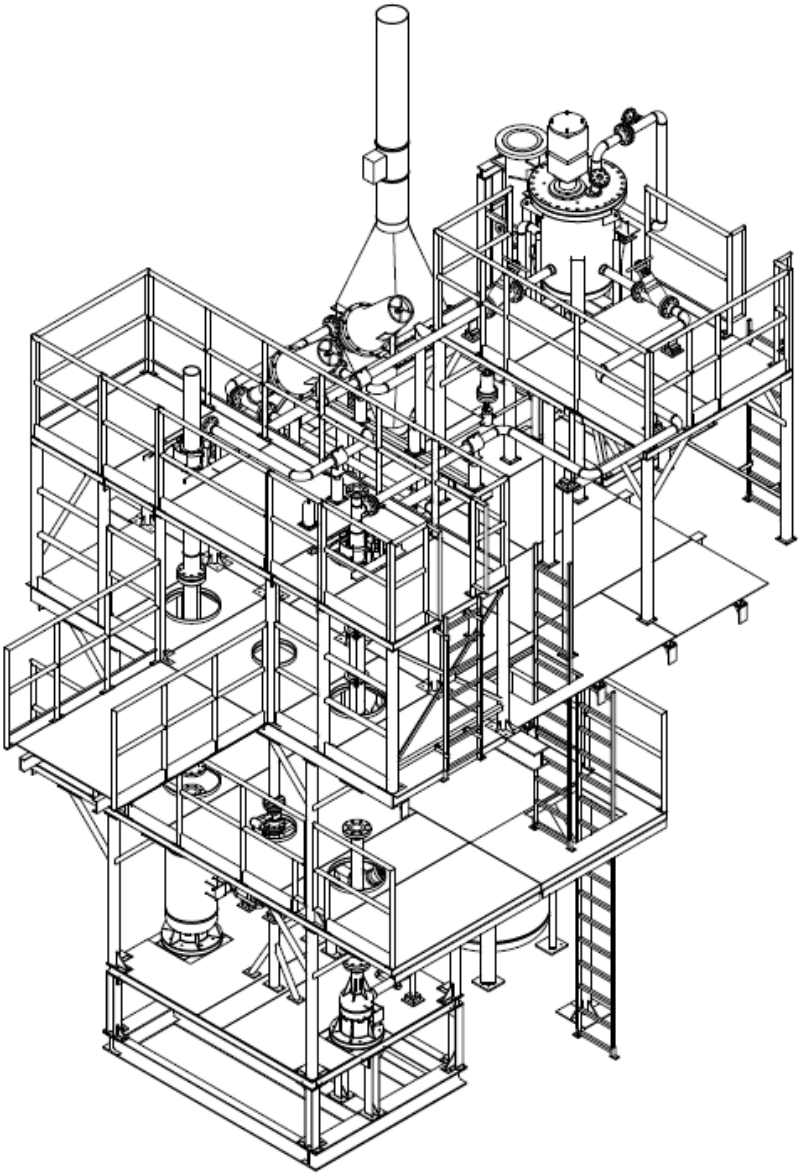

Facility: European Scaled Pool Experiment (E-SCAPE)

SCK•CEN, Belgium (Figure 12.4.12)

Planned operation: May 2014

- Objectives:
  - Investigations on liquid-metal pool thermal-hydraulics.
  - Tests on integral system behaviour.
  - Flow distribution.
  - Decay heat removal.

  - Tests on separate thermal-hydraulic phenomena.
  - Mixing and stratification.
  - Free surface oscillation.
- Operational parameters:
  - Heavy liquid metal: Lead-bismuth eutectic (LBE).
  - Maximum temperature: 350°C.
  - Minimum temperature: 200°C.
  - LBE volume: 2 500 l.
  - Flow rate: 0.8-40 m³/h.
  - Core simulator power: 100 kW.
  - Instrumentation: Flow and velocity measurements, pressure measurements, temperature measurements.

Figure 12.4.12: Schematic of E-SCAPE

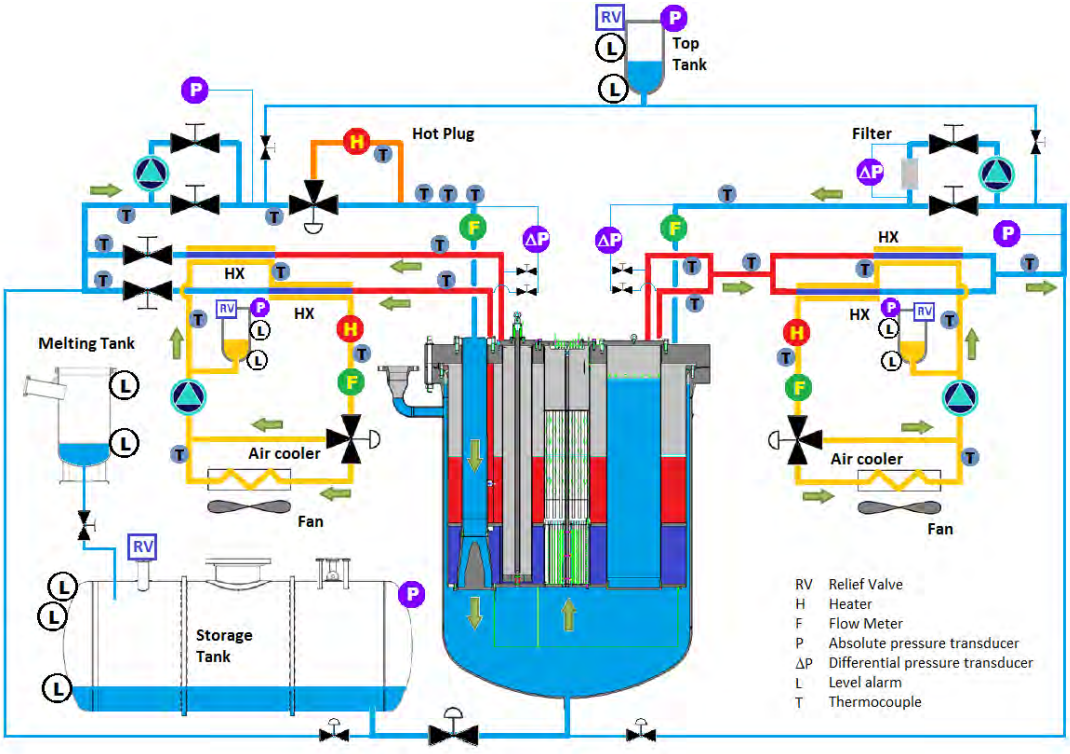

Table 12.4.1: Summary of the international heavy liquid metal test facilities

Association/ country	Name of facility	Type of facility	Objectives	OCS – O_2 probe	Tmax	Flow rate	Other information	CP*
Technological facilities								
KIT/D	THESYS	Loop	Development and testing of measurement techniques.	H_2/H_2O – yes	550°C	3.5 m^3/h	Heated pipe experiment . Heated rod experiment.	1
KIT/D	KOCOS	Loop	OCS development.	H_2/H_2O – yes	550°C		Diffusion coefficient measurement of oxygen in LBE.	3
ENEA/I	LIFUS 5	Static	Interaction HLM with water and simulate LOCA.	No	500°C	–	Facility relevant for safety-related experiments.	19
CEA/F	SOLDIF	Static	Solubilities, diffusivities, oxide layer characterisation.	? – yes	500°C	–		20
SCK•CEN/ BE	MEXICO	Loop	Investigations on the applicability of solid (PbO) OCS in large LBE loops, long-term testing of oxygen sensors in LBE as part of the OCS, oxygen mass transfer modelling and monitoring, particle filter testing, cold trap testing.	PbO – yes	500°C	1.8 l/s		4
SCK•CEN/ BE	HELIOS-3	Static	Investigations on the optimisation of LBE oxygen reduction, investigations on the feasibility of gas recycling, investigations on calamity recovery, component testing.	H_2/H_2O – yes	450°C	–		4
SCK•CEN/ BE	Liliputter	Loop	Investigations on filtration, investigations on mass transfer of impurities, component testing.	No – yes	450°C	0.5 l/s		4
SCK•CEN/ BE	RHAPTER	Pool	Investigations on moving mechanical components for robotics in LBE.	H_2/H_2O – yes	450°C		Instrumentation: torque sensor, position encoder, accelerometer, thermocouples, pressure gauges.	4
LANL-UNLV/ USA	LCS	Loop	Transfer and extend LBE technology to higher-temperature Pb.	Yes	700°C	0.25 m/s	ODS steel (MA956) construction.	6

See notes on page 901.

Table 12.4.1: Summary of the international heavy liquid metal test facilities (*cont.*)

Association/ country	Name of facility	Type of facility	Objectives	OCS – O_2 probe	Tmax	Flow rate	Other information	CP*
Technological facilities								
UNLV/USA	TC-1	Target	Long-term sustained operation of MHD pump for LBE loop; examine long-term performance of target systems under non-irradiation.	–	TBD (300°C at pump inlet)	TBD (15 m^3/h)		12
JAEA/JP	JLBL-1	Loop	Corrosion studies and development of flow measurement techniques.	H_2/H_2O	450°C	18 l/min	Two test sections.	9
TIT/JP	Steam injection and OCC	Apparat.	Oxygen sensor, oxygen potentials in LBE, LBE mist and impurities into steam flow, dissolved H_2 in steam and water chemistry and transport of metal elements in LBE.	H_2/H_2O – yes sensor	500°C			18
KIT/D	COSTA	Static	Corrosion mechanism investigation in controlled conditions.	H_2/H_2O – in the gas phase	1 000°C	–	200 specimens at 5 different T and 10 different O_2 activities in one run.	3
KIT/D	CORRIDA	Loop	Corrosion rate in controlled atmosphere.	H_2/H_2O – yes	550°C	2-4 m/s	Modelling of corrosion precipitation behaviour.	2
KIT/D	TELEMAT	Loop	High temperature corrosion in Pb.	H_2/H_2O – yes	700°C	2 m/s	Modelling of corrosion precipitation at high temperature.	1
KIT/D	CRISLA	Static	Creep-F-rupture in Pb and LBE.	H_2/H_2O – yes	650°C	–	Effect of oxide are also tested.	2
KIT/D	CORELLA	Dynamic	Corrosion on rotating samples.	H_2/H_2O – yes	650°C	1 200 rpm = 20m/s	Test on pump materials.	3
KIT/D	FRETHME	Dynamic	Fretting test in HLM.	H_2/H_2O – yes	650°C	–	Max. load: 500 N; max. frequency: 40 Hz.	3
ENEA/I	LECOR	Loop	Corrosion at low oxygen content, physico-chemistry, component testing.	H_2/O_2 – yes	500°C	4.5 m^3/h	Three test sections.	19
LANL-UNLV/ USA	LCS	Loop	Transfer and extend LBE technology to higher temperature Pb, corrosion tests in flowing Pb.	Yes	700°C	0.25 m/s	ODS steel (MA956) construction.	6
CEA/F	LEOX	Static	Effect of oxygen content on the corrosion mechanism.	Yes	600°C		Development of corrosion mechanism.	20

See notes on page 901.

Table 12.4.1: Summary of the international heavy liquid metal test facilities (*cont.*)

Association/ country	Name of facility	Type of facility	Objectives	OCS – O_2 probe	Tmax	Flow rate	Other information	CP*
Technological facilities								
CEA/F	COLIMESTA	Static	Effect of oxygen content on the corrosion mechanism.	H_2/H_2O – yes	600°C		Development of corrosion mechanism.	20
CEA/F	CICLAD	Rotating cylinder	Hydrodynamic effect on corrosion rate.	H_2/H_2O – yes	600°C	5 m/s	Development of corrosion mechanism.	20
CIEMAT/ES	FELIX	Static	Materials testing.	H_2/H_2O	600°C	–	Furnaces with controlled atmosphere.	5
CIEMAT/ES	LINCE	Loop	Long-term corrosion experiments and oxygen control system analysis.	Yes	500°C	2.5 m^3/h	LBE inventory 170 l, electrical power 80 kW.	5
JAEA/JP	JLBS	Static	Compatibility of materials.	OCS partially	600°C	–		7
JAEA/JP	JLBL-1	Loop	Corrosion studies and development of flow measurement techniques.	H_2/H_2O	450°C	18 l/min	Two test sections.	9
KAERI/KR	KPAL-1	Loop	OCS, corrosion, thermal-hydraulics.	Yes OCS, yes sensor	550°C	3.6 m^3/h		10
SNU/KR	HELIOS	Loop	OCS, materials and thermal-hydraulics (natural circulation capabilities in PEACER-300).	Yes OCS	450°C	200 cm/s	HELIOS has been designed by thermo-hydraulics scaling of PEACER-300.	16
REZ/CZ	COLONRI I	Loop	Corrosion in different conditions.	OCS indirectly	700°C	1-2 cm/s		11
ANL/USA	Natural Convection Quartz Harp	Loop	Long-term corrosion in Pb/LBE; thermo-mechanical behaviour between materials and Pb/LBE.	H_2/H_2O	800°C	0.01 m/s		13
MIT/US	H.H. Uhlig Corrosion Lab	Static/ rotating disc	Corrosion mechanism, benchmarking corrosion/precipitation; oxygen sensors.	O_2/He; H_2/He; H_2/H_2O	800°C	0-3 m/s	The liquid metal is contained in a ZrO_2 crucible, capability of the crucible is 4 L.	14
Univ. LILLE CNRS/F	Mechanical Properties in Liquid Metals	Static	Monotonic and cyclic properties of structural alloys in liquid metals.	OCS	600°C	Static	Purification of LBE by Ar/H; mechanical tests under Ar/H gas and in oxygen saturated or non-saturated LBE.	17

See notes on page 901.

Table 12.4.1: Summary of the international heavy liquid metal test facilities (*cont.*)

Association/ country	Name of facility	Type of facility	Objectives	OCS – O_2 probe	Tmax	Flow rate	Other information	CP*
Technological facilities								
TIT/JP	LBE Corrosion	Loop	Material corrosion in flowing LBE, oxygen control technique, oxygen sensor, electromagnetic flow meter, ultrasonic flow meter.	PbO Yes sensor	550°C	0.36 m^3/h		18
SCK•CEN/B	LIMETS 1	Static	Mechanical testing of materials and in LBE.	Ar/H_2 Yes	500°C	Static		4
SCK•CEN/B	LIMETS 2	Static	Mechanical testing of irradiated materials in LBE.	Ar/H_2	500°C	Static	SSRT, constant and raising load, CGR.	4
SCK•CEN/B	LIMETS 3	Static	Fatigue testing of materials in LBE.	Ar/H_2 Yes	500°C	Static	SSRT, constant and raising load, CGR.	4
SCK•CEN/B	LIMETS 4	Static	Mechanical testing of materials and in LBE.	Ar/H_2 Yes	500°C	Static		4
SCK•CEN/B	CRAFT	Loop	Corrosion rate in controlled atmosphere.	Ar/H_2 Yes	550°C	2-5 m/s	Investigations on the mechanisms and the kinetics of material/LBE interactions, modelling of corrosion/precipitation behaviour in LBE, investigations on the applicability of gas-liquid based OCS in large LBE loops, long-term testing of oxygen sensors in LBE as part of the OCS.	4
KIT/D	THEADES	Loop	Single effects, beam window, windowless, fuel elements, heat transfer.	H_2/H_2O Yes	450°C	100 m^3/h	Height of the test sections 3.4 m.	1
ENEA/I	CIRCE	Pool	Thermal-hydraulics, component development, large-scale exp. and liquid metal chemistry in pool configuration.	OCS yes No O_2 probe	450°C		8 540 l of LBE.	19
ENEA/I	HELENA	Loop	Thermal-hydraulics investigations and qualification of components and instrumentation.	–	500°C	35 kg/s at 3.5 bar		19

See notes on page 901.

Table 12.4.1: Summary of the international heavy liquid metal test facilities (*cont.*)

Association/ country	Name of facility	Type of facility	Objectives	OCS – O_2 probe	Tmax	Flow rate	Other information	CP*
Technological facilities								
KTH/SE	TALL	Loop	Thermal-hydraulics and heat transfer measurements, natural and forced transient flows, additional third leg with a pool-type test section for thermal stratification and mixing experiments for validation of coupled CFD and system codes.	No OCS	KTH/SE	TALL	Loop	22
JAEA/JP	JLBL-2	Loop	Flow studies in horizontal LBE target.	No	<450°C	50 l/min	Proof test of target – I.	9
JAEA/JP	JLBL-3	Loop	Thermal-fluid test loop.	Yes	450°C	500 l/min	Collaboration with MES.	8
SCK•CEN/B	COMPLOT	Loop	Investigations on hydraulics and hydrodynamics of MYRRHA components at full-scale: fuel assembly, spallation target, control rod and safety rod.	H_2/H_2O – yes	450°C	1.24-36 m³/h		4
SCK•CEN/B	E-SCAPE	Loop/pool	Investigations on liquid-metal pool thermal-hydraulics.	No	350°C	0.8-40 m³/h	Tests on integral system behaviour: flow distribution, decay heat removal. Tests on separate thermal-hydraulic phenomena: mixing and stratification, free surface oscillation.	4
LANL/US	DELTA	Loop	Corrosion tests in flowing LBE, corrosion/ precipitation and system kinetics models, oxygen sensors and control systems, thermal-hydraulics experiments, components testing, data acquisition and control systems.	Yes	550°C	2-5 m/s		6
UW/US	Wisconsin Tantalus facility	Loop	Multi-phase flow, heat transfer and flow stability/oscillations of steam/water injection into Pb/LBE.	–	550°C	1-10 g/sec		15

See notes on page 901.

Table 12.4.1: Summary of the international heavy liquid metal test facilities (*cont.*)

Association/ country	Name of facility	Type of facility	Objectives	OCS – O_2 probe	Tmax	Flow rate	Other information	CP*
Technological facilities								
KAERI/KR	KPAL-1	Loop	OCS, corrosion, thermal-hydraulics.	Yes OCS Yes sensor	550°C	3.6 m^3/h		10
SNU/KR	HELIOS	Loop	OCS, materials and thermal-hydraulics (natural circulation capabilities in PEACER-300).	Yes OCS	450°C	200 cm/s	HELIOS was designed by thermo-hydraulics scaling of PEACER-300.	16
TIT/JP	LBE-H_2O Direct Contact	Appar.	Operation technique of steam gas lift pump type LBE-cooled fast reactor, thermal-hydraulics of LBE-water direct contact boiling flow.		460°C	33.8 kg/h		18
HZDR/D	ELEFANT	Loop	Development and testing of components (EM pump, HX) and instruments as contactless flow meters.	No	550°C	0.3 l/s		21

* CP = Contact persons for the facilities. CP are listed in Table 12.4.2.

OCS – oxygen control system

Table 12.4.2: Contact persons as designated in Table 12.4.1

No.	Name/affiliation	Contact information
1	Professor Thomas Wetzel Institute for Nuclear and Energy Technologies (IKET) KIT	Tel: +49 (0) 721/608 23462 Fax: +49 (0) 721/608 24837 Email: thomas.wetzel@kit.edu
2	Dr. Juergen Konys Institute for Materials Research III (IMF III) KIT	Tel: +49 (0) 721/608 23720 Fax: +49 (0) 721/608 23956 Email: juergen.konys@kit.edu
3	Dr. Georg Müller Institut für Hochleistungsimpuls und Mikrowellentechnik (IHM) KIT	Tel: *49 (0) 721/608 24669 Fax: +49 (0) 721/608 22256 Email: georg.Mueller@kit.edu
4	Ir. Katrien Van Tichelen Head Unit LBE Components and Experiments Institute for Advanced Nuclear Systems SCK•CEN	Tel: +32 (0) 14/33 80 06 Fax: +32 (0) 14/32 13 36 Email: katrien.van.tichelen@sckcen.be
	Dr. Serguei Gavrilov Head Structural Materials Research Unit Institute for Nuclear Materials Science SCK•CEN	Tel: +32 (0) 14/33 30 67 Fax: +32 (0) 14/32 12 16 Email: serguei.gavrilov@sckcen.be
	CC to: Dr. Marc Schyns Head Nuclear Systems Research Institute for Advanced Nuclear Systems SCK•CEN	Tel: +32 (0) 14/33 34 41 Fax: +32 (0) 14/32 13 36 Email: marc.schyns@sckcen.be
	Dr. Paul Schuurmans Reactor Physics and MYRRHA Department SCK•CEN	Tel: +32 (0) 14/33 22 93 Fax: +32 (0) 14/32 15 29 Email: Paul.Schuurmans@sckcen.be

Table 12.4.2: Contact persons as designated in Table 12.4.1 *(cont.)*

No.	Name/affiliation	Contact information
1	Professor Thomas Wetzel Institute for Nuclear and Energy Technologies (IKET) KIT	Tel: +49 (0) 721/608 23462 Fax: +49 (0) 721/608 24837 Email: thomas.wetzel@kit.edu
2	Dr. Juergen Konys Institute for Materials Research III (IMF III) KIT	Tel: +49 (0) 721/608 23720 Fax: +49 (0) 721/608 23956 Email: juergen.konys@kit.edu
3	Dr. Georg Müller Institut für Hochleistungsimpuls und Mikrowellentechnik (IHM) KIT	Tel: *49 (0) 721/608 24669 Fax: +49 (0) 721/608 22256 Email: georg.Mueller@kit.edu
4	Ir. Katrien Van Tichelen Head Unit LBE Components and Experiments Institute for Advanced Nuclear Systems SCK•CEN Dr. Serguei Gavrilov Head Structural Materials Research Unit Institute for Nuclear Materials Science SCK•CEN *CC to:* Dr. Marc Schyns Head Nuclear Systems Research Institute for Advanced Nuclear Systems SCK•CEN Dr. Paul Schuurmans Reactor Physics and MYRRHA Department SCK•CEN	Tel: +32 (0) 14/33 80 06 Fax: +32 (0) 14/32 13 36 Email: katrien.van.tichelen@sckcen.be Tel: +32 (0) 14/33 30 67 Fax: +32 (0) 14/32 12 16 Email: serguei.gavrilov@sckcen.be Tel: +32 (0) 14/33 34 41 Fax: +32 (0) 14/32 13 36 Email: marc.schyns@sckcen.be Tel: +32 (0) 14/33 22 93 Fax: +32 (0) 14/32 15 29 Email: Paul.Schuurmans@sckcen.be
5	Dr. Dolores Gomez-Briceno Materials Project Head CIEMAT	Tel: +34 91 3466605 Fax: +34 91 3466661 Email: lola.gomezbriceno@ciemat.es
6	Dr. Magdalena Serrano de Caro Lead-alloys Technology Development DOE-SMR programme *CC to:* Dr. Keith Woloshun DELTA Loop DOE-SMR programme	Tel: +1 505 665 6680 Fax: +1 505 667 7443 Email: magda@lanl.gov Tel: +1 505 665 6822 Fax: +1 505 667 7443 Email: woloshun@lanl.gov
7	Dr. Yuji Kurata Nuclear Science and Energy Directorate JAEA	Tel: +81 (0) 29/282 5059 Fax: +81 (0) 29/282 6489 Email: kurata.yuji@jaea.go.jp
8	Dr. Shigeru Saito Center for Proton Accelerator Facilities JAEA	Tel: +81 (0) 29/282 5058 Fax: +81 (0) 29/282 6489 Email: saito.shigeru@jaea.go.jp
10	Dr. C.H. Cho HYPER Team KAERI *CC to:* Dr. T.Y. Song HYPER Team KAERI	Tel: +82-42-868-2914 Fax: +82-42-868-2080 Email: chcho@kaeri.re.kr Tel: +82-42-868-8924 Fax: +82-42-868-2080 Email: tysong@kaeri.re.kr

Table 12.4.2: Contact persons as designated in Table 12.4.1 (*cont.*)

No.	Name/affiliation	Contact information
11	Dr. Anna Brožová Div. of Integrity and Technical Engineering Dept. of Structural Properties and Corrosion Řež *CC to:* Dr. Dalibor Kárník Div. of Integrity and Technical Engineering Dept. of Structural Properties and Corrosion Řež	Tel: (+420-2) 6617 3432 Fax: (+420-2) 2094 0519 Email: bro@ujv.cz Tel: (+420-2) 6617 2617 Fax: (+420-2) 2094 0519 Email: kar@ujv.cz
12	Dr. Allen Johnson University of Nevada, Las Vegas	Tel: Fax: Email: allen.johnson@unlv.edu
13	Dr. James Sienicki Argonne National Laboratory Argonne, Illinois 60439	Tel: (+630) 252-4848 Fax: (+630) 252-4780 Email: sienicki@anl.gov
14	Professor Ronald G. Ballinger Dept. of Nuclear Engineering Dept. of Materials Science and Engineering H.H. Uhlig Corrosion Laboratory Massachusetts Institute of Technology	Tel: +1 617·253·5118 Fax: +1 617 253 0807 Email: hvymet@mit.edu
15	Dr. Michael Corradini Engineering Physics University of Wisconsin	Tel: 608-263-1648 Fax: 608-263-7451 Email: Corradini@engr.wisc.edu
16	Professor Il Soon Hwang Nuclear Materials Laboratory Nuclear Engineering Department Seoul National University Director, Nuclear Transmutation Energy Research Center of Korea (NUTRECK)	Tel: +82-2-880-7215 Fax: +82-2-889-2688 Email: hisline@snu.ac.kr
17	Professor Jean-Bernard Vogt Unité Matériaux et Transformations (UMET) Université Lille 1 UMR CNRS 8207 *CC to:* Dr. Ingrid Proriol Serre Unité Matériaux et Transformations (UMET) Université Lille 1 UMR CNRS 8207	Tel: +33 (0)3 20 43 40 35 Fax: +33 (0)3 20 43 40 35 Email: jean-bernard.vogt@univ-lille1.fr Tel: +33 (0)3 20 43 66 06 Fax: Email: ingrid.proriol-serre@univ-lille1.fr
18	Professor Minoru Takahashi Research Laboratory for Nuclear Reactors Tokyo Institute of Technology	Tel: Fax: Email: mtakahas@nr.titech.ac.jp
19	Alessandro Gessi Head of UTIS CPM ENEA CR Brasimone 40032 Camugnano (BO) Italy	Tel: +390534801273 Email: alessandro.gessi@enea.it

Table 12.4.2: Contact persons as designated in Table 12.4.1 (*cont.*)

No.	Name/affiliation	Contact information
20	Laure Martinelli DEN/DPC/SCCME/LECNA CEA *CC* to: Jean-Louis Courouau DEN/DPC/SCCME/LECNA CEA	Tel: +33 (0)1 69 08 16 13 Fax: +33 (0)1 69 08 15 86 Email: laure.martinelli@cea.fr Tel: +33 (0)1 69 08 16 43 Fax: +33 (0)1 69 08 15 86 Email: jean-louis.courouau@cea.fr
21	Dr. Sven Eckert Helmholtz-Zentrum Dresden-Rossendorf (HZDR) Institute of Fluid Dynamics	Tel: +49 351 260-2132 Fax: +49 351 260 1 2007 Email: s.eckert@hzdr.de
22	Professor Sevostian V. Bechta Head of Nuclear Power Safety Division Kungliga Tekniska Högskolan – KTH *CC to:* Dr. Pavel Kudinov Nuclear Power Safety Division Kungliga Tekniska Högskolan – KTH	Tel: +46 8 5537 8225 Fax: +46 8 5537 8830 Email: bechta@kth.se Tel: +46 8 5537 8826 Fax: +46 8 5537 8830 Email: bechta@kth.se

13. Safety guidelines*

Lead is a highly toxic substance (EPA, n.d.a, ILO, n.d.). Exposure to lead can cause irreversible health effects before signs and symptoms are seen or felt (Lewis, 1985). Rules and regulations, safety controls and practices have been developed to mitigate lead hazards over the years. Consequently, many occupational uses of lead now pose little risk of exposure if one takes precautions and follows procedures. However, when lead is used in a manner that is different from routine operations, the risk of exposure may increase. For researchers developing lead-alloy technologies, it is imperative that safety principles be closely observed, proper protective measures taken and formal procedures followed.

In the context of lead-alloy coolant technology, lead oxide hazards may exist as well. Lead oxide exists in one of the two forms: red to reddish-yellow tetragonal crystals stable at room temperature, and yellow orthorhombic crystals stable at above 489°C. Lead oxide presents severe health hazards, especially in the form of lead fumes or dusts, and should be treated with the same caution as with lead.

On the other hand, bismuth does not present severe hazards except under several special circumstances. For example, bismuth dust or powder can be flammable or even explosive at high concentrations and exposed to heat or flame. Generally bismuth may cause mild eye, skin and gastrointestinal irritation. Due to its low hazard ratings, the measures taken to mitigate lead hazards should be sufficient when bismuth is used together with lead. Hence bismuth hazards and controls will not be discussed here.

It is worth noting that safety practices are intrinsically linked to good and meaningful outcomes of experiments and tests, as they ensure proper control of the environment. Some practical implementations of coolant technology, on the other hand, can produce unique hazards if not performed correctly.

This chapter outlines the effects of lead on human health and the environment, the general rules and regulations governing the safe use and disposal of lead in many OECD countries (OSHA, n.d.), some common safety measures and procedures, and recommendations for routine R&D operations illustrated with several typical experiments. It should be used as a starting point to specific information available in the references. The scope is based on a balance between brevity (ease of use) and completeness (usefulness), and is much more extensive than that of the Materials Safety Date Sheets (MSDS). The main text is based on the training manual for lead awareness at Los Alamos National Laboratory (Grogin, 2001), with references on country-specific rules and additional regulations recommended by the expert working group members. A very comprehensive discussion on airborne lead hazards can also be found in a position paper by the EU Working Group on Lead (CEC, 1997). Many other reports have detailed information and analyses on different aspects of lead, waste and the environment (Holm, 2002; WHO, 1989).

It should be pointed out that under proton and neutron irradiation, lead and lead alloys all present varied, sometimes severe, radioactive hazards. These hazards and the conditions leading to their occurrence are complex and often system or alloy specific, e.g. ^{210}Po from irradiated bismuth (Cullen, 2003). They are not covered in this chapter. However, this is an extremely important topic for lead-alloy nuclear coolant application and should warrant a separate and detailed review in the future.

* Chapter lead: N. Li.

13.1 Effects of lead on human health and environment

Lead can enter human body in three different ways: inhalation (breathing), ingestion (eating or drinking), or absorption (through skin).

Figure 13.1.1: Absorption and storage of lead in human body

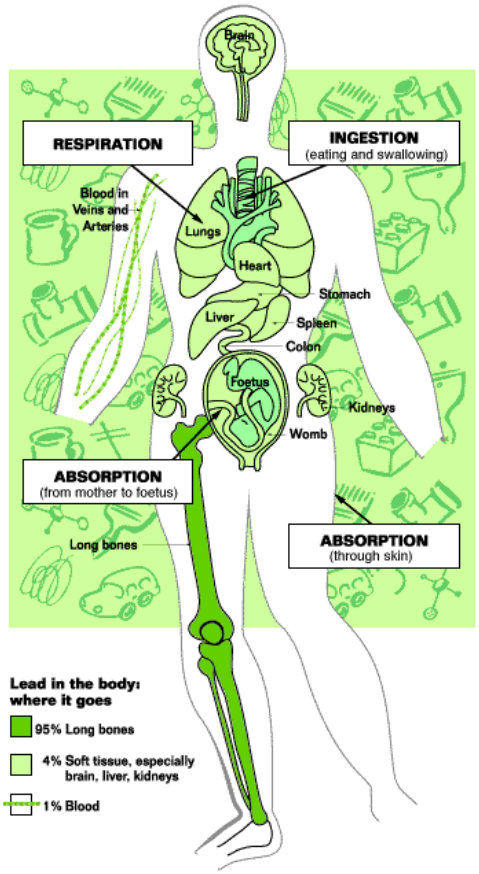

Source: Used with permission of the NSW.

Inhalation of airborne lead is the most common means by which lead can enter a human body in the workplace. Inhalation can occur when lead is scattered in the air as a dust, fume or mist. Inhaling small particles of lead allows the material to travel into the lungs, where it can be absorbed into the bloodstream.

The second most common way is by ingestion (swallowing). Ingestion of lead in the workplace is nearly always the result of poor hygiene practices. Lead can be ingested by handling food, using cigarettes or chewing tobacco, or applying cosmetics when hands are contaminated with lead.

Absorption of lead through the skin is rare, but it can occur if skin is exposed to certain organic forms of lead or if certain chemicals (such as dimethyl sulfoxide) capable of transporting heavy metals through the skin are present.

All of the lead that deposits in lungs and 10-15% of the lead ingested enters the bloodstream. In pregnant women, the amount of lead absorbed into the bloodstream through ingestion can increase to 50%. Once in the bloodstream, lead circulates throughout the body and is excreted at a steady rate. As exposure to lead continues, the amount stored in the body will increase if absorption is more than excretion. Of the total amount

of lead stored in the body, about 90% is found in the bones and teeth. If no further uptake occurs, accumulated lead is slowly released from the blood and soft tissues over a period of months, but is only released from the bones and teeth over a period of decades. If uptake continues, stored lead will eventually reach toxic levels, a condition known as lead intoxication. Accumulated lead can cause irreversible body damage before showing any signs or symptoms.

Exposure to lead through inhalation or ingestion can cause serious health effects in a variety of body systems. Such health effects may arise from acute (short-term) or chronic (long-term) exposures. The severity of an exposure depends upon the amount, or dose, of lead that enters the human body. A short-term, high-dose lead exposure can cause kidney, nerve, and brain damage that may lead to seizures, coma and death within a matter of days. Workplace exposures of this type are extremely rare but not impossible. Signs and symptoms of acute lead exposure are similar to many common ailments and, as a result, may not be immediately recognised. Signs and symptoms of acute lead exposure may include: blood in the urine or stool, paralysis, coughing, restlessness, digestive disorders, skin or eye irritation, disorientation, sleeplessness, drooling, sweating, fever and chills, thirst, frequent urination, tingling sensation, headache, vomiting, loss of memory, weakness, metallic taste, yellowing of the skin and eyes (jaundice) and muscle pain.

There is a condition specific to exposure to lead fumes called metal fume fever. It is an influenza-like illness caused by inhalation of freshly formed metal oxide particles with sizes below 1.5 microns, and usually between 0.02-0.05 microns. Symptoms may be delayed 4-12 hours and begin with a sudden onset of thirst, and a sweet, metallic or foul taste in the mouth. Other symptoms may include upper respiratory tract irritation accompanied by coughing and a dryness of the mucous membranes, lassitude and a generalised feeling of malaise. Fever, chills, muscular pain, mild to severe headache, nausea, occasional vomiting, exaggerated mental activity, profuse sweating, excessive urination, diarrhoea and prostration may also occur. Tolerance to fumes develops rapidly, but is quickly lost. All symptoms usually subside within 24-36 hours. Resistance to the condition develops after a few days of exposure, but is quickly lost in 1 or 2 days.

Long-term exposures to lead can damage the blood-forming system, impairing the replenishment of blood cells and the blood's ability to carry oxygen; the central nervous system and the brain; the kidneys, to the extent that kidney dialysis may be needed; and reproductive systems in both men and women. Signs and symptoms of chronic lead exposure can include: anaemia, lack of co-ordination, blue-black lines on the gums, twitching, high blood pressure, visual disturbances, loss of appetite and weight loss.

Chronic, high-dose exposures can impair the reproductive system of both men and women. Effects include decreased sex drive, impotence, and sterility in men and decreased fertility and abnormal menstrual cycles in women. There is an increased risk of miscarriage and stillborn children in women whose husbands were exposed to lead or who were exposed to lead themselves. There is also an increased risk of birth defects, mental retardation, behavioural disorders, or death during the first year in children born to such parents.

Lead may enter the environment during its usage and disposal (EPA, n.d.a). The initial means of entry is via the atmosphere. Lead will be retained in the upper 2-5 cm of soil, especially soils with at least 5% organic matter or a pH 5 or above. It is expected to slowly undergo speciation to the more insoluble sulphate, sulphide, oxide and phosphate salts.

Lead enters water from atmospheric fallout, runoff or waste water. Metallic lead is attacked by pure water in the presence of oxygen, but if the water contains carbonates and silicates, protective films are formed preventing further attack. That which dissolves tends to form ligands. Lead is effectively removed from the water column to the sediment by adsorption to organic matter and clay minerals, precipitation as insoluble salt, and reaction with hydrous iron and manganese oxide. Under most circumstances, adsorption predominates.

Figure 13.1.2: Effects of lead on human health

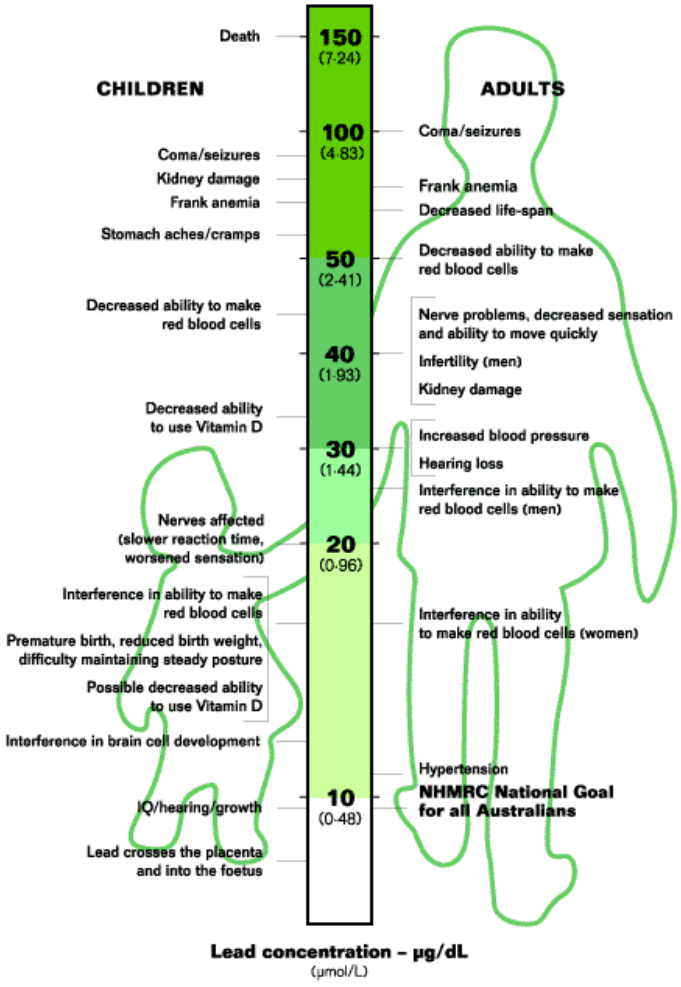

Source: Used with permission of the NSW.

Lake sediment micro-organisms are able to directly methylate certain inorganic lead compounds. Under appropriate conditions, dissolution due to anaerobic microbial action may be significant in subsurface environments. The mean percentage removal of lead during the activated sludge process was 82% and was almost entirely due to the removal of the insoluble fraction by adsorption onto the sludge and to a much lesser extent, precipitation.

The most stable form of lead in natural water is a function of the ions present, the pH and the redox potential. In oxidising systems, the least soluble common forms are probably the carbonate, hydroxide and hydroxycarbonate. In reduced systems where sulphur is present, PbS is the stable solid. The solubility of Pb is 10 ppb above pH 8, while near pH 6.5 the solubility can approach or exceed 100 ppb. Pb(0) and Pb(+2) can be oxidatively methylated by naturally occurring compounds such as methyl iodide and glycine betaine. This can result in the dissolution of lead already bound to sediment or particulate matter.

Elevated levels of lead in the water can cause reproductive damage in some aquatic life and cause blood and neurological changes in fish and other animals that live there.

Lead does not appear to bioconcentrate significantly in fish but does in some shellfish such as mussels. Evidence suggests that lead uptake in fish is localised in the mucous on the epidermis, the dermis and scales so that the availability in edible portions do not pose a human health danger.

Wild and domestic animals can ingest lead while grazing. They experience the same kind of effects as people who are exposed to lead. Low concentrations of lead can slow down vegetation growth near industrial facilities.

Figure 13.1.3: Sources and pathways of lead in the environment

Source: Used with permission of the NSW.

13.2 Rules and regulations

Lead is a technologically important metal throughout history. It is widely used in many industries and applications. Because of this wide presence and its toxic nature, lead work is also one the most regulated fields of labour. There are many rules and regulations in all industrial countries governing the use of lead.

Since regulations are country-specific and compliance is strictly required, it is beyond the scope of this handbook to present a comprehensive review of this topic. A compilation of the most significant standards and requirements is presented in Table 13.2.1. However, researchers should consult safety authorities within their own organisations/countries to determine specific requirements for compliance.

Nonetheless, there are several common features worth highlighting. First, since inhalation of airborne lead is the most common pathway for lead to enter human bodies, all regulations place a maximal allowable concentration (for an 8 hour shift, it is variably termed PEL – permissible emission level, or MPC – maximum permissible concentration, or MAK value – maximum allowable concentration in workstation at any time). PEL/MPC varies from 50-100 $\mu g/m^3$, while MAK value ranges from 100-150 $\mu g/m^3$.

Table 13.2.1: Regulations governing the safe use of lead in selected countries

PEL – Permissible Exposure Level, AL – Action Level

Country/ region	Regulations	In air, max permissible exposure level for 8-hr shift (PEL, microgram/m^3)	In air, action level (AL, microgram/m^3)	Monitoring frequency (month)			Record keeping (yr)	Max. Pb in blood (PbB, microgram/decilitre)	
				> PEL	< PEL & >= AL	< AL		Regular worker	Worker planning children
US	OSHA standards (www.osha.gov), 29 CFR, 1910.1025 – all occupational exposure to lead, and 1926.62 – all construction work where an employee may be occupationally exposed to lead	50 (100 MAK value)	30	3	6	Only when new risks are introduced through change of work, control	The longer of 40 or duration of employ; +20 (30 for construction worker)	40	30
Switzerland	Safety at Work is regulated by Federal Law (www.seco.admin.ch/dokumentation/01278/index.html?lang=fr) Classification of products is in the competence of the Federal Government (www.bag.admin.ch/index.html?lang=fr) Surveillance that regulations are applied is in the competence of SUVA	100 (workers < 18 years of age, pregnant women, anaemic persons excluded from working in areas > PEL)		2-6 depending on severity of exposure to be agreed upon with surveillance body	12	12		70 (male, female > 45 years of age)	30 (female < 45 years of age)
EU	Exposure to metallic lead and its ionic compounds (http://eur-lex.europa.eu/browse/summaries.html and www.ema.europa.eu/ema/)	150	75	3	3			70	
France	EU Directives								
Germany	EU Directives								
Sweden	Swedish Standards for Lead, AFS 1992:17, Swedish Standards for Air Control, AFS 1988:3, AFS 2000:3 (www.av.se)	50 (100 MAK value)	40	First 6 months, inspection required; afterwards, if Pb in air < 1/5 PEL, no more inspection is needed; if 1/5 PEL< Pb in air < 1/2 PEL, the authority decides the monitoring frequency; if 1/2 PEL< Pb in air < PEL, inspection is required every one year				PbB, micromol/litre, or 20.7 microgram/decilitre, value in () For women under 50: < 1.0 (0.8), no medical control; 1.0-1.5 (0.8-1.2), 6 months; 1.5-2.0 (1.2-1.5), 3 months; > 2.0 (1.2), measures taken to reduce PbB; > 2.5 (1.5), stop work	

Table 13.2.1: Regulations governing the safe use of lead in selected countries (*cont.*)

PEL – Permissible Exposure Level, AL – Action Level

Country/ region	Regulations	In air, max permissible exposure level for 8-hr shift (PEL, microgram/m^3)	In air, action level (AL, microgram/m^3)	Monitoring frequency (month)			Record keeping (yr)	Max. Pb in blood (PbB, microgram/decilitre)	
				> PEL	< PEL & >= AL	< AL		Regular worker	Worker planning children
UK	The Control of Lead at Work Regulations 2002 (www.hse.gov.uk/pubns/priced/l132.pdf)	150 (100 lead alkyls)		3 months if exposure from lead alkyls, or previous measurement > 100 microgram/m^3		12 months max if: exposure not from lead alkyls; no change; 2 previous consecutive tests show < 100 microgram/m^3	5 from date made	50 (young); 60 (others) (action levels: 40/50)	30 (action level: 25)
Japan	Safety at lead work is regulated by Japanese law and ordinance (www.jniosh.go.jp/icpro/jicosh-old/english/osh/outline/30.html and www.jisha.or.jp/english/link.html)	100				12	min. 5	40	
S. Korea		50							
Russian Federation		10							
Belgium	Exposure limits (www.werk.belgie.be/defaulttab.aspx?id=616#)	150		6	6	6	10	70	40

In practice, if we use the lead and LBE vapour pressures from the literature (Lyon, 1952; Morita, 2004), the 50-100 μg/m^3 PEL corresponds to 530-550°C for LBE and 500-520°C for Pb. Special care and controls must be taken to conduct experiments with exposed LBE and Pb above these temperatures. For airborne lead levels below PEL, the allowable work duration is lengthened proportionally so the total exposure equals to 8 hr times PEL.

Second, due to enhanced health threat (impairment of reproductive system and damage to children), the standards for young persons and pregnant women are more stringent. The Pb in blood (PbB) levels that require continued monitoring and work stoppage are lower for workers with heightened risks.

The monitoring frequency for airborne lead and PbB varies depending on severity from pervious measurement or whether changes in procedures and controls take place. It varies from 3 to 12 months, or longer when no changes occur. There are generally requirements on how long the workers' monitoring and medical records should be kept.

There are rules and regulations governing the limit value and monitoring of lead in ambient air and in wastes.

The National Ambient Air Quality Standard (NAAQS) is set by the US Environmental Protection Agency (US EPA) for pollutants that are considered to be harmful to public health and the environment; the NAAQS for lead is 1.5 μg/m^3, maximum arithmetic mean-averaged over a calendar quarter (EPA, nd.a, n.d.b).

The EU (1982, 1998) established a limit value for Pb in ambient air of 2 μg Pb/m^3, though some countries have reduced the limit to 0.5 μg/m^3. The sampling method is to collect atmospheric particles on a filter for subsequent determination of lead content. The reference method of analysis is atomic absorption spectrometry.

US EPA regulation sets the limit of Pb in solid waste to be 5 mg/L beyond which the waste is considered hazardous (EPA HW No. D008; CAS No. 2: 7439-92-1) (CFR, n.d.). This puts most of the lead-contaminated materials in coolant R&D in the category of hazardous wastes, including residues from polishing corrosion test specimens with a small amount of adhered Pb. The EU has been moving toward lead-free solder so the requirements might become even more stringent. The concentration limit in consideration is 0.1 wt.% for the EU and Japan (Soldertec, 2003).

For surface contamination, the following wipe sample clearance guidelines are recommended by the US HUD (LLNL, 2005):

- <100 μg/ft^2 (0.108 μg/cm^2) on uncarpeted floors;
- <500 μg/ft^2 (0.538 μg/cm^2) on interior window sills (stools);
- <800 μg/ft^2 (0.861 μg/cm^2) on window troughs (where the sash sits when closed);
- <800 μg/ft^2 (0.861 μg/cm^2) on exterior concrete.

These clearance guidelines are based on hazards to children, and are extremely low. In R&D work, higher limits may be acceptable at the discretion of responsible industrial hygienists. Although Pb vapour presence is minimal in common laboratory settings, long-term exposure without proper periodic clean-up could lead to high levels of Pb surface contamination.

Irradiated Pb and LBE may be considered low-level radioactive wastes. Their disposal is more difficult and their disposition sites very limited and country-dependent. This is beyond the scope of this chapter and should be treated in the future in the context of decommissioning and decontamination (D&D).

13.3 Common safety controls and practices

General controls can be used to reduce the potential for occupational exposure to lead. They can be categorised as engineering controls and administrative controls. Additionally there may be specific controls unique to the job. Industrial hygienists or other relevant safety specialists should be consulted about these controls, and approvals sought for operations involving lead.

Engineering controls are mechanical or structural systems used to minimise hazards. They include ventilation systems (e.g. fume hoods), isolation systems (e.g. glove boxes), adhesive mats at doorways, hygiene facilities (e.g. hand-washing basins), etc.

Administrative controls are used to direct, restrict or modify behaviour to prevent or minimise exposure to hazards. Specific requirements vary, but they generally include plans, procedures and permits, safe work practices, housekeeping, postings, access controls and training.

Plans, procedures and permits define the operating conditions that one may encounter, as might special precautionary measures to minimise workplace exposure to lead. When there is a potential for lead to become airborne in a manner that potentially increases risk of exposure, the activity hazard analysis or hazard control plan should identify the hazard and specify controls.

There are several general safe work practices and housekeeping rules to minimise or prevent exposure to lead, including:

- Wash hands and face before eating, drinking or applying cosmetics.
- Use only high-efficiency particulate air (HEPA) filter vacuums.
- Remove work clothes before entering eating areas, or use HEPA vacuums to clean dust off the clothes.
- Maintain all surfaces as free as practicable of accumulation of lead dust.
- Do not dry-sweep areas where lead may be present.
- Do not wear work clothes beyond the work area to prevent contamination.

For controls such as washing facilities, clean changing areas, separate clothes lockers, and showers to remain effective, workers must use them routinely and correctly.

Postings and access controls must be used in each work area where the permissible level is exceeded or as a precautionary measure where lead is present. Some areas may need access control to prevent unqualified personnel from entering.

Training is required for all personnel subject to lead exposure. Typically it consists of two components: a general lead awareness training covering the topics outlined here, and a facility or task-specific training provided by supervisors or facilities.

Personal protective equipment (PPE) is secondary protection that is used when other control measures are not feasible or not sufficiently effective at reducing exposures to lead. PPE can include coveralls, gloves, a face shield or vented goggles, booties and respirators. If respiratory protection is needed, proper training will be necessary.

When working with molten lead and lead-bismuth, toxic lead fumes are usually present, and the appropriate respirator should be selected if the concentration of fumes is above the permissible limit (PEL). Table 13.3.1 is based on US OSHA standards and represents the minimal respiratory protection at each action level.

Table 13.3.1: Respiratory protection for lead aerosols

Airborne concentration of lead or condition of use	Required respirator[1]
Not in excess of 0.5 mg/m^3 (10× PEL)	Half-mask, air-purifying respirator equipped with high-efficiency filters[2,3]
Not in excess of 2.5 mg/m^3 (50× PEL)	Full face-piece, air-purifying respirator with high-efficiency filters[3]
Not in excess of 50 mg/m^3 (1 000× PEL)	(1) Any powered, air-purifying respirator with high-efficiency filters;[3] or (2) Half-mask supplied-air respirator operated in positive-pressure mode[2]
Not in excess of 100 mg/m^3 (2 000× PEL)	Supplied-air respirators with full face-piece, hood, helmet, or suit, operated in positive-pressure mode
Greater than 100 mg/m^3, unknown concentration or fire fighting	Full face-piece, self-contained breathing apparatus operated in positive-pressure mode

1 Respirators specified for high concentrations can be used at lower concentrations of lead.

2 Full face-piece is required if the lead aerosols cause eye or skin irritation at the use concentrations.

3 A high-efficiency particulate filter means 99.97% efficient against 0.3 micron size particles.

13.4 Safe operations in HLM R&D

Using lead in heavy liquid metal coolant technology R&D has many operational aspects that can be hazardous if proper controls are absent and procedures are not followed. The hazards are multiplied many times in radiation environment, when alpha-emitting ^{210}Po, radioactive mercury isotopes and others are produced (see Chapter 8). Establishing the safety envelop and operating procedures, and getting approvals from safety authorities can be extremely labour intensive and time consuming, as the MEGAPIE project has demonstrated. This section, however, will not cover that but instead use several typical experimental operations with no irradiation to illustrate some safety practices in the more routine use of lead and LBE for HLM R&D. These are from observations and practices of many experiments and test facility operations around the world.

Many laboratories use small containers of LBE or lead to conduct experiments in the study of corrosion, wetting, embrittlement, oxygen control, etc. The generic operation steps may include setting up the apparatus, preparation, melting, filling, insertion, sealing, heating, gas injection, cooling, opening, extraction, cleaning and freezing. Transferring, draining, circulating, etc., are typically used in larger test loops and facilities, so covered separately later.

Setting up apparatus. The first consideration should be the location of the experiment and its environment. It should be in a dedicated laboratory or area separate from offices and eating areas with good ventilation and nearby washing facilities. The area should have non-porous, clean and uncluttered surfaces and walls to facilitate clean-up. Since leakage and spillage can occur, it is advisable to have metal drain pans underneath the apparatus and handling operations. If hoods or other active ventilation systems are used, HEPA filters should be installed.

The access should be controlled with proper warnings and contact information posted at prominent locations, including entrances, exits and next to the experiments. If large quantities of HLM are used, sticky mats on the floor at the exits may be used to limit contamination.

Periodic cleaning should be performed to eliminate deposited lead or its oxides. Wet wipes should be used for surfaces, and HEPA-filtered vacuum for floors. If a laboratory has been used for long time without frequent cleaning, surface sampling should be conducted to determine levels of contamination before cleaning is commenced.

Preparation. Solid LBE or lead ingots are typically used. Smalls amount of surface oxides can usually be dissolved into the melt (desirable at times if higher oxygen concentrations are needed), or cleaned up with mechanical means from the melt (e.g. picked up by a wire mesh scoop). If there is too much oxide, e.g. from long-term exposure to the environment, they should be discarded. Cleaning oxides in solid form may produce dangerous airborne lead dust, and should be avoided.

Melting. Melting ingots into a crucible or a vessel is straightforward. However, melting solidified LBE or lead in a container requires some caution and well-planned procedures. Significant differential volume expansion can occur during heat-up of HLM and containers, leading to stresses that in some situations cause crack or rupture. HLM should be melted from free surfaces into more confined volumes. For large containers, separate heating zones with correct heating sequences should be used. Some design features, e.g. a few degrees of slant in a melting tank wall (expanding toward the top), are better suited than others (e.g. a straight cylindrical tank is not as accommodating). A horizontal cylindrical melting tank more than half filled is not a good configuration. Due to such considerations, HLM is usually drained from the test apparatus with complex internal structures for freezing and melting.

Filling. If a large amount of LBE or lead is used for the first time, a pre-melting and transfer device is recommended, draining from the bottom into the experimental apparatus. Many suspended impurities, including oxide sludges, can be removed from the free surface by mechanical means. Such operations should be carried out at temperatures as low as possible, i.e. just high enough to prevent accidental freezing and plugging. The specific temperatures depend on the set-up, e.g. heating of the transfer line and the receiving vessel, but usually should be 150-180°C or slightly higher for LBE, and 380-400°C for lead. Such tasks can be carried out in open vessels, but the operators should wear respirators if more than a few kg of HLM is involved, and should in principle have air sampling done as well. While the vapour pressures at these temperatures are below permissible emission levels (PEL), the handling may create high levels of dust, including lead oxides. Cleaning the surroundings afterwards is necessary to prevent the spread of contaminations. Vacuuming with an HEPA-filtered vacuum cleaner for loose dust and wet-wiping of exposed surfaces are recommended.

The vessels and pipes to be filled should be properly pre-heated to temperatures not too different from the melt. Differences of a few tens of degrees are acceptable, but 50°C or more may produce thermal shocks that could damage the apparatus or sensors. Mitigation measures (e.g. use of bellows for joints) and procedural controls (e.g. slow fill when accidental freezing can be excluded) should be employed to reduce such effects. If there are areas not very accessible to pre-heating (e.g. pipes inside a vessel), caution must be taken to prevent accidental freezing (e.g. use a higher melt temperature for filling).

Insertion. Sensors, test samples and gas lines are often inserted after the filling. This should be performed at low temperatures. Since HLM is heavier than most materials, there will be some buoyancy so the fixtures should be sturdy and can prevent upward turning. Hanging is not an option. At this stage, the free surfaces of HLM should have already been cleaned up so the insertion does not contaminate the undersides with oxides and other floating impurities.

For all of the above operations involving open vessels, temperatures should be kept low both for safety reasons, and for avoiding excessive oxidation. While using an inert heavy cover gas (e.g. Ar) to reduce oxidation may be desirable, it is not necessary.

Sealing. Due to the needs for safety and good coolant chemistry control, tight seals are essential for experiments and operations. External rotating seals should be avoided. Flanges with gaskets in contact with high temperature HLM should be avoided as well, although some have worked reasonably well (graphite or spiral wound steel gaskets). Since even a small ingress of air will contaminate the HLM, a slightly positive cover gas pressure should be maintained during normal operations.

Due to relaxation of bolts from thermal cycles, flanges will loosen over time. Periodic retightening should be scheduled and performed. If leakage does occur, the experiment should be stopped, HLM drained into a melt tank, and the apparatus cooled down before repair and clean-up is performed. Liquid metal leakage detection can be based on simple conductivity probes in areas surrounding flanges or joints or likely collection basins, or inferred from loss of volume through level sensors and loss of pressure.

Heating. Heating up the HLM in the molten state is a quite simple process but may have consequences beyond the obvious. Very rapid heat-up may be detrimental to some components, especially ceramic parts (e.g. oxygen sensors). No definitive rule is reported, but a heating rate less than 50°C/hr is recommended for some Russian-made oxygen sensors. We have used much more rapid heating rates in small experiments with simple configurations. For large facilities, this should be determined carefully with analyses, simulations and testing.

Due to rapidly increasing solubility of elements in HLM with temperature, surface slags, especially lead oxides, will decrease and disappear. Oxidation of materials will also consume oxygen and clean up HLM surfaces. If no deliberate oxygen addition or air ingress takes place, the HLM at high temperatures usually has oxygen concentrations far below solubility or the so-called oxygen controlled range for corrosion mitigation. If no protective coatings or pre-oxidation has been applied to an apparatus built with steels, this could lead to rapid dissolution attack at high temperatures (above 500-550°C for 316L type austenitic steels, or T91 and HT-9 type ferritic and martensitic steels (see Chapter 6 for the steel compositions). Such dissolution attacks may even be accelerated if oxygen is added when the dissolution has already started by removing dissolved elements through oxidation in HLM. It is highly recommended that heating be carried out through planned stages during the initial start-up, or after insertion of fresh test specimens, so that protective oxidation can be initiated and established. Since many test apparatuses and loops are built with steels, such a precaution is essential in maintaining containment integrity and safety.

If in static tests at high temperatures the oxygen concentration is not first adjusted to sufficient levels, due to the slow diffusion of oxygen from cover gas into the depths of stagnant HLM and rapid local consumption of oxygen by oxidation, unprotected fresh test specimens made of steels may start to dissolve, setting up a competition of mass transfer processes between oxygen diffusion to the steels and dissolution products migrating toward high oxygen areas (e.g. free surface in contact with cover gases). This could render test results highly dependent upon heating rate, initial oxygen concentrations in HLM and the effectiveness of the mass exchange from gas to liquid. It may even be dependent upon placement of specimens, size of surfaces and other system specific conditions, which are usually not accounted for or reported.

Such scenarios can also arise in flow systems where gas exchange for oxygen control is conducted through a stagnant volume. In extreme cases, it could lead to much more rapid corrosion than expected and have severe safety consequences.

Gas injection. This is often done to adjust coolant chemistry, either by adding oxygen or using hydrogen to reduce oxygen, or using gas mixtures (e.g. steam and hydrogen, or CO and CO_2) to maintain oxygen levels. Sometimes, to create circulation (e.g. gas lift or stirrer), a high flow rate gas injection is applied.

It should be noted that even the highest purity supply gases usually contain ppm level of oxygen, which is too high for HLM if continuously applied over long periods of time. A getter system is needed to strip incoming gases of oxygen, unless adding oxygen is the goal. It is also not advisable to inject gases directly into the HLM melt, since a amount of residual oxygen will lead to slag formation and plugging of the injection line, and the transport of slags to other parts may lead to flow restriction or blockage. This is true even for hydrogen injection unless an oxygen getter system, pre-heating to complete reaction with hydrogen, or entrainment by flow for prolonged hydrogen retention, is used.

From the safety perspective, injecting gases with lead oxide formation may create aerosols in the cover gas space, leading to potentially very hazardous conditions when opening and repair are conducted (see *Opening* below). It is therefore emphasised that caution be applied when gas injection into liquid metal is deployed in experiments and operations.

Cooling. In the molten state, cooling should observe the same level of caution as heating. Rapid quench is not advisable.

The effects of cooling should be carefully considered when establishing procedures. Because solubility decreases with decreasing temperature, undesirable precipitation and deposition may occur in systems at hard-to-reach or technologically important sections. Once the solids deposit to walls, merely heating back up will not remove them since they either have low solubility or high melting temperatures. This could lead to reduced performance, restriction of flow and eventual blockage. It may also create unsafe conditions for maintenance and repair. The clean-up and restoration process can be very time consuming.

When temperature of HLM is lowered substantially from the operating conditions, oxygen concentration can reach saturation and precipitation will occur. Heating up quickly can lead to a deficiency in oxygen for corrosion protection. For example, the typical oxygen control point is 10^{-6} wt.%, or 10 ppb of oxygen in LBE. This corresponds to saturation at approximately 200°C. So cooling below that for an extended period will lead to significantly lower oxygen concentrations, and addition of oxygen will be necessary on re-heating if the precipitated oxides are somehow removed or left out (e.g. cooling is in the melt tank).

Opening. As in all open vessel operations, this should be conducted at temperatures as low as possible. Lower temperatures suppress oxidation and vapour emission.

The top concern upon opening vessels or pipes is the potential presence and release of fine oxides or aerosols. While good ventilation is necessary, strong air perturbation at the openings should be avoided. When possible, a small enclosure of suitable sheets may be used to contain any releases. Operators should wear respirators if opening is carried out through cutting or other means of strong disturbance.

Extraction. It should be done at low temperatures. Very often, reheating is needed to extract specimens or sensors after solidifying HLM in place, or being "welded" to holders or sheaths by the residual HLM.

Cleaning. Cleaning of specimens is a difficult and delicate task. There are a number of methods reported for removing the adhered LBE from the specimens, including simple swiping, boiling in glycerine, silicon oil, or acid, or dipping in sodium. The safety precaution for each is obvious and will not be discussed here. One should keep in mind that hazardous waste is usually generated, as is also the case for polishing, and disposal must comply with applicable rules and regulations. Therefore, minimising the use of supplies and recycling of some media should be attempted.

It is also a good practice to clean up the surrounding areas after each opening or after a certain time, to reduce surface contamination and spread beyond the laboratory.

Freezing. While it is desirable to keep the HLM molten at all times, especially in test facilities, HLM will often be allowed to freeze. Due to volume changes upon solidification, and continued changes during recrystallisation in LBE, caution and proper procedures must be applied. Freezing should start at more confined space toward free surfaces, and should be avoided in regions where complex and/or delicate components lie.

An important consequence of the freezing is the reduction of oxygen in HLM. Upon melting, a certain amount of time should be allowed for re-oxygenation before transferring and raising the temperature.

For large test facilities, there are several additional steps or functions. The generic forms are transferring, priming, circulation, active cooling, draining, etc. The actual procedures will be facility specific. However, similar safety precautions are required. In particular, because of the stored kinetic and thermal energy in the circulating liquid metals, local containment in the forms of pipe cladding, loop enclosure, drainage collection floor pan, with ventilation, will be necessary.

The danger posed by lead to human health and environment is very real and serious, and should not be overlooked in the research and development of lead-alloy coolant technology. It is also demonstrated in the world-wide use of lead throughout history that when rules and regulations are properly observed, and safe work practices and controls are employed and effectively utilised, lead hazards are manageable. It is imperative for this field of R&D and future applications that the safety guidelines are followed, and that workers and the environment not be harmed.

References

CEC (Commission of the European Communities) (1997), *Air Quality Daughter Directives Position Paper on Lead*, Working Group on Lead, Commission of European Communities, UE/AQ-5.2/EN, accessed 15 March 2015, http://ec.europa.eu/environment/air/pdf/pp_pb.pdf.

CFR (United States Code of Federal Regulations) (n.d.), Title 40, "Protection of Environment", Subsection 261.24, "Toxicity Characteristic", 40CFR261.24, accessed 15 March 2015, www.gpo.gov/fdsys/pkg/CFR-2002-title40-vol1/content-detail.html.

Cullen, D. and T. Allen (2003), internal report, Argonne National Laboratory (West), Los Alamos, NM.

EPA (United States Environmental Protection Agency) (n.d.a), "Lead", EPA webpage, accessed 15 March 2015, last updated 21 January 2015, www2.epa.gov/lead. Also "Lead Compounds", EPA webpage accessed 15 March 2015, last updated 18 October 2013 and www.epa.gov/ttn/atw/hlthef/lead.html. Also "Lead in Drinking Water", EPA webpage accessed 15 March 2015, last updated 29 July 2014, http://water.epa.gov/drink/info/lead/index.cfm. Also "Lead in Air", EPA webpage, accessed 15 March 2015, last updated 22 December 2014, www.epa.gov/air/lead.

EPA (n.d.b), "National Ambient Air Quality Standards (NAAQS)", EPA webpage, accessed 15 March 2015, last updated 21 October 2014, www.epa.gov/air/criteria.html.

EU (European Union) (1982), "EU Council Directive 82/884/EEC of 3 December 1982 on a Limit Value for Lead in the Air", accessed 15 March 2015, www.greenhome.co.me/fajlovi/greenhome/attach_fajlovi/eng/projects/green-resource-centar/2011/10/pdf/Directive_82_884_EEC_on_a_limit_for_value_for_lead_in_the_air.pdf.

EU (1998), "EU Council Directive 98/24/EC of 7 April 1998 on the Protection of the Health and Safety of Workers from the Risks Related to Chemical Agents at Work (Fourteenth Individual Directive Within the Meaning of Article 16(1) of Directive 89/391/EEC)", accessed 15 March 2015, https://osha.europa.eu/en/legislation/directives/exposure-to-chemical-agents-and-chemical-safety/osh-directives/75.

Grogin, P. et al. (2001), *Refresher: Lead Awareness*, LA-UR-01-5171, Los Alamos National Laboratory, Los Alamos, NM.

Holm, O. et al. (2002), *Heavy Metals in Waste – Final Report*, European Commission DG ENV. E3, Project ENV.E.3/ETU/2000/0058.

ILO (International Labour Organization) (n.d.), "Occupational Safety and Health", accessed 15 March 2015, www.ilo.org/safework/lang--en/index.htm.

Lewis, J. (1985), "Lead Poisoning: A Historical Perspective", *EPA Journal*, accessed 15 March 2015, www2.epa.gov/aboutepa/lead-poisoning-historical-perspective.

LLNL (Lawrence Livermore National Laboratory) (2005), "Safe Handling of Lead and Lead Compounds in General Industry and Construction Operations", LLNL ES&H Manual, Document 14.1, LLNL, Livermore, CA.

Lyon, R.N. (1952), "Liquid Metal Handbook", NAVEXOS, Government Printing Office, Washington, DC.

Morita, K. et al., "Thermophysical Properties of Lead-Bismuth Eutectic Alloy for Use in Reactor Safety Analysis", contribution to the *HLMC Handbook* (2004).

NSW (Australian Department of Environment and Conservation) (n.d.), "Lead", accessed 15 March 2015, last updated 27 November 2014, www.epa.nsw.gov.au/pesticides/lead.htm.

OSHA (United States Department of Labor, Occupational Safety and Health Administration) (n.d.), "Regulations (Standards - 29 CFR) - Table of Contents", OSHA webpage accessed 15 March 2015, www.osha.gov/pls/oshaweb/owadisp.show_document?p_table=STANDARDS&p_id=10030. Regulations by other agencies can be found in the web sites listed in Table 13.2.1.

Soldertec (2003), "Second European Lead-Free Soldering Technology Roadmap", Soldertec, accessed 15 March 2015, http://home.jeita.or.jp/tss/jisso_eas/japanese/leadfree/data/eu_roadmap_2003_ver2.pdf.

WHO (World Health Organization) (1989), *Environmental Heath Criteria for Lead – Environmental Aspects*, ISBN 92 4 154285 3, World Health Organization, Geneva, accessed 15 March 2015, www.inchem.org/documents/ehc/ehc/ehc85.htm.

14. Perspectives and R&D priorities of heavy liquid metal coolant technologies*

14.1 Introduction

HLM technologies are being developed for a number of advanced nuclear systems. These include accelerator-driven transmutation systems to "burn" high-level nuclear waste and HLM-cooled fast reactors. Accelerator-driven systems are presently under investigation in Europe (e.g. the MYRRHA project and related projects supported by the European Commission), China and India. Pb/lead-bismuth eutectic (LBE)-cooled fast reactors are one of the six concepts in the generation IV Nuclear Energy Systems initiative. Different missions can be envisaged, the more demanding of which include operating above 600°C for hydrogen production, or very long-life cores for non-traditional uses.

The most current knowledge of HLM technologies for applications below 600°C has been described in this second version of the handbook. Viewed from the perspective of programmatic applications for HLM technology and materials, there are still a number of technological gaps to be filled before a prototypic test/demonstration nuclear system (reactor or ADS) can be designed, constructed and operated based on lead or LBE cooling. There are also a number of scientific issues which need to be addressed for the upscale to prototypical dimensions, including fundamental physical, chemical and transport properties of HLM and materials, effects of environment, experimental and computational thermal-hydraulics, coolant chemistry, measurement techniques and instrumentation. However, with the exception of uncertainties in materials performance over very long service life in cores (20 years or longer) at temperatures over the 500-550°C range, no apparent conceptual barriers (i.e. "show-stoppers") exist for the eventual use of lead and LBE coolants in advanced nuclear applications.

For applications in the higher temperature ranges an extensive R&D programme on materials and coolant technology is needed. But this is not yet foreseen at the international level. A preliminary analysis of existing materials led to the following classification, depending on the upper operating temperatures:

- *Class I*. For temperatures below 550°C, it has been demonstrated that the existing technologies and some code qualified nuclear structural materials (austenitic and ferritic/martensitic steels) possess acceptable performance in short to medium durations and out of pile. These demonstrations need to be extended to longer durations and under irradiation. Some data under irradiation have been generated in the recent past, which have allowed a preliminary assessment of these steels. However, further experimental activities are needed to complete the database under irradiation and to define and execute a programme relevant for assessment under transient and off-normal conditions.
- *Class II*. For higher-temperature services envisioned in more advanced system concepts, materials and coolant technology developmental needs are much more extensive and the development much longer term. For reactor outlet temperatures

* Chapter lead: C. Fazio. For additional contributors please see Appendix 1.

up to 650-700°C for higher efficiencies, oxide dispersion strengthened (ODS) steels and/or advanced F/M steels are potential candidates. These materials, categorised as Class II, may be used with an extension of the LBE coolant technology. For this temperature range, it is likely that Pb, rather than LBE, will be used, although the use of LBE is more established.

- *Class III*. For operating temperature above 750-800°C in systems with more diverse energy products, including hydrogen production, refractory metal and alloys, ceramics and composites. These systems might require a very different coolant technology, design, construction and operating methodology. Compatibility is no longer the key obstacle. Other issues, including irradiation stability, fatigue strength, fabrication, joint, costs, etc., are challenging. The development of Class III materials is pursued though high temperature reactor and fusion technology development programmes. For this temperature range, Pb will likely be the only choice since LBE and the associated technologies no longer offer any intrinsic or experiential advantages.

14.2 Technology gaps, R&D needs and priorities for HLM systems operating at temperatures below 550°C

In Europe, HLM technology is being developed for the transmutation of high-level nuclear waste in subcritical systems and for generation IV lead-cooled fast reactors. Several projects (e.g. EUROTRANS, CDT, SEARCH, MAXSIMA) have been sponsored by the European Commission, with the aim of demonstrating the technical feasibility of transmutation of high-level nuclear waste using accelerator-driven systems. Within this objective the design of an experimental facility (e.g. FASTEFF and MYRRHA), should demonstrate the technical feasibility: *i)* of transmuting a sizable amount of waste; *ii)* of safely operating an ADS. In addition, a conceptual design of the European Facility for Industrial Transmutation (EFIT) is foreseen. The experimental facility and the EFIT are subcritical reactor systems cooled by liquid lead-bismuth eutectic (LBE) and Pb, respectively. For both systems, a liquid metal neutron spallation target is the reference design basis for the external neutron source as driver.

The current experimental facility and the EFIT design concepts foresee an outlet temperature for the HLM coolant no higher than 480°C and a maximum fuel cladding temperature of about 550°C under normal operating conditions.

Furthermore, the European Lead-Cooled System (ELFR) projects also sponsored by the European Commission have been charged with the study of an approximately 600 MWe lead-cooled fast reactor. These projects are the European contribution to the lead fast reactors (LFR) of the generation IV initiative. The HLM technology specifications for ELSY will benefit from the results emerging from the activities performed in the framework of ADS developments. Some specific Pb technology developments are foreseen, however, such as high temperature materials characterisation in Pb and steam generator tube rupture studies.

In the United States, HLM technology has been developed in the past through two advanced nuclear energy programmes: the Advanced Fuel Cycle Initiative (AFCI) and the generation IV LFR. There are a range of envisioned missions and system concepts in the United States, with the current focus being on a class of small- to medium-sized reactors with long-life cores (20 years or longer) and no on-site refuelling. The peak cladding temperature in the design is limited to 650°C, while core outlet temperature is approximately 560°C.

Previously, Japan conducted several programmes with the aim of developing HLM technology. At J-PARC, for example, it was intended to design, build and test an LBE-cooled

accelerator-driven transmutation system. At present the Japanese nuclear programme's future direction is under discussion.

Korea was developing HYPER (ADS) and PEACER (reactor) in collaboration with international partners. Seoul National University continues to operate an LBE loop (HELIOS) for research purposes.

14.2.1 *HLM thermal-physical properties*

This handbook contains the most relevant thermal and physical properties of Pb, Bi and LBE with recommended correlations. For the high temperature range, a set of thermodynamic and transport properties (thermal conductivity, viscosity and surface tension) of LBE has been developed for use in reactor safety analysis. However, due to a lack of experimental data published in the open literature, basic properties such as liquid density, vapour pressure and liquid adiabatic compressibility were estimated up to the critical point using semi-empirical models based on the extrapolation of low temperature data of LBE or its constituents. A recommendation to produce experimental data in the high temperature range has been made, which would be useful as a means to validate the computed values.

14.2.2 *HLM chemical properties*

The chemical properties data of solubility and diffusivity of oxygen and some metallic elements (e.g. Fe, Cr, spallation products as for instance Po, etc.) in the liquid metals and some oxides (e.g. iron oxides, chromium oxides, etc.) are of paramount importance for:

- the assessment of the materials corrosion rate;
- the design and engineering of HLM purification systems, for the development of a corrosion protection strategy that is based on protective oxide layers on the structural materials;
- the source term assessment and subsequent release of radioactive material from the coolant.

In this new version of the handbook new data have been added; however further effort is needed to complete the needed database for safety and licensing purposes.

14.2.3 *Materials*

The study of material properties changes in radiation environments, and specifically for HLM systems, the combined effects of radiation and corrosion, is a high priority R&D need. For instance the use of protective oxides as barriers against liquid metal corrosion may be compromised by radiation-enhanced transport of ions in oxides, resulting in uncertainties for in-core components such as fuel cladding. In addition, modelling tools are insufficient to analyse the varying test data and extrapolate the results to very long times, and only basic understanding of the triggers and kinetics of corrosion processes with long incubation periods, such as breakaway oxidation at high temperatures.

Furthermore, nuclear grade materials' manufacture, fabrication and qualification are gradually becoming high priority issues as HLM technology moves out of the laboratory and into test and demonstration facilities.

Reference structural materials are still under investigation for ADS systems developed in Europe. For instance, the operational limits of T91 martensitic steel (thought to be used for the highly loaded parts such as cladding, wrapper, spallation target structure) have been determined. As an alternative, the use of 15-15-Ti austenitic steel has been proposed. AISI 316L austenitic steel is the reference material for the vessel and in-vessel components.

In addition it has been agreed to characterise Fe-Al-based coatings, which are envisaged as an alternative protection method against oxide layer growth, for the fuel claddings.

For design concepts in other countries, similar materials are selected. For example, the reference materials for LFRs in the United States are HT-9 and 316L. Russia has developed some special alloys with added Si content for HLM-cooled reactors, most notably EP823.

For these materials the basic data on compatibility and mechanical property changes in the liquid metals are already available, mostly under out-of-pile conditions. However, for the specific design requirements the following data are needed with high priority:

- Long-term corrosion behaviour understanding and predictive model development of the steels and the coatings in order to identify reliable safety margins.
- Corrosion tests in LBE simulating transient conditions, e.g. low oxygen concentration.
- Studies on corrosion erosion and friction mechanism; first results are available, which can be included in design considerations. However, further activities might be needed to complete the overall assessment.
- Development of mass transfer model using reliable solubility and diffusivity data and corrosion data also for non-isothermal systems.
- Mechanical behaviour of the structural materials and the corrosion protection barriers in a representative temperature-stress field and more specifically:
  - creep;
  - fatigue and creep fatigue;
  - fracture mechanics;
  - creep and fatigue crack growth.

A very high priority is also placed on the assessment of mechanical properties in the liquid metal and of the steels and coatings under irradiation.

These properties need to be measured in the relevant ranges of temperature, neutron fluence, stresses and HLM flow velocity for the different components. At present the European design group for ADS has yet to produce a complete set of specifications to identify the testing ranges. Nevertheless, preliminary designs have allowed the definition of several irradiation experiments in LBE and Pb, e.g. HFR, BR2 and BOR60 reactors. These irradiation experiments have produced initial results and have shown the necessity to complete the irradiation and PIE campaign such as to complete the materials assessment.

Finally, the need to define standard procedures to perform corrosion and mechanical tests has been clearly expressed, as experimental data might be relevant for pre-normative research purposes and licensing issues.

A further relevant step will be the performance assessment of manufactured materials in well-defined shapes, e.g. tubing as fuel cladding.

14.2.4 Technologies

While much progress has been made in understanding the effect of coolant chemistry on materials corrosion, and measurement and control of oxygen in HLM in laboratory and small to medium test facilities, there are significant needs in scaling up to large systems, in particular pool-type and/or natural circulation systems. Oxygen sensors for higher temperatures, deep immersion in liquid metals, and enhanced robustness and reliability in plant-like environments requires continued improvement from the state of art. Oxygen control systems, filtration methods and oxygen activity maintenance and restoration after drainage, cool-down, freeze and thaw, will require further development and testing.

Alternative and/or expanded control ranges, coupled with materials development, are desirable. Most of these technological issues have priorities range from high to medium depending on specific concepts, programme development paths and time horizons.

Priorities might be envisaged for the development of:

- HLM purification systems for the control of aerosols and slags, to be applied in large scale and pool-type facilities.
- Reliable instrumentation (flow meters, pressure transducers, thermocouples, level sensors, pumps, etc.) for the long-term operation of HLM facilities.
- Reliable oxygen control methods and monitoring systems. Different methods have been envisaged to set the oxygen content in the liquid metal, which are based on liquid/gas or liquid/solid exchange. The efficiency of these systems needs to be assessed in order to make a selection of the most reliable and easiest method to be implemented in a nuclear system.
- Optimisation of on-line oxygen sensors in order to raise their reliability to nuclear standards. Effort is needed in the definition of a calibration strategy and to enhance their long-term performance and thermal shock resistance.
- Instrumentation for in-service inspection and repair (ISIR). These instruments need to be tested and calibrated in a combined LBE and irradiation environment.

A second issue with regard to technology development is the experimental validation of critical nuclear system components. The tests range from proof-of-principle up to qualification and reliability. Particular attention needs to be paid to those components that have a safety function or those where the behaviour is expected to significantly change because of the nature of the HLM coolant.

Component tests to be envisaged are:

- Control and safety rod systems. These components are essential for the operation of the nuclear system. Tests should include insertion speed and reliability tests.
- Fuel bundle behaviour in terms of mechanical stability and susceptibility to vibrations and as influenced by coolant properties.
- Fuel handling equipment. Fuel handling is a critical factor in the operation of nuclear systems. Handling in HLM poses different issues than fuel handling in other coolants and consequently appropriate testing is required.
- HLM pumping. Pumping a high density liquid to the requirements of a nuclear system is not straightforward. In particular the conditions imposed on the impeller of a mechanical pump in terms of erosion/corrosion are not met in “standard” materials tests where HLM velocities and turbulence patterns are different as compared to the case of a pump impeller. Experience from the liquid metal industry is not directly transferable, as the oxygen concentrations and operation temperatures are different.

14.2.5 *Thermal-hydraulics*

There are two kinds of open issues in this area. The first is related to the fundamental nature of heavy liquid metals. There are some needs in developing and validating a more suitable turbulent heat transfer model (or models) for computational thermal-hydraulics. Applications are found in complex geometries and critical components, e.g. the reactor core configuration and high-power spallation target windows in ADS. In addition, turbulent heat transfer in a pool configuration, i.e. for unconfined flows far away from a wall, requires further investigation, in particular in view of handling stratification and striping phenomena.

The second type of issues is technological and mostly related to the nature of the HLM-cooled system design and operation. Using coolant chemistry control and surface protective oxide formation to mitigate steel corrosion has consequences in heat transfer performance, particular for long-term or abnormal situations (e.g. build-up of oxides and high level of solid oxide particles). HLM-cooled nuclear reactors usually have open lattice configurations to reduce pumping power needs and enhance passive safety. Flow circulation methods, transients, flow stability and elimination of undesired instability are all important issues to be investigated.

According to present design choices, priority has been placed on thermal-hydraulics studies related to flow characterisation in the core region of ADS systems where normal and off-normal conditions need to be simulated. The experimental campaigns should be structured such as to have heavily instrumented test sections of fuel bundle in order to support the experimental data with CFD calculations. Moreover, additional tests in pool-type configurations in order to study turbulent heat transfer and to assess system code are also very much desirable to gain confidence in the design approaches.

14.2.6 Safety-related R&D

Safety-related research is difficult to categorise in a specific field since often an interplay of different phenomena occurs. On the other hand it might be argued that all research with regard to HLM-cooled nuclear systems is somehow safety-related. In any case, for licensing purposes a number of specific issues need to be investigated that are mostly linked to conditions beyond normal operation. The definition of the specific circumstances that need to be investigated will result from an iterative process from and interaction between (numerical) safety analyses of the nuclear system and experimental results. Particular issues that will require experimental investigation are the consequences of a clad failure including fuel-coolant and fuel-cladding-coolant interactions on the one hand and fuel dispersion phenomena on the other. A second example is the investigation of (violent) ingress of water in the coolant due to HEX tube failure. Issues to be studied include the impact of the water ingress on the chemistry control of the coolant, shock wave and damage propagation after a tube rupture, aerosol formation in the steam jet and (radioactive) release to the reactor hall.

15. Guidelines for thermo-hydraulics modelling of pressure drop of the heavy liquid metal-cooled loops*

15.1 Introduction

This chapter provides a set of guidelines for selecting correlations in the prediction of pressure losses induced from the wall friction and/or a change of flow area in liquid lead-alloy (lead-bismuth eutectic, LBE) cooled advanced nuclear energy systems (LACANES). The validity of guidelines described herein have been confirmed through an NEA benchmark effort using the HELIOS test loop and modelling by expert group participants, for the given range of experimental conditions (Cho, 2011). The guidelines are made for use in the prediction of both forced convection and natural circulation. The latter phenomenon is becoming important in new generation systems such as generation IV and small modular reactor (SMR) systems that pursue passive safety (Choi, 2011). The forced convection has been tested for relatively low flow rates. Thus, these guidelines can assist the predictions of both forced convection and natural circulation behaviour of the LBE coolant system, only for the given range of experiment. Also, in view of the fundamental thermal-hydraulic study of LBE fluid, these guidelines may provide an understanding of LBE coolant behaviours in comparison with water.

Due to the need for accurate prediction of pressure losses and heat transfers in LBE coolant an NEA benchmark programme was launched by an expert group designated as LACANES, in 2007. The main objectives of the NEA benchmark effort are to establish a set of best practices to model pressure loss and heat transfer as critical components of the thermo-hydraulic design and analysis tools with the goal to reduce the uncertainties and increase confidence in LACANES. Nine organisations (ENEA, RSE, GIDROPRESS, IAEA, IPPE, KIT/IKET, KIT/INR, SNU and RRC-KI) from five countries have been participating in the LACANES thermo-hydraulic study (Cho, 2011).

The raw database employed in the LACANES benchmark programme was produced experimentally from the 12 m tall LBE coolant integral test loop, known as HELIOS (Heavy Eutectic Liquid Metal Loop for Integrated Test of Operability and Safety of PEACER)[1] (Hwang, 2000; Jeong, 2006). The main purposes of HELIOS are the validation of both forced convection and natural circulation of LBE coolant systems as well as corrosion testing of structural materials and an integral validation of the operability of an LBE system.

15.2 Description of the LACANES benchmarking procedure

15.2.1 *Methods of LACANES benchmarking*

LACANES benchmarking is grouped into two phases consisting of a forced convection case (Phase I) and a natural circulation case (Phase II). All LACANES benchmarking procedures are illustrated in Figure 15.2.1.

* Chapter lead: I.S. Hwang.

1. PEACER: Proliferation-Resistant, Environment-Friendly, Accident-Tolerant, Continual and Economical Reactor. PEACER is a liquid LBE-cooled transmutation reactor conceptualised by Seoul National University.

Figure 15.2.1: Overall procedure of NEA LACANES benchmarking

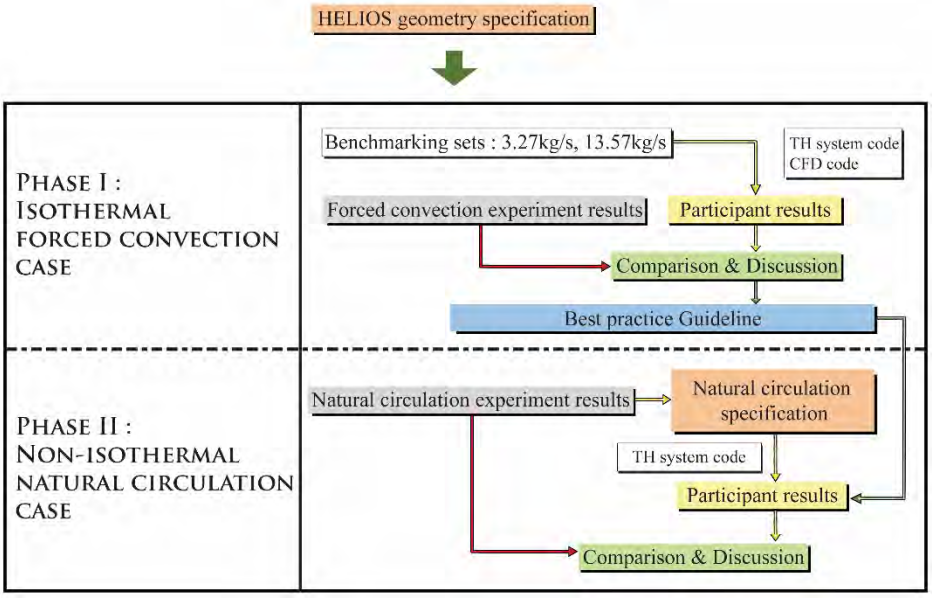

In Phase I, predictions of pressure losses calculated by programme participants were compared with measured data gathered from experimental results and supplementary information with other predictions. Participants used their own system codes to predict the pressure losses for all components of the HELIOS flow line. Furthermore, two CFD codes were simulated to obtain the pressure losses for specific components that have complicated geometries. The participants calculated pressure losses for two mass flow rate test conditions including low mass flow rate (3.27 kg/s) and high mass flow rate (13.57 kg/s) with an isothermal steady state of 250°C. Based on comparisons and discussions of benchmarking results, best practice guidelines to obtain the pressure loss coefficients on LACANES were constructed.

15.2.2 *Description of LBE thermo-hydraulic test loop HELIOS*

HELIOS was designed by scaling down with 5 000:1 ratio from its prototype PEACER-300 at Seoul National University. It has operated since May 2005 with the principle purposes of thermo-hydraulic experimentation and materials corrosion testing under LBE dynamic conditions. In the area of thermo-hydraulics, the verification of natural circulation capability that demonstrates the loss of flow accident (LOFA) condition of PEACER-300 is the main target scenario of HELIOS. Figure 15.2.2 shows an overall schematic design of PEACER-300 and the HELIOS demonstration LBE test loop.

Figure 15.2.3 shows the thermo-hydraulic loop configuration of the HELIOS system (except the support structure and material corrosion test section). It is comprised of the mock-up core, expansion tank, heat exchanger, mechanical pump, orifice, several gate valves and pipe system. The mock-up core generates heat by using four electrical heaters arranged in a square lattice as a principal heat source, having a maximum 60 kW thermal capacity. A heat exchanger removes the heat of LBE by flowing thermo-oil instead of water with counter-current flow between two fluids. In order to test the natural circulation capability of PEACER-300, the elevation difference between the heat source (a mock-up core) and the heat sink (a heat exchanger) is kept the same as that of PEACER-300, at about 7.4 m with a total height of 12 m.

Pressure losses and LBE temperatures are the main variables in the LACANES benchmarking study. Figure 15.2.3 also indicates four differential pressure metres[2] and ten thermocouples[3] installed at several regions. Four differential pressure metres have been installed in mock-up core, orifice, gate valve and a combined region that covers the area from core outlet to orifice outlet.

Figure 15.2.2: Design schematic of PEACER-300 and picture of demonstration LBE test loop, HELIOS

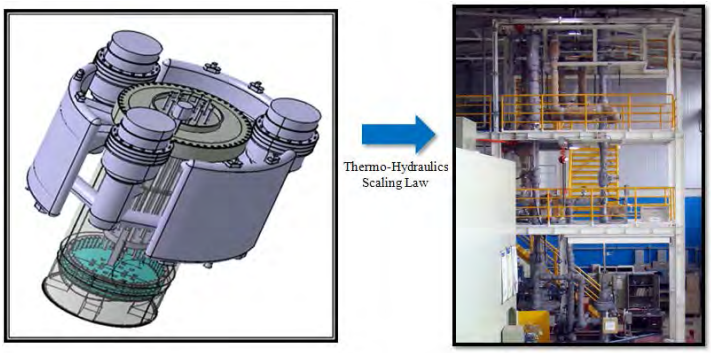

Figure 15.2.3: Entire loop configuration including several locations of differential pressure metres and thermocouples in HELIOS

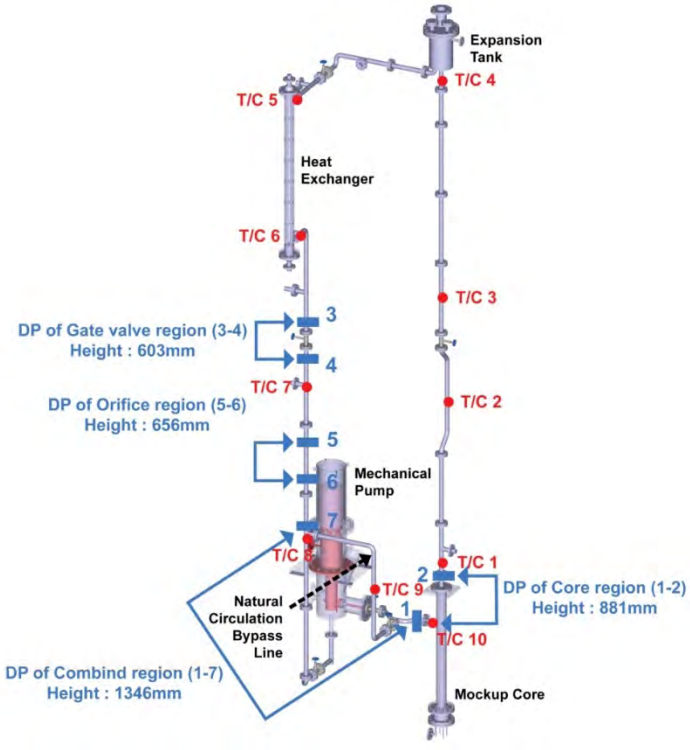

2. Rosemount-3051 CD3A, Rosemount Company, 2.5 bar measurement span with error of ±0.065% full scale.
3. Type K with stainless steel 304, calibrated with ±0.5°C error.

15.3 Pressure loss correlations used in design and analysis models

The thermal-hydraulic analysis of a complex cooling system is usually performed by means of system codes with suitable lamped models in order to describe all relevant physical phenomena and components. The increased calculation power has made possible the use of detailed local calculation by CFD codes for the most complex phenomena and components. Both system and CFD codes have been applied by different participants in LACANES. The different results are compared and analysed in the following sections so as to evaluate the code predictions and provide recommendations for the thermal-hydraulic modelling of the HLM loop.

15.3.1 *Design and analysis codes used in benchmarking*

The system codes applied in LACANES benchmarking Phase I were HETRAF, RELAP5, LegoPST, MARS-LBE and TRACE. CFD codes were CFX® and Star-CD®.

Table 15.3.1: All codes used in the LACANES benchmark programme

Code	Type	Reference
HETRAF	System code	Cheng (1994)
RELAP5	System code	INL (2001)
LegoPST	System code	Casamassima (2008)
MARS-LBE	System code	KAERI (2006)
TRACE	System code	US NRC (2007a, 2007b)
CFX®	Computational fluid dynamics	ANSYS (2009)
Star-CD®	Computational fluid dynamics	CD-adapco (2007)

Each system code has a module that calculates pressure losses by defining the friction loss coefficients and form loss coefficients with Eq. (15.3.1):

$$\Delta P_{total} = \frac{1}{2}\rho \sum_{i} V^2_{i(average)} \left(f\frac{L}{D} + K \right)_i \tag{15.1}$$

where P, i, ρ, V, f, L, D and K are pressure, the number of components, fluid density, average flow velocity, friction factor, length, the diameter of a component and the form loss coefficient, respectively.

The last term in the right hand side of Eq. (15.3.1) is defined as:

$$\text{Pressure loss coefficient} = \left(f\frac{L}{D} + K \right) \tag{15.2}$$

where $f(L/D)$ is the friction loss coefficient for a component with no change in cross-sectional dimensions.

Pressure loss coefficient for each geometry was calculated by the correlations located in the internal structure of code that was induced by the hydraulic-resistance handbooks. If there are no internal correlations or parameters for pressure loss coefficients in the system codes, it should be defined by users from the hydraulic-resistance handbooks. In the following sections, all correlations or parameters employed by participants to predict the pressure losses of HELIOS loops are introduced.

15.3.2 *Pipe wall friction loss correlations*

For the calculation of the distributed pressure loss all codes utilise a relation of Eq. (15.1), where the friction factor is evaluated with different correlations. These correlations are reported in Table 15.3.2 where information is provided on the range of applicability and literature references.

Table 15.3.2: Formulas for calculation of friction loss coefficients

		Correlations	Applicable range	Reference
Laminar flow		$f = \frac{64}{Re}$ (Hagen-Poiseuille law)	Up to $Re \approx 2\,000$	White (1986)
Transient or turbulent flow	1	$f_{L,T} = \left(3.75 - \frac{8250}{Re}\right)\left(f_{T,3000} - f_{L,2200}\right) + f_{L,2200}$ $f_{L,2200}$: Laminar friction factor at Re = 2 200 $f_{T,3000}$: Turbulent friction factor at Re = 3 000	2 200 < Re < 3 000	Colerbrook (1939) Zigrang (1985)
		$\frac{1}{\sqrt{f_T}} = -2\log_{10}\left\{\frac{\varepsilon}{3.7D} + \frac{2.51}{Re}\left[1.14 - 2\log_{10}\left(\frac{\varepsilon}{D} - \frac{21.25}{Re^{0.9}}\right)\right]\right\}$	Re > 3 000	
	2	$\frac{1}{\sqrt{f}} = -2\log_{10}\left\{\frac{\varepsilon}{3.7D} + \frac{2.51}{Re\sqrt{f}}\right\}$ (Colebrook's interpolation formula)	Re > 2 000	Idelchik (1994)
	3	$f = 0.11\left(\frac{68}{Re} + \frac{\varepsilon}{D}\right)^{0.25}$ (Altshul's approximate formula)	Re > 2 090·$(\varepsilon/D)^{0.635}$	Idelchik (1994)
	4	$f = \frac{1}{\left[2\log_{10}\left(\frac{2.51}{Re\sqrt{f}}\right) + \frac{\varepsilon}{3.7D}\right]^2}$	Re > 2 090·$(\varepsilon/D)^{0.635}$	Idelchik (1994)
	5	$f = \frac{0.3164}{Re^{0.25}}$ (Blasius)	4 000 < Re < 10^5	Idelchik (1994)
	6	$f = 8\cdot\left[\left(\frac{8}{Re}\right)^{12} + \frac{1}{(A+B)^{1.5}}\right]^{1/12}$ $A = \left\{2.457\cdot\ln\left[\left(\frac{7}{Re}\right)^{0.9} + 0.27\cdot\left(\frac{\varepsilon}{D}\right)\right]\right\}^{16}$ $B = \left(\frac{37530}{Re}\right)^{16}$ (Churchill's formula)	All ranges	Idelchik (1994)
	7	$f = \left(1.8\log_{10}\frac{8.25}{\frac{56}{Re} + \frac{\varepsilon}{D}}\right)^{-2}$	For turbulent flow	Slissky (1983)

f, r, D, Re_D and ε are friction factor, radius of pipe, diameter of pipe, Reynolds number and absolute surface roughness, respectively.

All correlations are expressed as function of the Reynolds number ($\rho V D/\mu$) and relative roughness (ε/D). Figure 15.3.1 shows all the correlations listed in Table 15.3.2. As Reynolds number increases, the tendency of friction factor is largely changed near the critical Reynolds number (about 2 000-3 000). All participants used the Hagen-Poiseuille law (see Table 15.3.2) for the laminar flow region ($Re < 2\,000$) which is an analytical solution for pipe wall friction. In the transient and turbulent flow region, all correlations are obtained from experimental results (the sixth correlation of Table 15.3.2, Churchill formulation, covers the full range of Reynolds number and relative roughness by linking friction factors of all range of Reynolds number).

Figure 15.3.1: Comparison of correlations for friction factor ($\varepsilon/D = 5{\cdot}10^{-5}$)

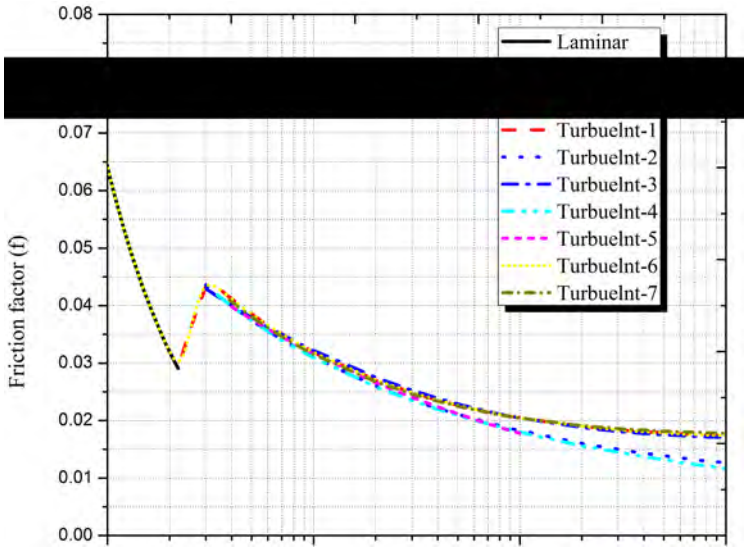

15.3.3 *Orifice*

In most fluid systems, an orifice is adopted to measure the mass flow rate by using the correlation between mass flow rate and pressure drop of fluid as in Eq. (15.2). As the Figure 13.3.2 flow area is sharply decreased in orifice tap in order to obtain a large decreasing of pressure, which indicates the mass flow rate. Afterwards the pressure is recovered by area expansion, but some of the pressure cannot be recovered due to irreversible energy loss. The pressure losses calculated in the benchmark are the latter, after recovery by expansion effect. Table 15.3.3 shows the pressure losses of an orifice region that corresponds to non-recovered pressure after expansion of flow.

Figure 15.3.2: Orifice geometry

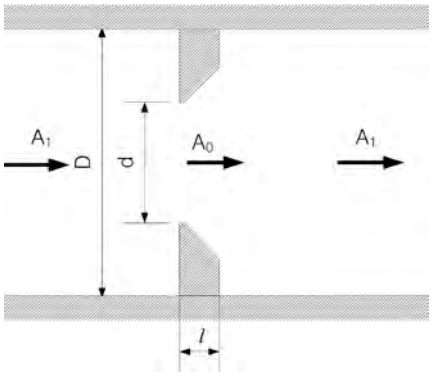

Table 15.3.3: Formulas for calculation of form loss coefficients in orifices

	Correlations	Applicable range	Reference
1	$K = \left(1 + 0.707\sqrt{1 - \frac{A_0}{A_1}} - \frac{A_0}{A_1}\right)^2 \left(\frac{A_1}{A_0}\right)^2$	$Re > 10^5$	Idelchik (1994)
2	$K = \left(1 - \frac{A_0}{A_1} + \sqrt{\xi}\left(1 - \frac{A_0}{A_1}\right)^{0.375}\right)^2 \left(\frac{A_1}{A_0}\right)^2$ where $\xi = 0.13 + 0.34 \times 10^{-\left[3.4(l/D) + 88.4(l/D)^{2.3}\right]}$	$Re > 10^4$	Idelchik (1994)
3	$K = \left(0.5\left(1 - \frac{A_0}{A_1}\right) + \left(1 - \frac{A_0}{A_1}\right)^2 + \tau\sqrt{1 - \frac{A_0}{A_1}}\left(1 - \frac{A_0}{A_1}\right)\right)\left(\frac{A_1}{A_0}\right)^2$ $\tau = (2.4 - \bar{l}) \times 10^{-\varphi(\bar{l})}$ $\varphi(\bar{l}) = 0.25 + \frac{0.535\bar{l}^{-8}}{0.05 + \bar{l}^{-8}}$	$Re > 10^3$	Idelchik (1994)

Where *f, r, D, Re_D* and ε are friction factor, radius of pipe, diameter of pipe, Reynolds number and absolute surface roughness, respectively.

All the correlations used in prediction of pressure loss for an orifice depend on the ratio of pipe flow area to orifice tap small area, regardless of Reynolds number, as shown in Figure 15.3.3. The area ratio (A_0/A_1) in the orifice of HELIOS is about 3.8. Experimental results (having a range of 10.9-11.6, almost constant independent of Reynolds numbers) show good agreement with used correlations.

Figure 15.3.3: Comparison of orifice correlations with experimental result

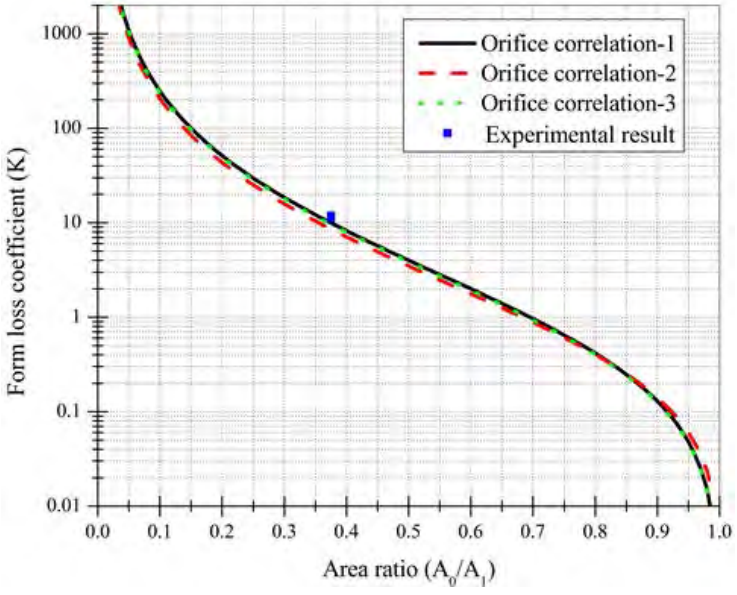

15.3.4 *Spacers*

Pressure losses of core or heat exchanger are dominant among those of the fluid system because of its small flow area and complex geometry. Grid spacers that support the core rods or steam generator tubes are the highest regions of pressure losses. Rehme (1973)

developed a correlation of grid spacer in a fuel bundle by many sets of grid spacers' experimental data that pronounced the effect of the blocking area ratio ($A_{grid\text{-}spacer}/A_{flow}$) as shown in the formulation of the Table 15.3.4.

Figure 15.3.4: Configuration of spacer

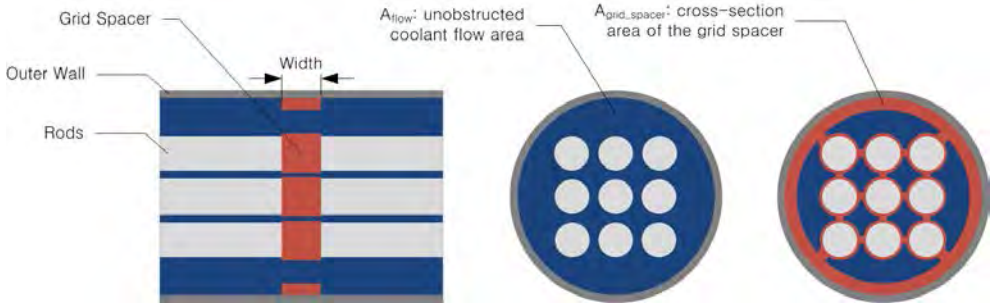

Table 15.3.4: Formulas for calculation of form loss coefficients in spacers

	Correlations	Reference
1	$K = C_v \left(\frac{A_{grid\text{-}spacer}}{A_{flow}} \right)^2$ $C_v = 3.5 + \frac{73.5}{Re^{0.264}} + \frac{2.79 \cdot 10^{10}}{Re^{2.79}}$ (C_v: modified drag coefficient)	Rehme (1973)

Where $A_{grid\text{-}spacer}$ and A_{flow} are the cross-section area of the grid spacer and the unobstructed coolant flow area, respectively.

In Rehme's correlation the predicted pressure losses of grid spacer depend on the area ratio of obstruction and flow ($A_{grid\text{-}spacer}/A_{flow}$), and on modified drag coefficient which is in turn determined as function of Reynolds number. However, experimental results from the HELIOS loop showed a discrepancy from those predictions with Rehme's correlation, as shown in Figure 15.3.5.

Figure 15.3.5: Comparison of grid spacer correlation (Rehme's correlation) with experimental result

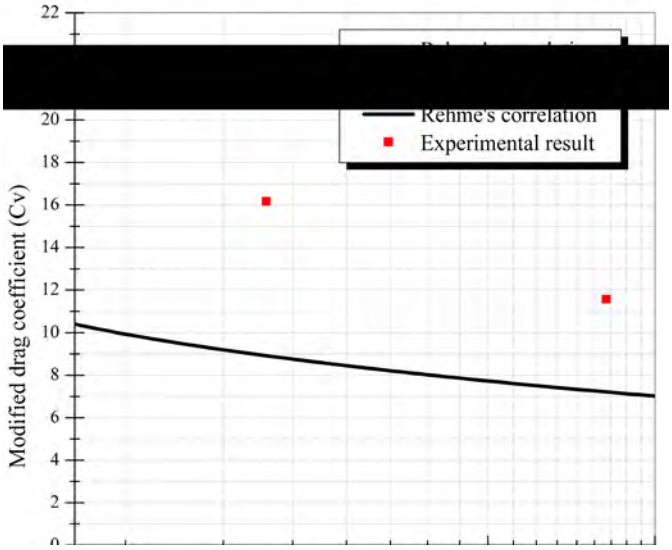

In contrast the detailed modelling of the complex geometry using CFD tools produced results that agree well with HELIOS experimental data, as shown in the figure above. It has been found that CFD modelling always provided more accurate results than experimental correlations (Cho, 2011). Further examples are given in Section 15.3.6.

15.3.5 *Sudden area change*

In regions like the gate valve and connecting piece of flange section, flow areas suddenly change, which disturbs the flow. The sudden area changes are illustrated in Figure 15.3.6 and correlations are listed in Table 15.3.5.

Figure 15.3.6: Geometries of sudden area changes

Sudden expansion (left), sudden contraction (right)

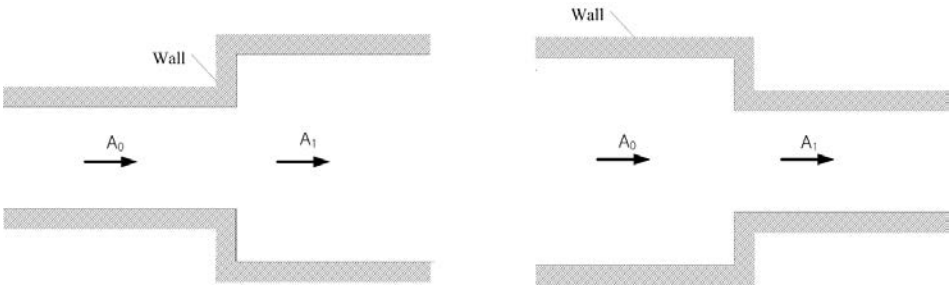

Table 15.3.5: Formulas for calculation of form loss coefficients in sudden expansion of flow area

Sudden expansion	Range	Reference
$K = \left(1 - \frac{A_0}{A_1}\right)^2$ Borda-Carnot's formula	$Re > 3.3 \cdot 10^3$	Idelchik (2000)

Table 15.3.6: Formulas for calculation of form loss coefficient in sudden contraction of flow area

	Sudden contraction	Range	Reference
1	$K = 0.5\left(1 - \frac{A_1}{A_0}\right)$	$Re > 10^4$	Idelchik (2000)
2	$K = 0.5\left(1 - \frac{A_1}{A_0}\right)^{3/4}$	$Re > 10^4$	Idelchik (1992)
3	$K = 0.5 - 0.7 \cdot \left(\frac{A_1}{A_0}\right) + 0.2 \cdot \left(\frac{A_1}{A_0}\right)^2$	$Re > 10^4$	Massey (1968)
4	$K = \left(1 - \frac{A_1}{A_c}\right)^2$ $\frac{A_c}{A_1} = 0.62 + 0.38\left(\frac{A_1}{A_0}\right)^3$	All range	Vennard (1961)

The sudden area changes depend only on the cross-sectional area ratio. The formula used for sudden expansion is that of Borda-Carnot, though different correlations are used for sudden contraction. All correlations are shown in Figure 15.3.7.

Figure 15.3.7: Comparison of correlations for sudden area change

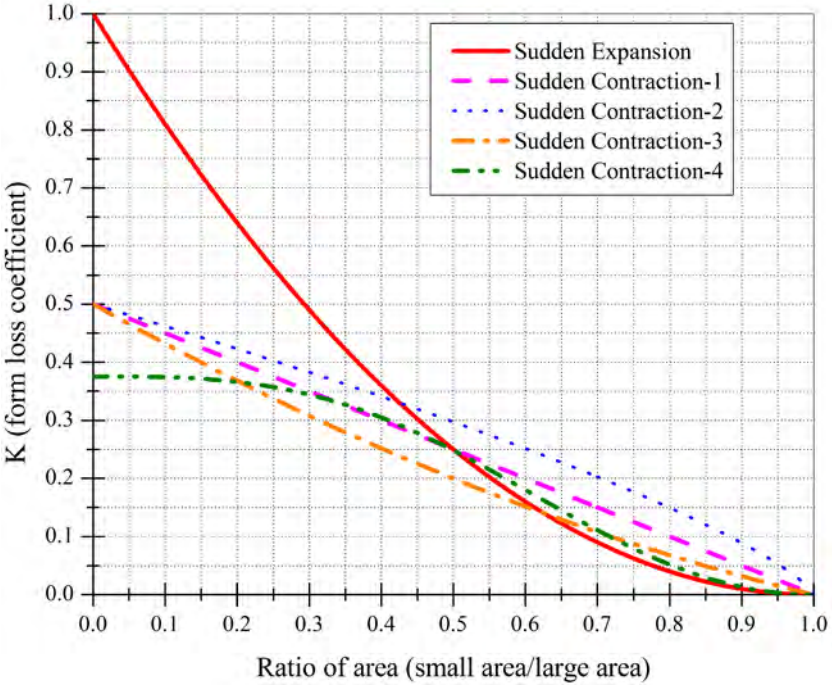

15.3.6 *CFD modelling and comparison with correlations for complex components*

Available friction loss coefficients for a straight pipe have shown to yield consistent values, suggesting that small variations among correlations can be attributed to their original development processes. On the other hand, the various correlations for a complex geometry used in the LACANES benchmark revealed quite significant discrepancies. The main reason for this scatter is that pressure loss correlations were derived from unique designs with specific arrangements of complicated components that are different from HELIOS cases. The CFD model has been extensively demonstrated to be an accurate numerical tool and effective for understanding complex flow patterns (Dhotre, 2004; Cheng, 2006). It provides consistent results with accurate experimental data for the range of measurements made in LACANES benchmarking. Therefore, CFD modelling has been recommended for complex geometry.

The core region of the HELIOS loop is shown in Figure 15.3.8. It consists of a 2 m long vessel with a concentric barrel containing a 1.4 m heating rod bundle in its centre. The flow enters the mock-up core vessel at approximately two-thirds the height through the vessel inlet. It then flows downwards in a gap between the vessel and the barrel, and the upward flow is heated by four rod bundles. Three grid spacers are located in the centric barrel to support the four rods having a 5 mm thickness (Jeong, 2006).

The boundary conditions of the CFX models are defined at inlet, outlet and walls. At the inlet, the mass flow rate of the fluid is specified and the direction of flow is defined normal to the cross-section area. At all walls, a no-slip between fluid and the wall is imposed. Neither buoyancy model nor a thermal energy calculation was conducted in the CFX models because experimental conditions for the forced convection are isothermal and steady state (250°C).

Figure 15.3.8: Flow pathways and drawings of the core region

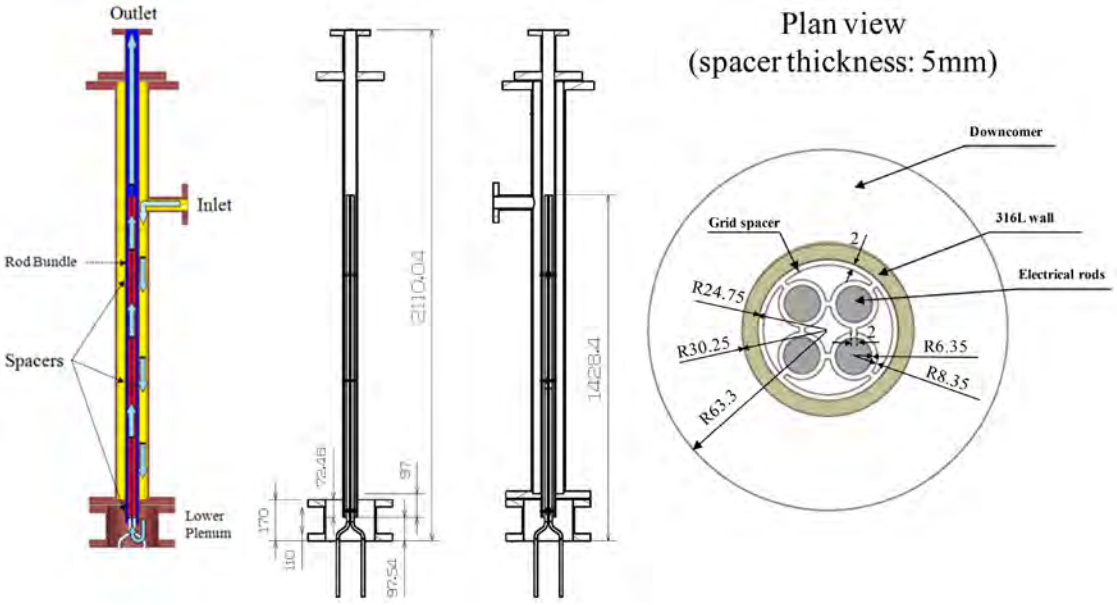

Figure 15.3.9: Results of pressure distribution by CFX simulation of the mock-up core at 13.57 kg/s condition

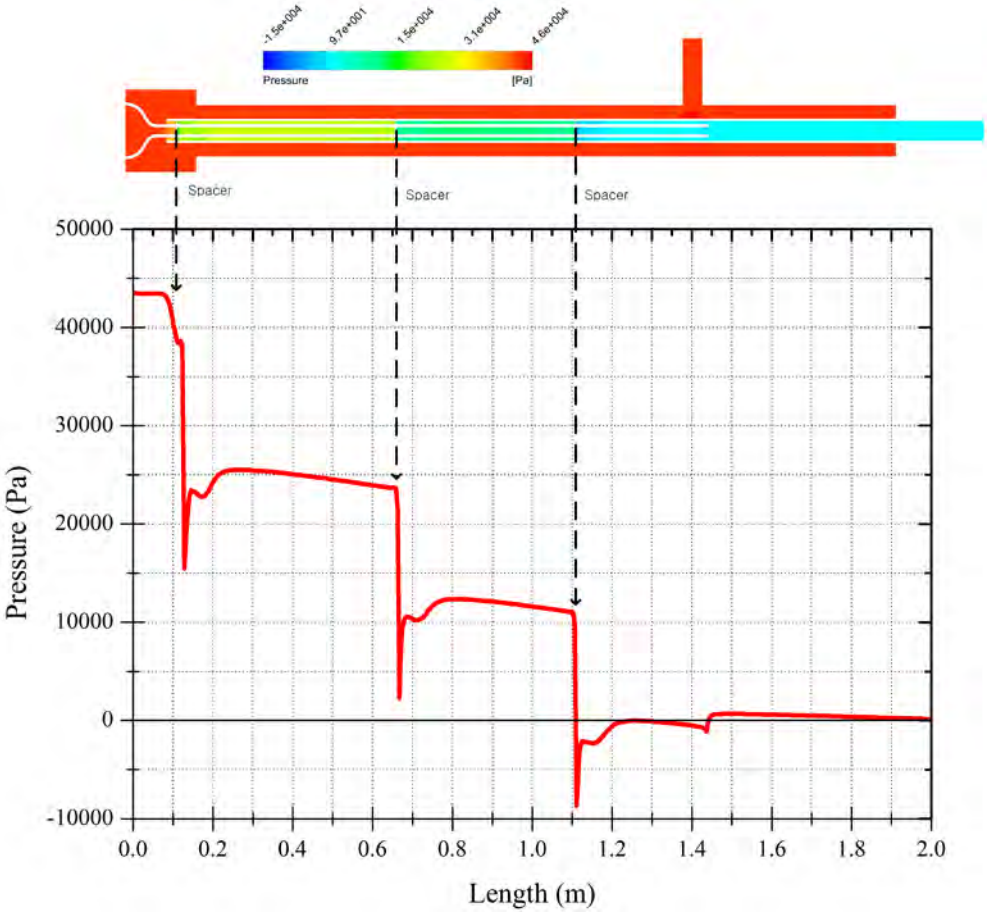

The most important feature of the computed pressure distribution is its step profile with near uniform pressure in the subchannels and large pressure jumps across each of the spacers. Pressure overshoots are predicted in the spacer regions because spacers have not only sudden expansions but also sudden contractions. As the flow area is suddenly contracted (to one-half of the flow area at the spacers' entrance), the pressure is sharply decreased. Then, pressure is recovered immediately after because flow area is suddenly expanded, having twice the flow area at the spacers' exit (Batta, 2010).

Based on the system code modelling of pressure losses in the mock-up core region, a substantial discrepancy from experimental data was found. CFD simulations for the mock-up core also showed that the pressure drop is dominated by spacer pressure losses. Each of the three spacers results in substantially different pressure losses due to different levels of flow development. Measured total pressure loss of the mock-up core (52.5 kPa) matches CFD results (46 kPa) very well.

15.4 Best practice guidelines

Based on findings from LACANES benchmarking, a set of best practice guidelines has been recommended in Table 15.4.1 for the prediction of pressure losses in LACANES. In the CFD simulations that provided accurate predictions, all prediction results were always in good agreement with experimental data within ±15% in pressure drop. When geometry is complicated and there is no available experimental data, CFD simulation can be recommended as the best practice.

Table 15.4.1: Recommended correlations

<table>
<tr><th>Components</th><th>Geometry</th><th>Recommended correlations</th><th>Reference</th></tr>
<tr><td>Orifice</td><td> 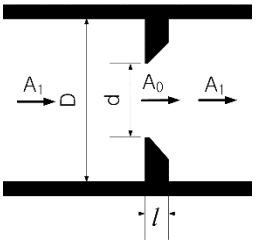
</td><td>$K = \left(1 + 0.707\sqrt{1 - \frac{F_0}{F_1}} - \frac{F_0}{F_1}\right)^2 \left(\frac{F_1}{F_0}\right)^2$
$Re > 10^5$</td><td>Idelchik (1994)</td></tr>
<tr><td>Discharge into a vessel</td><td> 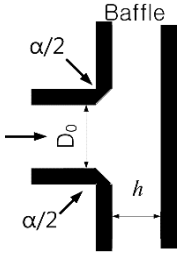
</td><td>
<table>
<tr><th rowspan="2">α deg</th><th colspan="10">h/D0</th></tr>
<tr><th>0.10</th><th>0.15</th><th>0.20</th><th>0.25</th><th>0.30</th><th>0.40</th><th>0.50</th><th>0.60</th><th>0.70</th><th>1.0</th></tr>
<tr><td>0</td><td>–</td><td>–</td><td>–</td><td>–</td><td>–</td><td>–</td><td>1.37</td><td>1.20</td><td>1.11</td><td>1.00</td></tr>
<tr><td>15</td><td>–</td><td>–</td><td>–</td><td>1.50</td><td>1.06</td><td>0.72</td><td>0.61</td><td>0.59</td><td>0.58</td><td>0.58</td></tr>
<tr><td>30</td><td>–</td><td>–</td><td>1.23</td><td>0.79</td><td>0.66</td><td>0.64</td><td>0.66</td><td>0.66</td><td>0.67</td><td>0.67</td></tr>
<tr><td>45</td><td>–</td><td>1.50</td><td>0.85</td><td>0.73</td><td>0.75</td><td>0.79</td><td>0.81</td><td>0.82</td><td>0.82</td><td>0.82</td></tr>
<tr><td>60</td><td>–</td><td>0.98</td><td>0.76</td><td>0.80</td><td>0.90</td><td>0.96</td><td>1.00</td><td>1.01</td><td>1.02</td><td>1.02</td></tr>
<tr><td>90</td><td>1.50</td><td>0.72</td><td>0.74</td><td>0.83</td><td>0.89</td><td>0.94</td><td>0.96</td><td>0.98</td><td>1.00</td><td>1.00</td></tr>
</table>
</td><td>Idelchik (1994)</td></tr>
<tr><td>Entrance in tubes</td><td> 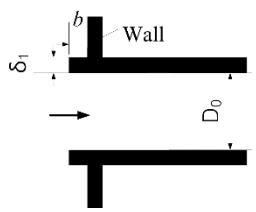
</td><td>
<table>
<tr><th rowspan="2">δ1/D0</th><th colspan="11">b/D0</th></tr>
<tr><th>0</th><th>0.002</th><th>0.005</th><th>0.010</th><th>0.020</th><th>0.050</th><th>0.100</th><th>0.200</th><th>0.300</th><th>0.500</th><th>∞</th></tr>
<tr><td>0</td><td>0.50</td><td>0.57</td><td>0.63</td><td>0.68</td><td>0.73</td><td>0.80</td><td>0.86</td><td>0.92</td><td>0.97</td><td>1.00</td><td>1.00</td></tr>
<tr><td>0.004</td><td>0.50</td><td>0.54</td><td>0.58</td><td>0.63</td><td>0.67</td><td>0.74</td><td>0.80</td><td>0.86</td><td>0.90</td><td>0.94</td><td>0.94</td></tr>
<tr><td>0.008</td><td>0.50</td><td>0.53</td><td>0.55</td><td>0.58</td><td>0.62</td><td>0.68</td><td>0.74</td><td>0.81</td><td>0.85</td><td>0.88</td><td>0.88</td></tr>
<tr><td>0.012</td><td>0.50</td><td>0.52</td><td>0.53</td><td>0.55</td><td>0.58</td><td>0.63</td><td>0.68</td><td>0.75</td><td>0.79</td><td>0.83</td><td>0.83</td></tr>
<tr><td>0.016</td><td>0.50</td><td>0.51</td><td>0.51</td><td>0.53</td><td>0.55</td><td>0.58</td><td>0.64</td><td>0.70</td><td>0.74</td><td>0.77</td><td>0.77</td></tr>
<tr><td>0.020</td><td>0.50</td><td>0.51</td><td>0.51</td><td>0.52</td><td>0.53</td><td>0.55</td><td>0.60</td><td>0.66</td><td>0.69</td><td>0.72</td><td>0.72</td></tr>
<tr><td>0.024</td><td>0.50</td><td>0.50</td><td>0.50</td><td>0.51</td><td>0.52</td><td>0.53</td><td>0.58</td><td>0.62</td><td>0.65</td><td>0.68</td><td>0.68</td></tr>
<tr><td>0.030</td><td>0.50</td><td>0.50</td><td>0.50</td><td>0.52</td><td>0.52</td><td>0.52</td><td>0.54</td><td>0.57</td><td>0.59</td><td>0.61</td><td>0.61</td></tr>
<tr><td>0.040</td><td>0.50</td><td>0.50</td><td>0.50</td><td>0.51</td><td>0.51</td><td>0.51</td><td>0.51</td><td>0.52</td><td>0.52</td><td>0.54</td><td>0.54</td></tr>
<tr><td>0.050</td><td>0.50</td><td>0.50</td><td>0.50</td><td>0.50</td><td>0.50</td><td>0.50</td><td>0.50</td><td>0.50</td><td>0.50</td><td>0.50</td><td>0.50</td></tr>
<tr><td>∞</td><td>0.50</td><td>0.50</td><td>0.50</td><td>0.50</td><td>0.50</td><td>0.50</td><td>0.50</td><td>0.50</td><td>0.50</td><td>0.50</td><td>0.50</td></tr>
</table>
</td><td>Idelchik (1994)</td></tr>
</table>

Table 15.4.1: Recommended correlations (*cont.*)

Components	Geometry	Recommended correlations	Reference
Straight pipe	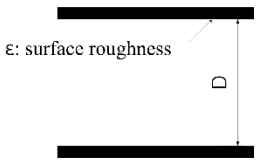	$f = 8 \cdot \left[\left(\frac{8}{Re} \right)^{12} + \frac{1}{(A+B)^{1.5}} \right]^{1/12}$ $A = \left\{ 2.457 \cdot \ln \left[\left(\frac{7}{Re} \right)^{0.9} + 0.27 \cdot \left(\frac{\varepsilon}{D} \right) \right] \right\}^{16}$ $B = \left(\frac{37530}{Re} \right)^{16}$	Idelchik (1994)
Sudden changes	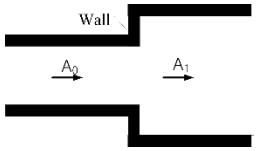	$K_{SE} = \left(1 - \frac{F_0}{F_1} \right)^2$ for sudden expansion	Idelchik (1994)
	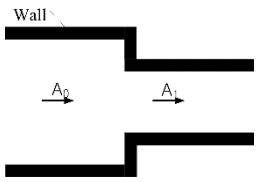	$K_{SC} = 0.5 - 0.7 \cdot \left(\frac{F_1}{F_0} \right) + 0.2 \left(\frac{F_1}{F_0} \right)^2$ for sudden contraction	Massey (1968)

15.5 Summary and recommendations for future work

Guidelines for the prediction of pressure losses were obtained based on a comparison between predictions calculated by system codes or CFD codes and experimental data from HELIOS measurements. The comparison included both simple geometries such as pipe and complicated ones such as the mock-up core region. For simple geometries existing correlations were found adequate for use in design and analysis. However, experimental data or CFD modelling is needed for complicated geometries.

These guidelines can be recommended only for the range of Reynolds number of the HELIOS experiments, i.e. $10^4 < Re_D < 2 \cdot 10^5$.

Future benchmarking with natural circulation will be used to verify that the best practice guidelines are applicable not only for forced convection but also for natural circulation, which is becoming increasingly important for passive safety assurance.

References

Ait Abderrahim, H.et al. (2001), "MYRRHA: A Multipurpose Accelerator Driven System for Research and Development", *Nuclear Instruments and Methods in Physics Research*, 463, pp. 487-494.

ANSYS, Inc. (2009), *ANSYS CFX Reference Guide*, ANSYS, Inc., Canonsburg, Pennsylvania.

Casamassima, V. and A. Guagliardi (2008), "A Modular Approach to Lead-Cooled Reactors Modelling", *Journal of Nuclear Materials*, 376, pp. 293-296.

Cheng, X. (1994), "Numerical Analysis of Thermally Induced Transients in Forced Flow of Supercritical Helium", *Cryogenics*, Vol. 34, 3, pp. 195-201.

Cheng, X. and A. Class (2008), "Analysis of Dynamic Behaviour of MEGAPIE Cooling System", *ICAPP'08*, Anaheim, CA, 8-12 June, paper 810.

Cheng, X. and N.I. Tak (2006), "CFD Analysis of Thermal-Hydraulic Behavior of Heavy Liquid Metals in Sub-Channels", *Nuc. Eng. Des.*, Vol. 236, 18, pp. 1874-1885.

Cho J.H.et al. (2011), "Benchmarking of Thermal Hydraulic Loop Models for Lead Alloy Cooled Advanced Nuclear Energy System (LACANES), Phase I: Isothermal Steady State Forced Convection", *Journal of Nuclear Materials*, Vol. 415, 3, pp. 404-414.

Choi, S.et al. (2011), "PASCAR: Long Burning Small Modular Reactor Based on Natural Circulation", *Nuclear Engineering and Design*, Vol. 241, 5, pp. 1486-1499.

Colebrook, C.F. (1939), "Turbulent Flow in Pipes with Particular Reference to the Transient Region Between Smooth and Rough Pipe Laws", *Journal of Institute of Civil Engineers*, 11, pp. 133-156.

Collier, A.M.et al. (2004), *User Documentation for KINSOL v2.2.0*, LLNL technical report UCRL-SM-208116, Lawrence Livermore National Laboratory, Livermore, CA.

Cori, R., G. Migliavacca and S. Spelta (1997), "A New Approach to LEGO Steady State Calculation for Power Plants Dynamic Models", *15th IMACS World Congress on Scientific Computation Modeling Applied Mathematics*, Berlin.

Dhotre, M.T. and J.B. Joshi (2004), "Two-Dimensional CFD Model for the Prediction of Flow Pattern, Pressure Drop and Heat Transfer Coefficient in Bubble Column Reactors", *Chemical Engineering Research and Design*, Vol. 82,6, 689-707.

Garbossa, G.et al. (1989), "A Model of Alto Lazio Boiling Water Reactor Using the Lego Code: Nuclear Steam Supply System Simulation", *7th Power Plant Dynamics, Control and Testing Symposium*, Knoxville, Tennessee, 15-17 May.

Hwang, I.S.et al. (2000), "The Concept of Proliferation-Resistant, Environment-Friendly, Accident-Tolerant, Continual and Economical Reactor (PEACER)", *Progress in Nuclear Energy*, Vol. 37, 1-4, pp. 217-222.

Idelchik, I.E. (1944), "Hydraulic Resistance During Flow Entrance in Channels and Passage Through Orifices", *Prom. Aerodin.*, Vol.2,pp. 27-57, BNT, NKAP.

Idelchik I.Eet al. (1986), *Handbook of Hydraulic Resistance*, 2nd edition, Hemisphere Publishing Corp., New York.

Idelchik, I.E. (1992), *Hydraulic Resistance Handbook*, Mashnostroenie, Moscow.

Idelchik, I.E. (2000), *Handbook of Hydraulic Resistance*, 3rd edition, CRC.

INL (Idaho National Laboratory) (2001), *RELAP5/Mod.3.3 Code Manual*, INL, Idaho Falls, Idaho.

Jaeger, W. and V. Sánchez (2008a), "Analyses of a LBE-Diphyl THT Heat Exchanger with the System Code TRACE", *Proc. of the 16th International Conference on Nuclear Engineering (ICONE-16)*, Orlando, Florida.

Jaeger, W. and V. Sánchez (2008b), "Influence of Oxide Layers on the Cladding Material in a Liquid Lead Environment: A Comparison Between MATRA and TRACE", *Proc. of the International Conference on Reactor Physics (PHYSOR-08)*, Interlaken, Switzerland.

Jaeger, W., V. Sánchez and B. Feng (2008c), "Analysis of an XADS Target with the System Code TRACE", *Proc. of the International Youth Nuclear Congress (IYNC-08)*, Interlaken, Switzerland.

Jeong, S.H. (2006), *Development of an Integral Test Loop, HELIOS and Investigation of Natural Circulation Ability for PEACER*, Nuclear Engineering Department, Seoul National University, Seoul.

KAERI (Korea Atomic Energy Research Institute) (2006), *MARS Code Manual Volume I – Code Structure, System Models, and Solution Methods*, Thermal Hydraulic Safety Research Department, KAERI, Korea.

Kirillov P.L., Yu.S. Yuriev and V.P. Bobkov (1990), "Heat-hydraulic Calculation Handbook", *Energoatomizdat*, Moscow.

Massey, B.S. (1968), *Mechanics of Fluids*, D. Van Nostrand Co., New York, pp. 217-219.

Meloni, P.et al. (2001), "Implementation and Preliminary Verification of the RELAP5/PARCS Code for Pb-Bi Cooled Subcritical System", *Proc. of the Int. Conference on Accelerator Applications (AccApp01)*, American Nuclear Society, Reno, NV.

Meloni, P.et al. (2002), "Natural Circulation of Lead-bismuth in a One-dimensional Loop: Experiments and Code Predictions", *Proc. of the International Conference ICONE-10*, Arlington, VA.

Meloni, P.et al. (2004), "Investigation of RELAP5 Capability to Simulate the LBE Cooling System Thermal-hydraulic", *Proc. of the 8th Information Exchange Meeting on Transmutation and Partitioning (IEMTP)*, Las Vegas, NV.

Meloni, P.et al. (2008), "Verification of the RELAP5 Code Against the MEGAPIE Irradiation Experiment", *10th Information Exchange Meeting on Transmutation and Partitioning (IEMTP)*, Mito, Japan, 6-10 October.

Rehme, K. (1973), "Pressure Drop Correlations for Fuel Element Spacers", *Nuclear Technology Review*, Vol. 17.

Slissky, P.M. (1983), "Methodical Recommendations to Calculation of Friction Factors in Tubes for Transition Zone", *Proc. of Sc.-Tech. Hydraulics*, pp. 31-44.

Spelta, S. (n.d.) *Confrontation du modèle LEGO-REP 900 MW CP2 avec l'essai d'ilotage de St. Laurent B1 du 22/7/81*, SEPTEN (EDF), Internal Report TH-85-09 A (DF07).

Spelta, S. (1985), "An Application of the LEGO Packages to PWR Power Plant Modeling", *Proc. of the 5th International Conference on Mathematical Modelling*, Berkley, CA.

Spelta, S.et al. (1989), "A Model of Alto Lazio Boiling Water Reactor Using the Lego Code: Balance of Plant Simulation", *7th Power Plant Dynamics, Control and Testing Symposium*, Knoxville, Tennessee, 15-17 May.

Todreas, N.E. and M.S. Kazimi (1990), *Nuclear System*, Hemisphere Publishing Corp., New York.

US NRC (United States Nuclear Regulatory Commission) (2007a), *TRACE V5.0 Theory Manual: Field Equations, Solution Methods and Physical Models*, US NRC, Washington, DC.

US NRC (2007b), *TRACE V5.0 User's Manual*, US NRC, Washington, DC.

VDI (Verein Deutscher Ingenieure) (ed.) (2006), *VDI-Wärmeatlas 3.0*, Springer Verlag, Berlin, Heidelberg.

Vennard, J.K. (1961), "One Dimensional Flow", *Handbook of Fluid Dynamics*, 1st ed., V.L. Streeter (ed.), McGraw-Hill, New York.

White, F.M. (1986), *Fluid Mechanics*, 2nd edition, McGraw-Hill.

Zigrang, D.J. and N.D. Sylvester (1982), "Explicit Approximations to the Solution of Colebrook's Friction Factor Equation", *AIChE Journal*, Vol. 28, No. 3, pp. 514-515.

Zigrang, D.J. and N.D. Sylvester (1985), "A Review of Explicit Friction Factor Equations", *Transactions of ASME, Journal of Energy Resource Technology*, 107, pp. 280-283.

Zrodnikov, A.V.et al. (2008), "Innovative Nuclear Technology Based on Modular Multi-purpose Lead-bismuth Cooled Fast Reactors", *Progress in Nuclear Energy*, Vol. 50, 2-6, pp.170-178.

Appendix 1. List of contributors

1. Introduction

C. Fazio (JRC-ITU, European Commission)

2. Thermophysical and electric properties of liquid lead, bismuth and lead-bismuth eutectic

V.P. Sobolev (SCK•CEN, Belgium)

A. Gessi (ENEA, Italy)

3. Thermodynamic relationships and heavy liquid metal interaction with other coolants

L. Martinelli (CEA, France)

S. Gossé (CEA, France)

P. Agostini (ENEA, Italy)

F. Balbaud-Célérier (CEA, France)

A. Ciampichetti (ENEA, Italy)

J-L. Courouau (CEA, France)

N. Li (Xiamen University, China)

H. Glasbrenner (ENSI, Switzerland)

V.P. Sobolev (SCK•CEN, Belgium)

A. Terlain (CEA, France)

4. Chemistry control and monitoring systems

J-L. Courouau (CEA, France)

5. Properties of irradiated LBE and Pb

J. Neuhausen (PSI, Switzerland)

A. Aerts (SCK•CEN, Belgium)

H. Glasbrenner (ENSI, Switzerland)

S. Heinitz (PSI, Switzerland)

M. Jolkkonen (KTH, Sweden)

5. Properties of irradiated LBE and Pb (*cont.*)

Y. Kurata (JAERI, Japan)

T. Obara (Tokyo Tech, Japan)

N. Thiollière (SUBATECH/EMN, France)

L. Zanini (PSI, Switzerland)

6. Compatibility of structural materials with LBE and Pb: Standardisation of data, corrosion mechanism and rate

F.J. Martín-Muñoz (CIEMAT, Spain)

A. Heinzel (KIT, Germany)

A. Weisenburger (KIT, Germany)

G. Müller (KIT, Germany)

S. Gavrilov (SCK•CEN, Belgium)

K. Lambrinou (SCK•CEN, Belgium)

7. Effect of LBE and lead on mechanical properties of martensitic and austenitic steels

J-B. Vogt (CNRS Lille, UMET, France)

I. Proriol-Serre (CNRS Lille, UMET, France)

D. Gorse (CNRS École Polytechnique ParisTech, France)

8. Irradiation effects on compatibility of structural materials with lead-bismuth eutectic (LBE)

Y. Dai (PSI, Switzerland)

S. Gavrilov (SCK•CEN, Belgium)

9. Corrosion protection in Pb and LBE at elevated temperatures

G. Müller (KIT, Germany)

G. Schumacher (KIT, Germany)

A. Heinzel (KIT, Germany)

A. Jianu (KIT, Germany)

A. Weisenburger (KIT, Germany)

10. Low Prandtl number thermal-hydraulics

J. Pacio (KIT, Germany)

L. Marocco (KIT, Germany)

R. Stieglitz (KIT, Germany)

11. Instrumentation

T. Wetzel (KIT, Germany)

R. Stieglitz (KIT, Germany)

M. Daubner (KIT, Germany)

S. Eckert (Helmholtz Zentrum Dresden-Rossendorf, Germany)

F. Stefani (Helmholtz Zentrum Dresden-Rossendorf, Germany)

D. Buchenau (Helmholtz Zentrum Dresden-Rossendorf, Germany)

T. Wondrak (Helmholtz Zentrum Dresden-Rossendorf, Germany)

12. Existing HLM facilities for experimental applications

C. Fazio (JRC-ITU, Germany)

K. Litfin (KIT, Germany)

13. Safety guidelines

N. Li (Xiamen University, China)

14. Perspectives and R&D priorities of heavy liquid metal coolant technologies

C. Fazio (JRC-ITU, European Commission)

P. Schuurmans (SCK•CEN, Belgium)

15. Guidelines for thermo-hydraulics modelling of pressure drop of the HLM-cooled loops

I.S. Hwang (SNU, Korea)

Appendix 2. Peer reviewers

1. Introduction

S. Maloy (LANL, United States)

M. Serrano de Caro (LANL, United States)

2. Thermophysical and electric properties of liquid lead, bismuth and lead-bismuth eutectic

C. Latgé (CEA, France)

3. Thermodynamic relationships and heavy liquid metal interaction with other coolants

S. Gossé (CEA, France)

4. Chemistry control and monitoring systems

T. Furukawa (JAEA, Japan)

5. Properties of irradiated LBE and Pb

M. Jensen (DTU, Denmark)

6. Compatibility of structural materials with LBE and Pb: Standardisation of data, corrosion mechanism and rate

F. Balbaud (CEA, France)

7. Effect of LBE and lead on mechanical properties of martensitic and austenitic steels

S. Maloy (LANL, United States)

8. Irradiation effects on compatibility of structural materials with lead-bismuth eutectic (LBE)

S. Maloy (LANL, United States)

9. Corrosion protection in Pb and LBE at elevated temperatures

F. Balbaud (CEA, France)

10. Low Prandtl number thermal-hydraulics

S. Keijers (SCK•CEN, Belgium)

M. Schyns (SCK•CEN, Belgium)

11. Instrumentation

S. Keijers (SCK•CEN, Belgium)

12. Existing HLM facilities for experimental applications

K. van Tichelen (SCK•CEN, Belgium)

13. Safety guidelines

N/A

14. Perspectives and R&D priorities of heavy liquid metal coolant technologies

M. Schyns (SCK•CEN, Belgium)

P. Schuurmans (SCK•CEN, Belgium)

15. Guidelines for thermo-hydraulics modelling of pressure drop of the HLM-cooled loops

M. Takahashi (Tokyo Institute of Technology, Japan)

Handbook on Lead-bismuth Eutectic Alloy and Lead Properties, Materials Compatibility, Thermal-hydraulics and Tehnologies

Heavy liquid metals such as lead or lead-bismuth have been proposed and investigated as coolants for fast reactors since the 1950s. More recently, there has been renewed interest worldwide in the use of these materials to support the development of systems for the transmutation of radioactive waste. Heavy liquid metals are also under evaluation as a reactor core coolant and accelerator-driven system neutron spallation source. Several national and international R&D programmes are ongoing for the development of liquid lead-alloy technology and the design of liquid lead-alloy-cooled reactor systems.

In 2007, a first edition of the handbook was published to provide deeper insight into the properties and experimental results in relation to lead and lead-bismuth eutectic technology and to establish a common database. This handbook remains a reference in the field and is a valuable tool for designers and researchers with an interest in heavy liquid metals.

The 2015 edition includes updated data resulting from various national and international R&D programmes and contains new experimental data to help understand some important phenomena such as liquid metal embrittlement and turbulent heat transfer in a fuel bundle. The handbook provides an overview of liquid lead and lead-bismuth eutectic properties, materials compatibility and testing issues, key aspects of thermal-hydraulics and existing facilities, as well as perspectives for future R&D.

Nuclear Energy Agency (NEA)
12, boulevard des Îles
92130 Issy-les-Moulineaux, France
Tel.: +33 (0)1 45 24 10 15
nea@oecd-nea.org www.oecd-nea.org

NEA No. 7268